Edited by
Daniel Abou-Ras, Thomas Kirchartz, and
Uwe Rau

Advanced Characterization Techniques for Thin Film Solar Cells

Edited by
Daniel Abou-Ras, Thomas Kirchartz, and Uwe Rau

Advanced Characterization Techniques for Thin Film Solar Cells

Volume 1

Second Edition

WILEY-VCH
Verlag GmbH & Co. KGaA

Editors

Dr. Daniel Abou-Ras
Helmholtz Center Berlin
for Materials and Energy
Hahn-Meitner-Platz 1
14109 Berlin
Germany

Prof. Dr. Thomas Kirchartz
Forschungszentrum Jülich GmbH
IEK-5 Photovoltaik
Leo-Brandt-Straße
52428 Jülich
Germany

Prof. Dr. Uwe Rau
Forschungszentrum Jülich GmbH
IEK-5 Photovoltaik
Leo-Brandt-Straße
52428 Jülich
Germany

Library of Congress Card No.: applied for

British Library Cataloguing-in-Publication Data
A catalogue record for this book is available from the British Library.

Bibliographic information published by the Deutsche Nationalbibliothek
The Deutsche Nationalbibliothek lists this publication in the Deutsche Nationalbibliografie; detailed bibliographic data are available on the Internet at <http://dnb.d-nb.de>.

Print ISBN: 978-3-527-33992-1
ePDF ISBN: 978-3-527-69901-8
ePub ISBN: 978-3-527-69904-9
Mobi ISBN: 978-3-527-69903-2
oBook ISBN: 978-3-527-69902-5

Cover Design Schulz Grafik-Design, Fußgönheim, Germany
Typesetting SPi Global, Chennai, India
Printing and Binding

Printed on acid-free paper

For Cíntia, Rafael, Teresa, Gabriel, and Julian

In memoriam Dr. Manuel J. Romero

Contents to Volume 1

Contents to Volume 2

List of Contributors

Daniel Abou-Ras
Helmholtz-Zentrum Berlin für Materialien und Energie GmbH (HZB)
Hahn-Meitner-Platz 1
14109 Berlin
Germany

Péter Ágoston
Technische Universität Darmstadt
Institut für Materialwissenschaft
Fachgebiet Materialmodellierung
Petersenstr. 23
64287 Darmstadt
Germany

Karsten Albe
Technische Universität Darmstadt
Institut für Materialwissenschaft
Fachgebiet Materialmodellierung
Petersenstr. 23
64287 Darmstadt
Germany

Jacobo Álvarez-García
Universitat de Barcelona
Department d'Electrònica
C. Martí i Franquès 1
08028 Barcelona
Spain

Marcus Bär
Renewable Energy
Helmholtz-Zentrum Berlin für Materialien und Energie GmbH (HZB)
Hahn-Meitner-Platz 1
14109 Berlin
Germany

Jan Behrends
Berlin Joint EPR Lab
Institute for Nanospectroscopy
Helmholtz-Zentrum Berlin für Materialen und Energie
Albert-Einstein-Str. 15
12489 Berlin
Germany

and

Berlin Joint EPR Lab Fachbereich Physik
Freie Universität Berlin
Arnimallee 14
14195 Berlin
Germany

Wolfhard Beyer
Forschungszentrum Jülich GmbH
Institut für Energie- und Klimaforschung (IEK-5)
Photovoltaik
52428 Jülich
Germany

Karsten Bittkau
Forschungszentrum Jülich GmbH
Institut für Energie- und Klimaforschung (IEK-5)
Photovoltaik
52428 Jülich
Germany

Varvara Brackmann
Leibniz Institute for Solid State and Materials Research (IFW) Dresden
Institute for Complex Materials
Helmholtzstraße 20
01069 Dresden
Germany

Torsten Bronger
Forschungszentrum Jülich GmbH
Institut für Energie- und Klimaforschung (IEK-5)
Photovoltaik
52428 Jülich
Germany

Rudolf Brüggemann
Carl von Ossietzky Universität Oldenburg
Fakultät V – Institut für Physik
AG GRECO
Carl-von-Ossietzky-Str. 9-11
26111 Oldenburg
Germany

Marc Burgelman
Universiteit Gent
Vakgroep Elektronica en Informatiesystemen (ELIS)
St.-Pietersnieuwstraat 41
9000 Gent
Belgium

Raquel Caballero
Universidad Autónoma de Madrid
Departamento de Física Aplicada
Calle Francisco Tomás y Valiente 7
28049 Madrid
Spain

Jose Chavez
The University of Texas at El Paso
Department of Electrical and Computer Engineering
500 West University Avenue
El Paso, TX 79968
USA

Oana Cojocaru-Mirédin
RWTH Aachen
I. Physikalisches Institut IA
Sommerfeldstraße 14
52074 Aachen
Germany

and

Max-Planck Institut für Eisenforschung GmbH
Max-Planck Straße 1
40237 Düsseldorf
Germany

Robert W. Collins
University of Toledo
Department of Physics and Astronomy
Wright Center for Photovoltaics Innovation and Commercialization (PVIC)
2801 West Bancroft Street
Toledo, OH 43606
USA

Koen Decock
Universiteit Gent
Vakgroep Elektronica en Informatiesystemen (ELIS)
St.-Pietersnieuwstraat 41
9000 Gent
Belgium

Carsten Deibel
Technische Universität Chemnitz
Institut für Physik
Optik und Photonik kondensierter Materie insbesondere für Sensorik und Analytik (OPKM/212064)
09107 Chemnitz
Germany

Kaining Ding
Forschungszentrum Jülich GmbH
Institut für Energie- und Klimaforschung (IEK-5)
Photovoltaik
52428 Jülich
Germany

Florian Einsele
Forschungszentrum Jülich GmbH
Institut für Energie- und Klimaforschung (IEK-5)
Photovoltaik
52428 Jülich
Germany

Matthias Fehr
Berlin Joint EPR Lab
Institut für Silizium-Photovoltaik
Helmholtz-Zentrum Berlin für Materialen und Energie
Kekuléstr. 5
12489 Berlin
Germany

Andreas Gerber
Forschungszentrum Jülich GmbH
Institut für Energie- und Klimaforschung (IEK-5)
Photovoltaik
52428 Jülich
Germany

Rene Gunder
Helmholtz-Zentrum Berlin für Materialien und Energie GmbH (HZB)
Hahn-Meitner-Platz 1
14109 Berlin
Germany

Levent Gütay
Carl von Ossietzky University of Oldenburg
Department of Physics
Carl-von-Ossietzky-Straße 9-11
26129 Oldenburg
Germany

Jennifer Heath
Linfield College
900 SE Baker Street
McMinnville, OR 97128
USA

Marc Daniel Heinemann
Helmholtz-Zentrum Berlin für Materialien und Energie GmbH (HZB)
Hahn-Meitner-Platz 1
14109 Berlin
Germany

Clemens Heske
University of Nevada
Las Vegas (UNLV)
Department of Chemistry and Biochemistry
4505 S. Maryland Pkwy
Las Vegas, NV 89154-4003
USA

and

Institute for Photon Science and Synchrotron Radiation (IPS)
Institute for Chemical Technology and Polymer Chemistry (ITCP)
Karlsruhe Institute of Technology (KIT)
ANKA Synchrotron Radiation Facility
Hermann-von-Helmholtz-Platz 1
76344 Eggenstein-Leopoldshafen
Germany

Volker Hoffmann
Leibniz Institute for Solid State and Materials Research (IFW) Dresden
Institute for Complex Materials
Helmholtzstraße 20
01069 Dresden
Germany

Vito Huhn
Forschungszentrum Jülich GmbH
Institut für Energie- und Klimaforschung (IEK-5)
Photovoltaik
52428 Jülich
Germany

Víctor Izquierdo-Roca
IREC – Catalonia Institute for Energy Research
C Jardins de les Dones de Negre 1
08930 Sant Adria del Besos
Barcelona
Spain

Ana Kanevce
National Renewable Energy Laboratory
15013 Denver West Pkwy
Golden, CO 80401-3305
USA

Christian A. Kaufmann
Helmholtz-Zentrum Berlin für Materialien und Energie GmbH (HZB)/Kompetenzzentrum Dünnschicht- und Naontechnologie für Photovoltaik Berlin (PVcomB)
Schwarzschildstrasse 3
12489 Berlin
Germany

Prakash Koirala
University of Toledo
Department of Physics & Astronomy and Wright Center for Photovoltaics Innovation & Commercialization (PVIC)
2801 West Bancroft Street
Toledo, OH 43606
USA

Thomas Kirchartz
Forschungszentrum Jülich GmbH
Institut für Energie- und Klimaforschung (IEK-5) Photovoltaik
52428 Jülich
Germany

and

Universität Duisburg-Essen
Fakultät für Ingenieurwissenschaften und CENIDE
47057 Duisburg
Germany

Denis Klemm
Sunfire GmbH
Gasanstaltstraße 2
01237 Dresden
Germany

Stephan Lehnen
Forschungszentrum Jülich GmbH
Institut für Energie- und Klimaforschung (IEK-5) Photovoltaik
52428 Jülich
Germany

Jian Li
University of Toledo
Department of Physics and Astronomy
Wright Center for Photovoltaics Innovation and Commercialization (PVIC)
2801 West Bancroft Street
Toledo, OH 43606
USA

Klaus Lips
Berlin Joint EPR Lab
Institute for Nanospectroscopy
Helmholtz-Zentrum Berlin für Materialen und Energie
Albert-Einstein-Str. 15
12489 Berlin
Germany

and

Berlin Joint EPR Lab Fachbereich Physik
Freie Universität Berlin
Arnimallee 14
14195 Berlin
Germany

Roland Mainz
Helmholtz-Zentrum Berlin für Materialien und Energie GmbH (HZB)
Hahn-Meitner-Platz 1
14109 Berlin
Germany

Sylvain Marsillac
Old Dominion University
Department of Electrical and Computer Engineering
Virginia Institute of Photovoltaics
231 Kaufman Hall
Norfolk, VA 23529
USA

Wyatt K. Metzger
National Renewable Energy Laboratory
15013 Denver West Pkwy
Golden, CO 80401-3305
USA

Thomas Christian Mathias Müller
Forschungszentrum Jülich GmbH
Institut für Energie- und Klimaforschung (IEK-5)
Photovoltaik
52428 Jülich
Germany

Melanie Nichterwitz
Helmholtz-Zentrum Berlin für Materialien und Energie GmbH (HZB)
Hahn-Meitner-Platz 1
14109 Berlin
Germany

Tim Nunney
Thermo Fisher Scientific
The Birches Industrial Estate
Imberhorne Lane
East Grinstead
West Sussex RH19 1UB
UK

Ulrich W. Paetzold
Forschungszentrum Jülich GmbH
Institut für Energie- und Klimaforschung (IEK-5)
Photovoltaik
52428 Jülich
Germany

and

IMEC v.z.w.
Kapeldreef 75
3001 Leuven
Belgium

Alejandro Pérez-Rodríguez
Universitat de Barcelona
Department d'Electrònica
C. Martí i Franquès 1
08028 Barcelona
Spain

and

IREC – Catalonia Institute for Energy Research
C Jardins de les Dones de Negre 1
08930 Sant Adria del Besos
Barcelona
Spain

Bart E. Pieters
Forschungszentrum Jülich GmbH
Institut für Energie- und Klimaforschung (IEK-5)
Photovoltaik
52428 Jülich
Germany

Paul Pistor
IREC – Catalonia Institute for Energy Research
Jardins de les Dones de Negre 1
08930 Sant Adrià de Besòs
Barcelona
Spain

and

Martin Luther University Halle-Wittenberg
Photovoltaics Group/ Institute of Physics
Von-Danckelmann-Platz 3
06120 Halle (Saale)
Germany

Nikolas J. Podraza
University of Toledo
Department of Physics and Astronomy
Wright Center for Photovoltaics Innovation and Commercialization (PVIC)
2801 West Bancroft Street
Toledo, OH 43606
USA

Johan Pohl
Technische Universität Darmstadt
Institut für Materialwissenschaft
Fachgebiet Materialmodellierung
Petersenstr. 23
64287 Darmstadt
Germany

Uwe Rau
Forschungszentrum Jülich GmbH
Institut für Energie- und Klimaforschung (IEK-5)
Photovoltaik
52428 Jülich
Germany

Angus A. Rockett
University of Illinois
Department of Materials Science and Engineering
1304 W. Green Street
Urbana, IL 61801
USA

Manuel J. Romero
National Renewable Energy Laboratory
1617 Cole Blvd.
Golden, CO 80401-3305
USA

Sascha Sadewasser
INL – International Iberian Nanotechnology Laboratory
Laboratory for Nanostructured Solar Cells
Av. Mestre José Veiga s/n
4715-330 Braga
Portugal

Roland Scheer
Martin-Luther-University Halle-Wittenberg
Photovoltaics Group/ Institute of Physics
Von-Danckelmann-Platz 3
06120 Halle (Saale)
Germany

Thomas Schmid
Federal Institute for Materials Research and Testing
Richard-Willstätter-Str. 11
12489 Berlin
Germany

Sebastian S. Schmidt
Helmholtz-Zentrum Berlin für Materialien und Energie GmbH (HZB)
Hahn-Meitner-Platz 1
14109 Berlin
Germany

Susan Schorr
Helmholtz-Zentrum Berlin für Materialien und Energie GmbH (HZB)
Hahn-Meitner-Platz 1
14109 Berlin
Germany

and

Freie Universität Berlin
Department for Geosciences
Malteserstr. 74-100
12249 Berlin
Germany

Michelle N. Sestak
University of Toledo
Department of Physics and Astronomy
Wright Center for Photovoltaics Innovation and Commercialization (PVIC)
2801 West Bancroft Street
Toledo, OH 43606
USA

Rolf Stangl
National University of Singapore
Solar Energy Research Institute of Singapore (SERIS)
Novel Cell Concepts & Simulation
7 Engineering Drive 1
Block E3A, #06-01
117574 Singapore
Singapore

Christiane Stephan
Bundesanstalt für Materialforschung und-prüfung (BAM)
Unter den Eichen 87
12200 Berlin
Germany

Daniel M. Többens
Helmholtz-Zentrum Berlin für Materialien und Energie GmbH (HZB)
Hahn-Meitner-Platz 1
14109 Berlin
Germany

Tobias Törndahl
Uppsala University
Solid State Electronics
PO Box 534
751 21 Uppsala
Sweden

Thomas Unold
Structure and Dynamics of Energy Materials
Helmholtz-Zentrum Berlin für Materialien und Energie GmbH
Hahn-Meitner Platz 1
4109 Berlin
Germany

Cornel Venzago
AQura GmbH
Rodenbacher Chaussee 4
63457 Hanau
Germany

Iris Visoly-Fisher
Ben-Gurion University of the Negev
Swiss Institute for Dryland Environmental and Energy Research
Jacob Blaustein Institutes for Desert Research
Sede Boqer Campus
Department of Solar Energy and Environmental Physics
8499000 Midreshet Ben-Gurion
Israel

Lothar Weinhardt
University of Nevada
4505 S. Maryland Pkwy
Las Vegas (UNLV)
Department of Chemistry and Biochemistry
Las Vegas, NV 89154-4003
USA

and

Institute for Photon Science and Synchrotron Radiation (IPS)
Institute for Chemical Technology and Polymer Chemistry (ITCP)
Karlsruhe Institute of Technology (KIT)
ANKA Synchrotron Radiation Facility
Hermann-von-Helmholtz-Platz 1
76344 Eggenstein-Leopoldshafen
Germany

Thomas Wirth
Bundesanstalt für Materialforschung und-prüfung
Unter den Eichen 87
12205 Berlin
Germany

Pawel Zabierowski
Warsaw University of Technology
Koszykowa 75
00-662 Warsaw
Poland

Xiaowang Zhou
Sandia National Laboratories
Mechanics of Materials Department
7011 East Avenue
Livermore, CA 94550
USA

David Zubia
The University of Texas at El Paso
Department of Electrical and Computer Engineering
500 West University Avenue
El Paso, TX 79968
USA

Preface of the Second Edition

Progress in photovoltaic devices is rarely revolutionary but most commonly a long, evolutionary process. Champion efficiencies of typical solar-cell technologies like crystalline silicon or $Cu(In,Ga)Se_2$ have increased over decades before they reached a (near) saturation level. In contrast to these long-term trends, the development in the last few years has been extraordinary and maybe even revolutionary in many respects. Several of the "classical" solar-cell technologies ($Cu(In,Ga)Se_2$, CdTe, crystalline Si) made substantial improvements in their champion cell efficiencies.

In addition to this notable progress, new materials or processing methods have been further developed in recent years. These include Si thin films grown by liquid-phase crystallization, vacuum- or solution-processed kesterites ($Cu_2ZnSn(S,Se)_4$), organic absorber layers, and in particular a completely new family of solution-processible photovoltaic absorber materials, which have reached astonishingly high efficiencies. This material family is a particular type of perovskites, comprising an organic molecule, a metal, and a halogen on different lattice positions. In spite of their already high conversion efficiencies of more than 20%, solar cells based on perovskite absorbers face numerous challenges such as stability and toxicity of the materials. The rise of metal-halide perovskites has also led to expansions of traditionally rather well-separated communities of inorganic and organic solar cells. There used to be a distinct separation between researchers working on solution-processible solar cells such as those made from organic or nanoparticular absorber materials and researchers working on vacuum-deposited thin-film materials such as $Cu(In,Ga)Se_2$, CdTe, and thin-film silicon. In recent years, these communities have started to share more and more interests and have therefore started to pursue more collaboration on single junction or tandem solar cells involving either materials like perovskites or material combinations involving organic and inorganic materials.

Thus, the second edition of the present handbook on characterization techniques for thin-film solar cells has to shift its focus slightly with respect to the first edition issued in 2011. The first edition was confined to characterization methods for the three traditional inorganic thin-film technologies, $Cu(In,Ga)Se_2$, CdTe, and thin-film silicon, whereas the new edition required a broader scope and therefore includes also aspects more commonly discussed in the community

of solution-processible semiconductor solar cells. These aspects include transient optoelectronic methods used in organic solar cells and related technologies and methods to study the absorption edge of semiconductors, using either purely optical techniques such as photothermal deflection spectroscopy or electrical techniques such as Fourier-transform photocurrent spectroscopy. In addition, we added chapters on in situ real-time characterization of thin-film growth and on molecular dynamics. Several chapters were rearranged, and further characterization and simulation techniques were added in order to account for new developments and possibilities.

As for the first edition, the editors would like to thank all authors of this handbook for their excellent and punctual contributions. We are especially grateful to Dr. Martin Preuss, Wiley-VCH, for helping in realizing this book project.

Berlin, Jülich, Germany
November 2015

Daniel Abou-Ras, Thomas Kirchartz, and Uwe Rau

Preface of the First Edition

Inorganic thin-film photovoltaics is a very old research topic with a scientific record of more than 30 years and tens of thousands of published papers. At the same time, thin-film photovoltaics is an emerging research field due to technological progress and the subsequent tremendous growth of the photovoltaic industry during recent years. As a consequence, many young scientists and engineers enter the field not only because of the growing demand for skilled scientific personnel but also because of the many interesting scientific and technological questions that are still to be solved. As a consequence, there is a growing demand for skilled scientific staff entering the field who will face a multitude of challenging scientific and technological questions. Thin-film photovoltaics aims for the highest conversion efficiencies and lowest possible cost. Therefore, a profound understanding of corresponding solar-cell devices and photovoltaic materials applied is a major prerequisite for any further progress in this challenging field.

In recent years, a wide and continuously increasing variety of sophisticated and rather specialized analysis techniques originating from very different directions of physics, chemistry, or materials science have been applied in order to extend the scientific base of thin-film photovoltaics. This increasing specialization is a relatively new phenomenon in the field of photovoltaics where during the "old days" everyone was (and had to be) able to handle virtually every scientific method personally. Consequently, it becomes nowadays more and more challenging for the individual scientist to keep track with the results obtained by specialized analysis methods, the physics behind these methods, and their implications for the devices.

The need for more communication and exchange especially among scientists and PhD students working in the same field but using very different techniques was more and more rationalized during recent years. As notable consequences, very well-attended "Young Scientist Tutorials on Characterization Techniques for Thin-Film Solar Cells" were established at Spring Meetings of the Materials Research Society and the European Materials Research Society. These tutorials were especially dedicated to mutual teaching and open discussions.

The present handbook aims to follow the line defined by these tutorials, providing concise and comprehensive lecture-like chapters on specific research methods, written by researchers who use these methods as the core of their scientific work and who at the same time have a precise idea of what is relevant

for photovoltaic devices. The chapters are intended to focus on the specific methods more than on significant results. This is because these results, especially in innovative research areas, are subject to rapid change and are better dealt with by review articles. The basic message of the chapters in the present handbook focuses more on how to use the specific methods, on their physical background, and especially on their implications for the final purpose of the research, that is, improving the quality of photovoltaic materials and devices.

Therefore, the present handbook is not thought as a textbook on established standard (canonical) methods. Rather, we focus on emerging, specialized methods that are relatively new in the field but have a given relevance. This is why the title of the book addresses "advanced" techniques. However, new methods also need to be judged by their implication for photovoltaic devices. For this reason, an introductory chapter (Chapter 1) will describe the basic physics of thin-film solar cells and modules and also guide to the specific advantages that are provided by the individual methods. In addition, we have made sure that the selected authors not only are established specialists concerning a specific method but also have long-time experience dealing with solar cells. This ensures that in each chapter, the aim of the analysis work is kept on the purpose of improving solar cells.

The choice of characterization techniques is not intended for completeness but should be a representative cross section through scientific methods that have a high level of visibility in the recent scientific literature. Electrical device characterization (Chapter 2), electroluminescence (Chapter 3), photoluminescence (Chapter 7), and capacitance spectroscopy (Chapter 4) not only are standard optoelectronic analysis techniques for solid-state materials and devices but also are well established and of common use in their specific photovoltaic context. In contrast, characterization of light trapping (Chapter 5) is an emerging research topic very specific to the photovoltaic field. Chapters 6, 8, and 9 deal with ellipsometry, the steady-state photocarrier grating method, and time-of-flight analysis, which are dedicated thin-film characterization methods. Steady-state photocarrier grating (Chapter 8) and time-of-flight measurements (Chapter 9) specifically target the carrier transport properties of disordered thin-film semiconductors. Electron spin resonance (Chapter 10) is a traditional method in solid-state and molecule physics, which is of particular use for analyzing dangling bonds in disordered semiconductors.

The disordered nature of thin-film photovoltaic materials requires analysis of electronic, structural, and compositional properties at the nanometer scale. This is why methods such as scanning probe techniques (Chapter 11) as well as electron microscopy and its related techniques (Chapter 12) gain increasing importance in the field. X-ray and neutron diffraction (Chapter 13) and Raman spectroscopy (Chapter 14) contribute to the analysis of structural properties of photovoltaic materials. Since thin-film solar cells consist of layer stacks with interfaces and surfaces, important issues are the analyses of their chemical and electronic properties, which may be studied by means of soft X-ray and electron spectroscopy (Chapter 15). Important information for thin-film solar-cell research and development is the elemental distributions in the layer stacks, analyzed by various

techniques presented in Chapter 16. Specifically for silicon thin-film solar cells, knowledge about hydrogen incorporation and stability is obtained from hydrogen effusion experiments (Chapter 17).

For designing photovoltaic materials with specific electrical and optoelectronic properties, it is important to predict these properties for a given compound. Combining experimental results from materials analysis with those from *ab initio* calculations based on density functional theory provides the means to study point defects in photovoltaic materials (Chapter 18). Finally, in order to come full circle regarding the solar-cell devices treated in the first chapters of the handbook, the information gained from the various materials analyses and calculations may now be introduced into one-dimensional (Chapter 19) or multidimensional device simulations (Chapter 20). By means of carefully designed optical and electronic simulations, photovoltaic performances of specific devices may be studied even before their manufacture.

We believe that the overview of these various characterization techniques is useful not only for colleagues engaged in the research and development of inorganic thin-film solar cells, from which the examples in the present handbook are given, but also for those working with other types of solar cells and optoelectronic, thin-film devices.

The editors would like to thank all authors of this handbook for their excellent and (almost) punctual contributions. We are especially grateful to Ulrike Fuchs and Anja Tschörtner, Wiley-VCH, for helping in realizing this book project.

Berlin, Germany; London, UK; and Jülich, Germany
August 2010

Daniel Abou-Ras,
Thomas Kirchartz,
and Uwe Rau

Abbreviations

1D	One-dimensional
2D	Two-dimensional
3D	Three-dimensional
A°X	Excitons bound to neutral acceptor
ac	Amplified current
ADC	Analog-to-digital converter
ADF	Annular dark field
ADXRD	Angle-dispersive X-ray diffraction
AES	Auger electron spectroscopy
AEY	Auger electron yield
AFM	Atomic force microscopy
AFORS-HET	Automat for simulation of heterostructures
ALDA	Adiabatic local density approximation
AM	Amplitude modulation
AM	Air mass
AMU	Atomic mass units
ARS	Angularly resolved light scattering
AS	Admittance spectroscopy
ASA	Advanced semiconductor analysis, a solar-cell device simulator
ASCII	American Standard Code for Information Interchange
a-Si	Amorphous silicon
A-X	Excitons bound to ionized acceptor
BACE	Bias-amplified charge extraction
BF	Bright field
BOP	Bond-order potential
BS	Beam splitter
BSE	Bethe–Salpeter equation
BSE	Backscattered electrons
c-AFM	Conductive AFM
CBD	Chemical bath deposition
CBED	Convergent-beam electron diffraction
CBM	Conduction-band minimum
CBO	Conduction-band offset
CC	Coupled cluster
CCD	Charge-coupled device
CE	Charge extraction

CELIV	Charge extraction with linearly increased voltage
CGI	[Cu]/([In]+[Ga])
CHA	Concentric hemispherical analyzer
CI	Configuration interaction
CIGS	$Cu(In,Ga)Se_2$
CIGSe	$Cu(In,Ga)Se_2$
CIGSSe	$Cu(In,Ga)(S;Se)_2$
CIS	$CuInSe_2$
CIS	$CuInS_2$
CISe	$CuInSe_2$
CL	Cathodoluminescence
CL	Core level
CMA	Cylindrical mirror analyzer
CN	Charge neutrality
CP	Critical point
CPD	Contact-potential difference
CSL	Coincidence-site lattice
CSS	Closed-space sublimation
CTEM	Conventional transmission electron microscopy
CV	Capacitance–voltage
cw	Continuous wave
D°h	Optical transitions between donor and free hole
D°X	Excitons bound to neutral donor
DAP	Donor–acceptor pair
db, DB	Dangling bond
dc	Direct current
DF	Dark field
DFPT	Density functional perturbation theory
DFT	Density functional theory
DFT	Discrete Fourier transform
DLCP	Drive-level capacitance profiling
DLOS	Deep-level optical spectroscopy
DLTS	Deep-level transient spectroscopy
DOS	Density of states
DSR	Differential spectral response
DT	Digital
D-X	Excitons bound to ionized donor
eA°	Optical transitions between acceptor and free electron
EBIC	Electron-beam-induced current
EBSD	Electron backscatter diffraction
EDMR	Electrically detected magnetic resonance
EDX	Energy-dispersive X-ray spectrometry
EDXRD	Energy-dispersive X-ray diffraction
EELS	Electron energy-loss spectrometry
EFTEM	Energy-filtered transmission electron microscopy
EL	Electroluminescence
ELNES	Energy-loss near-edge structure
EMPA	Eidgenössische Materialprüfungsanstalt
ENDOR	Electron nuclear double resonance
EPR	Electron paramagnetic resonance
ESCA	Electron spectroscopy for chemical analysis

ESEEM	Electron spin echo envelope modulations
ESI	Energy-selective imaging
ESR	Electron spin resonance
EXC	Free exciton transition
EXELFS	Extended energy-loss fine structure
FFT	Fast Fourier transformation
FIB	Focused ion beam
FIR	Far infrared
FM	Frequency modulation
FP-LAPW	Full potential linearized augmented plane wave
FT	Fourier transform
FTIR	Fourier transform infrared
FTPS	Fourier transform photocurrent spectroscopy
FWHM	Full width at half maximum
FX	Free excitons
FY	Fluorescence yield
GB	Grain boundary
GD-MS	Glow-discharge mass spectroscopy
GD-OES	Glow-discharge optical-emission spectroscopy
GGA	Generalized gradient approximation
GGI	[Ga]/([In]+[Ga])
GIXRD	Grazing-incidence X-ray diffraction
GNU	GNU's Not Unix (recursive acronym)
GPL	General public licence
GW	G for Green's function and W for the screened Coulomb interaction
HAADF	High-angle annular dark field
HFI	Hyperfine interaction
HOPG	Highly oriented pyrolytic graphite
HR	High resistance
HR	High resolution
HRTEM	High-resolution transmission electron microscopy
HT	High temperature
HWCVD	Hot-wire chemical vapor deposition
HZB	Helmholtz-Zentrum Berlin
IBB	Interface-induced band bending
IPES	Inverse photoelectron spectroscopy
IR	Infrared
JEBIC	Junction electron-beam-induced current
KPFM	Kelvin probe force microscopy
KS	Kohn–Sham
KSM	Kaplan–Solomon–Mott (model)
LAMMPS	Large-Scale Atomic/Molecular Massively Parallel Simulator
LBIC	Laser-beam-induced current
LCR meter	Inductance, capacitance, and resistance analyzer
LDA	Local density approximation
LED	Light-emitting diode
LESR	Light-induced ESR
LIA	Lock-in amplifier
LLS	Laser-light scattering
LO	Longitudinal optical
LR	Low resistance

LT	Low temperature
LVM	Localized vibrational modes
MBPT	Many-body perturbation theory
MD	Molecular dynamics
MIP	Mean-inner potential
MIR	Medium infrared
MIS	Metal–insulator–semiconductor
ML	Monolayer
MO	Metal oxide
MOS	Metal–oxide–semiconductor
MS	Molecular statics
MSE	Mean-square error
mw	Microwave
nc-AFM	Non-contact atomic force microscopy
NIR	Near-infrared
NIST	National Institute of Standards and Technology
NSOM	Near-field scanning optical microscopy
OBIC	Optical-beam-induced current
OES	Optical emission spectrometry
OTRACE	Open circuit corrected transient charge extraction
OVC	Ordered vacancy compound
PBE-GGA	Generalized gradient approximation by Perdew, Burke, and Ernzerhof
PC	Personal computer
PCSA	Polarizer–compensator–sample–analyzer
PDA	Photodetector array
PDE	Partial differential equations
PDS	Photothermal deflection spectroscopy
PECVD	Plasma-enhanced chemical vapor deposition
PES	Photoelectron spectroscopy
pESR	Pulsed electron spin resonance
PEY	Partial electron yield
PIPO	Photon-in photon-out
PL	Photoluminescence
PLL	Phase-locked loop
PMT	Photomultiplier tube
pp	Peak-to-peak
PV	Photovoltaic
PVD	Physical vapor deposition
QE	Quantum efficiency
QMA	Quadrupole mass analyzer
QMC	Quantum Monte Carlo
RDLTS	Reverse-bias deep-level transient spectroscopy
REBIC	Remote electron-beam-induced current
rf	Radio frequency
RGB	Red–green–blue, color space
RHEED	Reflection high-energy electrons
RIXS	Resonant inelastic (soft) X-ray scattering
RS	Raman spectroscopy
RSF	Relative sensitivity factor
RTP	Rapid thermal process
RTSE	Real-time spectroscopic ellipsometry

RZW	Ritter, Zeldov, and Weiser steady-state photocarrier method
S/N	Signal-to-noise (ratio)
SAED	Selected-area electron diffraction
SCAPS	Solar-cell capacitance simulator
SCM	Scanning capacitance microscopy
SE	Spectroscopic ellipsometry
SE	Secondary electron
SEM	Scanning electron microscopy
SIMS	Secondary-ion mass spectroscopy
SNMS	Sputtered neutral mass spectroscopy
SNOM, see also NSOM	Scanning near-field optical microscopy
SPICE	Simulation Program with Integrated Circuit Emphasis
SPM	Scanning probe microscopy
SQ	Shockley–Queisser (limit)
SR	Spectral response
SSPG	Steady-state photocarrier grating
SSRM	Scanning spreading-resistance microscopy
STEM	Scanning transmission electron microscopy
STM	Scanning tunneling microscopy
SWE	Staebler–Wronski effect
TCO	Transparent conductive oxide
TD	Trigger diode
TD-DFT	Time-dependent density functional theory
TDCF	Time-delayed collection field
TDS	Thermal desorption spectroscopy
TEM	Transmission electron microscopy
TEY	Total electron yield
TF	Tuning fork
TO	Transversal optical
TOF	Time of flight
TPC	Transient photocapacitance spectroscopy
TPD	Temperature-programmed desorption
TPV	Transient photovoltage
TU	Technical University
UHV	Ultrahigh vacuum
UPS	Ultraviolet photoelectron spectroscopy
UV	Ultraviolet
VBM	Valence-band maximum
VBO	Valence-band offset
Vis, VIS	Visible
WDX	Wavelength-dispersive X-ray spectrometry
WLR	White-light reflectometry
XAES	X-ray Auger electron spectroscopy
XAS	X-ray absorption spectroscopy
XES	X-ray emission spectroscopy
XPS	X-ray photoelectron spectroscopy
XRD	X-ray diffraction
XRF	X-ray fluorescence
ZFF	Zero filling factor
μc-Si	Microcrystalline silicon

Edited by
Daniel Abou-Ras, Thomas Kirchartz, and
Uwe Rau

Advanced Characterization Techniques for Thin Film Solar Cells

Edited by
Daniel Abou-Ras, Thomas Kirchartz, and Uwe Rau

Advanced Characterization Techniques for Thin Film Solar Cells

Volume 2

Second Edition

WILEY-VCH
Verlag GmbH & Co. KGaA

Editors

Dr. Daniel Abou-Ras
Helmholtz Center Berlin
for Materials and Energy
Hahn-Meitner-Platz 1
14109 Berlin
Germany

Prof. Dr. Thomas Kirchartz
Forschungszentrum Jülich GmbH
IEK-5 Photovoltaik
Leo-Brandt-Straße
52428 Jülich
Germany

Prof. Dr. Uwe Rau
Forschungszentrum Jülich GmbH
IEK-5 Photovoltaik
Leo-Brandt-Straße
52428 Jülich
Germany

Library of Congress Card No.: applied for

British Library Cataloguing-in-Publication Data
A catalogue record for this book is available from the British Library.

Bibliographic information published by the Deutsche Nationalbibliothek
The Deutsche Nationalbibliothek lists this publication in the Deutsche Nationalbibliografie; detailed bibliographic data are available on the Internet at <http://dnb.d-nb.de>.

Print ISBN: 978-3-527-33992-1
ePDF ISBN: 978-3-527-69901-8
ePub ISBN: 978-3-527-69904-9
Mobi ISBN: 978-3-527-69903-2
oBook ISBN: 978-3-527-69902-5

Cover Design Schulz Grafik-Design, Fußgönheim, Germany
Typesetting SPi Global, Chennai, India
Printing and Binding

Printed on acid-free paper

For Cíntia, Rafael, Teresa, Gabriel, and Julian

In memoriam Dr. Manuel J. Romero

Contents to Volume 1

Contents to Volume 2

List of Contributors

Daniel Abou-Ras
Helmholtz-Zentrum Berlin für Materialien und Energie GmbH (HZB)
Hahn-Meitner-Platz 1
14109 Berlin
Germany

Péter Ágoston
Technische Universität Darmstadt
Institut für Materialwissenschaft
Fachgebiet Materialmodellierung
Petersenstr. 23
64287 Darmstadt
Germany

Karsten Albe
Technische Universität Darmstadt
Institut für Materialwissenschaft
Fachgebiet Materialmodellierung
Petersenstr. 23
64287 Darmstadt
Germany

Jacobo Álvarez-García
Universitat de Barcelona
Department d'Electrònica
C. Martí i Franquès 1
08028 Barcelona
Spain

Marcus Bär
Renewable Energy
Helmholtz-Zentrum Berlin für Materialien und Energie GmbH (HZB)
Hahn-Meitner-Platz 1
14109 Berlin
Germany

Jan Behrends
Berlin Joint EPR Lab
Institute for Nanospectroscopy
Helmholtz-Zentrum Berlin für Materialen und Energie
Albert-Einstein-Str. 15
12489 Berlin
Germany

and

Berlin Joint EPR Lab Fachbereich Physik
Freie Universität Berlin
Arnimallee 14
14195 Berlin
Germany

Wolfhard Beyer
Forschungszentrum Jülich GmbH
Institut für Energie- und Klimaforschung (IEK-5)
Photovoltaik
52428 Jülich
Germany

Karsten Bittkau
Forschungszentrum Jülich GmbH
Institut für Energie- und Klimaforschung (IEK-5)
Photovoltaik
52428 Jülich
Germany

Varvara Brackmann
Leibniz Institute for Solid State and Materials Research (IFW) Dresden
Institute for Complex Materials
Helmholtzstraße 20
01069 Dresden
Germany

Torsten Bronger
Forschungszentrum Jülich GmbH
Institut für Energie- und Klimaforschung (IEK-5)
Photovoltaik
52428 Jülich
Germany

Rudolf Brüggemann
Carl von Ossietzky Universität Oldenburg
Fakultät V – Institut für Physik
AG GRECO
Carl-von-Ossietzky-Str. 9-11
26111 Oldenburg
Germany

Marc Burgelman
Universiteit Gent
Vakgroep Elektronica en Informatiesystemen (ELIS)
St.-Pietersnieuwstraat 41
9000 Gent
Belgium

Raquel Caballero
Universidad Autónoma de Madrid
Departamento de Física Aplicada
Calle Francisco Tomás y Valiente 7
28049 Madrid
Spain

Jose Chavez
The University of Texas at El Paso
Department of Electrical and Computer Engineering
500 West University Avenue
El Paso, TX 79968
USA

Oana Cojocaru-Mirédin
RWTH Aachen
I. Physikalisches Institut IA
Sommerfeldstraße 14
52074 Aachen
Germany

and

Max-Planck Institut für Eisenforschung GmbH
Max-Planck Straße 1
40237 Düsseldorf
Germany

Robert W. Collins
University of Toledo
Department of Physics and Astronomy
Wright Center for Photovoltaics Innovation and Commercialization (PVIC)
2801 West Bancroft Street
Toledo, OH 43606
USA

Koen Decock
Universiteit Gent
Vakgroep Elektronica en Informatiesystemen (ELIS)
St.-Pietersnieuwstraat 41
9000 Gent
Belgium

Carsten Deibel
Technische Universität Chemnitz
Institut für Physik
Optik und Photonik kondensierter Materie insbesondere für Sensorik und Analytik (OPKM/212064)
09107 Chemnitz
Germany

Kaining Ding
Forschungszentrum Jülich GmbH
Institut für Energie- und Klimaforschung (IEK-5)
Photovoltaik
52428 Jülich
Germany

Florian Einsele
Forschungszentrum Jülich GmbH
Institut für Energie- und Klimaforschung (IEK-5)
Photovoltaik
52428 Jülich
Germany

Matthias Fehr
Berlin Joint EPR Lab
Institut für Silizium-Photovoltaik
Helmholtz-Zentrum Berlin für Materialen und Energie
Kekuléstr. 5
12489 Berlin
Germany

Andreas Gerber
Forschungszentrum Jülich GmbH
Institut für Energie- und Klimaforschung (IEK-5)
Photovoltaik
52428 Jülich
Germany

Rene Gunder
Helmholtz-Zentrum Berlin für Materialien und Energie GmbH (HZB)
Hahn-Meitner-Platz 1
14109 Berlin
Germany

Levent Gütay
Carl von Ossietzky University of Oldenburg
Department of Physics
Carl-von-Ossietzky-Straße 9-11
26129 Oldenburg
Germany

Jennifer Heath
Linfield College
900 SE Baker Street
McMinnville, OR 97128
USA

Marc Daniel Heinemann
Helmholtz-Zentrum Berlin für Materialien und Energie GmbH (HZB)
Hahn-Meitner-Platz 1
14109 Berlin
Germany

Clemens Heske
University of Nevada
Las Vegas (UNLV)
Department of Chemistry and Biochemistry
4505 S. Maryland Pkwy
Las Vegas, NV 89154-4003
USA

and

Institute for Photon Science and Synchrotron Radiation (IPS)
Institute for Chemical Technology and Polymer Chemistry (ITCP)
Karlsruhe Institute of Technology (KIT)
ANKA Synchrotron Radiation Facility
Hermann-von-Helmholtz-Platz 1
76344 Eggenstein-Leopoldshafen
Germany

Volker Hoffmann
Leibniz Institute for Solid State and Materials Research (IFW) Dresden
Institute for Complex Materials
Helmholtzstraße 20
01069 Dresden
Germany

Vito Huhn
Forschungszentrum Jülich GmbH
Institut für Energie- und Klimaforschung (IEK-5)
Photovoltaik
52428 Jülich
Germany

Víctor Izquierdo-Roca
IREC – Catalonia Institute for Energy Research
C Jardins de les Dones de Negre 1
08930 Sant Adria del Besos
Barcelona
Spain

Ana Kanevce
National Renewable Energy Laboratory
15013 Denver West Pkwy
Golden, CO 80401-3305
USA

Christian A. Kaufmann
Helmholtz-Zentrum Berlin für Materialien und Energie GmbH (HZB)/Kompetenzzentrum Dünnschicht- und Naontechnologie für Photovoltaik Berlin (PVcomB)
Schwarzschildstrasse 3
12489 Berlin
Germany

Prakash Koirala
University of Toledo
Department of Physics & Astronomy and Wright Center for Photovoltaics Innovation & Commercialization (PVIC)
2801 West Bancroft Street
Toledo, OH 43606
USA

Thomas Kirchartz
Forschungszentrum Jülich GmbH
Institut für Energie- und Klimaforschung (IEK-5) Photovoltaik
52428 Jülich
Germany

and

Universität Duisburg-Essen
Fakultät für Ingenieurwissenschaften und CENIDE
47057 Duisburg
Germany

Denis Klemm
Sunfire GmbH
Gasanstaltstraße 2
01237 Dresden
Germany

Stephan Lehnen
Forschungszentrum Jülich GmbH
Institut für Energie- und Klimaforschung (IEK-5) Photovoltaik
52428 Jülich
Germany

Jian Li
University of Toledo
Department of Physics and Astronomy
Wright Center for Photovoltaics Innovation and Commercialization (PVIC)
2801 West Bancroft Street
Toledo, OH 43606
USA

Klaus Lips
Berlin Joint EPR Lab
Institute for Nanospectroscopy
Helmholtz-Zentrum Berlin für Materialen und Energie
Albert-Einstein-Str. 15
12489 Berlin
Germany

and

Berlin Joint EPR Lab Fachbereich Physik
Freie Universität Berlin
Arnimallee 14
14195 Berlin
Germany

Roland Mainz
Helmholtz-Zentrum Berlin für Materialien und Energie GmbH (HZB)
Hahn-Meitner-Platz 1
14109 Berlin
Germany

Sylvain Marsillac
Old Dominion University
Department of Electrical and Computer Engineering
Virginia Institute of Photovoltaics
231 Kaufman Hall
Norfolk, VA 23529
USA

Wyatt K. Metzger
National Renewable Energy Laboratory
15013 Denver West Pkwy
Golden, CO 80401-3305
USA

Thomas Christian Mathias Müller
Forschungszentrum Jülich GmbH
Institut für Energie- und Klimaforschung (IEK-5)
Photovoltaik
52428 Jülich
Germany

Melanie Nichterwitz
Helmholtz-Zentrum Berlin für Materialien und Energie GmbH (HZB)
Hahn-Meitner-Platz 1
14109 Berlin
Germany

Tim Nunney
Thermo Fisher Scientific
The Birches Industrial Estate
Imberhorne Lane
East Grinstead
West Sussex RH19 1UB
UK

Ulrich W. Paetzold
Forschungszentrum Jülich GmbH
Institut für Energie- und Klimaforschung (IEK-5)
Photovoltaik
52428 Jülich
Germany

and

IMEC v.z.w.
Kapeldreef 75
3001 Leuven
Belgium

Alejandro Pérez-Rodríguez
Universitat de Barcelona
Department d'Electrònica
C. Martí i Franquès 1
08028 Barcelona
Spain

and

IREC – Catalonia Institute for Energy Research
C Jardins de les Dones de Negre 1
08930 Sant Adria del Besos
Barcelona
Spain

Bart E. Pieters
Forschungszentrum Jülich GmbH
Institut für Energie- und Klimaforschung (IEK-5)
Photovoltaik
52428 Jülich
Germany

Paul Pistor
IREC – Catalonia Institute for Energy Research
Jardins de les Dones de Negre 1
08930 Sant Adrià de Besòs
Barcelona
Spain

and

Martin Luther University Halle-Wittenberg
Photovoltaics Group/ Institute of Physics
Von-Danckelmann-Platz 3
06120 Halle (Saale)
Germany

Nikolas J. Podraza
University of Toledo
Department of Physics and Astronomy
Wright Center for Photovoltaics Innovation and Commercialization (PVIC)
2801 West Bancroft Street
Toledo, OH 43606
USA

Johan Pohl
Technische Universität Darmstadt
Institut für Materialwissenschaft
Fachgebiet Materialmodellierung
Petersenstr. 23
64287 Darmstadt
Germany

Uwe Rau
Forschungszentrum Jülich GmbH
Institut für Energie- und Klimaforschung (IEK-5)
Photovoltaik
52428 Jülich
Germany

Angus A. Rockett
University of Illinois
Department of Materials Science and Engineering
1304 W. Green Street
Urbana, IL 61801
USA

Manuel J. Romero
National Renewable Energy Laboratory
1617 Cole Blvd.
Golden, CO 80401-3305
USA

Sascha Sadewasser
INL – International Iberian Nanotechnology Laboratory
Laboratory for Nanostructured Solar Cells
Av. Mestre José Veiga s/n
4715-330 Braga
Portugal

Roland Scheer
Martin-Luther-University Halle-Wittenberg
Photovoltaics Group/ Institute of Physics
Von-Danckelmann-Platz 3
06120 Halle (Saale)
Germany

Thomas Schmid
Federal Institute for Materials Research and Testing
Richard-Willstätter-Str. 11
12489 Berlin
Germany

Sebastian S. Schmidt
Helmholtz-Zentrum Berlin für Materialien und Energie GmbH (HZB)
Hahn-Meitner-Platz 1
14109 Berlin
Germany

Susan Schorr
Helmholtz-Zentrum Berlin für Materialien und Energie GmbH (HZB)
Hahn-Meitner-Platz 1
14109 Berlin
Germany

and

Freie Universität Berlin
Department for Geosciences
Malteserstr. 74-100
12249 Berlin
Germany

Michelle N. Sestak
University of Toledo
Department of Physics and Astronomy
Wright Center for Photovoltaics Innovation and Commercialization (PVIC)
2801 West Bancroft Street
Toledo, OH 43606
USA

Rolf Stangl
National University of Singapore
Solar Energy Research Institute of Singapore (SERIS)
Novel Cell Concepts & Simulation
7 Engineering Drive 1
Block E3A, #06-01
117574 Singapore
Singapore

Christiane Stephan
Bundesanstalt für Materialforschung und-prüfung (BAM)
Unter den Eichen 87
12200 Berlin
Germany

Daniel M. Többens
Helmholtz-Zentrum Berlin für Materialien und Energie GmbH (HZB)
Hahn-Meitner-Platz 1
14109 Berlin
Germany

Tobias Törndahl
Uppsala University
Solid State Electronics
PO Box 534
751 21 Uppsala
Sweden

Thomas Unold
Structure and Dynamics of Energy Materials
Helmholtz-Zentrum Berlin für Materialien und Energie GmbH
Hahn-Meitner Platz 1
4109 Berlin
Germany

Cornel Venzago
AQura GmbH
Rodenbacher Chaussee 4
63457 Hanau
Germany

Iris Visoly-Fisher
Ben-Gurion University of the Negev
Swiss Institute for Dryland Environmental and Energy Research
Jacob Blaustein Institutes for Desert Research
Sede Boqer Campus
Department of Solar Energy and Environmental Physics
8499000 Midreshet Ben-Gurion
Israel

Lothar Weinhardt
University of Nevada
4505 S. Maryland Pkwy
Las Vegas (UNLV)
Department of Chemistry and Biochemistry
Las Vegas, NV 89154-4003
USA

and

Institute for Photon Science and Synchrotron Radiation (IPS)
Institute for Chemical Technology and Polymer Chemistry (ITCP)
Karlsruhe Institute of Technology (KIT)
ANKA Synchrotron Radiation Facility
Hermann-von-Helmholtz-Platz 1
76344 Eggenstein-Leopoldshafen
Germany

Thomas Wirth
Bundesanstalt für Materialforschung und-prüfung
Unter den Eichen 87
12205 Berlin
Germany

Pawel Zabierowski
Warsaw University of Technology
Koszykowa 75
00-662 Warsaw
Poland

Xiaowang Zhou
Sandia National Laboratories
Mechanics of Materials Department
7011 East Avenue
Livermore, CA 94550
USA

David Zubia
The University of Texas at El Paso
Department of Electrical and Computer Engineering
500 West University Avenue
El Paso, TX 79968
USA

Preface of the Second Edition

Progress in photovoltaic devices is rarely revolutionary but most commonly a long, evolutionary process. Champion efficiencies of typical solar-cell technologies like crystalline silicon or $Cu(In,Ga)Se_2$ have increased over decades before they reached a (near) saturation level. In contrast to these long-term trends, the development in the last few years has been extraordinary and maybe even revolutionary in many respects. Several of the "classical" solar-cell technologies ($Cu(In,Ga)Se_2$, CdTe, crystalline Si) made substantial improvements in their champion cell efficiencies.

In addition to this notable progress, new materials or processing methods have been further developed in recent years. These include Si thin films grown by liquid-phase crystallization, vacuum- or solution-processed kesterites ($Cu_2ZnSn(S,Se)_4$), organic absorber layers, and in particular a completely new family of solution-processible photovoltaic absorber materials, which have reached astonishingly high efficiencies. This material family is a particular type of perovskites, comprising an organic molecule, a metal, and a halogen on different lattice positions. In spite of their already high conversion efficiencies of more than 20%, solar cells based on perovskite absorbers face numerous challenges such as stability and toxicity of the materials. The rise of metal-halide perovskites has also led to expansions of traditionally rather well-separated communities of inorganic and organic solar cells. There used to be a distinct separation between researchers working on solution-processible solar cells such as those made from organic or nanoparticular absorber materials and researchers working on vacuum-deposited thin-film materials such as $Cu(In,Ga)Se_2$, CdTe, and thin-film silicon. In recent years, these communities have started to share more and more interests and have therefore started to pursue more collaboration on single junction or tandem solar cells involving either materials like perovskites or material combinations involving organic and inorganic materials.

Thus, the second edition of the present handbook on characterization techniques for thin-film solar cells has to shift its focus slightly with respect to the first edition issued in 2011. The first edition was confined to characterization methods for the three traditional inorganic thin-film technologies, $Cu(In,Ga)Se_2$, CdTe, and thin-film silicon, whereas the new edition required a broader scope and therefore includes also aspects more commonly discussed in the community

of solution-processible semiconductor solar cells. These aspects include transient optoelectronic methods used in organic solar cells and related technologies and methods to study the absorption edge of semiconductors, using either purely optical techniques such as photothermal deflection spectroscopy or electrical techniques such as Fourier-transform photocurrent spectroscopy. In addition, we added chapters on in situ real-time characterization of thin-film growth and on molecular dynamics. Several chapters were rearranged, and further characterization and simulation techniques were added in order to account for new developments and possibilities.

As for the first edition, the editors would like to thank all authors of this handbook for their excellent and punctual contributions. We are especially grateful to Dr. Martin Preuss, Wiley-VCH, for helping in realizing this book project.

Berlin, Jülich, Germany
November 2015

Daniel Abou-Ras, Thomas Kirchartz, and Uwe Rau

Preface of the First Edition

Inorganic thin-film photovoltaics is a very old research topic with a scientific record of more than 30 years and tens of thousands of published papers. At the same time, thin-film photovoltaics is an emerging research field due to technological progress and the subsequent tremendous growth of the photovoltaic industry during recent years. As a consequence, many young scientists and engineers enter the field not only because of the growing demand for skilled scientific personnel but also because of the many interesting scientific and technological questions that are still to be solved. As a consequence, there is a growing demand for skilled scientific staff entering the field who will face a multitude of challenging scientific and technological questions. Thin-film photovoltaics aims for the highest conversion efficiencies and lowest possible cost. Therefore, a profound understanding of corresponding solar-cell devices and photovoltaic materials applied is a major prerequisite for any further progress in this challenging field.

In recent years, a wide and continuously increasing variety of sophisticated and rather specialized analysis techniques originating from very different directions of physics, chemistry, or materials science have been applied in order to extend the scientific base of thin-film photovoltaics. This increasing specialization is a relatively new phenomenon in the field of photovoltaics where during the "old days" everyone was (and had to be) able to handle virtually every scientific method personally. Consequently, it becomes nowadays more and more challenging for the individual scientist to keep track with the results obtained by specialized analysis methods, the physics behind these methods, and their implications for the devices.

The need for more communication and exchange especially among scientists and PhD students working in the same field but using very different techniques was more and more rationalized during recent years. As notable consequences, very well-attended "Young Scientist Tutorials on Characterization Techniques for Thin-Film Solar Cells" were established at Spring Meetings of the Materials Research Society and the European Materials Research Society. These tutorials were especially dedicated to mutual teaching and open discussions.

The present handbook aims to follow the line defined by these tutorials, providing concise and comprehensive lecture-like chapters on specific research methods, written by researchers who use these methods as the core of their scientific work and who at the same time have a precise idea of what is relevant

for photovoltaic devices. The chapters are intended to focus on the specific methods more than on significant results. This is because these results, especially in innovative research areas, are subject to rapid change and are better dealt with by review articles. The basic message of the chapters in the present handbook focuses more on how to use the specific methods, on their physical background, and especially on their implications for the final purpose of the research, that is, improving the quality of photovoltaic materials and devices.

Therefore, the present handbook is not thought as a textbook on established standard (canonical) methods. Rather, we focus on emerging, specialized methods that are relatively new in the field but have a given relevance. This is why the title of the book addresses "advanced" techniques. However, new methods also need to be judged by their implication for photovoltaic devices. For this reason, an introductory chapter (Chapter 1) will describe the basic physics of thin-film solar cells and modules and also guide to the specific advantages that are provided by the individual methods. In addition, we have made sure that the selected authors not only are established specialists concerning a specific method but also have long-time experience dealing with solar cells. This ensures that in each chapter, the aim of the analysis work is kept on the purpose of improving solar cells.

The choice of characterization techniques is not intended for completeness but should be a representative cross section through scientific methods that have a high level of visibility in the recent scientific literature. Electrical device characterization (Chapter 2), electroluminescence (Chapter 3), photoluminescence (Chapter 7), and capacitance spectroscopy (Chapter 4) not only are standard optoelectronic analysis techniques for solid-state materials and devices but also are well established and of common use in their specific photovoltaic context. In contrast, characterization of light trapping (Chapter 5) is an emerging research topic very specific to the photovoltaic field. Chapters 6, 8, and 9 deal with ellipsometry, the steady-state photocarrier grating method, and time-of-flight analysis, which are dedicated thin-film characterization methods. Steady-state photocarrier grating (Chapter 8) and time-of-flight measurements (Chapter 9) specifically target the carrier transport properties of disordered thin-film semiconductors. Electron spin resonance (Chapter 10) is a traditional method in solid-state and molecule physics, which is of particular use for analyzing dangling bonds in disordered semiconductors.

The disordered nature of thin-film photovoltaic materials requires analysis of electronic, structural, and compositional properties at the nanometer scale. This is why methods such as scanning probe techniques (Chapter 11) as well as electron microscopy and its related techniques (Chapter 12) gain increasing importance in the field. X-ray and neutron diffraction (Chapter 13) and Raman spectroscopy (Chapter 14) contribute to the analysis of structural properties of photovoltaic materials. Since thin-film solar cells consist of layer stacks with interfaces and surfaces, important issues are the analyses of their chemical and electronic properties, which may be studied by means of soft X-ray and electron spectroscopy (Chapter 15). Important information for thin-film solar-cell research and development is the elemental distributions in the layer stacks, analyzed by various

techniques presented in Chapter 16. Specifically for silicon thin-film solar cells, knowledge about hydrogen incorporation and stability is obtained from hydrogen effusion experiments (Chapter 17).

For designing photovoltaic materials with specific electrical and optoelectronic properties, it is important to predict these properties for a given compound. Combining experimental results from materials analysis with those from *ab initio* calculations based on density functional theory provides the means to study point defects in photovoltaic materials (Chapter 18). Finally, in order to come full circle regarding the solar-cell devices treated in the first chapters of the handbook, the information gained from the various materials analyses and calculations may now be introduced into one-dimensional (Chapter 19) or multidimensional device simulations (Chapter 20). By means of carefully designed optical and electronic simulations, photovoltaic performances of specific devices may be studied even before their manufacture.

We believe that the overview of these various characterization techniques is useful not only for colleagues engaged in the research and development of inorganic thin-film solar cells, from which the examples in the present handbook are given, but also for those working with other types of solar cells and optoelectronic, thin-film devices.

The editors would like to thank all authors of this handbook for their excellent and (almost) punctual contributions. We are especially grateful to Ulrike Fuchs and Anja Tschörtner, Wiley-VCH, for helping in realizing this book project.

Berlin, Germany; London, UK; and Jülich, Germany
August 2010

Daniel Abou-Ras,
Thomas Kirchartz,
and Uwe Rau

Abbreviations

1D	One-dimensional
2D	Two-dimensional
3D	Three-dimensional
A°X	Excitons bound to neutral acceptor
ac	Amplified current
ADC	Analog-to-digital converter
ADF	Annular dark field
ADXRD	Angle-dispersive X-ray diffraction
AES	Auger electron spectroscopy
AEY	Auger electron yield
AFM	Atomic force microscopy
AFORS-HET	Automat for simulation of heterostructures
ALDA	Adiabatic local density approximation
AM	Amplitude modulation
AM	Air mass
AMU	Atomic mass units
ARS	Angularly resolved light scattering
AS	Admittance spectroscopy
ASA	Advanced semiconductor analysis, a solar-cell device simulator
ASCII	American Standard Code for Information Interchange
a-Si	Amorphous silicon
A-X	Excitons bound to ionized acceptor
BACE	Bias-amplified charge extraction
BF	Bright field
BOP	Bond-order potential
BS	Beam splitter
BSE	Bethe–Salpeter equation
BSE	Backscattered electrons
c-AFM	Conductive AFM
CBD	Chemical bath deposition
CBED	Convergent-beam electron diffraction
CBM	Conduction-band minimum
CBO	Conduction-band offset
CC	Coupled cluster
CCD	Charge-coupled device
CE	Charge extraction

CELIV	Charge extraction with linearly increased voltage
CGI	[Cu]/([In]+[Ga])
CHA	Concentric hemispherical analyzer
CI	Configuration interaction
CIGS	$Cu(In,Ga)Se_2$
CIGSe	$Cu(In,Ga)Se_2$
CIGSSe	$Cu(In,Ga)(S;Se)_2$
CIS	$CuInSe_2$
CIS	$CuInS_2$
CISe	$CuInSe_2$
CL	Cathodoluminescence
CL	Core level
CMA	Cylindrical mirror analyzer
CN	Charge neutrality
CP	Critical point
CPD	Contact-potential difference
CSL	Coincidence-site lattice
CSS	Closed-space sublimation
CTEM	Conventional transmission electron microscopy
CV	Capacitance–voltage
cw	Continuous wave
D°h	Optical transitions between donor and free hole
D°X	Excitons bound to neutral donor
DAP	Donor–acceptor pair
db, DB	Dangling bond
dc	Direct current
DF	Dark field
DFPT	Density functional perturbation theory
DFT	Density functional theory
DFT	Discrete Fourier transform
DLCP	Drive-level capacitance profiling
DLOS	Deep-level optical spectroscopy
DLTS	Deep-level transient spectroscopy
DOS	Density of states
DSR	Differential spectral response
DT	Digital
D-X	Excitons bound to ionized donor
eA°	Optical transitions between acceptor and free electron
EBIC	Electron-beam-induced current
EBSD	Electron backscatter diffraction
EDMR	Electrically detected magnetic resonance
EDX	Energy-dispersive X-ray spectrometry
EDXRD	Energy-dispersive X-ray diffraction
EELS	Electron energy-loss spectrometry
EFTEM	Energy-filtered transmission electron microscopy
EL	Electroluminescence
ELNES	Energy-loss near-edge structure
EMPA	Eidgenössische Materialprüfungsanstalt
ENDOR	Electron nuclear double resonance
EPR	Electron paramagnetic resonance
ESCA	Electron spectroscopy for chemical analysis

ESEEM	Electron spin echo envelope modulations
ESI	Energy-selective imaging
ESR	Electron spin resonance
EXC	Free exciton transition
EXELFS	Extended energy-loss fine structure
FFT	Fast Fourier transformation
FIB	Focused ion beam
FIR	Far infrared
FM	Frequency modulation
FP-LAPW	Full potential linearized augmented plane wave
FT	Fourier transform
FTIR	Fourier transform infrared
FTPS	Fourier transform photocurrent spectroscopy
FWHM	Full width at half maximum
FX	Free excitons
FY	Fluorescence yield
GB	Grain boundary
GD-MS	Glow-discharge mass spectroscopy
GD-OES	Glow-discharge optical-emission spectroscopy
GGA	Generalized gradient approximation
GGI	[Ga]/([In]+[Ga])
GIXRD	Grazing-incidence X-ray diffraction
GNU	GNU's Not Unix (recursive acronym)
GPL	General public licence
GW	G for Green's function and W for the screened Coulomb interaction
HAADF	High-angle annular dark field
HFI	Hyperfine interaction
HOPG	Highly oriented pyrolytic graphite
HR	High resistance
HR	High resolution
HRTEM	High-resolution transmission electron microscopy
HT	High temperature
HWCVD	Hot-wire chemical vapor deposition
HZB	Helmholtz-Zentrum Berlin
IBB	Interface-induced band bending
IPES	Inverse photoelectron spectroscopy
IR	Infrared
JEBIC	Junction electron-beam-induced current
KPFM	Kelvin probe force microscopy
KS	Kohn–Sham
KSM	Kaplan–Solomon–Mott (model)
LAMMPS	Large-Scale Atomic/Molecular Massively Parallel Simulator
LBIC	Laser-beam-induced current
LCR meter	Inductance, capacitance, and resistance analyzer
LDA	Local density approximation
LED	Light-emitting diode
LESR	Light-induced ESR
LIA	Lock-in amplifier
LLS	Laser-light scattering
LO	Longitudinal optical
LR	Low resistance

LT	Low temperature
LVM	Localized vibrational modes
MBPT	Many-body perturbation theory
MD	Molecular dynamics
MIP	Mean-inner potential
MIR	Medium infrared
MIS	Metal–insulator–semiconductor
ML	Monolayer
MO	Metal oxide
MOS	Metal–oxide–semiconductor
MS	Molecular statics
MSE	Mean-square error
mw	Microwave
nc-AFM	Non-contact atomic force microscopy
NIR	Near-infrared
NIST	National Institute of Standards and Technology
NSOM	Near-field scanning optical microscopy
OBIC	Optical-beam-induced current
OES	Optical emission spectrometry
OTRACE	Open circuit corrected transient charge extraction
OVC	Ordered vacancy compound
PBE-GGA	Generalized gradient approximation by Perdew, Burke, and Ernzerhof
PC	Personal computer
PCSA	Polarizer–compensator–sample–analyzer
PDA	Photodetector array
PDE	Partial differential equations
PDS	Photothermal deflection spectroscopy
PECVD	Plasma-enhanced chemical vapor deposition
PES	Photoelectron spectroscopy
pESR	Pulsed electron spin resonance
PEY	Partial electron yield
PIPO	Photon-in photon-out
PL	Photoluminescence
PLL	Phase-locked loop
PMT	Photomultiplier tube
pp	Peak-to-peak
PV	Photovoltaic
PVD	Physical vapor deposition
QE	Quantum efficiency
QMA	Quadrupole mass analyzer
QMC	Quantum Monte Carlo
RDLTS	Reverse-bias deep-level transient spectroscopy
REBIC	Remote electron-beam-induced current
rf	Radio frequency
RGB	Red–green–blue, color space
RHEED	Reflection high-energy electrons
RIXS	Resonant inelastic (soft) X-ray scattering
RS	Raman spectroscopy
RSF	Relative sensitivity factor
RTP	Rapid thermal process
RTSE	Real-time spectroscopic ellipsometry

RZW	Ritter, Zeldov, and Weiser steady-state photocarrier method
S/N	Signal-to-noise (ratio)
SAED	Selected-area electron diffraction
SCAPS	Solar-cell capacitance simulator
SCM	Scanning capacitance microscopy
SE	Spectroscopic ellipsometry
SE	Secondary electron
SEM	Scanning electron microscopy
SIMS	Secondary-ion mass spectroscopy
SNMS	Sputtered neutral mass spectroscopy
SNOM, see also NSOM	Scanning near-field optical microscopy
SPICE	Simulation Program with Integrated Circuit Emphasis
SPM	Scanning probe microscopy
SQ	Shockley–Queisser (limit)
SR	Spectral response
SSPG	Steady-state photocarrier grating
SSRM	Scanning spreading-resistance microscopy
STEM	Scanning transmission electron microscopy
STM	Scanning tunneling microscopy
SWE	Staebler–Wronski effect
TCO	Transparent conductive oxide
TD	Trigger diode
TD-DFT	Time-dependent density functional theory
TDCF	Time-delayed collection field
TDS	Thermal desorption spectroscopy
TEM	Transmission electron microscopy
TEY	Total electron yield
TF	Tuning fork
TO	Transversal optical
TOF	Time of flight
TPC	Transient photocapacitance spectroscopy
TPD	Temperature-programmed desorption
TPV	Transient photovoltage
TU	Technical University
UHV	Ultrahigh vacuum
UPS	Ultraviolet photoelectron spectroscopy
UV	Ultraviolet
VBM	Valence-band maximum
VBO	Valence-band offset
Vis, VIS	Visible
WDX	Wavelength-dispersive X-ray spectrometry
WLR	White-light reflectometry
XAES	X-ray Auger electron spectroscopy
XAS	X-ray absorption spectroscopy
XES	X-ray emission spectroscopy
XPS	X-ray photoelectron spectroscopy
XRD	X-ray diffraction
XRF	X-ray fluorescence
ZFF	Zero filling factor
μc-Si	Microcrystalline silicon

Part I
Introduction

Advanced Characterization Techniques for Thin Film Solar Cells, Second Edition.
Edited by Daniel Abou-Ras, Thomas Kirchartz, and Uwe Rau.

1
Introduction to Thin-Film Photovoltaics

Thomas Kirchartz, Daniel Abou-Ras, and Uwe Rau

1.1
Introduction

From the early days of photovoltaics until today, thin-film solar cells have always competed with technologies based on single-crystal materials such as Si and GaAs. Owing to their amorphous or polycrystalline nature, thin-film solar cells always suffered from power-conversion efficiencies lower than those of the bulk technologies. This drawback was and still is counterbalanced by several inherent advantages of thin-film technologies. Because in the early years of photovoltaics space applications were the driving force for the development of solar cells, the argument in favor of thin films was their potential lighter weight as compared with bulk materials.

An extended interest in solar cells as a source of renewable energy emerged in the mid-1970s as the limitations of fossil energy resources were widely recognized. For terrestrial power applications the cost arguments and the superior energy balance strongly favored thin films. However, from the various materials under consideration in the 1950s and 1960s, only four thin-film technologies, namely, hydrogenated amorphous Si (a-Si:H) and the polycrystalline heterojunction systems CdS/Cu_xS, CdS/CdTe, and CdS/Cu(In,Ga)Se_2, entered pilot production. Activities in the CdS/Cu_xS system stopped at the beginning of the 1980s because of stability problems. At that time amorphous silicon became the front runner in thin-film technologies keeping almost constantly a share of about 10% in a constantly growing photovoltaic market with the remaining 90% kept by crystalline Si. Despite their high efficiency potential, polycrystalline heterojunction solar cells based on CdTe and Cu(In,Ga)Se_2 did not play an economic role until the turn of the century.

During the accelerated growth of the worldwide photovoltaic market since the year 2000, the market share of thin-film technologies was again at a level at or above 10%, with an increasing contribution of CdTe and Cu(In,Ga)Se_2. With annual production figures in the GW range, thin-film photovoltaics has become a multibillion-dollar business. In order to expand this position, further dramatic cost reduction is required combined with a substantial increase of

Advanced Characterization Techniques for Thin Film Solar Cells, Second Edition.
Edited by Daniel Abou-Ras, Thomas Kirchartz, and Uwe Rau.

module efficiency. In this context, material and device characterization becomes an important task not only for quality control in an expanding industry but remains also at the very heart of further technological progress.

In addition to the three inorganic thin-film technologies, also solar cells containing one or more organic materials were studied in particular from the 1990s onward. Two main variants of such organic solar cells are developed. The first one, the dye-sensitized solar cell (DSSC), uses organic dyes (later also inorganic nanoparticles) as light absorbers. In order to be able to use any well-absorbing material without putting any constraint on its ability to transport electrons and holes, a monolayer of that well-absorbing material (the dye) was attached to a mesoporous scaffold (usually made up of TiO_2) which was then immersed in a liquid and later also solid-state electrolyte infiltrating the pores of the scaffold. The tasks of light absorption as well as transport of the negative and positive charge carrier would then be performed by different materials, namely, the dye, the scaffold, and the electrolyte in this order. The second variant of an organic solar cell distributed the three tasks mentioned above over two materials: The first, usually a polymer, was used for light absorption and hole transport, while the second material (usually a fullerene) was used for electron transport and to a lesser degree also for light absorption. These technologies surpassed efficiencies of 10% and saw some attempts at commercialization, though so far on a smaller scale than, for example, CdTe. Within the last few years, the seemingly clear boundaries between the fields of organic and inorganic solar cells have started to become blurred by the advent of hybrid (organic–inorganic) metal-halide perovskites. The most widely used material in this class is $CH_3NH_3PbI_3$, which has an organic molecule (CH_3NH_3) on the A lattice position, lead on the B position, and iodine on the X position (for an ABX_3 perovskite). $CH_3NH_3PbI_3$ is one example of a class of materials that managed to surpass 20% efficiency on a cell level – the first time for an "organic" semiconductor. Given that these highly efficient perovskite solar cells are able to combine the tasks of light absorption as well as electron and hole transport just like the three typical inorganic thin-film technologies, the demands for and the methods used for device and material characterization in these perovskites are in many respects quite similar to the ones needed for inorganic thin-film solar cells.

The present book comprises a large range of characterization techniques used for photovoltaic devices and materials. The examples shown in the chapters concentrate on the three inorganic thin-film technologies – thin-film Si (a-Si:H, microcrystalline μc-Si:H, and combinations of both forming a tandem solar cell) – and the two heterojunction systems CdS/CdTe as well as $CdS/Cu(In,Ga)(Se,S)_2$ but sometimes include examples from organic and perovskite devices as well. These thin-film technologies have in common that they consist of layer sequences made up from disordered semiconductor materials that are deposited onto a supporting substrate or superstrate. This layer structure and the use of disordered materials define a fundamental difference to devices based on crystalline c-Si where a self-supporting Si wafer is transformed into a solar cell via a solid-state diffusion of dopant atoms. Thus, there are only the front

and the back surface as critical interfaces in the classical wafer solar cell (with the notable exception of the a-Si:H/c-Si heterojunction solar cell). In thin-film solar cells, the number of functional layers can amount to up to eight and more. Some of these layers have thicknesses as low as 10 nm. In large-area modules, these layers homogeneously cover areas of up to 6 m^2. These special features of the thin-film photovoltaic technologies define the field for the characterization techniques discussed in the present book.

Electrical characterization, electroluminescence and photoluminescence, capacitance spectroscopy, and characterization of light trapping as considered in Chapters 2–4 as well as 6, 8, 10, and 11 are common analysis techniques for photovoltaic devices. However, the specific properties of the thin-film systems like the disordered nature of the materials, the importance of features at the nanometer scale, and the fact that the film thicknesses are of the order or below the wavelength of visible light account for the special aspects to be considered when using these techniques. Chapters 5, 7, 8, and 9 deal with techniques like ellipsometry, photothermal deflection spectroscopy, the steady-state photocarrier grating method, and time-of-flight analysis, which are thin-film-specific methods, and moreover, some were even invented within the field of thin-film photovoltaics. Chapters 12–20 discuss classical methods for material characterization, each of them having special importance for at least one photovoltaic technology. Again, the specific features of photovoltaic thin films like the importance of dangling bonds and hydrogen passivation in disordered Si, the need for physical and chemical material analysis at the nanometer scale, or the prominence of interface chemistry and physics in thin-film solar cells define the focus of these chapters. Chapters 21–24 at the end of the handbook deal with the theoretical description of materials and devices. *Ab initio* modeling of semiconductor materials is indispensable, because even the basic physical properties of some of the wide variety of compounds and alloys used in thin-film photovoltaics are not satisfactorily known. Finally, successful modeling of the finished devices may be looked at as the definitive proof of our understanding of materials and interfaces.

The present introductory chapter yields a brief general introduction into the basic principles of photovoltaics, highlighting the specific material and device properties that are relevant for thin-film solar cells.

1.2 The Photovoltaic Principle

The temperature difference between the surface of the sun with a temperature of $T = 5800$ K and the surface of the earth ($T = 300$ K) is the driving force of any solar-energy conversion technology. Solar cells and solar modules directly convert the solar radiation into electricity using the internal photoelectric effect. Thus, any solar cell needs a photovoltaic absorber material that is not only able to absorb the incoming light efficiently but also to create mobile charge carriers, electrons and

holes, that are separated at the terminals of the device without significant loss of energy. Note that in *organic* absorber materials most light-absorption processes generate excitons and a first step of charge separation is necessary in order to dissociate the exciton into free carriers. In contrast, the low binding energy of excitons in *inorganic* semiconductors makes absorption and generation of mobile charge carriers in appropriate absorber materials of this type virtually identical. Thus, after light absorption electrons and holes are present in the absorber and must be directed toward the two different contacts of the absorber, that is, the final charge carrier separation step.

For a semiconductor acting as a photovoltaic absorber, its band-gap energy E_g is the primary quantity defining how many charge carriers are generated from solar photons with energy $E \geq E_g$. Maximizing the number of photons contributing to the short-circuit current density of a solar cell would require minimizing E_g. Since photogenerated electron–hole pairs thermalize to the conduction-band and valence-band edges after light absorption, the generated energy per absorbed photon corresponds to E_g regardless of the initial photon energy E. Thus, maximizing the band-gap energy E_g maximizes the available energy per absorbed photon. Therefore, one intuitively expects that an optimum band-gap energy exists between $E_g = 0$, maximizing the generated electron–hole pairs, and $E_g \to \infty$, maximizing the generated energy contained in a single electron–hole pair. Quantitatively, this consideration is reflected in the dependence of the maximum achievable conversion efficiency of a single-band-gap photovoltaic absorber material as discussed in the following section.

1.2.1
The Shockley–Queisser Theory

The maximum power-conversion efficiency of a solar cell consisting of single semiconducting absorber material with band-gap energy E_g is described by the Shockley–Queisser (SQ) [1] limit. In its simplest form, the SQ limit relies on four basic assumptions: (i) The probability for the absorption of solar light by the generation of a single electron–hole pair in the photovoltaic absorber material is unity for all photon energies $E \geq E_g$ and zero for $E < E_g$. (ii) All photogenerated charge carriers thermalize to the band edges. (iii) The collection probability for all photogenerated electron–hole pairs at short circuit is unity. (iv) The only loss mechanism in excess of the nonabsorbed photons of (i) and the thermalization losses in (ii) are spontaneous emission of photons by radiative recombination of electron–hole pairs as required by the principle of detailed balance.

In order to calculate the maximum available short-circuit current $J_{sc,SQ}$ as defined by (iii), we need the incoming photon flux ϕ_{inc} and the absorptance $A(E)$ defining the percentage of the incoming light at a certain photon energy E that is absorbed and not reflected or transmitted. The simplest approximation defined for an ideal absorber by condition (i) is a step function, that is, $A(E) = 1$ (for $E > E_g$) and $A(E) = 0$ (for $E < E_g$). Then we have under short-circuit conditions

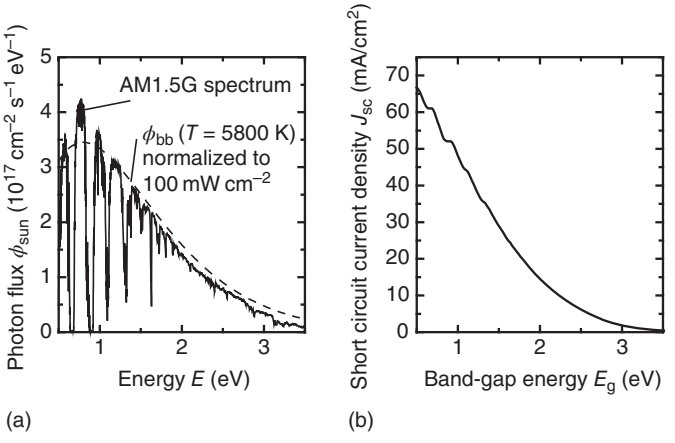

Figure 1.1 (a) Comparison of the AM1.5G spectrum with the blackbody spectrum of a body with a temperature $T = 5800$ K. Both spectra are normalized such that the power density is 100 mW/cm^2. (b) Using the AM1.5G spectrum and Equation (1.1), we obtain the short-circuit current density $J_{sc,SQ}$ in the Shockley–Queisser limit as a function of the band-gap energy E_g of the solar absorber.

(i.e., applied voltage $V = 0$ V)

$$J_{sc,SQ} = q\int_0^\infty A(E)\phi_{inc}(E)\mathrm{d}E = q\int_{E_g}^\infty \phi_{inc}(E)\mathrm{d}E, \tag{1.1}$$

where q denotes the elementary charge.

Figure 1.1a compares the spectral photon flux corresponding to the terrestrial AM1.5G norm spectrum with the blackbody spectrum at $T = 5800$ K, both spectra normalized to a power density of 100 mW/cm^2. Figure 1.1b illustrates the maximum short-circuit current density that is possible for a given band-gap energy E_g according to Equation 1.2.

Since light absorption by generation of free carriers and light emission by recombination of electron–hole pairs are interconnected by the principle of detailed balance, in thermodynamic equilibrium the photon emission ϕ_{em} is connected to the absorptance via Kirchhoff's law $\phi_{em} = A(E)\phi_{bb}(E, T)$, where $\phi_{bb}(E, T)$ is the blackbody spectrum at temperature T.

In an ideal solar cell under applied voltage bias, we use Würfel's [2] generalization of Kirchhoff's law to describe the recombination current $J_{rec,SQ}$ for radiative recombination according to

$$J_{rec,SQ} = q\int_0^\infty A(E)\phi_{bb}(E,T)\exp\left(\frac{qV}{kT}\right)\mathrm{d}E = q\int_{E_g}^\infty \phi_{bb}(E,T)\exp\left(\frac{qV}{kT}\right)\mathrm{d}E, \tag{1.2}$$

where the second equality again results from the assumption of a sharp band-gap energy E_g. Thus, Equation 1.2 describes the current density of a solar cell in

the dark if only radiative recombination of carriers is considered corresponding to condition (iv) and the carriers have the temperature T of the solar cell according to condition (ii). The total current density J under illumination is a superposition of this radiative recombination current density and the short-circuit current density defined in Equation 1.1. Thus, we can write

$$J(V) = J_{\mathrm{rec,SQ}}(V) - J_{\mathrm{sc,SQ}} = q\int_{E_g}^{\infty} \phi_{\mathrm{bb}}(E)\mathrm{d}E \exp\left(\frac{qV}{kT}\right) - q\int_{E_g}^{\infty} \phi_{\mathrm{inc}}(E)\mathrm{d}E. \quad (1.3)$$

There are two contributions to the incoming photon flux ϕ_{inc}, that is, the spectrum ϕ_{sun} of the sun and the photon flux ϕ_{bb} from the environment which has the same temperature as the sample. When we replace the incoming photon flux ϕ_{inc} with the sum $\phi_{\mathrm{sun}} + \phi_{\mathrm{bb}}$, Equation 1.3 simplifies to

$$J(V) = q\int_{E_g}^{\infty} \phi_{\mathrm{bb}}(E)\mathrm{d}E \left[\exp\left(\frac{qV}{kT}\right) - 1\right] - q\int_{E_g}^{\infty} \phi_{\mathrm{sun}}(E)\mathrm{d}E, \quad (1.4)$$

which is a typical diode equation with an additional photocurrent only due to the extra illumination from the sun. Now it is obvious that for 0 excess illumination and 0 V applied, the current becomes 0.

Figure 1.2 shows the current density/voltage (J/V) curves of an ideal solar cell according to Equation 1.4 for three different band-gap energies $E_g = 0.8$, 1.4, and

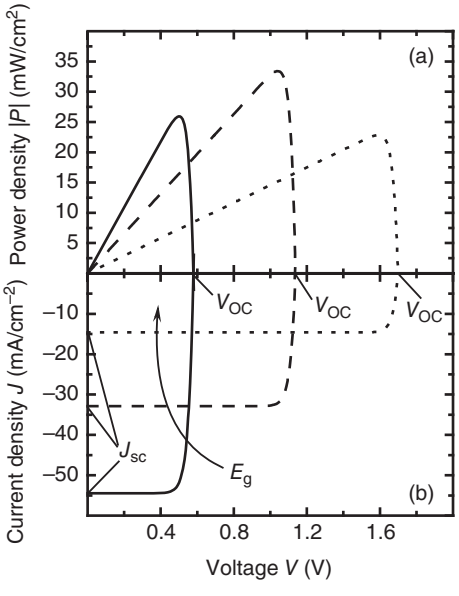

Figure 1.2 (a) Power density/voltage curves and (b) current density/voltage (J/V) curves of three ideal solar cells with band gaps $E_g = 0.8$, 1.4, and 2.0 eV, respectively. The higher the band gap E_g, the higher the open-circuit voltage V_{oc}, that is, the intercept of both power density and current density with the voltage axis. However, a higher band gap also leads to a decreased short-circuit current J_{sc} (cf. Figure 1.1b). The curves are calculated using Equation 1.4.

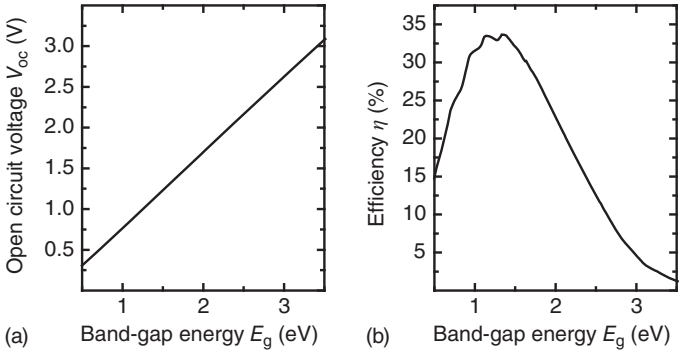

Figure 1.3 (a) Open-circuit voltage and (b) conversion efficiency as a function of the band-gap energy E_g in the Shockley–Queisser limit using an AM1.5G spectrum as illumination. The optimum band-gap energies for single-junction solar cells are in the range of 1.1 eV $< E_g <$ 1.4 eV with maximum conversion efficiencies around $\eta = 33\%$ under unconcentrated sunlight.

2.0 eV. If we evaluate Equation 1.4 under open-circuit conditions, that is, at $J = 0$, we find the maximum possible voltage in the fourth quadrant of the coordinate system in Figure 1.2. This voltage is called the open-circuit voltage V_{oc} and follows from Equation 1.4 as

$$V_{oc} = \frac{kT}{q} \ln\left(\frac{\int_{E_g}^{\infty} \phi_{sun}(E)\mathrm{d}E}{\int_{E_g}^{\infty} \phi_{bb}(E)\mathrm{d}E} + 1 \right) = \frac{kT}{q} \ln\left(\frac{J_{sc,SQ}}{J_{0,SQ}} + 1 \right). \tag{1.5}$$

Here, $J_{0,SQ}$ is the saturation current density in the SQ limit, that is, the smallest possible saturation current density for a semiconductor of a given band gap. The open-circuit voltage increases nearly linearly with increasing band gap as shown in Figure 1.3a.

From Equation 1.4, the power density follows by multiplication with the voltage. The efficiency η is then the maximum of the negative power density,[1)] that is,

$$\eta = \frac{-\max(J(V)V)}{P_{opt}} = \frac{-\max(J(V)V)}{\int_{E_g}^{\infty} E\phi_{sun}(E)\mathrm{d}E}. \tag{1.6}$$

Figure 1.3b shows the final result of the SQ theory: the efficiency as a function of the band-gap energy for illumination with the AM1.5G spectrum depicted in Figure 1.1a.

1) Negative current density means here that the current density is opposite to the current density any passive element would have. A negative power density means then that energy is extracted from the device and not dissipated in the device as it would happen in a diode, which is not illuminated.

1.2.2 From the Ideal Solar Cell to Real Solar Cells

The universality and simplicity of the SQ limit are due to the fact that all internal details of the solar cell are irrelevant for its derivation. However, these hidden details are the practical subjects of research on real solar cells and especially on thin-film solar cells. It is important to understand that some of these details idealized (or neglected) by the original SQ theory are not in conflict with the detailed balance principle [3].

Firstly, starting from a step function like absorptance toward a more complex spectral dependence of $A(E)$ is not in conflict with the radiative recombination limit (cf. Equations 2.1 and 2.2). A continuous transition from zero to unity is expected for any semiconductor material with finite thickness. Especially for thin-film absorbers, maximizing light absorption is an important task requiring additional means to confine the light as discussed in Section 1.2.3. Moreover, the disorder in thin-film absorbers may lead to additional electronic states close to the band gap (so-called band tails or band-gap fluctuations) with a considerable contribution to light absorption and emission. In consequence, the achievable conversion efficiency is reduced even in the radiative limit [4].

Secondly, proper extraction of the photogenerated electrons and holes requires sufficiently high carrier mobilities and selectivity of the contacts to make sure that all electrons and holes are collected in the n-type and in the p-type contact. Again, these requirements are valid even when restricting the situation to radiative recombination [5]. Since mobilities in disordered thin-film materials are generally lower than in monocrystalline absorbers, charge carrier extraction is an issue to be discussed with special care (Section 1.2.4).

Finally, recombination in thin-film solar cells is dominated by nonradiative processes. Thus, especially the achieved open-circuit voltages are far below the radiative limit. Section 1.2.5 and the major part of Chapter 2 will deal with understanding the efficiency limits resulting from all sorts of nonradiative recombination. It is important to note that even when considering nonradiative recombination, we must not necessarily abandon a detailed balance approach [6, 7] (cf. Chapter 3).

1.2.3 Light Absorption and Light Trapping

The first requirement for any solar cell is to absorb light as efficiently as possible. Solar-cell absorbers should therefore be nontransparent for photons with energy $E > E_g$. For any solar cell but especially for thin-film solar cells, this requirement is in conflict with the goal of using as little absorber material as possible. Additionally, thinner absorbers facilitate charge extraction for materials with low mobilities and/or lifetimes of the photogenerated carriers. This is why light trapping in photovoltaic devices is of major importance. Light trapping exploits randomization of light at textured surfaces or interfaces in combination with the fact that

semiconductor absorber layers have typical refractive indices n that are higher than that of air ($n = 1$) or glass ($n \approx 1.5$). Typical values for the real part of the refractive index are $n > 3.5$ in inorganic solar absorbers and $n \approx 2$ in organic materials. However, the light first has to enter the solar cell. In order to minimize reflection of incoming light at the front surface, a high refractive index is a disadvantage. The reflectance

$$R = \left(\frac{n-1}{n+1}\right)^2 \tag{1.7}$$

at the interface between air and the semiconductor (for normal incidence) will become higher, when the refractive index gets higher. However, the high reflection at the front surface is reduced by using several layers between air and absorber layer. The refractive indices of these layers increase gradually, and any large refractive index contrast (leading to strong reflection) is avoided.

For light trapping, however, a high refractive index has an advantage. When the direction of the incoming light is randomized by a scattering interface somewhere in the layer stack of the thin-film solar cell, part of the light will be guided in the solar-cell absorber by total internal reflection. The percentage of light kept in the solar cell by total internal reflection increases with the refractive index, since the critical angle $\theta_c = \arcsin(1/n)$ becomes smaller. For light with a Lambertian distribution of angles, the reflectance of the front surface for light from the inside is

$$R_i = 1 - \frac{(1-R_f)\displaystyle\int_0^{\theta_c} \cos\theta \sin\theta \mathrm{d}\theta}{\displaystyle\int_0^{\pi/2} \cos\theta \sin\theta \mathrm{d}\theta} = 1 - \frac{(1-R_f)}{n^2}. \tag{1.8}$$

Here, R_f is the reflectance at the front side of the absorber for normal incidence.

To visualize the effect the absorption coefficient and light trapping has on the absorptance of a solar cell, we present some calculations for a model system. Let us assume a direct semiconductor, which have absorption coefficients of the typical form

$$\alpha = \alpha_0 \sqrt{\frac{E - E_g}{1\,\mathrm{eV}}}. \tag{1.9}$$

Then, the absorptance $A(E)$, that is, the percentage of photons that are absorbed and not reflected or transmitted at a certain photon energy, is calculated for flat surfaces and for an absorber thickness much larger than the wavelength of light with

$$A = (1-R_f)\frac{(1-\mathrm{e}^{-\alpha d})(1+R_b\mathrm{e}^{-\alpha d})}{1-R_f R_b \mathrm{e}^{-2\alpha d}}. \tag{1.10}$$

Here, R_b is the reflectance at the backside. Equation 1.10 assumes an infinite number of reflections at the front and the back of the absorber layer. To calculate the real absorptance of any thin-film solar cell, it is rather useless for two reasons: (i) Thin-film solar cells usually consist of several layers and not only one, and (ii) the

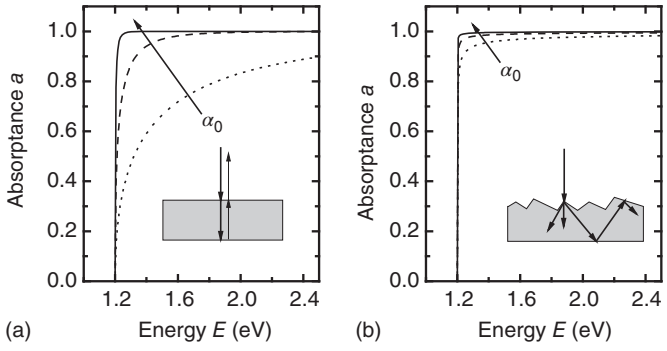

Figure 1.4 Absorptance as a function of photon energy for (a) a flat solar cell and (b) a textured solar cell with perfect light trapping. In both cases the absorption coefficient α_0 from Equation 1.9 is varied. The values are for both subfigures $\alpha_0 = 10^4$, $\sqrt{10} \times 10^4$, $10^5\,\mathrm{cm}^{-1}$. For the same absorption coefficient, the textured solar cell has absorptances that are much closer to the perfect step function than the flat solar cell.

layer thicknesses are of the same order than the wavelength of light and interferences cannot be neglected any more. Nevertheless Equation 1.10 is useful to test the influence of the absorption coefficient on the absorptance. Figure 1.4a compares the absorptance calculated according to Equation 1.10 for three different values of α_0, namely, $\alpha_0 = 10^4$, $\sqrt{10} \times 10^4$, $10^5\,\mathrm{cm}^{-1}$, and for a constant thickness d of the absorber of $d = 1\,\mu\mathrm{m}$. The reflectance at the front side is assumed to be $R_\mathrm{f} = 0$ and the reflectance at the backside is $R_\mathrm{b} = 1$.

To calculate the absorptance of a textured cell with light trapping, it is necessary to integrate over all angles. The resulting equations are rather complicated [8, 9]; however, a simple and useful approximation exists for the case $R_\mathrm{b} = 1$, namely, [10]

$$A = \frac{1 - R_\mathrm{f}}{1 + \dfrac{(1 - R_\mathrm{f})}{4n^2 \alpha d}}. \tag{1.11}$$

Figure 1.4b shows the result of applying the absorption coefficient defined in Equations 1.9–1.11. Again, the absorptance for the case of perfect light trapping is calculated for $\alpha_0 = 10^4$, $\sqrt{10} \times 10^4$, $10^5\,\mathrm{cm}^{-1}$, $d = 1\,\mu\mathrm{m}$, and $R_\mathrm{f} = 0$. The refractive index is assumed to be $n = 3.5$. It is obvious that for a given value of α_0, the absorptance of the textured solar cell comes much closer to the perfect step function like absorptance of the SQ limit.

To visualize the effect of light trapping on the short-circuit current density J_sc, Figure 1.5 compares the J_sc as a function of the product $\alpha_0 d$ for a flat and a Lambertian surface, that is, for absorptances calculated with Equation 1.10 and with Equation 1.11. The band gap is chosen to be $E_\mathrm{g} = 1.2\,\mathrm{eV}$ as in Figure 1.4 so the maximum J_sc for high $\alpha_0 d$ is the same as in the SQ limit (cf. Figure 1.1b), namely, $J_\mathrm{sc,max} \approx 40\,\mathrm{mA/cm}^2$. However, for lower $\alpha_0 d$, the J_sc with and without light trapping differ considerably and show the benefit from structuring the surface to enhance the scattering in the absorber layer. In reality the benefit from

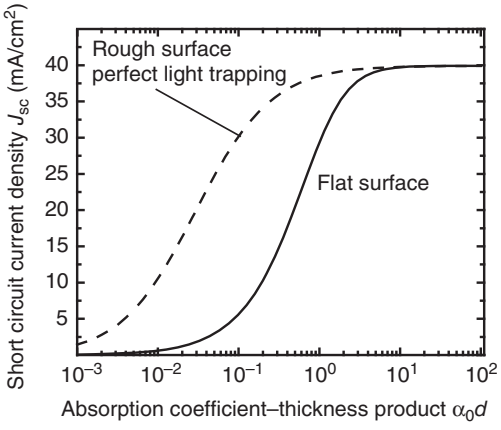

Figure 1.5 Comparison of the short-circuit current density of a flat (solid line) and a textured solar cell (dashed line) as a function of the product of α_0 and the thickness d assuming an absorption coefficient according to Equation 1.9 (with $E_g = 1.2$ eV). Especially for low absorption coefficients relative to the device thickness (low $\alpha_0 d$), light trapping increases the short-circuit current density drastically. The refractive index used for these simulations is $n = 3.5$ independent of photon energy.

light trapping will be smaller since the light has to be reflected several times at the front and especially at the back surface, where we assumed the reflection to be perfect. In reality any back reflector will absorb part of the light parasitically, that is, the light is absorbed but no electron–hole pairs are created, which could contribute to the photocurrent.

1.2.4 Charge Extraction

After an electron–hole pair is generated, the charge carriers must be extracted from the absorber layer. To get a net photocurrent, the electron must leave the device at the opposite contact than the hole. This requires a built-in asymmetry that makes electrons leave the device preferentially at the electron-extracting contact (cathode) and holes at the hole-extracting contact (anode).

Figure 1.6 introduces three device geometries that induce a built-in asymmetry that helps to extract oppositely charged carriers at opposite contacts. Figure 1.6a shows the band diagram of a p–n-junction solar cell under illumination, and Figure 1.6d shows the same cell with an applied voltage $V = 0.5$ V. The simulations were done by solving the Poisson equation and the continuity equations with the software ASA, which is described in Chapter 23. As typical for most solar cells with a p–n junction, the space charge region, where the bands are steep and the electric field is high, is at the very edge of the device. Most of the device consists in our example of a p-type base layer, where the field is practically zero. The transport of minority carriers (here electrons) to the space charge region is purely

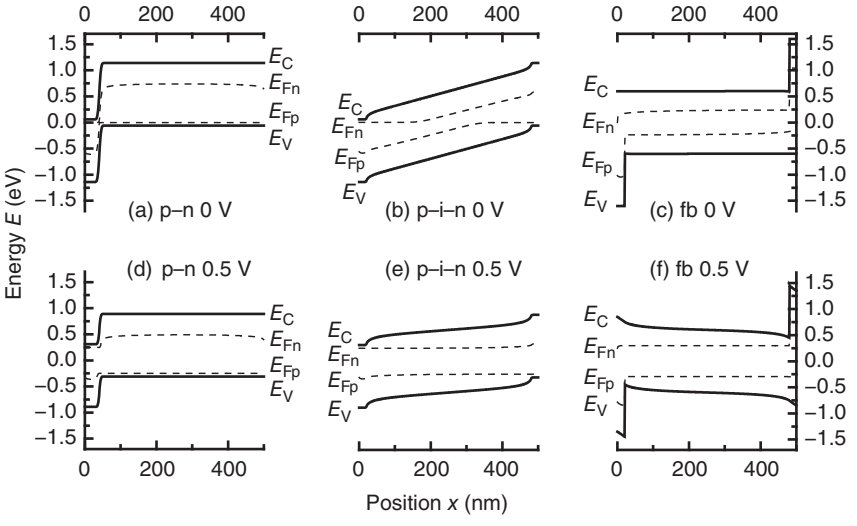

Figure 1.6 Simulation of the band diagrams of a (a, d) p–n-junction, a (b, e) p–i–n-junction, and a (c, f) flatband (fb) solar cell under illumination. Every type of geometry is depicted under short-circuit conditions and under an applied forward bias $V = 0.5$ V.

diffusive and independent from the applied voltage. That means application of a voltage only changes the electrical potential in the space charge region but not in the much larger neutral base.

The band bending at the junction leads to an asymmetry that separates the charges. Electrons are able to diffuse to the junction and then further to the n-type region and the electron contact. In addition the p–n junction serves as a barrier for holes which are in turn extracted by the back contact. Note that in the band diagram in Figure 1.6a and d, this back contact is not selective as is the p–n junction. Therefore, also electrons can leave the device at this contact, a fact that is usually considered as contact or surface recombination (cf. Chapter 2) and might be a major loss mechanism. Cu(In,Ga)Se_2 solar cells are examples for p–n (hetero)junctions.

For some disordered semiconductors like amorphous silicon, the electronic quality of doped layers is very poor. In addition, the mobilities and diffusion lengths are small; thus purely diffusive transport would not lead to efficient charge extraction. The solution to this problem is the so-called p–i–n-junction diode. Here the doped layers are very thin compared to the complete thickness of the diode. The largest share of the complete absorber thickness is occupied by an intrinsic, that is, undoped layer, in between the n- and p-type regions. Figure 1.6a shows the band diagram of such a p–i–n-junction solar cell under illumination, and Figure 1.6d shows the same cell with an applied voltage $V = 0.5$ V. At short circuit, the region with a nonzero electric field extends over the complete intrinsic layer. Only directly at the contacts the field is relatively small. When a forward

voltage is applied to the cell, the electric field becomes smaller as shown in Figure 1.6d. Solar cells made from a-Si:H as well as a-Si:H/μc-SiH tandem cells use the p–i–n configuration.

Both p–n-junction and p–i–n-junction solar cells have a built-in field, meaning that the bands are bended due to the different conductivity type of the layers. Theoretically, such a band bending is not necessary to separate charges as can be shown by a gedanken experiment [11]. Figure 1.6c shows the band diagram of a hypothetical flatband solar cell under short-circuit conditions. Like the p–i–n-junction solar cell, the flatband solar cell has an intrinsic layer sandwiched between two other layers that induce the asymmetry for charge separation. In this case, the asymmetry is not due to band bending and differently doped layers but instead due to band offsets at the heterojunction between two materials with different band gaps. Let us assume we find one contact material with zero band offset for the electrons and a high (in this case 1 eV) band offset for the holes and another material with the exact inverse properties. In this case the band diagram is completely flat at short circuit apart from the two band offsets. Like in the p–n-junction solar cell, the charge separation at short circuit is arranged via diffusive transport that is effective, when the diffusion length is high enough.

Under applied voltage the drawback of the flatband solar cell becomes obvious. The voltage has to drop somewhere over the absorber layer leading to an electric field, which creates a barrier for the extraction of charge carriers. While for a p–i–n-junction solar cell the field-assisted charge extraction becomes weaker with applied voltage, in a flatband solar cell the field hinders charge separation. This is why we consider in the following the flatband solar cell as a paradigmatic example for a device that exhibits poor charge separation properties. In fact, some typical features that show up in the numerical simulations in the following are indicative in practical (but faulty) devices for problems due to nonideal contact properties.

To illustrate the basic properties of the solar-cell structures introduced in Figure 1.6, we simulated the current/voltage curves for two different mobilities μ of electrons and holes. The recombination in the device was assumed to be dominated by one defect in the middle of the device with a Shockley–Read–Hall lifetime (see Section 1.2.5) $\tau = 100\,\text{ns}$ for electrons and holes. In addition, we assumed a surface recombination velocity $S = 10^5\,\text{cm/s}$ for the holes at the electron contact ($x = 0$) and the electrons at the hole contact ($x = 500\,\text{nm}$). The results are presented in Figure 1.7a ($\mu = 10^{-1}\,\text{cm}^2/\text{V s}$) and Figure 1.7b ($\mu = 10^{1}\,\text{cm}^2/\text{V s}$), demonstrating that short-circuit current density is substantially decreased when turning from the high to the low mobility. The fill factor FF, that is,

$$\text{FF} = \frac{P_{\text{mpp}}}{J_{\text{sc}} V_{\text{oc}}} \tag{1.12}$$

is relatively high for both cases. Here, P_{mpp} is the maximum power density that can be extracted from the device. Thus, the fill factor is understood as the largest

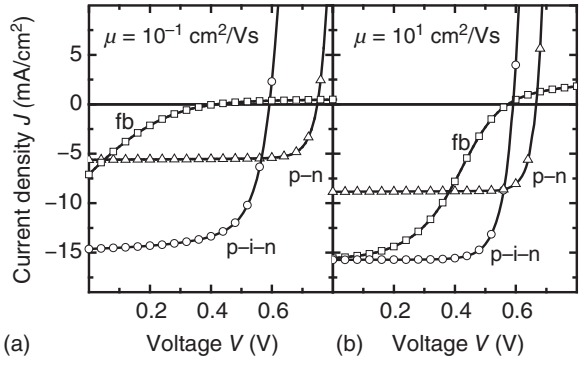

Figure 1.7 Simulated current/voltage curves of the three solar-cell geometries introduced in Figure 1.6 for two charge carrier mobilities, namely, (a) $\mu = 10^{-1}\,\mathrm{cm^2/V\,s}$ and (b) $\mu = 10^{1}\,\mathrm{cm^2/V\,s}$. The main influence of a decreased mobility is a lower short-circuit current for the p–n-junction solar cell and a lower fill factor for the p–i–n-junction and the flatband solar cell, which feature voltage-dependent charge carrier collection.

rectangle that fits between a *J/V* curve and the axis divided by the rectangle with the sides J_{sc} and V_{oc}.

For the p–n-junction solar cell, the open-circuit voltage also changes with mobility, which is due to increased surface recombination at high mobilities. This effect is pronounced in this simulation since the complete thickness of the absorber is rather thin (500 nm) and the surface recombination velocity is assumed to be rather high ($S = 10^5$ cm/s). The same effect also explains the relatively low short-circuit current density of the p–n-junction geometry since there is no built-in field or heterojunction that keeps the minorities away from the "wrong" contact (at $x = 500$ nm in Figure 1.6). Thus, the p–n-junction solar cell is sensitive to the lack of selectivity of the back contact, that is, to surface recombination.

The p–i–n junction has a much higher short-circuit current density changing also very little upon decrease of mobility from $\mu = 10^1\,\mathrm{cm^2/V\,s}$ (Figure 1.7b) to $\mu = 10^{-1}\,\mathrm{cm^2/V\,s}$ (Figure 1.7a). However, the fill factor decreases because of the reduced capability of the device to collect all charge carriers when, under forward bias voltage, the built-in field is reduced (cf. Figure 1.6e). This phenomenon is called bias-dependent carrier collection. Furthermore, the open-circuit voltage of the p–i–n cell is lower than that of its p–n-type counterpart. Nevertheless, the p–i–n structure delivers the highest output power under the assumed, unfavorable conditions, namely, relative low carrier mobilities and high surface recombination velocities.

The flatband solar cell has the most remarkable *J/V* curves. The *J/V* curves in both mobility cases are partly bended, leading to extremely low fill factors. This so-called S-shaped characteristic becomes more pronounced in the low-mobility case. Note that, in practice, such behavior is common in devices with faulty contacts and consequently insufficient carrier separation capabilities.

1.2.5
Nonradiative Recombination

The open-circuit voltage V_{oc} of any solar cell is considerably lower than its radiative limit, implying that nonradiative recombination mechanisms like Auger recombination [12] or recombination via defects, which is usually called Shockley–Read–Hall recombination [13, 14], dominate real-world devices. Figure 1.8 compares the three main recombination mechanisms. In case of radiative recombination (Figure 1.8a), the excess energy of the recombining electron–hole pair is transferred to a photon. In case of (Figure 1.8b) Auger recombination [15, 16], the excess energy serves to accelerate a third charge carrier (electron or hole) which thermalizes rapidly by emitting phonons. The third recombination mechanism is Shockley–Read–Hall recombination via states in the forbidden gap. Here, the excess energy is also transferred to phonons, leading to an increase in the lattice temperature of the absorber.

In very-high-quality devices from monocrystalline silicon, the recombination will be limited by Auger recombination and surface recombination. This means that even with a perfect bulk material without any defects, recombination in an indirect semiconductor like silicon will most likely not be limited by radiative recombination. However, typical thin-film solar cells are made from amorphous or microcrystalline semiconductors that are far from defect-free. Here, the most important recombination mechanism is recombination via states in the forbidden gap. These states can be, for instance, due to defects like dangling bonds [17] or due to band tails [18–20] arising from disorder in the material. Especially in amorphous Si, there is not only a single state in the band gap as indicated in Figure 1.8c but a continuous distribution of states in energy. The theory and modeling of such defect distributions will be described later in Chapter 23, while we want to restrict ourselves here to some simple examples with a single defect state.

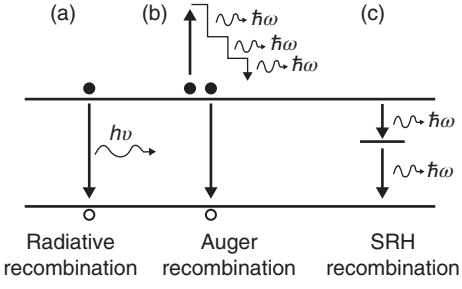

Figure 1.8 Overview over the three basic recombination mechanisms for photogenerated excess carriers in a semiconductor. The excess energy is either transferred to (a) a photon, (b) kinetic energy of an excess electron or hole, or (c) phonons. For case (b), in the so-called Auger recombination, the kinetic energy of the electron is lost by collisions with the lattice, which heats up. In case (c), the emission of phonons becomes possible by the existence of states in the forbidden gap. This recombination mechanism is called Shockley–Read–Hall recombination.

To visualize the influence of increased recombination rates on the current/voltage curve of solar cells, we made some numerical simulations using a very simple model for recombination. This model assumes recombination via a defect in the middle of the forbidden gap, assuming equal capture cross sections σ for electrons and holes. Then the recombination rate according to Shockley–Read–Hall statistics is

$$R = \frac{np - n_i^2}{(n+p)\tau}, \tag{1.13}$$

where τ is called the lifetime of the charge carrier. This lifetime depends on the density N_T of defect states, the capture cross section σ, and the thermal velocity v_{th} via

$$\tau = (v_{th}\sigma N_T)^{-1}. \tag{1.14}$$

Figure 1.9 shows the current/voltage curves of a (a) p–i–n-junction solar cell and (b) a p–n-junction solar cell for a constant mobility $\mu = 1\,\mathrm{cm}^2/\mathrm{V\,s}$ (for electrons and holes) and with a varying lifetime $\tau = 1\,\mathrm{ns}$, 10 ns, 100 ns, 1 µs, and 10 µs. All other parameters are defined in Table 1.1. It is important to note that a reduction of the lifetime has a different influence on the two geometries, which is in accordance with what we already observed when varying the mobility. For p–i–n-junction solar cells, a decrease of the lifetime leads to a decrease in open-circuit voltage, in fill factor, and in short-circuit current density. In contrast, the p–n-junction solar cell does not suffer from a decreased fill factor. The shape of the *J/V* curves stays practically the same. For low lifetimes (and/or low mobilities), the charge carrier collection in p–i–n-junction solar cells is

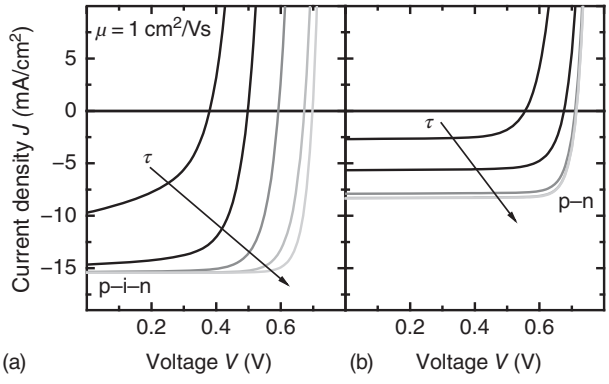

Figure 1.9 Current/voltage curves of (a) a p–i–n-junction solar cell and (b) a p–n-junction solar cell for a constant mobility $\mu = 1\,\mathrm{cm}^2/\mathrm{V\,s}$ (for electrons and holes) and with a varying lifetime $\tau = 1\,\mathrm{ns}$, 10 ns, 100 ns, 1 µs, and 10 µs. All other parameters are defined in Table 1.1. An increasing lifetime helps to increase V_{oc} in both cases up to the level defined by surface recombination alone. In case of the p–i–n-junction solar cell, the *FF* increases as well.

Table 1.1 Summary of all parameters for the simulations in this chapter that are not changed for the simulation.

Parameters for all simulations in this chapter	Values
Band gap E_g (eV)	1.2
Effective density of states N_C, N_V for conduction and valence band (cm^{-3})	10^{20}
Doping concentrations N_D, N_A in all doped layers of p–n- and p–i–n-junction solar cells (cm^{-3})	10^{19}
Total thickness d (nm)	500
Generation rate G ($cm^{-3}\ s^{-1}$)	2×10^{21}
Surface recombination velocity S (cm/s)	10^5

The mobilities and lifetimes, which are changed, are always given in the respective figure captions.

voltage dependent. For p–n-junction solar cells, this is not the case. But apart from the influence the carrier lifetime has on charge extraction, which is very similar to the effect of the mobility, the lifetime has a pronounced influence on the open-circuit voltage. The increase of V_{oc} with increasing lifetime τ, however, seems not to follow a simple relation. For high values of τ, V_{oc} saturates for both p–i–n-junction and p–n-junction solar cells. This saturation is due to surface recombination, which limits the maximum attainable open-circuit voltage V_{oc}.

1.3 Functional Layers in Thin-Film Solar Cells

Until now, we have discussed the photovoltaic effect, the requirements for the material properties to come close to a perfect solar cell, and the possible geometries to separate and extract charge carriers. In typical crystalline silicon solar cells, nearly all of these requirements and tasks have to be fulfilled by the silicon wafer itself. Charge extraction is guaranteed by diffusing phosphorus into the first several hundred nanometers of the p-type wafer to create a p–n junction. The wafer is texture etched to obtain a light-trapping effect and to decrease the reflection at the front surface. The only additional layers that are necessary are the metal grid at the front, an antireflective coating (typically from SiN_x), and the metallization at the back.

Thin-film solar cells are usually more complex devices with a higher number of layers that are optimized for one or several purposes. In general, there are two configurations possible for any thin-film solar cell as shown in Figure 1.10. The first possibility is that light enters the device through a transparent superstrate.

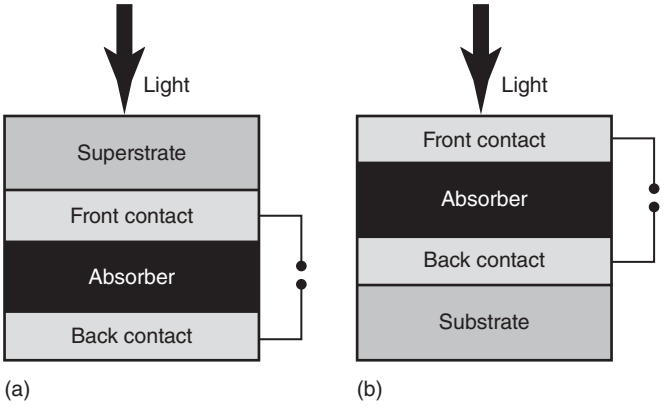

Figure 1.10 Sketch of the layer sequences to build up the system for thin-film solar cells in superstrate (a) and substrate configuration (b). The minimum number of layers in excess of the supporting sub- or superstrate consists of the transparent and conductive front contact, the absorber layer, and the back contact.

Table 1.2 List of the four types of layers in a thin-film solar cell together with their specific tasks and requirements necessary for an efficient solar cell.

Layer type	Possible tasks and requirements
Substrate/superstrate	Mechanical and thermal stability, transparency (superstrate)
Front contact	Light trapping, antireflection, electrical contact, charge extraction
Absorber	Absorb light, charge extraction, low recombination
Back contact	Light trapping, high reflection, electrical contact, charge extraction

The superstrate has to maintain the mechanical stability of the device while at the same time being extremely transparent. The superstrate is followed by layers which are part of the front contact, followed by the absorber layer and the layers that form the back contact. The second possibility is to inverse the layer stack, starting with the front contact, the absorber, and the back contact. These layers are all deposited on top of a substrate. Because light does not have to pass the substrate to enter the solar cell, the substrate can be transparent or opaque.

Table 1.2 summarizes the roles and the requirement for the three functional layers and the substrate or superstrate of thin-film solar cells. The substrate or superstrate provides mechanical stability. The functional layers are deposited onto the substrate or superstrate; thus, it has to be thermally stable up to the highest temperature reached during the complete deposition process.

The front contact and back contact layers have to provide the electrical contact of the solar cell to the outside world, that is, the layers need high conductivities and must make a good electric contact to the absorber layers. In addition, the built-in field required for efficient charge extraction (especially at higher voltage bias) of a p–i–n junction as depicted in Figure 1.6 requires doped contact layers. In devices that require efficient light trapping, usually the front and/or back contact layers are textured and have a lower refractive index than the absorber layer. Thus, the front contact layer additionally serves as an internal antireflective coating. In addition, a possible texture of the contact/absorber interface will lead to scattering of light and to increased path lengths of weakly absorbed light in the absorber layer. The back contact should have a high reflectivity so that weakly absorbed light is reflected multiple times.

The absorber layer is central to the energy conversion process, requiring a steep rise of the absorption coefficient above the band gap, a high mobility and low recombination rates for efficient charge collection, and a high open-circuit voltage potential. In case of a p–n-junction device, the absorber layer must be moderately doped either intentionally or by intrinsic doping due to defects. In case of a p–i–n-junction device, the main absorber layer, the i-layer, should be undoped.

1.4 Comparison of Various Thin-Film Solar-Cell Types

The basic schemes of the layer stack of a thin-film solar cell, as presented in Figure 1.10, are implemented in different ways in the different thin-film technologies. In the following, we will briefly discuss the main characteristics of the thin-film technologies that appear in examples in this book. These technologies are the $Cu(In,Ga)Se_2$ solar cell, the CdTe-based solar cell, the kesterite $Cu_2ZnSn(S,Se)_4$ solar cell, the thin-film silicon solar cell with amorphous and microcrystalline silicon absorbers, the perovskite solar cell, and the organic solar cell. We also discuss the main challenges in future developments and how characterization of materials and devices can help to improve the devices. For those readers who desire a more detailed insight in the physics and technology of the different thin-film solar cells, we refer to a number of books and review articles on the topic. The physics and particularly the fabrication of all types of thin-film solar cells are discussed in Refs [21–23], the physics of Cu-chalcopyrite solar cells in Refs [24, 25], the interfaces of CdS/CdTe solar cells in Ref. [26], the physics of amorphous hydrogenated silicon in Ref. [27], the physics and technology of thin-film silicon solar cells in Refs [28–32], the aspect of charge transport in disordered solids in Ref. [33], kesterite-type solar cells in Refs [34, 35], perovskite solar cells in Refs [36, 37], and organic solar cells in Ref. [38].

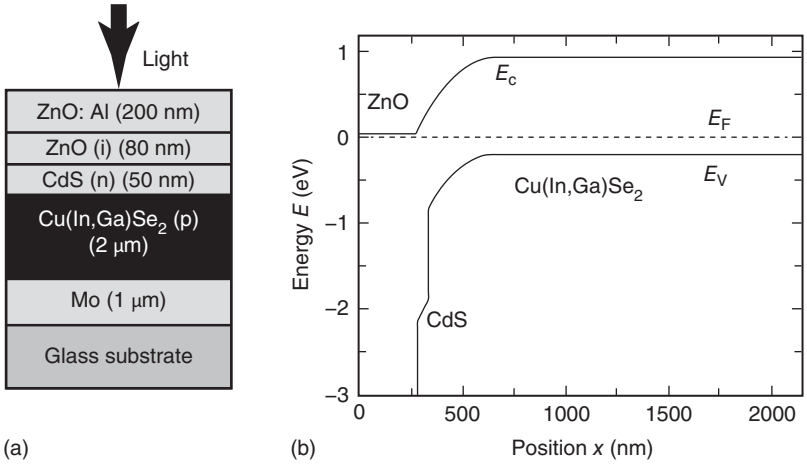

Figure 1.11 (a) Layer-stacking sequence and (b) energy band diagram of a typical ZnO/CdS/Cu(In,Ga)Se_2 heterojunction solar cell.

1.4.1
Cu(In,Ga)Se_2

1.4.1.1 Basic Properties and Technology

Solar cells with an absorber layer made from Cu(In,Ga)Se_2 are currently the state of the art of the evolution of Cu-based chalcopyrites for use as solar cells. Heterojunctions between CdS and Cu_2S were the basis for first approaches for thin-film solar cells since the 1950s [39–42]. In 1974 first work on the light emission and light absorption of CdS/$CuInSe_2$ diodes was published [43–45]. While $CuInSe_2$ was not further considered for applications as a near-infrared light-emitting diode (LED), its high absorption coefficient and its electronically rather passive defects make it a perfect choice for use as a microcrystalline absorber material. Inclusion of Ga atoms on the In lattice site such that the ratio of [Ga]/([Ga] + [In]) becomes around 20% shifts the band gap from 1.04 eV to around 1.15 eV, which is nearly perfect for a single-junction cell (cf. Figure 1.3). Today, thin-film solar cells with a Cu(In,Ga)Se_2 absorber layer are the most efficient thin-film technology with laboratory efficiencies up to 21.7% [46].

The classical layer stack for this type of solar cell is shown in Figure 1.11a. It consists of a typically 1 μm thick Mo layer deposited on a soda-lime glass substrate and serving as the back contact for the solar cell. Then, Cu(In,Ga)Se_2 is deposited on top of the Mo back electrode as the photovoltaic absorber material. This layer has a thickness of 1–2 μm. The heterojunction is then completed by chemical bath deposition of CdS (typically 50 nm) and by the sputter deposition of a nominally undoped (intrinsic) i-ZnO layer (usually of thickness 50–70 nm) and then a heavily doped ZnO:Al window layer.

The Cu(In,Ga)Se_2 absorber material yielding the highest efficiencies is prepared by coevaporation from elemental sources. The process requires a maximum

substrate temperature of ~550 °C for a certain time during film growth, preferably toward the end of growth. Advanced preparation sequences always include a Cu-rich stage during the growth process and end up with an In-rich overall composition in order to combine the large grains of the Cu-rich stage with the otherwise more favorable electronic properties of the In-rich composition. The first example of this kind of procedure is the so-called Boeing or *bilayer process* [47] which starts with the deposition of Cu-rich Cu(In,Ga)Se_2 and ends with an excess In rate to achieve a final composition that is slightly In poor. The most successful coevaporation process is the so-called three-stage process [48] where first $(In,Ga)_2Se_3$ (likewise In, Ga, and Se from elemental sources to form that compound) is deposited at lower temperatures (typically around 300 °C). Then Cu and Se are evaporated at an elevated temperature and finally again In, Ga, and Se to ensure the overall In-rich composition of the film even if the material is Cu rich during the second stage.

The second class of absorber preparation routes is based on the separation of deposition and compound formation into two different processing steps. High efficiencies are obtained from absorber prepared by selenization of metal precursors in H_2Se [49] and by rapid thermal processing of stacked elemental layers in a Se atmosphere [50]. These sequential processes have the advantage that approved large-area deposition techniques such as sputtering can be used for the deposition of the materials. The Cu(In,Ga)Se_2 film formation then requires a second step, the selenisation step typically performed at similar temperatures as the coevaporation process. Both absorber preparation routes are now used in industrial application.

Important for the growth of the Cu(In,Ga)Se_2 absorber is the active role of Na during absorber growth. In most cases, the Na comes from the glass substrate and diffuses into the absorber [51]. But there are also approaches where Na is incorporated by the use of Na-containing precursors [52, 53]. The explanations for the beneficial impact of Na are manifold, and it is most likely that the incorporation of Na in fact results in a *variety* of consequences (for a review see Ref. [54]).

1.4.1.2 Layer-Stacking Sequence and Band Diagram of the Heterostructure

Figure 1.11 displays the layer-stacking sequence (a) and the band diagram of the ZnO/CdS/Cu(In,Ga)Se_2 heterojunction (b). The back contact consists of a sputtered Mo layer. In excess of producing a functional, conductive contact, proper preparation of this layer is also important for adhesion of the absorber film and, especially, for the transport of Na from the glass substrate through the Mo layer into the growing absorber. A homogeneous and sufficient supply of Na depends much on the microstructure of this layer. In contrast, if Na is supplied from a precursor, additional blocking layers prevent out-diffusion of Na from the glass. Quantitative chemical depth profiling as described in Chapter 19 is a decisive tool to shed more light into the role of Na and on its way how it is functional during absorber growth.

The Cu(In,Ga)Se_2 absorber material grown on top of the Mo contact is slightly p-type doped by native, intrinsic defects, most likely Cu vacancies [55]. However, the net doping is a result of the difference between the acceptors and an almost

equally high number of intrinsic donors [56, 57]. Thus, the absorber material is a highly compensated semiconductor. Furthermore, the material features electronic metastabilities like persistent photoconductivity [58] which are theoretically explained by different light-induced defect relaxations [59]. However, final agreement on the observed metastability phenomena has not yet achieved, leaving an urgent need for further theoretical and experimental access to the complex defect physics of $Cu(In,Ga)Se_2$ (for a review of the present status, see Ref. [48]). Some experimental and theoretical methods helpful for further research are outlined in Chapters 11 and 21 of the present book.

Another puzzle is the virtual electronic inactivity of most grain boundaries in properly prepared polycrystalline $Cu(In,Ga)Se_2$ absorbers being one essential ingredient for the high photovoltaic efficiencies delivered by this material. A discussion of the present status is given in Ref. [60]. A great part of the structural analysis methods discussed in the present book (Chapters 13–15 and 17) describes tools indispensable for a better understanding of the microstructure of the $Cu(In,Ga)Se_2$ absorber material.

The surface properties of $Cu(In,Ga)Se_2$ thin films are especially important, as this surface becomes the active interface of the completed solar cell. The free surface of as-grown $Cu(In,Ga)Se_2$ films exhibits a very unique feature, namely, a widening of the band gap with respect to the bulk of the absorber material [61, 62]. This band-gap widening results from a lowering of the valence band and is effective in preventing interface recombination at the absorber–buffer interface [63, 64]. This surface layer has an overall Cu-poor composition and a thickness of 10–30 nm [65]. Understanding the interplay between this surface layer and the subsequently deposited buffer layer is one of the decisive challenges for the present and future research.

The 50 nm thick CdS buffer layer is in principle too thin to complete the heterojunction. In fact the role of the CdS buffer in the layer system is still somewhat obscure. It is however clear that the undoped (i) ZnO layer is also a vital part of a successful buffer/window combination. Furthermore, both interfaces of the CdS interlayer to the $Cu(In,Ga)Se_2$ absorber and to the (i) ZnO play a vital role [66]. Under standard preparation conditions, the alignment of the conduction bands at both interfaces is almost flat [67] such that neither barrier for electron transport occurs nor is the band diagram distorted in a way to enhance interface recombination. However, it turns out that a replacement of CdS by a less cumbersome layer is not straightforward. Though, while promising materials like In(OH,S), Zn(OH,S), In_2Se_3, ZnSe, and ZnS (for an overview see Ref. [68]) mostly in combination with standard ZnO double layer have been investigated in some detail, no conclusive solution has been found despite reported efficiencies of 18% using ZnS buffer layers [69]. Recent research [70] focuses at combinations of Zn(S,O,OH)/ZnMgO replacing the traditional CdS/(i) ZnO combination. Alternative buffer layers like ZnS also have the advantage of a higher band-gap energy $E_g = 3.6$ eV compared to that of CdS $E_g = 2.4$ eV. By the higher E_g, parasitic absorption in the buffer layer is restricted to a much narrower range, and the short-circuit current density in Cd-free cells can exceed that of standard devices by up to 3 mA/cm^2 [63]. However, all

technological improvements rely on our scientific understanding of the physics, chemistry, and microstructure of the heterointerfaces involved in the solar cell. Surface analysis methods as those discussed in Chapters 18 and 19 have already contributed much to our present knowledge and provide the promise to deepen it further.

1.4.2 CdTe

1.4.2.1 Basic Properties and Technology

Just as the CdS/Cu(In,Ga)Se_2 solar cell, also the CdS/CdTe devices are descendants of the first CdS/Cu_2S solar cells. In the mid-1960s, first experiments with tellurides were performed. Efficiencies between 5 and 6% were obtained for CdTe/$CuTe_2$ devices [71, 72]. Since Cu diffusion led to instabilities in these devices, instead, CdS and CdTe were combined to form a p–n heterojunction with efficiencies around 6% [73]. Thirty years later, the efficiency has increased to more than 21% [74]. In addition, CdTe solar modules represent the by far most successful photovoltaic thin-film technology with a share of about 10% in the global photovoltaic market (data from 2014) [75].

One decisive reason for this success is the relatively ease with which CdTe solar cells and modules are prepared. Several types of transparent conductive oxides (TCO) are used as front contact materials for preparation of CdTe solar cells, SnO_2:F and In_2O_3:F being the most common ones. Both materials, CdS and CdTe, forming the heterojunction of the solar cell, are grown with similarly fast and reliable methods, including closed-space sublimation, spraying, screen printing followed by sintering, and electrodeposition. Since CdS grows natively as n-type material and CdTe as p-type material, the p–n heterojunction forms automatically.

However, in order to improve the device efficiency substantially, an additional step, the $CdCl_2$ activation, is necessary. A vapor-based approach is most useful with regard to industrial applications [76]. The activation step leads to an intermixing of CdS and CdTe close to the heterointerface and to the formation of a Cu(Te,S) compound. In some cases, recrystallization of the CdTe film was observed after $CdCl_2$ treatment [77]. In any case, the intermixing process is decisive for the improvement of the device performance.

The major challenge for reliable manufacture of efficient devices is to produce a stable and ohmic back contact to the CdTe absorber with its high electron affinity. Often, back contacts are made with materials that contain Cu, such as Cu_2Te, ZnTe:Cu, or HgTe:Cu, enabling a relatively low contact resistance. However, Cu diffusion in CdTe is fast and extends deeply into the absorber, thereby affecting considerably the stability of the device [78]. Cu-free alternative contact materials include embrace, for example, Sb_2Te_3 [79]. Often, an etching step is used to produce a Te-rich interlayer, providing higher p-type doping and, consequently, a reasonably low-ohmic contact [80]. Recently, substantial advances in photovoltaic

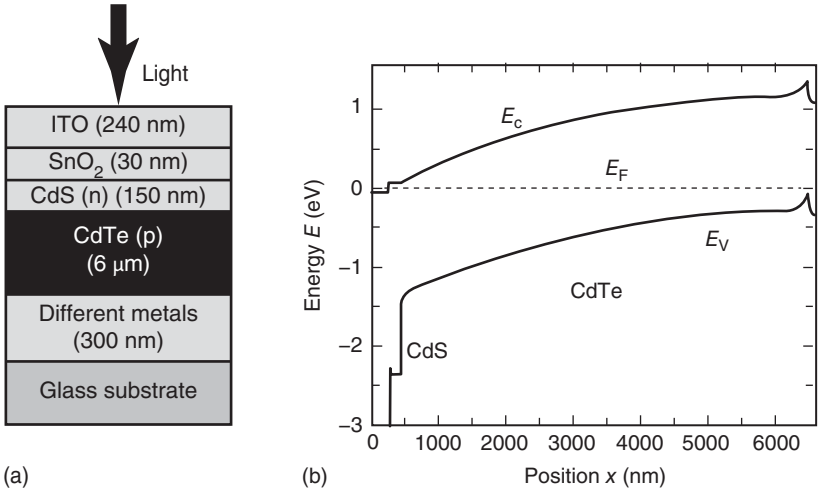

Figure 1.12 (a) Layer-stacking sequence and (b) energy band diagram of a typical CdTe-based solar cell following Ref. [82].

performance have been achieved by doping of the CdTe absorber [81] layer as well as by introducing compositional gradients.

1.4.2.2 Layer-Stacking Sequence and Band Diagram of the Heterostructure

From the point of view of the layer-stacking sequence and the band diagram shown in Figure 1.12a and b, the CdS/CdTe heterostructure is quite similar to those of the CdS/Cu(In,Ga)Se_2 heterostructure given in Figure 1.11. One obvious difference is the low doping density of the CdTe absorber, making the device somewhat a hybrid between a p–i–n and a p–n junction. The built-in field almost stretches from the heterointerface toward the back contact. As we have already seen, such a configuration is helpful for carrier collection but has the drawback of delivering lower open-circuit voltages than a p–n-type device with a relatively narrow space charge region if the density of recombination active defects doesn't depend on the doping concentration.

The band diagram at the back contact features a highly p-doped region due to Cu indiffusion or due to the formation of a Te-rich interlayer. This leads to a relatively thin yet high barrier for holes. Thus, the electrical contact is achieved via tunneling from the absorber into the back metal. The modeling of CdTe solar cells, including a proper approach to the back contact, which usually is by far not perfectly ohmic, represents a major challenge as discussed in Chapter 23.

The average grain sizes in the polycrystalline CdTe absorbers range from 1 to 2 mm, thus somewhat larger than in Cu(In,Ga)Se_2. However, the grain boundaries are considerably more electronically active than in Cu(In,Ga)Se_2. For instance, photocurrent concentration along grain boundaries [83] indicates type inversion of grain boundaries in CdTe. This could be helpful for current collection (along the grain boundaries) but also implies losses in open-circuit voltage. Again, connecting microstructural analysis with highly resolved measurements of electronic

properties by scanning techniques as described in Chapters 13 and 14 will clarify the picture in the future.

The favorable flat conduction-band alignment at the CdTe/CdS as well as at the CdS/TCO interface as featured by Figure 1.12b is similar to the situation for $Cu(In,Ga)Se_2$ devices. In CdTe solar cells this is basically a result of the $CdCl_2$ activation process and of intermixing [73].

1.4.3
$Cu_2ZnSn(S,Se)_4$

Photovoltaic devices with same thin-film stacking sequences as for $Cu(In,Ga)Se_2$ solar cells but replacing In and Ga in the absorber layer by the earth-abundant elements Zn and Sn have been developed during recent years as cost-effective alternatives. The tetragonal crystal structure of the compound $Cu_2ZnSn(S,Se)_4$, of kesterite type, is similar to the chalcopyrite-type structure of $Cu(In,Ga)Se_2$ [84]. A Cu/Zn disorder (referred to as "disordered kesterite") causes a high concentration of Cu_{Zn} and Zn_{Cu} antisite defects [76]. In the material system $Cu_2ZnSn(S,Se)_4$, it is possible to obtain band-gap energies of the compound semiconductors ranging from 1.0 to 1.5 eV by varying the [S]/([S] + [Se]) ratio from 0 to 1 [85]. Power-conversion efficiencies of 8.4% [86], 9.2% [87], and 12.6% [88] have been achieved by using $Cu_2ZnSn(S,Se)_4$ absorber layers with [S]/([S] + [Se]) ratios of 1 (Cu_2ZnSnS_4), 0 ($Cu_2ZnSnSe_4$), and about 0.25.

Since, according to the available phase diagrams [89, 90], the kesterite phase of $Cu_2ZnSn(S,Se)_4$ exhibits a small existence region with 1–2 at.% deviation in the composition at most growth temperatures of around 550 °C [35], secondary phases can be expected to be present when synthesizing $Cu_2ZnSn(S,Se)_4$ bulk crystals or thin films. Of the possible secondary phases, $Cu_2(S,Se)$, Zn(S,Se), Sn(S,Se), $Sn(S,Se)_2$, and $Cu_2Sn(S,Se)_3$ were reported to be most likely [91]. Some of these compounds can be considered to affect collection of charge carriers as well as radiative recombination in the photovoltaic devices [85]. However, recombination at the $CdS/Cu_2ZnSn(S,Se)_4$ interface was identified to influence the device performance more dominantly, probably due to a cliff-like conduction-band alignment in the solar cells with S-containing absorber layers. Therefore, further improvement of the power-conversion efficiencies to above 13% may be achieved by reducing this interface recombination [80], for example, by application of buffer layers other than CdS, or by reducing the density of secondary phases at this interface.

1.4.4
Thin-Film Silicon Solar Cells

1.4.4.1 Hydrogenated Amorphous Si (a-Si:H)

Central to the working principle of semiconductors is the forbidden energy gap derived from the periodicity of the crystal lattice. However, it is exactly this

strict periodicity that is lacking in amorphous semiconductors, which have a short-range order but no long-range order as their crystalline counterparts. The structural disorder caused by variations in bond lengths and angles has several implications for the electronic and optical properties of amorphous materials. The most important feature is the peculiar density of electronic states in amorphous silicon featuring localized states close to the band edges that arise from disorder and a distribution of deep states due to unpassivated, that is, dangling, bonds. In addition the word band gap is no longer adequate in amorphous semiconductors. Instead, an optical gap is defined from the onset of absorption, while a mobility gap is defined as the approximate demarcation line between localized and extended states [92]. Despite the fact that the mobility gap is not a forbidden zone for electrons but instead full of localized states, amorphous silicon still proves to be a useful material for thin-film devices like solar cells, photodetectors, and transistors [93].

While first crystalline silicon solar cells with reasonable efficiencies of about $\eta = 6\%$ were already developed in 1954 [94], the research on amorphous silicon first needed two breakthroughs before the fabrication of the first amorphous silicon solar cells in 1976 became possible [95]. The first breakthrough was the realization that the addition of considerable amounts of hydrogen helped to passivate dangling bonds in the amorphous material thereby leading to sufficiently low defect densities that hydrogenated amorphous silicon showed some of the important characteristics of useful semiconductors like dopability and photoconductivity [96]. The second breakthrough was the successful doping of amorphous silicon [97].

Despite the defect passivation with hydrogen, the defect densities in a-Si:H are still relatively high with diffusion lengths between 100 and 300 nm [98]. In doped a-Si:H layers, the defect density is two or three orders of magnitude higher, and the diffusion length is accordingly even lower. Thus, a p–n junction as used in crystalline silicon but also in Cu(In,Ga)Se_2 solar cells would not work for a-Si:H, since the diffusion length is too low. Because the absorber thickness cannot be made much thinner than the diffusion length due to the large losses because of insufficient light absorption, a p–i–n-junction configuration has to be used. The first advantage is that most of the absorber layer consists of intrinsic a-Si:H with its higher carrier lifetime than doped a-Si:H. The second advantage is that the built-in field helps with extracting charge carriers as shown in Figure 1.13. The advantage of the p–i–n configuration is that electron and hole concentrations are similar in a relatively large portion of the absorber volume, which increases defect recombination, which is automatically highest, when electron and hole concentrations are approximately equal.

Figure 1.13 shows the typical layer stack and band diagram of an a-Si:H p–i–n-type solar cell. Usually a superstrate configuration is used, although a substrate configuration is also possible. In the latter case, the solar cell is deposited on the substrate starting with the back contact and the n-type layer. Thus, such a solar cell is called nip solar cell, in which n–i–p represents the deposition order. In both cases of a substrate or superstrate configuration, the illumination is always from the p side. This is due to the lower mobility of holes in a-Si:H. It is therefore

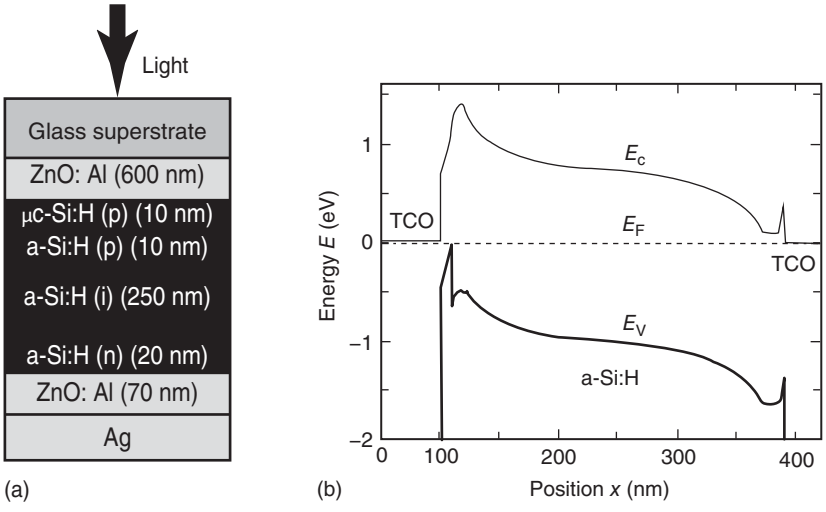

Figure 1.13 (a) Stacking sequence and (b) band diagram of a typical a-Si:H p–i–n solar cell. The main absorber layer is intrinsic, while the built-in field is due to the thin doped silicon layers. Due to the asymmetric mobilities between electrons and holes, the p-type layers will always be on the illuminated side, ensuring that the holes with their lower mobility have the shorter way to the contacts.

beneficial to have the hole contact on the illuminated side, where the generation rate is higher. With the hole contact on the illuminated side, the distance the slowest carrier has to travel to the contacts is minimized.

1.4.4.2 Metastability in a-Si:H: The Staebler–Wronski Effect

Shortly after the first reports on a-Si:H solar cells, Staebler and Wronski [99] published their findings on metastability in a-Si:H. Under illumination the conductivity of a-Si:H degrades but can be restored by annealing at temperatures of about 425 K. This degradation effect is known as the Staebler–Wronski effect. The metastable behavior is ascribed to the light-induced creation of additional defects. It is generally accepted that these metastable defects are additional dangling bonds that act like recombination centers in the material and that these dangling bonds are created by the breaking of weak or strained Si–Si bonds. Hydrogen plays an important role in the metastable behavior of a-Si:H; however, there is no consensus on the exact mechanisms involved and the role of hydrogen in the Staebler–Wronski effect [100–103]. The creation of additional recombination centers affects a-Si:H-based solar cells to such a degree that the Staebler–Wronski effect is a severe limitation for the application of a-Si:H in single-junction solar cells.

1.4.4.3 Hydrogenated Microcrystalline Silicon (μc-Si:H)

As can be seen by comparison with Figure 1.3b, the high optical gap of a-Si:H of approximately 1.75 eV (the exact value depending on the definition and on the hydrogen content) is too high for a single-junction solar cell. It was therefore

an important discovery in thin-film silicon solar-cell research to find a way to prepare hydrogenated microcrystalline silicon (μc-Si:H) with approximately the same band gap as crystalline silicon (E_g (c-Si) = 1.12 eV) that had a sufficient quality for use in solar cells. First μc-Si:H layers were deposited in the 1960s [104], and successful doping was achieved in the 1970s [105]. However, the material had insufficient electronic quality for use in solar cells. The use of gas purifiers in the 1990s by the Neuchâtel group made the fabrication of μc-Si:H layers with sufficiently low oxygen contents [106–108] and the successful fabrication of first μc-Si:H solar cells with reasonable efficiencies possible [109, 110].

1.4.4.4 Micromorph Tandem Solar Cells

One possibility to overcome [111] the efficiency limit of Shockley and Queisser is the use of a multijunction solar cell with absorber layers having different band gaps. The highest band-gap absorber should be on the illuminated side such that all high-energy photons are absorbed by the absorber with the higher band gap and the low-energy photons are absorbed by the cell or the cells with the lower band gap(s). If every absorber has its own p–n junction or p–i–n junction, then they can be deposited on top of each other such that one obtains two or more series connected solar cells on top of each other. This approach minimizes the losses due to thermalization of carriers and due to the transparency of any solar cell for photons with energies below the band gap of the absorber. With a similar approach as discussed in Section 1.2.1, the efficiency [112] and the optimal band-gap combinations can be calculated for multijunction solar cells in general and tandem (i.e., two-junction solar cells) in particular [113, 114]. It is a fortunate coincidence that the optimum combination for a tandem solar cell is close to the actual band gaps of amorphous (E_g (a-Si:H) ≈ 1.75 eV) and microcrystalline silicon (E_g (μc-Si:H) ≈ 1.2 eV). Although in principle efficiencies above the SQ limit for single-junction solar cells are possible with such a configuration, in reality the efficiencies are much lower than the SQ limit and even lower than efficiencies of real crystalline Si single-junction solar cells. Nevertheless, the tandem cell made from a-Si:H and μc-Si:H has achieved slightly higher efficiencies than either of the single-junction devices (see Ref. [29] for an overview). For these thin-film tandem cells with their relatively low mobilities, a second motivation arises for the use of tandem solar cells. Since the built-in field decreases for increasing thickness and since the charge collection becomes increasingly difficult with increasing distance to the contacts, thin solar cells have higher fill factors than thicker solar cells. The tandem approach is a useful way to keep individual cell thicknesses low and at the same time have a higher total thickness and a better absorptance.

1.4.4.5 Liquid-Phase Crystallized Si

Recently, substantial progress has been demonstrated in the development of polycrystalline Si solar cells on glass substrates. The defect concentration in the Si absorber layer, one of the main reasons for the so far limited device performance

(power-conversion efficiency of about 10%), has been reduced considerably by replacing the state-of-the-art solid-phase crystallization of the Si precursor layer by a laser-beam liquid-phase crystallization (LPC) process [115, 116]. This synthesis step can lead to large average grain sizes of several hundreds of micrometers, similar to those of multicrystalline Si wafers. As a result, the open-circuit voltage has increased to more than 650 mV, and power-conversion efficiencies of well above 11% have been demonstrated [117]. Solar cells based on LPC-Si thin films on glass substrates may emerge as low-cost alternatives to multicrystalline wafer-based Si solar cells, provided that light incoupling and contacting in the solar-cell stack can be further optimized.

1.4.5
Metal-Halide Perovskite Solar Cells

Semiconducting perovskites with one organic and one inorganic cation and three halogen atoms as anions were initially tested as dyes in DSSCs. The initial results were hardly promising in terms of stability, because the liquid electrolyte was quickly dissolving the perovskite layer [118]. However, once the liquid electrolyte was replaced by an organic hole transport layers, solar-cell efficiencies and stability were quickly improving. However, the stability still remains on a low level compared with inorganic materials. After it had become apparent that the most frequently used material $CH_3NH_3PbI_3$ was perfectly capable of light absorption as well as electron and hole collection [119], a large variety of device designs became possible, going way beyond the initial use in "DSSCs" with solid-state electrolytes.

$CH_3NH_3PbI_3$ exhibits an absorption coefficient similarly high as the one of $Cu(In,Ga)Se_2$ or GaAs and therefore can reach high photocurrent densities for rather low thicknesses [120]. The band-gap energy of $CH_3NH_3PbI_3$ is around 1.6 eV, that is, it is slightly too high for a single-junction device but close to the ideal band-gap energy for a tandem solar cell. The high conversion efficiencies [121] reached for a thin-film photovoltaic material with a band-gap energy as high as 1.6 eV make the perovskites rather unique, because of their use for tandem solar cells which has previously been possible only for the family of III – V semiconductors and by fabricating a-Si:H/μc-Si:H stacks. Charge carrier lifetimes in the material are frequently reported to exceed 100 ns, which is an excellent value for a polycrystalline semiconductor. Mobilities reported in the literature, however, vary from values around 100 $cm^2/V\,s$ for single crystals to values between 10^{-3} [122] and 10 $cm^2/V\,s$ [123] for thin films. Especially because the mobility values at the lower end of the spectrum of reported values belong to highly efficient devices with efficiencies approaching 20% [122], the understanding and measurement of charge transport properties seem to be currently a mostly unresolved challenge.

A major reason for the success but also some associated peculiarities of $CH_3NH_3PbI_3$ seems to be based on the defect physics of the material [124]. Due to the three lattice positions of the perovskite crystal (ABX_3), there are 12 possible

intrinsic defects, most of which are shallow in the case of $CH_3NH_3PbI_3$, doping the device rather than leading to recombination centers. The few deep defects exhibit large formation enthalpies and occur therefore less frequently than in many other polycrystalline materials. Nevertheless, the low concentration of deep defects still seems to control charge carrier recombination, which becomes apparent from the LED quantum efficiencies of LEDs being much smaller than one [125]. The shallow defects which are doping the device are able to diffuse through the device [126], thereby leading to a doping profile that is not constant as a function of time and bias voltage. This leads to hysteresis effects in the current/voltage curves, that is, depending on the voltage sweep direction and the speed of the voltage sweep, different efficiencies are measured [127].

While the efficiency of perovskite solar cells has recently surpassed 20% [121], future research efforts are likely directed toward topics such as improved long-term stability, reproducibility of device fabrication routines, alternatives for Pb as the inorganic cation [128], and the use of perovskites in tandem cells.

1.4.6 Organic Solar Cells

There exist a wide variety of solar cells that exploit the high absorption coefficients of organic molecules and use heterojunctions to cope with the high binding energies in these molecules. The most relevant among them are DSSCs [129], polymer–fullerene solar cells [130], small-molecule [131] solar cells, and polymer–nanoparticle solar cells [132]. DSSCs use the organic molecule as absorber, an inorganic mesoporous scaffold (typically TiO_2) as electron transporter, and a liquid- or solid-state electrolyte to transport the positive charge (a hole or an ion).

A second option is to merge the functions of absorption and transport of one charge carrier to produce a solar cell made up of two different types of materials, usually termed electron donor and electron acceptor. The electron donor may be a polymer or a highly absorbing small molecule. Originally, polymers were more widely used because they are solution processable (in contrast to many small molecules) and therefore do not require expensive equipment for solar-cell fabrication. However, nowadays, also solution-processable small molecules are used as electron donors [133], in addition to the classical concept of using evaporated small molecules.

The electron acceptor is typically a fullerene. In combination with solution-processable small molecules, fullerenes with side chains are used which are designed to improve the solubility of the fullerene. This allows for mixing the donor and the fullerene in solution and then spin coating or doctor blading the ink on a substrate. In the case of donor materials that have to be evaporated, usually pure C_{60} (without any side chains) is used and evaporated as well. Alternatives for fullerenes are other small molecules or polymers as well as inorganic nanoparticles. None of these concepts have so far been used in the highest

efficient devices. However, especially in the case of nonfullerene small-molecule acceptors, promising efficiencies have already been reached [134].

Independent of which material combination is used, the two types of materials are usually intimately mixed to form a so-called bulk heterojunction. The term bulk heterojunction implies that the bulk of the material consists of a blend of two different molecules or nanoparticles mixed so intimately that any point in the volume is "close" to a heterojunction between the two types of materials. "Close" means that for an efficient device, the heterojunction should be reached within the exciton diffusion length. If this is not the case, the excitons recombine before they are separated into electrons and holes.

Since 2001, organic bulk heterojunction solar cells have seen a steep increase in efficiency (from about 2% to 11%), mainly driven by the optimization of energy levels, in order to maximize light absorption as well as to minimize energy and recombination losses at the heterojunction. Future work will most likely focus on achieving enhanced electrical properties to allow charge extraction from thicker devices and to improve device stability.

1.5 Conclusions

The last 5 years have seen an amazing development in thin-film photovoltaics in terms of efficiency increase, in terms of new material options, and in terms of an improved understanding of processes and devices. This is true for the classical inorganic thin-film devices where, after more than 30 years of research performed, major progress in efficiencies has been demonstrated. Organic solar cells strive toward improved manufacturability. And finally a new class of materials, organic–inorganic metal halides with an unprecedented development of efficiencies, have opened an entirely new window of opportunity.

As a consequence the size of the scientific community concerned with thin-film photovoltaics is still increasing. In addition, more and more specialists for sophisticated physical and chemical analysis methods enter the field, improving our common understanding. Since photovoltaic devices are complex multicomponent systems, the most satisfying answers always will arise from a combination of a solid understanding of the photovoltaic principles with the results from various methods analyzing the electronic, chemical, and structural properties of all the layers and interfaces in the device.

Acknowledgments

The authors would like to thank Dorothea Lennartz for help with the figures. Special thanks are due to Bart Pieters (FZ Jülich) and Stephan Bücheler (EMPA) for discussions on thin-film silicon and CdTe solar cells.

References

1. Shockley, W. and Queisser, H.J. (1961) Detailed balance limit of efficiency of p-n junction solar cells. *J. Appl. Phys.*, **32**, 510.
2. aWürfel, P. (1982) The chemical potential of radiation. *J. Phys. C*, **15**, 3967–3985.
3. Bridgman, P.W. (1928) Note on the principle of detailed balancing. *Phys. Rev.*, **31**, 101.
4. Rau, U. and Werner, J.H. (2004) Radiative efficiency limits of solar cells with lateral band-gap fluctuations. *Appl. Phys. Lett.*, **84**, 3735–3737.
5. Mattheis, J., Werner, J.H., and Rau, U. (2008) Finite mobility effects on the radiative efficiency limit of pn-junction solar cells. *Phys. Rev. B*, **77**, 085203.
6. Rau, U. (2007) Reciprocity relation between photovoltaic quantum efficiency and electroluminescent emission of solar cells. *Phys. Rev. B*, **76**, 085303.
7. Kirchartz, T. and Rau, U. (2008) Detailed balance and reciprocity in solar cells. *Phys. Status Solidi A*, **205**, 2737–2751.
8. Green, M.A. (2002) Lambertian light trapping in textured solar cells and light-emitting diodes: analytical solutions. *Prog. Photovolt. Res. Appl.*, **10**, 235.
9. Mattheis, J. (2008) Mobility and homogeneity effects on the power conversion efficiency of solar cells. Dissertation, Universität Stuttgart. http://elib.uni-stuttgart.de/opus/volltexte/2008/3697/ (accessed 23 February 2010).
10. Tiedje, T., Yablonovitch, E., Cody, G.D., and Brooks, B.G. (1984) Limiting efficiency of silicon solar cells. *IEEE Trans. Electron Devices*, **31**, 711.
11. Würfel, P. (2002) *Physica E*, **14**, 18–26.
12. Green, M.A. (1984) Limits on the open-circuit voltage and efficiency of silicon solar cells imposed by intrinsic Auger processes. *IEEE Trans. Electron Devices*, **31**, 671.
13. Hall, R.N. (1952) Electron–hole recombination in Germanium. *Phys. Rev.*, **87**, 387.
14. Shockley, W. and Read, W.T. (1952) Statistics of the recombinations of holes and electrons. *Phys. Rev.*, **87**, 835.
15. Auger, P. (1925) Sur L'effet photoélectrique composé. *J. Phys. Radium*, **6**, 205.
16. Meitner, L. (1922) Über die β-strahlspektra und ihren zusammenhang mit der γ-strahlung. *Z. Phys. A Hadrons Nucleic*, **11**, 35.
17. Dersch, H., Stuke, J., and Beichler, J. (1981) Light-induced dangling bonds in hydrogenated amorphous silicon. *Appl. Phys. Lett.*, **38**, 456.
18. Tiedje, T., Cebulka, J.M., Morel, D.L., and Abeles, B. (1981) Evidence for exponential band tails in amorphous silicon hydride. *Phys. Rev. Lett.*, **46**, 1425.
19. Schiff, E.A. (1981) Trap-controlled dispersive transport and exponential band tails in amorphous silicon. *Phys. Rev. B*, **24**, 6189.
20. Fedders, P.A., Drabold, D.A., and Nakhmanson, S. (1998) Theoretical study on the nature of band tail states in amorphous Si. *Phys. Rev. B*, **58**, 15624.
21. Poortmans, J. and Arkhipov, V. (eds) (2006) *Thin Film Solar Cells – Fabrication, Characterization and Applications*, John Wiley & Sons, Ltd, Chichester.
22. Hamakawa, Y. (ed) (2004) *Thin-Film Solar Cells: Next Generation Photovoltaics and Its Applications*, Springer, Berlin.
23. Chopra, K.L., Paulson, P.D., and Dutta, V. (2004) Thin-film solar cells: an overview. *Prog. Photovolt. Res. Appl.*, **12**, 69.
24. Siebentritt, S. and Rau, U. (eds) (2006) *Wide-Gap Chalcopyrites*, Springer, Berlin.
25. Rau, U. and Schock, H.W. (2015) Cu(in,Ga)Se_2 and related solar cells, in *Clean Electricity from Photovoltaics*, 2nd edn (eds M.D. Archer and M.A. Green), Imperial College Press, London, p. 245.

26. Jaegermann, W., Klein, A., and Mayer, T. (2009) Interface engineering of inorganic thin-film solar cells – materials-science challenges for advanced physical concepts. *Adv. Mater.*, **21**, 4196.
27. Street, R.A. (1991) *Hydrogenated Amorphous Silicon*, Cambridge University Press.
28. Ballif, C., Despeisse, M., and Haug, F.-J. (2015) Thin-film solar cells based on amorphous and microcrystalline silicon, in *Clean Electricity from Photovoltaics*, 2nd edn (eds M.D. Archer and M.A. Green), Imperial College Press, London, p. 139.
29. Zeman, M. and Schropp, R.E.I. (1998) *Amorphous and Microcrystalline Silicon Solar Cells: Modeling, Materials and Device Technology*, Kluwer Academic Publishers, Norwell.
30. Shah, A.V., Schade, H., Vanecek, M., Meier, J., Vallat-Sauvain, E., Wyrsch, N., Kroll, U., Droz, C., and Bailat, J. (2004) Thin-film silicon solar cell technology. *Prog. Photovolt. Res. Appl.*, **12**, 113.
31. Schropp, R.E.I., Carius, R., and Beaucarne, G. (2007) Amorphous silicon, microcrystalline silicon, and thin-film polycrystalline silicon solar cells. *MRS Bull.*, **32**, 219.
32. Deng, X. and Schiff, E.A. (2003) Measurement amorphous silicon-based solar cells, in *Handbook of Photovoltaic Science and Engineering* (eds A. Luque and S. Hegedus), John Wiley & Sons, Ltd, Chichester, p. 505.
33. Baranovski, S. (ed) (2006) *Charge Transport in Disordered Solids – With Applications in Electronics*, John Wiley & Sons, Ltd, Chichester.
34. Ito, K. (2014) *Copper Zinc Tin Sulfide-Based Thin-Film Solar Cells*, John Wiley & Sons, Ltd, Chichester.
35. Siebentritt, S. and Schorr, S. (2012) Kesterites – a challenging material for solar cells. *Prog. Photovolt. Res. Appl.*, **20**, 512.
36. Stranks, S.D. and Snaith, H.J. (2015) Metal-halide perovskites for photovoltaic and light-emitting devices. *Nat. Nanotechnol.*, **10**, 391.
37. Green, M.A., Ho-Baillie, A., and Snaith, H.J. (2014) The emergence of perovskite solar cells. *Nat. Photonics*, **8**, 506.
38. Credgington, D. (2015) Organic photovoltaics, in *Clean Electricity from Photovoltaics*, 2nd edn (eds M.D. Archer and M.A. Green), Imperial College Press, London, p. 339.
39. Reynolds, D.C., Leies, G., Antes, L.L., and Marburger, R.E. (1954) Photovoltaic effect in cadmium sulfide. *Phys. Rev.*, **96**, 533.
40. Böer, K.W. (1976) Photovoltaic effect in CdS-Cu_2S heterojunctions. *Phys. Rev. B*, **13**, 5373.
41. Böer, K.W. and Rothwarf, A. (1976) Materials for solar photovoltaic energy conversion. *Annu. Rev. Mater. Sci.*, **6**, 303.
42. Pfisterer, F. (2003) The wet-topotaxial process of junction formation and surface treatments of Cu_2S–CdS thin-film solar cells. *Thin Solid Films*, **431–432**, 470.
43. Migliorato, P., Tell, B., Shay, J.L., and Kasper, H.M. (1974) Junction electroluminescence in $CuInSe_2$. *Appl. Phys. Lett.*, **24**, 227.
44. Wagner, S., Shay, J.L., Migliorato, P., and Kasper, H.M. (1974) $CuInSe_2$/CdS heterojunction photovoltaic detectors. *Appl. Phys. Lett.*, **25**, 434.
45. Shay, J.L., Wagner, S., and Kasper, H.M. (1975) Efficient $CuInSe_2$/CdS solar cells. *Appl. Phys. Lett.*, **27**, 89.
46. Jackson, P., Hariskos, D., Wuerz, R., Kiowski, O., Bauer, A., Friedlmeier, T.M., and Powalla, M. (2015) Properties of Cu(In,Ga)Se_2 solar cells with new record efficiencies up to 21.7%. *Phys. Status Solidi RRL*, **9**, 28.
47. Mickelsen, R.A. and Chen, W.S. (1980) High photocurrent polycrystalline thin-film CdS/$CuInSe_2$ solar cell. *Appl. Phys. Lett.*, **36**, 371–373.
48. Gabor, A.M., Tuttle, J.R., Albin, D.S., Contreras, M.A., Noufi, R., Jensen, D.G., and Hermann, A.M. (1994) High-efficiency $CuIn_xGa_{1-x}Se_2$ solar cells from $(In_xGa_{1-x})_2Se_3$ precursors. *Appl. Phys. Lett.*, **65**, 198–200.
49. Binsma, J.J.M. and Van der Linden, H.A. (1982) Preparation of thin $CuInS_2$

films via a two-stage process. *Thin Solid Films*, **97**, 237–243.

50. Probst, V., Karg, F., Rimmasch, J., Riedl, W., Stetter, W., Harms, H., and Eibl, O. (1996) Advanced stacked elemental layer progress for Cu(InGa)Se_2 thin film photovoltaic devices. *Mat. Res. Soc. Symp. Proc.*, **426**, 165–176.
51. Stolt, L., Hedström, J., Kessler, J., Ruckh, M., Velthaus, K.O., and Schock, H.W. (1993) ZnO/CdS/$CuInSe_2$ thin-film solar cells with improved performance. *Appl. Phys. Lett.*, **62**, 597–599.
52. Holz, J., Karg, F., and von Phillipsborn, H. (1994) *The Effect of Substrate Impurities on the Electronic Conductivity in CIGS Thin Films*. Proceedings of the 12th European Photovoltaic Solar Energy Conference, Amsterdam. H. S. Stephens & Associates, Bedford, pp. 1592–1595.
53. Nakada, T., Iga, D., Ohbo, H., and Kunioka, A. (1997) Effects of sodium on Cu(In,Ga)Se_2-based thin films and solar cells. *Jpn. J. Appl. Phys.*, **36**, 732–737.
54. Rocket, A. (2005) The effect of Na in polycrystalline and epitaxial single-crystal $CuIn_{1-x}Ga_xSe_2$. *Thin Solid Films*, **480**, 2–7.
55. Siebentritt, S., Igalson, M., Persson, C., and Lany, S. (2010) The electronic structure of chalcopyrite-bands, point defects and grain boundaries. *Prog. Photovolt. Res. Appl.*, **18**, 390.
56. Dirnstorfer, I., Wagner, M., Hofmann, D.M., Lampert, M.D., Karg, F., and Meyer, B.K. (1998) Characterization of CuIn(Ga)Se_2 thin films – II. In-rich layers. *Phys. Status Solidi A*, **168**, 163–175.
57. Bauknecht, A., Siebentritt, S., Albert, J., and Lux-Steiner, M.C. (2001) Radiative recombination via intrinsic defects in $Cu_xGa_ySe_2$. *J. Appl. Phys.*, **89**, 4391–4400.
58. Rau, U., Schmitt, M., Parisi, J., Riedl, W., and Karg, F. (1998) Persistent photoconductivity in Cu(In,Ga)Se_2 heterojunctions and thin films prepared by sequential deposition. *Appl. Phys. Lett.*, **73**, 223–225.
59. Lany, S. and Zunger, A. (2008) Intrinsic DX centers in ternary chalcopyrite semiconductors. *Phys. Rev. Lett.*, **100**, 016401.
60. Rau, U., Taretto, K., and Siebentritt, S. (2009) Grain boundaries in Cu(In,Ga)$(Se,S)_2$ thin-film solar cells. *Appl. Phys. A*, **96**, 221–234.
61. Schmid, D., Ruckh, M., Grunwald, F., and Schock, H.W. (1993) Chalcopyrite/defect chalcopyrite heterojunctions on basis of $CuInSe_2$. *J. Appl. Phys.*, **73**, 2902–2909.
62. Morkel, M., Weinhardt, L., Lohmüller, B., Heske, C., Umbach, E., Riedl, W., Zweigart, S., and Karg, F. (2001) Flat conduction-band alignment at the CdS/$CuInSe_2$ thin-film solar-cell heterojunction. *Appl. Phys. Lett.*, **79**, 4482–4484.
63. Dullweber, T., Hanna, G., Rau, U., and Schock, H.W. (2001) A new approach to high-efficiency solar cells by band gap grading in Cu(In,Ga)Se_2 chalcopyrite semiconductors. *Sol. Energy Mater. Sol. Cells*, **67**, 1–4.
64. Turcu, M., Pakma, O., and Rau, U. (2002) Interdependence of absorber composition and recombination mechanism in Cu(In,Ga)$(Se,S)_2$ heterojunction solar cells. *Appl. Phys. Lett.*, **80**, 2598–2600.
65. Kötschau, I.M. and Schock, H.W. (2003) Depth profile of the lattice constant of the Cu-poor surface layer in $(Cu_2Se)_{1-x}(In_2Se_3)_x$, evidenced by grazing incidence X-ray diffraction. *J. Phys. Chem. Solids*, **64**, 1559–1563.
66. Nguyen, Q., Orgassa, K., Koetschau, I., Rau, U., and Schock, H.W. (2003) Influence of heterointerfaces on the performance of Cu(In,Ga)Se_2 solar cells with CdS and $In(OH_x,S_y)$ buffer layers. *Thin Solid Films*, **431**, 330–334.
67. Weinhardt, L., Heske, C., Umbach, E., Niesen, T.P., Visbeck, S., and Karg, F. (2004) Band alignment at the i-ZnO/CdS interface in Cu(In,Ga)$(S,Se)_2$ thin-film solar cells. *Appl. Phys. Lett.*, **84**, 3175–3177.
68. Hariskos, D., Spiering, S., and Powalla, M. (2005) Buffer layers in Cu(In,Ga)Se-2 solar cells and modules. *Thin Solid Films*, **480**, 99–109.

69. Nakada, T. and Mizutani, M. (2002) 18% efficiency Cd-free Cu(In, Ga)Se_2 thin-film solar cells fabricated using chemical bath deposition (CBD)-ZnS buffer layers. *Jpn. J. Appl. Phys.*, **41**, L165–L167.
70. Hariskos, D., Fuchs, B., Menner, R., Naghavi, N., Hubert, C., Lincot, D., and Powalla, M. (2009) The Zn(S,O,OH)/ZnMgO buffer in thin-film Cu(In,Ga)$(Se,S)_2$-based solar cells part II: magnetron sputtering of the ZnMgO buffer layer for in-line co-evaporated Cu(In,Ga)Se_2 solar cells. *Prog. Photovolt. Res. Appl.*, **17**, 479–488.
71. Cusano, D.A. (1963) CdTe solar cells and photovoltaic heterojunctions in II–VI compounds. *Solid State Electron.*, **6**, 217.
72. Bonnet, D. (2004) *The Evolution of the CdTe Thin Film Solar Cell*. Proceedings of the European Photovoltaic Solar Energy Conference, June 2004, Paris. WIP Renewable Energies, Munich, p. 1657.
73. Bonnet, D. and Rabenhorst, H. (1972) *New Results on the Development of a Thin Film p-CdTe/n-CdS Heterojunction Solar Cell*. Proceedings of the 9th IEEE Photovoltaic Specialists Conference, May 1972, Silver Springs, MD. IEEE, New York.
74. First Solar, Inc. (2015) First solar achieves efficiency, durability milestones. Press release, February 15. http://investor.firstsolar.com/releasedetail.cfm?ReleaseID=895118 (accessed 23 February 2016).
75. http://www.ise.fraunhofer.de/de/downloads/pdf-files/aktuelles/photovoltaics-report-in-englischer-sprache.pdf.
76. McCandless, B.E., Qu, Y., and Birkmire, R.W. (1994) *A Treatment to Allow Contacting CdTe with Different Conductors*. Proceedings of the 24th IEEE Photovoltaic Specialists Conference. December 1994, Waikoloa, Hawaii, IEEE pp. 107–110.
77. Moutinho, H.R., Al-Jassim, M.M., Levi, D.H., Dippo, P.C., and Kazmerski, L.L. (1998) Effects of $CdCl_2$ treatment on the recrystallization and electro-optical properties of CdTe thin films. *J. Vac. Sci. Technol.*, **16**, 1251–1257.
78. Dobson, K.D., Visoly-Fischer, I., Hodes, G., and Cahen, D. (2000) Stability of CdTe/CdS thin-film solar cells. *Sol. Energy Mater. Sol. Cells*, **62**, 295–325.
79. Romeo, N., Bosio, A., Canevari, V., and Podesta, A. (2005) Recent progress on CdTe/CdS thin film solar cells. *Sol. Energy*, **77**, 795–801.
80. Bätzner, D.L., Romeo, A., Zogg, H., Tiwari, A.N., and Wendt, R. (2000) *Thin Solid Films*, **361–362**, 463–467.
81. Kranz, L., Gretener, C., Perrenoud, J., Schmitt, R., Pianezzi, F., La Mattina, F., Blösch, P., Cheah, E., Chirila, A., Fella, C.M., Hagendorfer, H., Jäger, T., Nishiwaki, S., Uhl, A.R., Buecheler, S., and Tiwari, A.N. (2013) Doping of polycrystalline CdTe for high-efficiency solar cells on flexible metal foil. *Nat. Commun.*, **4**, 2306–2312.
82. Fritsche, J., Kraft, D., Thissen, A., Mayer, T., Klein, A., and Jaegermann, W. (2002) Band energy diagram of CdTe thin film solar cells. *Thin Solid Films*, **403–404**, 252–257.
83. Visoly-Fisher, I., Cohen, S.R., Gartsman, K., Ruzin, A., and Cahen, D. (2006) Understanding the beneficial role of grain boundaries in polycrystalline solar cells from single-grain-boundary scanning probe microscopy. *Adv. Funct. Mater.*, **16**, 649–660.
84. Schorr, S. (2014) Crystallographic aspects of Cu_2ZnSnS_4 (CZTS), in *Copper Zinc Tin Sulfide-Based Thin-Film Solar Cells* (ed K. Ito), John Wiley & Sons, Ltd, Chichester.
85. Adachi, S. (2014) Physical properties, in *Copper Zinc Tin Sulfide-Based Thin-Film Solar Cells* (ed K. Ito), John Wiley & Sons, Ltd, Chichester.
86. Shin, B., Gunawan, O., Zhu, Y., Bojarczuk, N.A., Chey, S.J., and Guha, S. (2011) Thin film solar cell with 8.4% power conversion efficiency using an earth-abundant Cu_2ZnSnS_4 absorber. *Prog. Photovolt. Res. Appl.*, **21**, 72.
87. Repins, I., Beall, C., Vora, N., DeHart, C., Kuciauskas, D., Dippo, P., To, B., Mann, J., Hsu, W.C., Goodrich, A., and Noufi, R. (2012) Co-evaporated

$Cu_2ZnSnSe_4$ films and devices. *Sol. Energy Mater. Sol. Cells*, **101**, 154.

88. Wang, W., Winkler, M.T., Gunawan, O., Gokmen, T., Todorov, T.K., Zhu, Y., and Mitzi, D.B. (2014) Device characteristics of CZTSSe thin film solar cell with 12.6% efficiency. *Adv. Energy Mater.*, **4**, 1301465.
89. Dudchak, I.V. and Piskach, L.V. (2003) Phase equilibria in the $Cu_2SnSe_3 - SnSe_2 - ZnSe$ system. *J. Alloys Compd.*, **351**, 145.
90. Olekseyuk, I.D., Dudchak, I.V., and Piskach, L.V. (2004) Phase equilibria in the $Cu_2S - ZnS - SnS_2$ system. *J. Alloys Compd.*, **368**, 135.
91. Siebentritt, S. (2013) Why are kesterite solar cells not 20% efficient? *Thin Solid Films*, **535**, 1.
92. Pieters, B.E., Stiebig, H., Zeman, M., and van Swaaij, R.A.C.M. (2009) Determination of the mobility gap of μc-Si:H in pin solar cells. *J. Appl. Phys.*, **105**, 044502.
93. Street, R.A. (1991) *Hydrogenated Amorphous Silicon*, Cambridge University Press, pp. 363–403.
94. Chapin, D.M., Fuller, C.S., and Pearson, G.L. (1954) A new silicon p–n junction photocell for converting solar radiation into electrical power. *J. Appl. Phys.*, **25**, 676.
95. Carlson, D.E. and Wronski, C.R. (1976) Amorphous silicon solar cell. *Appl. Phys. Lett.*, **28**, 671.
96. Chittick, R.C., Alexander, J.H., and Sterling, H.F. (1969) The preparation and properties of amorphous silicon. *J. Electrochem. Soc.*, **116**, 77.
97. Spear, W.E. and LeComber, P.G. (1975) Substitutional doping of amorphous silicon. *Solid State Commun.*, **17**, 1193.
98. Zeman, M. (2006) Advanced amorphous silicon solar cell technology, in *Thin Film Solar Cells – Fabrication, Characterization and Applications* (eds J. Poortmans and V. Arkhipov), John Wiley & Sons, Ltd, Chichester, p. 204.
99. Staebler, D.L. and Wronski, C.R. (1977) Reversible conductivity changes in discharge-produced amorphous Si. *Appl. Phys. Lett.*, **31**, 292.
100. de Walle, C.G.V. and Street, R.A. (1995) Silicon–hydrogen bonding and hydrogen diffusion in amorphous silicon. *Phys. Rev. B*, **51**, 10615.
101. Stutzmann, M., Jackson, W.B., and Tsai, C.C. (1986) Annealing of metastable defects in hydrogenated amorphous silicon. *Phys. Rev. B*, **34**, 63.
102. Powell, M.J., Deane, S.C., and Wehrspohn, R.B. (2002) Microscopic mechanisms for creation and removal of metastable dangling bonds in hydrogenated amorphous silicon. *Phys. Rev. B*, **66**, 155212.
103. Branz, H. (1999) Hydrogen collision model: quantitative description of metastability in amorphous silicon. *Phys. Rev. B*, **59**, 5498.
104. Veprek, S., Marecek, V., and Anna Selvan, J.A. (1968) The preparation of thin layers of Ge and Si by chemical hydrogen plasma transport. *Solid State Electron.*, **11**, 683.
105. Usui, S. and Kikuchi, M. (1979) Properties of heavily doped GD-Si with low resistivity. *J. Non-Cryst. Sol.*, **34**, 1.
106. Kroll, U., Meier, J., Keppner, H., Littlewood, S.D., Kelly, I.E., Giannoulès, P., and Shah, A. (1995) Origin and incorporation mechanism for oxygen contaminants in a-Si:H and mc-Si:H films prepared by the very high frequency (70 MHz) glow discharge technique. *Mater. Res. Soc. Symp. Proc.*, **377**, 39.
107. Kroll, U., Meier, J., Keppner, H., Littlewood, S.D., Kelly, I.E., Giannoulès, P., and Shah, A. (1995) Origins of atmospheric contamination in amorphous silicon prepared by very high frequency (70 MHz) glow discharge. *J. Vac. Sci. Technol, A*, **13**, 2742.
108. Torres, P., Meier, J., Flückiger, R., Kroll, U., Selvan, J.A.A., Keppner, H., Shah, A., Littlewood, S.D., Kelly, I.E., and Giannoulès, P. (1996) Device grade microcrystalline silicon owing to reduced oxygen contamination. *Appl. Phys. Lett.*, **69**, 1373.
109. Meier, J., Dubail, S., Flückiger, R., Fischer, D., Keppner, H., and Shah, A. (1994) *Intrinsic Microcrystalline Silicon – A Promising New Thin Film Solar Cell Material*. Proceedings of the

1st World Conference on Photovoltaic Energy Conversion, December 1994, Hawaii, IEEE Hawaii. p. 409.

110. Flückiger, R. (1995) Microcrystalline silicon thin-films deposited by VHF plasma for solar cell applications. PhD thesis. Institute of Microtechnology, University of Neuchatel.

111. Green, M.A. (2001) Third generation photovoltaics: ultra-high conversion efficiency at low cost. *Prog. Photovolt. Res. Appl.*, **9**, 123.

112. Henry, C.H. (1980) Limiting efficiencies of ideal single and multiple energy gap terrestrial solar cells. *J. Appl. Phys.*, **51**, 4494.

113. de Vos, A. (1980) Detailed balance limit of the efficiency of tandem solar cells. *J. Phys. D: Appl. Phys.*, **13**, 839.

114. Coutts, T.J., Ward, J.S., Young, D.L., Emery, K.A., Gessert, T.A., and Noufi, R. (2003) Critical issues in the design of polycrystalline, thin-film tandem solar cells. *Prog. Photovolt. Res. Appl.*, **11**, 359.

115. Varlamov, S., Dore, J., Evans, R., Ong, D., Eggleston, B., Kunz, O., Schubert, U., Young, T., Huang, J., Soderstrom, T., Omaki, K., Kim, K., Teal, A., Jung, M., Yun, J., Pakhuruddin, Z.M., Egan, R., and Green, M.A. (2013) Polycrystalline silicon on glass thin-film solar cells: a transition from solid-phase to liquid-phase crystallised silicon. *Sol. Energy Mater. Sol. Cells*, **119**, 246–255.

116. Becker, C., Amkreutz, D., Sontheimer, T., Preidel, V., Lockau, D., Haschke, J., Jogschies, L., Klimm, C., Merkel, J.J., Plocica, P., Steffens, S., and Rech, B. (2013) Polycrystalline silicon thin-film solar cells: status and perspectives. *Sol. Energy Mater. Sol. Cells*, **119**, 112–123.

117. Haschke, J., Amkreutz, D., Korte, L., Ruske, F., and Rech, B. (2014) Towards wafer quality crystalline silicon thin-film solar cells on glass. *Sol. Energy Mater. Sol. Cells*, **128**, 190–197.

118. Kojima, A., Teshima, K., Shirai, Y., and Miyasaka, T. (2009) Organometal halide perovskites as visible-light sensitizers for photovoltaic cells. *J. Am. Chem. Soc.*, **131**, 6050.

119. Ball, J.M., Lee, M.M., Hey, A., and Snaith, H.J. (2013) Low-temperature processed meso-superstructured to thin-film perovskite solar cells. *Energy Environ. Sci.*, **6**, 1739.

120. De Wolf, S., Holovsky, J., Moon, S.-J., Löper, P., Niesen, B., Ledinsky, M., Haug, F.-J., Yum, J.-H., and Ballif, C. (2014) Organometallic halide perovskites: sharp optical absorption edge and its relation to photovoltaic performance. *J. Phys. Chem. Lett.*, **5**, 1035.

121. Yang, W.S., Noh, J.H., Jeon, N.J., Kim, Y.C., Ryu, S., Seo, J., and Seok, S.I. (2015) High-performance photovoltaic perovskite layers fabricated through intramolecular exchange. *Science*, **348**, 1234.

122. Ahn, N., Son, D.-Y., Jang, I.-H., Kang, S.M., Choi, M., and Park, N.-G. (2015) Highly reproducible perovskite solar cells with average efficiency of 18.3% and best efficiency of 19.7% fabricated via Lewis base adduct of lead(II) iodide. *J. Am. Chem. Soc.*, **137**, 8696.

123. Wehrenpfennig, C., Eperon, G.E., and Johnston, M.B. (2014) High charge carrier mobilities and lifetimes in organolead trihalide perovskites. *Adv. Mater.*, **26**, 1584.

124. Yin, W.-J., Shi, T., and Yan, Y. (2014) Unusual defect physics in $CH_3NH_3PbI_3$ perovskite solar cell absorber. *Appl. Phys. Lett.*, **104**, 063903.

125. Tvingstedt, K., Malinkiewicz, O., Baumann, A., Deibel, C., Snaith, H.J., Dyakonov, V., and Bolink, H.J. (2014) Radiative efficiency of lead iodide based perovskite solar cells. *Sci. Rep.*, **4**, 6071.

126. Xiao, Z., Yuan, Y., Shao, Y., Wang, Q., Dong, Q., Bi, C., Sharma, P., Gruverman, A., and Huang, J. (2015) Giant switchable photovoltaic effect in organometal trihalide perovskite devices. *Nat. Mater.*, **14**, 193.

127. Snaith, H.J., Abate, A., Ball, J.M., Eperon, G.E., Leijtens, T., Noel, N.K., Stranks, S.D., Wang, J.T.-W., Wojciechowski, K., and Zhang, W. (2014) Anomalous hysteresis in perovskite solar cells. *J. Phys. Chem. Lett.*, **5**, 1511.

128. Boix, P.P., Agarwala, S., Koh, T.M., Mathews, N., and Mhaisalkar, S.G. (2015) Perovskite solar cells: beyond

methylammonium lead iodide. *J. Phys. Chem. Lett.*, **6**, 898.

129. O'Reagen, B. and Gratzel, M. (1999) A low-cost, high-efficiency solar cell based on dye-sensitized colloidal TiO_2 films. *Nature*, **353**, 737.

130. Yu, G., Gao, J., Hummelen, J.C., Wudl, F., and Heeger, A.J. (1995) Polymer photovoltaic cells: enhanced efficiencies via a network of internal donor–acceptor heterojunctions. *Science*, **270**, 1789.

131. Peumans, P., Uchida, S., and Forrest, S.R. (2003) Efficient bulk heterojunction photovoltaic cells using small-molecular-weight organic thin films. *Nature*, **425**, 158.

132. Huynh, W.U., Dittmer, J.J., and Alivisatos, A.P. (2002) Hybrid nanorod-polymer solar cells. *Science*, **295**, 2425.

133. Sun, Y., Welch, G.C., Leong, W.L., Takacs, C.J., Bazan, G.C., and Heeger, A.J. (2012) Solution-processed small-molecule solar cells with 6.7% efficiency. *Nat. Mater.*, **11**, 44.

134. Cnops, K., Rand, B.P., Cheyns, D., Verreet, B., Empl, M.A., and Heremans, P. (2014) 8.4% efficient fullerene-free organic solar cells exploiting long-range exciton energy transfer. *Nat. Commun.*, **5**, 3406.

Part II
Device Characterization

Advanced Characterization Techniques for Thin Film Solar Cells, Second Edition.
Edited by Daniel Abou-Ras, Thomas Kirchartz, and Uwe Rau.

2
Fundamental Electrical Characterization of Thin-Film Solar Cells

Thomas Kirchartz, Kaining Ding, and Uwe Rau

2.1
Introduction

This chapter discusses device characterization methods, that is, methods to determine the response of a solar cell to optical and electrical excitation. Thus, device characterization deals directly with the finished product and is, thus, directly related to the final goal of all research efforts, namely, to produce an efficient solar cell. However, since the device is characterized as a whole, the interpretation of device measurements is complex because a large number of optical and electronic effects contribute to a relatively featureless result like the current/voltage characteristics. Thus, the challenge of device characterization lies not only in the measurement of the samples but mostly in the interpretation of data, which often goes hand in hand with device simulation as described in the third part of this book.

A variety of device characterization methods are conceivable. The current of a solar cell can be measured as a function of applied voltage, illumination intensity, wavelength of monochromatic illumination, illumination position, and sample temperature. In addition, the solar cell can be used as a light-emitting diode and its emission can be detected as a function of position, temperature, and photon wavelength. Finally, devices can be measured as a function of time after an electrical or optical excitation or as a function of the frequency of an applied alternating voltage. Part Two of this book will deal with these characterization methods in five chapters, while this chapter will restrict itself to the most fundamental characterization methods, that is, methods where the current of a solar cell is measured in response to a variety of illumination conditions and as a function of the applied voltage. Especially the measurement of the illuminated current/voltage (J/V) curves under standard measuring conditions is of crucial importance for determination and comparison of the efficiency of the optoelectrical energy conversion process.

Advanced Characterization Techniques for Thin Film Solar Cells, Second Edition.
Edited by Daniel Abou-Ras, Thomas Kirchartz, and Uwe Rau.

2.2
Current/Voltage Curves

2.2.1
Shape of Current/Voltage Curves and Their Description with Equivalent Circuit Models

In Chapter 1, the concept of the illuminated J/V curve and its basic features have already been discussed. We started our discussion on J/V curves with the ideal solar cell in the Shockley–Queisser limit [1]. In this case, thermodynamic arguments lead to a J/V curve of the form

$$J = J_0 \left[\exp\left(\frac{qV}{kT}\right) - 1 \right] - J_{sc}, \tag{2.1}$$

where kT/q is the thermal voltage. A J/V curve of such a shape – however with different values for the saturation current density J_0 and the short-circuit current density J_{sc} – follows also from a device simulation of a p–n-junction or p–i–n-junction solar cell as described in Chapter 23 as long as the recombination rate R is proportional to the product of electron and hole concentration ($R \propto np$) and as long as the carrier mobilities are sufficiently high to extract all charge carriers at all considered voltages. In this case, the recombination current density J_{rec} which is equal per definition to the dark current density J_d is simply

$$\begin{aligned} J_{rec} = J_d &= q\int_0^d R \; \mathrm{d}x = q\int_0^d B(np - n_i^2)\mathrm{d}x = qBn_i^2 d \left[\exp\left(\frac{qV}{kT}\right) - 1 \right] \\ &= J_0 \left[\exp\left(\frac{qV}{kT}\right) - 1 \right]. \end{aligned} \tag{2.2}$$

The requirement of sufficiently high mobilities means also that the quasi-Fermi levels will be flat and that it will be reasonable to assume $np = n_i^2 \exp[qV/(kT)]$ throughout the whole device thickness d, where n_i is the intrinsic carrier concentration. In the following, this will be illustrated by numerical simulations. Figure 2.1a and b shows the simulated dark and illuminated J/V curve of such an idealized device in the case when only radiative recombination is considered. The simulated device has a thick (2.5 µm) p-type layer and a thin (200 nm) n-type layer as is typical for most p–n-junction solar cells. The dark current density J_d is a simple exponential function with a slope of q/kT as rationalized from Equation 2.2 and the illuminated current density J_{il} is shifted by the value J_{sc} into the fourth quadrant of the coordinate system. Thus, the difference $J_{ph} = J_{il} - J_d$ between illuminated and dark J/V curve, the photocurrent, equals always the short-circuit current density J_{sc}.

Although a simple description of the J/V curve as in Equation 2.1 represents the main characteristics of most solar cell J/V curves, the reality looks slightly different in several respects. The first typical feature of any p–n-junction solar cell is shown in Figure 2.1c and d. Typically, the dominant recombination mechanism is not radiative recombination, and thus, the recombination rate does not scale directly with the np product. Instead, the typical recombination mechanism in

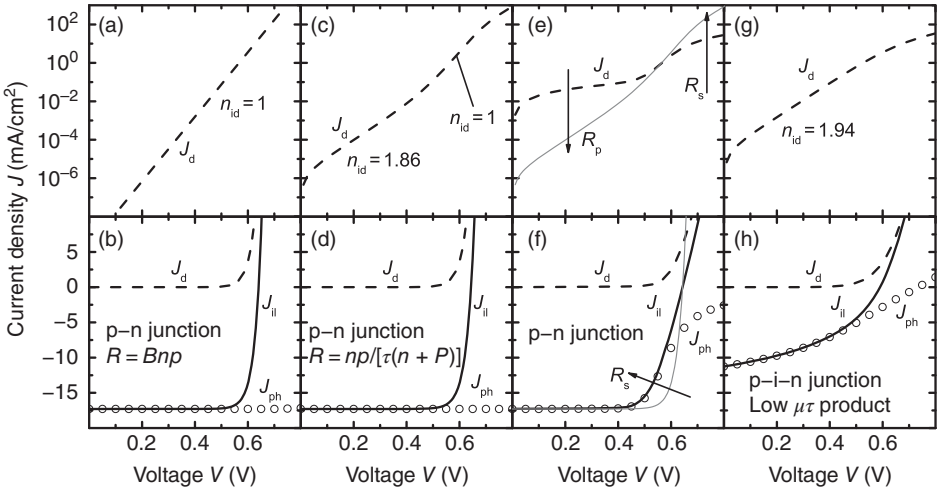

Figure 2.1 Semilogarithmic plots (a, c, e, g) of dark *J*/*V* characteristics and linear plots (b, d, f, h) of dark (dashed lines) and illuminated (full lines) *J*/*V* characteristics as well as of the difference $J_{ph} = J_{il} - J_d$ (open circles). In (a, b) the characteristics of a p–n-junction diode resulting from radiative recombination is shown leading to an ideal slope of the dark *J*/*V* with an ideality $n_{id} = 1$ and a voltage-independent photocurrent. (c, d) illustrate the departure from an ideal diode law in case of typical p–n-junction solar cells, where the low-energy part of the dark *J*/*V* features a second slope with a higher ideality factor $n_{id} = 1.86$ which originates from SRH recombination in the space charge region. (e, f) illustrate the addition of a series and parallel resistance with the gray line representing the case with $R_s = 0$ and $R_p = \infty$ for reference. Note that J_{ph} is voltage dependent despite the fact that carriers are efficiently collected. This can be used to determine the series resistance. (g, h) show a p–i–n junction with a low mobility-lifetime product and a subsequently strongly voltage-dependent photocurrent J_{ph}.

thin-film solar cells is Shockley–Read–Hall recombination [2, 3] via defects in the band gap. Assuming a defect in the middle of the band gap, the recombination rate scales with

$$R = \frac{np - n_i^2}{(n + p)\tau}, \tag{2.3}$$

where τ is the lifetime of electrons and holes, which we assume to be equal. Assuming such a recombination rate and a p–n-junction solar cell, the dark J/V curve as shown in Figure 2.1c differs considerably from the one for radiative recombination (Figure 2.1a). In addition to the voltage range $0.5\,\mathrm{V} < V < 0.7\,\mathrm{V}$, where the slope of the curve is q/kT, the slope is considerably smaller at lower voltages $V < 0.5\,\mathrm{V}$. At lower voltages, the recombination in the space charge region is dominant. Within the space charge region of a p–n junction (and similarly within the intrinsic layer of a p–i–n junction), the ratio of the carrier concentrations changes from $p \gg n$ (toward the p side) to $n \gg p$ (toward the n side). The maximum of the recombination rate R in Equation 2.3 is always found

within the junction for $n = p$, leading to

$$R(n = p) = \frac{np - n_i^2}{(n + p)\tau} \approx \frac{n}{2\tau} = \frac{\sqrt{np}}{2\tau}. \tag{2.4}$$

Assuming flat quasi-Fermi levels throughout the space charge region, the product np is proportional to $\exp(qV/kT)$, where the internal voltage V is the quasi-Fermi-level splitting (divided by the elementary charge). Thus, the recombination rate scales via

$$R(n = p) \propto \sqrt{\exp\left(\frac{qV}{kT}\right)} = \exp\left(\frac{qV}{2kT}\right) \tag{2.5}$$

with the internal voltage V. Obviously, the slope of the recombination rate and subsequently also the slope of the recombination current are now around $q/2kT$. We call this factor 2 in the denominator of the exponent in Equation 2.5 the ideality factor n_{id}, sometimes also the diode quality factor. When comparing this value with the according simulation in Figure 2.1c, we see that the actual value of the ideality factor is slightly smaller, that is, $n_{id} = 1.86$ at lower voltages, which is due to the fact that $n = p$ is only a limiting situation, which is exactly valid only at one position in the space charge region. The integration over the recombination in the space charge region then gives an ideality factor slightly smaller than 2 with an exact value that depends on the details of thicknesses, doping concentrations, and electrical parameters of the device.

An alternative explanation for ideality factors $1 < n_{id} < 2$ in thin-film solar cells can be Shockley–Read–Hall recombination via band tails [4] or other distributions of localized states in the band gap as described in Chapter 23. The explanation of $n_{id} > 2$ is not possible by considering recombination via a single recombination center. A multistep recombination process via a series of trap states distributed in space and energy would explain such large ideality factors for a recombination process situated in the space charge region [5]. This model is especially suited to describe the dependence of the ideality factor of CdS/CdTe heterojunction solar cells. Also the enhancement of recombination by tunneling – a process that makes the recombination rate dependent on the local electric field and, in consequence, from the applied bias voltage – predicts ideality factors that may exceed 2 [6]. This theory of tunneling-enhanced recombination especially applies to $Cu(In,Ga)Se_2$ with high Ga content or $CuGaSe_2$ solar cells [7].

The preceding discussion made clear that the ideality factor is strongly influenced by the recombination mechanism. However, the unique identification of recombination mechanisms via the ideality factor alone is not possible. Turning back to the simulations, we notice that at higher voltages, the ideality factor of the dark J/V curve in Figure 2.1c is again 1, as in Figure 2.1a, although the recombination mechanism is different. This is due to the fact that for the example in Figure 2.1c the recombination for voltages $V > 0.5$ V is dominated by recombination in the p-type layer of the p–n junction (which is assumed to be much thicker than the n-type layer). In the p-type layer in the dark and for not too high voltages,

the electron concentration is much smaller than the hole concentration ($n \ll p$). Simplifying Equation 2.3 yields

$$R(n \ll p) = \frac{np - n_i^2}{(n+p)\tau} \approx \frac{n}{\tau}. \tag{2.6}$$

Since the whole internal voltage V is now used to increase the minority carrier concentration,

$$R(n \ll p) \approx \frac{n}{\tau} \propto \exp\left(\frac{qV}{kT}\right) \tag{2.7}$$

holds. Obviously, the ideality factor is again unity, also for recombination via defects, as long as the concentration of one type of carrier is much smaller than the concentration of the other. With the same argument, also the recombination at surfaces of p–n junctions or p–i–n junctions will lead to ideality factors of one, since at the contacts usually $n \gg p$ or $p \gg n$ is fulfilled.

For p–n-junction solar cells, there are typically two voltage ranges with different ideality factors as shown in Figure 2.1c. At lower voltages, the ideality factor is close to but smaller than 2 (if multistep recombination or tunneling is absent), and the recombination is dominated by the space charge region. For higher voltages, the ideality factor is close to 1 indicating defect recombination in the volume or the surfaces of the absorber away from the space charge region. For this reason, determination of ideality factors in p–n-junction solar cells is usually done by fitting two-diode models to experimental data. The two-diode model in the dark has the form

$$J = J_{01}\left[\exp\left(\frac{qV}{n_{id1}kT}\right) - 1\right] + J_{02}\left[\exp\left(\frac{qV}{n_{id2}kT}\right) - 1\right], \tag{2.8}$$

where n_{id1} and n_{id2} are the two ideality factors and J_{01} and J_{02} are the two corresponding saturation current densities.

Up to now, we discussed the dependence of the recombination rate and the recombination current on the internal voltage V, defined as the quasi-Fermi-level splitting in the space charge region. We implicitly assumed that the voltage measured is equal to this internal voltage. Now, we have to distinguish the externally measured voltage V_{ext} from the internal voltage V_i which is equal to the quasi-Fermi-level splitting in the space charge region of the p–n junction. The external voltage is larger than the internal voltage by a term $\Delta V = V_{ext} - V_i$ that scales roughly in a linear way with current density J. The proportionality factor between ΔV and J is the series resistance R_s. The series resistance may originate from the finite conductivity of the absorber layers themselves or from the front and back contacts. For $V > 0.7$ V in Figure 2.1c, we already see that the simulated dark J/V curve (dashed line) has a lower current density at a given voltage than the solid line indicating the two-diode fit according to Equation 2.8. For this simulation, this is due to the finite mobility and thus finite conductivity of the p-type layer of the p–n junction.

For Figure 2.1e and f, we explicitly included an external series resistance and a finite shunt resistance to show its influence on the J/V curves under illumination

and in the dark. We add an external series resistance of $R_s = 5\,\Omega\,\mathrm{cm}^2$ and an external shunt resistance of $R_p = 5\,\mathrm{k}\Omega\,\mathrm{cm}^2$. The series resistance leads to an increased voltage at constant current density in case of the dark J/V curve, that is, more voltage has to be applied for the same current to flow since part of the voltage drops over the external resistance and not over the p–n junction. Under illumination, the curve with series resistance is shifted in the opposite direction. Now, the voltage at the junction must be higher than the voltage at the external contacts to drive a current through an external load resistance. The photocurrent J_{ph} defined as the difference between dark and illuminated J/V curve is no longer constant, since the voltage drop depends on the current, which is – at a given voltage – different under illumination and in the dark.

The shunt resistance R_p has a large influence on the dark J/V curve in the lower voltage range where the current increases drastically when compared to the J/V characteristics without R_p. In contrast, at higher voltages, the differential conductivity $G_d = \partial J/\partial V$ of the diode itself increases exponentially, while the conductivity of the shunt stays constant. Thus, for higher voltages, the shunt disappears and is also nearly invisible in the linear plot of dark and illuminated J/V curve.

Including both shunt and series resistance in the J/V curve leads to

$$J = J_{01}\left[\exp\left(\frac{q\left(V - JR_s\right)}{n_{id1}kT}\right) - 1\right] + J_{02}\left[\exp\left(\frac{q\left(V - JR_s\right)}{n_{id2}kT}\right) - 1\right] + \frac{V - JR_s}{R_p} - J_{sc}. \tag{2.9}$$

This equation is frequently used to analyze J/V measurements of p–n-junction solar cells. A useful property of this description of the J/V curve is that it consists entirely of basic circuit elements, like ideal diodes (defined by n_{id} and J_0), resistances (R_s, R_p), and a current source (J_{sc}) as depicted in Figure 2.2. Thus, such a description is particularly useful for two-dimensional modeling of solar cells and modules by solving networks of diodes, resistances, and current sources with appropriate software tools like SPICE (cf. Chapter 24).

Especially for disordered, low-mobility solar cells that are fabricated as p–i–n diodes such as amorphous and microcrystalline thin-film solar cells, an

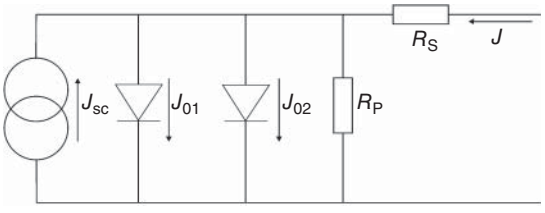

Figure 2.2 Equivalent circuit useful for the description of p–n-junction solar cells consisting of a current source representing the short-circuit current, two diodes for the recombination in the space charge region, and one series and parallel resistance. Note that a representation with an equivalent circuit is difficult for p–i–n-type solar cells, since there the photocurrent is inherently voltage dependent.

expression like Equation 2.9 is still insufficient to describe the measured results well. As shown in Chapter 19, the charge carrier collection of p–i–n-type devices is inherently voltage dependent. Thus, the short-circuit current density is not a voltage-independent constant anymore. Figure 2.1g and h shows the results of a simulation of a p–i–n-junction solar cell with relatively low mobility-lifetime product $\mu\tau = 10^{-9}\,\mathrm{cm}^2/\mathrm{V}$. Obviously, although there are no external series resistances assumed, the photocurrent is strongly voltage dependent and decays rapidly for increasing voltages, even changing its sign slightly below 0.8 V. The exact shape of the voltage-dependent photocurrent cannot be reproduced with analytical equations, but it must be calculated by numerical simulations as presented in Chapter 23. However, there are some analytical approximations, as, for example, that described in Refs [8, 9]. Thus, for low-mobility p–i–n-type diodes, the use of equivalent circuit models is difficult or impossible, depending on the specific needs of the given application.

2.2.2
Measurement of Current/Voltage Curves

Details concerning the correct measurement of J/V curves of solar cells under illumination have been discussed in Refs [10, 11]. Thus, we restrict ourselves here to a brief overview of the measurement itself. Illuminated J/V curves are usually measured under standard testing conditions, that is, a sample temperature of 25 °C and a predefined spectrum, which is for nonconcentrating solar cells usually the AM1.5G spectrum [12]. Figure 2.3 shows a typical setup for exact measurements of the illuminated J/V curve. The biggest challenge for this measurement is to have a light source generating a spectrum that resembles the solar spectrum as well as possible. Since the terrestrial solar spectrum is close to that of a blackbody with a

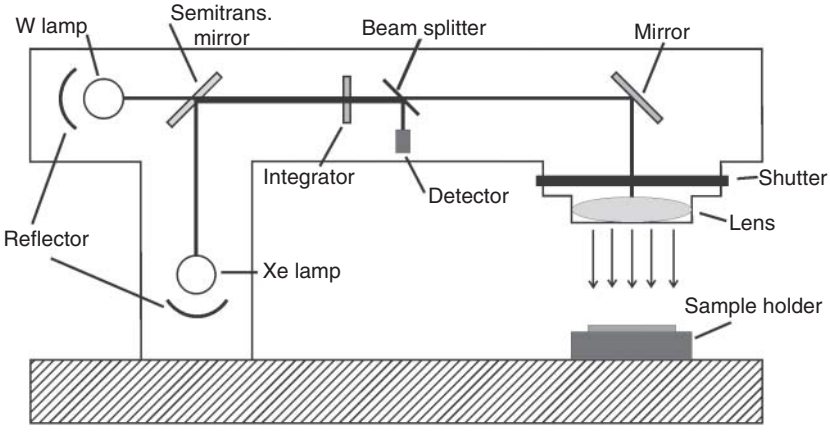

Figure 2.3 Schematic of a solar simulator for *J*/*V* measurements under illumination with a spectrum resembling the standard AM1.5G. To better approximate the solar spectrum, a W lamp and a Xe lamp are combined.

temperature of about 5800 K, any light bulb will have a blackbody spectrum with a much lower temperature since no element can withstand these temperatures without melting. The pure metal with the highest melting point (~3700 K) is W (tungsten), which is therefore commonly used in light bulbs. Since any blackbody source will not reach the temperature of the sun and thus the spectrum of the sun without melting, a W halogen lamp is usually combined with a Xe lamp to get a close match to the solar spectrum.

Assuming that the device under test is illuminated with a spectrum resembling the standard AM1.5G spectrum, the device is contacted and the load resistance is varied such that the voltage changes. The voltage and current are usually measured during the voltage sweep with a four-point probe technique, that is, the current measurement is connected in series with the load resistance, while the voltage measurement requires two separate probes. The circuit containing the voltage measurement has a high resistance and avoiding any resistive voltage drop affecting the measurement result.

2.2.3
Determination of Ideality Factors and Series Resistances

One part of the analysis of J/V curves is the determination of characteristic properties of the curve, as, for instance, the series resistance and the diode quality factor at various voltages. One method is to fit a one- or two-diode model (Equation 2.8) to the experiment. An alternative method for the determination of the series resistance in p–n-junction solar cells with voltage-independent charge carrier collection is the comparison of dark and illuminated J/V curves. As we have already seen in Figure 2.1f, the difference between dark and illuminated current/voltage curves is not a constant, when the series resistance $R_s > 0$ even when the actual charge carrier collection process is not voltage dependent. For a better understanding of this difference, let us shift the current density J_{il} under illumination by the AM1.5G spectrum by the short-circuit current density $J_{sc}^{AM1.5}$ at exactly this AM1.5G illumination to obtain the current density $J_{il} + J_{sc}^{AM1.5}$. Then the J/V curve reads

$$J_{il} + J_{sc}^{AM1.5} = J_0 \exp\left(\frac{q\left(V_{il} - \left(J_{il} + J_{sc}^{AM1.5}\right)R_s\right)}{n_{id}kT} - 1\right), \tag{2.10}$$

if parallel resistances are neglected, and assuming that the solar cell characteristic is well described by a one-diode model in the relevant voltage range. The voltage V_{il} at a given current density is consequently

$$V_{il} = \frac{n_{id}kT}{q} \ln\left(\frac{J_{il} + J_{sc}^{AM1.5}}{J_0} + 1\right) + J_{il}R_s. \tag{2.11}$$

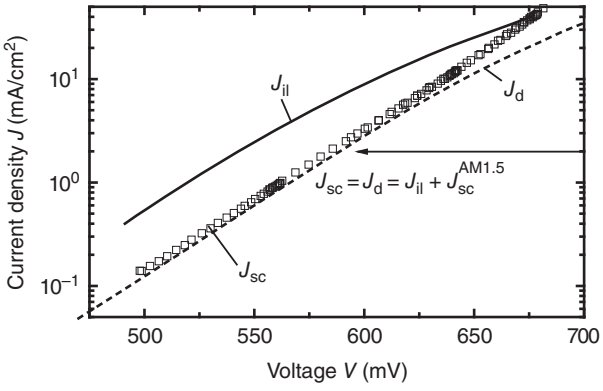

Figure 2.4 Dark current density J_d (dashed line), illuminated current density J_{il} (solid line), and illumination-dependent short-circuit current density J_{sc} (open squares) as a function of voltage or open-circuit voltage V_{oc} in case of the J_{sc} on a semilogarithmic scale. The J_{il}/V curve is shifted by the J_{sc} at AM1.5G conditions at which the J_{il}/V curve was measured. From the voltage differences at constant current densities in this plot, the series resistance of a p–n-junction solar cell can be calculated.

With similar arguments, the voltage V_d in the dark is

$$V_d = \frac{n_{id}kT}{q} \ln\left(\frac{J_d}{J_0} + 1\right) + J_d R_s. \tag{2.12}$$

If we now calculate the difference between the voltage in the dark and the voltage under illumination at a given current density $J_d = J_{il} + J_{sc}^{AM1.5}$, we obtain

$$V_d - V_{il} = J_d R_s - J_{il} R_s = J_{sc}^{AM1.5} R_s. \tag{2.13}$$

Consequently, the series resistance can easily be determined from the voltage difference in the dark and under illumination and the known short-circuit current density. Figure 2.4 shows the plot of the illuminated and dark J/V curves of a crystalline Si solar cell shifted into the first quadrant of the coordinate system and plotted with a logarithmic current axis. It can be seen that the voltage difference between dark and illuminated curves is relatively constant. At a current density $J_d = J_{il} + J_{sc}^{AM1.5} = 2\,\mathrm{mA/cm^2}$ (indicated by the black arrow), the series resistance is $R_s = \Delta V / J_{sc}^{AM1.5} = 45\,\mathrm{mV}/40.4\,\mathrm{mA/cm^2} \approx 1.1\,\Omega\mathrm{cm^2}$. With this method, the series resistance is determined as a function of the current density.

However, the method is only suitable as long as the series resistance does not depend on illumination conditions. For this situation, Aberle *et al.* [13] proposed to use the open-circuit voltage measured at different illumination conditions, yielding a so-called J_{sc}/V_{oc} curve. This curve follows the equation

$$V_{oc} = \frac{n_{id}kT}{q} \ln\left(\frac{J_{sc}}{J_0} + 1\right), \tag{2.14}$$

where J_{sc} denotes the variable short-circuit current density at various illumination intensities. From Equation 2.14 follows that V_{oc} is completely independent of series resistance, because no current flows at open-circuit conditions. The J_{sc}/V_{oc} curve is thus a series-resistance-free J/V curve. Consequently, the series resistance under illumination follows from

$$V_{oc} - V_{il} = -J_{il}R_s = (J_{sc} - J_{sc}^{AM1.5})R_s \tag{2.15}$$

and in the dark from

$$V_d - V_{oc} = J_d R_s = J_{sc} R_s \tag{2.16}$$

is obtained from comparison of the illuminated and the dark J/V curves with the J_{sc}/V_{oc} curve, which is shown in Figure 2.4 (open symbols).

A second useful property of the J_{sc}/V_{oc} representation is the fact that the voltage range, where the curve follows an exponential relation, is enlarged. In Figure 2.1e the voltage range, where the dark J/V is not heavily affected by either shunt or series resistance effects, is very small and it would be difficult to determine an ideality factor from the dark J/V curve. Since the J_{sc}/V_{oc} curve is independent of external series resistances, the determination of ideality factors from J_{sc}/V_{oc} curves becomes much easier using the slope of the J_{sc}/V_{oc} curve via

$$n_{id} = \frac{q}{kT}\frac{dV_{oc}}{d\ln(J_{sc})} = \frac{q}{kT}\frac{dV_{oc}}{dJ_{sc}}J_{sc}. \tag{2.17}$$

2.2.4 Temperature-Dependent Current/Voltage Measurements

The temperature is a useful parameter to vary, when analyzing a solar cell by means of J/V measurements. The temperature dependence of J/V curves is mainly due to the temperature dependence of the equilibrium concentrations of the charge carriers, either electrons, holes, or electrons *and* holes. To illustrate this statement, let us go back to the simple case of bulk recombination described by Equation 2.6. The recombination rate R scales with the minority carrier concentration n in this case. At a given voltage, $n \sim n_i^2/N_A$, where N_A is the acceptor concentration. Since the intrinsic carrier concentration n_i is given by

$$n_i^2 = N_C N_V \exp\left(\frac{-E_g}{kT}\right), \tag{2.18}$$

where N_C and N_V are the effective density of states of conduction and valence band, respectively, also the recombination rate in the volume should scale with a term $\exp(-E_g/kT)$. However, the activation energy E_a of the recombination rate is not always identical to the band gap E_g as in this example.

A typical task that is accomplished by temperature-dependent J/V analysis is the distinction between bulk and interface recombination. Figure 2.5 uses the band diagram to illustrate the different recombination mechanisms that can occur in a CdS/Cu(In,Ga)Se_2 solar cell. In case of interface recombination at the CdS/Cu(In,Ga)Se_2 interface (mechanism 1 in Figure 2.5), the respective

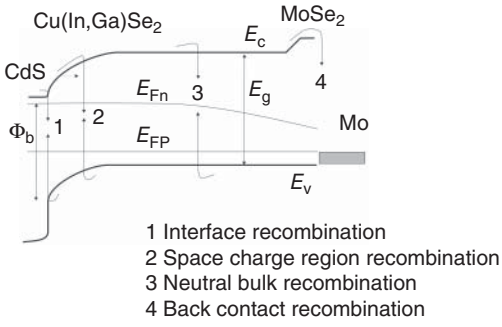

Figure 2.5 Schematic band diagram of a CdS/Cu(In,Ga)Se_2 solar cell showing the four main recombination mechanisms that can occur. The four different locations where recombination with different ideality factors and activation energies can take place are (i) the CdS/Cu(In,Ga)Se_2 interface, (ii) the space charge region, (iii) the neutral bulk, and (iv) the back contact (interface between Cu(In,Ga)Se_2 and Mo). The quantities E_C and E_V stand for the conduction and valence band, E_{fn} and E_{fp} stand for the quasi-Fermi levels of electrons and holes, and Φ_b is the interface barrier.

activation energy is the potential barrier height $\Phi_b = E_{fn} - E_V$ at the interface (E_{fn} being the electron Fermi level at the interface). This is due to the case that holes are the minorities at the interface and that subsequently the recombination rate at the interface scales with hole concentration [14]. The hole concentration in turn is given by

$$p = N_V \exp\left(\frac{qV - \Phi_b}{kT}\right), \tag{2.19}$$

which directly demonstrates that Φ_b is the activation energy of interface recombination. In contrast, the bulk recombination mechanisms 2 and 3 in Figure 2.5, that is, recombination in the space charge region and in the neutral region, are thermally activated by the band gap energy E_g. Due to the band offset between the Cu(In,Ga)Se_2 absorber and a thin $MoSe_2$ layer forming between the absorber and the metallic Mo back contact [15], the activation energy for this process 4 is even larger by this amount than E_g.

Obviously, a temperature-dependent study of the recombination current should be capable of determining the activation energy and subsequently discriminate between limitations by interface or volume recombination. Since the open-circuit voltage V_{oc} is the photovoltaic parameter, which is most directly affected by recombination, we now study the temperature dependence of V_{oc} at a given illumination intensity and thus a given short-circuit current density J_{sc}. The relation between the two is given by [16]

$$J_{sc} = J_0\left[\exp\left(\frac{qV_{oc}}{n_{id}kT}\right) - 1\right] = J_{00}\exp\left(\frac{-E_a}{n_{id}kT}\right)\left[\exp\left(\frac{qV_{oc}}{n_{id}kT}\right) - 1\right], \tag{2.20}$$

where J_{00} is a weakly temperature-dependent prefactor of the saturation current density J_0. The usefulness of such a description becomes obvious, when resolving

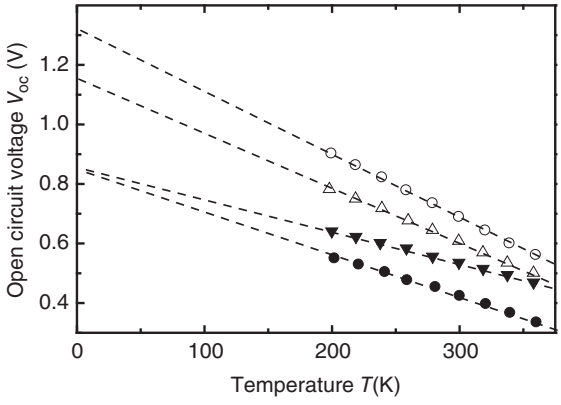

Figure 2.6 Temperature dependence of the open-circuit voltage V_{oc} for different Cu(In,Ga)(Se,S)$_2$ solar cells with different band gap energies due to different In/Ga and Se/S ratios. The open symbols correspond to devices that are grown with a Cu-poor final composition and have a band gap energy (as calculated from the stoichiometry) of $E_g = 1.49$ eV (circles) and 1.22 eV (triangles). The extrapolated open-circuit voltage V_{oc} ($T = 0$ K) roughly follows E_g, whereas for the devices grown under Cu-rich conditions V_{oc} ($T = 0$ K) is independent of E_g (1.15 eV, circles, and 1.43 eV, triangles). The latter finding points to the fact that recombination in such devices has an activation energy given by the height of the interface barrier Φ_b. (Redrawn after Ref. [17].)

for the open-circuit voltage. Now, we obtain

$$qV_{oc} = E_a - n_{id}kT \ln\left(\frac{J_{00}}{J_{sc}}\right), \tag{2.21}$$

that is, a direct relation between the open-circuit voltage V_{oc} and the activation energy E_a. The prefactor J_{00} is typically much larger than J_{sc}; thus, qV_{oc} is smaller than the activation energy by the roughly linearly temperature-dependent second term in Equation 2.21. A temperature-dependent measurement of V_{oc} should yield the activation energy as the extrapolated value of V_{oc} ($T = 0$ K) as long as J_{00} and J_{sc} are reasonably independent of temperature. As an example, Figure 2.6a shows the result of such a measurement for four different Cu(In,Ga)(Se,S)$_2$ solar cells [17]. The data with open symbols stem from samples with a Cu-poor composition. The extrapolated open-circuit voltage V_{oc} ($T = 0$ K) roughly follows their band gap energy E_g (as determined independently from their stoichiometry). The dominant recombination path for these devices therefore is bulk recombination. In contrast, samples with absorbers that are grown under Cu-rich conditions have low activation energies that are independent from the absorber's band gap energy. This finding points to the fact that their V_{oc} is limited by interface recombination and the activation energy corresponds to the interfacial barrier Φ_b.

Obviously, such an analysis of the dominant recombination mechanism requires investigation of a large series of samples (as done in Ref. [17]), and Figure 2.6 just illustrates exemplarily the experimental procedure. More examples covering different types of solar cells (CuInSe$_2$, CdTe, and a-Si:H) are found in Ref. [18].

2.3 Quantum Efficiency Measurements

2.3.1 Definition

A J/V measurement yields information on the absolute value of the short-circuit current density J_{sc} produced in a solar cell. However, this simple measurement does not yield information on the origin of the loss mechanisms that are responsible for the fact that not every photon in the solar spectrum contributes to J_{sc}. In an ideal solar cell, corresponding to the Shockley–Queisser limit as discussed in Chapter 1, every photon with a suitable energy $E > E_g$ leads to one electron–hole pair that is collected at the terminals of the solar cell. In real solar cells this is not the case and we are interested in knowing the reasons for these losses. An appropriate method to literally shed light into this problem is the spectrally resolved measurement of the short-circuit current, that is, $J_{sc}(E)$ likewise $J_{sc}(\lambda)$, depending on whether the result is plotted versus photon energy E or versus wavelength λ. The external quantum efficiency Q_e is defined as the number of electrons collected per photon incident on the solar cell according to

$$Q_e(E) = \frac{1}{q}\frac{dJ_{sc}(E)}{d\Phi(E)}, \tag{2.22}$$

where $d\Phi(E)$ is the incident photon flux in units of $[\Phi] = cm^{-2}\,s^{-1}$ in the (photon) energy interval dE that leads to the short-circuit current density dJ_{sc}.

A second frequently used quantity is the spectral response SR defined as the current produced per unit optical power incident on the solar cell. Consequently, the spectral response has the unit $[SR] = A/W$ and relates to the quantum efficiency via

$$SR = \frac{dJ_{sc}(E)}{d\Phi(E)}\frac{1}{E} = \frac{qQ_e}{E}. \tag{2.23}$$

In the ideal Shockley–Queisser case, we would have $Q_e(E) = 1$ for $E \geq E_g$ and $Q_e(E) = 0$ otherwise. In real solar cells we have $Q_e(E) < 1$ (even for $E \geq E_g$) resulting either from (i) optical or (ii) recombination losses. The optical losses can be further broken down to losses due to reflection and due to parasitic absorption within the device.

The reflection losses can be assessed by an additional measurement using a spectrometer, equipped with an integrating sphere determining the reflectance R, thus allowing us to quantify this loss mechanism separately. For an opaque solar cell, we know that all photons that are not reflected are absorbed in the device, that is, the absorptance A is given by $A = 1 - R$. The internal quantum efficiency Q_i is then defined as the number of collected electrons per number of photon *absorbed* in the solar cell according to

$$Q_i(E) = \frac{Q_e(E)}{1 - R(E)}. \tag{2.24}$$

Note that sometimes Q_i is defined as the number of collected electrons per number of photons *entering* the solar cell. This definition includes weakly absorbed light that enters the solar cell and leaves it after reflection at internal interfaces or surfaces. In this case, the overall reflectance R must be replaced by the front reflectance R_f.

In internal quantum efficiency spectra, the influence of (front surface) reflection is eliminated. However, it still contains information on optical as well as electrical properties of the device. For instance, the effect of a surface texture on the path length enhancement of weakly absorbed light (cf. Chapters 1 and 10) influences both internal and external quantum efficiencies. In addition, in a typical thin-film layer system, each layer, except for the photovoltaically active one(s), will lead to parasitic absorption. Therefore, the first step for the analysis of Q_i requires an *optical* model for the device to determine the absorptance A_i of each layer i in the system. Obviously, such a model requires the knowledge of thicknesses, refractive indices, and absorption coefficients determined, for example, with spectroscopic ellipsometry for reference layers from the respective materials. For thin layers, reflection, absorption, and transmission feature interference effects, which allow checking the accuracy of the simulation of the absorptance by comparison of measured and calculated reflectance. In case the absorptance A_i of a photovoltaically active layer is known, one may define an internal quantum efficiency Q_i^* for this layer via [19–21]

$$Q_i^*(E) = \frac{Q_e(E)}{A_i(E)}. \tag{2.25}$$

In the photovoltaically active layer, absorption is mainly due to generation of electron–hole pairs (neglecting a possible contribution from free-carrier absorption which may occur at long wavelengths in doped absorber materials). When neglecting free-carrier absorption, the absorptance A_i(E) is given by integrating the generation function $g(x, E)$ over the thickness d of the layer. Here, the generation function is the energy-resolved generation rate $G(x, E)$ normalized to the incoming photon flux. Losses within the active layer are then only due to recombination and only starting from this point an *electronic* model must be applied. Typically, such a model calculates the collection probability f_c(x) for electrons and holes such that at the very end of the analysis, we may use

$$Q_i^*(E) = \frac{Q_e(E)}{A_i(E)} = \frac{\int_0^d g(x,E) f_c(x) \mathrm{d}x}{\int_0^d g(x,E) \mathrm{d}x} \tag{2.26}$$

explaining the external quantum efficiency layer by layer.

2.3.2 Measurement Principle and Calibration

Figure 2.7 shows two typical quantum efficiency measurement setups: (a) a monochromator-based setup and (b) a setup with a filter wheel equipped

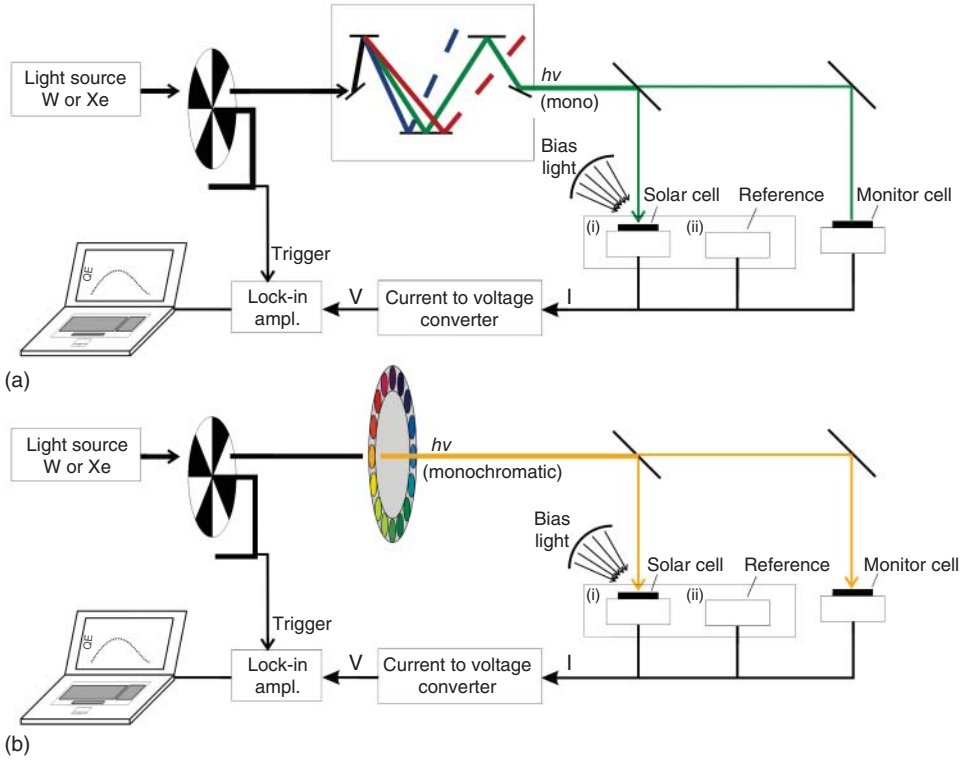

Figure 2.7 Scheme of two quantum efficiency setups – (a) a monochromator-based setup and (b) a setup with a filter wheel. In both cases, chopped monochromatic light illuminates first the reference (during calibration) and then the sample (during measurement). The current output of reference or sample is converted to voltage and then amplified with a lock-in amplifier triggered by the chopper wheel synchronization output. Temporal variations in intensity of the monochromatic light can be monitored with a monitor diode measuring intensity during calibration and during measurement.

with interference filters. The advantage of using monochromators is the high wavelength resolution and the broad spectral range. The wavelength resolution is especially high when double-stage monochromators are used. The disadvantage of double-stage monochromators compared with single-stage monochromators is the lower light throughput combined with a higher price and larger size. The advantage of filter wheels is the high optical throughput and the larger illuminated area. While monochromator-based setups illuminate only a small spot of few millimeters diameter, a filter wheel completely illuminates larger solar cells and minimodules of several centimeters edge length. In the following, we will first describe the operation and calibration of a monochromator-based system. Subsequently, we will discuss the aspects that are different for a setup with filter wheel.

In case of the setup with grating monochromator, first white light from a W halogen lamp or a Xe-arc lamp is chopped before entering the monochromator. The chopper is needed to obtain a periodic signal, which a lock-in amplifier can use. Care must be taken that higher modes due to shorter wavelengths (e.g., $\lambda/2$) are suppressed by the use of filters.

The monochromatic light is then focused on the (i) solar cell to be measured (during the actual measurement) or (ii) on the reference cell or detector (during the calibration). The reference used for calibration of the setup can either (i) be a pyroelectric radiometer for the relative calibration combined with a solar cell or photodiode for the absolute calibration at one wavelength or (ii) one reference solar cell for the whole spectral range. The advantage of using a pyroelectric radiometer lies in its spectrally independent sensitivity over a broad wavelength range. Thus, the calibration has a high quality for all wavelengths, where the intensity of the lamp is sufficient for a high signal-to-noise ratio in the radiometer. In case of the reference solar cell, not only the intensity of the lamp but also the quantum efficiency of the reference cell must be sufficiently high. Using a reference cell (without a radiometer) is particularly useful as long as the reference cell has a high quantum efficiency for all wavelengths of interest of the device under test. For instance, high efficiency crystalline silicon solar cells have a high quantum efficiency (>80%) in the spectral range where amorphous and microcrystalline silicon solar cells are sensitive.

In order to account for temporal variations in the absolute intensity of the light source, monitor solar cells are often used. Using a semitransparent mirror, part of the light leaving the monochromator or filter wheel is directed on a monitor solar cell, both during calibration and during measurement. For each wavelength, the ratio of intensity on the monitor cell during calibration and during measurement is multiplied with the resulting quantum efficiency value. When using monitor solar cells, it is important that the quantum efficiency of the monitor solar cell is sufficiently high in the complete spectral range of interest.

The current signal from the monitor and the test solar cell are then converted into a voltage by a current-to-voltage converter with a typical amplification ratio of $10^4 - 10^6$ V/A. The voltage output of the converter serves as input for the lock-in amplifier that uses the synchronization output of the chopper controller as trigger input. The amplified signal of the lock-in amplifier is then read and displayed by a computer.

The main difference in operation of a filter wheel-based setup concerns the calibration. As Figure 2.8 shows, the light from the monochromator is focused on the solar cell and illuminates only a small spot of typically 1 mm × 3 mm size. The filter wheel, however, illuminates larger areas. In order to measure the complete quantum efficiency of a solar cell of a certain size, the illuminated area must be much larger than the solar cell such that the complete cell area is illuminated homogeneously. This difference in illuminated area being either much smaller or larger than the sample requires different ways of calibration. While in the grating-based setup, the current of the reference device is measured and compared to the current of the sample, for filter wheel setups the current *densities* have to be used.

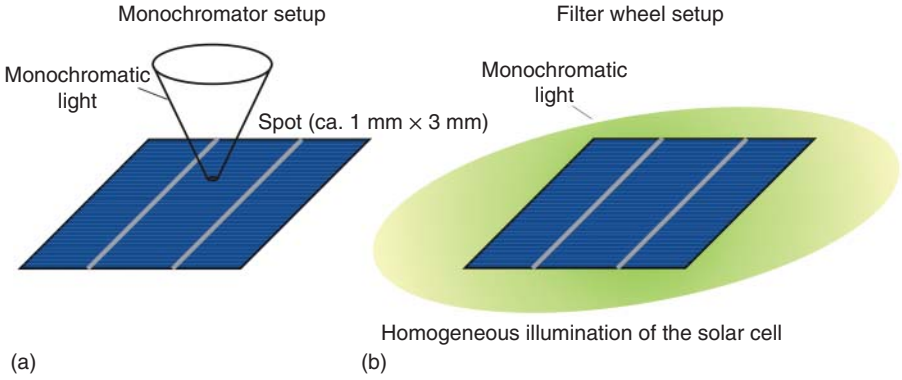

Figure 2.8 Schematic of the two possible approaches when illuminating a solar cell during a quantum efficiency measurement. (a) With a monochromator-based setup, a typical spot size is in the mm range and will be smaller than most investigated cells. Thus, the spot illuminates only a small part of the cell and the quantum efficiency will be a local quantity, which may change when moving the spot. (b) In case of a filter wheel setup, it is possible to illuminate solar cells or small modules homogeneously and thus get an average quantum efficiency.

In addition to filter wheel- or monochromator-based setups, it is also possible to measure the quantum efficiency of a solar cell using a Fourier spectrometer. The use of a Fourier spectrometer is particularly beneficial when a high dynamic range is required. The corresponding measurement technique to use a Fourier spectrometer for quantum efficiency measurements is called Fourier transform photocurrent spectroscopy (FTPS), and it is described in detail in Chapter 8 of this book.

2.3.3
Quantum Efficiency Measurements of Tandem Solar Cells

Especially in case of thin-film Si, organic, and perovskite solar cells, multijunction concepts are in the focus of research to make better use of the solar spectrum. Figure 2.9 shows the quantum efficiency of an a-Si:H/μc-Si:H tandem cell on textured ZnO:Al superstrate. The measurement of the two quantum efficiency spectra corresponding to both series-connected subcells requires the subsequent use of two bias light sources. In a first step, bias light with a short wavelength generates a photocurrent in the top cell that is *not* subject to the measurement. As a consequence, the bottom cell under investigation is limiting the output current of the tandem device. Now chopped monochromatic light with varied wavelength is used to produce the quantum efficiency spectrum of the bottom cell. A second measurement then uses longer wavelength light to generate a photocurrent in the bottom cell and the chopped light probes the quantum efficiency of the top cell. Care must be taken to ensure that for both measurements the bias light is in a spectral range where a pronounced difference in the quantum efficiency of top and bottom cell exists. Also the intensity of the bias light sources must be larger than that of the chopped light for all wavelengths [22–24].

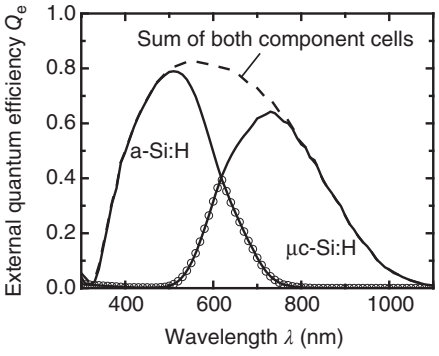

Figure 2.9 Example for the quantum efficiency of a-Si:H/μc-Si:H tandem cell on textured ZnO:Al superstrates. The quantum efficiencies of top and bottom cell are indicated as solid lines and are measured using a bias light to flood the respective other subcell. In addition, the sum of both is indicated as dashed line and the minimum value is indicated as open circles. The latter indicates the measurement result one would obtain, when measuring without bias light.

2.3.4 Differential Spectral Response Measurements

As defined in Section 2.3.1, the quantum efficiency measures the spectrally resolved photocurrent at *short circuit*. For many applications, and especially for thin-film solar cells, the restriction to the short-circuit situation does not give results that are representative for other operating points of the cells, too [25, 26]. A dependency of photocurrent on voltage or illumination is equivalent to a violation of the superposition principle in photovoltaics that has been discussed in Section 2.2. The main result was that the superposition principle is violated when the charge carrier collection depends on the density of charge carriers in the device and, thus, on the voltage and/or illumination bias. Such bias-dependent collection, in turn, originates either from a varying electric field in low-mobility devices as is the case for any p–i–n-type (cf. Figure 2.1h) solar cell or from a recombination rate $R \neq Bnp$. Recombination rates that are not proportional to the product np of electron and hole concentrations may result either from Shockley–Read–Hall recombination via (defect) states in the band gap or from Auger recombination (cf. Chapter 1).

In these situations, where the photocurrent is voltage and/or illumination bias dependent, the measurement of the quantum efficiency at various biases gives valuable information. As an example, in p–i–n-type solar cells, the comparison of the quantum efficiency at reverse voltages compared to those at short-circuit conditions or higher voltages allows distinguishing between collection losses and optical losses. This is because the lower the bias voltage V, the higher the electric field F in the intrinsic layer of the p–i–n diode, and the better the collection of carriers. If one can decrease the voltage V such that the quantum efficiency $Q_e(\lambda, V)$ does not increase any more with increasing reverse voltage, the electric

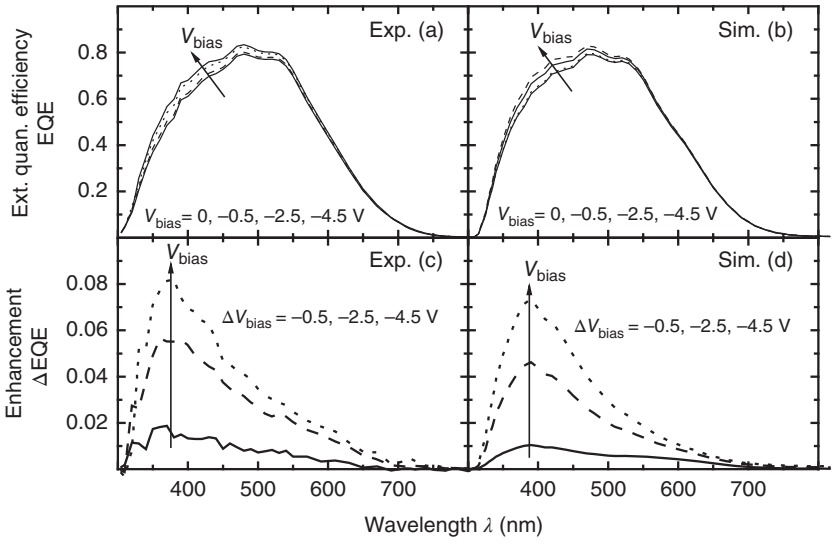

Figure 2.10 Bias-dependent quantum efficiency of the top cell in an a-Si:H/μc-Si:H tandem solar cell. (a, c) show the experiment and (b, d) the simulation. (a, b) show the quantum efficiency itself and (c, d) the difference in quantum efficiency compared to the short-circuit situation.

field F is sufficiently high to drive all photogenerated carriers to their respective junctions and the collection efficiency $f_c = 1$. The quantum efficiency at such reverse voltages is then equal to the absorptance and, thus, only determined by the optical properties of the device. Comparing the absorptance obtained from reverse biased quantum efficiency measurements with the quantum efficiency at higher bias voltages allows eventually the calculation of losses due to carrier collection at a certain voltage.

Figure 2.10 shows an example for a bias-dependent quantum efficiency measurement of an a-Si:H/μc-Si:H tandem solar cell. Presented is only the quantum efficiency of the top cell. This quantum efficiency is measured for different negative bias voltages to show the effect of the electric field in the p–i–n junction of the a-Si:H cell. The gain in quantum efficiency (b) is mainly in the wavelength range, where a considerable part of the light is absorbed in the p-layer, which has a poor electronic quality. Numerical simulations (c and d) as described in Chapter 19 have been used to analyze the electrical properties of the device.

2.3.5
Interpretation of Quantum Efficiency Measurements in Thin-Film Silicon Solar Cells

The interpretation of quantum efficiency measurements differs considerably depending on the solar cell type. For crystalline Si, for instance, the quantum efficiency in the wavelength range $780\,\text{nm} < \lambda < 950\,\text{nm}$ is typically used to determine the effective diffusion length of the base layer of the device [27–30].

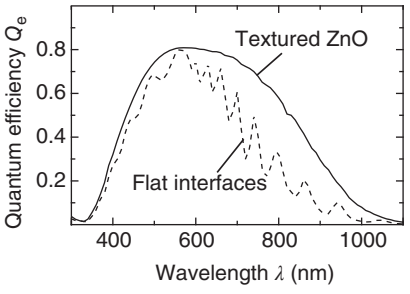

Figure 2.11 Comparison of the typical quantum efficiency of a μc-Si:H solar cell with a textured ZnO (solid line) and a flat ZnO.

For even higher wavelengths, information about the optical properties of the back contact are obtained. In CdS/Cu(In,Ga)Se_2 solar cells, different evaluation methods yield information about charge carrier collection properties of the buffer layer [31] or the absorber layer [32, 33]. Since a complete description of all methods is beyond the scope of this chapter, we focus here mainly on thin-film silicon solar cells and discuss the main challenges in interpretation of quantum efficiency measurements.

According to Equation 2.26, the quantum efficiency consists of contributions due to absorption of photons and generation of charge carriers as well as of contributions due to carrier collection. In order to show an example for the influence of optical properties of the device on the quantum efficiency, Figure 2.11 compares the external quantum efficiency of two μc-Si:H solar cells. The cell represented by the solid line is grown on a texture-etched ZnO:Al superstrate [34], while the cell with the dashed line is grown on the same superstrate but without etching. All thicknesses of the Si layers in the stack were the same, which was achieved by depositing the active layers at the same time during the same deposition process. There are two striking differences between the two curves. First, the textured solar cell has considerably higher quantum efficiency especially for higher wavelengths. Second, the quantum efficiency of the untextured solar cell shows interference patterns, which are absent for the textured solar cell.

The reason for the increased quantum efficiency of the textured solar cell lies in the concept of light trapping that was described in Chapters 1 and 5. Light that passes the interface between the textured ZnO and the Si is scattered by the rough interface and the refractive index difference (between 1.5 and 2 for ZnO:Al and between 3 and 5 for Si, depending on crystallinity and wavelength). The scattered light has now a high probability of being trapped in the absorber layer by total internal reflection. Thus, the weakly absorbed light, which travels in a flat cell only twice the cell thickness, is reflected multiple times in the textured cell. The increased optical path length of the light leads to the increased quantum efficiency at a given absorption coefficient and thickness. In case of the untextured solar cell, interference effects play a role since the cell thickness (thickness of all silicon layers is 1230 nm) is of the order of the wavelength of light and is smaller than the coherence length of the illumination. As a consequence, there are interferences that depend on the layer thicknesses and the refractive indices. For the

textured cell, these interference patterns are destroyed by the light scattering at the ZnO/Si interface.

Obviously, a more detailed analysis of the quantum efficiencies in Figure 2.11 would be of interest. This requires numerical simulations, which are described in more detail in Chapter 19. Analytical approaches to model both the optical part and the electronic part of the quantum efficiency are not possible in such thin p–i–n-type devices. This is due to the fact that (i) both electrons and holes are relevant for transport and recombination, which means that coupled differential equations for electron and hole transport have to be solved. For p–n-junction solar cells, most evaluation schemes rely on the fact that only one type of carrier dominates recombination. This is due to the fact that most p–n-junction devices have a thick base and a very thin emitter. Due to the large size difference, the minority carrier in the base is usually the relevant carrier and the solution of the continuity equation for the minority carrier in the base is sufficient to cover the electronic aspect of the problem.

The second challenge associated with p–i–n-junction thin-film solar cells is the fact that the wavelength of light and the cell thickness are comparable in magnitude and that geometric optics has to be abandoned in favor of wave optics. Calculating the absorption of a solar cell with perfectly flat interfaces is a simple numerical problem that is solved with a matrix transfer formalism [35]. The only prerequisite is a precise measurement of the optical properties of the individual layers by ellipsometry and photothermal deflection spectroscopy.

For textured surfaces, however, the calculation of the absorptance of the layers requires more sophisticated techniques. For research on light-trapping properties of a certain surface texture [36–39], Maxwell's equations have to be solved in three dimensions, which requires extensive computational resources. For a quick analysis of quantum efficiency measurements, more approximate methods [40] have to be used that do not consider interference effects for scattered light and that consider the interface properties only in the form of effective parameters such as haze (the ratio between light intensity that is scattered when being transmitted or reflected at an interface and the complete light intensity transmitted or reflected at an interface) and angular distribution function (describing the distribution of angles after the light is scattered at an interface) [41, 42]. Although the optical models for textured surfaces are far from being exact, a decent fit to the measured quantum efficiency is possible.

When all optical parameters of the layers are measured and the interface properties are determined such that the optical model allows a good description of the experiment, simulations of quantum efficiency measurements yield approximations of the major loss mechanisms affecting the short-circuit current. Figure 2.12 shows the absorptances of all relevant layers in (a) a μc-Si:H solar cell on textured ZnO:Al superstrate and (b) a CdS/Cu(In,Ga)Se_2 solar cell on a flat glass substrate simulated with ASA [43] and using the optical model genpro3 (a) and genpro1 (b). The major photocurrent losses for the μc-Si:H solar cell occur by absorption in the ZnO:Al layer and, especially, the p-type Si layer. These layers are the first ones that the light has to pass after the glass. Thus, the light has a high intensity

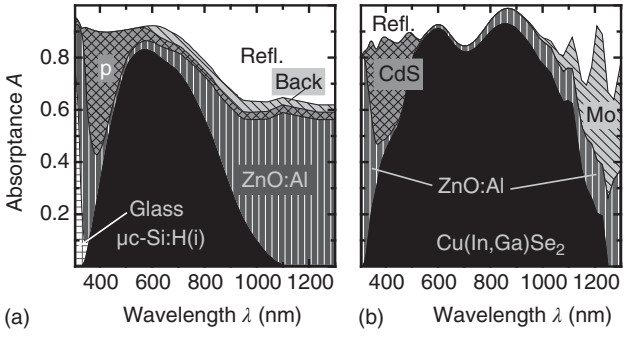

Figure 2.12 Comparison of the absorption in the different layers of (a) a typical μc-Si:H solar cell (redrawn from Ref. [44]) and (b) a typical $Cu(In,Ga)Se_2$ solar cell . The regions that are black indicate the absorption in the respective absorber layers. Since most of the photons absorbed there contribute to the short-circuit current, the black regions correspond well to the external quantum efficiency, while the other areas indicate how severe losses are in the different layers. (redrawn from Ref. [45].)

when passing through these layers and much of the light is absorbed there. While ZnO:Al exhibits a relatively low absorption coefficient but a high thickness (about 500 nm), the p-type Si layer is very thin (around 20 nm) but has a high absorption coefficient in the complete wavelength range also relevant for the absorber layer. For wavelengths higher than 900 nm, most light is absorbed again in the ZnO:Al layer since for higher wavelengths free-carrier absorption in the ZnO:Al becomes more dominant. In addition, the absorber layers become transparent and, thus, light is reflected multiple times in the cell and will be absorbed primarily in the thick front contact ZnO and the three back contact layers (n-type Si, ZnO, Ag).

In case of the $Cu(In,Ga)Se_2$ solar cell, the low wavelength regime is pretty similar to μc-Si:H. Part of the high-energy photons is absorbed in the ZnO:Al, and part is absorbed in the CdS, which has a similar role as the p-type Si in the μc-Si:H layer stack. The main difference between μc-Si:H and $Cu(In,Ga)Se_2$ becomes apparent for higher wavelengths. Here, the absorption in the $Cu(In,Ga)Se_2$ is much higher than in the μc-Si:H, because of the much higher absorption coefficient of $Cu(In,Ga)Se_2$ compared to μc-Si:H. Thus, even for wavelengths around 1100 nm, that is, just above the band gap of $Cu(In,Ga)Se_2$ and μc-Si:H, the absorptance of the $Cu(In,Ga)Se_2$ absorber is above 50%, while it is nearly zero in case of μc-Si:H. The higher absorptance of $Cu(In,Ga)Se_2$ in the infrared is possible despite the fact that no intentional texturing of the surface is required to achieve such a high absorptance in the long wavelength range as shown in Figure 2.12b. Note that the optical data for Figure 2.12 were measured [44] by means of ellipsometry and photothermal deflection spectroscopy (in case of the μc-Si:H cell) and the data for the $Cu(In,Ga)Se_2$ cell are taken from Ref. [45].

In addition to an entirely optical analysis of the quantum efficiency, the loss mechanisms of the photocurrent can also be analyzed in terms of optical losses and charge collection losses. However, this requires a careful determination of all electrical parameters, which has to be done by using a variety of different

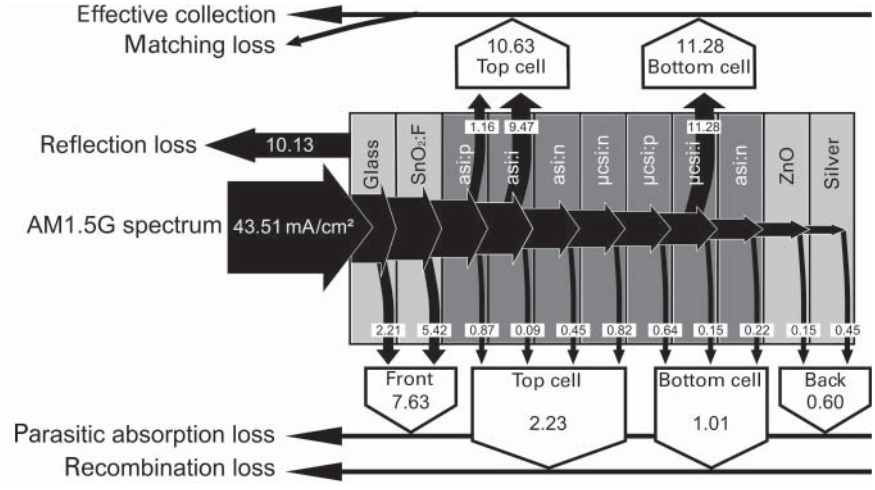

Figure 2.13 Using a simulation of an a-Si:H/µc-Si:H tandem solar cell, the losses in the different layers are calculated. The total incident photon flux of the AM1.5G spectrum between 300 and 1100 nm is taken as input leading to 43.51 mA/cm^2 as the maximum J_{sc} for a single-junction solar cell (and 0.5×43.51 mA/cm^2 for a tandem solar cell). Losses in the Si layers are denoted as recombination losses, while losses in the front and back contact layers are termed parasitic absorption losses although the distinction between the two is not strict.

measurement techniques. For the case of a-Si:H, µc-Si:H, and Cu(In,Ga)Se_2, an overview over typical parameters and the measurement techniques to obtain them is given in Refs [46–52]. For the case of an a-Si:H/µc-Si:H tandem solar cell, we performed a simulation of the losses in photocurrent in each layer as shown in Figure 2.13. We distinguished between parasitic absorption losses, recombination losses, and matching losses although this distinction does not discriminate between fundamentally different loss mechanisms. *Parasitic absorption* is defined here as absorption in a layer where either photogenerated electron–hole pairs will not reach the junction or where absorption does not lead to photogenerated electron–hole pairs at all. These layers are the transparent conductive oxide (TCO) layers and the silver back reflector. The glass superstrate contributes to parasitic absorption as well. *Recombination losses* are the losses in all silicon layers due to finite collection efficiencies and finite mobility-lifetime products. It becomes clear that the distinction between parasitic absorption loss and recombination loss is somewhat arbitrary, when it comes to generation of electron–hole pairs in layers that are of low electronic quality such as the TCO layers or the doped silicon layers. Only the free-carrier absorption, which is dominant in the TCO layers for higher wavelengths, is clearly parasitic absorption. The third loss mechanism is only relevant in multijunction solar cells. In these devices, the lowest photocurrent of the subcells limits the total photocurrent because of the series connection of the subcells. As a consequence, the additional photogenerated and collected carriers in the cell with the higher photocurrent

are lost by recombination. Thus, the matching loss in a multijunction solar cell is only a special type of recombination loss.

In conclusion, we can say that a loss analysis as detailed in Figure 2.13 is a useful tool to determine the major loss mechanisms of the photocurrent for a specific solar cell. It will be based on the measurement of the quantum efficiency Q_e and the numerical simulation of the measured Q_e. From the simulation, the losses in the solar cell are obtained. The critical point for analyses underlying Figures 2.12 and 2.13 is the assumption that a good fit of the simulated quantum efficiency to the measured one implies that the loss mechanisms in the real cell are the same as in the simulation. In order to make such an analysis reliable, all electrical and optical parameters have to be determined – at least approximately – with various additional methods. In addition, results of optical simulations of thin-film solar cells grown on rough substrates have to be critically examined due to the lack of reasonably fast and at the same time correct methods to simulate the absorptance of such layer stacks.

Acknowledgments

Also for these chapters, Dorothea Lennartz is gratefully acknowledged for the help with the figures. The authors of Chapter 3 thank Anke Helbig for her contributions.

References

1. Shockley, W. and Queisser, H.J. (1961) Detailed balance limit of efficiency of p–n junction solar cells. *J. Appl. Phys.*, **32**, 510.
2. Hall, R.N. (1952) Electron–hole recombination in germanium. *Phys. Rev.*, **87**, 387.
3. Shockley, W. and Read, W.T. (1952) Statistics of the recombinations of holes and electrons. *Phys. Rev.*, **87**, 835.
4. Van Berkel, C., Powell, M.J., Franklin, A.R., and French, I.D. (1993) Quality factors in a-Si:H nip and pin diodes. *J. Appl. Phys.*, **73**, 5264.
5. Nardone, M., Karpov, V.G., Shvydka, D., and Attygale, M.L.C. (2009) Theory of electronic transport in noncrystalline junctions. *J. Appl. Phys.*, **106**, 074503.
6. Rau, U. (1999) Tunneling-enhanced recombination in Cu(In,Ga)Se_2 heterojunction solar cells. *Appl. Phys. Lett.*, **74**, 111–113.
7. Nadenau, V., Rau, U., Jasenek, A., and Schock, H.W. (1999) Electronic properties of $CuGaSe_2$-based heterojunction solar cells. Part I. Transport analysis. *J. Appl. Phys.*, **87**, 584–593.
8. Crandall, R.S. (1983) Modeling of thin film solar cells: uniform field approximation. *J. Appl. Phys.*, **54**, 7176.
9. Hof, C. (1999) Thin film solar cells of amorphous silicon: influence of i-layer material on cell efficiency. Dissertation. Université de Neuchâtel.
10. Osterwald, C.R. (2003) Standards, calibration and testing of PV modules and solar cells, in *Practical Handbook of Photovoltaics* (eds T. Markvart and L. Castañer), Elsevier Ltd., Kidlington, p. 793.
11. Emery, K. (2003) Measurement and characterization of solar cells and modules, in *Handbook of Photovoltaic Science and Engineering* (eds A. Luque and S. Hegedus), John Wiley & Sons, Ltd, Chichester, p. 701.

12. ASTM Standard G173, *Standard Tables for Reference Solar Spectral Irradiances: Direct Normal and Hemispherical on 37° Tilted Surface*, American Society for Testing and Materials, West Conshohocken, PA, http://rredc.nrel.gov/solar/spectra/am1.5/ (accessed 12 March)
13. Aberle, A.G., Wenham, S.R., and Green, M.A. (1993) *A New Method for Accurate Measurements of the Lumped Series Resistance of Solar Cells*. Proceedings of the 23rd IEEE Photovoltaic Specialists Conference, Louisville, Kentucky, 10-14 May 1993, IEEE, New York, p. 133.
14. Scheer, R. (2009) Activation energy of heterojunction diode currents in the limit of interface recombination. *J. Appl. Phys.*, **105**, 104505.
15. Wada, T., Kohara, N., Negami, T., and Nishitani, M. (1996) Chemical and structural characterization of $Cu(In,Ga)Se_2$/Mo interface in $Cu(In,Ga)Se_2$ solar cells. *Jpn. J. Appl. Phys.*, **35**, L1253–L1256.
16. Rau, U. and Schock, H.W. (1999) Electronic properties of $Cu(In,Ga)Se_2$ heterojunction solar cells – recent achievements, current understanding, and future challenges. *Appl. Phys. A*, **69**, 131.
17. Turcu, M., Pakma, O., and Rau, U. (2002) Interdependence of absorber composition and recombination mechanism in $Cu(In,Ga)(Se,S)_2$ heterojunction solar cells. *Appl. Phys. Lett.*, **80**, 2598.
18. Hegedus, S.S. and Shafarman, W.N. (2004) *Prog. Photovoltaics Res. Appl.*, **12**, 155–176.
19. Slooff, L.H., Veenstra, S.C., Kroon, J.M., Moet, D.J.D., Sweelsen, J., and Koetse, M.M. (2007) Determining the internal quantum efficiency of highly efficient polymer solar cells through optical modeling. *Appl. Phys. Lett.*, **90**, 143506.
20. Dennler, G., Forberich, K., Scharber, M.C., Brabec, C.J., Tomis, I., Hingerl, K., and Fromherz, T. (2007) Angle dependence of external and internal quantum efficiencies in bulk-heterojunction organic solar cells. *J. Appl. Phys.*, **102**, 054516.
21. Law, M., Beard, M.C., Choi, S., Luther, J.M., Hanna, M.C., and Nozik, A.J. (2008) Determining the internal quantum efficiency of PbSe nanocrystal solar cells with the aid of an optical model. *Nano Lett.*, **8**, 3904.
22. Deng, X. and Schiff, E.A. (2003) Measurement amorphous silicon-based solar cells, in *Handbook of Photovoltaic Science and Engineering* (eds A. Luque and S. Hegedus), John Wiley & Sons, Ltd, Chichester, p. 549.
23. Burdick, J. and Glatfelter, T. (1986) Spectral response and I–V measurements of tandem amorphous-silicon alloy solar-cells. *Sol. Cells*, **18**, 310.
24. Müller, R. (1993) Spectral response measurements of 2-terminal triple junction a-Si solar-cells. *Sol. Energy Mater. Sol. Cells*, **30**, 37.
25. Hegedus, S.S. and Kaplan, R. (2002) Analysis of quantum efficiency and optical enhancement in amorphous Si p-i-n solar cells. *Prog. Photovoltaics Res. Appl.*, **10**, 257.
26. Hegedus, S.S. and Shafarman, W.N. (2004) Thin-film solar cells: device measurement and analysis. *Prog. Photovoltaics Res. Appl.*, **12**, 155.
27. Arora, N.D., Chamberlain, S.G., and Roulston, D.J. (1980) Diffusion length determination in p–n junction diodes and solar cells. *Appl. Phys. Lett.*, **37**, 325.
28. Basore, P.A. (1993) *Extended Spectral Analysis of Internal Quantum Efficiency*. Proceedings of the 23rd IEEE Photovoltaic Specialists Conference, Louisville, Kentucky, 10-14 May 1993, IEEE, New York, p. 147.
29. Hirsch, M., Rau, U., and Werner, J.H. (1995) Analysis of internal quantum efficiency and a new graphical evaluation scheme. *Solid-State Electron.*, **38**, 1009.
30. Brendel, R. and Rau, U. (1999) Injection and collection diffusion lengths of polycrystalline thin-film solar cells. *Solid State Phenom.*, **67–68**, 81.
31. Engelhardt, F., Bornemann, L., Köntges, M., Meyer, T., Parisi, J., Pschorr-Schoberer, E., Hahn, B., Gebhardt, W., Riedl, W., and Rau, U. (1999) $Cu(In,Ga)Se_2$ solar cells with a ZnSe buffer layer: interface characterization by quantum efficiency measurements. *Prog. Photovoltaics Res. Appl.*, **7**, 423.

32. Parisi, J., Hilburger, D., Schmitt, M., and Rau, U. (1998) Quantum efficiency and admittance spectroscopy on Cu(In,Ga)Se_2 solar cells. *Sol. Energy Mater. Sol. Cells*, **50**, 79.
33. Kniese, R., Lammer, M., Rau, U., and Powalla, M. (2004) Minority carrier collection in $CuGaSe_2$ solar cells. *Thin Solid Films*, **451–452**, 430.
34. Löffl, A., Wieder, S., Rech, B., Kluth, O., Beneking, C., and Wagner, H. (1997) *Al-Doped ZnO Films for Thin-Film Solar Cells with Very Low Sheet Resistance and Controlled Texture*. Proceedings of the 14th European Photovoltaic Solar Energy Conference, Barcelona, p. 2089.
35. Berning, P.H. (1963) Theory and calculations of optical thin films, in *Physics of Thin Films*, vol. **1** (ed G. Hass), Academic, New York, pp. 69–121.
36. Rockstuhl, C., Lederer, F., Bittkau, K., and Carius, R. (2007) Light localization at randomly textured surfaces for solar-cell applications. *Appl. Phys. Lett.*, **91**, 171104.
37. Rockstuhl, C., Lederer, F., Bittkau, K., Beckers, T., and Carius, R. (2009) The impact of intermediate reflectors on light absorption in tandem solar cells with randomly textured surfaces. *Appl. Phys. Lett.*, **94**, 211101.
38. Bittkau, K., Beckers, T., Fahr, S., Rockstuhl, C., Lederer, F., and Carius, R. (2008) Nanoscale investigation of light-trapping in a-Si:H solar cell structures with randomly textured interfaces. *Phys. Status Solidi A*, **205**, 2766.
39. Rockstuhl, C., Fahr, S., Lederer, F., Bittkau, K., Beckers, T., and Carius, R. (2009) Local versus global absorption in thin-film solar cells with randomly textured surfaces. *Appl. Phys. Lett.*, **93**, 061105.
40. Tao, G., Zeman, M., and Metselaar, J.W. (1994) Accurate generation rate profiles in a-Si:H solar cells with textured TCO substrates. *Sol. Energy Mater. Sol. Cells*, **34**, 359.
41. Krč, J., Zeman, M., Topič, M., Smole, F., and Metselaar, J.W. (2002) Analysis of light scattering in a-Si:H-based PIN solar cells with rough interfaces. *Sol. Energy Mater. Sol. Cells*, **74**, 401.
42. Krč, J., Smole, F., and Topič, M. (2003) Analysis of light scattering in amorphous Si:H solar cells by a one-dimensional semi-coherent optical model. *Prog. Photovoltaics Res. Appl.*, **11**, 15.
43. Pieters, B.E., Krč, J., and Zeman, M. (2006) *Advanced Numerical Simulation Tool for Solar Cells – ASA5*. Conference Record of the 2006 IEEE 4th World Conference on Photovoltaic Energy Conversion, 7-12 May 2006, Waikoloa Hawaii, IEEE, WCPEC-4 2, art. no. 4059936, pp. 1513.
44. Ding, K. (2009) Characterisation and simulation of a-Si:H/μc-Si:H tandem solar cells. Master thesis. RWTH Aachen.
45. Orgassa, K. (2004) Coherent optical analysis of the ZnO/CdS/Cu(In, Ga)Se_2 thin film solar cell. Dissertation. Universität Stuttgart.
46. Jiang, L., Lyou, J.H., Rane, S., Schiff, E.A., Wang, Q., and Yuan, Q. (2000) Open-circuit voltage physics in amorphous silicon solar cells. *Mater. Res. Soc. Symp. Proc.*, **609**, A18.3.1–A18.3.12.
47. Zhu, K., Yang, J., Wang, W., Schiff, E.A., Liang, J., and Guha, S. (2003) Bandtail limits to solar conversion efficiencies in amorphous silicon solar cells. *Mater. Res. Soc. Symp. Proc.*, **762**, 297.
48. Liang, J., Schiff, E.A., Guha, S., Yan, B., and Yang, J. (2006) Hole mobility limit of amorphous silicon solar cells. *Appl. Phys. Lett.*, **88**, 063512.
49. Willemen, J.A. (1998) Modelling of amorphous silicon single- and multi-junction solar cells. Dissertation. TU Delft. http://repository.tudelft.nl/assets/uuid:0771d543-af5f-4579-8a35-0b68d34a1334/emc_willemen_19981016.PDF (accessed 18 March 2010).
50. Pieters, B.E., Stiebig, H., Zeman, M., and van Swaaij, R.A.C.M.M. (2009) Determination of the mobility gap of intrinsic μc-Si:H in p–i–n solar cells. *J. Appl. Phys.*, **105**, 044502.

51. Pieters, B.E. (2008) Characterization of thin-film silicon materials and solar cells through numerical modeling. Dissertation. TU Delft, p. 105. http://repository.tudelft.nl/file/1218227/381966 (accessed 18 March 2010).

52. Gloeckler, M. (2005) Device physics of Cu(In,Ga)Se_2 thin-film solar cells. Dissertation. Colorado State University, Fort Collins. http://www.physics.colostate.edu/groups/photovoltaic/PDFs/MGloeckler_Thesis.pdf (accessed 18 March 2010).

3
Electroluminescence Analysis of Solar Cells and Solar Modules

Thomas Kirchartz, Vito Huhn, Andreas Gerber, Bart E. Pieters, and Uwe Rau

3.1
Introduction

Solar cells are large-area diodes optimized for light absorption and charge carrier collection. Inversing the normal operating mode by injecting charge carriers under applied forward bias leads to recombination in the device. Although most solar cells are not particularly efficient light emitters, part of the charge carrier recombination must be radiative, leading to detectable emission of photons with energies around the band gap of the solar-cell absorber. Electroluminescence (EL) characterization of solar cells has been used since the early 1990s [1–4]; however, the number of papers dealing with the field has risen substantially after a pioneering publication of Fuyuki *et al.* [5] featuring EL imaging with a charge-coupled device (CCD) camera. Within few years, EL imaging has become a valuable tool for fast and spatially resolved characterization of crystalline Si solar cells and modules [6–14].

Figure 3.1 depicts the two typical setups for EL characterization: (a) the EL imaging setup with a CCD camera, a power source, and a shielding against ambient light and (b) the EL spectroscopy setup with a monochromator and a cooled detector. The detector can be a Si CCD array, an InGaAs photodiode array, a Ge photodiode, or a photomultiplier, and especially in case of single photodiodes, it can be combined with a lock-in amplifier. For a good coverage of a wide wavelength range relevant for photovoltaics, often a combination of Si CCD and InGaAs photodiode arrays is used.

The attractiveness of EL imaging results partly from the high spatial resolution combined with its simplicity and swiftness, which is clearly superior to alternative techniques such as the light beam-induced current (LBIC) measurement. The measuring times of EL images are around two orders of magnitude shorter compared with LBIC. The technique can be used to survey entire modules but also to visualize microscopic defects on the micrometer scale. In addition, EL, that is, the emission of light by application of an electrical bias, is just the complementary reciprocal action of the photovoltaic effect taking place in solar cells and modules.

Advanced Characterization Techniques for Thin Film Solar Cells, Second Edition.
Edited by Daniel Abou-Ras, Thomas Kirchartz, and Uwe Rau.

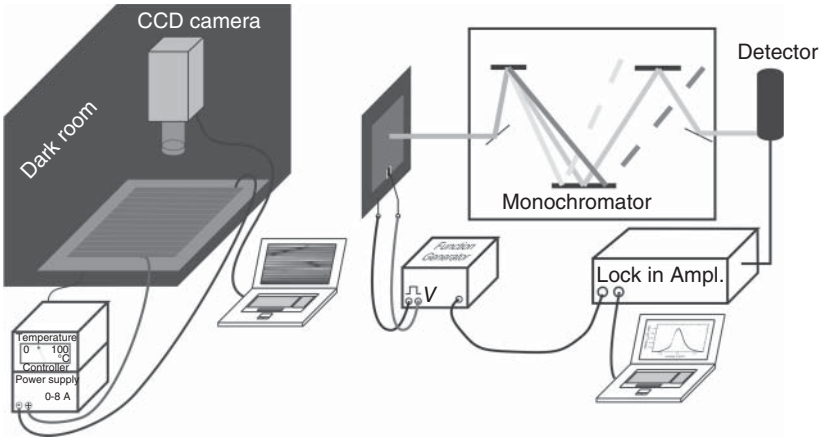

Figure 3.1 Schematic drawing of the measurement setups used for (a) spatially resolved EL imaging under forward or reverse bias and (b) EL spectroscopy.

Therefore, all important physical processes that influence the photovoltaic performance of a solar cell – such as recombination, resistive, and optical losses – are in a complementary way reflected in the EL of the same device. This fact guarantees the relevance of the method for photovoltaics. In addition to spatially resolved methods, also spectrally resolved EL [15–18] has proven to be a suitable tool for the analysis of solar cells. Finally, both spatially and spectrally resolved EL can be combined to a certain extent by the comparison of EL images made using different spectral filters [8, 19, 20].

This chapter starts with a brief comprehensive description of the basic theory underlying both spatially and spectrally resolved EL analysis. This description uses the convenience provided by the fundamental reciprocity between EL emission and photovoltaic action of solar cells [21]. Subsequently, Section 3.3 discusses recent results on spectrally resolved EL of different types of solar cells. Since the bulk of the literature on EL imaging studies crystalline Si solar cells, Section 3.4 reviews photographic surveying of Si wafer-based solar cells. Section 3.5 introduces EL images acquired on Cu(In,Ga)Se_2 modules and explains the determination of the sheet resistance of front and back contact. Section 3.6 discusses the differential analysis of EL images under illumination.

3.2 Basics

EL, that is, the emission of light in consequence to the application of a forward voltage bias to a diode, is the reciprocal action to the standard operation of a solar cell, namely, the conversion of incident light into electricity. According to the reciprocity theorem, the EL intensity ϕ_{em} of a solar cell emitted at any position

$\mathbf{r} = (x, y)$ of its surface is given by [21]

$$\begin{aligned}\phi_{\mathrm{em}}(E, \mathbf{r}) &= [1 - R(E, \mathbf{r})] Q_{\mathrm{i}}(E, \mathbf{r}) \phi_{\mathrm{bb}}(E) \exp\left(\frac{qV(\mathbf{r})}{kT}\right) \\ &= Q_{\mathrm{e}}(E, \mathbf{r}) \phi_{\mathrm{bb}}(E) \exp\left(\frac{qV(\mathbf{r})}{kT}\right), \end{aligned} \tag{3.1}$$

where kT/q is the thermal voltage, $V(\mathbf{r})$ is the internal junction voltage, E is the photon energy, and $Q_{\mathrm{e}}(\mathbf{r}) = [1 - R(\mathbf{r})] Q_{\mathrm{i}}(\mathbf{r})$ is the local external quantum efficiency determined by the front surface reflectance $R(\mathbf{r})$ and the internal quantum efficiency $Q_{\mathrm{i}}(\mathbf{r})$. The spectral photon density ϕ_{bb} of a blackbody

$$\phi_{\mathrm{bb}}(E) = \frac{2\pi E^2/(h^3 c^2)}{\exp(E/kT) - 1} \tag{3.2}$$

depends on Planck's constant h and the vacuum speed c of light. Recording the EL emission of a solar cell with a CCD camera, the EL signal $S_{\mathrm{cam}}(E, \mathbf{r})$ in each camera pixel is

$$S_{\mathrm{cam}}(\mathbf{r}) = \int Q_{\mathrm{cam}}(E) Q_{\mathrm{e}}(E, \mathbf{r}) \phi_{\mathrm{bb}}(E) \mathrm{d}E \exp\left(\frac{qV(\mathbf{r})}{kT}\right), \tag{3.3}$$

where Q_{cam} is the energy-dependent sensitivity of the detecting camera. Since in Equation 3.3 $\phi_{\mathrm{bb}}(E)$ and $Q_{\mathrm{cam}}(E)$ depend on energy but not on the surface position $\mathbf{r}$, lateral variations in the detected EL intensity emitted from different surface positions originate only from the lateral variations of the external quantum efficiency Q_{e} and of the internal voltage V. Hence, Equation 3.1 and thus Equation 3.3 consider all losses occurring in solar cells: The external quantum efficiency Q_{e} expresses the recombination and optical losses, while the internal voltage V reflects the resistive losses. As will be shown later, in some cases the exponential voltage-dependent term dominates the image, making EL analysis a tool that is especially suitable to analyze resistive losses.

In order to discriminate between recombination and optical losses that influence the detected and spectrally integrated EL spectrum on the one hand and resistive losses that only affect the absolute EL intensity on the other hand, a single EL image is insufficient. Measuring spectrally resolved EL at every position of the solar cell, however, would sacrifice the speed advantage of luminescent imaging. Thus, comparing the difference of images that use different spectral filters represents a viable compromise that combines spatial resolution with spectral information. Application of a spectral filter with transmittance T_{fil} changes Equation 3.3 to

$$S_{\mathrm{cam}}^{\mathrm{fil}}(\mathbf{r}) = \int Q_{\mathrm{cam}}(E) T_{\mathrm{fil}}(E) Q_{\mathrm{e}}(E, \mathbf{r}) \phi_{\mathrm{bb}}(E) \mathrm{d}E \exp\left(\frac{qV(\mathbf{r})}{kT}\right). \tag{3.4}$$

It is easily seen that the measurement of the contrast

$$C_{\mathrm{s}}(\mathbf{r}) = \frac{S_{\mathrm{cam}}^{\mathrm{fil},1}(\mathbf{r})}{S_{\mathrm{cam}}^{\mathrm{fil},2}(\mathbf{r})} = \frac{\int Q_{\mathrm{cam}}(E) T_{\mathrm{fil},1}(E) \phi_{\mathrm{em}}(E, \mathbf{r}) \mathrm{d}E}{\int Q_{\mathrm{cam}}(E) T_{\mathrm{fil},2}(E) \phi_{\mathrm{em}}(E, \mathbf{r}) \mathrm{d}E} \tag{3.5}$$

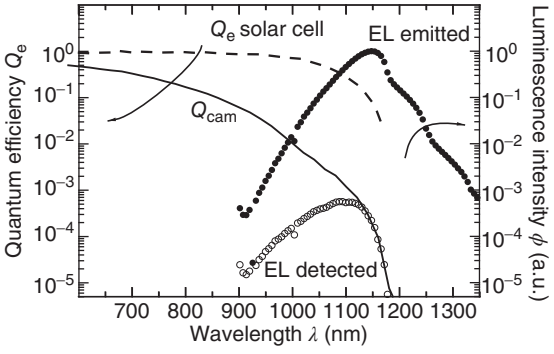

Figure 3.2 Comparison of the quantum efficiency of Si solar cell and Si CCD camera with the electroluminescence emitted by the solar cell and detected by the CCD camera. The connection between EL and quantum efficiency of the solar cell is given by Equation 3.1, and the connection between the camera sensitivity Q_{cam} and the EL detected by the camera is given by Equation 3.3.

between two EL images acquired at the same voltage V using two different filters as proposed by Würfel *et al.* [8] cancels out the voltage-dependent term in Equation 3.4. Thus, the combination of suitable filters isolates the optical properties and the recombination losses from the resistive losses.

Finally, for spectrally resolved EL measured integrally over the area of a solar cell, we obtain from Equation 3.3 for the detected signal

$$S_{det}(E) = Q_{det}(E)\phi_{bb}(E)dE \int Q_e(E, \mathbf{r}) \exp\left(\frac{qV(\mathbf{r})}{kT}\right) d\mathbf{r}, \tag{3.6}$$

where $Q_{det}(E)$ denotes the spectral sensitivity of the detector system including the detector itself as well as the monochromator. Depending on the details of the optics used in the experiment, the spatial integral in Equation 3.6 extends over a smaller or larger part of the cell area.

It becomes clear from Equations 3.5 and 3.6 that the spectral sensitivities $Q_{cam}(E)$ and $Q_{det}(E)$ of the camera or the detector are critical for the analysis of the EL emission. Most photographic EL setups use a Si CCD camera due to the lower noise and the lower price compared with an InGaAs camera. As shown in Figure 3.2 (solid line), the quantum efficiency (QE) of such a Si CCD camera is below 10^{-3} at the maximum of the EL emission. The integral EL intensity detected by the camera (open circles in Figure 3.2) is reduced by more than three orders of magnitude compared with the imaginary case of a perfect detector with a QE of unity over the whole spectral range of interest.

3.3 Spectrally Resolved EL

In the past, the bulk of spectroscopic luminescence investigations of photovoltaic materials have been done using optical and not electrical excitation. These

spectroscopic photoluminescence (PL) studies helped, for example, to determine the dislocation densities in multicrystalline Si wafers [22–24] or to investigate defects [25, 26] and the quasi-Fermi-level splitting in chalcopyrites [27] and thin-film Si solar cells [28]. Spectroscopic EL measurements have been rarely used for the characterization of solar cells, in spite of the fact that EL emission is the complementary action to the photovoltaic effect and is directly related to QE measurements. However, some recent publications [15–20] make use of the reciprocity between QE and EL (Equation 3.1) and explore the applicability of spectrally resolved EL for solar-cell characterization.

According to Equation 3.1, the EL spectrum contains in principle the same information as the QE spectrum. However, the spectral range where useful information can be gained is quite different for both methods, EL and QE. This is because the weighting factor in Equation 3.1, the blackbody spectrum ϕ_{bb}, depends exponentially on photon energy. This exponential energy dependency of ϕ_{bb} leads to the fact that EL is only measurable close to the band gap, since all higher energies E are damped by $\exp(-E/kT)$. In general, a QE measurement contains information on optical properties as well as on the recombination behavior of the solar cell. The optical properties, including the path length enhancement by the light-trapping scheme, the absorption coefficient of the absorber material, and the quality of the back reflector, dominate the QE especially at lower photon energies close to and below the band-gap energy. Thus, the Boltzmann factor of the blackbody spectrum emphasizes these optical properties, which are therefore relatively easy to extract from luminescence spectra as compared with QE spectra. One example is the determination of the absorption coefficient. Although it is possible to determine the absorption coefficient α of crystalline Si at room temperature by QE measurements [29], the determination via PL measurements has proven to be far more sensitive [30]. In case of Si, where the absorption coefficient is well known for energies below the band gap (cf. Refs [29, 30]), EL spectra reveal information on the light-trapping properties of the measured cell as, for instance, the path length enhancement factor [18, 31].

In contrast, the electronic properties of the solar cell, such as the diffusion length or the surface recombination velocity of the minority carriers, are usually extracted from the QE in an energy range slightly above the band-gap energy, where the QE is still close to its maximum. In this energy range, which corresponds to wavelength λ range around $780\,\text{nm} < \lambda < 920\,\text{nm}$ for crystalline Si, the QE has a much better signal-to-noise ratio than the EL. Thus, the determination of the effective diffusion length – using, for instance, the method of Basore [32] – is more easily achieved by a standard QE measurement than with EL.

A useful feature of Equation 3.1 is that it allows us to determine the so-called radiative saturation current density $J_{0,\text{rad}}$ [33]. This radiative and therefore lower limit of the saturation current density J_0 is defined by the photon flux keeping a solar cell in thermodynamic equilibrium. This photon flux cannot be measured directly, since it will not create excess carriers in a detector which is at the same

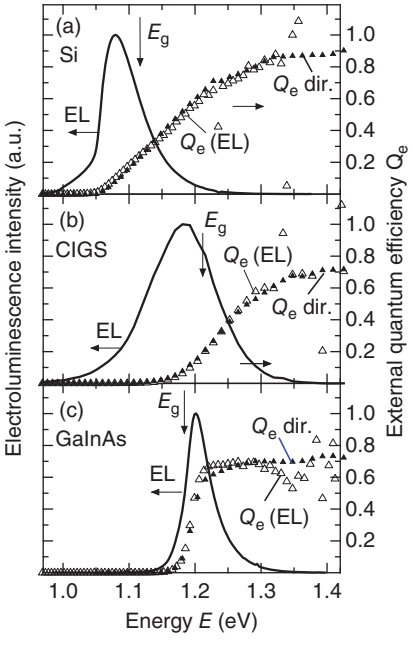

Figure 3.3 Comparison of EL spectra (lines) and quantum efficiencies (open triangles) of three different solar cells based on (a) crystalline Si, (b) Cu(In,Ga)Se_2 (CIGS), and (c) GaInAs. In addition to the directly measured quantum efficiencies, the filled triangles represent the quantum efficiencies that follow from the EL spectra using Equation 3.1. A relatively broad EL peak as for the indirect semiconductor Si and the disordered polycrystalline semiconductor Cu(In,Ga)Se_2 correlates with a slow rise from low to high QE. In contrast, the direct and crystalline semiconductor GaInAs features a sharp peak and a small transition region between high and low QE. (Data taken from Refs [15, 17].)

temperature as the device. However, the radiative recombination current

$$J_{\mathrm{rad}} = J_{0,\mathrm{rad}} \left[\exp\left(\frac{qV}{kT}\right) - 1 \right] \tag{3.7}$$

resulting from a voltage V that drops over the rectifying junction is accessible by making use of the reciprocity relation. With a calibrated setup (absolute number of photons per area and time interval is known), $J_{0,\mathrm{rad}}$ could be derived, provided the voltage V is known accurately. However, a much simpler way to determine $J_{0,\mathrm{rad}}$ is given by Equation 3.1. The measurement of the photovoltaic QE Q_e directly leads to the radiative saturation current density

$$J_{0,\mathrm{rad}} = q \int_0^\infty Q_e(E) \phi_{\mathrm{bb}}(E) \mathrm{d}E. \tag{3.8}$$

In practice, the simplest way is to scale the EL emission with the calibrated QE as shown in Figure 3.3 and then to integrate the EL emission to obtain the correct $J_{0,\mathrm{rad}}$. The quantity $J_{0,\mathrm{rad}}$ defines not only the lower limit for the actual saturation current density J_0 of a real solar cell but also the upper limit for the open-circuit voltage $V_{\mathrm{oc,rad}} = kT/q \ln(J_{\mathrm{sc}}/J_{0,\mathrm{rad}} + 1)$. Comparing the radiative open-circuit voltage $V_{\mathrm{oc,rad}}$ with the actual V_{oc} determined from a current/voltage (J/V) measurement gives the loss $\Delta V_{\mathrm{oc}} = V_{\mathrm{oc,rad}} - V_{\mathrm{oc}}$ due to nonradiative recombination. This voltage loss is a useful quantity to compare the quality of different solar-cell materials in terms of their recombination. Interestingly, there is a direct relationship between ΔV_{oc} and the QE Q_{LED} of a light-emitting diode (LED) since both quantities depend only on the ratio of nonradiative to radiative recombination [21].

Figure 3.3 shows the QE (solid triangles) and the EL spectrum (solid lines) of three different solar-cell materials, that is, (a) crystalline Si, (b) Cu(In,Ga)Se_2 (CIGS), and (c) GaInAs. In addition, we compare the QE measured with a QE setup as described in Chapter 2 with the QE obtained from the EL spectrum using Equation 3.1. Since the EL spectrum is measured only in relative units, the QE from EL is shifted in such a way that it fits best to the direct QE. The materials shown in Figure 3.3 are crystalline Si, an indirect semiconductor; Cu(In,Ga)Se_2, a polycrystalline, direct semiconductor; and GaInAs, a crystalline, direct semiconductor. While the first two samples are single-junction solar cells, the GaInAs solar cell is the middle cell of a triple-junction solar cell consisting of a GaInP/GaInAs/Ge stack [17]. Correspondingly, the shape of the absorption edge and the width of the EL spectrum are different for the three devices. In case of Si and Cu(In,Ga)Se_2, the peaks are broad and the absorption edge is smeared out, while for GaInAs, the spectrum is quite narrow and the QE changes abruptly from zero to its saturation value. The indirect band gap of Si explains the differences between Si and GaInAs: The lower probability of radiative transitions and correspondingly the lower and less abrupt absorption coefficient of the indirect band-gap semiconductor Si explain the broader transition region between high and low absorption and the broader peak. In case of Cu(In,Ga)Se_2, the reason for the broad peak lies in the disordered nature of the polycrystalline semiconductor. Both the intentional stoichiometric inhomogeneity, due to band-gap grading normal to the cell surface, and the unintentional band-gap variation [34], due to lateral changes in stoichiometry ([In]/[Ga] ratio), lead to a clear broadening of the EL peak and of the transition region between high and low absorption in the QE spectrum.

Despite the different nature of the three investigated samples, the QE derived from the EL (open triangles) fits well to the directly measured QE (solid triangles). For all three cells, we are able to calculate the radiative saturation current density $J_{0,\mathrm{rad}}$ and subsequently the radiative open-circuit voltage

$$V_{\mathrm{oc,rad}} = \frac{kT}{q} \ln\left(\frac{J_{\mathrm{sc}}}{J_{0,\mathrm{rad}}} + 1\right). \tag{3.9}$$

By comparing $V_{\mathrm{oc,rad}}$ with the open-circuit voltage $V_{\mathrm{oc,meas}}$ as derived from a J/V measurement, one obtains the voltage difference [21, 35]

$$\Delta V_{\mathrm{oc}} = V_{\mathrm{oc,rad}} - V_{\mathrm{oc,meas}} = -\frac{kT}{q} \ln(Q_{\mathrm{e}}^{\mathrm{LED}}), \tag{3.10}$$

which relates to the external quantum efficiency $Q_{\mathrm{e}}^{\mathrm{LED}}$ of the solar cell if operated as a LED.

For the previous examples we have $\Delta V_{\mathrm{oc}} = V_{\mathrm{oc,rad}} - V_{\mathrm{oc}} = 185\,\mathrm{mV}$ for the Si cell, $\Delta V_{\mathrm{oc}} = 216\,\mathrm{mV}$ for the Cu(In,Ga)Se_2 solar cell, and $\Delta V_{\mathrm{oc}} = 132\,\mathrm{mV}$ for the GaInAs cell. Thus, since the GaInAs as a direct, crystalline semiconductor has the best ratio between radiative and nonradiative recombination, it also possesses – relative to the band-gap energy – the best open-circuit voltage and is also the best LED of the three cells. Recently, similar investigations have also been

performed for organic bulk heterojunction solar cells, revealing that the LED QE in polymer/fullerene blends is much lower than in most inorganic solar cells [36]. Typical values for the LED QE of organic solar cells are in the range of $10^{-6}-10^{-7}$, leading to losses in open-circuit voltage that are typically >350 mV [37]. This implies that the ratio of radiative to nonradiative recombination is less favorable in current organic solar cells and explains the relatively low open-circuit voltages of these devices. Organic–inorganic perovskites are a solution-processable solar-cell technology with relatively high band gaps around 1.55–1.6 eV depending on the mode of measuring the band gap for the typical methylammonium lead iodide absorber. The radiative open-circuit voltage measured on $CH_3NH_3PbI_3$ devices is around 1.32–1.34 eV [38, 39] and measured open-circuit voltages have exceeded 1.1 V [40]. Thus, the loss ΔV_{oc} is in the range of just above 200 mV for the best perovskite solar cells and therefore on a similar level as Si or Cu(In,Ga)Se_2.

Green [41] calculated the radiative saturation current density $J_{0,rad}$ from the reported external quantum efficiencies of record solar cells of different technologies using Equation 3.1 as well as Equation 3.10 to obtain Q_e^{LED} (denoted as external radiative efficiency (ERE)). From the available data, Q_e^{LED} values over 20% for record efficiency GaAs devices, approximately 0.5% for the best Si solar cells, and approximately 0.2%/10^{-4}% for record Cu(In,Ga)Se_2/CdTe were deduced.

In recent years, efficiencies of thin-film GaAs solar cells have increased substantially to the current record value of 28.8% efficiency received by Alta Devices [42]. Part of the improvement was due to the fact that thin-film designs with good back reflectors make better use of photon recycling than previous designs of GaAs solar cells. Around open circuit, a GaAs solar cell is a good LED that illuminates itself, that is, photons created by radiative recombination are reabsorbed which increases the concentration of charge carriers at open circuit and therefore the voltage that can build up. However, this photon recycling effect boosts the open-circuit voltage only if parasitic absorption, for example, at a back mirror, is minimized [43]. Otherwise, the emitted photons are absorbed parasitically in the back contact and are not able to be reabsorbed and improve the voltage. A recent overview paper [44] discusses the influence of optics on the thermodynamics of the open-circuit voltage in more detail.

Multijunction solar cells offer another particularly interesting application for spectrally resolved EL measurements. Characterization of multijunction solar cells is generally impeded by the difficulty to measure the cells in a monolithic stack independently. Monolithic means here that all layers of the cell are grown on top of each other without the possibility to contact the individual cells. Since the band-gap energies of the cells in a multijunction solar cell are usually different to make best use of the solar spectrum, the EL spectra will be at different energetic positions close to these band-gap energies. Measuring, for example, one spectrum of a triple-junction solar cell will then contain three EL peaks corresponding to the different subcells [17]. According to Equation 3.1, the absolute amount of luminescence changes exponentially with the applied voltage. Thus, the logarithm of the EL intensity of the three peaks will then be linked to

the voltage applied to the corresponding subcell at a given injection current. By varying the injection currents and measuring the EL spectra, the internal voltages of the three subcells in a triple-junction solar cell could then be determined except for an additive offset voltage if the measurement was not calibrated for absolute photon fluxes. The determination of the unknown offset voltage is possible using the open-circuit voltage V_{oc} and the corresponding short-circuit current density J_{sc} at any illumination to scale the sum of the voltages of the subcells at an injection current density $J_{inj} = J_{sc}$ such that it corresponds to the open-circuit voltage of the complete cell.

3.4 Spatially Resolved EL of c-Si Solar Cells

The rapidly growing interest in EL as a characterization method for solar cells is due to the use of digital CCD cameras for image detection. Although the information contained in a single pixel is spectrally integrated information, the ability to get an image in very short time frames has made EL imaging a standard tool for the quality control of finished crystalline Si solar cells (for a recent review, see Ref. [13]). Possible reasons for spatial variations of the luminescence belong to two major categories:

1) The cell or part of the cell has a severe local failure such as a crack in the whole wafer or a broken finger that isolates a part of the cell from the rest as shown in Figure 3.4.
2) The optical or electronic properties of the solar cell vary locally, for instance, the minority-carrier diffusion length is lower close to dislocations or grain boundaries. Likewise, the surface recombination velocity is higher at the metal contacts of a point-contact mask (where the metal is in direct contact with the absorber layer) as compared with the parts of the back surface covered with a passivation layer.

Failure analyses, that is, investigations of category 1, need to detect a specific process-induced problem such as a crack or a broken finger, and they have to distinguish such a problem from causes such as locally reduced diffusion lengths. This is achieved either by additional visual inspection or by using properly programmed image processing software.

Investigations of category 2, that is, the quantitative determination of physical parameters from the EL image, require methods that go beyond the inspection of a single image. As pointed out in Section 3.2, every pixel in the EL image contains information on resistive, optical, and recombination effects that can be discriminated due to their different energy and voltage dependence. To determine optical and electronic parameters such as effective diffusion length or the backside reflectance, one has to isolate the energy-dependent parts of the EL from the voltage-dependent ones using filters as described in Refs [8, 31, 45]. Equation 3.5

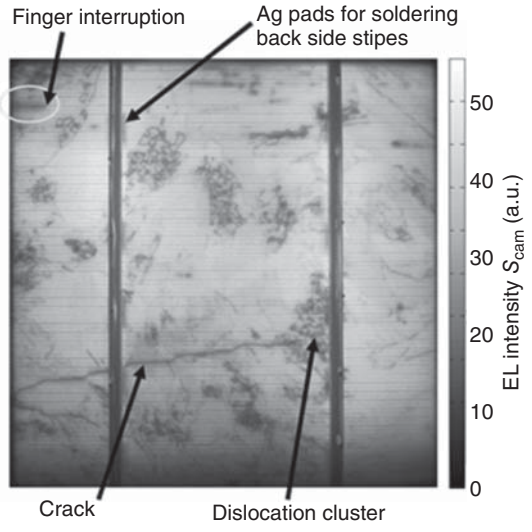

Figure 3.4 Example of an EL image of a $12.5 \times 12.5\,cm^2$ multicrystalline Si solar cell at 3 A featuring both process-induced failures such as locally reduced EL emission due to broken fingers or cracks as well as variations in the EL emission due to variations of electronic properties such as bulk diffusion lengths (e.g., reduced EL at dislocations) and the surface recombination velocity (e.g., reduced EL at unpassivated back side under Ag pads).

shows that the ratio of two EL images acquired using various filters but at the same voltage is free of any resistive effect. The exponential voltage dependence of the EL signal that is sensitive to any resistive effects cancels out, and only the changes in the image due to the different wavelength ranges selected by the filters remain.

Although giving absolute information on effective diffusion lengths from relative light intensities captured by a camera, the filter method is rather sensitive to the exact filter transmission and camera sensitivity. One approach to overcome these shortcomings was presented by Hinken *et al.* [46] using PL imaging instead of EL imaging. The method makes use of one additional degree of freedom present in PL imaging. While for EL only the voltage and injection current are variable, for PL imaging of solar cells, one can vary the voltage applied to the contacts of the solar cell independently from the injection of minority carriers which is done by illuminating the sample with a light source, for example, a laser. Thus, by comparison of images acquired at open-circuit and short-circuit conditions, the effective diffusion length is calculated [46].

In case of EL imaging, changing the voltage at the contacts is equivalent to changing the injection of minority carriers since no additional illumination is present. It is not possible to change the two independently, that is, one degree of freedom is reduced compared with PL imaging. However, the variation of the voltage still provides additional information on both resistive [10] and

recombination [47] effects. Especially the locally resolved determination of the series resistance via EL and PL has recently attracted interest. The series resistance R_s at the position $\mathbf{r} = (x, y)$ is usually [48] defined by

$$R_s(\mathbf{r}) = \frac{V_{ext} - V(\mathbf{r})}{J(\mathbf{r})}, \tag{3.11}$$

where V_{ext} is the external voltage at the contacts, $V(\mathbf{r})$ the local voltage, and $J(\mathbf{r})$ the local current density. The two quantities known are the external voltage V_{ext} and the total current I or the current density $J = I/A$ averaged over the area A. This leaves the local voltage and the local current density as the remaining quantities to be determined from EL. While the local voltage can easily be calculated from the logarithm of the local EL intensity according to Equation 3.1 (except for a constant offset), the local current density is the most critical quantity. The first attempt to determine the local series resistance by Hinken *et al.* [10] used an evaluation routine similar to Werner's [49] method to determine the local series resistance from the local emission and the first derivative of the EL emission for different voltages. This original method has the disadvantage that it assumes the local current density to be homogeneous. Thus, the method was only applicable to monocrystalline solar cells but not to multicrystalline Si solar cells. Attempts to improve this method were published by Haunschild *et al.* [48] and Breitenstein *et al.* [50]. Haunschild *et al.* [48] assumed that the EL intensity at low voltages, where resistive voltage losses are irrelevant due to the low differential conductance of the p–n junction at low voltages, is approximately proportional to the effective diffusion length. This assumption implies that the local current density is inversely proportional to the local EL intensity and can thus be obtained from one low-voltage EL image, again except for a constant factor. This method has still one disadvantage, namely, that it requires a measurement at relatively low voltages to make sure that there are no resistive effects. Low voltages imply a lower EL signal and in turn a long integration time. To improve the speed of the method, Breitenstein *et al.* [50] proposed an iterative computation scheme using different EL measurements taken at higher voltages with low integration times.

In addition, a solar cell with locally different current densities does no longer have a local series resistance that is a well-defined quantity. Theoretically, the series resistance according to Equation 3.11 depends not only on local properties but instead on all currents flowing everywhere in the device. This claim can be tested by assuming a network of two diodes with ohmic (voltage-independent) series resistances, and the diodes themselves are connected with resistances mimicking the emitter layer and the grid. If both diodes have different diode properties, then the apparent series resistance of one of the two diodes will always depend on the current flowing through the other diode and will therefore not be constant when varying the voltage.

It should be mentioned that apart from the methods using EL imaging, which are presented here, there are a large number of methods developed for PL imaging as well that allow similar investigations on solar cells and wafers [51–58].

3.5
EL Imaging of Thin-Film Solar Cells and Modules

EL analysis is becoming increasingly popular also for thin-film solar cells and modules [59–66]. The suitability and the potential of EL analysis of these devices are analogous to that of Si cells as long as two requirements are fulfilled: The thin-film solar cell should be a p–n-junction device and the emission should be due to recombination of free electrons and holes in contrast to, for example, tail-to-tail emission [67, 68]. Cu(In,Ga)Se_2 solar cells fulfill these requirements but not amorphous or microcrystalline solar cells [68]. The following discusses the investigation of a Cu(In,Ga)Se_2 module as a general example for the analysis of a thin-film module. Variations of the material quality and stoichiometry in Cu(In,Ga)Se_2 solar cells occur on relatively small length scales below 20 µm [34, 69, 70] and would therefore require microscopic investigations of the luminescence [71–75]. However, prominent features in EL images on the module level are predominantly due to resistive effects, that is, either caused by series resistances or by shunts. This can be seen from Figure 3.5 presenting EL images of a Cu(In,Ga)Se_2 module at two different current densities ($J = 6.25\,\mathrm{mA/cm^2}$ (a) and $J = 37.5\,\mathrm{mA/cm^2}$ (b)). The module consists of $N_c = 42$ cells connected in series with single cells of an area of $20 \times 0.4\,\mathrm{cm^2}$. The image acquired at the lower current density (Figure 3.5a) shows dark cells at the top of the module (i.e., for low x values) as the most striking feature. When increasing the current density to $J = 37.5\,\mathrm{mA/cm^2}$, there are no cells left that show a low emission over the whole width (i.e., extension in y direction).

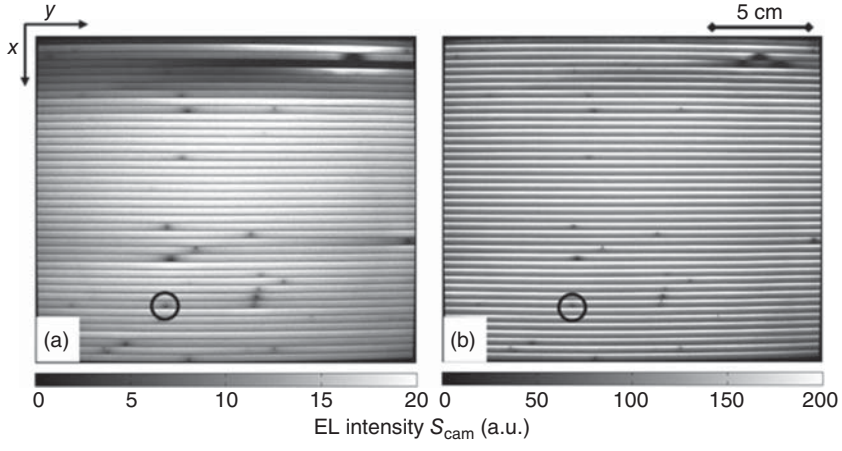

Figure 3.5 EL images at (a) $J = 6.25\,\mathrm{mA/cm^2}$ and (b) $J = 37.5\,\mathrm{mA/cm^2}$ of the same Cu(In,Ga)Se_2 module. Areas with quenched EL intensity are caused by shunts, which have a larger influence on the current distribution through the cell when current densities and therefore the differential conductance of the p–n junction are small as in (a). Since the differential conductance of the p–n junction increases with increasing current density, the EL intensity drop in the x direction becomes steeper as displayed in (b).

However, roughly circular dark spots, especially in the upper right corner, remain visible. In addition, every cell in Figure 3.5b shows a characteristic intensity gradient from high intensity at the top to low intensity at the bottom with little variation in y direction. This intensity gradient is not visible in Figure 3.5a for the image taken with the lower current density.

The macroscopic analysis discussed in the following is an example where it is reasonable to assume that $Q_e(E, \mathbf{r})$ is almost spatially independent, especially because the exponential dependence of the variations of the internal junction voltage $V(\mathbf{r})$ has a much stronger impact on the EL intensity than possible spatial variations of $Q_e(\mathbf{r})$. Thus, assuming a spatially and voltage-independent Q_e rearranges Equation 3.3 to

$$S_{cam}(\mathbf{r}) = \int Q_{cam}(E) Q_e(E) \phi_{bb}(E) \mathrm{d}E \exp\left(\frac{qV(\mathbf{r})}{kT}\right). \tag{3.12}$$

Consequently, we can determine from S_{cam} the voltage drop over the junction

$$\begin{aligned} V(\mathbf{r}) &= \frac{kT}{q}\left[\ln\left\{S_{cam}(\mathbf{r})\right\} - \ln\left\{\int Q_{cam}(E)\, Q_e(E) \phi_{bb}(E) \mathrm{d}E\right\}\right] \\ &= \Delta V(\mathbf{r}) + V_{offs} \end{aligned} \tag{3.13}$$

except for a spatially constant offset voltage V_{offs}.

Figure 3.6 visualizes the application of Equation 3.13 to the EL data from Figure 3.5 to obtain the relative voltage ΔV as a function of the coordinate x across all cells in the module. Note that we have generated the line scan by averaging over the y-coordinate, that is, over the whole length of the module. Two important features are immediately obvious from these line scans: first, the relatively low voltage drop across some cells due to the shunts, especially visible at low bias, and second, the voltage losses in x direction across individual cells due

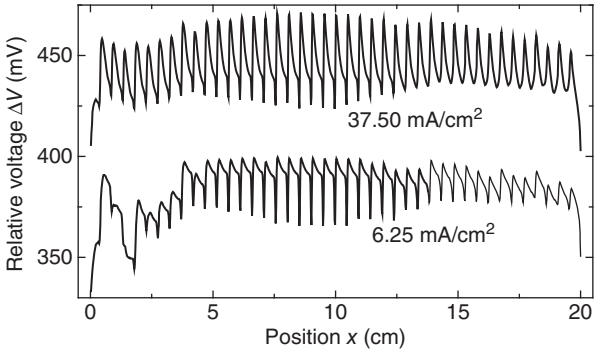

Figure 3.6 Internal voltage line scans (x direction) of the whole module of Figure 3.5 taken at different bias current densities ($J_D = 37.5$ and 6.25 mA/cm^2). The effect of shunts on the voltage is more pronounced for smaller than for higher injection current densities. This effect is most obvious for the cells located at positions 1 cm $< x <$ 4 cm. The line scans are averaged in y direction over the whole module length l.

to the sheet resistance of window and back contact layer, especially pronounced at large bias.

For a more quantitative access to the data in Figure 3.6, we need to model the voltage distribution along the whole width w of one subcell. This requires the solution of the coupled current continuity equations in the window layer and in the back contact [60]. In one dimension, we have

$$\frac{\mathrm{d}^2}{\mathrm{d}x^2} V_1 = -\rho_1^{\mathrm{sq}} \frac{\mathrm{d}}{\mathrm{d}x} j_1^{\mathrm{p}} = \rho_1^{\mathrm{sq}} J(V), \tag{3.14}$$

and

$$\frac{\mathrm{d}^2}{\mathrm{d}x^2} V_2 = -\rho_2^{\mathrm{sq}} \frac{\mathrm{d}}{\mathrm{d}x} j_2^{\mathrm{p}} = -\rho_2^{\mathrm{sq}} J(V), \tag{3.15}$$

where V_1, V_2 denote the voltages, j_1^{p}, j_2^{p} are the line current densities, and the ρ_1^{sq}, ρ_2^{sq} are the sheet resistances of the window layer and the back contact.

The solution of Equations 3.14 and 3.15 is given by

$$\Delta V = -\frac{j_{\max}^{\mathrm{p}} \rho_1^{\mathrm{sq}}}{\lambda} \sinh(\lambda x) + \frac{j_{\max}^{\mathrm{p}} [\rho_1^{\mathrm{sq}} \cosh(\lambda w) + \rho_2^{\mathrm{sq}}]}{\lambda \sinh(\lambda w)} \cosh(\lambda x) + \mathrm{const} \tag{3.16}$$

with the inverse characteristic length $\lambda = [G_{\mathrm{D}}(\rho_1^{\mathrm{sq}} + \rho_2^{\mathrm{sq}})]^{1/2}$ and $G_{\mathrm{D}} = \mathrm{d}J/\mathrm{d}V$ as the differential conductance at the given bias conditions.

For the investigation of the sheet resistances, EL images of a nonshunted region of the module were recorded with a higher spatial resolution. Figure 3.7 shows the calculated ΔV values calculated from the EL signals across a single nonshunted cell in x direction for three exemplary different bias current densities ($J = 50$, 25,

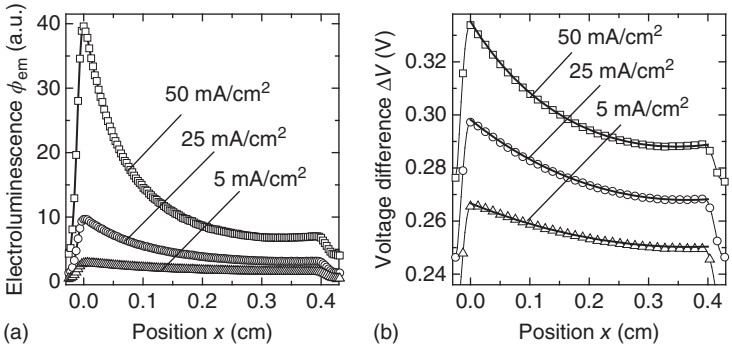

Figure 3.7 (a) Line scans of the electroluminescence intensity across one individual cell of the module shown in Figure 3.5 at different bias current densities ($J_{\mathrm{D}} = 50$, 25, 5 mA/cm^2). (b) Line scans of the relative internal voltages ΔV calculated from the EL line scans in (a) according to Equation 3.13. The solid lines represent fits of Equation 3.16 to the experimental voltage data (open symbols). The sheet resistances used in all fits are $\rho_{\mathrm{ZnO}}^{\mathrm{sq}} = 18.2\,\Omega/\mathrm{sq}$ and $\rho_{\mathrm{Mo}}^{\mathrm{sq}} = 1.1\,\Omega/\mathrm{sq}$ for the ZnO window layer and for the Mo back contact, respectively. Note that the experimental data are averages over 1376 lines in y direction (corresponding to a width of 3.8 cm). (Data taken from Ref. [60].)

5 mA/cm^2). Note that we have averaged the signals over 1376 lines in y direction (corresponding to a width of 3.8 cm).

To fit these experimental data, we have the choice either to determine the junction conductance G_D from an additional measurement of J_{sc}/V_{oc} independently (as in Ref. [60]) or to include the G_D values at each bias point into the fitting procedure. The latter method is based on the EL experiment alone and has the advantage of not needing an extra calibration measurement. The solid lines in Figure 3.7b show the result of a simultaneous fit of Equation 3.16 to the experimental data obtained for the different bias current densities. Fitting parameters are the sheet resistances ρ^{sq}_{ZnO} of the ZnO and ρ^{sq}_{Mo} of the Mo back contact as well as the differential junction conductance G_D at each bias point. The fitting of the data presented in Figure 3.7b and of similar data of the same module at six other voltages yields $\rho^{sq}_{ZnO} = 18.2\,\Omega/\text{sq}$ and $\rho^{sq}_{Mo} = 1.1\,\Omega/\text{sq}$. Since these values are very close to the results of the calibrated method ($\rho^{sq}_{ZnO} = 18.0\,\Omega/\text{sq}$, $\rho^{sq}_{Mo} = 1.25\,\Omega/\text{sq}$) [60], we conclude that the determination of the sheet resistances from the EL data alone is reasonably reliable. Note that the voltage curve across a cell must have a minimum to allow us to determine series resistances of both contacting layers. For the module investigated here, such a minimum is not visible until the current density $J = 50\,\text{mA/cm}^2$. The reason for that is the difference by a factor of 15 between both series resistance values. The voltage curve of a module with almost similar and high series resistances of both contacting layers would possess a minimum almost in the middle of the cell and that already at low current densities. In addition to the work described previously, recent practical applications of EL imaging concern the analysis of shunts due to line scribe failures [76] and areal defects [77] in Cu(In,Ga)Se$_2$ solar modules. Moreover, multispectral imaging [78] (i.e., the combination of spectrally and spatially resolved luminescence) opens new ways to gain additional insight into the optoelectronic properties especially of disordered materials with local variations of the band-gap energy.

Finally, we note that some complications for the aforementioned method for the interpretation of EL images in thin-film solar cells may occur because of light-induced transients in Cu(In,Ga)Se$_2$ and the effect of bulk series resistance [64, 79]. Furthermore, the assumption of radiative recombination as an "ideality one process," as assumed in Equation 3.1, is not necessarily true for any photovoltaic material [68]. For instance, in a-Si:H thin-film modules, a radiative ideality factor larger than one is detected in experiments [80] because of the spectral shift of the emission spectrum.

3.6
Electromodulated Luminescence under Illumination

Up to this point we have considered EL of cells and modules only without light bias. However, the combination of light and voltage bias is important, for example, to investigate the solar-cell devices under real working conditions. The emitted photon density ϕ_{em} in such a combination is given by the superposition of a PL

contribution ϕ_{sc} under short-circuit conditions and a term resulting from the application of a voltage V_j to the junction [81]

$$\phi_{em}(E,\mathbf{r}) = Q_e(E,\mathbf{r})\phi_{bb}(E)\exp\left(\frac{qV_j(\mathbf{r})}{kT}\right) + \phi_{sc}(E,\mathbf{r}). \tag{3.17}$$

Comparison of Equation 3.17 to Equation 3.1 shows that the difference of local emission $\phi_{em}(E,\mathbf{r})$ with and without illumination is just the short-circuit contribution ϕ_{sc}. Thus, a difference image $\Delta\phi_{em}(E,\mathbf{r}) = \phi_{em}(E,\mathbf{r},V_j > 0) - \phi_{em}(E,\mathbf{r},V_j = 0)$ just cancels the short-circuit term. Since this difference image is obtained by changing the voltage V_T at the terminals of the device, we denote the corresponding measurement *electromodulated luminescence*. It is important to note that in a real-world solar cell or module setting the terminal voltage $V_T = 0$ does not necessarily imply $V_j = 0$ at every location $\mathbf{r}$. This is because under illumination the collection of the photocurrent that is generated in the cell area causes a voltage drop $\Delta V(\mathbf{r})$ between this location and the terminal, that is, $V_j(\mathbf{r}) - V_T = \Delta V(\mathbf{r}) > 0$. However, under normal circumstances the junction voltages $V_j(\mathbf{r})$ at $V_T = 0$ will be much smaller than those under forward bias such that a difference image will cancel out the short-circuit part in Equation 3.17.

A small-signal electromodulation technique [82] allows one to determine the local photocurrent collection efficiency f_{PC} by a series of electromodulated luminescence images. The evaluation is based on the network theorem of Wong and Green [83]. This theorem describes that the quantity $f_{PC} = -\delta I_T^{PC}/\delta I_{\mathbf{r}}^{PC}$, that is, the probability that a small photocurrent $\delta I_{\mathbf{r}}^{PC}$ generated at location $\mathbf{r}$ contributes to the current $-\delta I_T^{PC}$ collected at the cell's terminal, equals the ratio between the voltage $\delta V_j(\mathbf{r})$ that drops over the junction at location $\mathbf{r}$ as a consequence of application of a small voltage variation δV_T at the terminal. Hence, the Wong/Green theorem

$$f_{PC}(\mathbf{r}) := -\frac{\delta I_T^{PC}}{\delta I_{\mathbf{r}}^{PC}}(\mathbf{r}) = \frac{\delta V_j(\mathbf{r})}{\delta V_T} \tag{3.18}$$

allows one to replace the meaningful but cumbersome measurement of the photocurrent collection efficiency, for example, by LBIC measurement, by a much simpler determination of the local junction voltage via luminescence measurements [82, 84].

Figure 3.8a shows a large-signal difference image of a CIGS solar cell with four grid fingers and the bus bar to the right. The image is gained as the difference

$$\begin{aligned}\Delta S_{cam}(V_T,\mathbf{r}) &= S_{cam}(V_j(V_T,\mathbf{r})) - S_{cam}(V_j(0,\mathbf{r}))\\ &= \left[S_0\exp\left(\frac{qV_j\left(V_T,\mathbf{r}\right)}{kT}\right) + S_{sc}\right]\\ &\quad - \left[S_0\exp\left(\frac{qV_j(0,\mathbf{r})}{kT}\right) + S_{sc}\right] \approx S_0\exp\left(\frac{qV_j\left(V_T,\mathbf{r}\right)}{kT}\right),\end{aligned} \tag{3.19}$$

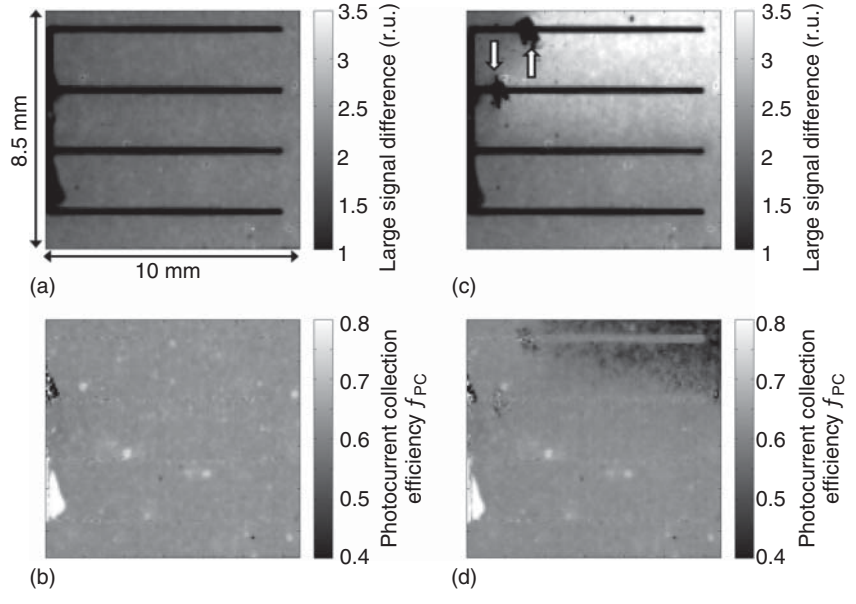

Figure 3.8 (a) Difference image ΔS of a Cu(In,Ga)Se_2 solar cell recorded at a terminal voltage of $V_T = 0.46$ V close to the maximum power voltage $V_{MPP} = 0.45$ V under one sun illumination intensity. (b) Photocurrent collection efficiency (f_{PC}) map derived according to Equation 3.20 from two images with $V_T = 0.47$ and $V_T = 0.45$ V, respectively. (c) Difference image and (d) photocurrent collection efficiency map of the same solar cell after removing a part of two upper grid lines (arrows in c) by scratching. The photocurrent collection efficiency in (d) is considerably deteriorated in the upper right part of the sample.

of one image at a terminal voltage $V_T = 0.46$ V and one image with signal S_{sc} at $V_T = 0$ V, i.e. at short circuit. The photocurrent collection efficiency f_{PC} is obtained as a differential or small-signal difference image according to

$$f_{PC}(\mathbf{r}) = \frac{\delta V_j(\mathbf{r})}{\delta V_T} = \frac{kT/q}{\delta V_T} \ln\left(\frac{\Delta S_{cam}\left(V_T + \delta V_T/2, \mathbf{r}\right)}{\Delta S_{cam}(V_T - \delta V_T/2, \mathbf{r})}\right). \tag{3.20}$$

Figure 3.8b shows such a photocurrent collection map that is gained from two difference images with $V_T = 0.47$ and $V_T = 0.45$ V, that is, the modulation voltage δV_T equals 0.02 V. The f_{PC} map shows a fairly uniform collection efficiency of approximately 0.65, showing that the sheet resistance of the window layer or the resistance of the grid fingers does not limit the photocurrent collection. In contrast upon scratching away the two upper grid fingers and part of the absorber (at the location of the arrows in Figure 3.8c) changes the large-signal difference image (mainly at the location of the scratches, Figure 3.8c) but also the f_{PC} map in upper right part of the cell (Figure 3.8d). Due to the interrupted grid fingers, the photocurrent collection efficiency deteriorates here to values as low as 0.4. We emphasize that the quantitative information gained by the

described methods does not rely on any assumption except for the validity of the reciprocity/superposition principle given by Equation 3.17.

Acknowledgments

Dorothea Lennartz is gratefully acknowledged for the help with the figures. The authors also thank Anke Helbig for her contributions.

References

1. Wang, K., Silver, M., and Han, D. (1993) Electroluminescence and forward bias current in p–i–n and p–b–i–n a-Si:H solar cells. *J. Appl. Phys.*, **73**, 4567.
2. Yan, B., Han, D., and Adriaenssens, G.J. (1996) Analysis of post-transit photocurrents and electroluminescence spectra from a-Si:H solar cells. *J. Appl. Phys.*, **79**, 3597.
3. Han, D., Wang, K., and Yang, L. (1996) Recombination and metastability in amorphous silicon p–i–n solar cells made with and without hydrogen dilution studied by electroluminescence. *J. Appl. Phys.*, **80**, 2475.
4. Feldman, S.D., Collins, R.T., Kaydanov, V., and Ohno, T.R. (2004) Effects of Cu in CdS/CdTe solar cells studied with patterned doping and spatially resolved luminescence. *Appl. Phys. Lett.*, **85**, 1529.
5. Fuyuki, T., Kondo, H., Yamazaki, T., Takahashi, Y., and Uraoka, Y. (2005) Photographic surveying of minority carrier diffusion length in polycrystalline silicon solar cells by electroluminescence. *Appl. Phys. Lett.*, **86**, 262108.
6. Ramspeck, K., Bothe, K., Hinken, D., Fischer, B., Schmidt, J., and Brendel, R. (2007) Recombination current and series resistance imaging of solar cells by combined luminescence and lock-in thermography. *Appl. Phys. Lett.*, **90**, 153502.
7. Kasemann, M., Schubert, M.C., The, M., Köber, M., Hermle, M., and Warta, W. (2006) Comparison of luminescence imaging and illuminated lock-in thermography on silicon solar cells. *Appl. Phys. Lett.*, **89**, 224102.
8. Würfel, P., Trupke, T., Puzzer, T., Schäffer, E., Warta, W., and Glunz, W.S. (2007) Diffusion lengths of silicon solar cells from luminescence images. *J. Appl. Phys.*, **101**, 123110.
9. Breitenstein, O., Bauer, J., Trupke, T., and Bardos, R.A. (2008) On the detection of shunts in silicon solar cells by photo- and electroluminescence imaging. *Prog. Photovoltaics Res. Appl.*, **16**, 325.
10. Hinken, D., Ramspeck, K., Bothe, K., Fischer, B., and Brendel, R. (2007) Series resistance imaging of solar cells by voltage dependent electroluminescence. *Appl. Phys. Lett.*, **91**, 182104.
11. Bothe, K., Ramspeck, K., Hinken, D., and Brendel, R. (2008) Imaging techniques for the analysis of silicon wafers and solar cells. *ECS Trans.*, **16**, 63.
12. Kasemann, M., Grote, D., Walter, B., Kwapil, W., Trupke, T., Augarten, Y., Bardos, R.A., Pink, E., Abbott, M.D., and Warta, W. (2008) Luminescence imaging for the detection of shunts on silicon solar cells. *Prog. Photovoltaics Res. Appl.*, **16**, 297.
13. Bothe, K. and Hinken, D. (2013) Quantitative luminescence characterization of crystalline silicon solar cells, in *Advances in Photovoltaics. Part 2: Semiconductors and Semimetals*, vol. **89** (eds G.P. Willeke and E.R. Weber), Elsevier, Amsterdam, p. 259.
14. Fuyuki, T. and Kitiyanan, A. (2009) Photographic diagnosis of crystalline silicon solar cells utilizing electroluminescence. *Appl. Phys. A*, **96**, 189.
15. Kirchartz, T., Rau, U., Kurth, M., Mattheis, J., and Werner, J.H. (2007)

Comparative study of electroluminescence from Cu(In,Ga)Se_2 and Si solar cells. *Thin Solid Films*, **515**, 6238.

16. Kirchartz, T. and Rau, U. (2007) Electroluminescence analysis of high efficiency Cu(In,Ga)Se_2 solar cells. *J. Appl. Phys.*, **102**, 104510.
17. Kirchartz, T., Rau, U., Hermle, M., Bett, A.W., Helbig, A., and Werner, J.H. (2008) Internal voltages in GaInP/GaInAs/Ge multijunction solar cells determined by electroluminescence measurements. *Appl. Phys. Lett.*, **92**, 123502.
18. Kirchartz, T., Helbig, A., Reetz, W., Reuter, M., Werner, J.H., and Rau, U. (2009) Reciprocity between electroluminescence and quantum efficiency used for the characterization of silicon solar cells. *Prog. Photovoltaics Res. Appl.*, **17**, 394.
19. Kirchartz, T., Helbig, A., and Rau, U. (2008) Note on the interpretation of electroluminescence images using their spectral information. *Sol. Energy Mater. Sol. Cells*, **92**, 1621.
20. Helbig, A., Kirchartz, T., and Rau, U. (2008) Quantitative information of electroluminescence images, in *Proceedings of the 23rd European Photovoltaic Solar Energy Conference* (eds D. Lincot, H. Ossenbrink, and P. Helm), WIP Renewable Energies, p. 426.
21. Rau, U. (2007) Reciprocity relation between photovoltaic quantum efficiency and electroluminescent emission of solar cells. *Phys. Rev. B*, **76**, 085303.
22. Koshka, Y., Ostapenko, S., Tarasov, I., McHugo, S., and Kalejs, J.P. (1999) Scanning room-temperature photoluminescence in polycrystalline silicon. *Appl. Phys. Lett.*, **74**, 1555.
23. Ostapenko, S., Tarasov, I., Kalejs, J.P., Haessler, C., and Reisner, E.-U. (2000) Defect monitoring using scanning photoluminescence spectroscopy in multicrystalline silicon wafers. *Semicond. Sci. Technol.*, **15**, 840.
24. Kittler, M., Seifert, W., Arguirov, T., Tarasov, I., and Ostapenko, S. (2002) Room-temperature luminescence and electron-beam-induced current (EBIC) recombination behaviour of crystal defects in multicrystalline silicon. *Sol. Energy Mater. Sol. Cells*, **72**, 465.
25. Bauknecht, A., Siebentritt, S., Albert, J., and Lux-Steiner, M.C. (2001) Radiative recombination via intrinsic defects in $Cu_xGa_ySe_2$. *J. Appl. Phys.*, **89**, 4391.
26. Hönes, K., Eickenberg, M., Siebentritt, S., and Persson, C. (2008) Polarization of defect related optical transitions in chalcopyrites. *Appl. Phys. Lett.*, **93**, 092102.
27. Bauer, G.H., Brüggemann, R., Tardon, S., Vignoli, S., and Kniese, R. (2005) Quasi-Fermi level splitting and identification of recombination losses from room temperature luminescence in Cu$(In_{1-x}Ga_x)Se_2$ thin films versus optical band gap. *Thin Solid Films*, **480–481**, 410.
28. Merdzhanova, T., Carius, R., Klein, S., Finger, F., and Dimova-Malinovska, D. (2004) Photoluminescence energy and open-circuit voltage in microcrystalline silicon solar cells. *Thin Solid Films*, **451–452**, 285.
29. Keevers, M.J. and Green, M.A. (1995) Absorption edge of silicon from solar cell spectral response measurements. *Appl. Phys. Lett.*, **66**, 174.
30. Daub, E. and Würfel, P. (1995) Ultralow values of the absorption coefficient of Si obtained from luminescence. *Phys. Rev. Lett.*, **74**, 1020.
31. Kirchartz, T., Helbig, A., and Rau, U. (2008) Quantification of light trapping using a reciprocity between electroluminescent emission and photovoltaic action in a solar cell. *Mater. Res. Soc. Symp. Proc.*, **1101**, KK01-04.
32. Basore, P.A. (1993) *Extended Spectral Analysis of Internal Quantum Efficiency*. Proceedings of the 23rd IEEE Photovoltaic Specialists Conference. 10–14 May 1993, Louisville, KY, IEEE, New York, p. 147.
33. Kirchartz, T., Mattheis, J., and Rau, U. (2008) Detailed balance theory of excitonic and bulk heterojunction solar cells. *Phys. Rev. B*, **78**, 235320.
34. Werner, J.H., Mattheis, J., and Rau, U. (2005) Efficiency limitations of polycrystalline thin film solar cells: case of Cu(In,Ga)Se_2. *Thin Solid Films*, **480**, 399.

35. Ross, R.T. (1967) Some thermodynamics of photochemical systems. *J. Chem. Phys.*, **12**, 4590.
36. Vandewal, K., Tvingstedt, K., Gadisa, A., Inganäs, O., and Manca, J.V. (2009) On the origin of the open circuit voltage of polymer-fullerene solar cells. *Nat. Mater.*, **8**, 904.
37. Yao, J., Kirchartz, T., Vezie, M.S., Faist, M.A., Gong, W., He, Z., Wu, H., Troughton, J., Watson, T., Bryant, D., and Nelson, J. (2015) Quantifying losses in open-circuit voltage in solution processable solar cells. *Phys. Rev. Appl.*, **4**, 014020.
38. Tvingstedt, K., Malinkiewicz, O., Baumann, A., Deibel, C., Snaith, H.J., Dyakonov, V., and Bolink, H.J. (2014) Radiative efficiency of lead iodide based perovskite solar cells. *Sci. Rep.*, **4**, 6071.
39. Tress, W., Marinova, N., Inganäs, O., Nazeeruddin, M.K., Zakeeruddin, S.M., and Grätzel, M. (2015) Predicting the open-circuit voltage of $CH_3NH_3PbI_3$ perovskite solar cells using electroluminescence and photovoltaic quantum efficiency spectra: the role of radiative and non-radiative recombination. *Adv. Energy Mater.*, **5**, 1400812.
40. Jeon, N.J., Noh, J.H., Yang, W.S., Kim, Y.C., Ryu, S., Seo, J., and Seok, S.I. (2015) Compositional engineering of perovskite materials for high-performance solar cells. *Nature*, **517**, 476.
41. Green, M.A. (2012) Radiative efficiency of state-of-the-art photovoltaic cells. *Prog. Photovoltaics Res. Appl.*, **20**, 472.
42. Green, M.A., Emery, K., Hishikawa, Y., Warta, W., and Dunlop, E.D. (2015) Solar cell efficiency tables (version 46). *Prog. Photovoltaics Res. Appl.*, **23**, 805.
43. Miller, O.D., Yablonovitch, E., and Kurtz, S.R. (2012) Strong internal and external luminescence as solar cells approach the Shockley–Queisser limit. *IEEE J. Photovoltaics*, **2**, 303.
44. Rau, U., Paetzold, U.W., and Kirchartz, T. (2014) Thermodynamics of light management in photovoltaic devices. *Phys. Rev. B*, **90**, 035211.
45. Giesecke, J.A., Kasemann, M., and Warta, W. (2009) Determination of local minority carrier diffusion lengths in crystalline silicon from luminescence images. *J. Appl. Phys.*, **106**, 014907.
46. Hinken, D., Bothe, K., Ramspeck, K., Herlufsen, S., and Brendel, R. (2009) Determination of the effective diffusion length of silicon solar cells from photoluminescence. *J. Appl. Phys.*, **105**, 104516.
47. Glatthaar, M., Giesecke, J., Kasemann, M., Haunschild, J., The, M., Warta, W., and Rein, S. (2009) Spatially resolved determination of the dark saturation current of silicon solar cells from electroluminescence images. *J. Appl. Phys.*, **105**, 113110.
48. Haunschild, J., Glatthaar, M., Kasemann, M., Rein, S., and Weber, E.R. (2009) Fast series resistance imaging for silicon solar cells using electroluminescence. *Phys. Status Solidi RRL*, **3**, 227.
49. Werner, J. (1988) Schottky barrier and pn-junction I/V plots – small signal evaluation. *Appl. Phys. A*, **47**, 291.
50. Breitenstein, O., Khanna, A., Augarten, Y., Bauer, J., Wagner, J.-M., and Iwig, K. (2010) Quantitative evaluation of electroluminescence images of solar cells. *Phys. Status Solidi RRL*, **4**, 7.
51. Trupke, T., Bardos, R.A., Schubert, M.C., and Warta, W. (2006) Photoluminescence imaging of silicon wafers. *Appl. Phys. Lett.*, **89**, 044107.
52. Abbott, M.D., Cotter, J.E., Chen, F.W., Trupke, T., Bardos, R.A., and Fisher, K.C. (2006) Application of photoluminescence characterization to the development and manufacturing of high-efficiency silicon solar cells. *J. Appl. Phys.*, **100**, 114514.
53. Abbott, M.D., Cotter, J.E., Trupke, T., and Bardos, R.A. (2009) Investigation of edge recombination effects in silicon solar cell structures using photoluminescence. *Appl. Phys. Lett.*, **88**, 114105.
54. Macdonald, D., Tan, J., and Trupke, T. (2008) Imaging interstitial iron concentrations in boron-doped crystalline silicon using photoluminescence. *J. Appl. Phys.*, **103**, 073710.
55. Kampwerth, H., Trupke, T., Weber, J.W., and Augarten, Y. (2008) Advanced luminescence based effective series resistance

imaging of silicon solar cells. *Appl. Phys. Lett.*, **93**, 202102.
56. Herlufsen, S., Schmidt, J., Hinken, D., Bothe, K., and Brendel, R. (2008) Photoconductance-calibrated photoluminescence lifetime imaging of crystalline silicon. *Phys. Status Solidi RRL*, **2**, 245.
57. Rosenits, P., Roth, T., Warta, W., Reber, S., and Glunz, S.W. (2009) Determining the excess carrier lifetime in crystalline silicon thin-films by photoluminescence measurements. *J. Appl. Phys.*, **105**, 053714.
58. Glatthaar, M., Haunschild, J., Kasemann, M., Giesecke, J., Warta, W., and Rein, S. (2010) Spatially resolved determination of dark saturation current and series resistance of silicon solar cells. *Phys. Status Solidi RRL*, **4**, 13.
59. Rau, U., Kirchartz, T., Helbig, A., and Pieters, B.E. (2009) Electroluminescence imaging of Cu(In,Ga)Se_2 thin film modules. *Mater. Res. Soc. Symp. Proc.*, **1165**, M03-04.
60. Helbig, A., Kirchartz, T., Schäffler, R., Werner, J.H., and Rau, U. (2010) Quantitative electroluminescence analysis of resistive losses in Cu(In,Ga)Se_2 thin-film modules. *Sol. Energy Mater. Sol. Cells*, **94**, 979.
61. Brown, G., Pudov, A., Cardozo, B., Faifer, V., Bykov, E., and Contreras, M. (2010) Quantitative imaging of electronic nonuniformities in Cu(In,Ga)Se_2 solar cells. *J. Appl. Phys.*, **108**, 074516.
62. Johnston, S., Unold, T., Repins, I., Sundaramoorthy, R., Jones, K.M., To, B., Call, N., and Ahrenkiel, R. (2010) Imaging characterization techniques applied to Cu(In,Ga)Se_2 solar cells. *J. Vac. Sci. Technol. A*, **28**, 665.
63. Paire, M., Lombez, L., Guillemoles, J.-F., and Lincot, D. (2011) Measuring sheet resistance of CIGS solar cell's window layer by spatially resolved electroluminescence imaging. *Thin Solid Films*, **519**, 7493.
64. Tran, T.M.H., Pieters, B.E., Ulbrich, C., Gerber, A., Kirchartz, T., and Rau, U. (2013) Transient phenomena in Cu(In,Ga)Se_2 solar modules investigated by electroluminescence imaging. *Thin Solid Films*, **535**, 307–310.
65. Gerber, A., Huhn, V., Tran, T.M.H., Siegloch, M., Augarten, Y., Pieters, B.E., and Rau, U. (2015) Advanced large area characterization of thin-film solar modules by electroluminescence and thermography imaging techniques. *Sol. Energy Mater. Sol. Cells*, **135**, 35–42.
66. Huhn, V., Gerber, A., Augarten, Y., Pieters, B.E., and Rau, U. (2016) Analysis of Cu(In,Ga)Se_2 thin-film modules by electro-modulated luminescence. *J. Appl. Phys.*, **119**, 095704.
67. Pieters, B.E., Kirchartz, T., Merdzhanova, T., and Carius, R. (2010) Modeling of photoluminescence spectra and quasi-Fermi level splitting in μc-Si solar cells. *Sol. Energy Mater. Sol. Cells*, **94**, 1851–1854.
68. Mueller, T.C.M., Pieters, B.E., Kirchartz, T., Carius, R., and Rau, U. (2014) Effect of localized states on the reciprocity between quantum efficiency and electroluminescence in Cu(In,Ga)Se_2 and Si thin-film solar cells. *Sol. Energy Mater. Sol. Cells*, **129**, 95–103.
69. Grabitz, P.O., Rau, U., Wille, B., Bilger, G., and Werner, J.H. (2006) Spatial inhomogeneities in Cu(In,Ga)Se_2 solar cells analyzed by an electron beam induced voltage technique. *J. Appl. Phys.*, **100**, 124501.
70. Bauer, G.H., Gütay, L., and Kniese, R. (2005) Structural properties and quality of the photoexcited state in $Cu(In_{1-x}Ga_x)Se_2$ solar cell absorbers with lateral submicron resolution. *Thin Solid Films*, **480**, 259.
71. Romero, M.J., Jiang, C.-S., Noufi, R., and Al-Jassim, M.M. (2005) Photon emission in $CuInSe_2$ thin films observed by scanning tunneling microscopy. *Appl. Phys. Lett.*, **86**, 143115.
72. Romero, M.J., Jiang, C.-S., Abushama, J., Moutinho, H.R., Al-Jassim, M.M., and Noufi, R. (2006) Electroluminescence mapping of $CuGaSe_2$ solar cells by atomic force microscopy. *Appl. Phys. Lett.*, **89**, 143120.
73. Gütay, L. and Bauer, G.H. (2005) Lateral variations of optoelectronic quality of $Cu(In_{1-x}Ga_x)Se_2$ in the submicron-scale. *Thin Solid Films*, **487**, 8.
74. Gütay, L. and Bauer, G.H. (2007) Spectrally resolved photoluminescence

studies on Cu(In,Ga)Se_2 solar cells with lateral submicron resolution. *Thin Solid Films*, **515**, 6212.

75. Bothe, K., Bauer, G.H., and Unold, T. (2002) Spatially resolved photoluminescence measurements on Cu(In,Ga)Se_2 thin films. *Thin Solid Films*, **403**, 453.
76. Misic, B., Pieters, B.E., Schweitzer, U., Gerber, A., and Rau, U. (2015) Defect diagnostics of scribing failures and Cu-rich debris in Cu(In,Ga)Se-2 thin-film solar modules with electroluminescence and thermography. *IEEE J. Photovoltaics*, **5**, 1179–1187.
77. Misic, B., Pieters, B.E., Theisen, J.P., Gerber, A., and Rau, U. (2015) Shunt mitigation in ZnO: Al/i-ZnO/CdS/Cu(In,Ga)Se_2 solar modules by the i-ZnO/CdS buffer combination. *Phys. Status Solidi A*, **212**, 541–546.
78. Delamarre, A., Paire, M., Guillemoles, J.-F., and Lombez, L. (2015) Quantitative luminescence mapping of Cu(In,Ga)Se_2 thin-film solar cells. *Prog. Photovoltaics Res. Appl.*, **23**, 1305–1312.
79. Mueller, T.C.M., Tran, T.M.H., Pieters, B.E., Gerber, A., Carius, R., and Rau, U. (2013) Effect of light soaking on the electro- and photoluminescence of Cu(In,Ga)Se_2 solar cells. *Appl. Phys. Lett.*, **103**, 183504.
80. Tran, T.M.H., Pieters, B.E., Schneemann, M., Muller, T.C.M., Gerber, A., Kirchartz, T., and Rau, U. (2013) Quantitative evaluation method for electroluminescence images of a-Si:H thin-film solar modules. *Phys. Status Solidi RRL*, **9**, 627–630.
81. Rau, U. (2012) Superposition and reciprocity in the electroluminescence and photoluminescence of solar cells. *IEEE J. Photovoltaics*, **2**, 169.
82. Rau, U., Huhn, V., Stoicescu, L., Schneemann, M., Augarten, Y., Gerber, A., and Pieters, B.E. (2014) Photocurrent collection efficiency mapping of a silicon solar cell by a differential luminescence imaging technique. *Appl. Phys. Lett.*, **105**, 163507.
83. Wong, J. and Green, M.A. (2012) From junction to terminal: extended reciprocity relations in solar cell operation. *Phys. Rev. B*, **85**, 235205.
84. Wong, J.; Sridharan, R.; Wang, Y. C.; Mueller, T. (2014) *Differential Electroluminescence Imaging and the Current Transport Efficiency of Silicon Wafer Solar Cells*. Proceedings of the 40th IEEE Photovoltaic Specialist Conference, 8–13 June 2014, Denver, CO, IEEE, pp. 0975–0979.

4
Capacitance Spectroscopy of Thin-Film Solar Cells

Jennifer Heath and Pawel Zabierowski

4.1
Introduction

The differential capacitance, or more generally, admittance, provides a window into the carrier dynamics within a diode-like device, such as a solar cell. The differential capacitance is the charge response, δQ, to a small change of voltage δV, $C = \delta Q/\delta V$. A number of experimental techniques exploit this response to study the electronic properties of buried layers within the device, especially to map out the subbandgap density of states, with the most broadly applied techniques being capacitance–voltage (CV) profiling, admittance spectroscopy (AS), and deep-level transient spectroscopy (DLTS). In addition to these, we will also discuss drive-level capacitance profiling (DLCP) and photocapacitance techniques. In this chapter, we endeavor to introduce these techniques from introductory concepts, while also commenting on the analysis of data from real photovoltaic materials, which is definitely an advanced topic. Although it is not possible to cover every scenario, we try to give examples as well as references to a wide range of resources.

The electronic states associated with defects and impurities are typically divided into two broad categories: "shallow" and "deep" states, corresponding, respectively, to centers with extended electronic wave functions and those that are strongly localized [1]. Generally speaking, the techniques discussed here are designed to detect nonradiative transitions involving deep states. Deep states act as traps and recombination centers, reducing the minority carrier mobility and in some cases pinning the Fermi energy deep in the gap. Energetically shallow states can also be observed in photocapacitance measurements as a valence (or conduction) band tail; these disorder induced traps reduce the drift mobility.

Much effort has gone into extending junction capacitance techniques to accurately measure properties of the more continuous densities of subbandgap states characteristic of imperfect materials. This includes early work by Losee [2] to treat generally the effect of gap states on admittance in Schottky devices, as well as experimental and numerical studies by Cohen and Lang [3, 4] to treat

Advanced Characterization Techniques for Thin Film Solar Cells, Second Edition.
Edited by Daniel Abou-Ras, Thomas Kirchartz, and Uwe Rau.

the case of continuous densities of states. In-depth discussions of the field are provided by Refs [5, 6].

Admittance measurements generally begin with a simple CV evaluation of the diode, which indicates whether significant shunt current exists and whether the film is fully depleted, and a rough estimate of doping density. For suitable devices, AS or DLTS data directly give the thermal trapping time of gap states, while DLTS or other transient measurements indicate whether these are majority or minority carrier traps. We will discuss ways in that additional information can also be gleaned from capacitance data, including the energetic position, density, and spatial variation of the defect transition; the carrier capture cross section; and, in some cases, the position of the Fermi energy. The photocapacitance techniques measure optical transitions involving defect states and are particularly valuable for studying optical properties of the buried absorber layers in working photovoltaic devices. The relationship between optical and thermal transition energies can also lead to a better understanding of lattice relaxation effects.

The techniques described here have generally been developed starting from the depletion approximation, as is standard for crystalline semiconductor diodes, and then considering the influence of trap states. This approximation and other assumptions are discussed in the following sections. When the dynamic response is dominated by other factors, such as contact resistance or transport mechanism, the data may provide different, but still useful, information. Examples are discussed in Refs [7–11].

4.2 Admittance Basics

This chapter makes use of the differential capacitance, $C = \delta Q/\delta V$, as opposed to the DC capacitance definition more commonly used in circuits, $C = Q/V$. These two definitions converge for standard capacitors. The differential capacitance describes the physical quantity measured in capacitance spectroscopy and applies to a more general situation where Q may not vary linearly with V; in diodes we approximate $Q \propto \sqrt{V_{\mathrm{bi}} - V}$ where V_{bi} is the built-in potential at the interface. However, in the small-signal approximation, we can still write $\delta Q \propto \delta V$.

When a small AC voltage is applied to a sample, the linear current response consists of both a component in phase with the applied voltage and a component that is 90° out of phase. We can represent the applied voltage V with amplitude V_{ac} and angular frequency ω as a function of time t:

$$V = V_{\mathrm{ac}} \exp(j\omega t) = V_{\mathrm{ac}}[\cos(\omega t) + j \sin(\omega t)].$$

For the ideal resistor, R, and capacitor, C, in parallel, we measure a total current, I:

$$I = V(R^{-1} + j\omega C).$$

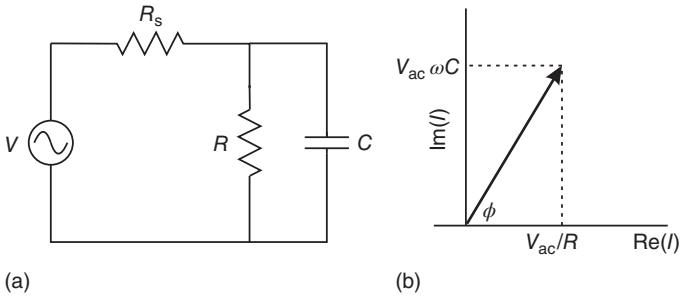

Figure 4.1 (a) Parallel circuit model for the device, with series resistor. (b) Phasor diagram for (a), neglecting R_s.

Note that information about the resistor and capacitor values are clearly separated into the real and imaginary parts of the current, and hence the admittance.

This current can be represented using a phasor diagram on the complex plane, as illustrated in Figure 4.1a and b, and analogous diagrams can be used to represent various types of data including the voltage difference between two measurement points and the impedance or admittance of the circuit element. The amplitude and phase of the phasor represent the measurement at time $t = 0$; the entire measurement as a function of time corresponds to the real component of the phasor as it rotates counterclockwise with angular velocity ω.

The small-signal response of any sample can be characterized by its complex admittance, $Y = Y' + jY''$, such that $I = YV$, where Y'' is the conductance, and Y'' is the susceptance. The complex impedance, $Z = Z' + jZ''$, is the inverse of the admittance, such that $V = IZ$. Here, Z' is the resistance, and Z'' is the reactance. Here, we focus on admittance measurements, since the complex admittance normally allows the diode capacitance to be clearly separated from the shunt conductance.

For diodes, including solar cell devices, authors frequently assume a simple circuit model, neglecting R_s, as illustrated in Figure 4.1a and b, such that $C = Y''/\omega$. The value Y''/ω is typically reported as the experimentally measured value of capacitance; however, note that this value results from the current itself; its meaning must be interpreted judiciously. Even in the case where this simple parallel circuit is applicable, "C" does not necessarily represent the accumulation of charge in any particular layer of the device.

A common shortcoming of the equivalent circuit is a too-high series resistance or frequency, such that the condition $\omega R_s C << 1$ or $R_s << R$ is violated; in this case the series resistance and capacitance essentially form a low-pass filter, and as ω increases, Y''/ω no longer accurately yields C [12]. This issue can originate either from resistance in the device and contacts or from spreading resistance in the contact and film. Problems with spreading resistance can be reduced by reducing the device area; however, this can in some cases increase the influence of stray capacitance from the edges of the device. At high frequencies, stray inductance may also be a complicating issue.

Assuming a simple model, as illustrated in Figure 4.1a and b, with a frequency-independent series resistance, a peak in the Y'/ω versus ω curve will be observed at $\omega R_s C = 1$, and as ω continues to increase, the apparent capacitance, Y''/ω, will decrease as ω^{-2}. The influence of R_s on the data can additionally be checked by intentionally adding a resistor in series with the device. Series resistance can also be estimated from the current–voltage data [13], but while the DC series resistance may provide a useful estimate, the admittance is an AC measurement, and the AC series resistance can be frequency dependent, perhaps originating from nonideal contacts or conduction mechanisms. The activation energy of the series resistance can then give useful information about charge transport in the device [7]. Note that just as AS naturally separates the components C and R in a parallel model with no R_s, impedance spectroscopy naturally applies to a series model with significant R_s, and so impedance spectroscopy approaches can be useful in understanding such devices [14]. A more complete discussion of dielectric response than is possible here is found in Ref. [15].

4.3 Sample Requirements

In general, any diode-like devices, including working solar cells, can be studied using the techniques described here. Of course, the diode quality must permit the capacitive response from the space charge region to be clearly distinguished. For simplicity, in this chapter we generally assume a single junction, either a one-sided p^+-n or n^+-p, or Schottky device, in which the lightly doped semiconductor is not fully depleted. The treatment discussed here is also consistent for MOS devices as long as they are measured in the depletion regime. Since the oxide is in series with the semiconductor, its effect on the capacitance can be subtracted. Interface states also contribute more strongly to the capacitance response in MOS devices, as discussed more in the following; this can either be a complication or an opportunity. In-depth treatments of the theory appropriate to these more complex device structures are provided elsewhere [5, 16]. Other multilayer devices, including p–i–n structures, can also be studied. In such devices, definitively tying experimental observations to a particular layer or interface of the device becomes more complicated.

In thin-film devices, the reproducibility of sample characteristics and measurement results has been problematic. Sensitivities to light, voltage, temperature, humidity, oxygen, and so on are well documented. In addition, comparisons between samples grown in different labs must be undertaken with caution.

4.4 Instrumentation

In order to measure admittance, the small AC current response to an applied AC voltage must be measured. This signal consists of two parts: the amplitude and

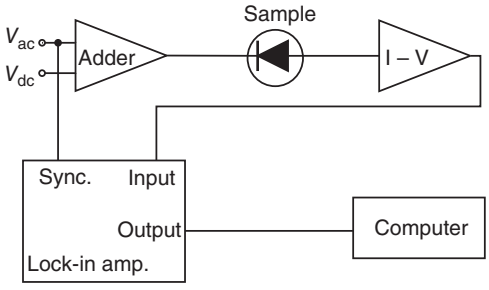

Figure 4.2 Schematic for a lock-in amplifier-based approach to measurement of complex admittance.

phase. Equivalently, it can be decomposed into components corresponding to the in-phase current and the current that is 90° out of phase. Many LCR meters (impedance analyzers) will directly provide this measurement. An alternative option is to employ a lock-in amplifier and transimpedance amplifier (current-to-voltage preamplifier) together to perform the same function, as illustrated in Figure 4.2. The ability to vary the AC frequency is essential. Generally, it is also important to control the AC voltage amplitude and apply a DC voltage offset.

In the case where transient signals must be evaluated, for example, after a voltage pulse, several approaches exist. The LCR or lock-in amplifier output can be displayed on an oscilloscope or collected directly by a data acquisition card and specialized software. In either case, the speed, accuracy, and timing or triggering of the digital data acquisition are essential considerations. The entire transient can be collected and stored for future analysis; collecting the data on a logarithmic timescale allows both short- and long-term contributions to the transient to be analyzed. This may be preferred for measurements of thin-film devices, allowing unusual behavior to be recognized and allowing the flexibility to attempt different analyzes. The analysis of exponential transient signals is discussed by Istratov and Vyvenko [17]. Some purpose-made DLTS equipment uses the Fourier transform approach discussed therein.

Regardless of the admittance measurement approach, careful calibration is required at each measurement frequency. Measurements at higher frequencies, above about 1 MHz, require extra attention to circuit components, connections, and calibration [18].

During the measurement, it is critical to monitor the relationship between conductance and susceptance, characterized by either the quality factor, Q, or dissipation factor D. These factors are defined such that $Q = D^{-1} = Y''/Y' = \tan(\phi)$, where ϕ is illustrated in Figure 4.1b. Typically, Q should be greater than ~0.1. When Q is small, such as for large leakage currents or low measurement frequencies, small errors in the measurement of ϕ can lead to large errors in determining Y'' and therefore C. It is wise to initially test the sensitivity and calibration of instrumentation with RC circuits constructed of known components.

In addition to the measurement of capacitance, sample temperature generally must be varied. The required temperature range will depend on the sample, with

lower temperatures allowing measurement of transitions from shallower states, but most authors find that a l-N_2 cryostat suffices. The importance of accurately measuring the stabilized sample temperature cannot be overemphasized as it directly influences the accuracy of parameter extraction. It is advisable to carefully consider the temperature sensor and location, calibration, and thermal design of the sensor–sample–cryostat system. For example, thin films grown on glass and placed in a cold finger-type cryostat in vacuum can lag the cold finger temperature significantly.

4.5 CV Profiling and the Depletion Approximation

The diode capacitance is traditionally analyzed using the depletion approximation. Although this approximation may not be very accurate for thin-film semiconductors, which can have significant densities of deep states, it is still a useful starting point for this discussion of admittance measurements. The depletion approximation assumes that the depletion region is precisely defined, ends abruptly, and is fully depleted of free carriers. In the depletion approximation, the depletion width will vary with applied bias, but the charge density $\rho(x)$ within the depleted region remains constant (where x is measured through the depth of the film, with $x = 0$ at the interface), while the bulk region remains neutral. Then, as long as the free-carrier relaxation time is short compared to the applied ac frequency, the capacitance response originates from the depletion edge, giving $C = \varepsilon\varepsilon_0 A/W$ where W is the width of the depletion region, A is the area of the device, and ε is the semiconductor dielectric constant.

For an abrupt, one-sided junction or Schottky junction,

$$W = \sqrt{\frac{2\varepsilon\varepsilon_0(V_{bi} - V_{dc})}{eN_B}}$$

where N_B is the doping concentration on the lightly doped side of the junction, e is the elementary charge, and V_{dc} is the applied dc bias, where V_{dc} is positive for forward bias [19]. Then,

$$C^{-2} = \frac{2(V_{bi} - V_{dc})}{e\varepsilon\varepsilon_0 A^2 N_B}.$$

So in a plot of C^{-2} versus V_{dc}, the intercept gives V_{bi}, and the slope yields the CV density, N_{CV}, which in this ideal situation is identical to N_B:

$$N_{CV} = -\frac{2}{e\varepsilon\varepsilon_0 A^2}\left[\frac{d\left(C^{-2}\right)}{dV_{dc}}\right]^{-1} = -\frac{C^3}{e\varepsilon\varepsilon_0 A^2}\left(\frac{dC}{dV_{dc}}\right)^{-1}. \tag{4.1}$$

Since, in the depletion approximation, the capacitance response originates solely from the edge of the depletion region, this result also holds true when N_B varies with position, x, through the thickness of the semiconductor [20]. So, $N_B(x)$ can be calculated using Equation 4.1 where $x = \varepsilon\varepsilon_0 A/C$ is measured from the junction.

Measurement of $C(V)$ can thus give a one-dimensional profile of the doping density N_B as a function of position through the thickness of the semiconductor, with a spatial resolution characterized by the Debye screening length L_D [21]. The parabolic band bending changes by kT/e over a distance of L_D, where $L_D = \sqrt{\varepsilon\varepsilon_0 kTe^{-2}N_B^{-1}}$. In order to neglect the transition region at the depletion edge, we require $W >> L_D$.

In crystalline materials, capacitance measurements as a function of voltage (CV) are considered a straightforward method to profile $N_B(x)$. However, the relatively large density of deep states in thin-film semiconductors can make it impossible to find the free-carrier density using CV, as further discussed in Section 4.7. Another complication can arise if the film is fully depleted or if $L_D \sim W$ [22]. In that case, N_{CV} is influenced by signal from the contacts or other layers, and $N_{CV} > N_B$. Many authors attempt to circumvent this difficulty by measuring in forward bias; however, interpretations of such measurements must be undertaken with caution. Forward bias does not reduce L_D, and can result in a significant injection of minority carriers; their impact depends on the particulars of the device. An exponential increase in capacitance indicates the depletion capacitance is becoming overwhelmed by the diffusion capacitance, also called the chemical capacitance [19]; or, depending on the dynamics of the film, this injection of minority carriers can instead result in a negative contribution to the capacitance. The negative capacitance itself is quite interesting but beyond the scope of this chapter [23–25].

4.6
Admittance Response of Deep States

When energy levels are present deeper in the bandgap, then the depletion approximation no longer necessarily holds true, and carrier capture and emission from these states must also be considered.

The electron capture rate, c_n, into an unoccupied state is

$$c_n = \sigma_n \langle \nu_n \rangle n$$

where σ_n is the capture cross section for electrons, and n is the density of free electrons moving with rms thermal velocity $\langle \nu_n \rangle$:

$$n = N_c \exp\left(-\frac{E_C - E_F}{kT}\right).$$

The principle of detailed balance states that in thermal equilibrium the capture and emission of electrons must be equal, and similarly the capture and emission of holes must balance. For electrons, this gives

$$e_n n_T = c_n (N_T - n_T)$$

where e_n is the emission rate of electrons, N_t is the total density of electron traps, and n_t is the density of occupied traps. Therefore, the fractional occupancy of the

trap in thermal equilibrium, which is also given by the Fermi–Dirac distribution function, can be used to relate the capture and emission times to the energetic position of the trap:

$$\frac{n_T}{N_T} = \frac{c_n}{c_n + e_n} = \left[1 + \frac{g_0}{g_1}\left(\frac{E_T - E_F}{kT}\right)\right]^{-1}.$$

This then gives the emission rate as

$$e_n = \sigma_n \langle \nu_n \rangle N_c \frac{g_0}{g_1} \exp\left(-\frac{E_c - E_T}{kT}\right),$$

where g_0 and g_1 represent the degeneracy of the initial and final states.

Since these values, particularly σ_n and E_T, may themselves depend on temperature, they can differ from the measured (apparent) capture cross-section σ_{na}, and thermal activation energy E_{na} of the trap determined from the thermally activated experimental data. This temperature dependence can have multiple origins. For deep states, a transition corresponds to a change from one charge state to another, so it is common for deep states to be charged, and therefore attractive or repulsive. Deep states may also reside in a larger, local concentration of traps that has an overall net charge and modifies the local free-carrier density [26, 27]. Additionally, the change in entropy with the change in trap state occupation may play a role as discussed in Section 4.12.

Electron emission from the defect is thus a thermally activated process with

$$e_n = \gamma \sigma_{na} T^2 \exp\left(-\frac{E_{na}}{kT}\right), \tag{4.2}$$

where, since we can approximate $N_c \propto T^{3/2}$ and $\langle \nu_n \rangle \propto T^{1/2}$, the temperature dependence of $N_c \langle \nu_n \rangle$ is isolated by defining $\gamma = N_c \langle \nu_n \rangle T^{-2}$ (assuming no temperature dependence of σ_{na}). For hole traps, Equation 4.2 has the identical form, with E_{pa} referenced to the valence instead of the conduction band edge.

This model assumes that the density of deep states obeys the principle of superposition, such that each deep state creates a set of discrete electronic energy transitions that can be added together to give the total density of states within the bandgap; interactions between states are neglected. Then, broad densities of states may originate from a single type of defect that is in a variety of different local environments. In real films, deep states can also interact with each other and with the lattice in complex ways that shift and broaden the density of states and can result in changes in the defect configuration or even diffusion of the trap center upon capture or emission of carriers (see, e.g., [28, 29]).

The differential capacitance of the sample originates from its response to a small voltage perturbation, δV. In the small-signal approximation, $\delta V < kT/e$. (Typical values of V_{ac}, around 30 mV, do not strictly satisfy this requirement, which may slightly impact the data [30, 31].) The resulting change in the band bending causes a change in trap state occupation at the location, x_T, where E_T is within kT of E_F, as illustrated in Figure 4.3. Thus, traps contribute to the capacitance in two ways: (i) traps modify the space charge density and therefore the depletion width W,

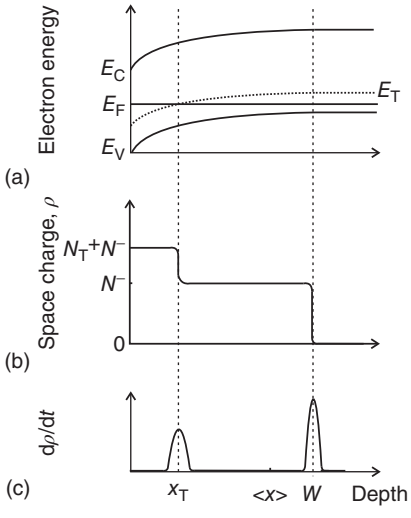

Figure 4.3 (a) Schematic of band bending with one deep trap state. (b) Charge density variation through the depletion region due to the trap state; same scale as (a). (c) In response to a changing bias, dV/dt, changes in space charge density $d\rho/dt$ can occur at both x_T and W as indicated.

and (ii) in the vicinity of x_T, the traps may be able to change their charge state dynamically, following the AC voltage, and contributing to $\delta Q/\delta V$.

The characteristic time of the capacitance measurement is defined by the angular frequency ω of the applied AC voltage such that states with emission rates $e_n > \omega$ respond to V_{ac}.[1)] By rewriting Equation 4.2, we can see that only states with apparent activation energies E_{na} up to the demarcation energy, E_e, will respond dynamically to the AC voltage, where

$$E_e = kT \ln\left(\frac{\gamma \sigma_{na} T^2}{\omega}\right). \tag{4.3}$$

Note that the demarcation energy depends on characteristics of the trap being measured, and so its determination might be difficult. The same combination of (ω, T) may probe different energies for physically different traps.

A general expression for the capacitance of the diode, which does not assume any specific density of states in the gap, can be derived starting from the identity

$$\frac{d}{dx}\left(x\frac{d\psi}{dx}\right) = \frac{d\psi}{dx} - x\frac{\rho}{\varepsilon\varepsilon_0},$$

where x is measured through the depth of the semiconductor ($x = 0$ at the interface), $\rho(x)$ is the depletion charge density, and $\psi(x)$ is the position-dependent potential in the depletion region and is defined to be zero far from the interface, such that $\psi(\infty) = 0$ and $d\psi/dx\,(\infty) = 0$. Then,

$$\int_0^\infty \frac{d}{dx}\left(x\frac{d\psi}{dx}\right)dx = 0 = \int_0^\infty \frac{d\psi}{dx}dx - \int_0^\infty x\frac{\rho}{\varepsilon\varepsilon_0}dx,$$

1) A better approximation in a depletion region dominated by a single deep trap level requires $e_t > \omega$, where $e_t = 2e_n\left(1 + \frac{x_t N_t}{W N_B}\right)$ [5].

and the value of ψ can be written as an integral over the charge density:

$$\psi(0) = -\int_0^\infty x\frac{\rho}{\varepsilon\varepsilon_0}\mathrm{d}x.$$

Application of a small voltage, δV, is equivalent to a voltage change at the interface of $-\delta V(0)$ since $\psi(0) = V_{\mathrm{bi}} - V_{\mathrm{a}}$ where V_{bi} is the built-in potential and V_{a} is the voltage applied across the junction. The charge response is $\delta Q = A\int_0^\infty \delta\rho(x)\mathrm{d}x$ where $\delta\rho$ is the change in charge density due to δV, and A is the area of the contact. Now the capacitance is

$$C = \frac{\varepsilon\varepsilon_0 A\int_0^\infty \delta\rho(x)\mathrm{d}x}{\int_0^\infty x\delta\rho(x)\mathrm{d}x} = \frac{\varepsilon\varepsilon_0 A}{\langle x\rangle}, \tag{4.4}$$

where $\langle x\rangle$ is the first moment of charge response, also called the center of gravity of the charge response.

Assumptions about the trap occupation and its response to AC and DC bias (and hence, its effect on $\langle x\rangle$) form the foundation of all the techniques discussed here. In both CV and DLTS, it is assumed that the frequency is chosen such that $\omega > e_{\mathrm{n,p}}$ for any deep traps; then, they do not respond dynamically to the AC bias, and $\langle x\rangle = W$. In CV it is also assumed that deep traps either do not change their charge state with the DC bias or are few enough not to have a significant influence on W. In contrast, in DLTS, the DC bias on the sample is assumed to have a strong effect on the trap state occupation. Indeed, the change in occupation of the traps in response to the DC bias yields the DLTS signal, as is further discussed in Section 4.8. In AS and DLCP, the AC frequency and/or the temperature are varied to ramp ω from values below $e_{\mathrm{n,p}}$ to above $e_{\mathrm{n,p}}$.

4.7 The Influence of Deep States on CV Profiles

Even if trap states do not respond to the AC voltage, they may adjust their charge state to the DC bias conditions, which results in artifacts in the CV profiles. To illustrate this behavior, we consider a SCAPS1D simulation of the n^+–p-junction containing uniform distributions of shallow and deep ($E_{\mathrm{T}} = E_{\mathrm{V}} + 0.3$ eV) acceptors of the concentrations $N_{\mathrm{A}} = 2\times10^{15}\,\mathrm{cm}^{-3}$ and $N_{\mathrm{T}} = 2\times10^{16}\,\mathrm{cm}^{-3}$, respectively [32, 33]. Figure 4.4a displays $N_{\mathrm{CV}}(\langle x\rangle)$, where N_{CV} and $\langle x\rangle$ are determined according to Equations 4.1 and 4.4, respectively. These values are simulated at two measurement frequencies: $\omega_{\mathrm{L}} < e_{\mathrm{p}}$ and $\omega_{\mathrm{H}} > e_{\mathrm{p}}$. In this simulation, the deep traps are assumed to be in equilibrium with the DC bias (similar to Figure 4.3). Then, the shallow acceptor density N_{A} is not reproduced at either frequency. At ω_{L}, $N_{\mathrm{CV}} = N_{\mathrm{A}} + N_{\mathrm{T}}$ is measured, while at ω_{H}, N_{CV} is a function of V_{dc}, with $N_{\mathrm{A}} \le N_{\mathrm{CV}} \le N_{\mathrm{A}} + N_{\mathrm{T}}$, since the static charge accumulated at deep states follows

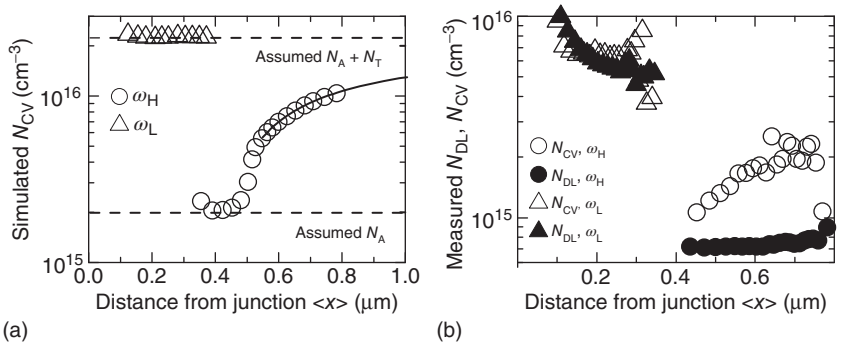

Figure 4.4 (a) Simulated CV profiles at two frequencies: low (ω_L, open triangles) and high (ω_H, open circles), as described in the text. The solid line is a fit using Equation 4.5. Best fit parameters are identical to assumed values of N_A and N_T and yield $\lambda = 0.45$. (b) Experimental CV (open symbols) and DLCP (closed symbols) data for a $CuInSe_2$ device. Device details are described elsewhere [34]. All data were collected at 11 kHz, which corresponds to a low frequency at 280 K (triangles) and a high frequency at 180 K (circles).

the DC voltage sweep and influences the capacitance. In this case the charge distribution delivered by CV profiling can be approximated by

$$N_{CV} = N_T(x_T)\left[1 - \frac{\lambda}{W}\right] + N_A(W), \tag{4.5}$$

where $\lambda = W - x_T$ is assumed to remain constant for applied DC voltages [35].

Thus, when trap densities are significant, the CV profile does not clearly yield the densities N_A and N_T nor indicate their uniformity. As discussed in Section 4.10 and illustrated in Figure 4.4a and b, DLCP can help sort out these issues. A longer discussion on the influence of deep states, including interface states, on CV and DLCP measurements, can be found in [34].

4.8
Deep-Level Transient Spectroscopy

In the standard approach, DLTS analysis consists of extracting the emission rates of deep levels from a transient capacitance signal as illustrated in Figure 4.5a–c. These transients result from a voltage or optical pulse applied to the junction. In its simplest application, DLTS allows for determination of deep trap parameters such as the type of the defect (majority or minority carrier trap), activation energy, capture cross sections, and trap concentration [36].

In order to understand the DLTS signal, we are interested in calculating how a change of a charge ΔQ at some distance x from the interface ($x = 0$) will influence the junction capacitance. It is assumed that the additional charge is trapped at defect states of the concentration N_T within a layer of the width Δx. Hence, $|\Delta Q| = q\Delta x N_T$. If we don't initially assume a one-sided junction, then this charge will induce a change of the depletion layer width $\Delta W = \Delta W_n + \Delta W_p$ where ΔW_n and

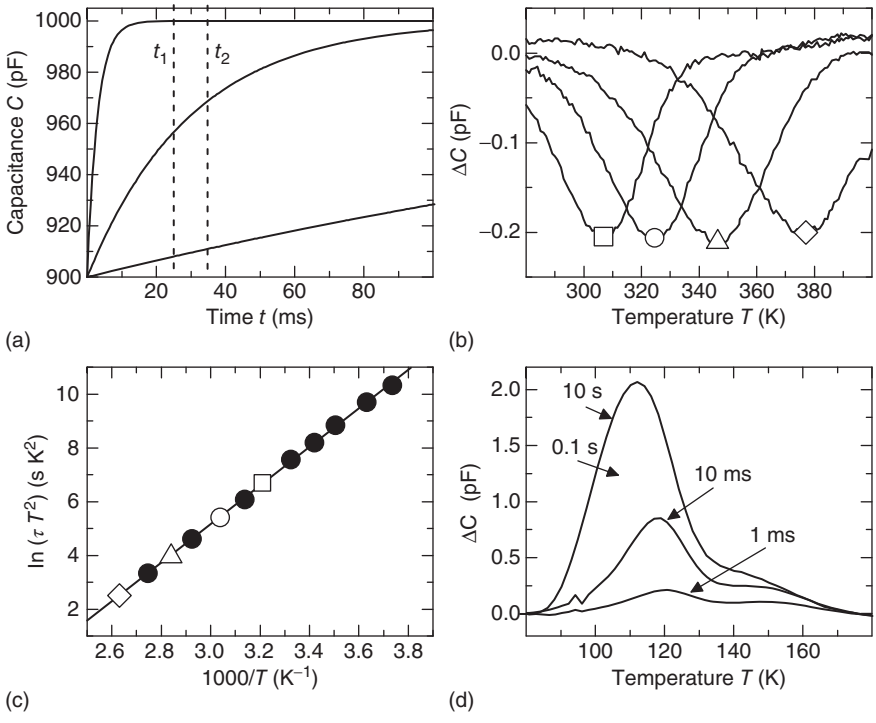

Figure 4.5 (a) Schematic transients. The DLTS signal, $[C(t_1) - C(t_2)]/C_0$, will be maximized when the rate window and emission rate match (Equation 4.11). (b) DLTS data for a GaAsN device. Each trace corresponds to a different rate window. (c) Arrhenius plot yielding E_{na} and σ_{na} of the trap. Data points corresponding to peaks in (b) are indicated with the same symbol. (d) Filling pulse dependence of the DLTS signal for the same sample; in this case data for a minority carrier trap is shown. The labels indicate filling pulse length. See Refs [37, 38] for further discussion. (Data courtesy of Steve Johnston, National Renewable Energy Laboratory.)

ΔW_p are the depletion widths on the n and p side of the junction, respectively. Small capacitance changes ($\Delta C << C$) can be approximated as

$$\frac{\Delta C}{C} \approx -\frac{\Delta W}{W} \tag{4.6}$$

By solving the Poisson equation, ΔW can be eliminated from Equation 4.6 yielding [39]

$$\frac{\Delta C}{C} \approx \mp \frac{N_T \Delta x}{W^2} \left(\frac{x + W_n}{N^-} - \frac{W_p - x}{N^+} \right), \tag{4.7}$$

where N^+ and N^- are the densities of ionized space charge on the n and p sides of the junction, respectively. The negative and positive signs correspond to decrease and increase of negative charge, respectively, or equivalently, an increase and decrease of positive charge. Rewriting Equation 4.7 for a spatial distribution of

trapping states within the depletion layer yields

$$\frac{\Delta C}{C} \approx \mp \int_{-W_n}^{W_p} \frac{N_T(x)}{W^2} \left(\frac{x + W_n}{N^-} - \frac{W_p - x}{N^+} \right) dx. \tag{4.8}$$

For highly asymmetrical junctions, (here $n^+ - p$), assuming a uniform defect distribution and neglecting the transition region, one arrives at

$$\frac{\Delta C}{C} \approx \mp \frac{N_T}{2N^-}. \tag{4.9}$$

Thus, by measuring the capacitance transient $\Delta C(t)$, one can easily monitor the occupation of deep levels while the system relaxes after the equilibrium has been disturbed, for example, by application of a voltage or a light pulse.

The previous equations show that the sensitivity of the capacitance change depends on the location of the trapped charge within the junction: it is highest at the border of the space charge layer and decreases toward the interface. For $x = 0$, that is, if the charge is accumulated at the very interface, the capacitance does not change at all ($\Delta C = 0$), since by charge neutrality $N^+ W_n = N^- W_p$. For this reason, an MIS-type structure can be an advantage in studying interface states with DLTS. Equations 4.8 and 4.9 also hold true for an MIS diode or for an $n^+ - i - p$ ($p^+ - i - n$) structure assuming the depletion width W_n (W_p) remains constant [40, 41].

Depending on the nature of the perturbing pulse and the characteristics of the trap states, the transient can be due predominately to either an emission or a capture of majority or minority carriers. In most materials, there may be many different trap states, and, assuming as in the SRH model that they are noninteracting and have discrete energy levels, the capacitance transient will consist of a sum over many exponentials.

In order to observe the emission of majority carriers, the junction is initially maintained in quasiequilibrium at reverse-bias $-U_R$. Majority carrier traps of the concentration N_T are ionized in a region of width $W(-U_R) = W_R$ and contribute to the junction capacitance $C(-U_R)$. During the bias pulse, the reverse-bias voltage and therefore depletion width are reduced for a time t_p, and these traps capture free carriers that appear in the previously depleted region. When the reverse bias is restored, the excess free carriers will be swept away. However, the trapped majority carriers reduce the space charge density, increasing the depletion width and causing the capacitance to drop below $C(-U_R)$ by ΔC. These trapped carriers are thermally emitted, and the capacitance gradually increases back toward $C(-U_R)$. This will be observed as a capacitance transient.

In the depletion region there are practically no free carriers and capture processes can be neglected [6]. For an $n^+ - p$-junction, assuming $e_p >> e_n$, which usually holds for acceptor-type defects located in the lower part of the bandgap, the capacitance transient $C(t)$ is characterized by a single time constant $\tau = 1/e_p$:

$$C(t) = C_\infty \left[1 - \frac{N_T}{2N^-} \exp\left(-e_p t\right) \right],$$

where C_∞ is the quasiequilibrium capacitance, in this case equal to $C(-U_R)$. An analogous equation is obtained for a p^+-n-junction.

In this kind of experiment, the charge state of minority carrier traps does not normally change during the pulse [42]. In order to investigate such defects, it is necessary to inject minority carriers into the depletion region by forward biasing the junction during the pulse or applying an optical pulse. For positively charged donors in p-type material, electron capture will prevail ($c_n >> c_p$), and at the end of the pulse, most of the traps will be occupied by electrons. Hence the negative space charge increases, which gives $\Delta C > 0$. After the pulse these electrons will be emitted, and the charge relaxation results in a capacitance transient characterized by a single time constant $\tau = 1/e_n$:

$$C(t) = C_\infty \left[1 + \frac{N_t}{2N^-} \exp\left(-e_n t\right)\right]$$

where N_t is the density of minority carrier (in this case, donor) traps in the material.

The sign of the capacitance transient $C(t)$ is always positive and negative for the emission of minority and majority carriers, respectively, independent of the conductivity type of the semiconductor (p or n). Note that significant series resistance can result in majority carrier traps appearing to have positive (minority carrier) transients. Apparent minority carrier transients should be checked by adding an additional series resistor to the device and observing its influence on the sign of the transient [37].

The normalized DLTS signal is defined as the difference of the capacitance at times t_1 and t_2 ($t_1 < t_2$):

$$S(T) = \frac{C(t_1) - C(t_2)}{\Delta C(0)}, \tag{4.10}$$

where $\Delta C(0)$ is the maximal capacitance change [36]. The $S(T)$ curve is called a DLTS spectrum. Since the emission rate[2] is an increasing function of temperature, $S(T) = 0$ for very slow (low T) and very fast (high T) transients. At intermediate temperatures $S(T)$ passes an extremum[3] as the time constant of the transient $\tau_{n,p}$ equals the rate window τ, defined as

$$\tau = \frac{t_1 - t_2}{\ln(t_1/t_2)}. \tag{4.11}$$

Activation energy and capture cross section of investigated traps can be calculated from the slope and intercept of an Arrhenius plot as illustrated in Figure 4.5c. The trap concentration can be evaluated using Equation 4.9, provided the shallow net doping level is known.

2) It is assumed that the response of a single level is observed. Ideally, different levels have significantly different emission rates, at a given temperature, and their responses can be clearly separated.
3) A maximum or a minimum occurs for minority and majority carrier traps, respectively.

4.8.1 DLTS of Thin-Film PV Devices

The aforementioned considerations were conducted under a number of simplifying assumptions, which very often are not fulfilled in thin-film PV devices. Typical complications that arise if one tries to apply the quoted standard formulas include:

1) In the so-called λ-effect, DLTS peak height is not related to deep trap concentration in a simple equation but depends on the energetic position of the defect level in the bandgap. In order to derive the more accurate formula, $\Delta C/C \approx f_\lambda N_T/2N^-$, where f_λ is a function of trap occupancy, one has to take into account the distance λ between the depletion edge and the point where the trap level and the quasi-Fermi level intersect [43].
2) The approximation $\Delta C/C \approx -\Delta W/W$ breaks down when deep trap concentrations are large, which has severe consequences for the DLTS signal analysis: (i) the capacitance transients become nonexponential, which influences the shape of DLTS peaks; (ii) DLTS peak position, and thus calculated activation energy and capture cross section, start to depend on the N_T/N^- ratio; and (iii) the λ-effect becomes more pronounced [44].
3) Since the emission of carriers occurs at large reverse biases, the emission rates can be influenced by the electrical field through Poole–Frenkel and tunneling effects [45, 46]. In order to avoid this kind of complication, reverse-bias DLTS (RDLTS) mode is used [47].
4) If a few closely spaced energy levels contribute to the capacitance transient in the same temperature range, the poor resolution of the standard (R)DLTS method does not allow for a clear separation of the individual components. Application of an inverse Laplace transform to the analysis of capacitance transients, called the Laplace DLTS method, increases the resolution by an order of magnitude [48, 49]. However, one has to be extremely careful while interpreting the emission rate spectrum since it is always a result of numerical calculations.
5) Nonexponential response, for example, due to defect relaxation, sometimes dominates capacitance transients and can be misinterpreted as the energetic distribution of defects within the bandgap. This issue is closely related to metastable phenomena, discussed in Section 4.14.
6) Barriers to carrier capture may require a fairly long filling pulse in order to fully populate the traps, as illustrated in Figure 4.5d. The dependence of DLTS signal on pulse length can allow the capture barrier energy to be measured [5]. This behavior can also be confused with metastable changes in the device.
7) Nonohmic contacts have been shown to give rise to DLTS response. Varying the pulse amplitude can help in identifying the parasitic signal [50].

4.9 Admittance Spectroscopy

Measurement of the sample admittance as a function of applied AC frequency and temperature is termed AS. This technique can yield the thickness of the film, the position of the Fermi energy in the bulk, the energetic position of dominant defect bands that occur between the Fermi energy and midgap, and an estimate of the density of those states. In contrast to both the DLTS and CV techniques, in AS the frequency (or temperature) is ramped so as to cross the transition frequency where the traps just start to respond. Note that AS can only detect traps between the band edge and midgap [51]. While an additional applied DC voltage is not fundamentally part of the AS measurement, it is typically crucial to making sense of the observed transitions. As noted in Section 4.1, while we assume the depletion approximation, in real devices many factors could contribute to a dynamic response; for example, measurements at differing DC bias can help distinguish between effects at the interface and in the bulk [3, 34]. Thus, interpretations of the AS transitions without additional bias-dependent investigation should be undertaken with caution.

When the sample is too cold, or the frequency too high, there is no time for carriers in the bulk, undepleted material to shift in and out of the depletion edge in response to the applied voltage, and a condition called freeze-out occurs. Under these conditions, the capacitance response will be that of the bulk dielectric, $C = \varepsilon\varepsilon_0 A/h$, where h is the distance between the top and back contacts. Increasing the temperature, T, or decreasing the frequency, f, eventually a step will be observed from $C = \varepsilon\varepsilon_0 A/h$ to $C = \varepsilon\varepsilon_0 A/W$.

The dielectric relaxation time, τ_R, is determined by $\tau_R = \rho_s \varepsilon\varepsilon_0$. The resistivity of the semiconductor, ρ_s, depends on the free-carrier density, which has a thermal activation energy of E_F, and the mobility. So, this initial step in the capacitance occurs at a characteristic energy of E_F as long as E_F does not vary strongly with T and the mobility is approximately constant. If the charge transfer is instead limited by mobility, usually seen at high frequencies, then these data may give the majority carrier mobility in the film [52].

As T continues to increase or f decrease, trap states can begin to respond. The demarcation energy E_e (Equation 4.3) determines the cut-off energy for trap response at a certain T, f data point. When $E_T = E_e$, the occupation of the state can follow the AC voltage, and its charge state will change at the location x_e. This causes $\langle x \rangle$ to move closer to the interface and C to increase from $\varepsilon\varepsilon_0 A/W$ to $\varepsilon\varepsilon_0 A/\langle x \rangle$ as shown in Figure 4.6a. Successively deeper trap states respond as E_e is further increased.

Steps in C correspond to peaks in G/ω, due to their causal relationship. This correspondence can be calculated using the Kramers–Kronig transformations, which relate the real and imaginary parts of the susceptibility, χ' and χ'', respectively [15]. A slight correction may be necessary to apply these transformations within the p–n-junction [53]. After measurement of one component of the data, the Kramers–Kronig transformations can be employed to construct the other,

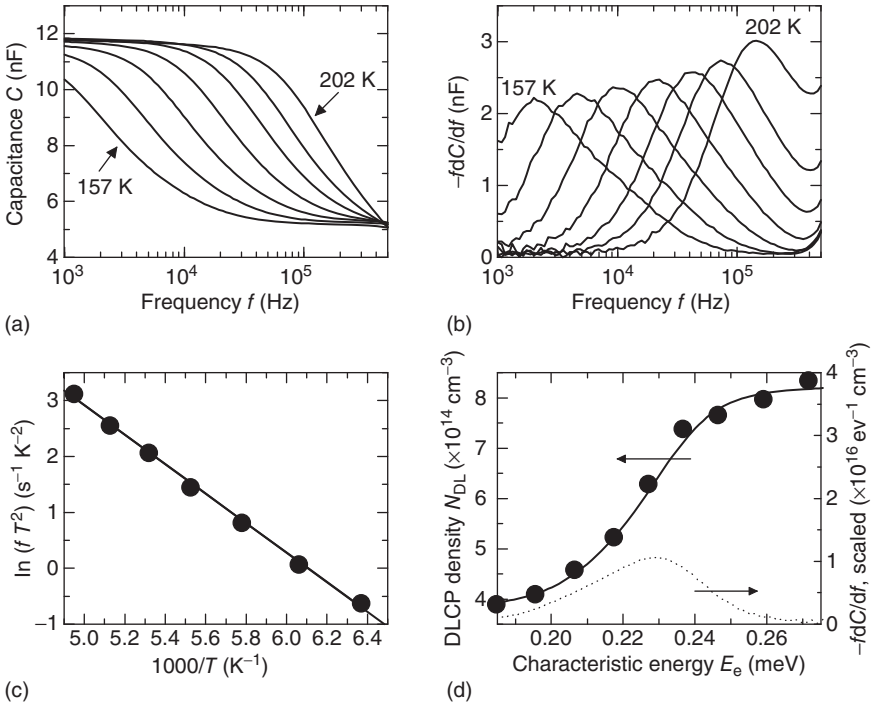

Figure 4.6 (a) Sample AS raw data for a CIGS device. Data was taken in 8 K increments from 157 to 202 K. (b) The AS data after applying Equation 4.12, showing the characteristic (peak) frequencies at each temperature. (c) Arrhenius plot of each peak (circles). A linear fit (line) yields $E_{na} = 0.23$ eV and $\gamma\sigma_{na} = 1.0 \times 10^7$ s^{-1} K^{-2}. (d) DLCP data (circles) collected at 45 kHz, at the location $\langle x \rangle = 1.3$–1.4 μm, and at temperatures ranging from 157 to 220 K. The integral over the 181 K AS ($-f$ dC/df) data (solid line) was scaled by a constant factor to show the close agreement of transition energy and magnitude between AS and DLCP. The raw AS ($-f$ dC/df) data at 181 K (dashed line), adjusted by the same scaling factor, thus represents the density of states for the 0.23 eV trap. (Data courtesy of Jian V. Li, National Renewable Energy Laboratory.)

although since frequencies are never truly measured from 0 to ∞, this is done with the assistance of approximations or fits to the data [54, 55]. Particularly in electrochemical measurements, it is common to use this procedure to verify the conductance measurement, but such tests are not necessarily definitive [56].

While the G/ω peaks can be a good way to observe the position of the capacitance step, they can be masked by the leakage conductance in some samples; analogous peaks can also be obtained from the derivative

$$\frac{\mathrm{d}C}{\mathrm{d}E_e} = -\frac{\omega}{kT}\frac{\mathrm{d}C}{\mathrm{d}\omega}, \tag{4.12}$$

as illustrated in Figure 4.6b. The (ω, T) data points from each peak can then be plotted on an Arrhenius plot; typically $\ln(\omega/T^2)$ is graphed as a function of $1000/T$

as shown in Figure 4.6c. Using Equation 4.2, the slope then yields the apparent activation energy E_{na}, while the intercept gives the apparent capture cross-section σ_{na}. These quantities may differ from the trap energy and the trap capture cross section, as discussed previously in Section 4.6. The graph of $\omega\,\mathrm{d}C/\mathrm{d}\omega$ versus ω can be transformed into $N_t(E_e)$ versus E_e by using the measured σ_{na} to rescale the ω axis to E_e and calculating $N_t(E)$ according to [51]

$$N_t(E_e) \approx -\frac{V_{bi}^2}{W[eV_{bi} - (E_{F\infty} - E_e)]}\frac{\omega}{kT}\frac{\mathrm{d}C}{\mathrm{d}\omega} \tag{4.13}$$

where $E_{F\infty}$ indicates the position of the Fermi energy in the bulk. The scaling provided by Equation 4.13 is typically limited by uncertainties in $E_{F\infty}$, W, and V_{bi}. Rescaling of the ω axis to E_e has been illustrated in Figure 4.6d; in that figure, the signal magnitude is scaled using DLCP data as described in the caption. For broad densities of states, a clear peak may not be observable in $\omega\,\mathrm{d}C/\mathrm{d}\omega$ versus ω, in which case the factor necessary to rescale the ω axis such that all of the $\omega\,\mathrm{d}C/\mathrm{d}\omega$ curves overlap can yield an estimate for σ_{na}.

The Arrhenius plot is commonly interpreted to directly yield E_T; however, in many materials, the apparently same trap response has been observed with differing E_{na} and σ_{na} values. These are often related by

$$\sigma_{na} = \sigma_{00}\exp\left(\frac{E_{na}}{E_{char}}\right), \tag{4.14}$$

such that a graph of $\ln\sigma_{na}$ versus E_{na} yields a straight line with slope E_{char}^{-1} and intercept $\ln\sigma_{00}$. A phenomenological relationship between the quantities E_{char} and σ_{00} exists, which is known as the Meyer–Neldel rule, and is further discussed in Section 4.12.

4.10 Drive-Level Capacitance Profiling

The technique of DLCP yields the density of states responding dynamically to the AC bias. Like AS, this technique allows different trap response energies to be isolated by adjusting the temperature and frequency of the measurement. At the same time, DLCP yields a density somewhat analogous to CV; however, in DLCP, the AC voltage amplitude, V_{ac}, is varied to determine the density.

The value of V_{ac} employed in DLCP no longer satisfies the small-signal condition, and the capacitance response, as a function of V_{ac}, is fit to yield higher-order corrections:

$$C = C_0 + C_1\delta V + C_2\delta V^2 + \cdots. \tag{4.15}$$

Note that, as V_{ac} is varied, at the same time the DC bias must be adjusted so that the maximum applied voltage remains constant, that is, the voltage waveforms are aligned at their peaks [57]. This gives an accurate value for the small-signal

capacitance, C_0, as well as an additional experimental parameter C_1. In DLCP, the values of C_0 and C_1 are used to find the gap state density according to [57]

$$N_{\mathrm{DL}} \equiv -\frac{C_0^3}{2e\varepsilon\varepsilon_0 A^2 C_1} = p + \int_{E_{\mathrm{F}}^{\infty}}^{E_{\mathrm{V}}+E_{\mathrm{e}}} g(E, x_{\mathrm{e}})\mathrm{d}E, \tag{4.16}$$

for a $\mathrm{n}^+-\mathrm{p}$ device, where an analogous equation can be written for a $\mathrm{p}^+-\mathrm{n}$ device. In Equation 4.16, N_{DL} is the free-carrier density plus the trap density that is able to respond at E_{e}, and $g(E, x_{\mathrm{e}})$ is the density of states in the gap at the location x_{e}.

Since DLCP is a purely AC measurement, the carriers contributing to N_{DL} are exactly those responding in an AS measurement. The same activation of trap response as a function of f, T can be observed, as illustrated in Figure 4.6d. In samples with deep traps, the high-frequency DLCP can give a more accurate estimation of free-carrier density than CV profiling data [34]. At low frequencies, DLCP should give the same result as CV profiling, where low frequencies are defined such that all traps that change their charge with the DC bias in CV also respond dynamically to the AC bias. DLCP gives the trap density more directly than AS, not requiring any particular knowledge about the device other than the dielectric constant.

The DLCP measurement can be repeated as a function of V_{dc}, to yield $N_{\mathrm{DL}}(\langle x \rangle)$, with the spatial sensitivity roughly determined by the Debye length [58]. The profile $N_{\mathrm{DL}}(\langle x \rangle)$ helps to identify spatial variations through the film [34, 59] and responses that are localized or at the interface. The issue of spatial variation is further discussed in Section 4.13.

4.11 Photocapacitance

Photocapacitance measurements come in many variations, all intended to measure the optical energy and cross section for transitions between traps and the conduction or valence band. The change in charge of the junction due to optical excitation of carriers into or out of defects results in a capacitance change that can be measured as a function of photon energy. While there is no space here to delve into the details of these measurements, we give a brief discussion of their benefits and references for further study.

Transient photocapacitance techniques allow a particular thermal transition to be clearly associated with its corresponding optical transition(s) and include both deep-level optical spectroscopy (DLOS) [60] and transient photocapacitance (TPC) spectroscopy [61], which are based upon the technique of DLTS. Essentially the DLTS experimental setup can be used, with the addition of a monochromatic light source, filters, and a shutter to control optical excitation of the sample. In these measurements, voltage or optical filling pulses are employed to alter trap occupation from its equilibrium value. The ensuing transient is observed under monochromatic optical excitation.

In DLOS, the transient rate is measured at times as close as possible to time = 0 (measured from the end of the filling pulse) to isolate the optically induced excitation of carriers out of the traps from the thermal relaxation. In TPC, transients in the light and in the dark are subtracted to remove the thermal part of the relaxation from the signal. The TPC technique utilizes a very low light intensity, selected such that the signal varies linearly with photon flux.

In both cases, the temperature and filling pulse are chosen carefully from either DLTS or AS data such that the optical response associated with particular thermal transients can be isolated. For example, following a majority carrier filling pulse, at high temperatures a trap may thermally empty very rapidly, before the beginning of the measurement, and perhaps more quickly than the response time of the electronics. In such measurements, little or no thermal transient is observed; the trap may still contribute to the optical part of the TPC signal, but the resulting signal magnitude will be limited by thermal quenching [62]. At a lower temperature, the same trap may have a time constant on the order of seconds, such that it is not significantly thermally emptied during the timescale of the measurement. Only in the latter case would the trap contribute to the optically enhanced transient in the way envisioned for this technique. By subtracting the high- and low-temperature spectra, the optical transition(s) associated with a specific defect, which has already been observed thermally, may be identified and characterized.

In some cases, dramatically different optical and thermal energies have been observed, allowing a better understanding of the lattice relaxation associated with changes in occupation of a trap; the DX centers in GaAs are a well-known example [63]. Finally, a similar measurement can be conducted while measuring the current, rather than capacitance, response of the device. This technique, dubbed transient photocurrent (TPI) spectroscopy, gives complementary information to TPC. This is because the capacitance response depends on net charge change, $p - n$, in the device, while the current transient is sensitive to the total concentration of carriers excited out of the traps, $p + n$. The difference between these spectra can be used to better understand minority carrier collection in the film [64].

These techniques allow what is essentially an optical absorption spectrum of the buried absorber layer in the complete, working device to be measured. Since many characteristics of the film can be altered due to deposition of ensuing layers (such as due to high temperatures, migration of elements, etc.), this can be a valuable tool, for example, to study the role of Ga and Na in CIGS [65, 66]. While the TPC and TPI spectra resemble steady-state photocurrent spectra with high dynamic range, such as in [67], the transient aspect of the TPC and TPI techniques offers additional experimental parameters with which to explore the device properties.

4.12 The Meyer–Neldel Rule

The Meyer–Neldel rule is a very general rule describing thermally activated processes for which the measured prefactors and energies in different samples are

interrelated by Equation 4.14. Meyer and Neldel observed that the activated DC conductivity of several related oxide semiconductors followed this relationship [68]. Since that time, many thermally activated processes have been observed to follow the Meyer–Neldel rule. In a-Si:H, it is observed in such seemingly disparate processes as the thermal annealing of defects and the activation of DC conductivity [69, 70]; AS spectroscopy data for CIGS following the Meyer–Neldel rule are discussed in Ref. [71]. The Meyer–Neldel rule is also known as the compensation rule when it is observed in thermally activated rate processes of chemical reactions (see, e.g., Ref. [72]).

The Eyring model, essentially the recognition that the measured transition corresponds to an increase in Gibbs free enthalpy, ΔG, for the thermodynamic system upon ionization, is the most generally accepted explanation of this behavior [73]. The trap energy is $E_T - E_V = \Delta G$ (for an acceptor-type trap). But, since ΔG is separated into entropy, ΔS, and enthalpy, ΔH, terms by $\Delta G = \Delta H - T\Delta S$ the measured thermal activation energy corresponds to ΔH rather than ΔG, and the value of ΔS affects the apparent capture cross section.

Then, Equation 4.2 becomes

$$e_n = \chi_n N_c \sigma_n \langle v_n \rangle \frac{g_0}{g_1} \exp\left(-\frac{\Delta H}{kT}\right),$$

where

$$\chi_n = \exp\left(\frac{\Delta S}{k}\right).$$

For deep states, ΔS is thought to predominantly originate from the change in lattice vibrations occurring with the change in occupancy, and bonding configuration, of the defect. A discussion of ΔS for traps in CIGS is given in [27]. When the electronic transition does not involve phonons, the localized state is not coupled to the local phonon modes, and the electronic degeneracy is neglected, then it has been shown that $\Delta S = 0$ and $\Delta G = \Delta H$ [74]. This includes transitions from the shallow, hydrogenic dopant states.

Explanations attempting to quantify ΔS and relate it to conduction in semiconductors focus on the electron–phonon interaction [75–77]. Unrelated mechanisms can cause apparent Meyer–Neldel behavior, especially when trends are only observed over one or two orders of magnitude. Examples for this phenomenon can be found in Refs [78, 79].

4.13
Spatial Inhomogeneities and Interface States

In thin-film solar cell materials, spatial inhomogeneities and interface states are often present. Here we consider only inhomogeneities through the depth of the film. Inhomogeneity could be observed in N_T, E_{na}, σ_{na}, or all of these. Since changes in band bending or E_F affect x_e, most of the techniques discussed here may probe a range of trap locations over the course of the measurement, and

inhomogeneity will lead to anomalous results. One exception is DLCP, in which the trap density can be measured by varying only the frequency, keeping T and V_{dc} constant (even so, the trap response and free-carrier response occur at two different locations in the film, and the spatial resolution is limited).

In most cases it is possible to test a hypothesis of inhomogeneity in AS by repeating the measurement at a different value of V_{dc}. For a uniform sample, the distance λ should remain constant with DC bias. So, $\langle x_H \rangle - \langle x_L \rangle = \varepsilon\varepsilon_0 A(C_H^{-1} - C_L^{-1})$ should not vary with V_{dc}, where C_H and C_L correspond to measurements above and below the transition frequency for the trap, respectively. However, this same identity could also hold true for an interface minority carrier trap or for a double-diode device with a nonohmic back contact.

An extremely important issue in thin-film photovoltaic devices are interface states, which represent a special case of inhomogeneity. The characteristic energy at which interface states respond dynamically to the AC bias corresponds to the Fermi energy at the interface. Assuming that E_F is not pinned at the interface, and that the density of interface states $N_I(E)$ is spread fairly uniformly over a wide range of energies, the apparent activation energy of interface states will shift with V_{dc} (and possibly T); such a measurement also allows the dependence of N_I on E to be determined. A shift of E_{na} with V_{dc} is highly suggestive of near-interface traps [16] but should not be confused with freeze-out of the mobility, which can also be bias dependent [52].

A spatially and energetically localized density of states (including near the interface) could appear as a peak in N_{CV} occurring at a particular value of V_{dc}, because W changes abruptly with V_{dc} as the trap state crosses from above to below E_F; such a peak should generally be suppressed in DLCP except at the exact T and f at which the trap state can respond to the AC voltage [59]. Hence, comparisons of results between different parameter values and different techniques can be extremely useful.

It is also possible for an interface minority carrier trap to be filled and emptied via the highly doped side of the junction. The barrier height for such a response may remain roughly constant with V_{dc}, since there is not a large potential drop on the highly doped side of the interface. This situation would appear like a bulk trap, where $\langle x_H \rangle - \langle x_L \rangle = \varepsilon\varepsilon_0 A(C_H^{-1} - C_L^{-1})$ is constant with V_{dc} [33, 80]. In some cases the two possibilities can be distinguished by the magnitude of $\langle x_H \rangle - \langle x_L \rangle$, which, in the case of an interface trap, will correspond to the relatively small depletion width on the highly doped side of the interface plus the thickness of any intrinsic buffer layer at the interface. Otherwise, variations in the sample preparation, such as replacement of the one-sided junction with a Schottky junction, are necessary to resolve this question.

Such a study has indeed yielded new information on a long-discussed trap in CIGS, showing that the trap response remains even in Schottky devices, and therefore is not at the p–n-junction interface [81]. In this case, the "trap" response may result from a nonohmic back contact, with an activation energy corresponding to the back barrier height. The falloff of capacitance in forward bias is indeed

suggestive of a double-diode device. However, forward bias can induce other complications including the injection of minority carriers and the addition of a negative component of capacitance, as mentioned in Section 4.5. The presence of a nonohmic back contact may be identifiable from $I-V-T$ measurements [82, 83].

In principle, DLTS is much less sensitive for charge changes in the vicinity of the interface. However, both majority and minority carrier traps at the interface can be effectively investigated by DLTS in MIS-like structures, as already indicated. This requires some modifications from the standard DLTS measurement discussed previously, and in particular, the pulse amplitude must be carefully chosen. The investigation of interface states in MIS structures by DLTS was discussed extensively by Murray *et al.* [40].

4.14 Metastability

An additional complication occurs when sample properties can be persistently changed by external factors like voltage stress or illumination and then recovered, perhaps, after heating the sample in a controlled environment and in the dark. In practice, such effects are common, but the details are characteristic to each specific material and indeed may depend on aspects of device preparation that are closely, but not identically, duplicated in different laboratories. Thus it is critical to carefully control the sample environment until its sensitivities are understood and to check for repeatability of measurements. Unfortunately, metastable effects may be observed under the conditions necessary for capacitance spectroscopy measurements, which then necessitates careful, and sometimes laborious, experimental procedures. An introduction to these issues for some common solar cell materials can be found in [41, 66, 84–88].

Acknowledgments

The authors gratefully acknowledge Steven W. Johnston and Jian V. Li for valuable discussions of the manuscript, as well as for assistance with the figures.

References

1. Feichtinger, H. (1991) Deep centers in semiconductors, in *Electronic Structure and Properties of Semiconductors* (ed W. Schröter), VCH Publishers Inc., New York, pp. 143–195.
2. Losee, D.L. (1975) Admittance spectroscopy of impurity levels in Schottky barriers. *J. Appl. Phys.*, **46**, 2204.
3. Lang, D.V., Cohen, J.D., and Harbison, J.P. (1982) Measurement of the density of gap states in hydrogenated amorphous silicon by space charge spectroscopy. *Phys. Rev. B*, **25**, 5285.
4. Cohen, J.D. and Lang, D.V. (1982) Calculation of the dynamic response of Schottky barriers with a continuous

distribution of gap states. *Phys. Rev. B*, **25**, 5321.
5. Blood, P. and Orton, J.W. (1992) *The Electrical Characterization of Semiconductors: Majority Carriers and Electron States*, Academic Press, Ltd, San Diego.
6. Schroeder, D.K. (2006) *Semiconductor Material and Device Characterization*, John Wiley and Sons, Inc., Hoboken.
7. Bozyigit, D., Lin, W.M.M., Yazdani, N., Yarema, O., and Wood, V. (2015) A quantitative model for charge carrier transport, trapping and recombination in nanocrystal-based solar cells. *Nat. Commun.*, **6**, 6180.
8. Almora, O., Zarazua, I., Mas-Marza, E., Mora-Sero, I., Bisquert, J., and Garcia-Belmonte, G. (2015) Capacitive dark currents, hysteresis, and electrode polarization in lead halide perovskite solar cells. *Phys. Chem. Lett.*, **6**, 1645.
9. Kleider, J.P., Alvarez, J., Brézard-Oudot, A., Gueunier-Farret, M.-E., and Maslova, O. (2015) Revisiting the theory and usage of junction capacitance: application to high efficiency amorphous/crystalline silicon heterojunction solar cells. *Sol. Energy Mater. Sol. Cells*, **135**, 8.
10. Bisquert, J. (2008) Beyond the quasistatic approximation: impedance and capacitance of an exponential distribution of traps. *Phys. Rev. B*, **77**, 235203.
11. Reislöhner, U. and Ronning, C. (2012) Maxwell–Wagner polarization in $Cu(In,Ga)(S,Se)_2$. *Appl. Phys. Lett.*, **100**, 252111.
12. Weiss, T.P., Redinger, A., Luckas, J., Mousel, M., and Siebentritt, S. (2013) Admittance spectroscopy in kesterite solar cells: defect signal or circuit response. *Appl. Phys. Lett.*, **102**, 202105.
13. Pysch, D., Mette, A., and Glunz, S.W. (2007) A review and comparison of different methods to determine the series resistance of solar cells. *Sol. Energy Mater. Sol. Cells*, **91**, 1698.
14. Crain, D.J., Rock, S.E., Garland, J.E., and Roy, D. (2013) Comparison of DC and AC electro-analytical methods for measuring diode ideality factors and series resistances of silicon solar cells. *Curr. Appl. Phys.*, **13**, 2087.
15. Jonscher, A.K. (1983) *Dielectric Relaxation in Solids*, Chelsea Dielectrics Press, Ltd, Chelsea.
16. Nicollian, E.H. and Brews, J.R. (1982) *MOS (Metal Oxide Semiconductor) Physics and Technology*, Wiley, USA.
17. Istratov, A.A. and Vyvenko, O.F. (1999) Exponential analysis in physical phenomena. *Rev. Sci. Instrum.*, **70**, 1233.
18. Callegaro, L. (2009) The metrology of electrical impedance at high frequency: a review. *Meas. Sci. Technol.*, **20**, 022002.
19. Sze, S.M. (1985) *Semiconductor Devices Physics and Technology*, John Wiley & Sons, New York.
20. Hilibrand, J. and Gold, R.D. (1960) Determination of the impurity distribution in junction diodes from capacitance–voltage measurements. *RCA Rev.*, **21**, 245.
21. Johnson, W.C. and Panousis, P.T. (1971) The influence of Debye length on the C–V measurement of doping profiles. *IEEE Trans. Electron Devices*, **18**, 965.
22. Kirchartz, T., Gong, W., Hawks, S.A., Agostinelli, T., MacKenzie, R.C.I., Yang, Y., and Nelson, J. (2012) Sensitivity of the Mott–Schottky analysis in organic solar cells. *J. Phys. Chem. C*, **116**, 7672.
23. Gommans, H.H.P., Kemerink, M., and Janssen, R.A.J. (2005) Negative capacitances in low-mobility solids. *Phys. Rev. B*, **72**, 235204.
24. Shulman, J., Xue, Y.Y., Tsui, S., Chen, F., and Chu, C.W. (2009) General mechanism for negative capacitance phenomena. *Phys. Rev. B*, **80**, 134202.
25. Bisquert, J. (2011) A variable series resistance mechanism to explain the negative capacitance observed in impedance spectroscopy measurements of nanostructured solar cells. *Phys. Chem. Chem. Phys.*, **13**, 4679.
26. Crandall, R.S. (1980) Trap spectroscopy of a-Si:H diodes using transient current techniques. *J. Electron. Mater.*, **9**, 713.
27. Young, D.L. and Crandall, R.S. (2005) Strongly temperature-dependent free energy barriers measured in a polycrystalline semiconductor. *Appl. Phys. Lett.*, **86**, 262107.

28. Branz, H.M. (1988) Charge-trapping model of metastability in doped hydrogenated amorphous silicon. *Phys. Rev. B*, **38**, 7475.
29. Branz, H.M. and Crandall, R.S. (1989) Ionization entropy and charge-state-controlled metastable defects in semiconductors. *Appl. Phys. Lett.*, **55**, 2634.
30. Los, A.V. and Mazzola, M.S. (2001) Semiconductor impurity parameter determination from Schottky junction thermal admittance spectroscopy. *J. Appl. Phys.*, **89**, 3999.
31. Los, A.V. and Mazzola, M.S. (2002) Model of Schottky junction admittance taking into account incomplete impurity ionization and large signal effects. *Phys. Rev. B*, **65**, 165319.
32. Burgelman, M., Nollet, P., and Degrave, S. (2000) Modelling polycrystalline semiconductor solar cells. *Thin Solid Films*, **361–362**, 527.
33. Ćwil, M., Igalson, M., Zabierowski, P., and Siebentritt, S. (2008) Charge and doping distributions by capacitance profiling in Cu(In,Ga)Se_2 solar cells. *J. Appl. Phys.*, **103**, 063701.
34. Heath, J.T., Cohen, J.D., and Shafarman, W.N. (2004) Bulk and metastable defects in $CuIn_{1-x}Ga_xSe_2$ thin films using drive-level capacitance profiling. *J. Appl. Phys.*, **95**, 1000.
35. Kimmerling, L.C. (1974) Influence of deep traps on the measurement of free-carrier distributions in semiconductors by junction capacitance techniques. *J. Appl. Phys.*, **45**, 1839.
36. Lang, D.V. (1974) Deep-level transient spectroscopy: a new method to characterize traps in semiconductors. *J. Appl. Phys.*, **45**, 3023.
37. Johnston, S.W., Kurtz, S., Friedman, D.J., Ptak, A.J., Ahrenkiel, R.K., and Crandall, R.S. (2005) Observed trapping of minority-carrier electrons in p-type GaAsN during deep-level transient spectroscopy. *Appl. Phys. Lett.*, **86**, 072109.
38. Kurtz, S., Johnston, S., and Branz, H.M. (2005) Capacitance-spectroscopy identification of a key defect in N-degraded GaInNAs solar cells. *Appl. Phys. Lett.*, **86**, 113506.
39. Kukimoto, H., Henry, C.H., and Merritt, F.R. (1973) Photocapacitance studies of the oxygen donor in GaP. I. Optical cross-sections, energy levels, and concentration. *Phys. Rev. B*, **7**, 2486.
40. Murray, F., Carìn, R., and Bogdanski, P. (1986) Determination of high-density interface state parameters in metal–insulator–semiconductor structures by deep-level transient spectroscopy. *J. Appl. Phys.*, **60**, 3592.
41. Zabierowski, P. (2011) Electrical characterization of CIGSe-based thin film photovoltaic devices, in *Thin Film Solar Cells: Current Status and Future Trends* (eds A. Romeo and A. Bossio), Nova Science Publishers, Inc., Hauppauge, New York.
42. For an example of an exception, see Grillot, P.N., Ringel, S.A., Fitzgerald, E.A., Watson, G.P., and Xie, Y.H. (1995) Minority- and majority-carrier trapping in strain-relaxed $Ge_{0.3}Si_{0.7}$/Si heterostructure diodes grown by rapid thermal chemical-vapor deposition. *J. Appl. Phys.*, **77**, 676.
43. Look, D.C. and Sizelove, J.R. (1995) Depletion width and capacitance transient formulas for deep traps of high concentration. *J. Appl. Phys.*, **78**, 2848.
44. Buchwald, W.R., Morath, C.P., and Drevinsky, P.J. (2007) Effects of deep defect concentration on junction space charge capacitance measurements. *J. Appl. Phys.*, **101**, 094503.
45. Frenkel, J. (1938) On pre-breakdown phenomena in insulators and electronic semiconductors. *Phys. Rev.*, **54**, 647.
46. Vincent, G., Chantre, A., and Bois, D. (1979) Electric field effect on the thermal emission of traps in semiconductor junctions. *J. Appl. Phys.*, **50**, 5484.
47. Li, G.P. and Wang, K.L. (1985) Detection sensitivity and spatial resolution of reverse-bias pulsed deep-level transient spectroscopy for studying electric field-enhanced carrier emission. *J. Appl. Phys.*, **57**, 1016.
48. Dobaczewski, L., Peaker, A.R., and Bonde Nielsen, K. (2004) Laplace-transform deep-level spectroscopy: the technique and its applications to the study of point defects in semiconductors. *J. Appl. Phys.*, **96**, 4689.

49. Zabierowski, P. and Edoff, M. (2005) Laplace-DLTS analysis of the minority carrier traps in the Cu(In,Ga)Se_2-based solar cells. *Thin Solid Films*, **480–481**, 301.
50. Lauwaert, J., Khelifi, S., Decock, K., Burgelman, M., and Vrielinck, H. (2011) Signature of a back contact barrier in DLTS spectra. *J. Appl. Phys.*, **109**, 063721.
51. Walter, T., Herberholz, R., Müller, C., and Schock, H.W. (1996) Determination of defect distributions from admittance measurements and application to Cu(In,Ga)Se_2 based heterojunctions. *J. Appl. Phys.*, **80**, 4411.
52. Lee, J.W., Cohen, J.D., and Shafarman, W.N. (2005) The determination of carrier mobilities in CIGS photovoltaic devices using high-frequency admittance measurements. *Thin Solid Films*, **480**, 336.
53. Dhariwal, S.R. and Deoraj, B.M. (1992) Contribution of bulk states to the depletion layer admittance. *Solid-State Electron.*, **36**, 1165.
54. León, C., Martin, J.M., Santamaría, J., Skarp, J., González-Díaz, G., and Sánchez-Quesada, F. (1996) Use of Kramers–Kronig transforms for the treatment of admittance spectroscopy data of p–n junctions containing traps. *J. Appl. Phys.*, **79**, 7830.
55. Milton, G.W., Eyre, D.J., and Mantese, J.V. (1997) Finite frequency range Kramers–Kronig relations: bounds on the dispersion. *Phys. Rev. Lett.*, **79**, 3062.
56. van de Leur, R.H.M. (1991) A critical consideration on the interpretation of impedance plots. *J. Phys. D: Appl. Phys.*, **24**, 1430.
57. Michelson, C.E., Gelatos, A.V., and Cohen, J.D. (1985) Drive-level capacitance profiling: its application to determining gap state densities in hydrogenated amorphous silicon films. *Appl. Phys. Lett.*, **47**, 412.
58. Unold, T. and Cohen, J.D. (1991) Enhancement of light-induced degradation in hydrogenated amorphous silicon due to carbon impurities. *Appl. Phys. Lett.*, **58**, 723.
59. Johnson, P.K., Heath, J.T., Cohen, J.D., Ramanathan, K., and Sites, J.R. (2005) A comparative study of defect states in selenized and evaporated CIGS(S) solar cells. *Prog. Photovolt.*, **13**, 1.
60. Chantre, A., Vincent, G., and Bois, D. (1981) Deep-level optical spectroscopy in GaAs. *Phys. Rev. B*, **23**, 5335.
61. Cohen, J.D. and Gelatos, A.V. (1988) Transient photocapacitance studies of deep defect transitions in hydrogenated amorphous silicon, in *Amorphous Silicon and Related Materials*, vol. **A** (ed H. Fritzsche), World Scientific Publishing Co., pp. 475–512.
62. Boucher, J.W., Miller, D.W., Warren, C.W., Cohen, J.D., McCandless, B.E., Heath, J.T., Lonergan, M.C., and Boettcher, S.W. (2014) Optical response of deep defects as revealed by transient photocapacitance and photocurrent spectroscopy in CdTe/CdS solar cells. *Sol. Energy Mater. Sol. Cells*, **129**, 57.
63. Lang, D. (1992) DX centers in III–V alloys, in *Deep Centers in Semiconductors: A State-of-the-Art Approach*, 2nd edn (ed S.T. Pantelides), Gordon and Breach Science Publishers, Yverdon, pp. 592–665.
64. Cohen, J.D., Unold, T., Gelatos, A.V., and Fortmann, C.M. (1992) Deep defect structure and carrier dynamics in amorphous silicon and silicon–germanium alloys determined by transient photocapacitance methods. *J. Non-Cryst. Solids*, **141**, 142.
65. Heath, J.T., Cohen, J.D., Shafarman, W.N., Liao, D.X., and Rockett, A.A. (2002) Effect of Ga content on defect states in $CuIn_{1-x}Ga_xSe_2$ photovoltaic devices. *Appl. Phys. Lett.*, **80**, 4540.
66. Erslev, P.T., Lee, J.W., Shafarman, W.N., and Cohen, J.D. (2009) The influence of Na on metastable defect kinetics in CIGS devices. *Thin Solid Films*, **517**, 2277.
67. Vanecek, M. and Poruba, A. (2002) Fourier-transform photocurrent spectroscopy of microcrystalline silicon for solar cells. *Appl. Phys. Lett.*, **80**, 719.
68. Meyer, W. and Neldel, H. (1937) Über die Beziehungen zwischen der

Energiekonstanten und der Mengenkonstanten *a* in der Leitwerts-Temperaturformel bei oxydischen Halbleitern. *Z. Tech. Phys.*, **12**, 588.

69. Street, R.A. (1991) *Hydrogenated Amorphous Silicon*, Cambridge University Press, Cambridge, p. 224.
70. Crandall, R.S. (1990) Defect relaxation in amorphous silicon: stretched exponentials, the Meyer–Neldel rule, and the Staebler–Wronski effect. *Phys. Rev. B*, **43**, 4057.
71. Herberholz, R., Walter, T., Müller, C., Friedlmeier, T., Schock, H.W., Saad, M., Lux-Steiner, M.C., and Albertz, V. (1996) Meyer–Neldel behavior of deep level parameters in heterojunctions to $Cu(In,Ga)(S,Se)_2$. *Appl. Phys. Lett.*, **69**, 2888.
72. Leffler, J.E. (1955) The enthalpy–entropy relationship and its implications for organic chemistry. *J. Org. Chem.*, **20**, 1202.
73. Glasstone, S., Laidler, K.J., and Eyring, H. (1941) *The Theory of Rate Processes*, McGraw-Hill, New York.
74. Almbladh, C.O. and Reese, G.J. (1982) Statistical mechanics of electronic energy levels in semiconductors. *Solid State Commun.*, **41**, 173.
75. Engström, O. and Alm, A. (1978) Thermodynamical analysis of optimal recombination centers in thyristors. *Solid State Electron.*, **21**, 1571.
76. Yelon, A. and Movaghar, B. (1990) Microscopic explanation of the compensation (Meyer–Neldel) rule. *Phys. Rev. Lett.*, **65**, 618.
77. (a) Yelon, A., Movaghar, B., and Branz, H.M. (1992) Origin and consequences of the compensation (Meyer–Neldel) law. *Phys. Rev. B*, **46**, 12244; (b) Viščor, P. (2002) Comment on "Origin and consequences of the compensation (Meyer–Neldel) law". *Phys. Rev. B*, **65**, 077201; (c) Yelon, A. and Movaghar, B. (2002) Reply to "Comment on 'Origin and consequences of the compensation (Meyer–Neldel) law'". *Phys. Rev. B*, **65**, 077202.
78. Widenhorn, R., Rest, A., and Bodegom, E. (2002) The Meyer–Neldel rule for a property determined by two transport mechanisms. *J. Appl. Phys.*, **91**, 6524.
79. Popescu, C. and Stoica, T. (1992) Meyer–Neldel correlation in semiconductors and Mott's minimum metallic conductivity. *Phys. Rev. B*, **46**, 15063.
80. Niemegers, A., Burgelman, M., Herberholz, R., Rau, U., Hariskos, D., and Schock, H.W. (1998) Model for electronic transport in $Cu(In,Ga)Se_2$ solar cells. *Prog. Photovoltaics Res. Appl.*, **6**, 407.
81. Eisenbarth, T., Unold, T., Caballero, R., Kaufmann, C.A., and Schock, H.-W. (2010) Interpretation of admittance, capacitance–voltage, and current–voltage signatures in $Cu(In,Ga)Se_2$ thin film solar cells. *J. Appl. Phys.*, **107**, 034509.
82. Niemegeers, A. and Burgelman, M. (1997) Effects of the Au/CdTe back contact on IV and CV characteristics of Au/CdTe/CdS/TCO solar cells. *J. Appl. Phys.*, **81**, 2881.
83. Demtsu, S.H. and Sites, J.R. (2006) Effect of back-contact barrier on thin-film CdTe solar cells. *Thin Solid Films*, **510**, 320.
84. Macdonald, D., Rougieux, F., Cuevas, A., Lim, B., Schmidt, J., Di Sabatino, M., and Geerligs, L.J. (2009) Light-induced boron–oxygen defect generation in compensated p-type Czochralski silicon. *J. Appl. Phys.*, **105**, 093704.
85. Nadazdy, V. and Zeman, M. (2004) Origin of charged gap states in a-Si:H and their evolution during light soaking. *Phys. Rev. B*, **69**, 165213.
86. Shimizu, T. (2004) Staebler–Wronski effect in hydrogenated amorphous silicon and related alloy films. *Jpn. J. Appl. Phys.*, **43**, 3257.
87. Balcioglu, A., Ahrenkiel, R.K., and Hasoon, F. (2000) Deep-level impurities in CdTe/CdS thin-film solar cells. *J. Appl. Phys.*, **88**, 7176.
88. Demtsu, S.H., Albin, D.S., Pankow, J.W., and Davies, A. (2006) Stability study of CdS/CdTe solar cells made with Ag and Ni back-contacts. *Sol. Energy Mater. Sol. Cells*, **90**, 2934.

5
Time-of-Flight Analysis

Torsten Bronger

5.1
Introduction

A large variety of transient optoelectronic methods are used to study charge transport, recombination, and the density of states of thin films for photovoltaics and related applications. Among those methods, the time-of-flight (TOF) method is arguably the most important technique that has been used for decades, especially to determine the mobility of low-conductivity samples and to measure the subgap density of states in disordered semiconductors. Thus, this chapter is dedicated only to the description of the TOF technique, while a large range of other transient methods are discussed more briefly in the following chapter.

TOF as described in this chapter has been used since the late 1960s to learn about material properties in various types of semiconductors. Although first attempts to probe the drift of photogenerated carries go back to 1949 [1], it was 20 years later that the first viable setup of the TOF experiment became popular [2]. During the 1970s, thorough theoretical examination by various authors led to a good understanding of the underlying processes of a TOF experiment. This development culminated in comprehensive theoretical models such as the multiple-trapping model around 1980, which were in good agreement with the experimental observations. Since then, these models haven't been modified significantly. However, they were extended in order to extract even more information out of TOF measurements, especially of the long-time regime.

Although it is not limited to them, TOF is especially suitable for low-conductivity materials (early intensively studied materials were highly disordered amorphous semiconductors such as vitreous As_2Se_3). Therefore, it is a good complement to other characterization methods such as conductivity or Hall measurements that have advantages when used with higher conductivity samples. One of the main challenges of the method is to be able to cover several orders of magnitude in dynamic range of the measured photocurrent. Among the crucial advantages of TOF relative to other transient methods discussed in the following chapter are the possibility to separately determine electron and hole mobilities and the possibility to only probe transport and charge trapping without charge

Advanced Characterization Techniques for Thin Film Solar Cells, Second Edition.
Edited by Daniel Abou-Ras, Thomas Kirchartz, and Uwe Rau.

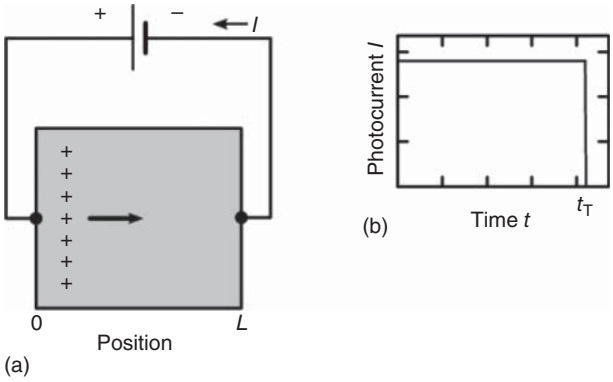

Figure 5.1 (a) Basic procedure of a time-of-flight experiment. (After Figure 1 in Ref. [3].) (b) Ideal photocurrent transient in the absence of any kind of dispersion.

recombination. These processes often occur simultaneously in other transient methods which are therefore more difficult to interpret.

5.2 Fundamentals of TOF Measurements

The left-hand sketch in Figure 5.1 depicts the basic principle of such an experiment: An intrinsic semiconductor specimen is put between two contact plates, and a voltage is applied. Then, electron–hole pairs are generated as a two-dimensional sheet at one contact in the specimen. This is usually done by illuminating the sample with a laser pulse with an absorption length that is much smaller than the sample thickness. The electric field caused by the applied voltage V helps separating the charge carriers. One type of carriers immediately leaves the sample through the nearby contact. The other type drifts through the whole sample to the opposite contact.

During the flight through the sample, the excess charge carriers modify the electric field leading to a step in the electric field at the position of the moving charge sheet. Without the charge, the electric field in the specimen would be $F_0 = V/L$, with L being the transit length for the charge carriers (for the usual setup, this is identical to the sample thickness). A positive charge sheet at position $0 \le x(t) \le L$ decreases the field strength behind and increases the field strength in front of the charge sheet. With F_{back} and F_{front} denoting the resulting electric field behind and in front of the moving charge sheet, respectively, this leads to

$$F_{\text{back}} = F_0 - \frac{Nq}{\varepsilon_r \varepsilon_0 A} \cdot \left(1 - \frac{x(t)}{L}\right) \quad \text{and}$$
$$F_{\text{front}} = F_0 + \frac{Nq}{\varepsilon_r \varepsilon_0 A} \cdot \frac{x(t)}{L}, \tag{5.1}$$

where t is the time, ε_r and ε_0 are the relative permittivity of the material and the vacuum permittivity, respectively, and qN is the charge density of the moving charge sheet.

In addition, the drifting charge generates a displacement current in the external circuit. If one electron drifts through the whole specimen, exactly one electron is pushed through the external circuit. The same happens if two electrons pass half of the specimen.

This is illustrated in Figure 5.1b. As long as the carriers are drifting in the sample, one measures the displacement current I in the external circuit. When they reach the contact, the current vanishes instantaneously. The integral of the current over time equals the generated excess charge. (Note, however, that we neglect the carriers of the opposite sign here. They would produce a delta peak at $t = 0$ and double the integral.)

Thus, the actual measurement quantity in a TOF experiment is the decay of the electrical current with time. This leads to the transit time t_T, which in turn yields the drift mobility μ_d by

$$\mu_d = \frac{v_d}{F} = \frac{L^2}{t_T V}, \tag{5.2}$$

where v_d is the drift velocity.

There are two popular methods for determining the transit time t_T:

1) The analysis of the photocurrent decay over time where a drop or kink in the curve marks the transit time.
2) Integration of the photocurrent and measurement of the collected charge over time. The transit time is then defined as the time, when half of the total charge is collected.

Note that in general, both methods yield slightly different values for t_T. Therefore, it is highly advisable not to mix both within one series of measurements.

5.2.1
Anomalous Dispersion

In general, the photocurrent curve in Figure 5.1 is heavily idealized. Various effects modify its shape, and these modifications contain valuable information about the material. In particular, they may contain information about the energetic distribution of trap levels, as we will see later.

Figure 5.2 shows two more realistic transients. Carrier diffusion leads to "normal dispersion." In this case, the spatial distribution has a Gaussian shape which broadens with time. The electrical current remains nearly constant during transit and the transit time t_T can be easily defined as long as the width of the charge sheet is small compared to the sample thickness.

Besides diffusion, other effects also lead to normal dispersion. One example is hopping between localized states of the same energy level if the distance between neighbor states is always the same. Then, the release times of the carriers fluctuate

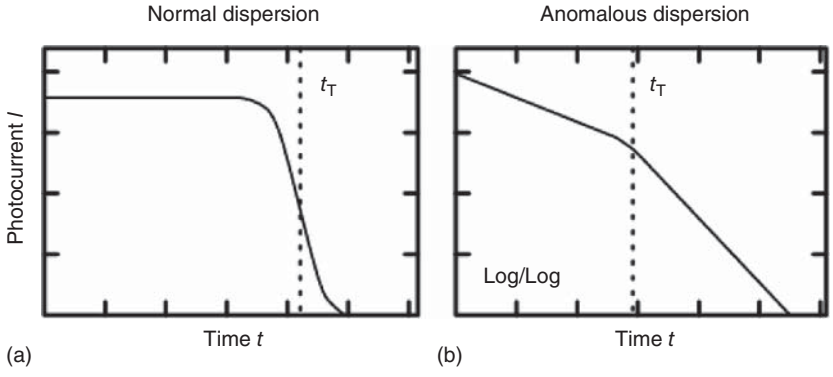

Figure 5.2 Two kinds of dispersive transport [4, p. 16]. Obviously, both cases are very different. While (a) consists of a constant phase followed by a sharp drop, (b) exhibits power-law behavior and has a much less distinct t_T. Note the logarithmic axes of the right-hand plot.

due to the random nature of the hopping process. Another example is trapping of carriers in a single trap level. Here, the reemission must be assisted by phonons, which is a statistical process. And last but not least, the initial width of the photogenerated charge sheet contributes to dispersion.

Typically for thin-film semiconductors, not only diffusion but also trapping in deep traps contributes to the spreading out of the electrical pulse. The resulting dispersion is called *anomalous dispersion*. While Section 5.4.1 will discuss the underlying physical effects in detail, the remainder of this section gives an overview of it.

As one can see in Figure 5.2b, anomalous dispersion is qualitatively different from normal dispersion. The electrical current strongly decays during the whole transit. Additionally, the current exhibits power-law behavior with different exponents. If the transit time t_T is defined as the kink in the curve, the part before t_T is called *pretransit* or *first branch*, and the part after it is called *posttransit* or *second branch*.

In contrast to normal dispersion, the posttransit decays slowly. This implies that a large fraction of carriers reaches the contact during the posttransit. Thus, while for normal dispersion, t_T is defined as the average transit time of the carriers, this is not true for anomalous dispersion. Instead, t_T denotes the transit time for the fastest carriers here (see Ref. [5, Section 2.2]).

Figure 5.3 shows a peculiar property of the current transient in the presence of anomalous dispersion: The *relative* dispersion is independent of the applied field and sample thickness. This means that if the time scale is normalized to the transit time t_T, the curves are congruent. This observation is called the "universality" of the current transient. The picture refers to measurements with different voltages; however, this universality can also be seen with different sample thicknesses.

As far as the underlying physical effects are concerned, it is typical of anomalous dispersion that the interaction of the excess carriers with the material doesn't reach a steady state during the experiment. Instead, as we will see later, the

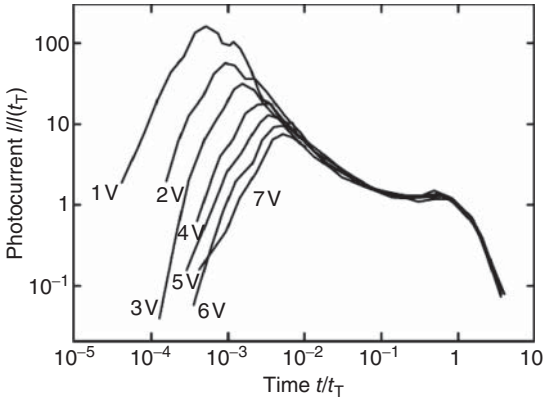

Figure 5.3 Universality of the current transient for different voltages. If the photocurrent is normalized to the photocurrent at the transit time and the time axis is normalized to the transit time, the decay curves lie on top of each other.

characteristic quantities (first and foremost the so-called demarcation energy) change continuously. This explains why the electrical current doesn't keep a constant level as in the case of normal dispersion.

5.2.2
Basic Electronic Properties of Thin-Film Semiconductors

Typically, mobilities in thin-film semiconductors are orders of magnitude smaller than in their bulk counterparts since their atomic arrangements are far away from the monocrystalline case. For example, while monocrystalline silicon has an electron mobility beyond 1000 $cm^2/V\,s$, amorphous or microcrystalline silicon only has mobilities in the range of 0.1 – 1 $cm^2/V\,s$. Numerous kinds of deviations from the ideal crystal may occur. Defects, stacking faults, clusters, or loss of long-range order in an amorphous phase may occur and lead to states in the forbidden gap of the semiconductor. Since these states represent local distortions of the atomic arrangement, they are *localized*. Carriers in these states cannot easily drift through the material. It is very important to note the fundamental difference to the *extended* states in the band: These states spread across the whole specimen, and mobilities of charge carriers in these states are high. In amorphous semiconductors and some other thin-film materials, both domains are separated by the *mobility edge*. Below the mobility edge (toward midgap), carrier mobility drops very quickly and in models like the ones described in Chapter 23 is considered to be zero.

Still, charge carriers in localized states can have a significant influence on the electronic properties of the material. For example, they can hop to neighbor states (close enough so that there is an overlap), especially at low temperatures, where almost no carriers occupy the extended states at higher energy levels anymore. Moreover, localized states can drag the Fermi level closer to midgap in doped

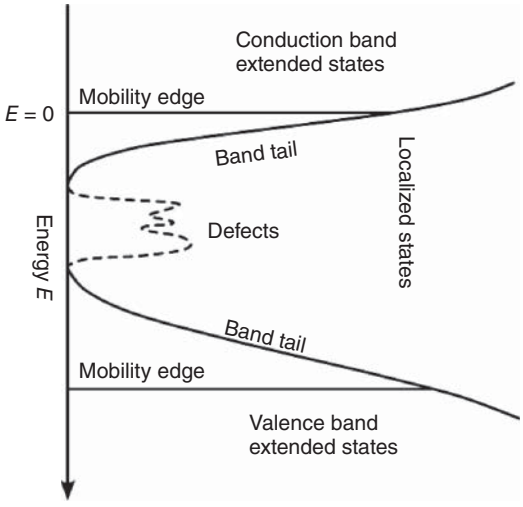

Figure 5.4 Model of the density of states in a disordered semiconductor.

semiconductors, and finally, they can trap carriers that are drifting in the extended states. Therefore, it is interesting to know the density of states of the material, both within the gap and close to the band edges.

Figure 5.4 shows a popular model of the density of states in a disordered semiconductor. The bands contain the extended states that you can also find in the ideal crystal. The band edges of the ideal crystal are replaced with the mobility edge. From the mobility edge toward midgap, the so-called band tails contain localized states. Their density of states drops exponentially. In some cases, further states close to midgap are assumed due to defects.

5.3 Experimental Details

Today, the most popular setup for TOF experiments is the light-induced generation of electron–hole pairs close to the top layer in a vertically stacked p–i–n diode. Figure 5.5 shows the basic concept: The sample layer is packed between two doped layers so that the whole stack forms a p–i–n diode. Ideally, the substrate is transparent, allowing for measuring the mobility of holes (illumination through the n-layer) and electrons (illumination through the p-layer) separately. The doped layers should be thin (<30 nm) so that they don't absorb the light pulse significantly.

Shortly before the light pulse, a reverse bias is applied to the sample. The blocking contact prevents electrical carriers entering the sample from the external circuitry. Thus, after the light pulse has generated the free carriers, only their transient through the sample is measured. Other techniques have been

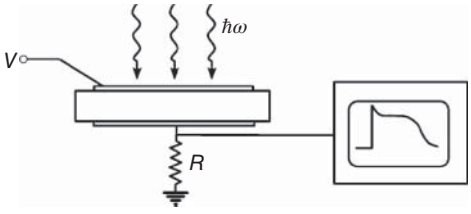

Figure 5.5 The basic principle used in vertical time-of-flight experiments. The resistor *R* builds a voltage divider together with the sample. This way, the current through the sample can be measured by the voltmeter to the right.

tested such as thin isolators between the contact pads and the sample, but diode configurations using p–n or Schottky junctions work more efficiently.

As far as the sample thickness and light pulse duration are concerned, several boundary conditions must be considered. First, the penetration depth of the light pulse – which determines the width of the generated charge sheet – should be much smaller than the sample thickness because otherwise the features of the current transient are blurred, and they are distorted by the transient of the charge carriers of the opposite sign. Besides, some assumptions in the theoretical models become invalid and interpretation of the experimental data becomes more difficult.

Secondly, the duration of the light pulse must be smaller than the transient time, that is, the time the charge carriers need to cross the sample, because a too long pulse means that the experiment has no well-defined starting point. The characteristic features of the TOF experiment are transformed to a steady-state experiment with less information.

The contacts may be connected to the external circuitry with metallic pads or conductive silver paste. If the substrate is transparent for illumination, a transparent conductive oxide (TCO) like ZnO, SnO, or ITO between the contact and the substrate may help contacting the back contact.

Figure 5.6 shows a detailed schematic for a TOF experiment. Every cycle starts with the laser emitting a short pulse. The laser is triggered either internally or externally (e.g., by a computer). The trigger frequency is of the order of seconds. Most often the laser is a nitrogen laser-pumped dye laser. The wavelength should be chosen such that the penetration depth is small and the quantum efficiency is high. For silicon samples, 488 and 500 nm are typical values.

Using a beam splitter a small fraction of the laser pulse is redirected to a photodiode which triggers the function generator. The function generator applies a reverse bias to the sample – usually between 0 and 10 V. This reverse bias is applied as a rectangular pulse which should be shorter than the dielectric relaxation time $t_d = \varepsilon_r \varepsilon_0 / \sigma$ (with σ being the conductivity) and much longer than the expected transit time. For example, for a 2 µm specimen with $\sigma = 10^{-9}$ S/cm, a good value for the length of the electrical pulse is 20 µs. Subsequently, the light is sent through an optical fiber with a typical length of 300 m in order to retard the light pulse by 1 ms. This is done so that electrical disturbances due to the switching on of the

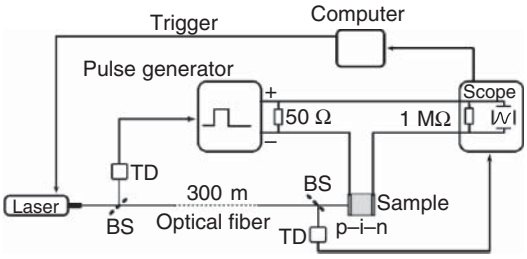

Figure 5.6 Setup for time-of-flight experiments. TD: trigger diode; BS: beam splitter.

voltage are diminished and the field in the sample is stabilized. The light pulse must pass another beam splitter which reflects the light to a second photodiode which triggers the oscilloscope. Immediately after that, the light pulse finally reaches the sample and is absorbed in its surface region. The photogenerated excess carriers drift through the external field, which causes a displacement current in the external circuit which is measured and stored by the oscilloscope.

Finally, the function generator switches off the voltage. Until the next measurement cycle, the sample should have time to get rid of space charge which could affect subsequent transient curves. In the worst case, the transient curve features change gradually from shot to shot. Normally, a few seconds of waiting time are enough for sample relaxation. If this doesn't help, one can ground both contacts between the cycles while still sending a couple of laser pulses onto the sample, so that the trapped charges can recombine with excited charges. (Section 5 in **Error! Bookmark not defined.**) Typically, this measurement cycle is repeated a couple of thousands of times and linearly averaged in the oscilloscope or in a computer.

5.3.1 Accompanying Measurements

There are a couple of measurements that support TOF experiments. They help with evaluating the TOF results and/or verify that the sample and the setup are suitable for a TOF experiment.

5.3.1.1 Capacitance

Capacitance measurements (see also Chapter 4) help to assure that the externally applied field is uniform across the sample. The expected value for the geometrical capacitance is $C = \varepsilon_r \varepsilon_0 A/d$, where ε_r, A, and d are the relative permittivity of the material, the area of the contacts, and the sample thickness, respectively. Any deviation from this means that there is an electric field caused by space charge within the sample which perturbs the external field.

One can determine the capacitance by measuring the RC time constant of the current decay. For this, a rectangular voltage signal is applied to the sample as a reverse bias by a function generator. Switching off of the signal triggers an oscilloscope, which then stores the current decay through its input resistance R.

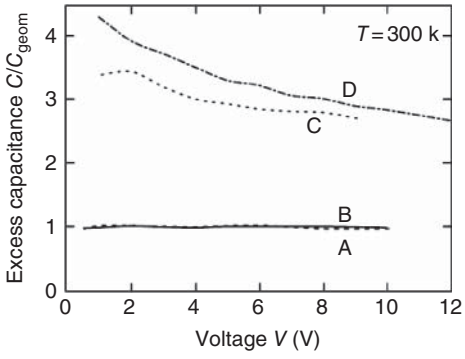

Figure 5.7 Capacitance measurements on µc-Si:H samples. The capacitances that are expected from the geometry of the samples are marked by the lines attached to the border on the right. (Redrawn after Ref. [4, p. 86].)

The resulting curve can be plotted half-logarithmically and RC can be extracted easily.

An alternative method is to connect the sample with its capacitance C_S and a known capacitor C_g in series. Then, the reverse-bias voltage V is applied to both capacitors. Since charge cannot be created or destroyed and it can only gather on the capacitor plates, both capacitors share the same amount of charge. This amount of charge can be determined by measuring the voltage drop V_g across the known capacitor. This yields

$$C_S = \frac{V_g \cdot C_g}{V - V_g}. \tag{5.3}$$

Figure 5.7 shows the voltage-dependent capacitance for four µc-Si:H samples. For each symbol, the geometrical capacitance expected from the sample geometry is indicated on the right. As you can see, two samples are very close to the expected result, whereas the two other samples exhibit way too high capacities. Additionally, these two samples have a voltage-dependent capacitance.

For TOF experiments, a uniform field is required. For this, the depletion layer of the p–i–n diode should be the whole i-layer. However, this excess capacitance means that the electric field is not uniform. Instead, space charge in the i-layer, probably close to the contacts, confines it to a fraction of the sample thickness. Thus, the effective thickness is reduced, which results in a higher capacity. Higher voltages reduce the relative effect of the space charge, but it doesn't vanish.

5.3.1.2 **Collection**

An important and simple test for a TOF setup is the total collected charge Q_0, which is defined as the time integral of the photocurrent. Theoretically, the number of electrons drifting through the sample and being eventually collected in one contact must equal the number of photons absorbed in the sample, which can be estimated by measuring the energy of one laser shot. Of course, there are several effects that cause deviations from this ideal picture, most notably the quantum

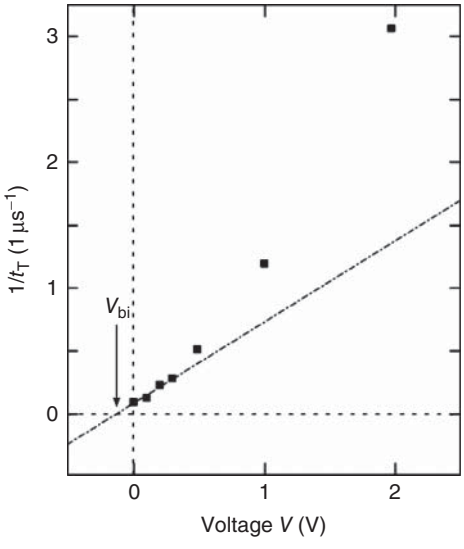

Figure 5.8 Dependence of inverse transit time on applied voltage. For small voltages, the dependence is linear. The extrapolation to infinite transit time yields the built-in voltage. (After Ref. [7].)

efficiency. Nevertheless, it is very helpful to check whether the total collection has the expected order of magnitude.

5.3.1.3 Built-In Field

The sample has a built-in voltage V_{bi} due to its p–i–n structure. This voltage should be determined because it enlarges the externally applied reverse-bias voltage. Thus, the actual drift mobility for a p–i–n diode is

$$\mu_d = \frac{d^2}{t_T(V + V_{bi})}. \tag{5.4}$$

Therefore, the built-in voltage is a significant parameter for an accurate interpretation of the results, especially at low voltages. In particular, it allows for a transient measurement even without an external field, and this in turn can be used to determine the built-in field itself [6].

Figure 5.8 visualizes how this can be done. The inverse transit time exhibits a linear dependence on the applied voltage in the small-voltage regime. With a linear regression one can extrapolate the voltage for which no transit takes place anymore which should correspond to the built-in voltage.

Figure 5.9 shows another method for determining the built-in field, the so-called Hecht plot. It depicts the dependence of the collected charge on the applied voltage. For small voltages, there is more-or-less linear behavior, which can be used to determine the built-in voltage as the extrapolated voltage for which no carriers are collected.

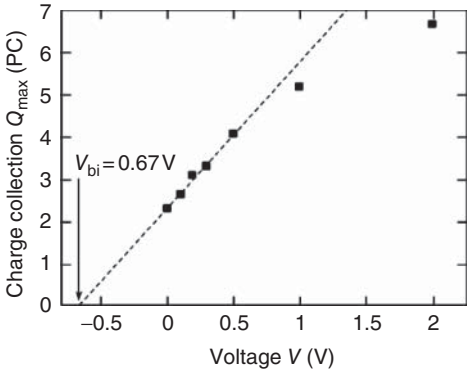

Figure 5.9 Dependence of total collection on applied voltage (Hecht plot). For small voltages, the dependence is linear. The extrapolation to vanishing charge collection yields the built-in voltage. (After Ref. [7].)

5.3.2 Current Decay

The best way to depict the photogenerated current decay is a log–log plot: The current is on the logarithmic y-axis, and the time is on the logarithmic x-axis. Most experimental and theoretical work has revealed power-law behavior of the photocurrent in disordered semiconductors, including the multiple-trapping model that will be explained later, so these axes help to visualize the dependency properly.

Figure 5.10 is such a plot for a 4.3 µm sample of µc-Si:H. The current decay is clearly visible, as are the linear sections of the curves, namely, the pre- and the posttransit, also known as the first and the second branch. The kink between both branches denotes the transit time t_T. For higher voltages, Equation 5.4 would predict shorter transit times, because at a given mobility a higher electric field corresponds to a higher drift velocity.

Figure 5.11 shows current transients for different input resistances of the oscilloscope. One can achieve different input resistances by applying a parallel resistor to the input of the oscilloscope. Apparently, while higher resistances are good for the posttransit regime where they lead to less noise due to higher voltages for the same current, they suppress the first part of the curve. By combining transients obtained with different input resistances, one can construct a transient with a high dynamic range.

As we will see later, the pretransit consists almost exclusively of carriers that drift through the sample according to $v_d = \mu F$. Consequently, one expects ohmic behavior of the pretransit. Therefore, Figure 5.12 plots the current decay $I(t)$ for different applied voltages, normalized by that voltage to get $\widetilde{I}(t)$:

$$\widetilde{I}(t) = I(t)\frac{d^2}{Q_0(V + V_{bi})}. \tag{5.5}$$

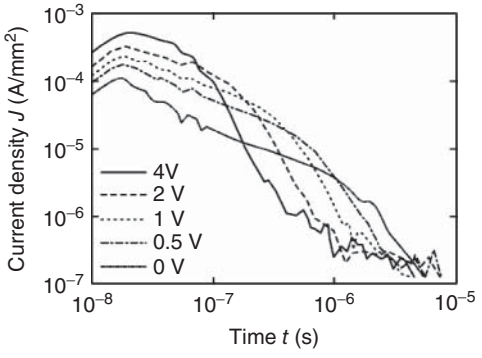

Figure 5.10 Transient photocurrent in μc-Si:H for different voltages. For higher voltages the kink moves to the left to shorter transit times. (After Ref. [4, p. 91].)

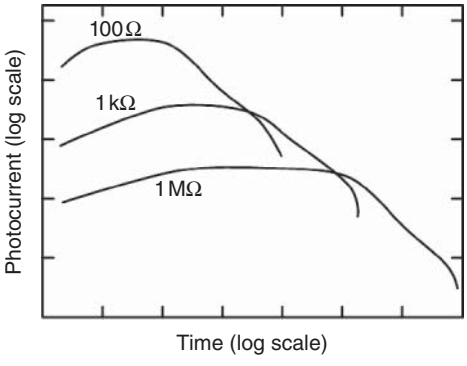

Figure 5.11 Schematic depiction of a sectioned transient photocurrent with different load resistors. The common right-hand part of the curves illustrates that one can increase the dynamic range of the measurement by using different resistors.

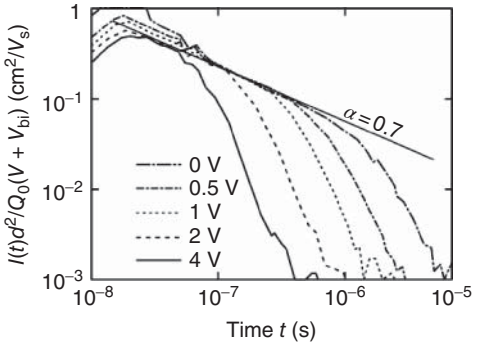

Figure 5.12 Normalized current transients for different voltages. The normalization leads to a common pretransit curve, which shows that all measurements share the same value of α. (After Ref. [4, p. 92].)

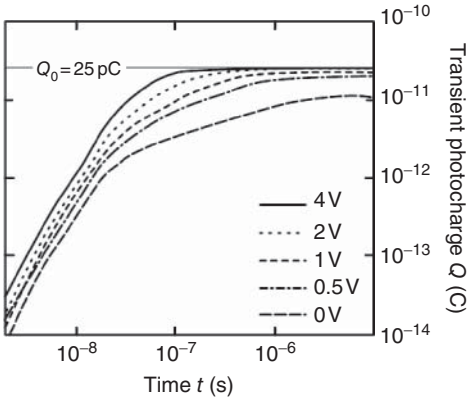

Figure 5.13 Charge collection of a μc-Si:H sample at various voltages. For higher voltages, the intersection with $Q_0/2$ moves to the left to shorter transit times. For 0 V, there is no intersection anymore. (After Ref. [4, p. 91].)

As one can see in Figure 5.12, there exists an envelope line which corresponds to a power law. In the multiple-trapping model that will be discussed in section 5.4.3.1, this envelope is $\mu_d(t)$ (note that the y-axis has the unit of a mobility). By using this plot, the exponent of the pretransit can be determined rather easily. Additionally, by finding the intersection with the $0.8 \cdot \mu(t)$ line, one has a quite well-defined transit time.

5.3.3
Charge Transient

Figure 5.13 shows a photocharge measurement on a sample at different applied voltages. As already explained, the upper limit of all curves, that is, the saturation value for $V \to \infty$, is called Q_0. Every single branch has its own saturation value $Q(\infty)$. The transit time t_T is reached when $Q_0/2$ is collected. Sometimes for small voltages, $Q_0/2$ is never reached. In this case, t_T cannot be determined by this method. Generally, it is advisable to use high voltages for the charge collection.

The choice between the methods of using the kink in the transient or the point of collecting $Q_0/2$ depends on whether the kink in the transient is reliably observable. If it is, the photocurrent measurement is more accurate, especially for voltage-dependent examinations. If the kink cannot be seen well, it is necessary to use the half-charge method.

Figure 5.14 demonstrates how a nonuniform field within the sample distorts the photocharge measurement. The screening of the electric field by the leading charge carriers causes a retarded transient, which can be seen in the dent of the curves. Such results do not allow for the determination of a transit time.

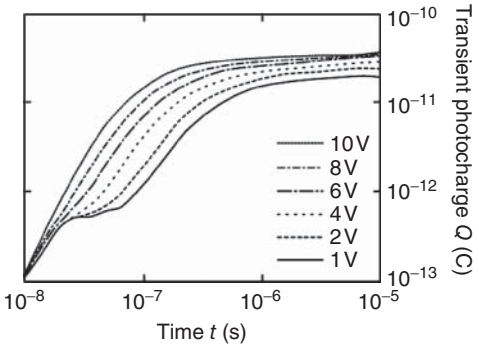

Figure 5.14 Transient photocharge in case of nonuniform field. The current breaks down already at very short times. Here, no accurate values for the transit time t_T can be extracted anymore. (After Ref. [4, p. 88].)

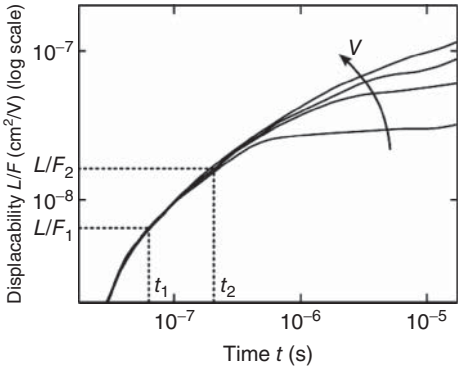

Figure 5.15 Displacability plot for the same sample as in Figure 5.13. By choosing the proper value of the displacability, that is, the ratio L/F of sample thickness L and electric field F, one can determine the transit time t_T for that case. (After Ref. [4, p. 28].)

Figure 5.15 illustrates an alternative approach to determine the transit time. By normalizing the photocharge according to

$$\widetilde{Q}(t) = Q(t)\frac{d^2}{Q_0(V + V_{bi})} = \frac{L}{F} \tag{5.6}$$

and reducing the photocharge curves to the pretransit $t << t_T$, one can eliminate the voltage dependence. Thus, different voltages can be plotted together and form a common continuous curve. The resulting quantity L/F is called *displacability*. This way, the transit time t_T can easily be extracted from the plot for various values of L/F. Section 5.4.3.1 will explain how information about the band tails can be obtained from these plots, too.

5.3.4 Possible Problems

There are some caveats with TOF measurements. In the following sections, some of them are discussed.

5.3.4.1 Dielectric Relaxation

The dielectric relaxation is a reaction of the sample material to the applied voltage. The free carriers drift in the external field, building up their own field which weakens the external one. The more conductive the material is, the quicker this screening field is created. The dielectric relaxation time,

$$t_\mathrm{d} = \frac{\varepsilon_\mathrm{r}\varepsilon_0}{\sigma_\mathrm{d}}, \tag{5.7}$$

is in general the ratio between the permittivity and the conductivity σ of the material. In the context of the TOF experiment, we use the dark conductivity σ_d to determine the dielectric relaxation time and do not consider the conductivity due to photogenerated excess carriers here (they may distort the applied field by their own which is discussed in the following).

The dielectric relaxation is a significant problem for the TOF experiment because due to the partial screening of the external field, the field is not well defined anymore. This may render the results difficult or impossible to interpret. Besides, the transient then takes extremely long and is blurred by carrier diffusion [8].

The only way to cope with dielectric relaxation is to keep the measurement time short enough so that the relaxation is insignificant during the time required for the measurement. In addition, it is necessary to keep the time during measurements when the applied voltage is switched out longer than the time when the voltage is switched on.

With respect to the problem of dielectric relaxation, the low conductivity of most thin-film materials is an advantage and one of the reasons why early TOF experiments were mostly done with very low-conductivity material: It was much simpler to ensure a homogeneous electric field throughout the sample.

5.3.4.2 Inhomogeneous Field

In addition to dielectric relaxation due to the dark conductivity of the sample, also photogenerated carriers may lead to deviations from the constant electric field used in the equations used to determine the mobility. If too many charge carriers are generated (i.e., their area density is larger than that of the charge carriers in the contacts), those that are close to the opposite contact screen out the external field for those following them, which means that the drift saturates for high light intensities.

Figure 5.16 shows the current transient in this case, compared with an ordinary transient. The first surprising feature is the strong initial peak. It is possibly due to

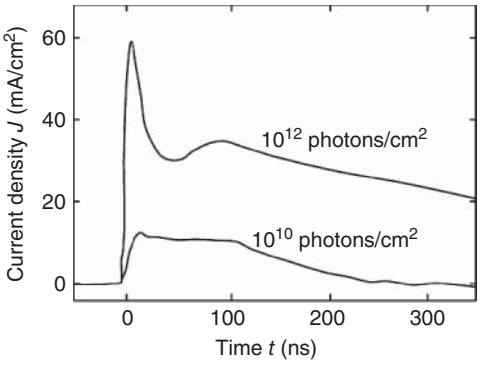

Figure 5.16 Effect of too many photoexcited carriers on the current transient. (After Ref. [8].)

carrier diffusion, which is not affected by the reduced field, and which is especially strong in the beginning of the experiment, when the concentration gradient is large. After the initial peak, the current goes through a minimum which is a typical feature of space charge-limited transport [8].

5.4 Analysis of TOF Results

5.4.1 Multiple Trapping

The "multiple-trapping" model is a popular approach to explain the anomalous dispersive transport in disordered semiconductors. The transport properties are determined by three basic assumptions:

1) Actual transport takes place only in the extended states at the mobility edge.
2) Charge carriers in extended states may be trapped in localized states below the mobility edge.
3) By thermal excitation, trapped carriers may be reemitted into the extended states (where retrapping is possible).

Then, the pronounced broadening of the packet of carriers in anomalous dispersive transport is mainly due to the exponential nature of the thermal excitation process out of the traps.

5.4.1.1 Overview of the Processes

The TOF experiment starts with the photoexcitation of carriers. At first, these excess carriers occupy states above the mobility edge in the conduction band. However, it takes only picoseconds for the carriers to thermalize down to the mobility edge (for amorphous silicon, see Ref. [9]).

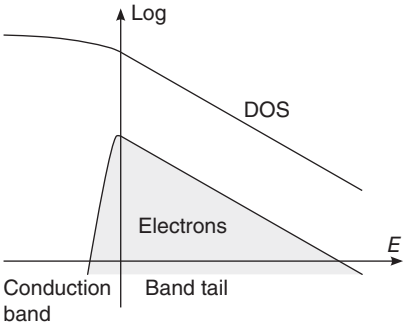

Figure 5.17 Distribution of carriers shortly after the very first trapping events (i.e., $t \approx \omega_0^{-1}$, where ω_0 is the attempt-to-escape frequency). In the tail, the density of electrons is proportional to the density of states.

Now, drift (and diffusion) at the mobility edge begins. However, every carrier has a certain probability to be trapped in a localized state. When this happens, the charge carrier becomes totally immobile, and the only way to get out of the trap is by thermal excitation into the extended states. There, the carrier drifts again, but it may be trapped and reemitted multiple times before it reaches the collecting contact.

Obviously, the time needed to be thermally excited out of a trap depends exponentially on trap depth. This makes a distinction possible between those carriers that have been trapped several times and those that have been trapped only once because it had been a deep trap.

As we will see later, this distinction is a pretty sharp energy level called demarcation energy. It separates the deep traps from the shallow traps. Carriers in shallow traps have continually switched between the shallow traps and the mobile extended states (unless, of course, they were unlucky enough to fall into a deep trap). By contrast, carriers in deep traps just stayed there. During the experiment, the demarcation energy moves downward, releasing carriers from the deep trap levels.

Throughout the model of multiple trapping, the so-called dispersion parameter α determines the behavior. For exponential band tails, it is

$$\alpha = \frac{k_B T}{E_{ch}}, \tag{5.8}$$

with E_{ch} being the width of the band tail. As we will see later, $\alpha = 1$ is an important special but not atypical case: For typical values of the bandwidth, it lies in the middle of the experimentally accessible temperature range (~100 °C).

5.4.1.2 Energetic Distribution of Carriers

The initial distribution of the photogenerated excess carriers is illustrated in Figure 5.17. Zero energy is at the mobility edge, increasing toward midgap. The solid line is the density of states. We assume here exponential band tails below the mobility gap and the crystalline square root behavior above it.

The filled shape denotes the states occupied by excess carriers. In its basic form, the multiple-trapping model assumes the same capture cross section for all traps. This means that the fraction f of occupied states of a certain energy level is the

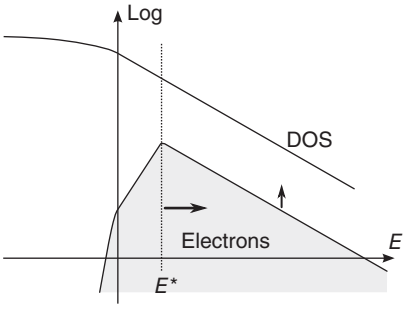

Figure 5.18 Distribution of carriers at the time $t >> \omega_0^{-1}$. The demarcation energy E^* separates shallow traps to the left from deep traps to the right. The arrows illustrate the development of E^* and the density of electrons with time.

same for all energies. Thus, the distribution of occupied states is parallel to the density of states on the logarithmic scale.

Note, however, that f is not constant in *time*. Instead, it obeys to a power law according to [10]

$$f(t) = \frac{N}{E_{ch} g_0} \frac{\sin(\alpha\pi)}{\alpha\pi} (\omega_0 t)^{\alpha}, \tag{5.9}$$

where N is the excitation density and ω_0 is the attempt-to-escape frequency, which in first order equals the phonon frequency. Let's make a rough estimation of the initial f for amorphous silicon: $\omega_0 t = 1$ (initial condition), $\alpha = 0.5$, $g_0 = 10^{22}\,\mathrm{cm^{-3}\,eV^{-1}}$, $E_{ch} = 50\,\mathrm{meV}$, and $N = (10\,\mathrm{pC}/e)/10^{-7}\,\mathrm{cm^3} = 6.2 \times 10^{14}\,\mathrm{cm^{-3}}$ leads to $f = 8 \times 10^{-7}$. Furthermore, one can estimate that even after 1 ms, f is still only at $0.03 << 1$. The mobility edge separates the mobile from the immobile carriers. At this early stage, a distinction between shallow and deep traps does not make sense.

Note that the theory of multiple trapping is valid only for $t \geq \omega_0^{-1}$. Actually, not before $t >> \omega_0^{-1}$ the predictions are really reliable. This is due to the fact that some aspects of the theory average over many trapping events, and there must be a sufficiently large number of them for meaningful statistics.

Let's have a look at the distribution of carriers after some arbitrary time t as shown in Figure 5.18.

The occupation probability f has increased because more and more carriers were trapped in deep traps and stayed there. This is indicated by the arrow pointing upward.

As already explained, carriers are constantly trapped and reemitted. The emission probability strongly depends on the trap depth and the number of emission events decreases exponentially with trap depth. At some point, the number of emission events during the time of the experiment becomes smaller than one. Since a fraction of an emission event is impossible, this means a very sharp drop. The energy where this happens is the demarcation energy

$$E^* = k_B T \ln \omega_0 t. \tag{5.10}$$

The demarcation energy moves to deeper levels with time, as indicated by the arrow pointing to the right. Below that energy ($E > E^*$), there are the *deep* traps

with no emissions so far. Because we assumed the same capture cross section for all localized states, the density of carriers is still parallel to the density of states for the deep traps.

Above E^*, there are the *shallow* traps with frequent trapping and emitting. This trapping and thermal emitting is much faster than all other actions in this model (e.g., carriers leaving the sample, shift of the distribution toward deeper energy levels). Therefore, the shallow traps are simply thermalized according to a Boltzmann distribution:

$$f_{\text{shallow}} = f \cdot \exp\left(\frac{E - E^*}{k_B T}\right). \tag{5.11}$$

This means that the distribution of carriers has a sharp maximum at E^* as can be seen in Figure 5.18. Tiedje and Rose [11] conclude that this effectively simplifies the trap distribution to one single trap level. Thus, the mobility can be expressed in terms of the concentration of excess carriers in extended states n_{free} and excess carriers in traps n_{trap}:

$$\mu_{\text{TOF}} = \mu_0 \frac{n_{\text{free}}}{n_{\text{free}} + n_{\text{trap}}} \approx \mu_0 \frac{n_{\text{free}}}{n_{\text{trap}}}. \tag{5.12}$$

As a further simplification, we assume that the density of traps at $E = 0$ equals the effective density of states in the band. Then, the TOF mobility is

$$\mu_{\text{TOF}} = \mu_0 \alpha (1 - \alpha)(\omega_0 t)^{\alpha - 1}. \tag{5.13}$$

Note that due to $\alpha < 1$, μ_{TOF} is decreasing in time. This is due to the shift of E^* to deeper traps. The resulting drift time for $\alpha < 1$ is

$$t_T = \omega_0^{-1} \left(\frac{1}{1 - \alpha} \frac{L}{\mu_0 F}\right)^{1/\alpha}. \tag{5.14}$$

While these equations for μ_0 and t_T can be used for fitting experimental data (see also Section 5.4.3.1), the results do not differ significantly from those obtained by examining the current decay curves as described in Section 5.3.3. In practice, the latter method is much easier and comparably accurate.

5.4.1.3 Time Dependence of Electrical Current

The direct measurement quantity is the electrical photocurrent. Therefore, its time dependence is of particular interest. From Equation 5.13 follows directly

$$I(t < t_T) = \mu_0 \frac{eFn(t = 0)}{L} \alpha (1 - \alpha)(\omega_0 t)^{\alpha - 1}, \tag{5.15}$$

where $n(t = 0)$ is the total number of electrons injected at $t = 0$. However, we must also explain the so-called "posttransit" (or "second branch") of the transient curve, that is, the photocurrent decay after the transit time t_T. The qualitative change of the transport between pre- and posttransit is very important for understanding why one can define a transit time t_T at all.

After the transit, the single trap level at $E^*(t)$ has moved down so much that the density of states at this level is very small. It is small enough so that the trapping

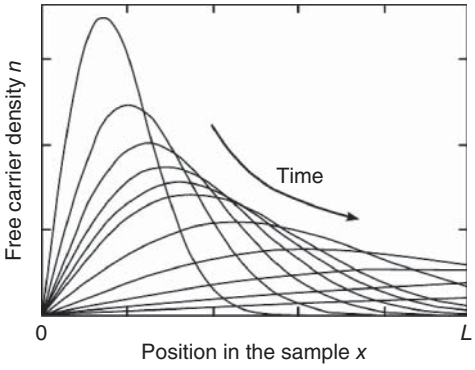

Figure 5.19 Spatial distribution of carriers at different times of the experiment.

probability is much smaller than the emitting probability. In other words, emitted carriers almost always leave the sample before they are retrapped at $E^*(t)$.

This is in contrast to the pretransit when carriers could thermalize down to $E^*(t)$ due to very many trapping-emitting events. But during posttransit, they wouldn't get that far. They rather leave the sample than being trapped in the region below $E^*(t_T) < E^*(t)$.

This makes the photocurrent during posttransit quite easy to describe: It simply consists of all thermally excited particles from the single trap level (which still is the maximum of the carrier distribution). This is

$$I(t > t_T) = \mu_0 \frac{eFn(t=0)}{L} \alpha(1-\alpha)(\omega_0 t_T)^{2\alpha}(\omega_0 t)^{-\alpha-1}. \tag{5.16}$$

5.4.2 Spatial Charge Distribution

The spatial distribution of charge carriers in the presence of anomalous dispersion is not identical to a simple charge sheet drifting through the sample while widening symmetrically due to diffusion. In fact, the problem can only be solved numerically for the general case. In Ref. [12], the special case $\alpha = 0.5$ is presented in detail because it can be calculated easily. Figure 5.19 shows the temporal development of the distribution of free excess carriers, assuming $\alpha = 0.5$.

5.4.2.1 Temperature Dependence

Since temperature is the primary parameter for thermal activation, which in turn is responsible for the emission of excess carriers into the mobile states, the dependence of the TOF experiment on temperature is significant.

In the multiple-trapping model, different temperatures lead to different dispersion parameters α. As already said, for exponential band tails, both quantities are proportional. Figure 5.20 shows the photocurrent on a log–log plot for a series of temperatures. For $T \to 0$, the dispersion becomes more and more pronounced, whereas for $T \to E_{ch}/k_B \Leftrightarrow \alpha \to 1$, the dispersion vanishes.

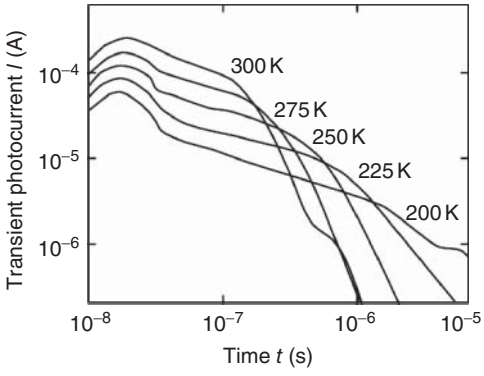

Figure 5.20 Transient curves for different temperatures. Obviously, the transit time t_T, if defined by the location of the kink, becomes larger for lower temperatures. (After Ref. [4, p. 94].)

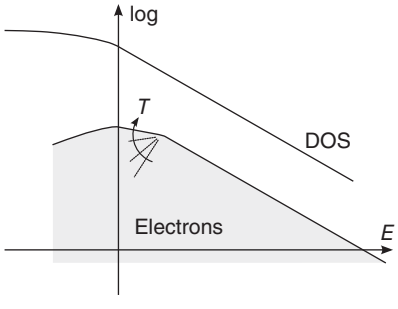

Figure 5.21 Distribution of carriers for high temperature $k_B T > E_{ch}$. The maximum of the carrier distribution no longer is in the tail but at the mobility edge.

Although the equations presented so far assumed $0 < \alpha < 1$, the theory of multiple trapping can easily be extended to $\alpha \geq 1$ or, in other words, to high temperatures.

Figure 5.21 depicts the energetic distribution of the excess carriers for exponential band tails if $T > E_{ch}/k_B$. Apparently, most of the carriers are now at the mobility edge. This is a qualitative difference to the low-temperature case. In particular, it means that there is no dispersive behavior anymore.

Consequently, the TOF mobility does not exhibit the time dependence of Equation 5.13, but instead [11]

$$\mu_{TOF} = \mu_0 \left(1 - \frac{E_{ch}}{k_B T}\right), \tag{5.17}$$

and the transit time t_T does not depend on the electric field or sample thickness.

5.4.3 Density of States

Beyond the deep understanding of the processes in the material and the sensible definition of a carrier mobility, the multiple-trapping model also greatly helps in determining the density of states in the material. Note, however, that one must first

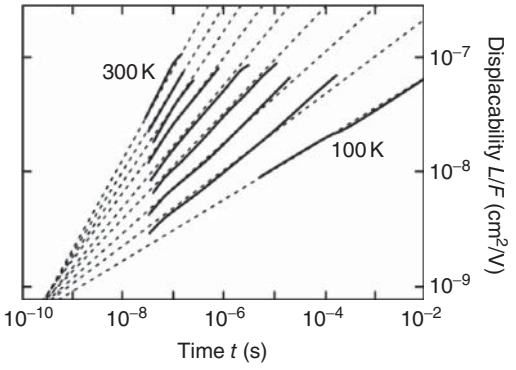

Figure 5.22 Displacability plots for different temperatures of a μc-Si:H sample with $d = 4.3$ μm and $V = 1$ V. The dashed lines are the fit curves. The fit yields μ_0, α, and ω_0 as fit parameters. (After Ref. [4, p. 96].)

assure that multiple trapping is the dominating process. Especially the time and temperature dependence of the photocurrent should follow the expected behavior.

5.4.3.1 Widths of Band Tails

Following the theory described by Schiff [10], the multiple-trapping model in case of exponential band tails leads to

$$\mu_{\mathrm{TOF}} = \mu_0 \frac{\sin(\alpha\pi)}{\alpha\pi} (\omega_0 t)^{\alpha-1}. \tag{5.18}$$

(Note that the prefactor in Schiff's calculation slightly differs from that in Equation 5.13 because Schiff uses slightly different approximations.) By integration over time, this yields for the displacability [4, p. 95]

$$\widetilde{Q}(t) = \frac{\sin(\alpha\pi)}{\alpha\pi(1-\alpha)} \left(\frac{\mu_0}{\omega_0}\right) (\omega_0 t)^{\alpha}. \tag{5.19}$$

Figure 5.22 revisits the displacability plots of Section 5.3.3. This time, the temperature is varied. Equation 5.19 can now be used to fit these curves. There is enough raw data so that one can obtain the fit parameters μ_0, α, and ω_0. For the density of states, α is the interesting parameter because it contains the band tail width E_{ch}.

5.4.3.2 Probing of Deep States

The posttransit curve contains information to deduce the density of states deep in the mobility gap. The more orders of magnitude in time the measurement covers, the deeper it will be able to probe the gap. Ideally, the time axis should span at least six decades. Therefore, this method is not feasible for high-mobility samples because their posttransit cannot be determined over a sufficient time scale. As an illustration of this effect, it can be noted that the determination of the valence band tail of amorphous silicon succeeded earlier than that of the conduction band tail, due to the much lower hole mobility in this material [13].

The main property of the posttransit that is exploited here is that it is dominated by thermal excitation of carriers at the demarcation energy as described in Section 5.4.1.3. As this energy moves deeper into the gap with time, the electrical current generated by the collected carriers samples the density of states.

After deconvoluting the current signal with an inverse Laplace transform [13], the density of states is

$$g(E) = \frac{2g(0)I(t)t}{Q_0 t_0 \omega_0}, \quad t \equiv \frac{1}{\omega_0} \exp\left(\frac{E}{k_B T}\right). \tag{5.20}$$

Here, $g(0)$ is the density of states at the mobility edge, Q_0 the total collected charge as in Section 5.3.3, ω_0 the attempt-to-escape frequency, and t_0 the free transit time, that is, the transit time for carriers that haven't been trapped. It can be estimated by $t_0 = d^2/\mu_0(V + V_{bi})$, with V being the applied voltage, V_{bi} the built-in voltage, and d the sample thickness.

An estimate for ω_0 for the material of interest can be taken from the fit of the previous section, or it can be calculated by applying Equation 5.10 to the temperature activation of t_T as done in Section C of [13]. A well-chosen ω_0 lets the density-of-state curves of different temperatures form a continuous line. Note that the conversion of time into energy of the right-rand side of Equation 5.20 is already known as the demarcation energy from Equation 5.10.

Since Equation 5.20 is equivalent to $g(e) \propto I(t) \cdot t$, a photocurrent decay of $I(t) \propto t^{-1}$ means a constant density of states (on the energy scale). If the photocurrent decays more slowly than $\sim t^{-1}$, this indicates a rise of the density of states, and a more rapid decay would indicate a decay of the density of states.

Note that this matches well with Equation 5.16, which suggests $t^{-\alpha-1}$ for the expected time dependence of the current. From $g(E) \propto t^{-\alpha-1} \cdot t = t^{-\alpha}$ and $\alpha = k_B T/E_{ch}$ follows

$$g(E) \propto \left[\exp\left(\frac{E}{k_B T}\right)\right]^{-k_B T/E_{ch}} = \exp\left(-\frac{E}{E_{ch}}\right), \tag{5.21}$$

which is exactly the assumed slope of the band tail.

Due to approximations made in its derivation, Equation 5.20 smoothes all sharp features in the density-of-state curve. More precisely, the curve appears as if a mollifier with a Lorentzian kernel of width $k_B T$ was applied to it. While this diminishes its usefulness for the deep-state region only slightly, it may distort band tails, except at low temperatures. More sophisticated analysis techniques exist which do not have this limitation [14], but Equation 5.20 is sufficient for most practical purposes.

The temperature-dependent mapping of the time axis to the energy axis by the right-hand side of Equation 5.20 means that by varying the temperature, different energy intervals of the density of states can be sampled. At low temperatures, it may even be possible to probe the rim of the band tail.

Figure 5.23 shows the density of states of a µc-Si:H sample, determined with the method as outlined in this section. The bump at 0.5 eV is defect states, and the drop on the left is the rim of the conduction band tail. As you can see, the three

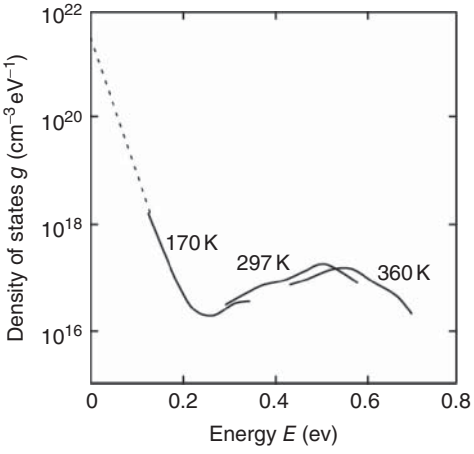

Figure 5.23 The density of states at the conduction band of μc-Si:H. The three TOF measurements at different temperatures can be used as patches for a continuous DOS curve. The dashed line is the extrapolated slope of the band tail [15].

TOF measurements at three different temperatures combine to a quite continuous and plausible density-of-state curve.

References

1. Haynes, J.R. and Shockley, W. (1949) Investigation of hole injection in transistor action. *Phys. Rev.*, **75**, 691–691.
2. Spear, W. (1969) Drift mobility techniques for the study of electrical transport properties in insulating solids. *J. Non-Cryst. Solids*, **1**, 197–214.
3. Tiedje, T. (1984) Hydrogenated amorphous silicon, *Topics. in. App. Phys.*, **21**, 207–238.
4. Dylla, T. (2004) Electron spin resonance and transient photocurrent measurements on microcrystalline silicon. PhD thesis. Freie Universität Berlin.
5. Marshall, J. (1983) Carrier diffusion in amorphous semiconductors. *Rep. Prog. Phys.*, **46**, 1235–1282.
6. Wyrsch, N., Beck, N., Meier, J., Torres, P., and Shah, S. (1998) Electric field profile in μc-Si:H pin devices. *Mater. Res. Soc. Proc.*, **420**, 801–806.
7. Lehnen, S. (2008) Elektronen- und Löcherbeweglichkeit am Übergang zwischen amorpher und mikrokristalliner phase von Silizium. Diploma thesis. Universität Köln, p. 52.
8. Tiedje, T., Wronski, C.R., Abeles, B., and Cebulka, J.M. (1980) Electron transport in hydrogenated amorphous silicon: drift mobility and junction capacitance. *Sol. Cells*, **2**, 301–318.
9. White, J.O., Cuzeau, S., Hulin, D., and Vanderhaghen, R. (1998) Subpicosecond hot carrier cooling in amorphous silicon. *J. Appl. Phys.*, **84**, 4984–4991.
10. Schiff, E.A. (1981) Trap-controlled dispersive transport and exponential band tails in amorphous silicon. *Phys. Rev. B*, **24**, 6189–6192.
11. Tiedje, T. and Rose, A. (1981) A physical interpretation of dispersive transport in disordered semiconductors. *Solid State Commun.*, **37**, 49–52.
12. Tiedje, T. (1984) Time-resolved charge transport in hydrogenated amorphous silicon, in *The Physics of Hydrogenated Amorphous Silicon II: Electronic and Vibrational Properties*, (eds J.D.

Joannopoulos and G. Lucovsky) vol. **56**, Springer, Berlin, pp. 261–300.

13. Seynhaeve, G.F., Barclay, E.P., Adriaenssens, G.J., and Marshall, J.M. (1989) Post-transit time-of-flight currents as a probe of the density of states in hydrogenated amorphous silicon. *Phys. Rev. B*, **39**, 10196–10205.
14. Main, C. (2002) Interpretation of photocurrent transients in amorphous semiconductors. *J. Non-Cryst. Solids*, **299–302**, 525–530.
15. Reynolds, S., Smirnov, V., Main, C., Carius, R., Finger, F., and Street, B. (2003) Localized states in microcrystalline silicon photovoltaic structures studied by post-transit time-of-flight spectroscopy. *Mat. Res. Soc. Proc.*, **762**, 327–332.

6
Transient Optoelectronic Characterization of Thin-Film Solar Cells

Carsten Deibel and Thomas Kirchartz

6.1
Introduction

There are a variety of transient methods that involve a time-dependent optical excitation of a semiconductor followed by the measurement of the voltage or current transient. An important example for such transient methods is the time-of-flight (TOF) technique that can be used to determine mobility and density of states, and is mostly used for disordered low-mobility semiconductors. While the TOF technique was discussed in detail in Chapter 5, the current chapter deals with other variations of transient optoelectronic methods that are mostly performed on solar-cell devices and do not always require special device structures like the TOF technique. Section 6.2 will introduce the typical measurement setup needed to perform these transient techniques. In the following (Section 6.3), we will first discuss the combination of charge extraction (CE) and transient photovoltage (TPV) measurements, which is frequently used to study charge carrier recombination in organic [1–10] and nanoparticle solar cells [11, 12]. In Section 6.3.4, we will continue with the determination of mobilities using CE at short circuit [3]. While the CE methods in Sections 6.3.2 and 6.3.4 just short-circuit the device at the same time as the bias light is switched off, charge extraction with linearly increased voltage (CELIV) uses a voltage ramp to extract charge carriers and allows the determination of charge carrier density, mobility, and lifetime (Section 6.4) [13–17]. The final section, Section 6.5, is devoted to the time-delayed collection field method (TDCF) which allows the separation of fast and slow recombination mechanisms and the study of field-dependent recombination [9, 18–24].

6.2
Measurement Setup

The experimental methods discussed in this chapter do not need a whole series of different setups. Instead one setup can be designed that allows the user to apply all of these methods to photovoltaic devices. The essential ingredients are shown

Advanced Characterization Techniques for Thin Film Solar Cells, Second Edition.
Edited by Daniel Abou-Ras, Thomas Kirchartz, and Uwe Rau.

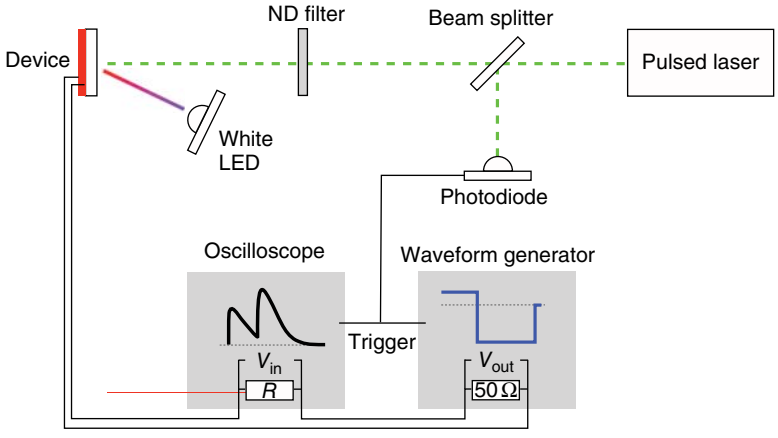

Figure 6.1 Schematic of a generic setup used for the transient optoelectronic experiments described in this chapter. The key functionalities are the ability to bias the device electrically (via the waveform generator) and optically (via the white LED) while at the same time being able to illuminate the sample with a pulsed laser. The transients created using a combination of these three perturbations are then recorded using an oscilloscope.

in Figure 6.1. There are two means of optically exciting the sample, one pulsed laser and a white light-emitting diode (LED). In addition, the voltage or current bias applied to the device has to be altered in a controlled way. This is achieved by a waveform generator. The final transient voltage or current is then recorded via an oscilloscope before further data processing is done using a computer. Some of the experiments described later only need a subset of the equipment (e.g., CE does not need the pulsed laser); however, due to the fact that commonly several methods are combined to better understand charge transport and recombination, it is useful to have the full set of tools as shown in Figure 6.1. In addition to building up the setup from the individual components, at least one commercial system is available that allows to do most of the methods described in the following.[1)]

6.3 Charge Extraction and Transient Photovoltage

The combination of CE and TPV is frequently used in particular in organic solar cells to determine the charge carrier lifetime as a function of charge carrier density. The data can be tested for consistency by attempting to predict the open-circuit voltage from the measured charge densities and lifetimes.

1) Fluxim Paios: see, www.fluxim.com

6.3.1 Transient Photovoltage

In order to measure recombination dynamics in organic, dye-sensitized, or nanoparticle solar cells, often the TPV technique is used. The term TPV refers to a small-signal measurement of the open-circuit voltage as a function of a time after a laser pulse and as a function of the steady-state bias light. Figure 6.2a shows the principle of the measurement. Initially, the sample is illuminated with bias light and an additional laser pulse and is kept at open circuit. This means that the density of states in a disordered semiconductor is filled approximately up to the quasi-Fermi levels with charge carriers caused by the bias light and the pulse. After the laser pulse (times $t > 0$), the sample is still kept at open circuit and illuminated by the bias light. However, the charge carriers created by the laser pulse recombine. At times sufficiently long after the pulse, the charge density, quasi-Fermi level splitting, and the open-circuit voltage V_{oc} should relax back to the level before the pulse. If the additional open-circuit voltage due to the charges created by the laser pulse is small compared to the total open-circuit voltage (typically in the range of 20 mV), the decay of V_{oc} after the pulse should be mono-exponential. By fitting an exponential of the form $\Delta V_{oc}(t) = \Delta V_{oc}(0) \exp(-t/\tau_s)$ to the data, a small-signal lifetime τ_s can be determined. Here, t is the time after the pulse and $\Delta V_{oc}(0)$ is the amplitude of the additional open-circuit voltage created by the pulse.

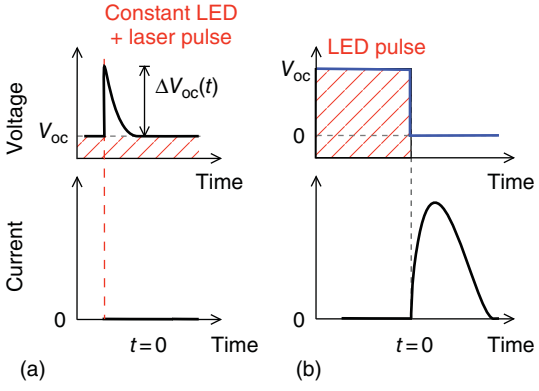

Figure 6.2 (a) Schematic principle of a transient photovoltage experiment. The device under test is held at open circuit using bias light. An additional weak laser pulse at $t = 0$ photogenerates charge carriers. After the pulse, the excess open-circuit voltage ΔV_{oc} created by the pulse decays because the excess charge recombines until a steady-state charge carrier concentration and open-circuit voltage are reached again. The decay constant of this decay of ΔV_{oc} is called the small-signal lifetime τ_s. (b) Schematic principle of the charge extraction measurement. The device under test is held at open circuit using LED illumination. The LED is switched off at $t = 0$ and the voltage is switched to zero so that the photogenerated excess charge is extracted.

By varying the bias light intensity, the small-signal lifetime can be determined as a function of open-circuit voltage or light intensity. For disordered semiconductors, typical recombination mechanisms are nonlinear with light intensity, and thus the small-signal lifetime is a strong function of bias light. In consequence, a single lifetime would not be sufficient for a fair comparison of a series of different solar cells. In order to guarantee such a fair comparison, lifetimes are usually presented as a function of charge carrier density, which can be determined, for instance, using the CE technique discussed in the next section.

6.3.2 CE at Open Circuit

CE measurements can be used to determine the average excess charge density at a given voltage and illumination condition. This information can then be used to make conclusions regarding the density of states and the reaction order of the main nongeminate recombination process.

Figure 6.3 shows the density of states of a disordered semiconductor schematically. Depending on the illumination condition, the density of states will be filled up to different levels which are approximately given by the quasi-Fermi levels E_{fn} for electrons and E_{fp} for holes. If the device is short-circuited at the same time as the bias light is switched off (see Figure 6.2b), the charge carriers will start flowing to the contacts. If charge collection is fast compared to recombination, most of the charge carriers will be collected and a current transient will be measured. The integral $Q = \int_0^{t_{max}} I(t)\mathrm{d}t$ of this current transient $I(t)$ yields the excess charge $\Delta Q = Q(V, \phi) - Q_0$ at a given voltage V and light intensity ϕ that is due to (sufficiently) mobile charge carriers of one polarity (electrons or holes) collected at a given electrode (cathode or anode). Here, Q_0 is the charge at short circuit in the

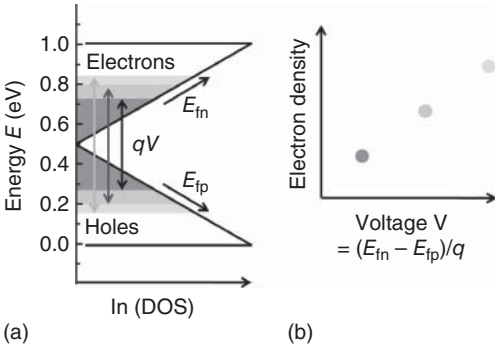

Figure 6.3 (a) Schematic depiction of the density of states of a disordered semiconductor filled to different levels due to, for example, different levels of bias light. If the charge stored in these states is collected by short-circuiting the device, the density of mobile excess electrons and holes can be extracted and plotted as a function of, for example, the voltage or the light intensity as shown schematically in (b).

dark, which includes all influences of, for example, doping. The charge Q_0 is not measured, but it needs to be taken into account, for example, if the measurement is simulated. The word "sufficiently" means here that the charge carriers have to be mobile enough to escape the device during the chosen upper limit t_{max} for the time integration without recombining. If charge collection is not fast compared to recombination, an iterative method has to be used to calculate the charge density that would have been collected if recombination was sufficiently small (see the supporting information in Ref. [25]).

From the charge, an average excess charge carrier density can be determined via $\Delta n_{av} = \Delta p_{av} = \Delta Q/(qAd)$, where A is the area of the device, d is the thickness of the active layer, and q is the elementary charge. If this operation is performed at different light intensities and open-circuit conditions, an increasing charge density is measured that is often associated with a density of states. In an intrinsic disordered semiconductor with an exponential density of tail states as shown in Figures 6.2 and 6.3, the excess charge carrier density (for instance for the case of electrons) is approximately given as

$$\Delta n_{av} = \Delta n_{av,0} \exp\left(\frac{qV}{2E_{ch}}\right), \tag{6.1}$$

where E_{ch} is the characteristic energy of the exponential (conduction band) tail, that is, the density N_{cbt} of states of the exponential tail is given by $N_{cbt} \sim \exp(E/E_{ch})$. This implies that in an ideal system approximated by Equation 6.1, the characteristic energy of the tail can be determined from a CE measurement. Obviously, this only works if certain assumptions are valid: (i) The situation needs to be completely symmetric for electrons and holes. That is, the density of states in conduction and valence band tail needs to be the same [26]. (ii) There must not be any doping, and the quasi-Fermi levels should be symmetric with respect to midgap. Otherwise the voltage cannot be split in two symmetric parts that increase the concentration of electrons and holes in the conduction and valence band tail by exactly a factor of $\exp(qV/2E_{ch})$. In case of higher doping concentrations, space charge effects lead to large spatial charge carrier gradients that lead to deviations from Equation 6.1, as discussed in Refs [26–28]. In reality, these conditions are rarely met, and CE can therefore be considered to give only a rough approximation of the density of states. Care should be taken in particular in the case of solar cells with active layer thicknesses, $d < 150$ nm. For such thin devices, the strong spatial gradient of the electron and hole concentration masks the energetic gradient caused by the density of states just as in the case of doping. Zero-dimensional models that ignore the spatial dependence of electron and hole concentrations are then insufficient to analyze the data [26, 29].

The CE method has difficulties dealing with devices where low mobilities or large thicknesses lead to insufficient charge collection at short circuit. In these cases, it is in principle possible to not short-circuit the device after switching off the bias light but to apply a reverse bias to sweep the charge carriers out of the device more quickly. This method has been proposed by Lange *et al.* [30] and was termed bias amplified charge extraction (BACE) by the authors.

6.3.3 Prediction of V_{oc} from CE and TPV

Using a combination of CE and TPV data, it is possible to predict the open-circuit voltage of a solar cell if nongeminate recombination is dominant [2]. The idea is that the current–voltage curve can be written as

$$\begin{aligned} J &= J_{\mathrm{rec}} - J_{\mathrm{gen}} \\ &= q\int_0^d R(x)\mathrm{d}x - q\int_0^d G(x)\mathrm{d}x, \end{aligned} \tag{6.2}$$

where R is the recombination rate, G is the optical generation rate, and J_{rec} and J_{gen} are the recombination current and photocurrent densities. The recombination current can be expressed as a function of electron density determined from CE and a large-signal lifetime τ_{l}. Typically, the recombination rate is approximately a power-law function of the extracted electron density, that is, $R = k\Delta n_{\mathrm{av}}^{\delta}$, where k is a constant and δ is often called a reaction order [26, 31]. This means that we can calculate the relation between small-signal and large-signal lifetimes via [32]

$$\begin{aligned} \tau_{\mathrm{l}} &= \frac{\Delta n_{\mathrm{av}}}{R} = \frac{1}{k\Delta n_{\mathrm{av}}^{\delta-1}}, \\ \tau_{\mathrm{s}} &= \frac{\mathrm{d}\Delta n_{\mathrm{av}}}{\mathrm{d}R} = \frac{1}{k\delta\Delta n_{\mathrm{av}}^{\delta-1}}, \\ \tau_{\mathrm{l}} &\approx \delta\tau_{\mathrm{s}}. \end{aligned} \tag{6.3}$$

Note that large-signal and small-signal lifetimes are exactly connected by $\tau_{\mathrm{l}} = \delta\tau_{\mathrm{s}}$ if the reaction order is a constant, as a function of charge carrier concentration. However in practice, the recombination rate is only approximately a power-law function of the charge carrier density; therefore the relation $\tau_{\mathrm{l}} \approx \delta\tau_{\mathrm{s}}$ is usually only approximate.

The recombination current in Equation 6.2 can then be expressed as

$$J_{\mathrm{rec}}(V_{\mathrm{oc}}) = q\int_0^d R(x)\mathrm{d}x = qd\frac{\Delta n_{\mathrm{av}}(V_{\mathrm{oc}})}{\tau_{\mathrm{l}}(V_{\mathrm{oc}})}. \tag{6.4}$$

If the analysis of recombination was correct, at any given light intensity, $J_{\mathrm{rec}}(V_{\mathrm{oc}})$ calculated as defined by Equation 6.4 should equal the photocurrent density J_{gen} at that same light intensity. The value of J_{gen} is usually taken from the saturation value of the light JV curve at reverse bias. Because there are various potential sources of error in the analysis and interpretation especially of the CE data, a consistency check using Equation 6.4 is valuable.

In the field of organic solar cells, there has been a long-standing discussion about the impact of field-dependent exciton splitting and therefore field-dependent charge generation [33–35]. This field-dependent charge generation is rather difficult to detect directly from current–voltage curves because it would be superimposed to the voltage-dependent charge collection that any low-mobility semiconductor likely shows. In the context of this scientific debate,

the finding $J_{rec}(V_{oc}) = J_{gen}$ has also often been interpreted as counterevidence for substantial field-dependent charge generation. Obviously, if J_{gen} is a function of electric field and therefore voltage, the method described previously would not capture this effect and $J_{rec}(V_{oc}) = J_{gen}$ therefore should not hold anymore [34]. For typical organic solar cells, the V_{oc} one would predict with the method described previously is equal to the actual V_{oc} by ±5 mV [7], which would correspond to a factor of $\exp(5\,\text{mV}/kT) = 1.2$ uncertainty in the value of J_{gen}. Thus, 20% of field-dependent change in charge generation would therefore be consistent with the observations [36].

6.3.4
CE at Short Circuit

The CE method as previously explained can also be used at short circuit in order to estimate the mobility of a material [3]. The sample is held at short circuit before and after the bias light is switched off. While the bias light is still on, the balance between charge generation, charge recombination, and CE controls the concentration of charge carriers in the device. As shown in Figure 6.4, the higher the light intensity, the more charge carriers will accumulate in the device at short circuit. In an efficient solar cell at short circuit, charge recombination should be negligible relative to charge collection. In this case, for a given rate of charge generation, it is essentially the mobility that controls the steady-state electron and hole density in the active layer at short circuit. In a drift-only approximation,

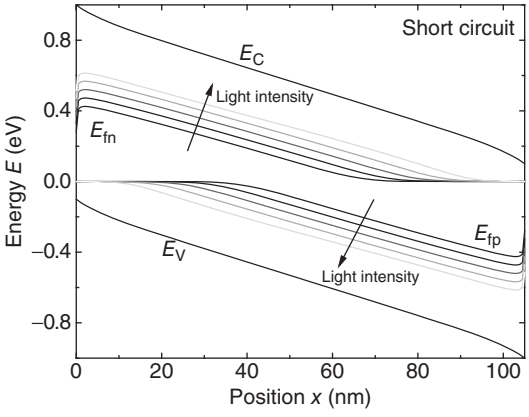

Figure 6.4 Band diagram of a thin solar cell at short circuit under illumination. The higher the illumination intensity, the higher the charge density should be at short circuit. Just as a higher light intensity increases the carrier concentration (moves the quasi-Fermi levels apart), a higher mobility would reduce the charge carrier concentration by sweeping the charges out of the device. Thus, from the knowledge of the carrier concentration in a device for a given light intensity information about the mobility can be extracted.

one could, for instance, equate the short-circuit current density J_{sc} with a drift current density and write

$$J_{sc} \approx q\mu_{eff}\Delta n_{sc}Ff(\delta), \tag{6.5}$$

where F is the electric field, Δn_{sc} is the excess electron density at short circuit under illumination relative to the dark, and $f(\delta)$ is a correction factor. Typically, F is determined using a constant field approximation $F = V_{bi}/d$, where V_{bi} is the built-in voltage and d the active layer thickness. Since the equation for a drift current density $J_{drift,n} \approx q\mu_n nF$ is always defined at a certain position x, using an electron density n is a function of x, Equation 6.5 requires a correction factor because it uses a spatially averaged charge density that is experimentally accessible. This was taken into account already in the original publication by Shuttle *et al.* [3], and a correction factor $f(\delta)$ was proposed that depends on the charge density dependence of mobility and electron density. If $\mu_n = \mu_0 n^\delta$, the mobility could be written as

$$\mu_{eff} \approx \frac{J_{sc}d}{qV_{bi}\Delta n_{sc}f(\delta)} \quad \text{with } f(\delta) = \frac{(2+\delta)(1+2\delta)}{(1+\delta)^2}. \tag{6.6}$$

Note that the correction factor does not depend very strongly on δ, and for typical values of δ between 0 and 1, the correction factor is between 2 and 2.25.

While this method to determine the mobility is relatively simple, especially if a CE setup is available already, the interpretation of the mobility is less straightforward. For instance, it is not obvious whether the mobility is due to electrons or holes or due to the faster or slower charge carrier. In the absence of simulation studies, focusing on this particular method, it may be useful to compare different samples all measured with this technique, but comparison of mobilities determined by CE with other methods such as space charge-limited current or TOF mobilities may not be easily possible.

6.4 CE with Linearly Increased Voltage

CELIV is another transient CE technique which can also determine the charge carrier density and charge carrier mobility simultaneously. It is similar to TDCF (see Section 6.5) and unlike TOF – in that it is suitable for investigating thin-film devices such as organic solar cells and in that electrons and holes cannot be distinguished. The technique was introduced by Petravichyus *et al.* [17] in 1975 for investigating the charge transport of holes in high-resistivity p-type CdSe crystal plates. Later, it was also applied to microcrystalline silicon [16] and organic solar cells [15]. While CELIV extracts dark charge carriers, in photo-CELIV, charge carriers are excited by a laser pulse.

The experimental setup requires a laser with pulses in the ns range, an oscilloscope, and an arbitrary waveform generator for voltage pulses. The pulse scheme for photo-CELIV is shown in Figure 6.5. A prebias voltage V_{off} is applied to the device under test, and then a laser pulse excites charge carriers. During

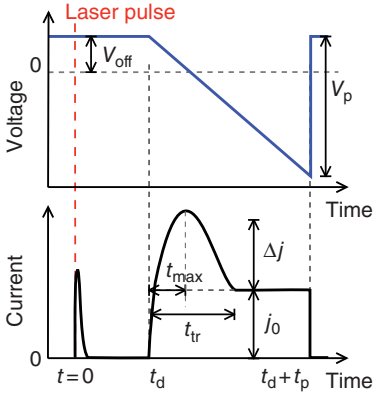

Figure 6.5 Schematic principle of the voltage and laser pulse scheme for the photo-CELIV measurement and the resulting extraction current. The offset voltage V_{off} is often selected so that the photocurrent directly due to the laser pulse at $t = 0$ is minimized. The triangular voltage pulse with slope V_p/t_p after delay time t_d leads to a capacitive response j_0 inversely proportional to the active layer thickness and an extraction current proportional to the extracted photogenerated charge carriers.

the delay time t_d recombination and extraction can occur, and afterwards the remaining charge carriers are extracted by a triangular collection voltage pulse $V(t) = A' \cdot (t\text{-}t_d)$ in reverse-bias direction, where $A' = V_p/t_p$. The same scheme applies to (dark) CELIV, just without laser and delay time. The triangular extraction pulse leads to a rectangular current response of height j_0 due to the geometric capacitance of the sample. In addition, the integral over the extraction current peak on top of j_0 with height Δj corresponds to the collected charge carrier density. The time t_{max} is a function of the charge carrier mobility. With CELIV, one restriction of TOF, namely, that the material dielectric relaxation time $\tau_\sigma \gg t_d, t_{tr}$ to avoid redistribution of the electric field within the transit time, is lifted [16]. In case the RC time is significant, the extraction current peak will be distorted, and the beginning of the geometric capacitance response will not be rectangular any more. Then, the maximum of the extraction peak is shifted to slower times, leading to an underestimation of the charge carrier mobility. Smaller sample areas and thicker samples – the latter potentially making the measurement less relevant due to the different conditions – can reduce the RC time.

The evaluation of the data in view of charge carrier concentration and mobility is the same for (dark) CELIV and photo-CELIV. The current $j_0 = C_{geo} \cdot A'$ is directly proportional to the geometric response of the device under test, $C_{geo} = \varepsilon_r \varepsilon_0 / d$, with active layer thickness d. The collected charge carrier density is $n = 1/d \cdot \int (j(t)\text{-}j_0) \mathrm{d}t$, the integral ranging from t_d to the transit time t_{tr} when all of the charges are extracted.

For photo-CELIV, charge carrier recombination can be studied by a variation of the delay time. For each delay time, the excess carrier concentration can be determined from the extraction current peak as described previously, and the longer the charge carriers are within the sample at V_{off}, the more of them recombine. Thus, the extraction peak is reduced with time. The time resolution of photo-CELIV, that is, the shortest accessible time at which a meaningful carrier concentration can be determined, is essentially limited by t_{max}. Therefore, the decay of the carrier concentration n in dependence of delay time is often best shown by $n(t_{max} + t_d)$. The

same limitation applies to the charge carrier mobility. In order to determine the recombination mechanism, the experimental charge carrier concentration decay $n(t_{max} + t_d)$ can be evaluated by fitting to the (excess) charge carrier continuity equation:

$$\frac{dn}{dt} = -R, \tag{6.7}$$

where, for the experimental data, $t = t_{max} + t_d$. The recombination rate to be tested could, for instance, be the Langevin recombination rate $R_L = k_L n^2$, where $k_L = q/\varepsilon\mu_{eff}$ with the effective charge carrier mobility μ_{eff} taken also from the CELIV experiment, as described later. Similarly, a reduced Langevin recombination rate $R_{L2} = \zeta k_L n^2$ with the reduction factor ζ as parameter or the empirical general decay $R = k_0 n^\delta$ can be determined, with the empirical parameter δ ($\delta \geq 1.5$) denoting the order of decay and k_0 being independent of n. Two factors should be considered: In analogy to the CE experiment, charge carriers may recombine also during extraction, which might have to be corrected in a similar fashion, as described previously. Also, dark charge carriers may influence the recombination, leading to an erroneous determination of δ if not considered properly. While the parameter δ is empirical (as is the prefactor k_0), it is possible [37] to interpret δ in view of an exponential density of tail states, in which case $\delta = E_{ch}/kT + 1$, with E_{ch} the characteristic tail energy and kT the thermal energy.

Also the charge carrier mobility can be determined using CELIV. Juska *et al.* [16] solved the continuity, drift, and Poisson equations for a simple case with only one charge carrier type and no traps. For extreme cases of high ($\Delta j > j_0$) and low conductivity ($\Delta j < j_0$), the resulting differential equation can be solved analytically. Lorrmann *et al.* [38] provided a complete analytic treatment of this simple case for all conductivity regimes. The numerical solution, essentially a parametric fit to the analytic result, is simpler to handle and allows approximate determination of the charge carrier mobility for intermediate conductivities (i.e., when $\Delta j \approx j_0$) according to

$$\mu = \frac{2\,d^2}{3A' t_{max}^2 \left(1 - B\frac{\Delta j}{j_0}\right)}. \tag{6.8}$$

Here, B is a fitting factor given as 0.36 [16] or, with lower deviations from the analytic result, 0.21 [38] to account for the level of conductivity and the corresponding electric field redistribution. We point out that Hanfland *et al.* [39] investigated the ability of CELIV to determine the charge carrier mobility in disordered semiconductors containing traps. They found that the traps distort the shape of the CELIV transients and that the resulting mobility may not reflect the real effective mobility accurately.

The determination of the decay of photogenerated charge carriers due to recombination can be performed with photo-CELIV as previously mentioned. However, the decay of the charge carrier concentration during the delay time t_d is generally due to a combination of charge recombination and extraction even before the extraction voltage pulse. Only under open-circuit conditions during the delay

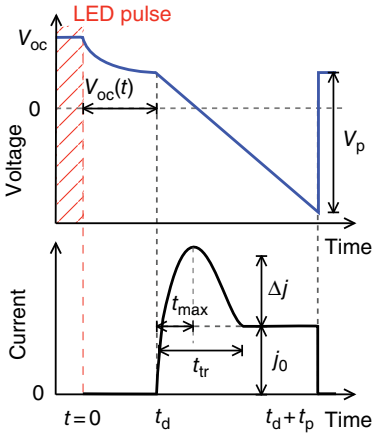

Figure 6.6 Schematic principle of the voltage and light pulse scheme for the OTRACE measurement and the resulting extraction current. The difference to photo-CELIV is that, here, a LED is used for illumination, which is switched off at $t = 0$. During the delay time t_d, the device is held under open-circuit voltage conditions so that no current leaves the device, as shown in the lower part of the figure. The extraction, starting at t_d, is the same as for CELIV.

time, no current would flow out of the device. If the CE during t_d is not considered, then the recombination rate will be overestimated. Therefore, in photo-CELIV, a constant offset voltage V_{off} has to be chosen to ensure that the current flow from the sample during t_d is as small as possible [13]. While this approach helps, an extension of photo-CELIV was developed by Baumann *et al.* [40] – open-circuit corrected transient charge extraction (OTRACE) by linearly increasing voltage – to reduce the current during the delay time to zero. Here, the open-circuit voltage decay $V_{oc}(t)$ upon a laser pulse is measured using a high-impedance input of the oscilloscope. The measured $V_{oc}(t)$ is then programmed into an arbitrary waveform generator to replace the constant V_{off}. The pulse scheme is shown in Figure 6.6. Therefore, in OTRACE, the device under test is under open-circuit conditions: No current flows during the delay time and the charge carrier recombination rate is not overestimated. Indeed, in Ref. [40], the authors used fast white LED instead of a laser and let the device under test reach steady-state conditions under constant illumination before switching it off at $t = 0$. Finally, OTRACE strongly reduces RC effects.

Two other extensions address a weakness of (dark) CELIV: In particular in organic semiconductors, the intrinsic charge carrier concentration is often so low that the extraction signal is below the noise level. Injection of charge carriers into the diode or metal–insulator–semiconductor capacitor can lift this limitation. The corresponding CELIV techniques are called i-CELIV [41] and MIS-CELIV [42].

6.5
Time-Delayed Collection Field Method

TDCF is a fast CE technique, in which charge carriers are photogenerated by an optical pump using short laser pulses under certain applied voltage. These charge carriers are probed by CE with strong reverse voltage applied after a delay time. The information which can be gained from TDCF is mainly the yield of the

extracted charge carriers in dependence on laser intensity, delay time, applied voltage, and so on. Direct information from the shape of the transients is often not used, which implies that RC effects are often not critical, which is why delay times down to a few nanoseconds are possible. TDCF was first reported by Mort *et al.* [43] in 1980 to study nongeminate recombination in amorphous Si:H. In 2002 it was applied to study geminate recombination in neat polymers [18], and from 2006 on it was used to investigate geminate and nongeminate recombination in organic solar cells [24].

The experimental setup requires a laser with pulse widths in the nanosecond range or below, an oscilloscope, and a voltage pulse generator. The pulse scheme is shown in Figure 6.7. A prebias voltage is applied to the device under test, and then the short laser pulse photogenerates charge carriers in the active layer. After a delay time t_d, during which the charge carriers can recombine, a collection voltage in reverse bias is applied to extract all charge carriers previously neither extracted nor lost to recombination. The collected charge corresponds to the integral over the current. The charge extracted during the delay time is termed Q_{pre}, the charge from t_d until the end of collection pulse at $t_d + t_e$ is Q_{col}, and the sum of both corresponds to the total extracted charge Q_{tot}. The extraction time t_e has to be chosen sufficiently long to ensure extraction of the complete photogenerated charge from the sample if possible.

TDCF can help to investigate different phenomena, on which the measurement conditions depend. If the field dependence of charge photogeneration and the counterprocess geminate recombination are investigated, the slower nongeminate charge carrier recombination has to be excluded as far as possible. Then, the shortest delay time slightly longer than geminate recombination lifetime has to be selected, 10 ns being commonly used. In addition, the laser intensity has to be low as nongeminate recombination scales (at least) quadratically with light intensity, but geminate recombination is independent of light intensity. To verify that geminate recombination dominates, the collected charge Q_{col} has to be measured as a function of light intensity. For low laser intensity, Q_{col} scales linearly with light intensity, and the photogeneration can be investigated. For higher intensities, it

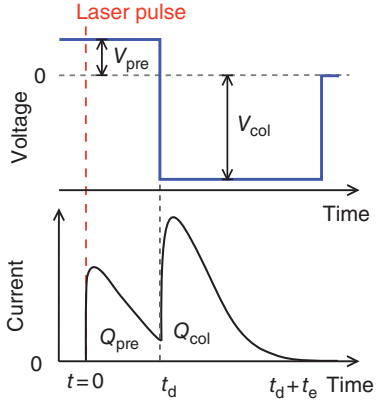

Figure 6.7 Schematic principle of the voltage and laser pulse scheme for the TDCF measurement and the resulting extraction current. The device is held at the prebias voltage V_{pre} when the laser pulse is incident at $t = 0$, until the end of the delay time t_d, resulting in an extracted charge Q_{pre}. The remaining charge Q_{col} is collected with a strong reverse-bias V_{col} with a sufficiently long pulse length t_e to extract all photogenerated charge.

deviates from the linear relation, and nongeminate recombination becomes dominant. Usually delay time is kept constant, and the prebias voltage is varied from about open-circuit to reverse-bias voltages. The field-dependent photogeneration can be investigated by considering Q_{tot} as a function of the internal electric field during the prebias. It is usually approximated by $(V_{bi}\text{-}V_{pre})/d$, with the built-in potential V_{bi} and the active layer thickness d.

For nongeminate recombination, usually the delay time is varied from shortest time to longest times in the microsecond regime at two or three fixed prebias voltages. Usually Q_{pre}, Q_{col} , and Q_{tot} are plotted versus delay time, and Q_{col} is fitted, for instance, by a second-order recombination rate $R = knp$, with recombination prefactor k, and electron and hole concentrations $n = p$. The charge carrier continuity equation has to be solved to determine k, for instance, by using an iterative scheme [21, 22] for discrete time steps Δt:

$$Q_{col}(t_d + \Delta t) - Q_{col}(t_d) = -(Q_{pre}(t_d + \Delta t) - Q_{pre}(t_d)) - \frac{k}{qAd}(Q_{col}(t_d)^2 + 2Q_{col}(t_d)\cdot Q_{dark})\Delta t, \quad (6.9)$$

with the active area A and dark charge Q_{dark}, which could, for example, be present due to injection of charge carriers under forward bias. According to Refs [21, 22], Q_{dark} should be considered, as otherwise the recombination prefactor will be overestimated. Q_{dark} can, for instance, be determined by CE experiments in the dark, as described in Section 6.3.

The charge carrier mobility can in principle also be measured with TDCF, although it will yield only effective values as electron and hole mobilities cannot be distinguished by this technique. The charge carrier extraction time is determined either by a linear fit of the photocurrent decays of the TDCF measurement [19] or an exponential fit, and the corresponding effective mobility is determined in analogy to the TOF method.

Acknowledgment

The authors would like to thank the DFG for the project "Radiative Recombination in Organic Solar Cells" (DE830-13/1).

References

1. Foertig, A., Wagenpfahl, A., Gerbich, T., Cheyns, D., Dyakonov, V., and Deibel, C. (2012) Nongeminate recombination in planar and bulk heterojunction organic solar cells. *Adv. Energy Mater.*, **2**, 1483.
2. Maurano, A., Hamilton, R., Shuttle, C.G., Ballantyne, A.M., Nelson, J., O'Regan, B., Zhang, W.M., McCulloch, I., Azimi, H., Morana, M., Brabec, C.J., and Durrant, J.R. (2010) Recombination dynamics as a key determinant of open circuit voltage in organic bulk heterojunction solar cells: a comparison of four different donor polymers. *Adv. Mater.*, **22**, 4987.
3. Shuttle, C.G., Hamilton, R., Nelson, J., O'Regan, B.C., and Durrant, J.R. (2010) Measurement of charge-density dependence of carrier mobility in an organic semiconductor blend. *Adv. Funct. Mater.*, **20**, 698.

4. Credgington, D., Hamilton, R., Atienzar, P., Nelson, J., and Durrant, J.R. (2011) Non-geminate recombination as the primary determinant of open-circuit voltage in polythiophene:fullerene blend solar cells: an analysis of the influence of device processing conditions. *Adv. Funct. Mater.*, **21**, 2744.
5. Dibb, G.F.A., Kirchartz, T., Credgington, D., Durrant, J.R., and Nelson, J. (2011) Analysis of the relationship between linearity of corrected photocurrent and the order of recombination in organic solar cells. *J. Phys. Chem. Lett.*, **2**, 2407.
6. Credgington, D., Jamieson, F.C., Walker, B., Nguyen, T.Q., and Durrant, J.R. (2012) Quantification of geminate and non-geminate recombination losses within a solution-processed small-molecule bulk heterojunction solar cell. *Adv. Mater.*, **24**, 2135.
7. Credgington, D. and Durrant, J.R. (2012) Insights from transient optoelectronic analyses on the open-circuit voltage of organic solar cells. *J. Phys. Chem. Lett.*, **3**, 1465.
8. Rauh, D., Deibel, C., and Dyakonov, V. (2012) Charge density dependent nongeminate recombination in organic bulk heterojunction solar cells. *Adv. Funct. Mater.*, **22**, 3371.
9. Foertig, A., Kniepert, J., Gluecker, M., Brenner, T., Dyakonov, V., Neher, D., and Deibel, C. (2014) Nongeminate and geminate recombination in PTB7:PCBM solar cells. *Adv. Funct. Mater.*, **24**, 1306.
10. Clarke, T.M., Lungenschmied, C., Peet, J., Drolet, N., and Mozer, A.J. (2015) A comparison of five experimental techniques to measure charge carrier lifetime in polymer/fullerene solar cells. *Adv. Energy Mater.*, **5**, Article no: 1401345.
11. Ip, A.H., Thon, S.M., Hoogland, S., Voznyy, O., Zhitomirsky, D., Debnath, R., Levina, L., Rollny, L.R., Carey, G.H., Fischer, A., Kemp, K.W., Kramer, I.J., Ning, Z.J., Labelle, A.J., Chou, K.W., Amassian, A., and Sargent, E.H. (2012) Hybrid passivated colloidal quantum dot solids. *Nat. Nanotechnol.*, **7**, 577.
12. Albero, J., Riente, P., Clifford, J.N., Pericas, M.A., and Palomares, E. (2013) Improving CdSe quantum dot/polymer solar cell efficiency through the covalent functionalization of quantum dots: implications in the device recombination kinetics. *J. Phys. Chem. C*, **117**, 13374.
13. Mozer, A.J., Sariciftci, N.S., Pivrikas, A., Osterbacka, R., Juska, G., Brassat, L., and Bassler, H. (2005) Charge carrier mobility in regioregular poly(3-hexylthiophene) probed by transient conductivity techniques: a comparative study. *Phys. Rev. B*, **71**, Article no: 035214.
14. Pivrikas, A., Sariciftci, N.S., Juska, G., and Osterbacka, R. (2007) A review of charge transport and recombination in polymer/fullerene organic solar cells. *Prog. Photovoltaics Res. Appl.*, **15**, 677.
15. Pivrikas, A., Juska, G., Mozer, A.J., Scharber, M., Arlauskas, K., Sariciftci, N.S., Stubb, H., and Osterbacka, R. (2005) Bimolecular recombination coefficient as a sensitive testing parameter for low-mobility solar-cell materials. *Phys. Rev. Lett.*, **94**, 176806.
16. Juska, G., Arlauskas, K., Viliunas, M., and Kocka, J. (2000) Extraction current transients: new method of study of charge transport in microcrystalline silicon. *Phys. Rev. Lett.*, **84**, 4946.
17. Petravichyus, A.D., Yushka, G.B., and Baubinas, R.V. (1975) Drift of holes in high-resistivity p-type CdSe crystal plates. *Sov. Phys. Semicond. USSR*, **9**, 1530.
18. Hertel, D., Soh, E.V., Bassler, H., and Rothberg, L.J. (2002) Electric field dependent generation of geminate electron–hole pairs in a ladder-type pi-conjugated polymer probed by fluorescence quenching and delayed field collection of charge carriers. *Chem. Phys. Lett.*, **361**, 99.
19. Albrecht, S., Schindler, W., Kurpiers, J., Kniepert, J., Blakesley, J.C., Dumsch, I., Allard, S., Fostiropoulos, K., Scherf, U., and Neher, D. (2012) On the field dependence of free charge carrier generation and recombination in blends of PCPDTBT/PC70BM: influence of solvent additives. *J. Phys. Chem. Lett.*, **3**, 640.
20. Vandewal, K., Albrecht, S., Hoke, E.T., Graham, K.R., Widmer, J., Douglas, J.D., Schubert, M., Mateker, W.R., Bloking, J.T., Burkhard, G.F., Sellinger,

A., Frechet, J.M.J., Amassian, A., Riede, M.K., McGehee, M.D., Neher, D., and Salleo, A. (2014) Efficient charge generation by relaxed charge-transfer states at organic interfaces. *Nat. Mater.*, **13**, 63.

21. Kniepert, J., Schubert, M., Blakesley, J.C., and Neher, D. (2011) Photogeneration and recombination in P3HT/PCBM solar cells probed by time-delayed collection field experiments. *J. Phys. Chem. Lett.*, **2**, 700.
22. Kniepert, J., Lange, I., van der Kaap, N.J., Koster, L.J.A., and Neher, D. (2014) A conclusive view on charge generation, recombination, and extraction in as-prepared and annealed P3HT:PCBM blends: combined experimental and simulation work. *Adv. Energy Mater.*, **4**, Article no: 1301401.
23. Kniepert, J., Lange, I., Heidbrink, J., Kurpiers, J., Brenner, T.J.K., Koster, L.J.A., and Neher, D. (2015) Effect of solvent additive on generation, recombination, and extraction in PTB7:PCBM solar cells: a conclusive experimental and numerical simulation study. *J. Phys. Chem. C*, **119**, 8310.
24. Offermans, T., Meskers, S.C.J., and Janssen, R.A.J. (2006) Time delayed collection field experiments on polymer: fullerene bulk-heterojunction solar cells. *J. Appl. Phys.*, **100**, Article no: 074509.
25. Shuttle, C.G., Maurano, A., Hamilton, R., O'Regan, B., de Mello, J. C., and Durrant, J.R. (2008) Charge extraction analysis of charge carrier densities in a polythiophene/fullerene solar cell: analysis of the origin of the device dark current. *Appl. Phys. Lett.*, **93**, 183501. See http://ftp.aip.org/epaps/apl_org_electron_photonics/E-APPLAB-93-043843/Supporting%20information043843APL.pdf for the supporting information (accessed 24 February 2016).
26. Kirchartz, T. and Nelson, J. (2012) Meaning of reaction orders in polymer: fullerene solar cells. *Phys. Rev. B*, **86**, 165201.
27. Deledalle, F., Kirchartz, T., Vezie, M.S., Campoy-Quiles, M., Tuladhar, P.S., Nelson, J., and Durrant, J.R. (2015) Understanding the effect of unintentional doping on transport optimization and analysis in efficient organic bulk-heterojunction solar cells. *Phys. Rev. X*, **5**, Article no: 011032.
28. Deibel, C., Wagenpfahl, A., and Dyakonov, V. (2009) Origin of reduced polaron recombination in organic semiconductor devices. *Phys. Rev. B*, 80, Article no: 075203.
29. Deledalle, F., Tuladhar, P.S., Nelson, J., Durrant, J.R., and Kirchartz, T. (2014) Understanding the apparent charge density dependence of mobility and lifetime in organic bulk heterojunction solar cells. *J. Phys. Chem. C*, **118**, 8837.
30. Lange, I., Kniepert, J., Pingel, P., Dumsch, I., Allard, S., Janietz, S., Scherf, U., and Neher, D. (2013) Correlation between the open circuit voltage and the energetics of organic bulk heterojunction solar cells. *J. Phys. Chem. Lett.*, **4**, 3865.
31. Deibel, C., Rauh, D., and Foertig, A. (2013) Order of decay of mobile charge carriers in P3HT:PCBM solar cells. *Appl. Phys. Lett.*, **103**, 043307.
32. O'Regan, B.C., Durrant, J.R., Sommeling, P.M., and Bakker, N.J. (2007) Influence of the $TiCl_4$ treatment on nanocrystalline TiO_2 films in dye-sensitized solar cells. 2. Charge density, band edge shifts, and quantification of recombination losses at short circuit. *J. Phys. Chem. C*, **111**, 14001.
33. Jamieson, F.C., Agostinelli, T., Azimi, H., Nelson, J., and Durrant, J.R. (2010) Field-independent charge photogeneration in PCPDTBT/PC70BM solar cells. *J. Phys. Chem. Lett.*, **1**, 3306.
34. Shuttle, C.G., Hamilton, R., O'Regan, B.C., Nelson, J., and Durrant, J.R. (2010) Charge-density-based analysis of the current–voltage response of polythiophene/fullerene photovoltaic devices. *Proc. Natl. Acad. Sci. U. S. A.*, **107**, 16448.
35. Clarke, T.M. and Durrant, J.R. (2010) Charge photogeneration in organic solar cells. *Chem. Rev.*, **110**, 6736.
36. Foertig, A., Rauh, J., Dyakonov, V., and Deibel, C. (2012) Shockley equation parameters of P3HT:PCBM solar cells determined by transient techniques. *Phys. Rev. B*, **86**, 115302.

37. Kirchartz, T., Pieters, B.E., Kirkpatrick, J., Rau, U., and Nelson, J. (2011) Recombination via tail states in polythiophene: fullerene solar cells. *Phys. Rev. B*, **83**, 115209.
38. Lorrmann, J., Badada, B.H., Inganas, O., Dyakonov, V., and Deibel, C. (2010) Charge carrier extraction by linearly increasing voltage: analytic framework and ambipolar transients. *J. Appl. Phys.*, **108**, Article no: 113705.
39. Hanfland, R., Fischer, M.A., Brutting, W., Wurfel, U., and MacKenzie, R.C.I. (2013) The physical meaning of charge extraction by linearly increasing voltage transients from organic solar cells. *Appl. Phys. Lett.*, **103**, Article no: 063904.
40. Baumann, A., Lorrmann, J., Rauh, D., Deibel, C., and Dyakonov, V. (2012) A new approach for probing the mobility and lifetime of photogenerated charge carriers in organic solar cells under real operating conditions. *Adv. Mater.*, **24**, 4381.
41. Armin, A., Velusamy, M., Burn, P.L., Meredith, P., and Pivrikas, A. (2012) Injected charge extraction by linearly increasing voltage for bimolecular recombination studies in organic solar cells. *Appl. Phys. Lett.*, **101**, Article no: 083306.
42. Armin, A., Juska, G., Ullah, M., Velusamy, M., Burn, P.L., Meredith, P., and Pivrikas, A. (2014) Balanced carrier mobilities: not a necessary condition for high-efficiency thin organic solar cells as determined by MIS-CELIV. *Adv. Energy Mater.*, **4**, Article no: 1300954.
43. Mort, J., Chen, I., Troup, A., Morgan, M., Knights, J., and Lujan, R. (1980) Nongeminate recombination of alpha-Si-H. *Phys. Rev. Lett.*, **45**, 1348.

7
Steady-State Photocarrier Grating Method

Rudolf Brüggemann

7.1
Introduction

The excess-carrier properties of a photoexcited semiconductor are important indicators of its quality with respect to applications in optoelectronic devices or for studying the recombination physics. In contrast to the majority-carrier properties, which can be determined rather straightforwardly by stationary photocurrent measurements, the minority-carrier properties can only be revealed by more sophisticated methods. In this respect the steady-state photocarrier grating (SSPG) method has had an enormous impact since it was suggested by Ritter, Zeldov, and Weiser, named RZW hereafter, in 1986 [1].

The SSPG method is based on the carrier diffusion under the presence of a spatial sinusoidal modulation in the photogeneration rate G, which induces a so-called photocarrier grating. From photocurrent measurements at different grating periods Λ, the ambipolar diffusion length L can be determined by an analysis that assumes ambipolar transport and charge neutrality.

The proposal by RZW, following papers on the analysis [2, 3], and the simple setup triggered a rapid widespread application [4–8]. In parallel, critical and more in-depth accounts on the underlying theory were given to put the technique on a firm ground or to describe its limits when applied to semiconductors with traps. Ritter *et al.* [9], Balberg [10, 11], Li [12], and Shah *et al.* [13] analyzed the transport equations, also with respect to the "lifetime" or "relaxation time" regimes. In the lifetime regime, the carrier lifetimes are longer than the dielectric relaxation time.

The previous publications were later criticized by Hattori *et al.* [14] who performed a second-order perturbation approach and pointed out deficiencies of other earlier analyses. Nevertheless, Hattori *et al.* showed that under the conditions in the "lifetime regime," the analysis and evaluation of the SSPG method are correct. These authors also suggested a correction method to avoid incorrect values of L.

A novel aspect was introduced by Abel *et al.* [15] who numerically solved the transport and Poisson equations and compared the solutions with a generalized theory which enables to study the SSPG results by the variation of Λ and/or

Advanced Characterization Techniques for Thin Film Solar Cells, Second Edition.
Edited by Daniel Abou-Ras, Thomas Kirchartz, and Uwe Rau.

electric field E. These authors derive their expressions in terms of the mobility-lifetime product $(\mu\tau)_{\text{min}}$ of the minority carriers, which can be determined from the SSPG method and related to L.

More recently, Schmidt and Longeaud [16] developed a generalized derivation of the solution of the SSPG equations at low E. They identified the shortcomings in the previous derivations which differ from the numerical solution. Their approach also allows the SSPG experiment to be used for the density-of-states (DOS) determination.

An important aspect is the aforementioned association of L with the $(\mu\tau)_{\text{min}}$ product of the minority carriers. Together with the majority-carrier mobility-lifetime product $(\mu\tau)_{\text{maj}}$ at the same G from the photoconductivity σ_{ph} via $\sigma_{\text{ph}} = eG(\mu\tau)_{\text{maj}}$, where e equals 1.6×10^{-19} C, the excess-carrier properties can be related to each other with the aim to consistently describe them in relation to models for recombination, the role of the Fermi level E_{f}, and the relevant DOS in the band gap [17].

The aforementioned brief and not complete description of SSPG-related aspects indicates that both the theoretical understanding and the variety of applications have evolved in the last 20 years. While some treatments point to modifications that may be needed for the correct determination of L and the corresponding $(\mu\tau)_{\text{min}}$, the original formulation and analysis by RZW is still often used as deviations are considered to be small.

7.2 Basic Analysis of SSPG and Photocurrent Response

7.2.1 Optical Model

Figure 7.1a sketches the arrangement of the SSPG experiment. Two coherent plane waves, which originate from one laser beam that has been split into the beams L_1 and L_2 with wavelength λ, impinge symmetrically onto a semiconductor where they suffer refraction according to Snell's law. The angle between the two beams changes from θ in air to θ' in the semiconductor with refractive index n_{s}. The wavelength changes from λ to λ' where $\lambda' = \lambda n_{\text{air}}/n_{\text{s}}$. These relations hold accordingly when the surrounding medium is not air but glass. The plane wave of L_1 can be described by the electric field $\vec{E}_1(\vec{r}) = \vec{E}_{10}\exp(i\vec{k}_1\cdot\vec{r} - i\omega t)$ in air and by $\vec{E}'_1(\vec{r}) = \vec{E}'_{10}\exp(i\vec{k}'_1\cdot\vec{r} - i\omega t)$ in the semiconductor, where the variables have their typical meanings. A similar expression holds for $\vec{E}_2(\vec{r})$ of L_2.

In Figure 7.1b, L_1 is perpendicular to the semiconductor surface so that no refraction occurs.

The local photon flux Φ in the semiconductor is related to the square of the local electric field by

$$\Phi(\vec{r}) \propto \left|\vec{E}'_1\left(\vec{r}\right) + \vec{E}'_2(\vec{r})\right|^2 = \left|\vec{E}'_{10}\exp\left(i\vec{k}'_1\cdot\vec{r} - i\omega t\right) + \vec{E}'_{20}\exp(i\vec{k}'_2\cdot\vec{r} - i\omega t)\right|^2, \quad (7.1)$$

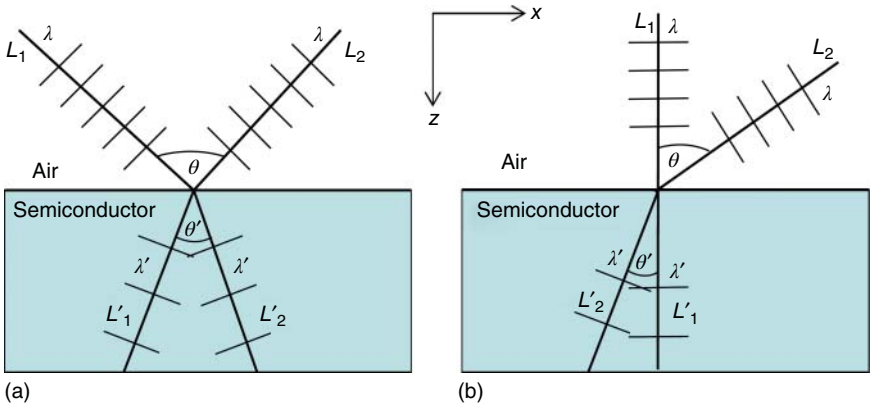

Figure 7.1 Schematics of the interference experiment with two plane waves L_1 and L_2 with wavelength λ. The coordinate system is sketched.

where $|\vec{k}|$ is given by $(2\pi n/\lambda)$ and we assume low absorption so that there is negligible decay of the photon flux. It is then found from Equation 7.1 that in the z-direction the value of Φ is constant. In the x-direction the influence of the refractive index change cancels. The sinusoidal modulation in the x-direction, sketched in Figure 7.2, which forms a so-called grating, has a grating period Λ given by

$$\Lambda = \frac{\lambda}{2\sin(\theta/2)}. \tag{7.2}$$

Assuming $\vec{E}_{10} = \vec{E}'_{10}$ and for a generation rate $G \approx \alpha\Phi$, independent in z, leads to a variation of G in x according to

$$G(\vec{r}) = G(x) = (G_1 + G_2) + 2\gamma_0(G_1G_2)^{0.5}\cos\left(\frac{2\pi x}{\Lambda}\right), \tag{7.3}$$

where $G_1 = \alpha\Phi_1$, $G_2 = \alpha\Phi_2$. The additional parameter γ_0 has been introduced here by RZW as a grating quality factor in order to account for a nonideal grating because of optical scattering, nonideal coherence, or mechanical vibrations. The amplitude of the modulation $2\gamma_0(G_1G_2)^{0.5}$ is typically larger than G_2 so that regions exist in which $G(x)$ with the two beams is less than G_1 only.

For the more explicit G profile within the semiconductor with the absorption coefficient α, one obtains [18]

$$G(x,z) = G(x) = (G_1 + G_2)\exp(-\alpha z)\left[1 + \frac{2\gamma_0\left(G_1G_2\right)^{0.5}}{G_1 + G_2}\cos\left(\frac{2\pi x}{\Lambda}\right)\right]. \tag{7.4}$$

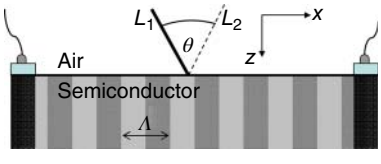

Figure 7.2 Schematic of the interference fringes between coplanar electrodes. The parallel planes of constant photon flux are perpendicular to the air–semiconductor interface.

An account of the influence of the polarization-dependent reflection on G was given by Nicholson [19].

In the asymmetric case of Figure 7.1b, in which the stationary beam hits the sample at right angle, the analysis yields that the fringes are no longer perpendicular to the surface but that they are tilted. This may cause problems by blurring of the relevant photocarrier grating relative to the electric field that probes its distribution.

7.2.2 Semiconductor Equations

Poisson's equation consists of the local total charge ρ to which the free carriers in the bands, trapped charge, and/or charged defects in addition to any charge from impurities or dopants contribute. In terms of E, it takes the form

$$\frac{1}{e}\frac{\mathrm{d}E}{\mathrm{d}x} = \frac{\rho}{\varepsilon\varepsilon_0}, \tag{7.5}$$

with the dielectric constants ε of the semiconductor and ε_0. For the special case of a homogeneous semiconductor with coplanar electrodes as in Figure 7.2, Poisson's equation reduces to $\rho = 0$ and E is given by the ratio of the applied voltage and the electrode distance.

In addition, with homogeneous free-carrier distributions, the current densities are determined by the electric field so that the current equation reduces to

$$j = j_\mathrm{n} + j_\mathrm{p} = (en\mu_\mathrm{n} + ep\mu_\mathrm{p})E = (\sigma_\mathrm{n} + \sigma_\mathrm{p})E, \tag{7.6}$$

with the free electron (hole) density n (p) and with the conductivities of the electrons (holes) σ_n (σ_p). The index denotes the respective carrier type of the electrical current density j and the extended-state mobility μ.

The continuity equations with $\mathrm{div}\, j_\mathrm{n} = \mathrm{div}\, j_\mathrm{p} = 0$ become

$$G = R \tag{7.7}$$

with the recombination rate R.

The special case under almost homogeneous G is used for the determination of the mobility-lifetime $(\mu\tau)_\mathrm{maj}$ product of the majority carriers. The measured photocurrent is assumed to be determined by one carrier type, say electrons. It is then given by the difference of the total to the dark current density. The photoconductivity is determined from Ohm's law $j_\mathrm{ph} = \sigma_\mathrm{ph}E$ and it is determined by the excess electron density n_ph.

The recombination lifetimes of the free electrons and holes τ_n and τ_p are defined by [20]

$$R = \frac{n_\mathrm{tot} - n_\mathrm{th}}{\tau_\mathrm{n}} = \frac{n_\mathrm{ph}}{\tau_\mathrm{n}} = \frac{p_\mathrm{tot} - p_\mathrm{th}}{\tau_\mathrm{p}} = \frac{p_\mathrm{ph}}{\tau_\mathrm{p}}, \tag{7.8}$$

where n_tot (p_tot) is the total electron (hole) density under illumination and n_th and p_th are the thermal equilibrium values. With Equation 7.7 and the substitution of

n_{ph}, it follows that

$$(\mu\tau)_n = \mu_n \tau_n = \left(\frac{\sigma_{ph}}{eG}\right), \tag{7.9}$$

which gives experimental access to the majority-carrier $(\tau)_{maj}$ product. Corresponding equations hold if holes are the majority carriers.

7.2.3 Diffusion Length: Ritter–Zeldov–Weiser Analysis

RZW devised the "SSPG technique for diffusion length measurement in photoconductive insulators." Their starting point of analysis are the transport equations of Chapter 23 under the assumption of ambipolar transport, so that only one carrier type is analyzed, and charge neutrality. They reduce to

$$\frac{1}{e}\frac{d}{dx}\left(-e\overline{D}\frac{dn(x)}{dx}\right) = G(x) - R(x), \tag{7.10}$$

where $\overline{D}$ is an effective diffusion coefficient and where $n(x)$ is the sum of the corresponding homogenous excess density n_0 and the modulated density $n(x) = n_0 + \Delta n(x)$. Splitting off the homogeneous terms results in a differential equation for $\Delta n(x)$ according to

$$\overline{D}\frac{d^2\Delta n(x)}{dx^2} = g(x) - \frac{\Delta n(x)}{\tau(n)}, \tag{7.11}$$

with $g(x) = 2\gamma_0(G_1G_2)^{0.5}\cos(2\pi x/\Lambda)$ and the carrier lifetime τ. The ansatz $\Delta n(x) = \Delta n_0 \cos(2\pi x/\Lambda)$ in phase with $g(x)$ results in

$$\Delta n_0 = \frac{2\gamma_0\sqrt{G_1G_2}}{1 + \left(\frac{2\pi L}{\Lambda}\right)^2}\tau, \tag{7.12}$$

where the ambipolar diffusion length L is introduced by

$$L = \sqrt{\overline{D}\tau}. \tag{7.13}$$

It is necessary to correctly account for a possibly G-dependent τ in Equation 7.13. Experimentally, the relation between photoconductivity or excess-carrier density and the generation rate is usually given by

$$n \propto G^{\gamma}, \tag{7.14}$$

with the power-law exponent γ. One may expand Equation 7.14 to eliminate τ in Equation 7.12 so that with $\tau \approx \gamma n_0/(G_1 + G_2)$ one determines

$$\Delta n_0 = \frac{2\gamma_0\sqrt{G_1G_2}}{1 + \left(\frac{2\pi L}{\Lambda}\right)^2}\frac{\gamma n_0}{G_1 + G_2}. \tag{7.15}$$

The local conductivity which is proportional to $n(x) = n_0(1 + \Delta n(x)/n_0)$ may now be written as

$$\sigma(x) = \sigma(L_1 + L_2)\left[1 + A\cos\left(\frac{2\pi x}{\Lambda}\right)\right], \tag{7.16}$$

where n_0 is related to $\sigma(L_1 + L_2)$. The photocarrier grating amplitude A is given by

$$A = \frac{2\gamma\gamma_0\sqrt{G_1 G_2}}{G_1 + G_2}\gamma_g, \tag{7.17}$$

in which the last term

$$\gamma_g = \frac{1}{1 + \left(\frac{2\pi L}{\Lambda}\right)^2} \tag{7.18}$$

with L and Λ describes the influence of the grating.

So far, the diffusion length L is related to the local conductivity $\sigma(x)$. What is needed for the electrical measurements is a relation between L and the measured current. In a next phenomenological step, RZW thus assumed that the magnitude of the average current density j_{coh} in the direction of the electric field under coherent conditions in the presence of the grating can be modeled by a series resistor model of local resistivities or inverse conductivities given by

$$\frac{j_{coh}(\Lambda, L_1 + L_2)}{E} = \sigma_{av}(\Lambda) = \frac{\Lambda}{\int_0^\Lambda \frac{dx}{\sigma(x)}} = \sigma(L_1 + L_2)\sqrt{1 - A^2}. \tag{7.19}$$

A problem with this approach is that, as j must be constant, $E(x)$ must oscillate if $\sigma(x)$ oscillates in contradiction to the assumption of no space charge and a constant E.

RZW also suggested that a lock-in technique may be used to determine the parameter β that, as will be shown in the following, is related to the diffusion length and is defined by RZW by

$$\beta(\Lambda) = \frac{U_{coh}(\Lambda)}{U_{inc}(\Lambda)}, \tag{7.20}$$

at a given grating period. Here $U_{coh}(U_{inc})$ denotes the lock-in amplifier (LIA) signal under coherent (incoherent) beam conditions. The LIA detects the difference in the currents with respect to the current density j_1 under the bias level of the beam L_1. The polarization change of 90° of L_1 together with the unchanged chopped L_2 results in a comparison of $j_{coh}(\Lambda, L_1 + L_2)$, under coherent condition, with $j_{inc}(\Lambda, L_1 + L_2)$, under incoherent condition. In terms of current densities, the parameter β is thus given by

$$\beta(\Lambda) = \frac{U_{coh}}{U_{inc}} = \frac{j_{coh}(\Lambda, L_1 + L_2) - j_1(\Lambda, L_1)}{j_{inc}(\Lambda, L_1 + L_2) - j_1(\Lambda, L_1)}. \tag{7.21}$$

The link between the experimentally determined β and the diffusion length L is adjusted by an approximation of the current densities with the assumed and also typically observed power-law dependence of the photocurrent density $j_{ph} \propto G^\gamma$

and the condition that $G_2/G_1 \ll 1$. The G terms can then be eliminated with, for example, $j_{\mathrm{inc}}(\Lambda, L_1 + L_2) - j_{\mathrm{inc}}(\Lambda, L_1) \propto (G_1 + G_2)^{\gamma} - (G_1)^{\gamma}$ and $j_{\mathrm{coh}}(\Lambda, L_1 + L_2)$ from Equation 7.19 so that $\beta(\Lambda)$ reads

$$\begin{aligned}\beta(\Lambda) &= \frac{[(1 + G_2/G_1)^{\gamma}\sqrt{1 - A^2} - 1]}{[(1 + G_2/G_1)^{\gamma} - 1]} \\ &\approx \frac{(1 + \gamma G_2/G_1)[1 - 2(\gamma\gamma_0\gamma_{\mathrm{g}})^2 G_2/G_1] - 1}{\gamma G_2/G_1} \approx 1 - 2\gamma(\gamma_0\gamma_{\mathrm{g}})^2, \end{aligned} \tag{7.22}$$

where the quadratic terms in G_2/G_1 have been neglected in the last step. Substituting γ_{g} from Equation 7.18 yields

$$\beta(\Lambda) = 1 - \frac{2Z}{\left[1 + \left(\frac{2\pi L}{\Lambda}\right)^2\right]^2} \tag{7.23}$$

with $Z = \gamma\gamma_0^2$.

7.2.3.1 Evaluation Schemes

Equation 7.23 is the central equation of the SSPG analysis: The data sets of the measured β values at different positions Λ can be analyzed with the fit function $\beta(\Lambda)$ and the two fit parameters: the diffusion length L and a fit parameter Z. While L has a physical meaning, the parameter Z is just a fit parameter. However, it can be evaluated for a self-consistency check of the analysis and the measured β data. From the Z value and the separate experimental determination of γ and γ_{d}, the grating quality factor γ_0 can be calculated. It should be "close to 1."

Balberg *et al.* [7] suggested rearranging the data according to a linear form as

$$\frac{1}{\Lambda^2} = \left[\frac{Z^{1/2}}{(2\pi L)^2}\right]\left[\frac{2}{(1-\beta)}\right]^{1/2} - (2\pi L)^{-2}, \tag{7.24}$$

with the ordinate values $1/\Lambda^2$ and the abscissa values $[2/(1-\beta)]^{1/2}$. The diffusion length L can be read from the extrapolation to the abscissa or from the fit parameters for the straight line.

In our laboratory it has been customary to plot the values related to the measured β as $(1-\beta)^{-1/2}$ on the ordinate scale by

$$(1-\beta)^{-1/2} = \left[(2Z)^{-1/2}\left(\frac{1}{L}\right)^2\right]\left(\frac{2\pi}{\Lambda}\right)^2 + (2Z)^{-1/2}. \tag{7.25}$$

This kind of linear plot was also used by Nicholson [19].

The advantage of any linear plot is that a disagreement from the theoretical expectation may more easily be identified by deviations from the linear behavior. Ambipolarity is not obeyed by charge separation under high electric fields [21], which can also be identified from a concave instead of a linear shape of the graph according to Equation 7.24. It is then still possible to evaluate the ambipolar diffusion length from portions of the data set. Any super- or sublinear behavior depends, of course, on the plot specification with respect to abscissa and ordinate

values. Balberg and Weisz [22] analyzed the measurement data for the identification of nonambipolarity under low-field conditions.

For identifying the effect of surface recombination, the rearrangement according to

$$\left[\frac{2}{(1-\beta)}\right]^{-1/2} = \left[\frac{L^2}{Z^{1/2}}\right]\left(\frac{2\pi}{\Lambda}\right)^2 + (Z)^{-1/2} g_s^2(\Lambda), \tag{7.26}$$

was suggested [18], where $g_s(\Lambda)$ is a function which is 1 for negligible surface recombination and which decreases with increasing Λ. In a linear plot, $g_s(\Lambda)$ thus takes effect at large ordinate values so that L can still be determined from the β data at shorter values of Λ. In the case of surface recombination, there is a sublinear increase in the plot.

7.2.4 More Detailed Analyses

Analyses of the SSPG method are available which give a more detailed account by including the effects of the dark conductivity, of traps, E at low and high values, and the aspect of space charge. They also relate, in more detail, the measured L with the minority-carrier ($\mu\tau$) product.

7.2.4.1 Influence of the Dark Conductivity

In a following paper [3], RZW also took into account the effect of the underlying dark conductivity σ_d. The introduction of σ_d in Equation 7.17 yields a slightly modified version of Equation 7.23.

With the dark-conductivity coefficient γ_d, given by

$$\gamma_d = \frac{\sigma_{ph}}{\sigma_{ph} + \sigma_d}, \tag{7.27}$$

Equation 7.23 reads

$$\beta(\Lambda) = 1 - \frac{2\gamma\gamma_d\gamma_0^2}{[1 + (2\pi L/\Lambda)^2]^2} = 1 - \frac{2Z}{[1 + (2\pi L/\Lambda)^2]^2}, \tag{7.28}$$

where now $Z = \gamma\gamma_d\gamma_0^2$. Formally, the fit functions (Equations 7.23 and 7.28) with the two fit parameters L and Z are the same.

7.2.4.2 Influence of Traps

In the original RZW approach, assumptions have been made. Especially with respect to semiconductors with band tails, it will be necessary to introduce the contributions of the trapping states and of the trapped charge. This is often accomplished by the introduction of effective or drift mobilities in which the reduction in mobility through the trapping and emission processes is expressed. We denote the reference to the total charge by a capital letter of the index so that

the drift mobilities read

$$\mu_{\mathrm{N}} = \mu_{\mathrm{n}} \frac{n}{N},$$
$$\mu_{\mathrm{P}} = \mu_{\mathrm{p}} \frac{p}{P}, \tag{7.29}$$

with the total density N and P. A ratio θ_{n},

$$N = n + n_{\mathrm{t}},$$
$$\frac{n}{N} = \theta_{\mathrm{n}}, \tag{7.30}$$

can be defined with the trapped electron density n_{t} and with a corresponding relation for the holes.

Poisson's equation then takes the form

$$\frac{1}{e}\frac{\mathrm{d}E}{\mathrm{d}x} = \frac{P - N}{\varepsilon\varepsilon_0}, \tag{7.31}$$

where the right-hand side is zero under charge neutrality with $N = P$.

The effective diffusion coefficient D_{N} may be introduced via the condition

$$\frac{kT}{e\mu_{\mathrm{n}}}\frac{\mathrm{d}n}{\mathrm{d}x} = D_{\mathrm{N}}\frac{\mathrm{d}N}{\mathrm{d}x}, \tag{7.32}$$

which yields [3]

$$D_{\mathrm{N}} = \frac{kT}{e\mu_{\mathrm{n}}}\left(\theta_{\mathrm{n}} + N\frac{\mathrm{d}\theta_{\mathrm{n}}}{\mathrm{d}N}\right), \tag{7.33}$$

where k is the Boltzmann constant and T is the temperature.

The ambipolar diffusion equation with $\Delta N = \Delta P$ and a common lifetime τ_{R} reads

$$\overline{D_{\mathrm{NP}}}\frac{\mathrm{d}^2\Delta N}{\mathrm{d}x^2} - \frac{\Delta N}{\tau_{\mathrm{R}}} + \Delta G(x) = 0, \tag{7.34}$$

which is similar to Equation 7.11. The ambipolar diffusion coefficient $\overline{D_{\mathrm{NP}}}$ is a rather complicated construct (see Equation B6 of Ritter *et al.* [3]). For Boltzmann statistics, $\overline{D_{\mathrm{NP}}} = 2(kT/e)\mu_N\mu_P/(\mu_N + \mu_P)$. It is noted that the parameters $\tau_{\mathrm{R}} = \tau_{\mathrm{n}}/\theta_{\mathrm{n}} = \tau_{\mathrm{p}}/\theta_{\mathrm{p}}$ and $\overline{D_{\mathrm{NP}}}$ contain the common response of the total electron and hole contributions and thus pertain to the ensemble of free and trapped carriers.

Upon inspection of the diffusion equation (Equation 7.34), the diffusion length L is defined by

$$L = \sqrt{\overline{D_{\mathrm{NP}}}\tau_{\mathrm{R}}}. \tag{7.35}$$

The same $\beta(\Lambda, \mathrm{L})$ function as in Equation 7.28 results from the analysis.

An effective lifetime t_θ is defined by Balberg [10] who obtains

$$L = \sqrt{2D_\theta t_\theta}, \tag{7.36}$$

with the effective diffusion coefficient D_θ. It can be shown that $\overline{D_{\mathrm{NP}}}\tau_{\mathrm{R}} = 2D_\theta t_\theta$.

7.2.4.3 Minority-Carrier and Majority-Carrier Mobility-Lifetime Products

To relate the diffusion length L with the individual mobilities and the individual lifetimes and their products of Equations 7.8 and 7.9, we rewrite $\overline{D_{\mathrm{NP}}}$ and τ_{R} according to

$$L = \sqrt{\overline{D_{\mathrm{NP}}}\tau_{\mathrm{R}}} = \sqrt{2\frac{kT}{e}\frac{\mu_{\mathrm{n}}\tau_{\mathrm{n}}\mu_{\mathrm{p}}\tau_{\mathrm{p}}}{\mu_{\mathrm{n}}\tau_{\mathrm{n}}+\mu_{\mathrm{p}}\tau_{\mathrm{p}}}}. \tag{7.37}$$

We can then associate either the electrons or the holes with the majority and minority carriers. Writing $(\mu\tau)_{\mathrm{min}} = \mu_{\mathrm{min}}\tau_{\mathrm{min}}$ and $(\mu\tau)_{\mathrm{maj}} = \mu_{\mathrm{maj}}\tau_{\mathrm{maj}}$ with the free-carrier mobilities μ_{min} and μ_{maj} and the free-carrier recombination lifetimes τ_{maj} and τ_{min} embraces the respective mobilities and lifetimes. The corresponding equation for L is

$$L = \sqrt{2\frac{kT}{e}\frac{(\mu\tau)_{\mathrm{min}}(\mu\tau)_{\mathrm{maj}}}{(\mu\tau)_{\mathrm{min}}+(\mu\tau)_{\mathrm{maj}}}}. \tag{7.38}$$

For the case that $(\mu\tau)_{\mathrm{min}} \ll (\mu\tau)_{\mathrm{maj}}$, Equation 7.38 takes the form

$$(\mu\tau)_{\mathrm{min}} \approx \frac{e}{2kT}L^2, \tag{7.39}$$

which allows the separate determination of $(\mu\tau)_{\mathrm{min}}$. As a rule of thumb, a room-temperature value of $L = 200$ nm corresponds to $(\mu\tau)_{\mathrm{min}} = 8\times10^{-9}$ cm^2/V.

The factor of 2 stems from the common contribution of the full electron and hole densities in an intrinsic-type semiconductor, with $n \gg n_0$, $p \gg p_0$, to the recombination rate. This relation is also deduced independently without SSPG background for the surface photovoltage experiment or collection lengths in solar cells [23]. If the aforementioned inequality is not met, the respective two unknowns $(\mu\tau)_{\mathrm{min}}$ and $(\mu\tau)_{\mathrm{maj}}$ can only be determined with the additional photoconductivity measurement and

$$\sigma_{\mathrm{ph}} = eG[(\mu\tau)_{\mathrm{min}}+(\mu\tau)_{\mathrm{maj}}]. \tag{7.40}$$

Equations 7.38 and 7.40 with the two unknowns allow the $(\mu\tau)_{\mathrm{min}}$ and $(\mu\tau)_{\mathrm{maj}}$ determination but no straightforward correlation whether the electrons or the holes are the majority/minority carriers.

In an analysis based on solutions for the free-carrier densities, Shah *et al.* [24] deduce the relation

$$L = \sqrt{C\frac{kT}{e}\frac{(\mu\tau)_{\mathrm{min}}(\mu\tau)_{\mathrm{maj}}}{(\mu\tau)_{\mathrm{min}}+(\mu\tau)_{\mathrm{maj}}}}, \tag{7.41}$$

which is similar to Equation 7.38. Here, C is a sample-dependent factor between 1 and 2 which depends on the photogeneration-rate dependence of the excess-carrier densities. For n-type a-Si:H samples, Shah *et al.* [25] estimate $C \approx 1$ so that a discrepancy of a factor of 2 exists in relation with Equation 7.39. For G-independent lifetimes, C can be shown to be equal to 2.

The factor 2 of Equation 7.39 also appears in the treatment by Schmidt and Longeaud [16] who suggest to fit Equation 7.28 and apply Equation 7.39 for an apparent $(\mu\tau)_{\mathrm{min}}^{\mathrm{app}}$ which can then be corrected.

Abel *et al.* [15] derive the relation

$$\beta(\Lambda) = 1 - 2\gamma \frac{1 + \left(\frac{2\pi}{\Lambda} \left(2\frac{kT}{e} (\mu\tau)_p \frac{\mu_n \tau_d^{rel}}{(\mu\tau)_n} \right)^{1/2} \right)^2}{\left[1 + \left(2\pi \left(\frac{kT}{e} \left[2(\mu\tau)_p + \mu_n \tau_d^{rel} \right] \right)^{1/2} / \Lambda \right)^2 + \left(2\pi \left(\frac{kT}{e} \left[(\mu\tau)_p \mu_n \tau_d^{rel} \right]^{1/2} \right)^{1/2} / \Lambda \right)^4 \right]^2}, \tag{7.42}$$

simplified for the case that electrons are the majority carriers and that the E-related drift terms can be neglected. If the term ${}_n\tau_d^{rel}$ with the effective dielectric relaxation time τ_d^{rel} can be neglected, because $\tau_d^{rel} = (n/N)\tau_d \ll \tau_d$, Equation 7.42 reduces to the RZW relation (Equation 7.23) combined with Equation 7.39 and $(\mu\tau)_{min} = (\mu\tau)_p$, including the factor of 2.

Hattori *et al.* [14] suggest using additional information from frequency-dependent lifetime measurements for a correction of L from the RZW analysis.

7.3 Experimental Setup

Figure 7.3 sketches two of the possible arrangements for the measurements of the β parameter as a function of the grating period Λ. The two beams hit the sample S in the gap between the electrodes. In Figure 7.3a the sample is moved on a linear stage to change the angle between the two beams split by the beam splitter BS. The mirrors M_1 and M_2 are rotated according to the sample position. The half-wave retardation plate H is positioned in the strong beam, alternatively placed between BS and M_1, in order to rotate the polarization. If H was in the weak beam, chopped by the chopper C, a photogeneration-rate change by H-rotation, e. g., from change

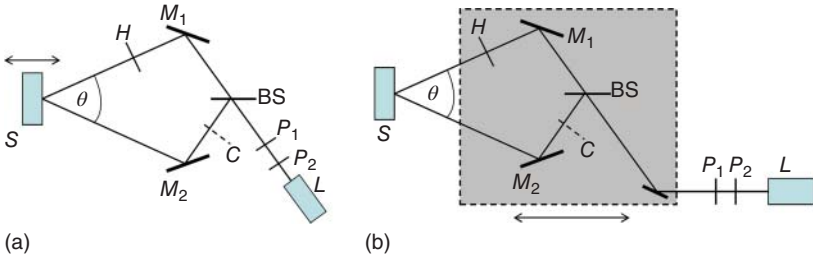

Figure 7.3 Schematics of experimental setups. The double arrows indicate that the sample is moved in (a) and an optical table is moved in (b) in order to change the angle between the two beams. (The setup of (b) has been devised by C. Longeaud and R. Brüggemann at LGEP, Paris, and at the University of Oldenburg.)

in reflection, would directly enter into the measured signal. In the strong beam, any intensity changes from the rotation of H would only change the light bias slightly. The optional polarization filters define the polarization and can also be used for a variation of ϕ by rotation of the polarizer P_2, keeping P_1 fixed.

The linear polarization is typically changed from 0° to +90° or −90°. A change from −45° to +45° can also be used in order to reduce the polarization-dependent reflection variations of L_1. A change of reflection upon rotating the polarization of L_1 is usually not taken further into consideration as it only slightly changes the bias level.

Figure 7.3b is different through the movement of an optical table on which most of the optical elements are arranged. The sample S is fixed, which gives a different option for the cryostat, compared with Figure 7.3a. The advantage here is that the length of the light path is almost the same for every Λ.

Arrangements with one perpendicular beam can also be found in the literature. Niehus and Schwarz [26] achieve long Λ by introducing an additional beam splitter. One beam is transmitted and the second beam is reflected on the beam splitter surface close to the other's transmission position which defines small angles θ.

A glass prism was employed by Nowak and Starczewska [27], while a compact goniometer-like setup is used at Utrecht University where the sample is rotated with no linear movement involved [28].

For T-dependent measurements, a suitable cryostat is incorporated into the setups. One should check that the grating quality factor is not reduced by the influence of the cryostat window or additional vacuum pump-related vibrations. For very thin samples, a cold finger with a hole may be helpful as a beam dump for the transmitted light.

The photocurrent is typically measured by an LIA. The photocurrents under coherent and incoherent illumination conditions for Equation 7.21 could also be measured in the steady state, for example, by an electrometer, but usually the LIA measurements will result in lower experimental errors.

Figure 7.4 sketches a strategy for the alignment of the two beams if their diameters are smaller than the electrode length. After adjusting L_1 and L_2 independently horizontally for maximum photocurrent signal, the vertical position must be optimized for overlap. A slight mismatch in the vertical direction may be difficult to assess by inspection with the eye. However, better alignment can be achieved by adjustment of the vertical position of L_2, as indicated by the double arrow in Figure 7.4a, and by monitoring the photocurrent or the LIA signal under coherent illumination. Best overlap is achieved when the LIA signal shows a minimum for maximum interference, as sketched in Figure 7.4b if β is positive.

For negative β, the phase shift of 180° must be taken into consideration. Depending on the experimenter's and the LIA options, the negative values of the real part or the amplitude can be maximized in this case.

One can always make a consistency check for the fitting results for L and Z. As pointed out in the literature [7, 18], the determined value of the fit parameter Z should be reasonable when comparing its value with $Z = \gamma\gamma_d\gamma_0^2$ of Equation 7.29 with the experimentally determined γ and γ_d and a grating quality factor γ_0 close

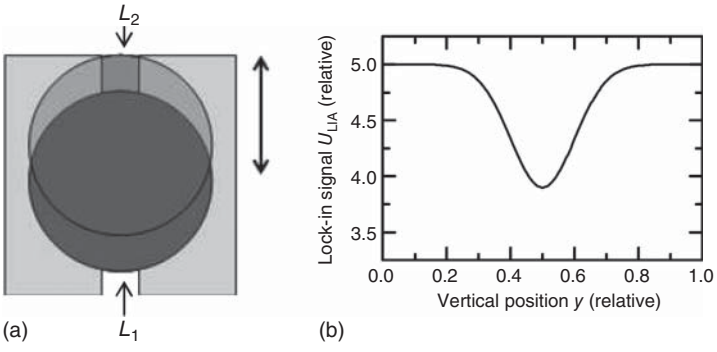

Figure 7.4 Schematic of the adjustment of L_1 and L_2 between the electrodes, (a). L_1 is fixed. The vertical movement of the lightly shaded L_2 results in the typical signal at the LIA, sketched in (b). The position of minimal signal results in optimized overlap, shown here for the Λ range with positive β.

to 1. During the measurements, a check of an approximately constant $j_{inc}(\Lambda)$ or LIA signal $U_{inc}(\Lambda)$ at the different grating periods is helpful. For the different measurement positions, the measured β data should decrease with increasing Λ. It may also be helpful initially, after having setup the experiment, to compare the β values measured with two different setups in order to check the data [29, 30].

7.4 Data Analysis

The experimental results comprise a set of values of the parameter β measured at a number of grating periods Λ. The (Λ, β) data can be evaluated according to one of the schemes from Equations 7.23–7.28. A comparison of the evaluation methods is discussed in [31]. Figure 7.5 illustrates graphical representations for long and short L. Through the large value for $L = 200$ nm and $Z = 0.8$, the β values in Figure 7.5a cover a wide range and do not even reach the limit $1-2Z = -0.6$ for long Λ. The β values with $Z = 0.1$ cover only a small range between 0.8 and 1 for $L = 200$ and 20 nm. This makes a precise L-determination difficult. There is almost no variation in β for $L = 20$ nm, even for $Z = 0.8$. Ritter *et al.* [3] consider that $L \approx 20$ nm can just be determined as a lower limit. It must be possible to measure at least some variation in β at the shortest experimental Λ to determine L. It is noted that results for determining β for $\Lambda < 500$ nm are difficult to achieve experimentally.

Figure 7.5b with the linear plots shows that the two cases for $Z = 0.1$ can be more easily distinguished compared to Figure 7.5a, but it has been pointed out [31] that any small variation in the large β values would lead to a large error because of the $(1 - \beta)$ term in the denominator of the linear plots.

The two full lines for $L = 20$ nm and the two dashed lines for $L = 200$ nm extrapolate to the same ordinate value, respectively, which represents L. Figure 7.5b has

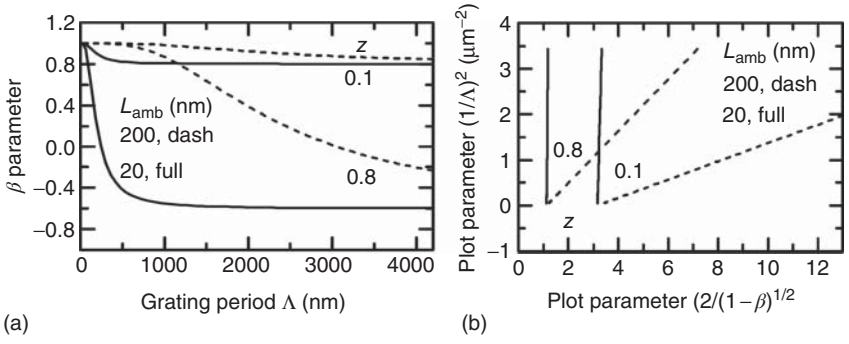

Figure 7.5 Analytical $\beta - \Lambda$ plot (a) and linear plot (b) for $L = 200$ and 20 nm and $Z = 0.1$ and 0.8. The β values are almost constant for $L = 20$ nm (a). The almost vertical lines of the data points correspond to $L = 20$ nm (b).

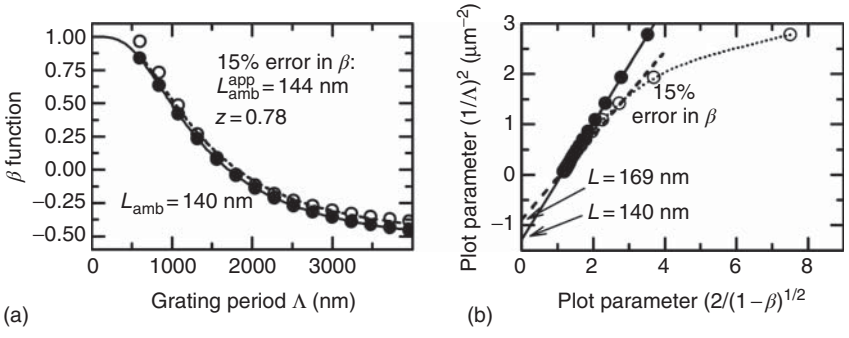

Figure 7.6 The symbols represent artificial measurement data (full symbols are ideal). A 15% error is imposed on β for $\Lambda > 500$ nm (upward shift, $L = 140$ nm, $Z = 0.8$, open symbols). The dashed curves show the fits in (a) and (b).

thus very steep straight lines for $L = 20$ nm because the ordinate intercept is a large negative value.

Figure 7.6 illustrates the effect of measurement errors in the determination of β. It is more likely that errors in the beam adjustments yield β values that are rather too large due to incomplete overlap or nonideal grating. The artificial data points with the full circles in Figure 7.6 represent the ideal $\beta(\Lambda)$ variations in Figure 7.6a and b with $L = 140$ nm. The open symbols show the shift by increasing β by 15%.

The dashed curve in Figure 7.6a shows the fit to the open symbols and is only slightly different compared to the full line which is the fit of the full symbols. Because a constraint in a (β, Λ) fit is given by $\beta(\Lambda = 0) = 1$ according to Equation 7.28, the fitting procedure according to Equation 7.28 is found to be less affected by too large a value of β at short Λ. The apparent L of 144 nm is close to the original value of 140 nm as is Z with $Z = 0.78$ instead of 0.8.

The nominally straight line in Figure 7.6b shows some curvature in the range of short Λ, that is, large ordinate values (open symbols). Restricting the linear fit in the range of abscissa values <4 results in a diffusion length $L = 169$ nm, which is

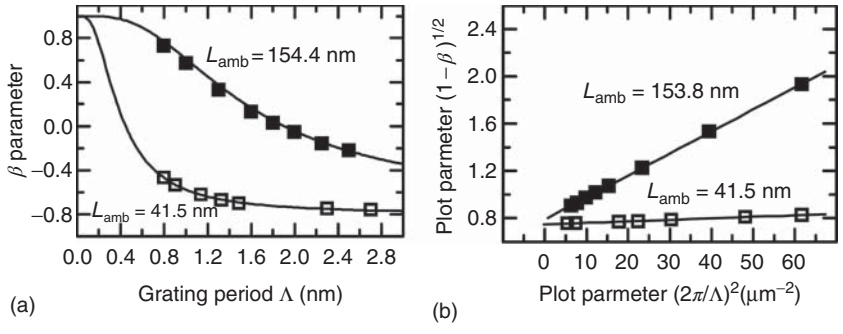

Figure 7.7 Experimental data in different representations in (a) and (b) for two undoped a-Si:H samples. There are data points with both negative and positive values of β.

quite a large discrepancy of 29 nm. Only if one restricts the fitting to a more linear region with abscissa values <2, an apparent value of $L < 150$ nm is achieved.

Figure 7.7 shows typical experimental data of a device quality and a high-defect a-Si:H sample in the $\beta(\Lambda)$ plot (Figure 7.7a) and in a linear plot (Figure 7.7b). There is very good agreement between the two evaluation schemes with $L = 154$ nm (and a good value of $\gamma_0 = 0.95$ from Z and γ) and $L = 41.5$ nm.

For the evaluation of the experimental data, the following analysis may be instructive. With say m values of (β, Λ), one can estimate the error in L by performing several fits with variations of $(m-1)$ or $(m-2)$ data points to determine the variation in L values. Single measurement data should be skipped if too large a disagreement between the two evaluation schemes is observed. Especially for large values of β, any of the linear plots with the term $(1-\beta)$ in the denominator suffers from error enhancement and should be handled with caution.

It is noted at the end of this section that the sample alignment in the SSPG experiment is quite robust against small variations in the sample orientation. Experimental tests in our laboratory have shown that such rotations of the sample, or the sample holder by a few degrees, do not lead to a significant variation in the measured β values. Unintentional misalignment of the sample is thus not severe. Any larger misalignment is easy to spot by the eye.

Substantial intentional rotation of the sample leads to a decrease of the effect of the modulation of the photocarrier grating. Balberg *et al.* [7] rotated the sample by 90° so that the photocurrent is parallel to the interference fringes. Meeting the requirements of the photocurrent measurement under incoherent conditions in this way, no half-wave plate is needed.

7.5 Results

This chapter presents and reviews results on a number of thin-film semiconductors. The limited and partially personal account that is given for each

semiconductor is restricted to the photoconductive properties in relation to the SSPG method, that is, the minority-carrier properties in the steady state. As these are linked with the majority-carrier properties, the latter will also be discussed in comparison when appropriate. Typically, Equation 7.39 is used to convert the experimental SSPG-derived L into $(\mu\tau)_p$.

7.5.1 Hydrogenated Amorphous Silicon

Hydrogenated amorphous silicon (a-Si:H) has been in the focus of SSPG applications since the early work by Ritter *et al.* [3, 32]. The main issues in a-Si:H-related research with SSPG deal with the identification of deficiencies of the method, the physics of recombination and its relation to the DOS, the effect of doping on the excess-carrier properties, and the role of the E_f position in general.

7.5.1.1 Temperature and Generation Rate Dependence

The monotonous decrease of $(\mu\tau)_p$ with decreasing T [33] in Figure 7.8 is a signature in a-Si:H. To demonstrate at least one example of numerical-modeling results of the photoresponse and the minority-carrier properties in particular, Figure 7.8b shows the simulated $(\mu\tau)_p$ that can roughly reproduce the experimental findings of Figure 7.8a [34].

At any T, $(\mu\tau)_p$ drops with increasing G. There has been some controversy in the literature about the consequences of the G dependence with respect to DOS models in the band gap of a-Si:H. Balberg and Lubianiker [35] suggested that one correlated dangling bond (DB) level is not sufficient to explain the experimental data while the Neuchatel group [36] pointed out that a proper balancing of charge

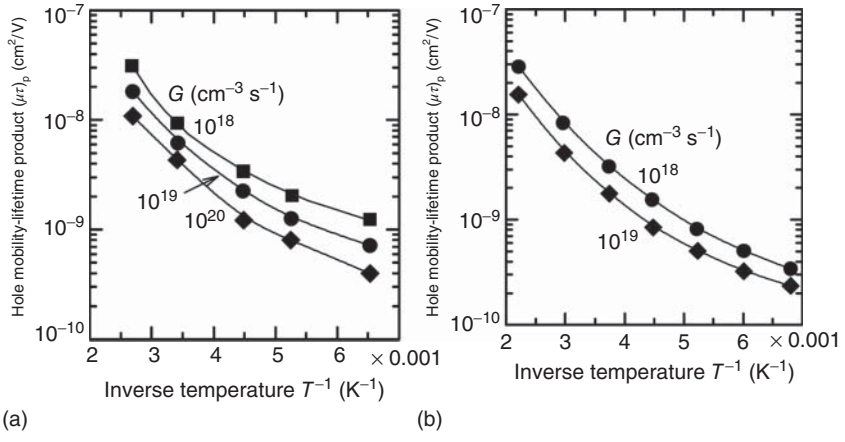

Figure 7.8 (a) T dependence of $(\mu\tau)_p$ of an undoped a-Si:H sample at different G. (After Ref. [33].) (b) Numerical simulation results with a free-hole mobility of 1 cm^2/(V s) which reproduce the decrease of $(\mu\tau)_p$ with decreasing T and increasing G. (After Ref. [34].)

in one correlated DB and in the band-tail states can also explain the experimental findings.

7.5.1.2 Surface Recombination

The application of Equation 7.26 is illustrated in Figure 7.9 with data, measured with a HeNe laser and an Ar laser [18]. From the β versus Λ plot in Figure 7.9a, the identification of deviations is not so easy, given that there is always an experimental error. A reduced L will be determined if all the circle data points are taken for the fit.

In Figure 7.9b, there is a curvature in the data for the Ar illumination especially in contrast to the linear behavior of the squares. It is noted that the β data at the longer Λ coincide from the two measurements. This means, as noted by Haridim *et al.*, that L can be determined in the usual way for longer Λ. For the HeNe measurements with the larger absorption depth, all data points are suitable.

Haridim *et al.* also determined the two surface recombination velocities at the air/a-Si:H and the a-Si:H/substrate by illuminating from the air and substrate sides and by fitting the experimental data with Equation 7.26 with suitable $g_s(\Lambda)$.

7.5.1.3 Electric Field Influence

In the early publications on SSPG, there has been concern with respect to the electric field limitations in two ways: E modulation due to space charge and phase shift in the modulation of $n(x)$ and $p(x)$ because E pulls these apart. Accounts on the "high"-E onset, the value at which such a deviation from the ideal behavior according to Equation 7.28 occurs, have been summarized by Schmidt and Longeaud [16]. They point out that depending on the theoretical approach, different E values for the low-field limit have been determined. Experimentally, one may study the β dependence on E and take a constant value of β as an indicator of

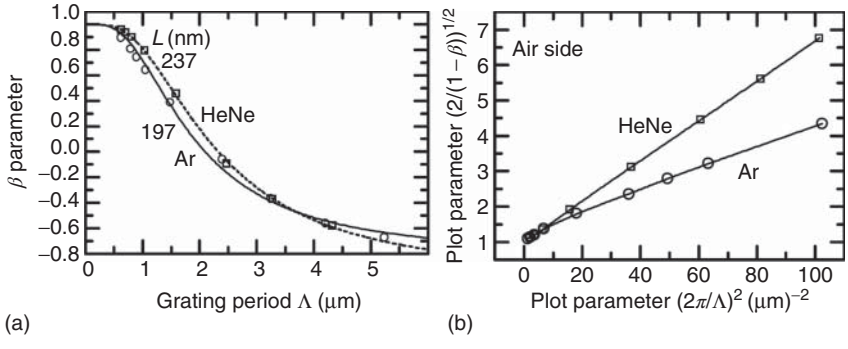

Figure 7.9 Digitized data from Haridim *et al.* [18] in a β versus Λ plot (a) and in the linear representation (b). The β values were determined under HeNe and under Ar illumination. A force fitting of the data results in a 40 nm different L of the latter. Note that at small abscissa and ordinate values in (b), the data points of the two kinds of experiments fall together.

the low-field limit. At higher field values, a drift length has been determined from the field dependence [3, 21].

The analysis by Abel *et al.* [15], which includes both the effect of space charge and external electric field, has been applied to study the β dependence on Λ and E. Good agreement could be achieved between the experiment and the fit function (Equation 7.42) for $\beta(\Lambda, E)$ [37]. Accounts on the effective dielectric relaxation time and space charge could thus be given.

7.5.1.4 Fermi Level Position

The aim of SSPG measurements with a-Si:H films was also to add complimentary information from the minority-carrier side to the majority-carrier properties from σ_{ph}.

Shortly after the SSPG proposal, the properties of boron-doped films were studied by Yang *et al.* [6]. Low-concentration boron doping was shown to lead to an increase in L. With higher doping level, L dropped drastically. These results were interpreted as a change in the minority-carrier type. For the higher doping levels and the shift of E_f toward the valence band edge, the electrons become the minority carriers, and the increasing defect density upon doping then leads to the reduction in L. An important observation was a benefit in L at small shifts of E_f toward midgap which was thought to be beneficial for the net *i*-layer carrier collection in a-Si:H-based *pin* solar cells.

In undoped a-Si:H with $E_c - E_f$ in the range of 0.65–0.75 eV, where $E_c - E_f$ is calculated from $E_c - E_f = kT \ln(\sigma_0/\sigma_d)$, with the prefactor $\sigma_0 = 150-200\,\Omega^{-1}\,\mathrm{cm}^{-1}$, the $(\mu\tau)_{maj}$ values are typically a factor of 50–100 higher than the $(\mu\tau)_{min}$ [17]. There is thus quite a variation in E_f for undoped a-Si:H samples, and this variation expresses itself in a variation in the mobility-lifetime products [38]. Typically, $(\mu\tau)_{maj}$ increases with decreasing $E_c - E_f$ [39] accompanied by a decrease in $(\mu\tau)_{min}$. This anticorrelated behavior is also seen when the electrons are the minority carriers in p-type a-Si:H, where $(\mu\tau)_{min}$ decreases with increasing $E_c - E_f > 0.8$ eV [36, 40–42].

In a field-effect configuration, the Fermi level in the conduction channel can be changed by the gate voltage. This effect was exploited by Balberg and Lubianiker [35] and also Schwarz *et al.* [43] to study the E_f-dependent variation of σ_{ph} and L without being hampered by a doping-dependent increase in the DB density.

7.5.1.5 Defects and Light-Induced Degradation

The time-dependent decrease of the photocurrent upon illumination is a signature of many a-Si:H films. Any increase in the defect density should also have an influence on the minority-carrier properties so that SSPG may reveal the underlying recombination physics. It is known in the literature that E_f shifts toward midgap upon light soaking [44]. In view of the aforementioned Fermi level-related discussion it is illustrative to point out the possibility that L may increase upon light soaking, as illustrated in Figure 7.10 [45]. Here, light soaking with the concomitant increase in $E_c - E_f$ leads to an increase in L while new defects are being created.

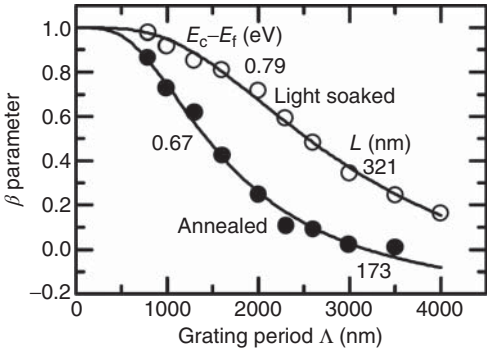

Figure 7.10 Increase of L upon light soaking of a-Si:H. (After C.D. Abel [45].)

Defects become less negative and thus less attractive for hole capture so that the minority-carrier properties improve.

It is usually reported that L does not change in the first hours of light soaking – with different interpretations. Wang and Schwarz [46] reported that for a-Si:H films with a low DB density, the main recombination channel is via band-tail states. An increase in the DB density upon illumination thus does not lead to a drop in L in the early stage of degradation.

The interpretation by the Neuchatel group [21] was different in that they assumed that the main recombination channel is via DB. Because of conversion of the newly created DB into *neutral* DB, they argued that these become then ineffective as the main capture process of holes is capture by *negatively* charged DB.

Sakata *et al.* [42] argued that errors have been made in the determination of L by Wang and Schwarz [46] because the measured L by SSPG should be corrected. They maintain that there is a drop in the true diffusion length also in the initial stages of degradation.

With respect to the influence of the $(\mu\tau)$ products on E_f and the reported change of E_f upon light soaking, it appears necessary to always monitor the dark current too. This has been done by Morgado [47] who determined $(\mu\tau)_p$, $(\mu\tau)_n$, and the E_f variation upon light soaking and also annealing.

7.5.1.6 Thin-Film Characterization and Deposition Methods

SSPG has also been applied in order to characterize the samples that were deposited by newly developed deposition methods, for example, hot-wire chemical vapor deposition (HWCVD). For example, Mahan *et al.* [48], Unold *et al.* [49], Lubianiker *et al.* [50], and Feenstra *et al.* [51] presented SSPG results with L in the range of 150–170 nm for typical device quality a-Si:H. These values were correlated with deposition parameters and, for example, with the hydrogen content of the films. Under specific deposition conditions, the so-called polymorphous silicon can be prepared. It has been shown to exhibit

favorable minority-carrier properties [52], which enhances the red response in solar cells.

7.5.2 Hydrogenated Amorphous Silicon Alloys

One of the first reports on the application of SSPG was given by Bauer *et al.* [4] on hydrogenated amorphous silicon–germanium (a-$Si_{1-x}Ge_x$:H) alloys. Typically, both σ_{ph} as a signature of the majority carriers and L as a signature of the minority carriers decrease with increasing x, but they are affected in a different way by the concomitant shift of E_f toward midgap.

Abel and Bauer [53] report on a decrease in $(\mu\tau)_p$ with increasing x in the range of x up to about 0.43. The values of $(\mu\tau)_p$ stay $>10^{-9}$ cm^2/V, that is, L of about 100 nm. Fölsch *et al.* [54] report slightly larger values in this x-range. These authors report a strong decrease in L for x larger than 0.5 at which the combination of increasing σ_d and decreasing σ_{ph} also makes L very difficult to measure.

The data by Gueunier *et al.* [55] on polymorphous silicon–germanium alloys (pm-$Si_{1-x}Ge_x$:H) range between 100 and 130 nm, that is, $(\mu\tau)_p$ between about 10^{-9} and 3×10^{-9} cm^2/V, for $x \leq 0.35$ at which the optical gap E_{04} (defined as the energy where the absorption coefficient $\alpha\,(E_{04}) = 10^4$ cm^{-1}) was 1.5 eV. Light soaking was shown to only affect the majority-carrier $(\mu\tau)_n$ product. An L-value of 100 nm was reported by Bhaduri *et al.* [56] in the range $x = 0.4-0.5$.

Li *et al.* [57] determined L for hydrogenated amorphous silicon carbide films (a-$Si_{1-x}C_x$:H) of different band gaps and different feedstock gases. These authors find a correlation between the increase of L and better solar-cell properties. They make it clear though that, as mentioned previously, the sole value of L may not be the only indicator of the defect density of a sample. They deduce from the complementary σ_d- and σ_{ph}-results that E_f-related occupation of defects may have lead to higher values of L of some of their a-$Si_{1-x}C_x$:H samples.

Mohring *et al.* [33] reported on the T-dependent and G-dependent $(\mu\tau)$ products of majority and minority carriers in optimized a-$Si_{1-x}C_x$:H with an optical band gap up to 1.95 eV. For the alloys, there is a monotonous decrease of $(\mu\tau)_p$ with decreasing T, similar to the findings for a-Si:H. At any T, $(\mu\tau)_p$ decreases with increasing alloy content which has been related by Mohring *et al.* to the previous observation of increased DB density with increasing x. For a-$Si_{1-x}C_x$:H with a band gap of 1.94 eV, the room-temperature values for $(\mu\tau)_p$ were $(1.2)\times10^{-9}$ cm^2/V and about a factor of 10 higher for $(\mu\tau)_n$.

7.5.3 Hydrogenated Microcrystalline Silicon

The application of SSPG to hydrogenated microcrystalline silicon (μc-Si:H) is rather straightforward on the one hand as, for example, sample geometries and relevant absorption coefficients are not significantly different. On the other hand,

there are some obstacles involved because of the typically higher σ_d and some possible effect of surface roughness, which reduces γ_0.

Goerlitzer *et al.* [58] and Droz *et al.* [59] find smaller Z in μc-Si:H because of the small ratio σ_{ph}/σ_d. With respect to optical scattering, Z was shown to increase after polishing the rough surface of μc-Si:H samples [32].

The T dependence of $(\mu\tau)_p$ of μc-Si:H was studied by Brüggemann and Kunz [60] and also by Balberg [61]. For the analysis, they also performed numerical simulations in order to correlate the experimental and simulation results. Other work is devoted to relating L with the deep defect density [29, 62–64] and the crystalline volume fraction and the deposition technique [29, 65].

There are indications that transport is inhomogeneous in μc-Si:H with respect to the transport path parallel or perpendicular to the film growth direction [66].

7.5.4
Hydrogenated Microcrystalline Germanium

Badran *et al.* [67] reported on L in microcrystalline germanium (μc-Ge:H). Because L was quite short, the conclusion was that μc-Ge:H appears suitable for diode applications as a sensor, as was demonstrated previously, under reverse bias but not as a solar cell.

7.5.5
Other Thin-Film Semiconductors

Thin-film chalcopyrite semiconductors were characterized soon after the SSPG method was proposed. Balberg *et al.* [5] determined the majority- and minority-carrier properties of $CuGaSe_2$ thin films. Here, electrons are the minority carriers for which the authors determined L of 115 nm. The reliability of the data was increased by a self-consistency check by comparing the fit parameters Z from SSPG and γ from σ_{ph}. From the intensity dependence of $(\mu\tau)_p$, it was concluded that there is a sharp drop in the DOS close to the band edges – in contrast to a-Si:H.

Menner *et al.* [68] report SSPG results on $CuGaSe_2$ thin films and determined the highest L for a Cu/Ga ratio at 0.95, that is, close to the stoichiometric point. SSPG measurements in the Cu-rich region were impossible because of the high σ_d. Menner *et al.* also aimed at revealing inhomogeneity in the growth process by application of a laser with a short absorption depth and by illumination from either the air/film or the substrate/film side. They concluded that a better crystal structure exists close to the substrate.

Belevich and Makovetskii [69] give an account of L measurements in polycrystalline p-type $CuInSe_2$. From their analysis they determine G-dependent minority-electron diffusion lengths between 360 and 420 nm, decreasing with increasing G. They relate the values of L to the dimension of the crystallites in the polycrystalline film.

Generally, it is noted that one should not be too optimistic with respect to the application of SSPG to the Cu(In,Ga)Se_2 system as it may be hampered by the large σ_d in Cu(In,Ga)Se_2, for which Zweigart *et al.* [70] determined L for some chemical compositions only. Because the dark current activation energy is also low, a decrease of T will only help if σ_{ph} does not decrease too much as well.

7.6 DOS Determination

Schmidt and Longeaud [16] developed an analysis of SSPG with emphasis on the DOS determination at the quasi-Fermi energy of the majority carrier. For the energy scale, the quasi-Fermi energy can be shifted by a variation of T or G so that a scan in energy can be performed. The experimentally determined DOS values are given by a combination of photocurrent and SSPG measurements. The application of the method was demonstrated on a-Si:H [16] and μc-Si:H [71].

7.7 Data Collection by Automization and Combination with Other Experiments

In line with the aim to collect complementary measurements on the same sample and ideally on the same spot and to measure reliably with high throughput for routine characterization of larger numbers of samples, Longeaud [72] developed a compact ($90 \times 60\,cm^2$), fast, reliable, and easy-to-use SSPG system that incorporates additional photoelectronic characterization techniques. For SSPG, a motor drives a mobile mirror which directs the laser beam to a number of adequately positioned fixed mirrors, each of which defines one grating period. For the modulation and for measurement in lock-in technique, an electro-optical modulator (EOM) is used [72, 73]. The combination of EOM and polarizer offers the versatility to combine SSPG together with steady-state photoconductivity (SSPC) and modulated photocurrent (MPC) experiments so that mobility-lifetime products and DOS information, the latter from both SSPG and MPC, can be obtained. As the sample position is fixed, a small cryostat may be introduced so that temperature-dependent measurements can also be achieved.

7.8 Summary

We have given an account of the SSPG method with some emphasis on the setup, on the necessary and complementary measurement steps, and on consistency checks with the aim to obtain a more complete picture on the excess-carrier properties. The evaluation of the experimental data on the basis of the RZW approach provides the basis of determining L when the experiment is performed under the

necessary condition of small modulation depth at low E, short enough dielectric relaxation time, and sufficiently high photocurrent values with distinctly different values between $(\mu\tau)_{min}$ and $(\mu\tau)_{maj}$. A simple relationship between L and $(\mu\tau)_{min}$ can then be applied.

Reference has been made to alternative and additional analyses by Ritter *et al.* [3], Balberg [10, 11], Li [12], Hattori *et al.* [14], Abel *et al.* [15], Schmidt and Longeaud [16], and Shah *et al.* [24] which cover possible shortcomings, limitations, and additional aspects. Some of the relevant literature on the applications of SSPG on thin-film amorphous and microcrystalline semiconductors and on chalcopyrite and other semiconductors was sketched. The examples illustrate the potential of the method for the characterization of the photoelectronic properties of thin-film semiconductors.

Acknowledgment

The author is grateful to M. Bayrak and O. Neumann for some measurements.

References

1. Ritter, D., Zeldov, E., and Weiser, K. (1986) Steady-state photocarrier grating technique for diffusion length measurement in photoconductive insulators. *Appl. Phys. Lett.*, **49**, 791.
2. Ritter, D. and Weiser, K. (1986) Ambipolar drift-length measurement in amorphous hydrogenated silicon using the steady-state photocarrier grating technique. *Phys. Rev. B*, **34**, 9031.
3. Ritter, D., Weiser, K., and Zeldov, E. (1987) Steady-state photocarrier grating technique for diffusion-length measurement in semiconductors – theory and experimental results for amorphous-silicon and semi-insulating GaAs. *J. Appl. Phys.*, **62**, 4563.
4. Bauer, G.H., Nebel, C.E., and Mohring, H.-D. (1988) Diffusion lengths in a-SiGe:H and a-SiC:H alloys from optical grating technique. *Mater. Res. Soc. Symp. Proc.*, **118**, 679.
5. Balberg, I., Albin, D., and Noufi, R. (1989) Mobility-lifetime products in $CuGaSe_2$. *Appl. Phys. Lett.*, **54**, 1244.
6. Yang, L., Catalano, A., Arya, R.R., and Balberg, I. (1990) Effect of low-level boron doping and its implication to the nature of gap states in hydrogenated amorphous-silicon. *Appl. Phys. Lett.*, **57**, 908.
7. Balberg, I., Delahoy, A.E., and Weakliem, H.A. (1988) Self-consistency and self-sufficiency of the photocarrier grating technique. *Appl. Phys. Lett.*, **53**, 992.
8. Liu, J.Z., Li, X., Roca i Cabarrocas, P., Conde, J.P., Maruyama, A., Park, H., and Wagner, S. (1990) *Ambipolar Diffusion Length in a-Si-H(F) and a-Si,Ge-H,F Measured with the Steady-State Photocarrier Grating Technique.* Conference Record 21st IEEE Photovoltaic Specialists Conference, p. 1606.
9. Ritter, D., Zeldov, E., and Weiser, K. (1988) Ambipolar transport in amorphous-semiconductors in the lifetime and relaxation-time regimes investigated by the steady-state photocarrier grating technique. *Phys. Rev. B*, **38**, 8296.
10. Balberg, I. (1990) The theory of the photoconductance under the presence of a small photocarrier grating. *J. Appl. Phys.*, **67**, 6329.
11. Balberg, I. (1991) Theory of the small photocarrier grating under the application of an electric-field. *Phys. Rev. B*, **44**, 1628.

12. Li, Y.M. (1990) Phototransport under the presence of a small steady-state photocarrier grating. *Phys. Rev. B*, **42**, 9025.
13. Hubin, J., Sauvain, E., and Shah, A.V. (1989) Characteristic lengths for steady-state transport in illuminated, intrinsic a-Si:H. *IEEE Trans. Electron Devices*, **36**, 2789.
14. Hattori, K., Okamoto, H., and Hamakawa, Y. (1992) Theory of the steady-state-photocarrier-grating technique for obtaining accurate diffusion-length measurements in amorphous-silicon. *Phys. Rev. B*, **45**, 1126.
15. Abel, C.-D., Bauer, G.H., and Bloss, W.H. (1995) Generalized theory for analytical simulation of the steady-state photocarrier grating technique. *Philos. Mag. B*, **72**, 551.
16. Schmidt, J.A. and Longeaud, C. (2005) Analysis of the steady-state photocarrier grating method for the determination of the density of states in semiconductors. *Phys. Rev. B*, **71**, 125208.
17. Brüggemann, R. (1998) Steady-state photoconductivity in a-Si:H and its alloys, in *Properties of Amorphous Silicon and Its Alloys* (ed T. Searle), INSPEC, London, p. 217.
18. Haridim, M., Weiser, K., and Mell, H. (1993) Use of the steady-state photocarrier-grating technique for the study of the surface recombination velocity of photocarriers and the homogeneity of hydrogenated amorphous-silicon films. *Philos. Mag. B*, **67**, 171.
19. Nicholson, J.P. (2000) Fresnel corrections to measurements of ambipolar diffusion length. *J. Appl. Phys.*, **88**, 4693.
20. Blakemore, J.S. (1987) *Semiconductor Statistics*, Dover, New York.
21. Sauvain, E., Shah, A., and Hubin, J. (1990) *Measurement of the Ambipolar Mobility-Lifetime Product and Its Significance for Amorphous Silicon Solar Cells.* Conference Record 21st IEEE Photovoltaics Specialists Conference, 1–8 May 1990, IEEE, Piscataway, NJ, Orlando, p. 1560.
22. Balberg, I. and Weisz, S.Z. (1991) Identification of nonambipolar transport in the application of a photocarrier grating to hydrogenated amorphous-silicon. *Appl. Phys. Lett.*, **59**, 1726.
23. Moore, A.R. (1984) *Semiconductors and Semimetals*, vol. **21** (ed. J.I. Pankove), Academic, Orlando, Part C, p. 239.
24. Shah, A., Sauvain, E., Hubin, J., Pipoz, P., and Hof, C. (1997) Free carrier ambipolar diffusion length in amorphous semiconductors. *Philos. Mag. B*, **75**, 925.
25. Shah, A., Hubin, J., Sauvain, E., Pipoz, P., Beck, N., and Wyrsch, N. (1993) Role of dangling bond charge in determining $\mu\tau$ products for a-Si:H. *J. Non-Cryst. Solids*, **164–166**, 485.
26. Niehus, M. and Schwarz, R. (2006) Diffusion lengths in GaN obtained from steady state photocarrier gratings (SSPG). *Phys. Status Solidi C*, **3**, 2103.
27. Nowak, M. and Starczewska, A. (2005) Steady-state photocarrier grating method of determining electronic states parameters in amorphous semiconductors. *J. Non-Cryst. Solids*, **351**, 1383.
28. Feenstra, K.F. (1998) Hot-wire chemical vapour deposition of amorphous silicon and the application in solar cells. PhD thesis. Utrecht University.
29. Okur, S., Gunes, M., Goktas, O., Finger, F., and Carius, R. (2004) Electronic transport properties of microcrystalline silicon thin films prepared by VHF-PECVD. *J. Mater. Sci. – Mater. Electron.*, **15**, 187.
30. Balberg, I., Epstein, K.A., and Ritter, D. (1989) Ambipolar diffusion length measurements in hydrogenated amorphous silicon. *Appl. Phys. Lett.*, **54**, 2461.
31. Brüggemann, R. (1998) Improved steady-state photocarrier grating in nanocrystalline thin films after surface-roughness reduction by mechanical polishing. *Appl. Phys. Lett.*, **73**, 499.
32. Ritter, D., Zeldov, E., and Weiser, K. (1987) Diffusion length measurements in a-Si-H using the steady-state photocarrier grating technique. *J. Non-Cryst. Solids*, **97**, 571.
33. Mohring, H.D., Abel, C.D., Brüggemann, R., and Bauer, G.H. (1991) Characterization of high electronic quality a-SiC-H films by mu-tau products for electrons and holes. *J. Non-Cryst. Solids*, **137**, 847

and (1997) Erratum. *J. Non-Cryst. Solids*, **210**, 306.

34. Brüggemann, R. (1993) Modellierung von Photoleitung in amorphen Halbleiterfilmen und pin-Strukturen (in German). PhD thesis. Philipps-Universität Marburg.
35. Balberg, I. and Lubianiker, Y. (1993) Evidence for the defect-pool model from induced recombination level shifts in undoped a-SiH. *Phys. Rev. B*, **48**, 8709.
36. Hubin, J., Shah, A.V., Sauvain, E., and Pipoz, P. (1995) Consistency between experimental-data for ambipolar diffusion length and for photoconductivity when incorporated into the standard defect model for a-Si:H. *J. Appl. Phys.*, **78**, 6050.
37. Brüggemann, R. and Badran, R.I. (2004) Electric-field dependence of photocarrier properties in the steady-state photocarrier grating experiment. *MRS Symp. Proc.*, **808**, 133.
38. Brüggemann, R. (2003) Parameters for photoelectronic characterisation and the Fermi level in amorphous silicon. *Thin Solid Films*, **427**, 355.
39. Anderson, W.A. and Spear, W.E. (1977) Photoconductivity and recombination in doped amorphous silicon. *Philos. Mag.*, **36**, 695.
40. Brüggemann, R., Abel, C.-D., and Bauer, G.H. (1992) *Implications of the Defect Pool Model for the Simulation of a-Si:H Solar Cells*. Proceedings of the 11th E.C. Photovoltaics Solar Energy Conference, 12–16 October 1992, Montreux, Switzerland (ed. L. Guimaraes, W. Palz, C. Reyff, H. Kiess, and P. Helm). Harwood Academic Publishers, Chur, p. 676.
41. Böhme, T., Kluge, G., Kottwitz, A., and Bindemann, R. (1993) Mobility-lifetime products of a-Si:H prepared at high deposition rate with triethylboron. *Phys. Status Solidi (a)*, **136**, 171.
42. Sakata, I., Yamanaka, M., and Sekigawa, T. (1997) Relationship between carrier diffusion lengths and defect density in hydrogenated amorphous silicon. *J. Appl. Phys.*, **81**, 1323.
43. Schwarz, R., Wang, F., and Reissner, M. (1993) Fermi-level dependence of the ambipolar diffusion length in amorphous-silicon thin-film transistors. *Appl. Phys. Lett.*, **63**, 1083.
44. Beyer, W. and Mell, H. (1996) Comparative study of light-induced photoconductivity decay in hydrogenated amorphous silicon. *J. Non-Cryst. Solids*, **198–200**, 466.
45. Abel, C.D. (1993) Photoelektronische Charakterisierung amorpher Halbleiter, PhD thesis, Universität Stuttgart, Germany.
46. Wang, F. and Schwarz, R. (1992) High-temperature annealing behavior of $\mu\tau$ products of electrons and holes in a-Si:H. *J. Appl. Phys.*, **71**, 791.
47. Morgado, E. (2002) Light-soaking and annealing kinetics of majority and minority carrier mobility-lifetime products in a-Si:H. *J. Non-Cryst. Solids*, **299**, 471.
48. Mahan, A.H., Carapella, J., Nelson, B.P., Crandall, R.S., and Balberg, I. (1991) Deposition of device quality, low H content amorphous silicon. *J. Appl. Phys.*, **69**, 6728.
49. Unold, T., Reedy, R.C., and Mahan, A.H. (1998) Defects in hot-wire deposited amorphous silicon: results from electron spin resonance. *J. Non-Cryst. Solids*, **227**, 362.
50. Lubianiker, Y., Balberg, I., Fonseca, L., and Weisz, S.Z. (1996) Study of recombination processes in a-Si:H by the temperature dependence of the two carriers phototransport properties. *MRS Symp. Proc.*, **420**, 777.
51. Feenstra, K.F., Werf, C.H.M., Molenbroek, E.C., and Schropp, R.E.I. (1997) Deposition of device quality amorphous silicon by hot-wire CVD. *MRS Symp. Proc.*, **467**, 645.
52. Kleider, J.P., Gauthier, M., Longeaud, C., Roy, D., Saadane, O., and Brüggemann, R. (2002) Spectral photoresponses and transport properties of polymorphous silicon thin films. *Thin Solid Films*, **403–404**, 188.
53. Abel, C.D. and Bauer, G.H. (1993) Evaluation of the steady-state photocarrier grating technique with respect to a-Si:H and its application to a-SiGe:H alloys. *Prog. Photovoltaics*, **1**, 269.
54. Fölsch, J., Finger, F., Kulessa, T., Siebke, F., Beyer, W., and Wagner, H. (1995)

Improved ambipolar diffusion length in a-$Si_{1-x}Ge_x$:H alloys for multi-junction solar cells. *MRS Symp. Proc.*, **377**, 517.

55. Gueunier, M.E., Kleider, J.P., Brüggemann, R., Lebib, S., Cabarrocas, P.R.I., Meaudre, R., and Canut, B. (2002) Properties of polymorphous silicon–germanium alloys deposited under high hydrogen dilution and at high pressure. *J. Appl. Phys.*, **92**, 4959.
56. Bhaduri, A., Chaudhuri, P., Williamson, D.L., Vignoli, S., Ray, P.P., and Longeaud, C. (2008) Structural and optoelectronic properties of silicon germanium alloy thin films deposited by pulsed radio frequency plasma enhanced chemical vapor deposition. *J. Appl. Phys.*, **104**, 063709.
57. Li, Y.M., Fieselmann, B.F., and Catalano, A. (1991) Novel feedstocks for a-SiC:H films and devices. Conference Record 22nd IEEE Photovoltaic Specialists Conference, 7–11 Oct 1991, Las Vegas, IEEE, Piscataway, NJ, p. 1231–1235.
58. Goerlitzer, M., Beck, N., Torres, P., Meier, J., Wyrsch, N., and Shah, A. (1996) Ambipolar diffusion length and photoconductivity measurements on "midgap" hydrogenated microcrystalline silicon. *J. Appl. Phys.*, **80**, 5111.
59. Droz, C., Goerlitzer, M., Wyrsch, N., and Shah, A. (2000) Electronic transport in hydrogenated microcrystalline silicon: similarities with amorphous silicon. *J. Non-Cryst. Solids*, **266**, 319.
60. Brüggemann, R. and Kunz, O. (2002) Temperature dependence of the minority-carrier mobility-lifetime product for probing band-tail states in microcrystalline silicon. *Phys. Status Solidi B*, **234**, R16.
61. Balberg, I. (2002) A simultaneous experimental determination of the distribution and character of the two band tails in disordered semiconductors. *J. Optoelectron. Adv. Mater.*, **4**, 437.
62. Brüggemann, R. (2005) Mobility-lifetime products in microcrystalline silicon. *J. Optoelectron. Adv. Mater.*, **7**, 495.
63. Brüggemann, R., Brehme, S., Kleider, J.P., Gueunier, M.E., and Bronner, W. (2004) Effects of proton irradiation on the photoelectronic properties of microcrystalline silicon. *J. Non-Cryst. Solids*, **338–340**, 77.
64. Günes, M., Göktas, O., Okur, S., Isik, N., Carius, R., Klomfass, J., and Finger, F. (2005) Sub-bandgap absorption spectroscopy and minority carrier transport of hydrogenated microcrystalline silicon films. *J. Optoelectron. Adv. Mater.*, **7**, 161.
65. Okur, S., Günes, M., Finger, F., and Carius, R. (2006) Diffusion length measurements of microcrystalline silicon thin films prepared by hot-wire/catalytic chemical vapor deposition. *Thin Solid Films*, **501**, 137.
66. Svrcek, V., Pelant, I., Kocka, J., Fojtik, P., Rezek, B., Stuchlikova, H., Fejfar, A., Stuchlik, J., Poruba, A., and Tousek, J. (2001) Transport anisotropy in microcrystalline silicon studied by measurement of ambipolar diffusion length. *J. Appl. Phys.*, **89**, 1800.
67. Badran, R.I., Brüggemann, R., and Carius, R. (2009) Minority-carrier properties of microcrystalline germanium. *J. Optoelectron. Adv. Mater.*, **11**, 1464.
68. Menner, R., Zweigart, S., Klenk, R., and Schock, H.W. (1993) Ambipolar diffusion length in $CuGaSe_2$ thin-films for solar-cell applications measured by steady-state photocarrier grating technique. *Jpn. J. Appl. Phys.*, **1** (32), 45.
69. Belevich, N.N. and Makovetskii, G.I. (1994) Ambipolar diffusion and ambipolar carrier drift in $CuInSe_2$ films. *Semiconductors*, **28**, 988.
70. Zweigart, S., Menner, R., Klenk, R., and Schock, H.W. (1995) Application of the steady-state photocarrier grating technique for determination of ambipolar diffusion lengths in $Cu(In,Ga)(S,Se)_2$-thin films for solar cells. *Mater. Sci. Forum*, **173**, 337.
71. Souffi, N., Bauer, G.H., and Brüggemann, R. (2006) Density-of-states in microcrystalline silicon from thermally-stimulated conductivity. *J. Non-Cryst. Solids*, **352**, 1109.
72. Longeaud, C. (2013) An automated steady state photocarrier grating experiment. *Rev. Sci. Instrum.*, **84**, 55101.
73. Fath-Allah, A., Ventosinos, F., and Longeaud, C. (2014) An automated experiment for determination of thin film semiconductor transport parameters. *J. Phys. Conf. Ser.*, **558**, 012011.

Part III
Materials Characterization

Advanced Characterization Techniques for Thin Film Solar Cells, Second Edition.
Edited by Daniel Abou-Ras, Thomas Kirchartz, and Uwe Rau.

8
Absorption and Photocurrent Spectroscopy with High Dynamic Range

Thomas Christian, Mathias Müller, and Thomas Kirchartz

8.1
Introduction

Semiconductors used for thin-film photovoltaics often feature a smeared out absorption edge with a range of subgap features that can be attributed to their electronic density of states close to and below their optical band gap. Because the subgap electronic density of states and the steepness of the absorption edge can have a huge influence on the device performance of solar cells and other electronic devices, there is a need to study spectroscopically the absorption edge of these materials. This should be done ideally with a high dynamic range to have access also to weaker transitions below the main absorption edge. This chapter will introduce two of these techniques: the photothermal deflection spectroscopy (PDS) and the Fourier transform photocurrent spectroscopy (FTPS). While PDS is a purely optical technique that studies the absorption of a semiconductor film, FTPS probes photocurrents and therefore requires electrical contacts to perform the measurements.

One of the main reasons why the study of the absorption edge of layers for thin-film photovoltaics is particularly important is that the density of states of the typically used amorphous, nanocrystalline, or microcrystalline semiconductors has more features below the band gap than highly crystalline semiconductors such as wafer-based Si or GaAs would have. Figure 8.1 shows the schematic density of states of disordered semiconductors. In contrast to crystalline semiconductors, there are electronic states between valence and conduction band edge. The shallow states, which are close to the band edges, can be assigned to disorder, for example, in bonding angles. This disorder leads to so-called band-tail states that can be measured in spectroscopic absorption measurements as Urbach tails. Deep states as shown in Figure 8.1 are due to defect states, a classical example being a dangling Si bond in amorphous Si. Both types of subgap states will have

Advanced Characterization Techniques for Thin Film Solar Cells, Second Edition.
Edited by Daniel Abou-Ras, Thomas Kirchartz, and Uwe Rau.

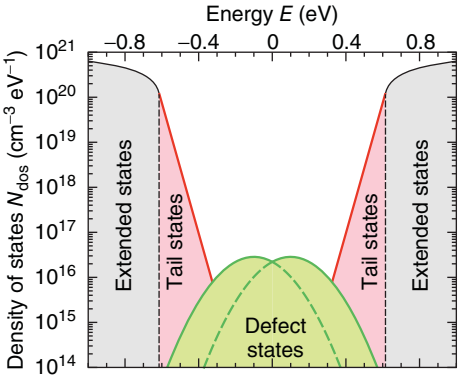

Figure 8.1 General band structure of density of electronic states in (disordered) semiconductors. Whereas highly ordered semiconductors are determined by the extended states only, disordered semiconductors are additionally influenced by localized states, the so-called tail and midgap defect states.

negative effects on charge transport and recombination; therefore, there is a need to characterize those states with transient or frequency-dependent methods such as admittance spectroscopy or time of flight as discussed in Chapters 4–6. However, there can also be optical transitions between these states that contribute to the absorptance or spectrally resolved photocurrent of an absorber layer or a solar cell.

The absorption coefficient

$$\alpha(E_\gamma) = \frac{C}{E_\gamma} \int n_o(E) n_u(E + E_\gamma) \mathrm{d}E \tag{8.1}$$

is the convolution of all initially occupied (n_o) with all unoccupied (n_u) states [1]. The photon energy is given by E_γ and the energy levels of the electronic states are given by E. The factor C depends on the refractive index and the momentum matrix elements. In the one-electron approximation, C is assumed to be constant for all optical transitions [1–3]. Figure 8.2 shows an example of α. The extended electronic states are above and below the conduction and valence band edge, respectively (see the gray-plotted areas in Figure 8.1). Transitions between these states are responsible for the maximum of light absorption labeled (bb) in Figure 8.2. Transitions between the tail states and between tail states and extended states are labeled (tt) and (tb/bt) in Figure 8.2, respectively. Electronic states deep in the band gap mostly have an amphoteric nature. In amorphous silicon, such states originate from dangling silicon–silicon bonds, which can be saturated by hydrogenation of the amorphous silicon. Transitions between these amphoteric deep defect states and the extended band and the localized band-tail states can be observed from (db/bd) and (dt/td) in Figure 8.2, respectively.

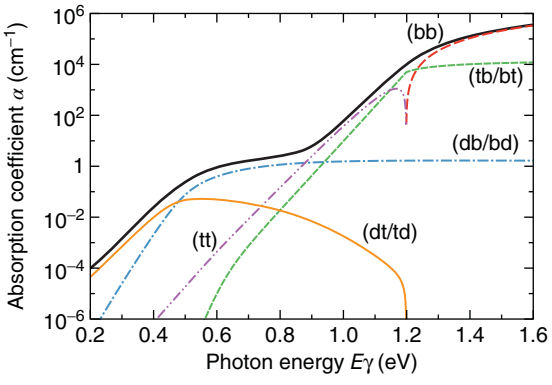

Figure 8.2 Calculated absorption coefficient (α) from convolution of different electronic states. Transitions are (bb) valence band → conduction band, (tb/bt) valence band → conduction band tail and valence band tail → conduction band, (db/bd) valence band → dangling bonds and dangling bonds → conduction band, (tt) valence band tail → conduction band tail, and (dt/td) valence band tail → dangling bonds and dangling bonds → conduction band tail.

8.2 Photothermal Deflection Spectroscopy

The simplest method to determine the absorptance of a semiconductor film is to measure its transmittance T and reflectance R, from which the absorptance

$$a(E_\gamma) = 1 - R(E_\gamma) - T(E_\gamma) \tag{8.2}$$

can be calculated as a function of photon energy E_γ.

The disadvantage of the method described earlier is that very low values of the absorptance cannot reliably be measured as a difference between two large numbers. If the reflection and transmission are measured below the band gap of the semiconductor, their sum will be close to one and already small errors in either R or T would lead to measured values of the absorptance that may be higher or lower than in reality by a large factor or even be negative. In order to be able to measure absorptances with a high dynamic range, it is necessary to find a way of directly measuring absorption without having to calculate it from the sum of other terms.

PDS is one way of overcoming the limitations of normal transmission-reflection measurements. PDS makes use of the fact that absorbed light causes a semiconductor film to warm up because absorbed light creates phonons by nonradiative recombination and thermalization of photogenerated carriers. In order to measure the temperature changes due to light absorption sensitively, one can make use of the mirage effect that also causes optical illusions, for example, in deserts.

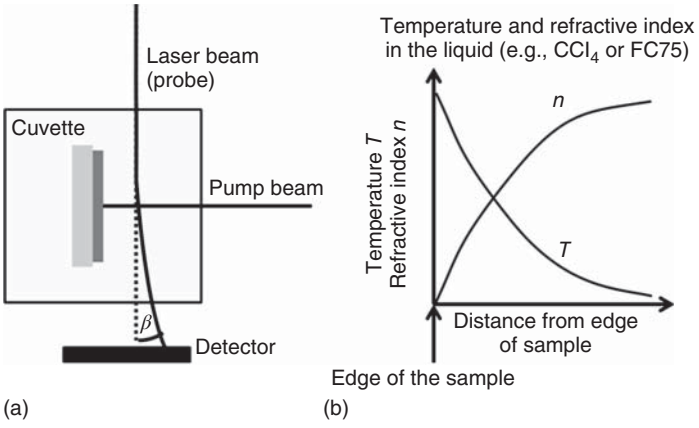

Figure 8.3 (a) Schematic of the PDS measurement principle. The monochromatic pump beam excites the sample, whose temperature will then increase. Within the cuvette, the temperature of the liquid (CCl_4 or FC75) will decrease with increasing distance from the sample surface, while its refractive index will do the opposite (b). Thus, the probe beam will be deflected away from the sample with an angle β that can be correlated to the amount of absorption by the probe beam.

The refractive index of media depends on temperature with higher temperatures typically leading to lower refractive indices. Thus, if a sample is illuminated with monochromatic light and at the same time placed in a cuvette filled with a liquid (typically CCl_4 or FC75), the refractive index of the liquid will change as a function of position as shown in Figure 8.3. In order to probe the refractive index gradient, a laser beam parallel to the sample surface can be used. This gradient in refractive index will lead to a deflection of the light beam away from the sample.

The angle β of the deflected light beam as shown in Figure 8.3 is detected using a quadrant detector. The change ΔV in voltage of the quadrant detector relative to the dc level V is proportional to the angle β [4], which is in turn proportional to the absorptance of the device and the power density of the monochromatic pump beam used to excite the sample [4, 5]. Thus, the measured signal $\Delta V/V$ from the position detector is directly proportional to the absorptance, and in order to determine the absorptance, the proportionality constant needs to be determined. One simple way of getting absolute values of the absorptance is now to measure the PDS signal over the spectral range accessible with the light source and monochromator and then to adjust the absolute value to a separately measured transmission and reflection measurement. Transmission and reflection measurements can also be included in the PDS setup as shown in Figure 8.4. Figure 8.5 shows an example for PDS measurements performed on microcrystalline and amorphous silicon layers on glass. The dynamic range of the measurement is about five orders of magnitude.

PDS has been used in photovoltaics mostly for disordered absorber layers as a means to study the absorption edge and subgap states. Jackson and Amer, for instance, used PDS to correlate defects seen in the subgap absorption spectra of

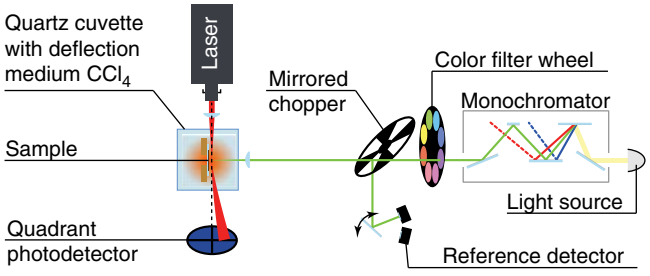

Figure 8.4 Schematic of the PDS setup.

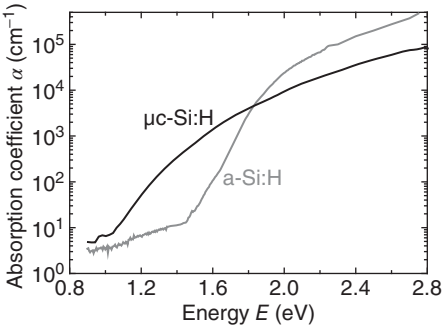

Figure 8.5 Example of PDS measurements of hydrogenated microcrystalline and amorphous silicon layers showing about five orders of magnitude dynamic range.

hydrogenated amorphous silicon with the defect density measured using electron-spin resonance measurements [6]. Also in the field of organic photovoltaics, PDS has been used frequently in order to study subgap states [7–10]. In the particular case of organics, the subgap features detected in PDS are usually transitions at the internal donor–acceptor interface which are often called charge-transfer state absorption. In particular, PDS has been used in combination with FTPS and luminescence spectroscopy to disprove the hypothesis of hot charge-transfer excitons being needed for charge separation in organic solar cells [9, 10].

8.3 Fourier Transform Photocurrent Spectroscopy

There are different ways of measuring spectrally resolved photocurrents of solar cells with a high dynamic range. In principle, this is possible with a normal quantum efficiency setup as described in Chapter 2 as long as a lock-in amplifier is used and filters are employed to suppress stray light sufficiently well for a high dynamic range. In a normal quantum efficiency setup with a grating monochromator, the illumination of the sample is done with a monochromatic light beam and the wavelength of this monochromatic light is scanned over the range of

wavelengths of interest [11]. A way of improving the signal-to-noise ratio is to measure the quantum efficiency of all wavelengths of interest at the same time using a Fourier spectrometer. The resulting technique of measuring spectrally resolved photocurrents and quantum efficiencies is called FTPS and is particularly suited for high dynamic range measurements [12, 13]. FTPS has been used in the past for a variety of purposes such as for the determination of the doping concentration in thin layers [14, 15]; the (*in situ*) study of degradation [16–19], thermal annealing [20], defects [13, 21–26], disorder [7, 19], and impurities [27]; the charge-transfer complex in bulk heterojunction photovoltaic cells [28–32]; the composition of nanocrystalline diamond films [33]; and the light scattering in silicon thin films [34].

The quantum efficiency

$$Q_e = \frac{\int_0^d f_c(z)G(z)\mathrm{d}z}{\phi} \tag{8.3}$$

depends on the charge carrier generation rate $G(z)$ and the collection probability $f_c(z)$ of charge carriers as a function of the position z (parallel to the surface normal). The corresponding flux of photons (per area, time, and energy interval) is given by ϕ. Since it is difficult to measure ϕ, the FTPS technique often measures a relative Q_e. Typically, the collection efficiency $f_c(z)$ is a function of position z. Thus, the shape of the quantum efficiency and the absorptance of a solar cell are typically different, except for photon energies where the generation rate $G(z)$ starts to become independent of z. This is the case for photon energies below the band gap, where the absorption coefficient–thickness product of the device becomes much smaller than one ($\alpha d << 1$). Thus, in particular for the quantum efficiencies below the gap that can be determined in FTPS measurements, the shape of the quantum efficiency will closely resemble the shape of the absorptance of the active layer.

8.3.1 FTIR Setup

The FTPS measurements usually use a common Fourier transform infrared (FTIR) spectrometer, which can be seen in Figure 8.6. Generally, an FTIR spectrometer needs three components, namely, a (i) light source, (ii) beam splitter, and (iii) light detector. To measure a spectrum, these three components have to match each other spectrally, that is, the beam splitter has to be transparent and the light detector has to be sensitive to the spectrum of the light source. A brief overview over the FTIR spectroscopy is also given in Refs. [35–37].

Different kinds of ***light sources*** exist. A tungsten lamp (up to 3000 K) in a quartz bulb is commonly used for the UV/VIS (visible) and near-infrared (NIR) range. A globar (silicon carbide, 1500 K) is used for medium-infrared (MIR) and far-infrared (FIR) illumination. Alternatively, a nickel-chromium or a Nernst lamp can be used, respectively. But instead of an internal light source, the optical inputs

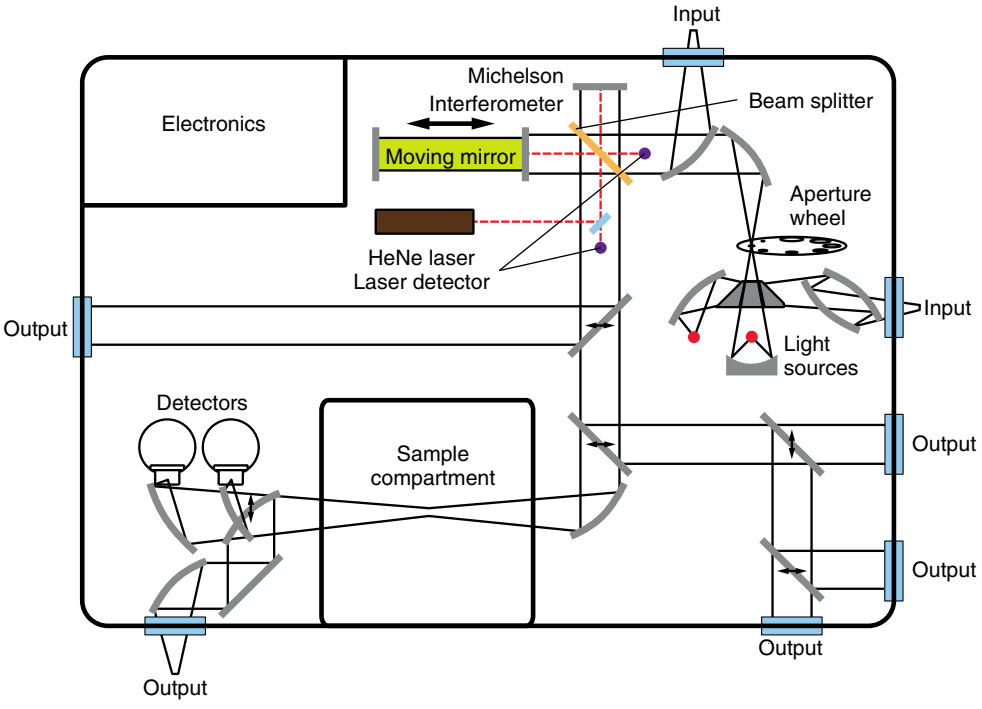

Figure 8.6 Sketch of Fourier transform infrared (FTIR) spectrometer. Such an FTIR spectrometer basically consists of a light source, a beam splitter for the Michelson interferometer, and a detector.

of an FTIR spectrometer allow for the use of any external light source. In case of FTPS, these optical inputs can be used for a more intense light source than the internal one. For the FTPS measurements of solar-cell applications, a UV/VIS, that is, a tungsten lamp, is the best choice.

The ***beam splitter*** is part of the central unit of an FTIR spectrometer, a Michelson interferometer. This interferometer consists of two mirrors and such a beam splitter, which ideally divides the incident light into two equal beams. One part transmits the beam splitter, while the other part is reflected, that is, a deflection of 90° as shown in Figure 8.6. The deflected beam hits a fixed mirror, while the transmitted beam hits a moving mirror. If the traveling distance of the moving mirror is x, the phase difference between both reflected light beams will be $2x$. For the UV/VIS and NIR region of the spectrum, beam splitters are made of coated SiO_2 (quartz) or CaF_2 (calcium fluoride). For the NIR and especially MIR region, beam splitters made of KBr (potassium bromide) are widely used.

To detect and control the position of the moving mirror, an (off-axis) laser beam is incident on the Michelson interferometer. A laser detector each at the entrance and the exit of the interferometer detects the interference of the laser while the mirror is moving. For a high precision of the positioning of the moving mirror, the laser needs to have a long coherence length. For this reason, a HeNe laser

(632.816 nm wavelength, 15802.4 cm^{-1} wavenumbers) is commonly used. For the normal use of an FTIR spectrometer, the mirror moves continuously forward and backward while the speed is kept constant. To ensure such a constant speed, the interference pattern of the laser (e.g., HeNe) is tried to keep in phase with a very precise oscillator. Technically, this is done by a so-called phase-locked loop.

The light beams exiting the Michelson interferometer, which interfere each other, are normally directed to the sample compartment. After passing the sample, the light beam hits an optical ***detector***. The detected signal is electrically gained and digitized to be used within a PC. Common digitalization depths are 16–24 bits. More enhanced FTIR spectrometers offer the opportunity to direct the beam paths to external optical outputs. This can be beneficial for FTPS for the purpose of measuring solar-cell modules, which do not fit the sample compartment. Also for the additional use of bias light for FTPS measurements or a probe scanning measurement, an external optical output can be beneficial. Note that in case of FTPS measurements, the sample coincides with the detector (see Section 8.3.3.1).

8.3.2 Data Processing

This section gives a brief overview of the processing of FTIR data. A further understanding of FTIR data processing is presented in a series by Herres and Gronholz [35–37]. Additionally, the textbooks [38–41] are recommended.

As mentioned earlier, the phase difference between two beams, which are split in the Michelson interferometer, is $2x$. This means that both light beams interfere constructively, if the optical retardation is a multiple of the wavelength λ, that is, if

$$2x = n\lambda, \tag{8.4}$$

where $n = 0, 1, 2, \ldots$. The interference pattern shows minima, that is, both beam paths interfere destructively, if

$$2x = \frac{n\lambda}{2}, \tag{8.5}$$

where $n = 1, 3, 5, \ldots$. This yields the general dependence of the measured signal (interferogram)

$$I(x) = S(\nu)\cos(2\pi\nu x) \tag{8.6}$$

of the intensity of a monochromatic line (S) as a function of the wavenumber ($\nu = 1/\lambda$), which is the inverse wavelength λ. This is outlined in Figure 8.7a, where in the upper part single interference patterns of light with three different wavelengths are shown. Every interference pattern separately corresponds to $I(x)$. By fitting Equation 8.6, one obtains the wavenumber (ν) and the wavenumber's corresponding intensity $I(\nu)$. Fitting all single interference patterns (for all wavenumbers) yields the spectrum, which is shown in Figure 8.7b. Since all interference patterns of all single light beams (single wavelengths) superimpose each other in

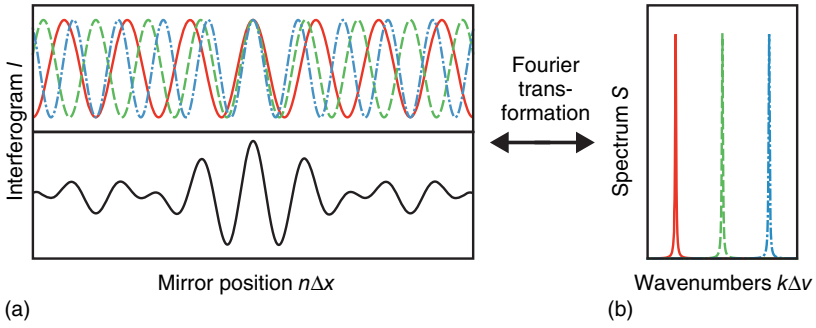

Figure 8.7 Sketch of Fourier transformation. (a) Light with different wavelengths (red, solid line; green, dashed line; blue, dash-dotted line) superimpose in the Michelson interferometer. This superposition yields an interferogram (*I*, black solid line) as it is measured with an FTIR spectrometer. (b) A Fourier transformation of the interferogram (*I*) then yields the spectrum (*S*).

the Michelson interferometer, the measured signal looks like the lower part in Figure 8.7a. This means that within an FTIR spectrometer, all wavelengths are measured in parallel. The fitting algorithm of the interferogram to yield the spectrum is the so-called Fourier transformation (FT). Generally, the FT determines the continuous different spectral components. However, since the interferogram is acquired at discrete points, the FT also has to be discrete. The spectrum

$$S(k\Delta\nu) = \sum_{n=0}^{N-1} I(n\Delta x)\mathrm{e}^{i2\pi \frac{nk}{N}} \tag{8.7}$$

is calculated via the discrete Fourier transformation (DFT), where N is the total number of acquired data points. Consequently, the continuous variables ν and x have been changed to $k\Delta\nu$ and $n\Delta x$, respectively. For each k, the sum over the whole interferogram multiplied with the sum of cosine and sine functions has to be calculated numerically. This multiplication leads to the highest values (Fourier coefficients) if the interference between the interferogram and the oscillating cosine and sine functions is highest. The spectral resolution (in wavenumbers)

$$\Delta\nu = \frac{1}{N\Delta x} \tag{8.8}$$

is directly related to the sample spacing in real space (Δx) and the total number of acquired data points (N). In fact, this means that the further the mirror in the Michelson interferometer moves, the higher the resolution, but in contrast, the longer the data acquisition time.

A real interferogram and its DFT, that is, its spectrum, are shown in Figure 8.8. It can be seen that the center burst in the interferogram (the point where the superposition of all light beams in the Michelson interferometer is highest) can be a very sharp peak with a high amplitude, i.e., the signal changes very fast. Additionally, the amplitude of the wings is small compared to the center burst, although these wings contain most of the useful information. This requires a high-frequency

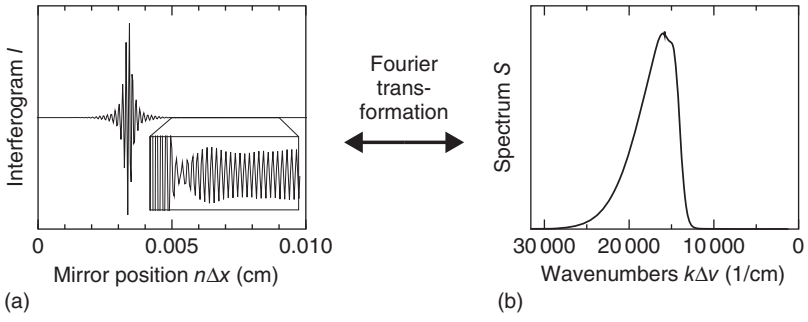

Figure 8.8 (a) Real interferogram and (b) spectrum after Fourier transformation.

bandwidth of the detector unit and a high bit depth for the analog-to-digital converter (ADC; see earlier). To gain a high-frequency bandwidth, the detector, the impedance converter, and even the ADC have to be well chosen.

Indeed, since the interferogram is reciprocally proportional to the spectrum, the narrower is the interferogram, the broader the spectrum, and vice versa. The amplitude of the interferogram center burst corresponds to the average spectral intensity, which can be derived from the inverse DFT.

The DFT is usually done by the software, which comes with an FTIR spectrometer. However, the software requires some parameters, which have to be set by the user. These parameters are (i) resolution, (ii) zero filling, (iii) undersampling, (iv) apodization, and (v) phase correction. The following sections give a brief overview over the meaning of these parameters.

8.3.2.1 Resolution in FTIR

As mentioned earlier (see Equation 8.8), the resolution is determined by the sampling distance (Δx) and the absolute number of sampling points (N), that is, the path length of the moving mirror in the Michelson interferometer. Figure 8.9 illustrates the relation between the spectrum in (a) and the corresponding interferogram in (b). The spectrum shows two sharp lines, which are separated

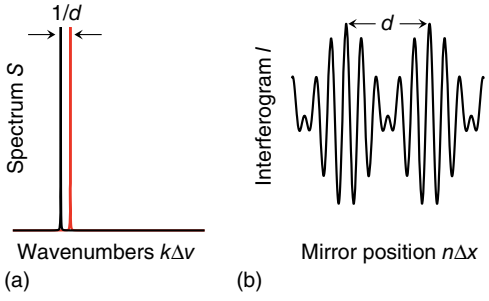

Figure 8.9 (a) Artificial spectrum, which consists of two Lorentzian peaks, which are separated by $1/d$ wavenumbers. (b) The two peaks from (a) produce repetitive patterns at a distance of d in the interferogram after Fourier transformation.

by $1/d$ wavenumbers. Due to this separation in the spectrum, the interferogram shows a periodic modulation pattern, which is repeated after a path length of d. This means that the closer both lines are, the greater is the distance between two repeated patterns in the interferogram. This fact is called the Rayleigh criterion.

Since the pathway in the Michelson interferometer in an FTIR and the sampling distance is limited by the wavelength of the internal laser, the resolution of an FTIR is finite. Common spectrometers have a resolution of $\Delta\nu \geq 0.2\,\mathrm{cm}^{-1}$. Quantum efficiency measurements of semiconductors, even highly ordered ones, do not need such high spectral resolution. A resolution of $\Delta\nu \approx 10\,\mathrm{cm}^{-1}$ for FTPS measurements is typically sufficient.

8.3.2.2 Zero Filling

Zero filling is a method to deal with the so-called picket-fence effect. Typical software for FT spectroscopy requires specifying the zero-filling factor (ZFF); therefore, we will briefly describe the picket-fence effect and the zero-filling method to compensate this effect, although the picket-fence effect is usually of minor importance for the specific application of FTPS.

The so-called picket-fence effect originates from the fact that the discrete FT only approximates the continuous FT. The data acquisition is performed at discrete sample points, which leads to an error if the interferogram contains frequencies which do not coincide with the frequency sample points ($k\Delta\nu$). In the worst case, someone could imagine that a frequency component lies exactly between two sample points. The resulting spectrum would then resemble the view through a picket fence. If the spectral components are broad enough (such as in FTPS) and spread over several sampling positions, this effect has little influence on the spectrum.

The zero-filling method to overcome the picket-fence effect adds zeros at the beginning or end of the interferogram before the DFT is performed. This increases the number of points in the interferogram, which therefore increases the number of points in the spectrum. The zero filling is equivalent to interpolating the spectrum, which therefore reduces the error and increases the spectral resolution [42, 43].

The influence of the zero filling is shown in Figure 8.10. The red solid line with the red open circles shows the absorption bands from water vapor without any zero filling, that is, $\mathrm{ZFF} = 1$. In comparison to this, the black solid line shows exactly the same measurement after a high zero filling of $\mathrm{ZFF} = 16$. The difference between both curves can be seen from the inset. While the spectrum without zero filling seems to look choppy, the zero-filled spectrum shows a quite smooth curve.

It should be noted that the measure of FTPS for solar-cell applications does not need any high ZFF. It is often recommended to chose at least $\mathrm{ZFF} = 2$ [35], since this procedure increases the signal-to-noise ratio by a factor of $\sqrt{2}$ [43]. Indeed, quantum efficiency spectra from semiconductors (as stated earlier) do not show very sharp and/or abrupt line shapes, even at very low sample temperatures.

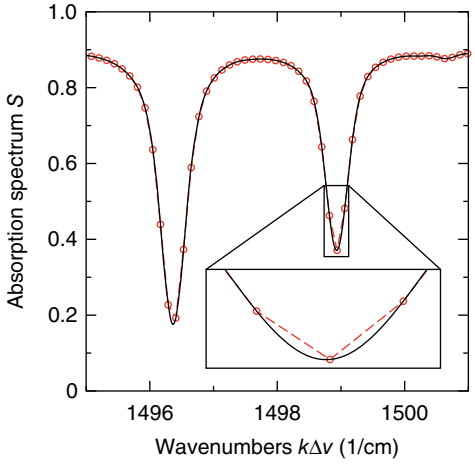

Figure 8.10 Spectra of sharp absorption bands from water vapor. Spectrum calculated with low zero filling ZFF = 1 (red dashed line with open circles), where the absorption bands look badly clipped, and spectrum calculated with high zero filling ZFF = 16 (black solid line).

8.3.2.3 **Undersampling**

The spectral range of an FTIR spectrometer is determined by the wavelength of its internal laser, which helps to control the position of the mirror in the Michelson interferometer. Since the wavelength of the laser triggers the data acquisition, frequencies which are higher than of the trigger itself are acquired too slowly. However, a common FTIR spectrometer is triggered at the zero crossing of the interference pattern of an internal HeNe laser, which emits light with $\nu = 15\,800\,\mathrm{cm}^{-1}$. This would mean that FTPS measurements are limited to this wavenumber at the upper end. It can be seen in the following that undersampling will help to expand the upper limit of the spectral range.

From Equation 8.7 it can be seen that the FT of an interferogram with N points only yields a redundant spectrum with $N/2$ points (see Figure 8.11a and b). The FT is mirror symmetric, that is,

$$S((N-k)\Delta\nu) = S(k\Delta\nu), \tag{8.9}$$

which can be easily seen with the identity

$$\mathrm{e}^{i2\pi k} = (\mathrm{e}^{i2\pi})^k = 1^k = 1. \tag{8.10}$$

If k is substituted by $N-k$, the spectrum S will not change. More generally spoken, the mirror-symmetric N-point sequence in Figure 8.11b is endless and periodically replicated, since also

$$S((k+mN)\Delta\nu) = S(k\Delta\nu) \tag{8.11}$$

is also valid, where $m = 1, 2, 3, \ldots$ (see Figure 8.11c). This replication of the spectrum is known as aliasing. To conclude, the upper limit of the spectrum is limited

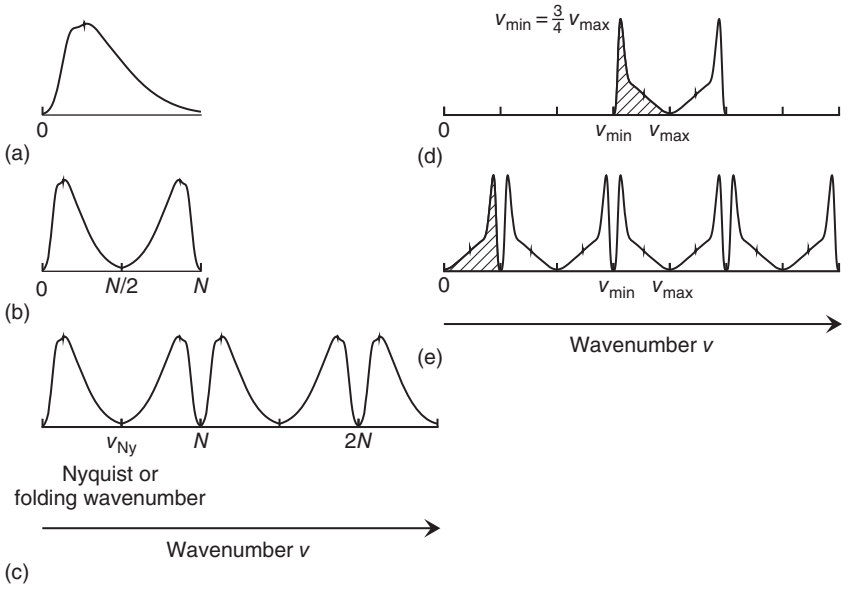

Figure 8.11 Effects of sampling. (a) Expected spectrum. (b) However, the Fourier transformation of the corresponding interferogram yields the expected spectrum and its mirror image. This means that only half of the interferogram points ($N/2$) contains useful information. The second half of the points is redundant and discarded. (c) Aliasing effect shows the endless replication of the spectrum on the wavenumber axis. If the spectrum has nonzero contribution in the wavenumber range $\nu \geq \nu_{max}$ and $\nu_{max} \geq \nu_f$, errors occur. These conditions are fulfilled if the sampling $\Delta x < 1/(2\nu_{max})$ is violated. (d) Undersampling can be realized without errors if the spectrum is actually limited to $\nu_{min} \leq \nu \leq \nu_{max}$. (e) The Fourier transformation with the use of undersampling also produces aliases.

to $N/2$ points, and therefore together with Equation 8.8 the so-called Nyquist wavenumber is

$$\nu_{Ny} = \frac{N}{2}\Delta\nu = \frac{1}{2\Delta x}. \tag{8.12}$$

Note that the factor of 2 is the reason why the spectral range is limited to the wavenumber of the internal laser, even with zero-crossing triggering (wave detection at wavelength $\lambda/2$) as mentioned earlier.

As a consequence of this aliasing, to measure clear and unchanged spectra with an FTIR, one has to ensure that the overlap of two mirroring spectra is zero, that is, the original spectrum has to be actually zero at $\nu \geq \nu_{Ny}$. To shift ν_{Ny} to higher wavenumbers, two solutions are possible. On the one hand, additional triggering points can be introduced. Modern FTIR spectrometer trigger the zero crossing and also the maxima/minima of the interference pattern of the internal laser, which yields four triggering points per wavelength and therefore shifts the upper wavenumber to $\nu_{Ny} = 31\,600\,\text{cm}^{-1}$. On the other hand, undersampling is also possible to shift the upper limit of the spectrum. Undersampling means that the lower

limit of the spectrum $\nu_{\min} > 0$. Since the sampling

$$\Delta x \leq \frac{1}{2|\nu_{\max} - \nu_{\min}|} \tag{8.13}$$

is determined by the upper ($\nu_{\max}$) and the lower spectral limit, not necessarily every sample point has to be triggered for data acquisition. By eliminating the spectral contribution from low wavenumbers, light with wavenumbers higher than the Nyquist wavenumber can be measured.

By sampling light with a wavenumber higher than the natural sampling (internal HeNe laser), the wavenumber of this light is underestimated. By knowing this and the fact that the spectrum has no contribution from low wavenumbers, the light with the underestimated wavenumbers can be interpreted as what it is, that is, light with a wavenumber beyond the Nyquist wavenumber. Figure 8.11d and e illustrates this. Since the Fourier transformation is periodic, the original spectrum (see Figure 8.11d) and its alias (Figure 8.11e), which starts at $\nu_{\min} = 0$, are equivalent. Only the wavenumber scaling has to be done afterward.

The upper limit of the spectrum

$$\nu_{\max} = n\nu_{\mathrm{HeNe}} \tag{8.14}$$

where $n = \ldots, 1/3, 1/2, 1, 2, \ldots$ must be a natural fraction or integer multiple of the wavenumber of the internal laser ($\nu_{\mathrm{HeNe}} = 15\,800$). The lower limit of the spectrum

$$\nu_{\min} = \frac{n-1}{n}\nu_{\max} \tag{8.15}$$

where $n = 1, 2, 3, \ldots$.

8.3.2.4 Apodization and Instrumental Line Shape

An additional effect arises from the difference between a continuous and a finite Fourier transformation (FT), as it is done within FTIR spectroscopy (compare Equation 8.7). While the continuous analytical FT of an analytical interferogram $I_{\mathrm{a}}(x)$ uses an infinite integral

$$S_{\mathrm{a}}(\nu) = \int_{-\infty}^{+\infty} I_{\mathrm{a}}(x)\mathrm{e}^{i2\pi\nu x}\ \mathrm{d}x, \tag{8.16}$$

the interferogram of a measured FTIR signal is limited by the pathway $N\Delta x$ of the moving mirror in the Michelson interferometer. This fact is known as *leakage.* To compensate the effect of the limited pathway of the mirror, the interferogram $I(x)$ is multiplied with an apodization function $A(x)$ such that the spectrum $S_{\mathrm{L}}(\nu)$ after apodization is given by

$$S_{\mathrm{L}}(\nu) = \int_{-\infty}^{+\infty} A(x)I(x)\ \mathrm{e}^{i2\pi\nu x}\mathrm{d}x. \tag{8.17}$$

If $A(x)$ is equal to a boxcar function, the FT of $A(x)$ yields the natural line shape of the FTIR spectrometer with finite resolution. Note that an infinite $A(x) = 1$ would also mean infinite resolution. The natural line shape is shown in Figure 8.12a. It

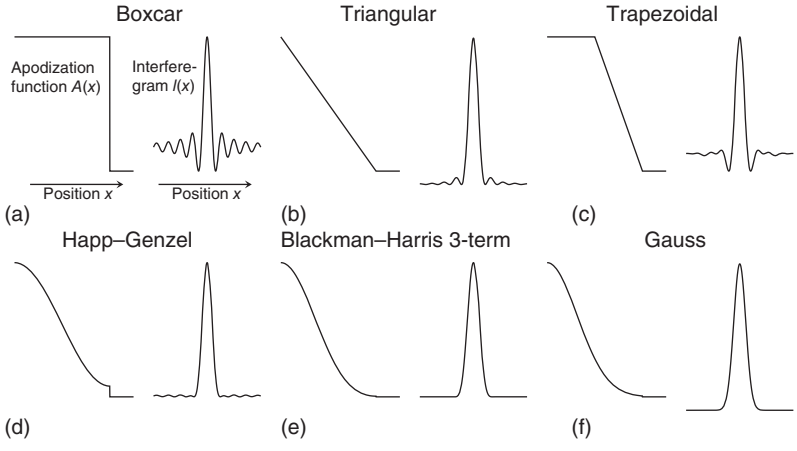

Figure 8.12 Several apodization functions (left) and its corresponding *instrumental line shapes*, that is, Fourier transformations (right). Generally, the broader the line shape, the less is the ripple (side lobes).

can be seen that this line shape is rather sharp compared to the other so-called *apodization* functions in Figure 8.12. However, the disadvantage of such a rather sharp line shape is numerous additional peaks beside the main peak, which are known as side lobes. These side lobes cause a displacement of the spectral intensity. The solution of this problem is the *removal of the feet*, which is the meaning of apodization. Instead of applying an FT with the natural line shape of an FTIR spectrometer, the user can choose to convolute the measured interferogram with such an apodization function. Some of the common functions and their line shapes are plotted in Figure 8.12. Choosing an apodization function always means a compromise between spectral resolution, that is, the width of the line shape, and artificial signals in the spectrum due to the side lobes. The choice of an apodization function therefore depends on the needs. If the highest resolution is needed, then the boxcar truncation is mandatory. The Happ-Genzel and the Blackman-Harris apodization functions yield a loss in resolution of 50% compared to the boxcar truncation. However, since these functions produce *wiggles* in the spectrum if the interferogram includes low-frequency components, that is, it may show an offset at the end, one should use an apodization function which is close to zero at the boundary. The triangular, trapezoidal, Blackman-Harris, or Gauss windows fulfill these requirements [36]. As the Blackman-Harris function shows almost the same narrow line shape as the triangular or Happ-Genzel function but at the same time the highest side lobe suppression and is further nearly zero at the interval ends, this function can be considered as the top performer of these three functions [36]. An extensive overview over the individual properties of numerous apodization functions can be found in [44, 45].

To summarize, spectra from FTPS measurements are often rather broad, and a Blackman – Harris window function is a proper choice for solar-cell applications.

8.3.2.5 Phase Correction

The last mathematical operation, which is performed on the Fourier transformation (FT) of an interferogram, is the phase correction. A phase correction is necessary, since the spectrum

$$S(\nu) = \mathrm{Re}(S(\nu)) + i\mathrm{Im}(S(\nu)) = S_0 e^{i\varphi(\nu)} \tag{8.18}$$

after FT of the interferogram is in general a complex number. The determination of the amplitude $S_0(\nu)$ can either be done by calculating the *power spectrum*

$$S_0(\nu) = \sqrt{[\mathrm{Re}(S(\nu))]^2 + [\mathrm{Im}(S(\nu))]^2} \tag{8.19}$$

or by multiplication of $S(\nu)$ by the inverse of $\varphi(\nu)$ and taking the real part of the result:

$$S_0(\nu) = \mathrm{Re}[S(\nu)e^{-i\varphi(\nu)}], \tag{8.20}$$

where the phase

$$\varphi(\nu) = \arctan\left[\frac{\mathrm{Im}\,(S\,(\nu))}{\mathrm{Re}(S(\nu))}\right]. \tag{8.21}$$

The correction of the phase via Equation 8.20 is known as *multiplicative phase correction* [36] or the *Mertz method* [46]. Note that Equations 8.19 and 8.20 are equivalent if the data is free of noise. However, the Mertz method in Equation 8.20 can reduce noise by a factor of $\sqrt{2}$ compared to the power spectrum in Equation 8.19 [36], since Equation 8.19 always yields a positive signal, that is, even noise, which fluctuates around zero, gets mirrored from the negative to the positive side. This means that FTIR interferograms should be phase corrected by this Mertz method to get the signal-to-noise ratio enhanced further. Additional to this, the phase $\varphi(\nu)$ contains useful information regarding the phase delays of either the optics, the detector/amplifier unit, or the electronic filters [36]. This means that a frequency-dependent delay of the charge carrier transport in solar cells can be determined from the phase $\varphi(\nu)$ in FTPS measurements.

8.3.3 Measurement Procedure

8.3.3.1 Sample Preparation

Three different configurations can be used for FTPS measurements (see Figure 8.13). The choice for any of these configurations depends on the requirements. Where the sample configuration in Figure 8.13a yields advantages for fast prototyping, since the preparation is easy, the configuration in Figure 8.13c uses whole solar-cell devices and an FTPS measurement would help understanding and analyzing the properties of the absorber layer and its charge carrier collection in a working solar cell and could be compared with other photovoltaic parameters.

The sample configuration in Figure 8.13a is a coplanar semiconducting layer on a substrate, which can be either transparent or opaque. The electrical contacts are

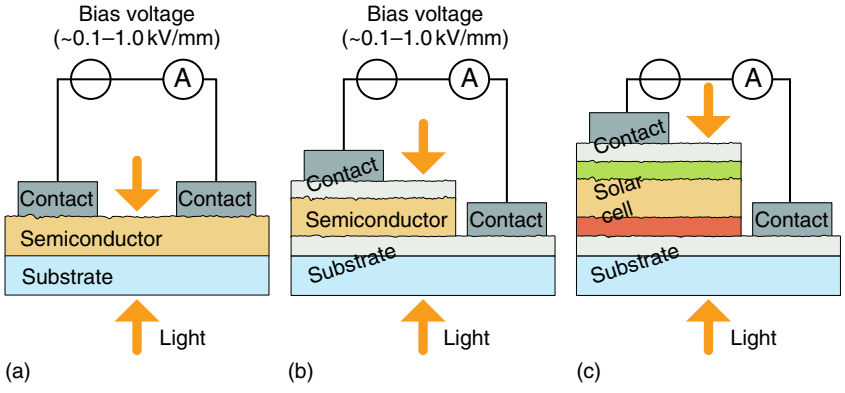

Figure 8.13 Different types of samples for FTPS measurements. (a) Coplanar semiconducting layer on a substrate where the electrical contacts are evaporated on top of the semiconducting layer. (b) Semiconducting layer sandwiched between two electrical contacts. (c) Working solar cell, which drives a photocurrent without any external voltage applied. Note that the light can be incident to the sample from both sides in each case.

evaporated on top of the semiconducting layer. An interdigital contact grid with narrow fingers and gaps between the fingers is highly recommended. This ensures high photogeneration of charge carriers in the semiconductor and low absolute bias voltages to drive the photoinduced current, if the layer stack should not be illuminated from the substrate side. The bias voltage, which drives the photoinduced current, should be in the range of $V_b \approx 0.1-1.0\,\mathrm{kV/mm}$. A low absolute bias voltage can be necessary to avoid any damage to the current/voltage amplifier. Therefore, to apply high electric fields at the same time, it is recommended to use interdigital electrical contacts with small gaps in between. However, Poruba *et al.* [34] recommend a spacing of 1.5 mm at least for scattering samples. The disadvantage is that this kind of samples does not correspond to material, which is grown on the same substrates as it is later used for solar-cell fabrication [47].

Figure 8.13b shows a semiconducting layer between two electrical contacts. One of these electrical contact layers is allowed to be opaque. At least one of both layers has to be transparent. This contact situation is more close to real conditions, for example, in solar-cell technology the semiconducting layers are often electrically connected by transparent conductive oxide layers (e.g., ZnO, SnO_2). The bias voltage is applied via these contacts, which means that the current in this case flows perpendicular to the layers. If the semiconducting layer is thin (up to a few micrometer), already small absolute bias voltages are sufficient to have electrical fields as high as $V_b \approx 0.1-1.0\,\mathrm{kV/mm}$ and efficiently extract charge carriers even in low mobility materials.

A whole working solar cell in Figure 8.13c can be typically measured without any applied bias voltage [48]. Nevertheless, we recommend a small reverse bias voltage of about $V_b \approx -10\,\mathrm{mV}$ to compensate the input impedance of a current/voltage amplifier. Any input impedance means an electrical load to the device, which hinders the photogenerated charge carriers to be extracted from

the device. The application of any forward bias voltage simulates real solar-cell working conditions [49].

8.3.3.2 Measurement Modes

The measurement procedure for FTPS depends on the choice of the sample (see Section 8.3.3.1). Three different measurement procedures are possible, that is, (i) steady-state measurement with spectrometer in step-scan mode, (ii) lock-in measurement with spectrometer in step-scan mode, and (iii) modulated measurement with spectrometer in scanning mode. The main difference is the modulation frequency of the optical signal.

The samples in Figure 8.13a and b are actually photoresistors. Light, which illuminates such a photoresistor, increases the conductivity by the ionization of defects in the semiconductor. The advantage of a photoresistor over a whole device (see Figure 8.13c) is the absence of any dark current. The disadvantage is its slow photoresponse. Photoresistors can be driven up to a modulation frequency $f = 300$ Hz. However, the scanning mode of an FTIR spectrometer uses modulation frequencies $f \geq 2.5$ kHz for light at $\lambda = 632$ nm wavelength, which means that only light at $\lambda \geq 5.3$ µm can be modulated with $f \leq 300$ Hz.

For this reason, in case (i), the moving mirror in the Michelson interferometer can be driven stepwise. In the so-called step-scan mode, the device has to be voltage biased and dc coupled to the current/voltage amplifier as well as to the analog/digital converter at the input of the spectrometer. The slow photoresponse leads to time-consuming measurements, which for the lack of averaging do only gain spectra with a dynamic range of two orders of magnitude.

A higher dynamic range can be achieved with the use of lock-in technique in case (ii). This technique can improve the signal-to-noise ratio about two orders of magnitude. For this mode the spectrometer is also used in the step-scan mode, the light is modulated by a chopper wheel (ideally close to or in the focal point of the light beam), and the sample is voltage biased and ac coupled to the current/voltage amplifier. The exit of this current/voltage amplifier has to be connected to a lock-in amplifier, which is triggered by the modulation frequency of the chopper. The dc signal from the lock-in amplifier can be digitized either by the lock-in unit itself or by the analog/digital converter of the spectrometer.

If the use of full working solar-cell devices is possible, in case (iii), FTPS measurements can be performed using the scanning mode of the spectrometer. As already mentioned, the modulation frequencies are high (~kHz). For this reason a current/voltage amplifier and analog/digital converter with a high bandwidth should be chosen to avoid spectral distortion, since the modulation frequency

$$f = 2\nu u \tag{8.22}$$

is a function of the wavenumber (ν) of the monochromatic light, where u is the steady velocity of the moving mirror in the Michelson interferometer, that is, light at $\nu = 25\,000$ cm^{-1} is modulated two times faster than light at $\nu = 12\,500$ cm^{-1}. The frequency response of the device depends on the electrical conductivity

$$\sigma = q[n(\varphi(\nu))\mu_e(\varphi(\nu)) + p(\varphi(\nu))\mu_h(\varphi(\nu))], \tag{8.23}$$

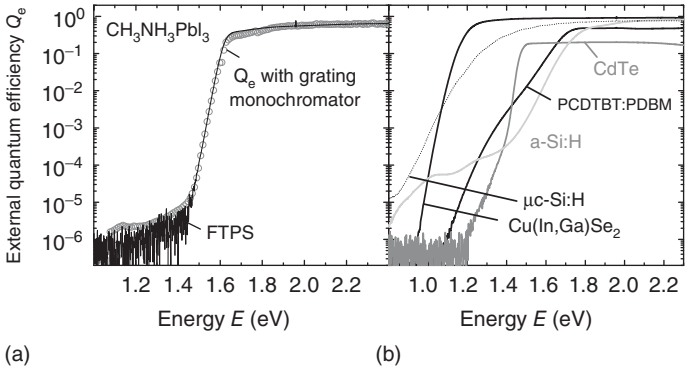

Figure 8.14 FTPS measurements (black solid lines) of different solar cells. In (a) the FTPS data (solid line) of a perovskite solar cell is compared to a quantum efficiency measured using a grating monochromator (open circles). Figure (b) compares FTPS measurements of hydrogenated amorphous silicon (a-Si:H), hydrogenated microcrystalline Si (µc-Si:H), cadmium telluride, copper indium gallium diselenide, and polymer-fullerene blend (PCDTBT:$PC_{71}BM$) solar cells.

which is a function of the electron (μ_h) and hole (μ_p) mobilities, respectively, and therefore also a function of the spectrum $\varphi(\nu)$. Beside the charge carrier mobilities, the electron (n) and hole (p) concentrations, respectively, influence the conductivity. Since n and p are also functions of $\varphi(\nu)$, the reliability of an FTPS measurement strongly depends on the spectrum. For this reason, the scanner velocity (modulation frequency) and the spectrum have to be altered to investigate any frequency damping of the device under test, which would yield a spectral distortion of the measured quantum efficiency of the device.

We measured FTPS of six state-of-the-art solar cells to demonstrate the measurement procedure and explain how to deal with the spectrum- and frequency-dependent conductivity. Figure 8.14a compares an FTPS measurement of a perovskite (methylammonium lead iodide, $CH_3NH_3PbI_3$) solar cell with a quantum efficiency measured using a quantum efficiency setup with a grating monochromator. While in the grating monochromator setup each wavelength has to be chosen separately altogether with color filters to eliminate higher orders of diffraction from the grating, in the FTPS setup all wavelengths are measured at the same time. This is known as the so-called *multiplex* or *Fellgett's* advantage. And due to the need of slits at the entrance and the exit of a monochromator, which defines the spectral resolution but also restricts the amount of light that passes through it, the FTPS setup can have a better signal-to-noise ratio of about two orders of magnitude. This fact is known as the *throughput* or *Jacquinot* advantage. Practically, these advantages lead to faster measurements with an FTPS setup compared to a grating monochromator setup.

Figure 8.14b shows further FTPS measurements of solar-cell devices with absorber layers made from hydrogenated amorphous silicon (a-Si:H), hydrogenated microcrystalline silicon (µc-Si:H), cadmium telluride (CdTe), copper

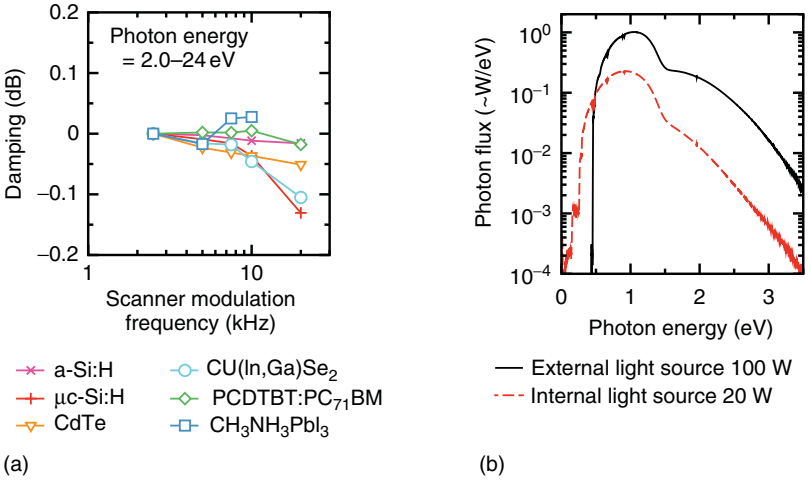

Figure 8.15 (a) Damping of the signal/spectrum versus the FTPS modulation frequency, which is chosen to be in the range $f = 2.5-20$ kHz. The damping is evaluated in the higher energy region of full absorptance (compare to Figure 8.14). (b) Comparison between internal and external light sources in use with *a Bruker Vertex 80v* FTIR spectrometer. The external light source shows higher output in the UV/VIS and NIR range compared to the internal light source.

indium gallium diselenide ($Cu(In,Ga)Se_2$), and a PCDTBT:$PC_{71}BM$ blend. The measurements are conducted with a *Bruker Vertex 80v* FTIR spectrometer, a *Femto DLPCA-200* current/voltage amplifier close to the sample in the sample compartment (variable gain 10^3-10^{11} V/A, bandwidth 500–1 kHz), an external light source, which is UV/VIS enhanced (see Figure 8.15b), and several optical cutoff filters.

In this measurement configuration, a single raw measurement is sufficient to obtain a dynamic range of four orders of magnitude. Together with the decrease of the photon flux of the light source to higher photon energies (see Figure 8.15b), where the absorptance of the samples is high, the dynamic range can be increased up to six orders of magnitude for a spectrally corrected FTPS measurement. However, the earlier mentioned spectral dependence of the conductivity (see Equation 8.23) requires the use of optical filters to enhance the reliability of the measurement. For example, an amorphous silicon device (compare Figure 8.14b) can show the influence of bias light in the low absorption region. A quantum efficiency measurement with a monochromator can show about two times less absorptance in the low energy region in comparison to the spectrally broad FTPS method. Similar to a dual beam constant photocurrent measurement, the spectrally broad illumination and therefore the high charge carrier concentration increases the FTPS signal at low subbandgap absorption. Since the subbandgap absorption of all other samples shows a much steeper decrease compared to the a-Si:H sample (see Figure 8.14b), the influence of any bias light is negligible.

Note that the signal-to-noise ratio is proportional to the square root of the spectral range [50], that is, it is better to use *smooth* filters, which do not totally eliminate high signal regions, instead of cutoff filters for enhancing the dynamic range [47]. This fact also arises from the earlier mentioned *multiplex* or *Fellgett's* advantage.

To further check the modulation frequency response of the samples, we varied the scanner velocity of the Michelson interferometer (see Figure 8.15a). The modulation frequency at the wavelength of the internal HeNe-reference laser is $f = 2.5 - 20$ kHz. The spectra are evaluated in the region of full absorption, that is, the photon energy range $E_\gamma = 2.0 - 2.4$ eV, where the modulation frequency is similar to the scanner modulation frequency. Whereas all absorber materials show almost no damping in the whole frequency range, the curves from μc-Si:H and $Cu(In,Ga)Se_2$ show a slight damping of almost −1.5 dB at $f > 10$ kHz compared to the signal at slowest modulation frequency. Further comparative studies of FTPS measurements for solar-cell applications can be found in Refs. [48, 49, 51–54].

Acknowledgment

The authors gratefully acknowledge the help from Reinhard Carius, especially for providing the data in Figure 8.5.

References

1. Vaněček, M., Kočka, J., Stuchlik, J., Kozisek, Z., Stika, O., and Triska, A. (1983) Density of the gap states in undoped and doped glow discharge a-Si:H. *Sol. Energy Mater.*, **8**, 411–423.
2. Vaněček, M., Abraham, A., Stika, O., Stuchlik, J., and Kočka, J. (1984) Gap states density in a-Si:H deduced from subgap optical absorption measurement on Schottky solar cells. *Phys. Status Solidi A*, **83**, 617–623.
3. Jensen, P. (1990) Deconvolution of CPM absorption spectra: a new technique. *Solid State Commun.*, **76**, 1301–1303.
4. Jackson, W.B., Amer, N.M., Boccara, A.C., and Fournier, D. (1981) Photothermal deflection spectroscopy and detection. *Appl. Opt.*, **20**, 1333–1344.
5. von Richthofen, J. (1995) Photothermische Deflektionsspektroskopie an Dünnschichtsolarzellen aus amorphem Silizium. Diploma thesis. RWTH Aachen University.
6. Jackson, W.B. and Amer, N.M. (1982) Direct measurement of gap-state absorption in hydrogenated amorphous silicon by photothermal deflection spectroscopy. *Phys. Rev. B*, **25**, 5559–5562.
7. Goris, L., Poruba, A., Hod'Ákova, L., Vaněček, M., Haenen, K., Nesládek, M., Wagner, P., Vanderzande, D., De Schepper, L., and Manca, J.V. (2006) Observation of the subgap optical absorption in polymer-fullerene blend solar cells. *Appl. Phys. Lett.*, **88**, 052113.
8. Benson-Smith, J.J., Goris, L., Vandewal, K., Haenen, K., Manca, J.V., Vanderzande, D., Bradley, D.D.C., and Nelson, J. (2007) Formation of a ground-state charge-transfer complex in polyfluorene/[6,6]-phenyl-C 61 butyric acid methyl ester (PCBM) blend films and its role in the function of polymer/PCBM solar cells. *Adv. Funct. Mater.*, **17**, 451–457.
9. Vandewal, K., Albrecht, S., Hoke, E.T., Graham, K.R., Widmer, J., Douglas, J.D., Schubert, M., Mateker, W.R.,

Bloking, J.T., Burkhard, G.F., Sellinger, A., Fréchet, J.M.J., Amassian, A., Riede, M.K., McGehee, M.D., Neher, D., and Salleo, A. (2013) Efficient charge generation by relaxed charge-transfer states at organic interfaces. *Nat. Mater.*, **13**, 63–68.

10. Lee, J., Vandewal, K., Yost, S.R., Bahlke, M.E., Goris, L., Baldo, M.A., Manca, J.V., and Van Voorhis, T. (2010) Charge transfer state versus hot exciton dissociation in polymer-fullerene blended solar cells. *J. Am. Chem. Soc.*, **132**, 11878–11880.
11. Street, R., Song, K., Northrup, J., and Cowan, S. (2011) Photoconductivity measurements of the electronic structure of organic solar cells. *Phys. Rev. B*, **83**, 165207.
12. Hod'áková, L., Poruba, A., Kravets, R., and Vaněček, M. (2006) Fast quantum efficiency measurement of solar cells by Fourier transform photocurrent spectroscopy. *J. Non-Cryst. Solids*, **352**, 1221–1224.
13. Poruba, A., Špringer, J., Mullerová, L., Vaněček, M., Repmann, T., Rech, B., Kuendig, J., Wyrsch, N., and Shah, A. (2003) *Fast and Sensitive Defect Characterization and Spectral Response Measurement of Thin Film Silicon Solar Structures*. Proceedings of the 3rd World Conference on Photovoltaic Energy Conversion, 5P-A9-07. 11-18 May 2003, Osaka, WCPEC-3 Organizing Committee.
14. Kravets, R., Vaněček, M., Piccirillo, C., Mainwood, A., and Newton, M.E. (2004) A quantitative study of the boron acceptor in diamond by Fourier-transform photocurrent spectroscopy. *Diamond Relat. Mater.*, **13**, 1785–1790.
15. Haenen, K., Nesládek, M., De Schepper, L., Kravets, R., Vaněček, M., and Koizumi, S. (2004) The phosphorous level fine structure in homoepitaxial and polycrystalline n-type CVD diamond. *Diamond Relat. Mater.*, **13**, 2041–2045.
16. Verkerk, A.D., Rath, J.K., and Schropp, R.E.I. (2010) Degradation of thin film nanocrystalline silicon solar cells with 1 MeV protons. *Energy Procedia*, **2**, 221–226.
17. Meillaud, F., Vallat-Sauvain, E., Niquille, X., Dubey, M., Bailat, J., Shah, A., and Ballif, C. (2005) *Light-Induced Degradation of Thin Film Amorphous and Microcrystalline Silicon Solar Cells*. Conference Record of the Thirty-First IEEE Photovoltaic Specialists Conference, 3-7 January 2005, Lake Buena Vista, FL, USA, IEEE, pp. 1412–1415.
18. Tomm, J.W., Jaeger, A., Barwolff, A., Elsaesser, T., Gerhardt, A., and Donecker, J. (1997) Aging properties of high power laser diode arrays analyzed by Fourier-transform photocurrent measurements. *Appl. Phys. Lett.*, **71**, 2233–2235.
19. Melskens, J., Schouten, M., Santbergen, R., Fischer, M., Vasudevan, R., van der Vlies, D.J., Quax, R.J.V., Heirman, S.G.M., Jäger, K., Demontis, V., Zeman, M., and Smets, A.H.M. (2014) In situ manipulation of the sub gap states in hydrogenated amorphous silicon monitored by advanced application of Fourier transform photocurrent spectroscopy. *Sol. Energy Mater. Sol. Cells*, **129**, 70–81.
20. Remes, Z., Kromka, A., Potmesil, J., and Vaněček, M. (2008) The influence of thermal annealing on the electronic defect states in nanocrystalline CVD diamond films. *Phys. Status Solidi A*, **205**, 2158–2162.
21. Kravets, R., Johnston, K., Potmesil, J., Vorlicek, V., and Vaněček, M. (2006) Defect spectroscopy of nanodiamond thin layers. *Diamond Relat. Mater.*, **15**, 559–563.
22. Vet, B. and Zeman, M. (2010) Comparison of a-SiC:H and a-SiN:H as candidate materials for a p-i interface layer in a-Si:H p-i-n solar cells. *Energy Procedia*, **2**, 227–234.
23. Vaněček, M. and Poruba, A. (2002) Fourier-transform photocurrent spectroscopy of microcrystalline silicon for solar cells. *Appl. Phys. Lett.*, **80**, 719–721.
24. Bozyigit, D., Volk, S., Yarema, O., and Wood, V. (2013) Quantification of deep traps in nanocrystal solids, their electronic properties, and their influence on device behavior. *Nano Lett.*, **13**, 5284–5288.

25. Poruba, A., Springer, J., Mullerova, L., Vaněček, M., Repmann, T., Rech, B., Kuendig, J., Wyrsch, N., and Shah, A. (2003) *Fast and Sensitive Defect Characterization and Spectral Response Measurement of Thin Film Silicon Solar Structures*. Proceedings of the 3rd World Conference on Photovoltaic Energy Conversion, 11-18 May 2003, Osaka, WCPEC-3 Organizing Committee, pp. 1631–1634.
26. Melskens, J., van Elzakker, G., Li, Y., and Zeman, M. (2008) Analysis of hydrogenated amorphous silicon thin films and solar cells by means of Fourier transform photocurrent spectroscopy. *Thin Solid Films*, **516**, 6877–6881.
27. Kromka, A., Kravetz, R., Poruba, A., Zemek, J., Perina, V., Rosa, J., and Vaněček, M. (2003) Detection of residual molybdenum impurity in CVD diamond. *Phys. Status Solidi A*, **199**, 108–112.
28. Haeldermans, I., Vandewal, K., Oosterbaan, W.D., Gadisa, A., D'Haen, J., Van Bael, M.K., Manca, J.V., and Mullens, J. (2008) Ground-state charge-transfer complex formation in hybrid poly(3-hexyl thiophene):titanium dioxide solar cells. *Appl. Phys. Lett.*, **93**, 223302.
29. Moghe, D., Yu, P., Kanimozhi, C., Patil, S., and Guha, S. (2011) Charge transfer complex states in diketopyrrolopyrrole polymers and fullerene blends: implications for organic solar cell efficiency. *Appl. Phys. Lett.*, **99**, 233307.
30. Gasparini, N., Katsouras, A., Prodromidis, M.I., Avgeropoulos, A., Baran, D., Salvador, M., Fladischer, S., Spiecker, E., Chochos, C.L., Ameri, T., and Brabec, C. (2015) Photophysics of molecular-weight-induced losses in indacenodithienothiophene-based solar cells. *Adv. Funct. Mater.*, **25**, 4898–4907.
31. Vandewal, K., Gadisa, A., Oosterbaan, W.D., Bertho, S., Banishoeib, F., Van Severen, I., Lutsen, L., Cleij, T.J., Vanderzande, D., and Manca, J.V. (2008) The relation between open-circuit voltage and the onset of photocurrent generation by charge-transfer absorption in polymer: fullerene bulk heterojunction solar cells. *Adv. Funct. Mater.*, **18**, 2064–2070.
32. Vandewal, K., Goris, L., Haeldermans, I., Nesládek, M., Haenen, K., Wagner, P., and Manca, J.V. (2008) Fourier-transform photocurrent spectroscopy for a fast and highly sensitive spectral characterization of organic and hybrid solar cells. *Thin Solid Films*, **516**, 7135–7138.
33. Remes, Z., Kromka, A., Vaněček, M., Ghodbane, S., and Steinmüller-Nethl, D. (2009) On the reduction of the non-diamond phase in nanocrystalline CVD diamond films. *Diamond Relat. Mater.*, **18**, 726–729.
34. Poruba, A., Fejfar, A., Remeš, Z., Špringer, J., Vaněček, M., Kočka, J., Meier, J., Torres, P., and Shah, A. (2000) Optical absorption and light scattering in microcrystalline silicon thin films and solar cells. *J. Appl. Phys.*, **88**, 148–160.
35. Herres, W. and Gronholz, J. (1984) Understanding FT-IR data processing. Part 1: Data acquisition and Fourier transformation. *Comput. Appl. Lab.*, **2**, 216–220.
36. Herres, W. and Gronholz, J. (1985) Understanding FT-IR data processing. Part 2: Details of the spectrum calculation. *Instrum. Comput.*, **3**, 10–16.
37. Herres, W. and Gronholz, J. (1985) Understanding FT-IR data processing. Part 3: Further useful computational methods. *Instrum. Comput.*, **3**, 45–55.
38. Alpert, N.L., Keiser, W.E., and Szymanski, H.A. (1970) *IR – Theory and Practice of Infrared Spectroscopy*, Plenum Press, New York.
39. Colthup, N.B., Daly, L.H., and Wiberly, S.E. (1990) *Introduction to Infrared and Raman Spectroscopy*, Academic Press by Elsevier, Boston.
40. Günzler, H. and Gremlich, H.-U. (2003) *IR-Spektroskopie: Eine Einführung*, Wiley-VCH Verlag GmbH & Co. KGaA, Weinheim.
41. Christy, A.A., Ozaki, Y., and Gregoriou, V.G. (2001) *Modern Fourier Transform Infrared Spectroscopy*, Elsevier, Amsterdam.
42. Lindon, J.C. and Ferrige, A.G. (1980) Digitisation and data processing in Fourier transform NMR. *Prog. Nucl. Magn. Rason. Spectrosc.*, **14**, 27–66.

43. Bartholdi, E. and Ernst, R.R. (1973) Fourier spectroscopy and the causality principle. *J. Magn. Reson.*, **11**, 9–19.
44. Bretzlaff, R.S. and Bahder, T.B. (1986) Apodization effects in Fourier transform infrared difference spectra. *Rev. Phys. Appl.*, **21**, 833–844.
45. Harris, F.J. (1978) On the use of windows for harmonic analysis with discrete Fourier transform. *Proc. IEEE*, **51**, 172–204.
46. Mertz, L. (1967) Auxiliary computation for Fourier spectrometry. *Infrared Phys.*, **7**, 17–23.
47. Holovský, J. (2011) Fourier transform photocurrent spectroscopy on non-crystalline semiconductors, in *Fourier Transforms – New Analytical Approaches and FTIR Strategies* (ed G. Nikolic), InTech, Rijeka, pp. 257–282.
48. Poruba, A., Vaněček, M., Rosa, J., Feitknecht, L., Wyrsch, N., Meier, J., Shah, A., Repmann, T., and Rech, B. (2001) *Fourier Transform Photocurrent Spectroscopy in Thin Film Silicon Solar Cells*. Proceedings of the 17th European Photovoltaic Solar Energy Conference, 22-26 October 2001, Munich, Germany, ETA-Florence, Italy and WIP-Munich, Germany, pp. 2981–2984.
49. Bailat, J. (2004) Growth, microstructure and electrical performances of thin film microcrystalline silicon solar cells. Diploma thesis. RWTH Aachen University.
50. Griffiths, P.R., Sloane, H.J., and Hannah, R.W. (1977) Interferometers vs monochromators: separating the optical and digital advantages. *Appl. Spectrosc.*, **31**, 485–495.
51. Vaněček, M. and Poruba, A. (2007) Fourier transform photocurrent spectroscopy applied to a broad variety of electronically active thin films (silicon, carbon, organics). *Thin Solid Films*, **515**, 7499–7503.
52. Poruba, A., Holovsky, J., Purkrt, A., and Vaněček, M. (2008) Advanced optical characterization of disordered semiconductors by Fourier transform photocurrent spectroscopy. *J. Non-Cryst. Solids*, **354**, 2421–2425.
53. Holovský, J., Poruba, A., Purkrt, A., Remeš, Z., and Vaněček, M. (2008) Comparison of photocurrent spectra measured by FTPS and CPM for amorphous silicon layers and solar cells. *J. Non-Cryst. Solids*, **354**, 2167–2170.
54. Holovský, J., Dagkaldiran, Ü., Remeš, Z., Purkrt, A., Ižák, T., Poruba, A., and Vaněček, M. (2010) Fourier transform photocurrent measurement of thin silicon films on rough, conductive and opaque substrates. *Phys. Status Solidi A*, **207**, 578–581.

9
Spectroscopic Ellipsometry

Jian Li, Robert W. Collins, Michelle N. Sestak, Prakash Koirala, Nikolas J. Podraza, Sylvain Marsillac, and Angus A. Rockett

9.1
Introduction

Over the past few decades, spectroscopic ellipsometry has emerged as a nondestructive, noninvasive optical technique for the characterization of thin-film solar-cell materials and devices [1–6]. *Ellipsometry* derives its name from the measurement of the output polarization ellipse which is generated after a beam of light with a known input polarization ellipse interacts specularly with a sample [7–9]. The polarization-modifying interaction can occur either when the light beam is transmitted through the sample, as in transmission ellipsometry, or more commonly when it is reflected obliquely from the sample surface, as in reflection ellipsometry. In the absence of depolarization effects (to be discussed in Section 9.3), the pure polarization state of the emerging beam is elliptical in general, and the analysis of this ellipse can provide useful optical and structural information about the sample including optical properties and multiple layer thicknesses.

The instrument that performs such polarization measurements is known as an *ellipsometer*, and one of the most popular instrument configurations of an ellipsometer is denoted PCSA [7–9]. In this configuration, an unpolarized, collimated light beam from a source is first polarized elliptically upon transmission through a polarizer (P) and compensator (C) and is then specularly reflected from the sample (S). The reflected beam passes through an analyzer (A), which is simply a second polarizer, before impinging on the detector. The source, polarizer, and compensator (also referred to as a retarder) work together to generate a known state of polarization before the light beam reaches the sample, whereas the analyzer and detector work together to detect the change in polarization state after the light beam reflects from the sample. Because the change in polarization state depends on wavelength, a *spectroscopic ellipsometry* experiment applies either a monochromator in conjunction with the source or a spectrometer in conjunction with the detector. Overall, a single ellipsometry measurement on an isotropic sample provides two important interaction parameters, ψ and Δ, at a given wavelength, which can be derived from the polarization state

Advanced Characterization Techniques for Thin Film Solar Cells, Second Edition.
Edited by Daniel Abou-Ras, Thomas Kirchartz, and Uwe Rau.

characteristics of the beam before and after reflection from the sample. These so-called ellipsometry angles are defined by

$$\tan\psi \exp(i\Delta) = \frac{r_p}{r_s},$$

where r_p and r_s are the complex amplitude reflection coefficients of the sample for p and s linear polarization states, for which the electric field vibrates parallel (p) and perpendicular (s) to the plane of incidence, respectively. The plane of incidence includes both the incident and reflected beam propagation vectors as well as the normal to the reflecting surface.

A single ellipsometry measurement performed at one wavelength can provide at most two sample parameters from the values of ψ and Δ determined in the experiment [7–9]. The simplest situation involves a reflecting sample that is nonmagnetic, isotropic, homogeneous, and uniform and at the same time presents a single interface to the ambient, meaning that it is atomically smooth and film-free. In this case, the optical property parameters of the sample including n, the real index of refraction, and k, the extinction coefficient ($n, k \geq 0$), can be determined from ψ and Δ. The optical property parameters (n, k) are functions of wavelength, that is, they exhibit dispersion, and are characteristic of the material from which the sample is composed. (The optical property parameters are often called "optical functions.") In fact, n and k serve as the real and imaginary parts of the complex index of refraction $N = n - ik$. The negative sign in this definition arises from the electric field phase convention adopted here. The determination of optical functions from spectra in the ellipsometry angles for a sample presenting a single ideal interface to the ambient medium will be described in Section 9.2.2.

In the early years of ellipsometry research, before the widespread use of computers, (ψ, Δ) data could be obtained only at one or a few selected wavelength values [10]. The most widespread application of such a measurement was to determine (n, k) and thickness of a thin film on a known substrate, which posed a data analysis challenge due to the limited number of data values. Starting in the 1970s, automatic ellipsometers were developed capable of collecting (ψ, Δ) point-by-point nearly continuously versus wavelength spanning from the ultraviolet (200–300 nm) to the near-infrared (800–900 nm) [11]. Acquisition times for *spectroscopic ellipsometry* (SE) ranged from several minutes to several hours depending on the number of wavelength points desired. Using this method, it is possible to extract N for one or more components of a sample structure as smooth functions of wavelength. Such optical functions can be further analyzed to provide the electronic structure such as the critical point parameters of a semiconductor material (fundamental and higher band-gap energies, critical point amplitudes and their widths) [9, 11–14]. A database of materials' optical functions in turn can provide useful information about complicated samples such as their void fraction, crystalline fraction, alloy composition, grain size, strain, and temperature, see for example Refs. [15–19]. The optical functions of many materials have been studied in depth and can be found, for example, in Refs. [20, 21].

The relatively long acquisition times of traditional SE precluded *in situ* and real-time measurements during thin-film deposition and processing; however, later

developments using high-speed array detectors enabled SE with acquisition times from tens of milliseconds to tens of seconds [9, 22]. The instrument for such measurements became known as the *multichannel ellipsometer*, and the technique was described as *real-time spectroscopic ellipsometry* (RTSE) which can be very useful in tracking the growth mechanisms of a thin-film material. The advantages of *in situ* RTSE include measurement of unoxidized surfaces in vacuum environments, the determination of surface roughness from the real-time data set and its correction for highly accurate spectra in N, and the resulting ability to develop a database of optical functions for a given material as a function of deposition parameters and measurement temperature. This optical function database is then useful for analyzing *ex situ* SE data. RTSE examples will be provided in this chapter since RTSE is the most informative type of ellipsometry currently available for photovoltaics research.

9.2 Theory

In order to understand the ellipsometry measurement, it is necessary to start with the basics of polarized light. Next the simplest problem is presented and solved, namely, that of a specularly reflecting single interface. This illustrates how ellipsometry can be used to determine the optical functions of a photovoltaic material.

9.2.1 Polarized Light

The electric field vector of a monochromatic plane wave of arbitrary polarization state traveling along the z direction can be written as [7]

$$\vec{E}(z,t) = [E_{0x}\cos(\omega t - kz + \delta_x)]\hat{x} + [E_{0y}\cos(\omega t - kz + \delta_y)]\hat{y}, \tag{9.1}$$

where E_{0x} and E_{0y} are the amplitudes of the electric field along the x and y axes ($E_{0x} \geq 0$; $E_{0y} \geq 0$), respectively; ω is the angular frequency of the wave; k is the magnitude of the propagation vector (not to be confused with k, the extinction coefficient); and δ_x and δ_y are the phase angles of oscillations along the x and y axes, respectively. In the most general case, the endpoint of the electric field vector traces out an ellipse as a function of time with period $\tau = 2\pi/\omega$ at a fixed position in space; however under special circumstances, the endpoint traces out a circle or a line resulting in circular or linear polarizations, respectively. In particular, when $E_{0y}/E_{0x} = 1$ and $\delta_y - \delta_x = \pm(\pi/2 + 2n\pi)$ ($n = 0, 1, 2, \ldots$) right (+) and left (−) circular polarization results; when $\delta_y - \delta_x = 2n\pi$, $\pm(\pi + 2n\pi)$ ($n = 0, 1, 2, \ldots$) linear polarization results. The handedness of circular and, more generally, elliptical polarization describes the sense of rotation of the electric field endpoint at a fixed position. For right- and left-handed polarization states, the electric field vector travels clockwise and counterclockwise, respectively. The handedness assignments for $\delta_y - \delta_x$ are valid when using the argument

($\omega t - kz + \delta$) in Equation 9.1. If an argument of ($kz - \omega t + \delta$) is used, the assignment is opposite (see, e.g., Refs [11, 23]). For the latter convention, the sign associated with the imaginary part of N becomes positive.

Thus, the elliptical polarization state can be defined most generally by four parameters: E_{0x}, E_{0y}, δ_x, and δ_y [7]. An alternative set of four parameters can be used, namely, the azimuthal angle Q, the ellipticity angle χ (whose sign defines the handedness), the amplitude A, and the absolute phase δ. The azimuthal angle Q ($-90° < Q \leq 90°$) of the ellipse is the angle between the major axis and a fixed reference direction (such as the p direction). The ellipticity angle χ ($-45° \leq \chi \leq 45°$) is defined as $\chi = \tan^{-1} e$, where $e = b/a$ ($-1 \leq e \leq 1$) and b and a are the lengths of the semiminor and semimajor axes of the ellipse, respectively. Usually only the shape of the polarization ellipse is of interest in an ellipsometry measurement (an exception being when ellipsometry is performed together with a polarized transmittance and/or reflectance measurement). As a result, the amplitude and absolute phase associated with the polarization ellipse are not of interest, and the key polarization state angles (Q, χ) can be derived from the field ratio E_{0y}/E_{0x} and the phase difference $\delta_y - \delta_x$.

9.2.2 Reflection from a Single Interface

Reflection from a single interface between the ambient and a non-magnetic, isotropic, homogeneous, and uniform medium ("the sample") provides the simplest example of how ellipsometry can be applied to determine N_s, the complex index of refraction of the given sample [7]. In this example, the front reflecting surface of the sample must be planar, atomically smooth, and film-free, and no light must be collected via reflection or scattering from the back surface of the sample or the sample holder. The latter condition is met if the reflecting material is opaque or if the sample is sufficiently thick that any back-surface reflection can be blocked with an aperture. Alternative methods to eliminate back-surface reflection for semitransparent samples include back-surface roughening to the point where the scattered irradiance is negligible or using wedge-shaped samples with planar but nonparallel surfaces.

For an isolated reflection from a single interface, the complex amplitude reflection coefficients for p and s polarized light are given by the Fresnel equations:

$$r_p = \frac{N_s \cos\theta_i - n_a \cos\theta_t}{N_s \cos\theta_i + n_a \cos\theta_t} \quad r_s = \frac{n_a \cos\theta_i - N_s \cos\theta_t}{n_a \cos\theta_i + N_s \cos\theta_t}. \tag{9.2}$$

In these equations, n_a is the real index of refraction of the ambient, $N_s = n_s - ik_s$ where n_s is the real index of refraction of the sample and k_s is its extinction coefficient, θ_i is the angle of incidence, and θ_t is the complex angle of transmission. Although these equations appear to have two complex unknowns, N_s and θ_t, Snell's law can be applied to eliminate θ_t. Then, the ellipsometry angles ψ and Δ can be expressed in terms of N_s, n_a, and θ_i through

$$\tan\psi \; e^{i\Delta} = \frac{r_p}{r_s} = \rho. \tag{9.3}$$

Upon inversion of the resulting equation, N_s can be determined from the measured ellipsometry angles ψ and Δ using the known quantities n_a and θ_i. The resulting equation becomes simpler in form when the optical functions are expressed instead as

$$\varepsilon_s = N_s^2 \quad \varepsilon_a = n_a^2, \tag{9.4}$$

where ε_s is the complex relative dielectric permittivity, the so-called complex dielectric function of the reflecting sample, and ε_a is the real dielectric function of the ambient. The final result, which relates the measured ellipsometry angles to the dielectric function of the sample, is given as

$$\varepsilon_s = \varepsilon_a \sin^2\theta_i \left[1 + \tan^2\theta_i \left(\frac{1-\rho}{1+\rho}\right)^2\right]. \tag{9.5}$$

For a single interface, the requirements on $\varepsilon_s = \varepsilon_{s1} - i\varepsilon_{s2}$, that is, that the imaginary part ε_{s2} be positive, imply that $0° \leq \psi \leq 45°$ and $0° \leq \Delta \leq 180°$.

9.3 Ellipsometry Instrumentation

Figure 9.1 shows the generic ellipsometer configuration that illustrates the principles of stepwise wavelength scanning SE used in *ex situ*, single-point, and off-line analysis whereby measurement speed is not critical [7–9]. The same basic configuration also applies to multichannel SE used in high-speed applications including

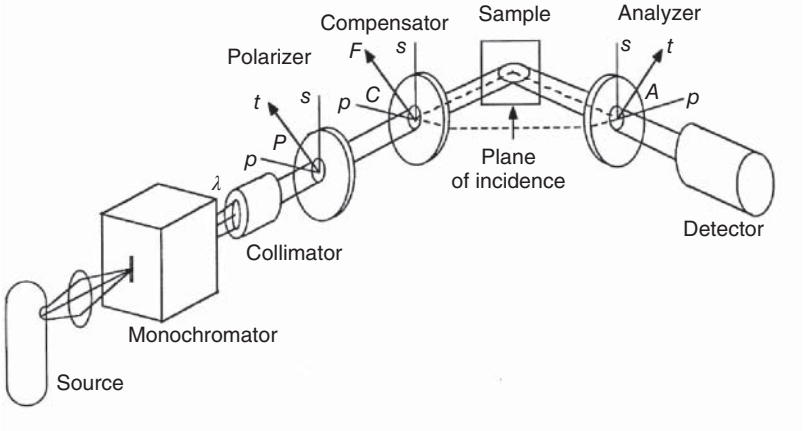

Figure 9.1 Generic spectroscopic ellipsometry (SE) configuration. The *p* and *s* directions are parallel and perpendicular to the plane of incidence, and *P* and *A* are the angles of the transmission axes *t* of the polarizer and analyzer, respectively, relative to the *p* direction (intersection of the plane of incidence with the surface of the device). *C* is the angle of the fast axis *F* of the compensator relative to the *p* direction.

in situ real-time, mapping, and online analysis [9, 24]. The principles and functions of the optical elements of Figure 9.1 are provided in Ref. [7]. Whereas the polarizer and analyzer extinguish the electric field component normal to the transmission axis, indicated by t in Figure 9.1, the compensator exerts a phase lag or retardance of δ_C on the electric field component normal to the fast axis indicated by F. As a result, for incident linear polarization with components both parallel and perpendicular to the fast axis, the polarization is modified to elliptical, in general, upon transmission through the compensator. Compensators are chromatic to varying extents depending on their design, meaning that δ_C depends on the wavelength. In wavelength scanning SE, the monochromator in Figure 9.1 is stepped from one wavelength point to the next, with an acquisition time of minutes to hours for complete spectra in (ψ, Δ). In this case, a single-element detector is used. In multichannel ellipsometry, the monochromator is eliminated from the source side of the instrument, and a detection system is used consisting of a spectrograph and linear detector array. Each pixel of the array collects photons over a narrow wavelength band, and array scanning for SE can occur at high speed (~5 ms) with (ψ, Δ) complete spectra acquisition times ranging from tens of milliseconds to tens of seconds.

The selected light sources and detectors for both types of instrument depend on the desired spectral range [9, 24–26]. For applications in photovoltaics, a range of ~200–2000 nm (about 0.6–6 eV) is ideal, covering the band-gap onsets and critical points of the key semiconductors. This typically requires a tandem light source, for example, a quartz–tungsten halogen lamp (400–2000 nm) with a see-through D_2 lamp (200–400 nm). In addition, at least two detectors are required: (i) Si-based detectors for wavelengths below 1000 nm and (ii) III–V-based detectors above 1000 nm. For wavelength scanning instruments, single-element photomultiplier tubes and Pb salt photodetectors can be used, for example, operating below and above 900 nm, respectively.

For both types of SE instruments, beam sizes are typically 1–5 mm, so that the measurement averages over a macroscopic area on the sample. If the sample is not uniform over this area, depolarization of the reflected beam will occur when the in-plane scale of the thickness or optical property variations is larger than the lateral coherence length of the beam (typically ~10 μm). For variations smaller than the lateral coherence length (i.e., ~0.05–5 μm), the specularly reflected beam will remain polarized; however in this case, nonspecular scattering is more likely to occur. In all cases of nonuniformity, SE can provide useful information on material properties and the uniformity of those properties through appropriate modeling [27]. For nonuniformities on a scale much less than the wavelength (<0.05 μm) (i.e., heterogeneities), effective medium theories are used in the modeling of SE data [28].

The most widely used experimental configurations in photovoltaics research are those in which one of the three polarization-modifying optical elements of Figure 9.1 rotates at a fixed angular frequency ω versus time t [29, 30]. The elements that can be rotated are (i) the polarizer with its transmission axis orientation given by $P(t) = \omega_P t - P_S$, (ii) the compensator with its fast axis orientation given by $C(t) = \omega_C t - C_S$, and (iii) the analyzer with its transmission axis orientation

given by $A(t) = \omega_A t - A_S$. In the expressions for $P(t)$, $C(t)$, and $A(t)$, the angular frequencies ω_P, ω_C, and ω_A describe the mechanical rotation of the polarizer, compensator, and analyzer, respectively, about their optical axes along which the beam propagates. The zero positions of these angles occur when the transmission or fast axis lies in the plane of incidence established by reflection from a sample. P_S, C_S, and A_S are offsets that account for arbitrary angular positions of the optical elements relative to the plane of incidence at $t = 0$, which is defined by the onset of data collection. In the following discussion, these offsets are neglected since they can be determined readily in calibration procedures and eliminated electronically or mechanically. For the wide spectral range of 200–2000 nm, the polarizer, compensator, and analyzer are fabricated from single-crystals of MgF_2 or SiO_2 (quartz). For the compensator, in fact, monoplates, biplates, or dual biplates that exploit such birefringent single crystals have been used. The monoplate is fabricated from an anisotropic single crystalline plate that exhibits a lower index of refraction for linearly polarization with its electric field vibrating along the fast axis relative to that along the slow axis. For MgF_2 and SiO_2 compensators, biplates with orthogonal fast axes are used to ensure a "zero-order" retardance (in the range of $0 < \delta_C < 2\pi$) for a manufacturable plate thickness. Operating in zero order ensures the weakest dispersion in the retardance $\delta_C(\lambda) = 2\pi\Delta n(\lambda)\Delta d/\lambda$, where $\Delta n(\lambda)$ is the wavelength-dependent birefringence and Δd is the thickness difference between the two plates. Dual biplates act as the combination of a polarization rotator and a compensator and are used to suppress further the wavelength dispersion of the retardance. As a result, a wide spectral range is possible in zero order without the appearance of a half-wave wavelength, where $\delta_C = \pi$ and incident linear polarization remains linear upon transmission through the compensator. Dual biplates yield more complicated data reduction equations, however, than those provided in the next sections [7, 26, 31].

9.3.1
Rotating-Analyzer SE for *Ex Situ* Applications

The most popular configuration for wavelength scanning ellipsometry incorporates the rotating analyzer principle of polarization state detection [29, 32, 33]. When the analyzer is rotating at an angular frequency ω_A such that $A = \omega_A t$, the light irradiance measured at the detector varies with time according to the following waveform:

$$I_{exp}(t) = I_0\{1 + \alpha\cos(2\omega_A t) + \beta\sin(2\omega_A t)\}. \tag{9.6}$$

The Fourier coefficients of the irradiance waveform include I_0, the dc coefficient, and α and β, the $2\omega_A$ cosine and sine coefficients normalized to the dc coefficient. In the straight-through configuration (source and detector colinear) without a compensator or sample, the light reaching the analyzer is linearly polarized and the irradiance at the detector follows Malus's law assuming that the polarizer and analyzer are ideal. If the fixed polarizer transmission axis is aligned with the analyzer transmission axis at $t = 0$, then $I_{exp}(t) = I_{out}\cos^2\omega_A t$, which implies that $\alpha = 1$ and $\beta = 0$ in Equation 9.6, with $I_0 = I_{out}/2$, where I_{out} is the output irradiance from

the fixed polarizer. With a sample in place and the analyzer–detector arm of the ellipsometer moved to collect the specularly reflected beam at oblique incidence, the light reaching the analyzer is elliptically polarized, in general.

For photomultiplier tube or solid-state detectors, the photocurrent is sampled at regular intervals (typically every ~5° of analyzer angle) triggered by an encoder mounted on the motor which drives the analyzer [33]. Assuming the detector is linear, the photocurrent is proportional to the incident irradiance of Equation 9.6, and Fourier analysis of the sampled current over one half mechanical rotation of the analyzer (one optical cycle) can provide the Fourier coefficients α and β. From the Fourier coefficients and the settings of the polarizer and optional compensator, the ellipsometry angles (ψ, Δ) can be determined. The compensator characteristics include not only the angle C of the fast axis F with respect to the p direction but also δ_C, which is the phase lag of the field component normal to F relative to that along F as described earlier in Section 9.3 [7]. If the fast axis of the compensator lies in the plane of incidence along p (so that $C = 0°$), then the following equations for (ψ, Δ) hold:

$$\tan\psi = \left|\sqrt{\frac{1+\alpha}{1-\alpha}}\right| |\tan P|, \tag{9.7}$$

$$\cos(\Delta + \delta_C) = \beta \left|\sqrt{\frac{1}{1-\alpha^2}}\right|. \tag{9.8}$$

The highest measurement precision occurs for the polarizer angle $P = \psi$ and for the compensator retardance $\delta_C = \pm 90° - \Delta$. Operation under these conditions is particularly advantageous when the light source is unstable. This motivates the use of a polarizer and compensator that can be adjusted automatically to achieve these conditions, wavelength point-by-point. For the compensator, a Berek monoplate design [31] can be used in which a MgF_2 plate is tilted slightly (~5–10°) about an axis either parallel or perpendicular to the fast axis, and this tilt angle is varied in order to vary δ_C. These two possible tilt axes form a right-handed coordinate system with the propagation vector of the light beam through the monoplate. A figure of the Berek compensator design is given in Ref. [31].

9.3.2
Rotating-Compensator SE for Real-Time Applications

In high-speed multichannel ellipsometry, it may not be possible to adjust the optical elements for optimization of instrument performance or to perform multiple measurements to resolve ambiguities [30]. As a result, the rotating analyzer ellipsometer has three limitations in applications whereby high speed is required. First, a rotating analyzer cannot detect depolarization by the sample or by optical element imperfections. When such effects are unrecognized and not modeled, they lead to experimental errors. Second, the sign of $\Delta + \delta_C$ is ambiguous, which means that there are two possible solutions for Δ. (When $\delta_C = 0°$, i.e., when no compensator is used, this simply means that one cannot determine the sign of Δ, i.e.,

the handedness of the general elliptical polarization state entering the rotating analyzer.) Third, there exists a low sensitivity to Δ for nearly linearly polarized light entering the rotating analyzer, which occurs when $\cos(\Delta + \delta_C)$ is an extremum or when $(\Delta + \delta_C) \sim 0°, 180°, 360°, \ldots$.

These three limitations are overcome by rotating the compensator rather than the analyzer [34, 35]. In this case, two SE configurations have been used, with the rotating compensator either in front of the sample, denoted as "PC_rSA," or behind the sample, denoted as "PSC_rA" (P, polarizer; C_r, rotating compensator; S, sample; and A, analyzer). In the PSC_rA configuration, the light beam incident on the sample is in a known time-independent (or unmodulated) polarization state. The unknown time-independent polarization state of the reflected beam is analyzed by the C_rA combination, serving as a polarization state detector [30]. Therefore, this configuration is conceptually simpler for understanding the principle of ellipsometry as a measurement of a polarization state change upon oblique reflection.

For the PC_rSA configuration, on the other hand, the polarization of the incident beam is continuously modulated by the rotating compensator through known states as described in the following paragraphs. In this case, the analysis with a fixed analyzer involves determining the capacity of the sample to change a continuous succession of polarization states upon reflection. Owing to the time reversal symmetry between the PSC_rA and PC_rSA configurations, however, their mathematical descriptions are closely related and can be obtained by the following interchanges: $P \leftrightarrow A$ and $\delta_C \leftrightarrow -\delta_C$. Operationally, however, instrument errors due to sample misalignment tend to be greater in the PSC_rA configuration. When a sample is misaligned in this configuration, the beam that passes through the compensator is also misaligned, and this generates greater errors relative to beam misalignment through a single polarizer (i.e., the analyzer). Sample misalignments are more common in real-time and mapping applications in which case alignment is more challenging or large-area samples may be nonplanar due to stress. In the PC_rSA configuration, the beam through the polarizer and compensator can be aligned once, and this alignment is not affected by the sample surface position. The PC_rSA configuration is more widely used owing to its incorporation in a popular commercial instrument and will be described in detail in this subsection.

For an ellipsometer with a compensator rotating at ω_C, irrespective of the position of the compensator (either before or after the sample), both $2\omega_C$ and $4\omega_C$ frequencies appear in the irradiance waveform, according to

$$I_{exp}(t) = I_0\{1 + \alpha_2 \cos(2\omega_C t) + \beta_2 \sin(2\omega_C t) + \alpha_4 \cos(4\omega_C t) + \beta_4 \sin(4\omega_C t)\}. \quad (9.9)$$

Here $2\omega_C$ can be understood as the fundamental optical frequency, and α_n and β_n ($n = 2, 4$) are the dc normalized $n\omega_C$ cosine and sine Fourier coefficients, respectively. A Fourier analysis of the irradiance waveform provides these coefficients which then can be related to ellipsometry angles ψ and Δ as described by the equations in the next paragraph.

Considering the PC_rSA configuration, the ellipsometry angles (ψ, Δ) can be overdetermined from the Fourier coefficients of Equation 9.9. The first step in this data reduction process is to apply the Fourier coefficients to extract the three parameters:

$$r_1 = \frac{r_0(\alpha_4 \cos 2P + \beta_4 \sin 2P)}{\sin^2(\delta_C/2)}, \tag{9.10}$$

$$r_2 = \frac{r_0(-\alpha_4 \sin 2P + \beta_4 \cos 2P)}{\sin^2(\delta_C/2)}, \tag{9.11}$$

$$r_3 = \frac{r_0(-\alpha_2 \sin 2P + \beta_2 \cos 2P)}{\sin \delta_C} \tag{9.12}$$

where

$$r_0 = \left(1 - \frac{\alpha_4 \cos 4P + \beta_4 \sin 4P}{\tan^2\left(\delta_C/2\right)}\right)^{-1}. \tag{9.13}$$

From these three parameters, the following equations can then be applied:

$$-N = -\cos 2\psi = \frac{r_1 - \cos 2A}{1 - r_1 \cos 2A}, \tag{9.14}$$

$$C = \sin 2\psi \cos \Delta = \frac{r_2 \sin 2A}{1 - r_1 \cos 2A}, \tag{9.15}$$

$$S = \sin 2\psi \sin \Delta = \frac{r_3 \sin 2A}{1 - r_1 \cos 2A}. \tag{9.16}$$

Equation 9.14 enables one to determine ψ without ambiguity over its full range of $0° \leq \psi \leq 90°$. Once ψ is known, then one can determine the value of Δ over the full range of $-180° < \Delta < 180°$ from Equations 9.15 and 9.16. Because $\sin 2\psi \geq 0$ over the full range of ψ, the signs of $\sin \Delta$ and $\cos \Delta$ enable direct identification of the quadrant of Δ. The determination of the four Fourier coefficients enables evaluation of the depolarization by the sample. The deviation from unity in the degree of polarization p, given by

$$p = (r_1^2 + r_2^2 + r_3^2)^{1/2} \tag{9.17}$$

is the appropriate measure of the depolarization in this ellipsometer configuration. By evaluating this parameter spectroscopically, one can identify the sources of depolarization, for example, variations in sample properties over the beam area, or collection of scattered light or back-surface reflections, that may generate data analysis problems if not taken into account.

Although the capacity of the sample to change the polarization state of the light upon specular reflection is described completely by the ellipsometry angles (ψ, Δ) as defined in Equation 9.3, this is an insufficient description of the sample if it generates a depolarized component upon reflection. In the case of sample depolarization, the formalism of Stokes vectors and Mueller matrices is best adopted [7]. This is a complication beyond the intended scope of this chapter.

9.4 Data Analysis

Rarely does a sample assume the simple form of a single interface; the most common sample structure consists of m layers on a substrate and $m+1$ interfaces. In order to extract one or more complex dielectric functions and the layer thicknesses from such multilayer samples from a pair of ellipsometry spectra (ψ, Δ), a model-based approach must be used [7–9, 24]. Two of the most commonly used approaches include exact numerical inversion and least-squares regression, which have different applications depending on the type of sample being analyzed. Both approaches are based on iterative application of the same three steps: (i) development of a model with starting parameters, (ii) determination of the best-fit parameters within the assumed model, and (iii) evaluation of the reasonableness of the results either through calculation of an error function or through an inspection of the smoothness and Kramers–Kronig consistency of the resulting dielectric function. A third approach, known as virtual interface analysis, is extremely useful for analysis of real-time data collected on complex graded layer structures in which case the focus of the analysis is on the near-surface region and not on the underlying multilayer structure.

9.4.1 Exact Numerical Inversion

Exact numerical inversion is useful for analysis of thin-film samples in which one of the complex dielectric functions of the sample is unknown, and only approximations to one or more of the thicknesses are available. The simplest inversion method utilizes a Newton–Raphson algorithm; however, more advanced algorithms exist [36, 37]. The first step in this method is to assign approximate values to the one or more thicknesses in the problem, as well as first-guess values of the real and imaginary parts of the one unknown complex dielectric function at one wavelength point (usually the largest value of λ in the case of a semiconductor). Then, (ψ, Δ) values at this wavelength are calculated and are compared to the experimental (ψ, Δ) data. Next, the inversion algorithm is used to bring the first-guess values of the complex dielectric function closer to the values required for an exact match to the experimental data. These steps are iterated until the calculated and experimental data values agree to within limits smaller than the precision, typically $<1 \times 10^{-4}$ [33]. The entire process is then repeated for the next spectral point, using the results from the previous spectral point as a first guess for the complex dielectric function. It is important to note that the first-guess value must be reasonably close to the actual solution; otherwise the inversion algorithm may diverge. Alternatively, multiple solutions may exist and an incorrect one may be erroneously identified. It should be noted that the final solution is associated with the particular approximate thickness values. There must be an additional iteration loop to identify improved thickness values based on the elimination of artifacts in the deduced complex dielectric

function. In addition, the result can be checked for Kramers–Kronig consistency (see, e.g., Ref. [9]).

9.4.2 Least-Squares Regression

Least-squares regression is the most commonly used method for extracting the complex dielectric function and thicknesses of a thin-film material from spectroscopic ellipsometry data (ψ, Δ) [38, 39]. The first step in this method is to develop models for the multilayer structure and any unknown complex dielectric functions of the layer components. In this case, in contrast to analysis by inversion, the dielectric functions are expressed as continuous analytical functions of wavelength. Thus, all parameters in the problem are wavelength independent; these parameters include those that describe the analytical functions as well as the thicknesses. Then, (ψ, Δ) spectra are calculated based on the first-guess values and are compared to the experimental (ψ, Δ) spectra. Next, the least-squares regression algorithm is used to bring the first-guess values closer to those that minimize the mean square error (MSE) between the calculated and experimental spectra. When the first-guess values reach the solution, the MSE will be minimized and the least-squares regression algorithm will be complete. It is important to note that the MSE will never vanish since there are more experimental data values than free parameters in the model, and these experimental data values incorporate both random and systematic errors [39].

9.4.3 Virtual Interface Analysis

Virtual interface analysis is useful for characterizing the near-surface region of a deposited film while minimizing the complexity of the model by approximating the underlying multilayer structure with a single interface to a pseudo-substrate. The method is particularly useful for characterizing compositionally graded thin films in real time during their deposition. When applied to RTSE data, this method assumes an initial pseudo-substrate with pseudo-dielectric function $<\varepsilon>$, which is obtained by applying Equation 9.5 to (ψ, Δ) values collected when $t = 0$ (no deposition). For all $t > 0$, an optical model is constructed which includes an outer layer of deposited material with complex dielectric function ε_o and thickness d_o on top of the pseudo-substrate just described. Using this model and the (ψ, Δ) values measured at multiple times, it is possible to determine the best dielectric function ε_o and the deposition rate required to fit the multiple (ψ, Δ) values. In this case, ε_o is interpreted as the dielectric function of the near-surface region of the deposited film. Repeating this procedure as a function of time will result in a depth profile in the optical functions, which can be further analyzed to extract a depth profile of the structural phase (as in thin-film Si:H that evolves from an amorphous to nanocrystalline phase) or the chemical composition (as in compositionally graded thin-film $CdTe_{1-x}S_x$ or CIGS solar-cell materials) [40, 41].

9.5
Spectroscopic Ellipsometry for Thin-Film Photovoltaics

In this section, results of SE studies of the three major thin-film technologies will be described in order of the level to which the capability has been advanced for each technology. For thin-film hydrogenated silicon (Si:H), significant progress has been made in understanding the growth processes using RTSE and in developing guiding principles for the optimization of both amorphous silicon (a-Si:H) and nanocrystalline silicon (nc-Si:H) solar cells [40]. For thin-film CdTe and $Cu(In_{1-x}Ga_x)Se_2$ (CIGS), significant advances in the application of SE, corroborated with other characterization techniques, such as electron microscopy and energy-dispersive X-ray spectroscopy, have been made only recently using the complex dielectric function databases developed previously. As a result, RTSE can now be performed with confidence to study the growth dynamics for the key component layers, such as CdTe, CdS, and CIGS, in challenging multilayer device configurations. In addition, with an appropriate apparatus for translating the device or the multichannel SE instrument, *ex situ* SE studies of complete modules enable contactless characterization that yields maps of properties such as layer thicknesses, carrier concentration, carrier mean free path, film stress, and alloy composition. These properties can be used further to predict the local external quantum efficiency (QE) and total short-circuit current density of the photovoltaic devices and to identify the origins of electrical and optical losses. Due to the specialized nature of the mapping measurements, examples of this capability will not be presented here but are provided in the references.

9.5.1
Thin Si:H

Thin-film Si:H is the most extensively studied of the thin-film solar-cell materials since it encompasses the prototypical amorphous and nanocrystalline semiconductors [42]. The highest-performance small-area solar cells from multijunctions of these materials yield roughly a factor of two lower efficiency than the highest-performance c-Si solar cells. In spite of this, thin-film Si:H cells can present certain advantages such as relaxed crystal momentum conservation and hence strong absorption for a much reduced thickness as well as the potential for low production costs [42]. The Si:H materials are deposited by plasma-enhanced chemical vapor deposition (PECVD), a low-temperature process (<300 °C), using a mixture of hydrogen and silane or disilane gases. As a result, these solar cells are excellent candidates for fabrication on flexible low-cost polymer substrates in roll-to-roll processes. By altering the deposition parameters, most notably the R value, which in the following examples is the ratio of hydrogen to silane or disilane gas flows, a Si:H thin film can be made fully amorphous, graded mixed phase, or fully nanocrystalline. These different structures of Si:H thin films have been studied in detail using RTSE as reviewed in this section [40, 43].

Figure 9.2 compares the deduced complex dielectric functions of pure amorphous and pure nanocrystalline phases of Si:H (a-Si:H and nc-Si:H, respectively) as measured by RTSE using a custom-made rotating-compensator multichannel spectroscopic ellipsometer. A calibrated c-Si substrate temperature of 200 °C was used during PECVD with a hydrogen dilution level of silane given by $R = [H_2]/[SiH_4] = 20$. In fact, the initial RTSE data before film growth can be used to calibrate the actual substrate temperature when the complex dielectric function of the substrate, a c-Si wafer in Figure 9.2, or that of its overlayers is accurately known as a function of measurement temperature. Because the final Si:H film of Figure 9.2 is graded from amorphous at the substrate interface to nanocrystalline at the top of the film, the analysis to deduce these dielectric functions was performed by applying a virtual interface model.

Although the overall shapes of the two dielectric functions in Figure 9.2 are similar, that of nc-Si:H shows two well-defined features near 3.4 and 4.2 eV, which are the vestiges of the critical points of single-crystal Si [14]. In contrast, the a-Si:H dielectric function is characterized by a single, much broader feature due to the loss of long-range order. This loss leads to a relaxation of crystal momentum (or electron ***k***-vector) conservation, and as a result, a larger imaginary part of the dielectric function than nc-Si:H is observed just above the a-Si:H band gap (1.7 eV). Thus, much stronger absorption is obtained over the photon energy range

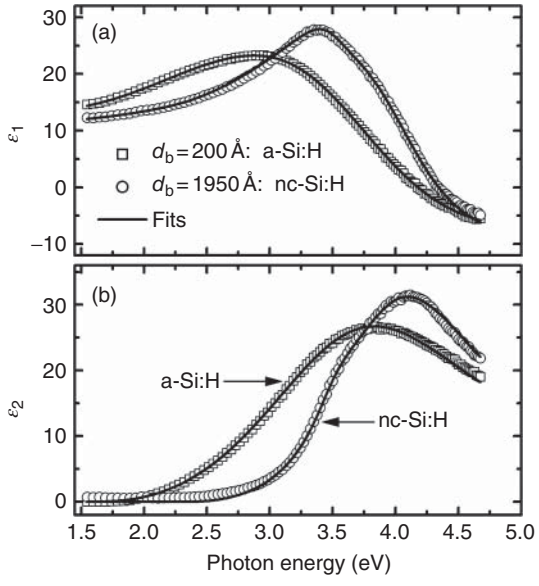

Figure 9.2 The real (a) and imaginary (b) parts of the complex dielectric functions of intrinsic amorphous and nanocrystalline Si:H (a-Si:H and nc-Si:H, respectively), measured at a calibrated substrate temperature of 200 °C in RTSE studies of a growing film with $R = [H_2]/[SiH_4] = 20$. The film thicknesses for these measurements of the a-Si:H and nc-Si:H dielectric functions were 20 and 195 nm, respectively. (Adapted from Ref. [43] with permission of Elsevier.)

of the visible spectrum from 1.8 to 3.1 eV. It is these differences that enable one to distinguish readily between the two phases using SE methods and to characterize the evolution of mixed-phase materials using RTSE [43]. Because the highest-quality a-Si:H and nc-Si:H materials are fabricated near the a-Si:H to nc-Si:H boundary in deposition parameter space, this capability is critically important for optimizing thin-film Si:H photovoltaic material deposition as will be demonstrated later in this subsection.

Figure 9.3a shows the surface roughness layer thickness as a function of the bulk layer thickness as deduced by RTSE for two different Si:H intrinsic layer depositions with hydrogen dilution levels of disilane given by $R = [H_2]/[Si_2H_6] = 60$ and $R = 150$ [44]. For the two depositions, all other PECVD parameters were fixed including a nominal substrate temperature of 200 °C [40]. (In the PECVD system used for the studies of Figures 9.3–9.5, the RTSE-calibrated temperature of 110 °C was found to be much lower than the nominal value of 200 °C.) The underlying substrate films for the depositions of Figure 9.3a were standard a-Si:H n-layers, which result in the layered configuration used for an amorphous n–i–p solar cell. Figure 9.3b shows the volume fraction of the nanocrystalline Si:H phase (f_{nc}) as a function of bulk layer thickness for the $R = 150$ i-layer which exhibited a graded mixed-phase structure. The structural parameters plotted in Figure 9.3b were determined by analysis of RTSE data using a virtual interface model which was applied in order to extract the complex dielectric function of the top ~1 nm of the growing film. In this way, a depth profile in f_{nc} is obtained by applying the Bruggeman effective medium approximation to the deduced dielectric functions assuming a mixture of fully amorphous and nanocrystalline phases. Because the film structure is locked-in as the film grows, Figure 9.3b represents a depth profile of the nanocrystalline content of the final film.

Figure 9.3a and b demonstrate specifically that for the $R = 150$ deposition, the Si:H i-layer film nucleates on the n-layer as amorphous Si:H, undergoes an amorphous-to-nanocrystalline transition after a thickness of ~10 nm as indicated by abrupt roughening, and then becomes fully nanocrystalline after a thickness of ~100 nm, at the onset of smoothening [44]. This behavior suggests that once Si:H nanocrystals nucleate from the amorphous phase, the deposition rate of the nc-Si:H is higher than that of a-Si:H, leading to inverted cone-like structures of nc-Si:H that protrude above the surface and coalesce after a sufficient thickness is deposited. A schematic of the proposed structure is shown in Figure 9.3c, which has been verified by electron microscopy. For the $R = 60$ deposition, a strong roughening effect is not observed and the film is found to remain amorphous throughout the deposition.

Similar depth profiles to that of Figure 9.3b obtained as a function of R, the H_2-dilution ratio of disilane, from $R = 80$ to 150 have been used to construct the growth-evolution diagram for the PECVD films in Figure 9.4a [40]. In this case, the Si:H i-layer films grown on a-Si:H n-layers remain amorphous throughout at least the first ~200 nm of bulk layer growth when $R \leq 80$. For higher R ($R \geq 100$), the Si:H i-layer films initially nucleate as a-Si:H but then undergo an amorphous-to-nanocrystalline transition at a thickness that shifts from greater

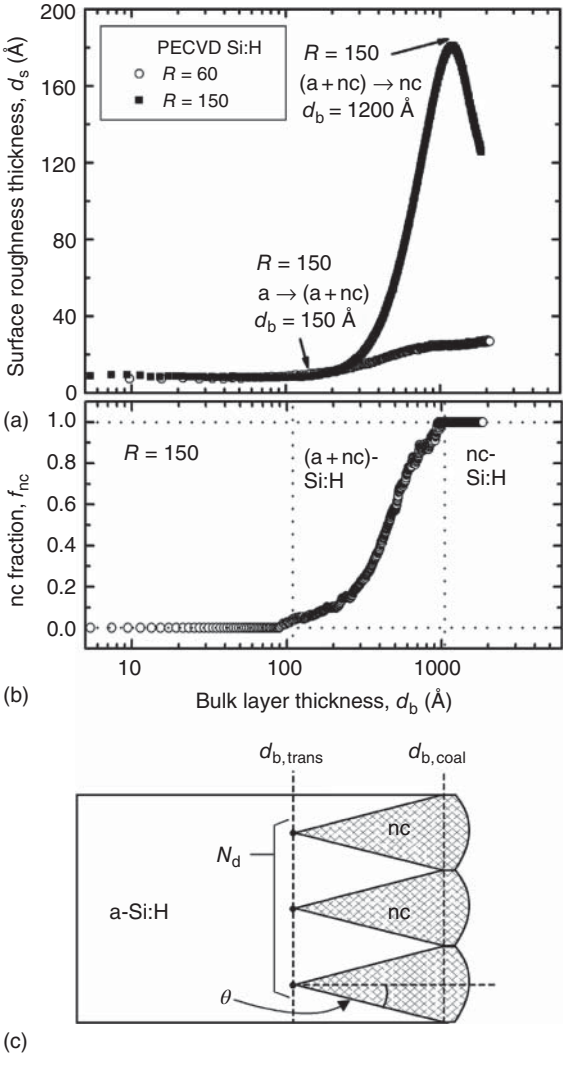

Figure 9.3 (a) Surface roughness layer thickness as a function of bulk layer thickness deduced by RTSE for two PECVD films with hydrogen dilution levels of disilane given by $R = 60$ and 150. For the two depositions, all other PECVD conditions were fixed including an actual substrate temperature of 110 °C. (Adapted from Ref. [44] with permission of Elsevier.) (b) Depth profile in the nanocrystalline volume fraction (f_{nc}) for the mixed-phase Si:H i-layer of (a) deposited under fixed conditions with $R = 150$ on top of an a-Si:H n-layer. (c) A schematic of nanocrystallite nucleation and coalescence where N_d describes the nuclei/area and θ is the cone half-angle. (Adapted from Ref. [44] with permission of Elsevier.)

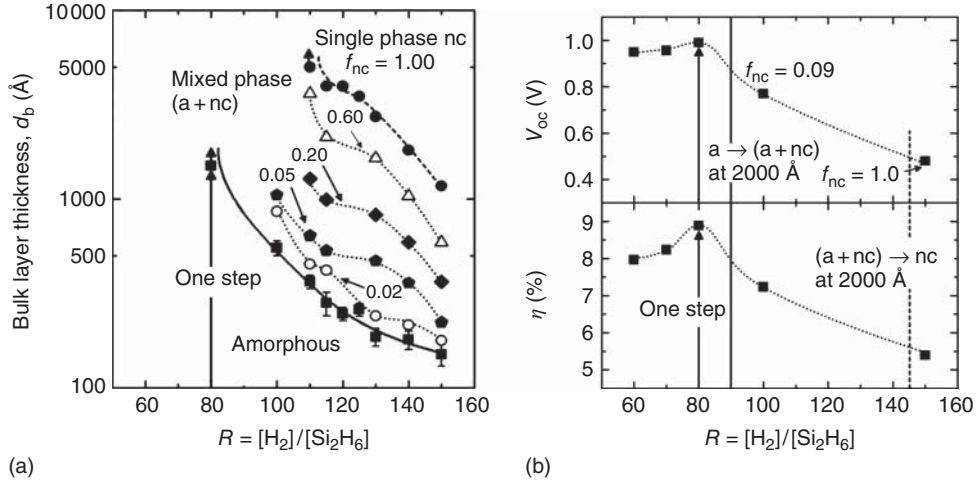

Figure 9.4 (a) Growth-evolution diagram deduced from virtual interface analysis of RTSE measurements performed during deposition of Si:H i-layers on a-Si:H n-layers in the n–i–p configuration used for a-Si:H solar cells (contours on the diagram indicate constant f_{nc} values). (b) V_{oc} and efficiency versus the Si:H i-layer R value for single-junction solar cells 200 nm thick. The n-layers used in these solar cells are pure a-Si:H. (Adapted from Ref. [40] with permission of IEEE.)

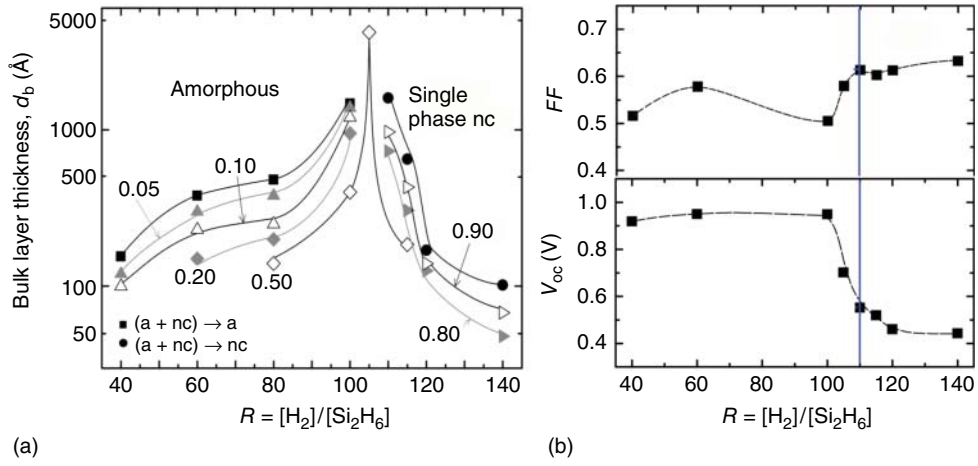

Figure 9.5 (a) Growth-evolution diagram for Si:H i-layers on nc-Si:H n-layer substrate films as deduced from virtual interface analysis of RTSE data. These i-layers are designed for incorporation into nc-Si:H solar cells (contours on the diagram indicate constant f_{nc} values). (b) V_{oc} and FF versus R for intended nc-Si:H solar cells in which case underlying nc-Si:H n-layers are used. The vertical line identifies the optimum nc-Si:H solar-cell performance as defined by the V_{oc}-FF product. (Adapted from Ref. [40] with permission of IEEE.)

than 200 nm to lower thicknesses with increasing R. Performance parameters of single-junction solar cells fabricated using a thickness of ~200 nm for the Si:H i-layer, and different R values are shown in Figure 9.4b [40]. The optimum V_{oc} and efficiency for this series of cells occurs when $R = 80$, which is the maximum R value possible such that the i-layer remains fully amorphous throughout its thickness. For a larger value of $R = 100$, the fraction of nanocrystallites as detected by RTSE in the near surface of the 200 nm i-layer is small (~0.09), but these nanocrystallites appear to degrade V_{oc} due to their presence at the i–p interface. This concept of maximum hydrogen dilution developed by RTSE is applied widely to optimize the performance of a-Si:H materials in devices [43]. In fact, RTSE has suggested extensions of this concept through Si:H layers deposited using multistep and continuously variable dilution ratios R for improvements over layers deposited using simple single-step processes.

Another growth-evolution diagram is shown in Figure 9.5a as obtained by virtual interface analysis of RTSE data collected on several Si:H i-layer depositions performed as a function of R. In this case, the i-layers were deposited on intended nanocrystalline Si:H (nc-Si:H) n-layers at a calibrated temperature of 110 °C [40]. This is the layer structure used for standard nanocrystalline n–i–p solar cells, and the resulting diagram differs significantly from that of the Si:H i-layers deposited on a-Si:H n-layers shown in Figure 9.4a. Mixed-phase Si:H growth in the initial stage results from a template effect due to the underlying nc-Si:H n-layer, which is itself mixed phase, consisting of ~0.5/0.5 vol. fraction ratio of a-Si:H/nc-Si:H. At lower dilution levels ($R < 105$), the mixed-phase i-layers evolve to a-Si:H due to a higher rate for amorphous Si:H growth. In this range of R, the mixed-phase nanocrystalline to amorphous [(a + nc) → a] transition shifts to larger thickness with increasing R. At higher dilution levels ($R > 105$), the initial mixed-phase material evolves rapidly to fully nc-Si:H due to the higher rate for nanocrystalline Si:H growth. In this range, the (a + nc) → nc transition shifts to lower thickness with increasing R. Figure 9.5a reveals a bifurcation value of $R = 105$, which divides the ultimate phase of the film between fully amorphous and fully nanocrystalline-even though the film nucleates as mixed-phase Si:H essentially independent of R. Such growth-evolution diagrams deduced in RTSE studies provide guidance for the optimization of nc-Si:H solar cells as described in the next paragraph.

In the case of 0.4–0.6 μm thick nc-Si:H i-layers used in solar cells with performance shown in Figure 9.5b, the optimum one-step deposition process occurs on the basis of the phase diagram at the smallest R value possible such that the i-layer evolves to predominantly nc-Si:H during its growth [40]. This minimum value occurs at $R = 110$. At $R = 100$ the (a + nc) → a transition occurs at a thickness of 150 nm, and it is clear from the V_{oc} value of 0.95 V in Figure 9.5b that the top of the film is a-Si:H. At $R = 120$ the (a + nc) → nc transition occurs at a thickness of 200 nm, and in this case, it is clear from the V_{oc} value of 0.46 V that the top of the film is nc-Si:H. The highest-performance nc-Si:H i-layer (i.e., the highest V_{oc}-FF product) in Figure 9.5b is obtained at $R = 110$, just before a more rapid drop in fill factor associated with the narrow bifurcation region. The continued lower fill factor for the low R Si:H films in Figure 9.5b relative to those of Figure 9.4b is attributed to the nc-Si:H phase transition in the i-layer, which for

the $R = 60$ deposition occurs at a thickness of about 40 nm as measured from the underlying n-layer. Overall, these results demonstrate clear correlations between structural evolution as determined from RTSE and device performance. Such correlations enable single-step, multistep, and graded layer optimization using the H_2-dilution ratio to control the phase of the film and its depth profile.

9.5.2 CdTe

The most successful thin-film photovoltaics technology from a commercial perspective is polycrystalline CdTe in the glass superstrate configuration [45]. CdTe serves as the p-type semiconductor absorber layer incorporated into the heterojunction solar cell with CdS commonly used as the n-type window layer. This subsection will focus on the application of SE (including RTSE) to CdTe thin-film photovoltaic devices.

9.5.2.1 RTSE Monitoring of CdS in CdTe Solar-Cell Devices

A critical need exists for measuring, monitoring, and controlling the properties of CdTe solar-cell component layers and multilayer structures in real time during their deposition in the sample configuration used for solar-cell production. Of particular interest is the CdS thickness since this layer is not electronically active and generates absorption losses in its role as the n-type window layer of the CdTe solar cell. In the RTSE analysis of the CdS window layer deposition process reviewed here, the layer was deposited by magnetron sputtering at a substrate temperature of 250 °C, a radio frequency (rf) power of 200 W, and an Ar pressure of 20 mTorr. The superstrate was NSG-Pilkington TEC-15 glass coated with a high resistivity transparent (HRT) SnO_2 layer. TEC-15 glass is soda-lime glass (SLG) overdeposited with a trilayer, yielding the structure SLG/SnO_2/SiO_2/SnO_2:F. The deposition time for the CdS layer was 14.5 min for an intended film thickness of 120 nm [46].

RTSE of CdS sputter deposition on the TEC-15/HRT structure was performed using a commercially available rotating-compensator multichannel spectroscopic ellipsometer [47, 48] having a spectral range of 0.75–6.5 eV (J.A. Woollam Co., M2000-DI). During CdS deposition, RTSE measurements were taken every 2.4 s, corresponding to an increment in CdS effective thickness (volume/area) of ~0.3 nm. The RTSE data were fit using a nonlinear least-squares regression algorithm to minimize the square root of the MSE between the experimental and best-fit ellipsometry data as defined in Equations 9.14–9.16. The RTSE data were analyzed using as input previously determined spectra in the complex dielectric function ε measured at 250 °C for each component of the multilayer stack. These components include SLG, SnO_2(I), SiO_2, SnO_2:F, SnO_2(II), and CdS, whereby two different versions of ε for SnO_2 are used. The second form (II) is the top-most HRT layer on which the CdS is deposited. The procedures for determining the ε spectra for these layers are described in Ref. [49].

Figure 9.6 depicts RTSE analysis results extracted in the nonlinear least-squares regression analysis. Because the SnO_2 HRT layer on which the CdS is deposited

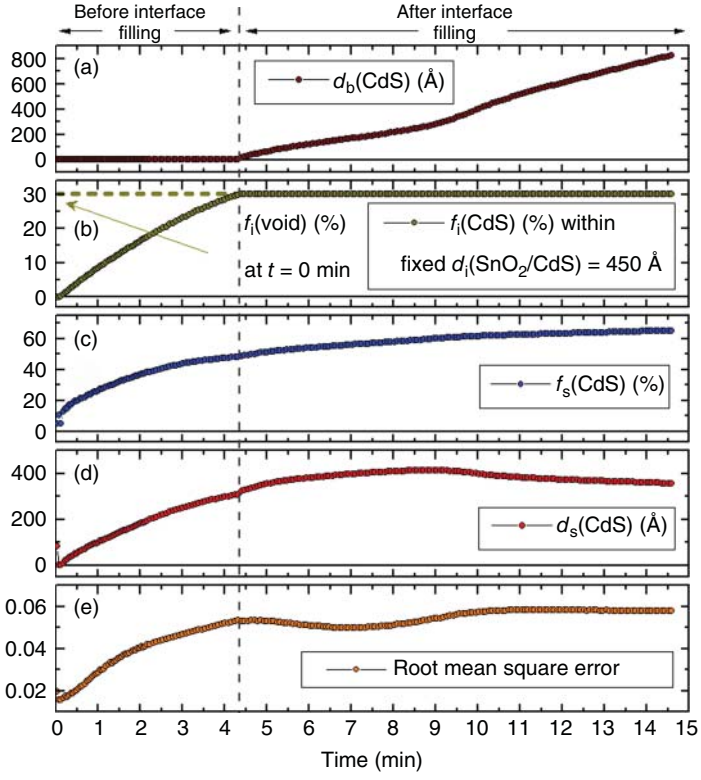

Figure 9.6 Structural parameters deduced by RTSE that describe the growth of a 120 nm CdS film on top of a rough SnO_2 HRT superstrate film, including (a) the CdS bulk layer thickness, (b) the CdS volume percentage in the 45 nm thick SnO_2/CdS interface roughness layer, (c) the CdS volume percentage in the CdS surface roughness layer, (d) the CdS surface roughness layer thickness, and (e) a measure of the quality of the fit to the RTSE data given as the square root of the MSE. (Adapted from Ref. [46] with permission of Elsevier.)

exhibits a considerable thickness of surface roughness, in fact 45 nm, a relatively complicated structural model is required and thus analysis challenges are generated. The required structural model simulates the evolution of the SnO_2 surface roughness layer into a SnO_2/CdS interface roughness layer and the simultaneous development of CdS surface roughness, both effects due to conformal coverage of the SnO_2 upon initial growth of the CdS. The RTSE results show very high sensitivity to the structural evolution of the CdS, as indicated by both the filling of the interface with CdS and the CdS layer surface roughness development. Figure 9.6 includes (a) the CdS bulk layer thickness, (b) the volume fraction of CdS within the fixed thickness (45 nm) roughness modulations of the SnO_2 surface as these modulations are transformed from surface to interface roughness, (c) the CdS volume fraction in the CdS surface roughness layer, and (d) the thickness of CdS surface roughness layer. Also shown in Figure 9.6e is the time evolution of the square root of the MSE, whose time average is minimized in

order to identify the appropriate structural and optical models for describing the experimental data.

The structural evolution of the CdS as depicted in Figure 9.6 can be understood as follows. At $t = 0$, the SnO_2 HRT layer on the superstrate presents a rough surface characterized by a roughness layer thickness of 45.0 ± 1.2 nm. The structural evolution of CdS on this surface can be described in terms of interface filling ($0 < t < 4.4$ min) and bulk layer growth ($4.4 < t < 14.5$ min) regimes. When the shutter is opened to initiate CdS deposition, two effects occur simultaneously in the interface filling regime. First, the voids associated with the valleys of the surface roughness layer of the top-most SnO_2 HRT begin to fill with CdS, whose volume percent in the roughness layer is given by f_i(CdS). Second, the CdS begins to conformally cover the peaks of the SnO_2 roughness, forming its own roughness layer of thickness d_s(CdS) and CdS volume percent f_s(CdS). In fact, a CdS component as low as 10 vol.% can be detected in the early stages of CdS roughness development ($d_s < 2$ nm) while interface filling is proceeding. The onset of bulk layer growth is observed upon completion of interface filling at $t = 4.4$ min, which occurs when f_i(void) $\rightarrow 0$. For $t > 4.4$ min in the bulk layer growth regime, the CdS volume percent in the interface roughness layer is fixed at its final value of $f_i(\text{CdS}) = 30.0 \pm 0.4$ vol.%, with the remainder being SnO_2. During bulk layer growth, $4.4 < t < 14.5$ min, the bulk layer thickness d_b(CdS) increases from the monolayer level to $\sim 83.0 \pm 0.8$ nm, approaching linearity as the CdS surface characteristics stabilize. At the end of deposition, the CdS surface roughness layer thickness and the CdS volume percent in the layer are given by $d_s(\text{CdS}) \sim 35.6 \pm 0.4$ nm and $f_s(\text{CdS}) \sim 65.3 \pm 0.4\%$, respectively.

The effective thickness of CdS at the end of deposition is given by $d_{\text{eff}} = f_i(\text{CdS})d_i + d_b + f_s(\text{CdS})d_s = 119.6 \pm 1.1$ nm, where $d_i = 45$ nm is the SnO_2/CdS interface layer thickness. The effective thickness matches the intended value of 120 nm. This thickness controls the quantum efficiency in the blue region of the solar spectrum (300–500 nm) and, in part, the current–voltage characteristics of the heterojunction diode. The final surface roughness on the CdS, of thickness $d_s(\text{CdS}) = 35.6 \pm 0.4$ nm, is controlled predominantly by the roughness on the underlying SnO_2 HRT layer; however, a weak smoothening effect is observed that depends on the CdS deposition conditions. In fact, this study has also been extended to explore the effect of deposition conditions on the structural evolution of the CdS, with consistent trends being observed. The CdS roughness evolution is important since its final thickness is expected to influence the nature of the heterojunction, as this junction is formed by the overdeposition of the CdTe on the rough CdS surface. Similar results to those in Figure 9.6 have been obtained for CdTe layer deposition on HRT/CdS to form the heterojunction.

9.5.2.2 *Ex Situ* SE and QE Simulation for CdTe Solar-Cell Devices

The multilayered structure of the CdTe solar cell presented in this review includes the TEC-15/HRT superstrate stack coated with magnetron sputtered CdS (~100 nm) and CdTe (~2.0 μm) [50]. In order to fabricate the device, the as-deposited stack is subjected first to a $CdCl_2$ treatment for 30 min at 387 °C, then to evaporations of ~3 nm of Cu and ~30 nm of Au, and finally to a 45 min

anneal at 150 °C for Cu diffusion. Solar-cell measurement under air mass (AM) 1.5 illumination yielded a short-circuit current density of 21.5 mA/cm^2, an open-circuit voltage of 0.815 V, a fill factor of 0.702, and a power conversion efficiency of 12.3%. *Ex situ* SE measurements of the completed device were performed through the SLG superstrate at a 50° angle of incidence over the range in photon energy E of 0.75 – 3.5 eV. The upper limit of E results from glass absorption. Spatial filtering enables separation and collection of the glass/film-stack second reflection, rejecting the ambient/glass first reflection as well as the higher reflections; in fact, the rejected reflections are almost fully blocked. The SE measurements were performed such that the incident beam reflects from the CdTe/Au back contact interface, and so this back contact region is included in the optical model.

In the analysis of the *ex situ* SE data for the CdTe solar cell, parameterized complex dielectric functions $\varepsilon(E)$ from an extensive database have been applied. As a result, variations in ε(E) have been generated through variations in wavelength-independent parameters related to material properties of interest. In general, analysis is initiated with the specification of the component material ε spectra and the wavelength-independent free parameters, if any, to be used in the analytical expressions for each. Starting with the semiconductors, CdTe and CdS, the spectra in $\varepsilon(E)$ are expressed as a sum of three oscillator terms:

$$\varepsilon(E) = \varepsilon_{1,\infty} + \varepsilon_{\mathrm{TL}}(E) + \sum_n \varepsilon_{\mathrm{CP},n}(E). \tag{9.18}$$

The energy-independent first term $\varepsilon_{1,\infty}$ is the constant offset to the real part of the complex dielectric function. The second term is a background Tauc – Lorentz (TL) oscillator $\varepsilon_{\mathrm{TL}}(E)$ whose imaginary part is forced to zero below the lowest critical point (CP) resonance energy E_0 of the semiconductor by fixing its band gap at E_0 [51]. Each CP oscillator in the last term of the sum is given by

$$\varepsilon_{\mathrm{CP},n}(E) = A_n\{\exp(i\phi_n)\}\left\{\frac{(\Gamma_n/2)}{[E_n - E - i(\Gamma_n/2)]}\right\}^{\mu_n}, \tag{9.19}$$

where A_n, E_n, Γ_n, μ_n, and ϕ_n are the amplitude, resonance energy, broadening parameter, exponent, and phase of the nth CP, respectively [51]. For CdTe, three critical points, E_0 ($n = 0$ in Equation 9.18), E_1, and $E_1 + \Delta_1$, contribute to the ε spectra over the 0.75 – 3.5 eV range. For single-crystal CdTe, the best-fit resonance energies of these three CPs are 1.49, 3.31, and 3.89 eV [52]. An Urbach tail of the form $\varepsilon_2(E) = \varepsilon_2(E_0)\exp[(E - E_0)/E_u]$, where E_u is the Urbach energy, is used to replace $\varepsilon_2(E)$ of Equation 9.18 for $E < E_0$. In the SE analysis using Equations 9.18 and 9.19 for CdTe, A_0, E_0, and Γ_0 serve as variables, whereas all other dielectric function parameters are linked to these variables. In fact, an approach has been developed that links $\varepsilon_{1,\infty}$ as well as the background TL oscillator, CP oscillator, and Urbach tail variables in Equations 9.18 and 9.19 for CdTe either to E_0, which depends on film stress [52], or to Γ_0, which depends on the mean free path of the excited electrons [53].

The (ψ, Δ) spectra of the final solar-cell structure are less sensitive to $\varepsilon(E)$ for CdS. As a result, it is necessary to reduce the number of parameters that describe

$\varepsilon(E)$ for the CdS, even from the three parameters (A_0, E_0, Γ_0) used for $\varepsilon(E)$ of CdTe. In order to address this problem, $CdCl_2$-treated structures were fabricated and studied in advance. These structures consist of glass/CdS/CdTe with the same CdS thickness of ~100 nm as is used in the solar cells. By depositing directly on glass, however, and eliminating the layer stack associated with TEC-15/HRT, which exhibits antireflection characteristics, enhanced sensitivity to the CdS $\varepsilon(E)$ spectra could be obtained. Thus, Equations 9.18 and 9.19 could be used with a single term in the CP sum associated with the E_0 transition. A comparison of the deduced E_0 CP parameters with those of $CdS_{1-x}Te_x$ studied previously [54] reveals that the strongest variations in $\varepsilon(E)$ for CdS in the solar-cell structure can be attributed to in-diffusion of Te from the overlying CdTe, an effect enhanced by the $CdCl_2$ treatment [55]. Thus, the composition x in the $CdS_{1-x}Te_x$ alloy can be used as a single free parameter that can in turn define the E_0 CP parameters (A_0, E_0, Γ_0) describing the variability in $\varepsilon(E)$ from untreated to variously treated CdS in the solar cell. In Figure 9.7, the analytically determined $\varepsilon(E)$ spectra are compared for the CdS in the $CdCl_2$-treated glass/CdS/CdTe structure, having a best-fit alloy composition $x = 0.066 \pm 0.007$, and for CdS deposited as an individual layer, having $x = 0$. In this case, the effects of alloying with Te due to overdeposition of CdTe and $CdCl_2$ treatment of the structure include a reduction in the CdS band gap E_0 and an increase in the broadening parameter Γ_0, as indicated in Figure 9.7 [54]. Also shown in Figure 9.7 is the parameterized dielectric function for $CdS_{1-x}Te_x$ predicted from the value $x = 0.05$ and used in the quantum efficiency simulations to be described later in this subsection.

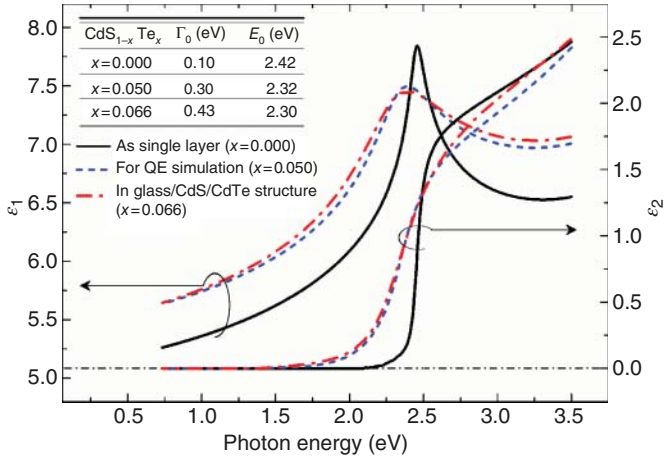

Figure 9.7 Complex dielectric function spectra $\varepsilon(E)$ for CdS layers related by a single variable parameter, the Te content x in $CdS_{1-x}Te_x$. Results are shown for CdS as an individual layer (solid lines; $x = 0$), as a layer within a glass/CdS/CdTe $CdCl_2$-treated structure (dot-dashed lines; $x = 0.066$), and as the CdS layer used in the quantum efficiency simulation (broken lines; $x = 0.050$). The table in the inset compares the resonance energies and the broadening parameters of the E_0 critical point, associated with the fundamental band gap for each of the three materials. (Adapted from Ref. [54] with permission of John Wiley and Sons.)

Turning next to the glass and top contact layers, the spectra in $\varepsilon(E)$ for the thickest layers in the TEC-15/HRT superstrate, which are the SnO_2:F and HRT, were each expressed as a sum of terms including the constant contribution to ε_1, an intraband term described by the Drude free electron expression, and a sum of CP oscillators for the interband transitions as given by the expression

$$\varepsilon(E) = \varepsilon_{1,\infty} + \varepsilon_{\mathrm{D}}(E) + \sum_{n} \varepsilon_{\mathrm{CP},n}(E). \tag{9.20}$$

The second term is given by the Drude expression, as follows:

$$\varepsilon_{\mathrm{D}}(E) = \frac{-\hbar^2}{\varepsilon_0 \rho(\tau \cdot E^2 + i\hbar E)}, \tag{9.21}$$

where $\hbar$ is Planck's constant h divided by 2π, ε_0 is the permittivity of free space, τ is the scattering time, and ρ is the resistivity. The resistivity in turn can be expressed by $\rho = m^*/Ne^2\tau = 1/e\mu N$, where m^* is the effective mass of the charge carrier, which is the electron in this case, and e, μ, and N are the electron charge, mobility, and concentration, respectively [56]. In SE analysis using Equations 9.20 and 9.21, $\varepsilon_{1,\infty}$, ρ, and τ for the SnO_2:F and $\varepsilon_{1,\infty}$ alone for the HRT serve as the variable parameters. Determination of $\varepsilon(E)$ for the glass and the thin layer components of SnO_2 and SiO_2 for the TEC-15/HRT superstrate, including the best-fit analytical models that describe the $\varepsilon(E)$ spectra, have been presented elsewhere [49].

Finally, the spectra in ε for the back contact Au component of the solar-cell structure were obtained from a 100 nm thick, opaque layer deposited onto an SLG substrate using the same evaporation conditions as are used for the solar-cell back contact. The results for $\varepsilon(E)$ were deduced by multiple angle SE performed *ex situ* immediately after deposition, applying a bulk/roughness optical model. These results were then parameterized with the analytical form of Equations 9.20 and 9.21. Two CP terms (see Equation 9.19) were used and the best-fit resonance energies were found to be 2.52 and 3.89 eV.

The analysis procedure for through-the-glass SE of the completed CdTe solar cell also includes the stress-induced birefringence in the glass, modeled as a shift in the ellipsometry angle Δ depending on photon energy E in accordance with the expression $\Delta[\Delta(E)] = E(a_1c_1 + a_2c_2E^2)$, where E is the photon energy in eV, a_1 and a_2 are unitless constants having magnitudes of 0.4032 and 0.0655, respectively, and c_1 and c_2 are the variable parameters used in the fitting.

Using the complex dielectric function database development described in previous paragraphs of this subsection, Figure 9.8 shows the experimental (points) and best-fit calculated (lines) spectra in (ψ, Δ). The resulting best-fit structural/optical model obtained from SE analysis of the device stack is shown in Figure 9.9. Figure 9.10 shows a cross-sectional electron micrograph (XTEM) of the solar cell used to corroborate the SE deduced thicknesses. In the micrograph, the layers of SnO_2:F and SnO_2 HRT are indistinguishable. The tabulated thicknesses of the layers were obtained as averages over a ~4 μm image length, and the effective thicknesses from SE are in reasonable accord with the XTEM results as shown in Figure 9.9. The overall agreement supports SE as a viable noninvasive

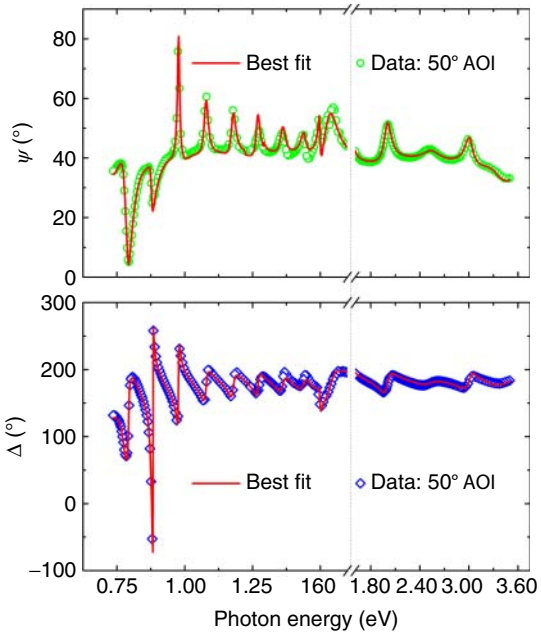

Figure 9.8 Experimental (ψ, Δ) spectra obtained at an angle of incidence of 50° and the corresponding best fit for a through-the-glass SE measurement of a completed CdS/CdTe solar cell.

Layer stack	SE	Effective SE	XTEM
CdTe/Au layer (0.26±0.02/0.74±0.02)	Opaque		
CdTe/Au interface (0.88±0.03/0.12±0.03)	184±10 nm		
CdTe bulk layer	1815±5 nm	1997 ± 15 nm	1932 nm
CdS/CdTe interface (0.48±0.10/0.52±0.10)	31±3 nm		
CdS bulk layer	67±4 nm	100 ± 6 nm	94 nm
HRT/CdS interface (0.45±0.08/0.55±0.08)	33±2 nm		
HRT layer	84±3 nm	403 ± 6 nm	428 nm
SnO_2:F layer	304±3 nm		
SiO_2 layer	27±1 nm		26 nm
SnO_2 layer	21±1 nm		24 nm
Soda-lime glass	3.16 mm		
Stress birefringence c_1	4.5 ± 1.2 deg/eV		
Stress birefringence c_2	−2.4 ± 1.0 deg/eV^3		

Figure 9.9 Results for the multilayer structure and best-fit parameters for a CdS/CdTe solar cell from the analysis of Figure 9.8, including the best-fit thicknesses and interface layer compositions along with their confidence limits. The second column of SE deduced thicknesses provides effective values obtained as the volume of the material per unit area, or the product of the material volume fraction and the thickness summed over all layers that include the material. The third column lists average thicknesses from the XTEM of Figure 9.10 for comparison with the SE results. (Adapted from Ref. [54] with permission of John Wiley and Sons.)

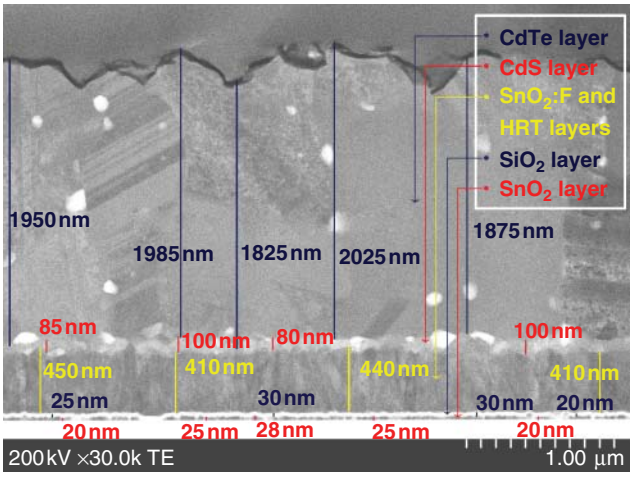

Figure 9.10 Cross-sectional transmission electron micrograph of the CdS/CdTe solar cell showing five distinct layers, starting from the superstrate: (i) SnO_2, (ii) SiO_2, (iii) SnO_2:F/HRT top contact, (iv) CdS, and (v) CdTe. The thicknesses of these layers, averaged over a length of ~4 µm, are given in Figure 9.9. (Adapted from Ref. [54] with permission of John Wiley and Sons.)

method for CdTe solar-cell analysis with the ability to extract several structural and optical parameters at a single point or in a mapping mode as in recently reported studies [57].

The results for the SnO_2:F layer of the TEC-15 yield a sheet resistance of $11.5 \pm 1.1\,\Omega$/sq, relatively close to the $15\,\Omega$/sq nominal value. Also from the resistivity and scattering time, a carrier concentration of $5.4 \times 10^{20}\,cm^{-3}$ and a mobility of $50\,cm^2/V\,s$ are deduced, assuming an electron effective mass for SnO_2:F of $m_e^* = 0.25m_e$ [56]. The best-fit values of E_0 and Γ_0 for the CdTe bulk layer have been used to estimate the stress in the layer as 0.07 ± 0.06 GPa and the excited electron mean free path as 320 ± 130 nm, at the lower and upper limits of sensitivity, respectively [52, 53]. Applying the same analysis before $CdCl_2$ treatment and back contact formation yields a higher stress value of 0.52 ± 0.07 GPa and a shorter mean free path of 26 ± 8 nm [57].

Figure 9.11 shows the measured QE spectrum along with the integrated current density for the cell of Figures 9.8–9.10, obtained under a reverse bias of −0.8 V, which is designed to maximize separation and collection of photoexcited electrons and holes. It should be noted that further increases in the reverse bias magnitude did not lead to additional current collection. The cell structure in Figure 9.9, along with the component layer $\varepsilon(E)$ spectra, enables simulation of both the QE spectrum and the integrated current density J also shown in Figure 9.11 [54, 58]. In the simulation, it is assumed that 100% collection occurs from the three layers containing at least 50 vol.% CdTe (see inset of Figure 9.11) and that no collection occurs from the CdS bulk layer and from the back CdTe/Au interface layer with 0.74 volume fraction of Au. In addition, due to the higher sensitivity that QE

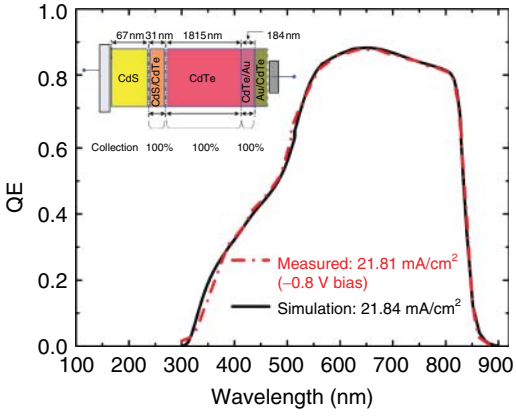

Figure 9.11 Measured quantum efficiency (QE) spectra at −0.8 V bias (red broken line) along with simulated QE spectra (black solid lines). The simulated results are based on 100% collection from (i) the 31 nm thick CdS/CdTe interface layer, (ii) the 1815 nm CdTe bulk layer, and (iii) the CdTe component of the 184 nm thick CdTe/Au interface layer, as shown in the inset schematics. (Adapted from Ref. [54] with permission of John Wiley and Sons.)

provides to the composition x in $CdS_{1-x}Te_x$, closer agreement between the simulation and the measurement is obtained by a slight adjustment of x in generating the $CdS_{1-x}Te_x$ $\varepsilon(E)$ spectra from $x = 0.066$ used in Figures 9.8 and 9.9 to $x = 0.050$. This modification, along with the assumptions described, yields a simulation in excellent agreement with the reverse bias QE. By modifying the database dielectric function for CdS to the $x = 0.050$ result, such fits can be obtained without free parameters.

9.5.3
$Cu(In_{1-x}Ga_x)Se_2$

Although several different processes exist for CIGS absorber layer fabrication, three-stage thermal coevaporation has generated the highest-efficiency CIGS devices. In this process, a CIGS film is produced by depositing a precursor film of $(In_{1-x}Ga_x)_2Se_3$ (IGS) at a moderate substrate temperature (~400 °C) in the first stage and exposing it to Cu and Se fluxes during the second stage. The IGS film is completely converted to CIGS throughout its ~2–3 μm thickness in the second stage, which is performed at an elevated temperature (~500–600 °C) relative to the first stage. Furthermore, by extending the second stage into a growth regime of Cu-rich film composition, a desirable $Cu_{2-x}Se$ phase is formed on the CIGS surface at the end of stage II. This $Cu_{2-x}Se$ phase, believed to exist as a semiliquid [59], is converted back to CIGS in the third stage through exposure to In, Ga, and Se fluxes while maintaining the film at the elevated temperature of stage II. The advantage of this three-stage process derives from its ability to yield large crystalline grains and a desirable band-gap profile, the latter due to the higher diffusion coefficient of In relative to Ga in the second and third stages.

9.5.3.1 RTSE for Three-Stage Coevaporation of CIGS

In the RTSE study to be reviewed here, three-stage coevaporation was performed on SLG substrates coated with optically opaque molybdenum [60]. At the start of stage I, In, Ga, and Se were coevaporated at a substrate temperature of 400 °C and at individual rates of 0.20, 0.06, and 2.00 nm/s, respectively. After an IGS precursor film of prescribed thickness was deposited (intended to be 65% of the desired final absorber layer thickness of 2.5 μm), the In and Ga source temperatures were reduced to terminate In and Ga coevaporation. The substrate temperature was then increased to 570 °C and stage II was initiated. During this stage, the source temperature of Cu was increased to obtain the desired rate, 0.17 nm/s, while continuing the coevaporation of Se throughout. As defined by the Cu-poor to Cu-rich transition, the Cu source temperature was reduced to terminate Cu evaporation. Defining the start of stage III, the In and Ga source temperatures were increased again to reach their stage I rates while maintaining the stage I and II Se flux and the stage II substrate temperature. At the end of stage III, identified relative to the Cu-rich to Cu-poor transition, the In and Ga sources were cooled to terminate coevaporation and the substrate temperature was steadily decreased. An energy-dispersive X-ray spectroscopy (EDS) measurement of the CIGS layer of this study, performed *ex situ* after the deposition, yielded $y = [\mathrm{Cu}]/\{[\mathrm{In}] + [\mathrm{Ga}]\} = 0.82$ and $x = [\mathrm{Ga}]/\{[\mathrm{In}] + [\mathrm{Ga}]\} = 0.25$.

Throughout the three-stage CIGS deposition process, a commercially available rotating-compensator multichannel ellipsometer (J.A. Woollam Co., M2000-DI) was used to collect ellipsometric spectra *in situ* and in real time at an angle of incidence of 70.3° with acquisition and repetition times of 3 and 5 s, respectively. In the optical models for analyzing the RTSE data, the complex dielectric functions of Mo, CIGS, and $Cu_{2-x}Se$ were obtained from databases developed by *in situ* and real-time SE at the relevant temperatures and compositions. For CIGS, the single-stage coevaporation process was used to deduce the database complex dielectric functions, and for $Cu_{2-x}Se$, the stage II deposition process in the absence of an IGS film was used for this purpose.

The optical model for stage I analysis incorporates a Mo/IGS interface roughness layer, an IGS bulk layer, and an IGS surface roughness layer. Figure 9.12 shows the structural evolution in the initial 90 s during the growth of IGS on the Mo-coated SLG substrate [60]. These results are characteristic of the stage I process for any thickness of three-stage CIGS. The surface roughness on the uncoated Mo layer is characterized by a layer 24.2 nm thick with 60 vol.% voids. All surface and interface roughness layers are modeled using the Bruggeman effective medium approximation assuming a mixture of underlying and overlying materials. In the initial stage of IGS growth, the voids existing in the valleys of the Mo surface roughness are filled by IGS, leading to the rapid increase in the IGS vol.% in the roughness layer from zero as shown in Figure 9.12a. Simultaneously, the surface roughness thickness d_s associated with the IGS film increases as the peaks of the Mo surface roughness are conformally covered by IGS as shown in Figure 9.12b. When the interface is almost completely filled, a bulk layer of thickness d_b can be incorporated into the model. During initial bulk layer growth, the

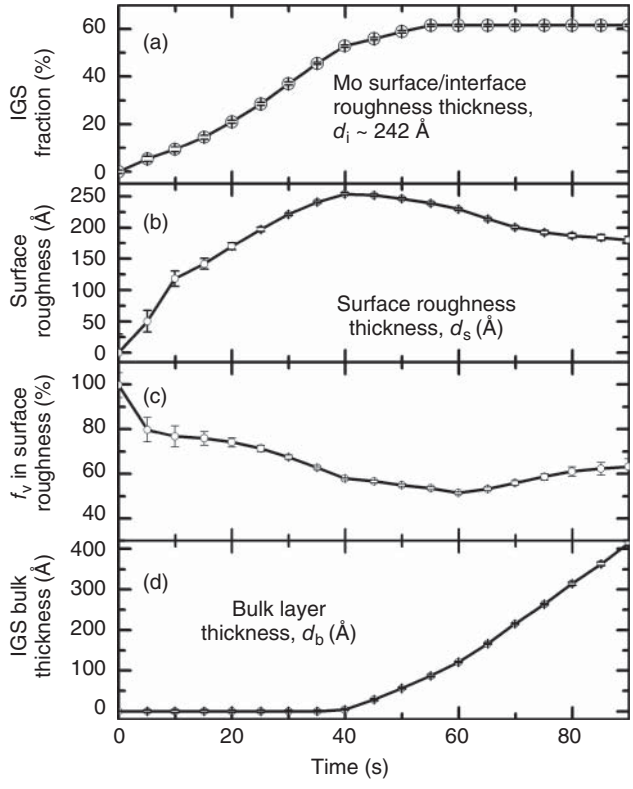

Figure 9.12 Initial structural evolution showing the first ~40 nm of $(In_{1-x}Ga_x)_2Se_3$ bulk layer growth on Mo-coated soda-lime glass: (a) IGS volume percentage filling the voids in the Mo surface roughness layer, (b) IGS surface roughness layer thickness, (c) void volume percentage in the IGS surface roughness layer, and (d) IGS bulk layer thickness. In this process, the substrate shutter was opened at $t = 0$ to start the first-stage deposition process. (Adapted from Ref. [60] with permission of IEEE.)

surface roughness on the IGS decreases in thickness indicating suppression of substrate-induced surface roughness due to structural coalescence.

Figure 9.13 depicts the continuation of IGS bulk layer growth after the completion of the Mo/IGS interface filling process as was shown in Figure 9.12. The termination of the IGS growth that ends stage I occurs at $t = 30$ min in Figure 9.13. Figure 9.13a depicts the bulk layer thickness evolution for the IGS process. An average deposition rate can be obtained in stage I by fitting the bulk layer thickness to a linear relationship as a function of time throughout IGS bulk layer deposition. This average rate can be used to evaluate the run-to-run reproducibility of the total incorporation rate of In + Ga in stage I. In addition to the average rate, the instantaneous rate can be tracked as well, giving insights into deposition source stability. In order to separate and characterize the individual In and Ga incorporation rates, the film composition is needed. This can be obtained from the complex

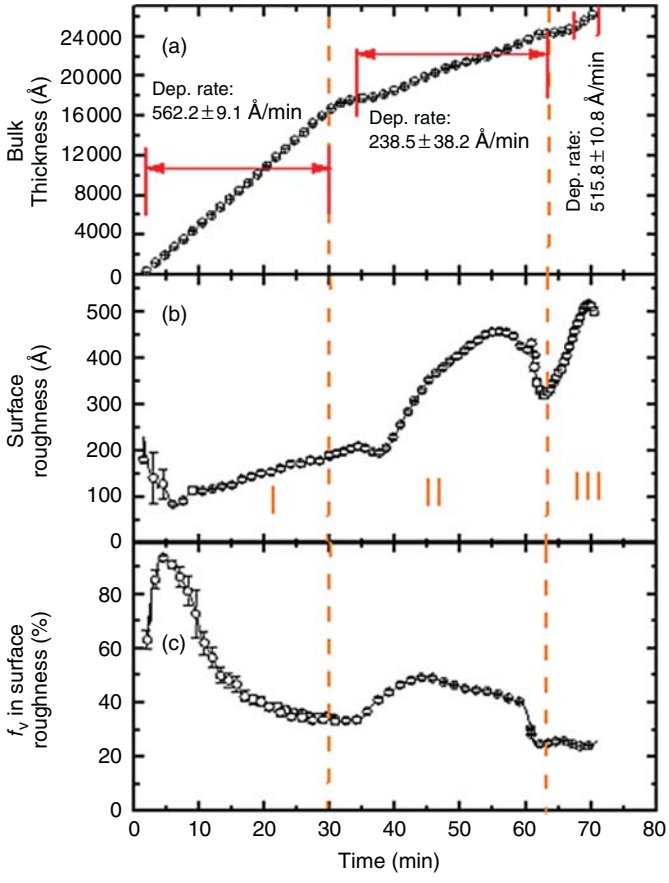

Figure 9.13 Evolution of (a) bulk layer thickness, (b) surface roughness layer thickness, and (c) void volume percentage in the surface roughness layer – all obtained throughout three-stage CIGS deposition yielding a ~2.5 μm thick CIGS layer. (Adapted from Ref. [60] with permission of IEEE.)

dielectric function at the end of IGS deposition. Application of virtual interface analysis throughout stage I may be possible for extracting changes in near-surface composition during the growth process. Figure 9.13b shows the evolution of the surface roughness layer throughout stage I, indicating continued smoothening in the first 300 nm of bulk layer growth followed by roughening until the end of deposition at a bulk layer thickness of 1.7 μm. Figure 9.13c shows gradual densification of the surface roughness layer after surface smoothening is complete.

RTSE analysis results for the structural parameters in stage II are also shown in Figure 9.13 for $30 < t < 63$ min. In this stage, a bulk conversion model is applied as represented using a mixture of IGS and CIGS in the Bruggeman effective medium approximation, whereby conversion of IGS to CIGS takes place uniformly throughout the IGS thickness [60]. Such a model would be consistent with diffusion of Cu along grain boundaries throughout the layer thickness, followed

by conversion of polycrystalline grains via slower in-plane diffusion. This is in contrast to a model in which IGS is converted to CIGS in a layer-by-layer process through spatially uniform diffusion from the IGS surface into the bulk. Much improved fits to the RTSE data are obtained for the bulk conversion model as compared to the layer-by-layer conversion model. The results for the IGS–CIGS conversion are shown in Figure 9.14 with the instantaneous thickness rate given in the inset. In addition to a bulk layer increase during stage II in Figure 9.13a, Figure 9.13b and c show a significant increase in roughness during IGS conversion and an increase in void fraction of the surface layer, followed by an apparent coalescence process near the end of stage II. In an attempt to corroborate the best-fit model that generated the stage II results of Figures 9.13 and 9.14, three-stage coevaporation of CIGS deposition was terminated halfway through stage II. Auger electron spectroscopy (AES) depth profiling was performed on this unfinished sample. Figure 9.15 presents the results for the AES depth profile,

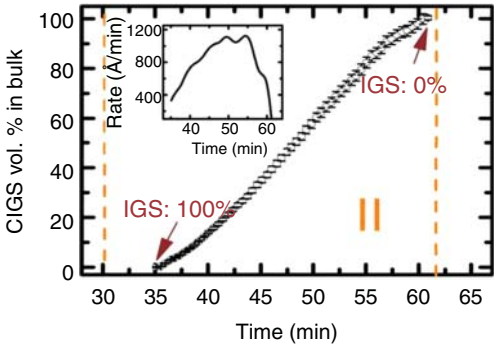

Figure 9.14 Conversion of IGS to CIGS during stage II growth of 2.5 μm CIGS. The IGS-to-CIGS conversion rate in terms of the increase in bulk layer thickness is shown in the inset. (Adapted from Ref. [60] with permission of IEEE.)

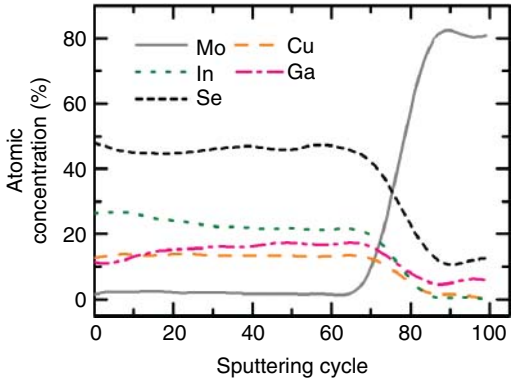

Figure 9.15 Auger electron spectroscopy depth profile of a film obtained after terminating the three-stage CIGS process during conversion of IGS to CIGS via the coevaporation of Cu and Se in stage II. (Adapted from Ref. [60] with permission of IEEE.)

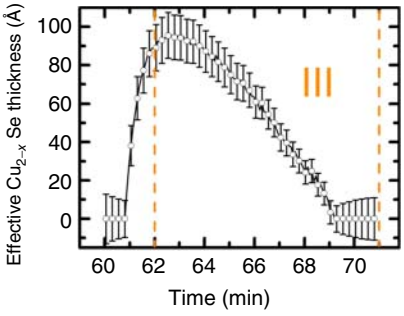

Figure 9.16 Effective thickness of $Cu_{2-x}Se$ formed near the surface at the end of stage II and throughout stage III for 2.5 μm CIGS. The effective thickness is the volume of $Cu_{2-x}Se$ material per unit area of substrate, or the product of the surface layer thickness and the $Cu_{2-x}Se$ volume fraction. (Adapted from Ref. [60] with permission of IEEE.)

which demonstrate a uniform distribution of Cu throughout the thickness at a composition of ~12 at.%, results that support the best-fit RTSE model.

In order to fit the RTSE data near the end of stage II at the Cu-poor to Cu-rich transition, a roughness region is required at the film surface that incorporates both CIGS and $Cu_{2-x}Se$. The behavior of the $Cu_{2-x}Se$ component in the surface layer near the end of stage II and throughout stage III is depicted in Figure 9.16. The effective thickness in Figure 9.16 is the volume per area, or the product of the surface layer thickness and $Cu_{2-x}Se$ volume fraction in the layer. After all IGS is converted to CIGS as shown in Figure 9.14 near the end of stage II, the $Cu_{2-x}Se$ phase rapidly develops as shown in Figure 9.16, increasing to an effective thickness of 9–10 nm. The surface layer smoothening and densification observed in Figure 9.13b and c at the end of stage II are expected to arise at least in part due to the $Cu_{2-x}Se$ formation as this material may preferentially fill the voids in the CIGS roughness layer. Finally, it is important to note that the magnitude of the observed smoothening and surface densification processes, as well as the maximum in the $Cu_{2-x}Se$ effective thickness, can be used to evaluate reproducibility of the stage II process and to correlate with solar-cell performance.

Finally in stage III, the dominant effect is the conversion of $Cu_{2-x}Se$ to CIGS in the near-surface region as quantified in Figure 9.16, and this effect is accompanied by an increase in bulk layer thickness associated with the conversion as well as an increase in surface roughness, as shown in Figure 9.13a and b, respectively. The stage III data allow one to identify the Cu-rich to Cu-poor transition, and a measure of the deposition rate at this time enables one to estimate the final Cu composition. The results of Figure 9.13 in general are consistent with the roughening effects as indications of grain growth processes in which crystallites grow above the film surface plane and smoothening effects as indications of coalescence processes. Based on this interpretation, one can conclude that grain growth and structural coalescence occur in each of the three stages. Most notably, rapid grain growth processes occur as IGS is converted to CIGS during stage II and as $Cu_{2-x}Se$ is converted to CIGS in stage III.

9.5.3.2 *Ex Situ* SE and QE Simulation for CIGS Solar-Cell Devices

The CIGS solar cells studied by *ex situ* SE were fabricated using the three-stage coevaporation process with an intended 2.2 μm thickness for the CIGS absorber layer [60]. The completed device structure includes the following components: SLG, dc-sputtered Mo back contact (~0.8 μm thick), the CIGS absorber layer,

chemical-bath-deposited (CBD) CdS (50–60 nm thick), RF-sputtered transparent conducting oxide bilayer of ZnO/ZnO:Al (300–400 nm thick), and electron beam-evaporated Ni/Al/Ni grids. The total cell area was 0.477 cm^2, as defined by mechanical scribing. After antireflection coating, solar-cell measurement under AM1.5 illumination yielded a short-circuit current density of 36.2 mA/cm^2, an open-circuit voltage of 0.638 V, a fill factor of 0.713, and a power conversion efficiency of 16.5%.

The strategy for analysis of *ex situ* SE data collected on CIGS solar-cell devices is similar to that applied for the CdTe devices as described in Section 9.5.2.2. Database spectra in ε have been developed for CIGS solar-cell component materials and, when possible, expressed as analytical functions of the material parameters of interest [61]. For CIGS, an important material parameter is the Ga content x, defined as the atomic ratio $[Ga]/\{[In]+[Ga]\}$. This ratio controls the band-gap and the above-gap absorption characteristics. The second compositional parameter is the Cu content, defined as the atomic ratio $y=[Cu]/\{[In]+[Ga]\}$. This compositional parameter has less influence on the CIGS dielectric function, and in most cases when RTSE is performed, a targeted value of $y \sim 0.9$ for optimum solar-cell performance can be obtained.

To determine the CIGS complex dielectric function ε as an analytical function of x, a series of CIGS thin films with $x=0.00$, 0.12, 0.26, 0.30, 0.37, and 0.48 were deposited onto native oxide-covered crystal silicon wafers at a substrate temperature of 570 °C. The value of x for each sample was determined from energy-dispersive X-ray spectroscopy (EDS) performed postdeposition. For highest possible accuracy in ε for CIGS thin films with different x values, specialized procedures were adopted including (i) single-stage coevaporation, which avoids depth-dependent nonuniformities, for example, in the composition and thus complex dielectric function; (ii) deposition to a thickness of ~60 nm on smooth native oxide-covered crystal silicon wafers, which minimizes the surface roughness on the film and thus the required corrections in data analysis; (iii) selection of a subset of samples with a nearly constant $y=0.90\pm0.03$ from a larger collection of samples, which reduces random variations; and (iv) characterization *in situ*, which minimizes ambient contamination and oxidation of the film surface. The resulting ε spectra for selected CIGS films are compared in Figure 9.17 where consistent trends versus x are observed [61]. Assuming an analytical form of Equations 9.18 and 9.19 with an Urbach tail for each of the ε spectra, oscillator parameters were obtained in best fits, and these parameters were fit in turn to polynomials in x. With the resulting database of polynomial coefficients, the ε spectra for any composition of CIGS can be generated from the single parameter, x.

Complex dielectric function spectra ε of other CIGS solar-cell components were determined from SE analyses in a similar approach as for CIGS, with the exception that the thicknesses were standardized to those used in the CIGS device. Individual layers were deposited onto c-Si wafers and measured by *in situ* SE. The resulting SE data were analyzed using an optical model incorporating bulk and surface roughness layers, and the complex dielectric function spectra were obtained by mathematical inversion using best-fit values for these thicknesses.

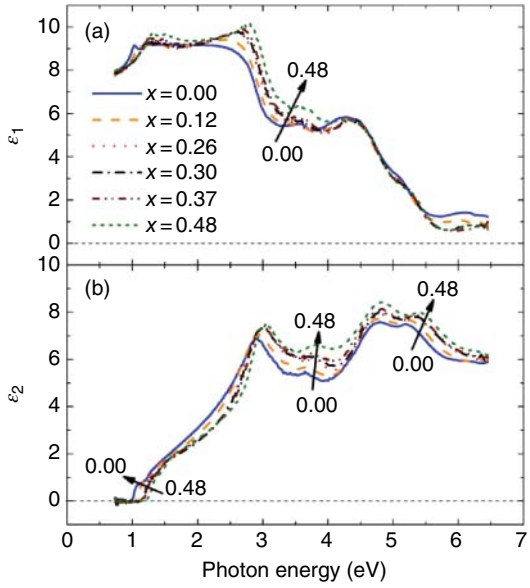

Figure 9.17 Room temperature spectra in ε for CIGS films with different Ga contents of $x = 0.00$, 0.12, 0.26, 0.30, 0.37, and 0.48 determined by applying numerical inversion to *in situ* SE data collected after single-stage CIGS deposition. (Adapted from Ref. [61] with permission of John Wiley and Sons.)

The inverted complex dielectric functions were then parameterized using analytical models similar to those developed for CdTe thin-film technology.

The complete CIGS solar-cell structure (without antireflection coating) was measured using *ex situ* SE at an angle of incidence of 70° [62]. Figure 9.18 shows the experimental data and best fit, using the database of ε spectra described in the preceding two paragraphs. In determining the compositional profile in CIGS that is generated as a result of the three-stage process, the CIGS layer was modeled with two linearly graded segments defined by the compositions at the junction (x_{HF}), at the back contact (x_{HB}), and at the minimum (x_L). In addition, the depth of the x_L composition from the junction is a fourth parameter required to determine the profile. The SE analysis of the complete solar cell yielded the structural and compositional parameters given in Figure 9.19. The two-segment Ga depth profile deduced from SE is shown in Figure 9.20, together with the corresponding profile obtained from secondary ion mass spectrometry (SIMS). Reasonable agreement between SE and SIMS measurement results is observed.

With the complex dielectric function database and the solar-cell structural and compositional parameters determined from SE, it is possible to simulate the QE spectrum as was done for the CdTe solar cell of Section 9.5.2.2 and to calculate the short-circuit current density under AM1.5 irradiance [62]. In Figure 9.21, the measured and optically simulated QE spectra are compared. It is assumed that separation and complete collection occurs for the electrons and holes generated

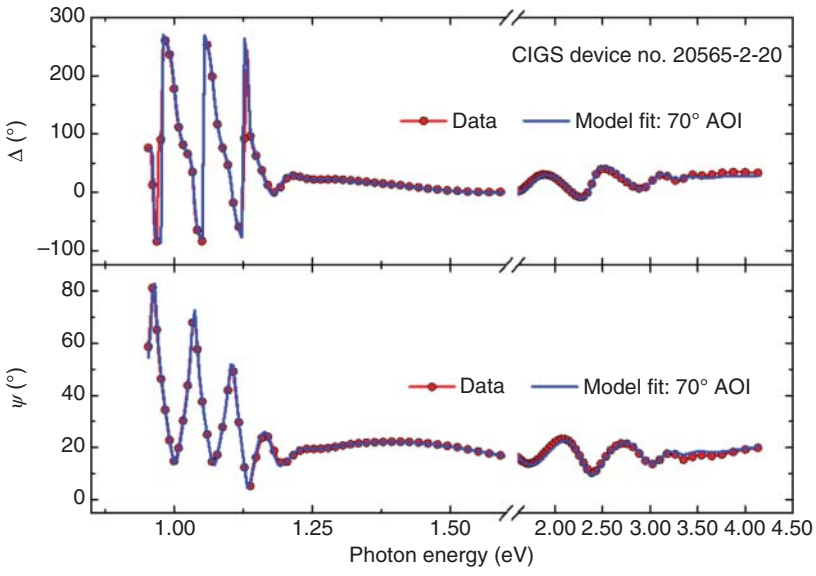

Figure 9.18 Measured *ex situ* SE data and best fit for an analysis of the CIGS solar-cell structure without an antireflection coating [62].

Layer (composition, properties)	Thickness
ZnO:Al/void roughness (0.69/0.31)	34.3 nm
ZnO:Al/void bulk (0.971/0.029)	112.0 nm
ZnO/ZnO:Al/void interface (0.218/0.753/0.029)	140.1 nm
ZnO/void bulk (1.000/0.000)	36.2 nm
CdS/ZnO/void interface (0.49/0.51/0.00)	44.5 nm
CdS/void bulk (1.00/0.00)	48.7 nm
CIGS/CdS/void interface (0.775/0.218/0.007)	59.1 nm
CIGS/void graded bulk (1.000/0.000) x_{HF} = 0.304 front composition d_F = 326.6 nm x_L = 0.182 minimum composition x_{HB} = 0.469 back composition d_B = 1851.1 nm	2177.7 nm
Mo/CIGS interface (0.82/0.18)	19.9 nm
Mo bulk	Opaque
Soda-lime glass	

Figure 9.19 Multilayer stack with best-fit structural and compositional parameters for the complete CIGS solar cell as deduced from the *ex situ* SE analysis of Figure 9.18. The Ga profile parameters are identified in Figure 9.20 [62].

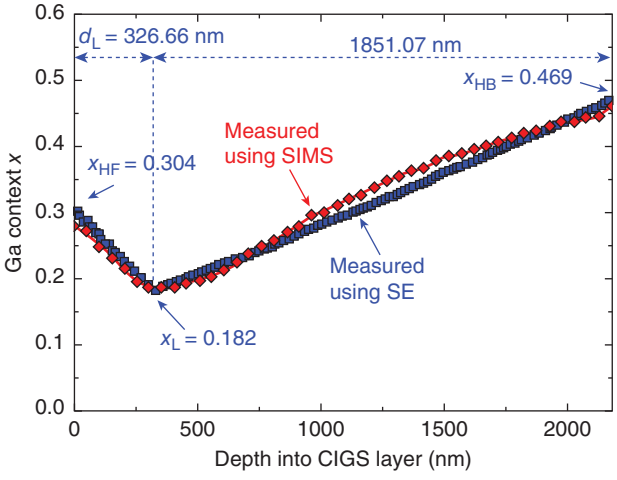

Figure 9.20 Ga compositional depth profile for the bulk CIGS absorber in the complete solar cell of Figures 9.18 and 9.19, deduced from *ex situ* SE analysis. The Ga profile associated with the three-stage CIGS coevaporation process is modeled using a two-segment gradient to deduce the four profile characteristics x_{HF}, x_L, d_L, and x_{HB} as shown. Also shown is the Ga profile obtained from secondary ion mass spectrometry (SIMS) for comparison [62].

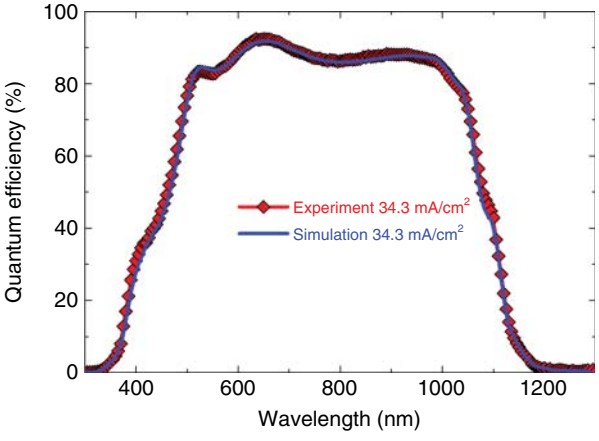

Figure 9.21 Measured and simulated quantum efficiency for the CIGS solar cell of Figures 9.19 and 9.20. The simulation is obtained by applying *ex situ* SE analysis results with no free parameters based on the assumptions that complete collection occurs from the CdS/CIGS interface layer and from the CIGS bulk layer [62].

in the CdS/CIGS interface layer and the CIGS bulk layer. The excellent agreement between the optically simulated QE spectrum (without any free parameters) and measured QE spectrum supports these assumptions and furthermore demonstrates the importance of the *ex situ* analysis in predicting the performance of CIGS solar cells.

9.6 Summary and Outlook

The optical technique of spectroscopic ellipsometry (SE) has become increasingly popular as the interest in developing and optimizing thin-film photovoltaic materials and devices has grown. Real-time SE (RTSE) allows one to study the characteristics of thin-film growth ranging from the initial nucleation and coalescence stage to the final film structural depth profile, as has been demonstrated for thin-film Si:H technology. Illustrative examples of the information that can be extracted from RTSE have been provided in this review. These examples include growth-evolution diagrams in Si:H thin-film technology; interface filling, bulk layer development, and surface roughness evolution in CdTe and CIGS thin-film technologies; and phase evolution in advanced multistage deposition in the CIGS technology. The significant challenge of state-of-the-art studies involves the use of device-relevant substrates such as thin-film metal back contacts and transparent conducting oxide top contacts that may exhibit significant surface roughness. These illustrative examples provide insights into why solar cells deposited under different conditions result in varying efficiencies, and in general, they help one to better understand the nucleation and growth of thin films deposited by different techniques such as PECVD, magnetron sputtering, and coevaporation.

The availability of databases of complex dielectric functions deduced from *in situ* and real-time SE enables *ex situ* SE analysis of complete solar-cell device structures using nonlinear least-squares regression analysis. Analytical expressions for the database dielectric functions in terms of material properties of interest such as composition allow one to deduce these properties as an outcome of the regression analysis. Such properties include not only composition but also free carrier concentration and lifetime, mean free path of excited carriers, and film stress, which can be deduced in the analysis in addition to the thicknesses of the layers that comprise the multilayer optical model. The resulting information on completed device structures enables the simulation of the external QE, the prediction of the current density for the device, and the identification of the origins of electronic or optical losses. Thus, insights are provided into the performance of solar cells and possible directions for improvements.

As shown in this chapter, various SE approaches are well established for the characterization of thin-film photovoltaic materials and devices in a research environment; however, excellent prospects also exist for expansion of the methodologies to the pilot-scale and full-scale production environments. For example, SE can be applied to the monitoring of solar-cell fabrication on flexible substrates such as polymer or steel foil in roll-to-roll processes [63]. In this case, one can track the initial start-up of the deposition process and the stability at a particular thickness point in the process. Also, using the dielectric function database obtained from *in situ* and real-time SE measurements, one can characterize completed solar devices *ex situ* for device-relevant information. This approach also motivates mapping spectroscopic ellipsometry, in which case thickness and compositional maps can provide insights into the uniformity of full-scale modules from production lines.

Definition of Polarization and Ellipsometry Variables

ψ and Δ	ellipsometry angles of a specularly reflecting sample
r_p and r_s	complex amplitude reflection coefficients of a sample for orthogonal p (parallel to plane of incidence) and s (perpendicular to plane of incidence) linear polarization states
n and k	real and imaginary parts of the complex index of refraction N ($N = n - ik$)
E_{0x} and E_{0y}	amplitudes of the electric field along orthogonal x and y axes
ω	angular frequency of an optical wave
k	magnitude of the optical propagation vector (not to be confused with k, the extinction coefficient)
δ_x and δ_y	phase angles of electric field oscillations along orthogonal x and y axes
τ	oscillation period of an optical wave
Q	azimuthal angle of a polarization ellipse
χ	ellipticity angle of a polarization ellipse (whose sign defines the handedness)
A	amplitude of an optical wave
δ	phase of an optical wave
θ_i	angle of incidence
θ_t	complex angle of transmission
n_s	real index of refraction of a sample
k_s	extinction coefficient of a sample
N_s	complex index of refraction of a sample
ε_s	complex dielectric function of a sample
n_a	real index of refraction of an ambient medium
ε_a	dielectric function of an ambient medium
I_0	dc Fourier coefficient of the reflected irradiance in an ellipsometry measurement
α and β	cosine and sine Fourier coefficients normalized to the dc coefficient of the reflected irradiance in an ellipsometry measurement
P_S, C_S, and A_S	offsets that account for arbitrary angular positions of optical elements (polarizer, compensator, analyzer) relative to the plane of incidence at $t = 0$, the onset of data collection in an ellipsometry measurement
p	degree of polarization

References

1. Boccara, A.C., Pickering, C., and Rivory, J. (eds) (1993) *Proceedings of the First International Conference on Spectroscopic Ellipsometry*, Elsevier, Amsterdam.
2. Collins, R.W., Aspnes, D.E., and Irene, E.A. (eds) (1998) *Proceedings of the Second International Conference on Spectroscopic Ellipsometry*, Elsevier, Amsterdam.

3. Fried, M., Humlicek, J., and Hingerl, K. (eds) (2003) *Proceedings of the Third International Conference on Spectroscopic Ellipsometry*, Elsevier, Amsterdam.
4. Arwin, H., Beck, U., and Schubert, M. (eds) (2007) *Proceedings of the Fourth International Conference on Spectroscopic Ellipsometry*, Wiley-VCH Verlag GmbH, Weinheim, Germany.
5. Tompkins, H.G. (ed) (2011) *Proceedings of the Fifth International Conference on Spectroscopic Ellipsometry*, Elsevier, Amsterdam.
6. Otani, Y., Tazawa, M., and Kawabata, S. (eds) (2014) *Proceedings of the Sixth International Conference on Spectroscopic Ellipsometry*, Elsevier, Amsterdam.
7. Azzam, R.M.A. and Bashara, N.M. (1977) *Ellipsometry and Polarized Light*, North-Holland, Amsterdam.
8. Tompkins, H.G., (1992) *A User's Guide to Ellipsometry*, Academic Press, New York.
9. Tompkins, H.G. and Irene, E.A. (eds) (2005) *Handbook of Ellipsometry*, William Andrew Publishing, Norwich, NY.
10. Passaglia, E., Stromberg, R.R., and Kruger, J. (eds) (1963) *Ellipsometry in the Measurement of Surfaces and Thin Films*, National Bureau of Standards, Washington, DC, Misc. Publ. 256.
11. Aspnes, D.E. (1976), "Spectroscopic ellipsometry," in: Seraphin, B.O. (ed), *Optical Properties of Solids: New Developments*, Amsterdam: North-Holland, pp. 799–846.
12. Wooten, F. (1972) *Optical Properties of Solids*, Academic Press, New York.
13. Lautenschlager, P., Garriga, M., Logothetidis, S., and Cardona, M. (1987) Interband critical points of GaAs and their temperature dependence. *Phys. Rev. B*, **35**, 9174–9189.
14. Lautenschlager, P., Garriga, M., Vina, L., and Cardona, M. (1987) Temperature dependence of the dielectric function and interband critical points in silicon. *Phys. Rev. B*, **36**, 4821–4830.
15. Aspnes, D.E., Potter, R.F., and So, S.S. (eds) (1981) *Optical Characterization Techniques for Semiconductor Technology*, *Proc. Soc. Photo-Opt. Instrum. Eng.* **276**, SPIE, Bellingham, WA.
16. Vedam, K., McMarr, P.J., and Narayan, J. (1985) Non-destructive depth profiling by spectroscopic ellipsometry. *Appl. Phys. Lett.*, **47**, 339–341.
17. Snyder, P.G., Rost, M.C., Bu-Abbud, G.H., Woollam, J.A., and Alterovitz, S.A. (1986) Variable angle of incidence spectroscopic ellipsometry: application to GaAs–$Al_xGa_{1-x}As$ multiple heterostructures. *J. Appl. Phys.*, **60**, 3293–3302.
18. Collins, R.W., Yacobi, B.G., Jones, K.M., and Tsuo, Y.S. (1986) Structural studies of hydrogen-bombarded silicon using ellipsometry and transmission electron microscopy. *J. Vac. Sci. Technol. A*, **4**, 153–158.
19. Irene, E.A. (1993) Applications of spectroscopic ellipsometry to microelectronics. *Thin Solid Films*, **233**, 96–111.
20. Palik, E.D. (ed) (1985) *Handbook of Optical Constants of Solids*, Academic Press, New York.
21. Palik, E.D. (ed) (1991) *Handbook of Optical Constants of Solids II*, Academic Press, New York.
22. Collins, R.W. (1990) Automatic rotating element ellipsometers, calibration, operation, and real time applications. *Rev. Sci. Instrum.*, **61**, 2029–2062.
23. Hecht, E. (2002) *Optics*, 4th edn, Addison-Wesley, San Francisco.
24. Fujiwara, H. (2007) *Spectroscopic Ellipsometry: Principles and Applications*, John Wiley & Sons, Ltd, Chichester.
25. Zapien, J.A., Collins, R.W., and Messier, R. (2000) Multichannel ellipsometer for real time spectroscopy of thin film deposition from 1.5 to 6.5 eV. *Rev. Sci. Instrum.*, **71**, 3451–3460.
26. Woollam, J.A., Johs, B., Herzinger, C.M., Hilfiker, J.N., Synowicki, R., and Bungay, C. (1999) Overview of variable angle spectroscopic ellipsometry (VASE): Parts I and II. *Proc. Soc. Photo-Opt. Instrum. Eng. Crit. Rev.*, **72**, 3–28.
27. Chen, C., Ross, C., Podraza, N.J., Wronski, C.R., and Collins, R.W. (2005) Multichannel Mueller matrix analysis of the evolution of the microscopic roughness and texture during ZnO:Al chemical etching, *Proceedings of the 31st IEEE Photovoltaic Specialists Conference*,

3–7 January, Orlando FL, USA, IEEE, New York, pp. 1524–1527.
28. Fujiwara, H., Koh, J., Rovira, P.I., and Collins, R.W. (2000) Assessment of effective-medium theories in the analysis of nucleation and microscopic surface roughness evolution for semiconductor thin films. *Phys. Rev. B*, **61**, 10832–10844.
29. Collins, R.W., An, I., and Chen, C. (2005), "Rotating polarizer and analyzer ellipsometry," in: Tompkins, H.G., and Irene, E.A. (eds), *Handbook of Ellipsometry*, Norwich, NY: William Andrew Publishing, pp. 329–432.
30. Collins, R.W., An, I., Lee, J., and Zapien, J.A. (2005), "Multichannel ellipsometry," in: Tompkins, H.G., and Irene, E.A. (eds), *Handbook of Ellipsometry*, Norwich, NY: William Andrew Publishing, pp. 481–566.
31. Tompkins, H.G. (2005), "Optical components and the simple PCSA (polarizer, compensator, sample, analyzer) ellipsometer," in: Tompkins, H.G., and Irene, E.A. (eds), *Handbook of Ellipsometry*, Norwich, NY: William Andrew Publishing, pp. 299–328.
32. Cahan, B.D., and Spanier, R.F. (1969) A high speed precision automatic ellipsometer. *Surf. Sci.*, **16**, 166–176.
33. Aspnes, D.E., and Studna, A.A. (1975) High precision scanning ellipsometer. *Appl. Opt.*, **14**, 220–228.
34. Hauge, P.S., and Dill, F.H. (1975) A rotating-compensator Fourier ellipsometer. *Opt. Commun.*, **14**, 431–437.
35. Aspnes, D.E. (1975) Photometric ellipsometer for measuring partially polarized light. *J. Opt. Soc. Am.*, **65**, 1274–1278.
36. Oldham, W.G. (1969) Numerical techniques for the analysis of lossy films. *Surf. Sci.*, **16**, 97–103.
37. Comfort, J.C., and Urban, F.K. (1995) Numerical techniques useful in the practice of ellipsometry. *Thin Solid Films*, **270**, 78–84.
38. Loescherr, D.H., Detry, R.J., and Clauser, M.J. (1971) Least-squares analysis of the film-substrate problem in ellipsometry. *J. Opt. Soc. Am.*, **61**, 1230–1235.
39. Jellison, G.E. Jr. (1998) Spectroscopic ellipsometry data analysis: measured versus calculated quantities. *Thin Solid Films*, **313–314**, 33–39.
40. Stoke, J.A., Dahal, L.R., Li, J., Podraza, N.J., Cao, X., Deng, X., and Collins, R.W. (2008) Optimization of Si:H multijunction n–i–p solar cells through the development of deposition phase diagrams, *Proceedings of the 33rd IEEE Photovoltaic Specialists Conference*, 11–16 May, San Diego CA, USA, IEEE, New York, Art. No. 413, pp. 1–6.
41. Li, J., Podraza, N.J., and Collins, R.W. (2007) Real time spectroscopic ellipsometry of sputtered CdTe, CdS, and $CdTe_{1-x}S_x$ thin films for photovoltaic applications. *Phys. Status Solidi (a)*, **205**, 901–904.
42. Deng, X., and Schiff, E.A. (2003), Amorphous silicon-based solar cells, in: Luque, A., and Hegedus, S. (eds), *Handbook of Photovoltaic Science and Engineering*, New York: John Wiley & Sons, Inc., pp. 505–565.
43. Collins, R.W., Ferlauto, A.S., Ferreira, G.M., Chen, C., Koh, J., Koval, R.J., Lee, Y., Pearce, J.M., and Wronski, C.R. (2003) Evolution of microstructure and phase in amorphous, protocrystalline, and microcrystalline silicon studied by real-time spectroscopic ellipsometry. *Sol. Energy Mater. Sol. Cells*, **78**, 143–180.
44. Stoke, J.A., Podraza, N.J., Li, J., Cao, X.M., Deng, X.M., and Collins, R.W. (2008) Advanced deposition phase diagrams for guiding Si:H-based multijunction solar cells. *J. Non-Cryst. Solids*, **354**, 2435–2439.
45. Green, M.A., Emery, K., Hishikawa, Y., Warta, W., and Dunlop, E.D. (2016) Solar cell efficiency tables (version 47). *Prog. Photovoltaics Res. Appl.*, **24**, 3–11.
46. Koirala, P., Attygalle, D., Aryal, P., Pradhan, P., Chen, J., Marsillac, S., Ferlauto, A.S., Podraza, N.J., and Collins, R.W. (2014) Real time spectroscopic ellipsometry for analysis and control of thin film polycrystalline semiconductor

deposition in photovoltaics. *Thin Solid Films*, **571**, 442–446.

47. Lee, J., Rovira, P.I., An, I., and Collins, R.W. (1998) Rotating-compensator multichannel ellipsometry: applications for real time Stokes vector spectroscopy of thin film growth. *Rev. Sci. Instrum.*, **69**, 1800–1810.
48. Johs, B., Hale, J., Ianno, N.J., Herzinger, C.M., Tiwald, T., and Woollam, J.A. (2001) Recent developments in spectroscopic ellipsometry for in-situ applications, in: Duparre, A., and Singh B. (eds), *Optical Metrology Roadmap for the Semiconductor, Optical, and Data Storage Industries, Proc. Soc. Photo-Opt. Instrum. Eng.* **4449**, Bellingham, WA: SPIE, pp. 41–57.
49. Chen, J., Li, J., Sainju, D., Wells, K.D., Podraza, N.J., and Collins, R.W. (2006) Multilayer analysis of the CdTe solar cell structure by spectroscopic ellipsometry, *Proceedings of the 4th World Conference on Photovoltaic Energy Conversion*, 7–12 May, Waikoloa HI, USA, IEEE, New York, pp. 475–478.
50. Plotnikov, V.V., Vasko, A.C., Compaan, A.D., Liu, X., Wieland, K.A., Zeller, R.M., Li, J., and Collins, R.W. (2009) Magnetron sputtering for II–VI solar cells: thinning the CdTe. *Mater. Res. Soc. Symp. Proc.*, **1165**, pp. M09-01: 1–9.
51. Collins, R.W., and Ferlauto, A.S. (2005), "Optical physics of materials", in: Tompkins, H. G., and Irene, E. A. (eds), *Handbook of Ellipsometry*, Norwich, NY: William Andrew Publishing, pp. 93–235.
52. Li, J., Chen, J., and Collins, R.W. (2011) Optical transition energies as a probe of stress in polycrystalline CdTe thin films. *Appl. Phys. Lett.*, **99**, 061905: 1–3.
53. Li, J., Chen, J., and Collins, R.W. (2011) Broadening of optical transitions in polycrystalline CdS and CdTe thin films. *Appl. Phys. Lett.*, **99**, 181909: 1–3.
54. Koirala, P., Li, J., Yoon, H.P., Aryal, P., Marsillac, S., Rockett, A.A., Podraza, N.P., and Collins, R.W. (2016) Through-the-glass spectroscopic ellipsometry for analysis of CdTe thin-film solar cells in the superstrate configuration. *Prog. Photovolt.: Res. Appl*. doi: 10.1002/pip.2759.
55. McCandless, B.E., and Sites, J.R. (2003), "Cadmium telluride solar cells," in: Luque, A., and Hegedus, S. (eds), *Handbook of Photovoltaic Science and Engineering* New York: John Wiley & Sons, Inc., pp. 617–662.
56. Kykyneshi, R., Zeng, J., and Cann, D.P. (2011), "Transparent conducting oxides based on tin oxide," in: Ginley, D., Hosono, H., and Paine, D. C. (eds), *Handbook of Transparent Conductors*, New York: Springer, pp. 171–191.
57. Koirala, P., Tan, X., Li, J., Podraza, N.J., Marsillac, S., Rockett, A., and Collins, R.W. (2014), "Mapping spectroscopic ellipsometry of CdTe solar cells for property-performance correlations," *Proceedings of the 40th IEEE Photovoltaic Specialists Conference*, 8–13 June, Denver CO, USA, IEEE, New York, pp. 674–679.
58. Aryal, P., Chen, J., Huang, Z., Dahal, L.R., Sestak, M.N., Attygalle, D., Jacobs, R., Ranjan, V., Marsillac, S., and Collins, R.W. (2012) Quantum efficiency simulations from on-line compatible mapping of thin-film solar cells, *Proceedings of the 37th IEEE Photovoltaic Specialists Conference*, 3–8 June, Austin TX, USA, IEEE, New York, pp. 2241–2246.
59. Abu-Shama, J., Noufi, R., Yan, Y., Jones, K., Keyes, B., Dippo, P., Romero, M., Al-Jassim, M., Alleman, J., and Williamson, D. L. (2001) Cu(In,Ga)Se_2 thin-film evolution during growth from $(In,Ga)_2Se_3$ precursors, *Mater. Res. Soc. Symp. Proc.*, **668**, pp. H.7.2: 1–6
60. Pradhan, P., Aryal, P., Ibdah, A.-R., Aryal, K., Li, J., Podraza, N.J., Marsillac, S., and Collins, R.W. (2014), "Real time spectroscopic ellipsometry analysis of the three-stages of $CuIn_{1-x}Ga_xSe_2$ co-evaporation," *Proceedings of the 40th IEEE Photovoltaic Specialists Conference*, 8–13 June, Denver CO, USA, IEEE, New York, pp. 2060–2065.
61. Aryal, P., Ibdah, A.-R., Pradhan, P., Attygalle, D., Koirala, P., Podraza, N. P., Marsillac, S., Collins, R. W., and

Li, J. (2016) Parameterized complex dielectric functions of $CuIn_{1-x}Ga_xSe_2$: applications in optical characterization of compositional non-uniformities and depth profiles in materials and solar cells. *Prog. Photovolt.: Res. Appl.*, doi: 10.1002/pip.2774.

62. Ibdah, A.-R., *Optical Physics of Cu(In,Ga)Se_2 Solar Cells and Their Layer Components*, Ph.D. Dissertation, University of Toledo, (2016, unpublished).

63. Dahal, L. R., Li, J., Stoke, J. A., Huang, Z., Shan, A., Ferlauto, A. S., Wronski, C. R., Collins, R. W., and Podraza, N. J. (2014), Applications of real-time and mapping spectroscopic ellipsometry for process development and optimization in hydrogenated silicon thin-film photovoltaics technology. *Solar Energy Mater. Solar Cells*, **129**, 32–56.

10
Characterizing the Light-Trapping Properties of Textured Surfaces with Scanning Near-Field Optical Microscopy

Karsten Bittkau, Stephan Lehnen, and Ulrich W. Paetzold

10.1
Introduction

In thin-film solar cells, the typical thicknesses of the absorbing layers are too small to absorb the majority of the impinging photons within one single path. The thicknesses are limited because of the small diffusion lengths of charge carriers in several absorber materials and the general demand of cost reductions. To increase the effective light path in the absorber layer, textured surfaces are commonly implemented. These textures provide light scattering which extends the light path in the absorber layer [1]. For larger scattering angles, total internal reflection occurs where the light cannot propagate throughout the absorber layer. This effect is called light trapping.

A common light-trapping approach is the use of textured contact layers, for example, aluminum- or boron-doped ZnO or fluorine-doped SnO_2 which is either textured by wet chemical etching or during the growth. The mechanisms result in a statistical surface morphology with different lateral sizes, heights, and shapes. By engineering the deposition and etching parameters, the distribution of surface features can be varied and optimized for each type of front contact layer and solar cell.

Since the technological effort and the parameter space are large and since each morphology consists of a special distribution of different features, this kind of optimization only leads to a local maximum of the total absorption. To achieve the overall optimum needs two things: a technology to prepare well-defined surface morphologies and a method to analyze the local light-scattering properties of individual surface features. The present chapter concentrates on the analysis of local light-trapping properties of textured surfaces with scanning near-field optical microscopy (SNOM).

In Section 10.2, the working principle of SNOM will be discussed. The role of evanescent light modes, which only occur in the optical near field, for the light-trapping properties of thin-film solar cells will be emphasized in Section 10.3. Fast Fourier transformation (FFT) will be discussed in Section 10.4

Advanced Characterization Techniques for Thin Film Solar Cells, Second Edition.
Edited by Daniel Abou-Ras, Thomas Kirchartz, and Uwe Rau.

as an analytical tool to extract local light-trapping properties from SNOM images. In Section 10.5, the investigation of an individual waveguide mode is exemplarily demonstrated. Finally, the light propagation within a thin absorber layer is investigated in Section 10.6.

10.2 How Does a Scanning Near-Field Optical Microscope Work?

SNOM (also found as NSOM) [2] is one kind of scanning probe microscopy (see Chapter 13) and works similar to an atomic force microscopy (AFM) in the non-contact mode.

There are in principle two different SNOM concepts: with and without aperture. The SNOMs with aperture normally make use of a tapered fiber tip which has a metallic coating in the tapered region to achieve a sufficient guidance of light. At the very end of the probe, a small hole is prepared into the coating which serves as an aperture. The fiber modes couple through this aperture to the light modes outside the tip. The optical resolution of such a microscope is defined by the size of the aperture which is much smaller than the wavelength of light. Therefore, spatial resolutions beyond the diffraction limit are achieved.

The apertureless SNOMs work without any fiber tip [3, 4]. Instead, an AFM probe is used, which is illuminated with focused laser light. As the tip serves as an antenna with strong field enhancement in the near field of the tip, light is scattered. The scattering behavior of the probe strongly depends on the interaction of the tip with the surface. This interaction becomes significant only in the near field. Apertureless SNOMs reach higher resolutions compared to SNOMs using an aperture, and the AFM probe is much more robust than a fiber tip. Nevertheless, it only works in the near field of the surface. The light propagation at larger distances cannot be studied with this kind of near-field microscope. The present chapter will focus on SNOMs with aperture, since the study of the light propagation is essential for the light scattering in thin-film solar cells.

The SNOM probe is an Al-coated tapered fiber tip. The aperture size is about 50–80 nm and defines the optical resolution of the system. The probe is scanning above the surface of the sample by a piezo controlling system. Distance controlling is achieved by shear-force techniques [5] since the tip is glued to a quartz tuning fork (see Figure 10.1) [6].

By this shear-force technique, the tuning fork is excited by a dither piezo, and the tip is oscillating laterally. The damping of this oscillation is measured, and the tip-to-sample distance is kept constant by a z-piezo. Therefore, topographic information can be obtained by the control voltage of the z-piezo. Additionally, the SNOM tip can collect the local light intensity at the position of the aperture. An incident plane wave illuminates the sample from the backside, and the tip collects the transmitted light at the surface [7]. This situation corresponds to the real device where the solar cell is illuminated from the substrate side (superstrate configuration) in p–i–n junctions.

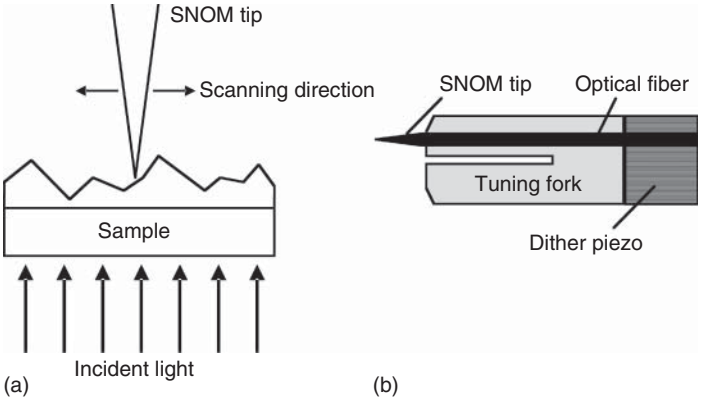

Figure 10.1 (a) Scheme of collection mode SNOM setup in transmission geometry. (b) Shear-force technique for distance controlling.

In addition to this so-called collection mode, an illumination mode is possible, where light is coupled to the fiber and the sample is illuminated by the small SNOM tip. The transmitted light is collected via a standard microscope objective. These experimental modes are not directly invertible. Also, the tip can both illuminate the sample and collect the light in the so-called luminescence mode, where the reemitted light is detected with subwavelength resolution. For solar-cell applications, this mode is used to study the local band-gap variations and lateral variations of the splitting of quasi-Fermi levels [8]. By using the sample itself as the detector, local photocurrent and photovoltages can be analyzed with SNOM in illumination mode [9–12]. A much more advanced mode takes advantage of applying two tapered fiber tips to illuminate the sample locally with the illumination tip and collect the light locally at a different position with the detection tip [13, 14]. Such a dual-probe SNOM can be used to investigate, for example, light propagation in thin films [15] or at surfaces [16]. For the kind of study described in the present chapter, the collection mode is most applicable. Therefore, most of the presented examples are obtained by this technique.

In Figure 10.2, the result of a measurement on a randomly textured ZnO surface is shown. In (a) the topography and in (b) the local light intensity at a wavelength of 658 nm are given. Both quantities are measured simultaneously by means of SNOM working in collection mode in transmission geometry. The surface consists of laterally distributed craters with different shapes and sizes. A typical lateral size of a crater is about 1 μm. By comparing the topography to the local light intensity, it can be found that at the edges of the craters, the highest light intensity is found. This behavior is typical for this kind of surface texture. The transmitted light is localized at the ridges between two (or more) craters owing to the strong curvature which leads to electric field enhancements.

Since the SNOM tip can be moved in three axes, the local light intensity distribution in the whole spatial domain above the surface can be obtained. A typical example is shown in Figure 10.3.

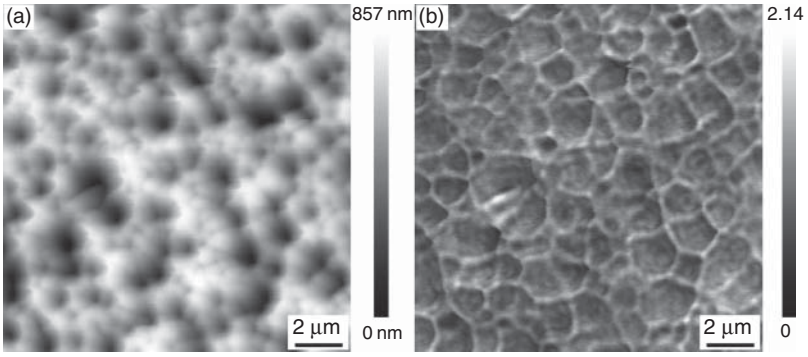

Figure 10.2 (a) Topography of randomly textured ZnO surface. (b) Local light intensity at a wavelength of 658 nm simultaneously measured with SNOM.

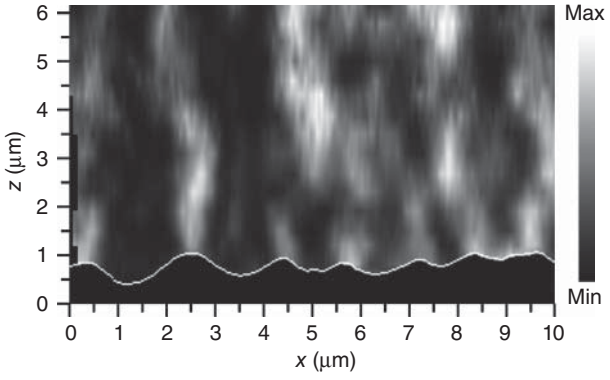

Figure 10.3 Local light intensity above a selected scanning line measured with SNOM at a wavelength of 658 nm.

For one selected scanning line, all measured intensities are plotted in a cross-sectional image. The spatial distance along the *z*-direction between two measurements was 350 nm. Missing data points are filled by interpolation [17]. It is found that there are strong localization effects above the surface with a jet-like shape. These jets are found at the highest curved edges in the topography.

10.3 The Role of Evanescent Modes for Light Trapping

In near-field optics, the so-called evanescent modes are very important. In the case of light trapping in solar cells, light, which is scattered inside the absorber layer into angles larger than the critical angle for total internal reflection, will be totally reflected at the interfaces to low refractive index material. Although light cannot propagate into the low refractive index material in this case, the electric

field intensity is finite but decreases exponentially with the distance from the interface in the order of the wavelength of light. The question is how the evanescent modes contribute to the total absorption in a thin film. Since the absorption in the layer is the most important quantity for optical study on thin-film solar cells and since evanescent modes are not detectable in far-field-based optical experiments (e.g., angularly resolved scattering, haze, reflection/transmission), this is indeed an important question. The answer will have an influence on the choice of experiment and also simulation tools to study the light-trapping properties of surface textures.

Here, a theoretical model was chosen, where Maxwell's equations are solved rigorously for a one-dimensional periodic grating. This model was developed by Chandezon *et al*. [18, 19] and is denoted as C method in the following. Within this method, Maxwell's equations are transformed into a curvilinear coordinate system where the surface is flat. By applying periodic boundary conditions, the field components are developed into Fourier series, resulting in an algebraic equation system instead of the differential equations. The C method provides two essential advantages: the comparably low demand of computer power and the possibility to separate the evanescent modes. This allows us to study the impact of surface modifications as well as to answer the question how evanescent modes contribute to the total absorption.

In Figure 10.4, the calculated electric field distribution for a single scanning line of an AFM measurement is shown [20]. The thin-film stack consists of a ZnO half space with a surface profile defined by the given scanning line. On top of this surface, a hydrogenated amorphous silicon (a-Si:H) layer with a thickness of 250 nm and a refractive index of $n_{\text{a-Si:H}} = 3.803 + 0.0022i$ is assumed [21]. At the top of this

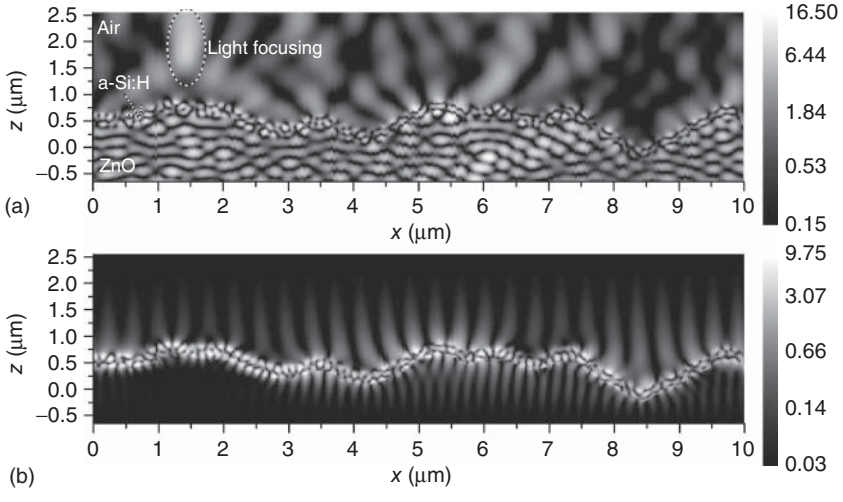

Figure 10.4 (a) Calculated electric field distribution for a single scanning line at a wavelength of 780 nm. (b) Calculated intensity distribution of evanescent part of light for the same scanning line [20]. For both figures, a logarithmic intensity scale was chosen.

layer, the profile is supposed to be conformal and the upper half space is air. The gray scale is logarithmic for enhanced visualization.

In Figure 10.4a, the distribution of the whole electric field is shown taking into account both propagating and evanescent part of light. In Figure 10.4b, only the intensity distribution of the evanescent part of light is shown. The light focusing effect which forms a jet-like shape (see Figure 10.3) can be seen in Figure 10.4a at, for example, an x coordinate of 1.5 µm and a z coordinate of 2 µm. In addition to the information which is collected by SNOM, the local light intensity inside the material can be obtained by these simulations. In the ZnO substrate, an intensity modulation is found, which results from the interference effects of the incident plane wave and the diffraction of the reflected waves. Inside the silicon layer, a finer interference pattern is found due to the larger refractive index. From the results of the evanescent part of light, it can be seen that inside the silicon layer, the interference pattern looks very similar to that for the total amount of light. This means that the behavior in the silicon is dominated by guided waves. The exponential decrease of these modes in the surrounding media can be seen in Figure 10.4b by the intensity spikes in air and ZnO.

In Figure 10.5, the calculated absorption enhancement for an a-Si:H thin film on top of a textured ZnO substrate is shown. With the results of the C method, the local absorption can be extracted. This absorption is integrated over the spatial domain of the silicon to get the total absorption. This value is normalized against the corresponding absorption for flat interfaces with an identical layer stack. This gives the enhancement of the absorption due to the texture. The measured surface profile is modified by stretching it along the z-axis. The new profile function is then given by $z(x) = sz_0(x)$. Here, $z_0(x)$ defines the measured profile and s the z scaling parameter. The absorption enhancement is calculated for both the total amount of light (solid curve) and the evanescent part (dashed curve). Obviously,

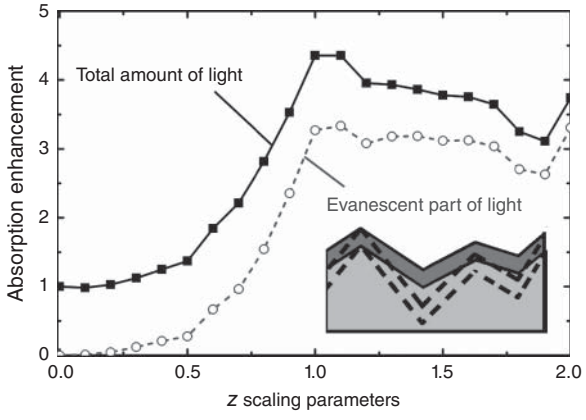

Figure 10.5 Calculated absorption enhancement for a selected scanning line with varying z scaling parameter for the total amount of light (solid curve) and the evanescent part of light (dashed line) [20]. The inset illustrates the kind of surface variation.

the total absorption can be increased by a factor of 4 for this kind of profile. The most important result is that the absorption of the evanescent modes nearly follows the absorption enhancement for the total amount of light. This means that the improvement in the quantum efficiency of textured solar cells is strongly dominated by light modes which are guided in the silicon layer. This result is found for all kinds of surface profiles and various kinds of modification.

In conclusion, it is demonstrated that light trapping in thin-film solar cells is strongly dominated by evanescent light modes, that is, light scattering at rough interfaces must be strong enough to excite these guided modes and that the experimental study must have an access to evanescent light. Since the intensity of these modes decreases exponentially with the distance to the surface, an optical near-field experiment is essential to study light trapping.

The following section will focus on the analytical methods for the extraction of evanescent mode intensity from SNOM measurements on textured surfaces.

10.4 Analysis of Scanning Near-Field Optical Microscopy Images by Fast Fourier Transformation

As shown in the previous section, the portion of light which is scattered into evanescent modes is essential for the study of light-trapping efficiency. Since these modes only have finite intensities in the optical near-field regime, where the distance to the surface is less than one wavelength, SNOM is a powerful tool to investigate local light-trapping efficiencies. Nevertheless, the analysis and interpretation of SNOM images is complex as the following questions arise: (i) How does the near-field probe influence the measured signal? (ii) Are the coupling efficiencies of different optical modes comparable? (iii) Since the measured optical modes couple to the same fiber mode, different modes cannot be directly distinguished. Is it possible to distinguish them indirectly? There are certainly more questions concerning the analysis and interpretation of SNOM images. But at this point, it should be enough to concentrate on these three.

The question whether the near-field probe influences the measured signal is reasonable since the tip is metallized and placed in the spatial domain which is in the focus of investigation. By comparing the measured cross-sectional images (see Figure 10.3) to numerical results from finite-difference time-domain simulations, disregarding the existence of the tip, a very good agreement is found for the investigated types of structure [22]. In the direct comparison of the local light intensities at a distance of 20 nm to the surface, deviations are found. A detailed investigation shows that this is mainly due to the finite size of the tip [23]. At the slope of a corrugated surface, the distance controlling system keeps the closest tip-to-sample distance constant which is achieved at the side of the tip. Therefore, the distance between the aperture and the surface might vary significantly. This has an impact on the detected light intensity due to the strong distance dependence of the evanescent modes.

The second question deals with the coupling efficiencies of different optical modes to the near-field probe. The optical fiber, with the tip at its end, has a finite angle of acceptance which means that the lateral wavevector of the optical mode inside the fiber is restricted. Optical modes with lateral wavevectors larger than the limit cannot couple directly into the fiber but via scattering at the conical tip which transfers the wavevector into the acceptance cone. Therefore, the coupling into the fiber is in principle possible for all optical modes. Nevertheless, the larger the lateral wavevector is, the stronger the scattering at the tip must be in order to detect it. Therefore, it is reasonable that optical modes with large planar wavevectors couple weaker to the fiber as modes which propagate nearly at normal incidence. This limitation affects the evanescent modes in particular.

The third question is the most interesting one. In the spatial domain of investigation, there are different optical modes: specularly scattered light, light with small scattering angles, strongly scattered light with nearly gracing angles, and light which is scattered into evanescent modes. By detecting all these modes by the SNOM probe, they will couple to the same fiber mode and are detected without any information about the lateral wavevector before scattering at the tip. For the study of the scattering behavior of textured surfaces, it is quite important to obtain the information about the transferred wavevectors. Especially, the extraction of evanescent modes is essential.

In Figure 10.6, the formation of periodic intensity patterns in SNOM images due to the interference of scattered light is illustrated. The wave fronts of the incident plane wave and the scattered light are shown. For the scattered light, only one possible scattering angle θ is depicted. The different wave fronts of the wave

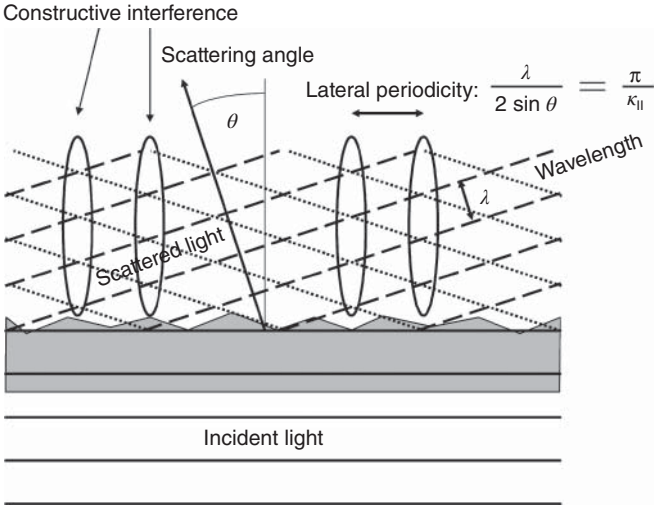

Figure 10.6 Incident and scattered wave fronts. The relation between the period of the interference pattern and the transferred planar wavevector is illustrated for a selected scattering angle.

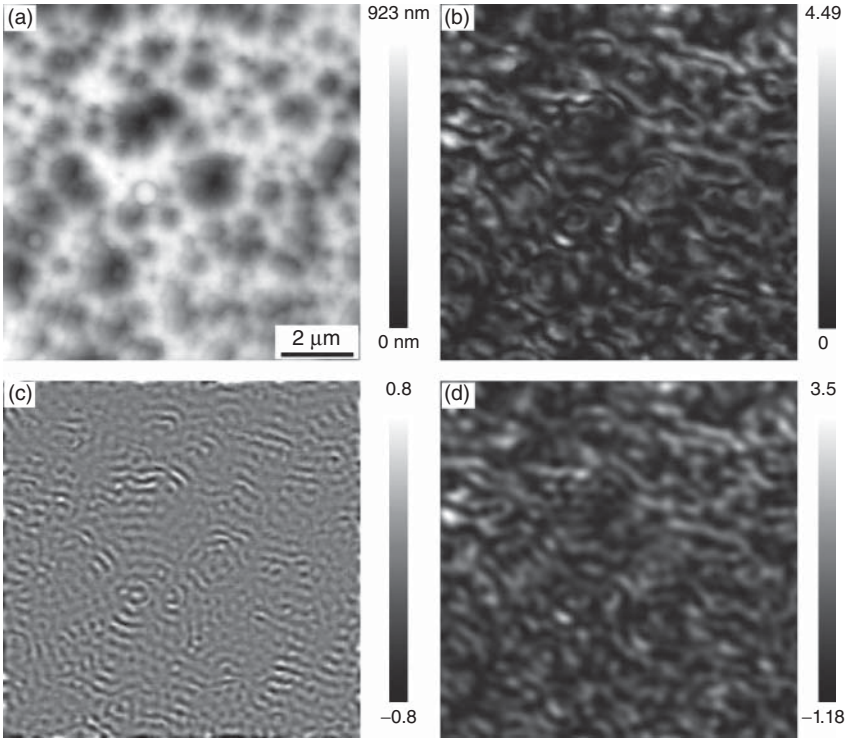

Figure 10.7 (a) Topography of an a-Si:H top cell with intermediate layer and µc-Si:H cap layer deposited on randomly textured ZnO. (b) Local light intensity at a wavelength of 705 nm measured with SNOM. In the lower part, the evanescent (c) and propagating (d) parts of the local light intensity are shown.

which is scattered to the left side interfere with the wave fronts of the light which is scattered to the right side. This leads to regions of constructive interference which are oriented perpendicular to the surface. The distance of the interference maxima is given by the scattering angle and, therefore, the transferred planar wavevector.

Considering all possible scattering angles gives a superposition of periodic light intensity patterns. The individual amplitude for each period can be extracted by FFT. This information can be used to generate individual images for the evanescent and propagating light. This is exemplarily shown in Figure 10.7.

In the upper part, the topography (a) and the local light intensity (b) at a wavelength of 705 nm are shown for an a-Si:H top cell deposited on a randomly textured ZnO layer. On top of the cell, an intermediate reflector consisting of SiO_x:H as well as a µc-Si:H cap layer is deposited. This layer stack describes the optical situation of a full tandem solar cell concerning the properties of the a-Si:H top cell [24]. The measured local light intensity is transformed by FFT, and the evanescent (c) and propagating (d) parts of transmitted light are extracted by high-pass and low-pass filters, where the spatial cutoff frequency was defined by $2/\lambda$. Between

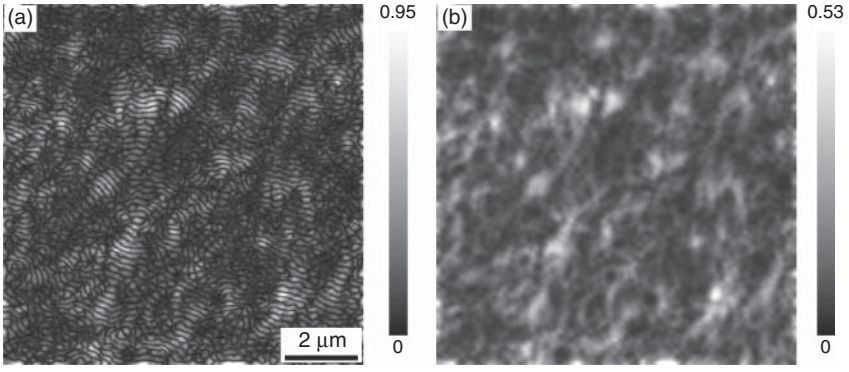

Figure 10.8 Evanescent part of light extracted from the SNOM measurement shown in Figure 10.7. (a) The norm of the FFT filtered values is plotted. Figure (b) shows a smoothed image to illustrate the envelope of the standing waves.

the measured image and the propagating part of light, strong similarities can be found. This means that the total transmitted light intensity is dominated by the propagating light modes. The evanescent part shows the light which is trapped inside the solar cell. The image appears a superposition of spherical waves with the craters as center positions.

In Figure 10.8 the evanescent part of light is shown as the norm of the back-transformed FFT image (see Figure 10.7c for comparison). Both the pure data (a) and smoothed data (b) are shown. In the intensity profile of the evanescent modes, nodes are found which are caused by standing waves. By smoothing the image, this oscillation is damped. Here, a better identification of regions with higher light-trapping efficiencies is possible. A detailed study of these images and the comparison to numerical results are necessary to extract the information relevant for further improvement of the surface texture.

10.5 Investigation of Individual Waveguide Modes

The coupling of incident light to waveguide modes is a very promising concept to improve the efficiency of thin-film solar cells that suffer from weak absorptance near the band gap of the absorber material [20, 25]. Nanophotonic light-trapping structures are implemented at different interfaces to diffract light into large angles inside the absorber material [26–29]. In the resonance case, optical waveguide modes propagate through the solar-cell absorber. Those modes show an increased absorption probability. An optical mode that is guided in a high refractive index material induces evanescent fields close to the interface. This allows an SNOM detecting such a waveguide mode in the optical near field of the absorber layer.

A particular planar waveguide mode is characterized by the polarization (either transversal electric (TE) or transversal magnetic (TM)), the propagation direction

(given by the planar wavevector), and the frequency (corresponds to the wavelength of incident light). The local light intensity distribution of such a waveguide mode shows a periodic pattern along the direction of propagation. The period corresponds to the planar wave vector.

With a special sample design, Paetzold *et al.* [30] investigated a particular waveguide mode in an a-Si:H solar cell. A squared part of the solar cell was nanopatterned with a two-dimensional cubic grating structure of 500 nm period. Each unit cell consists of a hemispherically shaped nanostructure. The cubic grating allows incident light to couple into waveguide modes in the absorber layer. The waveguide modes are able to propagate inside the film and will, therefore, also exist apart from the nanopatterned region. Generally, two different types of planar waveguide modes are separated: (i) transversal electric (TE) modes and (ii) transversal magnetic (TM) modes. In those modes, either the electric field or the magnetic field oscillates perpendicular to the propagation direction of the waveguide mode, respectively. At normal incident, the coupling to both TE and TM modes is always possible inside the nanopatterned region for any polarization of incident light due to the two-dimensional grating structure. Here, the grating allows diffraction along both planar coordinate axes, resulting in a twofold symmetry. Apart from the nanopatterned region, this symmetry is broken because the propagation direction is now fixed. Therefore, the coupling to a particular waveguide mode will show a strong polarization dependency. This is demonstrated in Figure 10.9.

Figure 10.9a schematically illustrates the top view of the measurement geometry. The corner of the periodically nanopatterned region is shown together with the two chosen scanning areas which are located mostly in the flat region of the solar cell including the edge to the nanopatterned part. In Figure 10.9b, the measured electric field intensity distributions are shown for both scanning areas and for both polarizations of incident light, parallel and orthogonal to the respective edge of the nanopatterned region. Due to the selection of the scanning areas, waveguide modes, which might be excited by the incident light due to the interaction with the grating structure, will propagate perpendicular to the edge of the nanopatterned region. In this case, a periodic electric field intensity distribution is expected in the same direction. This can be observed for polarization of incident light parallel to the edge of the nanopatterned region for both scanning areas. To support this, FFT of the selected part of the measured electric field intensity distributions are shown in Figure 10.9c. For polarization of incident light parallel to the edge of the nanopatterned region, distinct maxima are found in the FFT that reflect the periodic electric field intensity distribution. The position of the distinct peaks corresponds to the grating constant of 500 nm. For polarization of incident light orthogonal to the edge of the nanopatterned region, a diffuse ring-like structure is found in the FFT without any distinct maximum. This is caused by the interaction of incident light with small surface roughness which allows for light scattering in any direction. Due to the resonance condition, light is preferably scattered into the waveguide mode at this wavelength which is isotropic in lateral direction. Therefore, the ring-like structure in the FFT is expected. The results

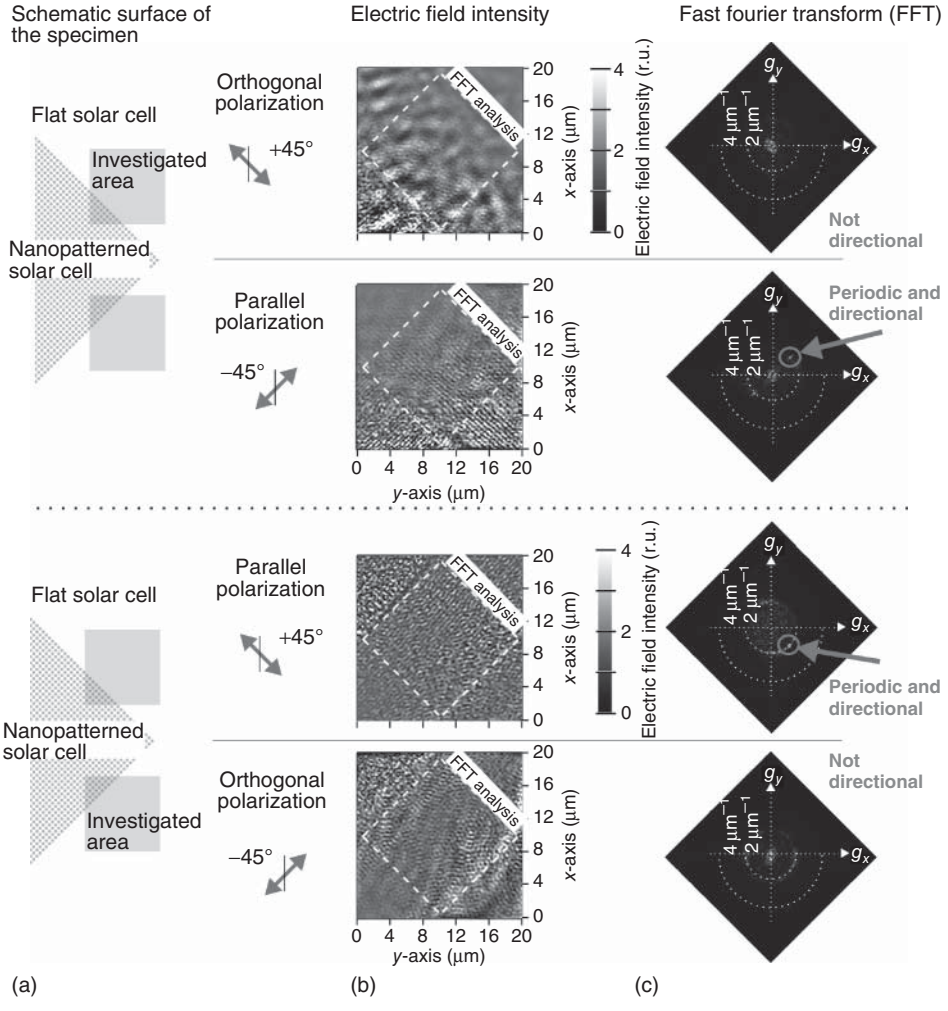

Figure 10.9 (a) Schematic illustration of the measured regions of the specimen. (b) Measured electric field intensity distributions at the surface of the area of investigation for incident monochromatic light of 750 nm and for incident polarization orthogonal and parallel to the respective the borderline of the nanostructured region. (c) Two-dimensional FFT of the measured electric field intensity distributions.

lead to the conclusion that the selected waveguide mode is a TE mode which is excited by the first diffraction order of the grating.

In order to identify the resonant light coupling to an individual waveguide mode, the wavelength of incident light is varied and the coupling efficiency for each wavelength determined. The coupling efficiency is defined by the peak intensity in the FFT of the electric field intensity distribution. The results are shown in Figure 10.10a. Figure 10.10b depicts the measured external quantum efficiency

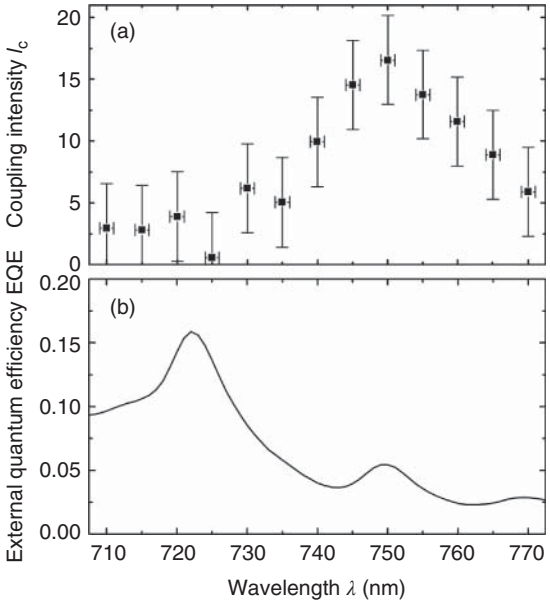

Figure 10.10 (a) Light coupling intensity I_c of incident light to a waveguide mode derived from a series of FFTs with a wide range of wavelengths. (b) External quantum efficiency of the nanophotonic solar cell as a function of the wavelength.

(EQE) of the nanopatterned solar cell for comparison. It can be clearly seen that the EQE shows local maxima at the wavelengths of 723 and 750 nm. In contrast, the coupling efficiency to the selected waveguide mode, measured by SNOM, shows a maximum only at a wavelength of 750 nm. From this, it can be concluded that only the resonance in the EQE at a wavelength of 750 nm is related to a TE mode which is excited by the first diffraction order of the grating.

10.6
Light Propagation in Thin-Film Solar Cells Investigated with Dual-Probe SNOM

For the coupling of incident light into the absorber material, the guidance of light inside the layer as well as the coupling of guided modes to propagating light in the surrounding half space is of great importance for solar cells. Textured interfaces are often used to support efficient coupling of incident light to the absorber layer. Anyway, those textures also influence the light guidance in particular in thin-film solar cells where coherent waveguide modes are present due to the low thickness of the absorber layer. Well-defined waveguide modes only exist in flat layers. Therefore, any kind of texture will have an impact on the guidance of light. Furthermore, the texture also supports the coupling of guided modes to the half space which will directly cause an optical loss for the solar cell as this light can no longer be absorbed.

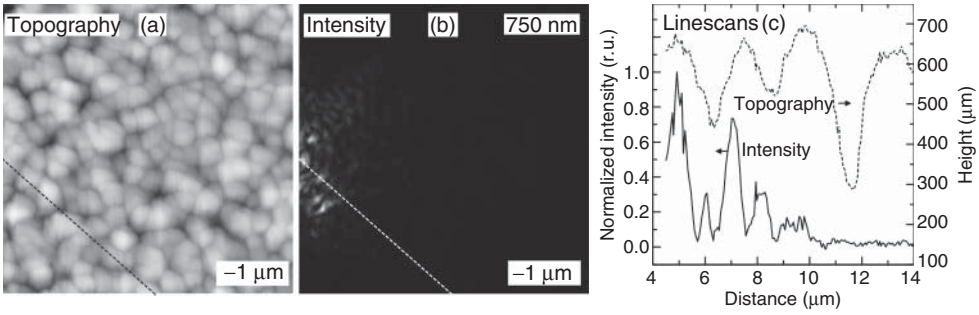

Figure 10.11 (a) Topography of a textured µc-Si:H thin-film solar cell. The height scale from min to max is 820 nm. The lateral size is $20 \times 20\ \mu m^2$. (b) Intensity map simultaneously measured at a wavelength of 750 nm in dual-probe mode. (c) Line scans at the positions shown by the dashed lines in (a) and (b).

An advanced dual-probe SNOM setup allows for the detailed characterization of those mechanisms by combining different advantages: (i) The illumination probe acts as a local point source which allows investigating local light coupling efficiencies into the solar cell. (ii) The detection probe allows studying of the optical losses due to light coupling to the half space. (iii) By variation of the relative positions of both probes, light propagation inside the absorber layer can be measured as the near-field effect of the SNOM probes allows the detection of evanescent waves that accompany waveguide modes.

In the simplest dual-probe configuration, the sample is illuminated through a tip at a fixed position. In the second, the collection probe is scanned across the surface and collects the local light intensity. In this configuration, light coupling into the layer is kept constant by the fixed illumination probe, whereas local light coupling from the guided modes to the collection probe is varied as well as the light path inside the layer by variation of the position of the collection probe. An example is shown in Figure 10.11. The topography, measured by the collection probe, is shown in Figure 10.11a, and the local light intensity measured by the collection probe is plotted in Figure 10.11b for a wavelength of 750 nm. The two dashed lines indicate the location of the line scans that are shown in Figure 10.11c. The line scan shows the exponential decay in light intensity due to absorption as well as a superimposed fine structure which correlates to the topographic information. At both maxima and minima in the topography, a stronger coupling of guided light to the collection probe is found which further reduces the remaining light intensity.

In order to measure the light intensity decrease as a function of the distance, the line scans from Figure 10.11c suffer from local light coupling efficiencies at the positions of the illumination and collection probes. Therefore, a more advanced configuration is illustrated in Figure 10.12. Here, the distance between both probes is kept constant during the scan. Generally, this can be achieved in two different ways: (i) Both probes are moved synchronously. (ii) The sample is

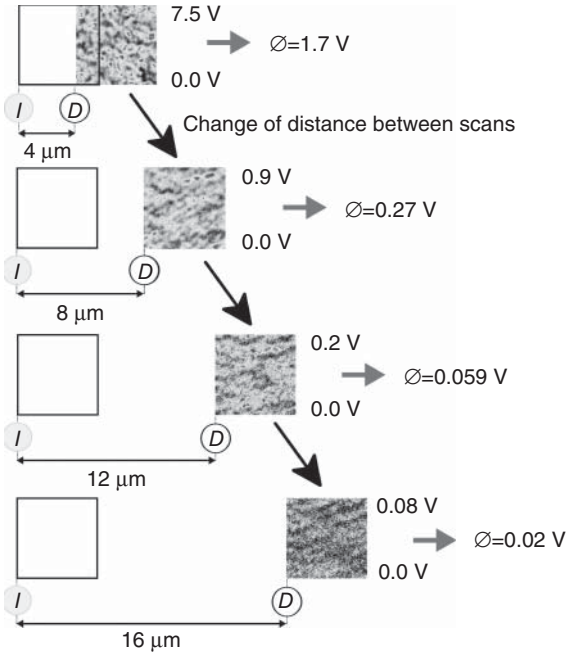

Figure 10.12 Illustration of the coupling-eliminated scan procedure. The black squares symbolize the scan area of the illumination probe, whereas the actual measured intensity maps are placed accordingly to the distance between the illumination probe (*I*) and the detection probe (*D*). The probe-to-probe distance is constant within a single measurement and changed stepwise in between the measurements. The images are plotted on a linear scale. The voltage is proportional to the intensity.

moved. From a practical point of view, it is much easier to move the sample and to keep the position of the probes constant. The scanning of the sample allows averaging the locally varying coupling efficiencies. Thereby, the intensity decrease due to light propagation through the absorber layer along the distance, as defined by the probe-to-probe distance, is measured. By incrementally increasing the probe-to-probe distance, the intensity decrease is extracted as a function of the distance.

Figure 10.13 shows the result of such a measurement performed on a µc-Si thin-film solar cell with a thickness of 1 µm. The effective absorption coefficient is extracted from the decrease of the average intensity of the measured light intensity distributions with the probe-to-probe distance. Due to the elongated light path inside the layer, the probe-to-probe distance is shorter than the effective light path. Therefore, intensity losses due to absorption are increased which is represented by the larger effective absorption coefficients compared to the macroscopic bulk values. Besides this, surface roughness leads to additional intensity losses inside the absorber layer due to coupling of guided light modes to outer half space.

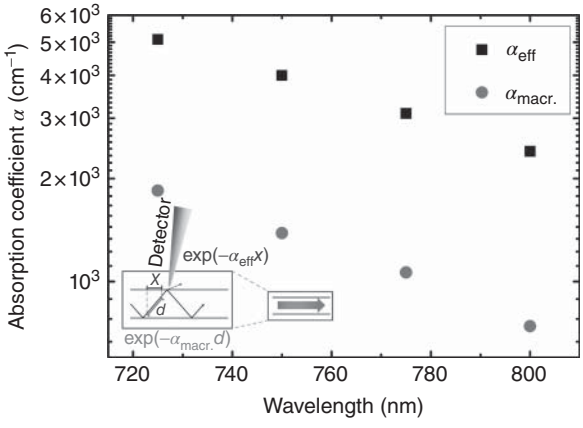

Figure 10.13 Absorption coefficient of a μc-Si:H layer with a thickness of 1 μm as a function of the wavelength. The circles represent the macroscopic values determined by photothermal deflection measurements on the same material. The squares were determined by dual-probe SNOM measurements and represent the effective absorption coefficient. The larger values for the SNOM measurement are explained by the increased light path inside the layer with respect to the lateral distance along the interface.

10.7 Conclusion

SNOM is found out to be an excellent tool to study the local light scattering and, therefore, the local light-trapping properties of thin-film solar cells on textured surfaces. Light scattering at textured surfaces must be understood in a wave picture. This is why the propagation of light inside the absorber layer is linked to guided modes. These modes can be obtained with high spatial resolution by SNOM experiment. The analytical techniques to characterize the potential of different morphological structures for the light trapping are established. For further improvement of surface texture, this information is essential and can only be obtained in optical near-field experiments.

Acknowledgments

The author thanks Thomas Beckers for parts of the measurements and Reinhard Carius for the helpful discussions. The Deutsche Forschungsgemeinschaft is acknowledged for the partial financial support through Grant No. PAK88.

References

1. Yablonovitch, E. and Cody, G.D. (1982) Intensity enhancement in textured optical sheets for solar cells. *IEEE Trans. Electron Devices*, **29**, 300–305.
2. Pohl, D.W., Denk, W., and Lanz, M. (1984) Optical stethoscopy: image recording with resolution λ/20. *Appl. Phys. Lett.*, **44**, 651–653.

3. Gleyzes, P., Boccara, A.C., and Bachelot, R. (1995) Near field optical microscopy using a metallic vibrating tip. *Ultramicroscopy*, **57**, 318–322.
4. Knoll, B. and Keilmann, F. (1998) Scanning microscopy by mid-infrared near-field scattering. *Appl. Phys. A*, **66**, 477–481.
5. Karrai, K. and Grober, R.D. (1995) Piezoelectric tip–sample distance control for near field optical microscopes. *Appl. Phys. Lett.*, **66**, 1842–1844.
6. Behme, G., Richter, A., Süptitz, M., and Lienau, C. (1997) Vacuum near-field scanning optical microscope for variable cryogenic temperatures. *Rev. Sci. Instrum.*, **68**, 3458–3463.
7. Betzig, E., Isaacson, M., and Lewis, A. (1987) Collection mode near-field scanning optical microscopy. *Appl. Phys. Lett.*, **51**, 2088–2090.
8. Gütay, L., Pomraenke, R., Lienau, C., and Bauer, G.H. (2009) Subwavelength inhomogeneities in Cu(In,Ga)Se_2 thin films revealed by near-field scanning optical microscopy. *Phys. Status Solidi A*, **206**, 1005–1008.
9. Gotoh, T., Yamamoto, Y., Shen, Z., Ogawa, S., Yoshida, N., Itoh, T., and Nonomura, S. (2009) Nanoscale characterization of microcrystalline silicon solar cells by scanning near-field optical microscopy. *Jpn. J. Appl. Phys.*, **48**, 91202.
10. McDaniel, A.A., Hsu, J.W.P., and Gabor, A.M. (1997) Near-field scanning optical microscopy studies of Cu(In,Ga)Se_2 solar cells. *Appl. Phys. Lett.*, **70**, 3555–3557.
11. Herndon, M.K., Gupta, A., Kaydanov, V., and Collins, R.T. (1999) Evidence for grain-boundary-assisted diffusion of sulfur in polycrystalline CdS/CdTe heterojunctions. *Appl. Phys. Lett.*, **75**, 3503–3505.
12. Leite, M.S., Abashin, M., Lezec, H.J., Gianfrancesco, A., Talin, A.A., and Zhitenev, N.B. (2014) Nanoscale imaging of photocurrent and efficiency in CdTe solar cells. *ACS Nano*, **8**, 11883–11890.
13. Kaneta, A., Fujimoto, R., Hashimoto, T., Nishimura, K., Funato, M., and Kawakami, Y. (2012) Instrumentation for dual-probe scanning near-field optical microscopy. *Rev. Sci. Instrum.*, **83**, 083709.
14. Fujimoto, R., Kaneta, A., Okamoto, K., Funato, M., and Kawakami, Y. (2012) Interference of the surface plasmon polaritons with an Ag waveguide probed by dual-probe scanning near-field optical microscopy. *Appl. Surf. Sci.*, **258**, 7372–7376.
15. Lehnen, S., Paetzold, U.W., Ermes, M., Bittkau, K., and Carius, R. (2014) *Analysis of Light Propagation in Thin-Film Solar Cells by Dual-Probe Scanning Near-Field Optical Microscopy*. 40th IEEE Photovoltaic Specialist Conference, June 8–13, 2014, Denver, Colorado, USA, pp. 3347–3351, doi:10.1109/PVSC.2014.6925652.
16. Dallapiccola, R., Dubois, C., Gopinath, A., Stellacci, F., and Dal Negro, L. (2009) Near-field excitation and near-field detection of propagating surface plasmon polaritons on Au waveguide structures. *Appl. Phys. Lett.*, **94**, 243118.
17. Bittkau, K., Beckers, T., Fahr, S., Rockstuhl, C., Lederer, F., and Carius, R. (2008) Nanoscale investigation of light-trapping in a-Si:H solar cell structures with randomly textured interfaces. *Phys. Status Solidi A*, **205**, 2766–2776.
18. Chandezon, J., Maystre, D., and Raoult, G. (1980) A new theoretical method for diffraction gratings and its numerical application. *J. Opt.*, **11**, 235–241.
19. Chandezon, J., Dupuis, M.T., Cornet, G., and Maystre, D. (1982) Multicoated gratings: a differential formalism applicable in the entire optical region. *J. Opt. Soc. Am.*, **72**, 839–846.
20. Bittkau, K. and Beckers, T. (2010) Near-field study of light scattering at rough interfaces of a-Si:H/μc-Si:H tandem solar cells. *Phys. Status Solidi A*, **207**, 661–666.
21. Vetterl, O., Finger, F., Carius, R., Hapke, P., Houben, L., Kluth, O., Lambertz, A., Mück, A., Rech, B., and Wagner, H. (2000) Intrinsic microcrystalline silicon: a new material for photovoltaics. *Sol. Energy Mater. Sol. Cells*, **62**, 97–108.
22. Rockstuhl, C., Lederer, F., Bittkau, K., and Carius, R. (2007) Light localization

at randomly textured surfaces for solar-cell applications. *Appl. Phys. Lett.*, **91**, 171104.

23. Ermes, M., Lehnen, S., Bittkau, K., and Carius, R. (2013) Reconstruction of SNOM near-field images from rigorous optical simulations by including topography artifacts. *Proc. SPIE*, **8789**, 87890I.
24. Rockstuhl, C., Lederer, F., Bittkau, K., Beckers, T., and Carius, R. (2009) The impact of intermediate reflectors on light absorption in tandem solar cells with randomly textured surfaces. *Appl. Phys. Lett.*, **94**, 211101.
25. Yu, Z., Raman, A., and Fan, S. (2010) Fundamental limit of nanophotonic light trapping in solar cells. *Proc. Natl. Acad. Sci. U.S.A.*, **107**, 17491–17496.
26. Bermel, P., Luo, C., Zeng, L., Kimerling, L.C., and Joannopoulos, J.D. (2007) Improving thin-film crystalline silicon solar cell efficiencies with photonic crystals. *Opt. Express*, **15**, 16986–17000.
27. Üpping, J., Bielawny, A., Wehrspohn, R.B., Beckers, T., Carius, R., Rau, U., Fahr, S., Rockstuhl, C., Lederer, F., Kroll, M., Pertsch, T., Steidl, L., and Zentel, R. (2011) Three-dimensional photonic crystal intermediate reflectors for enhanced light-trapping in tandem solar cells. *Adv. Mater.*, **23**, 3896–3900.
28. Kang, G., Park, H., Shin, D., Baek, S., Choi, M., Yu, D.-H., Kim, K., and Padilla, W.J. (2013) Broadband light-trapping enhancement in an ultrathin film a-Si absorber using whispering gallery modes and guided wave modes with dielectric surface-textured structures. *Adv. Mater.*, **25**, 2617–2623.
29. Brongersma, M.L., Cui, Y., and Fan, S. (2014) Light management for photovoltaics using high-index nanostructures. *Nat. Mater.*, **13**, 451–460.
30. Paetzold, U.W., Lehnen, S., Bittkau, K., Rau, U., and Carius, R. (2014) Nanoscale observation of waveguide modes enhancing the efficiency of solar cells. *Nano Lett.*, **14**, 6599–6605.

11
Photoluminescence Analysis of Thin-Film Solar Cells

Thomas Unold and Levent Gütay

11.1
Introduction

Luminescence describes the emission of light from a solid arising from deviations from thermal equilibrium, as distinct from blackbody radiation which is observed in thermal equilibrium [1, 2]. The thermal equilibrium state can be disturbed by various forms of excitation, such as the application of an external voltage (electroluminescence; see Chapter 3), an incident electron beam (cathodoluminescence; see Section 14.2.5), mechanical stress (mechanoluminescence), and a heating ramp releasing carriers from deeply trapped states (thermoluminescence), and also by the absorption of light of sufficient energy, which is commonly called photoluminescence (PL). The emission of PL radiation is caused by the transition of electrons from higher occupied electronic states into lower unoccupied states, under the emission of photons if the transition is dipole allowed. According to the laws of quantum mechanics, the transition rate can be calculated by first-order perturbation theory using Fermi's golden rule. Using this formalism, optical transitions from an occupied density of initial states to an unoccupied density of final states can be expressed by [2, 3]

$$R_{\mathrm{sp}}(E) \propto \int |M_{\mathrm{if}}|^2 f(E_{\mathrm{i}})(1 - f(E_{\mathrm{i}} + E))g(E_{\mathrm{i}})g(E_{\mathrm{i}} + E)\mathrm{d}E_{\mathrm{i}}, \tag{11.1}$$

where M_{if} represents the matrix element coupling the wavefunctions of the initial and final states, $f(E)$ represents the Fermi–Dirac occupation function, and $g(E)$ denotes the density of electronic states. Usually the optical transition matrix element is calculated in the semiclassical approximation, where the exciting light is treated by classical electrodynamics. Using the fact that the same transition matrix element and density of states govern absorption and emission events, a relationship between the absorption coefficient $\alpha(E)$ and the spontaneous emission rate was derived based on detailed balance arguments in thermal equilibrium [4]:

$$R^0_{\mathrm{sp}} = \frac{8\pi n_{\mathrm{r}}^2}{h^3 c^2} \frac{\alpha(E)E^2}{\exp(E/k_{\mathrm{B}}T) - 1}, \tag{11.2}$$

Advanced Characterization Techniques for Thin Film Solar Cells, Second Edition.
Edited by Daniel Abou-Ras, Thomas Kirchartz, and Uwe Rau.

where n_r is the refractive index of the material, h is Planck's constant, c is the speed of light, and k_B is the Boltzmann constant. Equation 11.2 is very useful in the sense that it directly relates the absorption coefficient of a material to its emission spectrum and in principle allows for calculating one quantity if the other quantity is known. Since in PL measurements we are interested in deviations from thermal equilibrium, we write the net spontaneous emission rate as

$$R_{sp} = R^0_{sp}\frac{np}{n_0 p_0} - R^0_{sp} = B(np - n_0 p_0) = Bn_i^2(\exp(\Delta\mu/k_B T) - 1), \tag{11.3}$$

where n and p are the total carrier densities, n_0 and p_0 are the equilibrium carrier densities related to the intrinsic carrier density by $n_i^2 = n_0 p_0$, $\Delta\mu = E_{Fn} - E_{Fp}$ represents the quasi-Fermi-level splitting between the quasi-Fermi levels for electrons E_{Fn} and for holes E_{Fp}, and B defines the material-specific radiative recombination coefficient [1]:

$$B = \frac{1}{n_i^2}\frac{8\pi}{h^3c^2}\int_0^\infty n_r^2\alpha(E)\exp(-E/k_B T)E^2\,\mathrm{d}E. \tag{11.4}$$

It is useful to distinguish the following experimental conditions: (i) $n \gg n_0$ and $p \gg p_0$. In this case, the PL photon flux is given by $Y_{PL} \propto Bnp$. This situation is referred to as the high-injection condition, where the radiative lifetime $\tau_{rad} = 1/(Bn)$ depends on the injection ratio. (ii) When $p \approx p_0$ for p-type material ($n \approx n_0$ for n-type material), then $Y_{PL} \propto Bnp_0$ and the PL flux depends on the majority carrier density with a radiative lifetime $\tau_{rad} = 1/(Bp_0)$ independent of the injection ratio. This situation is referred to as the low-injection condition. Typical values for the radiative coefficient and radiative lifetime assuming a doping level of $10^{16}\,\mathrm{cm}^{-3}$ are $B_{Si} = 2\times10^{-15}\,\mathrm{cm}^{-3}/\mathrm{s}$ and $\tau_{Si} = 0.025\,\mathrm{s}$ for silicon and $B_{CuInSe_2} \approx 6\times10^{-11}\,\mathrm{cm}^{-3}/\mathrm{s}$ and $\tau_{CuInSe_2} \approx 1\,\mu\mathrm{s}$ for $CuInSe_2$ [1, 5].

In most materials, nonradiative recombination occurs via deep defects in the energy band gap, limiting the recombination lifetime to significantly smaller values than the radiative lifetime since the total recombination rate comprises all individual recombination rates:

$$\tau_{tot}^{-1} = \tau_{rad}^{-1} + \tau_{nonrad}^{-1}. \tag{11.5}$$

From the ratio of measured lifetime to radiative lifetime, the PL efficiency of a material can be defined as $\eta_{PL} = \tau_{tot}/\tau_{rad}$.

So far, we have been mostly concerned with radiative transitions taking place within the sample. However, the correct calculation of the number of photons emitted from a sample in a PL experiment is much more complicated since details of the absorption profile, diffusion and drift and recombination of carriers with the sample, and the propagation of the emitted photons through the sample surface have to be taken into account. In most PL experiments, the information depth is given by the absorption length $1/\alpha$ of the exciting light or by the diffusion length of minority carriers, which ever of these two quantities is larger [2]. For an exact treatment, closed-form solutions are difficult to obtain and numerical simulation

has to be employed. However, assuming homogeneous material properties and flat quasi-Fermi levels and taking into account that light is emitted through the sample surface within a narrow emission cone $1/4n_r^2$, the photon flux detected outside the sample can be expressed by [6]

$$Y_{PL}(E) = \frac{1}{4\pi^2\hbar^3c^2}\frac{a(E)E^2}{\exp((E-\Delta\mu)/k_BT)-1}, \tag{11.6}$$

where the absorptivity is given by $a(E) = (1 - R_f)\,(1 - \exp(-\alpha(E)d))$ with the front surface reflectivity R_f and the sample thickness d. Equation 11.6 has been referred to as the generalized Kirchhoff's or generalized Planck's law because of its resemblance to these well-known relations valid for thermal equilibrium conditions. Note that Equation 11.6 is only valid if equilibration between the electronic states involved (e.g., carriers in the conduction band and carriers in the valence band) can occur on the timescale of the radiative recombination time. For most materials, this is true at room temperature for thermal-emission depths smaller than about $E_{gap} - 0.3\,V$. However, it is certainly not true for carriers in deep band-tail states at temperatures in the range of 10 K. Since the quasi-Fermi-level splitting $\Delta\mu$ contained in Equation 11.6 is related to the maximum open-circuit voltage, V_{oc}, achievable for a photovoltaic device, this relation can be used for predicting this device property using luminescence measurements at room temperature [6–9].

If measurements of the absolute magnitude of the luminescent photon flux emitted from a sample under photoexcitation are available, the quasi-Fermi-level splitting can be derived from the magnitude and spectral shape of the luminescence signal. This method in particular allows for the investigation of the influence of subsequent processing steps on the quality of an absorber material. If the optical constants are known for the material, the data may be evaluated using Equation 11.6 and the correct values for the spectral absorptivity. However, for thin-film compound semiconductor materials, the absorption coefficient very often is not exactly known, and one has to make simplifying assumptions. In this case, the high-energy wing of the PL signal may be evaluated at photon energies sufficiently larger than the band gap, where the absorptivity can be approximated to be constant and $a(E) \approx 1$ is a reasonable assumption. Then, Equation 11.6 can be rewritten as

$$\ln\left(\frac{Y_{PL}(E)}{10^{23}\,E^2/\mathrm{cm^2eV\,s}}\right) = -\frac{E-\Delta\mu}{kT} \tag{11.7}$$

allowing for an extraction of the quasi-Fermi-level splitting $\Delta\mu$ from a fit to the high-energy wing of the PL spectrum. Note that the equation assumes an absorber layer with homogeneous phase composition and constant quasi-Fermi levels throughout the material. For extracting the local optical threshold energy from a PL spectrum, the determined value $\Delta\mu$ is reinserted in Equation 11.6 which allows for the extraction of the spectral absorptivity $a(E)$ for the lower energetic region of the luminescence spectrum.

11.2 Experimental Issues

11.2.1 Design of the Optical System

A schematic of a typical PL setup is shown in Figure 11.1. The sample can be mounted in ambient conditions for fast room-temperature measurements or in a cryostat for low-temperature measurements in vacuum or, as is the case in dynamic cryostats, in helium or nitrogen atmosphere. As an excitation source, any light source of suitable luminance and appropriate wavelength range can be used. The most general light source would be a white light from a halogen or xenon lamp filtered by a monochromator, which allows for a wide range of excitation wavelengths, however, at the cost of very low excitation power. Because of the widespread availability and high monochromatic power, in most setups laser excitation sources are used, for example, gas lasers such as helium–neon (633 nm) or argon (514 nm) lasers or solid-state laser diodes. The excitation source is guided or focused onto the sample by a flat mirror or focusing device (lens or parabolic mirror). The luminescence radiation emitted from the sample is then collected by a light collection device, which again can be given by a lens or also by a parabolic or off-axis parabolic mirror. The collimated light passes an order-sorting filter system which prevents the detection of unwanted higher orders. For most applications, colored glass long-pass filters are chosen with cutoff wavelengths slightly larger than half the measurement wavelength. The luminescence light is then focused into the monochromator system through an entrance slit. As a general comment regarding the focusing assemblies in the whole luminescence setup, we point out that off-axis parabolic mirrors are considered first because they are dispersion free. The luminescence light exits the monochromator through an exit slit and reaches the radiation detector, which can be a photodiode, photomultiplier, or avalanche photodiode, or a one- or two-dimensional detection device such as a photodiode array or CCD array.

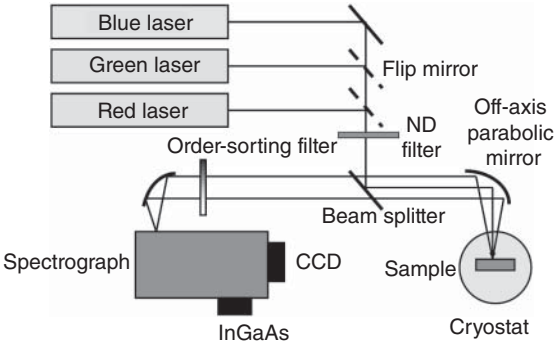

Figure 11.1 Experimental setup for room- and low-temperature PL measurements.

In the case of a single-area detector, the spectral resolution of the system is determined by the dispersion of the grating (nanometer/millimeter) times the entrance/exit slit width. Note that the focusing unit directing the light into the monochromator has to be designed to match the aperture of the monochromator specified by the f-number $f/\# = f/D$, where f is the focal length and D is the collimated beam diameter, to achieve an optimal illumination of the dispersion grating and mirrors inside the monochromator. If the focusing $f/\#$ is too small, then light is scattered inside the monochromator, and if the focusing $f/\#$ is too large, then the spectral resolution is decreased. In the case of a diode array, the exit slit is omitted, and the spectral resolution is determined by the dispersion times the diode width, which is typically 10–30 μm. The advantage of using a detector array is the possibility to record a single spectrum in one shot, without the need for scanning the grating. The advantage of using single-area detectors is the higher signal–noise ratio achievable by using low-noise amplification by avalanche diodes or photomultiplier tubes in combination with lock-in detection. The excitation signal can be modulated by an optical chopper wheel or by a direct electrical modulation of a laser diode.

If measurements with high spatial resolution are of interest, a microscope setup can be used [10]. In Figure 11.2, a PL setup utilizing a confocal microscope is outlined. In this configuration, the excitation source is focused onto the sample surface through a microscope lens. The luminescence light is collected through the same lens, separated from the exciting light beam by means of a beam splitter, and focused onto a fiber connected to the detecting system. This system exhibits diffraction-limited resolution of approximately 0.6λ/N.A., where N.A. is the

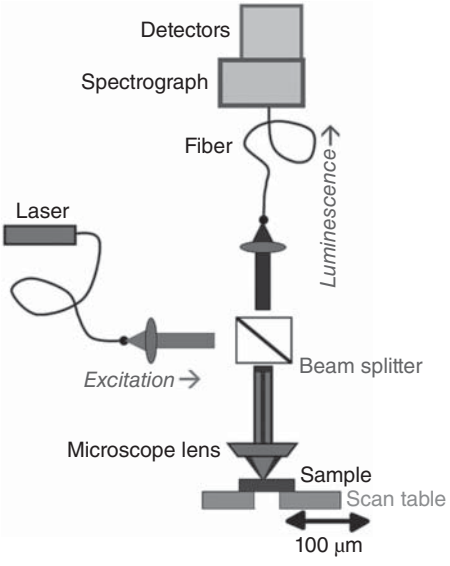

Figure 11.2 Setup for spatially resolved measurements using a confocal microscope.

numerical aperture of the microscope objective and λ is the wavelength of the detected luminescence signal. A spatial resolution of down to about 500 nm can be obtained in an optimized system investigating luminescence light of approximately 1000 nm. The sample is mounted on an xy-positioning table, which allows for a two-dimensional scan of the emitted luminescence radiation. As the excitation area in a micro-PL is in the range of 1 μm^2, very high excitation intensities can be achieved, which may lead to local heating and high-injection effects. This has to be kept in mind when analyzing the data. Efforts should be made to keep the excitation level as low as possible.

11.2.2 Calibration

The two most important calibrations to be performed are wavelength calibration of the monochromator and the determination of the transfer function of the complete optical system. The wavelength calibration is commonly performed using an argon or mercury–argon lamp, which is placed at the sample position. The atomic lines recorded by the detection system are then fitted to the known line spectrum of the lamp type which, for example, may be downloaded from the NIST website [11]. The transfer function contains the wavelength-dependent attenuation of the propagating luminescence signal after passing all optical components of the collection and detection system, that is, all lenses, mirrors, windows, filters, and gratings, and the quantum efficiency of the detector. To measure this function, a radiation source with known emission spectrum is placed at the sample position, and its emission spectrum is recorded with all optical components in place. If various filters or gratings are used, each one of these optical elements has to be considered. For absolute calibration of the luminescence photon flux, a blackbody calibration source with known emissivity and temperature is used. Calibrated tungsten-band lamps have been useful to perform this task.

In order to obtain the proper luminescence signal, the measured signal has to be multiplied by the transfer function and subsequently converted into energy space by taking into account the change from constant wavelength intervals to constant energy intervals, which requires a multiplication of the luminescence signal by a factor of λ^2.

11.2.3 Cryostat

If low-temperature measurements are of interest, a cryostat has to be used. Commonly used cryostats are either liquid helium or nitrogen flow or closed-cycle helium cryostats. The advantage of a closed-cycle cryostat is that no liquid helium is necessary, at the expense of mechanical vibrations of about ± 10 µm when compared with continuous-flow cryostats. Helium-flow cryostats allow for lower minimum temperatures of 1.5 K when compared to closed-cycle cryostat with which only 4 K can be reached. When performing low-temperature measurements on

thin-film materials, special care has to be taken to correctly determine the sample temperature during the measurement. Because the thin materials are commonly grown on glass substrates which are considerably bad thermal conductors, the temperature of the thin-film sample can differ considerably from the temperature of the cold finger of the cryostat. To properly calibrate the temperature, a second sensor mounted on a glass substrate identical to the sample glass substrate should be employed in the system.

11.3 Basic Transitions

A number of different transitions can occur in a PL measurement depending on the measurement conditions and the material properties (See Figure 11.3). In the following, we give a very brief description of the most important radiative transitions occurring in semiconductor materials. In general, the different transitions can be distinguished by their transition energy and by the change of the transition energy and luminescence yield with varying excitation intensity and temperature. Therefore, it is useful to define the following two dependencies. The luminescence yield of a transition line in general is found to obey the expression [1, 2]

$$Y_{\mathrm{PL}}(\phi) \propto \phi^{k}, \tag{11.8}$$

where ϕ is the excitation intensity and k is a characteristic parameter usually ranging between 0.5 and 2. The luminescence yield of transitions involving localized states generally decreases with increasing temperature owing to the thermal emission of the trapped carriers to the conduction or valence band. This dependence on temperature can be described by

$$Y_{\mathrm{PL}}(T) \propto \frac{1}{1 + C\exp(-E_{\mathrm{a}}/kT)}, \tag{11.9}$$

where E_{a} represents a characteristic activation energy and C is a constant which is proportional to $T^{3/2}$ if the thermal quenching involves thermal emission to the conduction or valence band [12, 13]. Bear in mind that the activation energies can differ significantly if or if not a $T^{3/2}$ dependence is included in the model.

The shift of transition energy with increasing temperature may be influenced by a shift in the optical gap with temperature [1]. Because this applies to all of the transitions discussed in the following section, this will not be discussed individually but only stated here. Typically, a decrease in the band gap with increasing temperature of the order of 10^{-4} eV/K is observed that may compensate positive peak shifts of the order of $k_{\mathrm{B}}T$ in the experiment. Radiative transitions can occur with or without the emission of phonons, depending on the electron–phonon coupling strength and the measurement temperature, thereby often leading to so-called phonon replica of the transitions. Because of limitation in space, these phonon replicas will not be discussed in the present section, and the interested reader is referred to the literature [1, 2].

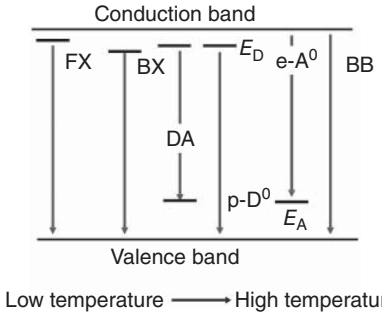

Figure 11.3 Optical transitions observable in luminescence measurements.

11.3.1 Excitons

The classical PL experiment is performed at low temperatures in the vicinity of 10 K. At this temperature, the luminescence efficiency can be considerably higher than at room temperatures as the ratio of radiative to nonradiative recombination rate is greatly increased and recombination events arising from electron–hole pairs bound to each other by their Coulomb interaction, so-called free excitons, may be observable. The transition energy of free excitons can be calculated using a simple hydrogenic model yielding

$$E_{FX} = E_g - E_x, \quad E_x = \frac{m_r e^4}{2(4\pi\varepsilon_0\varepsilon_r\hbar)^2 n^2}, \tag{11.10}$$

where E_x is the exciton binding energy and m_r is the reduced electron–hole mass $1/m_r^* = 1/m_e^* + 1/m_p^*$ [1]. The quantum number n specifies the possible excited states of the exciton. It is obvious from Equation 11.10 that the binding energy of excitons mostly depends on the dielectric constant ε_r and the reduced effective mass. For $CuGaSe_2$ thin films with a dielectric constant of about 13 and effective masses of $m_e^* \approx 0.14$ and $m_p^* \approx 1$, a free-exciton binding energy of 10 meV is expected, which agrees reasonably well with the experimentally determined value $E_{FE} = 13$ meV [14]. Exciton binding energies increase for large band-gap materials such as ZnO due to their smaller dielectric constants [15]. Optical transitions related to free excitons are only detectable at sufficiently low temperatures when $k_B T < E_x$ and will dissociate at higher temperatures. The thermal quenching of the free-exciton luminescence can be described by Equation 11.9, where the activation energy corresponds to the exciton binding energy if the quenching process corresponds to the dissociation of the excitons into free carriers. However, if many transitions are present, the activation energy in Equation 11.9 may not be unambiguously identified with the free-exciton transition. A more unambiguous determination of the binding energy is possible if excited states of the exciton can be detected [14, 16].

For the change of the PL yield with excitation intensity for free excitons, one expects $k = 1$ for resonant excitation and $k = 2$ for excitation above the band gap [17]. Schmidt *et al.* showed that if several transitions concur, the exciton k value can take values ranging from 1 to 2 depending on the material and experimental

conditions. Excitons do not exhibit a shift in their transition energy, if the excitation intensity is increased.

Free excitons get easily bound to impurities, which leads to a modification of their transition energy by the interaction with the impurity. The transition energy for bound-exciton emission is given by

$$E_{BX} = E_g - E_{BE}, \tag{11.11}$$

where the term E_{BE} represents the binding energy of the complex [2]. This term is typically a fraction of the ionization energy of the isolated impurity in the case of charged impurities and the sum of the free-exciton binding energy added to a fraction of the impurity binding energy in the case of neutral defects, as described by Haynes' rule [18, 19]:

$$E_{BE} = \begin{cases} c_n E_{A/D} + E_{FE} & \text{for neutral defects,} \\ c_i E_{A/D} & \text{for charged defects.} \end{cases} \tag{11.12}$$

The proportionality factors c_n and c_i depend on the effective mass ratio m_e^*/m_h^* and were estimated for donors in $CuGaSe_2$ to be of the order of $c_n \approx 0.3$ and $c_i \approx 1$ [14]. Considering the binding energy of 13 meV of free excitons in $CuGaSe_2$, binding energies of about 17 meV for excitons bound to shallow donors were obtained [14]. Excitons can also be bound to deeper impurities in which case their binding energy may be much larger than the binding energy of free excitons. The ratio between free- and bound-exciton emissions present in a PL experiment depends on the number of impurities present in the material and on the measurement temperature. According to Lightowlers [20], for impurity concentrations of $N > 10^{15}$ cm^{-3} in silicon, essentially all free excitons get captured by donors or acceptors and lead to bound-exciton luminescence.

Bound excitons do not have kinetic energy causing their line width to be much smaller than the line widths of order of $k_B T$ found for free excitons. Exciton transitions can also be broadened by inhomogeneities in the material properties such as composition variations and material strain. Since radiative emissions from free and bound excitons can occur with the additional emission of phonons, phonon replicas of the exciton emission lines are frequently detected and have to be distinguished from transitions arising from excitons bound at different impurities.

11.3.2 Free-Bound Transitions

In nonideal semiconductor materials, there are always localized states present due to donor or acceptor impurities which can give rise to carrier recombination by transitions between the free carriers in the bands and the localized states in the band gap, so-called free-to-bound (FB) transitions [1]. It is possible to detect both conduction-band-to-acceptor (e-A^0) and valence-band-to-donor-state (p-D^0) transitions. Shallow transitions from the conduction band to donors or from the valence band to acceptors are unlikely, because in these cases, the probability for phonon-related transitions is much higher than the probability of transitions involving the release of a photon [21].

Free-bound transitions can be identified by their spectral signature and specific temperature-dependent and intensity-dependent behavior. The transition line shape can be described by a modification of Equation 11.2 in which the square-root dependence of the density of states of parabolic conduction or valence bands in direct-gap semiconductors is considered [2, 22]:

$$Y_{\mathrm{PL}}(E) \propto E^2(E-(E_{\mathrm{g}}-E_{\mathrm{A/D}}))^{0.5}\exp((E_{\mathrm{g}}-E_{\mathrm{A/D}}-E)/kT), \tag{11.13}$$

where $E_{\mathrm{A/D}}$ is the donor or acceptor ionization energy. The peak position of the transition as obtained from setting the derivative of Equation 11.13 equal to zero is related to the optical gap by

$$Y_{\mathrm{PL}}(E)_{\max} \propto E_{\mathrm{g}}-E_{\mathrm{A/D}}+k_{\mathrm{B}}T/2. \tag{11.14}$$

Note that both these expressions strictly only apply to direct-gap semiconductors with ideal parabolic bands. The thermal quenching of the luminescence yield FB transitions is again described by Equation 11.9, where now the activation energy represents the ionization energy of the impurity state. For the excitation intensity dependence of FB processes, $k=1$ is expected in the ideal case since the transition rate depends on one free-carrier type, which depends linearly on the excitation intensity, and on the donor or acceptor density, which is independent of the excitation intensity. Note that when impurities are present in large densities, they begin to form impurity bands, which merge with the nearest intrinsic band, making the distinction between free-bound and band–band transitions difficult [1].

11.3.3
Donor–Acceptor Pair Recombination

If both donors and acceptors are present in significant concentrations and the temperature is low enough, it is possible to observe donor–acceptor pair (DAP) recombination processes, which involve transitions between two localized electronic states. These transitions originate from neutral donors and neutral acceptors (having previously captured a free carrier) which recombine to leave two oppositely charged defects [1]. The Coulomb energy between the ionized donor and acceptor is transferred to the emitted photon resulting in an emission energy of

$$E_{\mathrm{DA}} = E_{\mathrm{gap}}-E_{\mathrm{A}}-E_{\mathrm{D}}+E_{\mathrm{Coul}}. \tag{11.15a}$$

$$E_{\mathrm{Coul}} = \frac{e^2}{4\pi\varepsilon_0\varepsilon_{\mathrm{r}}r_{\mathrm{DA}}}, \tag{11.15b}$$

where E_{A} and E_{D} are the ionization energies of the donor and acceptor, respectively; E_{Coul} describes the Coulomb interaction between the ionized donor and acceptor; r_{DA} is the distance between the donor and the acceptor involved in the emission, which depends on the impurity density and the excitation density; and ε_{r} denotes the static dielectric constant. Since the effective distance between donors and acceptors decreases with the injection level, the effect of the Coulomb interaction is smallest for low excitation intensities and gets largest for high

excitation intensities. The dependence of the luminescence peak energy E_{DA} on the excitation intensity, ϕ_{exc}, can be empirically described by [23]

$$E_{DA}(\phi_{exc}) \propto E_{DA}(\phi_0) + \beta \log\left(\frac{\phi_{exc}}{\phi_0}\right) \tag{11.16}$$

where typical values of β are found to be around 1 – 5 meV per decade of excitation intensity. The maximum possible Coulomb energy-related shift of DAP transitions can be estimated from the binding energy of the spatially more extended defect, usually the donor level, in the hydrogenic impurity model given by [24]

$$E_{max} = \frac{e^4 m_e^*}{2(4\pi\varepsilon_r\varepsilon_0\hbar)^2}. \tag{11.17}$$

For typical values of $\varepsilon_r = 13.6$ and $m_e^* = 0.09$ for $CuInSe_2$, a maximum shift of $E_{max} = 6.6$ meV is estimated [25, 26]. Thermal quenching of DAP transitions is described by an equation similar to Equation 11.9, now containing two activation energies:

$$I_{PL} = \frac{1}{1 + C_1 \exp(-E_{a1}/kT) + C_2 \exp(-E_{a2}/kT)}, \tag{11.18}$$

where again the constants C_1 and C_2 are proportional to $T^{3/2}$ if the quenching occurs by thermal emission of charges to the valence band and conduction band, respectively [12]. Under the assumption that the constants C_1 and C_2 are of similar magnitude, the activation energy observed at lower temperature is related to the ionization energy of the shallower impurity state, and the activation energy observed at higher temperatures is related to the ionization energy of the deeper level. However, in some cases it is not possible to get meaningful fits using Equation 11.18, and the analysis of the data using the single activation energy contained in Equation 11.9 should be considered [13].

The change of the DAP line shape with increasing temperature is complicated, because the recombination process involves a tunneling step which depends on the distance of the recombination pairs. Briefly, for increasing temperatures more distant pairs get thermally reemitted to the bands before they recombine, increasing the number of close pairs in the radiative recombination. Due to the larger Coulomb term for the close pairs, this leads to a blueshift of the order of $k_B T$ of the emission spectrum with increasing temperature [1, 2]. For the luminescence yield as a function of excitation intensity, $k = 1$ is expected in the ideal case, but as was already discussed earlier, significantly smaller values than that may be observed in the case of different competing transition types. Schmidt *et al.* show that for certain experimental conditions the k values of the exciton and DAP transition are related to each other by $k_{exc} = 2k_{DAP}$ [17].

11.3.4
Potential Fluctuations

For high concentrations of donors and acceptors when $N_{A/D} a_B^3 > 1$, the Bohr radii $a_B^* = 4\pi\varepsilon_0\varepsilon\hbar^2/m^* e^2$ of the impurity wavefunctions start to overlap, leading

to impurity-related band formation [27]. If the donors' and acceptors' concentrations are of similar magnitude, the semiconductor becomes compensated, with a net doping density much lower than the dopant concentration. Since the distribution of dopants in the lattice is statistical, the band structure becomes distorted by potential fluctuations due to local variations in the fixed space charge, which cannot be screened by the low free-carrier density. Such potential fluctuations which are indicated in a schematic band diagram in Figure 11.4 strongly influence the optical and electrical properties as now transitions with significantly smaller transition energy than the standard DAP or FB transition energy become possible [26–30].

The average depth of the fluctuations, γ, can be estimated from the average charge fluctuations occurring within a certain volume defined by the screening radius r_s containing an impurity concentration $N_t = N_A^+ + N_D^-$ screened by a free-carrier density p by [27]

$$\gamma = \frac{e^2}{4\pi\varepsilon_r\varepsilon_0}(N_t r_s)^{0.5} = \frac{e^2}{4\pi\varepsilon_r\varepsilon_0}\frac{N_t^{2/3}}{p^{1/3}}, \tag{11.19}$$

where r_s given by $r_s = N_t^{1/3}p^{-2/3}$ for p-type material. Typical values for $CuInSe_2$ thin films can be estimated assuming $N_A = N_D = 10^{18}\,cm^{-3}$, $p = 10^{16}\,cm^{-3}$, and $\varepsilon_r = 13.6$ to yield $\gamma = 78$ meV with a screening length of $r_s \approx 270$ nm. Because DAP recombination involves tunneling between the two impurity sites, the transition energy can be significantly reduced in the presence of band fluctuations, which experimentally leads to a low-energy tail and broadening of the luminescence transitions. The emission energy of DAP recombination in highly compensated material can be estimated with

$$E_{PF\text{-}DA} = E_{DA} - 2\gamma, \tag{11.20}$$

where E_{DA} is given by Equation 11.15a [23]. It is obvious from Equations 11.19 and 11.20 that the emission energy for highly compensated DAP transitions depends on the number of impurities, the compensation ratio, and the free-carrier density which in turn depends on the excitation level in the experiment.

Therefore for increasing excitation level, a strong blueshift of the emission line is expected which can greatly exceed the $\beta = 1-2$ meV expected for the DAP

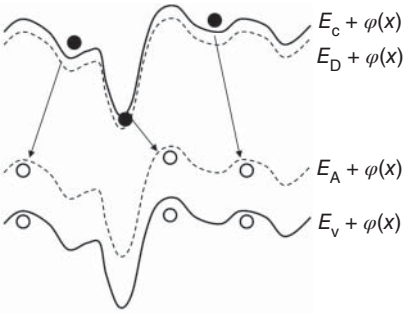

Figure 11.4 Effect of potential fluctuations on the band edges and the radiative transitions between trapped electrons and holes. $\varphi(x)$ denotes the spatial varying electrostatic potential arising from the potential fluctuations, and the dashed line represents an acceptor/donor level or band.

Coulomb term given in Equation 11.15b. Experimentally peak shifts as large as $\beta = 10-30$ meV are observed [26, 28, 29].

If the temperature is increased, the emission peak in strongly compensated semiconductors is found to redshift at low temperatures and low excitation intensities. This can be explained with a lack of complete thermalization of the carriers trapped in different potential wells, which leads to an incomplete filling of the lowest energetic wells. If temperature is increased, the carriers become more mobile and also populate the deepest wells, leading to a redshift of the emission line with increasing temperature. If the temperature is further increased, the more distant pairs are increasingly thermally emitted to the bands leaving the closer pairs and thus producing a blueshift, in accordance with the effect observed for DAP transitions. A detailed discussion of the effect of potential fluctuations in compensated semiconductors can be found in the literature [26, 27, 29–31].

11.3.5
Band–Band Transitions

With increasing temperature excitons and impurities become ionized, and the conduction and valence bands become increasingly occupied with photoexcited carriers such that band–band transitions become more probable. The line shape of band–band transitions can be described by Equation 11.2 using the appropriate absorption coefficient for band–band transitions. For a direct-gap semiconductor with parabolic bands, the following expression is obtained [2]:

$$Y_{\mathrm{PL}}(E) \propto E^2(E - E_{\mathrm{g}})^{0.5} \exp(-(E - E_{\mathrm{g}})/kT), \tag{11.21}$$

where E_{g} is the band gap of the material. This equation is very similar to the expression obtained for the free-bound emission stated earlier, which means that in order to distinguish between band–band transitions and free-bound transitions, knowledge of the value of the band gap determined by independent means is very helpful. As for free-bound transitions, the peak position increases with temperature as $k_{\mathrm{B}}T/2$. In band–band transitions, both free-carrier types are involved, both depend on the excitation intensity, and thus k values >1 can be observed. Note that in the case of high injection with band–band transitions dominating recombination $k = 1$ will be observed, because in this case the lifetime is inversely proportional to the injection level as discussed in Section 11.1.

11.4
Case Studies

In this section, we discuss some typical PL measurement results for chalcopyrite-type Cu(In,Ga)Se_2 thin films and also completed solar cells. The defect physics and therefore also the nature of the dominant PL transitions in this material are found to strongly depend on the film composition, most prominently on the [Cu]/[In]+[Ga] ratio. Sharp transitions are observed for material grown

under copper-rich conditions, whereas broad, mostly featureless transitions are observed in the case of copper-poor growth conditions [12, 25, 28, 29, 32]. We will also distinguish between low-temperature and room-temperature luminescence analyses. Both techniques have advantages and disadvantages depending on the material and the investigated material properties.

11.4.1
Low-Temperature Photoluminescence Analysis

In Figure 11.5, low-temperature PL spectra of a Cu-rich grown epitaxial $CuGaSe_2$ sample are shown. The sample was grown on GaAs(100) by metal organic vapor phase epitaxy (MOVPE). The Cu/Ga ratio of the sample was determined as $[Cu]/[Ga] \approx 1.1$ by energy dispersive X-ray analysis (EDX; see Section 14.2.3). The measurement was performed at 10 K, and the sample was illuminated by the 514.5 nm line of an Ar^+ laser using different excitation fluxes. The PL spectra exhibit distinct transition peaks at 1.72, 1.66, and 1.63 eV and a further peak occurring as a shoulder at 1.60 eV with full widths at half maximum (FWHM) of approximately 10, 19, 27, and 55 meV. These four peaks have been identified in the literature as an exciton-related transition (EXC) and three different donor–acceptor transitions (DA1, DA2, DA3) [14, 29].

This assignment can be justified by evaluating the peak energies and their shift with excitation intensity and also the corresponding k values describing the dependence of the PL yield on excitation intensity. In Figure 11.6a, the intensity of the DA1, DA2, and EXC transitions are plotted as a function of the excitation intensity using logarithmic scaling of the axes. A fit using Equation 11.8 yields k values of $k = 0.6$ for the DA1 and DA2 transitions and $k = 1.2$ for the EXC transition. Values of $k \leq 1$ are expected for donor–acceptor or free-bound transitions, whereas k values ≥ 1 are expected for exciton or band–band transitions. Considering the known value for the band gap $E_{gap} = 1.73$ eV of $CuGaSe_2$ at 10 K,

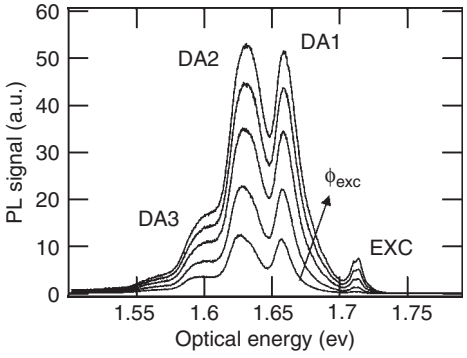

Figure 11.5 PL spectra for a Cu-rich grown epitaxial $CuGaSe_2$ thin film measured at various excitation fluxes and 10 K.

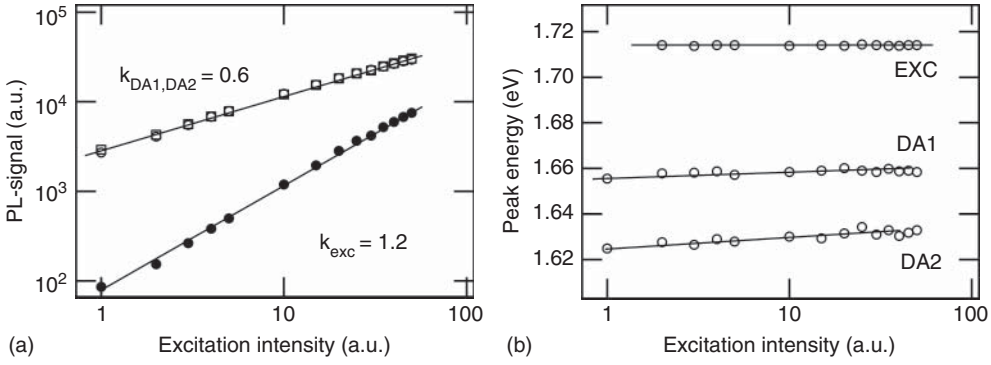

Figure 11.6 (a) Intensity dependence of the PL yield of transitions DA1, DA2, and EXC. (b) Shift of PL peaks as a function of excitation intensity.

the EXC transition energy is located 10 meV below the band gap, which agrees well with experimentally determined single-crystal free-exciton binding energies of 13 meV [14].

The shift of the peak energies with excitation intensity shown in Figure 11.6b indicates values of $\beta_{EXC} = 0$ meV, $\beta_{DA1} = 1.5$ meV, and $\beta_{DA2} = 4$ meV. The fact that the EXC transition does not shift with excitation intensity confirms the assignment to an exciton transition. In fact, a more detailed analysis of this transition shows that it can be deconvolved into two closely spaced transitions located at 1.7139 and 1.7105 eV, which have been identified with a free-exciton and a bound-exciton transition. A detailed discussion of this assignment can be found in the literature and is beyond the scope of this article [14]. Peak shifts of $\beta \sim 1-4$ meV are values typically observed for DAP recombination processes and may arise from the increasing contribution of the Coulomb interaction as the distance between the participating donors and acceptors is decreased when the density of photoexcited carriers increases with excitation intensity. This confirms an assignment of the transitions DA1 and DA2 to a DAP recombination. The fourth transition line (DA3) located at 1.6 eV could be related to a phonon replica of DA2 since its energetic distance between DA2 and DA3 ≈ 30 meV is comparable to typical LO-phonon energies $E_{ph} \approx 34$ meV in $CuGaSe_2$ [29]. However, it is also possible that DA3 is a separate DAP transition as has been suggested from cathodoluminescence measurements showing the spatial location of the DA3 transitions to be distinct from the spatial locations of the DA2 transition [33].

We note that although the observed k values are significantly smaller than the values of $k = 1$ and $k = 2$ expected for donor–acceptor and exciton transitions in the ideal case, these values agree well with the theory of Schmidt *et al.* [17] who predicted $k_{exc} \approx 2k_{DAP}$ for the situation of different concurring radiative and nonradiative transition.

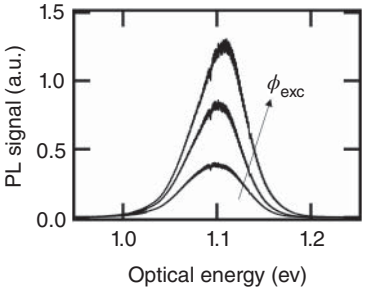

Figure 11.7 PL spectrum of Cu-poor $Cu(In,Ga)Se_2$ with [Cu]/([In]+[Ga]) = 0.9 and [Cu]/([In]+[Ga]) = 0.3 measured at 15 K.

Cu-poor prepared $Cu(In,Ga)Se_2$ films that generally lead to much higher solar conversion efficiencies than Cu-rich prepared films show a very different luminescence behavior at low temperature. In Figure 11.7, the PL spectrum of a coevaporated $Cu(In,Ga)Se_2$ thin-film solar cell with [Cu]/([In+Ga]) = 0.9 and [Ga]/([In+Ga]) = 0.3 in a glass/Mo/$Cu(In,Ga)Se_2$/CdS/ZnO stacking structure is measured at 15 K using a 660 nm laser diode as an excitation source.

Now a single but much broader transition is observed. The peak energy of this transition is 1.11 eV with an FWHM of 60 meV. A plot of the peak energy and intensity versus excitation intensity (not shown here) yields $\beta = 10$ meV and $k = 0.96$ at 15 K measurement temperature. Although this k value is compatible with the values observed for the DAP transitions of the Cu-rich sample, the β value is much larger than the 1–4 meV observed earlier and also much larger than the total shifts expected for DAP transitions in chalcopyrite materials. Such large β values are a clear indication of potential fluctuations due to strong compensation in the material as already discussed in Section 11.3.4. This assignment is corroborated by temperature-dependent measurements as shown in Figure 11.8a where the shift of the peak energy of the transition is plotted as a function of temperature.

It can be seen that the peak energy first shifts to smaller energies (redshift) at low temperatures and then to larger energies for temperatures above 50 K (blueshift). This behavior is a characteristic signature of potential fluctuations

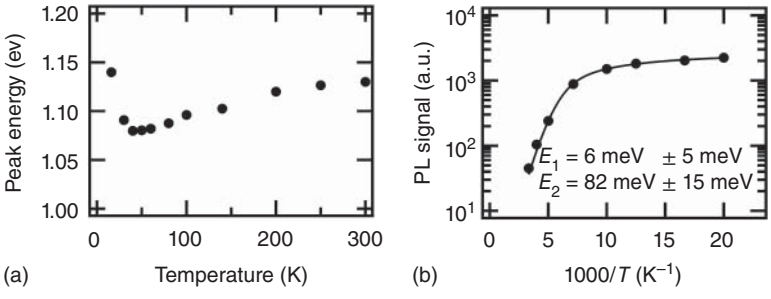

Figure 11.8 (a) PL-peak shift with temperature for Cu-poor $Cu(In,Ga)Se_2$. (b) Dependence of PL yield on temperature.

[25, 26, 29–31] as discussed earlier. An analysis of the PL yield in Figure 11.8b using Equation 11.18 yields activation energies of 6 and 82 meV assuming a $T^{3/2}$ dependence of the emission prefactors. Although the errors are relatively large, it can be concluded that a very shallow level at $E_1 = 6$ meV and a deep level at $E_2 = 82$ meV participate in the observed transition. However, we have to caution that the interpretation of transition energies and their temperature dependence is difficult in the presence of potential fluctuations, because thermal redistribution processes within the potential well landscape take place.

11.4.2
Room-Temperature Measurements: Estimation of V_{oc} from PL Yield

When the temperature is raised to room temperature, band–band transitions become very likely, as the bands are now sufficiently populated by photoexcited carriers. A room-temperature PL spectrum measured for the sample of Figure 11.7 is shown in Figure 11.9 exhibiting an even broader transition with a peak energy of 1.13 eV and an FWHM ≈ 100 meV (solid line, left scale).

An evaluation of the PL yield with excitation intensity gives a $k = 1.4$ and $\beta = 0$ meV, which allows to identify the recombination process as band–band transitions. Note that the exciton binding energy is of the order of tens of millivolts in this material leaving excitons fully ionized at 300 K.

Also included in the figure is a PL spectrum of a coevaporated Cu(In,Ga)Se_2 solar cell processed with similar but not identical preparation conditions and a [Ga]/([In+Ga]) ratio of 0.27 [9]. The device structure is glass/Mo/Cu(In,Ga)Se_2/CdS/ZnO with an active area of 0.5 cm^2. It can be seen that the spectral shape agrees well for these two samples, with a slight shift in the peak energy by 20 meV. For the measurement, the device was fully illuminated with light from a 780 nm laser diode. In order to allow a prediction of the open-circuit voltage corresponding to AM1.5 illumination conditions, the monochromatic excitation photon flux in the experiment was adjusted to correspond to the number of photons that would be absorbed for broadband AM1.5 excitation, which for a 1.1 eV band-gap

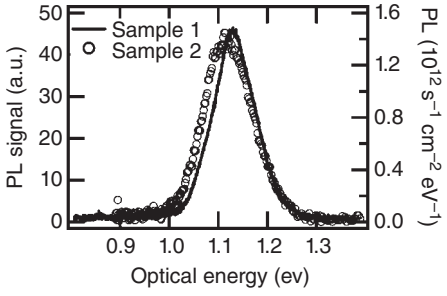

Figure 11.9 Room-temperature PL spectrum of the Cu-poor Cu(In,Ga)Se_2 device of Figure 11.7 (left scale, solid line) and a Cu-poor Cu(In,Ga)Se_2 device from a different coevaporation process measured in a setup with absolute calibration (right scale, open circles).

material is approximately 2×10^{17} cm^2/s or 60 mW/cm^2. The luminescence radiation was measured by a liquid nitrogen-cooled germanium detector in a setup calibrated to yield absolute photon numbers. According to the method outlined in Section 11.1, the absolute quasi-Fermi-level splitting is estimated by plotting the quantity $\ln(Y_{PL}(E)/10^{23}/E^2)$ versus energy and fitting the high-energy wing using Equation 11.7 as shown in Figure 11.10a. From the slope, m, the temperature of the photoexcited electron–hole ensemble $T = (1/k_B/m) = 320$ K, and from the y-axis intercept at $E = 0$ eV, a quasi-Fermi-level splitting of $\Delta\mu = 0.58$ eV is obtained. This value agrees very well with the experimentally determined open-circuit voltage for which $V_{oc} = 0.56$ V was obtained, using exactly the same illumination conditions [9]. The deduced temperature of $T = 320$ K is higher than the measurement temperature $T = 300$ K, most likely due to sample heating from the large-area illumination during the experiment. The good agreement between V_{oc} and $\Delta\mu$ demonstrates the feasibility of the method to judge the electronic quality of the material without need of electrical contacts or electrical measurements. On the other hand, it also shows that for this particular example very little losses occur in the functional layers and at the contacts, leading to a measured V_{oc} almost as high as the bulk value of the quasi-Fermi-level splitting.

As described in Section 11.1, the energy-dependent absorptivity function can be determined by plugging the values for the temperature and $\Delta\mu$ back into Equation 11.6. The resulting absorptivity function $a(E)$ is shown in Figure 11.10b (triangles, right scale). Using the approximation $a(E) \approx 1 - \exp(-\alpha(E)d)$ and assuming a homogeneous sample thickness of 1 µm, the absorption coefficient can then be derived from the absorptivity. The result is shown in Figure 11.10b (open circles, left scale). The absorption coefficient derived from the PL measurement may be compared to an absorption coefficient expected for a direct-gap semiconductor with ideal parabolic bands [1] $\alpha(E) = A(E - E_{gap})^{0.5}$, which is included in Figure 11.10b using a dashed line ($A = 10^5$ cm^{-1} and band-gap value $E_{gap} = 1.19$ eV). It can be seen that the theoretical curve agrees well with

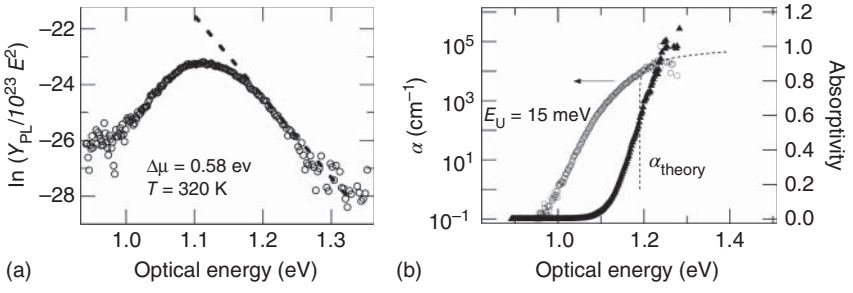

Figure 11.10 (a) Determination of the quasi-Fermi-level splitting from calibrated room-temperature PL measurement. (b) Absorptivity (triangles, right scale) and absorption coefficient (open circles, left scale) determined from the calibrated PL measurement. Also included is a direct-gap absorption coefficient with square-root dependence on energy (dashed line).

the experimental curve in the region above E_{gap}. For energies below E_{gap}, the experimental curve does not vanish rapidly but shows an exponentially decaying band tail with a characteristic energy of $E_0 = 15$ meV. Figure 11.10b shows that a defined value of the absorptivity, for example, $a(E) = 1/e$, may be used to derive an optical threshold from the PL measurement, which is related to the optical band gap of the material. This result will be used in the next section to map spatial inhomogeneities in the optical properties of a sample by PL.

11.4.3
Spatially Resolved Photoluminescence: Absorber Inhomogeneities

Thin semiconductor materials often show significant nonuniformities in their morphology, grain orientation, composition, and electronic and optoelectronic properties [34–39]. Although the knowledge of the impact of these inhomogeneities on cell performance is still limited, generally, spatial inhomogeneities of the absorber layer are considered to be disadvantageous for the cell efficiency, which was recently shown in several modeling approaches [5, 40, 41]. PL performed with microscopic spatial resolution can be used for investigating spatial inhomogeneities of absorber layers and for quantifying the variation of material properties on microscopic length scales [36, 42]. The experimental setup used in a PL-scanning experiment was described in Section 11.2.

In the following, micro-PL scans for a Cu(In,Ga)Se_2 thin-film sample with [Ga]/([In+Ga]) = 0.3 and [Cu]/([In+Ga]) ≈ 0.8 measured at room temperature are shown. The sample configuration was glass/Mo/Cu(In,Ga)Se_2/CdS. The sample was excited by a 532 nm laser at an excitation flux corresponding to $10^4 \times$ AM1.5. The detector system of the micro-PL setup was a spectrograph with a photodiode array, which allowed for straightforward measurements of a data set containing a complete PL spectrum for each point of the scan. An image of the spectrally integrated luminescence intensity, which is related to the local recombination lifetime, is shown in Figure 11.11. It can be seen that the integrated luminescence signal varies by a factor of 3 with typical structure sizes on the micrometer scale. To analyze the spatial variation of the quasi-Fermi-level splitting and of the optical threshold, the micro-PL spectra in Figure 11.11 are analyzed using the approach outlined earlier, extracting the quasi-Fermi-level

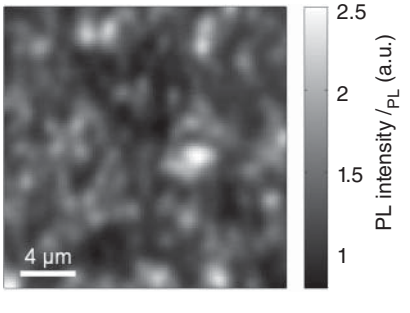

Figure 11.11 Two-dimensional scan of the spectrally integrated PL intensity for a Cu(In,Ga)Se_2 thin film at room temperature.

splitting from a fit to the high-energy tail of the data. Since in this experiment no absolute calibrated photon counts were recorded, only relative changes of the quasi-Fermi-level splitting can be extracted. The results for this quantity for the measured area are shown in Figure 11.12a. It can be seen from the images that the spatial variation closely resembles the variations seen for the integrated PL yield. In Figure 11.12b, a histogram of the distribution of $\Delta\mu$ is displayed showing a maximum variation of 40 meV and a distribution width of FWHM $\approx$ 13 meV. From each recorded PL spectrum, an absorptivity function $a(E)$ and an optical threshold E_{th} related to $a(E_{th}) = 1/e$ is derived by using the method described in the previous section, which we associate with the local optical band gap [42]. The resulting map of optical threshold values and the distribution histogram are shown in Figure 11.13a and b.

It can be seen that the maximum lateral variation of the band gap amounts to approximately 15 meV with an FWHM $\approx$ 6 meV, which is just less than half the value obtained for the distribution width of the quasi-Fermi-level splitting. In this example, we have considered the variation of the optical threshold energy

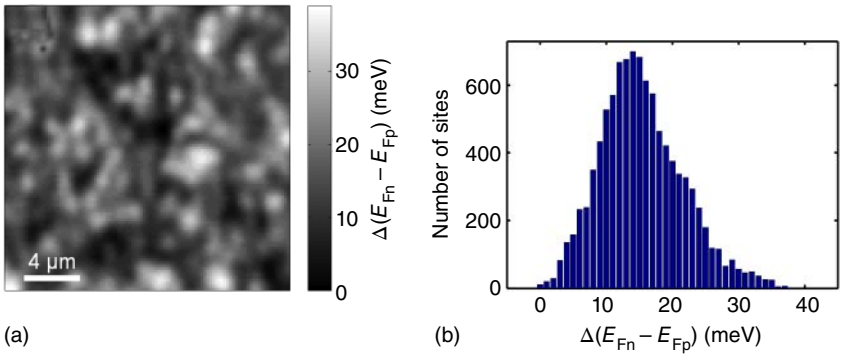

Figure 11.12 (a) Two-dimensional maps of the lateral variation of the quasi-Fermi-level splitting. (b) Corresponding statistical distributions of the 2D data.

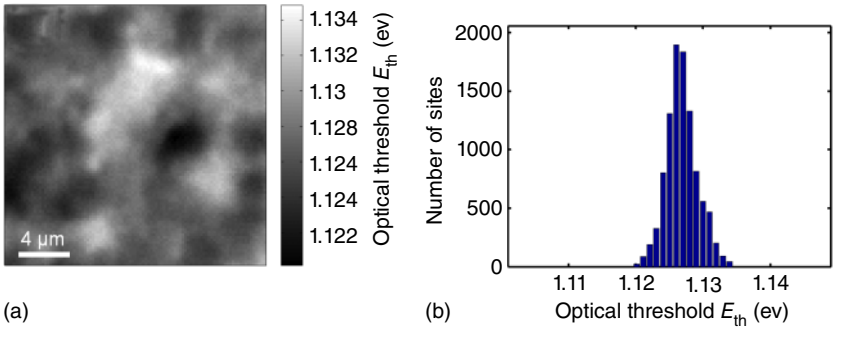

Figure 11.13 (a) Two-dimensional maps of the lateral variations of the optical threshold (local band gap). (b) Corresponding statistical distributions of the 2D data.

to be equal to a local variation of the band gap, which is expected from alloying inhomogeneities in Cu(In,Ga)Se_2, that is, a locally varying Ga content. Generally, the extracted local variation of the optical threshold energy can be caused by further effects than only a shift of the optical gap, such as large local variations of the absorber thickness or change in the characteristic band-tail energy. To strictly exclude thickness variations from the analysis, it would be necessary to monitor the local thickness, for example, by atomic force microscopy and include this information in the evaluation procedure [43]. We note that in general the variation of the quasi-Fermi-level splitting tends to decrease with increasing excitation level [44]. Although an excitation flux comparable to AM1.5 conditions would be desirable, it is generally very difficult to achieve for micro-PL measurements at room temperature because of the too small number of photons involved. In summary, the results shown here indicate that the absorber layer contains spatial variations of the quasi-Fermi levels splitting and of the local band gap. As the spatial variation of the optical threshold does not seem to correlate with the spatial variation in the quasi-Fermi-level splitting, and the distribution of the optical threshold values is significantly smaller than the distribution of $\Delta\mu$, we conclude that a local variation in recombination lifetime is the main cause of the observed variation in PL yield and $\Delta\mu$.

Acknowledgments

The authors would like to thank Jes Larsen (University of Luxembourg) for additional PL measurements. Raquel Caballero and Tim Münchenberg for preparation of samples and Steffen Kretzschmar for help with the measurements are gratefully acknowledged.

References

1. Pankove, J.I. (1971) *Optical Processes in Semiconductors*, Dover, New York.
2. Bepp, H.B. and Wiliams, E.W. (1972) Photoluminescence theory, in *Semiconductor and Semimetals*, vol. **8** (eds R.K. Willardson and A.C. Beer), Academic Press, New York.
3. Nelson, J. (2003) *The Physics of Solar Cells*, Imperial College Press, London.
4. Roosbroeck, W. and Shockley, W. (1954) Photon-radiative recombination of electrons and holes in germanium. *Phys. Rev.*, **94**, 1558.
5. Werner, J.H., Mattheis, J., and Rau, U. (2005) Efficiency limitations of polycrystalline thin film solar cells: case of Cu(In,Ga)Se_2. *Thin Solid Films*, **480**, 399.
6. Würfel, P. (1982) The chemical-potential of radiation. *J. Phys. C: Solid State Phys.*, **15**, 3967.
7. Würfel, P. (2009) *The Physics of Solar Cells*, Wiley-VCH, Weinheim.
8. Schick, K., Daub, E., Finkbeiner, S., and Würfel, P. (1992) Verification of a generalized Planck law for luminescence radiation from silicon solar cells. *Appl. Phys. A*, **54**, 109.
9. Unold, T., Berkhahn, D., Dimmler, B. and Bauer, G.H. (2000) *Open Circuit Voltage and Loss Mechanisms in Polycrystalline Cu(In,Ga)Se_2 Heterodiodes from Photoluminescence Studies*. Proceedings of the 16th European Photovoltaic Solar Energy Conference, Glasgow, United Kingdom, May

1–5, 2000 (eds H. Sheer, B. McNelis, W. Paltz, H.A. Ossenbrink and P. Helm), James & James, London, p. 737.
10. Wilson, T. (1990) *Confocal Microscopy*, Academic Press, New York.
11. Kramida, A., Ralchenko, Yu., Reader, J., and NIST ASD Team (2015). NIST Atomic Spectra Database (ver. 5.3), [Online]. Available: http://physics.nist.gov/asd. [2016, April 28]. National Institute of Standards and Technology, Gaithersburg, MD.
12. Siebentritt, S. (2006) Shallow defects in the wide gap chalcopyrite $CuGaSe_2$, in *Wide-Gap Chalcopyrites*, Springer Series in Materials Science, vol. **86** (eds S. Siebentritt and U. Rau), Springer, Heidelberg, p. 113.
13. Krustok, J., Collan, H., and Hjelt, K. (1996) Does the low-temperature Arrhenius plot of the photoluminescence intensity in CdTe point towards an erroneous activation energy? *J. Appl. Phys.*, **81**, 1442.
14. Bauknecht, A., Siebentritt, S., Alberts, J., Tomm, Y., and Lux-Steiner, M.C. (2000) Excitonic photoluminescence from $CuGaSe_2$ single crystals and epitaxial layers: temperature dependence of the band gap energy. *Jpn. J. Appl. Phys.*, **39**, 322.
15. Grundmann, M. (2006) *The Physics of Semiconductors*, Springer, Berlin.
16. Yakushev, M., Martin, R.W., Mudryi, A.V., and Ivaniukovich, A.V. (2008) Excited states of the A free exciton in $CuInS_2$. *Appl. Phys. Lett.*, **92**, 111908.
17. Schmidt, T., Lischka, K., and Zulehner, W. (1992) Excitation power dependence of the near-band-edge photoluminescence of semiconductors. *Phys. Rev. B: Condens. Matter Mater. Phys.*, **45**, 8989.
18. Haynes, J.R. (1960) Experimental proof of the existence of a new complex in silicon. *Phys. Rev. Lett.*, **4**, 361.
19. Atzmüller, H. and Schröder, U. (1978) Theoretical investigations of Haynes' rule. *Phys. Status Solidi B*, **89**, 349.
20. Lightowlers, E.C. (1990) Photoluminescence characterisation, in *Growth and Characterization of Semiconductors* (eds R.A. Stradling and P.C. Klipstein), Adam Hilger, Bristol and New York, p. 135.
21. Ascarelli, G. and Rodriguez, S. (1961) Recombination of electrons and donors in n-type germanium. *Phys. Rev.*, **124**, 1321.
22. Eagles, D.M. (1960) Optical absorption and recombination radiation in semiconductors due to transitions between hydrogen-like acceptor impurity levels and the conduction band. *J. Chem. Solids*, **16**, 76.
23. Yu, P.W. (1977) Excitation-dependent emission in Mg-, Be-, Cd-, and Zn-implanted GaAs. *J. Appl. Phys.*, **48**, 5043.
24. Zacks, E. and Halperim, A. (1972) Dependence of the peak energy of the pair-photoluminescence band on excitation intensity. *Phys. Rev. B: Solid State*, **6**, 3072.
25. Wagner, M., Dirnstorfer, I., Hofmann, D.M., Lampert, M.D., Karg, F., and Meyer, B.K. (1998) Characterization of $CuIn(Ga)Se_2$ thin films – I. Cu-rich layers. *Phys. Status Solidi A*, **167**, 131.
26. Schumacher, S.A., Botha, J.R., and Alberts, V. (2006) Photoluminescence study of potential fluctuations in thin layers of $Cu(In_{0.75}Ga_{0.25})(S_ySe_{1(y)})_2$. *J. Appl. Phys.*, **99**, 063508.
27. Shklovskii, B.I. and Efros, A.L. (1984) *Electronic Properties of Doped Semiconductors*, Springer, Berlin.
28. Dirnstorfer, I., Wagner, M., Hofmann, D.M., Lampert, M.D., Karg, F., and Meyer, B.K. (1998) Characterization of $CuIn(Ga)Se_2$ thin films – II. In-rich layers. *Phys. Status Solidi A*, **168**, 163.
29. Bauknecht, A., Siebentritt, S., Albert, J., and Lux-Steiner, M.C. (2001) Radiative recombination via intrinsic defects in $Cu_xGa_ySe_2$. *J. Appl. Phys.*, **89** (8), 4391.
30. Levanyuk, A.P. and Osipov, V.V. (1973) Theory of luminescence of heavily doped semiconductors. *Sov. Phys. Semicond.*, **7**, 721.
31. Krustok, J., Collan, H., Yakushev, M., and Hjelt, K. (1999) The role of spatial potential fluctuations in the shape of the PL bands of multinary semiconductor compounds. *Phys. Scr.*, **T79**, 179.
32. Zott, S., Leo, K., Ruckh, M., and Schock, H.W. (1997) Radiative recombination in $CuInSe_2$ thin films. *J. Appl. Phys.*, **82**, 356.

33. Siebentritt, S., Beckers, I., Riemann, T., Christen, J., Hoffmann, A., and Dworzak, M. (2005) Reconciliation of luminescence and Hall measurements on the ternary semiconductor $CuGaSe_2$. *Appl. Phys. Lett.*, **86** (9), 091909.
34. Sites, J.R., Granata, J.E., and Hiltner, J.F. (1998) Losses due to polycrystallinity in thin-film solar cells. *Sol. Energy Mater. Sol. Cells*, **55**, 43.
35. Eich, D., Herber, U., Groh, U., Stahl, U., Heske, C., Marsi, M., Kiskinova, M., Riedl, W., Fink, R., and Umbach, E. (2000) Lateral inhomogeneities of Cu(In, Ga)Se_2 absorber films. *Thin Solid Films*, **361**, 258.
36. Bothe, K., Bauer, G.H., and Unold, T. (2002) Spatially resolved photoluminescence measurements on Cu(In,Ga)Se_2 thin films. *Thin Solid Films*, **403**, 453.
37. Grabitz, P.O., Rau, U., Wille, B., Bilger, G., and Werner, J.H. (2006) Spatial inhomogeneities in Cu(In,Ga)Se_2 solar cells analyzed by an electron beam induced voltage technique. *J. Appl. Phys.*, **100**, 124501.
38. Yan, Y., Noufi, R., Jones, K.M., Ramanathan, K., Al-Jassim, M.M., and Stanbery, B.J. (2005) Chemical fluctuation-induced nanodomains in Cu(In,Ga)Se_2 films. *Appl. Phys. Lett.*, **87** (12), 121904.
39. Abou-Ras, D., Koch, C.T., Küstner, V., Aken, P.A., Jahn, U., Contreras, M.A., Caballero, R., Kaufmann, C.A., Scheer, R., Unold, T., and Schock, H.W. (2009) Grain-boundary types in chalcopyrite-type thin films and their correlations with film texture and electrical properties. *Thin Solid Films*, **517** (7), 2545.
40. Grabitz, P.O., Rau, U., and Werner, J.H. (2005) Modeling of spatially inhomogeneous solar cells by a multi-diode approach. *Phys. Status Solidi A*, **202** (15), 2920.
41. Kanevce, A. and Sites, J.R. (2007) *Impact of Nonuniformities on Thin Cu(In,Ga)Se_2 Solar Cell Performance. Thin-Film Compound Semiconductor Photovoltaics 2007*, Materials Research Society Symposium Proceedings, vol. 1012, Warrendale, PA, Materials Research Society (eds T. Gessert, S. Marsillac, T. Wada, K. Durose, and C. Heske), p. Y0802.
42. Gütay, L. and Bauer, G.H. (2007) Spectrally resolved photoluminescence studies on Cu(In,Ga)Se_2 solar cells with lateral submicron resolution. *Thin Solid Films*, **515**, 6212.
43. Gütay, L., Lienau, C., and Bauer, G.H. (2010) Subgrain size inhomogeneities in the luminescence spectra of thin film chalcopyrites. *Appl. Phys. Lett.*, **97**, 052110.
44. Gütay, L. and Bauer, G.H. (2009) Local fluctuations of absorber properties of Cu(In,Ga)Se_2 by sub-micron resolved PL towards "real life" conditions. *Thin Solid Films*, **517** (7), 2222.

12
Electron-Spin Resonance (ESR) in Hydrogenated Amorphous Silicon (a-Si:H)

Klaus Lips, Matthias Fehr, and Jan Behrends

12.1
Introduction

Hydrogenated amorphous silicon (a-Si:H) is frequently used as absorber layers in thin-film solar cells [1]. Its electrical properties are controlled by defect states which, among other factors, limit the efficiency of the solar cells [2]. The most prominent defects in a-Si:H are threefold coordinated silicon atoms (dangling bonds, db) and strained (weak) bonds that induce localized states in the band gap and act as traps for charge carriers. Latter states are known to limit the electronic mobility. Electron spin resonance (ESR), also often named electron paramagnetic resonance (EPR), is one of the few experiments which give structural information about such defect states. The defect spin acts as a local probe which very accurately senses the local magnetic field distribution in its vicinity. This is monitored by the line position and line shape of the corresponding ESR spectrum or its dynamics. The purpose of this chapter is to introduce the reader without ESR experience to the basic principles of ESR and its application to a-Si:H.

A necessary prerequisite for ESR is that the electronic state to be investigated is paramagnetic. A typical example is the neutral state of a broken silicon bond. If this state is not paramagnetic, for example, the state is not occupied, one has to change the occupancy of the state by shifting the (quasi-)Fermi level. This can be accomplished by charge injection, illumination, changing measurement temperature, or bombardment of the sample with high-energy electrons or ions.

ESR is also capable of quantifying the number of defects in a given sample volume with a sensitivity of about 10^{10-11} spins at 9 GHz. This mode is particularly interesting to material researchers that want to optimize the material quality. The main advantage of ESR is that almost any kind of sample geometry can be studied nondestructively, provided that the sample fits into the resonator of the ESR spectrometer. Typical sample volumes that can be studied are $4\,\text{mm} \times 4\,\text{mm} \times 10\,\text{mm}$ and the sample's state can be gaseous, liquid or frozen solution, powder, crystal, or thin film. The conductivity of the sample has to be small enough in order not to affect the properties of the ESR resonator. When studying thin films or interfaces, the sensitivity limit of ESR is easily reached. Here special sample preparation

Advanced Characterization Techniques for Thin Film Solar Cells, Second Edition.
Edited by Daniel Abou-Ras, Thomas Kirchartz, and Uwe Rau.

techniques or alternative ESR methods such as electrically detected magnetic resonance (EDMR) are mandatory.

The following paragraphs will introduce the reader to the theoretical and experimental principles of continuous-wave (cw) ESR focusing on those issues that are relevant for a-Si:H. In Section rau00332, the reader is introduced to the basic spectroscopic principle of ESR. In Section rau00333, the experimental details of ESR spectroscopy are presented with particular emphasis on the requirements that are necessary for studying thin-film samples. In Section rau00334, the influence of magnetic interactions and how they affect the ESR are discussed, whereas in Section rau0033c10-sec1-0005, the main experimental results from the a-Si:H literature are briefly presented and discussed. The readers interested in increasing the absolute sensitivity of the setup through electrical detection will find a brief introduction into EDMR spectroscopy in Section 12.6. For those who are interested in a more detailed treatise, we refer to the ESR textbooks of Atherton [3] or Poole [4].

12.2 Basics of ESR

A noninteracting electron in free space, often referred to as the free electron, is an ideal paramagnetic state with total spin, $S = 1/2$, to explain the basics of ESR spectroscopy. The free electron has a magnetic moment

$$\vec{\mu}_e = \gamma \vec{S} = -\frac{g_e}{\hbar}\frac{e\hbar}{2m_e}\vec{S} = -\frac{g_e}{\hbar}\mu_B\vec{S} \tag{12.1}$$

with γ the gyromagnetic ratio, $g_e = 2.002319$ the Landé factor of the free electron, and $\mu_B = 5.788 \times 10^{-5}$ eV/T the Bohr magneton, which is determined by the mass of the electron, m_e. If the electron is captured in an atomic orbital, its g value changes dramatically due to interaction with the magnetic fields induced by the orbital motion [3]. If the electron, however, is captured in a db state in a-Si:H ($g_{db} = 2.0055$), only a 0.16% shift is induced since the orbital momentum of the db is quenched by the crystal field (cf. Section 12.4.1).

Without an external magnetic field, the energy level with respect to the orientation of the electron spin expressed by the magnetic quantum number, which is either $m_S = 1/2$ or $-1/2$, is degenerated but will be split by an external magnetic field,[1] $B_0 = \mu_0 H_0$, into two Zeeman levels with energy $E = m_S \mu_B g_e B_0$ as shown by the solid lines in Figure 12.1. Between these two Zeeman levels, magnetic dipole transition can be induced through electromagnetic radiation which is in resonance with the energy splitting

$$\Delta E = h\nu = \mu_B g_e B_0. \tag{12.2}$$

In ESR spectroscopy, the frequency of the electromagnetic radiation, typically microwaves (mw), is kept fixed while B_0 is swept, thereby bringing the spins into

1) Note that magnetic fields in ESR are expressed in units of the magnetic flux density B, which is in tesla.

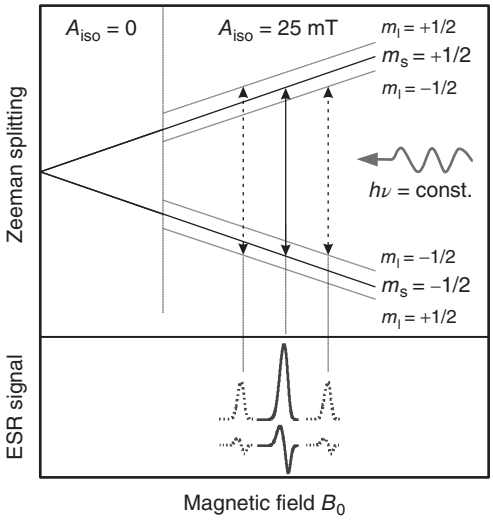

Figure 12.1 Energy levels of an electron ($S = 1/2$) as a function of the magnetic field for two cases: solid lines, without nuclear-spin interaction ($m_I = 0$, $A_{iso} = 0$), and dashed lines, with nuclear-spin interaction ($m_I = \pm 1/2$, $A_{iso} = 25$ mT). Details of the hyperfine interactions are explained in Section 12.4.2. The predicted ESR resonances are shown in absorption (pESR) and derivative mode (cw ESR).

spin resonance. Due to historical reasons, the frequencies are classified in different mw bands with the following nomenclatures: S band, 2–4 GHz; X band, 8–12 GHz; Q band, 30–50 GHz; and W band, 75–110 GHz. The selection rule for the ESR transition is $\Delta m_S = \pm 1$ and is observed in ESR as absorption (and sometimes as emission, not shown) of the mw at the resonant magnetic field B_0 (solid lines in Figure 12.1). The transition then is identified through the characteristic ESR spectrum, which directly appears as an absorption line when pulsed ESR (pESR) techniques are used or as the derivative in case of standard cw ESR. In X band, the required resonant magnetic field for free electrons is $B_0 \approx 0.35$ T inducing an energy splitting ΔE between the two spin levels of about 30 μeV, which corresponds to a temperature $T \approx 0.36$ K. The absorption of the mw is proportional to the occupation difference between the energetically upper and lower level in Figure 12.1. At thermal equilibrium, the fractional population of the upper and lower spin level can be easily calculated using Boltzmann's law as

$$\frac{N_{low} - N_{up}}{N_{low} + N_{up}} = \frac{\Delta N}{N} = \frac{1 - e^{-\Delta E/kT}}{1 + e^{-\Delta E/kT}} \tag{12.3}$$

with N the total number of spins in the measured volume, N_{low} and N_{up} the population of the lower and upper spin state, respectively, and k the Boltzmann factor. It becomes obvious from Equation 12.4 that for $g_e = 2$, $T = 300$ K, and $B_0 = 0.35$ T the fractional population (spin polarization) $\Delta N/N \approx 0.0008$, whereas at $T = 4$ K this value increases to $\Delta N/N = 0.058$. This shows that even for X band and cryogenic conditions, the population of $S = 1/2$ states are still almost equally populated

($\Delta N/N \ll 1$). This implies that both spin orientations, up and down, are almost equally likely to exist and hence the net magnetization, M, being the sum of all individual spin moments that can be polarized in a magnetic field, is rather small. To achieve a spin polarization of 93%, it requires $B_0 = 10\,\mathrm{T}$ and $T = 4\,\mathrm{K}$. Nevertheless, ESR can measure M with high accuracy even under environmental conditions by determining the mw absorption at spin resonance, thereby fulfilling Equation 12.2.

Since the mw absorption, I_{ESR}, is proportional to the population difference ΔN of both spin states, it can be easily shown from Equations 12.2 and 12.3 that [3]

$$I_{\mathrm{ESR}} \propto \Delta N = N_{\mathrm{low}} - N_{\mathrm{up}} \approx N\frac{g_{\mathrm{e}}\mu_{\mathrm{B}}B_0}{2kT}, \text{ when } \frac{\Delta E}{kT} \ll 1. \tag{12.4}$$

According to Equation 12.4, the mw absorption I_{ESR} (ESR response) is directly proportional to the total number of spins in the measured sample volume. Note that through the absorption process, the thermal equilibrium of the spin system is disturbed. The time that the spins need to relax back to thermal equilibrium is referred to as the spin–lattice relaxation time, T_1. This relaxation is accompanied by the emission of an mw photon and is a resonant process.

Since quite a number of experimental parameters such as mw power, mw field distribution within an ESR cavity or sample morphology, and sample shape determine the ESR response, reference measurements with a sample of comparable shape and morphology with known spin concentration are required for calibration purposes. Details on the procedure on how to determine the db concentration of thin-film silicon can be found in Section 12.3. Since I_{ESR} increases linearly with resonance field B_0 (which is equivalent to increasing mw frequency) and reciprocal with temperature, the signal-to-noise (S/N) ratio of an ESR experiment can be increased by measuring at higher mw frequency and/or lower T. Note that Equations 12.10 and 12.4 are only valid for isolated spins such as db states which are not coupled (low spin concentration). Equation 12.4 which is also known as Curie's law is definitely not valid for spins that are occupying conduction- or valence-band states (such as free electrons).

For the understanding of a-Si:H, it is also very beneficial to study the magnetic properties of their nuclear spins (cf. Section 12.4.2). Nuclear spins introduce internal magnetic fields through the hyperfine interaction (HFI, dashed lines in Figure 12.1), which can be very sensitively measured. Nuclear spins in a-Si:H are ^{1}H, ^{29}Si, and ^{31}P in typical concentrations of 10, 4.7, and below 0.1 at.%, respectively. The principal concept discussed so far also holds for nuclear spins. In the previous equations one only has to be replaced μ_{B} by μ_{N} (nuclear magneton) and g_{e} by g_{N}, the nuclear g value. Since the Bohr magneton is proportional to the reciprocal of the mass of the particle (see Equation 12.1), μ_{N} is a factor of 1836 smaller than μ_{B}. Hence, the nuclear-spin polarization is approximately three orders of magnitude smaller compared to electron spins. At the magnetic field used in ESR, the nuclear spins can be considered to be completely unpolarized (equal population of the spin states). The spectroscopy of nuclear spins (nuclear magnetic resonance (NMR)) is therefore orders of

magnitude less sensitive than ESR. On the other hand, the necessary frequency to induce a nuclear-spin transition (Equation 12.2) is also lower by three orders of magnitude and hence technically much easier to access and control. This is one of the reasons why time-domain NMR experiments were introduced decades before time-domain ESR.

12.3 How to Measure ESR

12.3.1 ESR Setup and Measurement Procedure

Figure 12.2 schematically shows the basic components of an ESR spectrometer. In contrast to most optical experiments, ESR is usually carried out as a reflection measurement in order to maximize the sensitivity. The sample is placed in an mw resonator, often referred to as cavity, which serves two purposes: First, the magnetic field, B_1, of the mw is well separated from the electric field, E_1, so that the detrimental interaction between the E_1 and the sample is minimized. Second, the cavity dramatically enhances B_1 – and concomitantly the sensitivity – at the sample position. The amplification of B_1 is quantified by the cavity quality factor

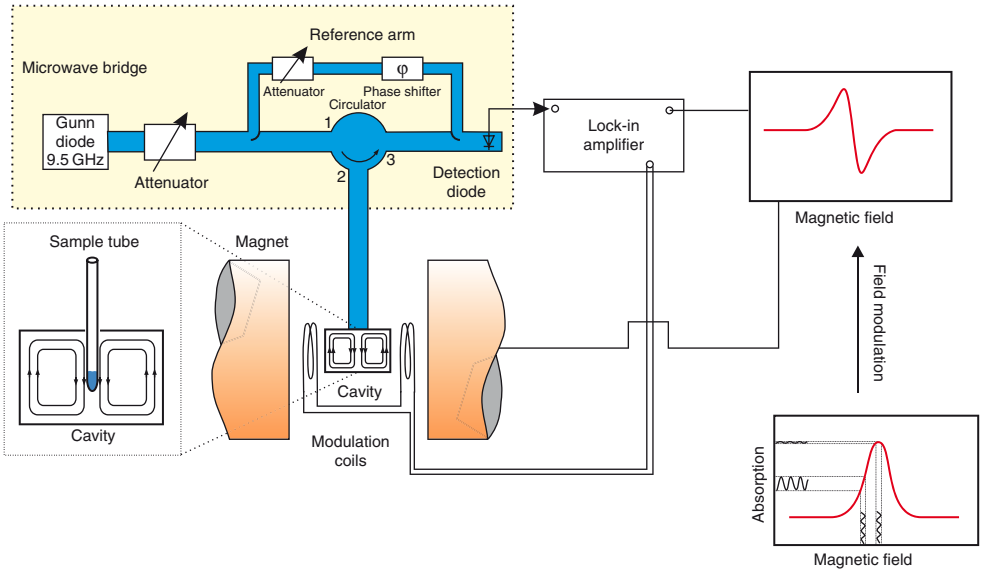

Figure 12.2 Simplified scheme of an ESR spectrometer. On the right side is shown how field modulation results in the derivative form of the ESR absorption signal. The B_1 distribution is indicated for a rectangular cavity. E_1 vanishes at the position of the sample in the center of the cavity at the maximum of B_1.

Q (specifies how much energy can be stored in the resonator) which amounts to a few 1000 for a typical X-band ESR cavity. Q is strongly determined by the design of the cavity. The mw frequency is tuned to the resonance frequency of the cavity, and the coupling between the mw waveguide and the resonator is adjusted in such a way that no mw are reflected but the energy is completely stored in the cavity. This adjustment procedure, which is referred to as *matching* and *coupling*, must be carried out whenever the sample is changed or when the experimental conditions that have an influence on resonance frequency or resonator coupling are varied. When cw mw radiation is absorbed by the sample at resonance, Q decreases. This leads to a change in the coupling and results in enhanced mw reflection from the resonator which is detected by an mw-sensitive detector (typically a diode or mixer). To ensure that only the reflected part of the mw reaches the diode, the signal is decoupled in a mw bridge configuration from the incoming mw radiation through a circulator (for details see Ref. [4]). The output current of the diode is recorded as a function of B_0. The current generated by the detector diode is proportional to the square root of the mw power, P_{mw}, only in a limited range (the *linear* regime). To ensure operation of the detector in this regime, a part of the mw power from the source bypasses the cavity (cf. Figure 12.2) and is directly guided to the detector via the *reference arm*. This mw bias is adjusted with respect to amplitude and phase in order to operate the detection diode in the optimum range and to match the phase at the detector.

Phase-sensitive detection can drastically improve S/N ratio because it minimizes the influence of noise or interfering signals. In analogy to optical experiments where the exciting light is chopped at a fixed frequency and lock-in detection is performed at the same frequency, it is likewise possible to modulate the mw amplitude in ESR. However, it turned out to be more favorable for most ESR experiments to modulate B_0 at frequency ν_{mod}. To this end a magnetic field with periodically changing amplitude (typically less than 1 mT) is superimposed with B_0. In consequence, the signal at the detection diode is modulated at the same frequency as well, and lock-in detection can be employed. Due to the magnetic field modulation, the signal measured is the derivative of the ESR absorption signal with respect to the magnetic field, that is, $\mathrm{d}I_{ESR}/\mathrm{d}B_0$. Consequently, the resonance line shape is the derivative of the associated absorption line. In order to achieve optimum S/N ratio, the modulation frequency is often set to the maximum value which is 100 kHz for most spectrometers.

In cw ESR, the line width is usually determined as the peak-to-peak width of the derivative of the absorption line, ΔB_{pp}. It has to be kept in mind that field modulation can dramatically distort the measured resonance line shape. To obtain the true resonance signal, $1/\nu_{\mathrm{mod}}$ has to be large compared to the spin relaxation times in the sample. Obeying this rule is particularly important when performing cw ESR measurements on disordered silicon at cryogenic temperatures. Here, the standard value $\nu_{\mathrm{mod}} = 100\,\mathrm{kHz}$ is usually too high, and hence experimentally obtained line shapes are likely to be affected. This is called *passage effect* [5], that is, the spins do not have sufficient time to relax between two successive modulation cycles. Further, the modulation amplitude, B_{mod}, should be smaller than

the narrowest line in the spectrum. Otherwise overmodulation will distort and increase the observed line width. $B_{mod} < 0.3 \cdot \Delta B_{PP}$ is sufficient in case that line shapes have to be determined accurately. As a rule of thumb, a good compromise between spectral resolution and S/N is achieved when $B_{mod} \approx \Delta B_{PP}$.

In an ESR spectrometer, P_{mw} can be set by an attenuator (see Figure 12.2). At low P_{mw}, $I_{ESR} \propto \sqrt{P_{mw}}$, and ΔB_{PP} is independent of P_{mw}. However, upon increasing P_{mw} beyond a value, which strongly depends on the type of sample and the experimental conditions, the increase in the ESR signal with mw power becomes weaker and finally even decreases. In addition, the experimentally obtained line is broadened. Both effects are called *saturation*. It means that at high P_{mw}, the population between both energy levels is equalized and the transition is thus saturated (see Equation 12.4). The mw power level where saturation sets in is determined by the interplay between P_{mw} and the spin relaxation times T_1 and T_2 (the latter will be defined in Section 12.4.3). It critically depends on the underlying line-broadening mechanisms (cf. Section 12.4.3). A detailed theoretical treatment of saturation is quite complex and beyond the scope of this chapter; a review can be found in Ref. [4]. The absence of saturation is a necessary prerequisite for determining line shapes and defect density. P_{mw} where saturation starts to influence the signal can easily be determined by measuring spectra for different power levels and analyze I_{ESR} as well as the line width as a function of $(P_{mw})^{1/2}$.

One of the main advantages of ESR is that the spin concentration can be determined, provided that the necessary experimental conditions are well established, that is, the sample volume contains enough spins. Increasing the sample volume generally leads to a gain in S/N until the sample starts to interact with E_1 which would lead to a reduction in Q. In consequence, obtaining optimum sensitivity on such "lossy" samples always requires a compromise between the number of paramagnetic centers and the sample volume that can be tolerated. Two categories of losses can be distinguished [6]: (i) dielectric losses in nonconducting samples which originate from mw absorption due to the imaginary part of the dielectric constant of the material and (ii) losses in conducting samples due to surface currents induced by the mw. Both effects are relevant when studying semiconductor materials and result in a decrease in Q. This is of fundamental importance when performing quantitative ESR measurements and comparing a (lossy) sample with an unknown spin concentration to a reference sample containing a known number of spins. In this case, both samples either have to be measured under identical conditions (e.g., in a double cavity, for details see Ref. [4]), or Q has to be explicitly included in the calculation. When the sample contains only a thin lossy layer, for example, a transparent conducting oxide on top of a semiconducting solar-cell absorber layer, the reduction in Q can be minimized by exact positioning of the sample so that the conductive layer is situated in the minimum of the electric field (usually in the center of the cavity).

States which are not paramagnetic can often be made paramagnetic by illuminating the sample with light. This technique is commonly referred to as light-induced ESR (LESR). For LESR, one has to choose the appropriate light intensity and frequency. Note that often LESR signals, in particular at low T, persist even

after switching off the light. To restore the dark situation, the sample has to be heated back to room temperature or illuminated with infrared (IR) light to depopulate the states. In cases when a white-light source like a halogen lamp is used, it is important to cut off the IR part since this may otherwise lead to a simultaneous depopulation of the spin states.

To further increase the S/N ratio or to reduce effects due to spin–lattice relaxation, the samples can be cooled, thereby enhancing $\Delta N/N$. Cooling is performed by placing the ESR sample in the flow of cooled N_2 or He gas. To decouple the sample from the environment, a glass Dewar is inserted into the center of the cavity. A heater in close proximity to the gas nozzle heats the cooling gas. Stabilization of sample temperature is achieved through a feedback loop with a temperature controller. It is worthwhile noting that water, which may condense in the cavity during low-T operation, leads to strong dielectric losses. To prevent the presence of water, the cavity should be purged with N_2 gas.

12.3.2 Pulsed ESR

Although cw ESR is the appropriate technique for the extraction of relevant interaction parameters or spin densities, the vast potential of ESR spectroscopy for the experimental investigation of structure and dynamics, in particular in the presence of disorder in the material, cannot fully be explored with traditional cw methods. While the technical demands are higher for pulsed (p) ESR (pESR), the experiments are often more easily interpreted, and less prior assumptions are needed as compared to cw ESR. pESR relies on the coherent manipulation of the electron spin by short (ns) intense mw pulses, instead of a steady perturbation as in cw ESR. Since it is beyond the scope of this chapter to cover the details of pESR, we instead refer to the excellent textbook by Schweiger and Jeschke [7].

Field-swept pESR spectra can be recorded by measuring the transient signal created by a sequence of mw pulses. The ESR spectrum is obtained by integrating the so-called Hahn echo [8] as a function of the external magnetic field. Since a field-swept echo experiment directly measures the absorption spectrum (referred to as echo-detected ESR) instead of the derivative spectrum resulting from magnetic field modulation in cw ESR (cf. Section 12.3.1), it is often superior to cw ESR for the detection of broad resonance lines due to better baseline stability. Another advantage is the absence of passage effects at low temperatures, suppression of broad fast-relaxing background signals. In addition, signal saturation – often a severe problem in solid-state cw ESR – is easily avoided by increasing the time span between repeating mw pulse sequences.

Since pESR is a time-domain technique, it provides direct experimental access to spin–relaxation times and the dynamics of spin-related processes (e.g., charge capture, separation, or emission). Small hyperfine couplings (cf. Section 12.4.2), which are often not resolved in the ESR spectrum, can be studied using double-resonance techniques such as electron-nuclear double resonance (ENDOR),

which is a combination of an ESR and NMR experiment, and electron-spin echo envelope modulation (ESEEM) [7].

12.3.3 Sample Preparation

To ensure that material parameters obtained from ESR measurements apply to the material incorporated in thin-film solar cells, deposition conditions and sample structures have to be identical for both ESR samples and solar cells. However, when studying device-grade material, the number of spins in a thin film of <1 μm is usually well below the detection sensitivity of conventional ESR, and the aforementioned requirement cannot be fulfilled. There are several ways to increase the ESR sample volume and accordingly the number of detectable paramagnetic defects. Three commonly applied approaches to prepare ESR samples are briefly described in Table 12.1 along with their advantages and disadvantages.

When the material has a high defect concentration, it can be deposited on a substrate which is likewise used as solar-cell substrate (e.g., glass). In this way, one can assure similar boundary conditions as for the layer growth during solar-cell preparation. Depending on the substrate thickness and resonator dimensions, several samples may be stacked in order to increase S/N. The maximum active sample volume of a typical X-band resonator is $10\,\text{mm} \times 5\,\text{mm} \times 5\,\text{mm}$. This volume is determined by the distribution of B_1 and B_{mod}. Note that in many cases thin-film silicon samples are grown in reactors where the substrate is constantly exposed to a plasma. This produces ions that impinge on the surface and can lead to the creation of paramagnetic defects. In other cases the substrate may contain defects even before deposition, for example, through a TCO or contact layers. Such ESR signals may superimpose the ESR spectrum of the silicon film and thus complicate the extraction of line shapes and defect densities. If such effects are not taken into account, large errors can easily be introduced for quantitative ESR.

Table 12.1 Properties of thin-film sample preparation techniques for ESR.

Sample structure	Advantage	Disadvantage
Thin film on substrate	Growth conditions like during solar-cell preparation	Low number of spins, parasitic signals from substrate, or TCO
Powder sample	Large sample volume and hence number of spins	Growth conditions differ from those used for solar-cell preparation, and removal of sacrificial substrate (or layer) may induce additional defects
Film on scotch tape	Growth conditions like during solar-cell preparation, large number of spins	Removal of sacrificial layer (TCO) may induce additional defects

When studying device-grade Si, the material is often deposited on Al foil (typical size 10 cm × 10 cm). Afterward, the film is removed from the substrate by diluted hydrochloric acid, and the Si flakes are collected in an ESR tube. This technique facilitates measurements on diluted spin systems; however, it is accompanied by the problem of different film growth conditions on Al foil compared to deposition on glass substrates. Moreover, the removal of the Al foil can introduce additional defects. Often it is also feasible to deposit Si on molybdenum foil. The samples can be peeled off by bending the metal substrate. In both cases, the Si powder has to be collected, weighed, and filled into sample tubes, which are then sealed under He atmosphere to ensure good thermal contact with the cooling gas. In addition, the He atmosphere prevents the samples from oxidizing.

Alternatively, Si may be deposited on ZnO-coated substrates which are also used as substrates for solar-cell preparation. After deposition, the film is covered with adhesive tape, and the ZnO sacrificial layer is subsequently etched away. This procedure maintains the initial structure of the film and at the same time allows a stack of many samples to be put into the resonator. It is worthwhile noting that the ZnO layer can be replaced by other materials, for example, SiN_X, provided that the acid for the etching process is changed accordingly.

12.4 The *g* Tensor and Hyperfine Interaction in Disordered Solids

In Section 12.2, we already noted that electron spins confined to solids or molecules exhibit a different g value than free electrons. This shift in g value is a direct consequence of the interaction of the electron spin with its environment and is therefore a significant source of information for the microstructure of the paramagnetic center. Moreover, the resonant magnetic field in ESR of the electron spin is influenced by superimposed internal magnetic fields of magnetic nuclei, acting as magnetic dipoles. This effect, known as HFI, contributes significantly to the spin's resonance frequency. Both Zeeman and HFI can be summarized in a quantum mechanical description with the following spin Hamiltonian:

$$H = \mu_B \vec{B}_0 \cdot g \cdot \frac{\vec{S}}{\hbar} + \sum_i \vec{I}_i \cdot \vec{A}_i \cdot \vec{S}, \quad \vec{A}_i = A_{\text{iso}} 1_{3\times3} + \vec{A}_{\text{dip}}, \tag{12.5}$$

where the first term describes the Zeeman energy and the second term the HFI, $\vec{S}$ and $\vec{I}_i$ denote the electron and nuclear-spin operators, while $\vec{g}$ and $\vec{A}_i$ are the g and HFI tensor, respectively, and $1_{3\times3}$ denotes the identity matrix. Note that in the aforementioned Hamiltonian, spin–spin interactions such as exchange coupling, dipolar coupling, as well as the nuclear Zeeman and quadrupolar interactions have been neglected. For a good overview of such effects, we refer to Ref. [3]. In the following, we will describe the two terms of the spin Hamiltonian in more detail, highlighting their physical origin and their potential for structural identification.

12.4.1 Zeeman Energy and *g* Tensor

The g value of an electron in a defect state is shifted with respect to the free electron value (g_e) due to the fact that the magnetic moment created by the electron spin interacts with the orbital angular momentum of the charge carrier. This spin–orbit coupling induces an additional term in the spin Hamiltonian that depends linearly on the spin–orbit coupling constant, λ (for details see Ref. [3]). Although the spin–orbit interaction in general is quite suitable to obtain microscopic information, it vanishes in first-order approximation, since the orbital momentum is quenched by the crystal field. Treating the spin–orbit interaction as a perturbation, the original ground state is mixed with other states, and a certain degree of orbital momentum L_{eff} is restored.

In the presence of B_0, an additional term in the Hamiltonian arises, which couples the partially restored orbital momentum to B_0:

$$H_{\text{SO}} = \lambda \vec{L}_{\text{eff}} \cdot \vec{S} = \mu_0 \vec{B}_0 \cdot [\Delta g] \cdot \vec{S}; \; [\overleftrightarrow{\Delta} g]_{ij} = -2\lambda \sum_{k \neq 0} \frac{\langle 0|L_i|k\rangle\langle k|L_j|0\rangle}{E_{\text{k}} - E_{\text{o}}}. \tag{12.6}$$

Here L_{eff} is the effective orbital angular momentum which depends on the wavefunctions of the defect ground and excited states, E_0 and E_k, respectively. The g tensor in Equation 12.7 is a function of the local defect symmetry and the chemical nature of the center, since it depends on λ which strongly depends on the nuclear charge of the center. Hence with increasing λ, strong shifts of g are observed in a-Si:H [9].

The g tensor of most paramagnetic centers is anisotropic due to asymmetries in their wavefunction and the crystal field. The Zeeman term in the spin Hamiltonian in Equation 12.5 is therefore influenced by the relative orientation of the external magnetic field and the principal axes of the g tensor. This is shown in Figure 12.3 for a threefold coordinated atom of a Si crystal (c-Si), a so-called dangling-bond defect. Such an ideal defect has axial symmetry with two principal components of the g tensor labeled g and $g_\perp$ as indicated in Figure 12.3. When the whole crystal is rotated with respect to the magnetic field B_0 in the plane of Figure 12.3, a variation in the g value (resonance position) as indicated will be observed, reflecting the symmetry of the defect state. Through such rotation experiments, a complete mapping of the g tensor and its symmetry is possible. For true powder samples, all crystal orientations appear with equal probability. In such orientationally disordered systems, all relative orientations between the B_0 field vector and principal axes of the g tensor occur with equal probability. Although a certain broadening of the ESR line shape by g-tensor anisotropy is introduced, the resulting spectra, usually referred to as powder patterns, still reflect the principal values and the symmetry of the g tensor. Solely its principal axes in the molecular frame cannot be analyzed in a powder pattern. In Figure 12.4, three exemplary spectra for different g-tensor symmetries are computed.

In the case of an isotropic g tensor, only a single symmetric line is observed as shown in Figure 12.4a. Paramagnetic centers with axial symmetry, like dbs

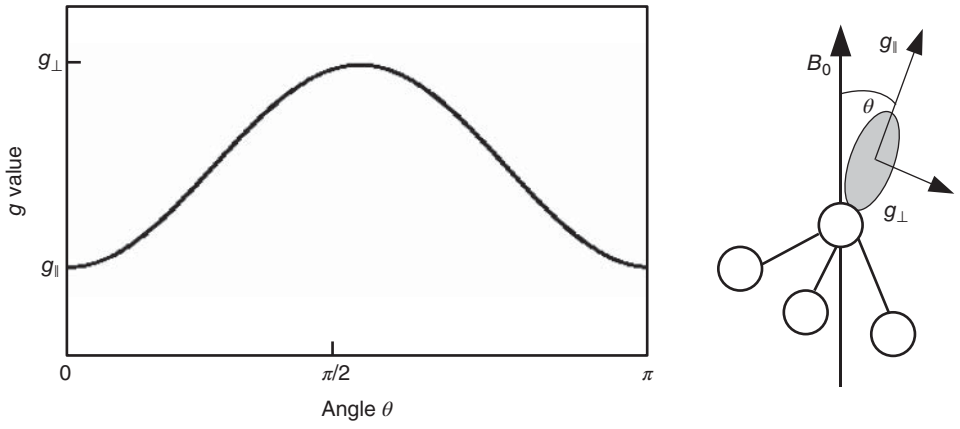

Figure 12.3 Schematic structure of a silicon db oriented in an angle θ with respect to B_0. The plot shows the variation of the observed g value when the db is rotated in the plane. The extremes of g at 0° and 90° denote the principal values $g_\parallel$ and $g_\perp$, respectively.

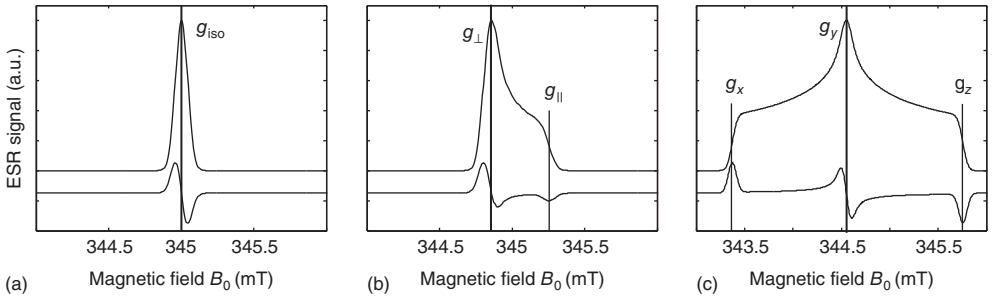

Figure 12.4 Numerical simulation of ESR powder patterns for different g-tensor symmetries. The ESR spectra are plotted as absorption lines (upper curves) and derivative spectra (lower curves) for (a) isotropic, (b) axial (using data obtained for dbs in a-Si:H [10, 11]), and (c) rhombic symmetry. The principal values of the g tensor for orientations of the magnetic field along the canonical directions are indicated. Simulations are carried out with the numerical simulation package *easyspin* [12] using the following parameters $\nu = 9.7$ GHz, $g_{iso} = 2.0055$, $g_\perp = 2.0065$, $g_\parallel = 2.0040$, $g_x = 2.0150$, $g_y = 2.0081$, $g_z = 2.0011$, Gaussian line broadening $\Delta B_{PP} = 0.1$ mT.

in a-Si:H with a sp-hybrid orbital, exhibit a typical powder pattern shown in Figure 12.4b. If B_0 is oriented along the symmetry axis of such a center, the effective g value is given by $g_\parallel$. If it is oriented perpendicular to the symmetry axis, the effective g value is given by $g_\perp$ (see also Figure 12.3). Since more orientations contribute to the latter situation, the spectral intensity at $g_\perp$ is larger than that at $g_\parallel$. In many cases, the microscopic structure of paramagnetic centers is more complex, and the axial symmetry is lifted. In that case, all three principal values of the g tensor, g_x, g_y, and g_z, are nondegenerate, and a rhombic powder pattern arises (Figure 12.4c).

It becomes obvious from Figure 12.4 that when line broadening is smaller than the g anisotropy, the principal g values and hence the symmetry of the spin-carrying center can be easily determined even for random distribution of the crystals (multi- or polycrystalline Si) or in an amorphous material like a-Si:H. If the orientation distribution in the thin film is not random (e.g., preferential orientation in crystal growth), deviation from the depicted powder pattern may occur. In case line broadening is stronger than the g anisotropy, the powder pattern features may be completely hidden.

12.4.2 Hyperfine Interaction

The magnetic interaction with nuclear spins present in the vicinity of an electron spin will introduce, in addition to the external magnetic field B_0, an internal magnetic field B_{int}. The interaction of the electron spin with B_{int} is referred to as HFI, which is determined by the sum of the magnetic interactions with the magnetic moments of all nuclei, I_i. The magnitude and orientation dependence of HFI are determined by the electron-spin density[2)] at the position of the respective nuclei and by the distance of the electron spin to the nuclear spins in its vicinity. Hence, to measure HFI is a very important source of information to identify the microscopic structure of a spin state.

The interaction with the nuclei is generally expressed by the HFI tensor A, which can be written as a sum of the isotropic Fermi contact interaction, A_{iso}, and the electron-nuclear dipole–dipole coupling, A_{dip} (see Equation 12.5). The Fermi contact interaction is given by

$$A_{\text{iso}} = \frac{2}{3}\frac{\mu_0}{\hbar} g_e \mu_e g_n \mu_n |\psi_0(0)|^2, \tag{12.7}$$

where $|\psi_0(0)|^2$ is the electron-spin density at the nucleus at position $r = 0$. If the electron spin is distributed over several nuclei, determination of the individual HFI allows a complete mapping of the spin density.

In Figure 12.5, the influence of $A_{\text{iso}} = 4.2$ mT on the Zeeman splitting of an electron spin is depicted, assuming that it is interacting with only one nuclear spin $I = 1/2$ as is the case for an electron trapped at a phosphorous donor atom (^{31}P) in crystalline silicon at low doping concentration ($N_D < 10^{17}$ cm^{-3}). Both Zeeman levels of the electron spin ($m_S = \pm 1/2$, dashed line in Figure 12.1) are split by the same amount in two levels belonging to the two nuclear-spin states with $m_I = \pm 1/2$. Since in an ESR experiment only the electron spin is in resonance and not the nuclear spin, the ESR selection rule is $\Delta m_S = \pm 1$ and $\Delta m_I = 0$. From this, it becomes evident that the ESR line is split into two resonances which are separated by $A_{\text{iso}} = 4.2$ mT symmetrically about the resonance position of the noninteracting spin (cf. Figures 12.1 and 12.5a). Note that the intensity of the lines is reduced by

2) In the a-Si:H ESR literature the number of paramagnetic centers per volume is also often referred to as the "spin density." To avoid confusion, the latter will be referred to as N_S or N_D (donor) through the article.

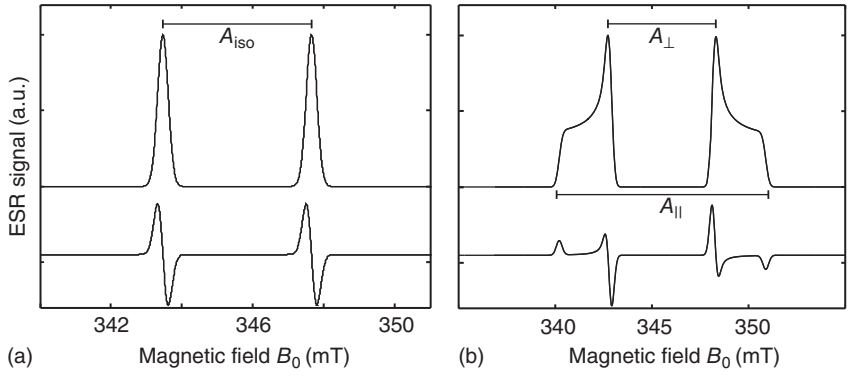

Figure 12.5 ESR powder pattern for a single electron spin $S = 1/2$ and a single nuclear spin $I = 1/2$, with an isotropic g tensor ($g_{iso} = 2.0055$): (a) $A_{iso} = 4.2$ mT (117 MHz) and (b) anisotropic HFI tensor ($A_\perp = 140$ MHz, $A_\parallel = 320$ MHz or $A_{iso} = 200$ MHz, $A_{dip} = 60$ MHz).

a factor of two since the total number of spins is not reduced but spread over two lines. According to Equation 12.7, the magnitude of the HFI is determined by the probability finding the electron at the site of the nucleus (position $r = 0$). Since for a p-type wavefunction $|\psi_0(0)|^2 = 0$, the isotropic HFI vanishes if spin-polarization effects due to spin–spin interaction are not important. This simple case already proves the strength of ESR spectroscopy in determining the local structure of paramagnetic states. Recent advances of numerical quantum chemical calculations, such as *ab initio* density-functional theory (DFT), improved the reliability of structure determination. They allow a quantitative evaluation of ESR parameters, instead of qualitative interpretation mainly based on symmetry analysis of the HFI tensor [13].

In contrast to isotropic Fermi contact HFI, anisotropic HFI induced by dipolar interaction depends on the relative orientation between B_0 and the vector connecting electron spin to nuclear spin. This anisotropic contribution to the HFI can be expressed by a tensor $\overleftrightarrow{A}^{dip}_{ij}$ [7]:

$$\overleftrightarrow{A}^{dip}_{ij} = \frac{\mu_0}{4\pi\hbar} g_e \mu_e g_n \mu_n \left\langle \psi_0 \left| \frac{3r_i r_j - \Delta_{ij} r^2}{r^5} \right| \psi_0 \right\rangle = \begin{pmatrix} A_x & 0 & 0 \\ 0 & A_y & 0 \\ 0 & 0 & A_z \end{pmatrix}, \tag{12.8}$$

where $\vec{r}$ is the vector connecting the electron spin to the nuclear spin. $\overleftrightarrow{A}^{dip}_{ij}$ is a traceless symmetric tensor which can be diagonalized to obtain the three principal hyperfine values $A_{x,y,z}$. Anisotropic HFI vanishes for electrons in s-orbital and is usually only important for electrons in orbitals with partial p-character. The wavefunction of dbs in a-Si:H can be described by a sp-hybrid orbital (cf. Section 12.5.1) with axial symmetry which is localized at an Si atom. If the Si isotope carries a nuclear spin $I = 1/2$, as is the case for ^{29}Si, strong HFI arises. For the principal axis perpendicular to the db symmetry axis, A_x and A_y are degenerated because of symmetry and will be denoted by $-A_{dip}$. Since the dipolar HFI tensor is traceless,

the principal value parallel to the symmetry axis A_z is given by $2A_{\mathrm{dip}}$. In addition to anisotropic HFI, the silicon db also exhibits isotropic HFI to its ^{29}Si host atom, due to its sp-orbital. The principal values of the full axially symmetric HFI tensor are then in analogy to the notation of g values given by

$$\begin{aligned} A_{||} &= A_{\mathrm{iso}} + 2A_{\mathrm{dip}} \\ A_{\perp} &= A_{\mathrm{iso}} - A_{\mathrm{dip}} \end{aligned} \tag{12.9}$$

The resulting ESR spectra, using typical isotropic and anisotropic HFI values for states in c-Si and a-Si:H, are shown in Figure 12.5b. Note that with the presence of anisotropic HFI, the spectrum becomes rather complex if the hyperfine contributions are not well separated or are masked by other ESR signals. To entangle such complex spectra, ESR measurements at various frequencies are mandatory.

If the electron spin is fairly well localized – a situation often encountered in disordered solids – we can approximate the spin as a magnetic point dipole, with all its spin density concentrated at one point. In this case, we can simplify $\overleftrightarrow{A}^{\mathrm{dip}}$ for this two-particle case as

$$\overleftrightarrow{A}^{\mathrm{dip}} = \frac{\mu_0}{4\pi\hbar}\frac{g_{\mathrm{e}}\mu_{\mathrm{e}}g_{\mathrm{n}}\mu_{\mathrm{n}}}{r^3}\begin{pmatrix} -1 & & \\ & -1 & \\ & & 2 \end{pmatrix} = \begin{pmatrix} -A_{\mathrm{dip}} & & \\ & -A_{\mathrm{dip}} & \\ & & 2A_{\mathrm{dip}} \end{pmatrix} \tag{12.10}$$

This point-dipole approximation is often applied to extract distances of the electron spin to weakly coupled nuclei, which allows a deep insight into the microscopic structure surrounding the paramagnetic center. Nevertheless, the applicability of this approximation in disordered solids has to be elaborated before conclusions about a microstructure can be made.

12.4.3 Line-Broadening Mechanisms

In the previous analysis, we assumed a certain intrinsic line width for the ESR resonance, which we now discuss in more detail. ESR resonances can be either homogeneously or inhomogeneously broadened. If all electron spins possess the same resonance frequency, which implies that their microscopic environment is identical (e.g., defect structure Figure 12.6a), the ESR line shape is homogeneous, and its line width $\Delta\omega$ and shape are determined by spin relaxation properties, that is, the lifetime determined spin coherence T_2 (often call spin–spin relaxation time) via the Heisenberg uncertainty principle: $\Delta\omega \approx 1/\hbar T_2$. The resulting line shape is a Lorentzian (Figure 12.6) and its width is defined by $2/T_2$. As shown in Figure 12.6, the EPR spectrum is the sum of a large number of identical spin packets producing identical lines with the same Larmor frequency (g value) and line width.

If the resonance frequencies are not identical for all electron spins, the ESR resonance is composed of different spin packets, each with its own distinct resonance frequency. Each of the individual spin packets is homogeneously broadened, with

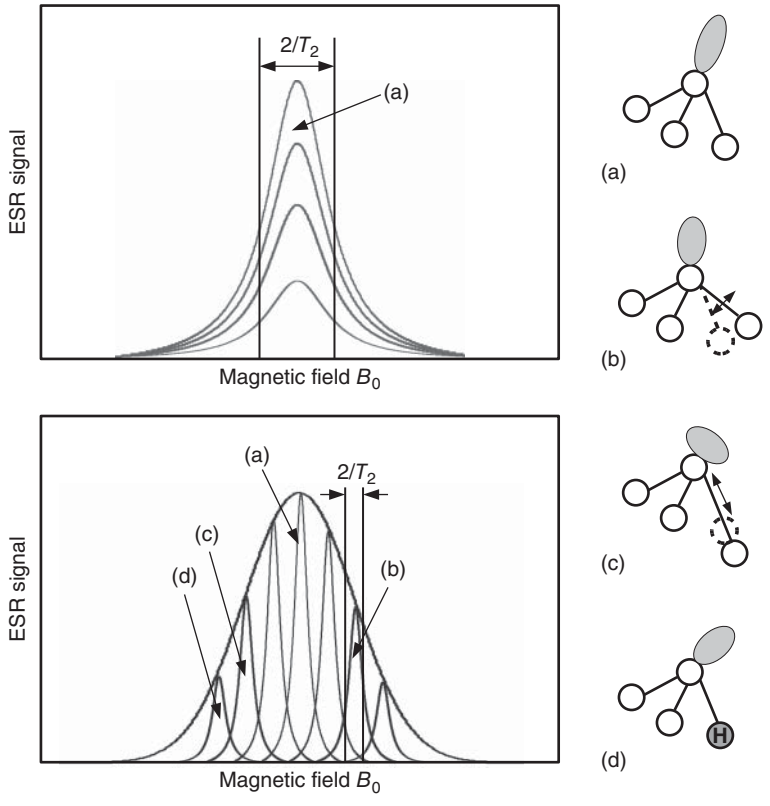

Figure 12.6 Upper plot: homogeneously broadened ESR line giving rise to a Lorentzian. The line is the superposition of many identical lines due to db structure (a). Lower plot: inhomogeneously broadened ESR line induced by variation in bond angle and bond length and due to unresolved HFI as indicated by defect structures (a)–(d), respectively. Each db structure produces its respective line as indicated in the plot leading to Gaussian broadening.

line width $2/T_2$ as in the case discussed before. The proliferation of resonance frequencies is induced by a variation of the spin interaction with its environment either by dipolar spin coupling, HFI, or a distribution of g values as in Figure 12.6 and giving rise to Gaussian line shape.

We will see that although the idealized analysis of the g-tensor symmetry allows the precise determination of the full g tensor, its application in materials with small g-tensor anisotropies, such as silicon, is usually hampered by inhomogeneous broadening. To illustrate this effect, we again consider the case of paramagnetic dbs in a-Si:H as indicated in Figure 12.6.

Inhomogeneous broadening of the db resonance due to HFI is induced by highly abundant magnetic nuclei, such as ^{1}H and ^{29}Si. Their random distribution in the matrix of localized dbs causes a variation in the dipolar HFI field experienced by each db. The matrix nuclei are located at a rather large distance from the electron

spin (>4 Å) [14]; hence the HFI is small and not resolved in the ESR spectrum. The inhomogeneous broadening due to unresolved HFI is frequency independent (see Equations 12.8 and 12.9) if the external magnetic field exceeds the HFI (high-field limit), a condition fulfilled in most ESR experiments. This nuclear-spin-induced disorder effect introduces a Gaussian line broadening, ΔA.

In amorphous materials like a-Si:H, the g-tensor analysis is further complicated by inhomogeneous broadening due to a distribution of g tensors. dbs are not well defined in terms of their microscopic structure due to disorder, which results in variation of bond lengths and bond angles as is shown on the right side of Figure 12.6. This induces a change in the wavefunction and tends to result in a distribution of g tensors. In the ESR literature, this is referred to as g strain, Δg, and leads to a significant field-dependent broadening (see Equation 12.2) of the ESR lines and ultimately limits the resolution of the full g tensor in the spectrum.

Both discussed inhomogeneous broadening mechanisms, ΔA and Δg, in X band are illustrated in Figure 12.7 for the line with axial g tensor shown in Figure 12.4b. Obviously, the powder pattern that is visible if no inhomogeneous broadening is present is completely masked in the X-band spectrum. In the case of unresolved

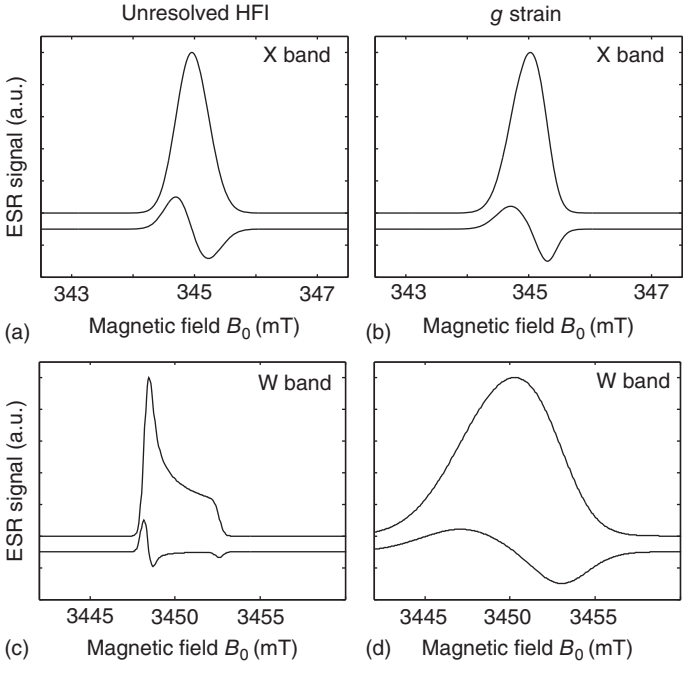

Figure 12.7 X-band ESR spectra (a) and (b) simulated assuming a defect with axial g tensor (see Figure 12.4b) but now assuming line-broadening effects due to (a) unresolved HFI ($\Delta A_{iso} = 15$ MHz) and (b) g strain ($\Delta g_{\perp} = 0.0037$, $\Delta g_{\parallel} = 0.0019$). Note that in both cases, the typical powder pattern can no longer be resolved. At W band (c, d), resolution enhancement can only be gained for the case of unresolved hyperfine (c) since the line-broadening mechanism is field (and hence frequency) independent.

HFI, the spectrum is almost symmetric and, without detailed knowledge, one is tempted to associate this with an isotropic g value. Note that although the lines in Figure 12.7a and b have the same g tensor, their peak position is different. Again one might associate this effect with a different g value and hence assign this to different defect states. In fact one might discover that both lines have an obvious asymmetry and associate this with the fact that two lines are superimposed. There is only one way out of this dilemma and that is to measure ESR spectra at higher mw frequency. This is performed in the simulation (Figure 12.7c and d) for W band, and due to the different frequency dependence of the broadening mechanism, the g tensor in case of unresolved HFI can now easily be recovered, whereas the line exhibiting g strain is only broadened at high frequency. This example shows how difficult sometimes ESR interpretations are if only X-band data are used for the evaluation of the line parameters. The concept of multifrequency ESR is now widely used in the community and commercial spectrometers from 1 GHz up to 263 GHz are now available.

12.5 Discussion of Selected Results

In the previous sections, we have discussed the essence of ESR spectroscopy focusing on thin-film materials. We have shown how microscopic parameters such as g value or HFI influence the ESR spectra and what the challenge is in the interpretation of the data in the presence of disorder. In this section, we will review how ESR has succeeded to unravel some very important aspects about the microstructure of a-Si:H. Nevertheless, it will become evident that many open questions remain, in particular, on light-induced degradation and on the interpretation of the ESR parameters. At the end of this section, we will highlight some of those challenges and address future research strategies to finally unravel the microstructure of defects in a-Si:H.

12.5.1 ESR on Undoped a-Si:H

The first report of ESR measurements in a-Si was by Brodsky and Title in 1969 [15]. They observed a Lorentzian-shaped line with $g = 2.0055$ with a paramagnetic defect density $N_S = 10^{20}\ \mathrm{cm}^{-3}$ (about one defects for every 500 Si atoms), which concomitantly resulted in material with very poor electronic quality. The ESR line width is determined by strong spin–spin interaction effects. Due to the similarity of the a-Si ESR line with that of dangling-bond defects observed at disordered c-Si surfaces [16], Brodsky and Title speculated that the ESR signal originates from ruptured Si–Si bonds, although they assumed that the structure of the material was microcrystalline. After the discovery that the introduction of hydrogen into the a-Si network dramatically reduces the defect density and improves the electronic quality [17], progress has been made over the years,

and today in device-grade a-Si:H $N_S < 10^{16}\,\mathrm{cm}^{-3}$ is easily reached [18]. The defect density of the $g = 2.0055$ line was used from early on as a measure of the electronic quality of a-Si:H although it is now well established that details of the deposition conditions also strongly influence the g value [18]. Currently no thorough understanding of this behavior exists. For ESR measurements on device-grade a-Si:H, powder samples with a volume between 0.01 and 0.1 cm^{-3} (5–50 mg weight) have to be prepared or many thin-film samples have to be stacked. In device-grade a-Si:H, the ESR line has Gaussian shape but is slightly asymmetric as shown in Figure 12.8a with an average g value (zero crossing of the field axis) $g = 2.005 - 2.0055$. The ESR line obeys almost a perfect Curie law behavior [20, 21], indicating that the defect configuration is rather robust and that its occupation is little affected by temperature. Stutzmann and Biegelsen analyzed the g tensor of the line according to the procedures as described before and found that the line shape at X band could be described with an axial symmetric g tensor with $g_{\parallel} = 2.004$ and $g_{\perp} = 2.008$ [10]. Due to structural disorder, the ESR spectrum of the db is broadened leading to an orientation-dependent Gaussian line shape due to strain with $\Delta H_{\parallel} = 0.38\,\mathrm{mT}$ and $\Delta H_{\perp} = 0.5\,\mathrm{mT}$ at X

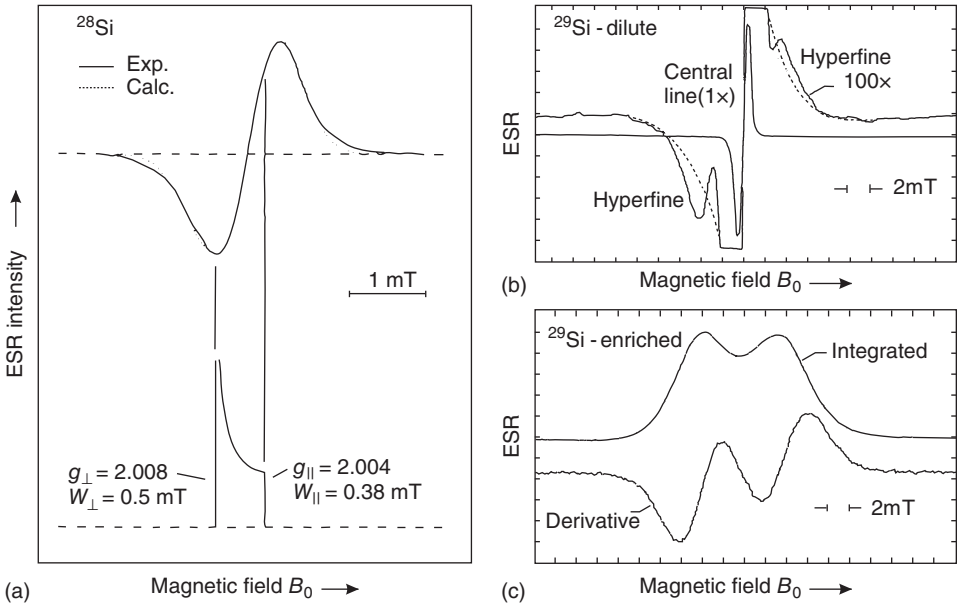

Figure 12.8 X-band ESR spectrum of undoped a-Si:H powder samples, which were (a, b) naturally abundant a-Si:H, and (c) ^{29}Si-enriched a-Si:H. Note that the sign reversal of the spectra results from a 180° phase shift of the lock-in amplifier setting with respect to the field modulation and is not due to an inversion of the spin population, which would lead to an emission line. Due to the strong amplification, the central line in (b) is clipped. ((a, b) Reprinted with permission from Ref. [10] by Stutzmann *et al.*). (c) Reprinted with permission from Ref. [19] by Biegelsen *et al.* Copyright (1989, 1986) by the American Physical Society.

band. Since the g strain in Ref. [10] is of the same order of magnitude as the g anisotropy, extending the range of ESR experiments to higher frequency did not introduce substantial improvement of data evaluation ($g_{\parallel} = 2.0039$, $g_{\perp} = 2.0063$, $\Delta g_{\parallel} = 0.0019$, $\Delta g_{\perp} = 0.0048$) [11]. When deuterium (D) is incorporated in the film replacing hydrogen during the deposition process, the line width of the 2.0055 line remains unchanged [19, 22]. This was an unexpected result, since the magnetic moment of D is smaller than that of H (H: $I = 1/2$ $g_N^H = 5.585$; D: $I = 1$, $g_N^D = 0.857$). From this experiment it was concluded that hydrogen (or D) is not located in the direct vicinity of the defect, for example, at a backbonded position. Since the g tensor in first-order approximation was found to have axial symmetry with the tensor's principal components being comparable to Pb-like defects at the c-Si/SiO_2 interface [23, 24], the ESR signal was associated with db states, supporting the early assignment of Brodsky and Title. Since the assignment of the 2.0055 line purely from g-tensor arguments is not possible in a-Si:H due to the small g shifts, the early speculation about its identification with dbs generated controversial discussions [10, 25–28].

One additional piece of information that is required is HFI of the db wavefunction with the ^{29}Si nuclei [10, 11, 19]. Naturally abundant silicon consists of 92.2 at.% ^{28}Si ($I = 0$) and 4.7 at.% ^{29}Si ($I = 1/2$) plus some other isotopes. When the magnetic field range and the amplification of the lock-in amplifier are extended, two small satellites can be observed in the ESR spectrum as shown in Figure 12.8b with the satellites on the low field side contributing to about 2.0(5)% of the total integrated signal intensity. When we assume that the spin density is located primarily at one atom and is not extended over many silicon atoms, only this nuclear spin can contribute to the total HFI. In that case, due to the abundance of ^{29}Si, each of the two HFI satellites is expected to contain 2.35% of the ESR signal. This is in good agreement with the experimental observation. When the a-Si:H was produced from 93 at.% ^{29}Si-enriched SiH_4, the $g = 2.0055$ line completely vanishes, and only two hyperfine satellites are observed as shown in Figure 12.8c.

The HFI observed in the ESR spectrum was clearly identified to originate from ^{29}Si. Here different situations have to be taken into account to understand the spectrum. The spin of the db can interact with nuclear spins that are in the vicinity of the db. Every Si atom including the threefold coordinated Si atom of the db defect itself can carry a nuclear spin with a certain probability depending on the isotope enrichment of ^{29}Si. In first-order approximation, from the isotropic HFI, the distribution of the spin density and hence the amount of s character of the wavefunction at the db state can be determined and from the anisotropic HFI its p-contribution. Unfortunately, disorder of the amorphous network induces considerable g strain, which makes it extremely difficult to extract the above HFI features from X-band data. Except for Q band [11], no further multifrequency ESR data were available. Nevertheless, a rough estimate of the HFI parameters $A_{iso} = 7$ mT and $A_{dip} = 2$ mT [10] assuming axial symmetry of the HFI could be deduced from spectra as shown in Figure 12.8 [10, 11, 19].

Watkins and Corbett introduced a local-hybrid model [29], approximating the wavefunction $|\Psi\rangle$ of the unpaired db electron ($g = 2.0055$) by a linear combination

of atomic orbitals (LCAOs):

$$|\Psi\rangle = \sum_i \alpha_i(\sigma_i|s?) + (\pi_i|p?) \text{ with } \sum_i \alpha_i^2 = 1, \sigma_i^2 + \pi_i^2 = 1, \tag{12.11}$$

where i indexes all atoms within the extend of $|\Psi\rangle$ ($i = 0$ being the db Si atom) and the projection coefficients α_i, σ_i, π_i of s-type and p-type contributions to the wavefunction. In case the db would be a pure sp^3 hybrid, one would expect $\alpha_0 = 1$, $\sigma_0 = \sqrt{1/4} = 0.5$, and $\pi_0 = \sqrt{3/4} = 0.87$. Assuming that the wavefunction of the 2.005 line is primarily localized at one atom, one can experimentally determine the projection coefficients by $\alpha_0^2\sigma_0^2 = A_{\text{iso}}/A(\text{s})$, $\alpha_0^2\pi_0^2 = A_{\text{dip}}/A(\text{p})$, and $\sigma_0^2 + \pi_0^2 = 1$, where $A(\text{s})$ and $A(\text{p})$ are the HFI constants of pure $|\text{s}\rangle$ and $|\text{p}\rangle$ orbitals as they were determined from Hartree–Fock calculations, respectively (for details see Ref. [29]). Assuming typical literature values for $A(\text{s})$ and $A(\text{p})$, it was found that $\alpha_0^2 = 0.45 - 0.69$, $\sigma_0^2 = 0.06 - 0.11$, and $\pi_0^2 = 0.89 - 0.94$ [10, 11]. Therefore, the sp hybridization has ≈10% s- and ≈90% p-character and the unpaired db electron is localized with more than 50% on the threefold coordinated Si atom itself. With the previous assumptions, it was shown that the a-Si:H db is similar to the P_b-like dangling-bond defects [30]; however, the P_b center is more localized as compared to the a-Si:H db. This picture of db defects in a-Si:H is up to now broadly accepted in the research community. However, it was pointed out that the local-hybrid model has serious deficiencies in reliably predicting spin-density distributions [31]. The model assumes that the atomic wavefunctions of Si are not perturbed in the solid state and completely neglects the influence of spin polarization due to exchange interaction on the HFI. It has been shown by DFT calculations that such effects are extremely important [32], especially for predicting isotropic HFI.

Despite the enormous efforts of the early years in determining the g-tensor and HFI parameters, it was recently shown within the German research cluster *EPR-Solar* [33] that with multifrequency ESR and pulsed ENDOR experiments, a much more complex picture of magnetic interaction parameters was determined, showing that simple axial symmetry is not sufficient in describing experiments [34]. In particular, it is shown that the g tensor has rhombic symmetry. This was already suspected from earlier calculations of the g-tensor and HFI parameters [22, 35].

In conjunction with other experimental data (for an overview see Ref. [2]), it was found that the db state is localized in the band gap and is amphoteric; hence the state can be occupied with 0, 1, or 2 electrons, thereby changing the charge of the state from positive to neutral to negative, respectively (Figure 12.9). Since a closed silicon bond is occupied by two electrons, a broken bond contains one electron and is a neutral state which is paramagnetic ($S = 1/2$). With the number of electrons residing on the localized state, the transition energy to populate or depopulate the state, $D^{0/+}$ or $D^{0/-}$, will shift with respect to the band edges by the correlation energy, U (Figure 12.9). U is determined by Coulomb repulsion between the two electrons and the energy shift induced by the change of the local bonding configuration. Since the temperature dependence of the db signal was shown to have an almost ideal Curie law behavior, $U = 0.2 - 0.3$ eV was estimated

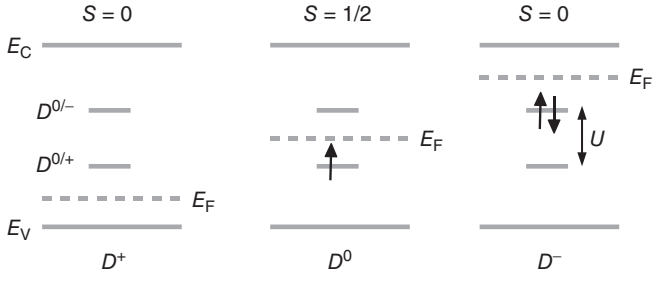

Figure 12.9 Energy transition levels of dangling bonds in their different charge and spin states. Both charged states, D^- and D^+, are not visible in ESR measurements.

from the deviations of the Curie law [21]. Note that if db states would have negative U, they would not be observable in ESR. Negative-U centers are well known in chalcogenide glasses and are characterized by having an unstable singly occupied state [36].

The occupation of the db can be changed either by doping or charge injection (light, applied bias) giving rise to D^+, D^0, and D^- as shown in Figure 12.9. The positively charged D^+ state (no electron, but two holes) has a total spin $S = 0$. To occupy this state with one electron, the Fermi level E_F has to move toward the conduction band. Once E_F passes the transition energy $D^{0/+}$, the db is turned into a neutral D^0 state. The db will stay paramagnetic until E_F passes the second transition energy $D^{0/-}$. Now it is energetically more favorable to have two electrons residing on one defect and turning it into the negatively charged D^- state. Due to the Pauli principle, both electrons must have an opposite spin orientation resulting in a vanishing total spin, $S = 0$. From this picture it becomes obvious that D^0 states must obey Curie's law in first-order approximation since the position of E_F is pinned by the db state itself when no doping is assumed. Deviations from this behavior are due to the fact that disorder in a-Si:H broadens the energy transition levels of the db states to Gaussian energy distributions and unintentional doping effects producing moderate n-type behavior [2]. Hence, when interpreting ESR paramagnetic defect-density results, one has to carefully consider E_F shifts.

12.5.2 LESR on Undoped a-Si:H

Despite the complexity of the microscopic structure of db states, many of the electronic properties of a-Si:H are determined through their interaction with excess charge carriers generated by light or through injection [2]. Such charge carriers may by trapped in localized states of the band and may change the ESR spectrum.

Using X-band LESR with above band-gap light, two additional ESR signals could be observed in undoped a-Si:H, a narrow line ($\Delta B_{PP} = 0.6$ mT) at $g = 2.004$ and a broad one ($\Delta B_{PP} = 2.0$ mT) at $g \approx 2.01 - 2.013$ [37, 38]. These signals were assigned to electrons ($g = 2.004$) and holes ($g = 2.01 - 2.013$) trapped in band-tail states of the conduction and valence band, respectively [38] (see Figure 12.10). Band-tail

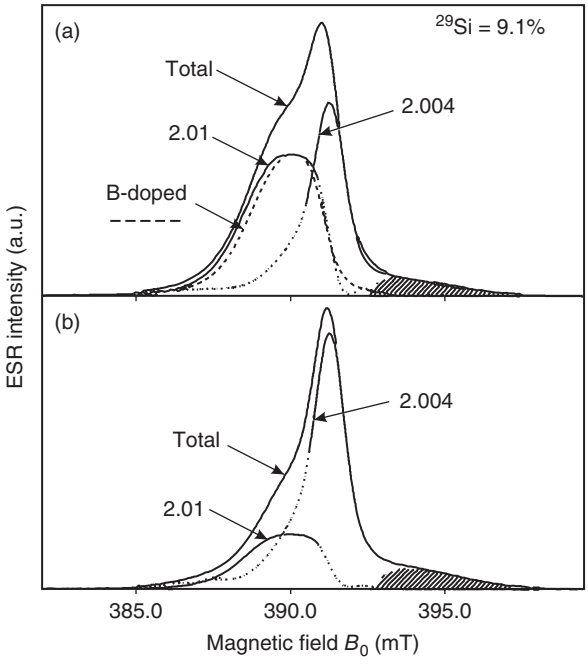

Figure 12.10 Echo-detected LESR spectra of ^{29}Si-enriched undoped a-Si:H measured at $T = 40$ K by (a) a two-pulse Hahn echo and (b) three-pulse stimulated echo. (Reprinted with permission from Ref. [39] by Umeda *et al*. Copyright (1996) by the American Physical Society.)

states are believed to originate from weak bonding and antibonding Si–Si bonds [40], which are induced by the variation in the disorder potential [41]. This leads to localized states that may act as trapping centers and thereby strongly reduces charge carrier mobility as compared to extended states [2]. In an alternative explanation, the LESR states were assigned to positively and negatively charged dbs that are made paramagnetic through trapping of light-generated charge carriers forming the $g = 2.004$ and 2.01 line, respectively [42–44]. These interpretations all assumed the presence of a high density of charged defects as it was introduced through the charged db models [42, 45].

In a more detailed pulsed LESR measurement by Umeda *et al.* [39] on undoped a-Si:H with varying ^{29}Si concentration, the HFI of the $g = 2.004$ line with ^{29}Si could be well resolved, partially due to the fact that the superimposed db and 2.01 signal in the LESR spectrum could be suppressed due to different relaxation behavior. As shown in Figure 12.10, the line at $g = 2.004$ contains on the high-field side clearly resolved shoulders (gray area) which stem from HFI with ^{29}Si. The intensity of the shoulder increased corresponding to the ^{29}Si concentration. However, the relative contribution to the central LESR line ($g = 2.004$) is about twice as large as what was reported for the db line (cf. Section 12.5.1). From this, Umeda *et al.* concluded that the wavefunction of the 2.004 center spreads equally over two Si atoms, different

from the ^{29}Si of the db line. This result is in good agreement with the assignment of the $g = 2.004$ line to an electron being localized on a weak Si–Si bond with its S-like wavefunction centered in between two Si atoms instead of on a threefold coordinated Si atom as is expected for charged dbs.

12.5.3 ESR on Doped a-Si:H

The assignment of the two LESR signals is nicely supported by the dependence of the ESR signal on substitutional doping by boron (B) and phosphorus (P). Doping is accomplished by introducing small amounts of PH_3 or B_2H_6 to the SiH_4 into the PECVD growth chamber. The ratio of the respective concentration is in the following considered as the doping concentration, for example, 1% P doping indicates $[PH_3] = 0.01 \cdot [SiH_4]$.

By B doping, E_F is shifted in the direction of the mobility edge of the valence band by P doping in the opposite direction. With increasing B concentration, an ESR line at $g = 2.01 - 2.013$ appears which has similar line parameters as the broad LESR line shown in Figure 12.10a [20, 38, 39]. This line was assigned to shallow band-tail states of the valence band. Through the shift of E_F, shallow doubly occupied band-tail states are depopulated into singly occupied paramagnetic states. With P doping, on the other hand, the intensity of the 2.004 signal is increased which is naturally explained by the fact that E_F is shifted in the conduction band tail [20]. In Figure 12.11, the measured spin concentrations of the respective ESR lines discussed so far are plotted as a function of E_F. The steep increase in N_S of the 2.01 and 2.004 lines toward the mobility edges is associated with the exponentially increasing density of states (DOSs) of the respective band tails. The fact that the db spin concentration, N_S^{db}, is reduced with increasing doping level, however, does not imply that the total db density (including charged dbs) is reduced when shifting E_F. On the contrary, with increasing [P] or [B],

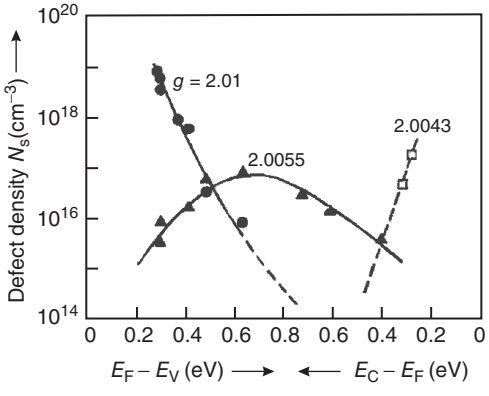

Figure 12.11 Dependence of spin densities on the distance of E_F from the respective mobility edges for the three discussed ESR resonances. (Reproduced with permission from Ref. [46] by Dersch *et al.*)

the db density increases dramatically due to doping-induced defect formation (often referred to as autocompensation) [2, 47]. Most P or B states form defect complexes which leads to nondoping configurations, for example, P_3^0 or B_3^0. The excess electrons and holes, which are introduced by the few active fourfold coordinated dopants, are captured at defect states rather than band-tail states, thereby positively or negatively charging the defects as becomes obvious from Figure 12.9. At high doping levels, such doping-induced defects are not visible in ESR, but they can be easily detected and analyzed through subband-gap optical and electrical spectroscopy [2].

Since it is believed that the neutral fourfold coordinated boron acceptor state in a-Si:H (B_4^0) lies energetically very close to the valence-band mobility edge, it can easily capture an electron from an energetically higher-lying band-tail state, thereby charging the boron (B_4^-) and making it diamagnetic and therefore invisible for ESR [48]. Due to the low doping efficiency and the high density of db and band-tail states, boron acceptor states cannot be made paramagnetic even for very high illumination levels. In compensated a-Si:H – this refers to the case when $[PH_3] = [B_2H_6]$ – the situation is different. Due to the compensation of both charges introduced into the a-Si:H network, E_F remains in the middle of the band gap. It was found that in this case, the db density is similar to that of undoped a-Si:H and that the doping efficiency is two orders of magnitude higher [48]. From this important result, it was concluded that defect formation in a-Si:H is related to the position of the Fermi energy in the material.

While the B-acceptor state is not observable in a-Si:H, the P donor is easily identified in the ESR spectrum through the HFI with the 100% abundant ^{31}P nuclei ($I = 1/2$). In c-Si, the P donor is observed at low temperatures when the electrons of the conduction band are trapped at P forming a paramagnetic state, P_4^0. This state reveals the typical P signature as shown in Figure 12.5a, namely, a signal split by an HFI with $A_{iso} = 4.2$ mT [49]. As shown in Figure 12.12 in 1% P-doped a-Si:H, also two satellites with equal intensity were observed [51]. Note that the splitting between the satellites is about six times larger than what is found for P in c-Si. The satellites are centered almost symmetrically around a strong narrow line with $g = 2.004$ (line is clipped in Figure 12.12). This 2.004 line has been discussed before with respect to LESR experiments and is associated with band-tail states of the conduction band. These states are populated by the doping-induced shift of E_F in the direction of the mobility edge of the conduction band. The correlation energy of the conduction band-tail states is about 20–30 meV as derived from LESR experiments [52]. The intensity of the satellites increased with the square root of $[PH_3]$, whereas the increase in the 2.004 line is less pronounced. To rule out other sources of HFI due to nuclear spins with $I = 1/2$ such as ^1H, ^{13}C, ^{15}N, or even $I = 1$ such as ^{14}N, Stutzmann and coworkers deposited 1% P-doped a-Si:D replacing H by D ($I = 1$) as well a similarly doped a-Si:H sample under ultrahigh vacuum (UHV) conditions, thereby minimizing the impurity concentration [50]. As shown in Figure 12.12, all three samples exhibit the same satellites lending support to the identification of the HFI with P_4^0.

For a quantitative evaluation of the HFI, second-order effects have to be taken into account [3]. The first-order HFI approximation is valid for $A_{iso} < 10$ mT

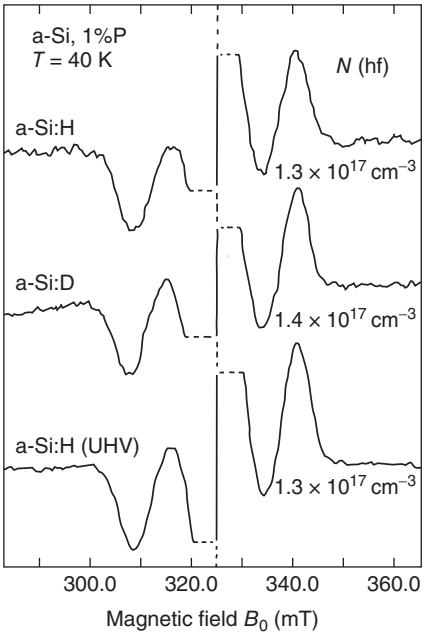

Figure 12.12 ESR spectra of 1% P-doped a-Si:H, a-Si:D, and a-Si:H deposited at UHV conditions. The central line of the ESR spectrum at $g = 2.004$ is clipped due to the large amplification. (Reprinted with permission from Ref. [50] by Stutzmann *et al*. Copyright (1987) by the American Physical Society.)

and produces $(2I + 1)$ satellites that are distributed equally spaced around the resonance position of the noninteracting spin. The second-order approximation introduces an additional quadratic term in B_0, which shifts all lines to lower fields, and the spacing between the lines increases from low field to high field. Assuming that the HFI in P-doped a-Si:H is isotropic, Stutzmann and Street determined $A_{iso} = 24.5$ mT taking into account a large distribution of HFI-coupling strengths induced by disorder. This is described by A strain (see Section 12.4.3) which for the case of P is found to be $\Delta A = 16$ mT. From second-order HFI, the g value of the P states can be calculated to ${g_P}^{a\text{-}Si} = 2.003(2)$ [50], which is similar to that of band-tail states identified through LESR and supports the assumption that the P states are distributed over a wide energy range among band-tail states of the conduction band. ${g_P}^{a\text{-}Si}$ is considerably larger than what is found in c-Si (${g_P}^{c\text{-}Si} = 1.9985$), which indicates that the P state in a-Si:H can no longer be approximated by a shallow, effective-mass state as in case of c-Si [50], since otherwise ${g_P}^{c\text{-}Si} < 2.0023$. The six times larger HFI interaction that is observed in a-Si:H is explained by the fact that the wavefunction of the neutral P atom in the a-Si matrix is much stronger localized as compared to c-Si. Stutzmann and Street estimate a donor radius from the HFI of about 9 Å [51] instead of 16.7 Å as found in c-Si [53]. As stated before, with P doping the db density dramatically increases, thereby reducing the doping efficiency. Stutzmann and coworkers estimated that

from 0.1% [PH_3] in the gas phase about 10^{20} cm^{-3}, P atoms are incorporated in the a-Si:H film. Of these, only about 10^{18} cm^{-3} are fourfold coordinated, and only 10% of them (10^{17} cm^{-3}) are P_4^0 states and hence observable in ESR [50].

Figure 12.13 summarizes the main achievements of ESR on doped and undoped a-Si:H. The sketch depicts the currently accepted picture of the DOS for nominally undoped a-Si:H as it is derived from many different experimental results [2]. From the mobility edges band-tail states with exponentially decreasing DOS with a slope of about 25 and 45 meV for the conduction and valence band tail with ESR signatures at $g = 2.01$ and 2.004, respectively, are observed. Only those states in region 1 are paramagnetic, and all other states are diamagnetic and will not be observed in ESR. By shifting the Fermi level in the respective tails either through illumination or doping, the ESR signatures of P_4^0 donor states or conduction- and valence-band-tail states can be observed. For strongly P- and B-doped materials, the db density strongly increases in regions 0 and 2, respectively, through the shift of E_F. These defects will no longer be observed in ESR since they are diamagnetic (see Figure 12.9).

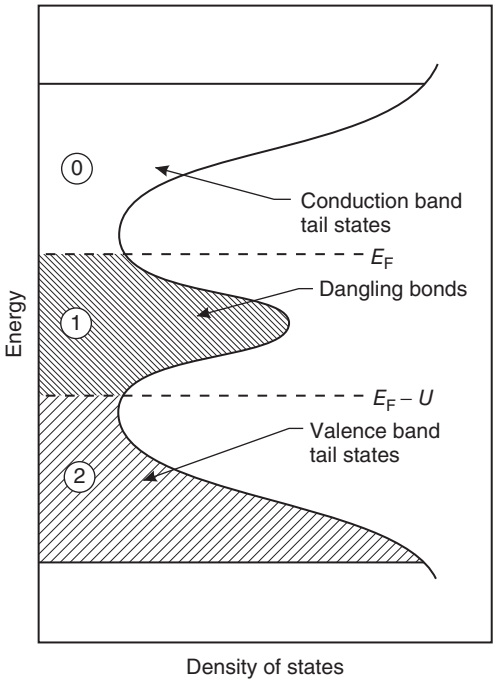

Figure 12.13 Density of states of a-Si:H showing the occupation of localized states for a certain position of the Fermi energy. States that lie within the correlation energy U energetically beneath E_F will be paramagnetic (region 1). Lower-lying states will be doubly occupied (region 2 and states above E_F are unoccupied. (Reprinted with permission from Ref. [54] by Stutzmann *et al*. Copyright (1983) by the American Physical Society.)

12.5.4
Light-Induced Degradation in a-Si:H

In 1977, Staebler and Wronski observed that intense light illumination of undoped electronic quality a-Si:H decreases both the dark conductivity and photoconductivity (Staebler–Wronski effect (SWE)) [55, 56]. They found that annealing to temperatures of about 150 °C completely reverses the effect. Subsequent investigations discovered that the observed conductivity decrease is due to a shift in the Fermi level toward midgap and a severe decrease in the excess charge carrier lifetime, while the mobility is essentially unchanged. It was not until 1980 that Dersch *et al.* [57] investigated a-Si:H by ESR methods realizing that the observed degradation is caused by a reversible increase in the db absorption signal. Today it is clear that the light-induced increase in the db concentration is the most important, but not the only degradation mechanism of a-Si:H [58]. dbs contribute most to the decrease in the excess charge carrier lifetime, which is strongly correlated to the defect-density N_s [40].

It was found experimentally that the number of metastable dbs increases with $N_s \propto t^{1/3} I^{0.6}$ under cw illumination for time t with light of intensity I and is independent of low impurity concentration in the material (cf. Figure 12.14). Several authors proposed intrinsic microscopic models for the SWE to explain these observations. Since a complete review of all published microscopic models for the SWE is beyond the scope of this publication, we discuss only the three following models.

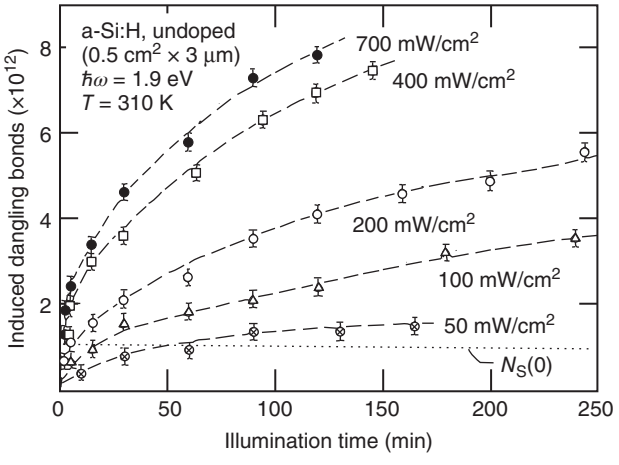

Figure 12.14 Number of light-induced dbs versus illumination time measured by ESR at various light intensities. Sample and illumination details are displayed in the upper left corner. The horizontal dotted line indicates the number of dbs $N_s(0)$ prior to illumination. (Reprinted with permission from Ref. [40] by Stutzmann *et al*. Copyright (1985) by the American Physical Society.)

12.5.4.1 Excess Charge Carrier Recombination and Weak Si–Si Bond Breaking

In a series of experiments, Staebler and Wronski showed that a metastable increase in the db concentration can also be generated by injecting excess charge carriers in a-Si:H pin diodes and can be prevented when light illumination is combined with a strong reverse bias to remove light-generated charge carriers from the *i*-layer. It is therefore clear that the degradation is induced by excess charge carrier trapping or recombination and not by the initial light-absorption event itself [59]. From these experiments, Stutzmann *et al.* [40] concluded that bimolecular recombination of excess charge carriers is the cause of db creation and derived a differential equation for the db concentration N_s:

$$\frac{dN_s}{dt} = c_{sw} np, \tag{12.12}$$

where n, p are the electron and hole concentrations, respectively, and c_{sw} denotes an empirical proportionality factor depending on microscopic details of the db creation mechanism. If there is already a certain amount of dbs available, Equation 12.12 can be easily solved by assuming that most of the recombination is taking place at db sites. In this monomolecular recombination limit, the charge carrier densities n and p are proportional to G/N_s, where G is the photocarrier generation rate. Together with Equation 12.12, we then obtain the experimentally observed db creation dynamics $N_s \propto t^{1/3}G^{2/3}$. This result also reproduces the intensity dependence, if we assume that G is proportional to the light intensity I. As for the microscopic process leading to db creation, Stutzmann *et al.* proposed a breaking of weak Si–Si bonds in the valence-band tail after trapping and bimolecular recombination of electrons with holes at the *same* weak bond site. In their model, the weak bond enters an excited state after trapping an electron–hole pair, which leads to the formation of two adjacent dbs (cf. Figure 12.15a). Since such a configuration is unlikely to be stable with an annealing energy barrier of 1.1 eV and is not compatible with the absence of strong exchange coupling in the ESR properties, the dbs must be separated on a short time scale after their creation.

Several microscopic models involving H were proposed in the literature to explain the separation of dbs. Among them are hydrogen bond switching [40, 60], dissociation of H_2^* complexes [61], and hydrogen migration on internal hydrogenated surfaces [62] (Figure 12.15b–d). All these models predict dbs which are spatially correlated to H atoms.

12.5.4.2 Si–H Bond Dissociation and Hydrogen Collision Model

The fact that ESR experiments do not show dbs spatially correlated to H atoms stimulated a variety of alternative microscopic models for the SWE. Direct emission of H atoms from Si–H bonds, leading to the formation of a db, and subsequent diffusion of H away from the broken bond were excluded as sources of the SWE, since these processes are irreversible [63]. Branz extended the Si–H bond dissociation model by proposing a collision step between mobile H atoms, originally emitted from Si–H bonds [64]. The two mobile H atoms form a metastable H-complex denoted by $M(Si–H)_2$ in a strongly exothermic reaction as shown in

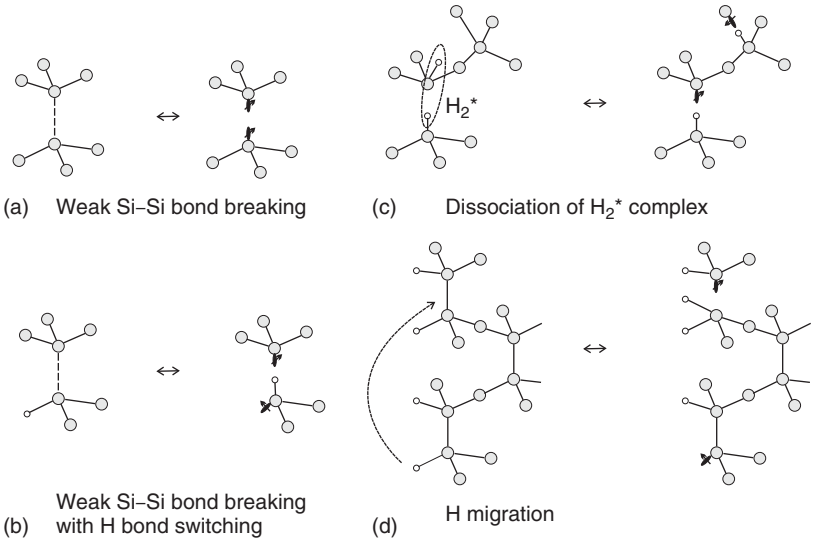

Figure 12.15 Different microscopic defect reactions proposed for the creation of metastable dbs in the SWE. (a) Breaking of weak Si–Si bonds, (b) hydrogen bond switching, (c) dissociation of H_2* complexes, and (d) hydrogen migration on internal hydrogenated surfaces. Gray objects denote Si atoms, open objects denote H atoms, and dbs are indicated by a schematic wavefunction and an arrow indicating the electron spins.

Figure 12.16. By annealing to 150 °C for several hours, the process is reversed, and the metastable complexes dissociate and saturate the dbs. The predicted time evolution of the db concentration is again $N_s \propto t^{1/3}G^{2/3}$, as in the case of the weak Si–Si bond-breaking model, but derived from different physical processes.

12.5.4.3 **Transformation of Existing Nonparamagnetic Charged Dangling-Bond Defects**
Another model accounting for the light-induced increase in paramagnetic dbs was introduced by Adler and proposes a charge transfer between originally charged dbs (D^+, D^-) with an effective negative correlation energy [42] (cf. Figure 12.17). This process does not create new dbs, but transforms nonparamagnetic centers into paramagnetic dbs, which are then observable by ESR. However, charged db densities appear to be too low in undoped a-Si:H to support this model, and the experimentally determined time evolution of the db density is not compatible with the one-carrier capture mechanism (see [64] and references therein).

In the preceding discussion we have seen that different models, based on completely different microscopic processes, do actually result in the same unusual sublinear time dependence. It is therefore most difficult to distinguish between the available theories by merely considering the time evolution of the db concentration. Another approach to deduce the microscopic origin and dynamics of the SWE is a microscopic investigation of the final metastable state by ESR. Here different models do actually predict quite different microscopic centers for

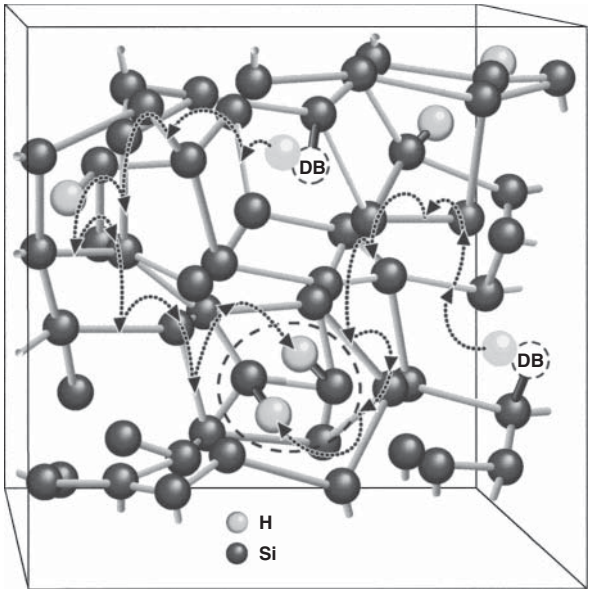

Figure 12.16 Schematic representation of the microscopic processes within the framework of the H collision model. (Figure reprinted with permission from Ref. [64] by Branz *et al*. Copyright (1999) by the American Physical Society.)

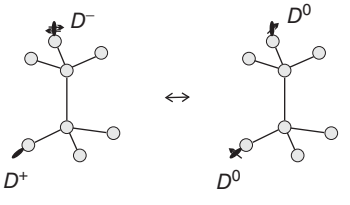

Figure 12.17 Schematic representation of the charge-transfer model proposed by Adler [42]. Gray objects denote Si atoms and dbs are indicated by a schematic wavefunction and an arrow indicating the electron spin.

the metastable state and its environment, for example, the hydrogen distribution around the defect, offering a possibility to test the available theoretical models.

In contrast to the H collision model (cf. Section 12.5.4.2), the weak Si–Si bond-breaking model (cf. Section 12.5.4.1) predicts a spatially correlated H distribution for light-induced dbs (light-soaked a-Si:H – state B) but not for native dbs (as-grown or annealed a-Si:H – state A) as noted earlier. We have seen in Section 12.4.2 that close magnetic nuclei like H induce a characteristic splitting of the db resonance by HFI. Since native dbs, present in as-deposited a-Si:H or in the annealed state A, do not exhibit the predicted defect-H correlation, db ESR spectra of degraded samples should differ significantly. Several studies were performed to address this question. Brandt *et al.* [65] carried out EDMR

experiments, while Isoya *et al.* [66] conducted ESEEM experiments to measure the HFI of H atoms directly.

ESEEM measurements clearly showed a contribution of distant matrix H atoms with a small HFI to the db, but no larger HFI, which would indicate the presence of close H atoms. Relying on these observations, Isoya *et al.* concluded that the immediate vicinity ($r < 4$ Å) is actually depleted from H, an interpretation which disagrees with the predictions of the model described in Section 12.5.4.1. In a recent contribution [14], pulsed ENDOR measurements showed that this interpretation is not correct, and the authors of Ref. [66] were misled by a typical artifact of two-pulse ESEEM experiments, observed in a wide range of disordered materials [67].

Brandt *et al.* [65] performed a more reliable experiment to determine the HFI of H atoms in the vicinity of dbs. By applying EDMR at low excitation frequencies ($\nu = 434$ MHz), contributions due to g anisotropy were avoided, and the line shape is only determined by HFI. Figure 12.18 compares EDMR spectra for native dbs (state A) and light-induced dbs (state B). The obtained spectra are nearly identical; hence no evidence for the presence of spatially correlated db–H pairs is found.

The fundamental problem inhibiting a complete resolution of the microscopic defect structure and its environment is the disorder-induced inhomogeneous broadening. Once spectral lines are subject to such excessive broadening, they become undetectable due to a finite experimental resolution and sensitivity. However, there is still room for improvement by the application of advanced ESR techniques at higher magnetic fields. We recently managed to increase resolution and sensitivity by the application of a Q-band pulse ENDOR technique at a

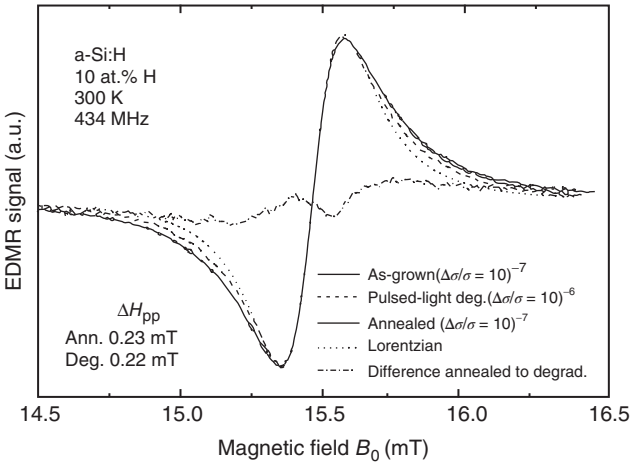

Figure 12.18 EDMR spectra of undoped a-Si:H at an excitation frequency of 434 MHz at room temperature for different sample conditions indicated in the legend. Samples are light-soaked by pulse light degradation. (Reprinted from Ref. [65] by Brandt *et al.* with permission from Elsevier.)

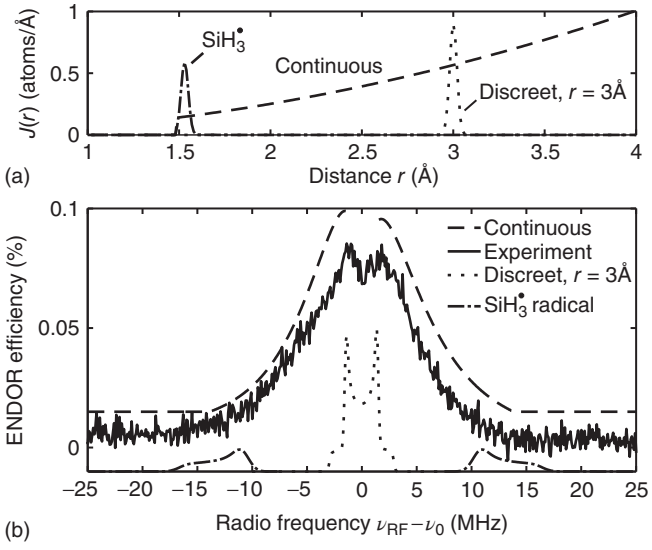

Figure 12.19 ENDOR spectroscopy of native db in undoped a-Si:H. (a) Radial distribution function $J(r)$ for a continuous (dashed line) and discreet (dotted line) distribution of H atoms around dbs. The position of H atoms in free SiH_3 radicals is shown by the dash-dotted line. (b) Corresponding ENDOR spectra for distributions in (a) and comparison with the experimental spectrum. The dashed, dotted, and dash-dotted spectra are offset vertically with respect to the experimental spectrum for better overview. For further details please refer to Ref. [14].

magnetic field of 1.2 T using a laboratory-built ESR resonator [14]. Investigation of HFI between native dbs in state A and H atoms shows that HFIs of up to 25 MHz are observed (see Figure 12.19a), indicating that H atoms can be very close to the db. By comparing the ENDOR spectrum with typical spectra for free SiH_3, we can conclude that a small amount of H atoms is bonded to db silicon atoms at a backbonded site. However, the results show that there is no observable short-range order and the H distribution is well described by a homogeneous distribution (see Figure 12.19b).

12.6 Alternative ESR Detection

The application of ESR to state-of-the-art a-Si:H thin films or even completely processed a-Si:H solar cells remains a challenge because the sensitivity of conventional ESR is usually not sufficient to reliably detect the paramagnetic defects. Moreover, it is often difficult to discriminate between signals from the cell structure, contact layers, or background signals from the substrate [68]. Although a correlation between the defect density as determined by ESR on powder samples and the efficiency of resulting solar cells is well established [69], it still remains

questionable if the defect properties of thin films in the device and in powder samples are identical, because the boundary conditions for the layer growth are different. The sensitivity limit of ESR, which prevents its successful application to thin-film devices, can be overcome by using indirect detection techniques. These methods do not rely on the detection of reflected (or absorbed) mw radiation, but monitor the influence of ESR on sensitively measurable macroscopic observables such as (photo)conductivity, capacitance, optical absorption, photoluminescence, or electroluminescence. To elucidate the impact of paramagnetic defects on charge transport in solar cells, the (photo)conductivity is an appropriate observable. For this reason, we restrict this paragraph to the description of EDMR. Due to the fact that we detect resonant changes in the (photo)current, only electrically active defect states contribute to the spectrum. In consequence, paramagnetic states which do not influence the conductivity and are thus not relevant for solar-cell operation (e.g., defects in the substrate) do not affect the EDMR signal.

12.6.1 History of EDMR

EDMR, which combines the microscopic selectivity of ESR with the sensitivity of a current measurement, has a long-standing history in the field semiconductor defect analysis. It was first demonstrated in 1966 by Maxwell and Honig [70, 71] as well as Schmidt and Solomon [72] who measured the influence of ESR on the photoconductivity in c-Si. The underlying mechanism was spin-dependent scattering of electrons at impurities. In 1972, Lepine utilized EDMR for the detection of charge carrier recombination via defect states at a silicon surface [73]. Since then, EDMR was applied to large variety of organic and inorganic semiconductors. In particular, this technique provided insight into transport and recombination pathways in a-Si:H thin films and devices (for a review see [74]). Until recently, EDMR experiments were exclusively carried out like cw ESR experiments, that is, the sample was continuously subjected to mw radiation while sweeping an external magnetic field and detecting the conductivity. Thus, spectroscopic information (e.g., g values, line widths, and line shapes) about the current-influencing paramagnetic states could be extracted. Toward the beginning of this century, the field of EDMR got a new impetus when the first pulse (p) EDMR (pEDMR) measurements employing short mw pulses were demonstrated [75]. By the use of pEDMR, it is not only possible to study the kinetics of spin-dependent transport and recombination processes but also to harness coherent spin effects [76] in a similar way like in pESR. An analysis of the time evolution in two-dimensional pEDMR measurements (ΔI vs B_0 and time) allows the deconvolution of spectrally overlapping signals [77]. In this way, pEDMR signals may be assigned to defect states in the individual layers of a pin solar cell. Moreover, for spin-dependent processes involving two different types of paramagnetic centers (e.g., a hopping process between conduction band-tail states and phosphorous donor states in n-doped a-Si:H), the contributing pairs of paramagnetic centers can be identified

based on the fact that the associated pEDMR signals exhibit the same time behavior.

The high sensitivity of EDMR originates from two effects: First, a current can be detected with high accuracy. Second, the EDMR signal intensity is not necessarily limited by the thermal polarization of the contributing paramagnetic centers which may be very small under standard ESR conditions. In fact, two spin-dependent mechanisms frequently encountered in disordered thin-film materials – namely, recombination and hopping transport via localized states – rely on a spin-pair mechanism in which the relative orientation of two spins determines the probability for a current-influencing transition. This model was developed by Kaplan *et al*. [78] and is referred to as the *KSM model*. It is equally applicable to spin-dependent recombination as well as hopping transport. Both processes are shown schematically in Figure 12.20.

In the case of a recombination process as shown in Figure 12.20a, the spin pair consists of two localized states with different energy. Although it would be energetically favorable if both electrons occupied the lower-lying state, owing to the Pauli principle this transition is only allowed when both spins are aligned antiparallel. Thus, invoking that the spin state is conserved during the process, the transition is blocked in the case of parallel spins. The application of mw radiation, which is resonant with either of the two spin-pair constituents, alters the respective spin state, and the initially forbidden transition becomes allowed. The recombination process is finally completed by the capture of a hole from the valence band. In addition, an electron from the conduction band can be trapped at the unoccupied defect state. All in all, one electron from the conduction band and one hole from the valence band are annihilated, resulting in a decrease in the sample conductivity. In the case of hopping transport as shown in Figure 12.20b, the spin pair consists of two states having similar energy close to E_F. Analogous to the recombination process, the transition between adjacent singly occupied states can be blocked by the relative spin orientation. Again, resonant mw radiation can flip one spin and enable an initially forbidden transition. The resonant enhancement of the

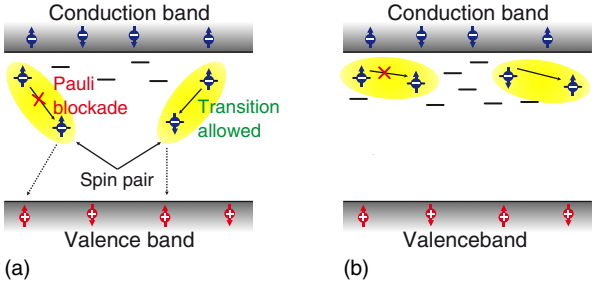

Figure 12.20 Spin-dependent processes involving localized states in the band gap as observed in thin-film silicon. For simplicity, only localized states in the upper half of the band gap are depicted. (a) Spin-dependent recombination. (b) Spin-dependent hopping transport. The arrows indicate the orientation of the electron and hole spins.

hopping rate can be considered to enhance the mobility in the hopping transport path. For a detailed review on spin-dependent hopping, see Ref. [79].

12.6.2 EDMR on a-Si:H Solar Cells

The application of EDMR to fully processed semiconductor devices dates back to the early days of EDMR. In 1976, Solomon performed spin-dependent conductivity measurements on a commercial diode based on crystalline silicon [80]. He observed an EDMR signal associated with recombination of excess charge carriers that were injected by applying a bias voltage and found a strong dependence of the signal intensity on the voltage. This voltage dependence could be modeled when taking into account the different recombination mechanisms (i.e., diffusion- and recombination-limited processes) that occur in p–n diodes. It was concluded that the spin-dependent signal is sensitive only to recombination in the space charge regions, which renders EDMR suitable to differentiate between diffusion- and drift-limited effects. Several studies on c-Si p–n diodes provided a quite detailed picture of spin-dependent recombination via intrinsic defects as well as impurity states and defect complexes [81–84]. Although the mechanisms of EDMR in devices can be quite complex in detail, an identification of the contributing defect states is often possible based on the line parameters which in many cases agree well with those found in ESR spectra of the respective material. In addition, extensive literature is available on EDMR in a-Si:H thin films [74].

After the demonstration that EDMR can successfully be applied to a-Si:H pin solar cells [85], spin-dependent recombination studies revealed a strong variation of the EDMR signal at room temperature with bias voltage and illumination conditions [86, 87]. Figure 12.21 shows EDMR spectra of an a-Si:H pin solar cell measured at different bias voltages without illumination. When the db states are brought into spin resonance, the recombination in the space charge region of the pin solar cell is enhanced. Since the dark currents in this bias regime are limited by recombination, an increase in the current is observed. The turnover between an enhancing and a quenching EDMR signal upon varying the bias voltage was shown to be related to the transition from diffusion- to drift-dominated behavior – similar to crystalline p–n diodes. Moreover, it was demonstrated by means of EDMR that charge transport and carrier collection are controlled by recombination in the bulk of the *i*-layer [87]. The finding that light-induced defect creation in this layer (cf. Section 12.5.4) is detrimental for the solar-cell performance together with the fact that EDMR probes recombination via db states makes this technique well suited to investigate degradation mechanisms in a-Si:H-based solar cells at ambient conditions [88]. Figure 12.22 illustrates this fact by comparing the bias-voltage dependence of the EDMR signal intensity recorded under dark forward bias injection conditions ($\Delta I/I$, with ΔI is the current change that is induced by the resonant mw) of annealed (Figure 12.22a) and degraded (Figure 12.22b) a-Si:H pin solar cells with varying *i*-layer thicknesses. The degradation was carried out by subjecting the cells to a

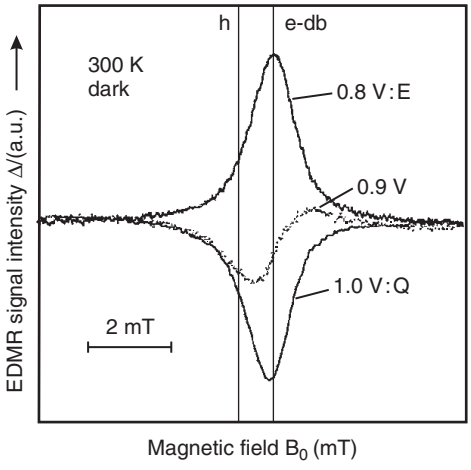

Figure 12.21 Dark EDMR spectrum obtained at $T = 300$ K on a-Si:H pin solar cell at different forward bias. Note that the signal changes sign at about 0.9 V. The peak of the resonance is at $g \approx 2.005$. (Reprinted with permission from Ref. [86] by Lips *et al*. Copyright (1993), American Institute of Physics.)

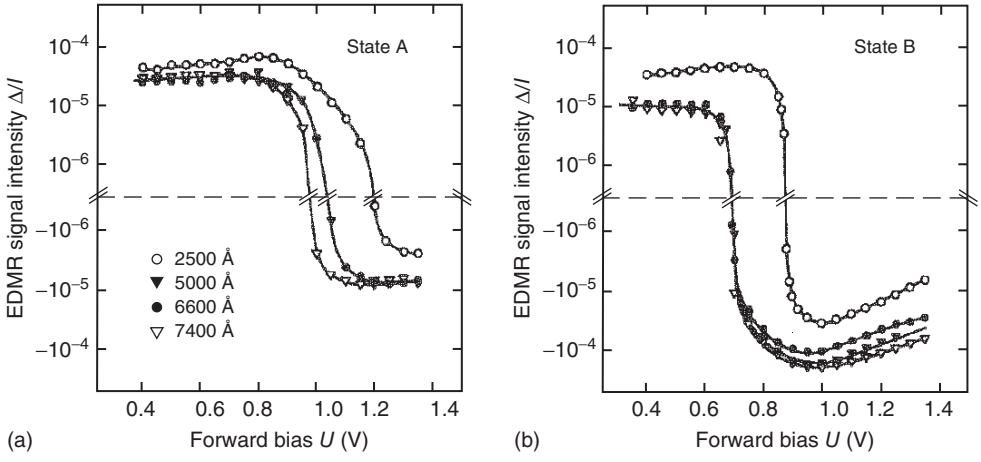

Figure 12.22 EDMR signal intensity ($\Delta I/I$) as a function of the bias voltage applied to a-Si:H pin solar cells for several thicknesses of the *i*-layer as given in the legend. (a) Annealed (state A). (b) Degraded (state B). (Reprinted from Ref. [88] by Lips *et al*. with permission from Elsevier.)

high forward current to ensure homogeneous degradation throughout the *i*-layer (150 mA cm^{-2} for 3 h). Figure 12.22 indicates a decrease in the turnover voltage (change of sign from positive to negative EDMR signal) by approximately 0.3 V upon degradation. Further, the quenching signal amplitude increases by more than one order of magnitude. The situation with respect to recombination in the solar

cell is very complex, and EDMR results cannot be interpreted right away since recombination may both enhance and decrease the dark current. Nevertheless it is possible to directly simulate EDMR with solar-cell simulation tools only assuming that through ESR the capture cross section of electrons in neutral db states is slightly increased by the mw [89]. From comparison to simulations, it became clear that degradation is predominantly a bulk effect in the *i*-layer of the pin a-Si:H solar cell. These observations demonstrate the sensitivity of EDMR with respect to defects created by degradation of a-Si:H pin solar cells.

Phosphorus-doped a-Si:H layers are frequently used in pin solar cells with microcrystalline silicon (μc-Si:H) absorber. Charge transport in these n-doped layers with typical thicknesses of a few 10 nm is relevant for solar-cell operation because electrons generated in the absorber have to transverse them in order to be collected at the metal electrode. Especially at low temperatures, transport in n-doped a-Si:H occurs via hopping among localized band tail and phosphorus donor states and can thus be observed by EDMR. Figure 12.23 shows a pEDMR spectrum of a μc-Si:H pin solar cell with amorphous *n*-layer which clearly reveals the ^{31}P hyperfine lines (with a splitting of ~25 mT) known from ESR measurements on n-doped a-Si:H powder samples (cf. Section12.5.3). The central line originates from spin-dependent hopping of electrons via conduction band-tail states in the n-doped a-Si:H layer as well as in the intrinsic μc-Si:H absorber [90]. Similar effects can be observed in high-efficiency heterojunction solar cells consisting of c-Si as absorber and n-doped a-Si:H as emitter layer [91].

These examples demonstrate that EDMR is capable of sensitively detecting electrically active paramagnetic states in fully processed solar cells and can identify the underlying transport and recombination mechanisms.

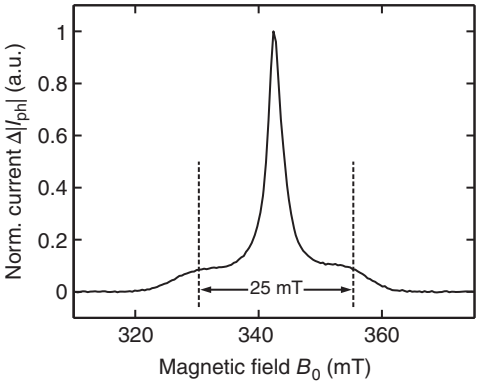

Figure 12.23 X-band pEDMR spectrum (resonant change in photoconductivity, $\Delta|I_{ph}|$, normalized to 1 as a function of the magnetic field) of a μc-Si:H pin solar cell with amorphous *n*-layer measured at $T = 10$ K. The experiment was performed under reverse bias ($U = -1.0$ V), and the sample was illuminated by a halogen lamp. The dashed vertical lines denote the positions of two ^{31}P hyperfine lines with their center of gravity at $g = 2.003$.

12.7 Concluding Remarks

ESR has contributed significantly to the understanding of the microscopic structure of defect states in a-Si:H. In particular, db states have been shown to be the dominant midgap defects in a-Si:H and are responsible for the electronic degradation of a-Si:H after light soaking. ESR was able to unravel the structure and influence of dopant states. However, most ESR results rely on experiments with only limited resolution and quantum chemical methods, which did not allow to link the magnetic interaction parameters with the defect structure and distribution. This generally insufficient resolution and detection sensitivity of conventional EPR has dramatically changed with the advent of novel multifrequency EPR spectrometers and detection schemes as well sophisticated DFT simulation tools, which allow determining information about spin-coupling parameters inaccessible until then. Recently, a German network called *EPR-Solar* was formed with the aim to transfer these advances in EPR instrumentation and theory to solve some of the remaining open questions related to defect states in a-Si:H materials, in particular the SWE [33]. Latest ESR results [34] and DFT calculations [92] show that db states in a-Si:H have a complex structure and cannot be described by simple sp-hybridized states. In order to transfer the obtained ESR results into the microscopic structure of defect states with their respective spin-density distribution, DFT calculations of the magnetic interaction parameters (e.g., HFI with ^{29}Si, g tensor) of many different db models are required. Currently such tools have become available [93–95] and are currently used by *EPR-Solar* to shed light on the microscopic structure of a-Si:H defects and their involvement in the SWE.[3)]

Acknowledgments

The authors greatly acknowledge Alexander Schnegg for helpful discussions and suggestions and proofreading the manuscript. The support from Christian Gutsche for updating our literature database and designing some of the graphs of this article is also greatly appreciated. Matthias Fehr is indebted to the German Federal Ministry of Research and Education (BMBF) for financial support through the Network project *EPR-Solar*, contract no. 03SF0328A.

References

1. Shah, A., Torres, P., Tscharner, R., Wyrsch, N., and Keppner, H. (1999) Photovoltaic technology: the case for thin-film solar cells. *Science*, **285**, 692.
2. Street, R.A. (1991) *Hydrogenated Amorphous Silicon*, Cambridge University Press, Cambridge, New York.
3. Atherton, N.M. (1993) *Principles of Electron Spin Resonance*, Ellis Horwood, PTR Prentice-Hall, New York.
4. Poole, C.P. (1983) *Electron Spin Resonance: A Comprehensive Treatise on Experimental Techniques*, Wiley, New York.

3) HFI parameters are often given in frequency units. For $g = 2$, 28 MHz is equivalent to 1 mT.

5. Weger, M. (1960) Passage effects in paramagnetic resonance experiments. *Bell Syst. Tech. J.*, **39**, 1013.
6. Feher, G. (1957) Sensitivity considerations in microwave paramagnetic resonance absorption techniques. *Bell Syst. Tech. J.*, **36**, 449.
7. Schweiger, A. and Jeschke, G. (2001) *Principles of Pulse Electron Paramagnetic Resonance*, Oxford University Press, Oxford, UK, New York.
8. Hahn, E.L. (1950) Spin echoes. *Phys. Rev.*, **80**, 580.
9. Stutzmann, M. and Stuke, J. (1983) Paramagnetic states in doped amorphous-silicon and germanium. *Solid State Commun.*, **47**, 635.
10. Stutzmann, M. and Biegelsen, D.K. (1989) Microscopic nature of coordination defects in amorphous-silicon. *Phys. Rev. B: Condens. Matter Mater. Phys.*, **40**, 9834.
11. Umeda, T., Yamasaki, S., Isoya, J., and Tanaka, K. (1999) Electron-spin-resonance center of dangling bonds in undoped a-Si:H. *Phys. Rev. B: Condens. Matter Mater. Phys.*, **59**, 4849.
12. Stoll, S. and Schweiger, A. (2006) Easy spin, a comprehensive software package for spectral simulation and analysis in EPR. *J. Magn. Reson.*, **178**, 42.
13. Vandewalle, C.G. and Blochl, P.E. (1993) 1st-principles calculations of hyperfine parameters. *Phys. Rev. B: Condens. Matter Mater. Phys.*, **47**, 4244.
14. Fehr, M., Schnegg, A., Teutloff, C., Bittl, R., Astakhov, O., Finger, F., Rech, B., and Lips, K. (2010) Hydrogen distribution in the vicinity of dangling bonds in hydrogenated amorphous silicon (a-Si:H). *Phys. Status Solidi A*, **207**, 552.
15. Brodsky, M.H. and Title, R.S. (1969) Electron spin resonance in amorphous silicon, germanium, and silicon carbide. *Phys. Rev. Lett.*, **23**, 581.
16. Walters, G.K. and Estle, T.L. (1961) Paramagnetic resonance of defects introduced near surface of solids by mechanical damage. *J. Appl. Phys.*, **32**, 1854.
17. Chittick, R.C., Alexande, J., and Sterling, H.F. (1969) Preparation and properties of amorphous silicon. *J. Electrochem. Soc.*, **116**, 77.
18. Astakhov, O., Carius, R., Finger, F., Petrusenko, Y., Borysenko, V., and Barankov, D. (2009) Relationship between defect density and charge carrier transport in amorphous and microcrystalline silicon. *Phys. Rev. B: Condens. Matter Mater. Phys.*, **79**, 104205.
19. Biegelsen, D.K. and Stutzmann, M. (1986) Hyperfine studies of dangling bonds in amorphous-silicon. *Phys. Rev. B: Condens. Matter Mater. Phys.*, **33**, 3006.
20. Dersch, H., Stuke, J., and Beichler, J. (1981) Temperature-dependence of electron-spin-resonance spectra of doped a-Si:H. *Phys. Status Solidi B*, **107**, 307.
21. Lee, J.K. and Schiff, E.A. (1992) Modulated electron-spin-resonance measurements and defect correlation energies in amorphous-silicon. *Phys. Rev. Lett.*, **68**, 2972.
22. Ishii, N., Kumeda, M., and Shimizu, T. (1982) The effects of H and F on the electron-spin-resonance signals in a-Si. *Jpn. J. Appl. Phys.*, **2** (21), L92.
23. Caplan, P.J., Poindexter, E.H., Deal, B.E., and Razouk, R.R. (1979) ESR centers, interface states, and oxide fixed charge in thermally oxidized silicon wafers. *J. Appl. Phys.*, **50**, 5847.
24. Poindexter, E.H., Caplan, P.J., Deal, B.E., and Razouk, R.R. (1981) Interface states and electron-spin resonance centers in thermally oxidized (111) and (100) silicon-wafers. *J. Appl. Phys.*, **52**, 879.
25. Pantelides, S.T. (1986) Defects in amorphous-silicon – a new perspective. *Phys. Rev. Lett.*, **57**, 2979.
26. Stutzmann, M. and Biegelsen, D.K. (1988) Dangling or floating bonds in amorphous-silicon. *Phys. Rev. Lett.*, **60**, 1682.
27. Pantelides, S.T. (1987) Defects in amorphous-silicon – a new perspective – reply. *Phys. Rev. Lett.*, **58**, 2825.
28. Fedders, P.A. and Carlsson, A.E. (1987) Energetics of single dangling and floating bonds in amorphous Si. *Phys. Rev. Lett.*, **58**, 1156.
29. Watkins, G.D. and Corbett, J.W. (1964) Defects in irradiated silicon – electron

paramagnetic resonance+electron-nuclear double resonance of Si-E center. *Phys. Rev. A*, **134**, 1359.

30. Brower, K.L. (1983) ^{29}Si hyperfine-structure of unpaired spins at the Si/SiO_2 interface. *Appl. Phys. Lett.*, **43**, 1111.
31. Cook, M. and White, C.T. (1988) Hyperfine interactions in cluster-models of the Pb defect center. *Phys. Rev. B: Condens. Matter Mater. Phys.*, **38**, 9674.
32. Neese, F. and Munzarova, M. (2004) Historical aspects of EPR parameter calculations, in *Calculation of NMR and EPR Parameters: Theory and Applications* (eds M. Kaupp, M. Bühl, and V.G. Malkin), Wiley-VCH.
33. http://www.helmholtz-berlin.de/forschung/enma/si-pv/projekte/bmbf/index_de.html (12 July 2010).
34. Teutloff, C., Fehr, M., Schnegg, A., Astakhov, O., Rech, B., Finger, F., Lips, K., and Bittl, R. (2010) Multifrequency EPR on defects in hydrogenated amorphous silicon, http://dx.doi.org/10.1103/PhysRevB.84.245203.
35. Ishii, N. and Shimizu, T. (1997) Cluster-model calculations of hyperfine coupling constants of dangling bond and weak bond in a-Si:H. *Solid State Commun.*, **102**, 647.
36. Shimakawa, K., Kolobov, A., and Elliott, S.R. (1995) Photoinduced effects and metastability in amorphous semiconductors and insulators. *Adv. Phys.*, **44**, 475.
37. Knights, J.C., Biegelsen, D.K., and Solomon, I. (1977) Optically induced electron-spin resonance in doped amorphous silicon. *Solid State Commun.*, **22**, 133.
38. Street, R.A. and Biegelsen, D.K. (1980) Luminescence and electron-spin-resonance studies of defects in hydrogenated amorphous-silicon. *Solid State Commun.*, **33**, 1159.
39. Umeda, T., Yamasaki, S., Isoya, J., Matsuda, A., and Tanaka, K. (1996) Electronic structure of band-tail electrons in a Si:H. *Phys. Rev. Lett.*, **77**, 4600.
40. Stutzmann, M., Jackson, W.B., and Tsai, C.C. (1985) Light-induced metastable defects in hydrogenated amorphous-silicon – a systematic study. *Phys. Rev. B: Condens. Matter Mater. Phys.*, **32**, 23.
41. Anderson, P.W. (1958) Absence of diffusion in certain random lattices. *Phys. Rev.*, **109**, 1492.
42. Adler, D. (1983) Origin of the photoinduced changes in hydrogenated amorphous-silicon. *Solar Cells*, **9**, 133.
43. Hautala, J. and Cohen, J.D. (1993) Esr studies on a-Si-H – evidence for charged defects and safe hole traps. *J. Non-Cryst. Solids*, **166**, 371.
44. Morigaki, K. (1981) Spin-dependent radiative and nonradiative recombinations in hydrogenated amorphous-silicon – optically detected magnetic-resonance. *J. Phys. Soc. Jpn.*, **50**, 2279.
45. Adler, D. (1981) Defects in amorphous chalcogenides and silicon. *J. Phys. (Paris)*, **42**, C43.
46. Dersch, H., Stuke, J., and Beichler, J. (1981) Electron-spin resonance of doped glow-discharge amorphous-silicon. *Phys. Status Solidi B*, **105**, 265.
47. Street, R.A., Biegelsen, D.K., and Knights, J.C. (1981) Defect states in doped and compensated a-Si-H. *Phys. Rev. B: Condens. Matter Mater. Phys.*, **24**, 969.
48. Stutzmann, M. (1987) Electron-spin resonance of shallow defect states in amorphous-silicon and germanium. *J. Non-Cryst. Solids*, **97–98**, 105.
49. Fletcher, R.C., Yager, W.A., Pearson, G.L., Holden, A.N., Read, W.T., and Merritt, F.R. (1954) Spin resonance of donors in silicon. *Phys. Rev.*, **94**, 1392.
50. Stutzmann, M., Biegelsen, D.K., and Street, R.A. (1987) Detailed investigation of doping in hydrogenated amorphous-silicon and germanium. *Phys. Rev. B: Condens. Matter Mater. Phys.*, **35**, 5666.
51. Stutzmann, M. and Street, R.A. (1985) Donor states in hydrogenated amorphous-silicon and germanium. *Phys. Rev. Lett.*, **54**, 1836.
52. Schumm, G., Jackson, W.B., and Street, R.A. (1993) Nonequilibrium occupancy of tail states and defects in alpha-SiH – implications for defect structure. *Phys. Rev. B: Condens. Matter Mater. Phys.*, **48**, 14198.

53. Feher, G. (1959) Electron spin resonance experiments on donors in silicon. 1. Electronic structure of donors by the electron nuclear double resonance technique. *Phys. Rev.*, **114**, 1219.
54. Stutzmann, M. and Biegelsen, D.K. (1983) Electron-spin-lattice relaxation in amorphous-silicon and germanium. *Phys. Rev. B: Condens. Matter Mater. Phys.*, **28**, 6256.
55. Staebler, D.L. and Wronski, C.R. (1977) Reversible conductivity changes in discharge-produced amorphous Si. *Appl. Phys. Lett.*, **31**, 292.
56. Staebler, D.L. and Wronski, C.R. (1980) Optically induced conductivity changes in discharge-produced hydrogenated amorphous-silicon. *J. Appl. Phys.*, **51**, 3262.
57. Dersch, H., Stuke, J., and Beichler, J. (1981) Light-induced dangling bonds in hydrogenated amorphous-silicon. *Appl. Phys. Lett.*, **38**, 456.
58. Fritzsche, H. (2001) Development in understanding and controlling the Staebler–Wronski effect in a-Si: H. *Annu. Rev. Mater. Res.*, **31**, 47.
59. Stutzmann, M. (1997) Microscopic aspects of the Staebler–Wronski effect, in *Amorphous and Microcrystalline Silicon Technology – 1997* (eds S. Wagner, M. Hack, E.A. Schiff, R. Schropp, and I. Shimizu), Materials Research Society, Warrendale.
60. Morigaki, K. (1988) Microscopic mechanism for the photo-creation of dangling bonds in a-Si-H. *Jpn. J. Appl. Phys., Part 1*, **27**, 163.
61. Zhang, S.B., Jackson, W.B., and Chadi, D.J. (1990) Diatomic-hydrogen-complex dissociation: a microscopic model for metastable defect generation in Si. *Phys. Rev. Lett.*, **65**, 2575.
62. Carlson, D.E. (1986) Hydrogenated microvoids and light-induced degradation of amorphous-silicon solar cells. *Appl. Phys. A: Solids Surf.*, **41**, 305.
63. Stutzmann, M., Jackson, W.B., Smith, A.J., and Thompson, R. (1986) Light-induced metastable defects in amorphous-silicon – the role of hydrogen. *Appl. Phys. Lett.*, **48**, 62.
64. Branz, H.M. (1999) Hydrogen collision model: quantitative description of metastability in amorphous silicon. *Phys. Rev. B: Condens. Matter Mater. Phys.*, **59**, 5498.
65. Brandt, M.S., Bayerl, M.W., Stutzmann, M., and Graeff, C.F.O. (1998) Electrically detected magnetic resonance of a-Si: H at low magnetic fields: the influence of hydrogen on the dangling bond resonance. *J. Non-Cryst. Solids*, **230**, 343.
66. Isoya, J., Yamasaki, S., Okushi, H., Matsuda, A., and Tanaka, K. (1993) Electron-spin-echo envelope-modulation study of the distance between dangling bonds and hydrogen-atoms in hydrogenated amorphous-silicon. *Phys. Rev. B: Condens. Matter Mater. Phys.*, **47**, 7013.
67. Höfer, P. (1994) Distortion-free electron-spin-echo envelope-modulation spectra of disordered solids obtained from 2-dimensional and 3-dimensional hyscore experiments. *J. Magn. Reson., Ser. A*, **111**, 77.
68. Lee, C., Ohlsen, W.D., Taylor, P.C., and Engstrom, O. (1987) ESR in pin structures based on a-Si:H, in *18th International Conference on the Physics of Semiconductors* (ed. O. Engstrom) World Scientific, Singapore, Stockholm, Sweden.
69. Neto, A.L.B., Lambertz, A., Carius, R., and Finger, F. (2002) Relationships between structure, spin density and electronic transport in 'solar-grade' microcrystalline silicon films. *J. Non-Cryst. Solids*, **299**, 274.
70. Honig, A. (1966) Neutral-impurity scattering and impurity Zeeman spectroscopy in semiconductors using highly spin-polarized carriers. *Phys. Rev. Lett.*, **17**, 186.
71. Maxwell, R. and Honig, A. (1966) Neutral-impurity scattering experiments in silicon with highly spin-polarized electrons. *Phys. Rev. Lett.*, **17**, 188.
72. Schmidt, J. and Solomon, I. (1966) Modulation De La photoconductivite dans le silicium a basse temperature par resonance magnetique electronique des impuretes peu profondes. *C. R. Seances Acad. Sci., Ser. B*, **263**, 169.

73. Lepine, D.J. (1972) Spin-dependent recombination on silicon surface. *Phys. Rev. B*, **6**, 436.
74. Stutzmann, M., Brandt, M.S., and Bayerl, M.W. (2000) Spin-dependent processes in amorphous and microcrystalline silicon: a survey. *J. Non-Cryst. Solids*, **266–269**, 1.
75. Boehme, C. and Lips, K. (2001) Time domain measurement of spin-dependent recombination. *Appl. Phys. Lett.*, **79**, 4363.
76. Boehme, C. and Lips, K. (2003) Electrical detection of spin coherence in silicon. *Phys. Rev. Lett.*, **91**, 246603.
77. Behrends, J., Schnegg, A., Fehr, M., Lambertz, A., Haas, S., Finger, F., Rech, B., and Lips, K. (2009) Electrical detection of electron spin resonance in microcrystalline silicon pin solar cells. *Philos. Mag.*, **89**, 2655.
78. Kaplan, D., Solomon, I., and Mott, N.F. (1978) Explanation of large spin-dependent recombination effect in semiconductors. *J. Phys. Lett.*, **39**, L51.
79. Boehme, C. and Lips, K. (2006) The investigation of charge carrier recombination and hopping transport with pulsed electrically detected magnetic resonance techniques, in *Charge Transport in Disordered Solids with Applications in Electronics* (ed S. Baranovski), Wiley, Chichester, England, Hoboken, NJ.
80. Solomon, I. (1976) Spin-dependent recombination in a silicon para-normal junction. *Solid State Commun.*, **20**, 215.
81. Rong, F., Poindexter, E.H., Harmatz, M., Buchwald, W.R., and Gerardi, G.J. (1990) Electrically detected magnetic-resonance in P–N-junction diodes. *Solid State Commun.*, **76**, 1083.
82. Christmann, P., Wetzel, C., Meyer, B.K., Asenov, A., and Endros, A. (1992) Spin dependent recombination in Pt-doped silicon P–N-junctions. *Appl. Phys. Lett.*, **60**, 1857.
83. Xiong, Z. and Miller, D.J. (1993) General expression for the electrically detected magnetic-resonance signal from semiconductors. *Appl. Phys. Lett.*, **63**, 352.
84. Müller, R., Kanschat, P., Aichberger, S., Lips, K., and Fuhs, W. (2000) Identification of transport and recombination paths in homo and heterojunction silicon solar cells by electrically detected magnetic resonance. *J. Non-Cryst. Solids*, **266–269**, 1124.
85. Homewood, K.P., Cavenett, B.C., Spear, W.E., and Lecomber, P.G. (1983) Spin effects in P+-I-N+ a-Si-H cells – photovoltaic detected magnetic-resonance (PDMR). *J. Phys. C: Solid State Phys.*, **16**, L427.
86. Lips, K. and Fuhs, W. (1993) Transport and recombination in amorphous P–I–N-type solar-cells studied by electrically detected magnetic-resonance. *J. Appl. Phys.*, **74**, 3993.
87. Fuhs, W. and Lips, K. (1993) Recombination in a-Si-H films and pin-structures studied by electrically detected magnetic-resonance (EDMR). *J. Non-Cryst. Solids*, **166**, 541.
88. Lips, K., Block, M., Fuhs, W., and Lerner, C. (1993) Degradation of a-Si-H P-I-N solar-cells studied by electrically detected magnetic-resonance. *J. Non-Cryst. Solids*, **166**, 697.
89. Lips, K., Boehme, C., and Fuhs, W. (2003) Recombination in silicon thin-film solar cells: a study of electrically detected magnetic resonance. *IEE Proc. – Circ. Dev. Syst.*, **150**, 309.
90. Behrends, J., Schnegg, A., Boehme, C., Haas, S., Stiebig, H., Finger, F., Rech, B., and Lips, K. (2008) Recombination and transport in microcrystalline pin solar cells studied with pulsed electrically detected magnetic resonance. *J. Non-Cryst. Solids*, **354**, 2411.
91. Boehme, C., Behrends, J., Maydell, K., Schmidt, M., and Lips, K. (2006) Investigation of hopping transport in n-a-Si:H/c-Si solar cells with pulsed electrically detected magnetic resonance. *J. Non-Cryst. Solids*, **352**, 1113.
92. Jarolimek, K., Groot, R.A., Wijs, G.A., and Zeman, M. (2009) First-principles study of hydrogenated amorphous silicon. *Phys. Rev. B: Condens. Matter Mater. Phys.*, **79**, 155206.
93. Pickard, C.J. and Mauri, F. (2002) First-principles theory of the EPR g tensor in solids: defects in quartz. *Phys. Rev. B: Condens. Matter Mater. Phys.*, **88**, 086403.

94. Gerstmann, U., Seitsonen, A.P., and Mauri, F. (2008) Ga self-interstitials in GaN investigated by ab-initio calculations of the electronic *g*-tensor. *Phys. Status Solidi B*, **245**, 924.

95. Ceresoli, D., Gerstmann, U., Seitsonen, A.P., and Mauri, F. (2010) First-principles theory of orbital magnetization. *Phys. Rev. B: Condens. Matter Mater. Phys.*, **81**, 060409.

13
Scanning Probe Microscopy on Inorganic Thin Films for Solar Cells

Sascha Sadewasser and Iris Visoly-Fisher

13.1
Introduction

Photovoltaic thin films are highly nonhomogeneous at the micron- and submicron scale, involving layers of different compositions, polycrystallinity, point, and extended defects. Spatially resolved characterization at high resolution is therefore adequate to resolve the properties of these different parts and their effect on the device properties, without averaging over the entire material. Scanning probe microscopy allows such characterization, as will be demonstrated in this chapter.

The invention of the scanning tunneling microscope (STM) by Binnig *et al*. in 1982 revolutionized the field of surface science [1]. The STM provided the means to obtain the first real space images showing atomic resolution on a Si(111) 7×7 surface. The STM uses the quantum mechanical tunneling current through a gap between a sharp metallic tip and the sample surface as a control parameter; therefore, it is limited to the study of conducting surfaces. A solution to this restriction was provided by the atomic force microscope (AFM), which employs a sharp tip supported by a cantilever beam as the measuring probe [2]. In AFM, the tip is in contact with the surface, and the deflection of the cantilever is monitored by optical beam deflection detection. Thus, the AFM also provided access to insulating surfaces. An additional technique in AFM was developed with the noncontact (or dynamic) mode [3], in which the cantilever is vibrated close to its resonance frequency. Tip–sample interaction changes the vibration amplitude or frequency, which serves as a feedback signal to maintain a constant distance to the sample surface while scanning across the sample. Forces exerted by the tip on the sample are minimal in noncontact mode; therefore, it is the method of choice for soft samples, such as biological or polymer samples.

In subsequent years the AFM was developed to a very versatile technique by combination with other measurement methods. This provided access to additional sample properties on a lateral scale in the nanometer range. Combination with the macroscopic Kelvin probe technique led to the development of the Kelvin probe force microscope (KPFM). Application of an ac bias and detection of the capacitance resulted in scanning capacitance microscopy (SCM).

Advanced Characterization Techniques for Thin Film Solar Cells, Second Edition.
Edited by Daniel Abou-Ras, Thomas Kirchartz, and Uwe Rau.

The measurement of currents in the contact mode of the AFM with an applied bias between tip and sample is the core of the conductive AFM (C-AFM). These and other techniques will be introduced in this chapter, providing the reader with the most important basics about each technique and allowing understanding experiments utilizing these techniques. Additionally, this chapter will also present some selected important results that have been obtained applying the various techniques to characterize thin-film solar cells. While only selected examples are discussed in this chapter, the interested reader is referred to the extensive list of references for further reading and exploration of the application of AFM- and STM-based techniques for the characterization of nanoscale properties of thin-film solar cell materials and devices.

13.2 Experimental Background

13.2.1 Atomic Force Microscopy

A typical AFM setup [2] consists of a probe in the shape of a cantilever with a small tip at its free end, a laser, a four-quadrant photodiode, and a scanner unit. The latter is usually constructed from piezoelectric elements. The laser beam is focused onto the back of the free end of the cantilever and from there reflected to the four-quadrant photodiode; this allows detecting the bending of the cantilever with high precision. While scanning the tip across a sample surface, the force interaction between tip and sample leads to changes either in the static bending of the cantilever (when the tip is in contact) or in the resonance frequency of the cantilever oscillation (when it is vibrated and the tip is at a small distance from the surface). The first operating mode is called contact mode and the second is called dynamic or noncontact mode. Both modes will be presented in detail in the subsequent subsections. Figure 13.1 schematically shows this basic AFM experimental setup.

The forces interacting between the tip and the sample consist of various contributions including the chemical binding force F_{chem}, the van der Waals force

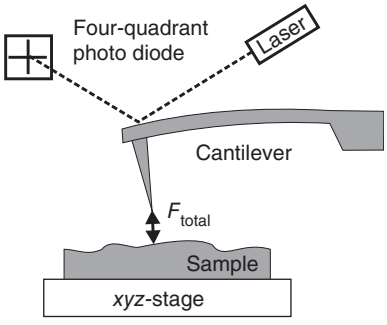

Figure 13.1 Working principle of an AFM showing the detection system, consisting of a laser and a position-sensitive photodiode, and the sample on a scanning *xyz*-stage.

F_{vdW}, electrostatic and magnetic forces, F_{el} and F_{mag}, respectively. The short-range chemical forces originate from a quantum mechanical overlap of the electron wave functions of the tip and sample surface. They can be described by an exponential distance dependence, and the interaction range is of the order of ~5 Å [4]. The long-range van der Waals force originates from electromagnetic field fluctuations. Typically, in AFM, it is described by the interaction between a sphere of radius R, representing the tip, and an infinite plane, representing the sample surface [5]:

$$F_{vdW} = -\frac{HR}{6z^2}, \tag{13.1}$$

where H is the Hamaker constant for the tip and sample materials and z the distance between the sphere and the plane. The electrostatic force F_{el} can be expressed by the capacitive force between the tip and the sample:

$$F_{el} = -\frac{1}{2}\frac{\partial C}{\partial z}V^2, \tag{13.2}$$

where C is the capacitance and V is the total voltage. In the case of AFM, only the force perpendicular to the surface along the z-direction has to be considered. More details on F_{el} will be given in Section 13.2.4, where Kelvin probe force microscopy is discussed. The magnetic force is not relevant, as only nonmagnetic tips and samples are considered here.

Chemical forces are responsible for atomic-scale contrast in AFM imaging. When experiments on a larger scale are performed, the tip–sample distance in noncontact AFM (nc-AFM) is typically larger than 5 Å and chemical forces do not have to be considered. In this case, topography imaging is governed by the long-range van der Waals and possibly by electrostatic forces.

13.2.1.1 Contact Mode

The point of contact between the tip and the sample surface is usually defined as the transition from attractive tip–surface forces (described in the previous section) to repulsive ones, originating from short-range Coulomb and Pauli repulsion between ion cores and electron clouds of atoms at the tip and the sample surfaces. Further reducing the tip–surface distance will result in a normal deflection of the cantilever, which is proportional to the repulsive force acting on it according to Hooke's law:

$$F = k_N z, \tag{13.3}$$

where k_N is the normal spring constant of the cantilever, determined by its material mechanical properties, shape, and dimensions. Typical spring constants of commercially available cantilevers range from 0.01 to 75 N/m, enabling detection of forces down to 10^{-9} N. For topography imaging, a feedback loop is used to keep the cantilever deflection constant by changing the probe height z while scanning in x and y. Thus, a nearly constant force is maintained between the tip and surface, and a map is created by recording the changes in z-position as a function of the x and y position, which can be interpreted as a topographical map. Lateral forces due to friction cause the cantilever to torque and can also

be followed by the four-quadrant photodiode. The lateral resolution of measurements is strongly dependent, among other factors, on the tip–surface contact area, which is increased as the tip and sample are driven toward each other. Several models can be used to calculate this contact area using the probe and surface mechanical properties [5]. Typically, this contact area will be circular with a diameter of 10–50 nm.

The advantages of the method include high lateral resolution and the ability to map the topography as well as adhesion forces and measure surface mechanical properties at high resolution. This scan mode is also used for conductive AFM mapping (see section 13.2.2). The disadvantages include potential harm to the tip and/or sample surface and relatively low force resolution, issues addressed by the noncontact imaging mode. Applications of contact-mode AFM mapping in thin-film solar cells include the characterization of surface morphology, grain size and shape and its distribution [6], grain orientation (by measuring the angles between grain facets) [7], surface defects, and detecting the presence of impurity particles by following the surface mechanical properties.

13.2.1.2 **Noncontact Mode**

In nc-AFM [8], the cantilever is mechanically oscillated at or close to its resonance frequency using a piezoelectric element. The four-quadrant photodiode signal is used to monitor the oscillation, which will be influenced by the tip–sample interaction. The oscillation of the cantilever is described by the equation of motion, where the tip is considered as a point-mass spring (mass m), and the motion in z-direction, perpendicular to the sample surface, is described by [5]:

$$m\ddot{z} + \frac{m\omega_0}{Q}\dot{z} + kz = F_0 \cos(\omega t) + F_{\text{total}}, \tag{13.4}$$

where Q and k describe the quality factor and spring constant of the cantilever, respectively, and F_0 and ω represent the amplitude and angular frequency of the driving force, respectively. The tip–sample interaction is given by F_{total}.

For the case of no tip–sample interaction, that is, when the tip is far away from the surface, the free resonance frequency ω_0 is given by

$$\omega_0 = \sqrt{\frac{k}{m}}, \tag{13.5}$$

where m is considered as the effective mass, which accounts for the specific geometry of the cantilever. When approaching the tip to the sample surface, forces between tip and surface become relevant; this influences the oscillation of the cantilever. As a result, the change in resonance frequency can be approximated via an effective spring constant [5]:

$$k_{\text{eff}} = k - \frac{\partial F_{\text{total}}}{\partial z}. \tag{13.6}$$

Essentially, the effective resonance frequency is modified according to the force gradient between tip and sample. For small force gradients and attractive forces, the resonance curve is shifted to lower frequencies and vice versa.

The approximation in Equation 13.6 is only valid for small oscillation amplitudes; the exact solution for larger amplitude can be found in Ref. [5].

Two different detection modes can be used in nc-AFM. In the amplitude modulation mode (AM mode), the tip–sample distance is controlled such that the oscillation amplitude remains constant [3]. For this purpose, the cantilever oscillation is excited at a constant frequency slightly off resonance. The AM mode is typically applied in measurements in air. When the AFM is introduced into a vacuum system, the quality factor Q of the cantilever increases significantly (typically above 10^5) as a result of the reduced damping. In this case, a very slow response time of the system results because of the reduced bandwidth [8]. Therefore, in vacuum typically the frequency modulation mode (FM mode) is used, in which the cantilever is always excited on resonance, and the shift of the resonance curve due to the tip–sample interaction is directly measured [8]. The resonance frequency is determined by a phase-locked loop (PLL) or a FM demodulator. The tip–sample distance is controlled by maintaining a constant frequency shift Δf with respect to the free resonance frequency f_0 of the cantilever [5]:

$$\Delta f = -\frac{f_0}{2k}\frac{\partial F_{\text{total}}}{\partial z}. \tag{13.7}$$

Both the AM and the FM modes measure the topography corresponding to a surface of constant force gradient.

13.2.2 Conductive Atomic Force Microscopy

One of the simplest ways of characterizing electrical properties at high resolution is by applying voltage between the sample and a C-AFM probe and measuring the resulting current flowing between them as a function of lateral tip location while scanning the sample surface. A current map is obtained in parallel with a topography map measured at constant force. Typically measured currents are in the range of picoampere to microampere. Conductive probes can be obtained by coating standard Si probes by a conductive layer or by making the probe entirely of conductive materials such as metals, doped diamond, or highly doped Si [9]. The coating may increase the size of the tip apex and is prone to damage by friction during scanning, whereas all-conductive probes are rare due to manufacturing difficulties. The choice of a specific conductive material also depends on work function matching between the tip and sample surface materials to reduce a possible current barrier upon contact [10]. The resolution of the current mapping is directly proportional to the tip–surface contact area, determined by the tip and surface mechanical properties and the applied force (see Section 13.2.1.1). Screening of the electrical potential limits the resolution in semiconductors to the relevant Debye length(s).

Historically, the method was developed by combining AFM with STM (see Section 13.2.5) to measure currents tunneling through an oxide layer on metal surfaces [11], which critically depend on the local oxide layer thickness, defects,

and charge traps. Such measurements require a more sensitive current amplifier, with a lower noise level, and are sometimes referred to as tunneling AFM (TUNA). Other than the characterization of dielectric films, the method can also be used to map samples of low conductivity, and typically measured currents are in the range of tens of femtoampere to hundreds of picoampere [12].

In cases where there is no significant surface current barrier (ohmic contact), and the sample can be considered a semi-infinite body of uniform resistivity, the current passes through the small probe–surface contact area and spreads laterally into a cone-shaped current path toward the large counterelectrode. The cone's dimensions and shape vary with the resistivity and homogeneity of the sample. This "spreading resistance" of the sample can be mapped by C-AFM and is referred to as scanning spreading resistance microscopy (SSRM). If an oxide layer is present on the sample surface, the tip must penetrate through it for SSRM. For a circular tip–sample contact area of radius r, the electrical resistance R is related to the SSRM measured resistivity ρ through

$$R = \frac{\rho}{4r}. \tag{13.8}$$

SSRM is commonly used to map variations in charge carrier density [13] and measures a wide range of currents (10 pA – 100 μA) often using a logarithmic current amplifier.

Examples of applications of C-AFM in inorganic thin-film solar cells include studies of current routes in these highly nonhomogeneous materials, and studying the effect of deposition parameters on the morphology–electrical properties relations in the dark and under illumination [14–17]. Photoconductive current mapping, using C-AFM under illumination, is particularly useful for correlating high-resolution current mapping with the photovoltaic device performance [18, 19]. A noted variation of this method is using scanning near-field optical microscopy (SNOM) for localized illumination while macroscopically measuring the resulting photocurrents [20].

13.2.3 Scanning Capacitance Microscopy

In SCM a conductive probe forms a capacitor with the sample surface in a configuration where no or negligible currents flow between them under bias. Small changes in the tip–sample capacitance are measured, which can be generated by changes in the tip–surface separation or by changes in the local dielectric properties of the sample. The first demonstration of the method used a profilometry-like apparatus [21] and was soon adopted in STM and nc-AFM-based systems [22, 23]. In these initial demonstrations the tip height was modulated, and variations in the capacitance, followed by a lock-in amplifier at the same frequency, were used as the input to the feedback loop, which acted to maintain a constant capacitance change by changing the tip–surface distance. The resulting map corresponded both to height variations and to changes in the dielectric properties. Nowadays, a normal force feedback in contact-mode AFM is commonly used to

control the tip–surface separation, and capacitance changes are measured, independently and simultaneously, by applying an ac bias of fixed amplitude and using lock-in detection [22, 24]. To avoid low-frequency noise of the capacitance sensor, the derivative of the capacitance with respect to bias dC/dV (phase signal) is recorded at high ac frequency, typically several kilohertz. As the capacitance with a contact area radius of a few nanometer is in the range of attofarads, the dynamic change in capacitance, that is, the derivative, is easier to measure using a special sensor circuit [22]. A circuit for direct ultralow capacitance measurements was also recently developed [25].

The charge carrier concentration in a semiconductor can be mapped using SCM and is interpreted through metal–oxide–semiconductor (MOS) capacitor physics, formed between the metal-coated probe, the semiconductor, and an intermediate dielectric surface layer such as SiO_2 (Figure 13.2). The MOS capacitance is voltage dependent, and the slope of the capacitance–voltage ($C-V$) curve depends on the type and concentration of the free charge carriers in the semiconductor. Due to the high ac frequency used for SCM detection, minority carriers cannot follow the change in voltage fast enough; hence only majority carriers affect the measured dC/dV signal. When positive bias is applied to the metal tip, electrons in an n-type semiconductor will accumulate at the semiconductor–oxide interface, and the measured capacitance will be that of the oxide layer only. When negative bias is applied to the metal tip, a depletion layer will develop in the semiconductor, acting as an additional dielectric layer in series with the oxide layer, and the capacitance will decrease. As the negative bias is increased, the depletion layer width will grow, and the capacitance will further decrease, until a breakdown field is reached. The velocity of the capacitance decrease with bias, that is, the slope of the $C-V$ curve, depends on the carrier concentration. The $C-V$ curve of a p-type semiconductor is a mirror image of that of an n-type semiconductor [10, 22]. Hence, the sign of the measured dC/dV signal points to the type of majority carriers in the device, and its magnitude can be interpreted in terms of the carrier concentration [26]. Quantification and analysis of the measured signal require detailed modeling [22] and is sometimes done by calibrating the SCM signal with similar samples of known carrier

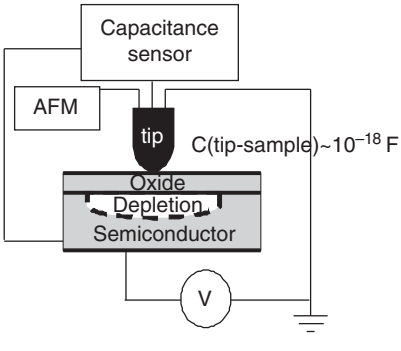

Figure 13.2 Schematic illustration of the metal–oxide–semiconductor (MOS) capacitor configuration in SCM.

concentration [27]. Metals and insulators display zero SCM signals, since their capacitance is not voltage dependent, and are thus difficult to distinguish by SCM.

The SCM resolution is determined not only by the tip–surface contact area but also by other factors such as the carrier concentration, with a lower carrier concentration resulting in wider depletion regions around the tip apex, hence lower resolution. Precise modeling can supply data at better resolution than the contact area [22]. A modification of the commonly used measurement method includes "closed loop" mapping, in which a second feedback loop is used to adjust the ac bias amplitude to preserve a constant dC/dV signal. The resulting ac bias amplitude is the measured quantity in this method. The advantage is that the depletion region width is constant hence the resolution is not modified between areas of different carrier concentrations in the sample. SCM was used to characterize inorganic thin-film solar cells despite the difficulty in modeling and quantification in nonhomogeneous materials. It was used for imaging carrier concentration profiles near grain boundaries and for detection of the electrical junction location in cross-sectional studies (see Section 13.3) [18, 28–35].

13.2.4
Kelvin Probe Force Microscopy

The KPFM uses a similar principle to the macroscopic Kelvin probe technique [36]. The electrostatic force between the AFM tip and the sample is compensated by applying a dc bias (V_{dc}) to the sample, which corresponds to the contact potential difference (CPD). The CPD is given by the work function difference between the tip and sample materials: $e \cdot V_{CPD} = \Phi_{sample} - \Phi_{tip}$ (e is the elementary charge). To detect the CPD, an additional ac bias (amplitude V_{ac}, frequency ω_{ac}) is applied (see Figure 13.3). This bias induces an oscillation of the cantilever, which results from the electrostatic force between tip and sample:

$$F_{el} = -\frac{1}{2}\frac{\partial C}{\partial z}(V_{dc} - V_{CPD} + V_{ac}\sin(\omega_{ac}t))^2. \tag{13.9}$$

Computing the square of the voltages, a spectral component at the frequency of the ac bias can be calculated as

$$F_{\omega_{ac}} = -\frac{\partial C}{\partial z}(V_{dc} - V_{CPD})V_{ac}\sin(\omega_{ac}t). \tag{13.10}$$

Additionally, a dc term F_{dc} results, which gives a constant contribution to the topography signal, and a term at frequency $2 \cdot \omega_{ac}$, which can be used to image the capacitance gradient [37]. Equation 13.10 shows that the induced oscillation of the cantilever at the frequency of the ac bias is reduced to zero when the dc bias is controlled to match the CPD. In many studies, the work function of the tip is calibrated on a reference sample with a known work function (e.g., highly oriented pyrolytic graphite, HOPG), and therefore the work function of the sample can be determined [7, 38, 39]. However, this is generally more suitable for measurements under ultrahigh vacuum (UHV) conditions since the work function of a sample is considerably modified by adsorbates and oxidation when experiments are performed in air [40].

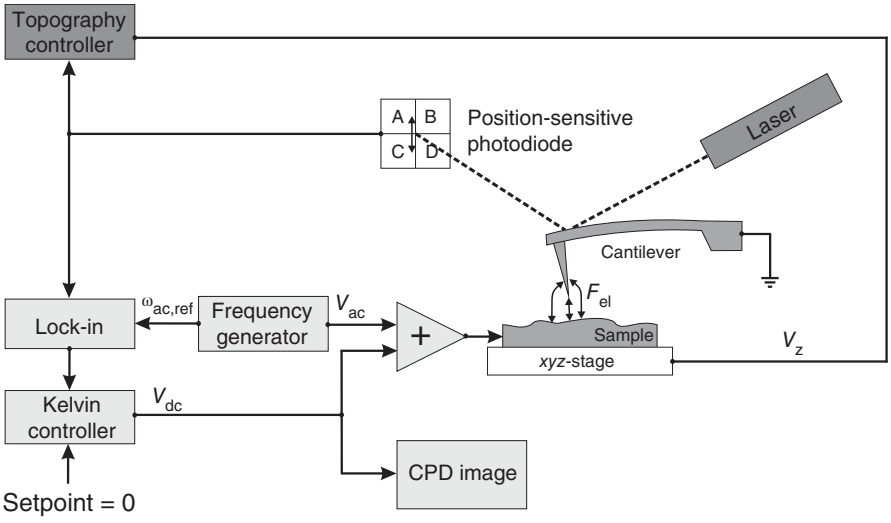

Figure 13.3 Schematic drawing of a typical KPFM setup for AM mode detection of the contact potential difference.

As in nc-AFM, KPFM measurements can also be performed in AM and FM modes. In this case, in AM mode, the dc bias is controlled by minimizing the amplitude of oscillation at ω_{ac}. For this purpose, the signal of the position-sensitive photodiode is analyzed by a lock-in amplifier tuned to the ac frequency. Frequently, ac frequencies of several kilohertz to several tens of kilohertz are used, and ac biases of 1–3 V have to be applied to get sufficient sensitivity [41, 42]. An improvement in sensitivity can be gained by tuning the ac frequency to a resonance mode of the cantilever. This resonance-enhanced detection allows using lower ac voltages, which is preferable for semiconductor samples to avoid tip-induced band bending effects [43]. One possible implementation uses a two-pass method, where in a first scan the topography is determined, and in a second scan the mechanical oscillation is switched off and instead an ac bias at the fundamental resonance is applied, while the tip retraces the same scan line [44]. A different realization uses a higher oscillation mode for the ac frequency, that is, the second oscillation mode [45, 46]; this provides the advantage of measuring simultaneously the topography and the CPD signal in one scan line. Due to a limitation of the bandwidth of the position-sensitive photodiode in many commercial AFM systems, the fundamental resonance frequency is limited to 70–80 kHz, which sets the second resonance mode at 400–470 kHz (the ratio between second and fundamental resonance frequency is ~6.3 for rectangular-shaped cantilevers) [47].

In FM mode KPFM, the ac bias-induced oscillation in the frequency shift signal Δf is used to detect the dc bias necessary to compensate the CPD. In this case, the ac bias is limited at the lower end by the bandwidth of the z-controller (if the ac bias is too low, the z-feedback will oscillate with the ac frequency), and at the higher

end by the bandwidth of the PLL or the FM demodulator (at high frequencies the Δf modulation cannot be resolved) [48]. Typically, for FM-KPFM ac frequencies between 1 and 3 kHz and ac voltages of 1 – 3 V are used.

The main difference between AM- and FM-KPFM is that AM-KPFM is sensitive to the electrostatic force, while FM-KPFM is sensitive to the electrostatic force gradient. As a consequence, the spatial resolution in AM-KPFM is limited due to the long-range character of the electrostatic forces [48, 49]. In this case, the electrostatic interaction between tip and sample is not confined to the tip apex but also part of the tip cone and possibly the cantilever contribute to the interaction and therefore decrease the spatial resolution [48, 50]. The FM mode promises to provide a better spatial resolution due to the more confined character of the electrostatic force gradient [48 – 50]. However, using resonance-enhanced AM-KPFM, recently even atomic-scale contrast in the CPD was demonstrated [51].

13.2.5
Scanning Tunneling Microscopy

The STM was the first development of a series of scanning probe microscopy methods and gained the inventors [1] the Nobel Prize in 1986. In STM the AFM probe consisting of a cantilever and tip is replaced by a sharp conducting tip. Typically, a PtIr or W sharpened wire is used as tip material. The tip is then approached to the sample until a tunneling current is detected. This quantum mechanical tunneling current shows an exponential distance dependence:

$$I \propto \rho_s V \mathrm{e}^{-2\kappa d}, \tag{13.11}$$

where ρ_s is the density of states of the sample close to the Fermi energy, V the applied voltage, d the distance between the tip and the sample, and κ is given by

$$\kappa = \frac{\sqrt{2m(U-E)}}{\hbar}, \tag{13.12}$$

where U is the vacuum barrier. From Equation 13.11 it becomes clear that the tunneling current is very sensitive to the distance between the tip and the sample surface. Thus, a distance controller can be used to adjust the tip – sample distance to maintain a constant tunneling current. It is important to recognize that STM does not image the surface morphology directly but rather represents a convolution of the electronic surface properties with the morphology. The map obtained by STM corresponds to a surface of constant density of electronic states. This is especially important when atomic-scale images are obtained.

An additional experimental possibility of STM is to perform spectroscopy measurements by maintaining the tip – sample distance constant (by switching off the feedback circuit) and performing a bias sweep of the applied voltage. Such a voltage spectroscopy measurement ramps the voltage from low to high values and provides information about the electronic structure of the sample surface. For negative voltages, electrons tunnel from occupied states of the sample into empty states of the tip. When the voltage increases, beyond the valence band

maximum, the tunneling current vanishes, as the Fermi level of the tip aligns within the bandgap of the sample. Only when the bias voltage is large (positive) enough, that is, when the Fermi level of the tip aligns with the conduction band minimum, electrons can tunnel from the tip into empty states in the conduction band of the sample. Thus, under ideal conditions, the bandgap of the sample can be locally determined. However, such measurements are easily impeded by surface defect states, tip-induced band bending, and surface contamination.

13.2.6 Issues of Sample Preparation

Thin-film solar cells are typically characterized by a rough top surface, which is coated by an electrical contact electrode in the completed device. This surface, lacking the contact, is typically used for scanning probe mapping using the methods described previously. Surface roughness can cause various artifacts in scanning probe microscopy. For example, changes in the local contact area at rough areas may locally change the signal in contact-mode AFM, C-AFM, and SCM, although no changes in the sample properties are present. Another effect is changes in the electrical field distribution at sharp features. A possible solution is to mechanically or chemically polish the sample surface. However, the resulting flat surface may not represent the true thin-film properties in the solar cell device, in which the film did not undergo polishing. Alternatively, rough surfaces can be characterized, provided variations in the mapped property are shown to be topography independent. This can be done, for example, by comparison to other samples with similar topography but different electrical properties or by showing that the property of interest varies with the measurement parameters.

Special care has to be taken when mapping cross-section samples of cleaved thin-film inorganic solar cells. Fracturing a multilayered, polycrystalline sample is likely to result in large height differences between the different layers. Such differences are hard to accommodate in a single AFM scan and should be avoided as much as possible. A way to achieve a relatively flat cross section is by fracturing the sample while the film is under tensile stress and the substrate is under compressive stress, as described in Ref. [52]. Polishing of such a cross section can be problematic since the different material layers may polish at different rates, and soft layer materials may spread over other layers' cross sections [9].

SCM requires careful surface preparation of the semiconductor, such that the oxide layer thickness is thick enough to block significant currents but thin enough to maximize the dC/dV signal. The oxide should effectively passivate semiconductor surface states and be free of charge traps, which significantly affect the measurement in SCM [22, 53].

It should be noted that many artifacts may affect mapping of electronic properties using AFM-based methods, which are different in different methods, and should be taken into account in the analysis of the obtained results. For example, C-AFM mapping of semiconductor surfaces at high bias may induce oxide formation on the scanned surface, attributed to chemical reactions induced

by the electric field involving the water layer adsorbed on the sample surface due to ambient humidity [17, 54]. This may affect subsequent mapping and can be avoided by using lower bias and/or scanning in a controlled humidity or vacuum environment.

13.3 Selected Applications

This chapter serves to describe a few examples of the application of the various scanning probe microscopy techniques and thereby allows the reader to see what kind of information is accessible by the various methods.

13.3.1 Surface Homogeneity

Typical thin-film solar cells employ a stack of various semiconductor and metal layers forming the device structure. After generation of the electron–hole pair by light absorption in the absorber material, it is separated in the built-in electric field of the p–n junction. In thin-film solar cells, the electronic p–n junction frequently coincides with a material junction or is very close to it. Thus, the main electronic transport is perpendicular to the material junctions, and charge carriers have to cross the interfaces of the layers. From an electronic point of view, this implies the transition of electric fields (represented by curvature of the bands in a band diagram) and band offsets due to interface dipoles (represented by vertical offsets in the band diagram). It is therefore highly important to study the spatial homogeneity of a material interface to obtain information of local variations in band bending or band offsets. One possible access to such information is to study the surface of the absorber material prior to the deposition of the subsequent layer. An example of this approach for a $CuGaSe_2$ absorber was presented by Sadewasser *et al*. [7] using KPFM. For this purpose a comparative study of $CuGaSe_2$ deposited on a Mo/glass substrate and on a ZnSe(110) single-crystalline substrate was performed [7]. Figure 13.4a and b shows the topography and work function of the $CuGaSe_2$/Mo/glass thin film, respectively. Comparison of the two images shows that areas of distinct and constant work function can be associated with specifically oriented facets of the individual grains seen in the topography image. A better understanding of this observation is gained by the experiments on the oriented $CuGaSe_2$ thin film on the ZnSe(110) substrate. By X-ray diffraction, the [220] direction of $CuGaSe_2$ was determined to be perpendicular to the substrate surface. Also here, the work function image (Figure 13.4d) shows areas of distinct but constant work function, where these areas coincide with specific facets as observed by comparison to the topography image in Figure 13.4c. The known orientation of the film in this case was used to perform a detailed analysis of the geometric angles between various facets of single grains and the substrate orientation. By this geometric analysis, the orientation of various facets could be

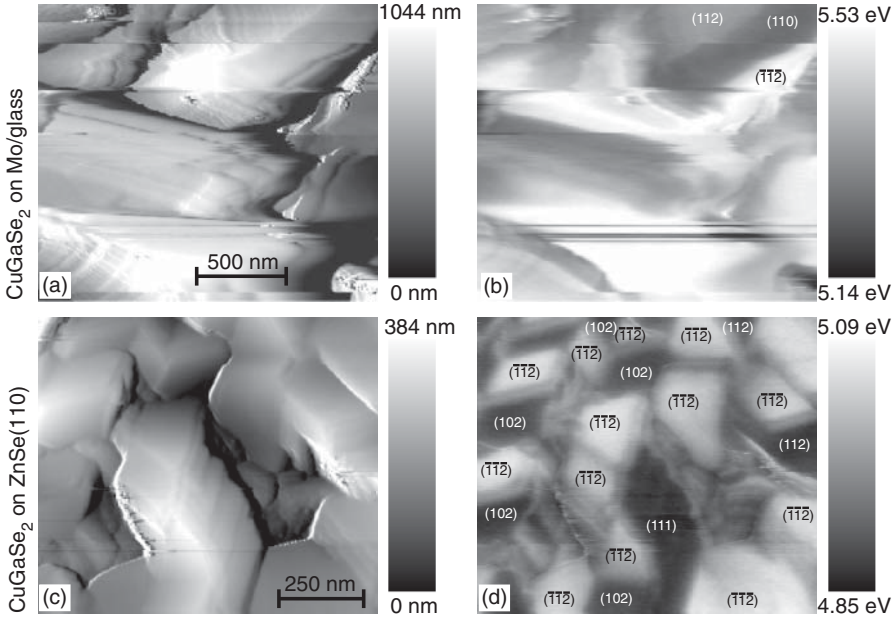

Figure 13.4 KPFM measurements on $CuGaSe_2$ thin films showing the different work function of differently oriented facets of individual grains [7]. (a) Topography of a $CuGaSe_2$ thin film on Mo/glass with height variations (grayscale) of 1044 nm and (b) the corresponding work function image ($\Delta\Phi = 5.14 - 5.53$ eV) with some indicated facet orientations. (c) Topography of $CuGaSe_2$ on ZnSe(110) with height variations of 384 nm and (d) the corresponding work function image ($\Delta\Phi = 4.85 - 5.09$ eV) with indicated facet orientations.

determined and is indicated in the work function image in Figure 13.4d. It is apparent that a majority of the facets show a {112} or $\{\overline{1}12\}$ orientation; this orientation is known to preferentially develop during crystal growth [55]; therefore it is not surprising to also frequently find this facet orientation in the present experiments.

The presence of distinct work function values for differently oriented facets can be explained by a surface dipole. This dipole will sensitively depend on the specific surface structure, that is, the atomic arrangement, surface relaxation, and reconstruction [56]. Specifically, the {112} facet is metal terminated, whereas the $\{\overline{1}12\}$ plane is Se terminated, which explains the assignment of the lower work function facets to the metal-terminated {112} facet.

Characterization of film morphology as a function of its deposition parameters is the most common use of scanning probe microscopy in thin-film inorganic solar cells [57]. Detection of currents routes in microcrystalline Si via C-AFM and STM mapping enabled Azulay *et al.* to develop a comprehensive model of conduction as a function of the crystalline content, resulting from the manufacturing conditions [58–60]. The optimized crystalline content for solar cell operation is suggested to be associated with a specific connectivity of a conductive structural network [59]. Ginger *et al.* [61] used a combination of KPFM and elemental

mapping by scanning electron microscopy/energy dispersive X-ray spectroscopy (SEM/EDS) to correlate local variations in the work function with stoichiometry changes in $Cu_2ZnSn(S,Se)_4$ films deposited from nanocrystal-based ink. They found that areas with a higher S/(S+Se) content showed a significantly higher work function, which was related to changes in the bandgap and a higher concentration of acceptor-like defects, harming the device operation efficiency [61].

When characterizing photovoltaic devices, it is also useful to study the surface homogeneity under illumination, which can point to photoactive defects and to subsurface inhomogeneities. Examples of such characterization were demonstrated using photovoltage mapping in SNOM of microcrystalline Si and $Cu(In,Ga)Se_2$/CdS/ZnO solar cells [62, 63]. In both cases, areas of lower photoresponse that are not related to clear topographical features, with dimensions of 100–250 nm, were noted. Such phenomena may arise not only from surface defects but also from defects in the internal, subsurface electrical junction, and reduce the effective active area of the device.

13.3.2 Grain Boundaries

Grain boundaries present the significant difference between poly- and single-crystalline material and likely influence material properties and consequently device performance. Crystal defects and impurities at grain boundaries can induce localized energy states within the bandgap, leading to trapped, localized charges. These form an electrostatic potential barrier (band bending) for majority carrier transport across grain boundaries [64], as well as enhanced recombination of photogenerated carriers [65]. Indeed, KPFM and SCM showed inconsistent charging of some grain boundaries in microcrystalline photovoltaic Si films, which was explained by the presence of impurities [32, 34], and photoconductive AFM mapping of a-Si:H films showed lower photocurrents near grain boundaries [19]. On the other hand, segregation of defects and impurities to the grain boundaries may be beneficial for improving the grain's crystalline quality. Characterizing a *single* GB using scanning probe microscopy obviates the need to average over different grain boundary lengths and directions, and over the entire inhomogeneous material, as is the case of macroscopic measurements. In some cases such characterization leads to realizing that the grain boundary potential profiles might be beneficial for the devices' photovoltaic performance, as described in the following. In the case of chalcopyrite-based solar cells, different models have been used to understand the physics of grain boundaries and their effect on device performance [64, 66–70]. KPFM has been used to study the electronic properties of grain boundaries, providing an excellent tool to access the properties of individual grain boundaries even in polycrystalline films with a typical grain size of the order of ~1 μm [71–76]. The main result of all these studies is the observation of a lower work function at the grain boundaries, with a drop of about 100 mV. As an example for these studies, we show results on a $CuGaSe_2$ absorber in Figure 13.5a–d. The sample was studied by UHV-KPFM, where the

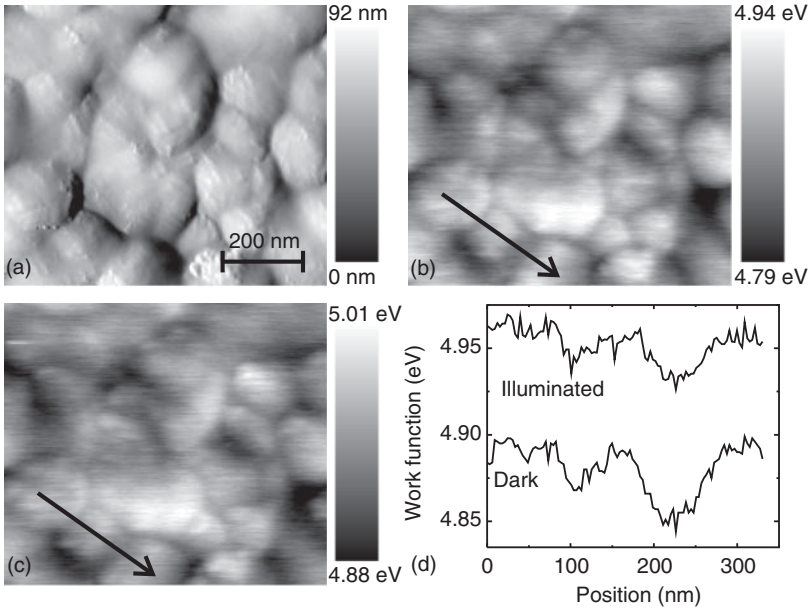

Figure 13.5 KPFM measurement on the back side of a $CuGaSe_2$ absorber film peeled off in UHV [74]. (a) Topography (height range = 92 nm), (b) work function in the dark ($\Delta\Phi = 4.79 - 4.94$ eV), (c) work function under illumination ($\Delta\Phi = 4.88 - 5.01$ eV). (d) Line profiles of the work function in the dark and under illumination along the line shown in (b) and (c).

measurements were taken on the backside of the absorber, obtained by peeling off the $CuGaSe_2$ thin film from the Mo/glass substrate inside the UHV [74, 77]. This ensures a clean and nonoxidized sample surface. The topography and work function of this surface are shown in Figure 13.5a and b, respectively. Clearly, a dip in the work function is observed along grain boundaries. Under illumination, the contrast of the work function image looks very similar (see Figure 13.5c); however, the values are elevated with respect to the dark measurement. This is also illustrated by the line profiles shown in Figure 13.5d showing two grain boundaries with a differently deep work function dip. Also the change of the work function dip under illumination is different for the two grain boundaries. This indicates that differently oriented grain boundaries have different electronic properties.

The shape of the work function decrease at $CuGaSe_2$ grain boundaries, observed in the previously presented experiments as well as many others, is in agreement with a space charge region, providing evidence for the presence of charged defects with a concentration of the order of $10^{11} - 10^{12}$ cm^{-2} [71]. More recent studies of $Cu(In,Ga)Se_2$ have reported grain boundaries exhibiting no potential change in addition to grain boundaries with upward band bending [33, 35, 78–80]. It was shown by simulations of the spatial resolution of KPFM that care has to be taken regarding absolute values of the band bending deduced from the potential change

at grain boundaries [81, 82]. Using a correction scheme to account for the limited resolution due to the long-range electrostatic forces acting in KPFM, Baier *et al*. extracted corrected values for the band bending with values up to ~400 mV, both for up- and downward band bending [80]. Cahen *et al*. noted that p- to n-type inversion at grain boundaries occurred more frequently in films with Ga-poor stoichiometry, while decreased such inversion was correlated with poorer current collection in devices with Ga-rich compositions [35]. Yang *et al*. showed that excess sulfurization degraded the grain boundary passivation in $Cu(In,Ga)Se_2$ [83].

A correlation between structural and electronic properties has also been achieved by investigation of single grain boundaries grown on epitaxial substrates [84–86]. These samples provided the possibility to comparatively investigate the grain boundary properties by electron backscatter diffraction (EBSD), Hall effect, and KPFM. On a $CuGaSe_2$ bicrystal containing a twin grain boundary [84, 85], no change of the work function was observed by KPFM, whereas for a higher disorder Σ9 grain boundary, a downward band bending was measured [86]. For both grain boundaries, Hall effect measurements showed a barrier for majority carrier transport, which led to the conclusion that a neutral barrier is present at the Σ3 twin grain boundary. This transport barrier can be represented as a localized offset in the band structure, which was supported by electron holography experiments and results from the lower valence electron density at the grain boundary [87]. The neutral barrier at the twin grain boundary is in agreement with theoretical predictions [66, 88]. These findings could also be confirmed on polycrystalline $CuInSe_2$ of device quality by combining KPFM with EBSD measurements on the same sample position [89]. C-AFM was used to identify current routes in photovoltaic thin films, and such current routes were found along grain boundaries in $CuInSe_2$ and $Cu(In,Ga)Se_2$ polycrystalline films deposited on glass/Mo substrates when the top surface (prior to CdS deposition) was mapped [15]. Using bias-dependent C-AFM mapping in the dark and under illumination, Azulay *et al*. showed evidence for grain boundary band bending in the order of 100 mV, in agreement with KPFM measurements, by a change in polarity of the measured photocurrent at that bias. However, higher currents observed along grain boundaries in the dark may imply an inversion of the dominant carrier type at the boundaries, requiring a much larger band bending there, of the order of 400 mV. The authors propose a spatially narrow band offset of 300 mV, which adds to the 100 mV band bending but is narrower than the KPFM spatial resolution hence cannot be detected. Current flow through the grains was mapped only at significantly higher bias (above 1 V), supporting this band offset [15]. Downward band bending was also detected by KPFM on $Cu_2ZnSn(S,Se)_4$ absorber layers [90], and these potential profiles were later correlated with enhanced minority carrier collection near grain boundaries by C-AFM [91].

Hole depletion near CdTe grain boundaries was previously deduced from measurements of a single grain boundary in a bicrystal and from macroscopic lateral transport measurements in CdTe polycrystalline films, with grain boundary

barrier heights ranging from 0.1 to 0.8 eV [92–95]. Visoly-Fisher *et al.* used a combination of several AFM-based methods for the electrical characterization of CdTe grain boundaries in CdTe/CdS solar cells [28, 96, 97]. Direct evidence for grain boundary depletion was obtained from SCM, showing brighter SCM signals (lower hole concentration) at the grain boundaries compared with those at the grain surface (Figure 13.6a), and from KPFM showing lower work function values at grain boundaries than the outer CdTe grain surface. The hole depletion width changed from one grain boundary to another, and extended for 100–300 nm on each side of the grain boundary, which is of the order of the Debye length (150 nm) in CdTe with a bulk charge carrier concentration of 7×10^{14} cm^{-3} [28]. Further mapping with high-resolution probes using C-AFM and SCM under illumination showed evidence for carrier-type inversion at the grain boundary core: surprisingly high photocurrents were observed at the cores of most grain boundaries, as well as SCM signals approaching zero at the core (Figure 13.6a), typical of insulating materials (with negligible concentration of free carriers, as in the case of inversion of the type of majority carriers) [97]. These unique grain boundary

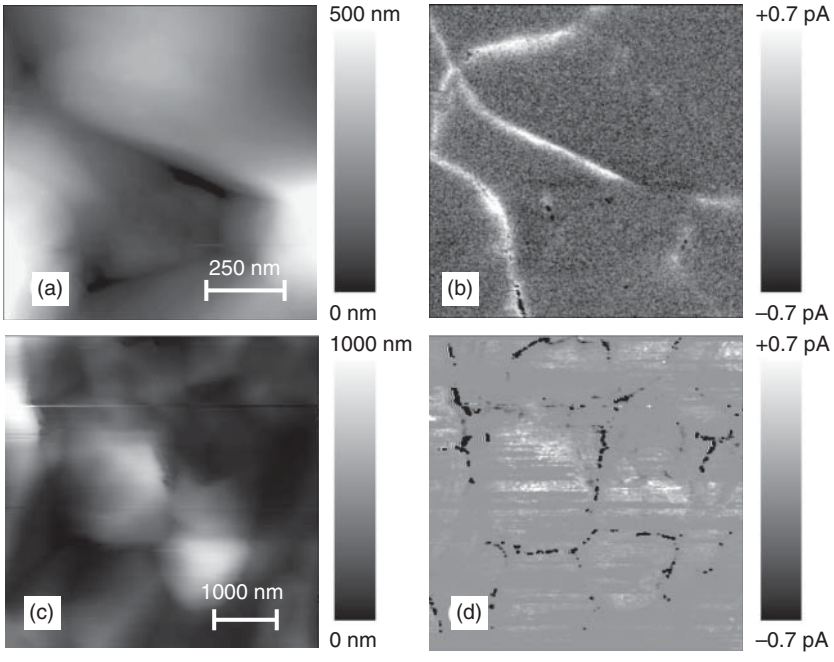

Figure 13.6 Mapping of the CdTe surface in CdTe/CdS cells without the back contact under illumination [96, 97]. (Copyright Wiley-VCH Verlag GmbH & Co. KGaA. Reproduced with permission). Simultaneously collected (a) AFM topography and (b) SCM images. Note the GB at the bottom left corner showing a lower SCM signal at its core. Scan size 2×2 μm, height range = 500 nm. Simultaneously collected (c) AFM topography and (d) C-AFM images. Scan size $5\ \mu m \times 5\ \mu m$, height range = 1000 nm, V_{dc} (CdTe) = 0.5 V (slightly lower than the cell's V_{oc}), current range = −0.7 to 0.7 pA. The current at GB cores is at opposite polarity to that at grain surfaces.

electronic properties develop during the $CdCl_2$ treatment used in the manufacture of CdTe/CdS cells [17, 96]. It was later found by C-AFM that the {111} Σ3 twin grain boundaries are more beneficial to microcurrent transport than other grain boundaries [98] and that long wavelength absorption is enhanced near CdTe grain boundaries, presumably due to a smaller bandgap [20].

Variations in the mapped photocurrent in CdTe/CdS samples as a function of applied bias generally followed those observed in cells, that is, the current reversed direction near the open-circuit voltage, V_{oc}. At grain boundary cores, however, a smaller bias was needed to reverse the current direction (Figure 13.6d), indicating a lower barrier in the CdTe/CdS junction at the points of intersection of grain boundaries with the junction compared with that away from these intersections. Thus, V_{oc}(grain boundary) < V_{oc}(grain surface), and the cell junction can be viewed as a series of junctions of varying barrier heights connected in parallel. Decreased V_{oc} at the grain boundaries is an additional evidence for depletion at grain boundaries [96]. The authors suggested that the unique doping profile that forms near grain boundaries is beneficial for cell performance by assisting in separation of photogenerated electron–hole pairs, followed by improved electron transport via the grain boundary core toward the junction. In this way, CdTe grain boundaries decrease the recombination rate (by improving the crystalline quality of the bulk because of gettering of defects, accompanied by a low recombination rate at the grain boundary core) and also increase the electron diffusion length in the absorber [96, 97].

13.3.3
Cross-Sectional Studies

The electronic working principle of a solar cell device can be illustrated and analyzed along the band diagram of the structure. However, experimental determination of the band diagram of a device is very difficult if not impossible. With techniques such as photoemission spectroscopy (see other chapters in this book), this problem is approached from the interface point of view. KPFM can be used to follow a different approach. The measurement of the work function along the cross section of a complete device provides valuable information about the electronic properties of the different layers [31, 38], the presence of impurity phases [99], and built-in electric fields [32, 79, 100–102].

As one example of cross-sectional KPFM, we illustrate here the investigation of the Ga-distribution in a $Cu(In_{1-x},Ga_x)S_2$ solar cell device [103]. A study by SEM/EDS showed that the absorber exhibits two distinct layers, where the $Cu(In_{1-x},Ga_x)S_2$ shows a significantly higher Ga content toward the Mo back contact and a significantly higher In content toward the CdS buffer layer. KPFM imaging was performed on the very same position of the cross section, thus allowing comparing the obtained electronic information to the compositional one. The KPFM image of the CPD and a line profile across the various layers are shown in Figure 13.7a and b, respectively. Clearly a higher work function for the back part of the absorber is observed. The fairly sharp transition between

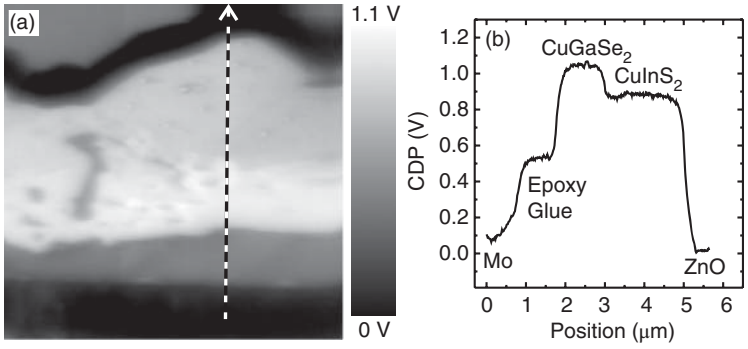

Figure 13.7 KPFM measurement on the cross section of a complete Mo/Cu(In_{1-x},Ga_x)S_2/CdS/ZnO solar cell device [103]. (a) Contact potential difference (CPD) image showing the variation with the different layers (color scale = 1.1 V). (b) Line profile of the CPD along the line in (a), clearly showing the different CPD for the In-rich front and the Ga-rich back part of the absorber.

the two work function regions coincides with the transition from the In- to the Ga-rich part of the absorber layer. This increase of the electric potential indicates the presence of a built-in electric field, which is oriented such that it accelerates electrons toward the In-rich region of the absorber layer and therefore keeps them away from the back contact of the solar cell. This proves the existence of a back surface field in the device, which reduces recombination at the back contact. The quantum efficiency (QE) of the device reveals an increased QE for photons with energies near the bandgap, which are absorbed deep inside the absorber. For the generated electron–hole pairs, collection is improved by the presence of this back surface field [103].

The metallurgical junction in heterojunction thin-film solar cells, defined by a change in overall chemical composition, does not necessarily coincide with the electronic junction, defined by the change in electrical properties. In the CdTe/CdS cell, Te from CdTe and Cu from the cell's back contact may, at sufficiently high concentrations, type-convert CdS [104]. S diffusion into the CdTe may type-convert some of the p-CdTe. Both effects would lead to a buried homo- rather than a heterojunction. Visoly-Fisher *et al*. have shown, by a combination of SCM and KPFM cross-section mapping, that the cell is a heterojunction, within the experimental uncertainty (50 nm), with no evidence for CdS-type conversion [29]. Figure 13.8 shows the layer sequence in the cell: the insulating glass substrate is coated with a low-resistance (LR) SnO_2:F layer of 300–500 nm thick. This layer shows unstable, noisy SCM signal probably related to unwanted current flow in the sensor circuit, due to high conductivity and lack of a surface dielectric layer, resulting in erroneous SCM results. The adjacent n-type layer (dark SCM signal under any dc bias between −2 and +2 V) consists of both a high-resistance (HR) SnO_2 layer and the CdS layer, which are electronically indistinguishable. A structure lacking the CdS layer showed a layer sequence similar to that of

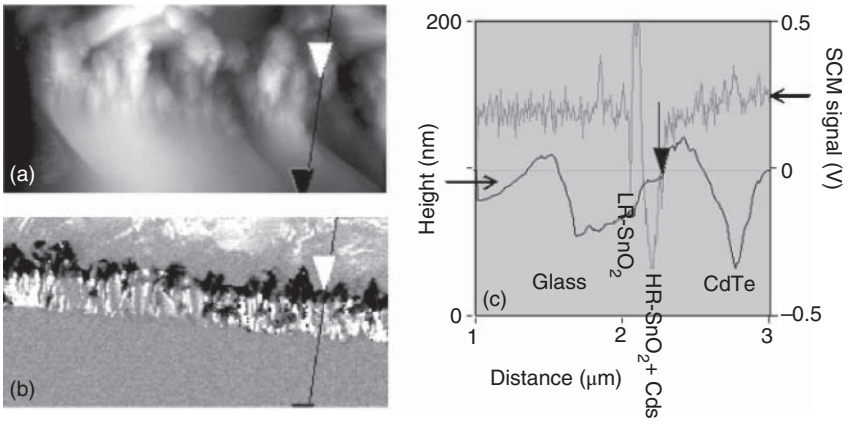

Figure 13.8 Glass/SnO_2:F/CdS/CdTe cell cross-section mapping [29]. (a) Topography image and (b) SCM image, taken simultaneously. (Reprinted with permission from Ref. [26]. Copyright [2003], American Institute of Physics.) The gray color of the glass substrate denotes a "zero" SCM signal of an insulator. Brighter colors denote p-type semiconductors; darker colors denote n-type semiconductors. Scan size $2\,\mu m \times 4\,\mu m$, $V_{ac} = 1\,V$, $V_{dc} = 0\,V$. (c) SCM and topography line profiles of the cross section. The lines in the images (a, b) indicate the locations of the line profiles. The black arrow in the line profiles shows the location of the white triangular markers in the images. At this point the metallurgical junction and the electronic junction are shown to coincide. The metallurgical junction is identified by the transition point between the layers in the topography image, and a sharp change in slope in the topography line section, and the electronic junction is identified as the transition point between bright positive, p-type signal to dark negative, n-type signal in the SCM image and zero SCM signal in the SCM line section.

a conventional cell, but with a 50–80 nm thinner n-type layer, adjacent to the CdTe. A layer of CdTe grains with very weak (almost zero) SCM signal is seen adjacent to the HR-SnO_2/CdS layer, 200–350 nm thick. These are interpreted to be recrystallized and regrown CdTe grains due to cell processing [105]. The SCM signal shows clear p-type behavior further into the CdTe layer.

A KPFM profile without external bias (not shown) indicates the change in CPD between the different layers expected from their different work functions [29]. The junction's built-in electric field is shown by a drop in the KPFM signal across certain layers, otherwise expected to show a constant signal related to their work function. Such voltage drop is noted across the HR-SnO_2 layer, indicating that this layer supports the junction's built-in electric field/open-circuit voltage. This indicates that to support the high open-circuit voltage, the n-type layer must have some minimal thickness (around 300 nm in the cells studied here). The role of the HR-SnO_2 that replaces part of the CdS is to improve the cell's blue response, due to its larger bandgap, and make good electrical contact to CdS, due to alignment of the conduction band minima. A thin CdS layer is still needed to provide a photovoltaic junction with low defect concentration and high open-circuit voltage [106]. This work demonstrates how combined SCM and KPFM of

CdTe/CdS cells show the location of the internal junctions and the roles of different layers in the structure.

13.4 Summary

Thin-film solar cells are made of complex materials, hence the prediction of device properties cannot rely on the properties of model systems and simple junction physics. Physical characterization of the polycrystalline films in use requires the understanding of their spatially resolved properties on the nanoscale. Such characterization, provided by scanning probe microscopy in its numerous variations, in combination with macroscopic analysis, can link the material properties and device performance and allow proper optimization of its energy conversion efficiency.

Acknowledgments

Iris Visoly-Fisher is grateful to David Cahen and Sidney R. Cohen for their contribution to results presented in this chapter. Sascha Sadewasser acknowledges support from Thilo Glatzel, David Fuertes Marrón, Marin Rusu, Roland Mainz, and Martha Ch. Lux-Steiner.

References

1. Binnig, G., Rohrer, H., Gerber, C., and Weibel, E. (1982) Surface studies by scanning tunneling microscopy. *Phys. Rev. Lett.*, **49**, 57–61.
2. Binnig, G., Quate, C.F., and Gerber, C. (1986) Atomic force microscopy. *Phys. Rev. Lett.*, **56**, 930–933.
3. Martin, Y., Williams, C.C., and Wickramasinghe, H.K. (1987) Atomic force microscope-force mapping and profiling on a sub 100-A scale. *J. Appl. Phys.*, **61**, 4723–4729.
4. Pérez, P., Payne, M.C., Stich, I., and Terukura, K. (1997) Role of covalent tip-surface interactions in noncontact atomic force microscopy on reactive surfaces. *Phys. Rev. Lett.*, **78**, 678–681.
5. García, R. and Pérez, R. (2002) Dynamic atomic force microscopy methods. *Surf. Sci. Rep.*, **47**, 197–301.
6. Al-Jassim, M.M., Yan, Y., Moutinho, H.R., Romero, M.J., Dhere, R.D., and Jones, K.M. (2001) TEM, AFM, and cathodoluminescence characterization of CdTe thin films. *Thin Solid Films*, **387**, 246–250.
7. Sadewasser, S., Th, G., Rusu, M., Jager-Waldau, A., and Lux-Steiner, M.C. (2002) High-resolution work function imaging of single grains of semiconductor surfaces. *Appl. Phys. Lett.*, **80**, 2979–2981.
8. Albrecht, T.A., Grütter, P., Horne, D., and Rugar, D. (1991) Frequency modulation detection using high-Q cantilevers for enhanced force microscope sensitivity. *J. Appl. Phys.*, **69**, 668–673.
9. Oliver, R.A. (2008) Advances in AFM for the electrical characterization of semiconductors. *Rep. Prog. Phys.*, **71**, 076501.

10. Sze, S.M. (1981) *Physics of Semiconductor Devices*, 2nd edn, Wiley-Interscience, New York.
11. Morita, S., Ishizaka, T., Sugawara, Y., Okada, T., Mishima, S., Imai, S., and Mikoshiba, N. (1989) Surface conductance of metal surfaces in air studied with a force microscope. *Jpn. J. Appl. Phys.*, **28**, L1634–L1636.
12. De Wolf, P., Brazel, E., and Erickson, A. (2001) Electrical characterization of semiconductor materials and devices using scanning probe microscopy. *Mater. Sci. Semicond. Process.*, **4**, 71–76.
13. De Wolf, P., Clarysse, T., Vandervorst, W., Snauwaert, J., and Hellemans, L. (1996) One- and two-dimensional carrier profiling in semiconductors by nanospreading resistance profiling. *J. Vac. Sci. Technol. B*, **14**, 380–385.
14. Shen, Z.H., Gotoh, T., Eguchi, M., Yoshida, N., Itoh, T., and Nonomura, S. (2007) Study of nano-scale electrical properties of hydrogenated microcrystalline silicon solar cells by conductive atomic force microscope. *Jpn. J. Appl. Phys.*, **46, Part 1**, 2858–2864.
15. Azulay, D., Millo, O., Balberg, I., Schock, H.W., Visoly-Fisher, I., and Cahen, D. (2007) Current routes in polycrystalline $CuInSe_2$ and $Cu(In,Ga)Se_2$ films. *Sol. Energy Mater. Sol. Cells*, **91**, 85–90.
16. Cavallini, A., Cavalcoli, D., Rossi, M., Tomasi, A., Pizzini, S., Chrastina, D., and Isella, G. (2007) Defect analysis of hydrogenated nanocrystalline Si thin films. *Phys. Rev. B: Condens. Matter Mater. Phys.*, **401**, 519–522.
17. Moutinho, H.R., Dhere, R.G., Jiang, C.S., Al-Jassim, M.M., and Kazmerski, L.L. (2006) Electrical properties of CdTe/CdS solar cells investigated with conductive atomic force microscopy. *Thin Solid Films*, **514**, 150–155.
18. Sadewasser, S., Abou-Ras, D., Azulay, D., Baier, R., Balberg, I., Cahen, D., Cohen, S., Gartsman, K., Ganesan, K., Kavalakkatt, J., Li, W., Millo, O., Rissom, T., Rosenwaks, Y., Schock, H.W., Schwarzman, A., and Unold, T. (2011) Nanometer-scale electronic and microstructural properties of grain boundaries in $Cu(In,Ga)Se_2$. *Thin Solid Films*, **519**, 7341–7346.
19. Kawai, M., Kawakami, T., Inaba, T., Ohashi, F., Natsuhara, H., Itoh, T., and Nonomura, S. (2010) Nano-scale current voltage characteristics of thin film solar cell with light irradiations. *Curr. Appl. Phys.*, **10**, S392–S394.
20. Leite, M.S., Abashin, M., Lezec, H.J., Gianfrancesco, A., Talin, A.A., and Zhitenev, N.B. (2014) Nanoscale imaging of photo current and efficiency in CdTe solar cells. *ACS Nano.*, **8**, 11883–11890.
21. Matey, J.R. and Blanc, J. (1985) Scanning capacitance microscopy. *J. Appl. Phys.*, **57**, 1437–1444.
22. Williams, C.C. (1999) Two-dimensional dopant profiling by scanning capacitance microscopy. *Annu. Rev. Mater. Sci.*, **29**, 471–504.
23. Williams, C.C., Hough, W.P., and Rishton, S.A. (1989) Scanning capacitance microscopy on a 25 nm scale. *Appl. Phys. Lett.*, **55**, 203–205.
24. Barrett, R.C. and Quate, C.F. (1991) Charge storage in a nitride-oxide-silicon medium by scanning capacitance microscopy. *J. Appl. Phys.*, **70**, 2725–2733.
25. Lee, D.T., Pelz, J.P., and Bhushan, B. (2002) Instrumentation for direct, low frequency scanning capacitance microscopy, and analysis of position dependent stray capacitance. *Rev. Sci. Instrum.*, **73**, 3525–3533.
26. Duhayon, N., Clarysse, T., Eyben, P., Vandervorst, W., and Hellemans, L. (2002) Detailed study of scanning capacitance microscopy on cross-sectional and beveled junctions. *J. Vac. Sci. Technol. B*, **20**, 741–746.
27. Smoliner, J., Basnar, B., Golka, S., Gornik, E., Loffler, B., Schatzmayr, M., and Enichlmair, H. (2001) Mechanism of bias-dependent contrast in scanning-capacitance-microscopy images. *Appl. Phys. Lett.*, **79**, 3182–3184.
28. Visoly-Fisher, I., Cohen, S.R., and Cahen, D. (2003) Direct evidence for grain-boundary depletion in polycrystalline CdTe from nanoscale-resolved measurements. *Appl. Phys. Lett.*, **82**, 556–558.

29. Visoly-Fisher, I., Cohen, S.R., Cahen, D., and Ferekides, C.S. (2003) Electronically active layers and interfaces in polycrystalline devices: cross-section mapping of CdS/CdTe solar cells. *Appl. Phys. Lett.*, **83**, 4924–4926.
30. Maknys, K., Ulyashin, A.G., Stiebig, H., Kuznetsov, A.Y., and Svensson, B.G. (2006) Analysis of ITO thin layers and interfaces in heterojunction solar cells structures by AFM, SCM and SSRM methods. *Thin Solid Films*, **511**, 98–102.
31. Matsumura, K., Fujita, T., Itoh, H., and Fujita, D. (2014) Characterization of carrier concentration in CIGS solar cells by scanning capacitance microscopy. *Meas. Sci. Technol.*, **25**, 044020.
32. Heath, J.T., Jiang, C.S. and Al-Jassim, M.M. (2010) *Diffused Junctions in Multicrystalline Silicon Solar Cells Studied by Complementary Scanning Probe Microscopy and Scanning Electron Microscopy Techniques*. 35th IEEE Photovoltaic Specialists Conference, pp. 227–232.
33. Jiang, C.S., Contreras, M.A., Repins, I., Moutinho, H.R., Yan, Y., Romero, M.J., Mansfield, L.M., Noufi, R., and Al-Jassim, M.M. (2012) How grain boundaries in Cu(In,Ga)Se_2 thin films are charged: Revisit. *Appl. Phys. Lett.*, **101**, 4.
34. Jiang, C.S., Moutinho, H.R., Liu, F., Romero, M.J., Al-Jassim, M.M. and IEEE, (2009) *Carrier Depletion and Grain Misorientations on Individual Grain Boundaries of Polycrystalline Si Thin Films*, 34th IEEE Photovoltaic Specialists Conference, vols 1–3, 2009, IEEE: New York. pp. 2106–2111.
35. Li, W.J., Cohen, S.R., Gartsman, K., and Cahen, D. (2012) Ga composition dictates macroscopic photovoltaic and nanoscopic electrical characteristics of Cu($In_{1-X}Ga_X$)Se_2 thin films via grain-boundary-type inversion. *IEEE J. Photovoltaics*, **2**, 191–195.
36. Kelvin, L. (1898) Contact electricity of metals. *Philos. Mag.*, **46**, 82.
37. Hochwitz, T., Henning, A.K., Levey, C., Daghlian, C., Slinkman, J., Never, J., Kaszuba, P., Gluck, R., Wells, R., Pekarik, J., and Finch, R. (1996) Imaging integrated circuit dopant profiles with the force-based scanning Kelvin probe microscope. *J. Vac. Sci. Technol. B*, **14**, 440.
38. Glatzel, T., Fuertes Marrón, D., Schedel-Niedrig, T., Sadewasser, S., and Lux-Steiner, M.C. (2002) $CuGaSe_2$ solar cell cross section studied by Kelvin probe force microscopy in ultra high vacuum. *Appl. Phys. Lett.*, **81**, 2017.
39. Sadewasser, S. (2006) Surface potential of chalcopyrite films measured by KPFM. *Phys. Status Solidi A*, **203**, 2571–2580.
40. Nonnenmacher, M., O'Boyle, M.P., and Wickramasinghe, H.K. (1991) Kelvin probe force microscopy. *Appl. Phys. Lett.*, **58**, 2921–2923.
41. Shikler, R., Meoded, T., Fried, N., Mishori, B., and Rosenwaks, Y. (1999) Two-dimensional surface band structure of operating light emitting devices. *J. Appl. Phys.*, **86**, 107–113
42. Shikler, R., Meoded, T., Fried, N., and Rosenwaks, Y. (1999) Potential imaging of operating light-emitting devices by Kelvin force microscopy. *Appl. Phys. Lett.*, **74**, 2972–2974.
43. McEllistrem, M., Haase, G., Chen, D., and Hamers, R.J. (1993) Electrostatic sample–tip interactions in the scanning tunneling microscope. *Phys. Rev. Lett.*, **70**, 2471–2474.
44. Rosenthal, P.A., Yu, E.T., Pierson, R.L., and Zampardi, P.J. (2000) Characterization of $Al_xGa_{1-x}As$/GaAs heterojunction bipolar transistor structures using cross-sectional scanning force microscopy. *J. Appl. Phys.*, **87**, 1937–1942.
45. Sommerhalter, C., Matthes, T.W., Glatzel, T., Jäger-Waldau, A., and Lux-Steiner, M.C. (1999) High-sensitivity quantitative Kelvin probe microscopy by noncontact ultra-high-vacuum atomic force microscopy. *Appl. Phys. Lett.*, **75**, 286–288.
46. Kikukawa, A., Hosaka, S., and Imura, R. (1996) Vacuum compatible high-sensitive Kelvin probe force microscopy. *Rev. Sci. Instrum.*, **67**, 1463–1467.

47. Butt, H.-J. and Jaschke, M. (1995) Calculation of thermal noise in atomic force microscopy. *Nanotechnology*, **6**, 1–7.
48. Glatzel, T., Sadewasser, S., and Lux-Steiner, M.C. (2003) Amplitude of frequency modulation-detection in Kelvin probe force microscopy. *Appl. Surf. Sci.*, **210**, 84–89.
49. Colchero, J., Gil, A., and Baró, A.M. (2001) Resolution enhancement and improved data interpretation in electrostatic force microscopy. *Phys. Rev. B: Condens. Matter Mater. Phys.*, **64**, 245403-1-11.
50. Zerweck, U., Loppacher, C., Otto, T., Grafström, S., and Eng, L.M. (2005) Accuracy and resolution limits of Kelvin probe force microscopy. *Phys. Rev. B: Condens. Matter Mater. Phys.*, **71**, 125424-1-9.
51. Enevoldsen, G.H., Glatzel, T., Christensen, M.C., Lauritsen, J.V., and Besenbacher, F. (2008) Atomic scale Kelvin probe force microscopy studies of the surface potential variations on the TiO_2(110) Surface. *Phys. Rev. Lett.*, **100**, 236104-1-4.
52. Ballif, C., Moutinho, H.R., Hasoon, F.S., Dhere, R.G., and Al-Jassim, M.M. (2000) Cross-sectional atomic force microscopy imaging of polycrystalline thin films. *Ultramicroscopy*, **85**, 61–71.
53. Bowallius, O. and Anand, S. (2001) Evaluation of different oxidation methods for silicon for scanning capacitance microscopy. *Mater. Sci. Semicond. Process.*, **4**, 81–84.
54. Avouris, P., Hertel, T., and Martel, R. (1997) Atomic force microscope tip-induced local oxidation of silicon: kinetics, mechanism, and nanofabrication. *Appl. Phys. Lett.*, **71**, 285–287.
55. Jaffe, J.E. and Zunger, A. (2001) Defect-induced nonpolar-to-polar transition at the surface of chalcopyrite semiconductors. *Phys. Rev. B: Condens. Matter Mater. Phys.*, **64**, 241304-1-4.
56. Mönch, W. (1993) *Semiconductor Surfaces and Interfaces*, *Springer Series in Surface Science*. vol. 26, Springer Verlag, Berlin.
57. Durose, K., Asher, S.E., Jaegermann, W., Levi, D., McCandless, B.E., Metzger, W., Moutinho, H., Paulson, P.D., Perkins, C.L., Sites, J.R., Teeter, G., and Terheggen, M. (2004) Physical characterization of thin-film solar cells. *Prog. Photovolt.: Res. Appl.*, **12**, 177–217.
58. Rezek, B., Stuchlik, J., Fejfar, A., and Kocka, J. (2002) Microcrystalline silicon thin films studied by atomic force microscopy with electrical current detection. *J. Appl. Phys.*, **92**, 587–593.
59. Azulay, D., Balberg, I., Chu, V., Conde, J.P., and Millo, O. (2005) Current routes in hydrogenated microcrystalline silicon. *Phys. Rev. B: Condens. Matter Mater. Phys.*, **71**, 113304-1-4.
60. Azulay, D., Millo, O., Savir, E., Conde, J.P., and Balberg, I. (2009) Microscopic and macroscopic manifestations of percolation transitions in a semiconductor composite. *Phys. Rev. B: Condens. Matter Mater. Phys.*, **80**, 245312-1-20.
61. Salvador, M., Vorpahl, S.M., Xin, H., Williamson, W., Shao, G.Z., Karatay, D.U., Hillhouse, H.W., and Ginger, D.S. (2014) Nanoscale surface potential variation correlates with local S/Se ratio in solution-processed CZTSSe solar cells. *Nano Lett.*, **14**, 6926–6930.
62. McDaniel, A.A., Hsu, J.W.P., and Gabor, A.M. (1997) Near-field scanning optical microscopy studies of Cu(In,Ga)Se_2 solar cells. *Appl. Phys. Lett.*, **70**, 3555–3557.
63. Gotoh, T., Yamamoto, Y., Shen, Z., Ogawa, S., Yoshida, N., Itoh, T., and Nonomura, S. (2009) Nanoscale characterization of microcrystalline silicon solar cells by scanning near-field optical microscopy. *Jpn. J. Appl. Phys.*, **48**, 091202-1-4.
64. Seto, J.Y.W. (1975) The electrical properties of polycrystalline silicon films. *J. Appl. Phys.*, **46**, 5247–5254.
65. Fahrenbruch, A.L. and Bube, R.H. (1983) *Fundamentals of Solar Cells: Photovoltaic Solar Energy Conversion*, Academic Press, New York.
66. Persson, C. and Zunger, A. (2003) Anomalous grain boundary physics in polycrystalline $CuInSe_2$: the existence of a hole barrier. *Phys. Rev. Lett.*, **91**, 266401-1-4.

67. Yan, Y., Jiang, C.-S., Noufi, R., Wei, S.-H., Moutinho, H.R., and Al-Jassim, M.M. (2007) Electrically benign behavior of grain boundaries in polycrystalline $CuInSe_2$ films. *Phys. Rev. Lett.*, **99**, 235504.
68. Metzger, W.K. and Gloeckler, M. (2005) The impact of charged grain boundaries on thin-film solar cells and characterization. *J. Appl. Phys.*, **98**, 063701-1-10.
69. Gloeckler, M., Sites, J.R., and Metzger, W.K. (2005) Grain-boundary recombination in $Cu(In,Ga)Se_2$ solar cells. *J. Appl. Phys.*, **98**, 113704-1-10.
70. Taretto, K., Rau, U., and Werner, J.H. (2005) Numerical simulation of grain boundary effects in $Cu(In,Ga)Se_2$ thin-film solar cells. *Thin Solid Films*, **480–481**, 8.
71. Sadewasser, S., Glatzel, T., Schuler, S., Nishiwaki, S., Kaigawa, R., and Lux-Steiner, M.C. (2003) Kelvin probe force microscopy for the nano scale characterization of chalcopyrite solar cell materials and devices. *Thin Solid Films*, **431–432**, 257.
72. Jiang, C.-S., Noufi, R., AbuShama, J.A., Ramanathan, K., Moutinho, H.R., Pankow, J., and Al-Jassim, M.M. (2004) Local built-in potential on grain boundary of $Cu(In,Ga)Se_2$ thin films. *Appl. Phys. Lett.*, **84**, 3477.
73. Jiang, C.-S., Noufi, R., Ramanathan, K., AbuShama, J.A., Moutinho, H.R., and Al-Jassim, M.M. (2004) Does the local built-in potential on grain boundaries of $Cu(In,Ga)Se_2$ thin films benefit photovoltaic performance of the device? *Appl. Phys. Lett.*, **85**, 2625.
74. Fuertes Marrón, D., Sadewasser, S., Glatzel, T., Meeder, A., and Lux-Steiner, M.C. (2005) Electrical activity at grain boundaries of $Cu(In,Ga)Se_2$ thin films. *Phys. Rev. B: Condens. Matter Mater. Phys.*, **71**, 033306.
75. Jiang, C.-S., Noufi, R., Ramanathan, K., Moutinho, H.R., and Al-Jassim, M.M. (2005) Electrical modification in $Cu(In,Ga)Se_2$ thin films by chemical bath deposition process of CdS films. *J. Appl. Phys.*, **97**, 053701.
76. Hanna, G., Glatzel, T., Sadewasser, S., Ott, N., Strunk, H.P., Rau, U., and Werner, J.H. (2006) Texture and electronic activity of grain boundaries in $Cu(In,Ga)Se_2$ thin films. *Appl. Phys. A*, **82**, 1.
77. Fuertes Marrón, D., Meeder, A., Sadewasser, S., Würz, R., Kaufmann, C.A., Glatzel, T., Schedel-Niedrig, T., and Lux-Steiner, M.C. (2005) Lift-off process and rear-side characterization of $CuGaSe_2$ chalcopyrite thin films and solar cells. *J. Appl. Phys.*, **97**, 094915.
78. Baier, R., Lehmann, J., Lehmann, S., Rissom, T., Alexander Kaufmann, C., Schwarzmann, A., Rosenwaks, Y., Lux-Steiner, M.C., and Sadewasser, S. (2012) Electronic properties of grain boundaries in $Cu(In,Ga)Se_2$ thin films with various Ga-contents. *Sol. Energy Mater. Sol. Cells*, **103**, 86–92.
79. Zhang, Z., Tang, X., Kiowski, O., Hetterich, M., Lemmer, U., Powalla, M., and Holscher, H. (2012) Reevaluation of the beneficial effect of $Cu(In,Ga)Se_2$ grain boundaries using Kelvin probe force microscopy. *Appl. Phys. Lett.*, **100**, 203903.
80. Baier, R., Leendertz, C., Abou-Ras, D., Lux-Steiner, M.C., and Sadewasser, S. (2014) Properties of electronic potential barriers at grain boundaries in $Cu(In,Ga)Se_2$ thin films. *Sol. Energy Mater. Sol. Cells*, **130**, 124–131.
81. Leendertz, C., Streicher, F., Lux-Steiner, M.C., and Sadewasser, S. (2006) Evaluation of Kelvin probe force microscopy for imaging grain boundaries in chalcopyrite thin films. *Appl. Phys. Lett.*, **89**, 113120.
82. Baier, R., Leendertz, C., Lux-Steiner, M.C., and Sadewasser, S. (2012) Toward quantitative Kelvin probe force microscopy of nanoscale potential distributions. *Phys. Rev. B: Condens. Matter Mater. Phys.*, **85**, 165436.
83. Yang, J., Lee, D., Huh, K., Jung, S., Lee, J., Lee, H., Baek, D., Kim, B., Kim, D., Nam, J., Kim, G., and Jo, W. (2015) Influence of surface properties on the performance of $Cu(In,Ga)(Se,S)_2$ thin-film solar cells using Kelvin probe force microscopy. *RSC Adv.*, **5**, 40719–40725.

84. Siebentritt, S., Sadewasser, S., Wimmer, M., Leendertz, C., Eisenbarth, T., and Lux-Steiner, M.C. (2006) Evidence for a neutral grain-boundary barrier in chalcopyrites. *Phys. Rev. Lett.*, **97**, 146601.
85. Siebentritt, S., Eisenbarth, T., Wimmer, M., Leendertz, C., Streicher, F., Sadewasser, S., and Lux-Steiner, M.C. (2007) A Σ3 grain boundary in an epitaxial chalcopyrite film. *Thin Solid Films*, **515**, 6168.
86. Hafemeister, M., Siebentritt, S., Albert, J., Lux-Steiner, M.C., and Sadewasser, S. (2010) Large neutral barrier at grain boundaries in chalcopyrite thin films. *Phys. Rev. Lett.*, **104**, 196602.
87. Schmidt, S.S., Abou-Ras, D., Sadewasser, S., Yin, W., Feng, C., and Yan, Y. (2012) Electrostatic potentials at $Cu(In,Ga)Se_2$ grain boundaries: experiment and simulations. *Phys. Rev. Lett.*, **109**, 095506.
88. Persson, C. and Zunger, A. (2005) Compositionally induced valence-band offset at the grain boundary of polycrystalline chalcopyrites creates a hole barrier. *Appl. Phys. Lett.*, **87**, 211904.
89. Baier, R., Abou-Ras, D., Rissom, T., Lux-Steiner, M.C., and Sadewasser, S. (2011) Symmetry-dependence of electronic grain boundary properties in polycrystalline $CuInSe_2$ thin films. *Appl. Phys. Lett.*, **99**, 172102.
90. Kim, G.Y., Jeong, A.R., Kim, J.R., Jo, W., Son, D.-H., Kim, D.-H., and Kang, J.-K. (2014) Surface potential on grain boundaries and intragrains of highly efficient $Cu_2ZnSn(S,Se)_4$ thin-films grown by two-step sputtering process. *Sol. Energy Mater. Sol. Cells*, **127**, 129–135.
91. Li, J.B., Chawla, V., and Clemens, B.M. (2012) Investigating the role of grain boundaries in CZTS and CZTSSe thin film solar cells with scanning probe microscopy. *Adv. Mater.*, **24**, 720–723.
92. Thorpe, T.P. Jr.,, Fahrenbruch, A.L., and Bube, R.H. (1986) Polycrystalline cadmium telluride. *J. Appl. Phys.*, **60**, 3622–3630.
93. Durose, K., Boyle, D., Abken, A., Ottley, C.J., Nollet, P., Degrave, S., Burgelman, M., Wendt, R., Beier, J., and Bonnet, D. (2002) Key aspects of CdTe/CdS solar cells. *Phys. Status Solidi B*, **229**, 1055–1064.
94. Vigil-Galán, O., Valliant, L., Mendoza-Perez, R., Contreras-Puente, G., and Vidal-Larramendi, J. (2001) Influence of the growth conditions and postdeposition treatments upon the grain boundary barrier height of CdTe thin films deposited by close spaced vapor transport. *J. Appl. Phys.*, **90**, 3427–3431.
95. Woods, L.M., Levi, D.H., Kaydanov, V., Robinson, G.Y. and Ahrenkiel, R.K. (1998) *Electrical Characterization of CdTe Grain-Boundary Properties from As Processed CdTe/CdS Solar Cells*, 2nd World Conference on Photovoltaic Solar energy Conversion, (eds J. Schmid, *et al.*), European Commission: Vienna, Austria. pp. 1043–1046.
96. Visoly-Fisher, I., Cohen, S.R., Gartsman, K., Ruzin, A., and Cahen, D. (2006) Understanding the beneficial role of grain boundaries in polycrystalline solar cells from single-grain-boundary scanning probe microscopy. *Adv. Funct. Mater.*, **16**, 649–660.
97. Visoly-Fisher, I., Cohen, S.R., Ruzin, A., and Cahen, D. (2004) How polycrystalline devices can outperform single-crystal ones: thin film CdTe/CdS solar cells. *Adv. Mater.*, **16**, 879–883.
98. Li, H., Liu, X.X., Lin, Y.S., Yang, B., and Du, Z.M. (2015) Enhanced electrical properties at boundaries including twin boundaries of polycrystalline CdTe thin-film solar cells. *Phys. Chem. Chem. Phys.*, **17**, 11150–11155.
99. Fuertes Marrón, D., Glatzel, T., Meeder, A., Schedel-Niedrig, T., Sadewasser, S., and Lux-Steiner, M.C. (2004) Electronic structure of secondary phases in Cu-rich $CuGaSe_2$ solar cell devices. *Appl. Phys. Lett.*, **85**, 3755.
100. Glatzel, T., Steigert, H., Sadewasser, S., Klenk, R., and Lux-Steiner, M.C. (2005) Potential distribution of $Cu(In,Ga)(S,Se)_2$-solar cell cross-sections measured by Kelvin probe force microscopy. *Thin Solid Films*, **480–481**, 177.
101. Zhang, Z., Hetterich, M., Lemmer, U., Powalla, M., and Holscher, H.

(2013) Cross sections of operating $Cu(In,Ga)Se_2$ thin-film solar cells under defined white light illumination analyzed by Kelvin probe force microscopy. *Appl. Phys. Lett.*, **102**, 023903.

102. Zhang, Z., Tang, X., Lemmer, U., Witte, W., Kiowski, O., Powalla, M., and Holscher, H. (2011) Analysis of untreated cross sections of $Cu(In,Ga)Se_2$ thin-film solar cells with varying Ga content using Kelvin probe force microscopy. *Appl. Phys. Lett.*, **99**, 042111.

103. Mainz, R., Streicher, F., Abou-Ras, D., Sadewasser, S., Klenk, R., and Lux-Steiner, M.C. (2009) Combined analysis of spatially resolved electronic structure and composition on a cross-section of a thin film $Cu(In_{1-x}Ga_x)S_2$ solar cell. *Phys. Status Solidi A*, **206**, 1017.

104. Bonnet, D. (1970) Preparation and properties of polycrystalline CdS_xTe_{1-x} films. *Phys. Status Solidi A*, **3**, 913–919.

105. Durose, K., Cousins, M.A., Boyle, D.S., Beier, J., and Bonnet, D. (2002) Grain boundaries and impurities in CdTe/CdS solar cells. *Thin Solid Films*, **403–404**, 396.

106. McCandless, B.E. (2001) *Thermochemical and Kinetic Aspects of Cadmium Telluride Solar Cell Processing*. II–VI Compound Semiconductor Photovoltaic Materials Symposium at the MRS Spring Meeting (eds R. Birkmire, *et al.*). MRS, Warrendale, PA, H1.6.1-12.

14
Electron Microscopy on Thin Films for Solar Cells

Daniel Abou-Ras, Melanie Nichterwitz, Manuel J. Romero, and Sebastian S. Schmidt

14.1
Introduction

Electron microscopy and its related techniques, be it on bulk samples in scanning electron microscopy (SEM) or on thin specimens in transmission electron microscopy (TEM), provides the possibilities not only to image positions of interest down to the angstroms range but also to analyze microstructures, compositions, as well as electrical and optoelectronic properties of individual layers and their interfaces in thin-film solar cells. It is the motivation of the present chapter to give an overview of these various techniques applied in SEM and TEM, highlighting their possibilities and also limitations. Also, an introduction into sample preparation for electron microscopy is given, which is often underestimated but eventually decides on the quality of the image data acquired and analysis results obtained.

Figure 14.1 represents an overview of the various electron and photon emissions occurring upon interaction of the impinging electron beam with a semiconducting thin film. The analysis techniques for these emission signals will be introduced in the following subsections.

14.2
Scanning Electron Microscopy

SEM is the technique applied most frequently for imaging of thin-film solar cells. Corresponding modern microscopes provide insight into layer thicknesses, surface topographies, and various other features in solar-cell thin-film stacks with resolutions down to below 1 nm. Also very frequently, scanning electron microscopes are equipped with energy-dispersive X-ray detectors, which are used for analyzing local elemental compositions in thin films. However, the possibilities of analysis in SEM go far beyond imaging and compositional analysis.

Advanced Characterization Techniques for Thin Film Solar Cells, Second Edition.
Edited by Daniel Abou-Ras, Thomas Kirchartz, and Uwe Rau.

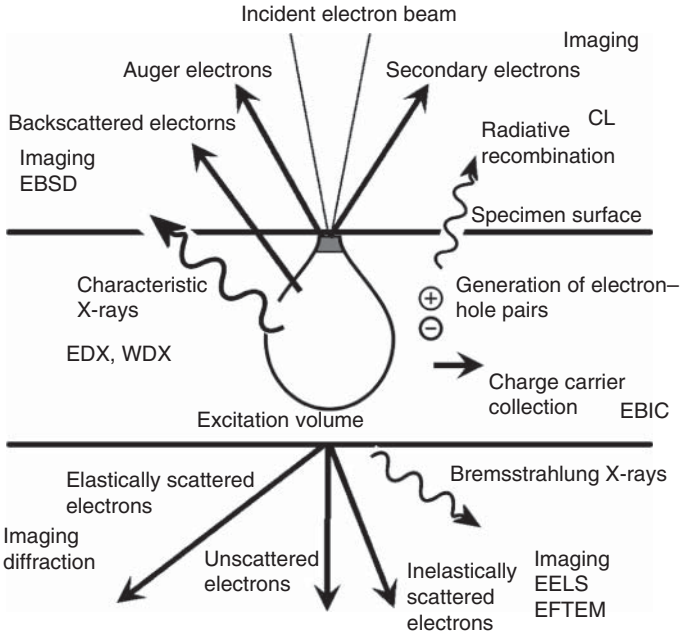

Figure 14.1 Various electron and photon emissions upon irradiation of a semiconducting specimen by an electron beam. Indicated are also the techniques making use of these emissions, that is, electron backscatter diffraction (EBSD), energy-dispersive spectrometry (EDX) and wavelength-dispersive X-ray spectrometry (WDX), cathodoluminescence (CL), electron-beam-induced current (EBIC) measurements, electron energy-loss spectroscopy (EELS), and energy-filtered TEM (EFTEM).

The present chapter gives an overview of the various imaging and analysis techniques applied on a scanning electron microscope. It will be shown that imaging is divided into that making use of secondary electrons (SEs) and of backscattered electrons (BSEs), resulting in different contrasts in the images and thus providing information on compositions, microstructures, and surface potentials. Also, it will be demonstrated how important it is to combine various techniques on identical sample positions in order to enhance the interpretation of the results obtained from applying individual SEM techniques.

Of particular importance for all SEM techniques are the energy of the incident electron beam E_b (adjusted via the acceleration voltage) and the electron-beam current I_B, which is adjusted by the current through the filaments of thermionic electron guns such as W or LaB_6 cathodes or by apertures for microscopes with field-emission guns. The electron-beam energy E_b defines the penetration depth R into the specimen material, which may be approximated via the empirical expression [1] $R = 4.28 \times 10^{-2}\,\mu\text{m}[\rho/(g/\text{cm}^3)]^{-1}(E_b/\text{keV})^{1.75}$, where ρ is the average density of the specimen material. On the other hand, the electron-beam current I_B affects the number of electrons per second in the electron beam and thus the electron-injection rate into the sample.

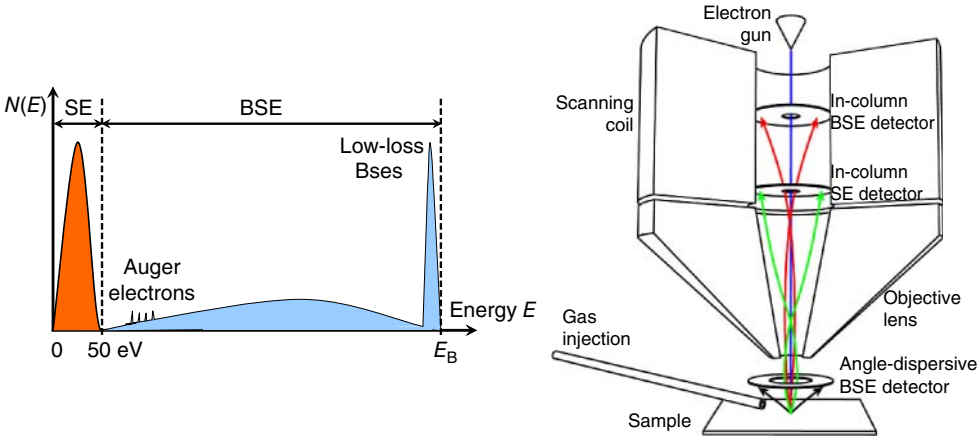

Figure 14.2 (a) Energy distribution of scattered SEs and BSEs. The spectrum features also peaks related to Auger electrons. (b) The electron trajectories in a typical scanning electron microscope, equipped with SE and BSE detectors as well as with a gas-injection system.

Electrons are focused by a series of electromagnetic lenses, resulting in electron-probe diameters on the specimen surface of down to below 1 nm. Scanning coils move the focused beam across the sample surface. Further extensive introductions into SEM and its related techniques can be found in various text books (e.g., Ref. [2]).

14.2.1 Imaging Techniques

Electrons used for imaging in a scanning electron microscope are either secondary electrons (SEs) or BSEs. Both types of electrons are emitted from the specimen upon electron irradiation (Figure 14.2). The emission spectrum also contains contributions from Auger electrons (used for surface analysis of samples; see Chapter 18 and Section 19.3), which are emitted after ionization of an inner-core shell, as alternative to characteristic X-rays (see Section 14.2.3). By convention, SEs exhibit energies between 0 and 50 eV, whereas BSEs cover the energy range between 50 eV and the energy of the primary beam E_b.

SEs are mostly collected outside of the microscope column by a positively biased collector grid and then accelerated on a scintillator layer in front of a photomultiplier (note that also low-energy BSEs are thus detected). Due to their very small exit depths of few nanometers and also due to the fact that the SE yield depends on the tilt of a given surface element, SEs are used to image the surface topography.

SEs are retarded by a positive bias and repelled by a negative one at the sample surface. Also, these electrons are affected by the electrical field present owing to differently biased regions. Thus, negatively charged regions appear bright and positively charged areas dark. Therefore, it is possible to obtain a voltage contrast and also information on the local doping [3].

SEs may also be detected inside the microscope column by use of annular detectors. As much as the electron beam is focused by the series of electrostatic and magnetic lenses when running from top to bottom, it is spread energetically when emitted from the specimen and traveling up the microscope column. SEs and BSEs exhibit substantially different trajectories, and therefore, two corresponding annular detectors at different vertical positions in the column may be used (Figure 14.2). Images recorded by the in-column SE detector rather contain information from the surface.

The in-column BSE detector collects mainly Rutherford-type BSEs, that is, multiple elastically scattered BSEs (by nucleus–electron interaction), emitted into rather small angles with respect to the impinging electron beam, and the energy of these BSEs depends on the atomic number Z. This is why the technique is often referred to as Z contrast imaging, that is, it allows for detecting phases exhibiting differences in Z. Additional energy filtering of these BSEs may reveal even small variations in compositions [4].

Apart from Rutherford-type BSEs, also Mott-type (single elastically scattered) BSEs are emitted, however, at much larger angles (with respect to the impinging beam). The exit volume is therefore also smaller, that is, the BSEs are emitted close to the surface, and in consequence, the corresponding detector is positioned just beneath the end pole piece of the microscope. Modern microscopes provide lens systems which separate the Mott BSEs, emitted at very large angles (>60°), from the Rutherford-type BSEs scattered into smaller angles [5]. Therefore, the contribution from Z contrast in the Mott BSE image is reduced substantially. Rather, the images exhibit a crystallographic contrast, also termed channeling contrast, resulting from the fact that the yield in BSEs is high when atomic columns in a grain are oriented (nearly) parallel to the trajectories of the BSEs, that is, the crystal forms channels for the BSEs. Then, the corresponding grain appears bright in the BSE image (else, lower intensities are obtained in the images). Sometimes, it is possible to obtain a channeling contrast also by use of an SE detector, which forms since channeled BSEs may lead to the release of SEs, carrying on the crystallographic contrast.

The use of gases injected on the specimen during imaging is an important issue, since, for example, in case of cross-sectional thin-film solar-cell specimens, the SEM imaging may be complicated by use of insulating materials such as glass or plastic foil substrates. The idea is to introduce a gas, for example, N_2, which is then cracked by the impinging electron beam, reducing charges present on the specimen surface. That is, the impinging electron beam is not substantially deflected, which may have considerable consequences on imaging and analysis.

14.2.2
Electron Backscatter Diffraction

BSEs may not only be used for imaging of thin films but also give information on crystal symmetry and orientation when diffracted at corresponding sets of atomic planes. This is the principle of electron backscatter diffraction (EBSD) [6], which

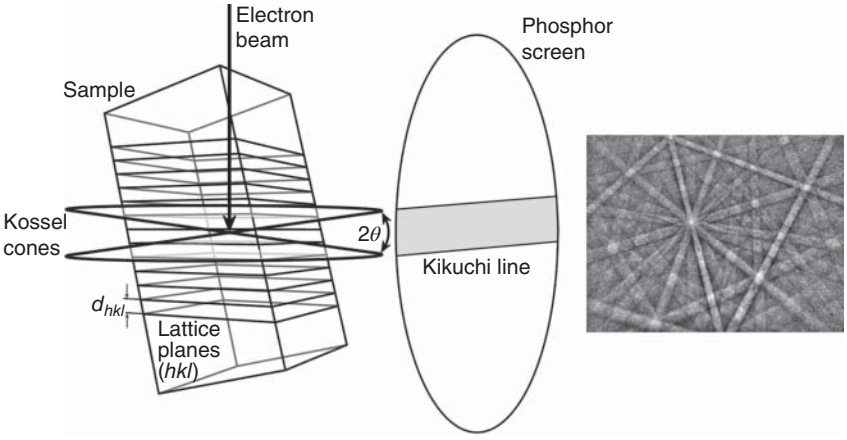

Figure 14.3 Schematics of the EBSD measurement (left) and a EBSD pattern from a $Cu(In,Ga)Se_2$ crystal (right).

is depicted in the schematics in Figure 14.3. When an electron beam impinges into a crystal residing within a polycrystalline thin film, BSEs are emitted in all directions, that is, some of these electrons meet the Bragg condition for a specific set of atomic planes in the crystal. Electron beams diffracted at a specific set of atomic planes form, when emerging from the specimen, a band on a planar detector, that is, a charge-coupled device (CCD) camera with a thin scintillator layer. The bands of the various sets of atomic planes in a crystal result in a diffraction pattern, which is referred to as Kikuchi or EBSD pattern.

It is apparent from Figure 14.3 that the sample surface is tilted substantially off the position perpendicular to the electron beam, which is done in order to reduce the absorption of BSEs by the surrounding material. The tilt angle usually applied of about 70° is a trade-off between reducing absorption of BSEs and still obtaining good resolution of the EBSD patterns. In a fully automated EBSD system, the positions (corresponding to the interplanar angles) and widths (related to the Bragg angles) of few bands are identified, and these bands are then indexed by comparison with simulated patterns from specific crystals. In order to increase the speed of evaluation, the diffraction bands in a given EBSD pattern are transformed to peaks in a radius–angle coordinate system, the so-called Hough space [6]. In present EBSD systems, EBSD patterns can be acquired and indexed at various points of a mesh, when scanning across a region of interest on the specimen, at velocities of up to above 600 patterns per second, resulting in an EBSD map.

It is important to point out that EBSD is a very surface-sensitive technique. In spite of the fact that at, for example, 20 kV, the penetration depth of the electron beam may be few micrometers for the typical absorber materials in inorganic thin-film solar cells, the exit depths for the BSEs contributing to the EBSD patterns are only few tens of nanometers. Therefore, the quality of the EBSD patterns and hence that of the EBSD maps depends mainly on the quality of the surface preparation of the specimen (see Section 14.4 for details). A very thin graphite layer

(few nanometers) on top of a polished cross-sectional specimen has shown to aid in preserving the surface for several weeks and also in reducing the drift during the EBSD measurement.

Since the local orientation of a crystal (with respect to a reference coordinate system) at a specific measuring point in the map can be identified, the EBSD patterns can be evaluated such that the EBSD map represents the local-orientation distribution, given by colors (see Figure 14.4, top, and legend therein). When acquiring EBSD patterns on a large area of about of 1 mm^2 or larger, integral film textures can be extracted which compare to those from texture measurements by means of X-ray diffraction (however, showing information depths of only few tens of nanometers, not several micrometers). Another way of representing EBSD data is to measure the sharpness of some diffraction bands (or peak intensities in the Hough space), which is typically expressed as gray values and termed pattern quality. The grain boundaries are visible in pattern-quality maps (see, e.g., Figure 14.4, bottom) as dark lines since, at the positions of grain boundaries, the EBSD patterns of two neighboring grains superimpose, resulting in zero solutions and therefore very low gray values.

Recently, a novel measurement setup for EBSD in the scanning electron microscope has been reported using electron transparent specimens, termed transmission EBSD (t-EBSD) [7] or transmission Kikuchi diffraction (TKD) [8]. This approach has led to a substantial improvement of the spatial resolution of EBSD, particularly useful for the analysis of nanocrystalline materials. Combined with modern acquisition software, microstructure features at scales of 5 – 10 nm can be resolved, with a perspective to even smaller values.

Since the local orientations of neighboring grains can be identified, also their relative orientations, that is, the so-called misorientations, can be quantified from the EBSD data. The misorientations can be parameterized by, for example, corresponding angle – axis pairs, where the point lattice of the first grain has to be rotated about the axis through the angle in order to result in the point lattice of the second grain. There are, depending on the crystal symmetry, various symmetrically equivalent angle – axis pairs, of which the one with the lowest angle is their representative, the so-called disorientation (where the disorientation angle can be used to classify grain boundaries in an EBSD map and to extract corresponding distributions). The superposition of the point lattices of two neighboring grains results in the so-called coincidence-site lattice (CSL). The ratio formed by the volume of the CSL unit cell and that of the point lattices is termed the Σ value, which corresponds to a specific disorientation (angle – axis pair) and therefore also can be used to classify grain boundaries. Note that grain boundaries always feature 5 macroscopic degrees of freedom, of which 3 parameters are represented by the disorientation (which can be measured by means of EBSD) and 2 parameters are related to the normal of the grain boundary plane (which can generally not be identified by EBSD).

A maximum misorientation angle in case of a contiguous grain is defined for neighboring pixels in an EBSD map. Thus, grain-size distributions of a polycrystalline thin film may be extracted at high accuracy. However, when acquiring an

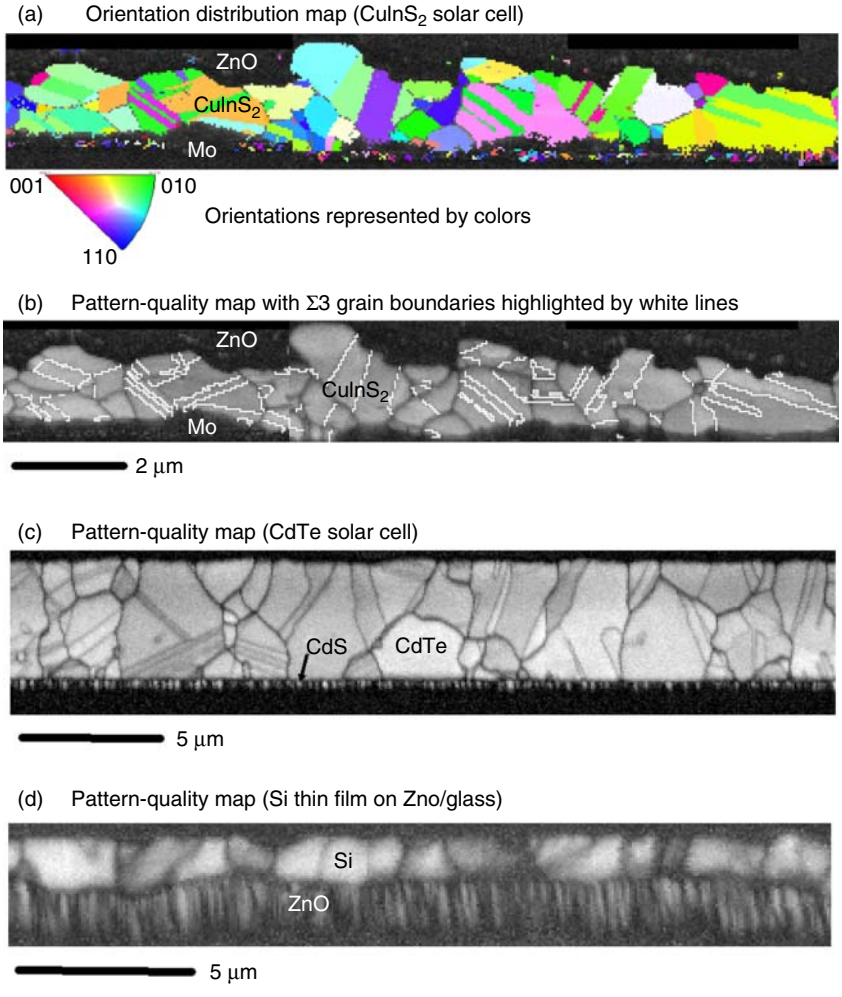

Figure 14.4 (a) Local-orientation distribution and (b) pattern-quality maps, extracted from the identical set of EBSD data, acquired on the cross-sectional specimen of a $CuInS_2$ thin-film solar cell (provided by J. Klaer, HZB, Berlin, Germany). (c) and (d) EBSD pattern-quality maps from a CdTe solar cell and a Si/ZnO/glass stack (also cross-sectional specimens; samples provided by A.N. Tiwari, EMPA, Dübendorf, Switzerland, and T. Sontheimer, HZB).

EBSD map on a region of interest, the microstructural information obtained is reduced to a two-dimensional section through the polycrystalline thin film, owing to the low information depth for EBSD of only a few tens of nanometers.

In order to overcome this obstacle, the EBSD technique may be combined with a scanning electron microscope equipped with a focused ion beam (FIB) (see Section 14.4 for details). The specimen is alternately sectioned by the FIB and analyzed by EBSD. A three-dimensional (3D) data cube is then reconstructed from the

resulting stack of EBSD maps. From this data cube, 3D grain-size distributions can be extracted, although a large volume has to be analyzed in order to obtain good statistics of the distributions, which is generally difficult for thin-film specimens. However, applying 3D EBSD analysis allows for imaging the 3D microstructure of a thin film at a specific region of interest, which is especially useful when studying grain boundaries by means of electron-beam-induced current (EBIC) or cathodoluminescence (CL), as will be further lined out in Section 14.2.7.

By evaluation of shifts of the diffraction bands in EBSD patterns acquired within an individual grain with respect to a reference pattern, microstrain information may be obtained [9, 10]. According to Britton *et al*. [11], modern EBSD systems with corresponding calibration routines allow for the detection of strain values on the order of 10^{-5}. Within individual grains in $CuInSe_2$ and $CuGaSe_2$ thin films, microstrain values of about 10^{-4} were measured [12].

14.2.3
Energy-Dispersive and Wavelength-Dispersive X-Ray Spectrometry

When an electron impinges on a specimen, it may scatter with an inner-shell electron of a specimen atom, transferring energy sufficient for the inner-shell electron to emerge from the specimen. The empty state is then reoccupied by an electron from an elevated state, and the difference in potential energy between the two states is either transferred to a bound electron, which then can leave the atomic bond as Auger electron, or is emitted as X-ray quantum. The difference in potential energy between two electronic states in an atom and therefore the energy of the X-ray quantum is characteristic for a specific element. Thus, by recording all X-rays emitted from a specimen upon electron-beam irradiation, the chemical composition can be analyzed.

There are two ways of X-ray detection. One is based on X-ray quanta from the specimen generating charge pulses in a field-effect transistor, which then are processed and assigned to slots according to their energies (right side of Figure 14.5). This is the principle of the energy-dispersive X-ray spectrometry (EDX). The EDX spectrum consists of X-ray lines at energy positions according to the characteristic energy differences between the states of inner-shell electrons. At high beam currents of several nanoamperes, fast acquisitions of EDX line scan or elemental distribution maps can be performed when scanning on a line or across a specific region of interest. The reader is referred to Section 19.5 for further details.

For the other way of X-ray detection, the X-rays emitted from the specimen are Bragg diffracted at single crystals, and by using crystals with various interplanar spacings, a large wavelength range in the spectrum is covered (left side of Figure 14.5). This is the principle of the wavelength-dispersive X-ray spectrometry (WDX). The X-ray line resolution of WDX and also its detection limit are by an order of magnitude lower than that of EDX, and therefore, WDX is predestined for analyses of compounds where X-ray lines are very close to or even superimpose each other and also for the analysis of rather light elements in compounds

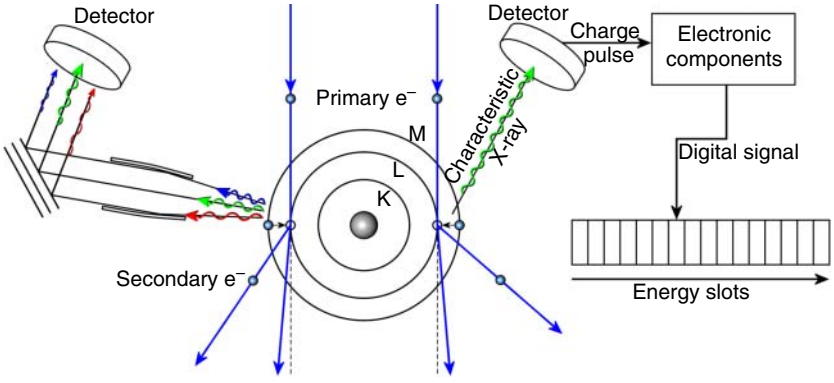

Figure 14.5 Schematics of principles of WDX (left) and EDX (right) measurements in a scanning electron microscope. While the characteristic X-rays are wavelength-dispersed by Bragg diffraction at crystals in the case of WDX, for EDX, the characteristic X-rays generate electron–hole pairs and thus current pulses in the detector, which are assigned to the corresponding energy slots in the spectrum.

and those present at small concentrations (down to about 0.01 at.%). It should be noted that by use of present EDX evaluation software, the deconvolution procedures of two superimposing X-ray lines have demonstrated quite effective. Also, when analyzing compounds with several elements by means of WDX, often different single crystals have to be used for each element, which is time consuming. Since WDX analyzes X-rays at rather flat angles with respect to the sample surface, owing to the geometries of analysis crystal and detector, rather high beam currents are needed in order not to suffer from long acquisition durations for decent statistics of the measurement.

Speaking of the spatial resolution, for example, in EDX or WDX elemental distribution maps, it is determined mainly by the excitation volume of the impinging electron beam (it is important to emphasize that in this sense, there is no difference between EDX and WDX). That is, high spatial resolution of down to about 100 nm can be achieved by reducing the acceleration voltage of the scanning electron microscope (e.g., to 5–7 keV). The spatial resolution also depends on the mean free path of the X-ray quantum of interest. For example, when regarding Cu-L X-ray quanta with energies of about 1 keV (EDX), the spatial resolutions extracted from corresponding elemental distribution maps may reach values of down to 100 nm, whereas they are substantially higher for maps using Cu-K X-rays (with energies of about 8 keV), which exhibit a much larger mean free path. In Figure 14.6, an SEM cross-sectional image is shown, which is superimposed by elemental distribution maps using Zn-L, Cd-L, Cu-L, and Mo-L signals. Although the CdS layer thickness is only about 50 nm, the corresponding Cd-L signals are clearly visible in between the Zn-L and Cu-L distribution maps. Also, although the energies for the Zn-L and Cu-L lines differ only by about 80 eV, the evaluation software was able to deconvolute the corresponding EDX peaks successfully.

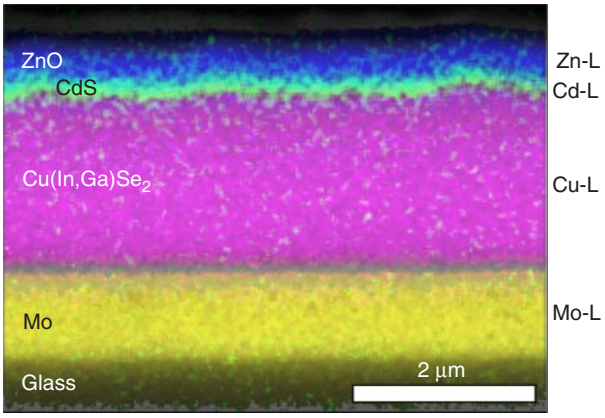

Figure 14.6 SEM cross-sectional image from a ZnO/CdS/Cu(In,Ga)Se_2/Mo/glass stack, superimposed by elemental distribution maps using Zn-L (blue), Cd-L (green), Cu-L (pink), and Mo-L (yellow) signals.

A different scenario for EDX measurements is given when analyzing specimens with thicknesses of only about 10–50 nm in a transmission electron microscope. Then, the excitation volume may be very small, when working with a highly focused electron probe even lower than 1 nm in extension, in spite of the high acceleration voltages of 100–300 keV. The resulting spatial resolutions may be below 1 nm [13]. Whenever working with such thin specimens, however, it is important to realize the substantial reduction in count rates and therefore the deterioration in statistics.

14.2.4
Electron-Beam-Induced Current Measurements

EBIC in a scanning electron microscope is a widespread method to characterize electronic properties of thin-film solar cells. Its principle is to measure the current of the solar cell or any other charge carrier separating and collecting structure during electron-beam irradiation.

Instead of light as in standard working conditions, the electron beam is used to generate free charge carriers/electron–hole (e–h) pairs in the semiconducting absorber material in a defined region around the position of irradiation. These charge carriers either recombine or they are collected and in this way measurable as an external current. The probability of collection depends on the position of generation and other parameters characteristic of the solar cell as, for example, diffusion lengths of charge carriers in the materials involved, charge distributions, and potential drops. By means of EBIC, these properties can be studied with a high spatial resolution. A good overview of the technique is given in a review by Leamy [14].

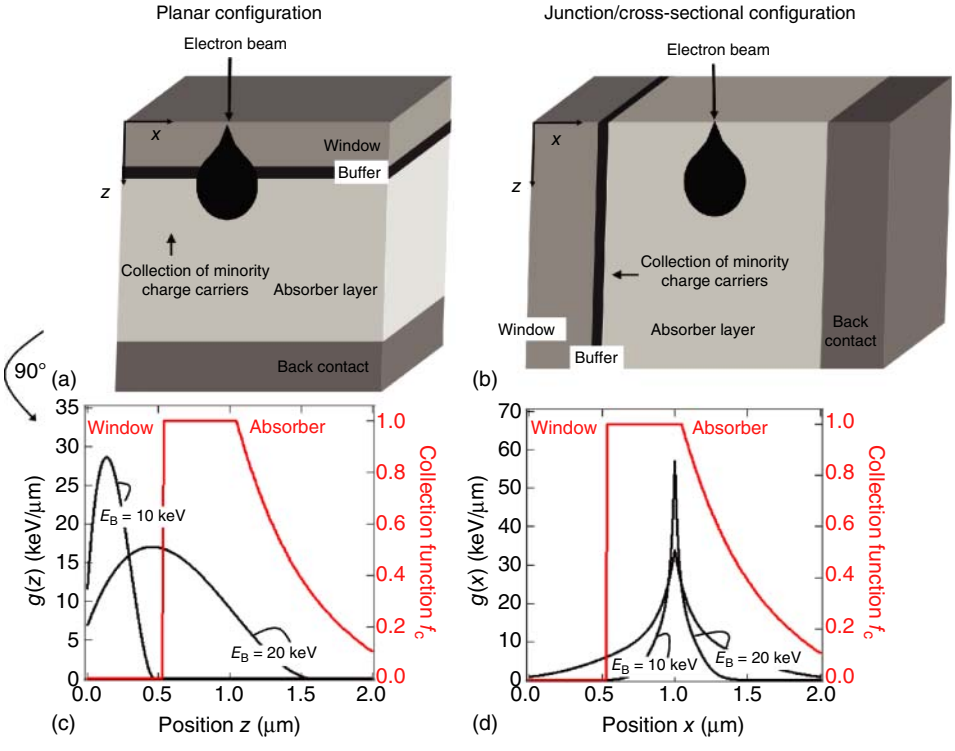

Figure 14.7 (a) Planar configuration of an EBIC experiment. (b) EBIC cross-sectional or junction configuration. (c) Depth-dependent generation function in $Cu(In,Ga)Se_2$ according to the equations in Ref. [1] and depth-dependent collection function f_c. (d) Lateral generation function [15] and collection function perpendicular to pn junction. f_c is the same in (c) and (d). For calculation of f_c in the quasineutral region, Equation 14.2 was used assuming $L = 500$ nm, $S_{BC} = 1 \times 10^5$ cm/s, $D = 1$ cm^2/s.

14.2.4.1 Electron-Beam Generation

Figure 14.7 shows schematically the setup of an EBIC experiment. The solar-cell sample is irradiated by a focused electron beam, and charge carriers are generated in a defined region around the position of irradiation.

The number of generated electron–hole pairs is assumed to be proportional to the band-gap energy E_g of the irradiated material [16], and the energy necessary to generate one electron–hole pair E_{eh} can be expressed as $E_{eh} = 2.1E_g + 1.3$ eV. In EBIC experiments, typical electron-beam energies E_b are between 3 and 40 keV. Varying E_b changes not only the number of charge carriers generated but also the extension of the generation region. The spatial distribution is proportional to the energy deposited by a primary electron along its path through the sample. For the description of this energy loss versus distance, different approaches have been chosen. Equations for mostly one-dimensional generation profiles in different materials have been derived experimentally by EBIC and luminescence

measurements [1, 17–19] via Monte Carlo simulations[11, 20] and analytically [21]. The lateral and depth-dependent generation functions shown in Figure 14.7 are derived from equations given in Refs [1, 9]. In Ref. [11], a comparison of various profiles gained from different measurements and simulations is shown, which illustrates that the results vary quite significantly.

Another problem occurs when analyzing a multilayer stack such as a solar cell. The problem of different densities of the irradiated materials can be solved by normalizing the spatial coordinate to the density of the corresponding material as shown in Ref. [9], but this procedure still neglects backscattering at the interfaces between the layers. Profiles for multilayer structures including this effect were obtained via Monte Carlo simulations or by a simple cut-and-paste method [14].

14.2.4.2 Charge Carrier Collection in a Solar Cell

For charge carrier collection within the solar cell, that is, for obtaining an external voltage or current, there need to be "selective" contacts for each type of charge carrier. Upon irradiation, a gradient of the Fermi levels of electrons and holes develops, which causes an electron current to one contact and a hole current to the second one. In a "regular" p–n-junction-based solar cell, this is provided by the potential drop of the space charge region of the p–n junction and ohmic (or low barrier) contacts to the external circuit.

The relevant equations describing charge carrier transport are the continuity equations for electrons and holes in the absorber material. When assuming low injection conditions (i.e., density of generated minority charge carriers much lower than density of majority charge carriers), the following equation for the collection function $f_c(\vec{x})$ can be derived via a reciprocity theorem [22, 23]:

$$D\Delta f_c(\vec{x}) + \mu\vec{E}\vec{\nabla}f_c(\vec{x}) - \frac{f_c(\vec{x})}{\tau} = 0, \tag{14.1}$$

where D is the diffusion constant of the minority charge carriers of the corresponding material, μ their mobility, τ their lifetime, and $\vec{E}$ a possible electric field. The collection function $f_c(\vec{x})$ stands for the probability of a charge carrier generated at position $\vec{x}$ to be collected. If translation invariance in the directions parallel to the p–n junction (y and z) is assumed, a one-dimensional equation can be used. Assuming as a boundary condition that the collection probability at the edge of the space charge region is one ($f_c(x_{SCR}) = 1$) and in case of an infinite semiconductor layer where $f_c(x) \to 0$ for $x \to \infty$, the solution for a field-free absorber layer ($E = 0$) is a simple exponential function $f_c(x) = \exp(-x/L)$, where L is the diffusion length of the minority charge carriers. Assuming a finite semiconductor limited by a back contact at position x_{BC}, the second boundary condition changes to $f_c'(x_{BC}) = S_{BC}/Df_c(x_{BC})$, where S_{BC} is the surface recombination velocity of the minority charge carriers at the back contact. A solution for $f_c(x)$ is

$$f_c(x) = \frac{1/L\cosh\left(\frac{x-x_{BC}}{L}\right) - S_{BC}/D\sinh\left(\frac{x-x_{BC}}{L}\right)}{S_{BC}/D\sinh\left(\frac{x_{BC}-x_{SCR}}{L}\right) + 1/L\cosh\left(\frac{x_{BC}-x_{SCR}}{L}\right)}. \tag{14.2}$$

In Figure 14.7 (red curve), an exemplary collection function of a Cu(In,Ga)Se_2 thin-film solar cell is shown. $f_c(x)$ is assumed to be zero in the window and buffer layers, one in the space charge region, and it is $L = 500$ nm and $S_{BC} = 1 \times 10^5$ cm/s.

14.2.4.3 Experimental Setups

In this section, an overview of the most commonly used experimental setups for EBIC measurements on thin-film solar cells is given: the junction, plan view, and edge-scan configurations. In a lot of cases, it is possible and reasonable to perform EBIC measurements not only on a completed p–n-junction solar cell but also on Schottky contacts produced by depositing a metal on the absorber layer. In this way, additional information about collection properties of the absorber layer is provided, especially when comparing EBIC results of Schottky contacts and p–n junctions. Since a sufficiently thin metal layer is partially transparent for electrons, it is possible to use a Schottky contact structure for all configurations described here.

Cross-Sectional or Junction EBIC Junction EBIC can be used to extract quantitative information about the solar cell like the width of its space charge region and the diffusion length of the minority charge carriers in the absorber layer. In junction EBIC, the cross section of the solar cell is irradiated by an electron beam, and the current signal is measured as a function of the position of irradiation a. An EBIC profile across the cross section of the solar cell perpendicular to the p–n junction can be described by integrating the collection function and the lateral generation profile over the coordinate x (see Figure 14.7):

$$I(a) = \int f_c(x) g(x - a) \mathrm{d}x. \tag{14.3}$$

It has to be taken into account that in this setup an additional free surface is present, where enhanced recombination due to surface defects might take place. Fitting of the measured profiles to theoretical ones obtained from the previous equations allows for the extraction of values for the width of the space charge region, the back contact recombination velocity S_{BC}, and a value not for the bulk diffusion length but for an effective diffusion length L_{eff}. L_{eff} is influenced by surface recombination and therefore depends on the depth of generation, that is, the electron-beam energy [24, 25]. Using the equations given in Refs [18, 19], describing the dependence of the effective diffusion length on the electron-beam energy E_b, it is possible to extract values for the bulk diffusion length and the surface recombination velocity [26]. An important assumption, which has to be fulfilled for this evaluation, is that the collection function is independent of the generation function (not always the case; see Section 14.2.4.4). In this way, the junction EBIC method can be used to extract quantitative information about important solar-cell properties with a high spatial resolution compared to other techniques.

Additionally, junction EBIC can be used to determine the position of the actual p–n junction [27, 28], to learn more about interface properties and charge and

defect distributions [20], and to investigate the behavior of grain boundaries [22, 29–32] and possible inhomogeneities in collection properties.

Planar EBIC from Front Side and Backside In such setups, the solar cell is either irradiated from the front side like it is under standard sunlight irradiation or from the backside. The EBIC can then be expressed as (Figure 14.7) $I = \int f_c(z)g(z)\mathrm{d}z$, where $g(z)$ is the depth generation profile of the electron beam. Information about collection properties like the minority charge carrier diffusion length and width of the space charge region can be obtained by measuring the collection efficiency (ratio of measured current to incident beam current) for different electron-beam energies E_b and consequently changed generation profiles $g(z)$. The evaluation of this data can be performed in different ways [33–35]. Compared with junction EBIC, planar EBIC from the front side provides the advantage that there is no artificial surface, which could influence charge carrier collection properties. The method can also be used to investigate the behavior of grain boundaries concerning charge carrier collection [29, 36]. One difficulty is the topography of the surface irradiated, which has a huge effect on absorption of incident electrons. This has to be taken into account especially when investigating grain boundary effects.

Edge-Scan Configuration In this configuration, a charge carrier collecting junction is deposited only on part of the surface of an absorber layer. The EBIC signal is measured in dependence of the distance of the position of irradiation to the junction [31, 37].

EBIC Measurements at Applied Bias When applying a voltage to a solar cell during an EBIC measurement, a background current through the device is induced (on the order of microampere or milliampere), which is by several orders of magnitude larger than the EBIC values (picoampere to nanoampere). In order to still obtain access to the (net) EBIC signals, an electron-beam blanker combined with lock-in amplification can be employed [38]. As a result, the collection of generated charge carriers can be investigated at operation conditions different from the short-circuit condition, which is particularly important when studying the effect of extended structural defects on the device performance at "realistic" solar-cell operation. Furthermore, the width of the space charge region (among other materials and device properties) can be extracted from EBIC profiles acquired on cross-sectional solar-cell specimens at various bias voltages (by use of Equation 14.2), and doping concentrations can be estimated [39].

14.2.4.4 Critical Issues

When using EBIC in order to investigate charge carrier collection properties of solar cells, it has to be taken into account that the generation of charge carriers in a semiconductor using an electron beam might be significantly different compared to the generation by sunlight. In the following different scenarios are discussed.

Injection Conditions The different spatial distribution of charge carrier generation as compared to sunlight generation might influence the charge distribution in the solar cell and therefore collection properties as, for example, shown in Ref. [40].

As mentioned earlier, the injection level, that is, the density of excess charge carriers compared to the equilibrium doping level of the semiconductor irradiated, plays an important role. Equation 14.2 describes the collection function of the quasineutral (i.e., field-free) region of an absorber layer only if low injection conditions are present. When the density of excess charge carriers is close to or higher than the doping density, the charge distribution within the device is influenced by these excess charge carriers, which also changes collection properties [41–43]. This effect can be used to estimate the doping density with a good spatial resolution, which can, for example, be used to exhibit differences in the doping level of grain boundaries [26].

Temperature When using high electron-beam intensities, it is possible that the sample heats up during the measurements, which may result in a modified charge carrier collection behavior of the device. An estimate of the maximum temperature change due to electron-beam irradiation is given by $\Delta T = E_b I_b r_b / K$ [44], where K is the thermal conductivity of the material irradiated, r_b the beam radius (in our case on the order of the extension of the generation volume), E_b the electron beam energy, and I_b the electron beam current. A more precise equation for a thin film–substrate structure is also given in Ref. [36].

Interactions of Sample and Electron Beam When investigating charge carrier collection properties by means of EBIC, one has to be aware of the fact that the electrons penetrating into the sample have much higher energies compared to light of the solar spectrum. There might also be reactions taking place which are not possible under standard conditions but might influence charge carrier collection properties. As an example, it was found that the electron beam works as a reducing agent and breaks oxygen bondings passivating compensating donors in a $Cu(In,Ga)Se_2$ layer, thereby changing its doping density [21].

Additional Interfaces/Surfaces The experimental setup might lead to additional surfaces or interfaces present in the charge carrier collecting device, which are not present under standard conditions using sunlight as excitation source. At these interfaces, there might be enhanced recombination due to an accumulation of defect states as mentioned earlier. A second effect might also be a different charge equilibrium due to structural reconstruction at the interface (dangling bonds, etc.). This results in band bending at the surface and therefore modified collection properties. As an example, it was shown that on InP an oxide causes band bending which assists charge carrier collection [45]. The EBIC signal results to be nearly constant with increasing distance to the collecting junction.

In the present section, EBIC was introduced as a powerful experimental technique to gain information about electrical properties of thin-film solar cells. There are different configurations in use complementing each other and allowing

a detailed insight into charge carrier collection properties. As the experimental setup and generation conditions differ from the ones under standard conditions using sunlight for generation, interpretation of EBIC data is not always straightforward, and care has to be taken. In solar-cell research, EBIC is not only used to derive values for relevant quantities like diffusion lengths or the width of the space charge region but also to learn about junction and interface properties as well as charge and potential distributions. In this way, it helps to develop a profound understanding of device properties and to improve solar-cell performance.

14.2.5 Cathodoluminescence

In semiconductors, the energy of impinging photons or the electron beam can promote electrons from the valence band to the conduction band, with the generation of electron–hole (e–h) pairs. The radiative recombination of these electrons and holes results in photoluminescence (PL) (see Chapter 11) upon photon excitation and cathodoluminescence (CL) as a result of electron irradiation. Therefore, the radiative processes in semiconductors are fundamentally similar in both PL and CL, only differing in the excitation source. CL thus benefits from the widespread use of photoluminescence for the interpretation of the emission spectra obtained.

Luminescence spectroscopies are very useful to determine composition in semiconductor compounds, assess crystal quality, and detect electronic levels associated with dopants (down to densities in the $10^{15}\,\mathrm{cm}^{-3}$ range) and electronically active defects, but do not provide high spatial resolution. Here is where the CL mode of operation of the electron microscope in both SEM and transmission electron microscopy (TEM) finds its application.

A summary of the radiative transitions that can be found in the emission spectrum of semiconductors is given in Figure 14.8. Process 1 describes the electron thermalization with intraband transition, a process that may lead to phonon-assisted luminescence or just phonon excitation. Process 2 is an interband transition involving the recombination of an electron in the conduction band and a hole in the valence band with the emission of a photon of energy $h\nu \approx E_g$. Process 3 is the exciton recombination, which is observable at cryogenic temperatures and, in some cases, in quantum structures at higher temperature. For the excitonic recombination, we can distinguish between free excitons (commonly denoted by FX) and excitons bound to an impurity (D^0X for a neutral donor, A^0X for a neutral acceptor; for the corresponding ionized impurities are D^-X and A^-X). Processes 1–3 are *intrinsic* luminescence because they are observed in undoped semiconductors. Processes 4–6 arise from transitions involving energy levels associated with donors and/or acceptors, and they are collectively known as *extrinsic* luminescence. Process 4 represents the transition between the energy level associated with a donor and a free hole (D^0h). Process 5 represents the transition between the free electron and the energy level associated with an acceptor (eA^0). Donor-to-acceptor pair (DAP) recombination is obtained if an electron bound to the donor state recombines with a hole bound to the acceptor state

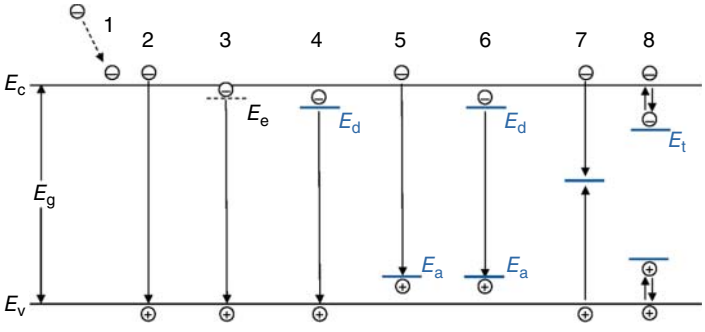

Figure 14.8 Schematic diagram of radiative transitions in semiconductors between the conduction band (E_c) and valence band (E_v) and transitions involving exciton (E_e), donor (E_d), and acceptor (E_a) levels. Nonradiative transitions via midgap states and traps are also shown.

(process 6). Finally, it is worth mentioning that all these radiative recombination processes will compete with each other, with other nonradiative recombination mechanisms (process 7, representing recombination through a midgap state without photon emission), and with trapping levels for both electrons and holes (process 8). The contribution of each process to the overall recombination will be reflected in the local emission spectrum and is ultimately the source of contrast in the photon intensity maps acquired by CL. The possibility to control the temperature and the excitation level during the experiment makes CL ideal for investigating in detail the recombination processes in semiconductors. CL has enabled imaging of the electronic and optical properties of semiconductor structures with an ultimate resolution of about 20 nm (although 100–500 nm is a more typical value) and can provide depth-resolved information by just varying the electron-beam energy (or acceleration voltage).

In general, the CL modes of the electron microscope can be divided into *spectroscopy* and *imaging*. In the *spectroscopy* mode, a spectrum is obtained over a selected area under observation in the SEM or TEM (a *point analysis* in the terminology of *X-ray microanalysis*, with the electron beam fixed over one location). In the *imaging* mode, an *image* of the photon intensity (when using a monochromator at the wavelength range of interest, a *monochromatic* image; when bypassing the monochromator, not resolved in energy, a *panchromatic* image) is acquired instead. Because *spectroscopy* and *imaging* cannot be operated simultaneously, information is inevitably lost.

Both modes can be combined in one single mode: *spectrum imaging*. The objective of the section of this chapter is introducing *spectrum imaging* as the most advanced instrumentation developed to date for CL measurements and illustrate how *spectrum imaging* can be applied to thin-film photovoltaics. Figure 14.9 shows the schematics of the instrumentation needed to setup the *spectrum imaging* mode in the SEM. The essential requirements for *spectrum imaging* are superior efficiency in the collection, transmission, and detection of the luminescence. High collection efficiency is achieved by a parabolic mirror

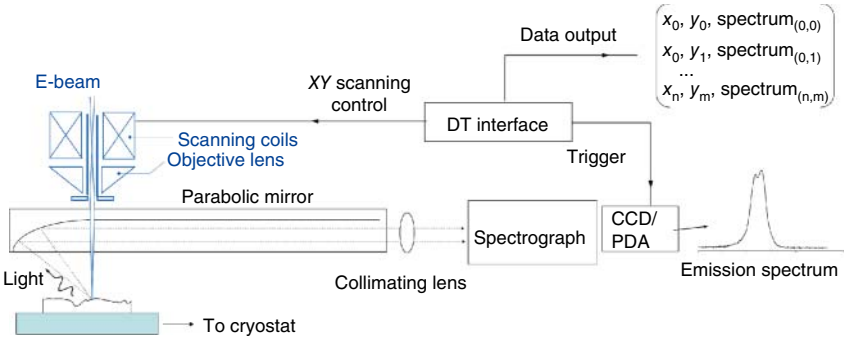

Figure 14.9 Schematics of the cathodoluminescence spectrum imaging setup in the SEM.

attached to the end of a *retractable* optical guide (the collection efficiency is estimated to be about 80% when positioning the specimen at the focal point of the mirror). A hole (about 500 µm in diameter) drilled through the parabolic mirror and aligned vertically with the focal point allows the electron beam through. The light transmitted by the optical guide is focused at the entrance slit of a spectrograph by a collimating lens. For the detection, multichannel photodetectors are needed. Both CCD and photodetector array (PDA) architectures are used for multichannel spectrum acquisition, where the choice of the photodetector material (Si, GaAs, InGaAs, etc.) depends on the wavelength of interest. Only at very low operating temperatures (using cryogenic liquids) is when CCDs and PDAs achieve the high sensitivity and superior performance required for this application (millisecond readout times, triggering, extremely low dark currents).

Up to this point, the described system is not yet able to perform *spectrum imaging*. The principal addition for implementing *spectrum imaging* is the digital electronics (DT interface in Figure 14.4) which (i) controls the $X-Y$ scanning of the electron beam, (ii) sends the *triggers* to the CCD/PDA electronics for the acquisition, and (iii) processes the *spectrum series* by associating each x_n, y_m pixel of the scanning with the corresponding spectrum. Thus, *spectrum imaging* combines *spectroscopy* and *imaging* in one single measurement by acquiring the emission spectrum at high speed (typically 10–100 ms) in synchronization with the scanning of the electron beam. With acquisition times of 10–20 ms by pixel on a 125 × 125 pixel scan, the time to acquire the entire *spectrum series* – consisting of 15 625 spectra, equivalent to more than 10 million data inputs – is about 5 min. This high-speed mode is routinely used when measuring thin films at cryogenic temperatures. When a very low excitation is needed to improve the resolution or when the emission is very low, we can increase the acquisition time per pixel (up to 500 ms to 2 s) at the cost of a much prolonged time for the measurement (hours instead of minutes). After the acquisition is complete, the *spectrum series* can be processed to:

- Reconstruct maps of the photon intensity, photon energy, or full width at half maximum (FWHM) at the wavelength range of interest selected over the spectrum
- Extract the spectrum from a selected area

- Output an ASCII file with any of the calculated parameters
- Perform quantitative measurements (relative contributions of different transitions, recombination rate at extended defects, etc.)
- Obtain pixel-to-pixel correlation between images that is inherent to *spectrum imaging*
- Display spectrum line scans
- Run spectrum fitting routines
- And much more

Once the spectrum series is saved, it can be reexamined in the future, even to answer one question that might be asked years after the measurements were completed.

Applications of *spectrum imaging* to the investigation of electronic properties in CdTe are presented in the remaining subsection. This is obviously a minor, although representative, demonstration of the results published to date, and the reader is welcome to explore the available literature on this subject.

14.2.5.1 Example: Spectrum Imaging of CdTe Thin Films

Record efficiencies in CdTe solar cells have been produced using *closed-space sublimation* (CSS) which, simply by the thermodynamics of the process, results in a high concentration of native cadmium vacancies (V_{Cd}). The need to provide a cost-effective solution by reducing capital and operating costs results in a CdTe thin film with a very high density of defects: (i) point defects (*intrinsic*, vacancies and interstitials associated with Cd and Te; *extrinsic*, introduced by incorporation of impurities to the CdTe) and (ii) extended defects (dislocations and grain boundaries). Because of this, we can anticipate that the emission spectrum will show all the radiative (and nonradiative) transitions described earlier (represented schematically in Figure 14.8). CdTe thin films are then a perfect example of what to be expected in most polycrystalline semiconductors used in solar cells, in which the crystal quality is good enough to see the *intrinsic luminescence* associated with related single crystals of high purity but is otherwise strongly influenced by the presence of defects.

A luminescence spectrum representative of CdTe thin films is shown in Figure 14.10 ($T = 15.7\,\text{K}$, $E_b = 10\,\text{keV}$, $I_b = 250\,\text{pA}$). At cryo temperatures, the spectrum consists of excitonic transitions (free excitons (FX) and bound excitons (BX)) and a very broad emission at lower energy, which is associated with DAP recombination. In CSS CdTe, the acceptors are complexes with participation of V_{Cd}, such as the center A or chlorine center A (after chlorine treatment) [46, 47]. The density of these complexes is so high that they interact with each other, forming a band (of acceptor character) located within the band gap. The fine structure of discrete transitions associated with the DAP recombination is lost, substituted for a very broad emission. The considerable broadening of the transitions in the emission spectrum is yet another manifestation of the high density of defects in polycrystalline semiconductors. *Spectroscopy* measurements from single crystals are often required for the interpretation of the spectrum in thin films.

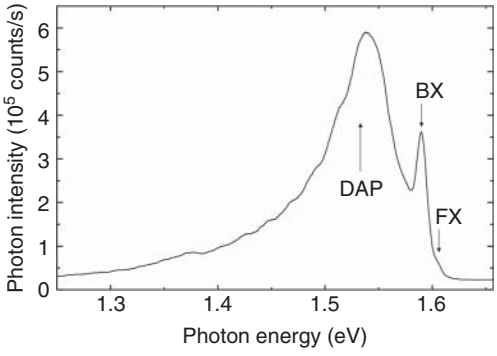

Figure 14.10 CL spectrum representative of CdTe thin films ($T = 15.7$ K, $E_b = 10$ keV, $I_b = 250$ pA). Excitonic transitions involving free excitons (FX) and bound excitons (BX), and a very broad emission associated with donor-to-acceptor (DAP) recombination can be resolved.

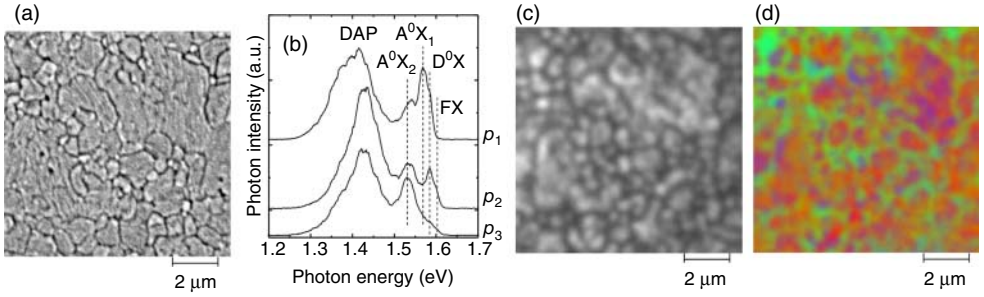

Figure 14.11 *Spectrum imaging* of CdTe thin films ($T = 15.7$ K, $E_b = 10$ keV, $I_b = 250$ pA). (a) Microstructure of the CdTe thin film, as seen by the secondary electron mode of the SEM. (b) A sequence of spectra selected over different locations of Figure 14.6d, p_1, p_2, and p_3, which reveals variations in the local density of donors and acceptors. (c) Photon intensity map corresponding to the free exciton (FX). (d) Photon energy map RGB (red, 1.530 eV; green, 1.570 eV; and blue, 1.600 eV) of the exciton recombination. The transition A^0X_1 at 1.570 eV is characteristic of grain boundaries; this is also shown in the spectrum at location p_1.

Spectrum imaging is very useful for the *microcharacterization* of the transitions identified in the emission spectrum and, more specifically, in determining the electronic properties of extended defects such as dislocations and grain boundaries. Results of *spectrum imaging* measurements completed on a CdTe thin film are summarized in Figure 14.11. The microstructure of the CdTe film is readily accessible to the electron microscope, as seen on Figure 14.11a, which reveals grains with 1–5 μm in diameter. When first examining the *spectrum series*, it becomes clear that there are large variations in the emission spectrum from location to location within the micrometer scale, an indication that the distribution of all the different electronic states present in the CdTe thin film is highly nonuniform. This is illustrated by the sequence of spectra in Figure 14.11b, selected over different

locations shown in Figure 14.11a and extracted from the *spectrum imaging* file. These local variations certainly contribute to the broadening seen in the emission spectrum acquired over large areas of the film. This is worth noting, but the best capability of *spectrum imaging* is the possibility of correlating directly electronic properties at the microscale with the microstructure of the film in a completely different dimension. This is especially interesting to investigate grain boundaries. Figure 14.11c shows the photon intensity image for the free exciton (FX) from where it may be concluded that recombination of free excitons is preferential at grain boundaries, because there, the photon intensity associated with the FX transition is largely reduced. When examining all the excitonic transitions and then mapping the photon energy of the dominant excitonic recombination (Figure 14.11d), it becomes evident that there is a characteristic excitonic transition associated with grain boundaries. To intuitively visualize this, the photon energy is displayed in an RGB scale covering the selected spectral interval (in this case red, 1.530 eV; green, 1.570 eV; and blue, 1.600 eV) – grain boundaries exhibit a green color in the map of Figure 14.11d. With this analysis, a *redshift* or *blueshift* is very intuitive and easy to recognize. In addition to this, and for a more quantitative analysis, an ASCII file can be produced with the energy of the transition(s) for each pixel, which can be further examined. This feature is unique to *spectrum imaging*. The distinct excitonic transition at grain boundaries (A^0X_1 at 1.570 eV) reveals that an acceptor with activation energy $\varepsilon_v + 30$ meV is preferentially located at grain boundaries, whereas an acceptor with activation energy level $\varepsilon_v + 70$ meV (A^0X_2 at 1.530 eV) is otherwise preferentially located in grain interiors. Shifting the energy level of the acceptor toward the valence band seems to be beneficial to the solar-cell performance.

14.2.6
Scanning Probe and Scanning Probe Microscopy Integrated Platform

Scanning probe microscopy (SPM) is becoming the instrument of choice in nanoscience characterization. In addition to providing excellent resolution and sensitivity, the tip (the central component of the microscope) represents *de facto* a *nanoprobe* that can be adapted to measure multiple properties in different modes of operation [48]. Among them, scanning tunneling microscopy (STM) (see Chapter 13), atomic force microscopy (AFM) (see Chapter 13), and near-field scanning optical microscopy (NSOM) (see Chapter 10) are routinely used in the laboratory. On the other hand, much progress remains to be made with novel modes of operation and applications. With this motivation, we have integrated *SPM* (STM/AFM/NSOM) with *SEM* in one integrated platform. There are obvious benefits from this approach: (a) the tip can be manipulated with high precision under constant observation in the SEM; (b) the tip and the electron beam are *two independent probes* that can be controlled simultaneously – one acting as *excitation probe* and the other acting as *sensing probe* – depending on the experimental configuration; and (c) SEM- and SPM-based measurements can be performed at the very same location during the same experiment. The final

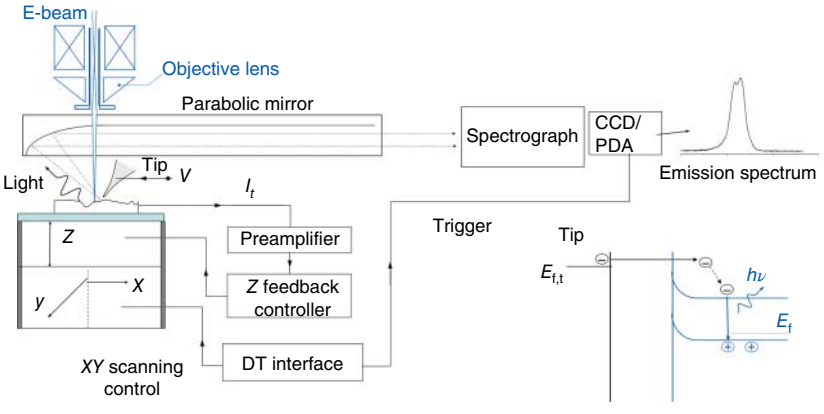

Figure 14.12 Schematics of the STM integrated inside the SEM. The STM is primarily designed to perform *tunneling luminescence* measurements. The inset shows the physics of the tunneling luminescence at low applied bias, in which minority carriers are injected by the tip in the semiconductor, recombining with available majority carriers.

subsection is dedicated to introducing the modes of operation that are available to this integrated platform as well as describing its application to *luminescence spectroscopy* and *electrical measurements* in thin-film solar cells.

Figure 14.12 shows the schematics of the STM integrated inside a scanning electron microscope equipped with *cathodoluminescence optics* (*which is described in the previous section dedicated to cathodoluminescence spectrum imaging*). The STM is based on a three-axis nanopositioning system (basically a digitally controlled *piezoscanner*, commercially available from various vendors) that can be mounted on top of the *mechanical stage* of the SEM. Inertial motion is used for the approaching of the STM tip, which is mounted on the side of the *piezoscanner*. Specialized cantilevered tips are needed to accommodate the tip between the parabolic mirror and the specimen, which is limited to 2–3 mm when the end of the tip is positioned at the focal point of the mirror. Another requirement to the geometry of the cantilevered tip is that the end of the tip must be observable in the *electron microscope*; otherwise both the electron beam (as the *excitation probe*) and/or the potential *luminescence* excited at the tip – depending on the experimental configuration – will be blocked by the tip itself. One of the advantages of this approach, though, is that the STM tip can be accurately positioned into the focal point of the parabolic mirror, improving dramatically the collection efficiency.

This setup is primarily intended to perform *tunneling luminescence microscopy*, in which tunneling electrons are responsible for the excitation of the luminescence. In semiconductors, the high localization of the tunneling electrons at the STM tip enables the controlled excitation of luminescence within a nanoscale volume underneath the tip. Therefore, *tunneling luminescence* exceeds the best spatial resolution of cathodoluminescence. On the other hand, the *quantum efficiency* of the tunneling luminescence is only about 10^{-4} photons/electron,

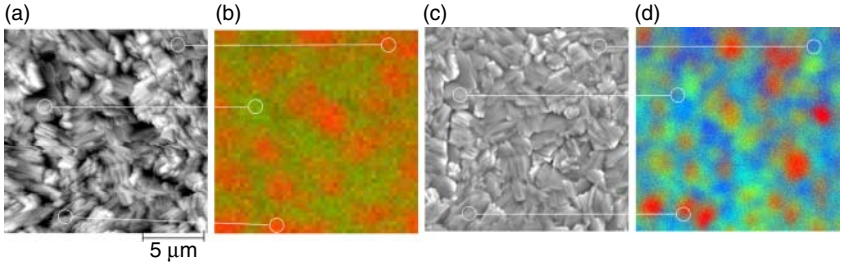

Figure 14.13 (a) STM image of a $Cu(In,Ga)Se_2$ thin film and (b) corresponding photon energy map of the tunneling luminescence ($V_t = -5$ V, $I_t = 50$ nA). (c) SEM image matching the previous STM and (d) corresponding photon energy map of the cathodoluminescence ($E_b = 5$ keV, $I_b = 750$ pA). The red–green–blue (RGB) scale in (b) and (d) corresponds to R: 1.17 eV, G: 1.20 eV, B: 1.22 eV.

and, therefore, a highly efficient collection optics is absolutely critical. With the optics of the cathodoluminescence setup, a *external quantum efficiency* as high as 10^6 photons/nA can be obtained, which is close to collecting every single photon. With this, the possibility of running *spectrum imaging* (*spectrum-per-pixel* measurements) of the *tunneling luminescence* is within reach. Now the *digital interface* (see Figure 14.12) controls the scanning of the STM tip and sends the *triggers* to synchronize the spectrum acquisition with the STM scanning. Because of the integration of both SEM and STM, *cathodoluminescence* and *tunneling luminescence spectroscopies* can be performed over the same location. This is very interesting for the thin films used in solar cells, in which the *surface electronics* can play a critical role in the solar-cell response. Because of the small volume of excitation, the STM-based luminescence can be used to measure the electronic states present near the *surface*. A comparison of the tunneling luminescence and cathodoluminescence spectra over the same location can be useful to compare the electronic properties of the surface against the bulk of the film.

For illustration of the capabilities of this STM–SEM platform, we present the results for $Cu(In,Ga)Se_2$ thin films, in which the *surface electronics* is critically involved in the formation of the junction [49]. Figure 14.13a and b shows the STM image and the corresponding photon energy map for the *tunneling luminescence* (color-coded so that *red-* and *blueshifts* in the emission spectrum are intuitive). Figure 14.13c and d shows the SEM image (over the same area) and the corresponding photon energy map for the cathodoluminescence excitation. This film is deposited in the regime of *selenium deficiency* and shows larger variations in energy from grain to grain when compared to the standard $Cu(In,Ga)Se_2$ deposited under Se *overpressure*, as clearly evidenced by the photon energy map of Figure 14.13d.

The most interesting result when comparing the photon energy maps (same RGB energy scale used in both) is that variations in the luminescence are largely mitigated at the $Cu(In,Ga)Se_2$ surface (Figure 14.13b). The naturally

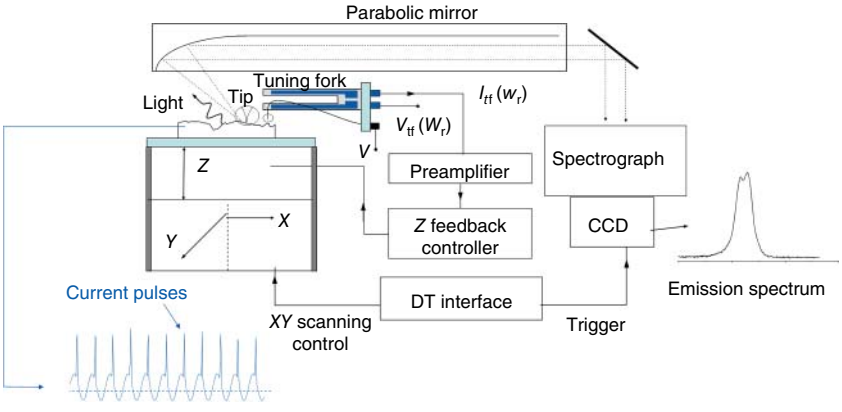

Figure 14.14 Schematics of the AFM integrated inside the SEM.

occurring depletion of Cu makes the surface more uniform than the underlying $Cu(In,Ga)Se_2$.

$Cu(In,Ga)Se_2$ is very accessible to observation in the STM, but for other systems, such CdTe, organic semiconductors, or silicon thin films, the *intrinsic* low conductivity will cause unstable operation of the STM under *constant current conditions* (*current feedback*), with the crashing of the STM tip as the most likely outcome. This can be solved by using the *force feedback* of the AFM instead. Figure 14.14 shows the schematics of the AFM implemented inside the SEM. The STM tip is now substituted by a force sensor consisting of an ultrasharp metallic tip attached to a self-sensing and self-actuating piezo tuning fork (TF). This is the most compact force sensor that can be built and inserted in the confined space between the parabolic mirror and the specimen. The TF is driven by an oscillating voltage source near its resonance frequency $V_{tf}(\omega_r)$. The interaction between the tip and the specimen causes a reduction of the oscillation amplitude [monitored by the current $I_{tf}(\omega_r)$] and a shift in the resonance frequency and phase of the oscillation. One maintains the distance Z constant by controlling the amplitude of the TF oscillation during the scanning of the tip while applying a voltage to the tip to create pulses of tunneling current in synchronization with the TF oscillation. Tunneling current pulses as high as about 100 nA have been observed without significant degradation of the AFM operation. In consequence, we can run *tunneling luminescence* measurements in both the STM and AFM configuration.

There are other benefits from using the AFM setup. First, the oscillation amplitude of the TF and the set point can be selected to drive the tip into the *intermittent-contact* or *tapping* mode. In this mode, the tip can establish a contact at the bottom of each oscillation. If, for example, a p–n junction is present in the specimen, the tip can locally forward bias the cell and excite *electroluminescence* (EL). A map of the AFM-based EL will be specific to the depletion region of the solar cell and not so much to the surface electronic states, such as in *tunneling luminescence* measurements, which are inherently noncontact measurements.

The second, and probably best, advantage of using the AFM is decoupling the Z-feedback from the electrical measurements that can be performed with the conductive tip (in the STM, the current is fed to the Z-feedback electronics to follow the topography of the film). This opens up the possibility of performing conductive AFM measurements (topography vs conductivity) and measuring local $I-V$ characteristics. This is available to any commercial AFM, however.

What is unique to the combination of AFM and SEM in the characterization of thin films is the possibility to measure the *lateral electron transport* across grain boundaries and estimate the *diffusion length* locally at individual grains. In this configuration, the lateral electron transport across a single grain boundary can be measured by maintaining the tip over one grain and measuring the difference in the *current/voltage* sensed by the tip when the electron–hole pairs are excited (by the e-beam) within the grain interior and the adjacent grain across the grain boundary. This is basically an EBIC measurement in which one of the terminal contacts is substituted by the AFM tip. Using this method, we have found evidence for a significant barrier for electron transport across grain boundaries in $CuGaSe_2$, which is not present in $CuInSe_2$ or $Cu(In,Ga)Se_2$. On the other hand, the exponential decay of the current (voltage) sensed by the tip when the electron beam moves away from the tip (similar to the method used by EBIC) can be applied to estimate the diffusion length locally at specific locations of interest in the film, under observation in the SEM.

Figure 14.15 illustrates the application of the AFM-based measurements of the electron transport to polycrystalline silicon films (of n-type polarity). Figure 14.15a and b shows SEM and AFM images revealing the microstructure of the film, and Figure 14.15c corresponds to an image of the current sensed by the tip at a specific location. There are two sources of contrast in the current images. First, the tip can establish a local Schottky diode, and the holes excited by the electron beam (minorities in n type) can be collected from regions close to the tip. This collected current, of positive polarity in our setup, extends from the tip the local (hole) diffusion length (see Figure 14.15c). Second, in this contact scheme with *remote* ground, the silicon film acts as a *current divider.* Thus, a fraction of the primary electrons from the electron beam (the specimen current) flows to the tip and the rest to the ground, depending on the relative resistance along these two different paths – this is referred to as *R*EBIC for *remote* EBIC [50]. This current is of negative polarity in this EBIC image. In the case of a film of uniform resistivity, the current detected by the picoamplifier is a straight ohmic line, but if there are grain boundaries impeding the electron transport, the ohmic baseline becomes stepped (meaning that the signal drops sharply at the boundary). This is because the slope of the detected current is proportional to the local value of resistivity. Figure 14.15c shows this sharp drop in the detected current when the electron beam moves across the grain boundaries, which is due to their high resistance to the electron flow. Although electrons flow with ease across certain grain boundaries (see, e.g., $A-B$ in Figure 14.15b and c), most of the boundaries present a very high energy barrier to the electron transport (see $A-C-D$ in the same figure), and the current toward the tip decreases rapidly when increasing

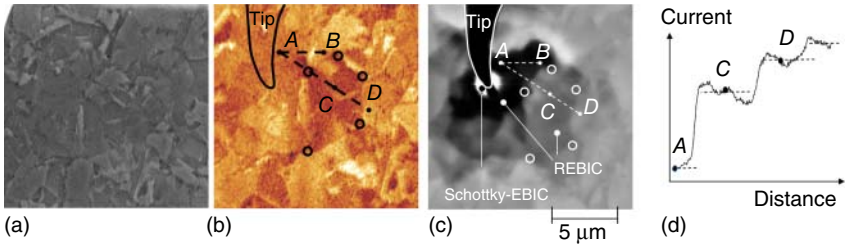

Figure 14.15 AFM-based EBIC measurements performed on polycrystalline silicon thin films. Figure (a) and (b) shows the SEM and AFM images acquired over the same area of the film. Figure (c) corresponds to an image of the current sensed by the tip (acquired during the scanning of the electron beam) with the tip making contact over the location at the end tip. The current line scan along *A*–*C*–*D* on (c) is shown in (d). Electron-beam energy $E_b = 15$ keV and current $I_b = 500$ pA. In order to enhance a correlation between these images, the contours of one grain are outlined for (b) and (c) (hollow circles).

the number of boundaries to be crossed by the electrons in order to reach the tip. This illustrates how the combination of SEM and AFM can be very useful to determine the electrical behavior of individual grain boundaries in microsized grain semiconductors.

14.2.7
Combination of Various Scanning Electron Microscopy Techniques

Apart from combining SEM and AFM imaging, it is also possible to unite various other SEM techniques in order to gain information on microstructure, composition, charge carrier collection, and radiative recombination, with high spatial resolutions of down to 20–100 nm. These are especially useful when acquired on the identical region of interest. Examples for an SE image, EBSD pattern quality and orientation distribution maps, monochromatic CL images, an EBIC image, and EDX elemental distribution maps, all acquired on the identical position on a ZnO/CdS/$CuInS_2$/Mo/glass cross-sectional specimen, are given in Figure 14.16. By combination of, for example, the EBSD maps and the CL images, it is possible to relate the local orientations to the local recombination behavior. The EDX maps suggest that the strongly varying local CL intensities are not due to a change in composition, and it is apparent that the EBIC intensities are high where the CL signals are rather low.

14.3
Transmission Electron Microscopy

Whenever aiming for imaging and analyses at scales of down to the angstroms range, TEM and its related techniques are appropriate tools. In many cases, also

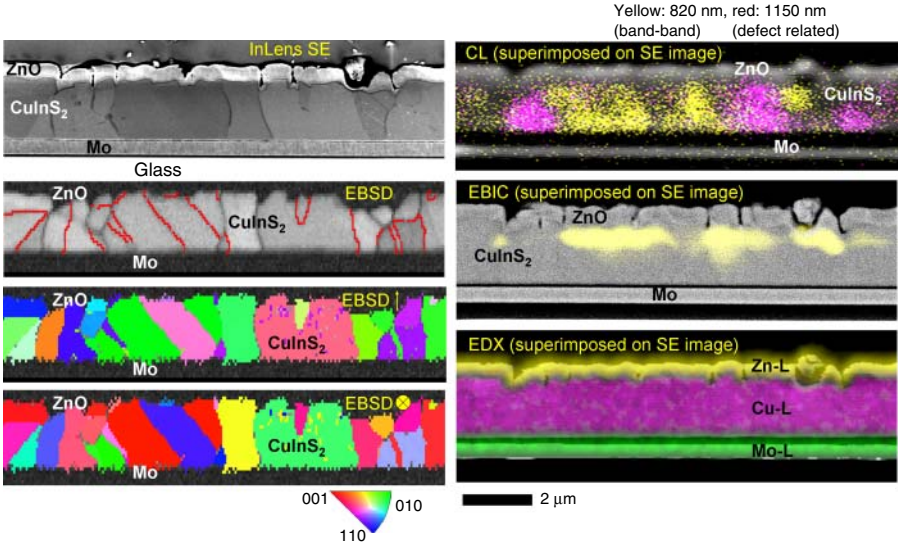

Figure 14.16 SE image (at 3 keV), EBSD pattern-quality (with Σ3 grain boundaries highlighted by red lines) and orientation distribution maps (at 20 keV), monochromatic CL images at 10 keV, 8 K, and at 820 (yellow, band–band transitions) and 1150 nm (pink, defect-related transitions), superimposed on an SE image, an EBIC image (8 keV) and EDX elemental distribution maps (7 keV) from Zn-L (yellow), Cu-L (pink), and Mo-L (green) signals. All images and maps were acquired on the identical position of a ZnO/CdS/$CuInS_2$/Mo/glass stack. (Provided by courtesy of Dr B. Marsen, HZB, Berlin, Germany; CL images in collaboration with Dr U. Jahn, Paul-Drude Institut Berlin, Germany.)

SEM techniques provide the access to various material properties of the individual layers, not requiring specimen preparation as time consuming as TEM techniques (details on the preparation can be found in Section 14.4). Still, TEM exhibits unique possibilities, especially when studying the properties of interfaces between individual layers, of grain boundaries, or of any other (sub)nanometer-scale features.

Transmission electron microscopes consist of an electron gun, emitting an electron beam, which is accelerated to energies typically ranging between 80 and 1200 keV. The way these electrons impinge on the sample differs for the conventional TEM (CTEM) and the scanning TEM (STEM) modes (Figure 14.17). In CTEM mode, the specimen is irradiated by a (nearly) parallel electron beam, and imaging as well as electron diffraction is performed on a specific region of interest. The beam may also be focused on a spot and scanned across this region of interest for modern microscopes with electron-probe sizes down to below 0.1 nm. This allows for imaging, electron diffraction, and compositional analysis of high spatial resolutions.

The present section will give an overview of the various techniques in CTEM and STEM modes, that is, imaging, electron diffraction, electron energy-loss spectroscopy, and electron holography. Details on TEM/EDX can be found in

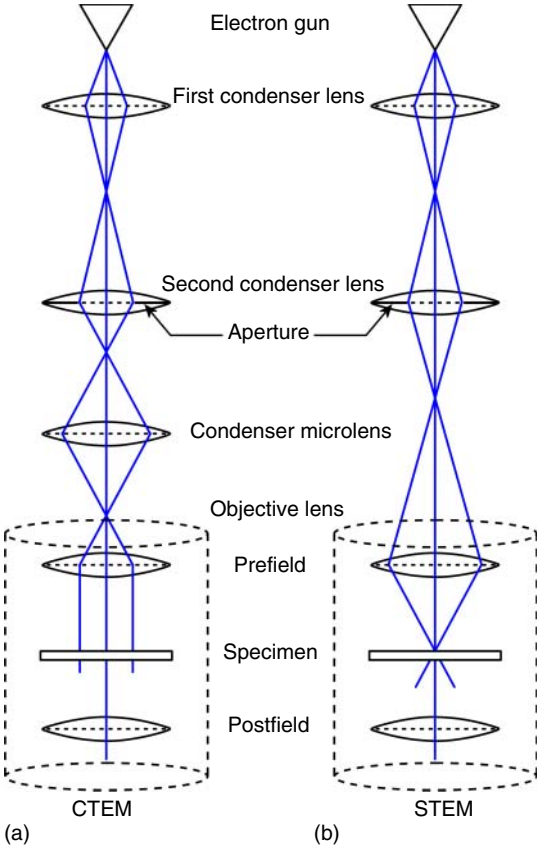

Figure 14.17 Schematics of the lens configurations in the upper part of transmission electron microscope and their influences on the electron-beam trajectories for CTEM (a) and for STEM (b). Note the results are a parallel beam for CTEM and a focused electron probe for STEM. (Reproduced from Ref. [43].).

Section 14.2.3. Further more detailed introductions into TEM can be found, for example, in Refs [51–53].

14.3.1 Imaging Techniques

14.3.1.1 Bright-Field and Dark-Field Imaging in the Conventional Mode

When a parallel electron beam is scattered at a crystalline specimen, a part of the electrons is diffracted at atomic planes. All electrons transmitted by the specimen are imaged by the objective lens into the image plane. The electrons diffracted into same angles go through the identical reflection in the diffraction pattern, which is formed in the back-focal plane of the microscope (Figure 14.18). The center reflection of the diffraction pattern (000) is generated by the direct (undiffracted)

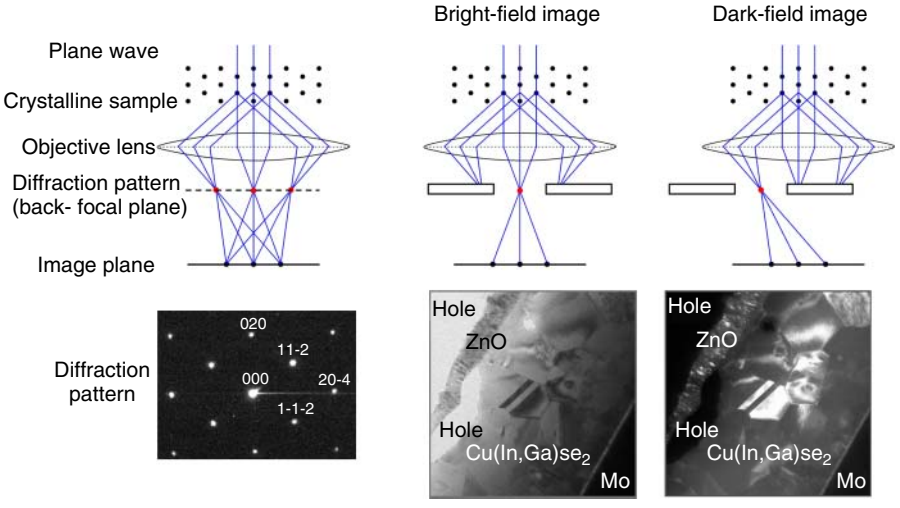

Figure 14.18 Schematics of BF and DF imaging in the CTEM mode of the microscope. The diffraction pattern is formed in the back-focal plane of the objective lens. Exemplary BF and DF images, acquired at the identical position on a cross-sectional specimen of a $Cu(In,Ga)Se_2$ thin-film solar cell, show the changes in contrast when selecting either direct or diffracted beams by means of the objective aperture.

beam, whereas the other reflections are indexed according to the *hkl* values of the set of atomic planes at which the electrons are diffracted. By use of projection lenses, either the image of the sample or the diffraction pattern can be projected on the view screen or the imaging device.

In order to enhance the contrast in a TEM image, an (objective) aperture may be introduced into the back-focal plane of the objective lens in order to select either direct or diffracted electron beams for imaging. When the objective aperture is positioned on the central (000) reflection in the diffraction pattern, mainly the direct electron beam contributes to the image, whereas diffracted beams are (at least in part) screened. The result is that the hole in the image (Figure 14.18) appears bright, and therefore the type of imaging is termed bright-field (BF). When diffracted beams are selected by use of the objective aperture, the hole becomes dark, which is why the method is called dark-field (DF) imaging. Grains with sets of atomic planes at which the impinging electron beam is diffracted into wide angles appear dark in a BF image and bright in the DF image (where the reflection is selected by the objective aperture corresponding to the set of atomic planes). It may be concluded that BF and DF imaging makes use of diffraction or amplitude contrasts.

14.3.1.2 High-Resolution Imaging in the Conventional Mode

In the present section, the term "high resolution" (HR) is used for imaging of the atomic lattice of polycrystalline thin films. In contrast to BF and DF imaging, where an objective aperture with rather small opening is applied in order to

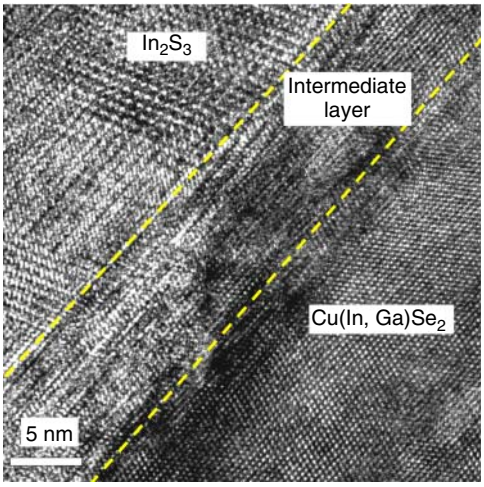

Figure 14.19 HR-TEM image from the interface between the p-type Cu(In,Ga)Se_2 absorber and the n-type In_2S_3 buffer. An intermediate layer of about 10 nm thickness formed between the absorber and the buffer (see Ref. [54] for further details).

select either the direct (including also forward scattered) or diffracted beams for HR-TEM, the objective aperture should be sufficiently large in order to include the direct and at least one diffracted beam [44]. HR-TEM images (as the one in Figure 14.19) must not be considered as direct images of the atomic lattice, but they are interference patterns formed by phase relationships of the direct and the diffracted beams. Therefore, HR-TEM imaging is based on phase contrast. Note that in order to image an atomic lattice, corresponding atomic columns have to be oriented parallel to the impinging electron beam, which is realized by tilting the specimen in the microscope. In addition, it is important to correct the aberrations of the objective lens as much as possible.

Then, spherical aberration and defocus are used to optimize phase-information transfer, resulting in an atomic lattice image since the interference fringes in HR-TEM images are related to the atomic positions. The appearance of these fringes is affected considerably by the focus and the specimen thickness (only for uncorrected transmission electron microscopes). By varying these parameters, contrasts may be inverted, that is, white spheres on black backgrounds (as in the HR-TEM image in Figure 14.19) may be changed into black spheres on white backgrounds. Therefore, the unambiguous interpretation of HR-TEM images requires in general the acquisition of a series of TEM images from the identical region of interest at varying focus and also the comparison of these experimental images with simulated ones [55]. Currently, high point resolutions of down to 0.05 nm [56] have been demonstrated by use of a series of lenses correcting for the spherical [57] and chromatic [58] aberrations of the objective lens (a similar corrector for spherical aberrations may be applied for the condenser system in order to enhance the point resolution in the STEM mode).

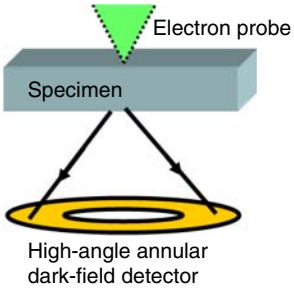

Figure 14.20 Schematics of HAADF imaging in the STEM mode of the microscope.

14.3.1.3 Imaging in the Scanning Mode Using an Annular Dark-Field Detector

Electrons transmitted through the sample in the STEM mode can be detected by use of either a BF detector, residing on the optical axis of the microscope, or a DF detector, which has the form of a ring and is therefore termed annular DF (ADF). By varying the camera length of the ADF detector, it is possible to image using mostly Bragg-diffracted electrons (large camera lengths), obtaining a crystallographic contrast, or to perform Z contrast imaging at high scattering angles (short camera lengths; see Figure 14.20). Note that the aim of Z contrast is to achieve images dominated by single-atom scattering, which is incoherent. The contrast in these images is then formed by differences in the average atomic number Z of the position probed since the intensity in the image I is proportional to about Z^2, according to the Rutherford scattering cross section. Modern microscopes providing an STEM mode are equipped with high-angle ADF (HAADF) detectors which exhibit a very large central aperture.

14.3.2 Electron Diffraction

14.3.2.1 Selected-Area Electron Diffraction in the Conventional Mode

The basic setup for electron diffraction in CTEM mode with (nearly) parallel illumination of the specimen has already been given in Figure 14.18. It was shown that the electron diffraction pattern forms in the back-focal plane of the objective lens. In order to confine the diffraction pattern to a specific region of interest, an aperture may be positioned on the corresponding position in the image plane. (Note that additional projection lenses – not shown in Figure 14.18 – project either the image of the sample in the image plane or the diffraction pattern in the back-focal plane on the view screen or the imaging device.) This is the concept of selected-area electron diffraction (SAED). The basic concepts of neutron and X-ray diffraction at materials, introduced in Chapter 15, apply also to electron diffraction. Thus, they shall not be addressed further at this point.

Aperture sizes of down to about 50 nm in diameter (on the specimen) may be applied. Similar as for HR-TEM, grains of interest are oriented such that atomic columns are parallel to the incident electron beam. An example of an SAED pattern acquired at the interface between a $Cu(In,Ga)Se_2$ absorber and an In_2S_3 buffer

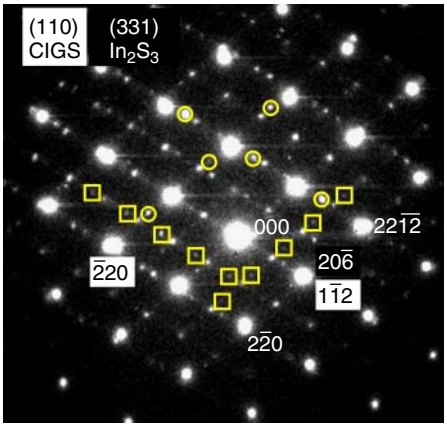

Figure 14.21 SAED pattern acquired at the interface between Cu(In,Ga)Se_2 absorber and In_2S_3 buffer. In addition to reflections attributed to the perfect crystals, also reflections from twin boundaries are visible, which are present in the Cu(In,Ga)Se_2 (circles) and In_2S_3 layers (squares).

layer is given in Figure 14.21. Note that in this diffraction pattern, it is possible to identify an orientation relationship between the Cu(In,Ga)Se_2 and the In_2S_3 layers since the corresponding $1\bar{1}2$ and $20\bar{6}$ as well as the 004 and $2\bar{2}0$ reflections superimpose each other. (Remark: The orientations of individual crystals with respect to the incident electron beam, also termed zone axes, have the notation [*uvw*] (*u*, *v*, and *w* being the coefficients of a vector in real space), whereas atomic planes (or rather the whole set of these) is given by *hkl* (*h*, *k*, and *l* being the coefficients of a vector in real space).)

14.3.2.2 Convergent-Beam Electron Diffraction in the Scanning Mode

Although SAED is very useful for giving information on the crystal structures of individual thin films and also on the orientation relationships of two neighboring layers, the region of interest probed is in general much larger than many crystalline features present in individual grains. Also, the crystallographic information obtained is in many cases not precise due to a relaxation of the Bragg conditions for a thin specimen and small grains present in the specimen. A technique overcoming these limitations is convergent-beam electron diffraction (CBED) in the STEM mode of the microscope. Using this technique, the illumination of the specimen is not parallel but convergent, with probe sizes in the range of few nanometers to few tens of nanometers, that is, sufficiently small in order to probe very small specimen volumes. The result is that instead of an array of sharp maxima as in SAED, the diffraction pattern in the back-focal plane consists of a pattern of disks of intensity. The size of these disks depends on the beam convergence angle, which is controlled by the size of the condenser aperture. The larger this angle, the larger the size of the CBED disks.

The camera length (magnification of the diffraction pattern) is also an important parameter since it defines the angular range of the pattern. At large camera lengths, mainly the central 000 disk is visible, whereas a wide area of the reciprocal space comes into sight for small-camera-length values, containing also electrons scattered into high angles. By acquiring CBED patterns at varying convergence angles and camera lengths, not only small deviations in lattice parameters within individual grains may be detected, but also specimen thicknesses and crystal symmetries of unknown materials may be determined.

14.3.3 Electron Energy-Loss Spectroscopy and Energy-Filtered Transmission Electron Microscopy

Two related analysis techniques in a TEM are electron energy-loss spectroscopy (EELS) and energy-filtered TEM (EFTEM, sometimes also referred to as energy-selected imaging (ESI). Both techniques are based on the loss of kinetic energy of the beam electrons due to the interaction with the specimen. The double-differential cross section of the interaction $d^2\sigma/(dE\, d\Omega)$ describes the angular distribution of the beam electrons after the scattering as a function of their energy loss. This distribution depends strongly on the elements and the bond types within the specimen and is a fingerprint of the material or compound under investigation. In EELS and EFTEM, the energy distribution of beam electrons after interaction with a specimen is exploited to analyze the specimen.

14.3.3.1 Scattering Theory

A good knowledge of electron scattering theory [59] is required, in order to interpret the acquired energy-loss spectra and energy-filtered images. In electron microscopy, beam electrons with kinetic energies E_B interact with the constituents of a specimen material via electromagnetic interactions. Two types of interactions are usually distinguished: elastic and inelastic interactions.

In elastic or quasielastic scattering, no or little energy is transferred between the beam electrons and the specimen. This is the interaction of the beam electrons with atomic nuclei in the specimen, which have a much larger rest mass than the beam electrons and phonons. Although the energy transfer is negligible, momenta may be transferred between the beam electrons and single nuclei or phonons. This transfer can change the momentum directions of the primary beam electrons but affects their absolute value only to a negligible extent.

In inelastic scattering, a significant amount of energy and momentum is transferred between the beam electron and the specimen. This is the interaction of the beam electron with electrons within the specimen. Due to the energy transfer, these specimen electrons can be excited from a lower into a higher unoccupied electronic state. This includes single-electron excitations as well as collective excitations such as plasma resonances (plasmons). The energy distribution of the

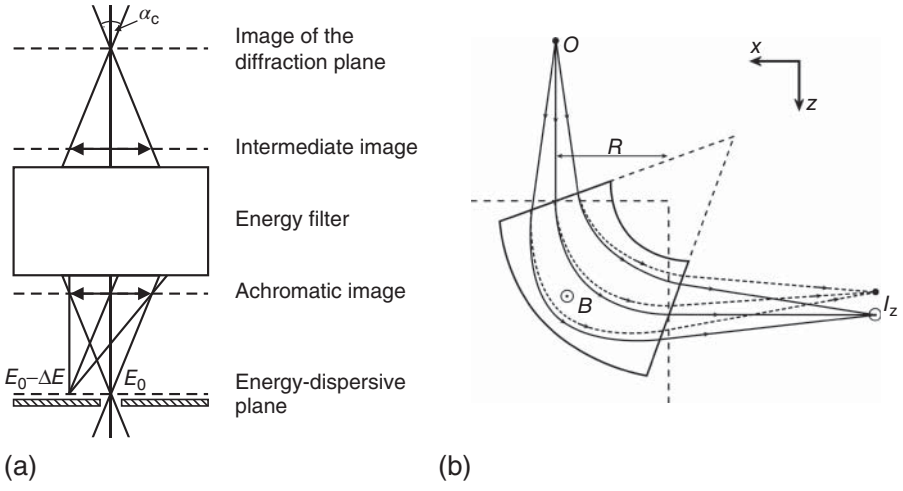

Figure 14.22 (a) The principle of an electron energy-loss spectrometer. Beam electrons with energy loss ΔE are focused on spots different from those for beam electrons with the initial energy E_0. α_c denotes the collection angle of the spectrometer. (b) Principle of a postcolumn energy filter. The magnetic field B deflects electrons emanating from the object point O on monochromatic spots along the z-axis, where the intensity distribution I_z is formed. The lines with arrows indicate the path of electrons without energy loss, and the dashed lines the path of electrons that lost some energy.

beam electrons having been scattered at the specimen is therefore strongly coupled with the electronic structure of the specimen.

14.3.3.2 Experiment and Setup

In general, both types of scattering, elastic and inelastic, occur and together determine the double-differential cross section of the interaction $d^2\sigma/(dE\, d\Omega)$, which is unique for each specimen. It is not (yet) convenient in TEM to record the total scattering intensity as function of scattering angle and energy loss. This is due to technical reasons and storing capacities. For EELS and EFTEM, only electrons within a specific angular range (i.e., within a cone) are utilized (see Figures 14.17 and 14.22a). The aperture angle α_c (i.e., the collection angle of the spectrometer; see Figure 14.22a) of this cone is either limited by the lens system or by an aperture in the optical path. In order to gain access to the energy distribution of the primary beam electrons scattered at the specimen, these electrons are focused on monochromatic spots, which are spatially separated along one axis according to their kinetic energies, as shown in Figure 14.22a. Ideally, the position of these spots in the resulting spectrum would be independent of the initial momentum of the electrons and the position of the interaction within the specimen. In practice, this is realized by means of imperfect electromagnetic prism devices (i.e., spectrometers and energy filters), within or below the TEM column. An example of a postcolumn filter installed below the TEM column is shown in Figure 14.22b. If

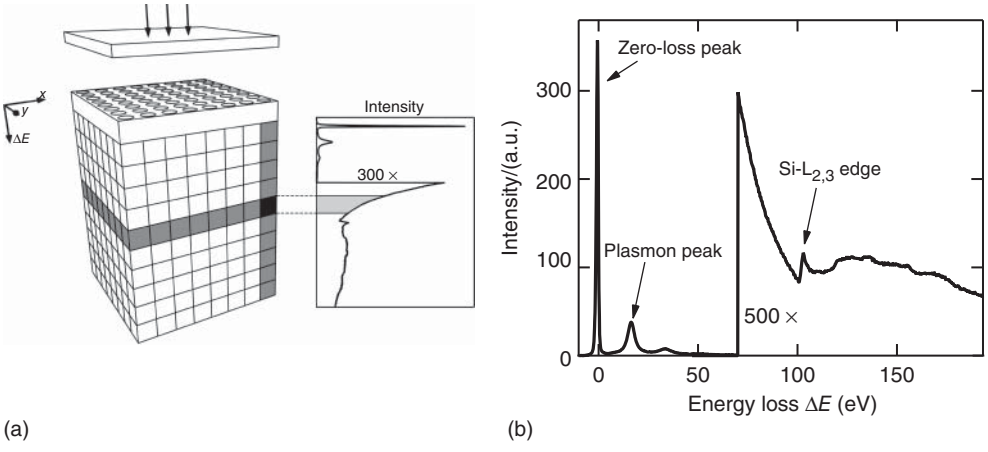

Figure 14.23 (a) Data cube of the intensity distribution $I(x, y, \Delta E)$. With EFTEM, the intensity distribution $I(x, y)$ for certain energy losses ΔE is acquired. EELS is applied to acquire the intensity distribution $I(\Delta E)$ for a sample positions x, y. (b) Electron energy-loss spectrum of a Si sample. The zero-loss peak, a plasmon peak, and the Si-$L_{2,3}$ edge are indicated.

properly aligned in a TEM, such spectrometers exhibit an energy-dispersive plane, containing the spectrum, and an image plane where the image or diffraction pattern of the sample is formed. For a review of EELS and EFTEM instrumentation and spectrometer devices, see Refs [51, 60].

The measured quantity in EELS and EFTEM is the electron intensity as function of sample position and energy loss $I(x, y, \Delta E)$ (sometimes also of scattering angles and energy loss $I(\varphi, \theta, \Delta E)$). These intensity distributions $I(x, y, \Delta E)$ are obtained by applying one of the following two approaches.

- *EELS*: Energy-loss spectra (diffraction spectra) $I(\Delta E)$ are acquired on positions (x, y) within a region of interest (see Figure 14.23a). For this approach, the projective lens system projects the spectrum (energy-dispersive) plane of the spectrometer on the detecting device (e.g., a CCD camera). The procedure described is performed in STEM mode.
- *EFTEM*: Images or diffraction patterns with intensity distributions $I(x, y)$ are acquired by use only of electrons within selected energy intervals (from ΔE to $\Delta E + \mathrm{d}E$) (see Figure 14.23a). For this approach, an energy-selecting slit (with width $\mathrm{d}E$) is placed into the spectrum plane of the spectrometer at position ΔE, and the projective lens system projects the image plane of the spectrometer on the detecting device (e.g., a CCD camera).

The energy resolution of the intensity distributions $I(x, y, \Delta E)$ is not only dependent on the quality of the spectrometers but also on the initial momentum and energy distribution of the beam electrons prior to the interaction with the specimen. The resolution can be improved substantially by applying monochromators to minimize the FWHM of the initial energy distribution.

14.3.3.3 The Energy-Loss Spectrum

Figure 14.23b shows an example of an electron energy-loss spectrum of a Si sample. In general, such a spectrum can be divided into several sections (corresponding to different causes for energy loss):

- *Zero-loss region (0 eV)*: The peak at zero energy loss is called "zero-loss" or "elastic" peak. Its intensity represents all electrons which traveled through the specimen without measurable energy loss within the resolution limit of the spectrometer, such as Bragg-diffracted electrons.
- *Low-loss region (0–50 eV)*: The first few hundred millielectron volt energy loss of the spectrum contains intensity fluctuations due to phonon scattering and intraband excitation. The subsequent region up to an energy loss of 50 eV contains beam electrons that have excited plasmons, Cherenkov radiation, and interband transitions. It is therefore possible to extract local band-gap energies [61] by evaluating the low-loss signals.

  While penetrating the specimen, beam electrons polarize the dielectric medium. In turn, the medium exerts a force on the beam electrons which results in energy loss. Hence, the energy-loss distribution is related to the polarizability of the specimen [51], and the low-loss region can be analyzed in order to determine the local complex dielectric function $\varepsilon(\Delta E)$ of the specimen [62]:
- *Ionization edges (50 eV to few kiloelectron volts)*: These edges or peaks (see Figure 14.23b) appear at approximately energy-loss values of the binding energy of electrons in core shells. Interactions with the beam electrons excite these inner-shell electrons into unoccupied electronic states or into the continuum. The heights of and the area under the edges are very sensitive to the local composition. Up to 50 eV beyond an ionization edge, the so-called energy-loss near-edge structure (ELNES) can be studied. This structure contains information on the binding state and the coordination of the involved atoms and depends on the joint density of states, which includes the density of ground and excited states. The two energy-loss spectra in Figure 14.24 show how the shape and the onset of the Si-$L_{2,3}$ edge changes from Si to SiO_2. In state-of-the-art microscopes, EELS and ELNES analyses can be performed down to the atomic scale [64] using the STEM mode.

  The extended energy-loss fine structure (EXELFS) covers a few hundred electron volts beyond the ionization edge and can be analyzed to obtain information about the distance of neighboring atoms. It arises through interference between the electron wave backscattered from neighboring atoms and the outgoing wave of the excited electrons.
- *Background*: Background signals, generated by various electron energy-loss processes, additional to the ones mentioned earlier, are superimposed on the characteristic features. These processes include beam electrons which excited quasi-free electrons and electrons that lost energy owing to bremsstrahlung. The local decrease of the background intensity at higher energy loss can be described well by a power law of the energy loss ΔE^{-n}. However, the exponent n may change with varying energy loss ΔE.

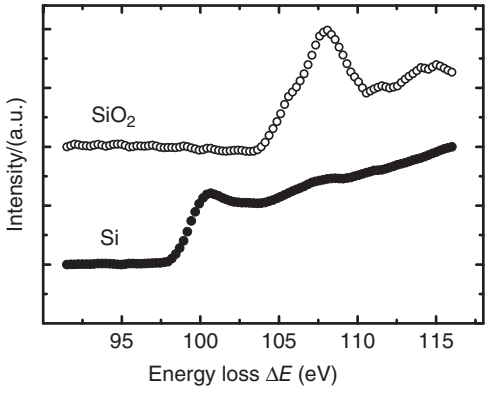

Figure 14.24 EEL spectra of the Si-$L_{2,3}$ edge acquired for a Si and SiO_2 sample [63]. The onset and the shape of the Si-$L_{2,3}$ edge change for different adjacent atoms.

- *Thickness effect*: The electron energy-loss spectrum is very sensitive to the collection angle (Figure 14.22a) and the thickness of the specimen. The thicker the sample, the higher the probability for multiple scattering of beam electrons in the specimen. The resulting energy loss of an electron is the sum of the energy losses of the individual scattering events.

For the evaluation of an EEL spectrum, a single-scattering distribution is favorable, where each electron has been scattered only once or not at all. It is therefore beneficial to work with specimen thicknesses smaller than the mean free path λ of electrons in the specimen material (which is typically 50 – 100 nm and can be estimated by use of an algorithm given in Ref. [51]). The effect of multiple scattering on a spectrum can be compensated in part by applying signal-processing methods, for example, Fourier-log or Fourier-ratio deconvolution [51].

Although sometimes obstructive, the thickness dependence is the reason why the local thickness of specimens can be measured with EELS and EFTEM. Assuming that the number of scattering events per electron follows a Poisson distribution, the specimen thickness t can be calculated from the ratio of the total electron intensity I_t and the intensity of the unscattered electrons I_0 according to $t/\lambda = \ln(I_t/I_0)$. A thickness distribution map from a region of interest can be computed from corresponding unfiltered and zero-loss filtered images:

Limitations: The energy and spatial resolutions of EELS and EFTEM are limited because of several effects. First of all, imperfect instrumentation affects these resolutions, which may be in part be compensated by the use of monochromators, aberration-corrected lenses, and spectrometers. However, not only the instrumentation has an effect but also the material and thickness of the specimen. Delayed or deformed ionization edges or edges at high energy losses are difficult to be evaluated. In addition to beam damage, contamination of the specimen surface with C or Si from the residual gas in the column can change the energy-loss spectrum substantially.

14.3.3.4 Applications and Comparison with Energy-Dispersive X-Ray Spectroscopy

With the information of the energy-loss distribution, a variety of specimen properties are accessible. However, the successful application of EELS and EFTEM requires good knowledge about the microscope and the scattering theory and may involve also modeling and simulation [65], as well as an optimized sample preparation.

One main application is the analysis of the local chemical composition of elements in the specimen, for which both techniques compete with energy-dispersive X-ray spectroscopy (EDX) in TEM. Sigle [66] gives an overview of state-of-the-art applications of EELS and EFTEM and a detailed comparison with EDX. A summary of this comparison is given in the following:

- *Resolution*: EELS in the STEM mode offers a slightly better spatial resolution than EDX (sub-angstrom), because the sample volume which provides the information can be defined by apertures confining the collection angle of the spectrometer [51]. This may compensate for beam broadening in the sample. The energy resolution, especially when using a monochromator, is much better in an electron energy-loss spectrum (<1 eV) compared with an EDX spectrum (down to few tens of electron volt, depending on the element). Therefore, EELS provides access to further specimen properties apart from composition (see preceding text).
- *Count rate and background*: In comparison with EDX, EELS profits from a better count rate but suffers from a higher background. This is partly because the X-ray fluorescence yield is very low, especially for light elements. In addition, the scattered electrons have an angular distribution peaked in forward direction, while characteristic X-rays are emitted isotropically. In the EDX signal, the background arises mainly from bremsstrahlung X-rays, whereas in the EELS signal, there are several contributions (see paragraph on "Background").
- *Quantification and detection limit*: Although EELS has advantages in the case of the detection of light elements, the detection limit strongly depends on the specimen material. In some cases, even single atoms can be detected [67]. The detection limit for EDX is approximately 0.1–1 at.%. Compared with EDX, EELS allows for a standardless quantification (without reference specimen) of the local composition. However, very thin specimens are required, and modeling is needed for a quantitative specimen analysis. While EDX in a TEM is a well-established acquisition technique, EELS is more demanding for the operator during acquisition and quantification.
- EELS is usually better for the detection and quantification of light elements, and EDX can be advantageous for the detection and quantification of heavy elements.
- *Information content*: In general, the information content is higher in EELS, since the spectra contain features like ELNES and EXELFS and information about the polarizability of the specimen and provide information about the specimen thickness.

14.3.4
Off-Axis and In-Line Electron Holography

In CTEM, the exit-plane electron wavefunction (i.e., of electrons emerging from the specimen at the bottom surface, having interacted or not) may be written in the form $a(x, y)\exp[i\varphi(x, y)]$, where a and φ are the amplitude and the phase of this wavefunction, whereas x and y are spatial coordinates. The objective lens of the microscope images this electron wave on the image plane of the objective lens. This image of the original wavefunction shall have the form $A(x, y)\exp[i\Phi(x, y)]$, where A and Φ are the corresponding amplitude and phase. The intensity distribution of a TEM image, $I(x, y)$, does not contain information on the phase of the electron wave since it can be considered the square of the corresponding amplitude distribution: $I(x, y) = A^2(x, y)$. Thus, in CTEM, the information on the spatial phase distribution $\Phi(x, y)$ and thus also that of the exit-plane wavefunction, $\varphi(x, y)$, is lost.

A way to overcome this obstacle is the application of off-axis electron holography [68]. Figure 14.25a shows a schematic representation of the experimental setup of this technique. The key principle is to make use of an unscattered reference electron wave (since the wave goes through a hole in the specimen) and the electron wavefunction of the scattered electrons (at the specimen) interfering with one another. This process results in a hologram, which contains the information on both the amplitude and the phase distribution $A(x, y)$ and $\Phi(x, y)$. The interference of the direct (unscattered) and the scattered electron wave is realized by a biprism, which is a positively charged wire. In a second step, the amplitude and phase distribution of the exit-plane wavefunction (i.e., $a(x, y)$ and $\varphi(x, y)$) are reconstructed from the hologram. Figure 14.25b and c shows the reconstructed amplitude and phase images from a ZnO/CdS/Cu(In,Ga)Se_2 layer stack. The amplitude image is governed mainly by the contrasts due to Bragg diffraction (mainly visible in the ZnO and Cu(In,Ga)Se_2 layers) and variations in thickness.

If the primary electron beam is not dynamically scattered (e.g., Bragg diffracted) in the specimen (for applying medium-resolution electron holography), the spatial phase distribution $\varphi(x, y)$ of the exit-plane electron wave is proportional to the electrostatic potential $V(x, y)$ via

$$\phi(x, y) = \sigma t(x, y)V(x, y), \tag{14.4}$$

where σ is an electron interaction constant dependent on the acceleration voltage and t is the effective specimen thickness, taking also in account possible contamination layers on the top and bottom surfaces of the specimen. That is, the contrasts in the phase image can be attributed to a spatially varying electrostatic Coulomb potential in the specimen which the impinging electrons experience when they travel through it. In a crystalline sample, the electrostatic potential $V(x, y)$ contains contributions from the ionic lattice of the crystal, also termed mean-inner potential (MIP), and from the redistribution of charges (via the Poisson equation). Twitchett *et al.* [70] demonstrated the application of phase imaging by means of off-axis electron holography at a bulk Si p–n junction. Since

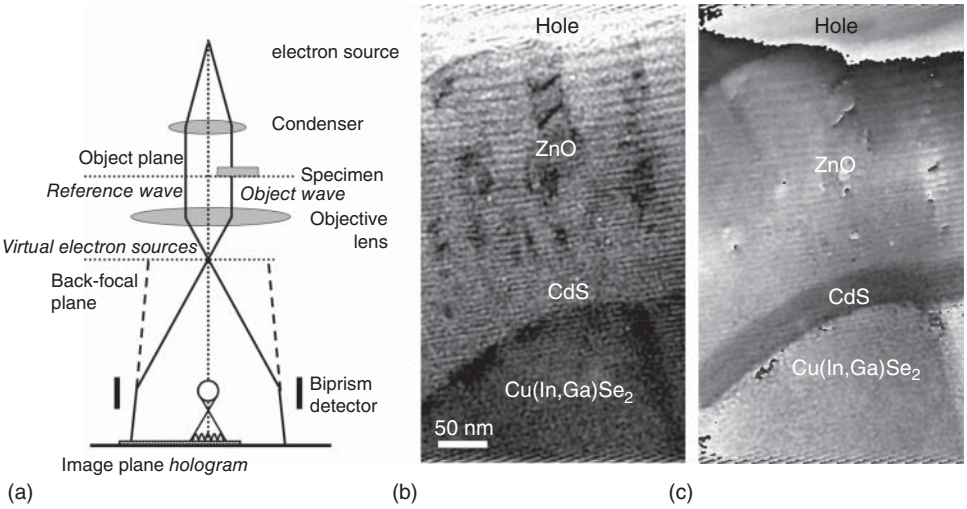

Figure 14.25 (a) Schematics of the experimental setup of off-axis electron holography. (Reproduced from Ref. [69].) Reconstructed amplitude (b) and phase (c) images from a ZnO/CdS/Cu(In,Ga)Se_2 layer stack. (Data by courtesy of M. Lehmann, TU Berlin/TU Dresden.)

the contribution from the ionic crystal lattice to $V(x, y)$ is the same for p-type and n-type Si, the contrast in the phase image is due to the distribution of space charges at the junction. However, this approach is complicated substantially when applied to a p–n heterojunction (as ZnO/CdS/Cu(In,Ga)Se_2 shown in Figure 14.25). It should also be noted that in general, off-axis holography (at medium resolution) is performed on specimens with thicknesses of few hundreds of nanometers in order to provide sufficiently high signal-to-noise ratios.

Even when working at a microscope without biprism, phase contrast images may still be obtained by the acquisition of a series of TEM images, for example, at varying focus, where the exit-plane electron wave interferes with itself. This technique (for medium resolutions) is termed Fresnel contrast analysis or in-line electron holography [71] and particularly useful at phase or grain boundaries, that is, where the phase is likely to change. The corresponding TEM images feature Fresnel fringes (Figure 14.26) at these boundaries, and the contrasts and spacings of these fringes vary with varying defocus value Δf. By use of a reconstruction algorithm [72], not only the spatial phase distributions $\varphi(x, y)$ but also the amplitude $a(x, y)$ of the exit-plane electron waves are calculated. From these distributions, corresponding electron-static potential images can be obtained via Equation 14.4.

If not measured by high-resolution TEM, the phase shift of atomic columns cannot be detected, and the images reconstructed from the through-focus series are, in the absence of superimposed electromagnetic fields [73], projections of the 3D potential. Note that, depending on the exact method and application, in-line

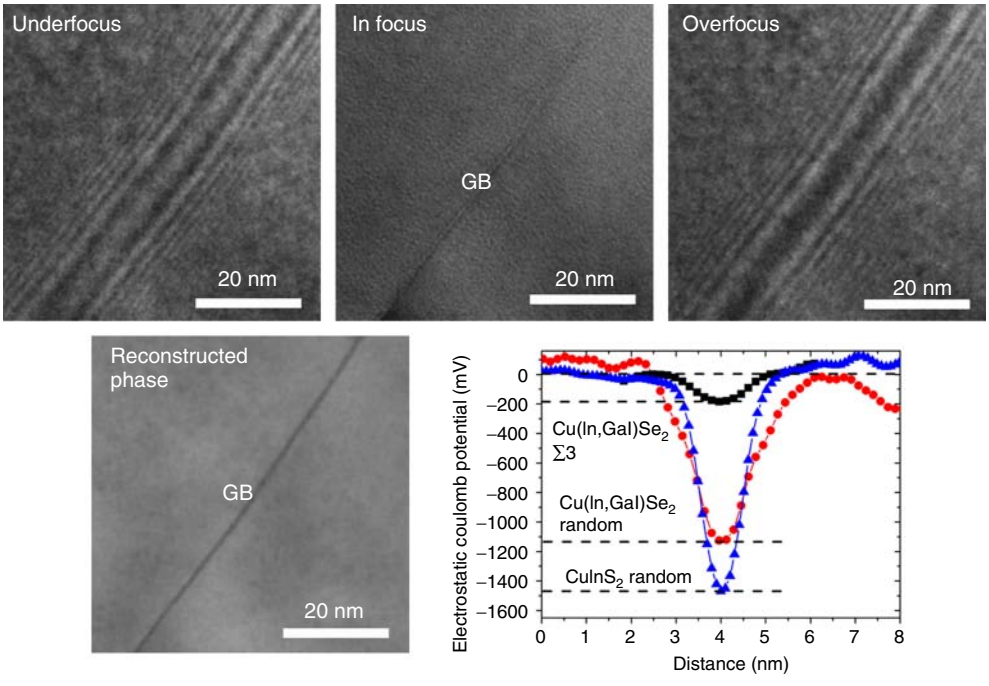

Figure 14.26 TEM images from a region around a grain boundary in a $CuInS_2$ thin film (top), acquired at varying focus value. In the images recorded at underfocus and overfocus conditions, Fresnel fringes around the grain boundary are visible. From this series of images, a phase distribution image was reconstructed (bottom). In addition, profiles across various grain boundaries in $Cu(In,Ga)Se_2$ and $CuInS_2$ absorber layers were extracted from electrostatic potential distribution images, calculated from corresponding phase distribution images by use of Equation 14.4.

electron holography may only give information about the *changes* in the phase (and not absolute values, as off-axis electron holography).

Unless intended by experienced users, the determination of the electrostatic potential by use of electron holography is more convenient when working on areas with constant thicknesses and by avoiding dynamical scattering conditions, that is, by tilting samples away from low-index zone axes, since dynamical scattering conditions can have a substantial influence on the exit-plane wave. In any case, simulation of the exit-plane wavefunction is necessary.

When extracting profiles from spatial distributions in the electrostatic potential obtained on $Cu(In,Ga)(S,Se)_2$ grain boundaries (Figure 14.26 shows an example from a $CuInS_2$ layer), the general result is potential wells with FWHM of about 1–2 nm and depths of 1–2 V. The width and depth of a potential well can depend on the grain boundary symmetry and may be interpreted in terms of whether varying space charge densities [74], changes in composition, or, more general, changes in the ionic lattice of the crystal are responsible for the changes in phase detected [75, 76]. The spatial resolution of the electrostatic potential profiles exhibits values

of about 0.4–0.6 nm and is limited by the size of the objective aperture. Note that the spatial amplitude distribution $a(x, y)$ was almost homogeneous around the phase object (in the present case, the grain boundary).

A decent comparison of off-axis and in-line holography and also a further introduction into the techniques can be found in Ref. [77].

14.4 Sample Preparation Techniques

The last section of the present chapter is dedicated to specimen preparation for electron microscopy. The position in the chapter suggests a minor importance; however, the preparation decides indeed on the quality of imaging and analyses. It is specifically the specimen surface to which one should always pay the greatest attention. All contamination, scratches, and further disturbances complicate the interpretation of images and the evaluation of the analysis data. Special care is advised when dealing with materials which are incongruently sputtered by an ion beam, for example, Cu(In,Ga)Se_2, since the surface treatment of these materials by ion beams may lead to the formation of agglomerates at the specimen surface [78].

The focus of the present section is put on the preparation of cross-sectional specimens. A more general introduction may be found in Ref. [79].

14.4.1 Preparation for Scanning Electron Microscopy

A very simple cross-sectional preparation not only for thin-film solar cells on glass substrates but also for those on foils is to fracture or cut the cell, which normally takes only seconds. However, since these solar cells in general consists of rather brittle materials, the result may be disappointing, yet justified when aiming for a quick glance on the sample or when surface roughness on the cross section is not a severe issue. Furthermore elaborated (and also more time-consuming) methods are described in the following:

- *Combination of mechanical and ion polishing*: Stripes of the solar cell are cut, which then are glued face-to-face together, best by use of epoxy glue which is suitable for high vacuum. From the resulting stack, slices are cut, of which the cross sections are mechanically polished. Care is advised not to apply too much pressure during the polishing, and the scratches remaining on the cross-sectional surface are in the range of 100 nm or smaller in depth. Then, this cross-sectional sample is introduced in an ion polishing machine, equipped with, for example, Ar ion beams. In order to obtain rather flat cross-sectional surfaces, small incident angles of about 4° should be chosen. A thin layer of graphite (of about 5 nm in thickness) reduces drift during the measurement and also preserves the cross-sectional surface, often for several weeks. The graphite

seems also to enhance the signal intensities for EBIC (Section 14.2.4) and CL (Section 14.2.5) measurements, probably since it reduces the surface recombination substantially.

- *FIB in a scanning electron microscope*: A focused Ga ion beam can be used to sputter trenches into specimens, exposing cross sections at positions of interest. In a scanning electron microscope, the progress of the sputtering can be monitored by corresponding electron detectors. Also, by alternately FIB slicing and SEM imaging, a 3D image of the specimen may be reconstructed. Similarly, also EBSD and EDX/WDX may be combined with FIB slicing. It is of advantage to be able to prepare cross-sectional specimens and perform imaging and analyses on these specimens without breaking the vacuum, that is, reducing the effects of surface contaminations substantially. It should be pointed out that by means of FIB, cross-sectional specimens from thin-film solar cells may be prepared independent of the substrate, which should be particularly helpful when working with, for example, sensitive foils as substrates.
- *Plasma etching in a glow-discharge apparatus*: Apart from polishing or slicing cross sections by means of ion beams, also plasmas may be used for this purpose [80]. Particularly, instruments used for glow-discharge optical emission or mass spectrometry (see Chapter 19.1 for details) may be employed. The specimen functions as cathode in the glow-discharge setup, and the Ar plasma ignited sputters the specimen atoms. Few seconds of sputtering is sufficient for reducing surface roughness substantially.

14.4.2
Preparation for Transmission Electron Microscopy

The ultimate goal is always to obtain specimens which are transparent for electrons, that is, which exhibit thicknesses ranging from few to several hundreds of nanometers (you would like to work, e.g., with rather thin specimens for HR-TEM and with relatively thick ones for off-axis electron holography). When aiming for very thin regions in the specimens, this is generally achieved by forming a hole, preferably at positions within the layer stacks of the thin-film solar cells. At the fringe of this hole, the layer thicknesses are rather small, which increase moving away from the hole according to the angle of the wedge formed (see Refs [81–84] for overviews and more details). Another very helpful preparation method is FIB, providing a tool for selecting precisely the position from where a lamella is to be extracted:

- *Combining mechanical and ion polishing*: An approach applied frequently for preparing cross-sectional specimens from thin-film stacks is the combination of mechanical and ion polishing. There are various ways to the final TEM specimen:
    - Stripes of the solar cell are cut, which then are glued face-to-face together by use of epoxy glue (similar as for the preparation of SEM specimens).

One may also glue a piece of Si single crystal to the sample stripe. The resulting stack is introduced into a small tube of about 3 mm in diameter, filled with epoxy glue. From the tube, disks are cut, which are polished on both sides down to thicknesses of about 100 µm. A dimple grinder introduces a circular deepening in the sample, so that the resulting minimum specimen thickness is about 20–30 µm. Finally, Ar-ion milling at rather small angles (3.5–6°) is performed until a hole forms, preferably at the interface between the two stripes of the solar cell (i.e., the fringe of the hole intersects the thin-film stacks; see Figure 14.27a).

- From the stack formed by gluing to stripes of solar cells together face-to-face, also directly disks may be cut. These disks are polished on both sides until they exhibit thicknesses of about 10 µm. Rings made of Mo or Ni are glued on these very thin cross-sectional specimens, which will then support them. The Ar-ion milling process is somewhat shorter than in the procedure described earlier, due to the reduced thickness of the specimen (Figure 14.27b). Also for this approach, the result is a specimen with a hole at the interface between the solar-cell stripes. That is, in side view, the specimen has the shape of a wedge, with decreasing thickness toward the hole (Figure 14.27c).

- *Tripod polishing*: The stack form by gluing two stripes of solar cells face-to-face together may also be polished by use of a so-called Tripod [85], where the polishing plane is defined by three points. Two points are given by Teflon legs, which are kept coplanar, while on the third point at a corresponding leg, the sample

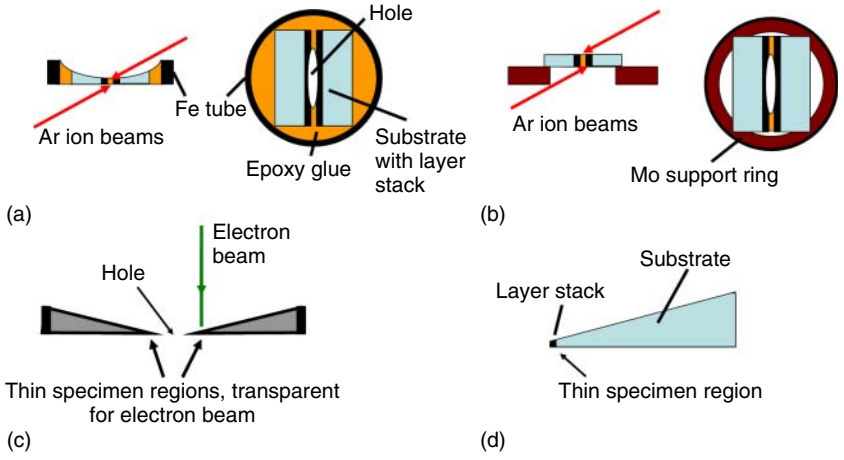

Figure 14.27 Schematics for conventional TEM preparation methods for cross-sectional specimens. (a) Forming a stack by gluing to two stripes of solar cells face-to-face together and embedding the stack in a Fe tube (cross-sectional and plan views). (b) Polishing the stack and gluing it to a Mo support ring (cross-sectional and plan views). (c) Cross-sectional view of the geometry of the final TEM specimen with respect to the incident electron beam. (d) Preparation of a wedge-shaped specimen by means of a Tripod. At the tip of the wedge, the specimen is transparent for the electron beam.

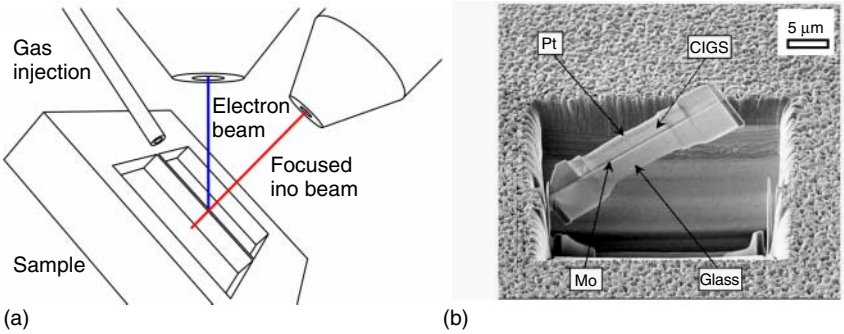

Figure 14.28 (a) Schematics of the configuration of the electron and Ga ion sources as well as of the gas injection in a focused ion beam system within a scanning electron microscope. The preparation of a TEM lamella is indicated. (b) SEM image of a TEM lamella prepared by FIB from a CdS/Cu(In,Ga)Se_2/Mo/glass stack.

is mounted. The pod heights are adjustable by micrometer screws. By use of a Tripod, either plan-parallel specimens may be polished, which are then glued to supporting rings (as described earlier), or wedge-shaped specimens may be produced (see Figure 14.27d). Often, specimens prepared by use of a Tripod are posttreated in an Ar-ion polishing machine in order to further reduce the thicknesses and to optimize the surface qualities.

- *Using an FIB in a scanning electron microscope*: Similarly as for SEM specimen preparation, trenches may be formed on two sides of a specific region of interest (Figure 14.28). The residual specimen lamella between the two trenches can be thinned further, until it is transparent for the electron beam. This lamella is then extracted by use of a micromanipulator needle and usually put on a TEM grid or welded (e.g., by use of Pt gas) to an appropriate TEM holder. Surface contamination layers formed as consequences of the ion-beam bombardment can be reduced substantially by decreasing the voltage and current of the impinging ion beam. FIB preparation may be also combined with polishing of the specimen in order to reduce the FIB milling duration. Further information of specimen preparation for TEM by use of an FIB can be found in, for example, Refs [86, 87].

Acknowledgments

The authors are grateful to Jaison Kavalakkatt for designing various figures and to Jürgen Bundesmann for technical support. Special thanks are due to Heiner Jaksch (Carl Zeiss NTS) and to Michael Lehmann (TU Berlin) for fruitful discussions and critical reading of the manuscript. Financial support by the Helmholtz Virtual Institute "Microstructure Control for Thin-film Solar Cells" (VI-520 MiCo) is gratefully acknowledged.

References

1. Everhart, T.E. and Hoff, P.H. (1971) Determination of kilovolt electron energy dissipation vs penetration distance in solid materials. *J. Appl. Phys.*, **42** (13), 5837–5846.
2. Reimer, L. (1985) *Scanning Electron Microscopy, Physics of Image Formation and Microanalysis*, Springer Series in Optical Sciences, vol. 45, Springer, Berlin.
3. Perovic, D.D., Castell, M.R., Howie, A., Lavoie, C., Tiedje, T., and Cole, J.S.W. (1995) Field-emission SEM imaging of compositional and doping layer semiconductor superlattices. *Ultramicroscopy*, **58**, 104–113.
4. Jaksch, H. (2008) *Low Loss BSE Imaging with the EsB Detection System on the Gemini Ultra FE-SEM. EMC 2008, Vol 1: Instrumentation and Methods*, Proceedings of the 14th European Microscopy Congress 2008, Aachen, Germany, September 1–5, 2008 (eds M. Luysberg, K. Tillmann and T. Weirich). Springer, Berlin. pp. 555–556.
5. Jaksch, H. (2008) *Strain Related Contrast Mechanisms in Crystalline Materials Imaged with AsB Detection. EMC 2008, Vol 1: Instrumentation and Methods*, Proceedings of the 14th European Microscopy Congress 2008, Aachen, Germany, September 1–5, 2008 (eds M. Luysberg, K. Tillmann and T. Weirich). Springer, Berlin. pp. 553–554.
6. Schwartz, A.J., Kumar, M., Adams, B.L., and Field, D.P. (eds) (2009) *Electron Backscatter Diffraction in Materials Science*, Springer, New York.
7. Keller, R.R. and Geiss, R.H. (2012) Transmission EBSD from 10 nm domains in a scanning electron microscope. *J. Microsc.*, **245**, 245–251.
8. Trimby, P.W. (2012) Orientation mapping of nanostructured materials using transmission Kikuchi diffraction in the scanning electron microscope. *Ultramicroscopy*, **120**, 16–24.
9. Troost, K.Z., van der Sluis, P., and Gravesteijn, D.J. (1993) Microscale elastic strain determination by backscatter Kikuchi diffraction in the scanning electron microscope. *Appl. Phys. Lett.*, **62**, 1110–1112.
10. Wilkinson, A.J. (1996) Measurement of elastic strains and small lattice rotations using electron back scatter diffraction. *Ultramicroscopy*, **62**, 237–247.
11. Britton, T.B., Maurice, C., Fortunier, R., Driver, J.H., Day, A.P., Meaden, G., Dingley, D.J., Mingard, K., and Wilkinson, A.J. (2010) Factors affecting the accuracy of high resolution electron backscatter diffraction when using simulated patterns. *Ultramicroscopy*, **110**, 1443–1453.
12. Abou-Ras, D., Kavalakkatt, J., Nichterwitz, M., Schäfer, N., Harndt, S., Wilkinson, A.J., Tsyrulin, K., Schulz, H., and Bauer, F. (2013) Electron backscatter diffraction: an important tool for analyses of structure–property relationships in thin-film solar cells. *JOM*, **65**, 1222–1228.
13. Watanabe, M., Ackland, D.W., Burrows, A., Kiely, C.J., Williams, D.B., Krivanek, O.L., Dellby, N., Murfitt, M.F., and Szilagyi, Z. (2008) Improvements in the X-ray analytical capabilities of a scanning transmission electron microscope by spherical-aberration correction. *Microsc. Microanal.*, **12**, 515–526.
14. Leamy, H.J. (1982) Charge collection scanning electron microscopy. *J. Appl. Phys.*, **53**, R53–R80.
15. Rechid, J., Kampmann, A., and Reinecke-Koch, R. (2000) Characterising superstrate CIS solar cells with electron beam induced current. *Thin Solid Films*, **361–362**, 198–202.
16. Holt, B. (1989) *SEM Microcharacterization of Semiconductors*, Academic Press, Ltd.
17. Bonard, J.M., Ganiere, J.D., Akamatsu, B., Araujo, D., and Reinhart, F.K. (1996) Cathodoluminescence study of the spatial distribution of electron–hole pairs generated by an electron beam in $Al_{0.4}Ga_{0.6}As$. *J. Appl. Phys.*, **79**, 8693–8703.

18. Werner, U., Koch, F., and Oelgart, G. (1988) Kilovolt electron energy loss distribution in Si. *J. Phys. D: Appl. Phys.*, **21**, 116–124.
19. Oelgart, G. and Werner, U. (1984) Kilovolt electron energy loss distribution in GaAsP. *Phys. Status Solidi A*, **85**, 205–213.
20. Mohr, H. and Dunstan, D.J. (1997) Electron-beam-generated carrier distributions in semiconductor multilayer structures. *J. Microsc.*, **187**, 119–124.
21. Kanaya, K. and Okayama, S. (1972) Penetration and energy-loss theory of electrons in solid targets. *J. Phys. D: Appl. Phys.*, **5**, 43–58.
22. Donolato, C. (1989) An alternative proof of the generalized reciprocità theorem for charge collection. *J. Appl. Phys.*, **66** (9), 4524–4525.
23. Donolato, C. (1985) A reciprocity theorem for charge collection. *Appl. Phys. Lett.*, **46** (3), 270–272.
24. Donolato, C. (1983) Evaluation of diffusion lengths and surface recombination velocities from electron beam induced current scans. *Appl. Phys. Lett.*, **43** (1), 120–122.
25. Jastrzebski, L., Lagowski, J., and Gatos, H.C. (1975) Application of scanning electron microscopy to determination of surface recombination velocity: GaAs. *Appl. Phys. Lett.*, **27** (10), 537–539.
26. Kniese, R., Powalla, M., and Rau, U. (2009) Evaluation of electron beam induced current profiles of Cu(In,Ga)Se_2 solar cells with different Ga-contents. *Thin Solid Films*, **517**, 2357–2359.
27. Matson, R.J., Noufi, R., Ahrenkiel, R.K., and Powell, R.C. (1986) EBIC investigations of junction activity and the role of oxygen in CdS/$CuInSe_2$ devices. *Solar Cells*, **16**, 495–519.
28. Romero, M.J., Al-Jassim, M.M., Dhere, R.G., Hasoon, F.S., Contreras, M.A., Gessert, T.A., and Moutinho, H.R. (2002) Beam injection methods for characterizing thin-film solar cells. *Prog. Photovolt.: Res. Appl.*, **10**, 445–455.
29. Liang, Z.C., Shen, H., Xu, N.S., and Reber, S. (2003) Characterization of direct epitaxial silicon thin film solar cells on a low-cost substrate. *Sol. Energy Mater. Sol. Cells*, **80**, 181–193.
30. Nichterwitz, M., Abou-Ras, D., Sakurai, K., Bundesmann, J., Unold, T., Scheer, R., and Schock, H.W. (2009) Influence of grain boundaries on current collection in Cu(In,Ga)Se_2 thin-film solar cells. *Thin Solid Films*, **517**, 2554–2557.
31. Edwards, P.R., Galloway, S.A., and Durose, K. (2000) EBIC and luminescence mapping of CdTe/CdS solar cells. *Thin Solid Films*, **361–362**, 364–370.
32. Galloway, S.A., Edwards, P.R., and Durose, K. (1999) Characterization of thin film CdS/CdTe solar cells using electron and optical beam induced current. *Solar Energy Mater. Sol. Cells*, **57**, 61–74.
33. Scheer, R. (1999) Qualitative and quantitative analysis of thin film heterostructures by electron beam induced current. *Solid State Phenom.*, **67–68**, 57–68.
34. Wu, C.J. and Wittry, D.B. (1978) Investigation of minority-carrier diffusion lengths by electron beam induced bombardment of Schottky barriers. *J. Appl. Phys.*, **49** (5), 2827–2836.
35. Sieber, B., Ruiz, C.M., and Bermudez, V. (2009) Evaluation of diffusion-recombination parameters in electrodeposited $CuIn(S,Se)_2$ solar cells by means of electron beam induced currents and modelling. *Superlattices Microstruct.*, **45**, 161–167.
36. Scheer, R. and Lewerenz, H.W. (1995) Diffusion length measurements on *n*-$CuInS_2$ crystals by evaluation of electron-beam induced current profiles in edge-scan and planar configurations. *J. Appl. Phys.*, **77** (5), 2006–2009.
37. Kuiken, H.K. and van Opdorp, C. (1985) Evaluation of diffusion length and surface recombination velocity from a planar collector geometry electron-beam-induced current scan. *J. Appl. Phys.*, **57** (6), 2077–2090.
38. Sekiguchi, T. and Sumino, K. (1995) Quantitative electron-beam tester for defects in semiconductors (CL/EBIC/SDLTS system). *Rev. Sci. Instrum.*, **66**, 4277–4282.
39. Abou-Ras, D., Schäfer, N., Baldaz, N., Brunken, S., and Boit, C. (2015) Electron-beam-induced current measurements with applied bias provide

insight to locally resolved acceptor concentrations at *p–n* junctions. *AIP Adv.*, **5**, 077191-1–077191-7.

40. Kniese, R., Powalla, M., and Rau, U. (2007) Characterization of the CdS/Cu(In,Ga)Se_2 interface by electron beam induced currents. *Thin Solid Films*, **515**, 6163–6167.
41. Schmid, D., Jäger-Waldau, G.J. and Schock, H.W. (1991) *Diffusion Length Measurement and Modeling of CuInSe$_2$–(Zn,Cd)S Solar Cells*, Proceedings of the 10th European Photovoltaic Solar Energy Conference, Lisbon, Portugal, April 8–12, 1991 (eds A. Luque, G. Sala, W. Palz, G. dos Santos and P. Helm). Kluwer Academic, Dordrecht, pp. 935–938.
42. Fossum, J.G. and Burgess, E.L. (1978) Silicon solar cell designs based on physical behaviour in concentrated sunlight. *Solid State Electron.*, **21**, 729–737.
43. Cavalcoli, D. and Cavallini, A. (1994) Evaluation of diffusion length at different excess carrier concentrations. *Mater. Sci. Eng.*, **B24**, 98–100.
44. Röll, K. (1980) The temperature distribution in a thin metal film exposed to an electron beam. *Appl. Surf. Sci.*, **5**, 388–397.
45. Hakimzadeh, R. and Bailey, S.G. (1993) Minority carrier diffusion length and edge surface recombination velocity in InP. *J. Appl. Phys.*, **74** (2), 1118–1123.
46. Castaldini, A., Cavallini, A., Fabroni, B., Fernandez, P., and Piqueras, J. (1996) Comparison of electrical and luminescence data from the A center in CdTe. *Appl. Phys. Lett.*, **69**, 3510–3513.
47. Hofmann, D.M., Omling, P., Grimmeiss, H.G., Meyer, B.K., Benz, K.W., and Sinerius, D. (1992) Identification of the chlorine *A* center in CdTe. *Phys. Rev. B: Condens. Matter Mater. Phys.*, **45**, 6247–6250.
48. Meyer, E., Jarvis, S.P., and Spencer, N.D. (2004) Scanning probe microscopy in materials science. *MRS Bull.*, **29**, 443–448.
49. Turcu, M., Pakma, O., and Rau, U. (2002) Interdependence of absorber composition and recombination mechanism in Cu(In,Ga)$(Se,S)_2$ heterojunction solar cells. *Appl. Phys. Lett.*, **80**, 2598–2600.
50. Holt, D.B., Raza, B., and Wojcik, A. (1996) EBIC studies of grain boundaries. *Mater. Sci. Eng. B*, **42**, 14–23.
51. Williams, D.B. and Carter, C.B. (2009) *Transmission Electron Microscopy, A Textbook for Materials Science*, Springer Science+Business Media, LLC.
52. Fultz, B. and Howe, J.M. (2008) *Transmission Electron Microscopy and Diffractometry of Materials*, Springer, Berlin.
53. Reimer, L. (1993) *Transmission Electron Microscopy, Physics of Image Formation and Microanalysis*, Springer, Berlin.
54. Abou-Ras, D., Rudmann, D., Kostorz, G., Spiering, S., Powalla, M., and Tiwari, A.N. (2005) Microstructural and chemical studies of interfaces between Cu(In,Ga)Se_2 and In_2S_3 layers. *J. Appl. Phys.*, **97** (12), 084908-1–084908-8.
55. Thust, A., Coene, W.M.J., Op de Beeck, M., and Van Dyck, D. (1996) Focal-series reconstruction in HRTEM: simulation studies on non-periodic objects. *Ultramicroscopy*, **64**, 211–230.
56. Kisielowski, C., Freitag, B., Bischoff, M., van Lin, H., Lazar, S., Knippels, G. *et al.* (2008) Detection of single atoms and buried defects in three dimensions by aberration-corrected electron microscope with 0.5-angstrom information limit. *Microsc. Microanal.*, **14**, 454–462.
57. Rose, H. (1994) Correction of aberrations, a promising means for improving the spatial and energy resolution of energy-filtering electron microscopes. *Ultramicroscopy*, **56**, 11–25.
58. Kabius, B., Hartel, P., Haider, M., Müller, H., Uhlemann, S., Loebau, U., Zach, J., and Rose, H. (2009) First application of C_c-corrected imaging for high-resolution and energy-filtered TEM. *J. Electron Microsc.*, **58** (3), 147–155.
59. Egerton, R.F. (1996) *Electron Energy-Loss Spectroscopy in the Electron Microscope*, Plenum Press, New York.
60. Reimer, L. (1995) *Energy-Filtering Transmission Electron Microscopy*, Springer, Berlin.
61. Gu, L., Ozdol, V.B., Sigle, W., Koch, C.T., Srot, V., and van Aken, P.A. (2010)

Correlating the structural, chemical, and optical properties at nanometer resolution. *J. Appl. Phys.*, **107**, 013501.
62. Ryen, L., Wang, X., Helmersson, U., and Olsson, E. (1999) Determination of the complex dielectric function of epitaxial $SrTiO_2$ films using transmission electron energy-loss spectroscopy. *J. Appl. Phys.*, **85**, 2828–2834.
63. Ahn, C.C. and Krivanek, O.L. (1983) *EELS Atlas*, Gatan, Inc., Pleasanton.
64. Muller, D.A., Kourkoutis, L.F., Murfitt, M., Song, J.H., Hwang, H.Y., Silcox, J., Dellby, N., and Krivanek, O.L. (2008) Atomic-scale chemical imaging of composition and bonding by aberration-corrected microscopy. *Science*, **319**, 1073–1076.
65. Verbeeck, J. and Van Aert, S. (2004) Model based quantification of EELS spectra. *Ultramicroscopy*, **101**, 207–224.
66. Sigle, W. (2005) Analytical transmission electron microscopy. *Annu. Rev. Mater. Res.*, **35**, 239–314.
67. Krivanek, O.L., Mory, C., Tence, M., and Colliex, C. (1991) EELS quantification near the single-atom detection level. *Microsc. Microanal. Microstruct.*, **2**, 257–267.
68. Lichte, H. (1986) Electron holography approaching atomic resolution. *Ultramicroscopy*, **20**, 293–304.
69. Lehmann, M. and Lichte, H. (2002) Tutorial on off-axis electron holography. *Microsc. Microanal.*, **8**, 447–466.
70. Twitchett, A.C., Dunin-Borkowski, R.E., Hallifax, R.J., Broom, R.F., and Midgley, P.A. (2004) Off-axis electron holography of electrostatic potentials in unbiased and reverse biased focused ion beam milled semiconductor devices. *J. Microsc.*, **214**, 287–296.
71. Dunin-Burkowski, R.E. (2000) The development of Fresnel contrast analysis, and the interpretation of mean inner potential profiles at interfaces. *Ultramicroscopy*, **83**, 193–216.
72. Bhattacharyya, S., Koch, C.T., and Rühle, M. (2006) Projected potential profiles across interfaces obtained by reconstructing the exit face wave function from through focal series. *Ultramicroscopy*, **106**, 525–538.
73. Saldin, D.K. and Spence, J.C.H. (1994) On the mean inner potential in high- and low-energy electron diffraction. *Ultramicroscopy*, **55**, 397–406.
74. Schmidt, S. S. (2011) Microscopic properties of grain boundaries in $Cu(In,Ga)Se_2$ and $CuInS_2$ thin-film solar cells studied by transmission electron microscopy. PhD thesis. Technical University Berlin.
75. Schmidt, S.S., Abou-Ras, D., Sadewasser, S., Yin, W., Feng, C., and Yan, Y. (2012) Electrostatic potentials at $Cu(In,Ga)Se_2$ grain boundaries: experiment and simulations. *Phys. Rev. Lett.*, **109**, 095506.
76. Abou-Ras, D., Schmidt, S.S., Caballero, R., Unold, T., Schock, H.-W., Koch, C.T., Schaffer, B., Schaffer, M., Choi, P.-P., and Cojocaru-Miredin, O. (2012) Confined and chemically flexible grain boundaries in polycrystalline compound semiconductors. *Adv. Energy Mater.*, **2**, 992–998.
77. Latychevskaia, T., Formanek, P., Koch, C.T., and Lubk, A. (2010) Off-axis and inline electron holography: experimental comparison. *Ultramicroscopy*, **110** (5), 472–482.
78. Abou-Ras, D., Marsen, B., Rissom, T., Frost, F., Schulz, H., Bauer, F., Efimova, V., Hoffmann, V., and Eicke, A. (2012) Enhancements in specimen preparation of $Cu(In,Ga)(S,Se)_2$ thin films. *Micron*, **43**, 470–474.
79. http://temsamprep.in2p3.fr/, accessed 14 March, 2016.
80. Shimizu, K. and Mitani, T. (2010) *New Horizons of Applied Scanning Electron Microscopy*, Springer Series in Surface Science, vol. 45, Springer, Berlin.
81. Bravman, J.C., Anderson, R.M., and McDonald, M.L. (Eds.) (1987) *Specimen Preparation for Transmission Electron Microscopy of Materials*. Proceedings of the MRS 1987 Fall Meeting, Boston, Massachusetts, USA, December 3, 1987, Materials Research Society Symposium Proceedings, vol. 115. Materials Research Society, Pittsburgh, Pennsylvania.
82. Anderson, R. (ed.) (1990) *Specimen Preparation for Transmission Electron Microscopy of Materials II*. Proceedings of the MRS 1990 Spring Meeting, San Francisco, USA, April 19–20, 1990,

Materials Research Society Symposium Proceedings, vol. 199. Materials Research Society, Pittsburgh, Pennsylvania.

83. Anderson, R., Tracy, B., and Bravman, John (eds) (1991) *Specimen Preparation for Transmission Electron Microscopy of Materials III*. Proceedings of the MRS 1991 Fall Meeting, Boston, Massachusetts, USA, December 5–6, 1991, Materials Research Society Symposium Proceedings, vol. 254. Materials Research Society, Pittsburgh, Pennsylvania.

84. Anderson, R.M., and Walck, S.D. (eds) (1997) *Specimen Preparation for Transmission Electron Microscopy of Materials IV*. Proceedings of the MRS 1997 Spring Meeting, San Francisco, USA, April 2, 1997, Materials Research Society Symposium Proceedings, vol. 480. Materials Research Society, Pittsburgh, Pennsylvania.

85. Ayache, J. and Albarède, P.H. (1995) Application of the ion-less tripod polisher to the preparation of YBCO superconducting multilayer and bulk ceramics thin films. *Ultramicroscopy*, **60**, 195–206.

86. Giannuzzi, L.A. and Stevie, F.A. (eds) (2005) *Introduction to Focused Ion Beams: Instrumentation, Theory, Techniques and Practice*, Springer, Berlin.

87. Mayer, J., Giannuzzi, L.A., Kamino, T., and Michael, J. (2007) TEM sample preparation and FIB-induced damage. *MRS Bull.*, **32**, 400–407.

15
X-ray and Neutron Diffraction on Materials for Thin-Film Solar Cells

Susan Schorr, Christiane Stephan, Tobias Törndahl, Rene Gunder, and Daniel M. Többens

15.1
Introduction

In order to understand natural and artificially produced materials, a detailed understanding of their crystal structures is required. This information is a basis for research in physics, chemistry, biology, and materials science. Among the various experimental methods, neutron and X-ray (photon) scattering have become key techniques of choice. Both techniques are complementary. In X-ray scattering, it is almost exclusively the electrons in atoms which contribute to the scattering, whereas neutrons interact with the atomic nuclei. This has an important consequence: The response of neutrons from light atoms (such as hydrogen or oxygen) is much higher than for X-rays, and neutrons easily distinguish atoms of comparable (or even equal) atomic number (see Figure 15.1). Due to the fact that neutrons interact with atoms via nuclear rather than electrical forces and nuclear forces are very short range (of the order of a few Fermis, i.e., 10^{-15} m), the cross section for such an interaction is very small. The size of a scattering center (nucleus) is typically 10^5 times smaller than the distance between the centers. As a consequence, neutrons can travel large distances through most materials without being scattered or absorbed. Thus, neutrons penetrate matter much more deeply than X-rays.

While neutron scattering provides insights into the crystal structure with high resolution, X-ray scattering has the advantage that (due to a larger scattering cross section) measurement durations are usually much shorter, compared with neutron scattering. Additionally, lab-scale X-ray sources are broadly available.

15.2
Diffraction of X-Rays and Neutron by Matter

Most of all inorganic, solid materials can be described as crystalline. When X-rays or neutrons interact with a crystalline substance, coherent elastic scattering may occur, which is also termed diffraction.

Advanced Characterization Techniques for Thin Film Solar Cells, Second Edition.
Edited by Daniel Abou-Ras, Thomas Kirchartz, and Uwe Rau.

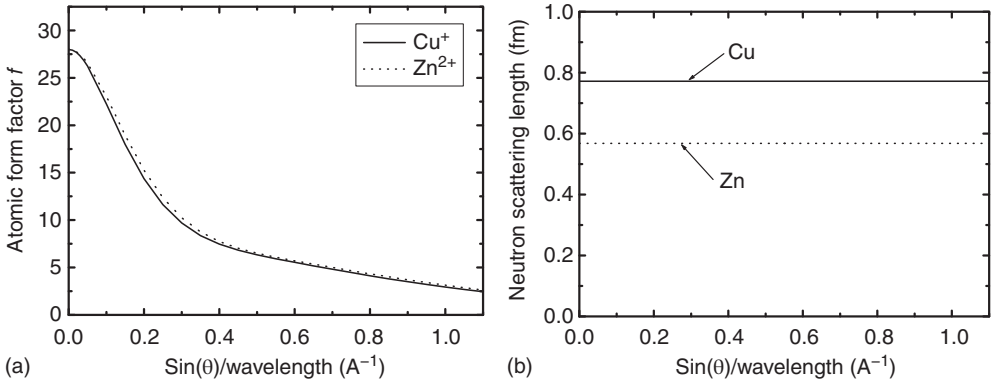

Figure 15.1 Example of scattering amplitudes of two isoelectric cations. (a) The atomic form factor f of Cu^+ and Zn^{2+}. For better visibility the atomic form factor of Ga^{3+} was not shown. (b) The coherent neutron scattering length b for Cu and Zn.

Elastic X-ray scattering can be described accurately in terms of classical electromagnetic theory. An electron in an alternating electromagnetic field will oscillate with the same frequency as the field. When an X-ray beam hits an atom, the electrons around the atom start to oscillate with the same frequency as the incoming beam. According to classical electromagnetic theory, an accelerated charge – here the oscillating electron – emits electromagnetic radiation. The sum of the contributions of these radiations to the scattered amplitude of all the electrons of an atomic species in the crystal is expressed by the atomic scattering factor f. At zero angle, all the scattered waves are in phase, and the scattered amplitude is the simple sum of the contributions from all Z (where Z is the atomic number of the atom) electrons, that is, $Z = f$. As the scattering angle increases, f becomes smaller than Z because of the increasing destructive interference effects between the Z-scattered waves (Figure 15.1a and b).

The scattering of neutrons by nuclei is a quantum mechanical process. Formally, the process has to be described in terms of the wave functions of the neutron and the electrostatic potential caused by the nucleus. The scattering of a neutron by a single nucleus can be described using the cross section σ, measured in barns ($1\,\text{barn} = 10^{-28}\,\text{m}^2$), which is equivalent to the effective area presented by the nucleus to the passing neutron. If the neutron "hits" this area, it is scattered isotropically. This is due to the fact that the range of the nuclear potential is very small compared with the wavelength of the neutron; thus, the nucleus is effectively a point scatterer. X-rays, on the other hand, are not scattered isotropically because the electron clouds around the atom are comparable in size to the wavelength of the X-rays. The amplitude of the neutron wave scattered by the nucleus depends on the strength of the interaction between the neutron and the nucleus. Because the scattered neutron wave is isotropic, its wave function can be written as $(-b/r)e^{i\boldsymbol{k}\boldsymbol{r}}$ if the scattering nucleus is in the origin of the coordinate system ($\boldsymbol{k}$ is the wave vector of the neutron with $k = 2\pi/\lambda$, and $\boldsymbol{r}$ is the position).

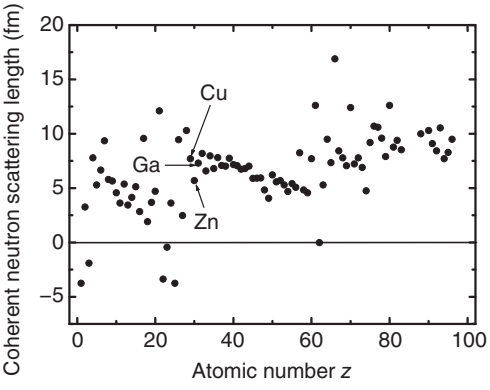

Figure 15.2 Coherent neutron scattering length in dependence on atomic number *Z*. Copper, zinc and gallium are marked.

The scattering amplitude, b, is referred to as the scattering length of the nucleus, which expresses the strength of the interaction between the neutron and the scattering nucleus. It varies in an irregular way with the atomic number (Figure 15.2). The relatively large scattering amplitudes of, for example, hydrogen and oxygen atoms in comparison with heavy metal atoms allow these atoms to be located within the unit cell. The scattering cross section σ is related to b by the simple relation $\sigma = 4\pi b^2$ [1].

The atoms in a crystal are arranged in a regular pattern. In almost all directions into which waves are scattered, destructive interference occurs. That is, the interfering scattered waves are out of phase, and not any residual energy leaves the solid sample. However, for a small fraction of these directions, the coincidence of the scattered waves results in constructive interference. The waves are in phase and scattered X-rays or neutrons leaving the sample into various directions. The scattering amplitude of a unit cell is determined by summing the scattering amplitudes f or b from all atoms in the unit cell, respectively. The summation must take into account the path or phase differences between all the scattered waves and is expressed by the dimensionless number F_{hkl}, the structure factor. F_{hkl} must not only express the amplitude of scattering from a lattice plane with the Miller indices hkl but also the phase angle of the scattered wave. Therefore, F_{hkl} is represented mathematically as a complex number, that is,

$$F_{hkl} = \sum_{n=0}^{N} f_n \exp\{2\pi i(hx_n + ky_n + lz_n)\} \quad \text{structure factor for X-rays}$$

$$F_{hkl} = \sum_{n=0}^{N} b_n \exp\{2\pi i(hx_n + ky_n + lz_n)\} \quad \text{structure factor for neutrons.} \tag{15.1}$$

In Equation 15.1, N is the number of symmetrically nonequivalent atomic positions in the unit cell, and x_n, y_n, and z_n are the atomic coordinates. The intensities

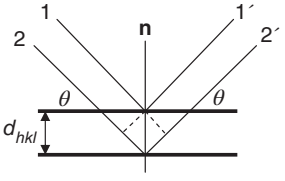

Figure 15.3 Schematic representation of the reflection of waves from lattice planes. The vector *n* is the normal of the plane; θ represents the diffraction or Bragg angle.

I_{hkl} of scattered X-ray or neutron waves are proportional to the squares of their amplitudes or F_{hkl} multiplied by its complex conjugate F^*_{hkl}; hence $I_{hkl} \propto |F_{hkl}|^2$.

The wavelengths λ of neutrons are related to their velocity v through de Broglie's equation $\lambda = h/mv$. Neutrons emerge from a nuclear reactor with a range of velocities and hence wavelengths of which the maxima are typically in the range 1–2 Å, that is, close to X-ray wavelengths. Similarly as for X-rays, useful single wavelength beams are achieved by the use of crystal monochromators. Therefore, neutron diffraction is geometrically similar to X-ray diffraction (XRD).

For simplicity, the scattering of X-rays and neutrons from a family of lattice planes *hkl* is often considered as reflection from a series of parallel planes inside the crystal. The two parallel incident rays 1 and 2 make an angle θ with these planes (Figure 15.3), which have a lattice plane distance d_{hkl}. A reflected beam of maximum intensity (Bragg peak) will result if the waves represented by 1′ and 2′ are in phase. The difference in path length between 1 and 1′ and 2 and 2′ must then be an integer multiple of the wavelength λ. This relationship is expressed mathematically in Bragg's law (Equation 15.2). The angle at which a reflected beam of maximum intensity occurs is termed Bragg angle θ:

$$n\lambda = 2d_{hkl} \sin\theta. \tag{15.2}$$

Polycrystalline diffraction methods may be classified as "fixed λ, varying θ" technique. For these techniques, a sufficiently large number of more or less randomly oriented crystallites are present in the specimen such that *hkl* planes in some of the crystallites are oriented, by chance, at the appropriate Bragg angles for reflection. The family of planes of a given d_{hkl} interplanar spacing reflects at the same 2θ angle with respect to the direct beam. In situations where the crystallites are randomly oriented, the diffracted intensities are uniform. Else, the analyzed ensemble of crystallites exhibits a texture or preferred orientation. The analysis of preferred orientations in thin films is important since it almost invariably arises as a consequence of the processes of crystallizations and recrystallizations or sintering during the growth processes of the thin films.

15.3
Grazing Incidence X-Ray Diffraction (GIXRD)

XRD from randomly oriented polycrystalline thin films often suffers from low peak intensity and poor peak to background ratio for symmetrical XRD measurements such as $\theta-2\theta$ powder diffraction techniques. The low diffraction intensity

from a thin top layer in a $\theta-2\theta$ scan is mainly related to the fact that the path length of the X-rays in the thin film is short. Therefore, most of the radiation instead interacts within the underlying substrate. In addition to lower peak intensity in $\theta-2\theta$ scans, the thin-film reflections may also be superimposed and difficult to distinguish from substrate reflections, which complicate the evaluation of the XRD data. To be able to improve the situation for weakly diffracting thin films, low-angle XRD techniques such as grazing incidence X-ray diffraction (GIXRD) have been developed. In a symmetric $\theta-2\theta$ measurement, the scattering vector is perpendicular to the sample surface, and only lattice planes in parallel to the substrate surface contribute to the diffractograms. Furthermore, the angle of the incoming X-rays to the sample surface is changed during the measurement to always be equal to θ, that is, half of the scattering angle 2θ. GIXRD is an asymmetric XRD scan where the path length of the X-rays in a thin film is increased by using a fixed angle of incidence, α, for the incoming X-rays. Since the GIXRD measurement is performed at a constant angle of incidence where only the detector is moved over a 2θ range of interest, it is also called a detector scan. In contrast to a $\theta-2\theta$ scan, the direction of the scattering vector changes during a grazing incidence (GI) measurement and is no longer perpendicular to the sample surface. This implies that the angle between the diffracting lattice planes and the sample surface changes during the course of a GIXRD measurement. A GIXRD measurement is best performed on a randomly oriented thin film in order to fulfill the Bragg condition for diffraction for every chosen angle of incidence, α (Figure 15.4).

A diffractogram measured by grazing incidence may in fact not show any reflections at all if the analyzed thin film is highly textured or epitaxial, because such thin layers all have their grains aligned to the underlying substrate in a specific way. However, a good way for thin-film analysis is to perform a symmetric $\theta-2\theta$ scan for information about the film texture in combination with an asymmetric GIXRD scan for information regarding the random orientation contribution from the same film.

For grazing incidence measurements, a nonfocusing diffractometer geometry is used since a divergent beam, which is commonly used in $\theta-2\theta$ focusing geometry setups, will not end up on the focusing circle of the diffractometer which leads to

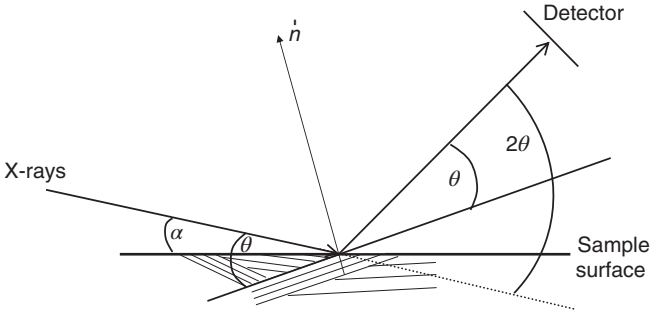

Figure 15.4 Principle geometry of a GIXRD experiment: α is the incident angle, θ the Bragg angle, and n the normal of the lattice plane which fulfills the Bragg equation.

large focusing errors. One example of a nonfocusing geometry, commonly used for GIXRD, is a parallel beam setup with a parabolic multilayer X-ray mirror on the primary side coupled with a parallel-plate collimator on the detector side. The advantage of the X-ray mirror is that it yields high intensities due to reflecting a large portion of the divergent X-rays from the X-ray tube in a parallel beam and that displacement errors or sample roughness do not lead to peak shifts in 2θ.

The attenuation of the intensity of an incoming X-ray beam in matter is defined by the Lambert–Beer law $I = I_0 e^{-\mu l}$. Here μ is the linear attenuation coefficient, l the traveled path length of the beam in the medium, and I_0 the intensity prior to entrance into the material. The linear attenuation coefficient is wavelength dependent and defined by $\mu = \mu_m \rho$, where μ_m is the mass absorption coefficient and ρ the density of the material. The mass absorption coefficient value, with the unit of square meter per kilogram, is usually tabulated instead of μ. For Cu-Kα radiation μ is normally found in the region from 10^4 to $10^6\ m^{-1}$, which corresponds to penetration depths of 1–100 μm. The traveled path length l of the X-rays in a sample can be described by $l = 2d/\sin\theta$ for a $\theta-2\theta$ scan and by $l = d(1/\sin\alpha + 1/\sin(2\theta - \alpha))$ for grazing incidence (GI) scan. The path length l is the sum of the distance traveled by the X-rays in the material prior to scattering takes place and the exit length after scattering occurs, and d is the penetration depth perpendicular to the sample surface. The problem for thin films is that the given penetration depth, d, for the X-rays is commonly much larger than the actual film thickness of the sample. Thus, the most obvious gain by using the grazing incidence technique is that the total diffraction volume is increased by increasing the path length of the X-rays within the thin film itself, which leads to higher peak intensities and overall improved statistics. For example, if a parallel beam setup with a beam width of 1 mm is used, which is typical for an X-ray mirror, the sample projection length is $(\sin\alpha)^{-1}$ mm. Thus, an α-value of 1° results in a projection length of 57 mm, which largely increases the total diffraction volume. At such an angle of incidence, less of the X-rays penetrate down into the substrate, and the presence of the substrate peaks in the diffractogram is reduced. However, caution is advised when performing small angle of incidence measurements because the projection length may extend the size of the analyzed sample. This may lead to unknown reflections in the diffractogram that originate from the sample holder.

The surface sensitivity of GIXRD may be increased further by using α-values of only a few tenths of a degree. For flat film surfaces, GIXRD measurements using small α-values cause the X-rays to be refracted at the air/sample interface. The reason for this refraction of the X-rays is that the refractive index, n, at X-ray energies is slightly smaller than 1, indicating that the X-rays traverse the air/sample interface into a less dense medium. n is approximated by $n = 1 - \delta - i\beta$, where both δ and β are in the 10^{-6} range for X-rays. One effect of refraction is that the X-rays are totally reflected if α is smaller than the critical angle for total external reflection, α_c. α_c is roughly dependent on the density of the thin film and is usually in the region of 0.1–0.5° for Cu-Kα radiation. For GIXRD measurements on flat samples, where $\alpha < \alpha_c$, the penetration depth of the X-rays is usually below 100 Å, which

makes the measurement very surface sensitive. At $\alpha > \alpha_c$, the penetration depth increases rapidly as it is influenced more strongly by the linear attenuation coefficient. One important effect for GIXRD measurements with α-values around the critical angle is that the measured scattering angle 2θ is different from the actual Bragg angle $2\theta_B$ due to the refraction of the X-rays at the sample surface. The corresponding peak shift $\Delta 2\theta$ is always positive and defined by $\Delta 2\theta = 2\theta - 2\theta_B$. The actual expression of $\Delta 2\theta$ has been derived by Toney and Brennan [2] and is expressed as

$$\Delta 2\theta \approx \alpha - 1/(2)^{1/2}\{[(\alpha^2 - {\alpha_c}^2)^2 + 4\beta]^{1/2} - {\alpha_c}^2 + \alpha^2\}^{1/2}. \quad (15.3)$$

From this expression it follows that the maximum value of $\Delta 2\theta$ is obtained close to the critical angle and is $\alpha_c - \beta^{1/2}$, which is α_c for $\beta = 0$. Furthermore, the peak shift is zero in GIXRD at zero and large angles of incidence, whereas $\Delta 2\theta$ varies linearly with α for $\alpha < \alpha_c$ and by using a small-angle approximation: ${\alpha_c}^2/2\alpha$ for $\alpha \gg \alpha_c$. Due to the peak shift that occurs in GIXRD close to the critical angle, it is important to make corrections to the measured data prior to analysis. This is especially true if properties that can depend on the actual 2θ value such as strain and film composition are to be evaluated. If the critical angle for a material is known, the measured data can be corrected if the diffractometer is carefully aligned. However, it may be a good idea to measure the position of the film reflections at α-values of a few degrees or even by a $\theta - 2\theta$ scan to estimate the peak shift, $\Delta 2\theta$. It is clear that the average information depth of a GIXRD measurement is dependent on the angle of incidence, where changing α and performing the same detector scan for several α results in depth resolved structural information of the analyzed sample. Thus, if a multilayer sample is analyzed by GIXRD, the intensity from peaks originating from the topmost layer increases with α for $\alpha < \alpha_c$, toward an intensity maximum reached for $\alpha = \alpha_c$. Above $\alpha > \alpha_c$ the intensity of the reflections from the top film decreases, and the intensity of the peaks from the underlying layers increases as the X-rays reach further down into the sample. An example of depth profiling by GIXRD is demonstrated by Toney *et al*. for iron oxide thin films [3]. The total diffraction volume at a certain angle of incidence is also dependent on the substrate surface roughness. For thin films on rough substrates, a maximum scattering intensity can sometimes be found at α-values higher than that of α_c.

15.3.1
Example: Microstructure of CZTSe Thin Films Studied by GIXRD

The microstructural analysis of polycrystalline thin films is performed by conducting a Le Bail analysis [4] using the program *WinPLOTR* [5] enclosed in the *FullProf Suite* software package. A Le Bail analysis is favorable because it enables an optimal fit of the peak profile, which is the most important parameter for the purpose of microstructural characterization since it relies on the (isotropic) peak broadening β_{sample} caused by microstrain and/or small average domain size. In contrast to the full width at half maximum Γ, the integral breadth β does include information on the integral intensity I_A, that is, the area enveloped by the peak ($\equiv \sum h \cdot \nu_{X\text{-ray}}$).

The integral breadth is calculated by the ratio between the integral intensity and the Γ and can be represented as the width of a rectangle, which is as high as I_{max} and includes the area of the peak.

In order to describe the shape of a peak appropriately, both Gaussian and Lorentzian profile usually must be considered in union. According to the Caglioti (Gaussian) function [6]

$$\Gamma_G^2 = U \cdot \tan^2\Theta_\Gamma + V \cdot \tan\Theta_\Gamma + W \tag{15.4}$$

and the Cauchy (Lorentzian) function (e.g., Ref. [7])

$$\Gamma_L = X \cdot \tan\Theta_\Gamma + Y/\cos\Theta_\Gamma, \tag{15.5}$$

the width of each peak is calculated at half the maximum intensity for the respective function, given in units of degrees (°).

The calculation of the integral breadth β by combining Γ_G and Γ_L is mandatory in order to perform a proper microstructural analysis. However, since the convolution of Gaussian and Lorentzian by applying the Voigt function is mathematically complex, they are treated by the approximating pseudo-Voigt function (e.g., Ref. [8]):

$$\beta_{pV} = 0.5 \cdot \eta \cdot \pi \cdot \Gamma_L + (1-\eta) \cdot 0.5 \cdot \Gamma_G \cdot \sqrt{\pi/\ln 2}, \tag{15.6}$$

where Γ is computed as

$$\Gamma = (\Gamma_G^5 + 2.69269\Gamma_G^4\Gamma_L + 2.42843\Gamma_G^3\Gamma_L^2 + 4.47163\Gamma_G^2\Gamma_L^3 + 0.07842\Gamma_G\Gamma_L^4 + \Gamma_L^5)^{1/5} \tag{15.7}$$

and the mixing parameter η is computed as

$$\eta = 1.36603(\Gamma_L/\Gamma) - 0.47719(\Gamma_L/\Gamma)^2 + 0.11116(\Gamma_L/\Gamma)^3. \tag{15.8}$$

This empirical expression for the pseudo-Voigt approximation is referred to as Thompson–Cox–Hastings pseudo-Voigt function [9]. The Caglioti function (Equation 15.3) was not considered for the microstructure analysis since only profile parameter U may be influenced by the microstructure, while V and W do exclusively reflect the profile emanating from the instrument. Consequently, only the profile parameters for the Lorentzian profile (i.e., X and Y in Equation 15.4) were used to deduce microstrain and domain size, respectively. The influence of the finite instrumental resolution was previously determined using standard reference material lanthanum hexaboride (NIST SRM 660b – LaB_6), from which, ultimately, an instrumental resolution function providing Gaussian and Lorentzian could be created. Once the integral breadth is known and corrected for the instrumental resolution, both the microstrain and the domain size of a sample can be obtained. The isotropic broadening due to the domain size β_{size} is separated from the total sample broadening β_{sample} by the Scherrer equation [10]:

$$\beta_{size} = \lambda_{X\text{-}ray}/D_{<V>} \cdot \cos\Theta \tag{15.9}$$

where $D_{<V>}$ refers to the volume averaged coherently scattering domain size. This means a particular grain or even a particular crystallite can contain several

domains if the periodicity of the three-dimensional arrangement of atoms is interrupted by, for instance, stacking faults and dislocations. So, the size broadening is caused by imperfections and, in principle, ranges between the limit cases "fully crystalline" (i.e., completely coherent) and "amorphous" (completely incoherent). That is why the domain size cannot be directly related to the grain or crystallite size, respectively. The domain size obtained from Equation 15.8 does deliver a volume weighted mean value because the columnar lengths being probed in a crystallite depend both on its shape and its orientation. In addition, the resolution limit of a laboratory XRD device restricts the detectable broadening β_{size} to $D_{<V>} \leq 100\,\text{nm}$, because larger domain sizes do not contribute significantly to incoherent scattering. The broadening β_{strain} induced by microstrain is extracted by the Wilson equation [11]:

$$\beta_{\text{strain}} = 4 \cdot \overline{\varepsilon} \cdot \tan\Theta, \tag{15.10}$$

where $\overline{\varepsilon}$ is treated as the volume averaged microstrain derived from the basic definition of the strain

$$e = \Delta d/d. \tag{15.11}$$

In contrast to the macrostrain, the microstrain emerges from a nonuniform stress field (related to the scale of probed sample volume) caused by lattice defects, chemical heterogeneities, or lattice mismatch at phase boundaries, though the reasons of microstrain also affect the domain size as they control the periodicity, but the different broadening effects can be separated in terms of the different angular dependencies (Refs [7, 11]; see Equations 15.8 and 15.9).

Kesterite-type compound semiconductors such as $Cu_2ZnSn(S,Se)_4$ (CZTSSe) have been investigated absorber layers for application in thin-film solar cells. This compound crystallizes in the kesterite-type structure with symmetry group $I\overline{4}$ but with a Cu–Zn disorder on the structural sites 2c and 2d [12, 13].

The polycrystalline CZTSe thin films studied for the present example were provided by IREC (Barcelona, Spain). These films were processed by a two-stage direct current magnetron sputtering process (PVD) on substrates (austenitic steel and soda-lime glass) already coated with a molybdenum back contact. In case of the steel substrate a chromium barrier layer was used to prevent the diffusion of iron and other contaminants into the back contact. Additionally, the thin films are equipped with a thin (~10 nm) ZnO layer in order to reduce the lattice mismatch between the CZTSe absorber and the Mo back contact. In the first stage the metals contained in kesterite-type CZTSe were supplied by corresponding targets and deposited sequentially at ambient temperature. The sputtering sequence of the metals is Cu/Sn/Cu/Zn. In the second stage the metallic stack is treated by a reactive annealing process under Se+Sn atmosphere (30 min at 400 °C and in the second step for 15 min at 550 °C).

The cation ratios of the absorber layer processed on austenitic steel resulted in [Cu]/([Zn]+[Sn]) = 0.75 and [Zn]/[Sn] = 1.25, whereas the layer processed on soda-lime glass shows values of [Cu]/([Zn]+[Sn]) = 0.81 and [Zn]/[Sn] = 1.14. The absorber thicknesses are on the order of 2 μm.

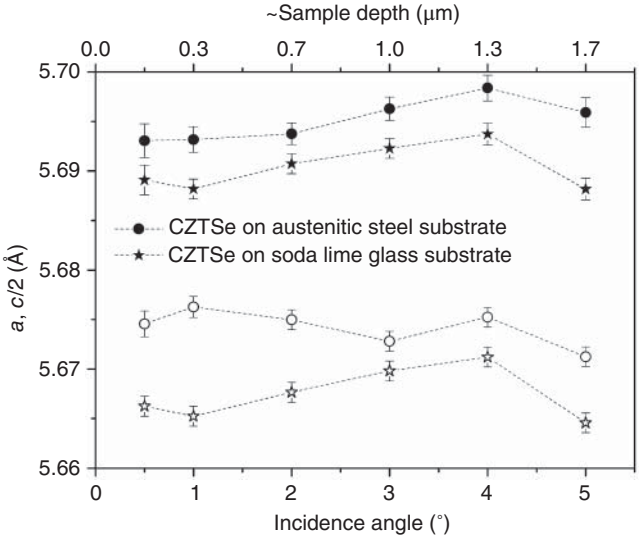

Figure 15.5 Lattice parameters *a* (closed symbols) and *c*/2 (open symbols) of CZTSe thin films deposited on different substrates, in dependence on the thin-film depth (corresponding to incident angle α).

The CZTSe thin films were analyzed in grazing-incidence configuration on a PANalytical X'Pert MPD Pro X-ray diffractometer operating with Cu-K_α radiation ($\lambda = 1.54059$ Å). Detector scans with various incident angles (0.5, 1, 2, 3, and 5) were acquired to probe different sample depths. The diffraction patterns were analyzed by the procedure described at the beginning of section 15.3.1.

Figure 15.5 shows the lattice parameters *a* and *c* of the CZTSe thin film in dependence on the sample depth. Figure 15.6 shows the resulting microstrain on the CZTSe absorber layer.

Using the glass substrate leads to lower microstrain in the CZTSe thin film, compared with the austenitic steel substrate. At the CZTSe/Mo interface, the microstrain of the CZTSe thin film on the austenitic steel substrate is considerably higher, which is probably induced by much larger lattice parameters found for the Mo back contact (i.e., compared with "unstrained" Mo). Unlike austenitic steel, glass substrate favors a [110] preferred orientation of the molybdenum. The microstrain of the CZTSe thin film processed on soda-lime glass, however, exhibits a strong increase not only in direction of the molybdenum back contact but also in the uppermost region of the absorber.

15.4
Neutron Diffraction of Absorber Materials for Thin-Film Solar Cells

Ternary and quaternary compound semiconductors used as absorber materials in thin-film solar cells often contain electronically similar elements, for example,

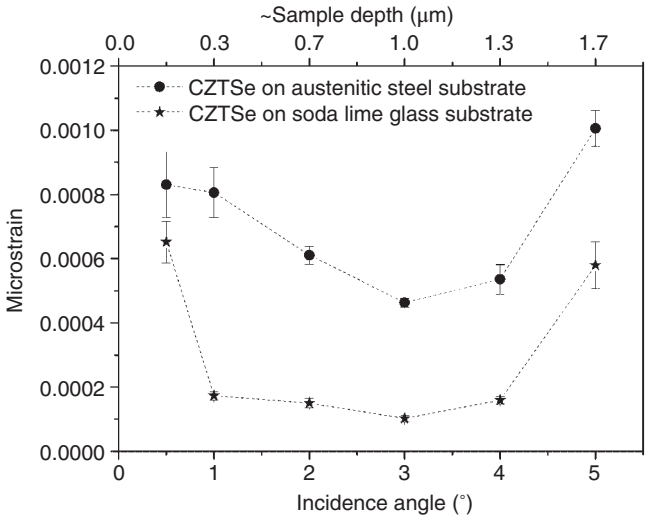

Figure 15.6 Microstrain of the CZTSe thin films on different substrates in dependence on the thin-film depth (incident angle α).

Cu and Ga (chalcopyrites $CuGaS_2$, $CuGaSe_2$, $Cu(In,Ga)S_2$, or $Cu(In,Ga)Se_2$) or Cu and Zn (kesterites Cu_2ZnSnS_4 and $Cu_2ZnSnSe_4$). The cations Cu^+, Ga^{3+}, and Zn^{2+} have the identical number of electrons (28). Since atomic scattering form factors f are proportional to the atomic number Z, the positions of the unit cell atoms of similar atomic number are not easy to be determined. Hence these cations named earlier are not distinguishable in the atomic structure by conventional XRD. The problem can be solved using neutron diffraction because of the different neutron scattering lengths of copper, gallium, and zinc ($b_{Cu} = 7.718(4)$ fm, $b_{Ga} = 7.288(2)$ fm, $b_{Zn} = 5.680(5)$ fm [14]).

Moreover, since atomic nuclei cross sections are very small, the destructive interference effects which in the case of X-rays lead to a decrease of the scattering amplitude with angle are also small, and neutron scattering amplitudes do not decrease rapidly with angle. This gives the advantage that in a neutron diffraction experiment, Bragg peaks with high intensity can be observed also in the high-Q region. In Figure 15.7a and b, the X-ray and neutron diffraction pattern of a kesterite sample are shown for comparison.

15.4.1
Example: Investigation of Intrinsic Point Defects in Nonstoichiometric $CuInSe_2$ by Neutron Diffraction

The concentration of intrinsic point defects in $Cu(In,Ga)Se_2$ can be determined by Rietveld analysis of X-ray and neutron powder diffraction data by using refined cation-site occupancy values [16]. This compound crystallizes in the chalcopyrite-type crystal structure with space group $I\bar{4}2d$. In general, $Cu(In,Ga)Se_2$ exhibits

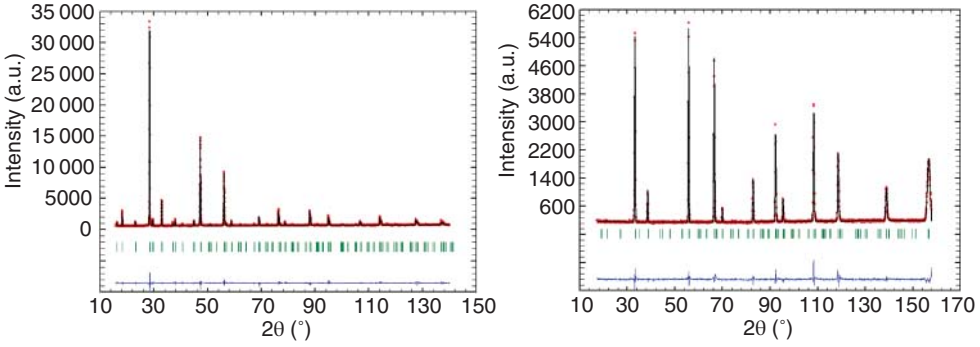

Figure 15.7 Rietveld analysis of a diffraction pattern of a kesterite sample with the chemical composition $Cu_{1.99}Zn_{0.49}Fe_{0.51}Sn_{1.01}S_4$ using X-rays (a) and neutrons (b) [15].

a nonstoichiometric composition, which can be expressed with the overall formula $Cu_y(In,Ga)_{1-y}(Se,S)_{1/2+y}$ (y ranging from 0 to 1). Within the chalcopyrite-type structure, monovalent Cu is situated on the positions 4a (0 0 0) and trivalent In or Ga on the positions 4b (0 0 1/2) in the unit cell. The cations are tetrahedrally coordinated by the anions and vice versa.

In principle, 12 different types of intrinsic point defects may exist in this crystal structure, which are vacancies, antisite, and interstitial defects. Introducing nonstoichiometry into the structure can cause various kinds of these defects. *Copper* deficiency in $Cu(In,Ga)Se_2$ leads to the presence of Cu vacancies (V_{Cu}). Moreover, unoccupied 4a sites in the unit cell may be occupied by In or Ga, where an In_{Cu} or Ga_{Cu} antisite defect is formed. For the determination of the fraction of the amount of In, Ga, Cu, and vacancies occupying the two possible cation positions 4a and 4b, neutron diffraction is applied. The distribution of the cations within the crystal structure can be revealed by the method of average neutron scattering length [17] on the basis of the refined site occupancy values. The average neutron scattering length $\overline{b}_j$ (j is either 4a or 4b) is given by

$$\overline{b}_j = Cu_j \cdot b_{Cu} + In_j \cdot b_{In} + Ga_j \cdot b_{Ga} + V_j$$
$$\overline{b}_j = Cu_j \cdot b_{Cu} + In_j \cdot b_{In} + Ga_j \cdot b_{Ga} + V_j \qquad (15.12)$$

where $b_{Cu} = 7.718\ (4)$ fm, $b_{In} = 4.065(2)$, and $b_{Ga} = 7.288\ (2)$ fm are the neutron scattering lengths of Cu, In, and Ga[2] and V_j is the vacancy fraction on the corresponding position. The requirement for the calculation of defect by this method is given by

$$Cu_j + In_j + V_j = 1. \qquad (15.13)$$

The procedure for calculation of defect concentrations after neutron diffraction experiment is explained using the example of nonstoichiometric $Cu_yIn_{1-y}Se_{1/2+y}$ ($y \neq 0.5$). First, the experimental average neutron scattering length $\overline{b}_j^{exp}$ for both cation positions has to be calculated using the site occupancy factors

resulting from the Rietveld analysis (occ_{4a} and occ_{4b}). The Rietveld method is a least-squares fit-based method for structural refinement of an experimentally determined diffraction pattern to a structure model and described in detail by Young [18]. Assuming in the Rietveld calculations that Cu is situated only on the 4a positions and In only on the 4b positions, the experimental average neutron scattering lengths $\overline{b}_{4a}^{\mathrm{exp}}$ and $\overline{b}_{4b}^{\mathrm{exp}}$ are defined as follows:

$$\overline{b}_{4a}^{\mathrm{exp}} = \mathrm{occ}_{4a} \cdot b_{\mathrm{Cu}} \quad \overline{b}_{4b}^{\mathrm{exp}} = \mathrm{occ}_{4b} \cdot b_{\mathrm{In}}. \tag{15.14}$$

The experimental average neutron scattering length has to be compared with a theoretical neutron scattering length ($\overline{b}^{\mathrm{calc}}$) calculated on the basis of a cation distribution model, defining the theoretical occupancies of Cu and In on the 4a and the 4b position:

$$\begin{aligned} \overline{b}_{4a}^{\mathrm{calc}} &= \mathrm{occ(Cu)}_{4a}^{\mathrm{theor}} \cdot b_{\mathrm{Cu}} + \mathrm{occ(In)}_{4a}^{\mathrm{theor}} \cdot b_{\mathrm{In}} + \mathrm{occ}(V)_{\mathrm{Cu}} \\ \overline{b}_{4b}^{\mathrm{calc}} &= \mathrm{occ(Cu)}_{4b}^{\mathrm{theor}} \cdot b_{\mathrm{Cu}} + \mathrm{occ(In)}_{4b}^{\mathrm{theor}} \cdot b_{\mathrm{In}} + \mathrm{occ}(V)_{\mathrm{In}} \end{aligned} \tag{15.15}$$

The sum of the theoretical occupancies of Cu and In on the 4a and 4b positions ($\mathrm{occ(Cu)}_{4a}^{\mathrm{theor}}$ and $\mathrm{occ(In)}_{4b}^{\mathrm{theor}}$) should not exceed the concentrations of Cu and In within the sample, which has to be determined by quantitative, compositional analysis, as, for example, wavelength-dispersive X-ray (WDX) spectrometry (see Chapter 14).

In order to determine the distribution of the cations Cu^+ and In^{3+} on the two possible positions (4a and 4b), the next step is to minimize the difference between $\overline{b}_{j}^{\mathrm{exp}}$ and $\overline{b}_{j}^{\mathrm{calc}}$ by building up a reasonable cation distribution model. Since $b_{\mathrm{Cu}} > b_{\mathrm{In}}$ a difference between experimentally determined and calculated average neutron scattering length of the 4a site like $\overline{b}_{4a}^{\mathrm{exp}} < \overline{b}_{4a}^{\mathrm{calc}}$ is caused by indium occupying this site (In_{4a}) or copper vacancies (V_{Cu}) that are present on this position. Thus, a dropping of $\overline{b}_{4a}^{\mathrm{exp}}$ can be caused by copper vacancies and/or indium on the 4a position. Moreover it has to be taken into account that in dependence of the Cu/In ratio (copper-rich or copper-poor $\mathrm{Cu}_y\mathrm{In}_{1-y}\mathrm{Se}_{1/2+y}$), both cations can also occupy interstitial positions. On the other hand, a $\mathrm{Cu}_{\mathrm{In}}$ defect would elevate the value of the experimental average neutron scattering length $\overline{b}_{4b}^{\mathrm{exp}}$ due to $b_{\mathrm{Cu}} > b_{\mathrm{In}}$.

In Figure 15.8, an example for the increase and decrease of the experimental average neutron scattering length of the two possible cation sites in the chalcopyrite-type structure ($\overline{b}_{4a}^{\mathrm{exp}}$, $\overline{b}_{4b}^{\mathrm{exp}}$) in dependence of stoichiometry in $\mathrm{Cu}_y\mathrm{In}_{1-y}\mathrm{Se}_{1/2+y}$ is shown. To prove the assumed cation distribution model, the experimental and theoretical average neutron scattering lengths of both cation sites have to be compared. First the amount of copper necessary to lift up $\overline{b}_{4b}^{\mathrm{exp}}$ is calculated and subtracted from the total amount of copper in the sample. The amount of copper left can be distributed on the 4a site (Cu_{4a}) and on interstitial positions (Cu_i). In the case of a copper-poor composition, the amount of copper left is required completely to achieve $\overline{b}_{4a}^{\mathrm{exp}} = \overline{b}_{4a}^{\mathrm{calc}}$; thus the possibility of a Cu_i defect can be excluded. This conclusion also corresponds with the high formation

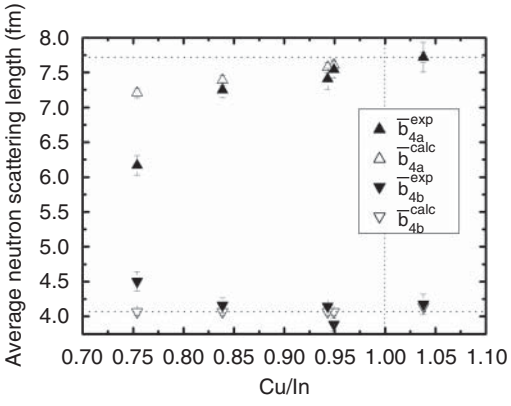

Figure 15.8 Experimentally determined average neutron scattering length of the 4a and 4b position in the chalcopyrite-type structure in comparison to the neutron scattering length of copper (b_{Cu}) and indium (b_{In}).

energy needed to form such a defect in copper-poor $CuInSe_2$ calculated by Zhang *et al*. [19]. The knowledge of the total amount of Cu_{In}, In_{Cu}, Cu_{Cu}, and In_{In} leads to an easy identification also of the fractions of V_{Cu} and V_{In}.

For further reading about the analysis of intrinsic point defects in chalcopyrite- and kesterite-type compound semiconductors by neutron diffraction, the corresponding book chapters in Refs [20, 21] are recommended.

15.5
Anomalous Scattering of Synchrotron X-Rays

Isoelectric cations can be distinguished in XRD analysis by making use of anomalous scattering effects. At wavelengths close to an absorption edge of an element, the scattering power of the atom changes. This allows an analysis of the refined site occupation factors similar to the method described for neutron diffraction (Section 15.4). As this is achieved by selecting specific wavelengths, the use of a tunable X-ray source is necessary. In praxis this requires synchrotron radiation. *Bremsstrahlung* from a sufficiently intense source, for example, a liquid metal jet, might offer an alternative. However, at the writing of the chapter, this is still untested.

The elastic scattering of X-rays by an atom is described by the atomic scattering or form factor $f = f_0(2\theta) + f'(\lambda) + if''(\lambda)$. In this sum, $f_0(2\theta)$ is the form factor *sensu stricto*. It is given by the Fourier transform of the electron density in the atom and decreases monotonously toward higher diffraction angles (see Section 15.2). Resonances of the inner-shell electrons change the scattering rates of the photons. This is considered by adding a complex term, the anomalous dispersion correction $f'(\lambda) + if''(\lambda)$ [22]. Both $f'(\lambda)$ and $f''(\lambda)$ depend on the wavelength of the radiation but are constant with respect to the diffraction angle.

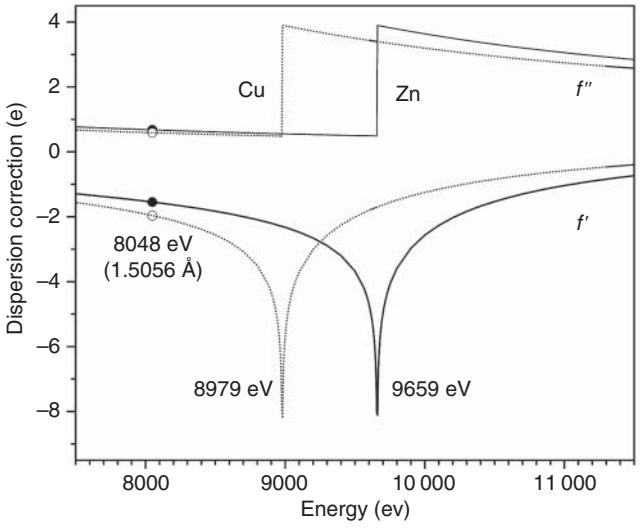

Figure 15.9 Dispersion correction for Cu (dotted) and Zn (solid) at the respective K-absorption edges. The data according to Cromer and Liberman [23, 24] are available online [25].

Under most experimental conditions the wavelength dependency of the anomalous dispersion is small, and correction terms for atoms with similar atomic number Z differ very little. This is different for photon energies close to the absorption edge of the respective element (Figure 15.9). Usually $f'(\lambda)$ and $f''(\lambda)$ are given as function of the photon energy, which is connected to the wavelength by the electromagnetic wave equation $E = hc/\lambda \approx 12398.42\,\text{Å/eV}/\lambda$. Plotted are the dispersion correction terms for copper and zinc. As these elements are neighbors in the periodic system, $Z(\text{Cu}) = 29$ and $Z(\text{Zn}) = 30$, their form factor is very similar and is even more so for the isoelectric cations Cu^+ and Zn^{2+}. At photon energy of 8048 eV, corresponding to the Cu-Kα_1 radiation widely used in laboratory X-ray powder diffractometers, their anomalous dispersion factors are close, too. The elements are nearly indistinguishable by XRD.

At the absorption edge of the respective element, the real term f' shows a sharp negative spike, and the imaginary term f'' increases abruptly. Close to the absorption edge, negative values of about eight electrons can be reached for f', which significantly reduces the scattering power for the respective element. The position of the absorption edge is different for different elements. As a result an energy range exists, at which anomalous dispersion factors differ quite significantly. Contrasts of about six electrons can be reached in the example of Cu and Zn.

Together with periodic tables of the energies of absorption edges, theoretical values for f' and f'' are readily available in the literature [25]. Most widely used are the calculations according to Cromer and Liberman [23, 24] and corrected for relativistic effects [26]. Those are in general sufficiently good to be used without further correction. However, this does not hold close to the absorption edge.

The anomalous dispersion correction is a function of the atomic electrons. As a result, the values of f' and f'' change with the electronic state of the element, which in turn is influenced by the charge of cations and anions as well as the geometry and type of neighboring atoms. Three effects are most important for practical purposes:

1) The position of the absorption edge can shift significantly. Close to the absorption edge, where changes in f' are large, such a shift translates into significant deviations of f'. Changes in f'' are smaller, as long as the shift does not result in a crossing of the edge. In example, the absorption edge for copper is typically given as 8978.9 eV. This is valid for the pure element as neutral atoms in its metallic form. For Cu^+ in Cu_2S the absorption edge is shifted by 0.7 eV toward higher energies; for Cu^{2+} in CuS the increase is 1.2 eV [27]. As a result, at an energy of 8974 eV, 5 eV below the tabulated edge, the absolute value of f' of Cu^+ is about $0.1e$ smaller than for neutral Cu. The change in total scattering power would result in deviations of the refined occupation factors in the range of 1%.
2) In real structures the geometry of the atoms at a specific site is not ideal but is subject to a range of deviations. This is especially true for disordered mixed crystals, which are the prime object of site occupation analysis. This results in a smoothing and broadening of $f'(\lambda)$ and $f''(\lambda)$. Most affected by this is the sharp spike in $f'(\lambda)$ close to the absorption edge. Achievable changes in f' are limited by this effect.
3) The influence of neighboring atoms gives rise to a fine structure of additional minima and maxima. Their positions and intensity reflect the bonding conditions of the atom. In XAS experiments, this fine structure is analyzed in order to gain information about the local coordination of an atom. The fine structure is more pronounced at the high energy side of the absorption edge. In anomalous diffraction experiments therefore energies at the low side of the edge should be used. Another reason is the increased background from fluorescence, which appears above the absorption edge.

Essentially, f' and f'' are different for each sample, even for each crystallographic site in a single sample. It is thus advisable to not rely blindly on the theoretically calculated values of f' and f''. While these generally are in good agreement, especially close to the absorption edge, significant deviations can be expected. Various methods for the experimental determination of the dispersion correction are described in the literature [22]. X-ray interferometry, total external X-ray reflection, X-ray refraction, and the Kramers–Kronig transformation of X-ray absorption data all can be used. Applied to a suitable calibration sample, they allow to derive proper values for f' and f''. For the purpose of site occupation analysis from structure refinement, it is most practical to employ the same method eventually to be used: Collection of diffraction data sets from a well-characterized calibration sample with known site occupancy factors for the respective elements and refining the values of f' and f'' instead of occupation factors.

In contrast to neutron diffraction, the anomalous atomic scattering power for X-rays is not defined by a constant. Instead, the atomic form factor $f = f_0(2\theta) + f'(\lambda) + if''(\lambda)$ is a complex value, depending both on diffraction angle and wavelength. This makes analysis of the data less straightforward. Two different approaches, valid both for single-crystal and powder diffractions, each have their own advantages and drawbacks:

1) The crystal structure could be refined simultaneously against multiple data sets. This allows the independent refinement of more than one occupation factor for the same crystallographic Wyckoff site. This approach avoids the need for approximations. Atomic form factors are modeled correctly, and all parameters are refined within a common least-squares matrix. However, depending on the algorithm used in the software, numerical instabilities can prevent convergence of the refinement. Even if this is avoided, extremely high correlation factors between structural parameters are common with this approach. In such a situation a single bad data set or a wrong assumption in the model can result to strong deviations from the correct results, without an obvious decrease in the overall quality of the fit. As the method effectively acts as a "black box," this is easily overlooked.
2) The alternative approach requires some approximations but is more robust. It is similar to the analysis of neutron diffraction data presented in the previous section. The crystal structure is modeled with only one species per site. Occupation factors are refined independently from individual data sets. It is easy to show that if a site j contains two elements A and B at occupancies occ(A) and occ(B) but is modeled only as element A, the refined value of the occupancy is

$$\mathrm{occ(A)}_\mathrm{j}^\mathrm{calc} = \mathrm{occ(B)}_\mathrm{j} \cdot \frac{f(\mathrm{B})_\mathrm{j}}{f(\mathrm{A})_\mathrm{j}} + \mathrm{occ(A)}_\mathrm{j}.$$

From two occupation factors $\mathrm{occ(A)}_\mathrm{j}^\mathrm{calc}$ refined from data sets with a different atomic scattering power ratio $f(\mathrm{B})_\mathrm{j}/f(\mathrm{A})_\mathrm{j}$, the site occupancy factors $\mathrm{occ(A)}_\mathrm{j}$ and $\mathrm{occ(B)}_\mathrm{j}$ can be derived in a straightforward way as zero-point intercept and slope, respectively. In order to transform the complex atomic form factor $f = f_0(2\theta) + f'(\lambda) + if''(\lambda)$ into a single number, two approximations are necessary: First, the effects of the imaginary term f'' are neglected, and second, the angular dependent term $f_0(2\theta)$ is replaced by a constant f_0. The correct value for f_0, resulting in a slope equal to $\mathrm{occ(B)}_\mathrm{j}$, to a degree, depends on the experiment conditions. It has to be determined either from a calibration sample or from simulated data. The advantage of this approach results from the linearity that is expected for multiple results derived at different energies at the absorption edges of A and B. Deviations from this linearity indicate problems with either experimental data or the analysis. (Többens, D. M., Gurieva, G. and Schorr, S. (2015) Thermal dependence of Cu/Zn ordering in CZTSe kesterites by anomalous diffraction, unpublished.)

15.5.1
Example: Investigation of Intrinsic Point Defects in Nonstoichiometric CZTSe by Anomalous Scattering of X-Rays

The second approach is demonstrated in Figure 15.2, showing the analysis of a sample of a Cu-poor, Zn-rich (B-type) off-stoichiometric kesterite-type CZTSe compound semiconductor ($Cu_{1.949}Zn_{1.059}Sn_{0.983}Se_4$) from a study on temperature-induced Cu/Zn disorder. (Többens, D.M. and Schorr, S. (2015) Quantitative anomalous powder diffraction analysis of photovoltaic kesterites, unpublished.) Powder diffraction data sets were collected at KMC-2, BESSY II [28], at a total of 10 different energies. Four each were taken 5–60 eV below the absorption edges of Cu and Zn, giving a range of f' from $-2e$ to $-7e$ for each element. Two data sets were taken at energies with nearly equal scattering power for Cu^+ and Zn^{2+}, at 8048 eV and between the absorption edges. From these the anion position could be refined without prior knowledge of the cation distribution. Extremely strong correlations between the structural parameters prevented simultaneous Rietveld refinement. On the other hand, the strong overdetermination from 10 energies allowed full exploitation of the strengths of the linearization method. The structure was modeled as ordered kesterite, space group $I\bar{4}$. In this structure type, Wyckoff sites 2a and 2c are occupied by copper, while 2d is occupied by zinc. The occupation factors derived from the final Rietveld refinements are plotted in Figure 15.10 as function of the

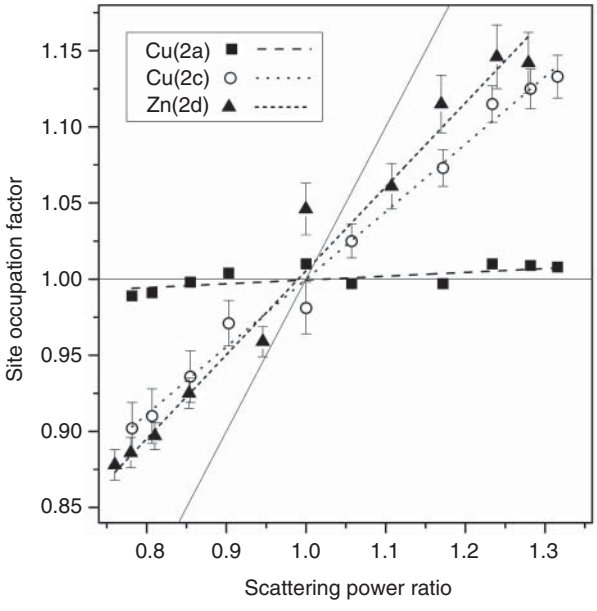

Figure 15.10 Refined site occupation factors for a disordered B-type (Cu-poor, Zn-rich) CZTSe kesterite plotted against scaled scattering power ratio of Cu and Zn. The thin, solid lines represent slopes of 0 and 1. See text for details on the interpretation.

respective scattering power ratios. For sites modeled as Cu, this is $f(\mathrm{Zn})/f(\mathrm{Cu})$ and $f(\mathrm{Cu})/f(\mathrm{Zn})$ for the 2d site modeled as Zn. In disordered kesterite, sites 2c and 2d would be evenly occupied by Cu and Zn, increasing the symmetry to $I\bar{4}2m$. The sample had been quenched from 225°C; therefore a high degree of disorder could be expected. This is confirmed by the results. The nearly horizontal line for 2a shows that this side is occupied by copper only, with only an insignificant fraction of zinc. Consequently, refinement of a model with Cu(2a) yields a constant occupation factor for all energies. On the other hand, the values for Cu(2c) and Zn(2d) give slopes of 0.44(2) and 0.55(3), respectively. As for a site modeled as Cu, the value of the slope is the amount of Zn and for a site modeled as Zn the amount of Cu; in this case copper and zinc are distributed evenly over the two sites. All lines cross through total occupation 1.0 at ratio 1.0, in agreement with fully occupied sites without vacancies. It should be noted that data acquired at the Cu edge and at the Zn edge are on the same line, each forming one of the branches. By doubling the range of scattering power ratios, this decreases the uncertainty of the results.

Acknowledgments

The authors gratefully acknowledge the support in the neutron diffraction experiments by Michael Tovar. Especially we thank E. Saucedo, S. López Mariño, and M. Espíndola Rodríguez (Catalonia Institute for Energy Research, Barcelona, Spain) for the CZTSe thin films.

References

1. Lovesey, S.W. (1984) *Theory of Neutron Scattering from Condensed Matter* vol. 2, Clarendon Press, Oxford.
2. Toney, M.F. and Brennan, S. (1989) Observation of the effect of refraction on X-rays diffracted in a grazing-incidence asymmetric Bragg geometry. *Phys. Rev. B: Condens. Matter Mater. Phys.*, **39** (11), 7963–7966.
3. Toney, M.F., Huang, T.C., Brennan, S., and Rek, Z. (1988) X-ray depth profiling of iron oxide thin films. *J. Mater. Res.*, **3** (2), 351–356.
4. Le Bail, A., Duroy, H., and Fourquet, J.L. (1988) Ab initio structure determination of $LiSbWO_6$ by X-ray powder diffraction. *Mater. Res. Bull.*, **23**, 447.
5. Rodriguez-Carvajal, J. (2011) *An introduction to the program Fullprof*.
6. Caglioti, G., Paoletti, A., and Ricci, F.P. (1958) Choice of collimators for a crystal spectrometer for neutron diffraction. *Nucl. Instrum.*, **3** (4), 223–228.
7. Young, R.A. (1995) *The Rietveld Method*, Oxford University Press.
8. Thompson, P., Cox, D., and Hastings, J. (1987) Rietveld refinement of Debye–Scherrer synchrotron X-ray data from Al_2O_3. *J. Appl. Crystallogr.*, **20** (2), 79–83.
9. Scherrer, P. (1918) Bestimmung der Größe und der inneren Struktur von Kolloidteilchen mittels Röntgenstrahlen. *Gott. Nachr.*, **26**, 98.
10. Stokes, A. and Wilson, A. (1944) The diffraction of X rays by distorted crystal aggregates – I. *Proc. Phys. Soc.*, **56** (3), 174.
11. Di Nunzio, P.E., Martelli, S., and Ricci Bitti, R. (1995) A Monte Carlo estimate of crystallite-size and microstrain distribution functions from X-ray line broadening. *J. Appl. Crystallogr.*, **28** (2), 146–159.
12. Schorr, S. (2011) The crystal structure of kesterite type compounds: a neutron

and X-ray diffraction study. *Sol. Energy Mater. Sol. Cells*, **95**, 1482–1488.
13. Ya Valakh, M., Dzaghan, V.M., Babichuk, I.S., Fontane, X., Perez-Rodriguez, A., and Schorr, S. (2013) Optically induced structural transformation in disordered kesterite Cu_2ZnSnS_4. *JETP Lett.*, **98**, 255–258.
14. Sears, V.F. (1992) Neutron scattering lengths and cross sections. *Neutron News*, **3** (3), 26–37.
15. Schorr, S., Höbler, H.-J., and Tovar, M. (2007) A neutron diffraction study of the stannite-kesterite solid solution series. *Eur. J. Mineral.*, **19** (1), 65–73.
16. Furrer, A., Mesot, J., and Straessle, T. (2009) Defects in solids, in *Neutron Scattering in Condensed Matter Physics*, 4th edn (eds J.L. Finney and D.L. Worcester), World Scientific, pp. 226–229.
17. Schorr, S., Tovar, M., Stuesser, N., Sheptiakov, D., and Geandier, G. (2006) Where the atoms are: cation disorder and anion displacement in (DX^{VI})-$(A^{I}B^{III}X^{VI}_{2})$ semiconductors. *Phys. Rev. B: Condens. Matter Mater. Phys.*, **385**, 571–573.
18. Young, R.A. (2000) *The Rietveld Method*, Oxford Science Publications.
19. Zhang, S.B., Wei, S.H., Zunger, A., and Katayama-Yoshida, H. (1998) Defect physics of the $CuInSe_2$ chalcopyrite semiconductor. *Phys. Rev. B: Condens. Matter Mater. Phys.*, **57** (16), 9642–9656.
20. Schorr, S., Stephan, C., and Kaufmann, C.A. (2015) Chalcopyrite thin-film solar cell devices, in *Neutron Applications in Materials for Energy* (eds V.K. Petersson and G.J. Kearley), Springer.
21. Schorr, S. (2014) Crystallographic aspects of Cu_2ZnSnS_4 (CZTS), in *Copper Zinc Tin Sulfide-Based Thin Film Solar Cells* (ed K. Ito), Wiley.
22. Lengeler, B. (1994) Experimental determination of the dispersion correction $f'(E)$ to the atomic scattering factor, in *Resonant Anomalous X-Ray Scattering – Theory and Applications* (eds G. Materlik, C.J. Sparks, and K. Fischer), Elsevier Science B.V., pp. 35–60.
23. Cromer, D.T. and Liberman, D.A. (1981) Anomalous dispersion calculations near to and on the long-wavelength side of an absorption edge. *Acta Crystallogr., Sect. A: Cryst. Phys., Diffr., Theor. Gen. Crystallogr.*, **37** (2), 267–268.
24. Cromer, D.T. (1983) Calculation of anomalous scattering factors at arbitrary wavelengths. *J. Appl. Crystallogr.*, **16**, 437.
25. Merritt, E.A., *Periodic table interface to X-ray absorption edge tabulations*. http://skuld.bmsc.washington.edu/scatter/AS_periodic.html (accessed 14 March, 2016).
26. Kissel, L. and Pratt, R.H. (1990) Corrections to tabulated anomalous-scattering factors. *Acta Crystallogr., Sect. A: Found. Crystallogr.*, **46**, 170–175.
27. Kumar, P., Nagarajan, R., and Sarangi, R. (2013) Quantitative X-ray absorption and emission spectroscopies: electronic structure elucidation of Cu_2S and CuS. *J. Mater. Chem. C*, **1** (13), 2448–2454.
28. Erko, A., Packe, I., Hellwig, C., Fieber-Erdmann, M., Pawlizki, O., Veldkamp, M., and Gudat, W. (2000) KMC-2: the new X-ray beamline at BESSY II. *AIP Conf. Proc.*, **521**, 415–418.

16
In Situ Real-Time Characterization of Thin-Film Growth

Paul Pistor, Roland Mainz, Marc Daniel Heinemann, Thomas Unold, and Roland Scheer

16.1
Introduction

Most of the characterization techniques presented in this book analyze thin films after completed fabrication and rely on their analysis far away from the preparation conditions. Information from the sample is generally obtained *ex situ*, analyzing the result of a preparation process after applying a set of conditions, while details of the sample during the growth process are missing.

In contrast, real-time *in situ* characterization techniques as described in the present chapter probe the sample properties continuously during deposition, giving insight into how the processing conditions influence the formation of the thin film. For this approach, a reasonable time resolution is necessary to allow monitoring of the entire evolution of the sample. This resolution in time can vary from below seconds to exceeding minutes, depending on the experimental conditions of the growth process. Real-time measurements allow the researcher to obtain a detailed portrait of the sample characteristics at different times of the processing, without a need to interrupt the process, to cool down the sample or to expose it to air.

In general, analytical real-time techniques can be helpful in research and production in two different ways: as an advanced growth analysis that elucidates details of the growth dynamics or as a real-time process control. In an advanced growth analysis, *in situ* measurements enable direct analytical access to the reaction routes of the thin films during their growth, allowing a detailed understanding of the reaction paths and their limitations. In research, *in situ* characterization techniques are often implemented into specialized equipment, designed for specific experiments aiming at the analysis of certain details of the process dynamics.

An example is the process chamber built for synchrotron-assisted growth analysis presented later on in the section on X-ray methods. The growth of compound semiconductors can be very complex, where the course of the film growth may crucially determine the final absorber characteristics. This means that even films with the same final composition are expected to show drastically different film

Advanced Characterization Techniques for Thin Film Solar Cells, Second Edition.
Edited by Daniel Abou-Ras, Thomas Kirchartz, and Uwe Rau.

properties and microcrystalline structure if they have been prepared following different reaction paths involving different transient and secondary phases at some point of their preparation.

A prominent example is the improvement of the electronic absorber properties and grain sizes if $Cu(In,Ga)Se_2$ thin films have passed through a Cu-rich growth phase [1]. For a knowledge-based improvement of complex thin-film deposition processes, a profound understanding of the phase evolution during the process is therefore of major interest. Together with posterior *ex situ* measurements of the specific thin-film properties, this growth analysis often allows to optimize processes in a more systematic manner.

In a production environment, process monitoring with real-time measurements greatly enhances the process control, as the analyzed parameters can be fed back into adjustments of the process parameters. For example, this may include monitoring the elemental composition of the films to adjust growth rates/times and to more accurately determine endpoints.

In this chapter, we will give an introduction into different real-time *in situ* characterization techniques. The focus will lay on the growth of $Cu(In,Ga)Se_2$ (CIGS) films, which will be taken as an example of how real-time methods can help to elucidate different aspects of the thin-film growth and in which way these methods and principles can be extended and adapted to different preparation methods. Following the introduction, the chapter is divided into three sections: In the first section, an overview over some of the most common real-time *in situ* characterization techniques will be given with short descriptions of the basic measurement principles accompanied by references. We will then provide some detailed examples on the use of X-ray-based techniques in the second section and light-scattering and reflection techniques in the third section. We will show how angle-dispersive X-ray diffraction (ADXRD) in a laboratory environment can monitor the phase transitions undergone during the growth process and which useful information can be extracted from the data interpretation. Due to the high brilliance of the excitation source, synchrotron-based energy-dispersive X-ray diffraction (EDXRD) allows tracking faster processes while taking advantage of additional X-ray fluorescence (XRF) and will be presented thereafter. The last section with details and examples of light-scattering techniques as growth monitor and process control is divided into the description of laser-light scattering (LLS) and white-light reflectometry (WLR).

16.2 Real-Time *In Situ* Characterization Techniques for Thin-Film Growth

For the application of an *in situ* method in a specific experimental setup, it has to be tolerant to potentially problematic process conditions for this application: rotating, nonstationary substrates, reactive gases, deposition of material on the viewports, rough samples at elevated temperatures, and so on. The specific process and growth conditions of the great variety of materials and deposition

Table 16.1 Real-time *in situ* measurement techniques (listed and explained in the following paragraphs).

Name	Probe	Feature
Optical		
Thermometry	Temperature	Phase transition
IR emission	IR radiation	Phase transition
LLS	Scattered light intensity	Thickness, phase transition
WLR	Reflected light intensity	Band gap, thickness, Urbach energy
Ellipsometry	Polarization angle and phase	Thickness, refractive index
Raman	Raman-scattered light	Crystalline phases, composition, defects
OES	Emitted light	Source flux
X-ray		
XRD	Diffracted X-rays	Crystalline phases, microstructure, stress
XRF	Fluorescent X-ray lines	Composition, thickness
Electrons		
RHEED	Diffracted high-energy electrons	Crystallographic properties of the surface

methods call for an equally great variety of *in situ* techniques, making an exhaustive enumeration a difficult task.

In this paragraph, a general introduction into some of the most common techniques is intended together with references for the further interested reader. This comprehensive overview is summarized in Table 16.1, which lists the abbreviated names, probed parameters, and features for the characterization techniques, which have been grouped in optical, X-ray, and electron-based techniques. In the following paragraphs, the principles and limitations of these techniques will be discussed in short:

Thermometry and IR emission Thermometry and infrared (IR) emission have been widely used in Cu(In,Ga)Se_2 three-stage growth, specifically to detect the Cu-rich growth phase. They go back to the work of Nishitani *et al.* [2] who reported that the infra-red (IR) emissivity of the samples is affected by the Cu/III ratio of the films. Both methods make use of the fact that Cu(In,Ga)Se_2 builds Cu-selenide secondary phases on the surface for Cu-rich stoichiometries. The appearance of these Cu selenides at the surface is the origin of drastic changes of the IR emissivity of the sample, which in turn can be used to detect the stoichiometry point when the Cu/III ratio exceeds 1. The change of emissivity can either be detected directly with a pyrometer [3] or analyzing a reflected/scattered IR signal [4]. Alternatively, the change in emissivity can be detected by thermometry [5]. Thermometry refers here to a simple measure of the sample temperature with a thermocouple. Applying a constant heating power, the substrate temperature varies when passing through the stoichiometric point due to the changed thermal

emissivity of the sample. Alternatively, a change in heating power can be detected if the heating power is adjusted to a set substrate temperature. The optical methods have the advantage of being noncontact techniques and also allow monitoring the deposition rate by an interpretation of the interference fringes.

LLS LLS is a standard process control technique for thin-film growth, for example, in the three-stage Cu(In,Ga)Se_2 growth process. A laser beam is directed onto the sample, and the intensity of the scattered light, off angle to the directly reflected beam, is detected during the process. Interferences cause oscillations of the detected LLS signal and can be used to monitor the film growth. More information on surface roughness and phase transitions can be obtained by this method as will be explained in more detail in the corresponding section on LLS (Section 16.4.1).

WLR Similar to LLS, WLR is based on the illumination of the sample and measurement of the reflected light. In contrast to LLS, the specular reflection is measured and the illumination and data acquisition are extended to a polychromatic spectral range. This extension allows the extraction of further valuable information of the sample including roughness, band gap, and Urbach energy as will be discussed in the corresponding section of this chapter (Section 16.4.2).

Ellipsometry Ellipsometry is a technique well established for the *in situ* monitoring of semiconductor thin-film growth in general but has not extensively been used in polycrystalline PV applications. An introduction into this technique is given in References [6, 7] as well as in Chapter 9 of the present book. The measurement principle consists of measuring the change in phase (Δ) and polarization angle (Ψ) of a polarized laser beam reflected from the sample surface. In conjunction with appropriate models, these measured (Δ, Ψ) data are used to derive sample thickness and refractive index, which in turn can be interpreted in terms of composition. As this measurement technique is highly accurate and sensitive down to subnanometer film growth, it has been widely applied in growth for thin-film coatings. Unfortunately, accurate measurements require relatively smooth surfaces, which is probably the reason why with few exceptions it has not been applied to the polycrystalline growth of thin-film PV materials (CdTe: [8, 9], Cu(In,Ga)Se_2: [10, 11]). Fujiwara states the maximal allowed surface roughness for optimized measurement conditions at 30% of the applied laser wavelength [6].

Raman spectroscopy Raman spectroscopy is introduced and explained in detail in Chapter 17. We will stick here only to the aspects most important for *in situ* applications. The features of the Raman signal can give detailed information on the crystalline phases present, as well as their composition and defects [12, 13]. Resonant multiwavelength Raman is especially suited for the detection of minor amounts of secondary phases. Its surface sensitivity makes it a valuable tool for the monitoring of the sample surface during the process. Some *in situ* applications can be found in Refs [14, 15].

Optical emission spectroscopy (OES) In OES (see also Chapter 19.2 of the present book), the detection of characteristic emission lines from excited atoms is used to determine the concentration of different species within a gas or plasma. It can be very useful to monitor the source flux during the deposition, for example, during sputtering processes, and has been applied in the preparation of $Cu(In,Ga)Se_2$ [16, 17] and CdTe [18] as well as thin-film silicon [19, 20].

X-ray diffraction (XRD) The principles of XRD are introduced in Chapter 15, and a more detailed description of its *in situ* applications will be given in Section 16.3. Main advantage of XRD is the access to global bulk crystallographic properties of the sample (phases, composition/defects, stacking faults). The need for appropriate security measures such as X-ray shielding, the limitation to crystalline phases, and the availability of bright X-ray sources for the synchrotron-based experiments are the major drawbacks of this technique.

XRF XRF is a standard technique commonly used as in-line composition control in many manufacturing processes. Yet it has also been used and developed in applications as an *in situ* characterization technique to control the reaction process [21]. In the energy-dispersive setup used for XRD with polychromatic X-ray excitation from a synchrotron, XRF can also be detected giving useful additional information on compositional changes within the sample [22]. This aspect will be handled in Section 16.3 of this chapter.

Reflection high-energy electron diffraction (RHEED) An introduction into the RHEED technique can be found in Refs [23, 24]. High-energy electrons (3–100 keV) are focused and strike the sample under low incident angles, limiting the interaction of the electrons to the sample surface. This way the electrons are only reflected by the two-dimensional surface crystal structure and cause a characteristic diffraction pattern on a phosphor screen or CCD camera mounted opposite to the electron gun. For well-defined RHEED patterns, a very clean and flat crystalline surface and high to ultrahigh vacuum conditions are needed, which is why the most common application of RHEED analysis is the measurement of epitaxial thin-film growth, for example, by molecular beam epitaxy. Introductions into the RHEED technology and examples for its use in photovoltaic thin-film growth are given in Refs [25–27].

16.3
X-Ray Methods for Real-Time Growth Analysis

In contrast to many surface-sensitive techniques, the main advantage of X-ray-based techniques such as XRD or XRF is their bulk sensitivity: The relatively long penetration depth of X-rays in common semiconductor materials allows probing the properties of thin films of several microns all the way from the surface to

the backside. In addition, due to its nondestructive nature, X-ray analysis is suitable to monitor bulk properties of thin films during the growth process. Here, we will elaborate on the use of XRD. Additionally, real-time XRF analysis will be introduced as it is measured simultaneously in EDXRD. The basic principles of XRD are explained in Chapter 15.

In ADXRD, monochromatic X-rays are used and the diffraction angle θ is varied to probe the different lattice planes according to the Bragg equation (see Chapter 15). In a standard laboratory XRD setup, the angle is typically varied by mechanically moving the goniometer. This way a high angular resolution can be achieved, but such measurements are time intense and therefore not very suitable for real-time measurements. However, acquisition times can be reduced with linear detector arrays or areal detectors that measure a given angular range all at once. With modern detectors, the time resolution is nowadays determined by the brilliance of the X-ray source rather than the photon counting speed of the detector. With a standard laboratory X-ray tube, a time resolution of some tens of seconds can be achieved. Advanced synchrotron X-ray sources allow acquisition times of around a second. Schematic drawings of two exemplary setups for an ADXRD and an EDXRD setup are depicted in Figure 16.1 and will be explained in more detail in the corresponding sections.

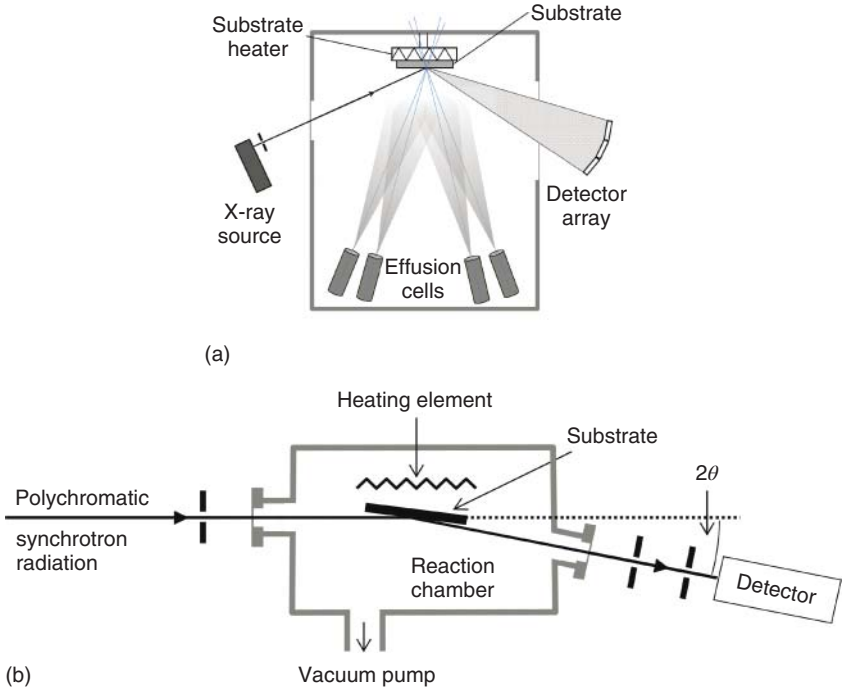

Figure 16.1 Schematic representation of (a) a laboratory-based ADXRD setup for the analysis of thin-film growth by coevaporation and (b) a synchrotron-based EDXRD setup for the analysis of the selenization of metallic precursors.

Table 16.2 Features of X-ray diffractograms and the information extracted from them.

Feature	Information
Peak positions	Identification of crystal phase, lattice spacing
Peak position shift	Thermal expansion, composition change, stress
Peak broadening (FWHM)	Domain size, microstructure, microstrain, structural defects, compositional gradients
Relative peak intensities	Crystallographic phases, preferential grain orientation (film texture), cation ordering

The detected diffraction pattern with its characteristic Bragg peaks holds information on the lattice spacings of the probed crystal structure. This is the main information gained by XRD and allows the identification of crystal phases. A variety of additional details can be extracted from the diffractograms: The intensity of the diffraction peaks as a whole relates to the probed volume of the thin film and can therefore give an indication for the changes in phase fraction and film growth. However, it has to be kept in mind that the peak intensities are influenced by a number of other factors (see Table 16.2). If the dependence between the lattice spacing and composition is known, shifts in XRD peak positions can in some cases be related to compositional changes. However, care has to be taken as thermal expansion and stress also induce peak shifts. In consequence and as the whole thin-film thickness is probed at once, compositional gradients are manifested and can be identified by a peak broadening [28]. But again, care has to be taken for the interpretation of the peak widths, as an increase of peak width may also be caused by a decrease of the average domain size or an increase of microstrain. In Table 16.2, we have summarized the information that in principle can be obtained from the different features of diffracted X-rays. From the table it is obvious that the interpretation of the data is often not unique, since several film properties may affect the XRD pattern in a similar way and a unique deconvolution of these factors is not always possible. Whole pattern fitting or Rietveld refinement (see Chapter 15) can help to increase the reliability of the data interpretation.

For high-quality XRD measurements, special attention has to be paid to provide a good sample alignment throughout the process even for varying temperatures. One possibility to adjust the sample height currently being implemented at the Martin-Luther-University is the use of a feedback system measuring the sample height in high resolution with an interferometer. If the viewports are not heated, one has to be aware of the damping of the signal as a result of the X-ray absorption of condensed materials on the entrance and exit windows.

The following sections will provide examples for the use of laboratory-based ADXRD techniques and more specialized approaches using polychromatic synchrotron X-ray excitation.

16.3.1 ADXRD: Angle-Dispersive X-Ray Diffraction

16.3.1.1 Experimental Setup

Figure 16.1a shows a schematic drawing of the laboratory XRD setup utilized at the Martin-Luther-University Halle-Wittenberg. Here, the monochromatic X-ray source is a Cu X-ray tube with a Ni filter mounted on a goniometer arm and located at the side of the system chamber. Inside the chamber, the X-rays hit the sample mounted upside down. The diffracted X-rays leave the chamber on the opposite wall and are detected by a linear detector array consisting of three segments. This detector array is also mounted on a goniometer arm and is capable of probing an angular range of 28° with a resolution of 0.007° within one single measurement. As no mechanical movement is required, integration times of 20–30 s are generally sufficient. The two windows through which the X-rays enter and leave the chamber are covered with fresh 125 μm thick Kapton foils before each new deposition run. Direct X-ray transmittance measurements before and after a process allow the estimation of beam attenuation due to window deposits and the subsequent intensity correction.

16.3.1.2 Example: Monitoring the Cu(In,Ga)Se_2 Three-Stage Coevaporation Process

The well-known three-stage process with Cu-poor/Cu-rich/Cu-poor growth regimes has been developed for the preparation of highest-efficiency Cu(In,Ga)Se_2 solar-cell absorbers exceeding power-conversion efficiencies of 20% [29]. The following section will show how *in situ* ADXRD can be used to monitor the evolution and transformation of phases during this process.

In the three-stage approach, the Cu(In,Ga)Se_2 absorber is deposited by coevaporation of the elements in a sequence of three phases: (I) In,Ga,Se, (II) Cu,Se, and (III) In,Ga,Se evaporation. During the whole sequence, a continuous excess of Se is offered, usually at a constant Se rate. Film growth starts with the deposition of $(In,Ga)_2Se_3$ precursor films in stage I at moderate temperatures (400 °C in this example). At the beginning of stage II (time t_1), the substrate temperature is increased to 600 °C and the evaporation of Cu is started. During this stage, the film undergoes various crucial phase transitions. Cu-deficient crystal phases such as $Cu(In,Ga)_5Se_8$ and $Cu(In,Ga)_3Se_5$ can be formed before the film reaches the chalcopyrite Cu(In,Ga)Se_2 stoichiometry (first stoichiometric point, s_1, in Figure 16.2 marked as dotted lines). Upon further Cu incorporation, the film becomes Cu rich and a Cu-selenide secondary phase starts to grow. At the end of stage II (t_2), the [Cu]/([In]+[Ga]) (CGI) ratio is usually around 1.1. As no further Cu is offered in stage III, the Cu_2Se_x is gradually consumed due to the ongoing In,Ga,Se supply. As a consequence, the CGI decreases again during this stage, and after passing through the second stoichiometric point (s_2), the film deposition is terminated at slightly Cu-poor compositions (CGI usually between 0.8 and 0.95).

Figure 16.2a shows the growth of an In-rich Cu(In,Ga)Se_2 absorber, with an overall [Ga]/([Ga]+[In]) ratio (GGI) of 0.33 as is commonly used for highest-efficiency devices. For comparison, in Figure 16.2b the growth of a Ga-rich

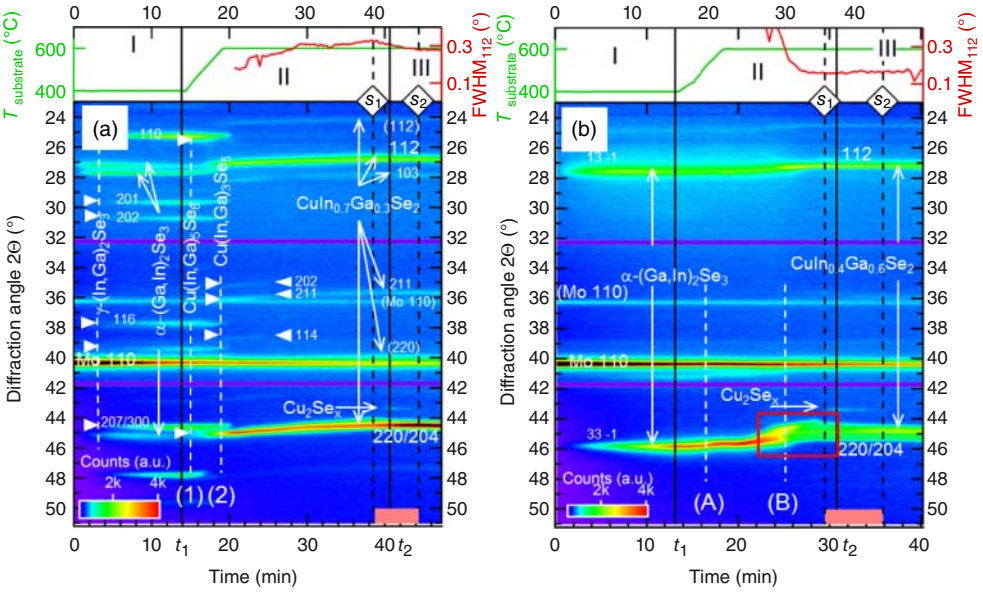

Figure 16.2 Examples of color-coded maps representing the XRD signature of chalcopyrite growth during a three-stage coevaporation for an (a) In-rich $Cu(In,Ga)Se_2$ (GGI = 0.33) and (b) Ga-rich $Cu(In,Ga)Se_2$ film (GGI = 0.55). Each column of this representation corresponds to a single full X-ray diffractogram taken at different times during the deposition. The intensity of the diffracted X-rays is color-coded in a logarithmic scale. The Cu-rich growth phase between the two stoichiometric points s_1 and s_2 is marked with a red bar at the bottom of the graphs. (Reprinted with permission from Ref. [30].)

$Cu(In,Ga)Se_2$ absorber (GGI = 0.55) is displayed. Following the description of the three-stage process previously, the sequence of (In,Ga) selenide, vacancy compounds, chalcopyrite, and Cu_2Se_x can be easily identified in these graphs. Several (In,Ga) selenide modifications might be observed during the $Cu(In,Ga)Se_2$ growth. The preference for one or the other is determined by the Se flux and the In/Ga ratio during the first stage and can in turn strongly influence the texture of the final chalcopyrite film [31]. For the In-rich film, the transition to the $Cu(In,Ga)_5Se_8$ and to the $Cu(In,Ga)_3Se_5$ vacancy phases can be observed, which are missing for the Ga-rich film.

Following the details given in Section 16.2 (Table 16.2), the complete mapping of the XRD features during the thin-film growth allows the discussion of the microcrystalline structure, texture, composition, and so on by an interpretation of peak shifts, peak broadening, and changing peak intensities. As an example, the Cu incorporation into the (In,Ga) selenide/chalcopyrite structure leads to an increase in the lattice spacing, which can be observed by a general shift of the $Cu(In,Ga)Se_2$ peaks to lower diffraction angles during the second stage. In Figure 16.2b, the chalcopyrite 220/204 peak is split into several very broad peaks before the stoichiometric point is reached. This region is marked in the color-coded map by a red rectangle and indicates phase segregations between In-rich

and Ga-rich regions in the sample. Similar phase segregations have often been reported in rapid sequential processes as a result of different diffusion coefficients for In and Ga [32]. In this sample, approximately 10 min. before the stoichiometric point is reached, a recrystallization takes place which is best observed in a strong decrease of the FWHM of the 112 peak (top graph of figure 16.2 b). While a drop of the FWHM has also been observed for pure $CuGaSe_2$ and $CuInSe_2$ samples, we repeatedly found increased FWHMs for the 112 peak in In-rich $Cu(In,Ga)Se_2$ samples [30]. Comparison with experimental compositional profiles has shown that this increased FWHM cannot be explained with GGI gradients alone and therefore its origin still remains unclear. A more detailed description of the experimental details and data interpretation can be found in Ref. [30]. This is an example of a typical growth process for device-grade absorbers grown in an evaporation chamber used for the evaporation of chalcopyrite and kesterite films on a regular basis. The advantage of this setup is that the full fingerprint of phase formations is always recorded for each deposition giving a detailed insight into the process evolution, which can then easily be correlated with other *ex situ* measurements and device properties.

16.3.1.3 Further Applications

ADXRD setups have also been used to monitor the growth of various other thin-film reaction processes. Examples include the selenization/sulfurization of metallic Cu–In–Ga precursors [33, 34] or the formation of kesterite thin films [35, 36]. The effect of $CdCl_2$ treatment on the structural properties of CdTe thin films has been studied with XRD in an *in situ* heating experiment [37]. Recently, the application range has been extended to monitor the phase formation of hybrid lead halide absorbers for perovskite thin-film solar cells and their decomposition [38, 39].

16.3.2 EDXRD/XRF: Energy-Dispersive X-Ray Diffraction and Fluorescence Analysis

16.3.2.1 Principle and Setup

In a standard ADXRD setup, the diffraction angle θ is varied and a monochromatic excitation at a constant wavelength λ is used. Instead, it is also possible to obtain a diffractogram by varying the wavelength λ at a constant diffraction angle θ as is done in EDXRD. The variation of wavelength is realized by the use of polychromatic (typically synchrotron) radiation in combination with an energy-dispersive detector. Since the photon energy E and its wavelength λ are related by $E = hc/\lambda$ (where h is Planck's constant and c is the speed of light), the Bragg equation (see Chapter 15) can be rewritten in its energy-dispersive form as

$$d_{hkl} = hc/(2E\sin(\theta)). \tag{16.1}$$

Polychromatic synchrotron radiation consists of a high flux of photons with a wide range of energies [40]. Only those photons which fulfill Equation 16.1 for a given interplanar distance d_{hkl} are diffracted in the direction of the detector kept at a fixed angle (additional to incoherent scattering), as shown in Figure 16.1b. Owing to the high intensity of synchrotron radiation and the high detection speed

of modern energy-dispersive detectors, it is still possible to obtain a complete diffractogram within seconds with an energy range of typically 6 – 100 keV [41].

An obvious difference to ADXRD is that in EDXRD the diffraction intensity is plotted versus energy E instead of the diffraction angle 2θ. In both cases the lattice spacings are calculated from the positions of the diffraction peaks using the Bragg equation in its angle-dispersive or energy-dispersive form. A major motivation for the use of EDXRD is that XRF signals are measured simultaneously and with the same high time resolution as the diffraction signals. XRF signals provide information about material adsorption and desorption as well as on elemental depth distributions [42, 43], which complement the information about phase formations, domain growth, and strain evolution obtained from the diffraction signals. Moreover, since the XRD signals are detected by the same detector as the diffraction signals, they stem from exactly the same sample volume. Hence, the combination of EDXRD and XRF (termed EDXRD/XRF) helps to gain a comprehensive understanding of the reaction and diffusion processes taking place during film growth. Disadvantages of EDXRD compared with ADXRD are a lower peak resolution stemming from the limited energy resolution of energy-dispersive detectors [40], and that for high time resolution, a highly brilliant polychromatic X-ray source of modern synchrotrons is needed.

In the following the potential of *in situ* EDXRD/XRF for the analysis of the growth of chalcopyrite thin films will be demonstrated. While *in situ* EDXRD has been used for the analysis of phase formations during film growth processes for several decades [44], the focus here will be on the combination of EDXRD and XRF analysis rather than on EDXRD alone.

16.3.2.2 Example: Rapid Thermal Processing of $Cu(In,Ga)Se_2$

In the first example a real-time investigation of the formation of $Cu(In,Ga)Se_2$ during selenization of a metallic Cu – In – Ga precursor film by a rapid thermal process (RTP) is shown [32]. For this fast process, knowledge about the incorporation velocity of Se into the film is important in order to be able to judge for how long a high Se pressure has to be maintained. Figure 16.3a presents time-dependent EDXRD/XRF spectra recorded during the selenization with a time resolution of 5 s. The diffraction signals reveal that the crystalline phases in the film evolve from the metallic phases present in the precursor (ternary $Cu_x(In,Ga)_y$ and pure In) via intermediate selenides – mainly InSe and In_4Se_3 – to the final $Cu(In,Ga)Se_2$ phase. Besides the diffraction signals, a number of fluorescence signals can be seen in the lower energy range in Figure 16.3a. The Se fluorescence signals (Se-K_α and Se-K_β) show a quick increase, indicating fast incorporation of Se into the film. The peak intensities plotted over process time shown in Figure 16.3b reveal that complete Se incorporation only takes around 30 s. In contrast, complete cation ordering of $Cu(In,Ga)Se_2$ (CIGS) in the chalcopyrite structure – indicated by the intensity increase of the CIGS 101 and 211 signals – takes up to 6 min and can therefore be identified here as the time-limiting reaction step. This means that already after 30 s the final film stoichiometry is reached, but five to six additional minutes are needed to enhance the crystal quality of the films and improve its electronic properties. (See Ref. [32] for more details.)

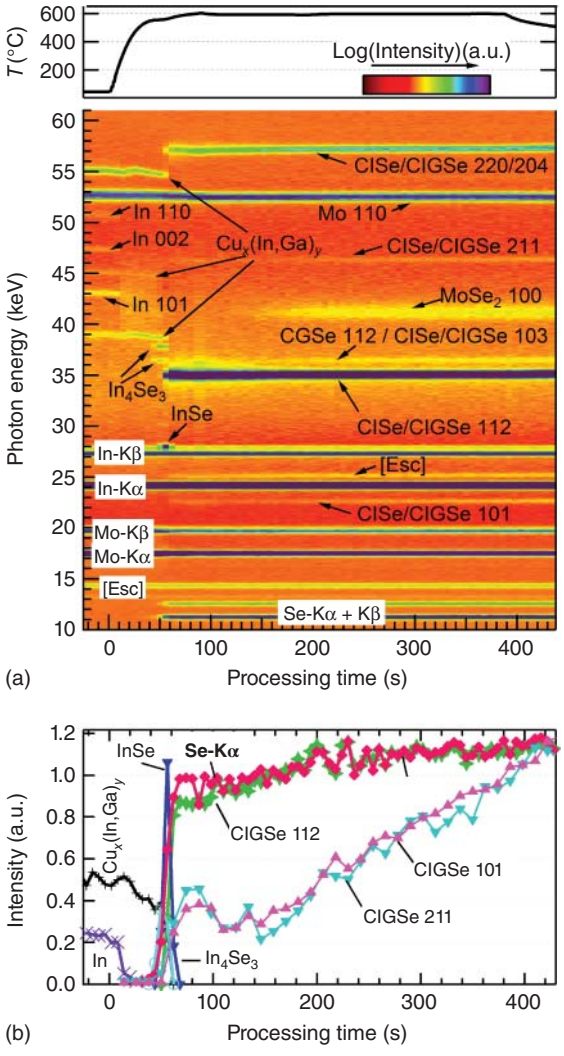

Figure 16.3 (a) Time-resolved EDXRD/XRF spectra during synthesis of $Cu(In,Ga)Se_2$ by a rapid thermal process (RTP). The complete reaction of the metallic precursor with selenium takes place within a few minutes. (b) Peak intensities versus time extracted from the time-resolved spectra in (a) by peak fitting. For more details see Ref. [32].

In contrast to the incorporation of Se described previously, volatile compounds can also evaporate off the sample during reactive annealing processes. This can cause a major problem for the development of reliable film growth processes, and therefore quantitative knowledge of the dependency of the compound evaporation on the process conditions is desirable. A well-known example is the loss of Sn during synthesis of kesterite-type Cu_2ZnSnS_4 and its relatives, which are used as absorber layers in thin-film solar cells [45]. EDXRD/XRF has been proven to be

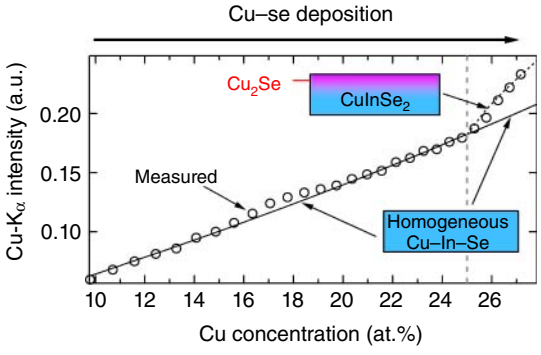

Figure 16.4 Measured and modeled Cu-K_α fluorescence intensities during deposition of Cu–Se onto a Cu–In–Se film in the second stage of a three-stage $CuInSe_2$ coevaporation process. For the calculation of the solid line, a homogeneous mixture of Cu, In, and Se during increasing Cu concentration was assumed. At higher Cu concentrations above 25%, a layered stack with a graded $CuInSe_2/Cu_2Se$ interface was assumed (dashed line). For more details see Refs [46, 47].

well suitable to study the dynamics of the Sn loss – detected by intensity changes of the Sn-K_α signals – and its interplay with phase formations during a wide range of process conditions [42].

16.3.2.3 Analysis of the depth distribution of phases with combined EDXRD/XRF

In the previously described examples, the intensity increase or decrease of the fluorescence signals is taken as a qualitative measure for the incorporation or loss of elements into or off the thin film. However, with a shallow incidence and/or exit angle, the fluorescence intensities are additionally influenced by the depth distributions of the elements inside the film due to the attenuation of incidence and fluorescence radiation in the sample. Therefore, fluorescence signal intensities contain information about depth distributions as a function of time. This is demonstrated in the example shown in Figure 16.4: The dots present Cu fluorescence intensities recorded during the second stage of a $CuInSe_2$ three-stage process, in which Cu and Se are deposited with a constant rate. In this graph the solid and dashed lines present simulated fluorescence intensities resulting from different depth distribution models [46]. In the beginning of the Cu–Se deposition, the increase of the measured Cu fluorescence intensity can be explained by a homogeneous incorporation of Cu into the Cu–In–Se film. However, at a Cu concentration near the $CuInSe_2$ stoichiometry, the slope of the measured fluorescence intensity suddenly becomes steeper, even though the deposition rate did not change. This increase can be explained with a growing Cu_2Se layer positioned on top of a $CuInSe_2$ layer (dashed line), whereas the model for homogeneous Cu incorporation clearly fails here (solid line). Hence, while diffraction shows that Cu_2Se forms somewhere in the film, the analysis of the Cu fluorescence intensity reveals the position of the Cu_2Se phase within the film. Using a double-detector setup for EDXRD/XRF, the segregation of Cu_2Se can be precisely correlated with relaxation of lateral stress, grain growth, and texture changes [47].

More complex depth profile evolutions, for example, during the chalcogenization of metallic precursors, can be resolved by taking into account several fluorescence signals for the comparison between modeling and measurement. A simple parameterization of the depth distributions – where the knowledge of phase formation gained from the simultaneously measured Bragg reflexes are taken as additional constrains – can been used to obtain qualitative *in situ* information about depth distributions and diffusion coefficients. The method has been applied to analyze depth distributions and diffusion parameters during sulfurization of Cu–In precursors [43]. The resolution of the method can be increased by using more than one detector to simultaneously measure fluorescence signals under different exit angles or in future possibly even by the usage of energy-dispersive area detectors.

16.4
Light Scattering and Reflection

16.4.1
LLS: Laser-Light Scattering

The measurement of the diffusively scattered light during thin-film growth is a very simple real-time *in situ* method. Light scattering, earlier introduced to assess surface finishes of metal films [48], has been used to monitor the growth of various semiconductors [49–53]. It can give information on film thickness, roughness, and even phase transitions. The reflectivity, that is, the intensity of diffusively scattered light, is measured at an angle (far) off the specular direction. In this way, the method can only be used for rough or structured surfaces. A typical LLS experimental configuration uses zenith angles Θ of 20–30° for both the incident (Θ_i) and scattered light (Θ_s). In order to avoid specular reflection, the difference between the azimuth angles $\varphi_{i,s}$ should be below 180° (see Figure 16.5a) [54]. A laser with a

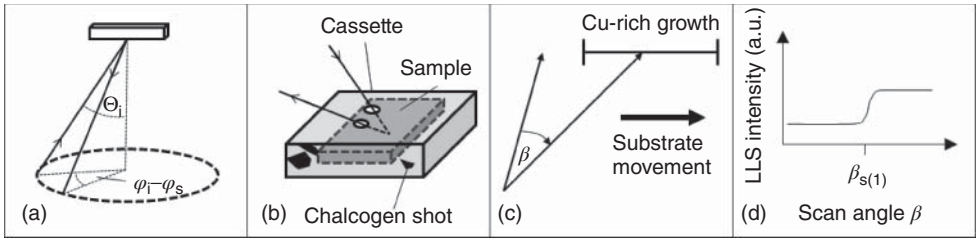

Figure 16.5 Sketches of different measurement geometries for LLS. (a) Angles at the stationary substrate. (b) Entrance and exit ports for measurement in a cassette. (c) and (d) Principle of scanning LLS to detect the entrance into the Cu-rich growth regime in an in-line deposition system. The substrate moves in direction of the arrow in (c). The laser scans along angle β while the detector is at a fixed position (not shown). At a certain angle $\beta_{s(1)}$, the laser hits the stoichiometry point s(1). As a result, the LLS signal varies as shown in (d) at the angle $\beta_{s(1)}$ in an intensity versus angle plot.

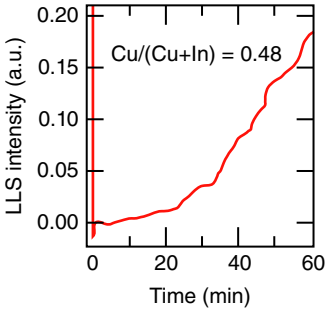

Figure 16.6 LLS transient of $CuInS_2$ epitaxial growth on Si(111) with Cu-poor composition. Substrate temperature was 400 °C and deposition rate 1.5 Å/s. Diode laser irradiation (633 nm) was operated at 0.5 mW. The reflected intensity measured by a photomultiplier at $\varphi_i - \varphi_s = 32°$ with respect to the specular beam. For further details see Ref. [57].

wavelength of 635 nm and roughly 1 mW CW power is typically appropriate. Also an infrared laser [55] or a white-light source [56] may be used. The detector can be a semiconductor diode covered with one or more interference filters to block stray light in the chamber. The use of the lock-in technique is recommended. The window ports may be heated in order to avoid absorbance from window deposits.

The intensity of scattered light from a film surface depends on the optoelectronic and morphological properties of the film, and often a combination of effects renders a clear assignment difficult. Therefore, empirical observations rather than analytical evaluations may be the basis for the application of this method for *in situ* monitoring. Nevertheless, the optical effects can sometimes be narrowed down to a particular event during film growth as will be shown later. A more comprehensive discussion of physical effects influencing the intensity of the scattered laser light can be found in Ref. [53].

In situ LLS basically is a dynamical method which detects the varying scattering power of the growing film. The simplest example is molecular beam epitaxy where the fluxes from evaporation sources are constant in time as in Figure 16.6. Here, a continuous signal increase is caused by film roughness increments where the size of surface features is less than the laser wavelength (633 nm). In addition, if interference fringes are observed, they can be used to monitor the increase in film thickness.

16.4.1.1 Example: Cu(In,Ga)Se_2 Three-Stage Process

A more complicated example is the growth using a follow-up of different growth phases. Again, we choose the example of the three-stage process for Cu(In,Ga)Se_2 growth by coevaporation with its different Cu – In – Ga flux sequences as described in Section 16.3.1. As explained there, the composition of the film varies during growth, and there is a period of excess Cu which leads to the formation of the secondary phase Cu_2Se [58]. In order to control a three-stage deposition process, we need to know the following:

- Thickness of the $(In,Ga)_xSe_y$ film at the end of stage I
- Ga/In ratio of the $(In,Ga)_xSe_y$ film at the end of stage I
- Time or position of Cu-poor→Cu-rich transition within stage II (s1)
- Time or position of Cu-rich→Cu-poor transition within stage III (s2)
- Cu/III_{final} ratio at the end of stage 3

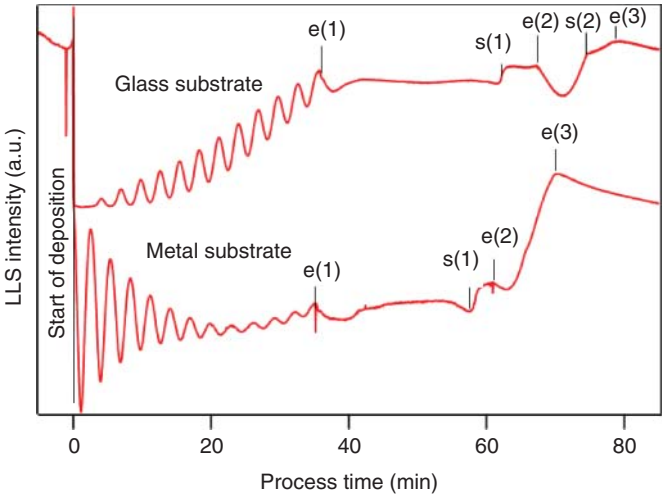

Figure 16.7 LLS transients during the growth of CIGS films within the three-stage process on glass substrate and on metal foil. Substrates are covered with Mo back contacts. Ga/III = 0.3 in final film. Substrate temperatures stage I (300 °C) and stages II and III (550 °C). Labels e(1)–e(3) mark the end of stages 1–3. Stoichiometry points s(1) mark the entrance into a Cu-rich growth regime. Stoichiometry point s(2) is only visible for the glass substrate and marks the exit from the Cu-rich growth regime.

Figure 16.7 gives the LLS transients of three-stage processes using glass and metal substrates. The layer thickness at e(1) (end of stage I) can be calculated from the number of interference fringes occurring between the start and e(1), provided that the Ga/In flux ratio is known. The thickness increase for one interference period is

$$\Delta d = \frac{\lambda}{2}\left(\frac{1}{\frac{n}{\cos\Theta_i'} + \tan\Theta_i' \sin\Theta_s \sin\left(90 - \phi_i + \phi_s\right)}\right), \tag{16.2}$$

where n is the refractive index of the $(In,Ga)_xSe_y$ film, $\Theta_{i,s}$ and $\varphi_{i,s}$ are the zenith and azimuth angles of the incident and scattered light, and $\Theta_i' = \arcsin(n^{-1}\sin(\Theta_i))$. For the film on glass, the amplitude of the interference oscillations increases with roughness but decreases with time. For the film on the metal substrate, the rough substrate leads to scattering from the start of the deposition. Here, the damping is dominant. As the band gap of $(In,Ga)_xSe_y$ increases with the Ga/In ratio, use of multiple light sources or even spectroscopic white-light scattering allows access to the Ga/In ratio by evaluating the damping of the interference fringes for different wavelengths (see next section on WLR). Another way to control the Ga/In ratio is to use multiple phases of In–Se and Ga–Se deposition, the length of which are determined by the interference periods. This procedure has successfully been used to achieve CIGS solar-cell efficiencies close to 19% [59]. It may, however, not be suitable for production.

The time of the Cu-poor to Cu-rich transition (s(1) in Figure 16.7) can be recognized from a step or peak [56] in the LLS transient. The particular type of the LLS feature (step or peak) at s(1) depends on the reflection geometry, laser wavelength, and process details. The optical constants of Cu_xSe differ from those of CIGS, and at s(1), the LLS signal increases due to the increased scattering from small Cu_xSe crystallites formed on the surface [56]. Figure 16.7 reveals that if the same deposition process is performed in the same deposition chamber but on different substrates, the s(1) LLS features are very similar. Knowing the time differences $t_{p2} = t_{s(1)} - t_{e(1)}$ and $t_{r2} = t_{e(2)} - t_{s(1)}$ and verifying a constant Cu – Se deposition rate in stage II allow one to calculate the maximum Cu excess during film growth [60] according to $R_2 = \mathrm{Cu/III}_{max} = 1 + t_{r2}/t_{p2}$.

Knowing the second stoichiometric point of the three-stage process is also important because it allows an estimation of the deposition rate in stage III and therefore adjustment of the final Cu deficiency in the film. Figure 16.7, however, already reveals that the s(2) transition is not always observable by LLS. For a stationary substrate, here, thermometry is the more reliable method [4]. Knowing the time interval $t_{r3} = t_{s(2)} - t_{e(2)}$ and $t_{p3} = t_{e(3)} - t_{s(2)}$ also allows determining $R_3 = \mathrm{Cu/III}_{final}$ at the end of stage III according to

$$R_3 = \frac{R_2}{1 + \frac{t_{p3}}{t_{r3}}\left(1 - \frac{1}{R_2}\right)} \tag{16.3}$$

if a constant flux of group III elements in the 3rd stage is assumed [60].

16.4.1.2 Further Multistage Applications

In the laboratory, LLS has been used to control the Se flux rate [4]. It is a very useful technique if it comes to low temperature deposition of CIGS [61]. In particular, the failure of Cu diffusion during the 2nd stage of the three-stage process can be detected [4]. White-light scattering using a CCD camera has been successfully tested [62]. The described methodology has also been used to monitor the growth and detect endpoints during the preparation of $Cu_2ZnSnSe_4$ thin films by coevaporation in multistage processes [36, 63].

16.4.1.3 In-Line Applications

We now turn to moving substrates. If a deposition process as in Figure 16.7 is accomplished in an in-line deposition, the period of Cu-rich growth needs to be detected. As there is an intensity step at s(1), we may be able to see a variation of the LLS signal if the laser is scanned along the substrate. Thus, imagine that the abscissa in Figure 16.7 is not the time but the position. Then s(1) would mark a particular point on the substrate axis in the direction of the moving substrate. LLS could be used to assess the process stability by requiring that the transition s(1) should be constant in space. In practice, it was suggested to move the laser across the substrate comparable to a bar code laser scanner [64]. The principle of this method is shown in Figure 16.5c and d. A step in an intensity versus angle plot would indicate the entrance into the Cu-rich growth regime and thus the position s(1). During constant substrate movement and under the assumption of

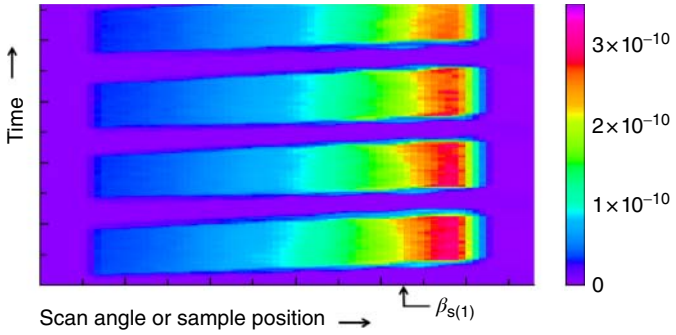

Figure 16.8 Example of scanning LLS for the growth of Cu(In,Ga)Se_2. The color represents the LLS intensity. On the abscissa is the position on the substrate. Different scans are plotted along the ordinate representing different scan times, thus different locations of the substrate in direction of the substrate movement. Constancy of the color contrast for the four substrates demonstrates the stability of the deposition process. (Reproduced with kind permission of Dr Stefan Paetel.)

stable deposition parameters, this angle $\beta_{s(1)}$ will be constant in time. A shift of the step in the LLS intensity toward smaller or larger β would indicate a change in the deposition rate (e.g., of the Cu source) and could be used as a control signal for the Cu source controller. Thus, stage 2 could be controlled. The technique has been realized in-line in a pilot Cu(In,Ga)Se_2 deposition line at ZSW, Germany [65]. Figure 16.8 shows an example of four substrates subsequently moving through the zone of the Cu-poor => Cu-rich transition in a three-stage deposition chamber. The position of the transition is clearly visible and stable, demonstrating the reliability of the LLS signal (and the deposition process). Using the same technique on stage I and II of a three-stage process, interference oscillations would be interpreted as due to the thickness at e(1) and would allow to control stage I.

16.4.1.4 **Example: Sulfurization of Cu-Rich Metallic Precursors in a Rapid Thermal Process**

Another example of LLS on stationary substrates is the reaction of metal films with sulfur or selenium during chalcogenide film formation. In Figure 16.9a, the characteristic LLS intensity variations are displayed. The dominating feature is the transition between metallic reflection and semiconductor reflection with a characteristic strong decrease in reflectance. But the LLS transients display more features; combining the LLS intensity variations with structural information from *in situ* XRD, it was possible to elucidate even phase transitions by LLS [57, 66]. The goal was to explore the method for production processes. In Figure 16.9b we see the same principle process as in (a) but with a pilot production type sulfurization furnace. Also here, the sulfurization process can be traced by *in situ* LLS. There are strong similarities between the LLS transients from the lab process (a)

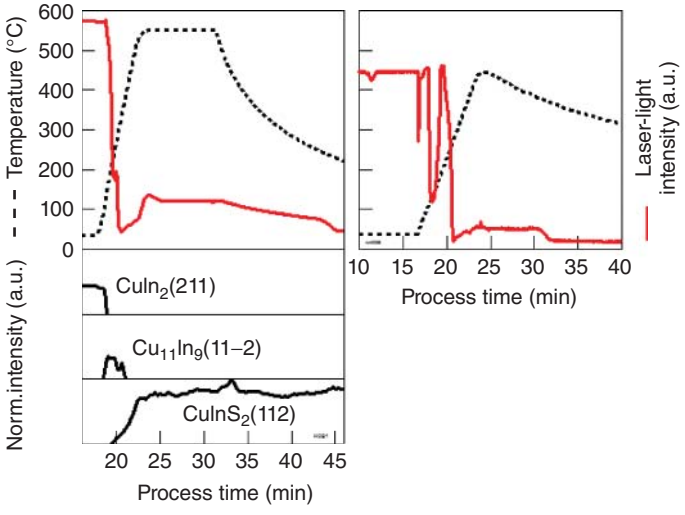

Figure 16.9 Sulfurization of Cu-rich metallic precursor layers, (a) in an experimental setup connected to *in situ* X-ray diffraction and (b) in a pilot line sulfurization chamber. In (a), the sulfurization was performed in a sulfur flux provided by a sulfur evaporation source. XRD pattern is recorded simultaneously and the XRD peak intensities are evaluated as a function of process time. Substrate size was $5 \times 5\,cm^2$. In (b), sulfurization was performed in a sealed graphite box housing elemental sulfur shots. The graphite box was equipped with glass windows for entrance of the laser beam and exit of the scattered light as depicted in Figure 16.5b. Indicated temperatures are nominal temperature readouts not displaying the real substrate temperature. The substrate size was $30 \times 30\,cm^2$.

and from the pilot production process (b). Accordingly, the sulfurization method with LLS control has been used in the former Sulfurcell company.

16.4.2
WLR: White-Light Reflectometry

Within the method of WLR, the full spectrum of the specular optical reflection from the growing film is analyzed. This allows obtaining absolute values for the surface roughness and the deposition rate as well as for optoelectronic material properties such as band gap and Urbach energy. Therefore, information extracted from WLR data recorded during film growth can give detailed insight into the evolution of the desired material properties and may serve to optimize or redesign the growth process. However, compared to LLS, WLR requires the use of more expansive equipment, as it requires a Si CCD and an InGaAs photodiode array. The light source can be a simple halogen lamp.

The method described here is based on the analysis of the specular reflection of white light from a semiconductor layer which grows onto an opaque reflecting substrate, for example, Mo-coated soda-lime glass as currently used for most

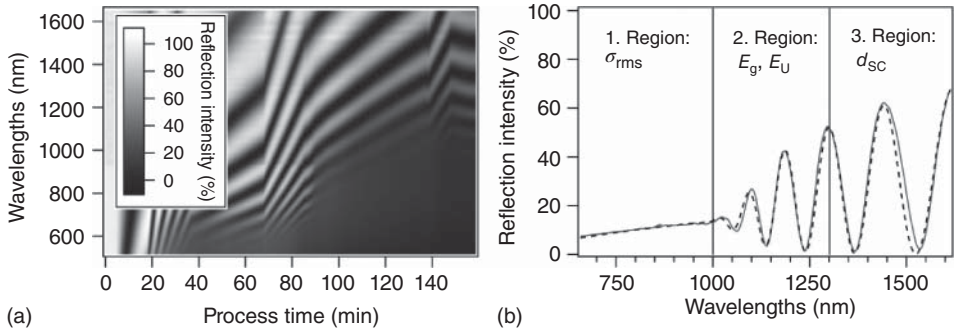

Figure 16.10 (a) Time development of the reflection spectra during a three-stage CIGS deposition process. (b) Isolated spectrum of the specular reflection, recorded after cool down of the sample to room temperature. The solid gray line shows the experimental data and the dashed line the fitted spectrum. From the different regions within the spectrum, it is possible to extract the surface roughness $\sigma_{RMS} = 60$ nm, layer thickness $d_{SC} = 2.17\,\mu m$, minimum band gap $E_g = 1.09\,eV$, and Urbach energy $E_U = 48\,meV$. Although this Urbach energy is higher than typically reported in the literature, it is consistent with values extracted from *T*/*R* measurements for this sample.

thin-film solar cells or modules. An example is presented in Figure 16.10a, which shows the time development of the reflection spectra during a three-stage CIGS deposition process as explained already in detail previously. In Figure 16.10b, the final reflection spectrum in the wavelength range of 700–1600 nm is depicted. The spectrum originates from the interference between the light reflected at the surface of the growing film and the surface of the metal substrate. Thus, the signal intensity I_{WLR} can be described by the sum of both waves, whose intensities are I_S and I_M:

$$I_{WLR} = I_S + I_M + 2\sqrt{I_S I_M}\cos\left[\frac{4\pi d_{SC} n_{SC}(\lambda)}{\lambda\cos(\Theta)}\right] + \Delta\delta. \tag{16.4}$$

Here, Θ is the angle to the substrate normal, d_{SC} the layer thickness, n_{SC} the refractive index of the semiconducting layer, and $\Delta\delta = \pi$ for the example of CIGS/Mo.

Three wavelength regions within the spectrum are marked in Figure 16.10b. From each region different information can be obtained. The wavelength region corresponding to photon energies above the band gap, which is between 600 and 1000 nm in this example, is determined by the specular reflection of the surface, I_S, which depends on the refractive index and the surface roughness. Thus, this part can be well described with the Fresnel equation combined with the scalar scattering theory for rough surfaces [67, 68]. Assuming a nonwavelength-dependent refractive index in this region, a fit to this part gives the refractive index and the surface roughness value. Comparison to measurements obtained from atomic force microscopy (AFM) shows a good correlation between the root mean square (RMS) roughness values obtained from AFM and from the fit to the optical data.

The second wavelength region is around the band-gap energy, which is between 1000 and 1300 nm in this example. The reflected signal in this region is strongly influenced by the absorption of the growing film, which allows extracting the absorption coefficient in this wavelength region. The envelope of the interferences is described by the prefactor of the cosine function in Equation 16.4, $2\sqrt{I_S I_M}$. I_S and I_M depend on the refractive index, the surface roughness, and the absorption coefficient. For a given refractive index, the absorption coefficient can be extracted from the amplitude of the interference. In a first approximation, the refractive index is used from the fit of the first region. From the shape of the wavelength-dependent absorption coefficient, the optical band gap and the Urbach energy can be extracted [69]. For graded semiconductors like Cu(In,Ga)Se_2, it is the minimum band gap which is obtained from the optical fit.

In order to calculate the absorption coefficient, the layer thickness is required. This can be obtained from the interference extrema in the part of the spectrum free of absorption losses. This is the third region in Figure 16.10b, which is between 1300 and 1700 nm in the given example. According to Equation 16.4, the interference minima are located at wavelengths whose multiples are equal to the optical path length, $d_{SC} n_{SC} / \cos(\Theta)$, within the growing film. By using the refractive index obtained from the subbandgap region as a first approximation, it is possible to extract the film thickness from the separation of two minima. The *in situ* monitoring of the thickness in real time thus also allows the calculation of the deposition rate. As a last step, the whole spectrum can be fitted to the experimental data by refining a parameterized wavelength dependence of the refractive index – which was previously kept constant. With the newly obtained refractive index, $n_{SC}(\lambda)$, the values for layer thickness, roughness, and absorption coefficient are recalculated. The process is repeated until convergence of the fit is achieved.

Care has to be taken for smooth films, since multiple reflections within the growing film cannot be neglected in the analysis. To analyze smooth films with RMS roughness values below 30 nm, it is recommended to extend the formalism to multiple reflections. Further, if the thin film is grown on nonopaque layers like transparent oxides or thick layers of $MoSe_x$ (>10 nm), a multilayer system has to be used. However, this makes the *in situ* data fitting more fragile.

The *in situ* determination of the properties obtained from WLR allows to control and to adjust the minimum band gap during the deposition process. Further, by knowing the Urbach energy, the process can be adjusted to minimize the Urbach energy and therefore increase the electronic quality of the deposited film. A process and quality control based on WLR is supposed to increase the reproducibility and the quality of the deposition of complex semiconductors like CIGS in the future. Further details about the method and the results of this method applied to a CIGS three-stage process as well as the correlation with structural data obtained from EDXRD are given in Ref. [70].

Spectral reflectometry has also been used *in situ* to determine the etch rate of polycrystalline silicon thin films [71]. In principle, the use of a CCD camera combined with adequate illumination and optics even enables the spectral imaging of the sample's reflectance [72]. In an *in situ* application, Urbanek *et al.* recorded

reflectance images during the growth of silicon nitride and silicon oxide thin films grown by ion beam sputtering and monitored the etching of thermally grown silicon oxide thin films using a monochromator to select different wavelengths from a simple halogen lamp [73].

16.5 Summary

In the present chapter, we showed that detailed growth analysis and advanced process control options motivate the use of *in situ* real-time characterization techniques during the growth of semiconductor thin films. In the first section of the chapter, a general overview of some of the most common real-time *in situ* characterization techniques has been given with short explanations on the principles and limitations of these techniques, providing further references for the interested reader.

We provided several detailed examples of the use of X-ray-based techniques and techniques based on light scattering/reflection for the characterization of the growth of chalcopyrite thin films. Laboratory-based ADXRD was demonstrated in the first example to be a powerful tool to monitor the complex phase transitions during the three-stage coevaporation process. Based on synchrotron-based polychromatic X-ray excitation and energy-dispersive detectors, EDXRD was used to resolve fast reaction processes within seconds in the second example. Here, the information on the crystalline phases from EDXRD could be correlated to compositional information from XRF detected simultaneously within the same ED X-ray detector to yield a more detailed picture on Se incorporation and modeling of depth profiles.

Light scattering has been introduced as a versatile tool to monitor phase changes and thin-film thicknesses. The power of LLS in the detection of the phase transitions during the CIGS growth (stoichiometric points in the coevaporation, phase transitions in rapid thermal processes) could be demonstrated for application in research and production. As last example, the method of WLR has been established and shown to provide access to real-time monitoring of diverse sample properties such as roughness, band gap, and Urbach energies.

Acknowledgments

The authors gratefully acknowledge the valuable contributions of Stefan Hartnauer to the ADXRD results and H. Rodriguez-Alvarez to the *in situ* EDXRD results. The work was partly funded by the ProFIT program of the Investitionsbank Berlin, Germany (project HighProCIS), by the Bundesministerium für Bildung und Forschung (project GRACIS, 03SF0359D), and by the European Commission (project JUMPKEST, Grant agreement number GA 625840).

References

1. Caballero, R., Kaufmann, C., Efimova, V., Rissom, T., Hoffmann, V., and Schock, H.W. (2013) Investigation of Cu(In,Ga)Se_2 thin-film formation during the multi-stage co-evaporation process. *Prog. Photovoltaics Res. Appl.*, **21**, 30–46.
2. Nishitani, M., Negami, T., and Wada, T. (1995) Composition monitoring method in $CuInSe_2$ thin film preparation. *Thin Solid Films*, **258**, 313–316.
3. Hunger, R., Sakurai, K., Yamada, A., Fons, P., Iwata, K., Matsubara, K., and Niki, S. (2003) In situ deposition rate monitoring during the three-stage-growth process of Cu(In,Ga)Se_2 absorber films. *Thin Solid Films*, **431–432**, 16–21.
4. Sakurai, K., Hunger, R., Scheer, R., Kaufmann, C.A., Yamada, A., Baba, T., Kimura, Y., Matsubara, K., Fons, P., Nakanishi, H., and Niki, S. (2004) In situ diagnostic methods for thin-film fabrication: utilization of heat radiation and light scattering. *Prog. Photovoltaics Res. Appl.*, **12**, 219–234.
5. Kohara, N., Negami, T., Nishitani, M., and Wada, T. (1995) Preparation of device-quality Cu(In,Ga)Se_2 thin films deposited by coevaporation with composition monitor. *Jpn. J. Appl. Phys.*, **34**, L1141–L1144.
6. Fujiwara, H. (2007) *Spectroscopic Ellipsometry: Principle and Applications*, John Wiley & Sons, Chichester.
7. Aspnes, D.E. (2014) Spectroscopic ellipsometry – past, present, and future. *Thin Solid Films*, **571**, 334–344.
8. Li, J., Chen, J., Podraza, N. and Collins, R. (2006) *Real Time Spectroscopic Ellipsometry of Sputtered CdTe: Effect of Growth Temperature on Structural and Optical Properties*. Conference Record of the IEEE 4th World Conference on Photovoltaic Power Conversion, May 2006, Waikoloa, pp. 392–395.
9. Koirala, P., Attygalle, D., Aryal, P., Pradhan, P., Chen, J., Marsillac, S., Ferlauto, A.S., Podraza, N.J., and Collins, R.W. (2014) Real time spectroscopic ellipsometry for analysis and control of thin film polycrystalline semiconductor deposition in photovoltaics. *Thin Solid Films*, **571**, 442–446.
10. Bundesmann, C.,Schubert, M., Ashkenov, N., Grundmann, M., Lippold, G. and Piltz, J. (2005) *Combined Raman Scattering, X-ray Fluorescence and Ellipsometry In-Situ Growth Monitoring of $CuInSe_2$-Based Photoabsorber Layers on Polyimide Substrates*. AIP Conference Proceedings, vol. 77, p. 165.
11. Simpson, L.J., Joshi, B.S., Gonzales, L.A., Verley, J. and Furtak, T.E. (2000) *A Parallel Detecting, Spectroscopic Ellipsometer for Intelligent Process Control of Continuously Deposited CIGS Films*. MRS Proceedings, vol. 616, p. 9.
12. Ferraro, J.R., Nakamoto, K., and Brown, C.W. (2003) *Introductory Raman Spectroscopy*, 2nd edn, Academic Press.
13. Smith, E. and Dent, G. (2005) *Modern Raman Spectroscopy: A Practical Approach*, John Wiley & Sons.
14. Rudigier, E., Djordjevic, J., von Klopmann, C., Barcones, B., Pérez-Rodríguez, A., and Scheer, R. (2005) Real-time study of phase transformations in Cu–In chalcogenide thin films using in situ Raman spectroscopy and XRD. *J. Phys. Chem. Solids*, **66**, 1954–1960.
15. Scheer, R., Perez-Rodriguez, A., and Metzger, W.K. (2010) Advanced diagnostic and control methods of processes and layers in CIGS solar cells and modules. *Prog. Photovoltaics Res. Appl.*, **18**, 467–480.
16. Gillespie, T.J., Marshall, C.H., Contreras, M., and Keane, J. (1999) Copper indium diselenide (CIS) process, control and manufacturing. *Sol. Energy Mater. Sol. Cells*, **59**, 27–34.
17. Posada, J., Jubault, M., Bousquet, A., Tomasella, E., and Lincot, D. (2015) In-situ optical emission spectroscopy for a better control of hybrid sputtering/evaporation process for the deposition of Cu(In,Ga)Se_2 layers. *Thin Solid Films*, **582**, 279–283.
18. Nawarange, A.V. (2011) *Optical emission spectroscopy during sputter deposition of CdTe solar cells and CuTe-based back*

contacts. Dissertation. University of Toledo.

19. Feitknecht, L., Meier, J., Torres, P., Zürcher, J., and Shah, A. (2002) Plasma deposition of thin film silicon: kinetics monitored by optical emission spectroscopy. *Sol. Energy Mater. Sol. Cells*, **74**, 539–545.
20. Lien, S.-Y., Chang, Y.-C., Cho, Y.-S., Chang, Y.-Y., and Lee, S.-J. (2012) Deposition and characterization of high-efficiency silicon thin-film solar cells by HF-PECVD and OES technology. *IEEE Trans. Electron Devices*, **59**, 1245–1254.
21. Eisgruber, I., Joshi, B., Gomez, N., Britt, J., and Vincent, T. (2002) In situ X-ray fluorescence used for real-time control of $CuIn_xGa_{1-x}Se_2$ thin film composition. *Thin Solid Films*, **408**, 64–72.
22. Rodríguez-Alvarez, H., Mainz, R., Caballero, R., Abou-Ras, D., Klaus, M., Gledhill, S., and Weber, A. (2013) Real-time study of Ga diffusion process during the formation of $Cu(In,Ga)Se_2$: the role of Cu and Na content. *Sol. Energy Mater. Sol. Cells*, **116**, 102–109.
23. Bozovic, I., Eckstein, I.N., and Bozovic, N. (2001) Reflection high-energy electron diffraction as a tool for real-time characterisation of growth of complex oxide, in *In-Situ Real-Time Characterisation of Thin Films* (eds O. Auciello and A.R. Krauss), John Wiley & Sons, Ltd, Chichester, pp. 29–56.
24. Koster, G. (2011) Reflection high-energy electron diffraction (RHEED) for in situ characterization of thin film growth, in *In Situ Characterization of Thin Film Growth* (eds G. Koster and G. Rijnders), Woodhead Publishing Limited, pp. 1–28.
25. Colegrove, E. (2014) *Fundamental investigations of CdTe deposited by MBE for applications in thin film solar photovoltaics*. Dissertation. University of Illinois at Chicago.
26. Cieslak, J. (2007) *Epitaxie von $Cu(In,Ga)S_2$ auf Si-substraten*. Dissertation. Friedrich-Schiller-Universität Jena.
27. Thiru, S., Asakawa, M., Honda, K., Kawaharazuka, A., Tackeuchi, A., Makimoto, T., and Horikoshi, Y. (2015) Investigation of $CuGaSe_2/CuInSe_2$ double heterojunction interfaces grown by molecular beam epitaxy. *AIP Adv.*, **5**, 02710.
28. Kötschau, I.M. and Schock, H.W. (2006) Compositional depth profiling of polycrystalline thin films by grazing-incidence X-ray diffraction. *J. Appl. Crystallogr.*, **39**, 683–696.
29. Friedlmeier, T.M., Jackson, P., Bauer, A., Hariskos, D., Kiowski, O., Wuerz, R., and Powalla, M. (2015) Improved photocurrent in $Cu(In,Ga)Se_2$ solar cells: from 20.8% to 21.7% efficiency with CdS buffer and 21.0 Cd-free. *IEEE J. Photovoltaics*, **5**, 1487–1491.
30. Pistor, P., Zahedi-Azad, S., Hartnauer, S., Wägele, L., Jarzembowski, E., and Scheer, R. (2015) Real time observation of phase formations by XRD during Ga-rich or In-rich $Cu(In, Ga)Se_2$ growth by co-evaporation. *Phys. Status Solidi A*, **212**, 1897–1904.
31. Abou-Ras, D., Contreras, M., Noufi, R., and Schock, H.-W. (2009) Impact of the Se evaporation rate on the microstructure and texture of $Cu(In,Ga)Se_2$ thin films for solar cells. *Thin Solid Films*, **517**, 2218–2221.
32. Mainz, R., Weber, A., Rodriguez-Alvarez, H., Levcenko, S., Klaus, M., Pistor, P., Klenk, R., and Schock, H.W. (2014) Time-resolved investigation of $Cu(In,Ga)Se_2$ growth and Ga gradient formation during fast selenisation of metallic precursors. *Prog. Photovoltaics Res. Appl.*, **23**, 1131–1143.
33. Jost, S., Schurr, R., Hölzing, A., Hergert, F., Hock, R., Purwins, M., and Palm, J. (2009) The formation of the thin-film solar cell absorber $CuInS_2$ by annealing of Cu–In–S stacked elemental layer precursors – a comparison of selenisation and sulfurisation. *Thin Solid Films*, **517**, 2136–2139.
34. Hölzing, A., Schurr, R., Jost, S., Palm, J., Deseler, K., Wellmann, P., and Hock, R. (2011) The influence of gallium on phase transitions during the crystallisation of thin film absorber materials $Cu(In,Ga)(S,Se)_2$ investigated by in-situ X-ray diffraction. *Thin Solid Films*, **519**, 7197–7200.

35. Wibowo, R.A., Yoo, H., Hölzing, A., Lechner, R., Jost, S., Palm, J., Gowtham, M., Louis, B., and Hock, R. (2013) A study of kesterite $Cu_2ZnSn(Se,S)_4$ formation from sputtered Cu–Zn–Sn metal precursors by rapid thermal processing sulfo-selenization of the metal thin films. *Thin Solid Films*, **535**, 57–61.
36. Kaune, G., Hartnauer, S., Syrowatka, F., and Scheer, R. (2014) Phase formation in $Cu_2ZnSnSe_4$ thin films deposited with multi-stage co-evaporation processes. *Sol. Energy Mater. Sol. Cells*, **120**, 596–602.
37. Kim, M.J., Lee, J.J., Lee, S.H., and Sohn, S.H. (2013) Study of CdTe/CdS heterostructure by $CdCl_2$ heat treatment via in situ high temperature XRD. *Sol. Energy Mater. Sol. Cells*, **109**, 209–214.
38. Pistor, P., Borchert, J., Fränzel, W., Csuk, R., and Scheer, R. (2014) Monitoring the phase formation of coevaporated lead halide perovskite thin films by in situ X-ray diffraction. *J. Phys. Chem. Lett.*, **5**, 3308–3312.
39. Borchert, J., Boht, H., Fränzel, W., Csuk, R., Scheer, R., and Pistor, P. (2015) Structural investigation of co-evaporated methyl ammonium lead halide perovskite films during growth and thermal decomposition using different PbX2 (X = I, Cl) precursors. *J. Mater. Chem. A*, **3**, 19842–19849.
40. Buras, B. and Gerward, L. (1989) Application of X-ray energy-dispersive diffraction for characterization of materials under high pressure. *Prog. Cryst. Growth Charact.*, **18**, 93–138.
41. Genzel, C., Denks, I.A., Gibmeier, J., Klaus, M., and Wagener, G. (2007) The materials science synchrotron beamline EDD for energy-dispersive diffraction analysis. *Nucl. Instrum. Methods Phys. Res., Sect. A*, **578**, 23–33.
42. Weber, A., Mainz, R., and Schock, H.W. (2010) On the Sn loss from thin films of the material system Cu–Zn–Sn–S in high vacuum. *J. Appl. Phys.*, **107** (1), 013516.
43. Mainz, R. and Klenk, R. (2011) In situ analysis of elemental depth distributions in thin films by combined evaluation of synchrotron X-ray fluorescence and diffraction. *J. Appl. Phys.*, **109** (12), 123515.
44. Ellmer, K., Mientus, R., and Rossner, H. (2001) In situ investigation by energy dispersive X-ray diffraction (EDXRD) of the growth of magnetron sputtered films. *Surf. Coat. Technol.*, **142–144**, 1094–1099.
45. Scragg, J.J., Ericson, T., Kubart, T., Edoff, M., and Platzer-Björkman, C. (2011) Chemical insights into the instability of Cu_2ZnSnS_4 films during annealing. *Chem. Mater.*, **23** (20), 4625–4633.
46. Rodriguez-Alvarez, H., Weber, A., Lauche, J., Kaufmann, C.A., Rissom, T., Greiner, D., Klaus, M., Unold, T., Genzel, C., Schock, H.-W., and Mainz, R. (2013) Formation of $CuInSe_2$ and $CuGaSe_2$ thin-films deposited by three-stage thermal co-evaporation: a real-time X-ray diffraction and fluorescence study. *Adv. Energy Mater*, **3**, 1381–1387.
47. Mainz, R., Rodriguez-Alvarez, H., Klaus, M., Thomas, D., Lauche, J., Weber, A., Heinemann, M.D., Brunken, S., Greiner, D., Kaufmann, C.A., Unold, T., Schock, H.-W., and Genzel, C. (2015) Sudden stress relaxation in compound semiconductor thin films triggered by secondary phase segregation. *Phys. Rev. B: Condens. Matter Mater. Phys.*, **92**, 155310.
48. Church, E.L., Jenkinson, H.A., and Zavada, J.M. (1977) Measurement of the finish of diamond-turned metal surfaces by differential light scattering. *Opt. Eng.*, **16** (4), 360.
49. Rouleau, C.M. and Park, R.M. (1993) In-situ, real-time diffuse optical reflectivity measurements during GaAs cleaning and subsequent ZnSe/GaAs heteroepitaxy. *J. Vac. Sci. Technol. A*, **11** (4), 1792.
50. Celii, F.H., Files-Sesler, L.A., III, E.A.B., and Liu, H.-Y. (1993) In-situ detection of InGaAs strained-layer relaxation by laser light scattering. *J. Vac. Sci. Technol. A*, **11** (4), 1796.
51. Pidduck, A.J., Robbins, D.J., Cullis, A.G., Gasson, D.B., and Glasper, J.L. (1989) In situ laser light scattering. *J. Electrochem. Soc.*, **136** (19), 3083.
52. Pietzker, C., Rudigier, E., Bräunig, D. and Scheer, R. (2001) *Laser Light Scattering and Real-Time XRD Studies on the Sequential Formation of $CuInS_2$*

Films: Towards a Simple and Stable Process Control. Proceedings of the 17th European Photovoltaic Solar Energy Conference, edited by B. McNelis, W. Palz, H. A. Ossenbrink and P. Helm (WIP, Munich), vol. II, p. 1031.

53. Scheer, R., Perez-Rodriguez, A., and Metzger, W. (2010) Advanced diagnostic and control methods of processes and layers in CIGS solar cells and modules. *Prog. Photovoltaics*, **18** (6), 467.
54. Sakurai, K., Neumann, T., Hesse, R., Abou-Ras, D., Jablonski, P., Neisser, A., Kaufmann, C., Niki, S., Scheer, R., and Schock, H.-W. (2007) Characteristics of scattered laser light signals from $Cu(In,Ga)Se_2$ films. *Thin Solid Films*, **515** (15), 6222–6225.
55. Hartnauer, S., Wägele, L.A., Syrowatka, F., Kaune, G., and Scheer, R. (2015) Co-evaporation process study of $Cu_2ZnSnSe_4$ thin films by in situ light scattering and in situ X-ray diffraction. *Phys. Status Solidi A*, **212**, 356–363.
56. Scheer, R., Neisser, A., Sakurai, K., Fons, P., and Niki, S. (2003) $Cu(In_{1-x}Ga_x)Se_2$ growth studies by in situ spectroscopic light scattering. *Appl. Phys. Lett.*, **82** (13), 2091.
57. Scheer, R., Pietzker, C. and Bräunig, D., (2001) *Laser Light Scattering In-Situ Studies on the Growth of Chalcopyrite Thin Films*. Proceedings of the Spring Meeting of the Materials Research Society, Symposium H, edited by MRS (San Francisco), vol. 668, p. H7.3.
58. Gabor, A.M., Tuttle, J.R., Albin, D.S., Contreras, M.A., Noufi, R., and Hermann, A.M. (1994) High efficiency $CuIn_xGa_{1-x}Se_2$ solar cells made from $(In_xGa_{1-x})_2Se_3$ precursor films. *Appl. Phys. Lett.*, **65** (2), 198.
59. Hesse, R., Caballero, R., Abou-Ras, D., Unold, T., Kaufmann, C.A., and Schock, H.-W. (2007) A reliable optical method for in-situ process control for deposition of $Cu(In,Ga)Se_2$ thin layers for photovoltaics, in *Photovoltaic Cell and Module Technologies*, vol. **6651** (eds B.v. Roedern and A.E. Delahoy), SPIE, p. 665108-1.
60. Repins, I.L., Fisher, D., Batchelor, W.K., Woods, L., and Beck, M.E. (2005) A non-contact low-cost sensor for improved repeatability in co-evaporated CIGS. *Prog. Photovoltaics Res. Appl.*, **13**, 311–323.
61. Kaufmann, C.A., Neisser, A., Klenk, R., and Scheer, R. (2005) Transfer of $Cu(In,Ga)Se_2$ thin film solar cells to flexible substrates using an in situ process control. *Thin Solid Films*, **480–481**, 515–519.
62. Hesse, R., Rodriguez-Alvarez, H., Mainz, R., Lauche, J., Herdin, P., Abou-Ras, D., Unold, T. and Schock, H-W. (2008) *In-Situ Monitoring of Rapid Thermal Processes (RTP) of Cu(In,Ga)(S,Se)$_2$ by Optical Methods*. SPIE Proceedings 7045 – Photovoltaic Cell and Module Technologies II, vol. 7045, p. 704505.
63. Hartnauer, S., Wägele, L.A., Syrowatka, F., Kaune, G., and Scheer, R. (2014) Co-evaporation process study of $Cu_2ZnSnSe_4$ thin films by in situ light scattering and in situ X-ray diffraction. *Phys. Status Solidi A*, **212**, 356–363.
64. Neisser, A. and Scheer, R. (2004) *Verfahren zur Herstellung einer Chalkogenid-Halbleiterschicht mit optischer in-situ-Prozesskontrolle und Vorrichtung zur Verfahrensdurchführung*. Deutschland Patent No. DE10256909 (29.07.2004).
65. Powalla, M., Jackson, P., Witte, W., Hariskos, D., Paetel, S., Tschamber, C., and Wischmann, W. (2013) High-efficiency $Cu(In,Ga)Se_2$ cells and modules. *Sol. Energy Mater. Sol. Cells*, **119**, 51–58.
66. von Klopmann, C., Djordjevic, J., Rudigier, E., and Scheer, R. (2006) Real-time studies of phase transformations in Cu–In–Se–S thin films 2. Sulfurization of Cu–In precursors. *J. Cryst. Growth*, **289** (1), 121–133.
67. Bennett, H. and Porteus, J. (1961) Relation between surface roughness and specular reflectance at normal incidence. *JOSA*, **51** (2), 123–129.
68. Carniglia, C. (1979) Scalar scattering theory for multilayer optical coatings. *Opt. Eng.*, **18** (2), 182104.
69. Kirchartz, T. and Rau, U. (2007) Electroluminescence analysis of high efficiency $Cu(In,Ga)Se_2$ solar cells. *J. Appl. Phys.*, **102** (10), 104510.
70. Heinemann, M.D., Mainz, R., Rodriguez-Alvarez, H., Greiner, D.,

Kaufmann, C.A. and Unold, T., *In-situ Analysis of Band Gap, Urbach Energy, Growth Rate and Roughness during Thin Film Cu(In,Ga)Se_2 Absorber Growth*, submitted for publication.

71. Benson, T.E., Kamlet, L.I., Klimecky, P., and Terry, R.L. (1996) In-situ spectroscopic reflectometry for polycrystalline silicon thin film etch rate determination during reactive ion etching. *J. Electron. Mater.*, **25**, 955–964.
72. Necas, D., Ohlidal, I., Franta, D., Cudek, V., Ohlidal, M., Vodak, J., Slodkova, L., Zajckova, L., Elias, M., and Vizda, F. (2014) Assessment of non-uniform thin films using spectroscopic ellipsometry and imaging spectroscopic reflectometry. *Thin Solid Films*, **571**, 573–578.
73. Urbanek, M., Spousta, J., Behounek, T., and Sikola, T. (2007) Imaging reflectometry in situ. *Appl. Opt.*, **46**, 6309.

17
Raman Spectroscopy on Thin Films for Solar Cells

Jacobo Álvarez-García, Víctor Izquierdo-Roca, Paul Pistor, Thomas Schmid, and Alejandro Pérez-Rodríguez

17.1
Introduction

In the present chapter, the capabilities of Raman spectroscopy for the advanced characterization of thin films for solar cells are reviewed. Raman spectroscopy is an optical nondestructive technique based on the inelastic scattering of photons with elemental vibrational excitations in the material. The line shape and position of the Raman bands are determined by the crystalline structure and chemical composition of the measured samples, being sensitive to the presence of crystalline defects, impurities, and strain. The presence of peak characteristic of different phases also allows for the identification of secondary phases that are strongly related to the growth and process conditions of the films. All these aspects account for a strong interest in the analysis of the Raman spectra, providing a powerful nondestructive analytical tool for the structural and chemical assessment of the films. In addition, the combination of a Raman spectrometer with an optical microscope also allows for achieving a high spatial resolutions (of below 1 μm) when mapping surfaces and analyzing depth-resolved phase distributions in thin films.

The present chapter is divided into four main sections: The two first ones are devoted to a revision of the fundamentals of Raman spectroscopy (Section 17.2) and vibrational modes in crystalline materials (Section 17.3). Section 17.4 deals with the main experimental considerations involved in the design and implementation of a Raman scattering setup. This is followed by a detailed description of the application of Raman scattering for the structural and chemicophysical analysis of thin-film photovoltaic materials (Section 17.5), with the identification of crystalline structure and secondary phases, evaluation of film crystallinity, analysis of chemical composition of semiconductor alloys, and characterization of nanocrystalline and amorphous layers, stress effects, and crystal orientations. This includes the description of corresponding state-of-the-art and recent case examples that illustrate the capabilities of the Raman technique for the advanced

Advanced Characterization Techniques for Thin Film Solar Cells, Second Edition.
Edited by Daniel Abou-Ras, Thomas Kirchartz, and Uwe Rau.

characterization of layers and process monitoring in thin-film photovoltaic technologies.

17.2 Fundamentals of Raman Spectroscopy

Raman spectroscopy relies on the analysis of the electromagnetic radiation inelastically scattered by a material. The macroscopic theory, introduced in this section, provides a simple and consistent description of the underlying physical processes. Nevertheless, in order to fully describe the light–matter interaction process, it is necessary to take into account quantum mechanical considerations. A detailed description of light-scattering theory can be found in Ref. [1]. Further detailed information on the fundamentals of Raman scattering and its application for the analysis of semiconductor materials is given in Refs [2–4].

Transmission, *reflection*, *refraction*, and *absorption* constitute the fundamental processes that describe most of the photon–matter interactions. However, a small fraction of light undergoes different interaction mechanisms resulting in the radiation of electromagnetic energy. These processes are known as *light scattering* and typically account for <1% of the photon–matter interactions. When a photon is scattered by a medium, it may either retain its energy (*elastic scattering*) or lose part of it (*inelastic scattering*).

In the case of the interactions between light and semiconducting materials, light scattering is a straightforward consequence of the dielectric properties of the medium. In the presence of an externally applied electric field, atoms within a dielectric material redistribute their electrical charge, creating an internal electric field (polarization), which tends to compensate the external field. In linear and isotropic materials, the polarization response $\vec{P}$ is linear with the electric field of the incoming radiation, according to

$$\vec{P} = \chi \cdot \vec{E}_{\mathrm{I}} = \chi \cdot \vec{E}_{\mathrm{I}}^{0} \cdot \cos(\vec{k}_{\mathrm{I}} \cdot \vec{r} - \omega_{\mathrm{I}} \cdot t). \tag{17.1}$$

In this equation, $\vec{E}_{\mathrm{I}}^{0}$ is the amplitude of the electric field from an electromagnetic incident wave with wavevector $\vec{k}_{\mathrm{I}}$ and frequency ω_{I}. The factor χ is the electrical susceptibility of the medium and may be interpreted as the density of electric dipoles per unit volume, which is a characteristic of the material. When the applied field is oscillating, such as the one associated with the electromagnetic radiation, the induced polarization field is also time dependent, and therefore, according to the basic electrodynamic theory, it radiates energy. Consequently, light scattering may be interpreted as a result of the radiative processes associated with the existence of electric dipoles at the atomic scale, distributed throughout the material.

While the previous description provides a simple picture of elastic light scattering, Raman scattering involving inelastic interactions requires a more accurate analysis of the polarization mechanisms. Polarization is caused by the redistribution of charges within the atoms forming a solid. However, in a semiconducting crystal at temperatures above 0 K, atoms do not occupy static positions, but they

oscillate around their equilibrium positions with a characteristic frequency Ω. Such periodic oscillations modulate the dielectric response of the medium, leading to the occurrence of radiative polarization fields oscillating at a frequency different to the frequency of the external electric field.

To illustrate this argument mathematically, one may consider a perfect crystal in which all the atoms are oscillating at a frequency Ω. Notice that for the sake of simplicity, we will restrict this discussion to the analysis of a single collective oscillation mode in a crystal (phonon), characterized by a frequency Ω and wavevector $\vec{q}$ – in a more general approach, an expansion in terms of Fourier components may be considered. Under these assumptions, the amplitude of the oscillations of an atom in the crystal may be expressed as

$$\vec{X}(\vec{r},t) = \vec{X}^0(q,t) \cdot \cos(\vec{q}\cdot\vec{r} - \Omega \cdot t). \tag{17.2}$$

In terms of this frequency-dependent amplitude, the susceptibility of the crystal can be expressed as a first-order Taylor expansion:

$$\chi(\vec{q},\Omega) = \chi_0 + \left(\frac{\partial\chi}{\partial X^j}\right) \cdot X^j(\vec{q},\Omega). \tag{17.3}$$

In the previous expression, the index *j* runs over the three crystallographic directions. Using Equations 17.1 and 17.3 and basic trigonometric relations, the polarization vector may be expressed as

$$\begin{aligned}\vec{P} =& \chi \cdot \vec{E}_{\mathrm{I}}^0 \cos(\vec{k}_{\mathrm{I}} \cdot \vec{r} - \omega_{\mathrm{I}} \cdot t) + \left(\frac{\partial\chi}{\partial X^j}\right) \cdot X^j(\vec{q},\Omega) \cdot \vec{E}_{\mathrm{I}}^0 \cdot \cos(\vec{k}_{\mathrm{AS}} \cdot \vec{r} - \omega_{\mathrm{AS}} \cdot t) \\ &+ \left(\frac{\partial\chi}{\partial X^j}\right) \cdot X^j(\vec{q},\Omega) \cdot \vec{E}_{\mathrm{I}}^0 \cdot \cos(\vec{k}_{\mathrm{S}} \cdot \vec{r} - \omega_{\mathrm{S}} \cdot t),\end{aligned} \tag{17.4}$$

where

$$\begin{aligned}\vec{k}_{\mathrm{S}} &= \vec{k}_{\mathrm{I}} - \vec{q} \quad & \omega_{\mathrm{S}} &= \omega_{\mathrm{I}} - \Omega \\ \vec{k}_{\mathrm{AS}} &= \vec{k}_I + \vec{q} \quad & \omega_{\mathrm{AS}} &= \omega_I - \Omega.\end{aligned} \tag{17.5}$$

The first term of Equation 17.4 corresponds to a wave equation with the same frequency and wavevector as the incoming field (zero-order term) and is responsible for the elastic contribution to the scattering radiation, sometimes called *Rayleigh scattering*. The second and third terms in Equation 17.4 contain a factor proportional to the first derivative of the susceptibility and account for the two terms responsible for the Raman scattering processes. This factor makes the inelastic contribution much less intense than the elastic term. Typically, the Raman scattering intensity is $10^6 - 10^9$ times less intense than the Rayleigh signal.

On the other hand, it is worth to notice that the Raman scattering signal consists of two contributions, symmetrically shifted in frequency with respect to the frequency of the excitation light ω_{I}. The magnitude of this shift (ω), known as *Raman shift*, is directly equal to the vibration frequency of the crystal (Ω). The Raman shift is usually expressed as a wavenumber (inverse wavelength), and it is related to the

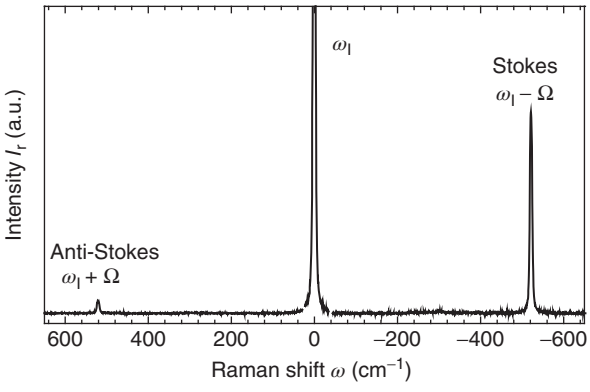

Figure 17.1 Scattering spectrum of crystalline Si showing two inelastic contributions shifted to higher (anti-Stokes) and lower (Stokes) energy. The energy shift is the energy of the phonon involved in the photon–phonon interaction. The observed peak corresponds to a triple-degenerate phonon band at 520 cm^{-1}, as described in Section 8.3.

excitation (λ_I) and scattered (λ_{scatt}) wavelengths by

$$\omega\,(\mathrm{cm}^{-1}) = \frac{1}{\lambda_{scatt}(\mathrm{cm})} - \frac{1}{\lambda_I(\mathrm{cm})}. \tag{17.6}$$

For practical analytical purposes, the information provided by the two inelastic contributions is redundant, and usually only the low-frequency signal (Stokes component) is analyzed, since its intensity is higher than the high-frequency component (anti-Stokes band), as shown in Figure 17.1. Normally, Raman spectra are plotted as function of the absolute value of the Raman shift.

The frequency, intensity, and bandshape of the Raman bands provide useful information in relation to the way in which atoms vibrate in a crystalline lattice. These parameters, in turn, indirectly depend on a number of physical and chemical factors, including the chemical composition and crystallographic structure of the material and the presence of impurities, stress, or crystalline defects. Such interdependence between the Raman spectra and different physical properties allows inferring basic material properties based on the analysis of the spectra and constitutes the fundamentals of the technique.

17.3
Vibrational Modes in Crystalline Materials

In the previous section, we had assumed a simplified case in which all the atoms in a crystal oscillate at a unique frequency. However, in real crystals, the lattice dynamics is characterized by the existence of multiple collective oscillation modes (phonons), which can be described in terms of their frequency (Ω) and

wavevector ($\vec{q}$) [5]. As a result, the band structure of Raman spectra of real materials is usually complex, particularly in those cases in which the crystal symmetry is low. Nevertheless, there exists an important restriction that must be taken into account, which significantly reduces the complexity of the Raman spectra. In a perfect crystalline material, any inelastic photon–phonon interaction must fulfill two fundamental relations, given by Equation 17. A first relation stands for the energy conservation law, which requires that the energy balance in the scattering process must be properly preserved. Likewise, the conservation of the crystalline quasimomentum requires also that the difference between the wavevectors of the scattered and incoming photon must be equal to $\pm\vec{q}$ (wavevector of the phonon involved in the scattering process). Furthermore, since the energy of visible photons is about three orders of magnitude greater than the typical energy of lattice oscillations, inelastic scattering at practical experimental conditions occurs without a significant change of the photon energy and, accordingly, without any substantial change in its wavevector module. Consequently, the conservation of the crystalline quasimomentum requires that phonons involved in inelastic scattering processes must have a wavevector module close to zero: $|\vec{q}| = 0$. According to these conservation laws, the Stokes process can be interpreted as the process of creation of a phonon with frequency (Ω) and wavevector ($\vec{q}$) by the incident photon, resulting in a scattered photon with lower energy, while the anti-Stokes process would correspond to the annihilation of a phonon with frequency (Ω) and wavevector ($\vec{q}$) by the incident photon, resulting in a scattered photon with higher energy.

The previous argument related to the energy and quasimomentum conservation laws allows predicting the number of optically active bands for any given crystalline structure. Raman active phonons correspond necessarily to long-wave oscillation modes (or zone-center phonons, in relation to their position in the Brillouin zone), which involve the in-phase displacement of all the equivalent atomic positions in the crystal. Therefore, the number of optical vibrational modes in three-dimensional crystalline structures is always $3(N-3)$, where N is the number of atoms in the crystal base (notice that this formula takes into account the fact that three normal modes necessarily correspond to pure translations in the crystal).

At this point, it is worth to mention that the symmetry characteristics of a particular crystalline structure may lead to additional restrictions in the characteristics of the Raman spectrum. A first restriction deals with the fact that some of the optically active modes may be symmetrically equivalent, thus leading to Raman modes with the same frequency. When this happens, the corresponding Raman mode is said to be *degenerated*. On the other hand, a second noticeable particularity of some lattice vibrations is their lack of Raman activity. Non-Raman active modes necessarily involve the displacement of atoms in the lattice in such a way that the terms in the derivative of the electrical susceptibility are null or they cancel each other. From Equation 17.4, it is clear that under this condition, the Raman intensity is zero.

In order to illustrate the concepts described in the previous paragraphs, we shall consider now the crystalline structure of Si as a practical example. Si crystallizes in a diamond-like face-centered cubic structure, in which two Si atoms occupy the nodes of the crystal unit cell, at positions given by $\vec{u}_1 = (0, 0, 0)$ and $\vec{u}_2 = (1/4, 1/4, 1/4)$ (space group $Fd\bar{3}m$). Therefore, one may expect three Raman active phonons for this structure, which in principle may occur at different frequencies. In this case, due to the high symmetry characteristics of the Si structure, the frequency of these three active modes is the same (the mode is said to be triple degenerated), and therefore, one single band is observed in the (Stokes) Raman spectrum of crystalline Si, as shown in Figure 17.1.

The previous simple example already reveals that a complete comprehension of the Raman spectrum of a material necessarily requires a detailed analysis of the symmetry properties of the crystal structure. Nevertheless, in addition to the previous considerations, it must be taken into account also the fact that in polar oscillation modes (those involving an asymmetric displacement of ions in the lattice, which result in a net electric field over the crystal), the photon–phonon coupling results in a splitting of the phonons with propagation vector parallel (longitudinal) and perpendicular (transverse) to the electric field. Such splitting is known as LO–TO *splitting*, and from a practical point of view, it results in the occurrence of two bands in the spectrum for each polar mode, occurring at different frequencies. As a representative example of LO–TO splitting, we may consider the case of the GaAs crystal. The crystalline structure of GaAs is essentially the same as the one of Si, replacing each of the two atoms in the atomic base by one atom of Ga and As. Though this modification results in a different symmetry space group ($F\bar{4}3m$), it is possible to show that the three optical modes in this crystalline structure are also degenerated. However, unlike in the case of the Si crystalline structure, these modes involve the displacement of ions with different charges, which results in a net electric field (polar modes) that is responsible for the LO–TO splitting of the mode. The experimentally measured frequencies for these two bands are 268 and 292 cm^{-1}, corresponding to the TO and LO modes, respectively.

17.4 Experimental Considerations

From the experimental point of view, Raman spectroscopic measurements require a relatively simple setup, consisting of a laser source, focusing and collection optics, and a sensitive spectrophotometer. Figure 17.2 shows a schematic diagram of the experimental setup required for these measurements. From the different elements constituting the system, the spectrometer unit is the most critical one.

The following subsections intend to introduce the most important considerations in the selection of an adequate Raman setup.

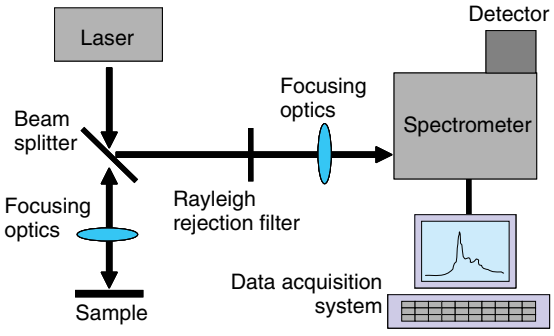

Figure 17.2 Schematic diagram of Raman scattering experimental setup.

17.4.1 Laser Source

Continuous gas lasers with powers ranging from some tens of milliwatt to a few watts have been traditionally used as light sources in Raman spectroscopy. Recently, highly temperature-stabilized solid-state lasers have also become a good alternative to conventional gas lasers.

17.4.1.1 Laser Power

Since the intensity of the Raman signal linearly increases with laser power, in order to reduce data acquisition times, the incident laser power should be kept as high as possible. However, increased laser power also means severing the thermal impact on the sample.

Even at moderate laser powers, thermal effects may cause subtle changes in the spectra, which may lead to wrong interpretations of the spectra. Asymmetric band broadening and redshift of the Raman bands are usually the first observable thermal effects. The impact of sample warming is difficult to predict a priori, as it depends on spot size, thermal stability, thermal conductivity, and heat capacity of the measured sample. It is therefore of most importance to determine the threshold below which spectral changes due to heating of the sample can be excluded for every new material measured with Raman in a dedicated power series, as this threshold can vary in a quite wide range depending on the setup and sample.

Thermal effects can be especially important when working with a micro-Raman configuration, because, in this case, the incident excitation power is concentrated in a very small (micrometric) volume, which can lead to very high power densities. Apart from reversible effects on the spectra due to a simple warming of the sample, high power densities may easily cause severe irreversible thermal damages to the sample (bear in mind that a typical power of 10 mW on a spot of 100 μm diameter is related to a power density of roughly 100 W/cm^2).

An instructive example for irreversible thermal damages is given by the analysis of organic–inorganic lead halide perovskites such as the methylammonium

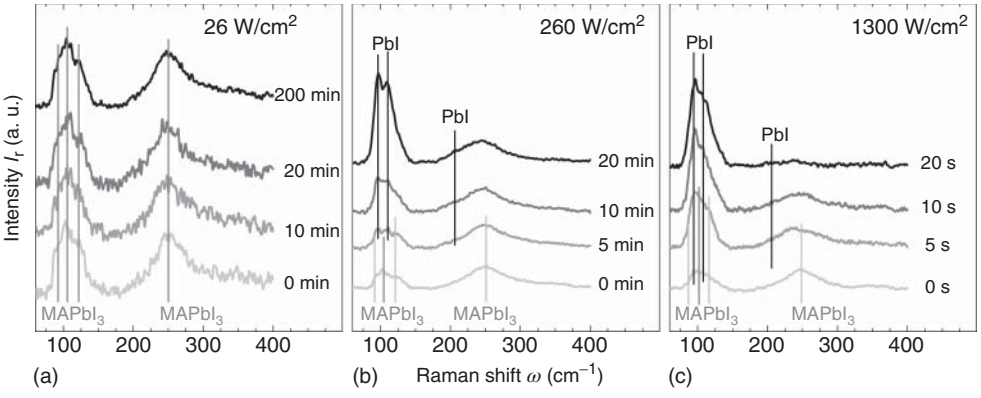

Figure 17.3 Raman spectra measured on a $MAPbI_3$ sample with different times of exposure to the excitation laser and different power excitation densities ($\lambda_{ex} = 532$ nm). Measurements were made with the sample encapsulated in an Ar ambient.

(CH_3NH_3 or MA) lead halide $CH_3NH_3PbI_3$. In Figure 17.3, an example for laser-induced degradations of $MAPbI_3$ films is given. Here, in order to avoid humidity-induced degradation, the sample was measured in a dry Ar atmosphere. Under standard excitation with a green laser (514 nm/532 nm) and a low power density ($\leq$26 W/cm^2), the Raman spectrum of $MAPBI_3$ is characterized by stable broadbands centered at 106 and 250 cm^{-1} (Figure 17.3a). However, for increased power density of $\geq$260 W/cm^2, the Raman spectrum starts to show a clear time-dependent behavior (Figure 17.3b). For an excitation time below 5 min, the Raman features correspond to those measured under low power density excitation. After 5–20 min, the broadband centered at 106 cm^{-1} increases in intensity in comparison with that centered at 250 cm^{-1}, and new bands close to 97 and 109 cm^{-1} appear with increasing intensities. These two bands correspond to the reported main PbI_2 Raman peaks [6]. This evolution can be interpreted as a laser-induced thermal decomposition of the perovskite layer into lead iodine. If the power density is further increased to 1300 W/cm^2, it becomes impossible to measure the pristine perovskite layer, as the decomposition occurs within seconds (Figure 17.3c). While the case of sensible materials such $MAPbI_3$ is an extreme example, it is important to exclude thermal effects observed in Raman measurements of all kinds of materials as these easily may lead to misinterpretation of the obtained data.

17.4.1.2 Laser Wavelength

Inelastic Raman scattering occurs regardless of the excitation wavelength. In this sense, laser wavelength is not a critical parameter in many applications. Nevertheless, some considerations should be kept in mind when selecting a proper wavelength. First, the Raman cross section increases with a ω_I^4 factor. Thus, shorter wavelengths are normally expected to yield better Raman signals. However, this is not always the case due to the fact that the Raman scattering intensity is also

proportional to the scattering volume, which normally decreases exponentially with light frequency due to light absorption. Therefore, light penetration is a relevant factor, which has not only an impact on the Raman intensity but also on the volume probed by the measurement. This is interesting in the analysis of semiconductors with high optical absorption in the visible region, as those involved in thin-film solar cells: In this case the direct comparison of spectra measured with different excitation wavelengths (and, hence, with different penetration depths of the scattered volume) provides a simple procedure to analyze the in-depth homogeneity of the layers, even if this is normally achieved at an estimative low depth resolution level. On the other hand, as a consequence of the dependence of the light absorption on the excitation wavelength, the thermal impact of the Raman measurements will also depend on the excitation wavelength. This implies the need to analyze the potential presence of thermal effects in the spectra for each of the excitation wavelengths used in the measurements.

A second consideration in relation to the selection of the laser wavelength deals with the possible existence of *resonant Raman* effects [7]. Resonance occurs when the excitation wavelength matches (or is close to, in the preresonant case) the energy of an electronic transition in the material. This coupling leads to a strong enhancement of the intensity of the Raman peaks, mainly in the case of those corresponding to LO modes. In the case of semiconductors, these effects take place mainly when the excitation energy approaches that of the optical band gap. Tuning the excitation photon energy to this value allows to obtain a selective enhancement of the Raman peaks related to a specific phase in the sample, and this can be applied for the high sensitivity detection of secondary phases, as will be described in Section 17.5.1. Finally, it is worth to mention that near-infrared (NIR) or ultraviolet (UV) excitation wavelengths may be a particularly adequate choice in cases in which, under visible excitation light, the Raman signal cannot be resolved due to the existence of a strong background fluorescence signal. In those cases, the use of excitation wavelengths far away from the electronic absorption bands of the material (as those at NIR or UV regions) constitutes an effective means to reduce background fluorescence.

17.4.2 Light Collection and Focusing Optics

In many cases, Raman spectra are acquired within the so-called *backscattering* configuration, in which the light scattered at 180° with respect to the incident laser beam is analyzed. Optical systems based either on conventional optical discrete elements or fiber optics are used for light-focusing and collection purposes, commonly in conjunction with beam splitting optics.

17.4.2.1 Raman Microscopy

As Raman spectroscopy is most often performed in the visible or NIR spectral range, combination with optical microscopy is straightforward, and in recent years Raman spectroscopy in general has gained interest with the commercial

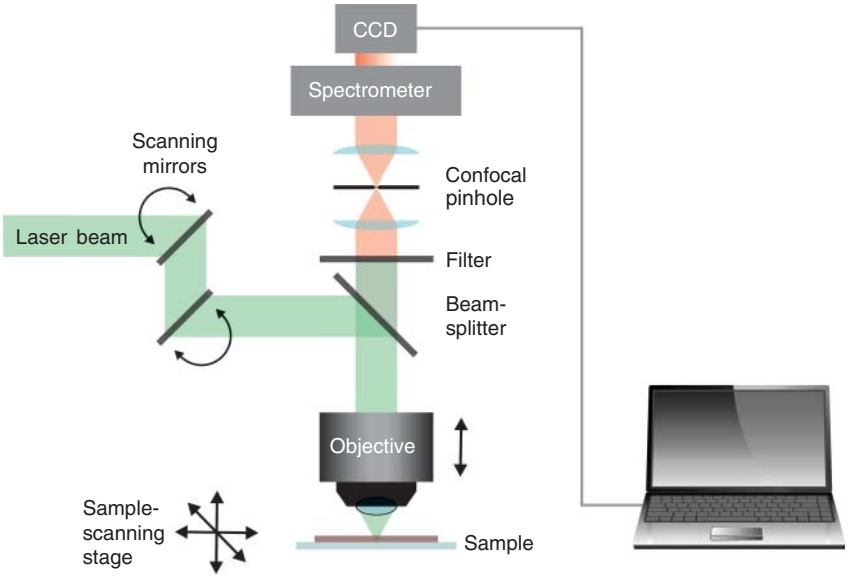

Figure 17.4 Schematic setup of a Raman microscope.

availability of Raman microscopes (also known as *Raman microprobes*). Figure 17.4 depicts the general principle of a Raman microscope [8]. Indeed, there are several different types of Raman microscopes available, including inverted and upright microscopes. Here, the upright configuration is shown, which is most commonly used for the investigation of thin-film solar-cell materials.

A microscope objective lens is employed for both focusing of laser light onto a specimen and collection of the light backscattered by the sample. The collected light passes notch or edge filters (in some configurations working as 45° beam splitters) for rejection of the reflected or elastically (Rayleigh) scattered light. Typically, a grating-based spectrometer disperses the light and projects it onto a CCD camera. Most commercially available micro-Raman setups include spatial filtering of the collected light by the principle of confocal microscopy, where the typical approach is to place an adjustable pinhole in front of the spectrometer entrance to reject out-of-focus contributions to the signal. Also available are alternative approaches that, for example, use arrays of apertures and slits that can be inserted individually into the beam [9] or a spectrometer entrance slit for spatial filtering in one dimension and binning of only a few rows on the CCD for spatial filtering in the perpendicular direction [10].

Raman microscopes most often allow sample observation by white-light microscopy and specific choice of the measurement spot on the micrometer scale. Furthermore, Raman microscopes are equipped with mirrors for scanning the laser beam over the sample and/or sample-scanning stages for movement of the sample through the laser focus. Both cases allow raster scanning of samples

with collection of the full spectroscopic information in every pixel [9]. Thus, a Raman spectroscopic mapping experiment yields a data cube that is defined by the x and y coordinates and the wavenumber axis of the Raman spectra, in which each element contains the Raman intensity at a specific sample position and wavenumber. Data processing software can extract distributions of, for example, intensities of selected marker bands or wavenumber positions of bands, which are spectroscopic images (sometimes also termed *chemical images*) of the sample reflecting the distributions of chemical constituents or physicochemical properties.

17.4.2.2 Spatial Resolution

According to Abbe [11] and Rayleigh [12], the resolution of optical focusing systems is limited by optical diffraction and depends on the numerical aperture (N.A.) of the focusing element and the wavelength of light. The N.A. is a measure for the focusing angle and is defined by

$$\text{N.A.} = n \sin\theta. \tag{17.7}$$

Here, n represents the refractive index of the medium between the objective front lens and the specimen and θ is the half-angle of the maximum cone of light that can enter or exit the lens. The latter depends on the focal length and diameter of the lens. By definition, a lens working in air can theoretically reach a maximum N.A. of 1. For practical reasons, the corresponding focusing angle of 180° can only be reached by parabolic mirrors [13]. With immersion objectives, higher N.A. are accessible (e.g., water, $n = 1.33$; modern synthetic immersion oils, $n \leq 1.6$). Together with the magnification, the N.A. is usually indicated on the housing of the objective.

According to the Rayleigh criterion [12], the resolution R of an optical system – defined as the minimum distance of two objects allowing to identify them as two barely separated (but overlapping) objects – is 0.61 times the ratio of wavelength λ and N.A:

$$R = 0.61 \frac{\lambda}{\text{N.A.}}. \tag{17.8}$$

As a rule of thumb, the diffraction-limited lateral resolution of a system is on the order of $\lambda/2$ when working with immersion objective lenses (assuming N.A. ≈ 1.2) and on the order of λ when working with air objectives (assuming N.A. ≈ 0.6). This relates to lateral resolutions in the visible spectral range from approximately 200 nm to >1 µm. To our experience, a typical value in the investigation of thin-film solar-cell materials is 400 nm ($\lambda = 632.8$ nm, 100×/N.A. = 0.9 air objective lens). Note that this is the distance allowing to barely identify two overlapping Airy disks of two light-scattering microscopic (or nanoscopic) objects, which corresponds to approximately the full width at half maximum (FWHM) of the Airy disk. The focus diameter – if defined as the distance between the first intensity minima on both sides of the Airy disk maximum – is approximately twice this number.

As the laser focus in transparent media is much less confined in the axial (i.e., z) direction than in lateral (i.e., x and y) directions, the depth resolution of a Raman microscope can be on the order of several tens of micrometers when working with open pinhole aperture. By lowering the confocal pinhole diameter from, for example, 1 mm (open pinhole) down to few tens of micrometers, the depth resolution can be improved down to 1–6 µm [8, 14]. Indeed, signal intensities are reduced by closing the pinhole. As in thin-film solar-cell absorbers the optical penetration depth δ is much smaller than the confocal resolution, the axial measurement spot size is limited by δ, which is defined as the distance over which the incoming light intensity is reduced to $1/e \approx 37\%$ of its initial value. For example, the optical penetration depth in $CuInSe_2$ is approximately 70 nm, due to its high absorption coefficient of approximately 150 000 cm^{-1} in the visible range around $\lambda = 600$ nm [15]. Thus, in this material only approximately the top 100 nm layer contributes to the Raman signal.

Optical microscopy techniques which break the diffraction limit can reach higher spatial resolutions. In tip-enhanced Raman spectroscopy (TERS), a sharp silver or gold tip with radius at the apex on the order of only 10 nm is introduced into the laser focus [16]. Such tips can enhance the Raman signal within their optical near field by some orders of magnitude due to plasmonic and other enhancement effects known from surface-enhanced Raman scattering (SERS). In typical alignments of such experiments, the normal (far-field) Raman signal can be neglected, and thus, the lateral (and depth) resolution of this technique is on the order of only 10 nm. Even though "TERS-ready" instruments start to become commercially available, this technique is still performed in specialized research labs only and is not employed for routine analysis. As an example for TERS imaging of solar-cell materials, we would like to mention the pioneering work of Zhang *et al.* on organic solar cells [17, 18].

17.4.3
Spectroscopic Module

Due to the narrow bandwidth of the Raman bands, particularly in the case of semiconducting materials, high spectral resolution (wavelength resolution $\Delta\lambda < 0.1$ nm) is desirable. Besides, the low intensity of the Raman signal requires the use of sensitive CCD detectors, which are usually actively cooled to minimize dark current noise. The excellent performance of currently available multichannel CCD detectors makes them the preferred choice for most applications in front of photomultiplier-based systems, which require using scanning monochromators.

Special attention should be paid to the performance of the selected optical system in terms of stray light rejection. Since the Raman bands appear at spectral positions relatively close to the much more intense laser excitation light, stray light must be necessarily considered. For this reason, double or triple grating spectrometers are often the best choice for laboratory systems. In the case of single grating spectrometers, it is necessary to use a Rayleigh rejection filter in order to minimize the intensity of the laser light directly going into the spectrometer.

17.5
Characterization of Thin-Film Photovoltaic Materials

17.5.1
Identification of Crystalline Structures

As earlier discussed, bands in the Raman spectra of thin-film crystalline materials essentially provide the phonon energy of the zone-center phonons in the corresponding crystalline structure. The analysis of the frequency and number of bands in the spectra allows determining the crystalline structures present in the film. However, unlike with other techniques such as X-ray diffraction (XRD), simulation techniques for predicting the Raman spectrum of a given material are significantly complex, and more often, crystalline structure and phase identification is accomplished by comparing the spectra with data from reference materials. In any case, in order to avoid wrong interpretations of the spectra, it is always desirable to analyze cautiously the reference spectrum of the material under investigation. Once this is done, Raman spectroscopy can be effectively used to investigate the crystallographic properties of thin-film materials, providing useful information on the existence of secondary phases with a submicron spatial resolution. Even though the required integration time depends on the experimental setup, the film characteristics, and the type of analysis to be performed, in general it is possible to perform a measurement within a few seconds to a few minutes. Moreover, when combined with a motorized stage, the technique can be used in order to make a chemical mapping of the surface of the film (*Raman mapping*).

We shall now introduce the potential of Raman spectroscopy as an analytical tool by considering a particular example in some detail. We will discuss the case of the chalcopyrite-type structure, which is characteristic of many thin-film photovoltaic materials, including $CuInSe_2$, $CuInS_2$, $CuGaSe_2$, and related alloys [19, 20]. From the crystallographic point of view, the chalcopyrite-type structure is significantly more complex than type IV or III–V materials, and correspondingly, the Raman spectrum reflects the existence of more modes in which atoms in the lattice can oscillate. The unit cell in the chalcopyrite-type structure is occupied by two formula units, leading to a total of 21 vibrational modes. These modes are classified according to the symmetry of the atomic displacements and expressed in group theory notation as

$$\Gamma_{\text{opt}} = A_1 \oplus 2A_2 \oplus 3B_1 \oplus 3B_2 \oplus 6E. \tag{17.9}$$

Equation 17.9 is interpreted in the following way. The zone-center phonon spectrum in the chalcopyrite-type structure contains one A_1 symmetry mode, two A_2 modes, and so on. By convention, double-degenerate modes are designed by the letter E, while letters A and B are reserved to totally symmetric and antisymmetric nondegenerate vibrational modes, respectively. Therefore, in this case, the 21 vibrational modes are grouped into 9 nondegenerate modes and 6 double-degenerate modes. By analyzing in more detail the symmetry of each vibration, it can be shown that the two A_2 modes are not active by Raman, while B_2 and E type

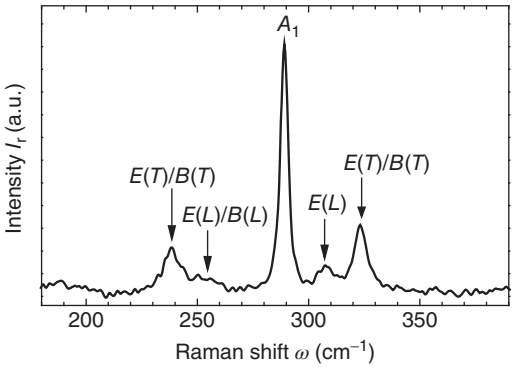

Figure 17.5 Raman spectrum of a $CuInS_2$ film, showing characteristic chalcopyrite-type Raman bands.

modes involve polar displacements, resulting in LO – TO splitting of these modes. The experimental Raman spectrum of a representative chalcopyrite compound, $CuInS_2$, is shown in Figure 17.5.

The spectrum of $CuInS_2$ is characterized by a dominant band at 290 cm^{-1}, corresponding to the A_1 symmetry phonon mode. This is in fact a common characteristic to all chalcopyrite-type materials, for which the A_1 mode involves only the displacement of the lighter anions while the heavier cations remain at rest, yielding higher scattering intensity. On the other hand, due to the relatively poor intensity of the other bands and the fact that they overlap, their identification necessarily requires a more accurate spectral analysis based on the use of polarized light and special light excitation/collection geometries. In this way, it is possible to figure out particular experimental configurations in which Raman scattering is only allowed for selected symmetry phonons. The dependence of the scattering intensity with the polarization and the scattering geometry is a consequence of the symmetry characteristics of the derivative susceptibility tensor and gives rise to configurations in which certain symmetry-type phonons are forbidden (*selection rules*). Even though these methodologies are extremely useful for fundamental studies, they have limited applicability in the case of thin-film polycrystalline materials, in which multiple randomly oriented crystals are excited simultaneously.

Once the basic spectral properties of chalcopyrite-type materials have been introduced, we will consider now the case of more complex structures in which multiple crystalline phases may occur. Figure 17.6 shows the Raman spectrum of a $CuInSe_2$ precursor grown by electrodeposition. Single-step electrodeposition of $CuInSe_2$ followed by recrystallization under sulfurizing conditions allows the fabrication of high crystalline quality $CuIn(S,Se)_2$ absorbers [21]. Electrodeposition-based processes have interest because of their higher potential to achieve a significant reduction in fabrication costs in relation to standard physical vapor deposition (PVD) processes.

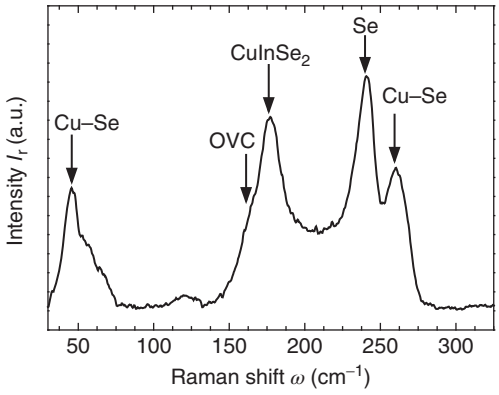

Figure 17.6 Raman spectrum of a $CuInSe_2$ electrodeposited precursor, in which different secondary phases are identified.

This spectrum shows the presence of mode characteristic of both Cu-rich and Cu-poor secondary phases, which coexist with the desired chalcopyrite-type phase [22]. The existence of chalcopyrite-type $CuInSe_2$ can be inferred from the observation of a characteristic A_1 band at 173 cm^{-1}. Nevertheless, additional bands in the spectra appear, in relation to the precipitation of elementary Se and binary Cu_xSe phases, as indicated in the figure. The presence of these phases is related to the used electrodeposition conditions that lead to precursor layers with overall Se-rich and Cu-rich composition, and they play a significant role in the recrystallization of the layers during the sulfurizing step. Moreover, special attention should be paid to the low-frequency shoulder observable in the region of 153 cm^{-1}. This shoulder is associated with the presence of an ordered vacancy compound (OVC) phase, with chemical composition $CuIn_3Se_5$ [23]. A more detailed analysis of the crystallographic structure of this OVC phase reveals that it is closely related to the chalcopyrite-type structure. Essentially, the OVC structure can be derived by randomly introducing in the chalcopyrite-type lattice complex defects in the form of (In_{Cu}^{2+}) antisites and Se vacancies (V_{Se}^{2-}) and imposing the preservation of the charge neutrality in the lattice. For example, the $CuIn_3Se_5$ OVC structure may be readily obtained by introducing in a defect-free chalcopyrite lattice a combination of two In_{Cu} and one V_{Se} for every three molecular formula units ($CuInSe_2$). Likewise, other combinations of defects in the primary chalcopyrite structure lead to a variety of OVC structures characterized by different stoichiometries. By using group theory methods combined with simple lattice dynamic models, it is possible to show that the spectrum of the OVC structure should be also characterized by a totally symmetric A_1 band, in which the displacement of the anions is equivalent to those involved in the A_1 mode of the chalcopyrite-type structure. Nevertheless, in good agreement with the experimental findings, the expected frequency of the A_1 band for the OVC

phase is lower, due to the fact that the introduced (V_{Se}^{2-}) vacancies lead to an effective weakening of the average anion–cation bonding constant.

Enhanced detection of the OVC phase can be achieved when working with a 785 nm excitation wavelength. This determines a preresonant excitation of the *E*/*B* symmetry OVC Raman peaks located in the 228–235 cm^{-1} spectral region, because of the coupling of the excitation energy with the band-gap energy of the OVC (close to 1.3 eV, depending on the stoichiometry of the compound). The content of the OVC phase at the surface region of the absorber has been found to have a relevant impact on the efficiency of electrochemical-based Cu(In,Ga)Se_2 solar cells [24].

Another example of identification of secondary phases can be found in the CdTe system. In this case, Raman scattering is very sensitive to the presence of Te aggregates that can be present in CdTe thin films depending on their growth and processing conditions [25]. Te has characteristic vibrational modes at 123 (*E*) and 141 cm^{-1} (A_1). The frequency of the A_1 mode coincides with that of the TO mode from CdTe, which has also an LO mode at 167 cm^{-1}. Observation of the modes related to Te aggregates in the film is favored by the fact that Te has at least two orders of magnitude larger scattering cross section compared to that of CdTe.

In the previous examples, Raman spectroscopy provided particularly useful information in relation to the identification of phases present in the film. In particular, detection of OVC phases in chalcopyrites constitutes a good alternative to XRD analysis due to the strong overlapping between the different XRD peaks from the different crystalline structures. Use of resonant Raman strategies has also been demonstrated as a powerful methodology for the high sensitivity selective detection of secondary phases in kesterite $Cu_2ZnSnS_4(Se_4)$ (CZTS(Se)) compounds and their alloys [26, 27]. The highest-performing kesterite devices are made from absorbers with nonstoichiometric Cu-poor (Cu/(Zn+Sn) < 1) and Zn-rich (Zn/Sn > 1) compositions, which favor formation of secondary phases such as ZnS(Se) or Sn–S(Se) compounds. Control in the occurrence of these phases is critical to achieve high-efficiency devices. Detection of these phases by XRD is strongly compromised by the strong overlapping of the main diffraction peaks from the different compounds of the Cu–Zn–Sn–S(Se) systems. Secondary phases that can be detected with resonant Raman scattering measurements in CZTS(Se) layers include ZnS (with 325 nm excitation wavelength), ZnSe (with 441 nm or 457 nm excitation wavelengths), Sn(S,Se) (with 785 nm excitation wavelength), and SnS_2 (with 514 excitation wavelength).

Furthermore, in many occasions the formation of secondary phases occurs primarily at the interface regions, which makes its detection by means of other techniques not necessarily straightforward. In relation to this aspect, we will consider now another example in which the high spatial resolution provided by micro-Raman spectroscopy allowed investigating the chemical characteristics of the interface of a photovoltaic absorber. Figure 17.7 shows a spectrum measured with a Raman microprobe with the laser spot directly focused on the cross section of a $CuInS_2$ film grown onto Mo-coated glass. The spectrum measured with the laser probe located on the region close to the $CuInS_2$/Mo interface shows the

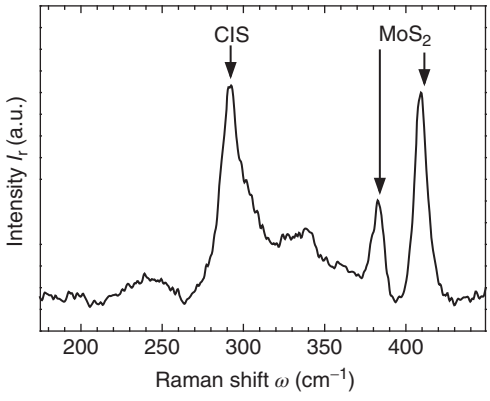

Figure 17.7 Cross-sectional Raman spectrum of a $CuInS_2$ film grown onto Mo-coated glass, revealing the formation of a MoS_2 phase at the $CuInS_2$/Mo interface.

presence of two bands at about 380 and 410 cm^{-1} that correspond to the main vibrational mode characteristic of the hexagonal structure of MoS_2 [28].

MoS_2 and $MoSe_2$ interfacial phases have been observed at the interface region between the Mo back contact and the absorber layer in chalcogenide-based solar cells (including both chalcopyrite $Cu(In,Ga)(S,Se)_2$ and kesterite $Cu_2ZnSn(S,Se)_4$ solar cells). The presence of such phases has a relevant effect on the characteristic of the devices, as they prevent the formation of a Schottky barrier at the back region of the cell. On the other hand, they might be also responsible in some cases for film adhesion failure [28–30].

Analysis of interfaces and of the distribution of crystalline phases in thin-film solar-cell materials can also be achieved by the use of Raman mapping experiments. Maps collected on cross-sectional samples of such materials reveal their layer structure and compositional changes across the layers. This has been applied for the analysis of $CuInS_2$/Mo samples prepared by the spray ion layer gas reaction (ILGAR) method [31], investigating the occurrence of the CuAu-ordered $CuInS_2$ polytype in the processed samples [19, 32]. In this crystal structure, cations form alternating Cu and In planes, similar to the copper–gold crystal structure. Occurrence of this phase in $CuInS_2$-based devices is favored by the fact that its formation energy is only about 2 meV per atom. The presence of this secondary phase has been recently reported as beneficial for high-efficiency devices, being related to the existence of a release of strain in the $CuInS_2$ absorbers [32].

17.5.2
Evaluation of Film Crystallinity

The crystalline quality of a photovoltaic absorber is important in order to ensure its adequate optoelectronic properties. The presence of crystalline defects may result in changes in the doping levels, density of states (DOS), and electronic transport properties. Crystalline defects embrace several modifications of the

crystalline lattice of the material, which result in the breakage of the symmetry of the crystal. Point defects, such as vacancies, interstitials, or antisites, are zero-dimensional defects affecting only ions in the lattice. Other crystalline defects, such as dislocations or grain interfaces, are physically extended over one or two dimensions in the space.

Some crystalline defects result in characteristic changes in the Raman spectrum. In particular, the introduction of impurities in a crystal often results in characteristic localized vibrational modes (LVM) that may be active by Raman. This is the case, for example, for N atomic impurities in GaAs lattice [33], which give rise to an LVM at about 475 cm^{-1}. Furthermore, the relative intensity of the LVM can be used to determine the impurity concentration in the host lattice. Usually, impurity concentrations above 1% are required in order to be able to resolve LVM.

Raman spectroscopy is also sensitive to lattice disorder. For example, variations in the cation arrangement in ternary tetrahedral compounds often result in additional Raman bands, which are often described as *disorder-activated modes*. In some cases, these bands arise from noncenter phonons which become active by the relaxation of the quasicrystalline momentum conservation law, caused by the breakage of the crystalline symmetry. In general, either point or extended defects can be responsible for such activation of noncenter phonons because of the breakage of the momentum conservation law. These effects determine a characteristic change in the shape of the main peaks in the spectra, with the appearance of a shoulder at the low- or high-frequency side that is due to the contribution of the modes at the vicinity of the center of the Brillouin zone [3–38]. The location of this contribution in relation to the frequency of the Raman peak is determined by the dispersion curves of the phonons involved in the process in the vicinity of the point where $q = 0$: In Si, this contribution appears at the low-frequency side of the Raman peak [36], while semiconductors as $CuInS_2$ and $CuInSe_2$ show this disorder-induced contribution at the high-frequency side of the main Raman mode [37]. Kesterite CZTS and CZTSe semiconductors show this disorder-induced contribution at the low-frequency side of the main Raman peaks, similar to the case of Si [38]. The resulting shape of the band can be modeled, assuming a correlation length model that is described in Section 17.5.4. Estimation of the correlation length allows obtaining a quantitative estimation of the degree of disorder in the crystals related to the presence of a high density of defects.

In some cases, Raman scattering can also be used to analyze the presence of specific defects. Introduction of point and extended defects can lead to changes in the chemical bonds among the atoms in the material that can be related to either the breakage of certain bonds or to the formation of new ones. This determines changes in the intensity of the corresponding peaks in the Raman spectra. An interesting example of these effects is described in Ref. [39], which reports the impact of the presence of different kinds of point defect clusters ($[Zn_{Cu}+V_{Cu}]$, $[2Zn_{Cu}+Zn_{Sn}]$, $[Cu_{Zn}+Sn_{Zn}]$) in the Raman spectra from $Cu_2ZnSnSe_4$.

Finally, the analysis of the Raman bandwidth provides an additional method to evaluate the density of defects in the material. The bandwidth of a Raman band

is inversely proportional to the phonon lifetime, which obviously depends on the density of defects that promote phonon scattering. Therefore, a thin-film material with a high density of defects is characterized by the increased width of their bands, with respect to the natural bandwidth of the defect-free crystal. In the case of chalcopyrite-type $CuInS_2$ and $CuInSe_2$ photovoltaic absorbers, the increased bandwidth of the A_1 Raman band has been confirmed to be correlated with a degradation of the film crystallinity, as corroborated by a comparative study using XRD and electron microscopy [29, 40]. Furthermore, a correlation between the FWHM of the A_1 band and photovoltaic parameters, such as the open-circuit voltage and the fill factor [41, 42], was found.

17.5.3
Chemical Analysis of Semiconducting Alloys

Alloying obviously leads to changes in the lattice dynamics of the crystal, which manifest in the Raman spectra. In the simplest case, alloying results in a gradual change of the force constants and effective mass that causes a Raman band to shift its frequency. Although it is not always the case, the shift of the Raman band is often linear with the degree of alloying. Even if it is not linear, the frequency of the Raman band can still be used to unambiguously determine the composition of the alloy. $Cu(In,Ga)Se_2$ and $Cu(In,Ga)S_2$ are representative examples of this mode behavior [43–45]. In these cases, the A_1 dominant band in the spectrum is observed to shift linearly from the reference position of the $CuInSe_2(S_2)$ compound ($CuInSe_2$, 173 cm^{-1}; $CuInS_2$, 290 cm^{-1}) to the frequency of the band at the $CuGaSe_2(S_2)$ crystal ($CuGaSe_2$, 183 cm^{-1}; $CuGaS_2$, 310 cm^{-1}). Nevertheless, in some cases, two bands instead of one single band are observed for a given vibrational mode. In such case, the alloy is said to present a *bimodal behavior* – in opposite to the previous *one-mode behavior.* A representative photovoltaic material presenting this behavior is $CuIn(S,Se)_2$. In this case, the A_1 band splits into two modes, which are referred to as *Se-like* and *S-like* bands, since they appear closer to the respective positions of the reference ternary compounds at 173 and 290 cm^{-1}, respectively [46]. Moreover, the dependence of the frequency of both modes with the degree of alloying is significantly different. While the *Se-like* mode is clearly affected by the variation of the Se/S ratio in the quaternary alloy, the *S-like* band is nearly unaffected by the change in the film stoichiometry. This can be seen in Figure 17.8, which corresponds to the plot of Raman spectra from S-rich alloys with different composition. The dependence of these modes on the degree of alloying has allowed the development of a simple methodology that has been proposed in [47] for the quantitative determination of the S/(S+Se) content ratio in $CuIn(S,Se)_2$ based on the analysis of their relative integral intensities. This methodology does not depend on the experimental conditions used for the measurement of the Raman spectra.

A more complex behavior has been reported in the case of the $Cu_2ZnSn(S,Se)_4$ (CZTSSe) solid solutions [48]. The Raman spectra from these samples show

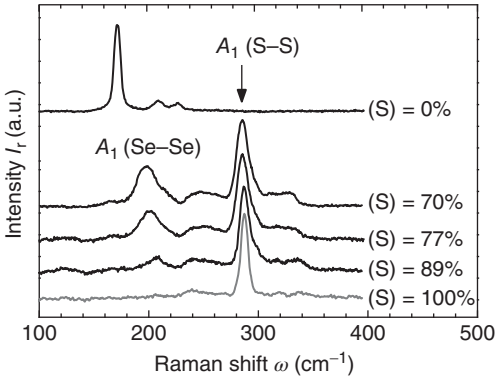

Figure 17.8 Raman spectrum from $CuIn(S,Se)_2$ alloys with different composition. For comparison, spectra from $CuInSe_2$ (top) and $CuInS_2$ (bottom) layers are also shown. Notice that the Se-like mode significantly shifts with the alloy composition, while the frequency of the S-like band remains nearly unaffected.

dominant CZTS-like peaks in the $280-400\,cm^{-1}$ frequency region (related to S vibrational modes), dominant CZTSe-like peaks in the $170-205\,cm^{-1}$ frequency region (related to Se vibrational modes), and additional peaks in the $205-280\,cm^{-1}$ frequency region that are related to vibrational modes involving both S and Se anions. A similar behavior with the appearance of additional Raman peaks has also been observed for the Si_xGe_{1-x} and $Cu(S_xSe_{1-x})$ solid solutions [49, 50]. In the case of CZTSSe, the analysis of the dependence of the integral intensity of the Raman bands sensitive to anion vibrations with the S/(S+Se) composition ratio has allowed to observe the existence of a simple linear relationship. The calibration of the fitting parameters used in this analysis provides a simple methodology for the quantitative measurement of the S/(S+Se) content ratio in the CZTSSe solid solution, as reported in [51]. As in the case of $CuIn(S,Se)_2$, this methodology does not depend on the experimental conditions used for the measurement of the Raman spectra.

These methodologies provide also an effective means of establishing a compositional mapping of the films and allow investigating the existence of in-depth resolved composition inhomogeneities. This can be done by Raman microprobe measurements performed with the laser probe focused at different positions from the cross section of the layers [52, 53]. Figure 17.9 shows an example of such measurements performed on a $CuIn(S,Se)_2$ layer synthesized with a gradual change in the S to Se content ratio [53]. In this figure, the spectra from the surface region are characterized by a dominant S-like mode which points out the existence of a S-rich surface region. Moving the laser spot toward the back region leads to a decrease of this peak and a corresponding increase of the Se-like mode, which correlates with the existence of a Se-rich alloy at the back region of the layer. In addition, the spectra measured close to the interface with the back Mo contact show the peaks characteristic of the interfacial $MoSe_2$ phase.

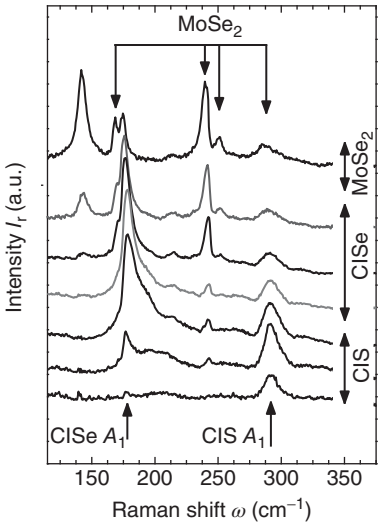

Figure 17.9 Micro-Raman spectra measured with the laser spot at different positions through the cross section of a $CuIn(S,Se)_2$ layer with graded composition on a Mo-coated glass substrate.

This kind of in-depth resolved measurements is of interest because in this case there is no need for a special preparation of the specimens before their observation.

Lateral resolution in these measurements is limited by optical diffraction, but by using high-N.A. objective lenses (even without immersion oil), resolutions of 300–400 nm in the visible spectral region are accessible. With an N.A. = 0.9 objective lens providing approximately 400 nm lateral resolution at 632.8 nm, gradual changes of the relative gallium concentration [Ga]/([Ga]+[In]) in a 2.2 μm thick $Cu(In,Ga)Se_2$ layer in a ZnO/CdS/$Cu(In,Ga)Se_2$/Mo layer stack could be determined [54]. A line scan with step sizes of approximately 80 nm – tentatively oversampling the diffraction-limited resolution – was performed across the absorber layer, and band shifts within approximately 2.5 cm^{-1} were observed for the A_1 mode of $Cu(In,Ga)Se_2$ due to compositional changes as described earlier.

Another option is the use of an Ar^+ ion beam for the selective sputtering of the layer to different depths [55]. This allows us to obtain a depth resolution of the order of 100 nm because of the high light absorption of these semiconductors. However, in this case, the choice of the sputter conditions requires special care in order to minimize the presence of damage-induced effects in the spectra.

Both methods, Raman mapping of cross sections and depth profiling by sputtering, resulted in Ga gradients of the same $Cu(In,Ga)Se_2$ samples, which are in good agreement with each other and agree well with the results of independent (mostly elemental analysis) methods [54].

17.5.4
Nanocrystalline and Amorphous Materials

In the previous sections we have restricted our discussion to the analysis of crystalline and polycrystalline materials. For practical purposes, a defect-free

nanocrystal with diameters above 100–200 nm may be regarded as an infinite crystal. This is due to the fact that the phonon frequency and Raman scattering cross section are mostly dependent on the short-range ordering of the crystal lattice, up to a few atomic neighbors. In this sense, it is worth to highlight that Raman spectroscopy is much more sensitive to the local environment of the atoms in the crystal than XRD techniques (Chapter 15). As discussed in Section 17.5.2, a remarkable consequence of this characteristic is the activation of LVM caused by the introduction of impurities in the lattice.

When the effective correlation length over which the material can be considered crystalline is further reduced over this limit (100–200 nm), spectral effects become measurable. In the case of nanocrystalline materials, the phonon correlation length may be physically limited by the size of the crystal itself, but more generally, it may be restricted by the presence of crystalline defects, resulting in a higher phonon scattering probability. When the phonon correlation length cannot longer be considered infinite, the breakage of the crystalline symmetry leads to a relaxation of the quasimomentum conservation law and the activation of noncenter phonon modes with $\vec{q} \neq 0$. As a result, the bandshape of the Raman bands is modified, resulting in an effective asymmetric broadening and shift with respect to the crystalline band. In this case, the modeling of the spectrum allows estimating the effective correlation band of the material, which, in the case of nanostructured films, can be associated with the grain size.

Phonon confinement effects in nanocrystalline Si have been extensively studied [34, 35]. Moreover, the Raman spectrum of nanocrystalline Si can be accurately modeled based on the simplifying assumption that the phonon dispersion curve can be described by a parabola. Then, the Raman bandshape of the Si band may be expressed according to the equation

$$I(\omega) \propto \int_0^{\frac{2\pi}{a_0}} \frac{e^{-\frac{q^2L^2}{8}} \cdot 4\pi q^2 \cdot dq}{[\omega - \omega(q)]^2 + \left[\frac{\Gamma_0}{2}\right]^2}, \tag{17.10}$$

which for any particular case allows extracting the correlation length (L) by fitting the experimental spectrum.

The validity of the correlation length model is conditioned by the assumption that the material has some degree of crystalline ordering. When the phonon correlation length is further reduced, additional considerations must be taken into account. In particular, when a solid material progressively loses its crystalline order, any phonon can contribute to inelastic light scattering. Therefore, the resulting spectrum is conditioned by the phonon DOS, which determines which interactions are more probable. In general, the spectra of amorphous materials are characterized by the presence of broadbands resembling the phonon DOS.

An important practical application of Raman spectroscopy in the field of photovoltaic materials deals with the determination of the amorphous fraction in Si thin films. This parameter has a significant importance from the technological point of view, since it affects the open-circuit voltage of the cell and, at the same

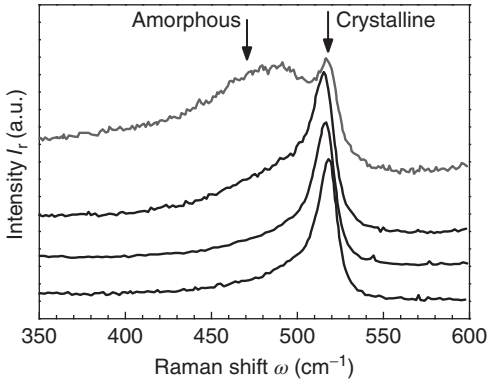

Figure 17.10 Raman spectra of Si films containing a mixture of amorphous and microcrystalline phases.

time, is strongly dependent on the film deposition conditions. Figure 17.10 shows characteristic Raman spectra from layers exhibiting a variable content of amorphous (a-Si) and microcrystalline (μc-Si) phases [36].

As may be appreciated in this figure, the presence of an a-Si phase in the films leads to a broadband in the region of 480 cm^{-1}, for which the Si phonon DOS has a maximum. The integral intensity of this band in relation to the intensity of the crystalline peak at 520 cm^{-1} provides a direct indication of the amorphous/microcrystalline ratio. Moreover, the following model may be used for quantification purposes:

$$\varphi_c = \frac{I_c}{I_c + \gamma I_a}, \tag{17.11}$$

where the parameter γ is an empirical constant, ϕ_c is the crystalline/amorphous fraction, and I_c and I_a are the intensity of the crystalline and amorphous bands.

17.5.5 Evaluation of Stress

In a crystalline material, the frequency of the Raman bands is a characteristic inherent to the crystalline structure and the chemical composition of the material. However, the phonon frequency may be modified by means of introducing an external force able to modify the internal energy of the crystal. When a mechanical stress is applied to a crystal, it results in microscopic atomic displacements, resulting in a net strain. Such strain modifies the interatomic distance and, consequently, the ionic and covalent bonding forces between neighbor atoms. This mechanism is responsible for the variation of the phonon frequency. In principle, even though one should take into account the tensor nature of stress and strain magnitudes, a compressive stress results in a reduction of the interatomic distance, increasing the interatomic forces, which leads to a positive (*blue*)shift of

the phonon frequency. When a tensile stress is applied, the phonon frequency is decreased (or *redshifted*).

The existence of stress in thin-film materials can be assessed by Raman spectroscopy by means of accurately determining the frequency of the Raman modes. In the case of crystalline Si and for a uniaxial or biaxial stress, the frequency shift can be related to the magnitude of the stress by the following expression [56]:

$$\sigma\ (\mathrm{MPa}) = -434\Delta\omega\ \ (\mathrm{cm}^{-1}). \tag{17.12}$$

Note that the magnitude of the Raman shift associated with typical stress values is in the range of 1 cm^{-1}. Therefore, the performance of these measurements requires a high-resolution spectrometer. Furthermore, special attention should be paid to the stabilization of the sample temperature and the avoidance of laser-induced local heating. In the case of Si, the magnitude of the thermally induced Raman shift of the band is in the range of 0.024 $\mathrm{cm}^{-1}\ \mathrm{K}^{-1}$, which leads to the fact that a local temperature increase of just 20 °C may lead to an error in the determination of the stress magnitude of about 210 MPa.

Just as other physicochemical properties of thin-film solar-cell materials described earlier, stress can also be used as contrast in Raman images. As an example, we show a Raman map collected on the surface of a polycrystalline $CuInSe_2$ layer. On an area of 25 μm × 25 μm (pixel size 200 nm, diffraction-limited resolution ~400 nm at 632.8 nm), changes in A_1 mode position of approximately 1 cm^{-1} were observed. Tanino *et al.* [57] and González *et al.* [58] investigated the relation between the A_1 mode Raman shift and applied pressure for this material, and both found a proportionality factor of approximately 5 $\mathrm{cm}^{-1}\ \mathrm{GPa}^{-1}$:

$$\Delta\omega\ (\mathrm{cm}^{-1}) = 5\sigma\ (\mathrm{GPa}). \tag{17.13}$$

The stress obtained by this equation can be converted into strain ε based on well-known Young's modulus E of this material [59]:

$$\varepsilon = \sigma/E = \sigma\ (\mathrm{GPa})/68.8\,\mathrm{GPa}. \tag{17.14}$$

According to these equations, the A_1 mode band positions in a Raman map were converted into stress, expressed in gigapascal. Here, all values were related to the average Raman shift observed in this experiment (arbitrarily set to 0), and thus, only relative changes of stress were calculated. That way, potential effects of differences in spectrometer calibration are excluded, which might significantly change the result of this conversion, which is based on functions determined by other authors using different instruments [57, 58]. Subsequently, stress values have been further converted into strain.

Figure 17.11a shows the optical micrograph of the polycrystalline $CuInSe_2$ surface, revealing that the boundaries between individual crystals are optically not visible. In Figure 17.11b the wavenumber positions of the A_1 mode of $CuInSe_2$ are plotted as a function of lateral coordinates and converted into stress and strain. As even the high-resolution spectrometer grating with 1800 grooves/mm used in this measurement leads to a resolution that is limited to approximately 0.3 cm^{-1}/CCD pixel in the investigated spectral range, the

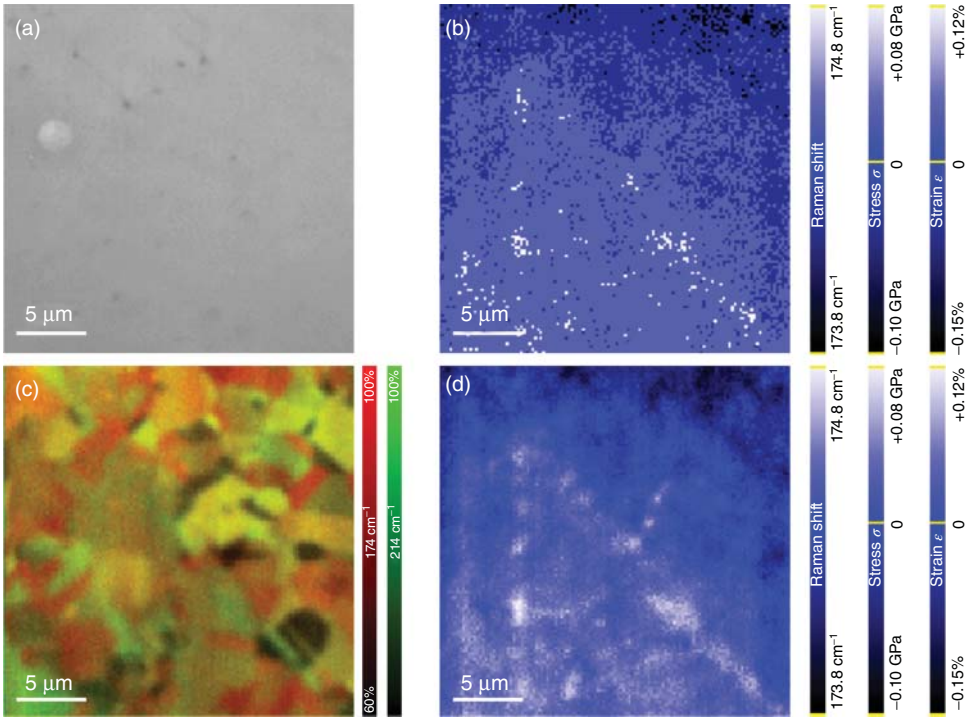

Figure 17.11 Raman map of a polycrystalline $CuInSe_2$ surface revealing stress, strain, and crystal orientations: (a) optical micrograph, (b) A_1 mode band positions and their conversion into stress and strain, (c) band intensities of A_1 and B_2 modes revealing individual crystals and their orientations, and (d) A_1 band positions, stress, and strain evaluated based on the peak positions of Gaussian functions fitted to all A_1 bands in the map.

observed changes within 1 cm^{-1} are resolved into only four steps. Becker *et al.* used the same instrument configuration and showed that fitting of Raman bands and using the peak positions of the fit functions improve the resolution down to approximately 0.05 cm^{-1} [60]. Gaussian fitting of the A_1 Raman modes in the map shown in Figure 17.11 leads to a clear improvement of resolution, as shown in Figure 17.11d. Comparison of Figure 17.11b and d reveals that only the resolution within the observed 1 cm^{-1} change is improved. Neither the wavenumber range is significantly changed by peak fitting, nor other artifacts are introduced by this data treatment method. A comparison of Raman microscopy with other methods for the determination of stress in $CuInSe_2$ has shown that all of them yield values in the same order of magnitude, even though comparison of different techniques is not straightforward, especially due to different spatial resolutions or measurement spot sizes, respectively [61]. Compared with other techniques, Raman microscopy combines the possibility of mapping relatively large areas of several hundreds of square micrometer with the submicrometer resolution that

is accessible with high-N.A. objective lenses. Furthermore, local changes of stress and strain can be directly related to crystal sizes, shapes, and even orientations, which can be derived from the same spectra and are thus determined on the exactly same sample spots, as described in the following section.

17.5.6
Evaluation of Crystal Orientations

As described previously, a step in the Raman process is the induction of a polarization field in a molecule or crystal. As typically linearly polarized lasers are used as excitation sources, the efficiency of this process as well as the spatial distribution of the induced field depends on the relative orientation of a molecule or crystal with respect to the polarization direction of the laser. Different vibrational modes are excited to a different extent depending on their individual orientations with relation to the exciting electric field. Therefore, the Raman bands of a material change their relative intensities as a function of relative orientation of the crystal under investigation. The Raman map of $CuInSe_2$ shown in Figure 17.11 clearly reveals this effect. Here, a laser with polarization direction parallel to the vertical axis of the map was used for excitation, and no polarization optics were placed in the detection path, that is, all collected polarization directions were detected simultaneously. The different efficiencies of excitation of the A_1 ($\sim$174 cm^{-1}, locally changing due to stress) and B_2 modes ($\sim$213 cm^{-1}, with contributions of an E mode) led to very significant changes in relative band intensities. The plot of these band intensities in Figure 17.11c in the form of a two-color map reveals all crystals of this polycrystalline material, which are not visible in a conventional microscopy image (Figure 17.11a). This was proofed by comparing Raman maps with electron backscatter diffraction (EBSD) maps of the exactly same areas of a $CuInSe_2$ sample [62]. In the same study, we showed that the behavior of relative band intensities for different polarization directions is in good agreement with theory and is specific for the actual crystal facet and orientation.

17.6
Conclusions

This chapter gives an overview of the capabilities of Raman spectroscopy for the advanced characterization of thin-film photovoltaic materials. The applicability of the technique for the microstructural and chemicophysical analysis of the films is illustrated by the description of state-of-the-art and recent examples that corroborate the potential of Raman scattering for these applications. This includes features related to the identification of crystalline structures and secondary phases, the evaluation of the film crystallinity and presence of defects, the measurement of the composition of semiconductor alloys, the quantification of the amorphous to microcrystalline fraction in partially amorphous films, and the analysis of stress and crystal orientations. Recent developments of Raman

microscopy-based techniques for the advanced lateral and in-depth resolved characterization of the films with high spatial resolution are also described. The relevant impact of all these features on the characteristics of the solar cells gives a strong interest to Raman spectroscopy not only for the fundamental characterization of the films but also as a nondestructive process monitoring tool applicable in a production line of thin-film cells and modules.

Acknowledgments

The authors are grateful to Tariq Jawhari and Lorenzo Calvo-Barrio from the Scientific and Technological Centers of the University of Barcelona (CCiTUB) as well as to Edgardo Saucedo and Xavier Fontané from IREC for fruitful discussions and suggestions. A. Pérez-Rodríguez and V. Izquierdo-Roca belong to the M-2E (Electronic Materials for Energy) Consolidated Research Group and the XaRMAE Network of Excellence on Materials for Energy of the "Generalitat de Catalunya." T. Schmid is grateful for the support of the Helmholtz Virtual Institute "Microstructure Control for Thin-Film Solar Cells" (VI-520 MiCo). P. Pistor acknowledge funding from the EU FP7 program under GA N° 625840 ("JUMPKEST")

References

1. Cardona, M. (1975) *Light Scattering in Solids*, vol. **I**, Springer-Verlag, Heidelberg, New York.
2. Ferraro, J.R., Nakamoto, K., and Brown, C.W. (2003) *Introductory Raman Spectroscopy*, 2nd edn, Academic Press.
3. Smith, E. and Dent, G. (2005) *Modern Raman Spectroscopy: A Practical Approach*, John Wiley & Sons.
4. Jawhari, T. (2000) Micro-Raman spectroscopy of the solid state: applications to semiconductors and thin films. *Analysis*, **28**, 15–21.
5. Yu, P. and Cardona, M. (1996) *Fundamentals on Semiconductors*, Springer, Berlin.
6. Zallen, R. and Slade, M.L. (1975) Interpolytype conversion and layer–layer coupling in PbI_2. *Solid State Commun.*, **17**, 1561–1566.
7. Paillard, V., Puech, P., Laguna, M.A., Temple-Boyer, P., Caussat, B., Couderc, J.P., and de Mauduit, B. (1998) Resonant Raman scattering in polycrystalline silicon thin films. *Appl. Phys. Lett.*, **73**, 1718–1720.
8. Opilik, L., Schmid, T., and Zenobi, R. (2013) Modern Raman imaging: vibrational spectroscopy on the micrometer and nanometer scales. *Annu. Rev. Anal. Chem.*, **6**, 379–398.
9. Zhao, J. (2006) Raman spectroscope. US Patent 7,102,746.
10. Bennett, R., Day, J.C.C., Meaden, G.M. (2006) Spectroscopy apparatus and method. US Patent 7,139,071.
11. Abbe, E. (1873) Beitraege zur theorie des mikroskops und der mikroskopischen wahrnehmung. *Arch. Mikrosk. Anat.*, **9**, 413–468.
12. Rayleigh, L. (1879) Investigations in optics, with special reference to the spectroscope. *Philos. Mag.*, **8**, 261–274.
13. Stadler, J., Stanciu, C., Stupperich, C., and Meixner, A.J. (2008) Tighter focusing with a parabolic mirror. *Opt. Lett.*, **83**, 681–683.
14. Everall, N.J. (2009) Confocal Raman microscopy: performance, pitfalls, and best practice. *Appl. Spectrosc.*, **63**, A245–A262.

15. Theodoropoulou, S., Papadimitriou, D., Anestou, K., Cobet, C., and Esser, N. (2009) Optical properties of $CuIn_{1-x}Ga_xSe_2$ quaternary alloys for solar-energy conversion. *Semicond. Sci. Technol.*, **24**, 015014-1–015014-8.
16. Schmid, T., Opilik, L., Blum, C., and Zenobi, R. (2013) Nanoscale chemical imaging using tip-enhanced Raman spectroscopy: a critical review. *Angew. Chem. Int. Ed.*, **52**, 5940–5954.
17. Zhang, D., Wang, X., Braun, K., Egelhaaf, H.J., Fleischer, M., Hennemann, L., Hintz, H., Stanciu, C., Brabec, C.J., Kern, D.P., and Meixner, A.J. (2009) Parabolic mirror-assisted tip-enhanced spectroscopic imaging for non-transparent materials. *J. Raman Spectrosc.*, **40**, 1371–1376.
18. Wang, X., Zhang, D., Braun, K., Egelhaaf, H.J., Brabec, C.J., and Meixner, A.J. (2010) High-resolution spectroscopic mapping of the chemical contrast from nanometer domains in P3HT:PCBM organic blend films for solar cell applications. *Adv. Funct. Mater.*, **20**, 492–499.
19. Álvarez-García, J., Barcones, B., Pérez-Rodríguez, A., Romano-Rodríguez, A., Morante, J.R., Janotti, A., and Wei, S.-H. (2005) Vibrational and crystalline properties of polymorphic $CuInC_2$ (C=Se,S) chalcogenides. *Phys. Rev. B: Condens. Matter Mater. Phys.*, **71**, 054303-1–054303-9.
20. Rincón, C. and Ramírez, F.J. (1992) Lattice vibrations of $CuInSe_2$ and $CuGaSe_2$ by Raman microspectrometry. *J. Appl. Phys.*, **72**, 4321–4324.
21. Lincot, D., Guillemoles, J.F., Taunier, S., Guimard, D., Sicx-Kurdi, J., Chaumont, A., Roussel, O., Ramdani, O., Hubert, C., Fauvarque, J.P., Bodereau, N., Parissi, L., Panheleux, P., Fanouillere, P., Naghavi, N., Grand, P.P., Benfarah, M., Mogensen, P., and Kerrec, O. (2004) Chalcopyrite thin film solar cells by electrodeposition. *Sol. Energy*, **77**, 725–737.
22. Izquierdo-Roca, V., Saucedo, E., Ruiz, C.M., Fontané, X., Calvo-Barrio, L., Álvarez-García, J., Grand, P.-P., Jaime-Ferrer, J.S., Pérez-Rodríguez, A., Morante, J.R., and Bermúdez, V. (2009) Raman scattering and structural analysis of electrodeposited $CuInSe_2$ and S-rich quaternary $CuIn(S,Se)_2$ semiconductors for solar cells. *Phys. Status Solidi A*, **206**, 1001–1004.
23. Xu, C.-M., Xu, X.-L., Xu, J., Yang, X.-J., Zuo, J., Kong, N., Huang, W.-H., and Liu, H.-T. (2004) Composition dependence of the Raman A_1 mode and additional mode in tetragonal Cu–In–Se thin films. *Semicond. Sci. Technol.*, **19**, 1201–1206.
24. Insignares-Cuello, C., Broussillou, C., Bermúdez, V., Saucedo, E., Pérez-Rodríguez, A., and Izquierdo-Roca, V. (2014) Raman scattering analysis of electrodeposited $Cu(In,Ga)Se_2$ solar cells: impact of ordered vacancy compounds on cell efficiency. *Appl. Phys. Lett.*, **105**, 021905-1–021905-4.
25. Rai, B.K., Bist, H.D., Katiyar, R.S., Chen, K.-T., and Burger, A. (1996) Controlled micro oxidation of CdTe surface by laser irradiation: a micro-spectroscopy study. *J. Appl. Phys.*, **80**, 477–481.
26. Fontané, X., Calvo-Barrio, L., Izquierdo-Roca, V., Saucedo, A., Pérez-Rodríguez, A., Morante, J.R., Berg, D.M., Dale, P.J., and Siebentritt, S. (2011) In-depth resolved Raman scattering analysis for the identification of secondary phases: characterization of Cu_2ZnSnS_4 layers for solar cell applications. *Appl. Phys. Lett.*, **98**, 181905.
27. López-Marino, S., Sánchez, Y., Placidi, M., Fairbrother, A., Espindola-Rodríguez, M., Fontané, X., Izquierdo-Roca, V., López-Garcá, J., Calvo-Barrio, L., Pérez-Rodríguez, A., and Saucedo, E. (2013) ZnSe etching of Zn-rich $Cu_2ZnSnSe_4$: an oxidation route for improved solar-cell efficiency. *Chem. Eur. J.*, **19**, 14814–14822.
28. Álvarez-García, J., Pérez-Rodríguez, A., Romano-Rodríguez, A., Morante, J.R., Calvo-Barrio, L., Scheer, R., and Klenk, R. (2001) Microstructure and secondary phases in coevaporated $CuInS_2$ films: dependence on growth temperature and chemical composition. *J. Vac. Sci. Technol., A*, **19**, 232–239.
29. Kohara, N., Nishiwaki, S., Hashimoto, Y., Negami, T., and Wada, T. (2001) Electrical properties of the

Cu(In,Ga)Se_2/$MoSe_2$/Mo structure. *Sol. Energy Mater. Sol. Cells*, **67**, 209–215.

30. Abou-Ras, D., Kostorz, G., Bremaud, D., Kälin, M., Kurdesau, F.V., Tiwari, A.N., and Döbeli, M. (2005) Formation and characterisation of $MoSe_2$ for Cu(In,Ga)Se_2 based solar cells. *Thin Solid Films*, **480–481**, 433–438.
31. Schmid, T., Camus, C., Lehmann, S., Abou-Ras, D., Fischer, C.-H., Lux-Steiner, M.C., and Zenobi, R. (2009) Spatially resolved characterization of chemical species and crystal structures in $CuInS_2$ and $CuGa_xSe_y$ thin films using Raman microscopy. *Phys. Status Solidi A*, **206**, 1013–1016.
32. Moreau, A., Insignares-Cuello, C., Escoubas, L., Simona, J., Bermúdez, V., Pérez-Rodríguez, A., Izquierdo-Roca, V., and Ruiz, C. (2015) Impact of Cu–Au type domains in high current density $CuInS_2$ solar cells. *Sol. Energy Mater. Sol. Cells*, **139**, 101–107.
33. Panpech, P., Vijarnwannaluk, S., Sanorpim, S., Ono, W., Nakajima, F., Katayama, R., and Onabe, K. (2007) Correlation between Raman intensity of the N-related local vibrational mode and N content in GaAsN strained layers grown by MOVPE. *J. Cryst. Growth*, **298**, 107–110.
34. Fauchet, P.M. and Campbell, I.H. (1988) Raman spectroscopy of low-dimensional semiconductors. *Crit. Rev. Solid State Mater. Sci.*, **14**, S79–S101.
35. Gouadec, G. and Colomban, P. (2007) Raman spectroscopy of nanomaterials: how spectra relate to disorder, particle size and mechanical properties. *Prog. Cryst. Growth Charact. Mater.*, **53**, 1–56.
36. Garrido, B., Pérez-Rodríguez, A., Morante, J.R., Achiq, A., Gourbilleau, F., Madelon, R., and Rizk, R. (1998) Structural, optical and electrical properties of nanocrystalline silicon films deposited by hydrogen plasma sputtering. *J. Vac. Sci. Technol., B*, **16**, 1851–1859.
37. Camus, C., Rudigier, E., Abou-Ras, D., Allsop, N.A., Unold, T., Tomm, Y., Schorr, S., Gledhill, S.E., Köhler, T., Klaer, J., Lux-Steiner, M.C., and Fischer, C.-H. (2008) Phonon confinement and strain in $CuInS_2$. *Appl. Phys. Lett.*, **92**, 101922-1–101922-3.
38. Dimitrievska, M., Fairbrother, A., Pérez-Rodríguez, A., Saucedo, E., and Izquierdo-Roca, V. (2014) Raman scattering crystalline assessment of polycrystalline Cu_2ZnSnS_4 thin films for sustainable photovoltaic technologies: phonon confinement model. *Acta Mater.*, **70**, 272–280.
39. Dimitrievska, M., Fairbrother, A., Saucedo, E., Pérez-Rodríguez, A., and Izquierdo-Roca, V. (2015) Influence of compositionally induced defects on the vibrational properties of device grade $Cu_2ZnSnSe_4$ absorbers for kesterite based solar cells. *Appl. Phys. Lett.*, **106**, 073903.
40. Izquierdo-Roca, V., Pérez-Rodríguez, A., Morante, J.R., Álvarez-García, J., Calvo-Barrio, L., Bermudez, V., Grand, P.P., Parissi, L., Broussillon, C., and Kerrec, O. (2008) Analysis of S-rich $CuIn(S,Se)_2$ layers for photovoltaic applications: influence of the sulfurisation temperature on the crystalline properties of electrodeposited and sulfurised $CuInSe_2$ precursors. *J. Appl. Phys.*, **103**, 123109-1–123109-7.
41. Rudigier, E., Enzenhofer, T., and Scheer, R. (2005) Determination of the quality of $CuInS_2$-based solar cells combining Raman and photoluminescence spectroscopy. *Thin Solid Films*, **480–481**, 327–331.
42. Izquierdo, V., Pérez-Rodríguez, A., Calvo-Barrio, L., Álvarez-García, J., Morante, J.R., Bermudez, V., Ramdani, O., Kurdi, J., Grand, P.P., Parissi, L., and Kerrec, O. (2008) Raman scattering microcrystalline assessment and device quality control of electrodeposited $CuIn(S,Se)_2$ based solar cells. *Thin Solid Films*, **516**, 7021–7025.
43. Tanino, H., Deai, H., and Nakanishi, H. (1993) Raman spectra of $CuGa_xIn_{1-x}Se_2$. *Jpn. J. Appl. Phys., Part 1*, **32** (3 suppl), 436–438.
44. Papadimitriou, D., Esser, N., and Xue, C. (2005) Structural properties of chalcopyrite thin films studied by Raman spectroscopy. *Phys. Status Solidi B*, **242**, 2633–2643.
45. Álvarez-García, J. (2002) *Characterisation of $CuInS_2$ Films for Solar Cell Applications by Raman spectroscopy*,

University of Barcelona, http://www.tdx.cesca.es/TDX-0122103-094011/index.html.

46. Bacewicz, R., Gebicki, W., and Filipowicz, J. (1994) Raman scattering in $CuInS_{2x}Se_{2(1-x)}$ mixed crystals. *J. Phys. Condens. Matter*, **6**, L777–L780.
47. Insignares-Cuello, C., Oliva, F., Neuschitzer, M., Fontané, X., Broussillou, C., Goislard de Monsabert, T., Saucedo, E., Ruiz, C.M., Pérez-Rodríguez, A., and Izquierdo-Roca, V. (2015) Advanced characterization of electrodeposition-based high efficiency solar cells: non-destructive Raman scattering quantitative assessment of the anion chemical composition in $Cu(In,Ga)(S,Se)_2$ absorbers. *Sol. Energy Mater. Sol. Cells*, **143**, 212–217.
48. Dimitrievska, M., Xie, H., Fairbrother, A., Fontané, X., Gurieva, G., Saucedo, E., Pérez-Rodríguez, A., Schorr, S., and Izquierdo-Roca, V. (2014) Multiwavelength excitation Raman scattering of $Cu_2ZnSn(S_xSe_{1-x})_4$ $(0 \leq x \leq 1)$ polycrystalline thin films: vibrational properties of sulfoselenide solid solutions. *Appl. Phys. Lett.*, **105**, 031913.
49. Pagès, O., Souhabi, J., Torres, V.J.B., Postnikov, A.V., and Rustagi, K.C. (2012) Re-examination of the SiGe Raman spectra: percolation/one-dimensional-cluster scheme and ab initio calculations. *Phys. Rev. B: Condens. Matter Mater. Phys.*, **86** 045201.
50. Ishii, M., Shibata, K., and Nozaki, H. (1993) Anion distributions and phase transitions in $CuS_{1-x}Se_x$ $(x = 0–1)$ studied by Raman spectroscopy. *J. Solid State Chem.*, **105**, 504–511.
51. Dimitrievska, M., Gurieva, G., Xie, H., Carrete, A., Cabot, A., Saucedo, E., Pérez-Rodríguez, A., Schorr, S., and Izquierdo-Roca, V. (2015) Raman scattering quantitative analysis of the anion chemical composition in kesterite $Cu_2ZnSn(S_xSe_{1-x})_4$ solid solutions. *J. Alloys Compd.*, **628**, 464–470.
52. Takei, R., Tanino, H., Chichibu, S., and Nakanishi, H. (1996) Depth profiles of spatially-resolved Raman spectra of a CuInSe-based thin-film solar cell. *J. Appl. Phys.*, **79**, 2793–2795.
53. Izquierdo-Roca, V., Fontané, X., Álvarez-García, J., Calvo-Barrio, L., Pérez-Rodríguez, A., Morante, J.R., Ruiz, C.M., Saucedo, E., and Bermúdez, V. (2009) Electrochemical Synthesis of $CuIn(S,Se)_2$ alloys with graded composition for high efficiency solar cells. *Appl. Phys. Lett.*, **94**, 061915-1–061915-3.
54. Abou-Ras, D., Caballero, R., Fischer, C.H., Kaufmann, C.A., Lauermann, I., Mainz, R., Mönig, H., Schöpke, A., Stephan, C., Streeck, C., Schorr, S., Eicke, A., Döbeli, M., Gade, B., Hinrichs, J., Nunney, T., Dijkstra, H., Hoffmann, V., Klemm, D., Efimova, V., Bergmaier, A., Dollinger, G., Wirth, T., Unger, W., Rockett, A.A., Perez-Rodriguez, A., Alvarez-Garcia, J., Izquierdo-Roca, V., Schmid, T., Choi, P.P., Müller, M., Bertram, F., Christen, J., Khatri, H., Collins, R.W., Marsillac, S., and Kötschau, I. (2011) Comprehensive comparison of various techniques for the analysis of elemental distributions in thin films. *Microsc. Microanal.*, **17**, 728–751.
55. Fontané, X., Izquierdo-Roca, V., Calvo-Barrio, L., Pérez-Rodríguez, A., Morante, J.R., Guettler, D., Eicke, A., and Tiwari, A.N. (2009) Investigation of compositional inhomogeneities in complex polycrystalline $Cu(In,Ga)Se_2$ layers for solar cells. *Appl. Phys. Lett.*, **95**, 261912-1–261912-3.
56. Wu, X., Yu, J., Ren, T., and Liu, L. (2007) Micro-Raman spectroscopy measurement of stress in silicon. *Microelectron. J.*, **38**, 87–90.
57. Tanino, H., Maeda, T., Fujikake, H., Nakanishi, H., Endo, S., and Irie, T. (1992) Raman spectra of $CuInSe_2$. *Phys. Rev. B: Condens. Matter Mater. Phys.*, **45**, 13323–13330.
58. González, J., Quintero, M., and Rincón, C. (1992) Pressure dependence of the Raman A1 mode and pressure-induced phase transition in $CuInSe_2$. *Phys. Rev. B: Condens. Matter Mater. Phys.*, **45**, 7022–7025.
59. Berger, L.I. (1997) *Semiconductor Materials*, CRC Press.
60. Becker, M., Scheel, H., Christiansen, S., and Strunk, H.P. (2007) Grain orientation, texture, and internal stress optically

evaluated by micro-Raman spectroscopy. *J. Appl. Phys.*, **101**, 063531.

61. Schäfer, N., Wilkinson, A.J., Schmid, T., Schulli, T., Chahine, G.A., Marquardt, J., Schorr, S., Winkelmann, A., Klaus, M., Genzel, C., Rissom, T. and Abou-Ras, D. (2015) Assessing strain distributions in $CuInSe_2$ thin films by electron backscatter diffraction, X-ray diffraction, and Raman microscopy, submitted for publication.
62. Schmid, T., Schäfer, N., Levcenco, S., Rissom, T., and Abou-Ras, D. (2015) Orientation-distribution mapping of polycrystalline materials by Raman microspectroscopy. *Sci. Rep.*, **5**, 18410.

18
Soft X-ray and Electron Spectroscopy: A Unique "Tool Chest" to Characterize the Chemical and Electronic Properties of Surfaces and Interfaces

Marcus Bär, Lothar Weinhardt, and Clemens Heske

18.1
Introduction

In view of the complexity of thin-film solar cells, which are composed of a multitude of layers, interfaces, surfaces, elements, impurities, and so on, it is critically important to characterize and understand the chemical and electronic properties of these components. As a first step, systems (that have generally been *empirically* optimized) need to be characterized, and a detailed understanding of the inner workings and limitations (optimization barriers) need to be achieved. In a second step, concepts and process modifications to overcome the barriers need to be developed and implemented, and the results obtained in the first step form the experimental basis to help in such "brainstorming" processes. In step three, finally, the characterization approaches will need to ascertain whether the implemented process modifications were successful and whether, from a chemical and electronic perspective, the modifications indeed modified the targeted aspects of the chemical and electronic structure derived in the first step.

To fulfill such demands, a combination of various techniques, illuminating different aspects of the electronic and chemical structure, needs to be employed. It is the purpose of the present chapter to discuss and demonstrate the power of a "tool chest" comprised of soft X-ray and electron spectroscopies to illuminate the electronic and chemical properties from a variety of different perspectives. These techniques are in part very old (in fact, almost as old as the initial discovery of X-rays by W.C. Röntgen in 1895) and in part brand new, with the up-to-date most comprehensive approach to study the electronic bulk structure of a material (the so-called RIXS map approach [1–5]) being developed in the late 2000s.

The techniques in the tool chest require unique experimental environments. Some of them can be performed in ultrahigh vacuum surface science systems in a single-investigator laboratory; others require high-brightness X-ray radiation from a third-generation synchrotron radiation source. These techniques need to be coupled with optimally selected sample series: either custom designed to address a specific question, from a world-record (or lab-record) batch to establish a benchmark picture, taken directly from industrial preparation processes to shed

Advanced Characterization Techniques for Thin Film Solar Cells, Second Edition.
Edited by Daniel Abou-Ras, Thomas Kirchartz, and Uwe Rau.

light on the peculiarities of the "real-world" systems, or, simply, from failed cells to investigate failure mechanisms (e.g., after prolonged stress testing). The answers that can be derived from the spectroscopic results will be as good as the questions that are being asked, and thus experiment planning is a further central component to a successful approach to study, understand, and optimize the chemical and electronic structure of materials, surfaces, and interfaces for thin-film solar cells.

The chapter is arranged as follows: Section 18.2 will describe the here-demonstrated characterization techniques of the "soft X-ray and electron spectroscopy tool chest", together with two short examples on band gap determination and the RIXS map approach. In Section 18.3, a detailed example will be given that demonstrates the unique capabilities of the tool chest for characterizing the *chemical* properties of surfaces in thin-film solar cell devices. Section 18.4 describes examples of *electronic* interface structure investigations, and Section 18.5 summarizes the main messages of the present chapter.

18.2 Characterization Techniques

When a soft (ca. 50–1500 eV) X-ray photon impinges on a material surface, it interacts with the sample by exciting an electron from an occupied to an unoccupied electronic state. Numerous secondary electronic processes can follow, including the excitation of secondary electrons by inelastic scattering of the initially excited electron and the relaxation of electrons with lower binding energy into the hole created by the initial excitation. The energy gained in the latter process can be used to emit a secondary photon or electron, which in turn can undergo inelastic scattering to produce further secondary electrons and/or photons. Additional processes occur when the sample is exposed to electrons (as opposed to photons), giving rise to a similar (but different) cascade of secondary processes. The spectroscopic techniques discussed in this chapter make use of these cascades of events in various different ways.

Figure 18.1 presents an overview of the various spectroscopic techniques that probe specific aspects of the interaction cascade. Table 18.1 lists the techniques together with the corresponding depth sensitivity and the probed electronic states. In photoelectron spectroscopy (PES [6]), the kinetic energy of the originally excited electron is probed. A typical PES spectrum thus records the number (intensity) of emitted electrons as a function of kinetic energy E_{kin}, which is then conveniently converted into a "binding energy" E_{B} scale by using Einstein's well-known equation (all energies related to the Fermi energy):

$$E_{\mathrm{kin}} = h\upsilon - E_{\mathrm{B}} \tag{18.1}$$

When excited with soft X-rays from a lab source, PES is generally denoted as "**XPS**," while UV excitation gives spectra denoted as "**UPS**" spectra. Due to the short inelastic mean free path (IMFP) of electrons [7, 8] at kinetic energies attainable with soft X-ray excitation, PES spectra give a surface-sensitive view of

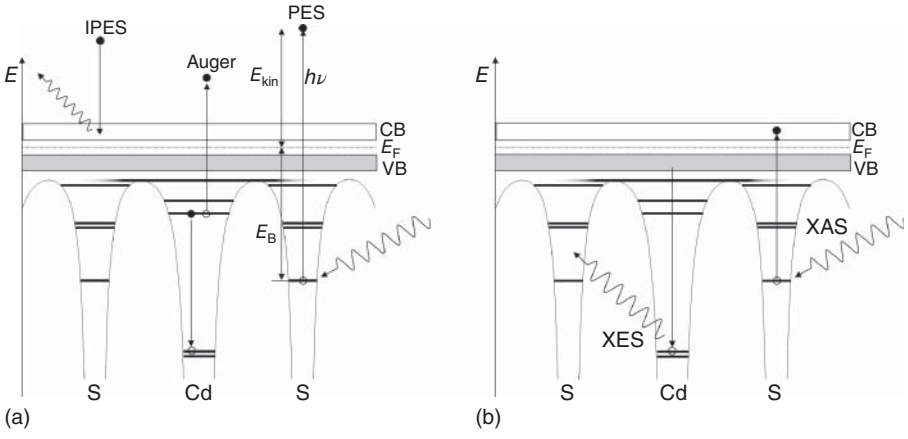

Figure 18.1 Schematic energy diagram of CdS, illustrating the various electron ((a) "PES", "IPES", and "Auger") and X-ray ((b) "XES" and "XAS") spectroscopies discussed in this chapter. For definition of the abbreviations, see text.

the occupied core level (CV) and valence level states present at the surface of the sample. This, in turn, gives detailed insights into the electronic structure (e.g., the band structure of the valence band) and the chemical properties (e.g., the local chemical environment of a specific atomic species, giving rise to a distinct binding energy).

As PES, X-ray emission spectroscopy (XES) probes the *occupied* states and hence can be used to investigate the chemical and electronic structure of samples. For XES, a core-level electron is excited by (soft) X-ray photons. The created core hole is filled by a lower binding energy (most often valence) electron, causing the emission of a photon, which is detected by a wavelength-dispersive X-ray spectrometer. The probability for this process (compared with that of, e.g., direct PES) is very small, demanding the experiments to be performed at high-brightness synchrotron radiation sources. Because the radiative relaxation process involves a localized core hole, XES is an excellent tool to probe the *local* structure near select atomic species. In contrast to PES, XES is a photon-in-photon-out (PIPO) technique, and thus the information depth is determined by the $1/e$-attenuation length of soft X-rays in matter [9], which is material-dependent and roughly two orders of magnitude larger than the IMFP in PES. Consequently, XES probes the near-surface *bulk* of the sample with typical attenuation lengths of 20–200 nm.

The overwhelming majority of the core holes created by the initial excitation process (giving rise to PES) are filled by Auger transitions, as sketched in the center of the scheme in Figure 18.1a. In the Auger process (here denoted as XAES for "X-ray-excited Auger electron spectroscopy"), a characteristic electron is emitted that reveals atom-specific information about the chemical state of the emitting atom, as in the case of PES in a surface-sensitive fashion. Due to different initial and final states involved in the Auger process as compared with the PES process, the chemical sensitivity is complementary to that of the PES process.

Table 18.1 Overview of the spectroscopic methods in the "soft X-ray and electron spectroscopy tool chest".

Measurement technique		Excited by	Detection of	Depth sensitivity	Probed electronic states
UPS	UV photoelectron spectroscopy	UV photons	Electrons	Surface	Occupied valence levels
XPS	X-ray photoelectron spectroscopy	X-ray photons	Electrons	Surface	Core levels
IPES	Inverse photoelectron spectroscopy	Electrons	UV photons	Surface	Unoccupied valence levels
XAES	X-ray-excited Auger electron spectroscopy	X-ray photons	Electrons	Surface	Occupied valence levels and core levels
XES	X-ray emission spectroscopy	X-ray photons	X-ray photonsSample currentAuger electrons	Near-surface bulk Surface	Occupied valence levels and core levels
XAS	X-ray absorption spectroscopy	X-ray photons	X-ray photonsSample currentAuger electrons	Near-surface bulk Surface Surface	Unoccupied valence levels and core levels
RIXS	Resonant inelastic X-ray scattering	X-ray photons	X-ray photons	Near-surface bulk	Occupied and unoccupied valence levels and core levels
UV–Vis		UV–visible photons	UV–visible photons	Bulk	Occupied and unoccupied valence levels

Auger transitions are generally named according to the principal quantum numbers of the three involved electronic levels. For example, sodium Auger transitions that involve a 1s core hole and 2p electrons for the relaxing and emitting electrons, respectively, are denoted as "Na KLL." For a complete description of the nomenclature, see Ref. [10].

While PES, XES, and XAES probe occupied electronic states, X-ray absorption spectroscopy (XAS [11]) and inverse photoemission spectroscopy(IPES) [12] investigate *unoccupied* electronic states. XAS is an element-specific technique, sensitive to the bonding environment and geometry. It involves the excitation of a core electron into an unoccupied state of the conduction band. For this, the

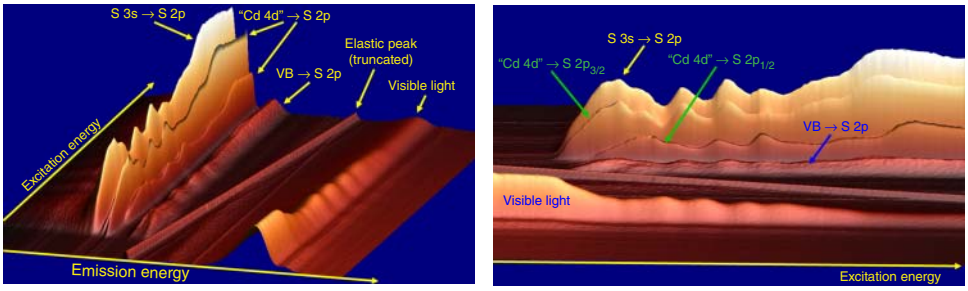

Figure 18.2 RIXS map of CdS. XES spectra are represented along the "emission energy" (detection energy) axis, while XAS spectra are represented along the "excitation energy" (beamline energy) axis. The peak heights correspond to photon intensity, as recorded by a soft X-ray spectrometer. All labels pertain to the relaxation transitions in CdS, giving rise to photon emission (the "visible light" line is due to visible fluorescence from the sample).

excitation energy is scanned across the absorption edge of the investigated core level, and secondary processes such as soft X-ray fluorescence due to radiative decay (fluorescence yield, (FY)), the current drawn by the sample to maintain charge neutrality (total electron yield, (TEY)), the number of electrons emitted above a certain threshold (partial electron yield, (PEY)), or the number of Auger electrons emitted in the corresponding Auger emission process (Auger electron yield AEY) are used as detection channels. The information depth of XAS is determined by the detection mode (yield) and varies from bulk sensitivity to surface sensitivity in the order given earlier. If an entire XES spectrum is recorded for each (or a select number of) point(s) in an XAS spectrum near the absorption edge, the combination of XAS and XES is referred to as "resonant inelastic (soft) X-ray scattering" (RIXS). A RIXS map, as shown in Figure 18.2 for CdS, thus gives the most complete spectroscopic information about both the occupied and unoccupied electronic states. RIXS can be used to "test" calculated band structures [13–15].

In IPES, a slow electron is directed at the surface, and a UV photon that stems from the electronic relaxation into a lower unoccupied electronic state is detected. By scanning the initial electron energy and detecting UV photons of a fixed photon energy, information on the conduction band (including, in particular, the position of the conduction-band minimum (CBM) with respect to the Fermi energy) can be obtained. Alternatively, the electron energy can be kept constant, and the detected photon energy is varied using a grating spectrometer.

In combining PES and IPES, or XES and XAS, the band gap of the surface (PES/IPES) or near-surface bulk (XES/XAS) of the sample can be determined. Such data can be complemented by optical (UV–Vis) absorption, which gives insight into the bulk band gap energy of the material. Apart from the differences in depth sensitivity, this band gap information also may include additional aspects. For example, the PES/IPES band edge positions can be given with respect to the Fermi energy, while this is not the case for XES/XAS and UV–Vis (because these approaches measure the energetic *difference* between two electronic states

without relation to the Fermi energy). In XES/XAS, in contrast, the band gap is derived near the atoms of a specific species (due to the involvement of a core level), while PES/IPES and UV–Vis are not element-specific. An example for a band gap determination with these techniques is given in Figure 18.3, which illustrates the band gap widening of chalcopyrite $Cu(In,Ga)(S,Se)_2$ thin-film

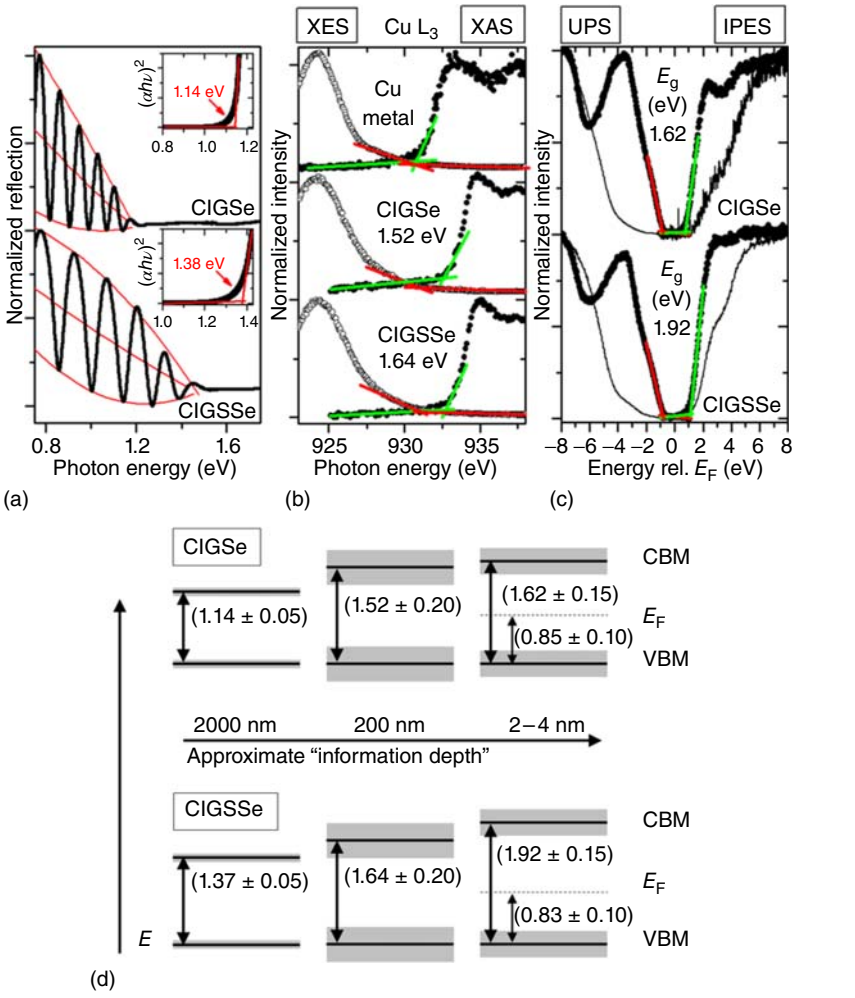

Figure 18.3 (a): Optical (UV–Vis) reflection spectra of $Cu(In,Ga)Se_2$ (CIGSe) and $Cu(In,Ga)(S,Se)_2$ (CIGSSe) thin films. Insets: E_g determination (±0.05 eV) using an approximated absorption coefficient. (b): Cu L_3 XES (left) and XAS (right) spectra of CIGSe, CIGSSe samples, and metallic Cu. The lower bound for the ground-state band-gap values are determined by linear extrapolation of the leading edges (±0.20 eV). (c): UPS (left) and IPES (right) for the as-introduced (thin solid lines) and cleaned samples (dots). Band-gap error bars are ±0.15 eV. (d): Schematic representation of the derived band gaps as a function of the approximate experimental information depth (keeping in mind the exponentially decaying information profile of the various experimental techniques). (Reproduced with permission from Bär [16] of American Institute of Physics.)

solar-cell absorbers toward the surface [17, 18], as seen in the band-gap energy progression as the experimental techniques become more surface sensitive.

It should be noted that none of these techniques (or, for that matter, *any* experimental technique) exclusively probe(s) the ground state of the system. Rather, any experimental probe will influence the system, in our case, by measuring the transition probability between an initial state and a final state under the influence of a quantum mechanical operator (Fermi's golden rule) that describes the photon field (for PES, XES, XAS, UV – Vis, and IPES), the Coulomb interaction (for Auger transitions), or the two-photon processes (described by the Kramers – Heisenberg formalism for RIXS). While the ground state might be involved as the initial state (only for PES and RIXS), this is not the case in general. Even more importantly, it is not directly evident how the best approximation of the initial state can be obtained, especially in the presence of core (XES, XAS, RIXS) or valence (UV – Vis) excitons, but a variety of "best-practice" approaches have been established. These include the use of extrapolation of spectral leading edges [19 – 21] and direct comparison with theoretically derived spectra [1, 14, 22] (i.e., using Fermi's golden rule or the Kramers – Heisenberg formalism).

In the following two sections, the here-described techniques will be put to work. In Section 18.3, we will use the example of wet chemical treatments of chalcopyrite thin-film solar-cell absorbers to demonstrate the chemical sensitivity of the characterization techniques. In Section 18.4, we will discuss determinations of the electronic structure at thin-film solar-cell interfaces.

18.3
Probing the Chemical Surface Structure: Impact of Wet Chemical Treatments on Thin-Film Solar Cell Absorbers

In this section, the prominent example of wet chemical treatments of chalcopyrite thin-film solar-cell absorbers will be used to demonstrate the capabilities of combining PES (here: XPS), XAES, and XES to reveal treatment-induced modifications of the chemical absorber surface.

Today, the standard ZnO/buffer/$Cu(In_{1-X}Ga_X)(S_YSe_{1-Y})_2$/Mo/glass structure of chalcopyrite thin-film solar cells contains a thin CdS buffer layer (~50 nm), usually prepared by chemical bath deposition (CBD). Record efficiencies both on a laboratory scale (21.7% [23]) and for large-area commercial modules (15.7% for 9703 cm^2 [24]) have thus been achieved. However, there is a strong impetus to replace CdS by other compounds for ecological as well as economical reasons. The simple omission of the buffer layer, however, does not result in high-efficiency solar cells [25]. This situation can be improved by a (pre)treatment of the $Cu(In_{1-X}Ga_X)(S_YSe_{1-Y})_2$ ("CIGSSe") absorber in an aqueous solution of ammonium hydroxide and Cd^{2+}-ions (i.e., identical to the CBD solution but without the S source) prior to ZnO deposition. This leads to an increase in short-circuit current density, open-circuit voltage, and fill factor [26]. Such a Cd^{2+}/NH_3 treatment was first proposed for $CuInSe_2$ thin-film solar-cell absorbers

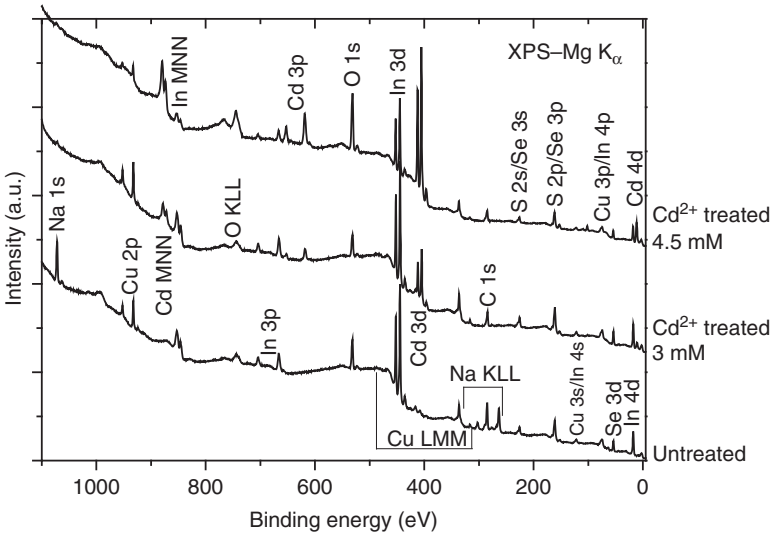

Figure 18.4 XPS survey spectra of an untreated and two Cd^{2+}/NH_3-treated $CuIn(S,Se)_2$ thin-film solar-cell absorbers (3 mM and 4.5 mM Cd^{2+} concentration). The different photoemissions and Auger lines are identified as indicated.

by Ramanathan *et al*. [25] and later successfully employed also by several other groups [27–29]. Even though Cd is still involved, this process is advantageous, since the amount of Cd-containing waste is largely reduced because, in contrast to the batch-type CBD, the solution can be reused repeatedly. In the following it will be shown how a combination of XPS, XAES, and XES is capable of giving a detailed insight into the modifications of the chemical surface structure induced by the Cd^{2+}/NH_3 treatment.

XPS survey spectra for the untreated $CuIn(S,Se)_2$ absorber and after Cd^{2+} treatment at two concentrations (3 and 4.5 mM) are exemplary shown in Figure 18.4. A wealth of information can be derived from such spectra. For example, the strong decrease of the intensity of the Na 1s line at ~1070 eV shows that surface Na (stemming from the glass substrate and diffusing through the $CuIn(S,Se)^2$/Mo during the absorber preparation at about 550 °C) is removed by the Cd^{2+}/NH_3 treatments. Furthermore, a slight reduction of the "native" O content at the surface of the (air-exposed) $CuIn(S,Se)^2$ absorbers is found when using Cd^{2+} concentrations of up to 3 mM, while concentrations of 4.5 mM and above (not shown) lead to a pronounced *enhancement* of the O signal. After all Cd^{2+}/NH_3 treatments, Cd is detected on the $CuIn(S,Se)^2$ surface (see Ref. [30] for a more detailed discussion of peak intensities).

Before demonstrating how the soft X-ray and electron spectroscopies can help to identify the Cd species, first the surface composition of the untreated $CuIn(S,Se)^2$ absorber, especially the S/(S+Se) = Y ratio, is determined. In Figure 18.5, the corresponding detail XPS spectrum of the S 2p and Se 3p region

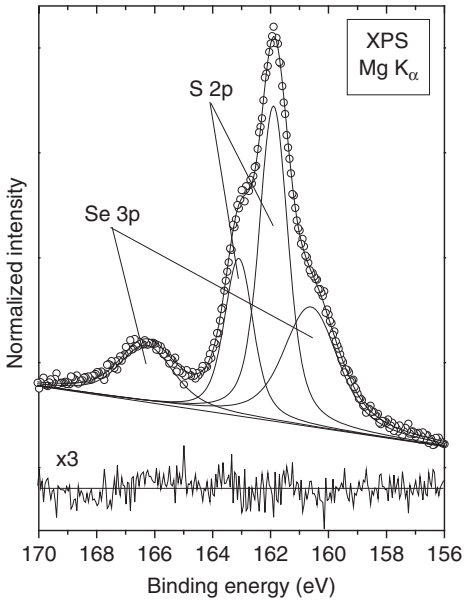

Figure 18.5 S 2p and Se 3p XPS detail spectrum of the investigated $CuIn(S,Se)_2$ thin-film solar-cell absorber. The continuous lines show the corresponding fits, together with their (threefold magnified) residuum.

is shown. In order to compute the [S]/([S]+[Se]) ratio, the peak areas were determined by fitting them with Voigt line shapes (which is a convolution of Gauss- and Lorentz-shaped contributions and represents the best description of core level peaks for materials with a significant band gap) and a linear background, coupling the line widths of the two (spin–orbit split) S 2p and Se 3p lines, respectively. Furthermore, the spin–orbit splitting of S 2p (1.2 eV [31, 32]) and Se 3p (5.7 eV [31, 32]) and the 2 : 1 peak ratio (which corresponds to the multiplicity $2j + 1$) of the $j = 3/2$ and $j = 1/2$ components were kept constant. No peak area correction for the energy-dependence of the analyzer transmission and the IMFP of the electrons is necessary, since the S 2p and Se 3p electrons have very similar kinetic energies. The surface [S]/([S]+[Se]) ratio can then simply be derived from the fit-derived areas, corrected by photoionization cross sections from [33]. Here it is found to be 0.75 (i.e., significantly S rich).

The Cd $M_{45}N_{45}N_{45}$ Auger emission line is shown in Figure 18.6. As indicated, the Cd "deposition" takes place in two different concentration regimes, up to 3 mM Cd^{2+} and 4.5 mM Cd^{2+} and above. For the higher concentration regime, the Cd Auger line is shifted to lower kinetic energies, in parallel with a strong increase in peak intensity. The dashed and dotted lines represent a spectral decomposition of the 4.5 mM spectrum, revealing two different Cd species in the high-concentration regime. In parallel, an enhancement in the O 1s and Cd 3d XPS intensity is found. Further information can be obtained by computing the "modified Auger parameter" [α^*(Cd) = binding energy (Cd $3d_{5/2}$) + kinetic energy

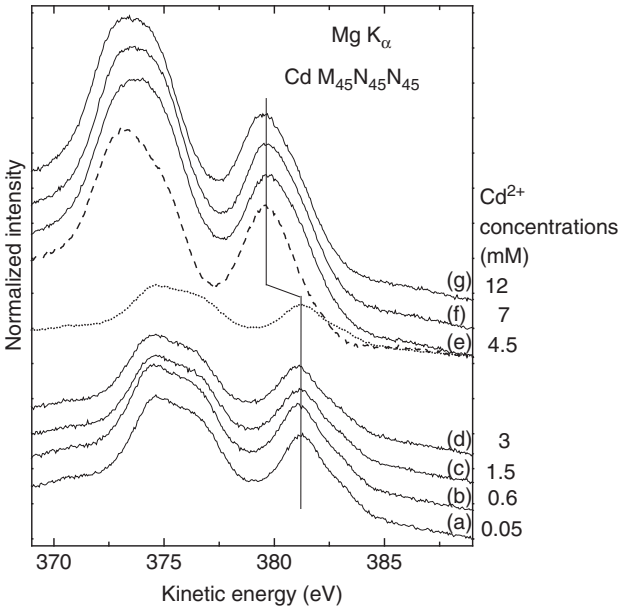

Figure 18.6 Cd $M_{45}N_{45}N_{45}$ XAES spectra of $CuIn(S,Se)_2$ absorbers after Cd^{2+}/NH_3 treatment with different Cd^{2+} concentrations (0.05–12 mM, spectra a–g), indicating two different Cd species in the different concentration regimes. The dashed and dotted spectra below (e) are discussed in the text [30].

(Cd $M_4N_{45}N_{45}$)]. The value of 785.3 eV in the high-concentration regime suggests the formation of $Cd(OH)_2$ [31, 34]. As mentioned, a second Cd species in addition to the now-identified $Cd(OH)_2$ is present, as found for lower Cd^{2+} concentrations. While XPS and XAES can clearly distinguish the two different species and even give strong evidence for a $Cd(OH)_2$ deposition in the high-concentration regime, the identification of the second species is more difficult. XPS and XAES line positions and Auger parameters point toward CdS and/or CdSe, which are not easily distinguishable [31, 34]. In order to resolve this problem, an additional spectroscopic viewpoint is needed, and thus XES experiments for an untreated and a Cd^{2+}/NH_3-treated (1.5 mM) $CuIn(S,Se)_2$ absorber were performed.

The S $L_{2,3}$ XES spectra shown in Figure 18.7 reveal the changes in local chemical bonding undergone by the S atoms upon Cd^{2+}/NH_3 treatment (1.5 mM Cd^{2+} concentration). A detailed discussion of the various features included in this spectrum can be found in Ref. [35]. As already discussed in Section 18.2, XES, as a "PIPO" technique, is more bulk sensitive than XPS and XAES. Here, the majority of the spectrum is associated with approximately the upper 100 nm of the $CuIn(S,Se)_2$ film. To get information about the changes induced by the Cd^{2+}/NH_3 treatment at the absorber *surface*, the spectrum of the untreated absorber (a) was subtracted from that of the Cd^{2+}/NH_3-treated film (b) in Figure 18.7, yielding the (magnified) difference spectrum (c). Comparison with a CdS reference (Figure 18.7e) suggests the formation of CdS at the absorber surface, particularly by noting the two peaks

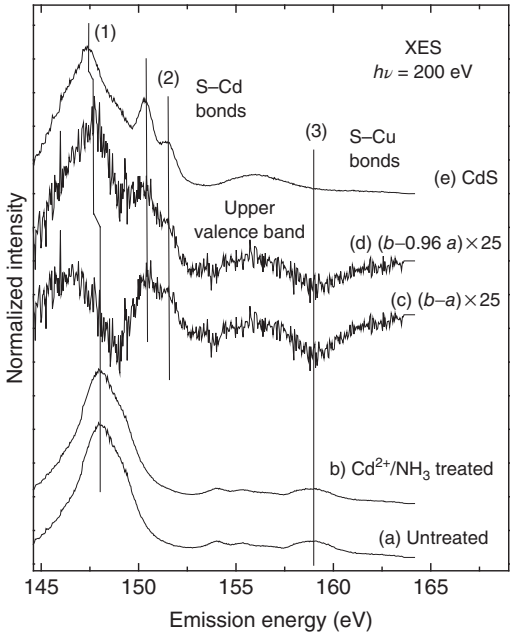

Figure 18.7 S $L_{2,3}$ X-ray emission spectra of (a) an untreated and (b) a Cd^{2+}-treated $CuIn(S,Se)_2$ absorber (1.5 mM Cd^{2+} concentration). The spectrum (c) shows the enlarged (×25) difference of (a) and (b). The spectral features at lines (2) indicate the presence of S–Cd bonds. Spectrum (d) was obtained by subtracting 96% of spectrum (a) from spectrum (b). For comparison, spectrum (e) shows a CdS-reference film [30].

at 150.4 and 151.5 eV (marked by the vertical lines (2)). These peaks correspond to valence electrons with strong Cd 4d character decaying into the S $2p_{1/2}$ and $2p_{3/2}$ core holes, respectively, and thus indicate S–Cd bonds. Additionally, the upper valence band of CdS can be observed at about 156 eV. Consequently, for spectrum (d), a suitable amount (96%) of spectrum (a) was subtracted from (b). This subtraction assumes that 96% of the signal is due to S atoms in the $CuIn(S,Se)_2$ environment and 4% to S atoms in a different environment. The derived difference spectrum (d) now very closely resembles the CdS reference spectrum with the exception of a "dip" at 159 eV, which is associated with Cu 3d-derived states and hence gives a direct probe of S–Cu bonds [35]. In the present case, the Cd^{2+}/NH_3 treatment apparently induces the breaking of some of these bonds in the favor of the formation of S–Cd bonds. This is in agreement with the experimental finding of Cu in used Cd^{2+}/NH_3-treatment solutions after extended absorber soaking [27] and can be explained by an ion exchange via the corresponding Cd and Cu ammine complexes in the Cd^{2+}/NH_3-treatment solution [36].

The assumed 4% of CdS signal intensity correspond to approximately one monolayer of CdS. Using the IMFP of the electrons (λ) calculated by the QUASES-IMFP-TPP2M code [37], this is in agreement with the respective layer thickness determined from the attenuation of XPS and XAES substrate signals [30]. Hence,

the dominant Cd species formed in the low-concentration regime is CdS, and a significant amount of Cd in a Se environment can be excluded (in agreement with the *S-rich* nature of the investigated $CuIn(S,Se)_2$ surface). XES measurements of Cd^{2+}/NH_3-treated $CuIn(S,Se)_2$ samples treated in high-concentration solutions also indicate the formation of S–Cd bonds [38] which, together with the XAES finding of the formation of two Cd species (see Figure 18.6) for these Cd^{2+} concentrations ($\geq$4.5 mM), are indicative for the formation of a $Cd(OH)_2$/CdS bilayer in that concentration regime.

In summary, soft X-ray and electron spectroscopies allow us to derive the following picture of the Cd^{2+}/NH_3-treatment process. In the low-concentration regime, that is, for Cd^{2+}-ion concentrations up to 3 mM, the formation of S–Cd bonds can be found on the S-rich chalcopyrite absorber surface. The deposited amount of "CdS" is nearly independent of the Cd^{2+} concentration. The S atoms forming the S–Cd bonds stem from the absorber surface, as evidenced by the breaking of S–Cu bonds. The latter can be explained by an ion exchange via the corresponding Cd and Cu ammine complexes in the Cd^{2+}/NH_3-treatment solution [36]. Without additional diffusion processes, the "CdS" amount is limited to the equivalent of one monolayer, that is, to a state in which all S surface atoms are bound to Cd atoms, as corroborated by the intensity behavior of XPS and XAES signals and by the spectral deconvolution of XES spectra. For concentrations of 4.5 mM and above, a "CdS"/$Cd(OH)_2$ bilayer is formed.

It is the combination of the various spectroscopic techniques, using different aspects of chemical sensitivity and different information depths, together with a suitably designed sample series, and a well-posed initial question, that leads to deep insights into the chemical properties of thin-film solar-cell absorber surfaces and the chemical modifications induced by a "real-world" chemical treatment. Such insights are extremely valuable for a better understanding of empirically optimized processes and can lead the way to performance enhancements in real-world solar-cell systems.

18.4 Probing the Electronic Surface and Interface Structure: Band Alignment in Thin-Film Solar Cells

The electronic structure, in particular the alignment of the transport levels (i.e., the CBM and the valence-band maximum – VBM) plays a crucial role for the charge transport in every electronic device and thus also for solar cells. In principle, there are three general ways how the conduction bands may align at an interface, as depicted in Figure 18.8. The situation shown in Figure 18.8a, that is, a downward step in the conduction band and hence a negative conduction-band offset (CBO, also called "cliff"), can lead to a reduced recombination barrier (as indicated by the arrow in Figure 18.8), with potential consequences for the performance of the associated cell [39, 40]. The alignment with an upward step in the conduction band and hence a positive CBO (also called "spike"), which is shown in Figure 18.8c,

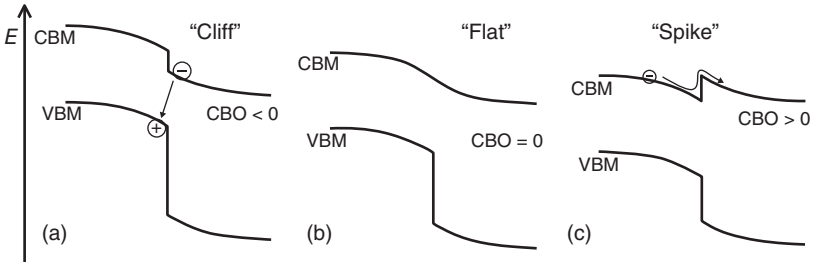

Figure 18.8 Possible (conduction) band alignments at a semiconductor heterointerface: (a) downward step ("cliff"), (b) vanishing band offset ("flat"), and (c) upward step ("spike").

might also be undesirable since the electron transport across the interface may be impeded [41]. Finally, the transition point between a cliff and a spike, that is, a flat conduction-band alignment, is shown in Figure 18.8b.

In the following, we will show how the CBO of an interface can be measured, using the example of CdS/Cu(In,Ga)$(S,Se)_2$ thin-film solar cells. Particularly important for a correct determination are the complex properties of the different layers of the Cu(In,Ga)$(S,Se)_2$ cell. For example, high-efficiency Cu(In,Ga)$(S,Se)_2$ films generally exhibit different structural and chemical properties at the surface (or back surface) than in the bulk of the film (e.g., the band-gap energy, as mentioned in Section 18.2). Thus, great care has to be exercised in determining the band alignments at interfaces in such complex systems, analyzing both the conduction and valence bands separately and taking the chemical structure of the interface into account.

As a first example, we will now discuss the interface band alignment of CdS/$CuInSe_2$ (i.e., with a Ga- and S-free absorber surface) in detail in Ref. [18]. The samples were taken from the (former) Shell Solar pilot line, prepared by a rapid thermal annealing of elemental layers on Mo-coated soda-lime glass. CdS films were deposited by CBD. The $CuInSe_2$ layers also contain Ga, but it is localized near the back contact of the cell and thus only trace amounts of Ga can be found at the $CuInSe_2$ surface.

The determination of the band alignment is now done in two steps:

1) In the first step, the band edge position of the $CuInSe_2$ surface as well as of the CdS surface on the $CuInSe_2$ absorber is determined by UPS and IPES.
2) The values derived in the first step are corrected by the changes in band bending which occur due to the formation of the interface. This can be done by using core-level lines measured by XPS, as will be discussed later.

Figure 18.9 shows the UPS and IPES spectra of the absorber surface (a–f) and of a thick CdS film. Since the samples were taken from a large-scale industrial production line, they were exposed to air for a (minimized) period of time prior to the measurements and thus exhibit surface contaminants. As visible in Figure 18.9, most prominently in the UPS spectra, these contaminants obscure the measurement with very surface-sensitive techniques like UPS or IPES. For this reason the

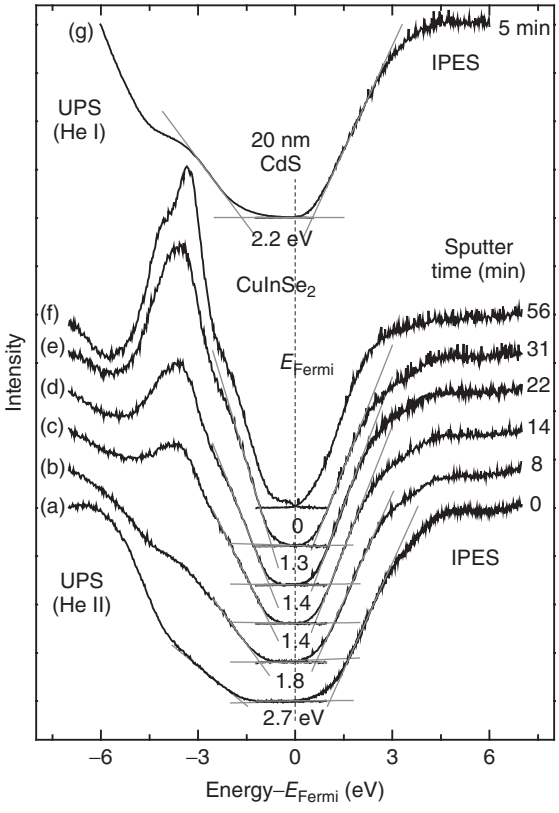

Figure 18.9 UPS and IPES spectra of a $CuInSe_2$ thin-film solar-cell absorber and of a 20 nm CBD-CdS/$CuInSe_2$ interface sample. The spectra were acquired after subsequent Ar^+-ion sputter steps, as listed on the right-hand side. Gray lines indicate the linearly extrapolated band edges; the determined band gaps are given in the center [18].

samples were cleaned by using low-energy (500 eV) Ar^+ ions at a current density of 1 μA/cm^2 and low and varying angles. More recently, it was found that ion energies as low as 50 eV are very efficient at removing surface contaminants from chalcopyrite surfaces while effectively avoiding any sputter-induced damage to the surface (see also discussion in the following text) [42].

For a variety of reasons [19–21], a linear extrapolation of the leading edge in the spectra can be used to approximate the positions of VBM and CBM in the spectra. While the as-introduced sample (Figure 18.9a) is dominated by the surface contaminations and thus results in an artificially increased "band-gap energy" of 2.7 eV, a band-gap energy of 1.4 eV can be derived for the sample surface at intermediate stages of the cleaning process (Figure 18.9c and d). Note that it is found that the surface contaminants are also removed during the CBD process [30, 43]. Hence, the surface band-gap energy derived after the sputter treatment is expected to be a good approximation of the $CuInSe_2$ band gap directly

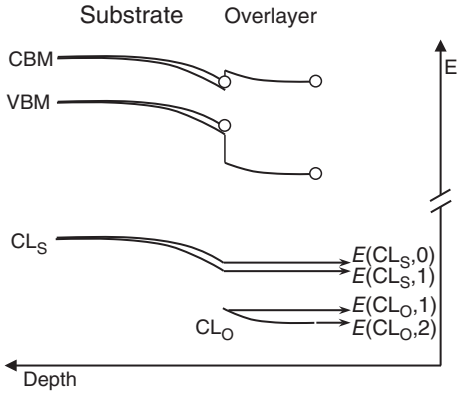

Figure 18.10 Schematic (potential) impact of interface formation on the position of the electronic levels in the substrate. The energy positions of the core levels can be used to quantify this "interface-induced band bending."

at the CdS/$CuInSe_2$ interface. Further Ar^+ ion bombardment leads to a further reduction of the derived values to 1.3 eV and, finally, to the emergence of a Fermi edge after prolonged sputter treatment, indicating the formation of metallic surface species (Figure 18.9f). This is consistent with earlier investigations, in which metallic species (both Cu and In) are found after prolonged sputter treatment of the $CuInSe_2$ surface [44–47]. The such-derived surface band-gap energy of the $CuInSe_2$ film of 1.4 (±0.15) eV is in accordance with the surface band-gap widening described in Section 18.2, presumably due to Cu depletion at the surface of the film [17, 48, 49]. The derived band edge positions are −0.8 (±0.1) eV for the VBM and 0.6 (±0.1) eV for the CBM, respectively.

The band edge positions and the surface band gap energy of the CdS buffer layer were determined in a similar way (a sputter time of 5 min was sufficient to clean the surface). Values of −1.8 (±0.1) eV for the VBM and 0.4 (±0.1) eV for the CBM were derived. It is interesting that the resulting surface band gap of 2.2 (±0.15) eV is below that of a CdS bulk film (2.4 eV). This reduction of the band gap can be ascribed to a pronounced intermixing of S and Se at the interface [50, 51], which leads to the formation of a Cd(S,Se) film.

In the first (crude) approximation, the determined values indicate a CBM of the $CuInSe_2$ absorber 0.2 eV above that of the CdS buffer layer, which would indicate a small cliff. However, this value has to be corrected for changes in band bending occurring during the interface formation, as is illustrated in Figure 18.10. The UPS and IPES measurements described above measure the energetic levels at the surface of the respective films, that is, at the $CuInSe_2$/vacuum and CdS/vacuum interface. These positions are marked with open circles in Figure 18.10.

The deposition of an overlayer on a substrate will generally induce a charge transfer both localized at the interface (i.e., the formation of chemical bonds) as well as a longer-range charge transfer to equilibrate the electrochemical potentials. This may lead to the formation of an interface dipole (or, more precisely,

a modification of the previously present surface dipole) and a change in band bending in the absorber film. This is indicated in Figure 18.10 by the difference of the dotted line (without overlayer) and the continuous line (with overlayer). Further band bending may occur in the overlayer, as also shown in Figure 18.10. Both "shifts" can be determined by measuringcore level (CL) energies by means of XPS and by computing the interface-induced band bending (IBB) correction, as will be described in the following. Since the described shifts are caused by surface/interface charges basically generating an electric field, all electronic levels (VBM, CBM, and all CLs) will shift by the same amount. If (at least) one sample with a sufficiently thin overlayer is available, such that both CL signals from the substrate, as well as from the overlayer, can be detected, then the actual positions of the VBMs and CBMs of substrate and overlayer at the interface and thus the band alignment can be determined. The necessary IBB correction can be computed with the positions of a substrate core level CL_S with energies $E(CL_S,0)$ without overlayer and $E(CL_S,1)$ with thin overlayer, and those of an overlayer core level CL_O with energies $E(CL_O,1)$ with thin overlayer and $E(CL_O,2)$ with thick overlayer, as follows:

$$\mathrm{IBB} = E(\mathrm{CL_S}, 0) - E(\mathrm{CL_S}, 1) + E(\mathrm{CL_O}, 1) - E(\mathrm{CL_O}, 2) \tag{18.2}$$

Using this value and the VBM and CBM positions, we can compute the VBO and the CBO energies:

$$\begin{aligned} \mathrm{VBO} &= E(\mathrm{VBM_O}) - E(\mathrm{VBM_S}) + \mathrm{IBB} \\ \mathrm{CBO} &= E(\mathrm{CBM_O}) - E(\mathrm{CBM_S}) + \mathrm{IBB} \end{aligned} \tag{18.3}$$

where CBM_O (VBM_O) are the energies of the CBM and VBM of the overlayer and CBM_S (VBM_S) the corresponding energies of the substrate.

In the discussed case of the $CdS/CuInSe_2$interface, IBB values using five different CL of the substrate and three different core levels of the overlayer were computed and averaged to minimize the influence of chemical shifts occurring during the interface formation. An average value of IBB = 0.2 (±0.1) eV was found. The resulting band alignment picture is summarized in Figure 18.11. It is characterized by a flat conduction-band alignment, that is, a CBO of 0.0 (±0.2) eV and a VBO of 0.8 (±0.2) eV. Due to the strong intermixing of S and Se at the interface mentioned earlier, we can assume that the offset is not abrupt but rather "smeared out" over an interfacial region, as indicated in Figure 18.11 by the dashed and curved line in the valence-band region.

The result of a flat conduction-band alignment is of large relevance for the understanding of CISe-based thin-film solar cells. As discussed earlier, such an alignment is an intermediate case between a barrier for electron transport (a spike) and cliff-like arrangement that could lead to enhanced recombination. Experiments on interface structures involving absorbers with increased bulk band gap (e.g., a $Cu(In,Ga)S_2$ absorber) show that such cliffs indeed exist, even for optimized solar-cell systems, as shown in Figure 18.12 [42]. Such findings may explain why the very high efficiencies expected for wide-gap chalcopyrite absorbers have so far been elusive. In general, the gain in open-circuit voltage of

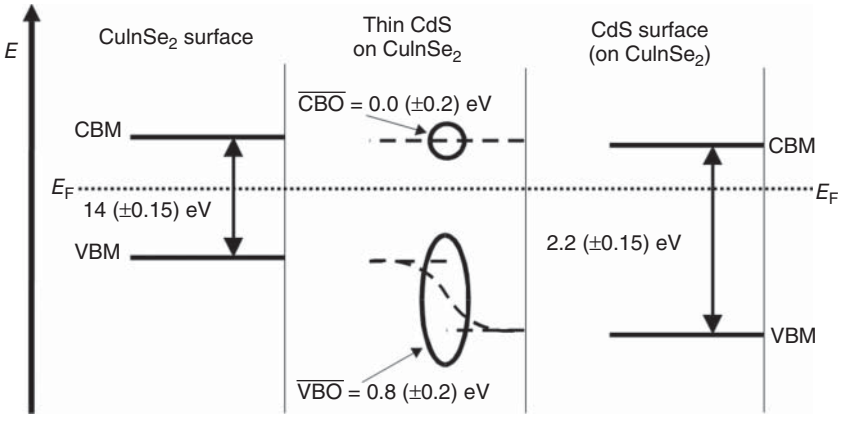

Figure 18.11 Schematic summary of the experimental band alignment results at the CdS/$CuInSe_2$ interface. The left and right parts of the figure represent the level alignment at the surfaces of the $CuInSe_2$ and CdS films, respectively (solid lines). The central part displays the level alignment directly at the interface (dashed lines), which, in addition to the energy positions far away from the interface, also takes an interface-induced band bending as well as interdiffusion into account [18].

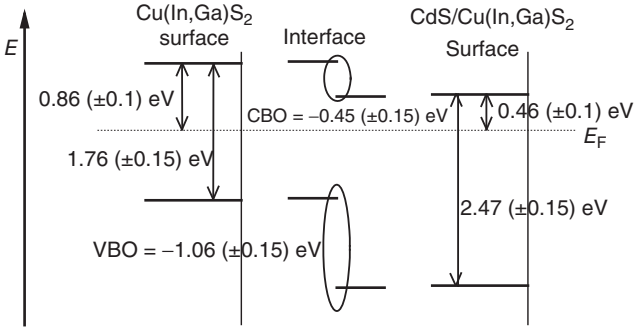

Figure 18.12 Schematic summary of the experimental band alignment results at the CdS/Cu(In,Ga)S_2 interface. The left and right parts of the figure represent the level alignment at the surfaces of $CuInSe_2$ and CdS films, respectively. The central part displays the level alignment directly at the interface, which, in addition to the energy positions far away from the interface, also takes an interface-induced band bending correction into account. (Reproduced with permission from Weinhardt [42] of American Institute of Physics.)

these devices is smaller than what would be expected by the increase of the bulk band gap, which is in accordance with the finding of a sizeable (unfavorable) cliff in the conduction-band alignment.

In summary, thus, the results demonstrate the intricate details of interfaces and their electronic structure in real-world thin-film solar cells, in particular in view of the band offsets between different heterojunction partners. Since such offsets are fundamental properties influencing the charge carrier transport

and thus performance of solar cells, a detailed knowledge of the electronic structure is of crucial importance for insight-based optimization approaches. The here-described combination of experimental methods, namely, PES with UV and X-ray excitation, coupled with IPES, allows a detailed assessment of both the occupied and unoccupied electronic states as a function of overlayer thickness and thus can contribute significant insights into the complicated nature of high-efficiency, real-world thin-film solar cells.

18.5 Summary

In order to aid in the development of high-efficiency, thin-film solar-cell devices, a unique tool chest of characterization techniques is available that uses soft X-rays and electrons to probe the electronic and chemical properties of surfaces and interfaces. By applying a variety of different viewpoints, that is, by varying the depth sensitivity and by combining methods that probe occupied and unoccupied electronic states, a comprehensive picture of the complex processes at empirically optimized real-world semiconductor surfaces and heterojunctions can be drawn. Such insights can be used to propose novel optimization approaches and, furthermore, be employed to monitor the success of deliberately introduced modifications. By analyzing the electronic properties on the most microscopic scale, for example, by using localized core holes and their wave function overlap with delocalized bands, a detailed understanding of both, long-range electronic properties and local chemical bonding can be obtained.

As an outlook, it should be mentioned that some of the here-described methods are PIPO techniques. Due to their $1/e$-attenuation lengths in the order of a few tens to a few hundreds of nanometers, PIPO techniques have recently been successfully employed to investigate samples under nonvacuum conditions [3, 4, 52–56] and thus in the future will lend themselves to monitor the electronic and chemical properties of thin-film solar-cell interfaces *while they are being formed*. This promises new and exciting insights into the interface formation dynamics and will open up a new avenue for deliberate optimization of thin-film solar cells.

Acknowledgments

The authors gratefully acknowledge (in alphabetically order) M. Blum, J.D. Denlinger, N. Dhere, C.-H. Fischer, O.Fuchs, T. Gleim, D. Gross, A. Kadam, F. Karg, S. Kulkarni, B. Lohmüller, M.C. Lux-Steiner, M. Morkel, H.-J. Muffler, T. Niesen, S. Nishiwaki, S. Pookpanratana, W. Riedl, W. Shafarman, G. Storch, E. Umbach, W. Yang, Y. Zubavichus, and S. Zweigart for their contributions to the results presented in this chapter. Valuable discussions with L. Kronik and J. Sites are also acknowledged. The research was funded through the Deutsche Forschungsgemeinschaft (DFG) through SFB 410 (TP B3), the National Renewable Energy

Laboratory through Subcontract Nos. XXL-5-44205-12 and ADJ-1-30630-12, the DFG Emmy Noether Programme, and the German BMWA (FKZ 0329218C). The Advanced Light Source is supported by the Office of Basic Energy Sciences of the US Department of Energy under Contract Nos. DE-AC02-05CH11231 and DE-AC03-76SF00098.

References

1. Weinhardt, L., Fuchs, O., Fleszar, A., Bär, M., Blum, M., Weigand, M., Denlinger, J., Yang, W., Hanke, W., Umbach, E., and Heske, C. (2009) Resonant inelastic soft X-ray scattering of CdS: a two-dimensional electronic structure map approach. *Phys. Rev. B: Condens. Matter Mater. Phys.*, **79**, 165305.
2. Fuchs, O., Weinhardt, L., Blum, M., Weigand, M., Umbach, E., Bär, M., Heske, C., Denlinger, J., Chuang, Y., McKinney, W., Hussain, Z., Gullikson, E., Jones, M., Batson, P., Nelles, B., and Follath, R. (2009) High-resolution, high-transmission soft X-ray spectrometer for the study of biological samples. *Rev. Sci. Instrum.*, **80**, 063103.
3. Fuchs, O., Zharnikov, M., Weinhardt, L., Blum, M., Weigand, M., Zubavichus, Y., Bär, M., Maier, F., Denlinger, J., Heske, C., Grunze, M., and Umbach, E. (2008) Comment on "Isotope and temperature effects in liquid water probed by X-ray absorption and resonant X-ray emission spectroscopy" – Fuchs et al. reply. *Phys. Rev. Lett.*, **100**, 249802.
4. Weinhardt, L., Fuchs, O., Blum, M., Bär, M., Weigand, M., Denlinger, J., Zubavichus, Y., Zharnikov, M., Grunze, M., Heske, C., and Umbach, E. (2010) Resonant X-ray emission spectroscopy of liquid water: Novel instrumentation, high resolution, and the "map" approach. *J. Electron Spectrosc Relat. Phenom.*, **177**, 206–211.
5. Blum, M., Weinhardt, L., Fuchs, O., Bär, M., Zhang, Y., Weigand, M., Krause, S., Pookpanratana, S., Hofmann, T., Yang, W., Denlinger, J.D., Umbach, E., and Heske, C. (2009) Solid and liquid spectroscopic analysis (SALSA) – a soft X-ray spectroscopy endstation with a novel flow-through liquid cell. *Rev. Sci. Instrum.*, **80**, 123102.
6. Hüfner, S. (2003) *Photoelectron Spectroscopy*, Springer.
7. Seah, M.P. and Dench, W.A. (1979) Quantitative electron spectroscopy of surfaces: a standard data base for electron inelastic mean free paths in solids. *Surf. Interface Anal.*, **1**, 2–11.
8. Tanuma, S., Powell, C.J., and Penn, D.R. (1994) Calculations of electron inelastic mean free paths. V. Data for 14 organic compounds over the 50–2000 eV range. *Surf. Interface Anal.*, **21**, 165; QUASES-IMFP-TPP2M code for the calculation of the inelastic electron mean free path, Version2.2, http://www.quases.com/.
9. Henke, B.L., Gullikson, E.M., and Davis, J.C. (1993) X-ray interactions: photoabsorption, scattering, transmission, and reflection at E=50–30000 eV, Z=1–92 *At. Data Nucl. Data Tables*, **54**, 181–342; http://www-cxro.lbl.gov/optical_constants/atten2.html.
10. Briggs, D. and Seah, M.P. (1990) *Practical Surface Analysis - Auger and X-ray Photoelectron Spectroscopy*, 2nd edn, Wiley Interscience.
11. Stöhr, J. (1992) *NEXAFS Spectroscopy*, Springer.
12. Smith, N.V. (1988) Inverse photoemission. *Rep. Prog. Phys.*, **51**, 1227–1294.
13. Carlisle, J.A., Shirley, E.L., Hudson, E.A., Terminello, L.J., Callcott, T.A., Jia, J.J., Ederer, D.L., Perera, R.C.C., and Himpsel, F.J. (1995) Probing the graphite band structure with resonant soft-X-ray fluorescence. *Phys. Rev. Lett.*, **74**, 1234–1237.
14. Eich, D., Fuchs, O., Groh, U., Weinhardt, L., Fink, R., Umbach, E., Heske, C., Fleszar, A., Hanke, W., Gross, E., Bostedt, C., Von Buuren, T., Franco, N., Terminello, L., Keim, M., Reuscher, G.,

Lugauer, H., and Waag, A. (2006) Resonant inelastic soft X-ray scattering of Be chalcogenides. *Phys. Rev. B: Condens. Matter Mater. Phys.*, **73**, 115212.

15. Lüning, J., Rubensson, J., Ellmers, C., Eisebitt, S., and Eberhardt, W. (1997) Site- and symmetry-projected band structure measured by resonant inelastic soft X-ray scattering. *Phys. Rev. B: Condens. Matter Mater. Phys.*, **56**, 13147–13150.
16. Bär, M., Nishiwaki, S., Weinhardt, L., Pookpanratana, S., Fuchs, O., Blum, M., Yang, W., Denlinger, J., Shafarman, W., and Heske, C. (2008) Depth-resolved band gap in Cu(In,Ga)$(S,Se)_2$ thin films. *Appl. Phys. Lett.*, **93**, 244103.
17. Schmid, D., Ruckh, M., Grunwald, F., and Schock, H.W. (1993) Chalcopyrite/defect chalcopyrite heterojunctions on the basis of $CuInSe_2$. *J. Appl. Phys.*, **73**, 2902–2909.
18. Morkel, M., Weinhardt, L., Lohmüller, B., Heske, C., Umbach, E., Riedl, W., Zweigart, S., and Karg, F. (2001) Flat conduction-band alignment at the CdS/$CuInSe_2$ thin-film solar-cell heterojunction. *Appl. Phys. Lett.*, **79**, 4482–4484.
19. Eich, D., Ortner, K., Groh, U., Chen, Z.H., Becker, C.R., Landwehr, G., Fink, R., and Umbach, E. (1999) Band Discontinuity and Band Gap of MBE Grown HgTe/CdTe(001) Heterointerfaces Studied by k-Resolved Photoemission and Inverse Photoemission. *Phys. Status Solidi A*, **173**, 261–267.
20. Gleim, T., Heske, C., Umbach, E., Schumacher, C., Faschinger, W., Ammon, C., Probst, M., and Steinrück, H.-P. (2001) Reduction of the ZnSe/GaAs(100) valence band offset by a Te interlayer. *Appl. Phys. Lett.*, **78**, 1867–1869.
21. Gleim, T., Heske, C., Umbach, E., Schumacher, C., Gundel, S., Faschinger, W., Fleszar, A., Ammon, C., Probst, M., and Steinrück, H.-P. (2003) Formation of the ZnSe/(Te/)GaAs(100) heterojunction. *Surf. Sci.*, **531**, 77–85.
22. Weinhardt, L., Fuchs, O., Umbach, E., Heske, C., Fleszar, A., and Hanke, W. (2007) Resonant inelastic soft X-ray scattering, X-ray absorption spectroscopy, and density functional theory calculations of the electronic bulk band structure of CdS. *Phys. Rev. B: Condens. Matter Mater. Phys.*, **75**, 165207.
23. Jackson, P., Hariskos, D., Wuerz, R., Kiowski, O., Bauer, A., Friedlmeier, T.M., and Powalla, M. (2015) Properties of Cu(In,Ga)Se_2 solar cells with new record efficiencies up to 21.7%. *Phys. Status Solidi RRL*, **9**, 28–31.
24. Green, M.A., Emery, K., Hishikawa, Y., Warta, W., and Dunlop, E.D. (2015) Solar cell efficiency tables (Version 46). *Prog. Photovoltaics Res. Appl.*, **23**, 805–812.
25. Ramanathan, K., Bhattacharya, R.N., Granata, J., Webb, J., Niles, D., Contreras, M.A., Wiesner, H., Hasoon, F.S., and Noufi, R. (1997) *Properties of Cd and Zn Partial Electrolyte Treated CIGS Solar Cells*, Proc. 26th IEEE PVSC, IEEE, New York, p. 319.
26. Bär, M., Muffler, H., Fischer, C., Zweigart, S., Karg, F., and Lux-Steiner, M.C. (2002) ILGAR-ZnO window extension layer: an adequate substitution of the conventional CBD-CdS buffer in Cu(In,Ga) $(S,Se)_2$ based solar cells with superior device performance. *Prog. Photovoltaics Res. Appl.*, **10**, 173–184.
27. Ramanathan, K., Wiesner, H., Asher, S., Niles, D., Bhattacharya, R.N., Keane, J., Contreras, M.A., and Noufi, R. (1998) *High Efficiency Cu(In,Ga)Se_2 Thin Film Solar Cells without Intermediate Buffer Layers*, Proceedings of 2nd World Conference Photovoltaics: Energy Conversion, European Commission, Italy, p. 477.
28. Wada, T., Hayashi, S., Hashimoto, Y., Nishiwaki, S., Sato, T., Negami, T., and Nishitani, M. (1998) *High Efficiency Cu(In,Ga)Se_2 (CIGS) Solar Cells with Improved CIGS Surface*, Proceedings of 2nd World Conference of Photovoltaics Energy Conversion, p. 403.
29. Canava, B., Guillemoles, J.-F., Yousfi, E.-B., Cowache, P., Kerber, H., Loeffl, A., Schock, H.-J., Powalla, M., Hariskos, D., and Lincot, D. (2000) Wet treatment based interface engineering for high efficiency Cu(In,Ga)Se_2 solar cells. *Thin Solid Films*, **361–362**, 187–192.

30. Weinhardt, L., Gleim, T., Fuchs, O., Heske, C., Umbach, E., Bär, M., Muffler, H., Fischer, C., Lux-Steiner, M., Zubavichus, Y., Niesen, T., and Karg, F. (2003) CdS and $Cd(OH)_2$ formation during Cd treatments of $Cu(In,Ga)(S,Se)_2$ thin-film solar cell absorbers. *Appl. Phys. Lett.*, **82**, 571–573.
31. NIST X-ray Photoelectron Spectroscopy Database, NIST Standard Reference Database 20, Version 3.4, http://srdata.nist.gov/xps/.
32. Wagner, C.D., Riggs, W.M., Davis, L.E., and Moulder, J.F. (1979) in *Handbook of X-ray Photoelectron Spectroscopy* (ed G.E. Muilenberg), Perkin-Elmer Corporation, Eden Prairie.
33. Scofield, J.H. (1976) Hartree-Slater subshell photoionization cross-sections at 1254 and 1487 eV. *J. Electron. Spectrosc. Relat. Phenom.*, **8**, 129–137.
34. Wagner, C.D. (1990) in *Practical Surface Analysis, Vol. 1* (eds D. Briggs and M.P. Seah), John Wiley & Sons, p. 595.
35. Heske, C., Groh, U., Fuchs, O., Umbach, E., Franco, N., Bostedt, C., Terminello, L., Perera, R., Hallmeier, K., Preobrajenski, A., Szargan, R., Zweigart, S., Riedl, W., and Karg, F. (2001) X-ray emission spectroscopy of $Cu(In,Ga)(S,Se)_2$-based thin film solar cells: electronic structure, surface oxidation, and buried interfaces. *Phys. Status Solidi A*, **187**, 13–24.
36. Bär, M., Weinhardt, L., Heske, C., Muffler, H., Lux-Steiner, M., Umbach, E., and Fischer, C. (2005) Cd^{2+}/NH_3 treatment of $Cu(In,Ga)(S,Se)_2$ thin-film solar cell absorbers: a model for the performance-enhancing processes in the partial electrolyte. *Prog. Photovoltaics*, **13**, 571–577.
37. S. Tougaard, QUASES-IMFP-TPP2M code for the calculation of the inelastic electron mean free path, Version 2.2, http://www.quases.com/.
38. Bär, M. (2004) Novel Cd-free window structure for chalcopyrite-based thin film solar cells, PhD thesis, TU Berlin, http://opus.kobv.de/tuberlin/volltexte/2004/687/.
39. Hengel, I., Neisser, A., Klenk, R., and Lux-Steiner, M.C. (2000) Current transport in $CuInS_2$:Ga/CdS/ZnO-solar cells. *Thin Solid Films*, **361-362**, 458–462.
40. Klenk, R. (2001) Characterisation and modelling of chalcopyrite solar cells. *Thin Solid Films*, **387**, 135–140.
41. Liu, X. and Sites, J.R. (1996) *Calculated Effect of Conduction-Band Offset on $CuInSe_2$ Solar-Cell Performance*, Proceedings of the AIP conference, Lakewood, p. 444.
42. Weinhardt, L., Fuchs, O., Gross, D., Storch, G., Umbach, E., Dhere, N., Kadam, A., Kulkarni, S., and Heske, C. (2005) Band alignment at the $CdS/Cu(In,Ga)S_2$ interface in thin-film solar cells. *Appl. Phys. Lett.*, **86**, 062109.
43. Kylner, A. (1999) The chemical bath deposited $CdS/Cu(In,Ga)Se_2$ interface as revealed by X-ray photoelectron spectroscopy. *J. Electrochem. Soc.*, **146**, 1816–1823.
44. Heske, C., Fink, R., Umbach, E., Riedl, W., and Karg, F. (1996) Surface preparation effects of polycrystalline $Cu(In,Ga)Se_2$ thin films studied by XPS and UPS. *Cryst. Res. Technol.*, **31**, 919–922.
45. Niles, D.W., Ramanathan, K., Hasoon, F., Noufi, R., Tielsch, B.J., and Fulghum, J.E. (1997) Na impurity chemistry in photovoltaic CIGS thin films: investigation with X-ray photoelectron spectroscopy. *J. Vac. Sci. Technol., A*, **15**, 3044–3049.
46. Otte, K., Lippold, G., Frost, F., Schindler, A., Bigl, F., Yakushev, M.V., and Tomlinson, R.D. (1999) Low energy ion beam etching of $CuInSe_2$ surfaces. *J. Vac. Sci. Technol., A*, **17**, 19–25.
47. Weinhardt, L., Morkel, M., Gleim, Th., Zweigart, S., Niesen, T.P., Karg, F., Heske, C., and Umbach, E. (2001) *Band Alignment at the $CdS/CuIn(S,Se)_2$ Heterojunction in Thin Film Solar Cells*, Proceedings of 17th European Photovoltaics Solar Energy Conference, Munich, 1261.
48. Dullweber, T., Hanna, G., Rau, U., and Schock, H.W. (2001) A new approach to high-efficiency solar cells by band gap grading in $Cu(In,Ga)Se_2$ chalcopyrite semiconductors. *Sol. Energy Mater. Sol. Cells*, **67**, 145–150.

49. Klein, A. and Jaegermann, W. (1999) Fermi-level-dependent defect formation in Cu-chalcopyrite semiconductors. *Appl. Phys. Lett.*, **74**, 2283–2285.
50. Heske, C., Eich, D., Fink, R., Umbach, E., van Buuren, T., Bostedt, C., Terminello, L.J., Kakar, S., Grush, M.M., Callcott, T.A., Himpsel, F.J., Ederer, D.L., Perera, R.C.C., Riedl, W., and Karg, F. (1999) Observation of intermixing at the buried CdS/Cu(In,Ga)Se_2 thin film solar cell heterojunction. *Appl. Phys. Lett.*, **74**, 1451–1453.
51. Weinhardt, L., Bär, M., Pookpanratana, S., Morkel, M., Niesen, T., Karg, F., Ramanathan, K., Contreras, M., Noufi, R., Umbach, E., and Heske, C. (2010) Sulfur gradient-driven Se diffusion at the CdS/CuIn(S,Se)$_2$ solar cell interface. *Appl. Phys. Lett.*, **96**, 182102.
52. Heske, C., Groh, U., Fuchs, O., Weinhardt, L., Umbach, E., Schedel-Niedrig, T., Fischer, C., Lux-Steiner, M., Zweigart, S., Niesen, T., and Karg, F. (2003) Monitoring chemical reactions at a liquid–solid interface: water on CuIn(S,Se)$_2$ thin film solar cell absorbers. *J. Chem. Phys.*, **119**, 10467–10470.
53. Heske, C. (2004) Spectroscopic investigation of buried interfaces and liquids with soft X-rays. *Appl. Phys. A*, **78**, 829–835.
54. Fuchs, O., Zharnikov, M., Weinhardt, L., Blum, M., Weigand, M., Zubavichus, Y., Bär, M., Maier, F., Denlinger, J., Heske, C., Grunze, M., and Umbach, E. (2008) Isotope and temperature effects in liquid water probed by X-ray absorption and resonant X-ray emission spectroscopy. *Phys. Rev. Lett.*, **100**, 027801.
55. Weinhardt, L., Blum, M., Fuchs, O., Benkert, A., Meyer, F., Bär, M., Denlinger, J.D., Yang, W., Reinert, F., and Heske, C. (2013) RIXS investigations of liquids, solutions, and liquid/solid interfaces. *J. Electron. Spectrosc. Relat. Phenom.*, **188**, 111–120.
56. Benkert, A., Blum, M., Meyer, F., Wilks, R.G., Yang, W., Bär, M., Reinert, F., Heske, C., and Weinhardt, L. (2014) Setup for in situ investigation of gases and gas/solid interfaces by soft X-ray emission and absorption spectroscopy. *Rev. Sci. Instrum.*, **85**, 015119.

19
Accessing Elemental Distributions in Thin Films for Solar Cells

Volker Hoffmann, Denis Klemm, Varvara Brackmann, Cornel Venzago, Angus A. Rockett, Thomas Wirth, Tim Nunney, Christian A. Kaufmann, Raquel Caballero, and Oana Cojocaru-Mirédin

19.1
Introduction

The present chapter will give a technical and experimental overview for a number of methods that are broadly available for determining elemental distributions regarding the matrix- and trace-element concentrations in multilayer stacks. These techniques are glow-discharge optical emission spectroscopy (GD-OES) and glow-discharge mass spectroscopy (GD-MS) (Section 19.2), secondary ion mass spectroscopy (SIMS) and sputtered neutral mass spectroscopy (SNMS) (Section 19.3), Auger electron spectroscopy (AES) (Section 19.4), and X-ray photoelectron spectroscopy (XPS) (Section 19.5). In addition, energy-dispersive X-ray spectroscopy (EDX) (Section 19.6) in a scanning electron microscope may be applied on fractured cross-sectional specimens of these multilayer stacks, providing a quick way of analyzing the spatial distribution of the matrix elements. Finally, when aiming at spatial resolutions for the analysis of elemental distributions of both matrix and trace elements, atom probe tomography (APT) (Section 19.7) may be performed on tip-shaped specimens of thin-film stacks.

AES, XPS, SIMS, and SNMS exhibit a good lateral resolution, and depth-resolved information may be obtained in combination with a sputtering process. Thereby, ions are accelerated toward the surface of the sample and collide with the atoms in the region near the surface. The resulting collision cascade leads to the emission of sample material from the surface and forms a more or less flat crater. While AES and XPS only use this process to expose the region of interest, SIMS and SNMS analyze the sputtered material. Because of practical reasons, different sputtering rates are employed at times, that is, fast sputtering for removing sample material and slow sputtering during the analysis.

Advanced Characterization Techniques for Thin Film Solar Cells, Second Edition.
Edited by Daniel Abou-Ras, Thomas Kirchartz, and Uwe Rau.

XPS, AES, and SIMS work under ultrahigh vacuum conditions and must be performed at high acceleration voltages in order to obtain high sputtering yields. These techniques make use of a scanning ion beam for sputtering, which allows the discrimination of crater edge effects. For the SIMS analysis, only an electronically gated area is used for the analysis. Similarly, in AES and XPS measurements, only secondary electrons from the inner, flat part of the crater contribute to the analysis. In order to reduce the sputtering-enhanced roughness, sputtering conditions need to be optimized and sample rotation may be applied, where ultimate depth resolution is needed [1].

The sputtering process may change the properties of the material owing to ion damage at the sample surface. At acceleration voltages of several tens of kilovolt, significant mixing of the material occurs, which deteriorates the depth resolution. This effect is less pronounced for techniques, which use lower voltages, such as GD-OES and GD-MS. After several collisions, the energy of the sputtering particles is reduced to about 50 eV, and only a small number of atom layers participates in the collision process. These collisions also cause a nearly uniform angle distribution of the sputtering particles, which reduces the sputtering-enhanced roughness. The higher current density in the high-pressure (several hectopascals) sputtering instruments (GD-OES and GD-MS) results also in a higher thermal load on the sample. Therefore, pulsed discharges are preferred in the case of heat-sensitive samples. Even when applying pulsed discharges, the erosion rate is much higher for GD-OES and GD-MS than for XPS, AES, and SIMS.

Last but not least, it should be mentioned that all sputtering techniques suffer from preferential sputtering, which means that sputtering of light elements is preferred in comparison with heavier elements. For techniques that analyze the sputtered material itself, such as SIMS or SNMS, after a short time equilibrium is achieved. XPS and AES, however, analyze the modified surface. Therefore, if the sample consists of elements with very different sputtering yields, preferential sputtering must be taken into account during quantification. Sputtering yields vary with varying surface-binding potential, which often differs between different phases or crystal orientations at the surface. Consequently this may lead to preferential sputtering and roughening of the sample surface.

Most of the examples given in the present chapter are analytical results from $Cu(In,Ga)(S,Se)_2$ thin films applied as solar absorber materials. The in-depth In and Ga distributions across these layers are in general not homogeneous and depend strongly on the method used for the film deposition, the process parameters involved, and aging/storage conditions [2, 3].

Although in an ideal single-junction solar-cell device, the band-gap energy of the absorber is considered constant across the absorber layer, a designed band-gap profile may yield a considerable efficiency enhancement in a device affected by recombination loss at the various internal interfaces. For $Cu(In,Ga)Se_2$ thin-film solar-cell devices, the Ga distributions in $Cu(In,Ga)Se_2$ thin films are proportional to those of the corresponding band-gap energies [2, 4]. The measurement of the

in-depth Ga and In distributions is, hence, a key issue to be considered for device optimization. The recording of Ga and In profiles has contributed immensely to an advanced understanding of the formation of such gradients over the last few years [5, 6] and their impact on the final functionality of the thin film as absorber layer within a solar-cell device [7, 8]. This has even sparked the development of numerical models for in-depth gradient formation [9, 10]. Further a widespread interest in the comparability of a multitude of different methods for measurement of in-depth compositional gradients has been noted [11].

Impurities in chalcopyrite thin films, such as alkali ions or Fe, are of importance for the quality of the final device [12, 13]. Especially the methods detailed in the present chapter using mass spectroscopy, GD-MS, SIMS, and APT, are dedicated for the detection of impurity elements. Their influence on the growth process and the electronic properties of the semiconductor material and also their final distribution within the thin film may have a serious impact on the electronic quality of the material grown and hence also on the solar conversion efficiency of the final device. Appropriate analysis tools for the concentrations and distributions of these trace elements are therefore needed.

19.2 Glow-Discharge Optical Emission Spectroscopy (GD-OES) and Glow-Discharge Mass Spectroscopy (GD-MS)

GD-OES and GD-MS are among the most important techniques for the direct analysis of solids. The short time for the analysis (typically 5 min (OES) – 50 min (MS) for a thin film of about 5 µm thickness) is caused by the high erosion rate – for OES typically 1 – 6 µm/min and for MS 0.1 – 1 µm/min. Also, the capability to analyze many elements, including the light elements, simultaneously makes GD-OES and GD-MS powerful techniques. The introduction of the radio-frequency (rf) mode in OES expanded the application to the analysis of nonconducting materials [14, 15].

When the sputtering conditions are optimized, depth profiling is possible with a depth resolution of about 5 – 10% of the investigated depth. Since the development of fast and cheap personal computers for data acquisition, nearly all GD-OES instruments are suitable and used for both bulk analysis and depth profiling. Also modern GD-MS instruments are prepared for depth profiling, but mostly in direct current (dc) mode for conducting samples. A number of rf-GD-MS instruments exist as prototypes in the research environment.

19.2.1 Principles

Glow discharge (GD) set-up works in a noble-gas (generally Ar) atmosphere at pressures ranging from about 100 to 1000 Pa. All GD instruments work under

obstructed conditions (when no positive column is built), provided by a short distance between the cathode and the anode with the analytical sample of interest serving as the cathode. During the discharge, the cathode is bombarded by positive noble gas ions and atoms. Material is sputtered from the sample, which is then partly ionized and excited to emit photons corresponding to the characteristic spectral lines. The GD gives information on the elemental composition of the analytical material removed layer-by-layer from the cathode. It can be estimated that the number of Ar atoms in the discharge exceeds the number of sputtered sample atoms approximately by a factor of 1000. This explains why GD calibration curves are usually linear over a wide range of elemental concentration and matrix effects are less important. The separation of sputtering and excitation in space and time is also essential for the low matrix effects. The atoms and ions from the sample are highly dissolved in the argon gas and have no more information about former neighbors in the solid sample.

19.2.2 Instrumentation

19.2.2.1 Plasma Sources

Most GD instruments use the Grimm-type design (see Figures 19.1 and 19.2), where the anode has a ring shape, whose annular front is situated only 0.1 – 0.2 mm away from the surface of the sample [16]. Thus, the discharge is restricted to a sample area, which is equal to the inner aperture of the anode tube (typically 2 – 10 mm). This source configuration is not only suitable for flat and vacuum-tight samples, but also special sample holders exist for cylindrical, spherical, or pin-type samples.

In GD-MS, many instruments are of the type VG9000, which exhibits a source design for low power and low gas-flow conditions and with possible cryogenic cooling of sample and source. Most of these instruments are only equipped with a pin-geometry source. Later, also flat-type sources were introduced. Therefore,

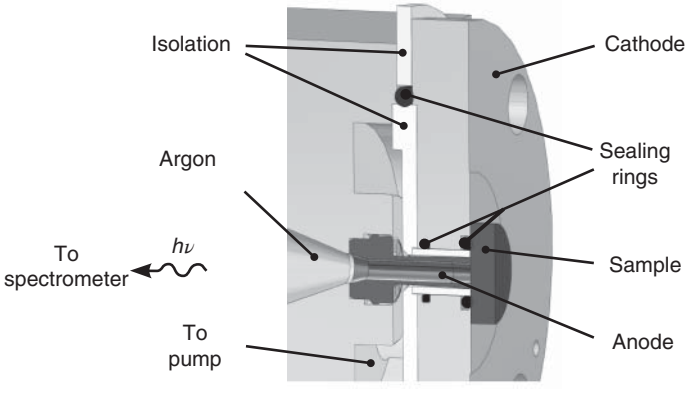

Figure 19.1 Diagram of a typical glow-discharge source used for dc-GD-OES analysis.

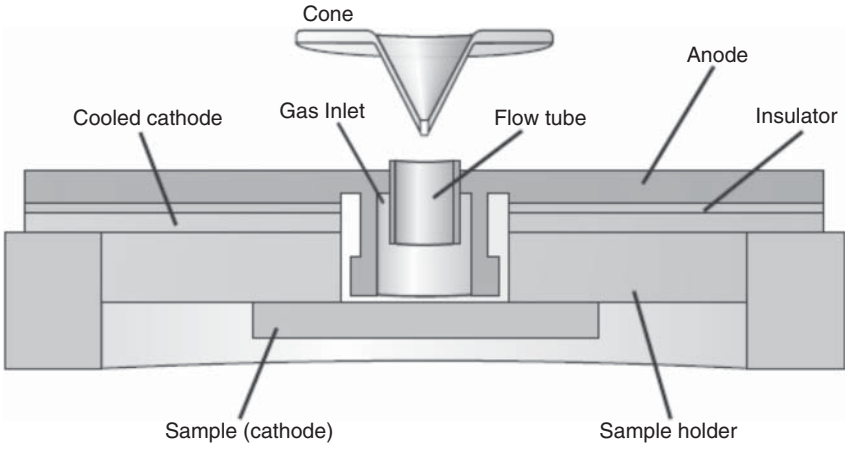

Figure 19.2 Diagram of the glow-discharge source of the ElementGD. (Reprinted with permission from Thermo Fisher Scientific (Bremen) GmbH.)

GD-MS became available for thin-layer analysis. Additionally, developments on the ElementGD-type instrument introduced microsecond pulsed discharge by a pulsed voltage generator [17]. This approach allows much tighter control of sputter rates and therefore also GD-MS analyses in the low micrometer and nanometer range.

19.2.2.2 **Plasma Conditions**

Under constant discharge conditions, the spectral line intensities and ion currents are proportional to the number densities of sputtered atoms in the plasma and hence the element concentration in the investigated sample. In order to maintain reproducible excitation and ionization conditions in the GD source, the discharge conditions (i.e., the argon pressure, voltage, and current) are controlled carefully. The current/voltage characteristics, which describe the discharge, depend on pressure and matrix composition of the thin-film sample analyzed. Thus, for different matrix compositions, it is only possible to keep two of the three discharge parameters constant. It turns out that the pressure has the lowest influence on the sputtering rate and also on the light emission [18]. Therefore, voltage and current are kept constant in dc mode. Standard conditions for a 4 mm source in GD-OES are 700 V and 20 mA, and a VG9000-type instrument with a 10 mm source uses 1000 V and 3–10 mA in most cases. The ElementGD is mostly used in the range from 30 to 60 mA at 500–800 V.

Conductive material can be analyzed with a constant potential drop across cathode and anode (dc mode). If the potential varies at radio frequencies (rf), nonconductive samples such as thin-film solar cells on glass substrates may be also analyzed. Both dc and rf excitation can be applied continuously or in a pulsed mode. However, only pulsed rf generators are offered commercially with repetition rates of up to 10 kHz. In rf mode, the measurement of the plasma current is

difficult, and therefore, other parameters, such as constant power and constant voltage, are preferred.

19.2.2.3 Detection of Optical Emission

The optical radiation of the excited sample atoms is detected end-on through a window with an appropriate transmittance. MgF_2 is most commonly used as window material.

Apart from the GD source with its associated gas and power supplies, vacuum pumps, and controls, the optical system is the most important part of a GD instrument. In order to make use of the analytical capability of the discharge source, the spectrometer must exhibit sufficient resolving power in an adequate spectral range. Commercial optical GD spectrometers cover the wavelength range from 110 to 800 nm, which contains the most sensitive lines of all elements. The high spectral resolution is required in order to avoid spectral interference with lines of other elements and molecules, in particular of the discharge gas Ar. A monochromator can be used for sequential analysis or as additional wavelength channel.

In most common polychromator systems for GD-OES, each detection channel is equipped with a photomultiplier tube (PMT) and a corresponding high-voltage supply. The rapid development in the performance of charge-coupled devices (CCDs) and related detection techniques makes CCD detection systems very attractive. These systems are available for bulk and depth profile analysis and allow flexible selection of nearly all lines and simultaneous measurement of signal and background. However, they still suffer from lower sensitivity and speed of data acquisition in comparison with PMT systems.

19.2.2.4 Mass Spectroscopy

Most installed GD-MS instruments are equipped with a double-focusing, reversed Nier–Johnson geometry mass spectrometer [19]. This geometry provides high mass resolution measurement (with $m/\Delta m$ up to 10 000), which is crucial for the determination of concentrations of trace elements in complex matrices. The ions are extracted through an exit orifice by the pressure difference into the mass spectrometer. Signal detection in GD-MS is performed by means of ion-counting detectors (secondary electron multipliers or Daly detectors) and analog ion-current detectors (secondary electron multipliers or Faraday cups). In combination, both detection principles (analog and counting) are able to measure the ion current within 12 orders of a linear dynamic range. The disadvantage of these mass spectrometric systems (spectrometer with detector) for thin-layer analyses is that they record the mass spectrum sequentially, that is, they are considered slow in comparison to simultaneously recording instruments.

Time-of-flight (TOF) mass spectrometers [20] have the advantage of very fast simultaneous detections of full-range mass spectra and therefore deliver the capability to analyze even thinner layers that can be investigated by use of double-focusing MS. On the other hand, they suffer from a lower dynamic range than double-focusing instruments.

19.2.3 Quantification

19.2.3.1 Glow-Discharge Optical Emission Spectroscopy

Because of the complex nature of the discharge conditions, GD-OES is a comparative analytical method. Therefore, standard reference materials must be used in order to establish a relationship between the measured line intensities and the elemental concentration. In quantitative bulk analysis, which has been developed to very high standards, the calibration is performed with a set of calibration samples of compositions similar to those of the unknown samples. Normally, an element present at high concentration in the sample is used as reference, and the internal standard method is applied [21]. This method is not generally applicable in depth profile analysis of a multilayer stack, because the various layers on which a depth profile was acquired often comprise largely different types of materials, that is, a common reference element is not available [22].

The quantification algorithm most commonly used in dc-GD-OES depth profiling is based on the concept of constant emission yield R_{ik} [11]. It was found that the number of photons with wavelength k emitted per atom or ion of element i in a plasma (i.e., emission yield R_{ik}) is almost matrix and pressure independent. The statement is only valid if the source is operated under constant excitation conditions, that is, mainly at constant voltage and current. The given line intensity I_{ik} then depends further on the concentration c_i of element i in the sample j and on the sputtering rate q_j, which is the total sputtered mass of sample j per time:

$$I_{ik} = c_i \cdot q_i \cdot R_{ik}. \tag{19.1}$$

From this equation, the emission yields of elements can be determined by the analysis of standard samples. For a standard sample, the concentrations of all elements and the sputtering rate must be known. When line intensities of all elements present in the sample were measured and the corresponding emission yields are known, the element concentrations of unknown samples and the sputtering rate can be determined using Equation 19.1. These concentrations can be converted into the depth of the craterz if we assume that the density ρ of the sample is an average of the density of the pure element densities ρ_i:

$$\rho = \sum (c_i \cdot \rho_i) \tag{19.2}$$

$$z = \sum \left(\frac{q}{\rho} \cdot A \cdot \Delta t \right) \tag{19.3}$$

where q is the sputtering rate of the sample, Δt is sputtering duration, and A is the sputtering area.

19.2.3.2 Glow-Discharge Mass Spectroscopy

GD-MS is a unique quantitative technique, exhibiting low matrix dependence and a very high linear range compared with other solid-state analytical techniques.

In addition, the relative sensitivity factors (RSFs) are matrix independent over a wide range of concentrations, which is an advantage, especially when determining very low concentrations. The RSF – a term used by VG9000 users and software – simply means the reciprocal slope of a virtual calibration curve (relative sensitivity coefficient (RSC) is therefore a more correct term) based on the theory that the calibration curve is linear and does not have an intercept [23]. All of these facts allow for performing GD-MS analyses routinely by using typical RSFs determined on various matrices. Such an RSF data set is called the standard RSF. RSF data in this set is normalized to Fe, that is, the RSF for Fe equals 1. Because the RSFs for various elements vary only within about one order of magnitude, semiquantitative analysis becomes possible even without any standard and calibration:

$$\mathrm{RSF}_{x/y} = \frac{I_y}{I_x} \cdot c_{x/y} \tag{19.4}$$

where I_x is the ion intensity (corrected for ion abundance) of element x and $c_{x/y}$ is the certified concentration of element x in matrix y of the calibration sample. The normalization of the analyte- and matrix-specific RSF is performed in the following way:

$$\mathrm{StdRSF}_x = \frac{\mathrm{RSF}_{x/y}}{\mathrm{RSF}_{\mathrm{Fe}/y}} \tag{19.5}$$

where StdRSF_x is the standard RSF of element x normalized to Fe, that is, $\mathrm{RSF}_{\mathrm{Fe}} = 1$. The standard RSF set contains a large list of standard RSFs for many elements from experimental results. Finally, for the quantification of an analytical result, the standard RSFs are applied as follows (for the example of determining the Na concentration in a Si matrix):

$$c_{\mathrm{Na/Si}} = \frac{I_{\mathrm{Na}}}{I_{\mathrm{Si}}} \cdot \frac{\mathrm{StdRSF}_{\mathrm{Na}}}{\mathrm{StdRSF}_{\mathrm{Si}}}. \tag{19.6}$$

19.2.4 Applications

19.2.4.1 Glow-Discharge Optical Emission Spectroscopy

Figure 19.3a shows GD-OES in-depth elemental distribution profiles from a $Cu(In,Ga)Se_2$ thin film on Mo-coated glass substrates acquired by means of pulsed rf-GD. In Figure 19.3b, these profiles are given quantified according to the procedure described in Section 19.2.3.1. Layers of $CuInSe_2$ and $CuGaSe_2$ on Mo-coated glass substrates were used as standards. The results of the quantification were confirmed by means of XRF results (measuring the integral compositions of the $Cu(In,Ga)Se_2$ layer). The gradients of Ga and In in the layer show a good agreement with energy-dispersive X-ray diffraction [24] (see Chapter 13.5 for an introduction) and AES measurements (see Section 19.4.7).

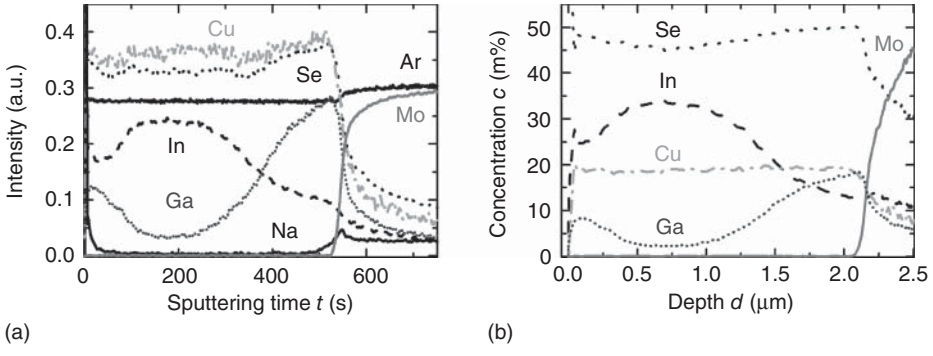

Figure 19.3 Measured (a) and quantified (b) in-depth elemental distribution profiles from a Cu(In,Ga)Se_2/Mo/glass stack using $U_{peak-peak}$ 1000 V, 3.5 hPa, 350 Hz, 7% duty cycle.

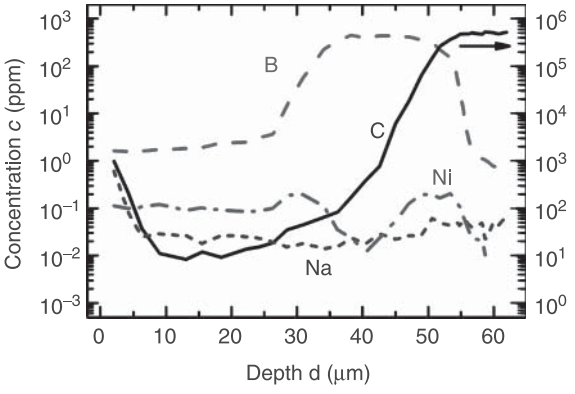

Figure 19.4 Trace and matrix concentrations of a Si-layer system on a SiC substrate (C concentration scaled by the right axis).

19.2.4.2 **Glow-Discharge Mass Spectroscopy**

Figure 19.4 shows a system of Si layers on a SiC substrate acquired with continuous dc at 800 V and 6 mA on a VG9000 instrument with concentration distributions from ppb range for impurities and doping elements together with matrix concentrations of Si and C.

Figure 19.5 shows an example of the capabilities of a pulsed dc-GD-MS source on an ElementGD instrument (900 V, 1.0 kHz, 50 μs pulse width, 295 ml/min Ar) for matrix- (a) and trace-element distributions (b) in two 2.5 μm thick layers on Mo-coated glass substrates from different $CuInS_2$ deposition runs. These two $CuInS_2$ layers do not exhibit a large difference in matrix-element distributions but large differences in trace-element distributions. Since only dc-GD-MS was used, analyses of the Mo layer and of the glass substrate were not possible.

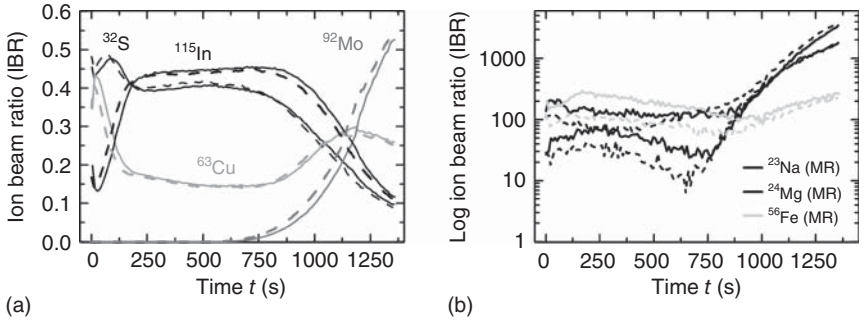

Figure 19.5 (a) Matrix-element distributions, given in terms of ion-beam ratio concentrations, from two $CuInS_2$/Mo/glass stacks (solid and dotted lines) analyzed by pulsed dc-GD-MS and acquired at mass resolution ($m/\Delta m = 4000$). (b) Trace-element distributions of the identical multilayer stacks. Note that the time t is related to the depth of the sputtering crater.

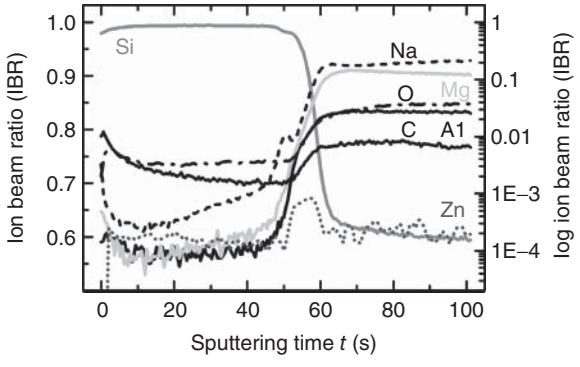

Figure 19.6 rf-GD-TOF data from a 100 nm Si layer on a glass substrate, ion-beam ratio of trace elements to the sum of all measured elements (matrix element Si: linear scale – left, all other elements: log scale – right), 50 W, 1.8 ms pulse length, 45% duty cycle.

Figure 19.6 shows the analysis results obtained on a thin Si layer (100 nm) on a glass substrate, measured by a prototype rf-GD-TOF system [25], exhibiting also signals from the interface between Si and glass, as well as from the glass substrate. Increased intensities of Zn and Na signals are found in the interface region between Si and glass. The analysis of this transition into the nonconductive substrate glass and of the glass itself is only possible since rf-GD could be used.

19.3 Secondary Ion Mass Spectrometry (SIMS)

SIMS [26, 27] is one of the most sensitive composition depth profiling techniques available. In many cases, ion count rates may exceed 10^9 counts/s for pure

elements with background signals of less than 1 count/s. Thus, it is possible under these analysis conditions to detect part per trillion level impurities in some cases. Sensitivities in the part per million range are routine for almost all elements. Even difficult species such as N can be detected in the form of molecular ions, and inert gases such as Ar can also be measured. Furthermore, SIMS can provide quantitative depth scales with good accuracy based on sputtered crater depth measurements. Because virtually every ion emitted from the surface can be detected, very slow sputtering rates can still permit useful analyses. The result is that SIMS can also be operated in a "static" mode, in which there is effectively no sputtering of the surface (only a fraction of a monolayer is removed). This allows near-surface analysis without alteration of the composition. Many higher-end instruments also provide the ability to map the location of individual atoms on the probed surface with micron-scale (and sometimes submicron) resolution. SIMS is best for analyzing trace impurity depth profiles in known matrices or measuring relative changes in a matrix constituent in the absence of major changes in the chemistry of the matrix.

19.3.1 Principle of the Method

SIMS is a method in which ionized species are sputtered from a sample surface into vacuum and accelerated by an electric field. Energy and mass of these species are then analyzed and detected with high efficiency. Given the high efficiency of the ion detector and the probability of an atom leaving the surface as an ion, it is possible to detect very small impurity concentrations in a solid. The technique can often provide an image of the surface from the detected ions and can measure molecular species, in some instruments to very high masses. A typical SIMS instrument is shown schematically in Figure 19.7.

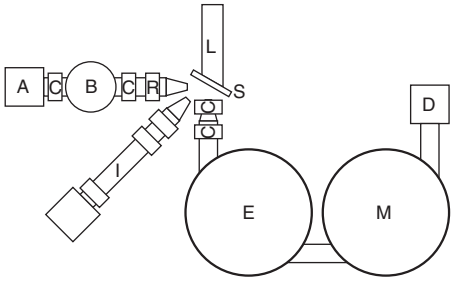

Figure 19.7 A schematic illustration of a typical SIMS instrument. The various parts shown are as follows. (A) gas source, (B) optional mass analyzer for the primary ion beam that sputters the sample, (C) magnetic or electrostatic lenses to focus the primary beam, (D) ion-detection electronics (usually a multichannel plate, electron multiplier, or Faraday cup), (E) energy analyzer (usually electrostatic), (I) optional depth profiling sputter gun (for time-of-flight instruments), (L) sample introduction load-lock, (M) mass analyzer (time-of-flight, magnetic sector, or quadrupole mass spectrometer), (R) raster plates to deflect the primary ion beam across the sample, and (S) sample.

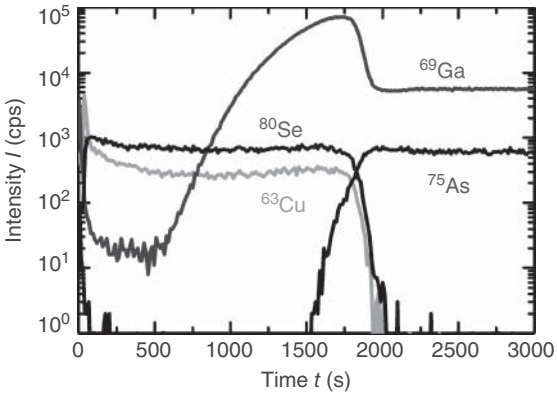

Figure 19.8 A typical SIMS profile for a single-crystal epitaxial layer of Cu(In,Ga)Se_2 on GaAs. Note the change in signal intensity for Ga between the Cu(In,Ga)Se_2, which contains only about 5 at.% Ga, and the GaAs which is 50 at.% Ga. The change is because the ion yield for Ga from GaAs is much lower than for Ga in Cu(In,Ga)Se_2.

The method for removing species from the sample surface is sputtering, generally by use of an ion beam rastered across the surface. This beam can be composed of electropositive (e.g., Cs^+), electronegative (e.g., O_2^+), or inert gas (e.g., Ar^+) ions. The electronegativity of the sputtering ion increases the yield of ions of the opposite electronegativity. An exemplary SIMS depth profile from a Cu(In,Ga)Se_2 layer on GaAs single-crystal substrate is shown in Figure 19.8.

The primary methods for measuring the sputtered species mass include TOF, magnetic sector, or quadrupole mass spectrometers. In all cases, kinetic energy is measured first, for example, by deflection by an electric field through an aperture. Once the kinetic energy of the ion is known, the charge-to-mass ratio can be determined. In the TOF method, the mass is found based on the ion velocity determined by the kinetic energy, E, as $E = 1/2mv^2$ where m is the ion mass and v is the velocity of the ion. The energy is determined by the secondary ion accelerating field. From the time required for the ion to emerge from the sample to the detector, its mass can thus be calculated. For this method, it is necessary that the analyzed ion beam is pulsed very rapidly such that the time at which an ion is emitted from the sample can be determined very precisely. This requires a very-high-performance ion gun operating on a very small duty cycle. Therefore, a second ion gun is applied for the sputtering, removing sample ions down to a fixed depth (forming a crater), and no analysis takes place during that sputtering duration. Note that TOF-SIMS operates essentially as static SIMS between sputtering steps.

The magnetic sector mass spectrometer uses the cyclotron radius due to the Lorentz force of the ion moving at a known velocity in a known magnetic field. Thus, by detecting ions at a given angle, the mass-to-charge ratio is determined. In such an instrument, the magnetic field is typically swept to select a mass while keeping the ion energy constant. Finally, a quadrupole mass spectrometer includes

an electromagnetic field that permits ions of a given mass and energy to pass through an rf electromagnetic field while rejecting other ions. The TOF instrument has a high mass resolution (sufficient to distinguish between $^{30}Si^{1}H$ at a mass of 30.9816 atomic mass units (AMU) and ^{31}P at 30.97376 AMU) and the advantage of recording the entire mass spectrum for every analysis pulse. For the magnetic sector approach, high resolutions may be achieved, similar as for the TOF instruments with in average very high signal levels and consequently excellent detection limits. The lowest mass resolution and the highest detection limit exhibit the quadrupole mass spectrometer.

A variant technique is secondary neutral mass spectrometry (SNMS) [28–30]. In this method, a highly ionized gas plasma is generated near to the sample surface for the purpose of ionizing neutral species sputtered from the sample. In the case of SIMS, only a small fraction (a few percent at most) of the sputtered species leaves the surface as ions. Also, the ion yield fluctuates substantially in a broad range from 10^{-5} to few percent. By ionizing sputtered neutral species, the fraction of species ionized is increased to nearly 100%, and thus, the sensitivity of the technique is enhanced correspondingly. Furthermore, if the ionization probability were independent of the composition of the sample surface, many of the artifacts of conventional SIMS associated with ion yield fluctuations may be avoided. While SNMS is an attractive approach, it is important to realize that the ionization probability in a plasma changes considerably when metal ions of various species are introduced into the gas. Therefore, while many ions are produced, the ion yield has strong matrix effects, and the yield changes based on what was recently sputtered from the sample surface. At the same time, the transmission of ions through the gas phase and into the detector is not as high as for SIMS, that is, the sensitivity of SNMS is not necessarily improved.

19.3.2 Data Analysis

Analysis of SIMS data begins with the instrument setup, in order to eliminate instrumental artifacts. Some of these artifacts include changes in secondary ion yield, interferences, and degradation of depth resolution by displacement of atoms during sputtering. A brief summary of some of these issues is presented in the following.

Two typical mass spectra obtained by SIMS from a $Cu(In,Ga)Se_2$ thin film are shown in Figure 19.9. Comparison of the two mass spectra in Figure 19.9 reveals that there are many signals that result from molecular interferences. For example, the large number of peaks beyond In at masses 113 and 115 AMU is due to molecular species. One may take advantage of the fact that an atom sputtered from the sample surface can have up to a few tens of electron volt of kinetic energy in addition to the energy provided by the extraction lens, which accelerates the ions away from the sample surface. Molecular species exhibit much smaller kinetic energies because attempting to sputter a molecule with a high kinetic energy generally leads to its fragmentation. Therefore, by closing the spectrometer apertures (field

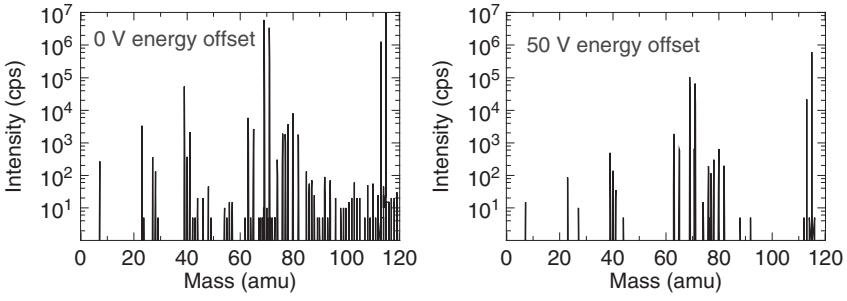

Figure 19.9 Two mass spectra from $Cu(In,Ga)Se_2$ thin films. The mass spectrum (a) was acquired under conditions maximizing sensitivity, while the acquisition of spectrum (b) was optimized for eliminating molecular interferences. The additional peaks in figure (a) are mostly compounds of elements in spectrum (b) with Na and O.

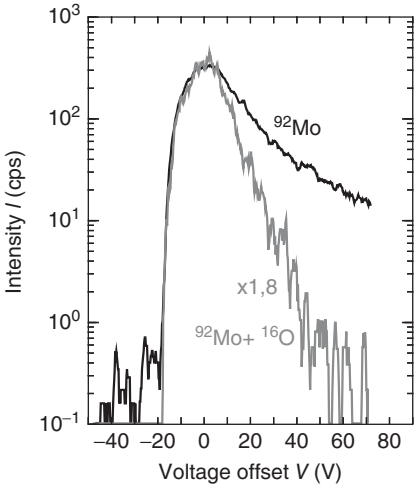

Figure 19.10 Energy spectra for the 92 AMU atomic species ^{92}Mo (gray) and the 108 AMU molecular species $^{92}Mo+^{16}O$ (scaled such that the maximum signals are roughly equal). Note that at about 60 V offset, the signal intensity from atomic species is increased by a factor of 100 relative to that of the molecular species.

and contrast diaphragms and energy slit), the detection of atomic species can be favored over molecular species. However, this also reduces sensitivity. Examples of energy spectra for an atomic and a molecular species are shown in Figure 19.10. Adjusting the energy analyzer to an energy greater than what the extraction lens provides is selective for atomic species. This method is not necessary with an TOF instrument because it has such a high mass resolution that molecular species can be easily separated from atomic species.

The output of a SIMS analysis is quite simple, plotting number of counts of ions per second as the sample is sputtered. However, the secondary ion yield depends significantly on the chemistry of the surface from which the ion is emitted, the sputtering rate depends on the matrix being analyzed, and complex changes can take place that can locally alter the sputtering yield at an interface. In the exemplary depth profile shown in Figure 19.8, the profiles from the volume of the

$Cu(In,Ga)Se_2$ thin film are relatively smooth for each matrix element. However, close to the interface between and the GaAs substrate, one can see the Ga signal at the back of the $Cu(In,Ga)Se_2$ film, well above the steady-state level in the GaAs. This is the case in spite of the fact that the $Cu(In,Ga)Se_2$ film contains at most 10 at.% Ga, while the substrate is 50 at.% Ga. The reason for the change is the ion yield, which is much higher for Ga in $Cu(In,Ga)Se_2$ than for Ga in GaAs. There is no way to eliminate such ion yield changes. One may correct for such a change if the ion yield is determined separately in each matrix. By calculating the fraction of the two matrices present, one can adjust the count rate in order to reduce the effect.

Because the ion yield depends upon the number of electronegative and electropositive species, sputtering with one species or the other changes the yield [31, 32]. A clean surface that has not been analyzed contains few of the sputtering beam species. As sputtering begins and large concentrations of sputtering atoms are implanted into the surface, the ion yields will change [33]. The onset of sputtering also typically amorphizes the sample, which alters ion yields. Likewise, there are strong ion yield effects typically found in the presence of variable concentrations electronegative or electropositive species in the sample. For example, O in samples profiled using a Cs^+ ion beam affects ion yields, typically increasing the yield of electropositive species and decreasing the yield of electronegative species. The details of how to detect and avoid such interferences are too lengthy to describe here and in any case are an art rather than a science. However, altering the depth profile conditions, for example, by changing the primary ion species and the polarity of the detected species and by looking for common elements that cause yield changes such as O, is a big help. In order to really quantify the data, one requires a relatively constant composition area in a sample and a known standard profiled immediately before or after the sample in question for comparison.

19.3.3 Quantification

Quantitative analysis of SIMS data can – in theory – be conducted based on tabulated ion yields. However, this is generally unreliable. As described earlier, the ion yield varies considerably from one matrix to another, with the presence of impurities (especially electropositive or electronegative elements) and with the details of the analysis condition. This may even extend to the location within a sample holder in which a sample is mounted (because of fluctuations in the secondary ion accelerating field). Therefore, it is necessary for quantitative analysis to perform all measurements under as identical conditions as possible. This often means measuring a standard sample immediately before or after measuring a test specimen. Even so, most SIMS operators will be lucky to obtain quantitative compositions to within a factor of 2. The ideal way of quantifying low-concentration impurity elements is to work with a standard sample into which a known concentration of this impurity element has been implanted. This approach provides quite

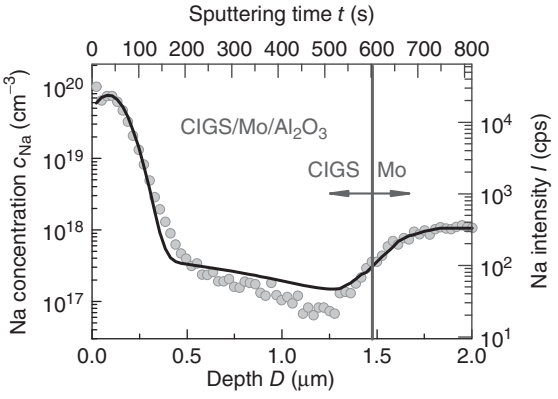

Figure 19.11 A SIMS composition depth profile (circles) of Na in a polycrystalline $Cu(In,Ga)Se_2$ thin film and a fit to the data based on a Gaussian curve and a baseline count rate in the bulk of the sample.

a reliable ion yield standard for a given analysis. An example of an implant profile from a $Cu(In,Ga)Se_2$ thin-film sample is shown in Figure 19.11. Both atomic concentrations and depth were quantified.

From the dose of the implant, the height of the Gaussian can be calculated in atoms per cubic centimeter, and the data thus quantified. The depth scale can also be determined from the peak of the implant, as done in the example here, although it is easier to measure the crater depth with a profilometer. Note that the depth scale ends in the $Cu(In,Ga)Se_2$ thin film because the sputtering rate of Mo is different from that of $Cu(In,Ga)Se_2$ and must be calibrated separately. This is best done by measuring craters of several depths, some ending in the $Cu(In,Ga)Se_2$ thin film and some in the Mo layer.

19.3.4 Applications for Solar Cells

SIMS is used extensively in solar cell manufacture in order to detect the presence of impurities, to determine doping profiles, to analyze interdiffusion at heterojunctions, and to acquire compositional depth profiles of matrix elements. Considering the application of SIMS in some of the major solar cell technologies, we may expect the following. In crystalline Si solar cells, the primary application is determination of the in-depth elemental distributions of dopants. During process development, impurity detection is important, but usually Si processing can (must) not introduce significant numbers of impurities. O and C are common trace elements in Si and are easily detected in SIMS in a mode detecting negative secondary ions. In amorphous Si solar cells, impurity detection and characterization of dopant distributions, studies of the movement of dopants during processing, and profiling of the complete structure of multijunction structures are important. Research has shown that in extremely high-efficiency solar cells made

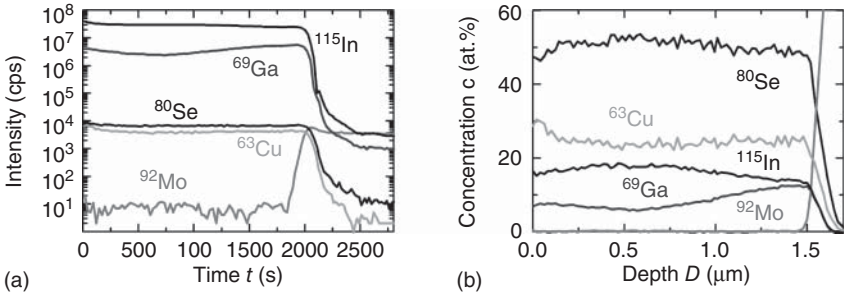

Figure 19.12 (a) Raw SIMS depth profiles from a Cu(In,Ga)Se_2 polycrystalline film on Mo-coated glass and (b) this SIMS data as quantified depth profiles. The ion yields for the various elements were quantified by comparison with energy-dispersive X-ray and X-ray photoelectron spectroscopy measurements, giving the integral concentrations of the matrix elements in the sample.

by chemical vapor deposition, in some cases, the growth process may result in dopant diffusion and interdiffusion of layers. Proper choice of the growth process may reduce these effects substantially. SIMS is an important method used to study such changes in dopant and matrix-element distributions. In CdTe devices, SIMS is used for characterizing the results of processes such as the $CdCl_2$ treatment. Finally, SIMS has been used regularly to study elemental distributions in Cu(In,Ga)Se_2 solar absorbers on Mo/glass substrates (see Figure 19.12). SIMS can also be used to resolve questions concerning, for example, diffusion of beneficial impurities such as Na [34, 35] and harmful impurities such as Fe [36] into the absorber from substrates such as soda-lime glass and stainless steel.

19.4 Auger Electron Spectroscopy (AES)

19.4.1 Introduction

AES is an analytical technique applied in order to determine the elemental composition and, in any case, to gather information on chemical bonding from the surface region of a solid material. Compositional depth profiles can be obtained by combining AES with ion-beam sputtering. AES is broadly used for an extensive variety of materials applications, especially those requiring surface sensitivity and high spatial resolution.

19.4.2 The Auger Process

The emission of electrons as a result of the ionization process shown in Figure 19.13 was discussed in 1922 by Meitner [37] and described in 1925 by

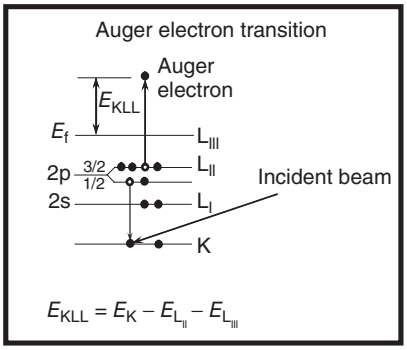

Figure 19.13 Schematics of an Auger electron emission process.

Auger [38], who observed their tracks in a Wilson cloud chamber and correctly explained their origin. Figure 19.13 shows the atom immediately after K-shell ionization by an incident primary particle. The Auger process starts when an electron from an elevated energy state occupies the empty state in the K shell (as shown in Figure 19.13 for an L electron). The energy released by this transition is either emitted as a photon or given to another L electron. If this energy is sufficient, an electron can emerge from the atom. The process described earlier is termed a KLL Auger transition. The kinetic energy of an Auger electron is equal to the energy difference of the singly ionized initial state and the doubly ionized final state. For an atom of atomic number Z undergoing an Auger process involving the levels WXY, the Auger electron kinetic energy is given by the difference in the binding energies of energy levels W, X, and Y. Therefore, the resulting kinetic energy E_{KLL} is described by $E_{KLL} = E_K - E_{L_{II}} - E_{L_{III}}$, whereas all energies are referenced to the Fermi level E_f. The energies and relative intensities of WXY Auger transitions (KLL, LMM, and MNN) show a systematic behavior with increasing atomic number Z. In heavier elements, which exhibit more energy levels, more Auger transitions are possible.

Auger emission can be initiated bombarding a sample by electrons, X-rays, or ions. However, Auger instruments are typically equipped with electron guns because electron beams can be focused to very small areas.

19.4.3 Auger Electron Signals

As outlined earlier, Auger electrons are characterized by their kinetic energies. They can be detected by measuring the energy distribution $N(E)$ of secondary electrons, where E is the electron energy. The Auger electrons appear as prominent features together with small loss peaks on the $N(E)$ curve among the various secondary electrons ejected. Most loss peaks obtained in secondary electron spectra are either plasmon or ionization losses (plasmons are the result of collective oscillations of valence electrons against the positive atom cores).

Auger electrons may be emitted from all elements except for H and He, and therefore, the element may be identified by its Auger spectrum, that is, by the

energy positions of the peaks attributed to the transitions WXY mentioned earlier. The concentration of an element is related to the intensity of its peaks. Due to the dependence of the atomic energy levels, the energy-loss spectrum, and the valence-band structure on the local bonding, the energy positions and the shapes of Auger peaks are a result of the chemical environment of the atom. These features in the Auger electron spectrum may be interpreted accordingly.

19.4.4 Instrumentation

AES is performed in an ultrahigh-vacuum system in order to minimize surface contamination during analysis. Gas molecules colliding with the surface would deposit roughly one atomic monolayer per second at 1.3×10^{-4} Pa, assuming all the molecules stick to the surface. However, sticking probabilities are usually much smaller than 1, especially after adsorption of the first monolayer. Therefore, Auger analysis should be performed at pressures $p < 1 \times 10^{-6}$ Pa, in order to inhibit reactions with adsorbates, which may alter the surface composition.

In 1967, Palmberg [39] and, separately, Tharp and Scheibner [40] reported on the measurement of Auger electrons by using a low-energy electron diffraction system. Harris [41, 42] showed the advantage of using the first derivative of the direct spectrum in order to identify Auger peaks on the large secondary electron background. In 1969, Palmberg *et al*. [43] introduced the cylindrical mirror analyzer (CMA) and obtained Auger spectra with improved sensitivity and with subsecond data acquisition duration.

Nowadays, an Auger system is equipped with an electron gun emitting the primary electron beam for Auger electron excitation, an electron energy analyzer and detector measuring the emitted electrons from the specimen, a secondary electron detector acquiring secondary electron images, an ion gun for surface cleaning and for performing depth profile analysis, and a sample manipulator to locate the area of interest at the analyzer focal point.

The electrons are emitted either from a LaB_6 cathode (older systems) or from a Schottky field emitter. Schottky field emission sources may provide 1 nA of current into probe diameters of about 10 nm (electron-beam energies $E_p = 10$ keV), which is sufficient for Auger analysis if channel plates for signal detection are used.

The most commonly used energy analyzers are the CMA shown in Figure 19.14 or the concentric hemispherical analyzer (CHA), which is described in Section 19.5.2.

The basic construction of the CMA consists of a pair of coaxial cylinders with entrance and exit slits and a detector. An electric field between the two cylinders deflects electrons toward the detector to an extent dependent on their kinetic energy. Scanning the electric field sweeps electrons of different energies across the detector, thus generating the spectrum. The electron gun is located coaxially within the CMA. The advantage of this arrangement is a minimization of shadowing in case of rough surfaces. The CMA is a suitable tool for investigating samples

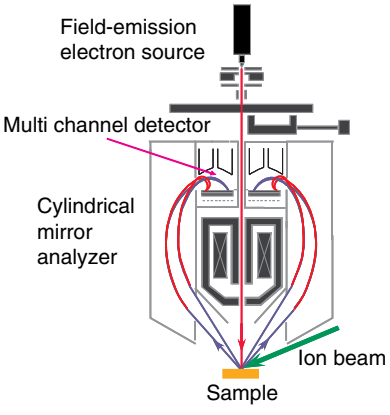

Figure 19.14 Scheme of the cylindrical mirror analyzer. (Reprinted with permission from Physical Electronics GmbH.)

with rough surfaces. The intensity response of a CMA is relatively constant as a function of sample angle over a wide range of angles.

An important parameter of all energy analyzers is the resolution ΔE, which is generally determined by the full width at half maximum (FWHM). ΔE varies proportionally with the energy E, and for a given analyzer geometry, the relative resolution, $\Delta E/E$, is constant. The relative energy resolution of CMAs is between 0.3% and 1.2%. As mentioned earlier, the FWHM of peaks measured by the CMA increase with E; however, the angular acceptance of electrons is defined by the input slit geometry and remains constant with energy. Therefore, the measured spectrum cannot be expressed by $N(E)$ but is described by the product E times $N(E)$.

The detector is usually a single-channeltron electron multiplier or a microchannel-plate electron multiplier. More detailed additional information about the CMA as well as other energy analyzers is available in the literature [44].

In Figure 19.15a the $EN(E)$ surface spectrum of the active layer of a solar cell is presented. As mentioned in Section 19.4.3, the various Auger peaks appear on

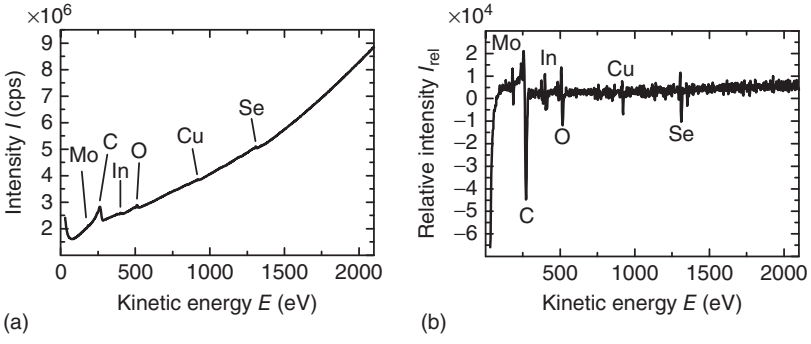

Figure 19.15 $EN(E)$ spectrum (a) and $E\,dN(E)/dE$ spectrum (b) of the top surface of a $CuInSe_2$/Mo/glass stack (exciting primary electron energy was 5 keV at 20 nA primary electron-beam current).

a varying background. Figure 19.15b shows the same spectrum after differentiation, which may be carried out either electronically (older systems) or by applying a suitable algorithm such as the Savitzky–Golay filter [45]. The Auger peaks in the filtered spectrum (Figure 19.15b) appear as characteristic features on a low varying background. The peak intensity can be easily determined from the distance between peak maximum and peak minimum. Identification of Auger peaks will be commonly carried out by comparing peak energies and peak shapes with the standard spectra collected in Ref. [46].

19.4.5
Auger Electron Signal Intensities and Quantification

Figure 19.16 illustrates the effects within the sample created by the incident electron beam. Size and shape of the interaction volume depend on the energy of exciting primary electrons and the atomic number of the sample material. Auger electrons are created both in the near-surface region and within greater depths of the analyzed sample. However, only those electrons which are excited within the near-surface region can escape the sample. Electrons that are scattered by interactions with the electrons of the sample atoms incurring energy losses form loss structures on the low energy side of the Auger peaks, and electrons experiencing random and multiple loss processes form the continuous background. The distance an electron travels without energy loss is referred to as λ, the inelastic mean free path. It specifies the detected volume from which Auger electrons can escape the sample. λ depends on the material and the energy E_{WXY} and it is independent of the energy of the primary electrons. Experimentally determined values are presented in Ref. [47]. The smallest λ values occur near 75 eV. Between 100 and 2000 eV, λ increases approximately as $E^{1/2}$ but rises more rapidly thereafter, and below about 75 eV, λ again increases. Low-energy electrons can escape from only the first several atom layers of a surface because

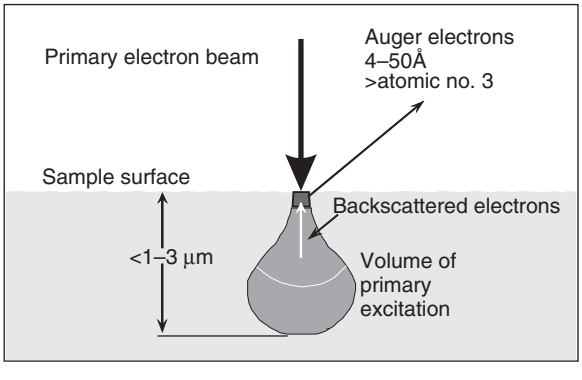

Figure 19.16 Electron beam–sample interaction. (Reprinted with permission from Physical Electronics GmbH.)

they have short mean free paths in solids, for example, they are strongly absorbed by even a monolayer of atoms. This property gives AES its high surface sensitivity.

Two further important factors are the ionization cross section σ and the backscattering factor r. σ depends on the energy of the primary electrons E_p, on the critical energy for ionization E_W, and on the ionized species. Maximum ionization should occur near to about $E_p/E_W = 3$. However, extra ionization caused by backscattered electrons increases the ratio to about $E_p/E_W = 6$. The backscattering factor r depends on E_p and on the atomic number Z. For increased E_p and Z values, an enhanced ionization contribution is obtained due to the effect from backscattered electrons.

Surface roughness is also an important issue. The escape probability of electrons from rough surfaces is smaller than for flat ones. Electrons emerging from a rough surface may be reabsorbed by the surrounding material. Using an analyzer with a large acceptance angle such as a CMA, this roughness effect is minimized [1].

19.4.6 Quantification

Various procedures exist for quantifying Auger peak intensities. A quantification approach commonly used in the AES community introduces an atomic sensitivity factor S_i [39] of an element i. The atomic concentration c_A of a given element A in a sample can then be expressed as

$$c_A = (I_A/S_A)/\Sigma_i(I_i/S_i), \tag{19.7}$$

where I_A is the Auger intensity of WXY transition of element A and I_i is the Auger intensity of WXY transition of element i.

Equation 19.7 can only be applied if minor variations of r, λ and the Auger transition probability γ of the WXY transition appear, such as for homogeneous samples. For these samples, a set of RSFs may be used, determined for each beam voltage, normalized to a reference material [39].

However, in the case of alloys or compounds, sensitivity factors determined on pure elemental standard samples may lead to incorrect results. The atomic density of element i, N_i, r, and λ can sometimes vary considerably, and also changes in peak shape, induced by the changed chemical environment of the emitting atom, can appear. In that case either sensitivity factors determined on samples of the same composition or correction factors, as proposed in the literature [48, 49], have to be applied for quantification.

19.4.7 Application

If the electron beam is scanned across the sample surface along with a secondary electron detector, corresponding images can be acquired, which is useful when localizing the region of interest on the sample surface. Auger

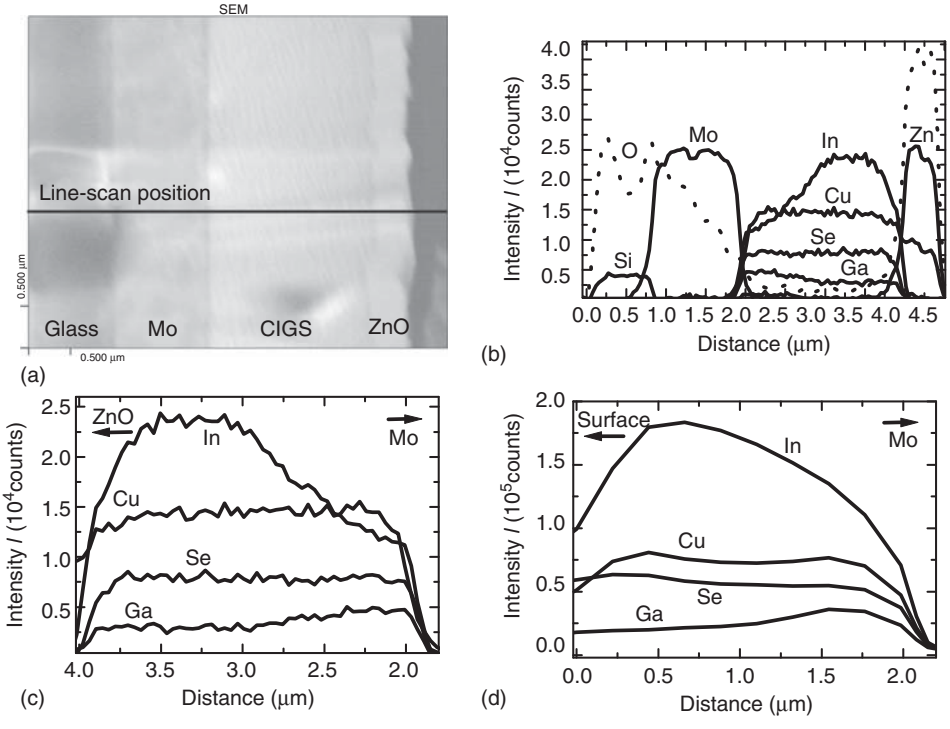

Figure 19.17 (a) Scanning electron micrograph from a cross section of a glass/Mo/Cu(In,Ga)Se_2 (CIGS)/CdS/ZnO stack. (b) Line scan across this stack by means of scanning Auger electron spectroscopy. (c) Detail of the line scan presented in (a). (d) Auger in-depth elemental distribution profiles of the layer of the identical stack, performed at 5 keV Ar^+ ion sputtering.

line scans or maps can be recorded by measuring the intensity of a certain Auger peak while scanning the electron beam across a region of interest. In Figure 19.17a–c, a secondary electron image from a cross-sectional sample of a glass/Mo/Cu(In,Ga)Se_2/CdS/ZnO stack and the corresponding line scans across this stack are presented (the distribution profiles shown in Figure 19.17c are details of the ones given in Figure 19.17b). A primary electron beam of 10 keV at 1 nA was applied.

The ZnO layer appears on the right-hand side of the line scan (Figure 19.17b), followed by the Cu(In,Ga)Se_2 thin film, the Mo layer, and the glass substrate. Since the glass substrate is an electrically insulating material, charging effects caused by the primary electron beam appear. Charging can be reduced substantially either by applying low primary beam energies and currents, by tilting the sample to a grazing-incidence angle of the primary electron beam, or by neutralizing charging by low-energy ion bombardment. In the present case, the sample was tilted (60° to the surface normal). Additionally, the surface was flooded by low-energy ions (70 eV).

When applying ion-beam sputtering on the identical thin-film stack, in-depth elemental distribution profiles were obtained. Commonly, alternating AES and sputtering is performed. The resulting profile is shown in Figure 19.17d. The analysis was performed applying 5 keV at 5 μA Ar^+ ion sputtering as well as 5 keV primary electron-beam excitation ($I = 20$ nA). Intensity quantification was not possible since no appropriate sensitivity factors for the Cu(In,Ga)Se_2 layer were available. The depth was calculated from the sputtering time by introducing the sputtering rate, which was determined from in-depth elemental distribution profiles of a standard layer of known thickness.

The in-depth profile agrees well with the line scan acquired on the cross-sectional sample, shown in Figure 19.17c. While Cu and Se signal intensities are constant throughout the layer, those of Ga and In signals exhibit gradients already found by GD-OES and SIMS (see Sections 19.2.4.1 and 19.3.4). The decrease of the In, Cu, Se, and Ga signals at the surface is caused by covering the C contamination layer.

Substantial roughness may be found at the bottom of the sputter crater. The results are a decrease of the depth resolution and intensity structures as well as a broadening of signals at interfaces in the thin-film stack. Furthermore, strong roughness leads to a decrease of intensities. These effects can be clearly seen in Figure 19.17d, where the structured course of In, Cu, Se, and Ga signals is smoothed, their intensities are lower than in the line scan analysis, and the signals at the Cu(In,Ga)Se_2/Mo as well as Mo/glass interfaces are slightly broadened. In this context it should be noted that roughness may be minimized by rotating the sample during sputtering.

19.5 X-Ray Photoelectron Spectroscopy (XPS)

19.5.1 Theoretical Principles

XPS or electron spectroscopy for chemical analysis (ESCA) is probably one of the most widely used surface science techniques. It utilizes X-ray photons to ionize atoms and analyzes the kinetic energies of the ejected photoelectrons. As the core electron binding energies of the elements are distinctive, photoelectron spectroscopy can be a valuable tool in determining material composition. Furthermore, chemically inequivalent atoms of the same element are known to show measurably differing binding energies. This "chemical shift" information can be most useful in investigating surface reactions or changes in the state of the surface, as induced by, for example, oxidation.

At its heart, XPS is based on the photoelectric effect outlined by Einstein in 1905 [50] and was developed by Siegbahn *et al*. in the 1950s and 1960s [51]. The Einstein relationship relates the kinetic energy of the emitted photoelectron E_{KE} excited by a photon of energy $h\nu$ to the binding energy of the electrons in the atom

E_{BE} referenced to the vacuum level. For photoemission from solids, the binding energy is referenced to the Fermi level of the material, resulting in Equation 19.8:

$$E_{KE} = h\nu - E_{BE} - \phi \tag{19.8}$$

where ϕ is the work function of the solid. Equation 19.8 assumes that the photoelectrons suffer no change in energy between emission from the surface and detection in the spectrometer, that is, the process is elastic. In practice, the loss of energy due to the work function of the spectrometer also needs to be included in Equation 19.8. This offset is typically handled by the instrument data system internally. If the experiment is conducted by use of incident photons of much greater energy than the work function, the kinetic energy spectrum will correlate directly to the discrete binding energies of the electrons in the solid. However, there are a finite number of electrons that lose energy due to inelastic collisions in the solid. This results in the photoelectron peaks detected against a background increasing from high to low kinetic energy [52].

Once an incident photon has interacted with a solid and a photoelectron has been ejected, the solid is left with a vacancy in a core electron level. This is generally occupied by an electron from a higher energy level, and the subsequent deexcitation of the atom may occur by either emission of an Auger electron or X-ray fluorescence. The resultant spectrum is a combination of peaks attributed to photoelectrons and Auger electrons.

Figure 19.18a shows a typical wide-scan (or "survey") XPS spectrum, and Figure 19.18b a high-resolution scan of the Si2p region for a Si wafer coated with a thin oxide layer. The area under each peak in the spectrum is directly related to the amount of the substance present in the irradiated area. This allows standardless, quantitative analysis of the surface or thin film to be performed.

XPS is a surface-sensitive technique. The sensitivity toward surface atoms is due to the relatively short path that a photoelectron can travel before it is subject to an inelastic scattering process, that is, spectra are the product of atoms in

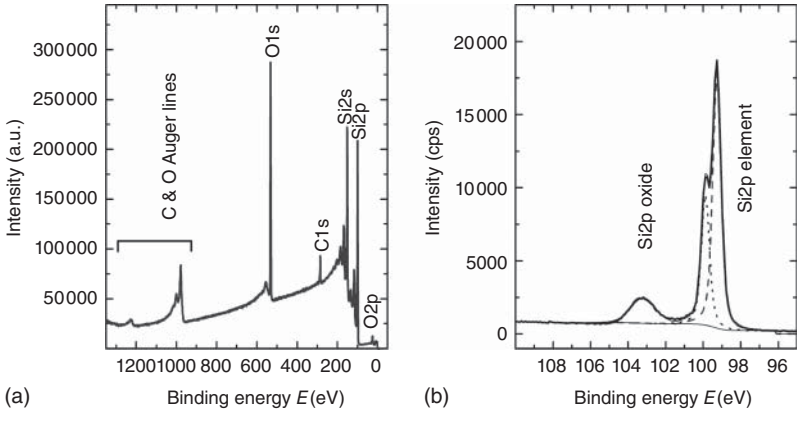

Figure 19.18 A typical XPS survey spectrum (a) and a high-resolution scan of the Si2p region (b) from a Si wafer sample, showing the chemical state information available.

the outer 10 nm of the sample surface. For the analysis of thin films, cycles of ion bombardment followed by analysis are performed, extending the depth that can be investigated to a few microns, with accurate determination of compositional changes at interfaces between layers, which is possible due to the narrow electron escape depth.

19.5.2 Instrumentation

A schematic of the typical internal components of an XPS system required for thin-film solar-cell analysis is shown in Figure 19.19. XPS analyses have to be performed in high or ultrahigh vacuum. Primarily this is to prevent the emitted photoelectrons colliding with gas molecules, which would significantly attenuate the signal. The vacuum also assists in increasing the time before an impurity-free surface adsorbs gas molecules from the background in the chamber sufficiently to influence the analysis.

The X-ray photon source used for the XPS experiment varies according to the desired resolution and power required, from simple, low-power X-ray "guns" to the use of synchrotron sources. Lab instruments generally have either a monochromated X-ray source, which are usually configured to expose the sample to only Al-Kα X-rays, or a nonmonochromated source. Modern instruments tend to have monochromated sources, which offer better spectral resolution, good sensitivity, and the possibility of focusing the beam on a smaller area. The X-rays are monochromated by reflecting the beam from a quartz crystal, which has a suitable Bragg constant to transmit the Al-Kα X-rays only.

Most instruments include a CHA for the accurate analysis of the kinetic energy distribution of the photoelectrons. Electrons are focused on the entrance of the analyzer by a series of lenses. A potential difference, called the pass energy, is applied across the two hemispherical plates which allows electrons within a narrow kinetic energy range to be transmitted through the analyzer. Electrons are collected at the exit by a detector, either channeltrons or a multichannel plate. XPS analyzers typically run in a constant energy mode, that is, the pass energy is fixed, and a retarding potential is applied before the analyzer slit in order to select the kinetic energy. By scanning the energy range, the spectrum is generated.

No special sample preparation is required for XPS. Both conducting and insulating samples can be analyzed. For conducting samples, the ejected photoelectrons

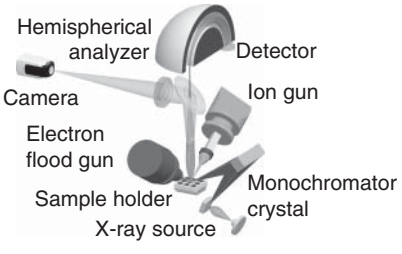

Figure 19.19 Schematic of a typical XPS instrument configuration. (The schematic of the K-Alpha XPS instrument used with kind permission from Thermo Fisher Scientific.)

are replaced by conduction from the ground through the sample holder. Insulating samples, such as thin-film solar cells deposited on a glass substrate, require an external source of electrons to prevent an excessive buildup of charge at the surface, which distorts the appearance of the spectrum. Electrons are typically supplied from a low-energy flood source, which generates a beam slightly larger than the analysis area with the aim of either neutralizing any buildup of charge or overcompensating by gas ions to eliminate excess negative charge, which may be present on the sample and deflect the flood gun beam.

The final component required is an ion source for removing surface material, forming a crater in which the chemical composition is measured. Ar^+ is the most commonly used ion, with typical acceleration energies in the range of 0.1 – 5 keV. A typical depth profile experiment is carried out by alternating spectral acquisition and periods of ion sputtering. The sample is usually rotated during the etching cycle in order to minimize sputter-induced roughness in the direction of the ion beam and to reduce the possibility of heavier elements migrating into lower layers, both of which can cause a significant reduction in depth resolution [1].

The main limitation of XPS is that the best possible spatial resolution using a lab instrument is around 3 µm. This is due to the twin difficulties of focusing the X-ray beam below 10 µm and the low signal level when operating the analyzer to give the ultimate spatial resolution of 3 µm. Acquisition times can also be large, with several hours required for depth profile experiments on large areas of interest or thick layers.

19.5.3
Application to Thin-Film Solar Cells

XPS can be applied to the analysis of the surface chemistry, layer compositions, and compositional gradients within thin-film solar cells. Figure 19.20 shows a

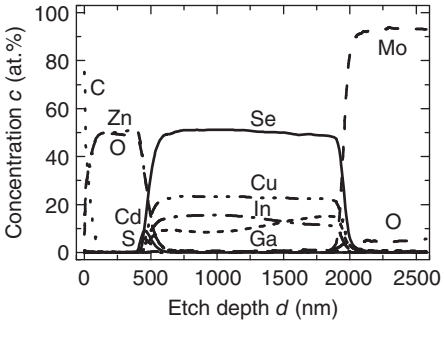

Figure 19.20 XPS depth profile of a $Cu(In,Ga)Se_2$ solar cell. The data was collected using a 150 µm X-ray spot (Al-Kα 1486.6 eV) and a 180° hemispherical analyzer fitted with a 128-channel detector. The sample was sputtered using 2 kV/2 µA Ar^+ ions, over a 2 mm × 4 mm area, and it was rotated during etching. The total acquisition time was 6 h.

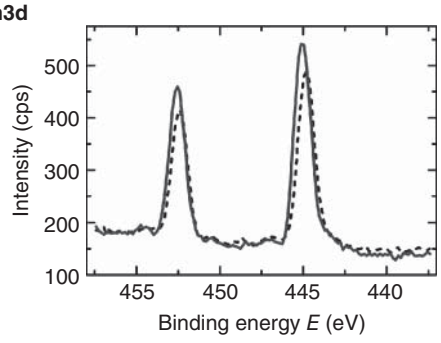

Figure 19.21 In3d spectra for regions near the CdS layer (dashed line) and near the Mo layer (solid line).

depth profile through a complete device, from the ZnO front contact to the Mo back contact. By initially considering only the variation in each elemental signal, it is possible to obtain direct quantification of the composition of each layer. The signals are quantified by measuring the area of a peak due to the emission electron from a particular orbital and normalizing it via an RSF based on the ionization potential of that electron in that element. There are two main groups of sensitivity factors, based either on calculation [53] or experimental observation [54]. The Scofield set is more widely used, as it covers the entire periodic table. This is of particular interest in the Cu(In,Ga)Se_2 layer, where the In and Ga elemental distributions can be measured with good depth resolution, which is of the order of a few tens of nanometers, and can be less than 3 nm (in this case the structure of each of the interfacial layers is quite rough, and so the interface resolution measured in this experiment is in the range 50–80 nm. Some variation in the ZnO stoichiometry is also evident from the elemental profile. These two examples demonstrate the rich information that can be obtained from a simple level of data processing.

By close examination of the spectra, it is possible to identify changes in chemical state. For example, at the interface of two layers, it is possible that there could be an interaction between components that influences the performance of a device. This interaction layer could be only a few nanometers in thickness but would be evident in several levels of the XPS depth profile.

Figure 19.21 shows In3d spectra from an area near the CdS layer and one near the Mo back contact. The small variation in peak position indicates that the chemistry at the two positions is slightly different. This is most likely to be due to the change in the [In]/[Ga] ratio between these two regions. Information such as this can indicate problems in the manufacturing process, such as unwanted oxidation (cf. the presence of a low level of oxygen detected in the Mo layer in Figure 19.20).

XPS depth profiling analysis is destructive, and accurate calibration of the etching rate through multilayered samples is challenging. Often depth scale calibration relies on another technique (e.g., an SEM cross section) or is based on the etch rate measured using a standard of known thickness, such as Ta_2O_5/Ta or SiO_2/Si.

The limit in the spatial resolution means that identifying the precise location of submicron surface defects is impossible and that rough interfaces will have an average depth resolution measured by the experiment.

Despite these limitations, XPS has proven to be an important technique for the investigation of elemental distributions in solar-cell devices, failure analysis, and quality assurance applications. Advances in instrument design and software capability have enabled significant reductions in acquisition time and detection limits. The ability to analyze samples with no special preparation steps required permits both initial research developments and finished devices to be measured. In summary, the ability to directly quantify the concentrations and subtle variations in the chemistry of material present, with extreme surface selectivity, makes XPS a useful addition to the armory of the materials analyst.

19.6 Energy-Dispersive X-Ray Analysis on Fractured Cross Sections

In order to detect small traces of possibly light elements, such as Na, energy-dispersive X-ray spectroscopy (EDX) is certainly not an appropriate technique to be used as the detection limit in particular for light elements is not sufficient. But if in need of a fast method with virtually no sample preparation involved, which can provide valuable information regarding the in-depth matrix-element distributions of the deposited thin film (e.g., the In and Ga distributions in $Cu(In,Ga)Se_2$ thin films), EDX on a cross-sectional sample in a scanning electron microscope may be the method of choice.

19.6.1 Basics on Energy-Dispersive X-Ray Spectroscopy in a Scanning Electron Microscope

As part of the inelastic interaction of sample atoms with the electron beam in an SEM, X-rays characteristic for these atoms are emitted (Chapter 14.2.3). These X-rays can be used to identify constituent elements of the sample under investigation. Depending on the detector in use, both the wavelength and the energy of the emitted X-rays can be used for a compositional analysis [55]. Since sample drift can be an issue when recording elemental distribution profiles on a solar cell cross section, the use of high acquisition rates is often advantageous.

When investigating homogeneously composed samples, EDX is a well-suited method for the quantitative determination of the sample composition [56]. It is, however, important to realize that, performing SEM–EDX on multilayer stacks in a cross-sectional configuration, the spatial extension of the interaction volume of the electron beam with the specimen always comprises inhomogeneous material distributions. This will render efforts to obtain reliable quantified information futile in the vast majority of cases. However, in general the qualitative distribution of a matrix element that is obtained by referring to the net counts

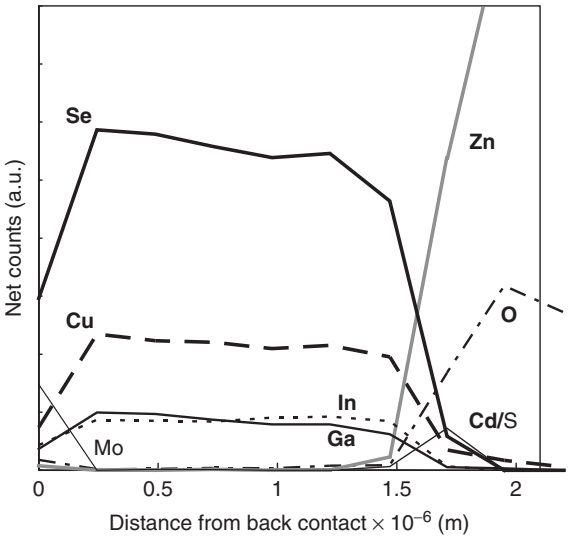

Figure 19.22 Net-count SEM–EDX line scan from a ZnO/CdS/Cu(In,Ga)Se_2/Mo/glass stack, recorded using acceleration voltage of 7 keV and a beam current of 250–300 pA.

may be transformed into a corresponding concentration distribution by relating the average net count of a specific element to its average concentration, which may be determined, for example, by means of X-ray fluorescence [57]. For good comparability of various measurements, it is necessary to either ensure identical measurement conditions or, alternatively, to perform normalization to an element of which ideally the concentration is assumed to be constant throughout the depth of a particular layer.

In order to ensure a favorable ratio of the characteristic X-ray line signal and the background, the kinetic energy of the exciting electrons should – as a rule of thumb – be at least twice as high as the maximum line energy used for analysis. Hence, the position of the characteristic X-ray lines for the relevant elements and their possible overlap determine the minimum acceleration voltage to be applied for the SEM–EDX analysis.

Figure 19.22 shows a net-count line scan from the fractured cross section of a ZnO/CdS/Cu(In,Ga)Se_2/Mo/glass stack, in which the Cu(In,Ga)Se_2 layer was deposited by standard multistage coevaporation [55]. The acceleration voltage was 7 kV, using a beam current of 250–300 pA. The value for the acceleration voltage was chosen according to the excitation energy for the In-L line (3.4 keV). The line scan consists of 10 measurement points between the Mo back contact and the ZnO front contact of the solar-cell device. Although the thickness of the CdS buffer layer is only in the range of about 50 nm, it is clearly visible. Apparently, Ga and In are not homogeneously distributed. The corresponding elemental distributions exhibit in-depth gradients.

19.6.2 Spatial Resolutions

Several approaches have been published [48, 58–60], which estimate the extension R of the interaction volume of an electron beam with a compound, considerations which are relevant for all-electron-beam-related techniques (see also Chapter 14). In SEM–EDX, the value R represents an intuitive and reliable limit for the spatial resolution. For Cu(In,Ga)Se_2 thin-film solar-cell devices at an acceleration voltage of 7 kV R varies from 130 to 270 nm, depending on the material hit by the electron beam. A definition of the spatial resolution similar to the one for analytical transmission electron microscopy (TEM) [61] is difficult to obtain in the case of SEM–EDX due to the usually large specimen thickness, that is, the comparably large interaction volume of the electron beam with the sample. The signal quality and also possible superpositions of characteristic lines with those of the background have a certain impact on the minimum expansion of the patterns to be resolved. It is hence highly recommended to determine the lateral resolution experimentally for the material system and measurement conditions used. Other error sources to be considered are the measurement-system error, the error introduced by sample drift during signal acquisition, the error caused by the roughness of the surfaces and interfaces of and within the sample that is analyzed, and, in connection with the sample surface roughness and sample orientation, errors introduced by reabsorption of emitted characteristic X-rays and subsequent fluorescence processes [48].

19.6.3 Applications

Modern SEM–EDX systems are often equipped with the possibility to record spectral images of an area of interest. That is, EDX spectra are recorded on a defined, spatially resolved pattern and can be analyzed after the measurement. This enables the acquisition of elemental maps and/or "wide" line scans that provide for a certain lateral averaging. Figure 19.23 shows a cross-sectional scanning electron micrograph from a ZnO/CdS/Cu(In,Ga)Se_2/Mo/glass stack. Also indicated is the region of interest in which EDX data acquisition was performed using the identical measurement setup, with 250–300 pA and with 4–5 nA electron-beam current.

A net-count line scan along the arrow was extracted from the collected EDX data and is displayed in Figure 19.24a for the In-L, Ga-L, and Se-L lines. As the acquisition durations were comparable in range, the number of net counts is considerably higher for the measurement at 4–5 nA. The Cu(In,Ga)Se_2 thin film depicted in Figure 19.23 is fabricated at a nominal substrate temperature of 330 °C. Standard processes are normally performed at temperatures above 500 °C, and a comparison with Figure 19.22 shows that at the low process temperature, a much stronger Ga gradient forms in the Cu(In,Ga)Se_2 layer.

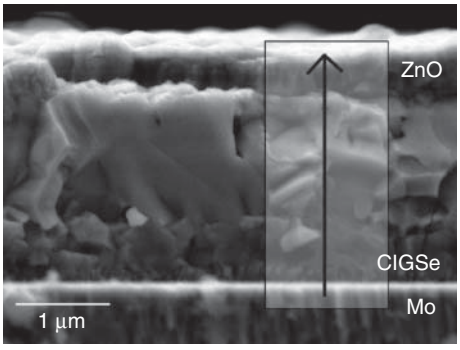

Figure 19.23 Cross-sectional SEM image from a ZnO/CdS/Cu(In,Ga)Se_2/Mo(/glass) stack, for which the Cu(In,Ga)Se_2 (CIGSe) absorber was deposited at the rather low nominal substrate temperature of 330 °C; the acquisition area for spectral imaging is indicated by the shaded area.

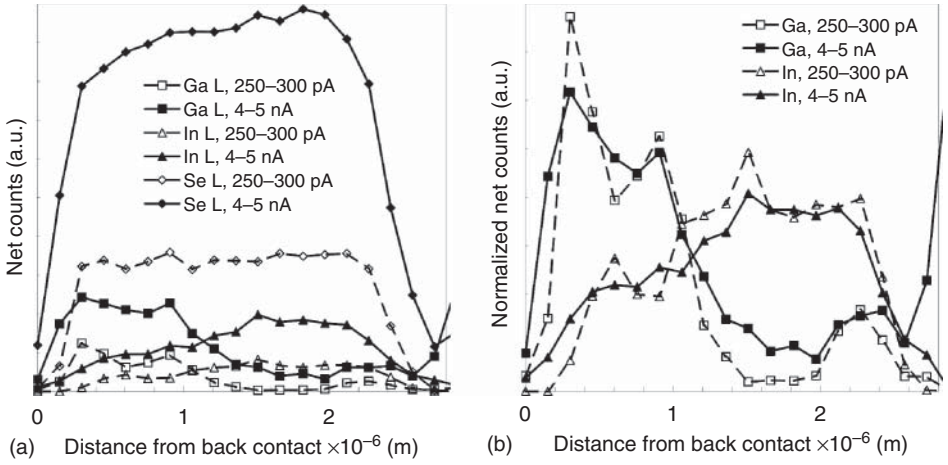

Figure 19.24 SEM–EDX line scans from the ZnO/CdS/Cu(In,Ga)Se_2/Mo/glass stack given in Figure 19.23: (a) net counts as recorded and (b) net counts normalized to Se-L.

It was already mentioned earlier that, in order to improve comparability of individual measurements, the normalization to an element with a constant concentration throughout the layer may be of use. In the case of Cu(In,Ga)Se_2 thin films fabricated by coevaporation, the Se concentration is assumed to comply with this requirement [50].

Figure 19.24b shows Ga and In signals normalized to the Se concentration. Due to the roughness of the investigated surface, the effect of reabsorption, which is higher for lower beam energies, needs to be considered. It is important to be aware that a possible error introduced by reabsorption of Se-L X-rays is enhanced when normalization to the Se-L line is carried out for high-energy signals. On the other hand, it may also have a compensating effect for low-energy lines. After

normalization, the line scans that were performed with the different beam currents show a good match. Both Ga-L and Ga-K signal distributions indicate features with spatial extensions as low as approximately 150 nm. These are the two distinct peaks, which designate a particularly high Ga content for distances below 1 μm away from the back contact and a peak in the Ga signal above 2 μm distance. All of these features can be ascribed to particular stages of the $Cu(In,Ga)Se_2$ deposition process [3, 55]. It is interesting to note the slight difference in resolution for the line scan recorded at 4–5 nA when compared with the line scan acquired at 250–300 pA. The peak width seen in the normalized spectra is slightly increased for the use of a beam current of 4–5 nA. Also, at distances larger than 2.6 μm from the back contact, the line scan at 4–5 nA exhibits an increase of the Ga signal, while the line scan at 250–300 pA does not. This may be the consequence of the proximity of the Zn-L and Ga-L lines and an EDX signal misinterpretation due to the larger interaction volume for the higher beam current. However, the use of higher beam currents allows for a much reduced measurement duration, which reduces the risk of drift and still shows a reasonable lateral resolution.

19.6.3.1 Sample Preparation

Cross-sectional specimens for SEM–EDX can simply be prepared by fracturing or cutting of the sample. Care should be taken regarding contacting of the sample in order to avoid electrical charging during the measurement as this may lead to additional drift. The use of finished solar-cell devices for depth profiling of the absorber layer is one way to circumvent more laborious methods of increasing the sample surface conductivity like the deposition of a very thin carbon layer. At times, it may also be advantageous to prepare polished cross-sectional specimens (see Chapter 14) in order to minimize errors that may be introduced by rough cross-sectional surfaces.

19.7 Atom Probe Tomography and Correlated Microscopies

A general view of nanotechnology includes the design of novel devices whose properties are controlled or influenced by features at the nanometric scale such as impurity segregation at grain boundaries (GBs) or interfaces, clustering, nanolayers, nanowires, and so on. To develop the full potential of these materials and understand their properties, their chemical changes at the atomic level must be characterized. APT is a new technique for this purpose [62–65]. The advantage of this powerful tool is that it provides access to both the structure and the composition of materials at the atomic scale, that is, about 0.2 nm for the lateral resolution and about 0.1 nm for the depth resolution [66]. Impurities at levels as low as 10–30 ppm (depending on the background level and on the position in the mass spectrum) can be traced. Another advantage is that the elemental distributions can be explored in three-dimensional (3D) view within the studied material, with

typical dimensions of the analyzed volume of about 50 nm × 50 nm × 300 nm for state-of-the-art instruments.

19.7.1 Theoretical Principles

In APT, the atoms from the apex of a needle-shaped sample are successively removed by a field-evaporation process, applying a high electric field necessary to remove an atom from the surface (about few tens of volt per nanometer). The removal of an atom from the sample surface involves both desorption of an atom from the surface and ionization of the removed atom [67]. The desorption phenomenon implies breaking the atomic bonds of a specific atom to remove it from the surface, while the ionization phenomenon implies that this atom is pulled away from the surface as an ion when a sufficiently high electric field is applied.

The high electric field at the surface of the sample is achieved by using a needle-shaped tip sample with a radius of curvature ≤50 nm. The electric field generated at the apex of the tip can be defined as

$$F = \frac{V}{kR} \tag{19.9}$$

where k is the field factor, V is the voltage, and R is the radius of curvature. The constant k can range from 3 to 8, as calculated for a W tip, and its value depends mostly on the tip shape [68, 69].

19.7.2 Instrumentation

Figure 19.25 shows a tip-shaped specimen placed in an ultrahigh vacuum chamber with a base pressure of $\sim 10^{-9}$ Pa. The tip is cooled down to very low temperatures between 20 and 80 K to preserve the position of the surface atoms subjected to high electric field and to reduce the thermal agitation energy, $k_B T$, of the atoms at the instant of their evaporation, thus providing high spatial resolution. Moreover, a local electrode or microelectrode with inner diameter of about 30 μm (e.g., for a LEAP 3000X HRTM [70]) is positioned within several tens of micrometers from the apex of the tip. Its main task is to enhance the field at the apex of the tip, thus enabling a longer lifetime of the tip during the APT analysis [71].

Applying either high-voltage or laser pulses to a positively biased APT tip induces controlled field evaporation of surface atoms. The field-evaporated atoms are accelerated toward a position-sensitive detector that records their TOF and impact positions. A 3D elemental map can be reconstructed from the collected data using an inverse projection of the detector coordinates (x_D, y_D) to the tip surface (x, y). A point-projection model is used, which assumes that the trajectory of the ions depends strictly on the distribution of the field lines and not on its mass or applied voltage [72] as shown in Figure 19.26. For this model, the apex of

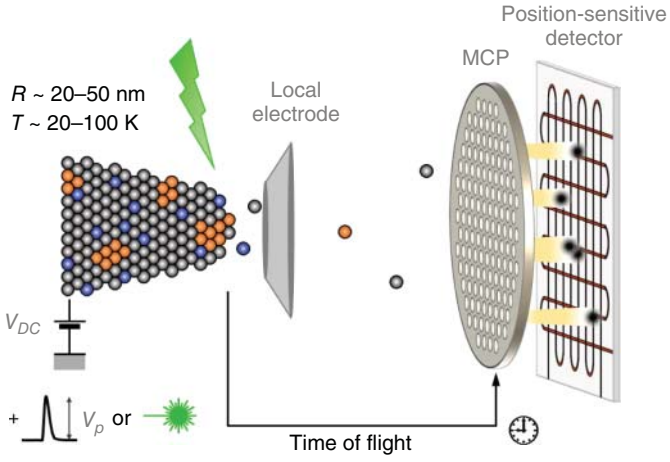

Figure 19.25 Schematics of the experimental setup used for atom probe tomography and, more specifically, of the local electrode atom probe (LEAP). (Reproduced with kind permission from Dr. Ivan Povstugar from Max-Planck Institut für Eisenforschung GmbH, Düsseldorf.)

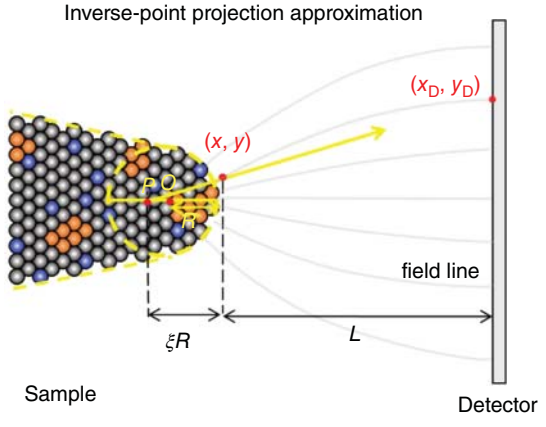

Figure 19.26 Schematics of the point-projection model used for the 3D reconstruction of the APT data. Here, P is the projection point, O is the center of the hemispherical cap, R is the radius of curvature, L is the flight length, ξ is the image compression factor, and x, y (x_D,y_D) are the coordinates of the atoms at the apex of the tip (on the detector).

the tip is considered as a truncated cone with a hemispherical cap, although for real APT tips, deviations from this geometry are found.

By using the point-projection model, the magnification by projection parameter, M, can be defined as the ratio between the flight path, L, and the product ξR:

$$M = \frac{L}{\xi R}. \tag{19.10}$$

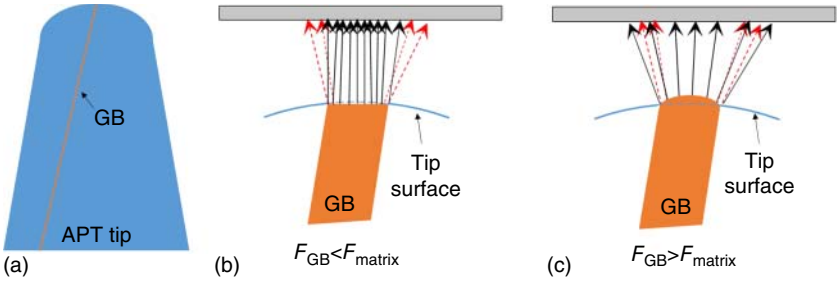

Figure 19.27 (a) Schematics of an APT tip containing a grain boundary (GB) (b) and (c) of the local magnification effect in the case of low- and high-field GB.

The constant ξ is the image compression factor, and its value ranges between 1 and 2 [73]. The parameter M is instrument dependent, since L may vary between a straight-flight-path (~10 cm) and reflectron (~36 cm) systems.

19.7.3 Artifacts in Atom Probe Tomography

One of the most encountered artifacts in APT is the local magnification effect (LME) [74]. This effect occurs owing to local variation in the evaporation field, causing local protrusion at the tip surface and hence trajectory deviation in flight path. These local variations in evaporation field are produced mainly by the existence of another phase inside the APT tip, such as a GB or a precipitate [75]. Figure 19.27 shows the trajectory aberrations and the density variations due to the GB, which has a lower or a higher field evaporation than the matrix (Figure 19.27b and c). The LME is very easily detected in the reconstructed 3D APT map owing to the atomic density variations in the reconstructed GB region. An effective way to reduce these LMEs is to place the GB perpendicular to the tip axis (z axis), since the LME increases continuously as the GB approaches an orientation parallel to the tip axis [76].

19.7.4 Sample Preparation

The APT data quality is determined very much by the sample preparation. Indeed, the APT tip surface is often prone to *ex situ* or *in situ* contaminations, which reduce substantially the tip lifetime during the APT measurements.

In the present subsection, standard and site-specific sample preparation using combined microscopies will be described.

19.7.4.1 Standard Sample Preparation

For APT investigations, a very thin needle with a tip radius of $R \leq 50$ nm should be prepared from the material of interest. There are several methods applied for tip preparation, such as electropolishing of metallic wires/rods and focused ion beam

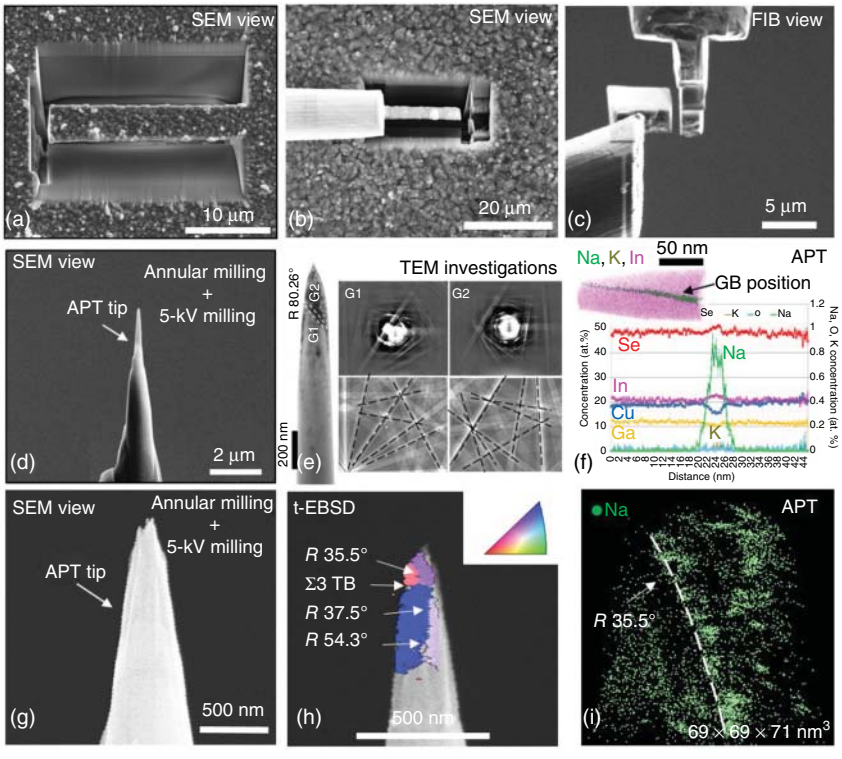

Figure 19.28 (a) Milling of a chunk for lift-out, (b) attaching the micromanipulator to the chunk by Pt deposition, (c) attaching the micromanipulator to the chunk by Pt deposition, (d, g) annular milling and final 5 kV milling to obtain APT sharpened tips for transmission electron microscope (TEM), electron backscatter diffraction (EBSD), and APT investigations, (e) TEM investigations showing the grain orientation determination based on the Kikuchi diffraction pattern, (f) APT results showing the Na and K segregation at the random high-angle GB noted by *R* 80.26° in (e), (h) EBSD measurement directly on the APT tip, and (i) APT results showing the Na segregation and clustering at the *R* 35.5° GB shown in (h).

(FIB) milling of any solid material. The FIB lift-out method [77] has been shown to be well appropriate for the preparation of APT tips from semiconductor materials such as $Cu(In,Ga)Se_2$ and $Cu_2ZnSn(S,Se)_4$ thin-film materials. The main steps of a standard lift-out process are shown in Figure 19.28a–c.

The lift-out process involves:

1) Defining the region of interest on the $Cu(In,Ga)Se_2$ surface
2) Milling of two rectangular trenches using a tilt angle of 22°, that is, a chunk is obtained (Figure 19.28a)
3) Performing a first free-cut on the left side of the chunk
4) Attaching the micromanipulator to the chunk by depositing a Pt weld by ion-beam-induced chemical vapor deposition

5) Performing the final free-cut on the right side of the chunk (Figure 19.28b)
6) Lifting out the freestanding chunk and attaching it on the Mo pins using Pt deposition
7) Performing a free-cut to finally obtain only a small part of the chunk (about 2 µm in width) on the top of the Mo pin (Figure 19.28c)

After mounting the desired material on the Mo support tips, annular milling [77] is applied to obtain a tip-shaped sample for the APT investigations. Moreover, the annular milling parameters such as ion-beam energies and currents are specially optimized for the material under investigation to avoid Ga contamination and amorphization of the APT tips. For Cu(In,Ga)Se_2 and $Cu_2ZnSn(S,Se)_4$, the voltage was kept at 2–5 kV at the end of the annular milling to restrict the Ga implantation to a region of about 5 nm below the surface [78].

19.7.4.2 Site-Specific Sample Preparation Using Combined Microscopies

Novel site-specific preparation procedures have recently been developed [78], providing the ability to analyze the structural properties of a specific Cu(In,Ga)Se_2 GB prior to the APT investigations. Thus, the relationship between structural and chemical properties for GBs in polycrystalline Cu(In,Ga)Se_2 layers can be determined.

These site-specific preparation procedures combine the FIB lift-out method either with TEM or with electron backscatter diffraction (EBSD) as shown in Figure 19.28e and h. At the end, APT analyses on the preinvestigated tips were performed, as shown Figure 19.28f and i. In the APT maps, each point corresponds to one atom, clearly showing the APT capability to analyze the desired area at the nanometer scale. Moreover, these APT results give evidence for Na and K impurity segregations at random high-angle GBs, indicated by "R" in Figure 19.28e, f, h, and i with misorientation angles of 80.36° and 35.5°. The segregation of alkali metals at GBs can be expected, since these elements are present in the soda-lime glass used as substrate material for the solar cells. However, for long, it has remained unknown in which quantities these elements segregate to Cu(In,Ga)Se_2 GBs and how they are distributed. Indeed, as a mass spectrometry method, APT is one of the few techniques which can give information on Na and K concentrations and also 3D localization at GBs within Cu(In,Ga)Se_2 thin films [75, 78–81].

19.7.5 Application to Thin-Film Solar Cells

As demonstrated in the previous sections, APT is a very powerful tool able to trace any chemical changes at the atomic scale and in 3D. This information becomes important when the properties of thin-film solar cells are controlled by nanoscale features, such as nanodots or clusters of secondary phases or extended structural defects as GBs. In the following, two examples are shown in Figures 19.29 and 19.30 for which the nanoscale features have considerable impact on the solar-cell performance.

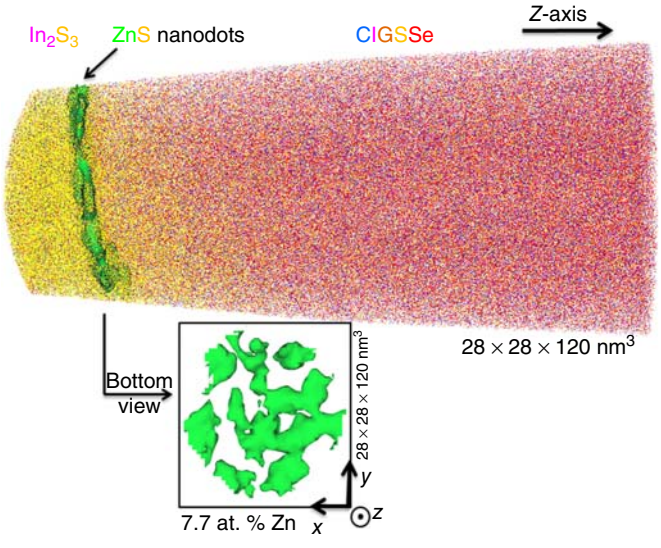

Figure 19.29 APT 3D map showing the distribution of In (pink), S (yellow), Zn (light green), Cu (blue), Ga (orange), and Se (red). The presence of the ZnS nanodots at the In_2S_3/Cu(In,Ga)Se_2 interface is apparent in the bottom view element envelope map (see inset) [82]. (Reproduced with permission from Ref. [82].)

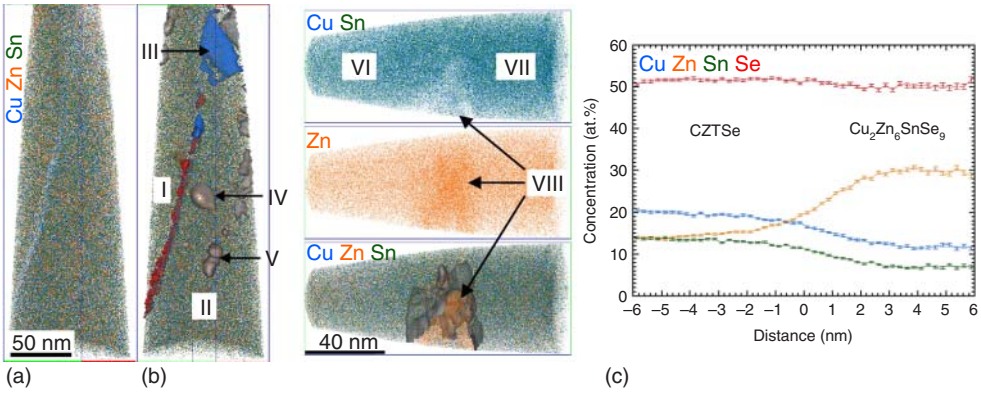

Figure 19.30 (a) and (b) Three-dimensional elemental maps of Cu (blue), Zn (orange), and Sn (green) with isoconcentration surfaces of 20.0 at.% Zn (gray), 22.5 at.% Cu (red), and 25.0 at.% Cu (blue). (c) Proximity histogram (proxigram) across the 20.0 at.% Zn isoconcentration surface of region VIII [83].

In the first example, a buffer layer for Cu(In,Ga)Se_2 solar cells, consisting of mixed In_2S_3–ZnS nanodots deposited by spray-ion layer gas reaction (ILGAR), as alternative to CdS, is presented. The Cu(In,Ga)Se_2 solar cell containing this mixed, alternative buffer layer showed a 1% (absolute) higher conversion efficiency than the solar cell containing a pure In_2S_3 buffer layer. Thus, the insertion of the ZnS nanodots into In_2S_3 affected the device performance considerably [82]. APT

provided chemical and structural information, such as ZnS nanodot composition, size, shape, and distribution, as shown in Figure 19.29.

Another example concerns the precipitation of secondary phases in $Cu_2ZnSn(S,Se)_4$ thin films for solar cells. These phases are generally considered to be detrimental to the conversion efficiency, as they can lead to an increase in series resistance [84] and/or a decrease in open-circuit voltage [85]. Hence, reliable and accurate characterization of precipitates containing secondary phases in terms of composition, size, and distribution is essential for understanding solar-cell properties and for controlling synthesis and process parameters. Moreover, detection of secondary phases remains a great challenge, as many of them are structurally similar to the $Cu_2ZnSn(S,Se)_4$ matrix and can be present as nanoprecipitates or inclusions. Thus, the APT measurements were necessary for characterizing the possible secondary phases in the $Cu_2ZnSn(S,Se)_4$ layers and their composition, size, and distribution. Figure 19.30 shows that indeed, Zn-rich precipitates with diameters of about 50 nm and a stoichiometry corresponding to $Cu_2Zn_5SnSe_8$ and $Cu_2Zn_6SnSe_9$ were formed in a $Cu_2ZnSnSe_4$ layer. Although their size is rather small, Schwarz *et al*. [86] showed that these Zn-rich precipitates can act as a barrier for photogenerated charge carriers, increasing the series resistance. Furthermore, it can contribute to the recombination activity by increasing the reverse saturation current.

Acknowledgments

Volker Hoffmann, Varvara Brackmann (IFW Dresden), Dennis Klemm (sunfire GmbH) and Cornel Venzago from AQura GmbH gratefully acknowledge the financial support from the FP6 Research Training Network GLADNET (No. MRTN-CT-2006-035459). The group from IFW Dresden thanks the Spectruma Analytik GmbH and HZB, Berlin for good collaborations. Cornel Venzago wishes to thank Agnés Tempez from Horiba Jobin Ivon for collaboration with rf-GD-TOF measurements. Christian A. Kaufmann and Raquel Caballero are grateful to Jürgen Bundesmann for technical support. Oana Cojocaru-Mirédin greatfully acknowledges financial support by the German Federal Ministry of Education and Research (Contract 03X5522A). She also thanks Pyuck-Pa Choi, Torsten Schwarz, and Purvesh Soni for the help in APT data acquisition, analysis and understanding.

References

1. Reniers, F. (2009) In-depth analysis: methods for depth profiling, in *Handbook of Surface and Interface Analysis: Methods for Problem-Solving* (eds J.C. Riviere and S. Myhra), Taylor & Francis Group, LLC, p. 273.
2. Gabor, A.M., Tuttle, J.R., Bode, M.H., Franz, A., Tennant, A.L., Contreras, M.A., Noufi, R., Jensen, D.G., and Hermann, A.M. (1996) Band-gap engineering in $Cu(In,Ga)Se_2$ thin films grown from $(In,Ga)_2Se_3$ precursors. *Sol. Energy Mater. Sol. Cells*, **41–42**, 247–260.
3. Kaufmann, C.A., Caballero, R., Unold, T., Hesse, R., Klenk, R.,

Schorr, S., Nichterwitz, M., and Schock, H.-W. (2009) Depth profiling of Cu(In,Ga)Se_2 thin films grown at low temperatures. *Sol. Energy Mater. Sol. Cells*, **93**, 859–863.

4. Gloeckler, M. and Sites, J.R. (2005) Band-gap grading in Cu(In,Ga)Se_2 solar cells. *J. Phys. Chem. Solids*, **66**, 1891–1894.
5. Caballero, R., Kaufmann, C.A., Efimova, V., Rissom, T., Hoffmann, V., and Schock, H.W. (2013) Investigation of Cu(In,Ga)Se_2 thin-film formation during the multi-stage co-evaporation process. *Prog. Photovolt.: Res. Appl.*, **21**, 30–46.
6. Mainz, R., Weber, A., Rodriguez-Alvarez, H., Levcenko, S., Klaus, M., Pistor, P., Klenk, R., and Schok, H.-W. (2015) Time-resolved investigation of Cu(In,Ga)Se_2 growth and Ga gradient formation during fast selenisation of metallic precursors. *Prog. Photovolt.: Res. Appl.*, **23**(9), 1131–1143.
7. Chirila, A., Buecheler, S., Pianezzi, F., Bloesch, P., Gretener, C., Uhl, A.R., Fella, C., Kranz, L., Perrenoud, J., Seyrling, S., Verma, R., Nishiwaki, S., Romanyuk, Y.E., and Tiwari, A.N. (2011) Highly efficient Cu(In,Ga)Se_2 solar cells grown on flexible polymer films. *Nat. Mater.*, **10**, 857–861.
8. Schubbert, C., Eraerds, P., Richter, M., Parisi, J., Riedel, I., Dalibor, T., and Palm, J. (2015) A simulation study on the impact of band gap profile variations and secondary barriers on the temperature behavior, performance ratio, and energy yield of Cu(In,Ga)$(Se,S)_2$ solar cells. *Phys. Status Solidi A*, **212** (2), 336–347.
9. Rodriguez-Alvarez, H., Mainz, R., and Sadewasser, S. (2014) A one-dimensional Fickian model to predict the Ga depth profiles in three-stage Cu(In,Ga)Se_2. *J. Appl. Phys.*, **115**, 2049131.
10. Zweschke, A. and Wellmann, P.J. (2015) Numerical reactive diffusion modeling of stacked elemental layer rapid thermal annealed chalcopyrite absorber layer formation. *Thin Solid Films*, **582**, 397–400.
11. Abou-Ras, D., Caballero, R., Fischer, C.-H., Kaufmann, C.A., Lauermann, I., Mainz, R., Mönig, H., Schöpke, A., Stephan, C., Streek, C., Schorr, S., Eicke, A., Döbeli, M., Gade, B., Hinrichs, J., Nunney, T., Dijkstra, H., Hoffmann, V., Klemm, D., Efimova, V., Bergmaier, A., Dollinger, G., Wirth, T., Unger, W., Rockett, A.A., Perez-Rodriguez, A., Alvarez-Garcia, J., Izquierdo-Roca, V., Schmidt, T., Choi, P.-P., Müller, M., Bertram, F., Christen, J., Khatri, H., Collins, R.W., Marsillac, S., and Kötschau, I. (2011) Comprehensive comparison of various techniques for the analysis of elemental distributions in thin films. *Microsc. Microanal.*, **17**, 728–752.
12. Sakurai, K., Shibata, H., Nakamura, S., Yonemure, M., Kuwamore, S., Kimura, Y., Ishizuka, S., Yamada, A., Matsubara, K., Nakanishi, H., and Niki, S. (2005) Properties of Cu(In,Ga)Se_2:Fe thin films for solar cells. *Mater. Res. Soc. Symp. Proc.*, **865**, 417–421.
13. Caballero, R., Kaufmann, C.A., Eisenbarth, R., Cancela, M., Unold, T., Eicke, A., Klenk, R., and Schock, H.W. (2009) The influence of Na on low temperature growth of CIGS thin film solar cells on polyimide substrates. *Thin Solid Films*, **517**, 2187–2190.
14. Payling, R., Delwyn, J.G., and Bengtson, A. (eds) (1997) *Glow Discharge Optical Emission Spectrometry*, John Wiley & Sons, New York, Weinheim, Brisbane, Singapore, Toronto.
15. Marcus, K.R. (1993) *Glow Discharge Spectroscopies*, Plenum Press, New York.
16. Grimm, W. (1968) Eine neue Glimmentladungsquelle für die optische Emissionsspektralanalyse. *Spectrochim. Acta Part B*, **23** (7), 443–454.
17. Voronov, M., Hofmann, T., Smid, P., and Venzago, C. (2009) Microsecond pulsed glow discharge applied to a sector-field mass-spectrometer. *J. Anal. At. Spectrom.*, **24**, 676–679.
18. Bengtson, A. and Nelis, T. (2006) The concept of constant emission yield in GDOES. *Anal. Bioanal. Chem.*, **385** (3), 568–585.
19. Adams, F., Gijbels, R., and Van Grieken, R.E. (eds) (1988) *Inorganic Mass Spectrometry*, John Wiley &

Sons, New York, Chichester, Brisbane, Toronto, Singapore.
20. Hohl, M., Kanzari, A., Michler, J., Nelis, T., Fuhrer, K., and Gonin, M. (2006) Pulsed r.f.-glow-discharge time-of-flight mass spectrometry for fast surface and interface analysis of conductive and non-conductive materials. *Surf. Interface Anal.*, **4**, 292–295.
21. Nelis, T. (1997) Calibration, in *Glow Discharge Optical Emission Spectrometry* (eds R. Payling, D.G. Jones, and A. Bengtson), John Wiley & Sons, New York, Weinheim, Brisbane, Singapore, Toronto, pp. 413–417.
22. Bengtson, A. (1994) Quantitative depth profile analysis by glow discharge. *Spectrochim. Acta Part B*, **49** (4), 411–429.
23. Vieth, W. and Huneke, J.C. (1991) Relative sensitivity factors in glow discharge mass spectrometry. *Spectrochim. Acta Part B*, **46B** (2), 137–153.
24. Rissom, T., Mainz, R., Kaufmann, C.A., Caballero, R., Efimova, V., Hoffmann, V., and Schock, H.-W. (2011) Examination of growth kinetics of copper rich Cu(In,Ga)Se_2-films using synchrotron energy dispersive X-ray diffractometry. *Sol. Energy Mater. Sol. Cells* **95**(1), 250–253.
25. Lobo, L., Pisonero, J., Bordel, N., Pereiro, R., Tempez, A., Chapon, P., Michler, J., Hohl, M., and Sanz-Medel, A. (2009) A comparison of non-pulsed radiofrequency and pulsed radiofrequency glow discharge orthogonal time-of-flight mass spectrometry for analytical purposes. *J. Anal. At. Spectrom.*, **24**, 1373–1381.
26. Wilson, R.G., Stevie, F.A., and Magee, C.W. (eds) (1989) *Secondary Ion Mass Spectrometry: A Practical Handbook for Depth Profiling and Bulk Impurity Analysis*, Wiley, New York.
27. Benninghoven, A., Werner, H.W., and Rüdenauer, F.G. (eds) (1987) *Secondary Ion Mass Spectrometry: Basic Concepts, Instrumental Aspects, Applications and Trends*, Wiley, New York.
28. Szymczak, W. and Wittmaack, K. (2003) Ion-to-neutral conversion in time-of-flight secondary ion mass spectrometry. *Appl. Surf. Sci.*, **203–204**, 170–174.
29. Veryovkin, I.V., Calaway, W.F., Moore, J.F., Pellin, M.J., Lewellen, J.W., Yuelin, L., Milton, S.V., King, B.V., and Petravic, M. (2004) A new horizon in secondary neutral mass spectrometry: post-ionization using a VUV free electron laser. *Appl. Surf. Sci.*, **231–232**, 962–966.
30. Oechsner, H., Getto, R., and Kopnarski, M. (2009) Quantitative characterization of solid state phases by secondary neutral mass spectrometry. *J. Appl. Phys.*, **105** (6), 063523.
31. Magee, C.W. and Frost, M.R. (1995) Recent successes in the use of secondary ion mass spectrometry in microelectronics materials and processing. *Int. J. Mass Spectrom. Ion Processes*, **143**, 29–41.
32. Williams, P. and Baker, J.E. (1980) Quantitative analysis of interfacial impurities using secondary-ion mass spectrometry. *Appl. Phys. Lett.*, **36** (10), 842–845.
33. Bryan, S.R., Linton, R.W., and Griffis, D.P. (1987) Characterization and removal of ion yield transients in the near surface region of secondary ion mass spectrometry depth profiles. *J. Vac. Sci. Technol. A*, **5** (1), 9–14.
34. Rockett, A., Granath, K., Asher, S., Al Jassim, M.M., Hasoon, F., Matson, R., Basol, B., Kapur, V., Britt, J.S., Gillespie, T.S., and Marshall, C. (1999) Na incorporation in Mo and $CuInSe_2$ from production processes. *Sol. Energy Mater. Sol. Cells*, **59**, 255–264.
35. Bodegård, M., Granath, K., Stolt, L., and Rockett, A. (1999) The behaviour of Na implanted into Mo thin films during annealing. *Sol. Energy Mater. Sol. Cells*, **58**, 199–208.
36. Batchelor, W.K., Beck, M.E., Huntington, R., Repins, I.L., Rockett, A., Shafarman,W.N., Hasoon, F.S. and Britt, J.S. (2002) *Substrate and Back Contact Effects in CIGS Devices on Steel Foil*. Conference Record of the 29th IEEE Photovoltaics Specialists Conference, New Orleans, Louisiana, USA, May 19–24, 2002. IEEE, Piscataway, New Jersey, pp. 716–719.
37. Meitner, L. (1922) Über die β-Strahl-Spektra und ihren Zusammenhang mit der γ-Strahlung. *Z. Phys. A: Hadrons Nucl.*, **11**, 35–54.

38. Auger, P. (1925) Sur l'effet photoélectrique composé. *J. Phys. Radium*, **6**, 205–208.
39. Palmberg, P.W. (1967) Secondary emission studies on Ge and Na-covered Ge. *J. Appl. Phys.*, **38**, 2137–2147.
40. Tharp, L.N. and Scheibner, E.J. (1967) Energy spectra of inelastically scattered electrons and LEED studies of tungsten. *J. Appl. Phys.*, **38**, 3320–3330.
41. Harris, L.A. (1968) Analysis of materials by electron-excited Auger electrons. *J. Appl. Phys.*, **39** (3), 1419–1427.
42. Harris, L.A. (1968) Some observations of surface segregation by Auger electron emission. *J. Appl. Phys.*, **39** (3), 1428–1431.
43. Palmberg, P.W., Bohn, G.K., and Tracy, J.C. (1969) High sensitivity Auger electron spectrometer. *Appl. Phys. Lett.*, **15**, 254–255.
44. Rivière, J.C. and Myhra, S. (2009) *Handbook of Surface and Interface Analysis*, 2nd edn, Methods for Problem-Solving, pp. 46–55.
45. Savitzky, A. and Golay, M.J.E. (1964) Smoothing and differentiation of data by simplified least squares procedures. *Anal. Chem.*, **36** (8), 1627–1639.
46. Childs, K.D., Carlson, B.A., LaVanier, L.A., Moulder, J.F., Paul, D.F., Stickle, W.F., and Watson, D.G. (1995) in *Handbook of Auger Electron Spectroscopy*, 3rd edn (ed C.L. Hedberg), Physical Electronics, Inc., MN, USA.
47. Czanderna, A.W. (1975) Methods of surface analysis, in *Methods and Phenomena* (eds S.P. Wolski and A.W. Czanderna), vol. 1, Elsevier Scientific Publishing Company, Amsterdam, Oxford, New York, p. 164.
48. Mathieu, H.J. and Landolt, D. (1981) Experimental study of matrix effects in quantitative Auger analysis of binary metal alloys. *Surf. Interface Anal.*, **3** (4), 153–156.
49. Wirth, T. (1992) Quantitative Auger electron spectroscopy of silicides by extended matrix correction using $dN(E)/dE$ spectra. *Surf. Interface Anal.*, **18** (1), 3–12.
50. Einstein, A. (1905) On a heuristic viewpoint concerning the production and transformation of light. *Ann. Phys.*, **17**, 132–148.
51. Siegbahn, K., Nording, C.N., Fahlman, A., Nordberg, R., Hamrin, K., Hedman, J., Johansson, G., Bermark, T., Karlsson, S.E., Lindgren, I., and Lindberg, B. (1967) *ESCA: Atomic, Molecular and Solid State Structure Studied by Means of Electron Spectroscopy*, Almqvist and Wiksell, Uppsala, Sweden.
52. Watts, J.F. and Wolstenholme, J. (2003) *An Introduction to Surface Analysis by XPS and AES*, Wiley, UK.
53. Scofield, J.H. (1976) Hartree–Slater subshell photoionization cross-sections at 1254 and 1487 eV. *J. Electron Spectrosc.*, **8**, 129–137.
54. Wagner, C.D. (1981) Empirical atomic sensitivity factors for quantitative analysis by electron spectroscopy for chemical analysis. *Surf. Interface Anal.*, **3**, 211–225.
55. Brümmer, O., Heydenreich, J., Krebs, K.H., and Schneider, H.G. (eds) (1980) *Handbuch Festkörperanalyse mit Elektronen, Ionen und Röntgenstrahlen*, Friedr. Vieweg & Sohn, Braunschweig.
56. Colby, J.W. (1968) Quantitative microprobe analysis of thin insulating films. *Adv. X-Ray Anal.*, **11**, 287–305.
57. Luysberg, M., Tillmann, K. and Weirich, T. (2008) *Elemental Distribution Profiles Across Cu(In,Ga)Se_2 Solar-Cell Absorbers Acquired by Various Techniques*. (eds Abou-Ras, D., Kaufmann, C.A., Schöpke, A., Eicke, A., Döbeli, M., Gade, B., Nunney, T.) Proceedings of the 14th European Microscopy Congress 2008, September 1–5, 2008, Aachen, Germany. Springer. "EMC 2008", Vol. 1: Instrumentation and Methods, pp. 741–742.
58. Grün, A.E. (1957) Lumineszenzphotometrische Messungen der Energieabsorption im Strahlungsfeld von Elektronenquellen – Eindimensionaler Fall in Luft. *Zeitschrift für Naturforschung*, **12a** (2), 89–95.
59. Rechid, J., Kampmann, A., and Reineke-Koch, R. (2000) Characterising superstrate CIS solar cells with electron beam induced current. *Thin Solid Films*, **361–362**, 198–202.

60. Mohr, H. and Dunstan, D.J. (1997) Electron-beam-generated carrier distributions in semiconductor multilayer structures. *J. Microsc.*, **187** (2), 119–124.
61. Michaels, J.R. and Williams, D.B. (1987) A consistent definition of probe size and spatial resolution in the analytical electron microscope. *J. Microsc.*, **47** (3), 289–303.
62. Blavette, D., Bostel, A., Sarrau, J.M., Deconihout, B., and Menand, A. (1993) An atom-probe for three dimensional tomography. *Nature*, **363**, 432–435.
63. Cerezo, A., Godfrey, T.J., Sijbrandij, S.J., Smith, G.D.W., and Warren, P.J. (1998) Performance of an energy-compensated three-dimensional atom probe. *Rev. Sci. Instrum.*, **69**, 49–58.
64. Gault, B., Vurpillot, F., Vella, A., Gilbert, M., Menand, A., Blavette, D., and Deconihout, B. (2006) Design of a femtosecond laser assisted tomographic atomprobe. *Rev. Sci. Instrum.*, **77**(4), 043705
65. Kelly, T.F. and Miller, M.K. (2007) Atom probe tomography. *Rev. Sci. Instrum.*, **78**, 031101.
66. Gault, B., Moody, M.P., Cairney, J.M., and Ringer, S.P. (2012) *Atom Probe Microscopy*, Springer Series in Material Science 160, Springer Science+Business Media, New York.
67. Miller, M.K. and Forbes, R.G. (2014) *Atom-Probe-Tomography: The Local Electrode Atom Probe*, Springer Science+Business Media, New York.
68. Sakurai, T. and Müller, E.W. (1973) Field calibration using the energy distribution of field ionization. *Phys. Rev. Lett.*, **30**, 532–535.
69. Sakurai, T. and Müller, E.W. (1977) Field calibration using the energy distribution of a free-space field ionization. *J. Appl. Phys.*, **48** (6), 2618–2625.
70. Kelly, T.F., Gribb, T.T., Olson, J.D., Martens, R.L., Shepard, J.D., Wiener, S.A., Kunichi, T.C., Ulfig, R.M., Lenz, D.R., Strennen, E.M., Oltman, E., Bunton, J.H., and Strait, D.R. (2004) First data from a commercial local electrode atom probe (LEAP). *Microsc. Microanal.*, **10** (3), 373–383.
71. Seidman, D.N. (2007) Three-dimensional atom-probe tomography: advances and applications. *Annu. Rev. Mater. Res.*, **37**, 127–158.
72. Vurpillot, F., Bostel, A., Menand, A., and Blavette, D. (1999) Trajectories of field emitted ions in 3D atom-probe. *Eur. Phys. J. Appl. Phys.*, **6** (2), 217–221.
73. Gault, B., de Geuser, F., Stephenson, L.T., Moody, M.P., Muddle, B.C., and Ringer, S.P. (2008) Estimation of the reconstruction parameters for atom probe tomography. *Microsc. Microanal.*, **14**, 296–305.
74. Vurpillot, F., Cerezo, A., Blavette, D., and Larson, D.J. (2004) Modelling image distortions in 3DAP. *Microsc. Microanal.*, **10**, 384–390.
75. Cojocaru-Mirédin, O., Choi, P., Abou-Ras, D., Schmidt, S.S., Caballero, R., and Raabe, D. (2011) Characterization of GBs in CIGS films using atom-probe tomography. *IEEE J. Photovoltaics*, **1**, 207–212.
76. Blavette, D., Duval, P., Letellier, L., and Guttmann, M. (1996) Atomic-scale APFIM and TEM investigation of grain boundary microchemistry in astrology Ni base superalloys. *Acta Mater.*, **44**, 4995–5005.
77. Thompson, K., Lawrence, D., Larson, D.J., Olson, J.D., Kelly, T.F., and Gorman, B. (2007) In situ site-specific specimen preparation for atom probe tomography. *Ultramicroscopy*, **107**, 131–139.
78. Cojocaru-Mirédin, O., Stoffers, A., Soni, P., Wuerz, R., and Raabe, D. (2015) Viable approaches of grain boundary characterization in multicrystalline and polycrystalline photovoltaic materials using correlative microscopies. *Ultramicroscopy*, in preparation.
79. Cojocaru-Mirédin, O., Schwarz, T., Choi, P.P., Herbig, M., Wuerz, R., and Raabe, D. (2013) Atom probe tomography studies on the Cu(In,Ga)Se_2 grain boundaries. *J. Visualized Exp.*, **74**, 50376.
80. Abou-Ras, D., Schmidt, S.S., Caballero, R., Unold, T., Schock, H.-W., Koch, C.T., Schaffer, B., Schaffer, M., Choi, P.-P., and Cojocaru-Mirédin, O. (2012) Confined and chemically flexible grain boundaries in polycrystalline compound semiconductors. *Adv. Energy Mater.*, **2**, 992–998.

81. Couzinie-Devy, F., Cadel, E., Barreau, N., Arzel, L., and Pareige, P. (2015) Na distribution in Cu(In,Ga)Se_2 thin films: investigation by atom probe tomography. *Scr. Mater.*, **104**, 83–86.

82. Cojocaru-Mirédin, O., Fu, Y., Kostka, A., Sáez-Araoz, R., Beyer, A., Knaub, N., Volz, K., Fischer, C.-H., and Raabe, D. (2014) Interface engineering and characterization at the atomic-scale of pure and mixed ion layer gas reaction buffer layers in chalcopyrite thin-film solar cells. *Prog. Photovolt.: Res. Appl.*, **23** (6), 705–716.

83. T. Schwarz (2015) On the nano-scale characterization of kesterite thin-films. PhD thesis. RWTH Aachen 2015. Shaker-Verlag Aachen GmbH, Aachen.

84. Mitzi, D.B., Gunawan, O., Todorov, T.K., Wang, K., and Guha, S. (2011) The path towards a high-performance solution-processed kesterite solar cell. *Sol. Energy Mater. Sol. Cells*, **95**, 1421–1436.

85. Siebentritt, S. and Schorr, S. (2012) Kesterites – a challenging material for solar cells. *Prog. Photovolt.: Res. Appl.*, **20**, 512–519.

86. Schwarz, T., Marques, M., Bott, S., Mousel, M., Redinger, A., Siebentritt, S., Cojocaru-Mirédin, O., Raabe, D., and Choi, P. (2015) Detection of novel $Cu_2Zn_5SnSe_8$ and $Cu_2Zn_6SnSe_9$ phases in co-evaporated $Cu_2ZnSnSe_4$ thin-films. *Appl. Phys. Lett.*, submitted for publication.

20
Hydrogen Effusion Experiments

Wolfhard Beyer and Florian Einsele

20.1
Introduction

In an effusion experiment, a sample is heated to high temperatures, and released (effused) gases are detected. In particular for incorporated hydrogen in thin films, effusion measurements have been established as a fairly fast method for the measurement of hydrogen concentration and the kinetics of its release and thus on its incorporation stability [1]. Knowledge about hydrogen incorporation and stability is of particular interest for silicon-based thin-film solar cell materials like hydrogenated amorphous silicon (a-Si:H), microcrystalline silicon (μc-Si:H), related (alloy) materials, and amorphous and microcrystalline germanium (a-Ge:H and μc-Ge:H, respectively). These materials contain typically 10 at.% of hydrogen. More recently, this class of materials has gained interest also for application as undoped surface passivation layers and doped contact layers in amorphous/crystalline silicon heterojunction solar cell technology [2]. The process of hydrogen effusion may also be of importance in the technology of crystalline silicon on glass (or on SiO_2) if plasma-grown a-Si:H films are used as a starting material [3]. Furthermore, hydrogen incorporation and its release is of interest (and has been studied) for transparent conducting oxide (TCO) materials like tin oxide (SnO_2) and zinc oxide (ZnO) which are widely applied in thin-film solar cell technology. Although the incorporated hydrogen concentration in these TCO films is typically much smaller than in a-Si:H, hydrogen is the topic of intensive research [4] since it may act as a dopant [5]. In addition, during a-Si:H deposition on TCO-coated glass substrates, hydrogen may reduce the oxygen-bonded Sn or Zn atoms to the metallic phase [6].

Gas effusion measurements in general have turned out to provide a fast structural characterization of thin films, since the effusion of gas atoms and molecules from the film interior depends on the atomic density and is strongly modified by the presence of empty spaces (voids). This is particularly true for effusion of rare (inert) gas atoms like He, Ne, and Ar which do not react with the host material [7]. These gas atoms can be brought into the material during deposition or by ion implantation.

Advanced Characterization Techniques for Thin Film Solar Cells, Second Edition.
Edited by Daniel Abou-Ras, Thomas Kirchartz, and Uwe Rau.

The aim of this chapter is to review some effusion measurement techniques, the data analysis, and selected results. Hydrogen effusion (also termed hydrogen evolution) measurements were first applied in thin-film silicon technology by Triska *et al*. [8] in 1975. Gas effusion measurements in general, however, go back to much earlier work, in particular in surface science where this technique has been widely used for characterizing the desorption of atomic or molecular species. Here, the technique is often termed temperature-programmed desorption (TPD) or thermal desorption spectroscopy (TDS). Basic work has been published in extensive review articles like those by Redhead [9] and Pétermann [10].

20.2 Experimental Setup

Two different experimental setups are commonly applied for hydrogen effusion measurements, the "closed" and the "open" effusion systems. In the "closed" system, a sample is heated inside a closed vacuum container, and the hydrogen pressure is recorded as a function of time [11–15]. Provided that readsorption of hydrogen to the sample and adsorption/desorption of hydrogen at the walls of the container are negligible and the gas temperature remains constant, according to the gas equation

$$pV = \nu RT = NkT \tag{20.1}$$

(with the pressure p, the gas volume V, the number of gas atoms/molecules $N = \nu N_A$, the Avogadro number N_A, the gas constant R, and the Boltzmann constant k), the time derivative of the pressure is proportional to the effusion rate $\mathrm{d}N/\mathrm{d}t$.

In an "open" system, the vacuum container where the sample is heated is constantly evacuated by a turbomolecular pump [16]. Due to the constant pumping speed of turbomolecular pumps over a wide pressure range, the hydrogen pressure at the pumping port is a measure of the effusion rate, if the adsorption/desorption at the container walls is negligible and the hydrogen flow is not inhibited by the size of the vacuum lines.

In many cases, quadrupole mass analyzers (QMAs) are applied for partial pressure detection so that not only hydrogen but other desorbing gases can be measured. Such instruments typically require pressures $\leq 10^{-3}$ mbar. In particular at this point, the "open" system has some advantages to the "closed" system, as it is less sensitive to the total amount of effused gases. Both setups allow, in principle, line-of-sight mass spectrometry where effusing gas atoms or molecules can proceed without collision directly into the orifice of the quadrupole instrument. By line-of-sight mass spectrometry, desorbing gas species can clearly be identified, while upon collision, different gas species may form. Since quadrupole instruments only measure ions, usually at the entrance port of the quadrupole instrument, a heated filament generates free electrons

which are accelerated by an applied voltage and cause the ionization of atoms or molecules. Typically voltages up to 100 V are applied, and positive ions are measured. Under these conditions, molecules are partially decomposed showing up in the mass spectra as characteristic cracking patterns, tabulated in the literature [17]. For example, water (molecular weight 18) gives a cracking pattern with the masses 18, 17, 16, 2, and 1, neglecting some presence of deuterium. Thus, even for effusion of several hydrogen-bearing molecule species at the same time, the identification of the effusion of the individual molecule species may be possible. As a heating schedule, most commonly a linear increase of the sample temperature as a function of time is used, but the application of a linear variation of the reciprocal temperature has also been discussed [9].

In the United States and Europe, effusion setups are commonly self-assembled, and there is no standard commercial product. In Japan, there is a commercial product for basic measurements by ESCO Company (ESCO EMD-WA1000S). In the following, we describe the experimental procedures of effusion measurements for the setup realized in the Forschungszentrum Jülich. This latter apparatus has been applied successfully for thin-film characterization for almost 30 years. In Figure 20.1, the setup is shown schematically. It is an "open" system and allows absolute calibration of the effusion rate of various gases. In this effusion system, the samples are placed in a quartz tube (16 mm outer diameter) which is sealed at one side and is constantly pumped by turbomolecular pump at a nominal pumping speed of 150 l/s at the other side. Within the quartz tube, the samples can be moved using a small thin metal boat made of nickel that can be manipulated from the outside of the quartz tube via a small magnet. For the measurement, a sample is placed in the end part of the quartz tube which is heated by an oven. The remaining samples are stored in the cold parts of the quartz tube outside of the heated range. The oven is of relatively low mass in order to ensure a fast heating and cooling and is only 10 cm in length. It has a maximum power consumption of about 0.4 kW and allows heating rates >40 K/min up to a maximum temperature of 1200°C. At this maximum oven temperature, the sample within the quartz tube attains a temperature of about 1050 °C. While a maximum temperature of about 1000 °C is sufficient for measurement of hydrogenated silicon, we note that for alloys of silicon with nitrogen or carbon, higher temperatures may be required for all hydrogen to leave the sample. Higher temperatures (by 150–200 °C) are no problem for the quartz tube but for the oven a special construction may be necessary. Typical (linear) heating rate is 20 K/min (applied for most effusion measurements in this chapter).

For the QMA, a Q-200 (with Faraday cup detector) by Leybold–Heraeus was employed in the original Jülich apparatus. This device is no longer produced, but high-quality apparatus (e.g., Hiden HAL 301/3F) is on the market. For the effusion experiment, various masses (at Jülich up to about 20) are measured sequentially by the quadrupole instrument while the temperature rises. Measurements of different masses require a time delay in order to account for the RC time of

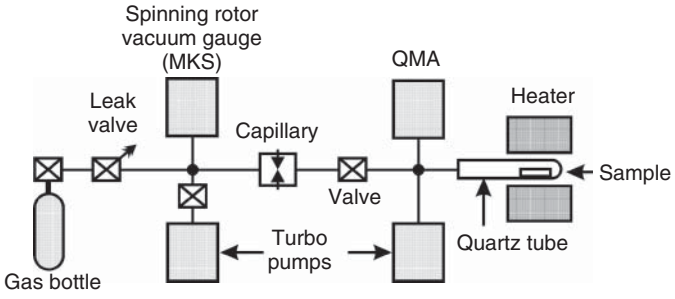

Figure 20.1 Schematic illustration of hydrogen effusion setup employed at Jülich. Samples are placed in a quartz tube which is evacuated by a turbopump. Upon heating, effusing gases are detected by a quadrupole mass analyzer (QMA). The left part of the effusion setup (separated by a valve) is used for calibration (see text).

the Faraday cup signal amplifier. The data are recorded via PC. The apparatus described so far can provide relative measurements only. In order to achieve absolute measurements, a calibration system as also shown schematically in Figure 20.1 has been implemented.

Calibration is achieved by inserting well-known flows of calibration gases into the apparatus and by comparing the quadrupole reading of the calibration gas flow with that from the sample. In order to establish the calibration gas flow, a capillary is used with dimensions chosen such that a pressure p on the higher pressure side of the capillary of $p \approx 10^{-3} - 10^{-2}$ mbar results in a gas flow of about 10^{16} atoms/s through the capillary. Since such a flow causes only a weak rise of pressure (up to $10^{-5} - 10^{-4}$ mbar) in the main turbopumped chamber, the pressure drop within the capillary exceeds two orders of magnitude. Then the gas flow through the capillary $\mathrm{d}N/\mathrm{d}t$ given by the Knudsen formula for molecular flow

$$\mathrm{d}N/\mathrm{d}t = C_1 p (M)^{-1/2} \tag{20.2}$$

depends only on the gas type (molecular mass M), the capillary dimensions, and the pressure p at the higher pressure side of the capillary. The latter is measured at Jülich by a highly accurate *spinning rotor vacuum gauge* (MKS).

The constant C_1 can be determined by establishing a well-known flow $\mathrm{d}N/\mathrm{d}t$ of a calibration gas of molecular mass M_0, for example, by using a well-known volume as a source of the calibration gas and monitoring the pressure drop in this volume as a function of time. While this pressure drop yields with Equation 20.1 the rate $\mathrm{d}N/\mathrm{d}t$, with the pressure p measured at the higher pressure side of the capillary and $M = M_0$, the constant C_1 in Equation 20.2 is obtained.

Once C_1 is known, the flows $\mathrm{d}N/\mathrm{d}t$ of other gases can be calculated according to Equation 20.2, using the measured pressure p and the known molecular mass M. With this setup, only the flows of highly pure gases can be calibrated which means that highly pure calibration gases are required (supplied, e.g., in the MINICAN system by Linde), the system must be highly leak tight, and when switching

from one calibration gas to another, the calibration system needs to be pumped to low pressure (typically 5×10^{-7} mbar). At Jülich, a turbopump with a nominal pumping speed of 50 l/s is employed in the calibration system.

For an accurate measurement of a quadrupole signal for a given mass, one needs to account for two sources of signal drifts. One possibility of an error arises because the signal height of a given mass is not measured at the peak center of the quadrupole signal but rather in the flanks. This drift is usually fairly long term, and it has proven sufficient to optimize the measuring window to the peak maximum once per week. The other possible error arises because the sensitivity of a quadrupole may change (it typically decreases) as a function of time, likely due to changes of the degree of ionization of the incoming gas species. The sensitivity factors of different gases were found to vary only slightly relative to each other. To account for this effect, we determined in calibration procedures prior to and after the actual effusion experiment the sensitivity factors S_X^A of a given gas molecule X by comparing the quadrupole reading with the actual gas flow calculated by Equation 20.2. In addition to the gases expected to arise from the effusion experiment, a reference gas with the sensitivity factor S_Y^R (Y typically He, Ne, or Kr) is also calibrated. From these calibration runs relative sensitivity factors S_X^A/S_Y^R for a given molecule X are obtained. To determine the actual sensitivity S_X^A during an effusion run, the reference gas is kept flowing, and the actual value of S_Y^A is monitored. The actual value of S_X^A is then determined by $S_X^A = S_Y^A \left(S_X^R/S_Y^R\right)$ [18]. By monitoring a reference gas flow during an effusion run, irregularities of the effusion system like nonconstant pumping speed or sudden changes in quadrupole sensitivity (which sometimes occur when effused gases like fluorine contaminate the QMA system) are also detected. Besides the calibration described here, effusion measurements at Jülich have often been calibrated by measuring samples which had been implanted with a well-known dose of H or He ions, or by comparing the effusion results with impurity concentrations measured otherwise.

Important for successful H effusion measurements is also the choice of the film substrate which should affect the effusion process as little as possible. In early work, often aluminum foils or rock salt substrates were employed which were removed by hydrochloric acid or water prior to effusion [12, 15]. Metal substrates are usually not well suited as they often contain dissolved hydrogen leading to a high hydrogen background signal. Moreover, at the interface to amorphous silicon layers, silicide formation or metal-induced crystallization may occur in certain temperature ranges leading to modifications of the effusion spectra. Glass often leads to a high hydrogen background signal, and problems may arise as it gets soft and melts at elevated temperature. We obtained best results with crystalline silicon, germanium (both only moderately doped), or sapphire platelets as substrates. In these cases, the hydrogen background signal is low, arising primarily from surface-adsorbed water. However, for certain deposition conditions, the films on the latter substrates tend to form blisters and pinholes [19] typically near 300–400 °C causing modifications of the effusion spectra [16]. The reason is presumably that these latter substrates have a low solubility for molecular hydrogen

so that H_2 precipitates at the film–substrate interface. The effect can be avoided by a thin coating with SiO_2 which provides a higher H_2 solubility and diffusivity. Fused quartz substrates usually do not show pinhole formation, but hydrogen in-diffusion at 500–650°C and out-diffusion above 700 °C have been reported [16].

The detection limit for the effusion of molecular hydrogen (molecular mass 2) of the Jülich system is near 10^{13} molecules/s. It is caused primarily by a background mass 2 signal due to H_2O desorption from parts of the apparatus which are not heated out (e.g., the quartz-metal connection) when pumping down the effusion apparatus. Since the hydrogen isotope deuterium (present in natural hydrogen at about 0.015 at.%) has a much lower background and thus a lower detection limit, deuterated materials are often prepared and measured. Note that for hydrogen effusion from silicon, the results for the two different hydrogen isotopes, namely, H_2 proper and D_2 (deuterium), are quite similar, that is, there is no significant isotope effect visible in hydrogen effusion [20].

Recently it was demonstrated by Kherani *et al*. [21] that effusion measurements of radioactive tritium (T) from a-Si:H:T films are possible without high vacuum. Here, effusing tritium (primarily HT molecules) moves in an argon atmosphere to an ionization chamber where the radioactive decay of T is monitored. The effusion spectra for tritium from amorphous silicon were not found to differ significantly from those for hydrogen or deuterium. Due to the high sensitivity of tritium decay measurements, this method can give a much lower detection limit for effusing hydrogen than obtained for the nonradioactive isotopes of hydrogen.

20.3 Data Analysis

If hydrogen effusion measurements are only performed to measure the absolute hydrogen concentration, the effusion rate is integrated over the time and temperature, that is,

$$N_{\mathrm{H}} = \int (\mathrm{d}N/\mathrm{d}t)\mathrm{d}t. \tag{20.3}$$

Additional measurement techniques like secondary ion mass spectrometry (SIMS), infrared absorption, and others may be necessary to assure that after completion of the experiment all hydrogen has left the material. As mentioned in Section 20.2, a relatively simple check of calibration is the measurement of a well-known implantation dose of a given gas species.

If the aim of the experiment is the study of hydrogen stability and processes of its release, some knowledge is required on the distribution of hydrogen within the thin film and on its bonding state, namely, if hydrogen is predominantly present as a molecule or if it is bonded to atoms of the amorphous network. The hydrogen depth profile can be conveniently measured, for example, by SIMS profiling (see Section 19.2); the bonding state can be evaluated, for example, by infrared absorption measurements which give information on the concentration of hydrogen in bonds to amorphous network atoms (Si, C, etc.).

In the following we describe the data analysis assuming a constant hydrogen concentration for the as-deposited material throughout the film depth, the bonding of hydrogen primarily to atoms of the host material (little H_2) and the measurement of hydrogen effusion in a high vacuum system applying a constant heating rate.

Hydrogen effusion involves then surface desorption of hydrogen which can be described for a single process by the rate equation [1, 9, 10]

$$\mathrm{d}(N/N_0)/\mathrm{d}t = (kT/h)(1 - (N/N_0))^n \exp(-\Delta G/kT) \tag{20.4}$$

(with N_0 and N denoting the original and effused hydrogen concentrations, k and h the Boltzmann and Planck constants, respectively, n the order of reaction, and ΔG *the free energy of desorption*). For simplicity, the transmission coefficient [10] is set equal to unity in Equation 20.4. For a temperature T rising as $T = T_0 + ßt$ ($ß$ the linear heating rate), Equation 20.4 describes an effusion rate $\mathrm{d}N/\mathrm{d}t$ first rising and then falling as a function of temperature and time. However, this surface desorption formula will only describe the measured effusion curves or part of them as long as surface desorption is the rate-limiting step for effusion. As we are dealing with thin films, diffusion of hydrogen as an atom or a molecule to the film surface may also be a rate-limiting step. Therefore, the analysis of the effusion data requires the identification of rate-limiting processes and the identification of the diffusing species (molecular or atomic hydrogen). Since in an effusion measurement a sample is heated to high temperatures, structural changes may occur which will also influence the effusion curves, in particular by changing the diffusion process.

20.3.1
Identification of Rate-Limiting Process

Methods for analysis of effusion data and for the identification of rate-limiting effusion processes are demonstrated in the following part of Section 20.3 for a-Si:H and a-Ge:H films. Typical hydrogen (deuterium) effusion transients (also termed effusion spectra [9]) for such material are shown in Figure 20.2a [22] and b [18]. These films were deposited by plasma decomposition of SiH_4 and GeD_4 gases, respectively, at different substrate temperatures T_S. Film thickness was approximately 1 µm. For this deposition method, the hydrogen (deuterium) concentration in the films decreases significantly with increasing T_S so that films deposited near room temperature have hydrogen concentrations >20 at.%, decreasing to below 5 at.% for the highest substrate temperatures shown.

For identification of the rate-limiting process of hydrogen effusion, the effusing species must be known. For a-Si:H, line-of-sight mass spectrometry [23] demonstrates that only molecular hydrogen desorbs, that is, no atomic H and no SiH_x species ($x = 1-4$) were seen. The situation for a-Ge:H is likely to be similar. This means that the primary rupture of Si:H or Ge:H bonds and the diffusion of molecular or atomic hydrogen to the film surface could be rate-limiting steps. In the case of diffusion of atomic hydrogen, a surface recombination step of atomic

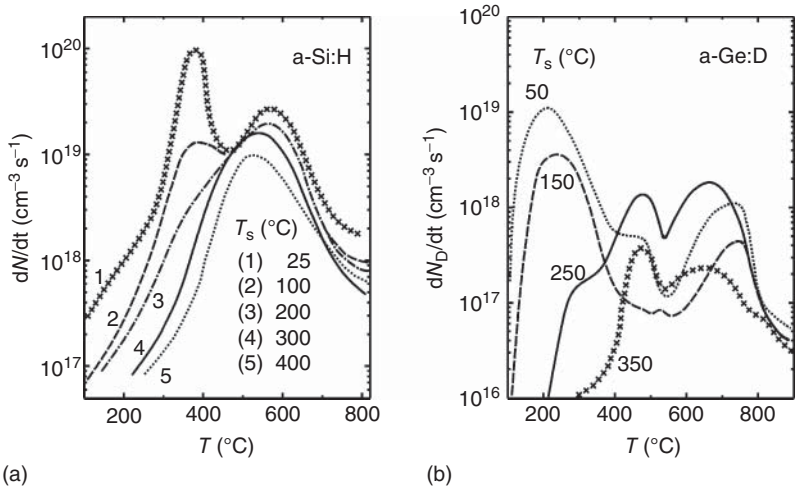

Figure 20.2 Effusion spectra of undoped (a) a-Si:H (Reproduced from Beyer *et al*. [22] with permission of Springer) and (b) a-Ge:D (Reproduced from Beyer *et al*. [18] with permission of Taylor & Francis) deposited at various substrate temperatures T_S.

hydrogen to form hydrogen molecules could also limit the hydrogen effusion rate. In addition, as mentioned before, changes in effusion rate with the result of effusion maxima or minima can arise if the structure of a material changes in a narrow temperature range. In particular the H diffusion processes may be affected by structural changes. A major structural change of amorphous films occurs upon crystallization.

According to differential thermal analysis measurements performed at heating rates close to the present one, crystallization of a-Si:H is known to take place at $T = 700 - 800\,°C$ [24] and of a-Ge:H near 500 °C [25]. In Figure 20.2, crystallization is particularly visible in the effusion spectra of a-Ge:D by the effusion dip near 500 °C. In the case of a-Si:H, crystallization is often barely visible since at high temperatures $T > 700\,°C$, little hydrogen is commonly present.

Up to the crystallization temperature (see Figure 20.2a and b), the effusion spectra of a-Si:H and a-Ge:D show basically one or two effusion peaks with maximum effusion rates for a-Si:H near 400 and 600 °C and for a-Ge:H near 200 and 450 °C. At high substrate temperatures ($T_S \geq 200\,°C$ for a-Si:H and $T_S \geq 250\,°C$ for a-Ge:H), only the high-temperature (HT) peaks remain.

Several experiments then allow the identification of the rate-limiting effusion process for each effusion peak. An effusion process limited by diffusion of hydrogen atoms or hydrogen molecules can be detected (i) by measuring hydrogen depth profiles by SIMS as a function of annealing or (ii) by measuring the effusion spectra of identical films of different thickness. In the first case, a decrease in hydrogen concentration toward the film surface and for many substrates also toward the film–substrate interface is expected. In the second case, the (average)

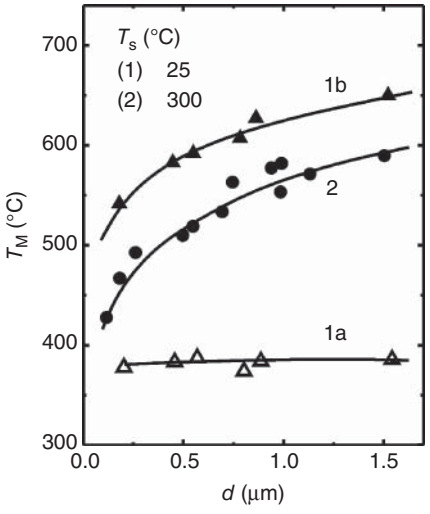

Figure 20.3 Temperature T_M of hydrogen effusion maximum versus film thickness d for plasma-grown a-Si:H. Curves 1a and 1b refer to the low-temperature and high-temperature effusion peaks of $T_S = 25\,°C$ material, respectively, curve 2 to the effusion peak of $T_S = 300\,°C$ material. (Reproduced from Beyer [22] with permission of Springer.)

diffusion length for hydrogen species required to leave the film rises with increasing film thickness. Accordingly, the effusion peak will shift to higher temperature [13, 16]. In Figure 20.3, the temperature T_M of maximum effusion rate of the two effusion peaks is plotted for a-Si:H films as a function of film thickness d [22]. It is seen that the low-temperature peak is practically independent of film thickness, while the high temperature peaks shift to higher temperature.

Accordingly, it can be concluded that in the low temperature peaks in Figure 20.2a, hydrogen effusion from a-Si:H is not limited by diffusion but by the rupture of Si:H bonds. In contrast, in the high temperature peaks of Figure 20.2a, diffusion is the rate-limiting step. For both a-Si:H and a-Ge:H, the analysis of the results shown in Figure 20.4 leads to the same conclusion for both materials.

Here, the effusion rate of molecular H_2, HD, and D_2 is plotted as a function of temperature for sandwich structures of deuterated (or partly deuterated) material embedded into two layers of hydrogenated material. Note that in these samples, as verified by SIMS depth profiling, hydrogen effuses both at the actual surface and at the film–substrate interface. The fact that the effusion maxima of H_2, HD, and D_2 in the low temperature (LT) peak lie all nearly at the same temperature demonstrates that effusion is here not limited by diffusion. In the high temperature (HT) peaks, on the other hand, the HD and D_2 peaks show up at higher temperature than the H_2 peaks demonstrating that the effusion rate of hydrogen is limited by diffusion.

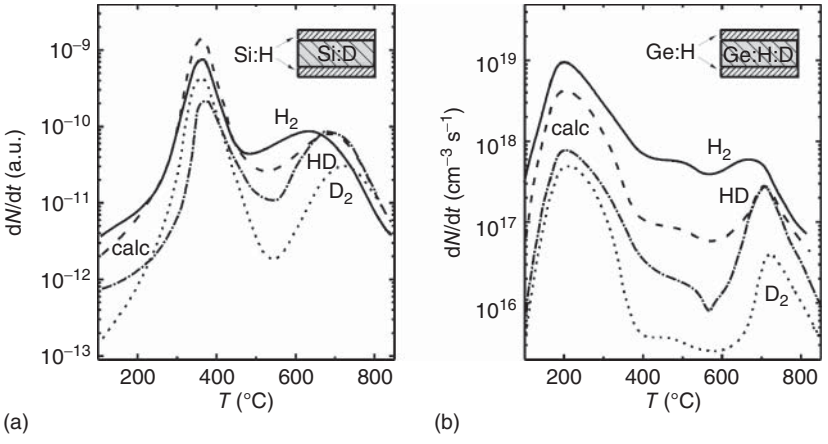

Figure 20.4 H_2, D_2, and HD effusion rates versus temperature T for sandwich samples of (a) undoped a-Si:H/a-Si:D/a-Si:H (substrate temperature $T_S = 25\,°C$) (Reproduced from Beyer [22] with permission of Springer) and (b) a-Ge:H/a-Ge:H:D/a-Ge:H ($T_S = 50\,°C$). Dashed curves give the HD effusion rate calculated according to Equation 20.5. (Reproduced from Beyer [18] with permission of Taylor & Francis)

20.3.2 Analysis of Diffusing Hydrogen Species from Hydrogen Effusion Measurements

The effusion curves in Figure 20.4 can also be used for the identification of the diffusing hydrogen species. If the diffusing species is *molecular* hydrogen (deuterium), little effusion of HD is expected which may arise only from the interface areas between hydrogenated and deuterated layers and from interaction of diffusing *molecular* hydrogen (deuterium) with bound deuterium (hydrogen). In the other case of diffusion of *atomic* hydrogen (deuterium), a large effusion rate of HD is expected as HD is then formed at the film surface by a recombination process. If dN_H/dt and dN_D/dt are the effusion rates of H_2 and D_2, respectively, the effusion rate dN_{HD}/dt of HD is given by

$$dN_{HD}/dt = 2((dN_H/dt)(dN_D/dt))^{1/2}. \quad (20.5)$$

This effusion rate of HD follows from the rate equation (Equation 20.4) for $n = 2$, yielding

$$dN_H/dt + dN_{HD}/dt + dN_D/dt = \text{constant}(N_H + N_D)^2 \exp(-\Delta G/kT). \quad (20.6)$$

The results in Figure 20.4 thus demonstrate that in the low temperature effusion peaks, primarily molecular hydrogen is diffusing for both a-Si:H and a-Ge:H. The fact that the effusion maxima of H_2, HD, and D_2 for this LT peak occur at the same temperature (implying that H_2 effusion is not limited by diffusion) shows that diffusion of molecular hydrogen in these materials is very fast. In the HT peaks, on the other hand, the measured and (according to Equation 20.5) calculated HD signals coincide, suggesting diffusion by atomic H. Since the deuterated peaks

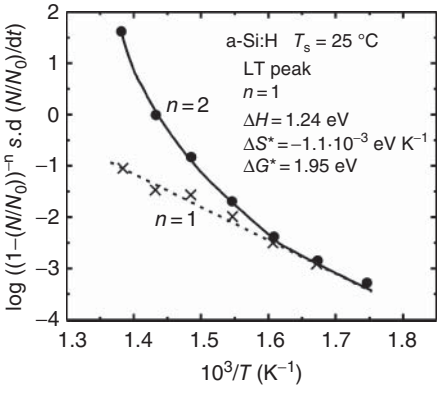

Figure 20.5 Analysis of LT hydrogen effusion peak of undoped a-Si:H ($T_S = 25\,°C$) in terms of Equation 20.4. (Reproduced from Beyer [22] with permission of Springer).

occur at higher temperature than the hydrogenated ones, effusion is apparently limited by diffusion. Thus, in this case, surface recombination of atomic hydrogen is not limiting the effusion rate. Similar results as for the HT peaks of the low substrate temperature samples of Figure 20.4a and b are obtained for H/D/H sandwich samples deposited at higher substrate temperature, showing one (HT) effusion peak only.

Thus hydrogen effusion measurements are found to provide an important structural information, namely, that for plasma-grown a-Si:H and a-Ge:H films of low substrate temperature and high hydrogen content, hydrogen molecules are diffusing very fast, while for high substrate temperatures and low hydrogen content, apparently a more dense material is present where molecular hydrogen (with a molecular diameter of about 2.5 Å) cannot diffuse and H diffusion takes place at much slower rate by atomic hydrogen.

After assigning the hydrogen release process of a given effusion peak to structural changes or to desorption or diffusion, the appropriate kinetic parameters in the latter case, in particular the energies involved, can be determined.

20.3.3
Analysis of H_2 Surface Desorption

For an effusion peak limited by surface desorption, Equation 20.4 is applicable for describing the effusion curves. The order of reaction can be determined by an analysis of the peak shape [9, 14] if there is one fixed free energy of desorption ΔG only. One expects $n = 1$ if immobile neighboring hydrogen atoms form H_2 molecules during desorption, whereas for a surface recombination process of mobile atomic hydrogen, the order of reaction should be $n = 2$. According to Equation 20.4, a plot of $\log(\mathrm{d}(N/N_0)/\mathrm{d}t)\ (1 - (N/N_0))^{-n}$ versus $1/T$ should yield (for a single ΔG) for $n = 1$ a straight line if the order of reaction is unity. The results of Figure 20.5 [22] demonstrate for the low temperature effusion of a-Si:H that this is indeed the case.

Since $\Delta G = \Delta H - T\Delta S$ (ΔH the enthalpy and ΔS the entropy of the reaction), from the slope of the straight line in Figure 20.5, the enthalpy ΔH can be determined. From the intercept I of the straight line at $1/T = 0$, the (experimental) entropy ΔS follows as $I = (kT/h)\exp(\Delta S/k)$, and thus ΔG ($\Delta G \approx 1.95$ eV for a-Si:H) is obtained.

An alternative way to determine ΔH, ΔS, and thus ΔG is the measurement of the effusion peak as a function of the heating rate $ß$. According to Beyer and Wagner [26], for a linear heating rate $ß$, the formula

$$\ln(\beta/kT_M{}^2) = \ln[n(kT_M/h)(\exp \Delta S/k)(1 - N_M/N_0)^{n-1}/\Delta H] - \Delta H/kT_M \quad (20.7)$$

is valid. Here, N_M is the hydrogen concentration effused at the temperature T_M. In the case of the first-order reaction, this formula simplifies and leads to the approximation formula [9]

$$\Delta G/kT_M = \ln(\nu_1 T_M/\beta) - 3.64 \quad (20.8)$$

with $ß$ the linear heating rate, $T = T_0 + ßT$, and the characteristic frequency $\nu_1 = kT/h$ approximately equal to the phonon frequency, that is, $\nu_1 \approx 10^{13}\ s^{-1}$.

The analysis of the effusion curves in terms of kinetic parameters becomes difficult or impossible when dealing with several overlapping processes (with different ΔG) rather than with a single process. In particular, a peak shape analysis like the one using Equation 20.4 will become rather meaningless. In this case, Equations 20.7 and 20.8 may still be applicable describing then the dominant effusion process only.

20.3.4
Analysis of Diffusion-Limited Effusion

If the effusion process is limited by diffusion, the effusion peak temperature T_M is related to the diffusion coefficient near this latter temperature. The correlation between effusion and diffusion parameters is obtained by solving the diffusion equation for out-diffusion of hydrogen from a film of thickness d at constant heating rate $ß$. If out-diffusion toward both surface and film–substrate interface sides of a film is assumed, the relation

$$\begin{aligned}\ln(D/E_D) &= \ln(d^2\beta/\pi^2 kT_M{}^2) \\ &= \ln(D_0 E_D) - E_D/kT_M \end{aligned} \quad (20.9)$$

is obtained [26]. Also assumed for this relation is that the hydrogen diffusion coefficient D can be expressed by the Arrhenius dependence

$$D = D_0 \exp(-E_D/kT) \quad (20.10)$$

with D_0 the diffusion prefactor and E_D the diffusion energy. The diffusion parameters D_0 and E_D can be obtained according to Equation 20.9 by plotting $\ln(d^2ß/\pi^2 kT_M{}^2)$ versus $1/T_M$ either for a series of identical films prepared with different thickness d or of samples measured with a different heating rate $ß$.

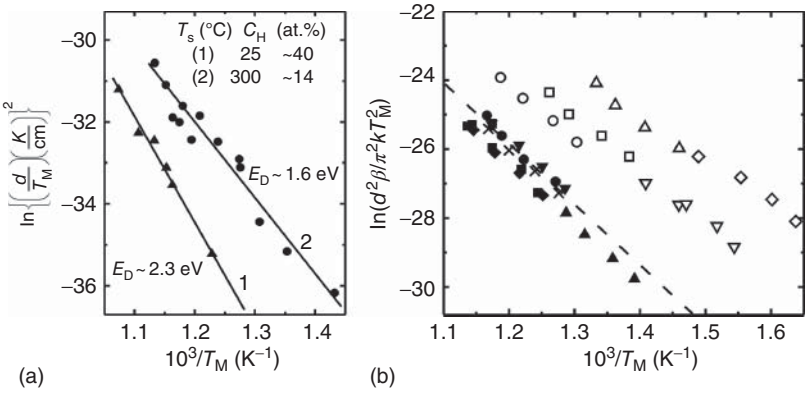

Figure 20.6 (a) Plot of $\ln((d/T_M)^2)$ versus $1/T_M$ for (diffusion-limited) effusion data of Figure 20.3. (Reproduced from Beyer [22] with permission of Springer.) (b) Plot of $\ln(d^2\beta/\pi^2kT_M^2)$ versus $1/T_M$ for samples measured at a different heating rate β. Closed symbols undoped, open symbols boron doped, x: phosphorus doped [26], dashed curve: data by Ref. [27].

Two examples for the application of Equation 20.9, in order to determine the hydrogen diffusion parameters, are shown in Figure 20.6a and b. A close agreement with results for hydrogen diffusion from SIMS hydrogen–deuterium interdiffusion measurements ($D_0 = 1.17 \times 10^{-2}$ cm^2/s, $E_D = 1.53$ eV [27]) is observed as long as the material is not changing its structure significantly between the annealing temperature of the SIMS diffusion measurements (typically 300–450 °C) and the temperature of the evaluated H effusion peak (typically 600 °C). This condition is fulfilled for curve 2 of Figure 20.6a and for all samples in Figure 20.6b. The dashed line in Figure 20.6b shows the results of hydrogen and deuterium interdiffusion measurements by Carlson and Magee [27] for undoped material demonstrating the close agreement for the H diffusion data obtained by the different methods. The results give for undoped a-Si:H deposited between 280 and 300 °C hydrogen diffusion prefactors between 8×10^{-3} and 1.2×10^{-2} cm^2/s and diffusion energies E_D between 1.49 and 1.54 eV.

One may ask to what degree the experimental effusion curves are fitted by a single H diffusion process, that is, by a single Arrhenius dependence. Using $D_0 = 1.1 \times 10^{-2}$ cm^2/s and $E_D = 1.49$ eV determined by the procedure employed in Figure 20.6b for a given sample, the corresponding effusion rate was calculated [22] according to Equation 8 in Ref. 26 and normalized to fit the experimental data in the effusion maximum. The results of experimental and calculated effusion curves are shown in Figure 20.7. A good agreement is found in a wide temperature range $T \leq T_M$. A deviation between experimental and calculated curves occurs primarily at $T > T_M \approx 550$°C suggesting that in this high temperature range, diffusion processes with higher diffusion energy and/or material changes are involved.

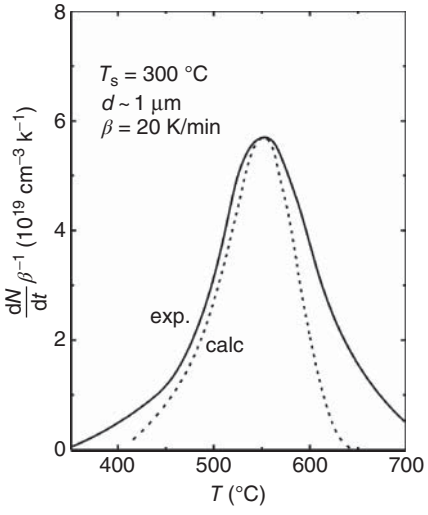

Figure 20.7 Calculated and experimental hydrogen effusion rate of plasma-grown a-Si:H (dense material) versus temperature. (Reproduced from Beyer [22] with permission of Springer.)

A much stronger structural change than for the material of Figure 20.7 occurs, however, for the low substrate temperature a-Si:H material (curve 1 in Figure 20.6a). This material was analyzed in Sections 20.3.1 and 20.3.2 to be void rich up to annealing temperatures of 400 °C and dense for annealing temperatures of 500–600 °C. It is likely that due to material reconstruction (upon release of much hydrogen in the LT effusion peak), the HT effusion peak is here retarded, causing the changed diffusion parameters of curve 1 in Figure 20.6a, as discussed also by Kherani *et al*. [21].

If measurements of the maximum effusion rate T_M as a function of film thickness or heating rate are unavailable, the diffusion energy E_D may be roughly estimated from T_M by using Equation 20.9 and assuming, for example, for D_0 the theoretical diffusion prefactor

$$D_0 = (1/6)\nu_1 a^2 \approx 10^{-3} \text{ cm}^2/\text{ s} \tag{20.11}$$

for a-Si:H (a is the interatomic distance) [28]. For the data in Figure 20.7, $E_D \approx 1.33$ eV is obtained.

20.3.5
Analysis of Effusion Spectra in Terms of Hydrogen Density of States

Jackson *et al*. [29] proposed to analyze hydrogen effusion measurements in terms of a hydrogen density of states, in analogy to deep-level transient spectroscopy (DLTS) measurements giving the electronic density of trap states. They relate the effusion rate dN/dt at a particular time t of the effusion experiment with the position of the hydrogen chemical potential $\mu(t)$ relative to a surface barrier energy

(for hydrogen desorption) or transport energy E for hydrogen diffusion (k is the Boltzmann constant)

$$dN_H/dt = C \exp(-(E - \mu(t))/kT(t)). \quad (20.12)$$

For the hydrogen density of states $g_H(E)$, the relation

$$g_H(\mu) \approx \partial N_H/\partial \mu \quad (20.13)$$

is assumed to be valid. According to Equation 20.12 and for a fixed prefactor C, the experimental effusion rate gives the time dependence of the chemical potential $\mu(t)$ relative to the energy E. Equation 20.13 then yields the hydrogen density of states near the H chemical potential μ. The authors assume $C = 10^{27}\,cm^{-2}\,s^{-1}$ for hydrogen surface desorption and $C \approx 10^{25} - 10^{26}\,cm^{-2}\,s^{-1}$ for diffusion-limited effusion for a sample of 0.5 µm film thickness. The results for sputtered deuterated a-Si:H films gave for hydrogen surface desorption (LT effusion peak) a relatively sharp H density-of-states distribution at an energy of about 1.85 eV. This energy corresponds to the value of $\Delta G \approx 1.9$ eV characterizing the LT hydrogen effusion peak of undoped hydrogen-rich a-Si:H (see Section 20.3.3). For the diffusion-related effusion, the authors evaluated a relatively broad hydrogen density of states extending between energies of about 1.6 and about 2.2 eV below the hydrogen transport path.

Drawbacks of the method are that the determined $g_H(E)$ involves any change of H effusion due to structural changes, like crystallization, densification, or formation of bubbles. Actually such structural changes are obscured, as such changes are recognized in the effusion spectra at characteristic temperatures (like the crystallization temperature) but appear in the H density-of-states distribution at certain energies defined by the value of C used. Furthermore, in particular at low hydrogen content, hydrogen (mass 2) signals arising from H_2O and CH_4 effusion will also contribute to the "hydrogen density of states." The analysis, furthermore, is questionable for diffusion-limited effusion as hydrogen atoms (at some depth L from the next film surface) set free to move in the transport path related to a decrease in H chemical potential will not immediately be desorbed. Due to the diffusion-limited effusion process, this hydrogen will desorb after the time $t = L^2/4$ $D(t, T)$, approximately. Here, $D(t, T)$ is the H diffusion coefficient at the given time and temperature. Thus, it appears unlikely that this method could detect any particular H density-of-states feature except for the case where the samples are extremely thin.

20.3.6
Analysis of Film Microstructure by Effusion of Implanted Rare Gases

In the past few years, it was demonstrated that the effusion of rare (noble) gases like He, Ne, or Ar provides a fast characterization of thin films [7]. Since these atoms do not bind to atoms of the host material, the effusion curves are affected primarily by the material density and by the presence of various types of voids. These atoms can be brought into the material either during deposition or by ion

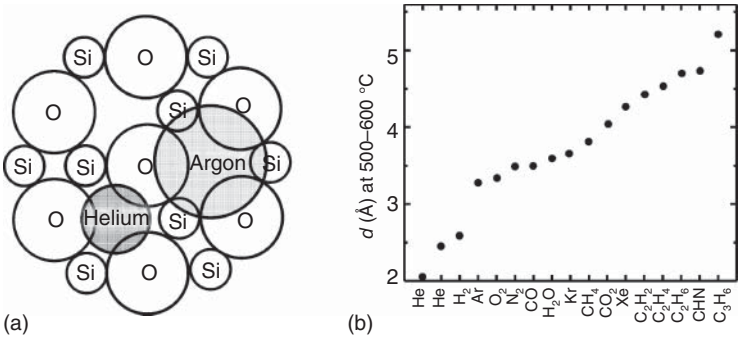

Figure 20.8 (a) Schematic illustration of helium and argon incorporation in quartz (from Ref. [32]). (b) Diameter *d* of atoms and molecules ordered according to size from gas viscosity measurements. (Reproduced from Eucken [33] with permission of Springer.)

implantation. In the latter case, the dose needs to be as small as possible to avoid ion bombardment damage which usually densifies a given material but may also lead to formation of bubbles (isolated voids) filled with the rare gas. In general, the implantation dose should be $\leq 10^{16}\,\mathrm{cm}^{-2}$ [7, 30]. The implantation energy is typically chosen such that the maximum of the implanted atom distribution lies near half of the film thickness. Diffusion of rare gases in a solid has been described by the process of doorway diffusion, first applied to the diffusion of rare gases in glass [31]. Considering rare gas atoms sitting in cages of a host material (see Figure 20.8a), diffusion of a given atom is considered to proceed if, by thermal vibrations, the doorway of a given cage opens wide enough so that the atom can move from one cage to another.

By classical modeling, Anderson and Stuart [31] derived the formula

$$E_\mathrm{D} = CGr_\mathrm{D}(r - r_\mathrm{D})^2 \tag{20.14}$$

with a constant C, a shear modulus G, a doorway radius r_D, and a radius r of the diffusing atoms. In Figure 20.8b, approximate sizes of various atoms and molecules are given, determined by viscosity measurements [33]. Note that these measurements give temperature-dependent sizes and that the diameters shown here refer to (mostly) $T \approx 500-600\,^\circ\mathrm{C}$. Note also that the size of neon and H_2 is quite similar, so that neon out-diffusion can be used to predict H_2 diffusion, which is of great importance for hydrogen stability issues [28].

According to Equation 20.14, a strong dependence of the diffusion energy E_D on the size of the diffusing atoms and molecules is expected, and the corresponding effusion peaks often show such a dependence, as depicted in Figure 20.9a. Note that also the widths of the rare gas effusion peaks give structural information on the material, namely, about its homogeneity, since broader effusion structures indicate the presence of more inhomogeneous materials or of material structure which is more strongly changing with rising annealing temperature. If we assume for the diffusion coefficients of the rare gases Arrhenius dependences $D = D_0 \exp(-E_\mathrm{D}/kT)$, the diffusion energy E_D can be estimated from T_M by

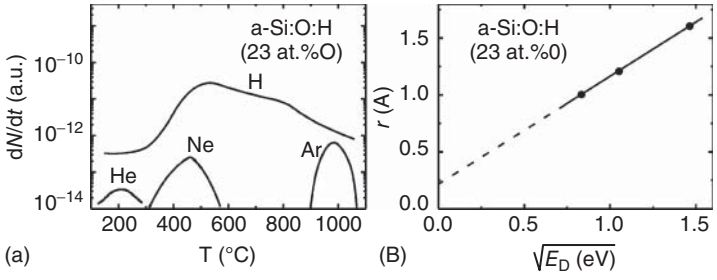

Figure 20.9 (a) Effusion spectra of hydrogen and implanted He, Ne, and Ar for plasma-deposited a-Si:O:H (oxygen concentration ≈ 23 at.%). (b) Atomic radius r of diffusing rare gas atoms in a-Si:O:H of (a) versus square root of diffusion energy.

Equation 20.9, using the theoretical diffusion prefactor D_0 (Equation 20.11). According to Equation 20.14, a plot of the atomic radius r versus $(E_D)^{1/2}$ should give a straight line with the intercept r_D at $E_D = 0$. In Figure 20.9b, the atomic radius r is plotted versus $(E_D)^{1/2}$ for the effusion results of Figure 20.9a. A nearly straight line is obtained with an intercept $r_D \approx 0.2$ Å. It must be noted, however, that this analysis for the present a-Si:O:H material is not expected to give accurate values for r_D. The broad hydrogen effusion spectrum in Figure 20.9a indicates that structural changes occur with rising annealing temperature so that the assumption of a constant r_D up to the annealing temperature of about 1000 °C appears quite unlikely.

For characterization of microstructure, the analysis of helium effusion peaks turned out to be highly useful [7]. This is demonstrated in Figure 20.10a and b, showing the effusion of implanted He for plasma-grown a-Si:H and a-Ge:H films, deposited at different substrate temperatures T_S.

For higher substrate temperatures T_S, the results show He effusion maxima near $T_M = 400$ °C for a-Si:H and near 370 °C for a-Ge:H. Similar peak effusion temperatures are obtained when He is implanted in crystalline silicon or germanium, and in fact, from literature data of the diffusion of helium in crystalline Si and Ge [34], similar effusion peak temperatures are calculated according to Equation 20.9. In the picture of doorway diffusion, the difference between silicon and germanium may be related to the different bond length of about 2.35 Å for silicon and about 2.45 Å for Ge [35]. With decreasing substrate temperatures, the He effusion temperature decreases, indicating a more open structure (increasing doorway radius in Equation 20.14). Qualitatively, this structural change agrees with the results of hydrogen effusion (see Section 20.3.1). Another interesting feature in Figure 20.10a and b is the appearance of a second He effusion peak at high temperatures $T > 500$ °C for substrate temperatures near 200 °C for a-Si:H and 300 °C for a-Ge:H. Such peaks have been explained by the presence of isolated voids [7]. If He enters such void, it can leave only (except that the voids disappear by structural changes) if according to the gas equation (Equation 20.1) the pressure within the void gets such high that He returns into the network. Thus the temperature of this high temperature He peak will depend primarily on the

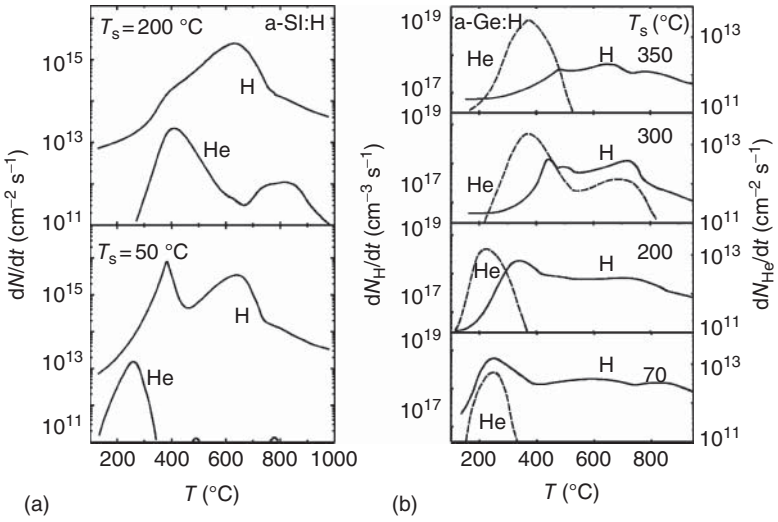

Figure 20.10 Effusion spectra of hydrogen and (implanted) helium for undoped (a) a-Si:H and (b) a-Ge:H, deposited at different substrate temperatures T_S.

void size and the amount of He. Since this high temperature He effusion usually occurs when the material has crystallized (for a-Si:H and a-Ge:H), this void size has unlikely much relation to the original material and is not evaluated. Instead, the ratio F^{HT} of high temperature to total He effusion is analyzed. The concept is that F^{HT} describes the probability for diffusing He atoms to get trapped in isolated voids, that is, F^{HT} is a measure of the concentration of isolated voids, present from the deposition process.

In Figure 20.11a and b, the results for T_M and F^{HT} for plasma-grown a-Si:H and a-Ge:H films are compared. It is seen that the decrease of T_M with decreasing substrate temperature T_S (and increasing hydrogen content) takes place quite gradually for a-Si:H, while it occurs in a rather narrow temperature range between 200 and 250 °C for a-Ge:H under the applied deposition conditions. Another interesting result is the enhanced formation of isolated voids near $T_S = 200$ °C for (plasma-grown) a-Si:H and near $T_S = 250$ °C for a-Ge:H, while isolated voids show up in much smaller concentration at low substrate temperatures ($T_S < 200$ °C) and high T_S (>300 °C). This formation of isolated voids has been explained by diffusion effects of hydrogen in the subsurface region (close to the surface where the network is still fairly flexible) at the temperature of deposition, resulting in hydrogen (H_2) precipitation and thus in the formation of voids [7, 30]. However, voids may also arise by the H effusion process if much hydrogen leaves the material (see Section 20.4.1.1). No isolated voids trapping helium are expected when the material is permeable to diffusion of H_2 at low substrate temperatures. At high substrate temperatures, the concentration of isolated voids in both materials gets small, presumably because the concentration of incorporated hydrogen gets small as well.

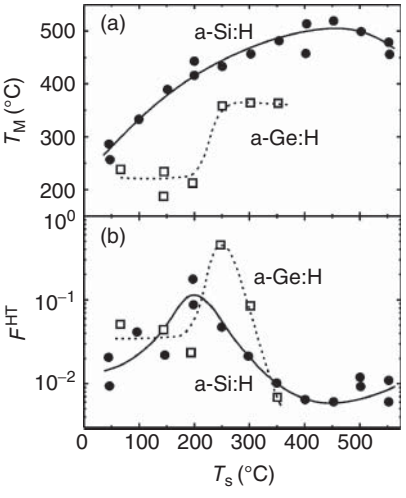

Figure 20.11 (a) Temperature T_M of (lower temperature) He effusion peak and (b) ratio F^{HT} of a-Si:H and a-Ge:H films as a function of substrate temperature T_S [30].

20.4
Discussion of Selected Results

20.4.1
Amorphous Silicon and Germanium Films

20.4.1.1 Material Density versus Annealing and Hydrogen Content

In the previous section, the effusion results of amorphous silicon and germanium films have been used to illustrate the evaluation of hydrogen and helium effusion measurements. The general picture obtained from such measurements is that at low substrate temperatures a hydrogen-rich material grows with interconnected voids (or decreased material density) such that molecular hydrogen (H_2) can move rapidly without diffusion processes delaying H_2 release. After annealing to about 400 °C and thus after having released a high amount of hydrogen, the same film appears as a rather dense material where diffusion of hydrogen takes place by hydrogen atoms. Thus a strong structural change must have taken place during annealing near $T_A = 400$ °C. Indeed, such changes can be monitored by various methods, like measurements of the film density [36] or of changes in He effusion [7]. In Figure 20.12, some results are shown.

In Figure 20.12a it is seen that the film thickness d of low T_S plasma-grown a-Si:H decreases (and thus the material density increases) considerably in the temperature range of low temperature hydrogen effusion at about 300–400 °C. In Figure 20.12b, shifts of the He effusion peak to higher temperature show that plasma-grown a-Si:H deposited at lower substrate temperature T_S densifies much stronger than material deposited at higher T_S. Still, some densification effects are observed also for a-Si:H grown at $T_S = 300$ °C. It is also seen in Figure 20.12b that the concentration of isolated voids increases upon annealing, as the fraction F^{HT} of HT He effusion rises. For $T_S = 50$ °C material, this annealing effect is

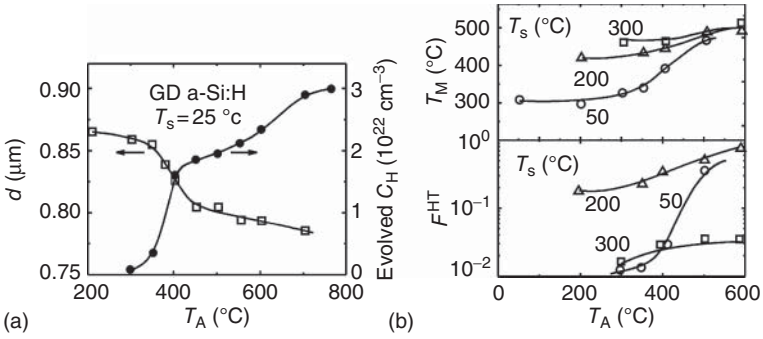

Figure 20.12 (a) Thickness d and evolved H concentration C_H of (undoped) plasma-deposited a-Si:H of low substrate temperature and high H content as a function of annealing temperature T_A. Annealing time was 5 min [36]. (b) Temperature T_M of (low-temperature) He effusion peak and fraction of high-temperature (related to isolated voids) He effusion F^{HT} as a function of annealing temperature T_A (annealing time: 5 min) [7].

likely related to the change of interconnected voids to isolated ones as the material shrinks upon annealing [7]. For $T_S = 200$ and 300 °C, however, H effusion paired with an incomplete shrinkage of the material presumably causes this increase of isolated voids [37]. Note that this latter mechanism could also result in the trapping of the implanted helium atoms in voids generated by hydrogen effusion. In fact, the enhanced values of F^{HT} at $T_S = 150-300$ °C in Figure 20.11b could be caused by such an effect.

20.4.1.2 Effect of Doping on H Effusion

Significant changes of hydrogen effusion by doping were first noted by Beyer *et al*. [16]. It was found that in particular by boron doping both low temperature and high temperature hydrogen effusion peaks of plasma-grown a-Si:H are shifted to lower temperature. This is illustrated in Figure 20.13a for low substrate temperature material. It was demonstrated later [1, 20] that the effect originates from a Fermi level dependence of both the hydrogen desorption free energy ΔG and the hydrogen diffusion energy, as shown in Figure 20.13b. Note that due to defect generation during (low temperature) hydrogen effusion, the Fermi level in the doped material may shift toward midgap so that the HT effusion may not always show a doping dependence.

20.4.2
Amorphous Silicon Alloys: Si:C

Alloys of amorphous silicon with carbon, nitrogen, oxygen, or germanium can be fairly easily prepared by plasma deposition by the addition of, for example, methane, ammonia, carbon dioxide, or germane, respectively, to silane. Thus the band gap can be varied from near 1 eV (a-Ge:H) to more than 2.5 eV (a-Si:C:H,

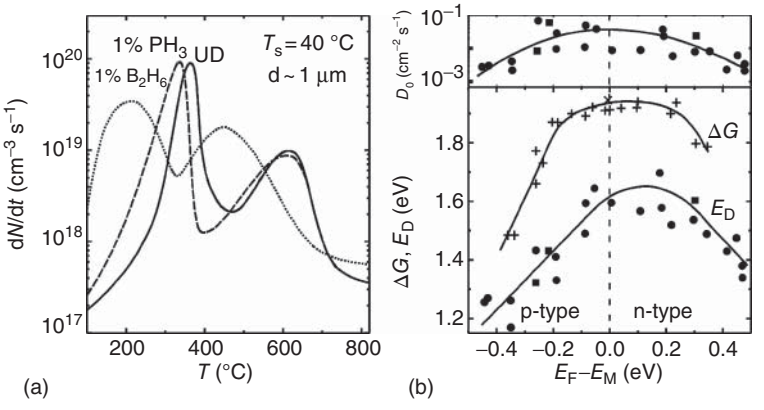

Figure 20.13 (a) Hydrogen effusion rate for a-Si:H, deposited at $T_S = 40\,°C$, undoped (UD) and doped with 1% diborane (B_2H_6) and 1% phosphine (PH_3) [1]. (b) Hydrogen free energy of desorption ΔG, hydrogen diffusion prefactor D_0, and hydrogen diffusion energy E_D (the latter two determined by HD interdiffusion experiments measured by SIMS) versus Fermi energy E_F relative to midgap E_M [1].

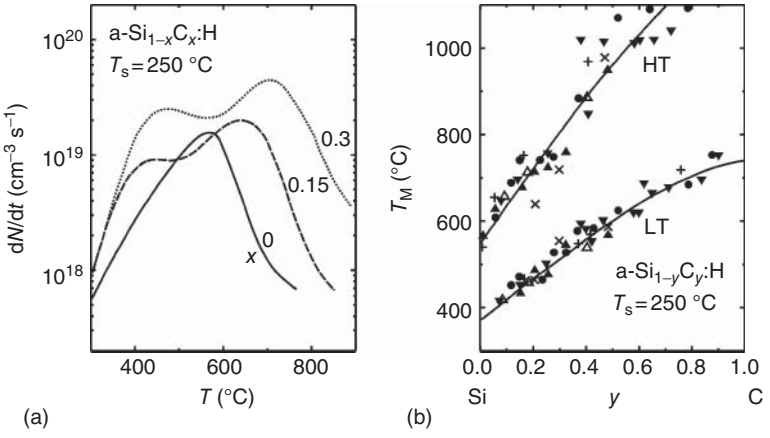

Figure 20.14 (a) Hydrogen effusion rate dN/dt for a-Si:C:H prepared from SiH_4-CH_4 gas mixtures at $T_S = 250\,°C$ [1]. (b) Temperature T_M of LT and HT effusion peaks versus film composition y of a-$Si_{1-y}C_y$:H films ($T_S = 250\,°C$) prepared from various gas mixtures. (Reproduced from Beyer [38] with permission of Springer International Publishing AG.)

a-Si:N:H, and a-Si:O:H). However, when alloy atoms are added to silicon, the tendency to grow material with an interconnected void structure is enhanced. Typical results of hydrogen effusion of a-Si:C:H films are shown in Figure 20.14a and b.

The results show that already upon the addition of 15% carbon, an low temperature hydrogen effusion peak appears. The temperature T_M of both H effusion maxima shifts rapidly with increasing carbon content to higher temperature.

These effects can be understood by an increase of (average) hydrogen binding energy as carbon is incorporated. While the effusion spectra in Figure 20.14a look similar to those in Figure 20.2a, it must be noted that the effusion temperature in the HT peak of a-Si:C:H is often not found to be diffusion limited (on the scale of film thickness), in contrast to typical plasma-grown a-Si:H films. This may be attributed to the presence of a granular material in a-Si:C:H. For a-Si:C:H alloys with carbon concentrations exceeding about 20 at.%, a significant hydrogen effusion in the form of hydrocarbon molecules was observed, predominantly in the temperature range where low temperature hydrogen effusion takes place. By mass spectrometric analysis, the hydrocarbon molecules methane, ethylene, and propene were identified as the primary desorbing species [38].

20.4.3
Microcrystalline Silicon

Microcrystalline silicon films have a much stronger tendency to show microstructure effects (voids at grain boundaries) than a-Si:H films. However, deposition conditions (usually at conditions close to the amorphous – microcrystalline transition) can be found to prepare fairly dense material with diffusion-limited hydrogen effusion [39]. Figure 20.15 shows effusion results for a series of samples deposited at different substrate temperatures. Under the conditions used, the samples of $T_S = 150$ and 200 °C are void rich; those deposited at 250 and 300 °C compact with similar hydrogen diffusion coefficients as in a-Si:H. The nature of the various LT hydrogen effusion peaks is not fully clarified.

The microstructure effects visible in hydrogen effusion are also seen by effusion measurements of implanted He and Ne. The results shown in Figure 20.16 (for μc-Si:H deposited at somewhat different deposition conditions as compared to the samples of Figure 20.15) demonstrate the growth of relatively dense μc-Si:H at higher ($T_S = 200$ °C) substrate temperatures (He effusion near 400 °C and

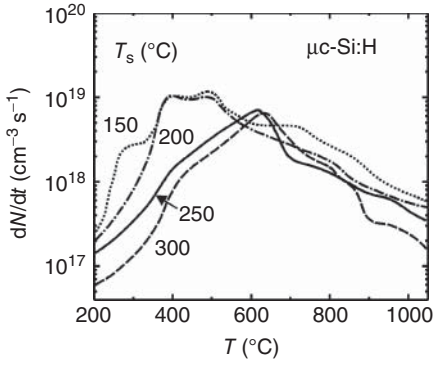

Figure 20.15 Hydrogen effusion spectra for a series of microcrystalline Si:H films deposited at different substrate temperatures T_S. (Reproduced from Beyer [39] with permission of Materials Research Society.)

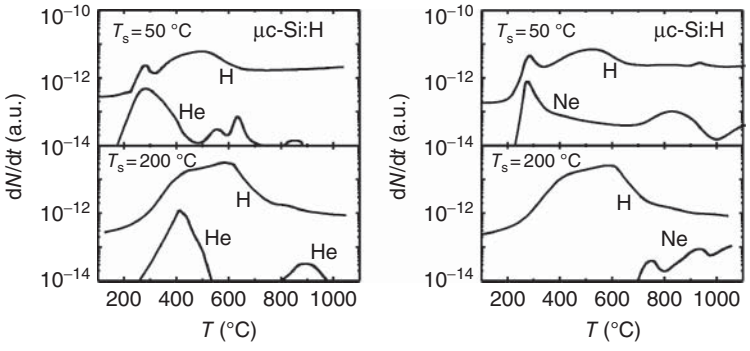

Figure 20.16 Effusion spectra of hydrogen and (a) implanted He and (b) implanted Ne for microcrystalline Si:H films deposited at $T_S = 50$ and 200 °C (W. Beyer (2009), unpublished).

near 900 °C, hydrogen effusion maximum near 600 °C, and neon effusion above 700 °C only). In contrast, at $T_S \approx 50$ °C material with interconnected voids grows as indicated by a He effusion peak below 200 °C, a hydrogen effusion maximum near 500 °C, and Ne effusion starting near 200 °C but extending up to 900 °C and higher. Note that this latter very broad effusion process suggests the presence of a rather inhomogeneous material, as noted in Section 20.3.6.

20.4.4
Zinc Oxide Films

Hydrogen effusion measurements of zinc oxide crystals and thin films were performed by Nickel *et al*. [4, 40] and, more recently, by Beyer *et al*. [41]. Nickel derived hydrogen diffusion energies by effusion measurements, varying film thickness and heating rate. Hydrogen density-of-states measurements were presented, but the drawbacks discussed in Section 20.3.5 apply.

In Figure 20.17a–c, results of effusion of implanted He and Ne are presented for LPCVD grown, sputter (SP)-grown, and single-crystal ZnO, respectively. The results show rather void-rich material in the first case, more dense material in the second case, and highly dense material (no visible neon effusion) in the third case. The width of the He and Ne effusion peaks suggests a rather inhomogeneous material (see Section 20.3.6) in the first case and the most homogeneous material (as expected) in the last case.

20.5
Comparison with other Experiments

As discussed in Section 20.3, the characterization of thin-film material should never rely on effusion measurements alone, since there are chances for erroneous conclusions for poorly defined material. For example, SIMS depth profiling is often

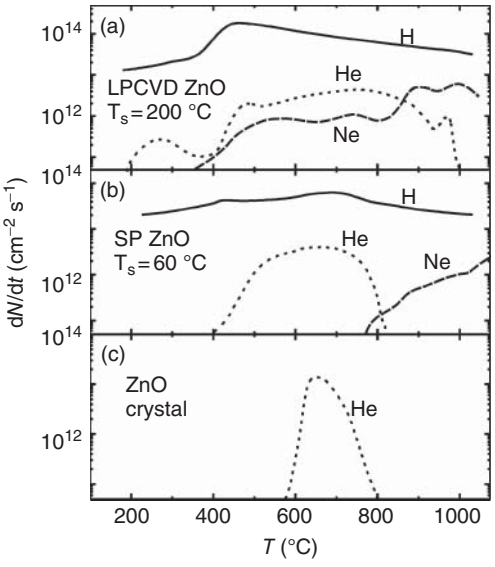

Figure 20.17 Effusion spectra of implanted He and Ne for (a) LPCVD grown, (b) sputter (SP) grown, and (c) single-crystal ZnO. Also shown is the hydrogen effusion rate versus temperature of the thin-film ZnO material. (Reproduced from Beyer [41] with permission of Materials Research Society.)

indispensable for assuring that hydrogen is evenly distributed within the film. Interdiffusion experiments of hydrogen and deuterium can be of great importance for verifying the evaluation of effusion measurements in terms of the H diffusion coefficient. Infrared absorption measurements are necessary to assure the presence of, for example, silicon-bonded hydrogen in contrast to molecular hydrogen. Furthermore, a comparison of microstructure data from effusion measurements with those from small-angle scattering is highly recommended for assuring important issues with regard to material structure.

20.6 Concluding Remarks

While the technique of hydrogen effusion was primarily developed for the quantification of incorporated hydrogen and of the thermal stability of hydrogen in amorphous Si:H films, the more recent successful structural characterization of various materials by rare gas effusion opens a wide range of further applications of the method, namely, for microstructure analysis of thin films in general. For amorphous silicon and related technology, effusion measurements have been applied widely, and a wealth of information was obtained. However, further work like the modeling of diffusion of hydrogen atoms and molecules, rare gas atoms, and other species in thin films is highly welcome. Drawbacks of the method involve its

destructive nature, the special substrates required, the costly high vacuum equipment, and the limited throughput which is a few samples per day, not counting the effort of rare gas implantations. Part of these obstacles may get overcome, in the future, by, for example, confining to small spots heated by a laser, if advanced hydrogen or rare gas detection methods are developed and applied. In any case, a further successful development of thin-film silicon solar cells appears hardly thinkable without applying sophisticated microstructure analysis like the gas effusion method.

Acknowledgments

The authors wish to thank Dorothea Lennartz and Pavel Prunici for valuable technical support. Support and interest by Uwe Rau is gratefully acknowledged.

References

1. Beyer, W. (1991) Hydrogen effusion: a probe for surface desorption and diffusion. *Physica B*, **170**, 105–114.
2. Tanaka, M., Taguchi, M., Matsuyama, T., Sawada, T., Tsuda, S., Nakano, S., Hanafusa, H., and Kuwano, Y. (1992) Development of new a-Si/c-Si heterojunction solar cells: ACJ-HIT (artificially constructed junction-heterojunction with intrinsic thin-layer). *Jpn. J. Appl. Phys.*, **31**, 3518–3522.
3. Matsuyama, T., Terada, N., Baba, T., Sawada, T., Tsuge, S., Wakisaka, K., and Tsuda, S. (1996) High-quality polycrystalline silicon thin film prepared by a solid phase crystallization method. *J. Non-Cryst. Solids*, **198–200**, 940–944.
4. Nickel, N.H. (2006) Hydrogen migration in single crystal and polycrystalline zinc oxide. *Phys. Rev. B: Condens. Matter Mater. Phys.*, **73**, 195204-1–195204-9.
5. Van de Walle, C.G. (2000) Hydrogen as a cause of doping in zinc oxide. *Phys. Rev. Lett.*, **85**, 1012–1015.
6. Beyer, W., Hüpkes, J., and Stiebig, H. (2007) Transparent conducting oxide films for thin film silicon photovoltaics. *Thin Solid Films*, **516**, 147–154.
7. Beyer, W. (2004) Characterization of microstructure in amorphous and microcrystalline Si and related alloys by effusion of implanted helium. *Phys. Status Solidi C*, **1**, 1144–1153.
8. Triska, A., Dennison, D., and Fritzsche, H. (1975) Hydrogen content in amorphous Ge and Si prepared by r.f. decomposition of GeH_4 and SiH_4. *Bull. Am. Phys. Soc.*, **20**, 392.
9. Redhead, P.A. (1962) Thermal desorption of gases. *Vacuum*, **12**, 203–211.
10. Pétermann, L.A. (1972) Thermal desorption kinetics of chemisorbed gases. *Prog. Surf. Sci.*, **3**, 1–61.
11. Brodsky, M.H., Frisch, M.A., Ziegler, J.F., and Lanford, W.A. (1977) Quantitative analysis of hydrogen in glow discharge amorphous silicon. *Appl. Phys. Lett.*, **30**, 561–563.
12. Fritzsche, H., Tanielian, M., Tsai, C.C., and Gaczi, P.J. (1979) Hydrogen content and density of plasma-deposited amorphous silicon–hydrogen. *J. Appl. Phys.*, **50**, 3366–3369.
13. Biegelsen, D.K., Street, R.A., Tsai, C.C., and Knights, J.C. (1979) Hydrogen evolution and defect creation in amorphous Si:H alloys. *Phys. Rev. B: Condens. Matter Mater. Phys.*, **20**, 4839–4846.
14. McMillan, J.A. and Peterson, E.M. (1979) Kinetics of decomposition of amorphous hydrogenated silicon films. *J. Appl. Phys.*, **50**, 5238–5241.
15. Oguz, S. and Paesler, M.A. (1980) Kinetic analysis of hydrogen evolution from reactively sputtered amorphous silicon–hydrogen alloys. *Phys. Rev.*

B: Condens. Matter Mater. Phys., **22**, 6213–6221.
16. Beyer, W., Wagner, H., and Mell, H. (1981) Effect of boron-doping on the hydrogen evolution from a-Si:H films. *Solid State Commun.*, **39**, 375–379.
17. Cornu, A. and Massot, R. (1966) *Compilation of Mass Spectral Data*, Heyden and Son, London.
18. Beyer, W., Herion, J., Wagner, H., and Zastrow, U. (1991) Hydrogen stability in amorphous germanium films. *Philos. Mag. B*, **63**, 269–279.
19. Shanks, H., Fang, C.J., Ley, L., Cardona, M., Demond, F.J., and Kalbitzer, S. (1980) Infrared spectrum and structure of hydrogenated amorphous silicon. *Phys. Status Solidi B*, **100**, 43–56.
20. Beyer, W., Herion, J., Mell, H., and Wagner, H. (1988) Influence of boron doping on hydrogen diffusion and effusion in a-Si:H and a-Si alloys. *Mater. Res. Soc. Symp. Proc.*, **118**, 291–296.
21. Kherani, N.P., Liu, B., Virk, K., Kosteski, T., Gaspari, F., Shmayda, W.T., Zukotynski, S., and Chen, K.P. (2008) Hydrogen effusion from tritiated amorphous silicon. *J. Appl. Phys.*, **103**, 024906-1–024906-7.
22. Beyer, W. (1985) Hydrogen incorporation in amorphous silicon and processes of its release, in *Tetrahedrally-Bonded Amorphous Semiconductors* (eds D. Adler and H. Fritzsche), Plenum Press, New York, pp. 129–146.
23. Matysik, K.J., Mogab, C.J., and Bagley, B.G. (1978) Hydrogen evolution from plasma-deposited amorphous silicon films. *J. Vac. Sci. Technol.*, **15**, 302–304.
24. Tsai, C.C. and Fritzsche, H. (1979) Effect of annealing on the optical properties of plasma deposited amorphous hydrogenated silicon. *Sol. Energy Mater.*, **1**, 29–42.
25. Jones, S.J., Lee, S.M., Turner, W.A., and Paul, W. (1989) Substrate temperature dependence of the structural properties of glow discharge produced a-Ge:H. *Mater. Res. Soc. Symp. Proc.*, **149**, 45–50.
26. Beyer, W. and Wagner, H. (1982) Determination of the hydrogen diffusion coefficient in hydrogenated amorphous silicon from effusion experiments. *J. Appl. Phys.*, **53**, 8745–8750.
27. Carlson, D.E. and Magee, C.W. (1978) A SIMS analysis of deuterium diffusion in hydrogenated amorphous silicon. *Appl. Phys. Lett.*, **33**, 81–83.
28. Beyer, W. (2003) Diffusion and effusion of hydrogen in hydrogenated amorphous and microcrystalline silicon. *Sol. Energy Mater. Sol. Cells*, **78**, 235–267.
29. Jackson, W.B., Franz, A.J., Jin, H.C., Abelson, J.R., and Gland, J.L. (1998) Determination of the hydrogen density of states in amorphous hydrogenated silicon. *J. Non-Cryst. Solids*, **227–230**, 143–147.
30. Beyer, W. (2004) Microstructure characterization of plasma-grown a-Si:H and related materials by effusion of implanted helium. *J. Non-Cryst. Solids*, **338–340**, 232–235.
31. Anderson, O.L. and Stuart, D.A. (1954) Calculation of activation energy of ionic conductivity in silica glasses by classical methods. *J. Am. Ceram. Soc.*, **37**, 573–580.
32. Norton, J.F. (1953) Helium diffusion through glass. *J. Am. Ceram. Soc.*, **36**, 90–96.
33. Eucken, A. (1950) *Landolt-Börnstein, Atom- und Molekularphysik I*, Springer Verlag, Berlin, Germany, p. 325 and pp. 369–371.
34. Van Wieringen, A. and Warmoltz, N. (1956) On the permeation of hydrogen and helium in single crystal silicon and germanium at elevated temperatures. *Physica*, **22**, 849–865.
35. Kennard, O. (1978) Bond lengths between carbon and other elements, in *CRC Handbook of Chemistry and Physics*, 58th edn (ed R.C. Weast), CRC Press, West Palm Beach, Florida, USA, p. F-215.
36. Beyer, W. and Wagner, H. (1983) The role of hydrogen in a-Si:H – results of evolution and annealing studies. *J. Non-Cryst. Solids*, **59–60**, 161–168.
37. Beyer, W., Hilgers, W., Lennartz, D., Maier, F.C., Nickel, N.H., Pennartz, F., and Prunici, P. (2014) Effect of annealing on microstructure in (doped and

undoped) hydrogenated amorphous silicon films. *Mater. Res. Soc. Symp. Proc.*, **1666** DOI: 10.1557/opl.2014.667

38. Beyer, W. and Mell, H. (1987) Composition and thermal stability of glow discharge a-Si:C:H and a-Si:N:H alloys, in *Disordered Semiconductors* (eds M.A. Kastner, G.A. Thomas, and S.R. Ovshinsky), Plenum Press, New York, pp. 641–658.
39. Beyer, W., Hapke, P., and Zastrow, U. (1997) Diffusion and effusion of hydrogen in microcrystalline silicon. *Mater. Res. Soc. Symp. Proc.*, **467**, 343–348.
40. Nickel, N.H. and Brendel, K. (2003) Hydrogen density-of-states distribution in zinc oxide. *Phys. Rev. B: Condens. Matter Mater. Phys.*, **68**, 193303-1–193303-4.
41. Beyer, W., Breuer, U., Hamelmann, F., Hüpkes, J., Stärk, A., Stiebig, H., and Zastrow, U. (2009) Hydrogen diffusion in zinc oxide thin films. *Mater. Res. Soc. Symp. Proc.*, **1165-M05-24**, 209–214, DOI: http://dx.doi.org/10.1557/PROC-1165-M05-24.

Part IV
Materials and Device Modeling

Advanced Characterization Techniques for Thin Film Solar Cells, Second Edition.
Edited by Daniel Abou-Ras, Thomas Kirchartz, and Uwe Rau.

21
Ab Initio Modeling of Defects in Semiconductors

Karsten Albe, Péter Ágoston, and Johan Pohl

21.1
Introduction

The characterization of semiconductors applied in photovoltaic devices by means of *ab initio* methods has become an emerging field over recent years. This is not only because of the increasing availability of more powerful computers but mostly due to the development of refined numerical and theoretical methods.

Explaining and predicting solid-state properties require an understanding of the behavior of electrons in solids. First-principles or *ab initio* calculations are those that start directly at the Hamiltonian of the Schrödinger equation, containing the kinetic energy operators and the potential energy due to electrostatic interactions of electrons and nuclei. The value of *ab initio* methods lies in the fact that material properties can be calculated from scratch without experimental input or empirical parameters. Obtaining materials data from *ab initio* calculations may serve various purposes. Firstly, they allow for validating experimental results and therefore contribute to a better understanding of material properties. Secondly, calculated data can be used for identifying new properties or mechanisms. Thirdly, by calculating specific properties for a large database of various structures, new materials with optimized properties may be designed. In semiconductor research, *ab initio* methods are now frequently used for calculating structural, thermomechanical, and electronic properties. In practice, however, the feasibility of an *ab initio* approach always depends on the problem at hand and may be limited for conceptual reasons. Most importantly, the computational costs which scale with the system size, that is, the number of electrons necessary to calculate a certain property of a material, restrict the applicability of *ab initio* methods. Moreover, it is often very crucial to balance accuracy and computational cost by choosing the appropriate method for the problem at hand. The most accurate approach of treating a complex system consisting of many interacting particles, such as a semiconducting crystal, is *ab initio* methods, solving the many-body Schrödinger equation directly. This includes quantum Monte Carlo (QMC) [1], configuration interaction (CI), and coupled cluster (CC) methods [2], which are computationally expensive and therefore more often applied for studying small systems, like

Advanced Characterization Techniques for Thin Film Solar Cells, Second Edition.
Edited by Daniel Abou-Ras, Thomas Kirchartz, and Uwe Rau.

molecules and clusters, rather than solids. The most established *ab initio* methods for describing electrons in solids are based on density functional theory (DFT), of which we give a brief exposition in the following. We then describe exemplarily how the defect chemistry of a semiconductor may be determined from *ab initio* calculations and present results on the point defect chemistry of ZnO as a case study.

21.2 DFT and Methods

In DFT, the complexity of a many-body system of N interacting electrons in the presence of ionic cores is reduced to the optimization of an electron density, which depends only on three spatial coordinates independent of the number of electrons. Hohenberg and Kohn showed in 1964 [3] that the energy E of an interacting electron gas in an external potential $V(\mathbf{r})$ due to ionic cores and external fields can be expressed by a functional $F[n(\mathbf{r})]$ of the electron density $n(\mathbf{r})$ and that the ground-state energy is equivalent to $E_{\mathrm{GS}} = \min \int V(\mathbf{r})n(\mathbf{r})\mathrm{d}\mathbf{r} + F[n(\mathbf{r})]$. The proof itself, however, does not provide a recipe of how to construct an explicit functional $F[n(\mathbf{r})]$. Later, Kohn and Sham showed that the problem of many interacting electrons may be transformed into a problem of noninteracting particles moving in an effective potential, which may in principle include all many-body effects including exchange and correlation, and is only a functional of the electron density [4]. Within the Kohn–Sham method, the ground-state total energy E for a collection of electrons interacting with one another and with an external potential V_{ext} (including the interaction of the electrons with the nuclei) can be written as

$$E[n] = \sum_a f_a \left\langle \Psi_a \left| \left(\frac{1}{2}\nabla^2 + V_{\mathrm{ext}} + \frac{1}{2}\int \frac{n\left(r'\right)\mathrm{d}r'^3}{|r-r|} \right) \right| \Psi_a \right\rangle + E_{\mathrm{xc}}[n] + E_{\mathrm{II}},$$

where f_a is the occupation of a single-particle state ψ_a usually taken from a Fermi function, while E_{II} describes the ion–ion interaction. All many-body effects are hidden in the exchange–correlation $E_{\mathrm{xc}}[n]$ term.

By construction, DFT is an exact theory given that the exchange–correlation functional is known. In praxis, however, the functional has to be approximated. Since the foundations of DFT have been completed with the Hohenberg–Kohn theorem and the Kohn–Sham ansatz, subsequent progress in the theory has focused on efficient numerical implementations and improved exchange–correlation functionals.

21.2.1 Basis Sets

Finding a mathematically convenient basis set representing the Kohn–Sham orbitals within DFT calculations is essentially a balance of computational performance and accuracy. Any basis can be made more complete and therefore more

accurate by adding more basis functions. For a plane-wave or real-space basis, this can be systematically done by simply increasing the spectral range. Usually, core electrons, for which the wavefunctions exhibit strong oscillations, are excluded and replaced by so-called pseudopotentials representing the combined potential of the ionic core and core electrons. Exclusion of the core electrons results in an improved performance, especially for plane-wave basis sets, and is often a prerequisite for treating extended systems. Using a localized basis set, such as a Gaussian or numerical atomic orbital basis function, may have advantages concerning the scalability of the method with respect to the system size. However, in that case, more effort is needed to check the completeness of the basis set. A combination of a localized basis and a plane-wave representation is the full-potential linearized augmented plane-wave (FP-LAPW) method, which represents an accurate yet efficient all-electron approach [5].

21.2.2 Functionals for Exchange and Correlation

21.2.2.1 Local Approximations

In the local density approximation (LDA), the exchange–correlation energy as a functional of the density is described by a homogeneous electron gas. The correlation energy of the homogeneous electron gas can be obtained by highly accurate QMC simulations [6], while the exchange energy is known analytically. The LDA is sufficiently accurate for many problems in solid-state physics, especially for describing electrons in simple metals which behave very much like free electrons. Because of its simplicity and limited computational costs, the LDA is very useful for describing large systems as well as for obtaining approximate energies and wavefunctions that can then be refined by more sophisticated levels of theory. An improvement of the LDA has been achieved by recognizing that the exchange–correlation energy can be described more accurately by including gradients of the electron density. In contrast to LDA, different variants exist of how the gradient is included. Nowadays, however, the generalized gradient approximation (GGA) by Perdew *et al*. [7] (PBE-GGA) is most widely used.

Although improving on many calculated material properties in comparison with the local approximation, the GGA still has deficiencies in various aspects. Most importantly, both the LDA and the GGA fail to reasonably describe the fundamental band gap, which is generally underestimated (sometimes by more than 50%) in both approximations. This issue is known as the band-gap problem in DFT. Approaches to improve the exchange–correlation energy by including higher derivatives of the electron density have failed, and it is now generally accepted that improvements require to properly account for nonlocality.

21.2.2.2 Functionals beyond LDA/GGA

A direct extension of the LDA and the GGA functionals is obtained by adding an on-site Coulomb repulsion term to specific orbitals representing the electrostatic repulsion between localized electrons. This approach is motivated by the

lattice-based Hubbard model [8], which describes the repulsion of electrons within a narrow band, that is, electron correlation, by an empirical parameter U. Similarly, a density functional that partially corrects specific localized orbitals for the electron correlation can be designed by introducing the repulsion parameter U (LDA + U or GGA + U) [9].

The +U method has become a popular approach, which allows for a partial correction of the correlation and self-interaction error of the LDA and significantly improves the description of Mott insulators, such as transition metal oxides (MOs). Nowadays, the method is widely applied due to its relative accuracy at very reasonable computational costs. As a by-product, the calculated band gaps of semiconductors can be improved by using the +U approach because the increased repulsion between specific orbitals leads to an enhanced localization. However, LDA + U and GGA + U still underestimate the band gap. In addition, it is often not *a priori* clear how and for which orbitals U parameters should be applied. Further details on the LDA + U method can be found in a review by Anisimov *et al*. [10].

The LDA and the GGA functionals considerably underestimate the exchange energy but properly account for the correlation energy. The Hartree–Fock method by definition properly accounts for the exchange interaction but in turn cannot access the correlation energy. Therefore, one may conclude that the true answer to the problem must lie somewhere in between. This is the starting point for the development of hybrid functionals. The basic idea for hybrid functionals is thus to mix the exchange–correlation energy of the traditional LDA or GGA functionals with a fraction of exact or Hartree–Fock exchange. In recent years, it turned out that hybrid functionals are indeed able to give a much better description of the exchange and the correlation energy than traditional functionals. Also, the band gaps are significantly improved. This, however, comes at a price: Hybrid functionals are generally at least two orders of magnitude more computationally expensive than their local or semilocal counterparts. Typical examples of hybrid functionals that have been engineered in such a way are B3LYP [11], PBE0 [12], and HSE06 [13, 14], just to name the most prominent ones. The hybrid functional PBE0 should clearly be distinguished from PBE, which is a semilocal GGA functional (see Section 21.2.2.1). A review on hybrid functionals applied to solids and an assessment of their accuracy in comparison to experiment have recently been given by Marsman *et al*. [15]. Another review focusing more on the general theoretical framework has been authored by Kümmel and Kronik [16] who also discuss the issue of the band-gap problem in the case of hybrid functionals.

For a more detailed general introduction into *ab initio* total energy calculations, we refer the reader to a review paper by Payne *et al*. [17]. A highly recommendable full treatise on electronic structure calculations including recent developments in DFT methods can be found in a recent book by Martin [18]. The different approximative functionals in DFT may be ordered into a hierarchy starting with the most basic, the LDA, and then increasing in accuracy. Such a hierarchy is sometimes called the Jacobs ladder of DFT. A table which puts the different *ab initio* methods and functional approximations into such a scheme is shown in Table 21.1.

Table 21.1 Overview of *ab initio* total energy and electronic structure methods.

Method	Description	References
Density functional theory		
Local and semilocal functionals		
LDA	A local functional describing exchange–correlation energy that depends only on the local electron density and is obtained from the solution for the homogeneous electron gas	[6]
GGA	The exchange–correlation energy also depends on the gradient of the electron density	[7]
Orbital-dependent and hybrid functionals		
LDA + U/GGA + U	An on-site Coulomb repulsion term, represented by the parameter U, is included for specific orbitals. Description of exchange and correlation is improved if U is chosen properly	[9]
Hybrid functionals (HSE06, PBE0, B3LYP, etc.)	Improved accuracy of the exchange–correlation energy by mixing local or semilocal functionals with a fraction of exact exchange or Hartree–Fock exchange. Provides a good alternative to local and semilocal functionals but is computationally more expensive. In certain cases, hybrid functionals alleviate the band-gap problem	[15, 16]
Many-body approaches		
GW	Allows for an improved description of charged excited states by treatment of the screened Coulomb interaction. It delivers a good description of band structures, but it is difficult to obtain total energies	[19]
BSE	Explicit treatment of neutral excitations within the framework of MBPT	[20]
Time-dependent DFT	Explicit treatment of neutral excitations within the framework of DFT	[20]
QMC	True many-body wavefunction approach; highly accurate but also computationally expensive; currently forces are still hard to obtain	[21]

21.3
Methods Beyond DFT

More sophisticated methods that potentially alleviate the band-gap problem of DFT need to take explicitly into account the many-body interactions of excited states, in particular the Coulomb screening and the interaction of electrons and holes. The three main approaches to this problem are the *GW*[1)] method [19], methods based on the Bethe–Salpeter equation (BSE) [20], and time-dependent density functional theory (TD-DFT) [20]. While being very useful for the calculation of excited-state properties, all of these methods suffer from their extreme computational cost, which finally limits their applicability to the study of very small systems.

GW is the method of choice when realistic electron addition and removal energies, such as measured in direct and inverse photoemission experiments, are of interest. The *GW* method is thus able to give much more accurate energies for charged excited states than standard DFT. *GW* is based on a perturbative treatment of standard DFT calculations and is therefore also referred to as a many-body perturbation theory (MBPT) approach. *GW* provides an approximation to the electron self-energy Σ based on a perturbative evaluation with Kohn–Sham orbitals. Pioneered already in 1965 with the work of Hedin [22], it was not until the 1980s that calculations for silicon showed that the *GW* method has the potential to alleviate the band-gap problem for real materials.

For an accurate treatment of neutral excitations in semiconductors such as electron–hole pairs (excitons), one has to resort to either the BSE or the TD-DFT. These methods are able to predict, for example, optical and electron energy-loss spectra. As with DFT, the accuracy of TD-DFT is limited by the accuracy of the available functionals. For example, optical spectra calculated by TD-DFT within the adiabatic local density approximation (ALDA), which is the time-dependent analog of the LDA, show very good agreement with experiments for molecular materials. For solids, better agreement has been found using BSE approaches. Due to their computational complexity, however, BSE approaches are limited to relatively simple materials. The efficient description of electron–hole excited states is therefore still considered to be an unsolved problem. A review comparing *GW*, BSE, and TD-DFT is given in Ref. [20].

A method that does not quite fit the scheme of Table 21.1 is the QMC method [21]. QMC is the only method presented here, which is completely independent of DFT. It is a ground-state method based solely on the many-body wavefunction as the basic object. Therefore, it takes a fundamentally different approach to the problem of electron correlation compared to all the methods described previously (see Section 21.2.2), which are all in some way based on the electronic density. The basic idea is to sample the many-body wavefunction using random numbers. QMC is in principle able to give the correct total energy, and

1) In *GW*, the *G* stands for Green's function and the *W* stands for the screened Coulomb interaction, which both enter the electron self-energy Σ.

therefore an exact treatment of exchange and correlation is possible. However, this is only true for an infinitely long simulation run. The error in the total energy of a system given by QMC is an entirely statistical error, which scales as the inverse square root of the number of time steps. It is the extreme computational cost of this method, which limits its usefulness in practice. For very small systems it can, however, be a very valuable tool if very accurate total energies are needed. In praxis, the forces on the ions are hard to obtain and computationally much more expensive than the total energy, which make structural relaxations difficult. A good review on QMC methods has been given by Foulkes *et al*. [21].

21.4 From Total Energies to Materials Properties

In principle, DFT calculations allow to predict material properties that can directly be derived from total energies and atomic forces of any atomic arrangement of interest. Moreover, electronic properties as described by the KS orbitals are directly accessible. Before we specifically discuss the use of DFT calculations for studying point defects in semiconducting materials, we will first give a brief survey of properties obtainable by considering the electronic system in the ground state.

Properties which are conceptually easy to calculate include those that can be directly derived from total energy differences. To this group belong, for example, cohesive energies, defect formation enthalpies, or energies of various configurations. The latter can be used in the cluster expansion method that, together with Monte Carlo simulations, allows to calculate configurational entropy and free energy differences as well as phase diagrams [23].

Being conceptually relatively simple, however, does not mean that accuracy is easily achieved. The calculation of most material properties involves the use of a supercell, that is, a cell which contains several identical primitive cells in a periodic arrangement. The use of a supercell, however, can introduce finite-size errors, especially if defective structures are considered. In practice, finite-size scaling procedures allow for minimizing these effects. For example, the cohesive energy of a crystal is calculated as the energy difference between the perfect crystal and the free atom. While one does not have to worry about finite-size errors for the perfect crystal, calculations of the free atom involve finite-size effects because the free atom interacts with itself through the periodic boundary conditions. Therefore, one has to make sure that the energy of the free atom is sufficiently converged with respect to the size of the cell, that is, the amount of vacuum around the atom. The same reasoning applies to surface energy calculations, where slab geometries are used, and convergence both with respect to the thickness of the slab and to the vacuum layer has to be ensured. Also, in calculation of point defect formation enthalpies, cell size effects are an important issue [24].

The next class of properties is obtained from derivatives of the total energy with respect to continuous variables. First-order derivatives with respect to atomic

positions, strain, and electric fields directly yield atomic forces, stress states, and polarization. Lattice constants and elastic moduli are usually calculated by fitting total energies to a thermodynamic equation of state relating energy and volume. From high-order (including mixed) derivatives, force constants, elastic moduli, polarizabilities, dielectric susceptibilities, or piezoelectric tensors, to name only a few, can be obtained [25]. In principle, derivatives can be obtained by calculating energy variations due to a direct perturbation, like atomic displacements, by applying perturbation theory [26, 27] or by evaluation of time correlations (Green–Kubo formalism) in molecular dynamics (MD) simulations.

These alternative routes can be exemplified by the phonon density of states, which allows to access thermodynamic properties like the heat capacity and differences in free energy. The most common method is the frozen-phonon method, where the energy of all different phonon modes is calculated by displacing atoms in an appropriately sized supercell. By diagonalization of the force constant matrix, the eigenfrequencies and thus the phonon dispersion relation and the phonon density of states are subsequently obtained. Alternatively, the density functional perturbation theory (DFPT) [26, 27] can be used. The third method to access the phonon density of states is by means of *ab initio* MD. *Ab initio* MD yields the velocities of the atoms and their trajectories as a function of time. By means of spectral analysis, one can then obtain the phonon density of states from the velocity autocorrelation function.

Electronic properties such as the fundamental band gap, valence-band offsets, and defect transition levels can be obtained consistently from DFT within the limits defined by the functionals used for exchange and correlation. This is because the only physically meaningful properties directly generated by DFT calculations are the total energy, the ground-state electronic density, and the energy of the highest occupied state. A word of caution is in order here because the quasiparticle eigenstate energies of DFT and especially the ones of the unoccupied excited states are sometimes confused with the true energies of excited-state electrons. In particular, the optical band gap may not be determined from total energy differences, while the fundamental band gap can. In practice, these two quantities are often close, but this cannot be taken for granted. In case true excited-state properties (in particular the optical band gap and absorption spectra) are of interest, one has to resort to methods beyond DFT. The story is a bit different in case of hybrid functionals, for which the unoccupied states may in fact be interpreted as an approximation to excited-state energies within a generalized Kohn–Sham framework [16].

21.5 *Ab initio* Characterization of Point Defects

One of the most powerful applications of first-principles electronic structure theory is the modeling of point defect in solids, whose presence controls the functional properties of many semiconductors. Therefore, in this final part, we

will guide the reader through the procedures relevant for calculating defect properties in semiconductors. In order to see the necessity of first-principles calculations in the context of point defects, it is worth mentioning some quantities of interest which can be calculated. The formation energies of intrinsic defects like vacancies, interstitials, antisites, or more complex defect arrangements can be compared in order to identify the predominant defect species. In the case of extrinsic impurities, the calculated formation energies provide insights into the solubility of the impurities. The stable charge states of intrinsic or extrinsic defects can be obtained, which in turn classify the defects as acceptors or donors in a specific host material. Furthermore, the activation energies for changing the charge state, that is, the ionization energies of the defects, can be obtained and therefore allow to identify appropriate donors and acceptors for device development. In this context, *ab initio* methods have made significant contributions to the understanding of AX and DX centers[2)] in II–VI semiconductors and particularly in GaAs [29–31].

Defect-induced states within the band gap affect the optical properties, for example, in the case of color centers, or can act as recombination centers. The assignment of these levels to specific defects is experimentally difficult but possible with the aid of DFT calculations. Apart from the thermodynamic stability, the mobility of point defects can also be assessed. The free energy of defect migration determines the kinetic stability of intrinsic point defects and impurities under nonequilibrium conditions. In the case of more than just one defect, their interactions can be studied by calculating binding energies. The characteristics of extrinsic point defects are sometimes heavily influenced by the presence of intrinsic point defects, for example, due to defect association.

Also, the association of solely intrinsic point defects is a key for understanding the materials behavior as it is the case for chalcopyrites [32]. Another important application is the determination of doping limits, which can be estimated by first-principles calculations. Alternatively it is possible to choose one specific defect and even focus on a single certain charge state in order to calculate properties of interest which in turn can be used for the experimental identification or characterization of this specific defect.

Various experiments capable of identifying point defects can be simulated from first principles with, however, varying reliability. For example, it is possible to calculate the formation volume of defects to study their impact on the crystal lattice parameter [33]. Calculating ionization energies enables to estimate the conductivities which can then be measured [34]. It is possible to identify the defect-related magnetic moment and derive parameters for electron

2) A DX center is a substitutional donor which may behave like an acceptor depending on the position of the Fermi level. Similarly, an AX center is an acceptor, which may behave like a donor. This behavior is usually associated with large lattice relaxations and bond breaking. In the AX and DX denomination, A stands for acceptor and D for donor. These substitutional donors and acceptors were previously thought to associate with unknown point defects, represented by the symbol X, which was not confirmed later. The denominations AX and DX center, however, remained [28].

paramagnetic resonance measurements [35]. It is even possible to model the positronic trapping state at a defect location and derive from it the characteristic lifetimes in order to compare them with results obtained by positron annihilation spectroscopy [36].

In the case of localized defect-related states, optical spectra are the primary means for defect identification. The calculation of optical properties is, however, often difficult in the case of solids. Using simple LDA/GGA-DFT in most cases, it is at least possible to identify whether an absorption feature can be expected or not. The absorption energy on the other side is clearly an excited-state property and affected by the difficulties mentioned previously. A good example for the calculation of a defect excitation can be found in Ref. [37], where the full methodology of MBPT was applied to the excitation of a negatively charged nitrogen-vacancy color center in diamond.

In the following, we present a list of guidelines that should allow the interested reader to judge the reliability of defect calculations and their particular strengths and drawbacks:

- Energy differences are reliable even within the LDA.
- The determination of the defect geometry (relaxation and volume changes) is reliable.
- Energy differences between structures of similar bonding type and geometry are more reliable than those between different ones (e.g., ionic solid vs molecule). This is due to error cancelations important for the success of first-principles calculations. For example, the calculation of the migration energy is often more reliable than the calculation of the formation energy (reference energies can involve metals or molecules).
- The characterization of neutral defects is usually more reliable than of charged defects. This is especially true for defects, which involve highly localized defect states. In the case of delocalized defect states, that is, for defects which are naturally charged, a neutral calculation often leads to an overestimation of their formation energy.
- In the case of charged defects, a higher charge state is not necessarily less accurately described. The reliability as a function of charge state depends on the specific defect type.
- The characterization of localized defect states is more difficult for small-gap materials than for materials with larger band gaps.
- Excited-state properties are especially difficult to obtain in the case of defects in solids. The reliability of such calculations can be even difficult to estimate.

Although in many cases these guidelines are valid, exceptions can always be found. In the following we will focus on how to calculate the formation energies of intrinsic point defects for a two-component system. This covers many aspects of the defect modeling. By using a two-component system, the example provides sufficient generality.

21.5.1 Thermodynamics of Point Defects

The key quantity for accessing the thermodynamics of point defects in solids is the Gibbs free energy of defect formation (ΔG_f). Ultimately, one is interested in defect concentrations which can be calculated from the formation energy for the dilute limit ($c < 10^{-3}$) through

$$c = c_0 \exp\left(-\frac{\Delta G_f}{k_B T}\right) = c_0 \exp\left(-\frac{\Delta E_f + p\Delta V_f - T\Delta S_f}{k_B T}\right) \tag{21.1}$$

Here, c_0 is the concentration of available positions for the defect in the lattice, k_B is the Boltzmann constant, and T is the temperature. The quantities ΔE_f, ΔV_f, and ΔS_f are the formation energy, formation volume, and formation entropy of the corresponding defect, respectively. The discussion now focuses on the formation energy, which is usually the dominating contribution and sufficient for low-temperature and low-pressure conditions. The other two contributions can, however, also be calculated within electronic DFT.

At this stage, two systematic paths can be followed. It is possible to construct defect pairs or clusters which are charge neutral and conserve the particle numbers. This method leads to the well-known Kröger–Vink notation of defect reactions. A typical example is the so-called Schottky defect equilibrium which in the case of a simple MO could be

$$0 \rightleftharpoons V_O^{2+} + V_M^{2-}. \tag{21.2}$$

The defect equilibrium and therefore the concentrations can be expressed in terms of Gibbs free energy of defect formation $\Delta G_{Schottky} \approx \Delta E_{Schottky}$. The strength of this method is that by conserving charge as well as particle numbers, the formation energy does not depend on external reservoirs other than the material itself. In the case of a first-principles approach, $\Delta E_{Schottky}$ is calculated by constructing a supercell of the MO, remove a cation and an anion from arbitrary positions, and calculate the formation energy $\Delta E_{Schottky}$ from total energy differences via

$$\Delta E_f = E^Z_{defect} - E^Z_{ideal}. \tag{21.3}$$

Here, E^Z_{ideal} and E^Z_{defect} are the total energies as obtained by a total energy calculation for the supercells containing the ideal and the defect structure, respectively. This approach uses only the DFT total energies and returns relatively accurate numbers. There are, however, some pitfalls using this approach. Apparently, the charge states in Equation 21.3 were simply guessed and could well differ from $q = \pm 2$. It is of course possible to check the charge state via the electron density output of the DFT code, which is always available. In case the charge state is different for either the oxygen or cation vacancy (the oxygen vacancy could be a color center or single donor), this supercell calculation cannot represent the ground state of the defect. For the case that V_O is only singly charged, one could insert two V_O in order to reestablish the ground state. Then, the conservation of particle numbers has to be omitted. In complex oxides (e.g., in sesquioxides), defect

reactions are even more complicated as exemplified by the following reaction:

$$0 \rightleftharpoons 3V_{\mathrm{O}}^{2+} + 2V_{\mathrm{M}}^{3-}. \tag{21.4}$$

It can be seen that the number of defects (five in this case) increases dramatically with the complexity of the materials stoichiometry. Considering typical cell sizes accessible by present DFT calculations ($50 < N_{\mathrm{atoms}} < 1000$), the assumption of dilution is not fulfilled, and the resulting numbers will surely depend on the actual arrangement of the defects within the cell. Therefore, this approach is neither unique nor flexible. Following the ideas of Zhang and Northrup [38], it is more efficient to calculate the formation energies of individual defects sequentially and in different charge states so that charge as well as particle conservation do not need to be fulfilled. Defect reactions are constructed at a later stage from the individual defects with the lowest formation energies. Since the constraints of constant particle numbers and charge are neglected, the free energy of defect formation depends on the chemical potentials and electrochemical potential of the reservoirs:

$$\Delta G_{\mathrm{f}} = \Delta E_{\mathrm{f}} + p\Delta V_{\mathrm{f}} - T\Delta S_{\mathrm{f}} - \sum_i n_i \mu_i + qE_{\mathrm{F}} \tag{21.5}$$

Here, n_i is the number of exchanged particles of type i in order to construct the defect, and subscript i is the corresponding reference chemical potentials. The reference electrochemical potential for the electrons is the Fermi energy E_{F}, and q is the charge state of the defect.

Figure 21.1 illustrates the process of defect formation as a subsequent exchange of (neutral) atoms and electrons with their respective reservoirs. The chemical

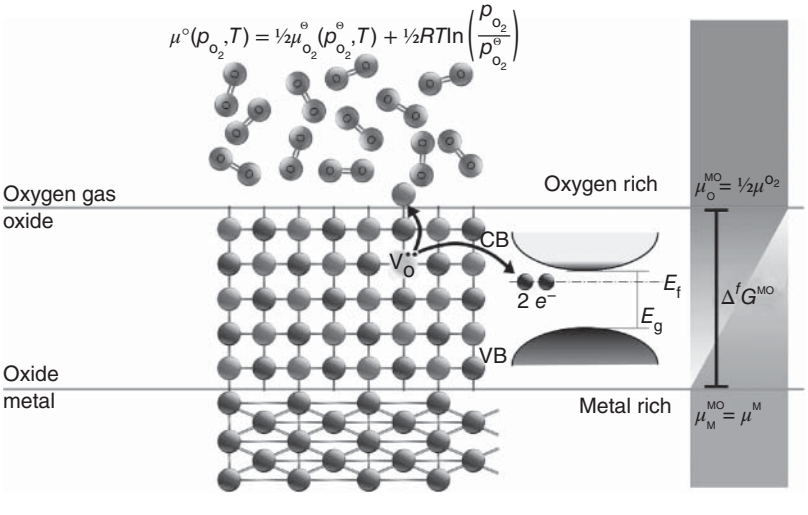

Figure 21.1 Defective metal oxide and possible reservoirs for anions, cations, and electrons. Here, as an example, we show the case of an oxygen vacancy in charge state $q = +2$, which is formed by releasing a neutral oxygen atom to the gas reservoir with chemical potential $\mu_{\mathrm{O}}^{\mathrm{MO}} = \frac{1}{2}\mu^{\mathrm{O}_2} = \mu^{\mathrm{O}}(p_{\mathrm{O}_2}, T)$ and by moving two electrons into the electron reservoir with the Fermi energy E_{F}.

potentials of the relevant atomic species i and the Fermi energy E_F are experimental control variables. The Fermi energy is also sometimes referred to as the chemical potential of the electrons. Conceptually, the Fermi energy can be controlled or influenced by dopants and impurities. The control over the chemical potentials is often difficult to establish experimentally. The chemical potentials i are related to the species activities a_i via $\mu_i = \mu_i^\Theta + RT \ln a_i$, where μ_i^Θ is the reference chemical potential in the chemical standard state. In case of a reference reservoir in the gas phase, the chemical potential may be related to the partial pressure p_i via the ideal gas law. For the oxygen gas phase, for example, this allows to relate the chemical potential of oxygen O to the oxygen partial pressure p_{O_2}, via

$$\mu^O(p_{O_2}, T) = \frac{1}{2}\mu^\Theta_{O_2}(p^\Theta_{O_2}, T) + \frac{1}{2}RT \ln\left(\frac{p_{O_2}}{p^\Theta_{O_2}}\right),$$

where $p^\Theta_{O_2}$ refers to the partial pressure in the standard state. In the case that the reference chemical potentials are the ones of solid phases, it is difficult to establish precise experimental control. However, the activities and therefore the chemical potentials are always closely related to the availability of the respective species during production of the material. In applied studies the chemical potential of metallic species is therefore often treated as a free parameter, expressed as deviations from the cohesive energies $\mu_i = \mu_i^{el} + \Delta\mu_i$ of the most stable elemental reference phases μ_i^{el}. The chemical potential of the solid phase is equal to its cohesive energy and serves as a reference for the metal-rich limit ($\mu_M^{MO} = \mu^M$ in Figure 21.1). The maximal deviations from the elemental reference values are restricted by the heat of formation of the compound ΔH_f, which can also be calculated from first principles:

$$\Delta H_f^{MO} = \Delta\mu_M + \Delta\mu_O \tag{21.6}$$

It is common to plot the defect formation energies as a function of the Fermi energy at specific chemical potentials of interest.

At this stage, it may appear irritating that the defect stability, which depends on the Fermi energy, influences the Fermi energy itself, as defects are charged. Once the formation energies of all (predominant) defects are known, the determination of the concentrations is achieved as follows: First, a specific environment is chosen by fixing the atomic chemical potentials. Next, the formation energies and concentrations are expressed as a function of the Fermi energy. The actual value of the Fermi energy is obtained by additional physical constraints. At the resulting Fermi energy, the total charge (including also free charge carriers and dopants) should vanish (charge neutrality (CN)), and none of the defects should have a negative formation energy. A detailed description of this process is given in Ref. [34].

Although the Fermi energy always assumes a fixed value in thermodynamic equilibrium, it is instructive to plot the formation energies of all defects as a function of this parameter. In this representation, it is most convenient to discuss the changes of the defect equilibria upon extrinsic doping and changes of the environment.

In Figure 21.2, several well-known defect equilibria are translated into this representation. The first panel (Figure 21.2a) represents the Schottky reaction

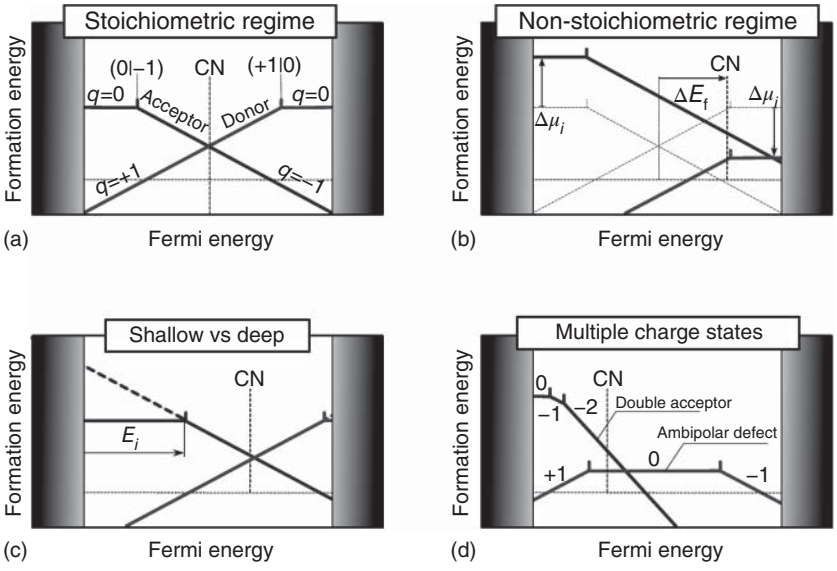

Figure 21.2 Examples for prototype defects: (a) a Schottky/Frenkel defect pair and stoichiometric defect reaction. (b) Shift toward a nonstoichiometric regime due to changes of the μ_i. (c) A deep acceptor and a shallow donor defect. (d) Examples for multiple charge states: an ambipolar defect and a double acceptor defect. The (approximate) point of CN is indicated for all examples.

of Equation 21.3. The slope of each line represents the charge state of the defect (Equation 21.6). In this case, the acceptor and donor formation energies are totally symmetric with respect to each other, and the CN is easily found at the point where the formation energy of both defects has the same value. Charge states can change as they are denoted by the changing slopes of the defects. The apparent symmetry between donor and acceptor formation energies is not necessarily present in real materials. The situation changes especially when a different environmental condition (Δ_i) is chosen.

In the case of our metal oxide, the second panel (Figure 21.2b) shows the effect of a lower oxygen pressure and/or higher temperature and a consequently lower chemical potential of oxygen and a correspondingly higher chemical potential of the metal. Under these conditions, the formation energy of the oxygen vacancy is lower and that of the cation vacancy higher. The Fermi energy necessarily shifts to the right (n type) since negative formation energies are unphysical. The CN is now more difficult to determine since three species significantly contribute to it. Positive charge carriers are the oxygen vacancies whereas cation vacancies and electrons in the conduction band (CB) are negative compensating charges. The exact numbers have to be determined numerically and now also depend on the density of states in the CB. We also see that in this case, the fact that the oxygen vacancy can transform into a neutral color center may further affect the CN.

The third panel (Figure 21.2c) displays the situation when the ionization energy of the acceptor and donor differs from each other. The ionization energy of the defect is given by the distance of the charge-state transition energy to the VBM for acceptors and to the CBM for donors. The donor is shallow (low ionization energy), while the acceptor is deep (high ionization energy). Only very shallow donors are able to keep their charge even at a Fermi energy close to the band edges. These defects are generally good candidates to produce free charge carriers. This is necessary but not a sufficient condition. In order to obtain the free charge carriers, the defects of opposite charge should additionally have high formation energy. In Figure 21.2c, for example, this is not the case. The point of CN is well below the CBM. In this situation, even with the help of additional extrinsic donors, the Fermi level can hardly move higher. This is because the formation energy of the acceptor becomes negative for a Fermi energy well below the CBM. This is usually referred to as Fermi-level pinning, a situation which leads to difficulties of n-type doping, for example, in chalcopyrites due to the presence of negatively charged copper vacancies. The probability for the existence of such pinning levels generally increases with larger band gaps. Therefore, the larger the band gap, the fewer materials can be found which are still dopable to a significant extent. This is because the intervals of the Fermi level for which negative defect formation energies occur, are potentially larger for wide-gap materials. While small band-gap materials like silicon or GaAs can usually be doped n as well as p type, one type of doping usually predominates for wide-gap materials, while the other is more difficult or even impossible to achieve. Finally, for insulating materials often neither n- nor p-type doping can be achieved.

In the last example (Figure 21.2d), it is shown that defects can potentially exist in multiple charge states. It is possible that donors and acceptors have two or more ionization levels. Consequently, they exhibit two or more different charge states. It is further also possible that defects exist in negative as well as positive charge states, that is, ambipolar defects. Important defects of this class are, for example, vacancies and interstitials in silicon as well as hydrogen in many semiconductors. In the case of hydrogen, the switching from donor to acceptor does not occur via a neutral charge state. The omission of a charge state is called a negative *U* behavior and is usually related to large structural relaxations and conformational changes of the defect.

21.5.2
Formation Energies from *Ab Initio* Calculations

After giving some examples, we now show the process of obtaining the formation energies of point defects from the output of first-principles calculations. First, an appropriate variant of first-principles methodology is chosen, which reproduces most of the relevant properties of the bulk material and still allows to calculate at least 100 atoms. Bulk calculations are performed, and the accuracy of the (DFT) method is tested with the semiconductor and all relevant reference phases (metal and the oxygen molecule in the case of an oxide). From a band

structure calculation of the host semiconductor, the positions of the VBM and CBM and their corresponding energies are determined. In the next step, neutral defects are placed into a supercell of a sufficient size and the structures are optimized usually at constant volume conditions. The size of the supercell should be as large as possible. However, this sensitively depends on the material, the method, and the available computational resources. The calculations are usually conducted within periodic boundary conditions, and the defects in the supercells should be separated by at least two neighboring shells. The defects are subsequently charged, and the total energies are calculated for each charge state. When periodic boundary conditions are used, a homogeneous countercharge is added to avoid energy divergence. Unfortunately, this measure introduces spurious cell size effects. In the case of potentially magnetic defects, additional spin-polarized calculations have to be conducted in order to avoid spin contamination. The formation energies for each charge state can now be obtained for a Fermi energy at the VBM by evaluating Equation 21.5 and setting $E_f = 0$. Normally, only the line segments for the charge states with the lowest formation energy are plotted for each defect (see Figure 21.2). As discussed previously, defect formation energies are usually plotted under specific chemical potential of its constituents, which are of interest. It is often instructive to plot the formation energies under the most extreme conditions, which give upper and lower limits to the formation energies of specific defects. In the case of the metal oxide (see Figure 21.1), this would be $\Delta\mu_O = 0$; $\Delta\mu_M = H_f^{MO}$ in the oxygen-rich (high oxygen pressure) limit, whereas $\Delta\mu_O = H_f^{MO}$; $\Delta\mu_M = 0$ in the reducing limit (low oxygen pressure).[3)]

At this stage, the formation energies are still affected by so-called supercell size effects. The magnitude of these effects can well be on the order of electron volts. For example, charged defects interact electrostatically with their periodic replicas in calculations with periodic boundary conditions. In the case of very extended defect-localized wavefunctions, it is additionally possible that the defect-related state shows a significant band dispersion, which in turn leads to usually overestimations of the total energy. Several other supercell size effects have been pointed out previously for charged but also for neutral defects. They are reviewed extensively in the literature [39–42].

21.5.3
Case Study: Point Defects in ZnO

In order to illustrate the formalism presented before, we show results for ZnO, an important semiconducting material. The data presented in Figure 21.3a and b corresponds to the calculated formation energies according to Ref. [33]. This study was undertaken using the so-called LDA + U approach in order to calculate the formation energies of all intrinsic defects. In a second step, the formation energies were corrected for supercell size effects by an extrapolation technique, which involves the calculation of the formation energy in supercells with different sizes.

3) The Gibbs free energy of formation G_f is equal to the formation enthalpy H_f when the entropy of formation is neglected. This is usually a safe approximation at room temperature.

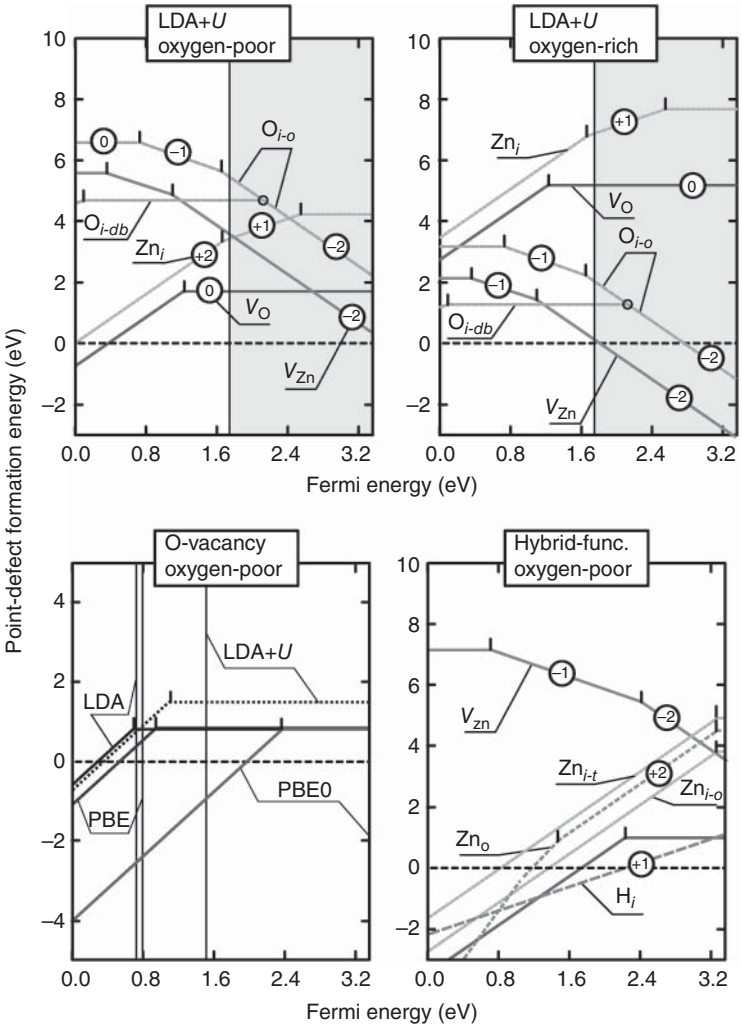

Figure 21.3 Formation energies of intrinsic point defects of ZnO in the LDA with *U* corrections in the oxygen-poor (a) and oxygen-rich (b) limiting cases according to Ref. [33]. (c) A comparison of different exchange–correlation functionals applied to the oxygen vacancy [43]. Vertical lines denote the band gaps corresponding to the respective functional. (d) Comparison of several donor defects including hydrogen interstitials and using hybrid-functional methodology according to Ref. [44].

The formation energies are shown for oxygen-poor (Figure 21.3a) and oxygen-rich (Figure 21.3b) conditions. These are the stability limits of ZnO toward decomposition into metal + oxygen gas (oxygen poor) on the one side and zinc peroxide formation on the other side (oxygen rich). The corresponding environmental conditions can be estimated with the help of the ideal gas law and electrochemical tables. Exemplarily, the oxygen pressure range is $10^{-26} - 10^{16}$ Pa

for a temperature of 600 °C. In the following, the defect energetics are discussed with respect to the calculated band gap (shaded area), which is generally too low using local exchange–correlation functionals. This deficiency is further discussed later in this section.

In the oxygen-poor regime, only oxygen vacancies have low formation energies. This defect is the primary donor of ZnO and exists in the charge states $q = +2/0$. The fact that the charge state $q = +1$ is not present indicates the existence of large lattice relaxations. In the charge state $q = +2$, the energy gain due to lattice relaxations is so high that the removal of an electron from the neutral charge state results in the immediate ejection of the second electron (negative U effect). The Zn interstitials (Zn_i) on the other side have higher transition levels, that is, they are shallow donors with higher formation energies. It is interesting to note that the oxygen vacancy has relatively high ionization energy (color center) but low formation energy on the one side, whereas the Zn_i has a low ionization energy but high formation energy on the other side. This means that both defects cannot lead to high intrinsic electron concentrations but due to different reasons. This finding is at odds with the experimental observation of high intrinsic electron concentrations, especially in reduced ZnO samples. This issue has been extensively discussed in the literature and will not be reviewed here. The most commonly cited theories resolving this controversy can be found in Refs [32, 45].

Among the acceptor defects, the Zn vacancy (V_{Zn}) has the lowest formation energy, which is comparatively large in the oxygen-poor limit but rather low in the oxygen-rich limit. Therefore, by increasing the oxygen partial pressure, the formation of V_{Zn} can be favored over V_O. Additionally, at lower Fermi energy in the oxygen-rich limit, oxygen interstitials in a dumbbell configuration have a low formation energy. Similar to the oxygen vacancies, this defect shows the interesting effect of omitting a charge state ($q = -1$). The most stable charge state is $q = 0$. In this dumbbell configuration, the oxygen atoms have a net charge of −1 (obtained via direct analysis of the charge density) and can, therefore, be classified as peroxo ions which are closed (electronic-)shell configuration of the oxygen dimer. Consequently, additional electrons cannot be accommodated within this geometry. Upon electron addition the dimer breaks and oxygen reoccupies a regular oxygen site, whereas the other oxygen moves to the more symmetrical octahedral interstitial position within the wurtzite lattice. In the final configuration, both anions have a net charge of −2, so that in total two electrons are needed to accomplish this rearrangement. It is important to note that ZnO is often strongly n-type doped. The formation energy of acceptors (especially V_{Zn}) intersects the zero formation energy line. This point depends on the oxygen chemical potential and denotes a pinning level for n-type doping in this material. Under high n-type doping, the V_{Zn} will cause a decay of the doping efficiency in this material. In summary, the defect equilibria of ZnO are mainly determined by oxygen and zinc vacancies similar to situation (b) of Figure 21.2.

Up to this point, we have discussed the defect energetics with respect to the calculated band gap, which is strongly underestimated. The use of different

exchange–correlation functionals results in different band-gap energies. In Figure 21.3, the calculated band gaps of several functionals are indicated together with the resulting formation energies for the oxygen vacancies in ZnO [43].

While there are significant differences in the band-gap energies for different functionals, it is interesting that the formation energy of the neutral charge state is comparably constant. LDA and GGA-PBE give very similar results, and their band-gap energies are very close. In contrast, the hybrid functional (PBE0) results in a decrease in the formation energy of more than 3 eV for the positive charge state. The electronic transition energy is consequently shifted upward, while the formation energy of the zero charge state is essentially the same as in LDA calculations. In contrast, the LDA + U approach leads to both a higher formation energy and higher transition energy for the oxygen vacancies. In the LDA + U approach, the band gap is still significantly underestimated, while the PBE0 is able to reproduce the correct band gap. The relatively constant formation energies for the neutral charge state express the fact that total energies are reliable even when obtained with the LDA. Whenever the ionization of a defect is considered, however, complications due to band-gap errors arise. Since the hybrid functional is able to reproduce the band gap of ZnO, it is interesting to reexamine also the energetics of other defects. Figure 21.3d shows the defect energetics of several intrinsic defects and hydrogen interstitials in ZnO. The results are taken from Ref. [44], which were obtained by the hybrid-functional method in a plane-wave implementation [46]. Also in this case, the formation energies were corrected for finite-size effects by using increasingly larger supercells up to a size of 784 atoms and an extrapolation technique.

For the common defects, the diagram looks similar to the LDA + U result, apart from the pronounced shift to higher Fermi energy. The order of the defect energetics is essentially the same as in the case of the LDA + U calculations. For example, the energetic difference between V_O and Zn_i is comparable. What changes are mainly the positions of the band edges with respect to the transition energies and to a smaller extent the relative positions of the transition energies with respect to each other. In contrast, the formation energies of the neutral charge states change to a much lesser extent.

As an example for extrinsic defects, hydrogen, a potentially important donor for ZnO, is also displayed in Figure 21.3d. This defect has a positive slope throughout the whole band gap and is therefore a very shallow donor. It can be found as interstitial or substitutional defect. In this case, the formation energy of the defect is related to the solubility of hydrogen.

21.6 Conclusions

Over the last decades, powerful theoretical and numerical methods were developed that have triggered the deployment of computational materials science as an entirely new discipline, providing information about materials properties and

processes. Quantum mechanical methods have gained significant importance, especially in the context of understanding point defects in semiconductors, since they allow to systematically study a variety of material properties including those that are not directly accessible by experiments. Therefore, by systematically combining first-principles methods and experiments, further improvement of materials for photovoltaic materials can be expected. This chapter has outlined the principle concepts of electronic DFT and presented its application to intrinsic point defects in oxide materials.

Acknowledgments

The authors are grateful for the support by the Sonderforschungsbereich 595 "Ermüdung von Funktionsmaterialien" of the Deutsche Forschungsgemeinschaft (DFG).

References

1. Mitas, L. (1997) Quantum Monte Carlo. *Curr. Opin. Solid State Mater. Sci.*, **2**, 696–700.
2. Szabo, A. and Ostlund, N.S. (1996) *Modern Quantum Chemistry: Introduction to Advanced Electronic Structure Theory*, Dover, New York.
3. Hohenberg, P. and Kohn, W. (1964) Inhomogeneous electron gas. *Phys. Rev.*, **136**, B864.
4. Kohn, W. and Sham, L.J. (1965) Self-consistent equations including exchange and correlation effects. *Phys. Rev.*, **140**, A1133.
5. Singh, D.J. and Nordstrom, L. (eds) (2006) *Planewaves, Pseudopotentials, and the LAPW Method*, Springer, Berlin.
6. Ceperley, D.M. and Alder, B.J. (1980) Ground state of the electron gas by a stochastic method. *Phys. Rev. Lett.*, **45**, 566–569.
7. Perdew, J.P., Burke, K., and Ernzerhof, M. (1996) Generalized gradient approximation made simple. *Phys. Rev. Lett.*, **77**, 3865.
8. Hubbard, J. (1963) Correlations in narrow energy bands. *Proc. R. Soc. London, Ser. A*, **276**, 238.
9. Anisimov, V.I., Zaanen, J., and Andersen, O.K. (1991) Band theory and Mott insulators: Hubbard U instead of Stoner I. *Phys. Rev. B: Condens. Matter Mater. Phys.*, **44**, 943.
10. Anisimov, V.I., Aryasetiawan, F., and Lichtenstein, A.I. (1997) First-principles calculations of the electron structure and spectra of strongly correlated systems: the LDA+U method. *J. Phys. Condens. Matter*, **9**, 767.
11. Becke, A.D. (1993) Density-functional thermochemistry. III: The role of exact exchange. *J. Chem. Phys.*, **98**, 5648.
12. Adamo, C. and Barone, V. (1999) Toward reliable density functional methods without adjustable parameters: the PBE0 model. *J. Chem. Phys.*, **110**, 6158.
13. Heyd, J., Scuseria, G., and Ernzerhof, M. (2003) Hybrid functionals based on a screened Coulomb potential. *J. Chem. Phys.*, **118**, 8207.
14. Heyd, J., Scuseria, G., and Ernzerhof, M. (2006) Hybrid functionals based on a screened Coulomb potential (vol. 118, p. 8207, 2003). *J. Chem. Phys.*, **124**, 219906.
15. Marsman, M., Paier, J., Stroppa, A., and Kresse, G. (2008) Hybrid functionals applied to extended systems. *J. Phys. Condens. Matter*, **20**, 064201.
16. Kümmel, S. and Kronik, L. (2008) Orbital-dependent density functionals: theory and applications. *Rev. Mod. Phys.*, **80**, 3.
17. Payne, M.C., Teter, M.P., Allen, D.C., Arias, T.A., and Joannopoulos, J.D. (1992) Iterative minimization techniques

for *ab initio* total-energy calculations: molecular dynamics and conjugate gradients. *Rev. Mod. Phys.*, **64**, 1045.
18. Martin, R.M. (2004) *Electronic Structure: Basic Theory and Practical Methods*, Cambridge University Press, Cambridge.
19. Friedrich, C. and Schindlmayer, A. (2006) Many-body perturbation theory, in *Computational Nanoscience: Do It Yourself!* vol. 31 (eds J. Grotendorst, S. Blügel, and D. Marx), John von Neumann Institute for Computing, Jülich, Germany, pp. 335–355.
20. Onida, G., Reining, L., and Rubio, A. (2002) Electron excitations: density-functional versus many-body Green's-function approaches. *Rev. Mod. Phys.*, **74**, 601.
21. Foulkes, W.M.C., Mitas, L., Needs, R.J., and Rajagopal, G. (2001) Quantum Monte Carlo simulation of solids. *Rev. Mod. Phys.*, **73**, 33.
22. Hedin, L. (1965) New method for calculating the one-particle Green's function with application to the electron-gas problem. *Phys. Rev.*, **139**, 796.
23. Lerch, D., Wieckhorst, O., Hart, G.L.W., Forcade, R.W., and Müller, S. (2009) Uncle: a code for constructing cluster expansions for arbitrary lattices with minimal user-input. *Modell. Simul. Mater. Sci. Eng.*, **17**, 055003.
24. Erhart, P., Juslin, N., Goy, O., Nordlund, K., Muller, R., and Albe, K. (2006) Analytic bond-order potential for atomistic simulations of zinc oxide. *J. Phys. Condens. Matter*, **18** (29), 6585–6605.
25. Wu, X., Vanderbilt, D., and Hamann, D.R. (2005) Systematic treatment of displacements, strains, and electric fields in density-functional perturbation theory. *Phys. Rev. B: Condens. Matter Mater. Phys.*, **72** (3), 035105.
26. Baroni, S., Gironcoli, S., Corso, A., and Giannozzi, P. (2001) Phonons and related crystal properties from density-functional perturbation theory. *Rev. Mod. Phys.*, **73**, 515.
27. Gonze, X., Allan, D.C., and Teter, M.P. (1992) Dielectric tensor, effective charges, and phonons in alpha-quartz by variational density-functional perturbation-theory. *Phys. Rev. Lett.*, **68**, 3603.
28. Morgan, T.N. (1986) Theory of the DX center in $Al_xGa_{1-x}As$ and gas crystals. *Phys. Rev. B: Condens. Matter Mater. Phys.*, **34**, 2664.
29. Chadi, D.J. (1999) Predictor of p-type doping in II–VI semiconductors. *Phys. Rev. Lett.*, **59** (23), 15181.
30. Chadi, D.J. and Chang, D.J. (1989) Energetics of DX-center formation in GaAs and $Al_xGa_{1-x}As$ alloys. *Phys. Rev. B: Condens. Matter Mater. Phys.*, **39**, 10063.
31. Wei, S.-H. and Zhang, S.B. (2002) Chemical trends of defect formation and doping limit in II–VI semiconductors: the case of CdTe. *Phys. Rev. B: Condens. Matter Mater. Phys.*, **66**, 155211.
32. Lany, S. and Zunger, A. (2005) Anion vacancies as a source of persistent photoconductivity in II–VI and chalcopyrite semiconductors. *Phys. Rev. B: Condens. Matter Mater. Phys.*, **72**, 035215.
33. Erhart, P., Albe, K., and Klein, A. (2006) First-principles study of intrinsic point defects in ZnO: role of band structure, volume relaxation and finite size effects. *Phys. Rev. B: Condens. Matter Mater. Phys.*, **73**, 205203.
34. Erhart, P. and Albe, K. (2008) Modeling the electrical conductivity in $BaTiO_3$ on the basis of first-principles calculations. *J. Appl. Phys.*, **104** (4), 044315.
35. Walle, C.G. and Blöchl, P.E. (1993) First-principles calculations of hyperfine parameters. *Phys. Rev. B: Condens. Matter Mater. Phys.*, **47**, 4244.
36. Puska, M.J. and Nieminen, R.M. (1994) Theory of positrons in solids and on solid-surfaces. *Rev. Mod. Phys.*, **66**, 841.
37. Ma, Y.C., Rohlfing, M., and Gali, A. (2010) Excited states of the negatively charged nitrogen-vacancy color center in diamond. *Phys. Rev. B: Condens. Matter Mater. Phys.*, **81**, 041204.
38. Zhang, S.B. and Northrup, J.E. (1991) Chemical potential dependence of defect formation energies in GaAs: application to Ga self-diffusion. *Phys. Rev. Lett.*, **67**, 2339.
39. Persson, C., Zhao, Y.-J., Lany, S., and Zunger, A. (2005) n-type doping of $CuInSe_2$ and $CuGaSe_2$. *Phys. Rev. B: Condens. Matter Mater. Phys.*, **72**, Art no: 035211.

40. Hine, N.D.M., Frensch, K., Foulkes, W.M.C., and Finnis, M.W. (2009) Supercell size scaling of density functional theory formation energies of charged defects. *Phys. Rev. B: Condens. Matter Mater. Phys.*, **79**, 024112.

41. Castleton, C.W.M., Höglund, A., and Mirbt, S. (2006) Managing the supercell approximation for charged defects in semiconductors: finite-size scaling, charge correction factors, the band-gap problem, and the *ab initio* dielectric constant. *Phys. Rev. B: Condens. Matter Mater. Phys.*, **73**, 035215.

42. Christoph, F., Blazej, G., Tilmann, H., Jörg, N., Georg, K., Anderson, J., and Chris, G.V. (2014) First-principles calculations for point defects in solids. *Rev. Mod. Phys.*, **86**, 253.

43. Ágoston, P., Albe, K., Nieminen, R.M., and Puska, M.J. (2009) Intrinsic n-type behavior in transparent conducting oxides: a comparative hybrid-functional study of In_2O_3, SnO_2, and ZnO. *Phys. Rev. Lett.*, **103**, 245501.

44. Oba, F., Togo, A., Tanaka, I., Paier, J., and Kresse, G. (2008) Defect energetics in ZnO: a hybrid Hartree–Fock density functional study. *Phys. Rev. B: Condens. Matter Mater. Phys.*, **77**, 245202.

45. Walle, C.G. (2000) Hydrogen as a cause of doping in zinc oxide. *Phys. Rev. Lett.*, **85**, 1012–1015.

46. Paier, J., Marsman, M., Hummer, K., Kresse, G., Gerber, I.C., and Ángyán, J.G. (2006) Screened hybrid density functionals applied to solids. *J. Chem. Phys.*, **124**, 154709.

22
Molecular Dynamics Analysis of Nanostructures

Xiaowang Zhou, Jose Chavez, and David Zubia

22.1
Introduction

In this chapter we discuss how molecular dynamics (MD) simulations can be used to understand nanostructure and defect formation during growth of solar cells and how the insights gained can be used to reduce defects. Section 22.2 explains the basic concept of MD. Section 22.3 discusses MD simulation methods for vapor deposition. Section 22.4 introduces numerical tools for extracting information on defects from MD results. Section 22.5 presents a case study in which MD is used to understand and reduce defects in CdTe/CdS solar cells.

22.2
Molecular Dynamics Methods

A molecular dynamics simulation essentially solves atom positions as a function of time from Newton's equations of motion. As a simple example, Figure 22.1a shows a crystal with dimensions L_x, L_y, and L_z in the x-, y-, and z-directions. This material system is simulated in MD as an assembly of atom coordinates that can be designated according to structure, orientation, and lattice constant of the crystal. A system temperature can be established by further assigning velocities to this assembly of atoms according to a Boltzmann distribution. Periodic boundary condition can be used in simulations. This simply means that the system shown in Figure 22.1a is periodically repeated in the x-, y-, and z-directions with the periodic length being L_x, L_y, and L_z. As a result, the surfaces are removed and the system can be viewed as infinitely large.

Atoms in MD models are subject to interatomic forces. In general, the force acting on a given atom equals the derivative of system energy with respect to a displacement of the atom. Hence, all interatomic forces can be calculated once an interatomic potential model [1] is available to define the system energy as a function of atom positions. Based on the forces calculated from the potential model, MD simulations integrate atom positions and velocities as a function of time from

Advanced Characterization Techniques for Thin Film Solar Cells, Second Edition.
Edited by Daniel Abou-Ras, Thomas Kirchartz, and Uwe Rau.

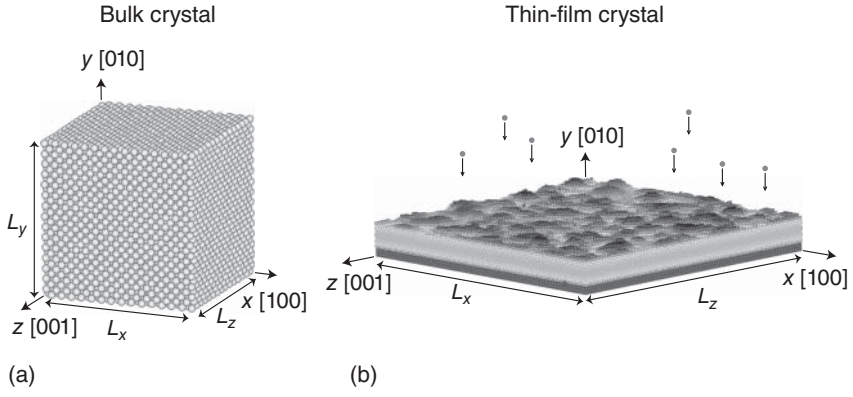

Figure 22.1 Example MD systems. (a) Bulk and (b) thin-film crystal systems.

Newton's equation of motion. The simplest MD simulations conserve energy and do not change system size (given by the periodic lengths L_x, L_y, L_z). Such constant energy and constant volume simulations do not allow temperature and pressure to be controlled. Alternatively, MD simulations can be performed under a constant temperature condition (e.g., using Nose–Hoover dragging forces [2] to increase or decrease atom kinetic energies depending on whether the temperature is lower or higher than the desired value). MD integration can also be performed under a constant pressure condition (e.g., using Parrinello–Rahman algorithm [3] to allow the periodic lengths L_x, L_y, and L_z to change in responding to external pressure).

MD simulations allow complex material problems to be numerically studied. When the system contains no defects, such as the one shown in Figure 22.1a, MD simulations can be used to study phonon vibration spectra and thermal transport properties. If systems contain point defects, MD simulations can be used to study the diffusion of these defects. If external forces/loads are applied to atoms, MD simulations can be used to study a variety of other problems including deformation, fracture, and structure evolution. As another example, Figure 22.1b shows a thin-film crystalline structure where periodic boundary conditions are used only in the x- and z-directions, whereas a free boundary condition is used in the y-direction. During simulations, adatoms are continuously injected to the top y-surface from random locations far above the surface, and positions of all atoms are solved from Newton's equation of motion. In this case, MD simulations can be used to simulate the structure evolution during vapor deposition synthesis processes.

The large-scale atomic/molecular massively parallel simulator (LAMMPS) [4, 5] is perhaps the most widely applied MD code today. LAMMPS is popular because it is publically available [4], has incorporated different types of interatomic potentials, contains flexible functionalities, and can be easily extended. In addition to MD simulations, LAMMPS can be used to perform energy minimization by molecular statics (MS) simulations. Here, the goal is not to examine the dynamic behavior of the material, but rather to find out the lowest

energy structure. This is useful because the initial structure of MD simulations is often guessed, which may be far away from equilibrium. MS simulations will allow the guessed structure to be relaxed, enabling the determination of the equilibrium structure (e.g., relaxed to the correct lattice constant when the initial lattice constant is off).

22.3 Vapor Deposition Simulations

Direct MD simulations of vapor deposition for material synthesis have unique advantages over other techniques for (structural) defect studies. For example, quantum mechanical calculations [6] are computationally much more expensive. As a result, they can only be applied for small systems, and the calculations of defect properties rely on the use of "guessed" defect configurations as the input. Continuum models [7] are not as predictive, and therefore, they require more assumptions. In direct MD vapor deposition simulations, however, defects are naturally formed without any assumptions. Using the Stillinger–Weber potential [8] for the II–VI elements Zn–Cd–Hg–S–Se–Te [9], we demonstrate two MD simulations [9] that help reveal defects in II–VI compound thin films.

In the first case, we show in Figure 22.2a the atomic configuration obtained from an MD simulation of vapor deposition of an alloyed $(Cd_{0.28}Zn_{0.68}Hg_{0.04})(Te_{0.20}Se_{0.18}S_{0.62})$ compound on a (010) zinc-blende (zb) ZnS substrate, where the initial ZnS substrate containing eleven (010) layers is shaded. During the simulation, the bottom two (040) layers are held fixed to prevent crystal shift upon adatom impact on the top surface. The next seven (040) layers are isothermally controlled at a growth temperature $T = 1200$ K. This leaves the top two layers free where the motion of atoms is solely determined by Newton's equations of motion.

Growth of the alloy is simulated by injecting Cd, Zn, Hg, Te, Se, and S atoms from random locations far above the surface. All adatoms have an initial incident direction perpendicular to the surface and an initial far-field incident kinetic energy $E_i = 5.0$ eV. The relative injection frequencies of different species are chosen to give a $(Cd_{0.28}Zn_{0.68}Hg_{0.04})(Te_{0.20}Se_{0.18}S_{0.62})$ film composition and an overall deposition rate of $R = 0.2$ nm/ns. This deposition rate is much higher than experimental values but has to be used in order to grow sufficient material for the analysis within the MD time scale (due to the computational cost, MD time scales are usually limited to within tens of nanoseconds). However, by maintaining the substrate at an elevated temperature, adatoms can often relax to low energy configurations even within the short time constraint imposed by the high deposition rate. As a result, the effects of accelerated deposition rates on structures are mitigated. Indeed, Figure 22.2a convincingly verifies that MD vapor deposition simulations can predict crystalline growth.

Based on the final atom coordinates, we find a small antisite fraction of 0.0051 for anion (Te, Se, S) to occupy cation (Cd, Zn, Hg) sites and a smaller antisite fraction of 0.0003 for cation to occupy anion sites. The data also allows us to quantify

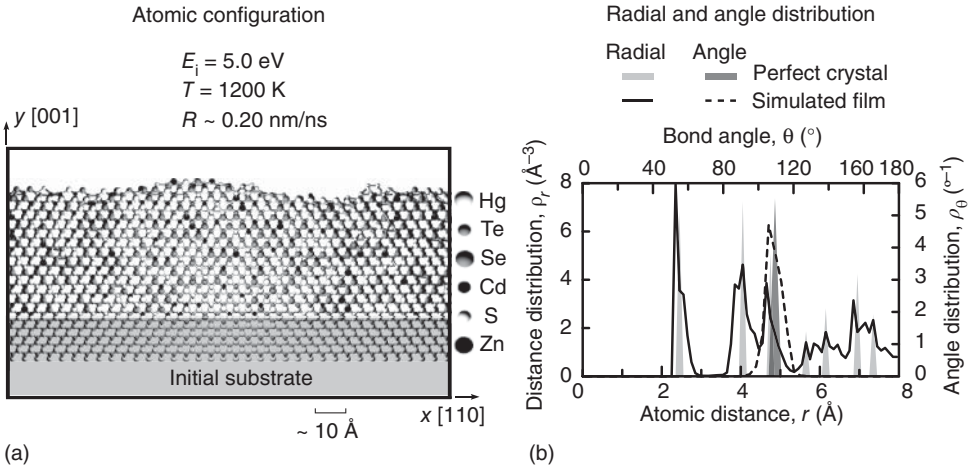

Figure 22.2 MD simulation of growth of a superalloyed $(Cd_{0.28}Zn_{0.68}Hg_{0.04})(Te_{0.20}Se_{0.18}S_{0.62})$ layer on (010) zinc-blende ZnS. (a) Atomic configuration and (b) radial and bond-angle distribution function.

in Figure 22.2b structural characteristics such as radial (solid line) and bond angle (dash line) distribution functions, where reference values obtained from perfect zinc-blende structure are included as the shaded regions. Figure 22.2b indicates that the peak radial positions obtained from the deposited film align well with the reference peaks and the bond angles center around the tetrahedral angle of about 109°. Hence, the film obtained from the MD simulations has a good crystallinity of the zinc-blende structure.

In the second case, we demonstrate in Figure 22.3 the atomic configuration obtained from an MD simulation of vapor deposition of HgTe/CdSe/ZnS multilayers. The simulation approach is the same as described earlier, except that different growth conditions are used to grow different layers as indicated in the figure. Figure 22.3 reveals various defects. For example, misfit dislocations exhibiting extra half planes about 145° from the y-axis in the smaller lattices are found at both CdSe/ZnS and HgTe/CdSe interfaces. Interestingly, two types of misfit dislocations are observed, one exhibiting only one extra half plane and the other exhibiting two extra half planes. The spacing of these misfit edge dislocations is on the order of 30–40 Å, leading to significant tilting of the (001) growth surface that causes small-angle grain boundaries between neighboring domains (subgrains). Stacking faults are observed in the HgTe layer. Various point defects such as antisites, interstitials, and isolated S atoms in the CdSe layer can also be seen in Figure 22.3 (marked by circles). Although these defects can affect the materials properties, they are not easily identifiable in experiments. MD simulations allow for virtual synthesis of the materials, in which these defects can be reduced by manipulation of growth conditions and design of nanoscale structures. They can also help interpret the phenomena observed from the experimental microscopic analyses.

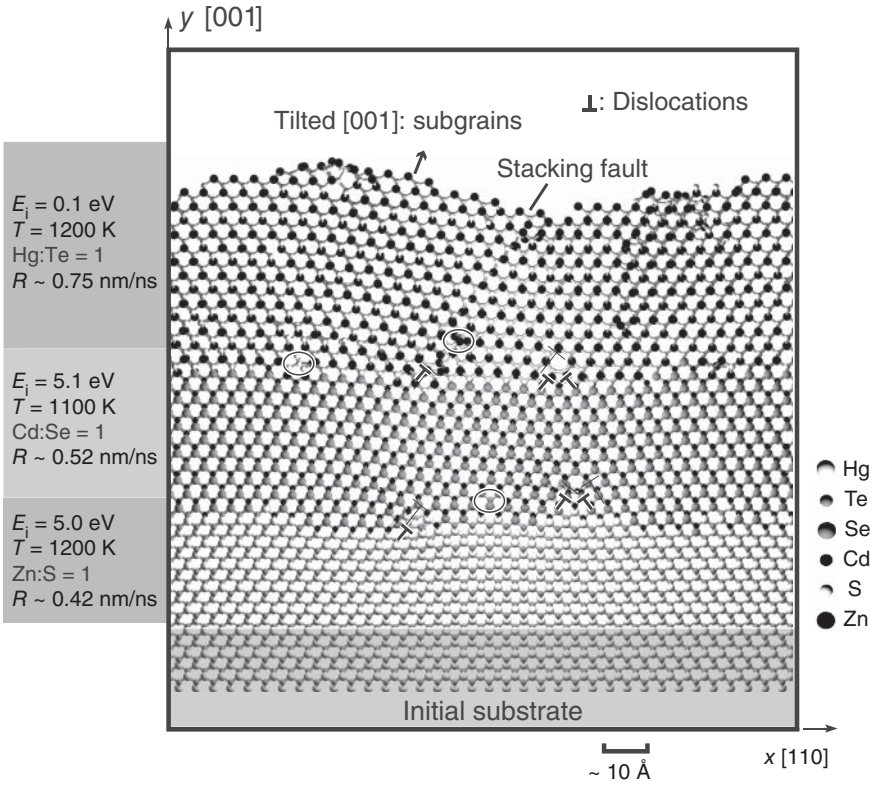

Figure 22.3 Atomic configuration of HgTe/CdSe/ZnS multilayers grown on (010) zinc-blende ZnS obtained from an MD simulation.

22.4
Defect Extraction Algorithms

Typical MD result files consist of three-dimensional (3D) coordinates of a large number of atoms. The data sets contain information about crystallographic and defect structures. Various algorithms have been developed to extract the crystallographic and defect information contained within the numerical data [10]. Based on such information, visualization software can then provide graphical representation of various structural characteristics. Here, we illustrate three different visualizations of the same CdTe sphalerite crystal containing an individual stacking fault bounded between two partial dislocations. In Figure 22.4a, a visualization tool [11] is used to illustrate this system with Cd and Te atoms represented by black and gray circles, respectively. While the stacking fault and the two partial dislocations (indicated by the arrows) can be recognized, they are not particularly easy to analyze. This type of image can be directly compared with experimental data [12, 13], that is, with high-resolution transmission electron microscopy (HRTEM) images for validation of the predicted defect structures. A distinct advantage in the

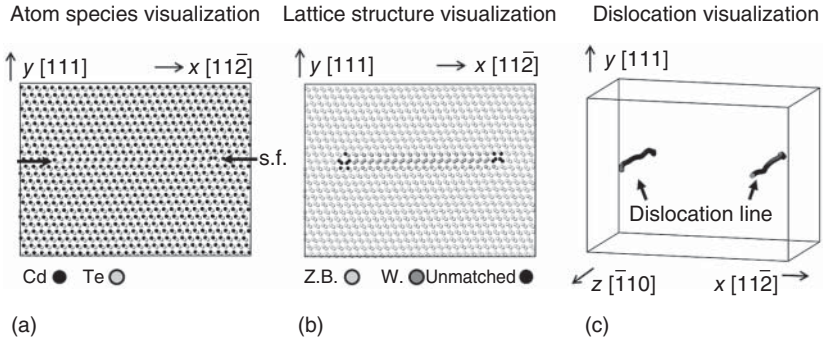

Figure 22.4 Atomistic visualization and analysis of a CdTe (111) crystal with one intrinsic stacking fault. (a) The illustration of Cd and Te species; (b) the distinction of wurtzite, sphalerite, and unmatched crystal structures; and (c) the extraction of dislocation line segments.

MD simulated data over experimental HRTEM is that it can be cleaved along any arbitrary direction and viewed along any arbitrary zone axis.

The algorithm given in Ref. [11] can be used to determine the lattice type of each atom by comparing positions of its neighboring atoms to a catalog of reference positions of various lattices. Figure 22.4b shows the same configuration as Figure 22.4a except that the light gray, dark gray, and black colors are now used to distinguish sphalerite, wurtzite, and unmatched lattices where "unmatched" simply means that the lattice does not match sphalerite nor wurtzite. The dark gray dots (wurtzite region) highlight the stacking fault, and the black dots (unmatched lattice) identify the two partial dislocations.

Multiple strategies have been employed to detect and extract other defects within atomistic data sets [14, 15]. In Figure 22.4c, an algorithm [16, 17] that extracts dislocation line segments from atomistic data is employed to analyze the same CdTe crystal. In this case, only two dislocation line segments associated with partial dislocations are shown, further confirming that the system analyzed contains a stacking fault bounded by two partials.

22.5 Case Study: CdTe/CdS Solar Cells

22.5.1 Validation of MD Methods

Using a bond order potential (BOP) [13, 18], MD simulations are performed to grow CdTe on (0001) wurtzite CdS [12]. The simulated atomic structures are compared to experimental HRTEM images of CdTe/CdS layers [19] shown in Figure 22.5. The predicted image in the top frame of Figure 22.5a shows two misfit dislocations as manifested by extra planes in the CdS layer. The configuration and density of the predicted misfit dislocations agree well with those found in the HRTEM image shown in the bottom frame of Figure 22.5a. Furthermore,

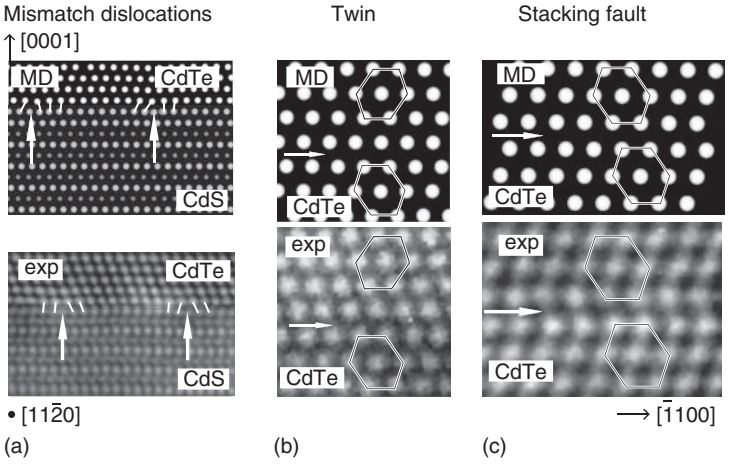

Figure 22.5 Comparison of MD predicted and experimentally detected defects in CdTe thin films on CdS substrates. (a) Misfit dislocations, (b) twin, and (c) stacking fault. The arrows mark the position of dislocation cores and twin/stacking fault planes. (Reproduced with permission from Yan [19] of American Institute of Physics.).

the simulation indicates the formation of twin and stacking fault as shown in the top frames in Figure 22.5b and c, in remarkably good agreement with the experimental images shown in the bottom frames. These results validate the capability of MD simulations for defect studies, relevant to the experimental length scales. They also confirm that for the CdTe/CdS multilayered films with a large lattice mismatch strain of $\varepsilon_0 \sim 0.11$, the misfit dislocation density is very high. For instance, Figure 22.5a indicates that the distance between the dislocations is about 10 times the interplanar distances.

22.5.2
Reducing Defects via Nanostructuring

As described earlier, multilayered films always contain a high misfit defect density. One idea to reduce defects is shown in Figure 22.6, where a SiO_2 layer is first deposited on CdS and patterned to expose the CdS layer underneath in small windows. CdTe is then selectively grown on the exposed CdS surface but not on the mask surface [20]. This creates CdTe nanoislands. Experimentally exploring this idea is expensive and prolonged, especially when the dimension of the islands reduces below 100 nm. Alternatively, MD simulations allow defect density to be quantified as a function of island size prior to any experiments.

22.5.3
MD Informed Continuum Analysis

MD simulations can provide continuum models with information to calculate misfit dislocation densities in nanoislands. First, MD simulations are performed

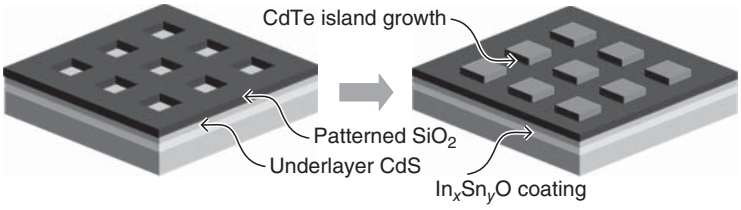

Figure 22.6 Growth of CdTe nanoislands on CdS using nanopatterning technology.

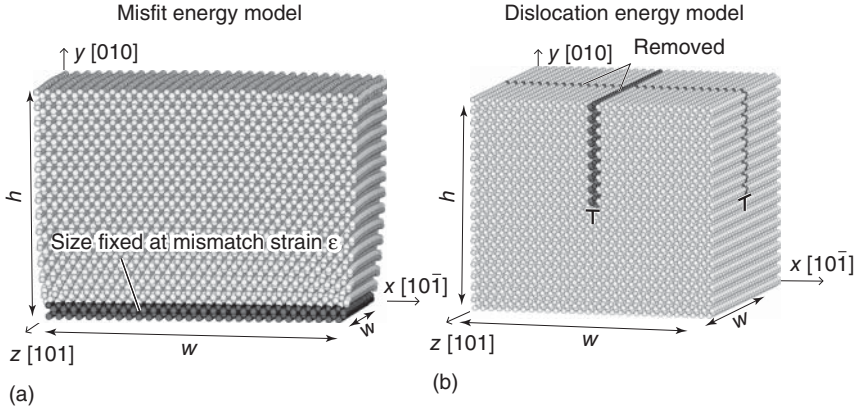

Figure 22.7 Atomistic models for (a) misfit strain energy density and (b) misfit dislocation energies.

to derive the density of misfit strain energy and dislocation line energy as functions of island dimensions and lattice mismatch. Atomistic models for calculating these quantities during island growth are shown in Figure 22.7a and b. For the strain energy density, a CdTe island with a width w and a height h is relaxed using energy minimization simulations under the condition that the bottom layer of this island, represented by dark spheres in Figure 22.7a, is strained by a lattice mismatch strain ε_0 that remains fixed during simulation. The density of the misfit strain energy is calculated from the energy difference between the strained and the unstrained (i.e., $\varepsilon = 0$) islands per unit volume. For the misfit dislocation energy, these line defects are introduced into the island by removing corresponding planes, as shown in Figure 22.7b. After energy minimization simulations, the misfit dislocation energy is calculated as the difference of the relaxed energies between the dislocated and the dislocation-free islands per unit of dislocation length [21].

These misfit strain energy density and dislocation energy functions obtained from MD simulations are then used in classic misfit dislocation theory [22, 23] to calculate the dislocation density in nanopatterned multilayers. In this theory, the system energy is a sum of misfit strain and dislocation energies. Increasing dislocations increases dislocation energy but reduces misfit strain energy. The equilibrium dislocation density can be obtained by minimizing the total system

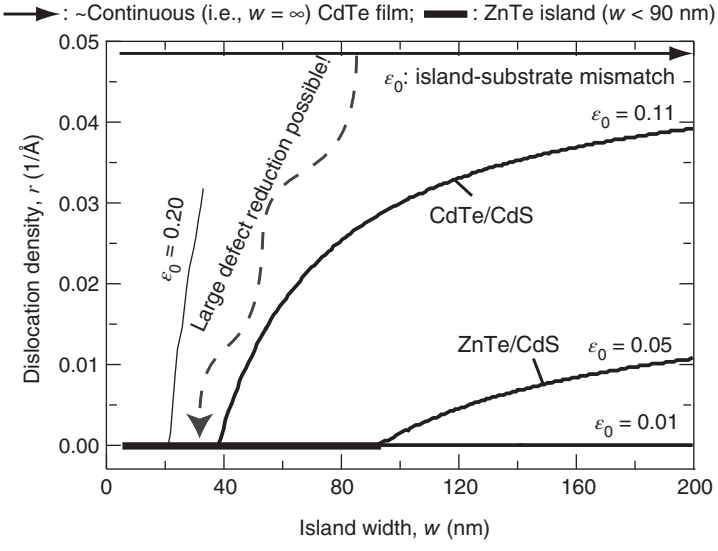

Figure 22.8 Predicted misfit dislocation density ρ as a function of island width w and lattice mismatch strain ε_0.

energy with respect to the number of dislocations. By using the BOP [13, 18], our calculated equilibrium dislocation density ρ is shown in Figure 22.8 as a function of island width w at four different lattice mismatch strains of $\varepsilon_0 = 0.20, 0.11$ (corresponding to CdTe/CdS), 0.05 (corresponding to ZnTe/CdS), and 0.01, respectively. For reference, the dislocation density obtained for continuous (i.e., island width $w = \infty$) CdTe/CdS films is included with a line and an arrow. Figure 22.8 indicates that continuous CdTe/CdS multilayers have an extremely high misfit dislocation density near 0.05 $Å^{-1}$. By utilizing nanopatterning, the dislocation density can be reduced according to the $\varepsilon_0 = 0.11$ line until dislocation-free CdTe/CdS multilayers are obtained when the island width is below a critical value of about 40 nm. However, the critical island width can be increased to 90 nm for a better lattice mismatched ZnTe/CdS system. This implies that by using composition grading where the Zn content is slowly decreased along the thickness of a $Cd_{1-x}Zn_xTe$-on-CdS island, dislocation-free CdTe/graded layer/CdS multilayers can be achieved when the island size is below 90 nm. Note from Figure 22.8 that for a smaller lattice mismatch of 0.01, the critical island width is larger than 200 nm, whereas for a larger lattice mismatch of 0.20, the critical island width is reduced to 20 nm.

22.5.4 Direct MD Simulations

The effect of island size on defect density can also be directly studied by MD simulations of selective-area deposition of CdTe on a nanopatterned substrate [24]. In Figure 22.9a we show CdTe islands grown on nanopatterned CdS [0001] using the Stillinger–Webber potential [9]. In a similar way to the experimental approaches

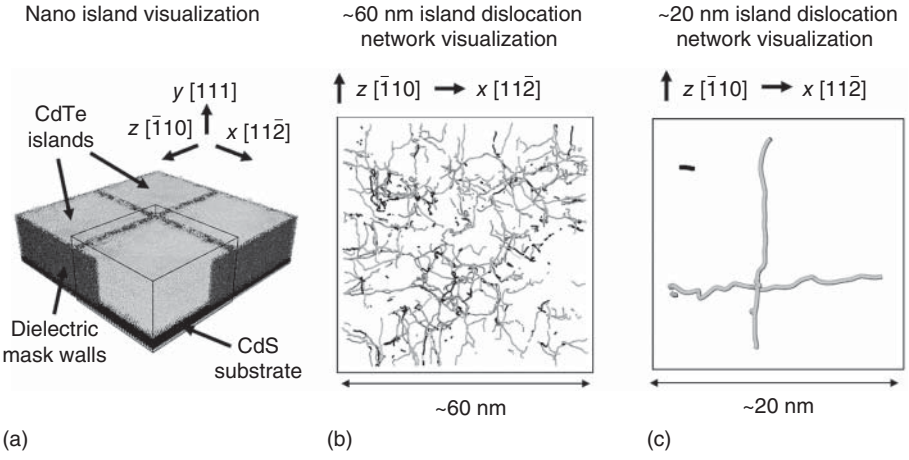

Figure 22.9 (a) Atomistic visualization of CdTe nanoisland structures, (b) dislocations in the 60 nm island, and (c) dislocations in the 20 nm island.

described in previous sections, the simulated selective-area deposition incorporates a patterned dielectric layer. The dark gray areas in Figure 22.9a are the growth mask (patterned dielectric layer) used to achieve selective-area growth. The lighter gray areas are the CdTe nanoislands. The patterned dielectric layer is created by decreasing the sticking coefficient of the atoms to effectively create an artificial material that inhibits adatom nucleation similar to experimental dielectric materials such as SiO_2 and Si_3N_4. All other vapor deposition simulation settings are similar to those described earlier. The growth height of the CdTe nanoislands is nominally 15 nm. In these simulations, two different island widths (60 and 20 nm) are used to study the effect of island size on defect density. Figure 22.9b shows a significant number of dislocation line segments in the 60 nm CdTe nanoisland. An analysis of the Burgers vectors of these segments indicates that the $1/6\langle 112\rangle$ Shockley partial dislocations (light gray) are most numerous, while $1/2\langle 110\rangle$ perfect dislocations (dark gray) are also present. In comparison, Figure 22.9c shows a drastic reduction in dislocation segments in the 20 nm CdTe nanoisland. This suggests that crystal quality improves when the size of the nanopatterning is reduced. This trend is in good agreement with experimental data reported in literature [20].

22.6 Concluding Remarks

Molecular dynamics provides an accurate simulation method to study the microstructures of materials under conditions where experiments are challenging. On the other hand, MD simulations are limited to extremely short time scales. With this understood, properly designed MD simulations can still replicate the experimental observations (e.g., a high temperature can be used to offset the short time scale). More importantly, MD simulations are effective in revealing

mechanisms and trends in spite of the simulated conditions. MD simulations are also accurate when deriving thermodynamic (energies of various structures) and kinetic (energy barriers of various evolution events) properties. These properties can be used in continuum models to overcome the MD time scale issue. Future MD models will continuously improve with emergence of better interatomic potentials and faster computers.

Acknowledgments

Sandia National Laboratories is a multiprogram laboratory managed and operated by Sandia Corporation, a wholly owned subsidiary of Lockheed Martin Corporation, for the US Department of Energy's National Nuclear Security Administration under contract DE-AC04-94AL85000. This work was performed under a DOE Project No. EE0005958.

References

1. Finnis, M. (2003) *Interatomic Forces in Condensed Matter*, Oxford Series on Materials Modelling, Oxford University Press, Oxford.
2. Hoover, W.G. (1985) Canonical dynamics: equilibrium phase-space distributions. *Phys. Rev. A: At. Mol. Opt. Phys.*, **31**, 1695–1697.
3. Parrinello, M. and Rahman, A. (1981) Polymorphic transitions in single crystals: a new molecular dynamics method. *J. Appl. Phys.*, **52**, 7182.
4. LAMMPS download site: lammps.sandia.gov.
5. Plimpton, S. (1995) Fast parallel algorithms for short-range molecular-dynamics. *J. Comput. Phys.*, **117**, 1–19.
6. Griffiths, D.J. (2014) *Introduction to Quantum Mechanics*, Pearson Education Limited, London.
7. Fan, D. and Chen, L.Q. (1997) Computer simulation of grain growth using a continuum field model. *Acta Mater.*, **45**, 611.
8. Stillinger, F.H. and Weber, T.A. (1985) Computer simulation of local order in condensed phases of silicon. *Phys. Rev. B: Condens. Matter Mater. Phys.*, **31**, 5262.
9. Zhou, X.W., Ward, D.K., Martin, J.E., van Swol, F.B., Cruz-Campa, J.L., and Zubia, D. (2013) Stillinger–Weber potential for the II–VI elements Zn–Cd–Hg–S–Se–Te. *Phys. Rev. B: Condens. Matter Mater. Phys.*, **88**, 085309.
10. Li, J. (2005) *Atomistic Visualization, Handbook of Materials Modeling*, Springer, Columbus, Netherlands, pp. 1051–1068.
11. Stukowski, A. (2010) Visualization and analysis of atomistic simulation data with OVITO – the Open Visualization Tool. *Modell. Simul. Mater. Sci. Eng.*, **18**, 015012.
12. Zhou, X.W., Ward, D.K., Doty, F.P., Zimmerman, J.A., Wong, B.M., Cruz-Campa, J.L., Nielson , G.N., Chavez J.J., Zubia, D., and McClure, J.C. (2015) A prediction of dislocation-free CdTe/CdS photovoltaic multilayers via nano-patterning and composition grading. *Prog. Photovoltaics Res. Appl.*, **23**, 1837–1846.
13. Chavez, J.J., Ward, D.K., Wong, B.M., Poty, F.O., Cruz-Campa, J.L., Nielson, G.N., Gupta, V.P., Zubia, D., McClure, J.C., and Zhou, X.W. (2012) Defect formation dynamics during CdTe overlayer growth. *Phys. Rev. B: Condens. Matter Mater. Phys.*, **85**, 245316.
14. Li, D., Wang, F.C., Yang, Z.Y., and Zhao, Y.P. (2014) How to identify dislocations

in molecular dynamics simulations? *Sci. China: Phys., Mech. Astron.*, **57**, 2177.

15. Stukowski, A. (2012) Structure identification methods for atomistic simulations of crystalline materials. *Modell. Simul. Mater. Sci. Eng.*, **20**, 045021.
16. Stukowski, A. and Albe, K. (2010) Extracting dislocations and non-dislocation crystal defects from atomistic simulation data. *Modell. Simul. Mater. Sci. Eng.*, **18**, 085001.
17. Stukowski, A., Bulatov, V.V., and Arsenlis, A. (2012) Automated identification and indexing of dislocations in crystal interfaces. *Modell. Simul. Mater. Sci. Eng.*, **20**, 085007.
18. Ward, D.K., Zhou, X.W., Wong, B.M., Doty, F.P., and Zimmerman, J.A. (2012) Analytical bond-order potential for the cadmium telluride binary system. *Phys. Rev. B: Condens. Matter Mater. Phys.*, **85**, 115206.
19. Yan, Y., Dhere, R.G., Jones, K.M., and Al-Jassim, M.M. (2001) Influence of substrate structure on the growth of CdTe thin films. *J. Appl. Phys.*, **89**, 5944.
20. Aguirre, B.A., Zubia, D., Ordonez, R., Anwar, F., Prieto, H., Sanchez, C.A., Salazar, M.T., Pimentel, A.A., Michael, J.R., Zhou, X., McClure, J.C., Nielson, G.N., and Cruz-Campa, J.L. (2014) Selective growth of CdTe on nano-patterned CdS via close-space sublimation. *J. Electron. Mater.*, **43**, 2651.
21. Zhou, X.W., Ward, D.K., Wong, B.M., Doty, F.P., and Zimmerman, J.A. (2012) Molecular dynamics studies of dislocations in CdTe crystals from a new bond order potential. *J. Phys. Chem. C*, **116**, 17563.
22. Payne, A.P., Nix, W.D., Lairson, B.M., and Clemens, B.M. (1993) Strain relaxation in ultrathin films: a modified theory of misfit-dislocation energetics. *Phys. Rev. B: Condens. Matter Mater. Phys.*, **47**, 13730.
23. Nix, W.D. (1989) Mechanical properties of thin films. *Metall. Trans.*, **20**, 2217.
24. Chavez, J.J., Zhou, X., Ward, D.K., Cruz-Campa, J.L., and Zubia, D. (2014) A molecular dynamics study on defect reduction in thin film $Cd_{1-x}Zn_xTe$/CdS Solar Cells. *2014 IEEE 40th Photovoltaic Specialist Conference*, 1593–1595.

23
One-Dimensional Electro-Optical Simulations of Thin-Film Solar Cells

Bart E. Pieters, Koen Decock, Marc Burgelman, Rolf Stangl, and Thomas Kirchartz

23.1
Introduction

In this chapter, we discuss the simulation of thin-film solar cells, that is, the application of detailed mathematical models to describe the physics relevant to the operation of thin-film solar cells. These models should describe both the optical and the electronic processes in the device. We will first discuss the fundamentals of device simulation. In Section 23.3, we discuss the simulation of various thin-film materials used in solar cells, including a-Si:H, μc-Si:H, Cu(In,Ga)Se_2, and CdTe. Section 23.4 deals with commonly used optical models. Various popular tools used for the simulation of thin-film devices are discussed in Section 23.5.

23.2
Fundamentals

The semiconductor equations consist of the Poisson equation

$$\nabla \cdot (\varepsilon \nabla \Psi_{\mathrm{vac}}) = -\rho, \tag{23.1}$$

and the continuity equations for electrons and holes

$$\begin{aligned} \frac{\partial n}{\partial t} &= \frac{1}{q}\nabla \cdot \vec{J}_{\mathrm{n}} + G - R \\ \frac{\partial p}{\partial t} &= -\frac{1}{q}\nabla \cdot \vec{J}_{\mathrm{p}} + G - R, \end{aligned} \tag{23.2}$$

where Ψ_{vac} is the potential related to the local vacuum level; ρ is the space charge density; n and p refer to electron and hole concentrations in the extended conduction and valence band, respectively; J_{n} and J_{p} are the electron and hole current

Advanced Characterization Techniques for Thin Film Solar Cells, Second Edition.
Edited by Daniel Abou-Ras, Thomas Kirchartz, and Uwe Rau.

density, respectively; t is the time; G is the generation rate; and R is the recombination rate.

The electron and hole current densities are, respectively, described by

$$\vec{J}_{\mathrm{n}} = \mu_{\mathrm{n}} n \nabla E_{\mathrm{Fn}}$$

$$\vec{J}_{\mathrm{p}} = \mu_{\mathrm{p}} p \nabla E_{\mathrm{Fp}}, \tag{23.3}$$

where E_{Fn} and E_{Fp} are the quasi-Fermi levels for electrons and holes, respectively.

Using the Maxwell–Boltzmann approximation for the carrier concentrations as a function of the quasi-Fermi levels and the effective density of states in the valence (N_{v}) and conduction (N_{c}) band, we can write

$$n = N_{\mathrm{c}} \exp\left(\frac{E_{\mathrm{Fn}} - E_{\mathrm{c}}}{kT}\right) = N_{\mathrm{c}} \exp\left(\frac{E_{\mathrm{Fn}} - \left(E_{\mathrm{vac}} - q\chi\right)}{kT}\right)$$

$$p = N_{\mathrm{v}} \exp\left(\frac{E_{\mathrm{v}} - E_{\mathrm{Fp}}}{kT}\right) = N_{\mathrm{v}} \exp\left(\frac{\left(E_{\mathrm{vac}} - q\chi - E_{\mu}\right) - E_{\mathrm{Fp}}}{kT}\right), \tag{23.4}$$

where E_{vac} is the vacuum potential, χ is the electron affinity, and E_{μ} is the mobility gap. In a crystalline semiconductor, the mobility gap is identical to the band gap. In disordered semiconductors like a-Si:H or μc-Si:H, the band gap is no longer a well-defined quantity and the mobility gap – defined as the energy range where states are localized and carriers have a negligible mobility – takes over its role.

In equilibrium the product of n and p is equal to

$$n_{\mathrm{i}}^2 = N_{\mathrm{c}} N_{\mathrm{v}} \exp\left(\frac{E_{\mathrm{v}} - E_{\mathrm{c}}}{kT}\right) = N_{\mathrm{c}} N_{\mathrm{v}} \exp\left(-\frac{E_{\mu}}{kT}\right), \tag{23.5}$$

where n_{i} is the intrinsic carrier concentration.

To solve the semiconductor equations, the boundary conditions to the simulated domain need to be specified. Typically device simulators offer the possibility to use an ohmic (flatband) model or a Schottky contact (i.e., including a barrier). In addition to the possible presence of a barrier at the contact, the surface recombination rates can typically be specified. Surface recombination is described by

$$\vec{J}_{\mathrm{n}} = -qR_{\mathrm{n}}^{\mathrm{surf}} = -qS_{\mathrm{n}}(n - n_{\mathrm{eq}})$$

$$\vec{J}_{\mathrm{p}} = -qR_{\mathrm{p}}^{\mathrm{surf}} = -qS_{\mathrm{p}}(p - p_{\mathrm{eq}}), \tag{23.6}$$

where S_{n} and S_{p} are the surface recombination velocities of electrons and holes, respectively, and n_{eq} and p_{eq} are the equilibrium concentrations at the contacts for electrons and holes, respectively. Commonly infinite surface recombination velocities are assumed for thin-film silicon devices. However, the theoretical maximum value of the surface recombination velocity is the thermal velocity.

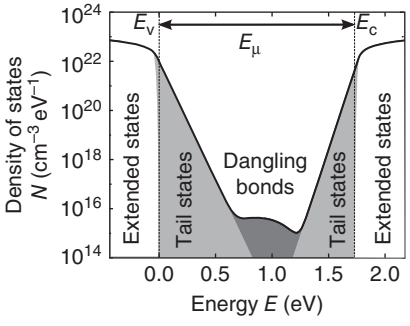

Figure 23.1 Schematic representation of the density of states in a-Si:H.

23.3 Modeling Hydrogenated Amorphous and Microcrystalline Silicon

23.3.1 Density of States and Transport of Hydrogenated Amorphous Silicon

The schematic density of states in a-Si:H is shown in Figure 23.1. Indicated are the extended states in the valence and conduction band, the valence and conduction band tails, and the states originating from dangling bonds. Due to the localized nature of band-tail states and states from structural defects, the mobility of electrons and holes at these states is much lower as compared to the nonlocalized states in the valence and conduction band, where the carriers are considered free. The energy separation of localized and nonlocalized states is rather sharp [1], and, consequently, this dividing energy has been termed "mobility edge." The energy difference between the valence-band mobility edge and conduction-band mobility edge is the so-called mobility gap E_μ. As the energy separation of localized and nonlocalized states is sharp, electronic transport in a-Si:H is dominated by the carriers in the states just below the valence-band mobility edge and just above the conduction-band mobility edge; hence for electronic transport, the mobility gap is the amorphous equivalent of the band gap. In Figure 23.1, the mobility edges of the valence and conduction band are indicated by E_v and E_c, respectively. A typical value of the mobility gap in a-Si:H is 1.75 eV [2].

In a-Si:H, there are distributions of localized band-tail states. The localized tail states are single-electron states, that is, they can be occupied by either 0 or 1 electron. Tail states belonging to the conduction band exhibit acceptor-like behavior, meaning that the states are neutral when unoccupied and negatively charged when occupied by an electron. Tail states belonging to the valence band, on the other hand, exhibit donor-like behavior and are positively charged when unoccupied and neutral when occupied by an electron. The tail-state densities of the conduction and valence band decay exponentially into the gap [3]. The density of tail states can be described by

$$N_{\mathrm{cbt}} = N_{\mathrm{c}} \exp\left(\frac{E - E_{\mathrm{c}}}{E_{\mathrm{c0}}}\right)$$
$$N_{\mathrm{vbt}} = N_{\mathrm{v}} \exp\left(\frac{E_{\mathrm{v}} - E}{E_{\mathrm{v0}}}\right), \tag{23.7}$$

where N_{v0} and N_{c0} are the density of tail states at the mobility edges of the valence and conduction band, respectively, and E_{v0} and E_{c0} are the characteristic energies (or Urbach energies) of the valence and conduction band tails, respectively. In a-Si:H, the valence band tail is much broader than the conduction band tail. Typical values of the characteristic energies of the tail states in device quality a-Si:H are 45 meV for the valence band tail and 30 meV for the conduction band tail. The characteristic energies of the band tails are, however, temperature dependent [4, 5]. For the valence band tail, the following relation is often used [4]:

$$E_{\mathrm{v0}}(T) = \sqrt{E_{\mathrm{v0}}(0)^2 + (kT)^2}. \tag{23.8}$$

Aljishi *et al*. [5] suggested that the temperature dependency of the band tails exhibits a freeze-in temperature, above which the tail slope becomes temperature dependent.

Defect states arising from dangling bonds are *amphoteric* in nature, that is, the dangling bond is multivalent and can have three charged states, namely, positively charged when the state is unoccupied by electrons, neutral when the dangling bond is occupied by one electron, and negatively charged when the dangling bond is occupied by two electrons. A dangling bond, therefore, has two energy levels: the $E^{+/0}$ level related to the transition between the positively and neutrally charged states of the dangling bond and the $E^{0/-}$ level related to the transition between the neutrally and negatively charged states of the dangling bond. The energy difference between the $E^{+/0}$ and $E^{0/-}$ levels of the dangling bond is the correlation energy, U. It is generally accepted that in a-Si:H, the correlation energy is positive, that is, the $E^{0/-}$ level is higher than the $E^{+/0}$.

For the distribution of dangling-bond states in the mobility gap of a-Si:H and related materials, the most frequently used models are the standard model and the defect-pool model. The standard model is a simple approach where the distribution of dangling-bond states is assumed to be Gaussian. The distribution of dangling-bond states as characterized by their $E^{+/0}$ transition level is

$$N_{\mathrm{db}}^{+/0} = N_{\mathrm{db}} \frac{1}{\sigma_{\mathrm{db}}\sqrt{2\pi}} \exp\left(-\frac{\left(E - E_{\mathrm{db0}}^{+/0}\right)^2}{2\sigma_{\mathrm{db}}^2}\right), \tag{23.9}$$

where $N_{\mathrm{db}}^{+/0}$ is the distribution of energy levels arising from the $E^{+/0}$ transition level and N_{db} is the total dangling-bond concentration of which the $E^{+/0}$ are distributed around the energy level $E_{\mathrm{db0}}^{+/0}$ with a standard deviation of σ_{db}. Note that Equation 23.9 can easily be transformed to describe the distribution of $E^{0/-}$ transition levels by replacing $E_{\mathrm{db0}}^{+/0}$ with $E_{\mathrm{db0}}^{0/-} = E_{\mathrm{db0}}^{+/0} + U$.

The defect-pool model, of which several versions exist [6–9], is an elaborate thermodynamical model that describes chemical equilibrium reactions where weak Si–Si bonds break to form two dangling bonds and the reverse reaction (the weak-bond to dangling-bond conversion model [10]). Hydrogen plays a key role in the equilibration processes in a-Si:H. At normal deposition temperatures of a-Si:H, the hydrogen in the material is mobile. The establishment of a chemical equilibrium between weak bonds and dangling bonds requires structural changes in the material, for which the mobile hydrogen provides the required atomic motion [11, 12]. The central idea behind the defect-pool models is that the concentration of dangling-bond states depends on the formation energy of the dangling bonds. Furthermore, the formation energy of a dangling bond depends on charged state of the dangling bond and thereby on the position of the Fermi level and the energy levels of the amphoteric dangling-bond state [13]. In defect-pool models, the energy distribution of the dangling-bond states is computed such that the free energy of the system is minimized [8], resulting in equilibrium defect-state distributions that depend strongly on the position of the Fermi level in the material. An important result is that the defect-pool model can account for the observed differences in energy distribution of defect states in undoped and doped a-Si:H [9].

In the following section, we will briefly introduce the defect-pool model as it was formulated in 1996 by Powell and Deane [8] (in 1993 a similar defect-pool model was published by Powell and Deane [7]). The defect-pool function, $P(E)$, describes the probability distribution that if a dangling bond is created, it is created at energy level E. Usually the defect-pool function is assumed to be a Gaussian distribution:

$$P(E) = \frac{1}{\sigma_{\mathrm{dp}}\sqrt{2\pi}} \exp\left(-\frac{\left(E - E_{\mathrm{dp}}\right)^2}{2\sigma_{\mathrm{dp}}^2}\right), \tag{23.10}$$

where σ_{dp} is the standard deviation of the Gaussian defect pool and E_{dp} is the mean energy of the Gaussian defect pool. Note that the final distribution of defects is *not* Gaussian as the formation energy, and thus the equilibrium concentration of dangling bonds depends on the energy level. Using this Gaussian defect-pool function and taking into account the influence of the formation energy of dangling bonds on the equilibrium concentration thereof, Powell and Deane derived the following expression for the energy distribution of dangling-bond defect states:

$$\begin{aligned} N_{\mathrm{db}}^{+/0}(E) &= \gamma\left(\frac{2}{F_{\mathrm{eq}}^0(E)}\right)^{kT/2E_{\mathrm{v0}}} P\left(E + \frac{\sigma_{\mathrm{dp}}^2}{2E_{\mathrm{v0}}}\right) \\ \gamma &= N_{\mathrm{v0}}\left(\frac{H}{N_{\mathrm{SiSi}}}\right)^{kT/4E_{\mathrm{v0}}} \left(\frac{2E_{\mathrm{v0}}^2}{2E_{\mathrm{v0}} - kT}\right) \exp\left(-\frac{1}{2E_{\mathrm{v0}}}\left[E_{\mathrm{p}} - E_{\mathrm{v}} - \frac{\sigma_{\mathrm{dp}}^2}{4E_{\mathrm{v0}}}\right]\right), \end{aligned} \tag{23.11}$$

where F_{eq}^0 is the equilibrium occupation function for neutral dangling-bond states, N_{SiSi} is the concentration of electrons in Si–Si bonding states taking four electrons per Si atom and is approximately 2×10^{29} m^{-3} [8], and H is the concentration of

hydrogen in the a-Si:H and is approximately 5×10^{27} m^{-3}[8]. The thermal equilibrium occupation functions for amphoteric dangling-bond states are given by [14, 15]

$$F_{\mathrm{eq}}^{+} = \frac{1}{1 + 2\exp\left(\frac{E_{\mathrm{f}} - E^{+/0}}{kT}\right) + \exp\left(\frac{2E_{\mathrm{f}} - E^{+/0} - E^{0/-}}{kT}\right)}$$

$$F_{\mathrm{eq}}^{0} = \frac{2\exp\left(\frac{E_{\mathrm{f}} - E^{+/0}}{kT}\right)}{1 + 2\exp\left(\frac{E_{\mathrm{f}} - E^{+/0}}{kT}\right) + \exp\left(\frac{2E_{\mathrm{f}} - E^{+/0} - E^{0/-}}{kT}\right)}$$

$$F_{\mathrm{eq}}^{-} = \frac{\exp\left(\frac{2E_{\mathrm{f}} - E^{+/0} - E^{/-}}{kT}\right)}{1 + 2\exp\left(\frac{E_{\mathrm{f}} - E^{+/0}}{kT}\right) + \exp\left(\frac{2E_{\mathrm{f}} - E^{+/0} - E^{/-}}{kT}\right)}, \tag{23.12}$$

where F_{eq}^{+} and F_{eq}^{-} are the equilibrium occupation functions for positively charged and negatively charged dangling-bond states, respectively.

Figure 23.2 shows the defect-state distributions computed with the 1996 defect-pool model for three positions of the Fermi level (as indicated by the arrows). In the case the Fermi level is around midgap ("i type"), the total dangling-bond concentration is lower than that when the Fermi level is close to the conduction band ("n type") or close to the valence band ("p type"). The defect-pool model thus predicts a inhomogeneous distribution of defects in the absorber layer as the defect densities are highest near (and in) the doped layers, thus leading to relatively more recombination closer to the p type and n type as compared with the assumption of a constant density of dangling bonds through the absorber layer.

23.3.2
Density of States and Transport of Hydrogenated Microcrystalline Silicon

In literature μc-Si:H is used as a general term for a mixed-phase material consisting of varying amounts of c-Si nanocrystallites, a-Si:H, and grain boundaries. The presence of crystalline grains, the grain boundaries, the columnar structure, and the presence of a-Si:H tissue all influence the transport properties in μc-Si:H. As this chapter deals with one-dimensional (1D) device modeling, we cannot take all

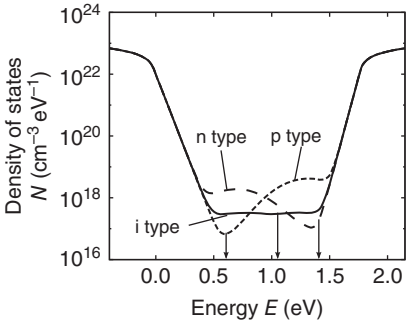

Figure 23.2 Defect-state distributions in a-Si:H according to the 1996 defect-pool model for three positions of the Fermi level: close to the conduction-band mobility edge ("n type"), the intrinsic position ("i type"), and close to the valence-band mobility edge ("p type"). The three positions of the Fermi level are indicated with arrows.

the effects of such a mixed phase into account. We will, therefore, use effective models, that is, we pretend the material is homogeneous.

It was suggested by Overhof *et al*. [16] that conduction through μc-Si:H takes place primarily through the crystalline phase, that is, along a percolation path. From this percolation theory, it is to be expected that the effective medium properties of μc-Si:H are dominated by the properties of the crystalline phase.

The density of states in μc-Si:H looks similar to the density of states in a-Si:H. Besides the extended states, there are band tails and dangling-bond defects. Both time of flight and photoluminescence indicate the presence of exponential band tails [17–20]. Both the valence and conduction band tails have about the same characteristic energy, $E_{v0} \approx E_{c0} \approx 31$ meV. It is difficult to infer from the measurements carried out whether the tails are temperature dependent like in a-Si:H [21].

From electron spin resonance (ESR) spectroscopy, it has been found that there are two dangling-bond distributions with different paramagnetic properties in μc-Si.H [22]; presumably these two dangling-bond distributions are separated spatially where one distribution is located within the crystallites and the other in the a-Si:H tissue [23]. The total defect density was found to be in the range $5 \times 10^{15} - 1 \times 10^{16}$ cm^{-3}. As we are interested in parameter values for the effective media approximation and we assume transport predominantly to take place through the crystalline part of the material, the effective density of defect states could be lower than the total defect-state density. The total dangling-bond distribution can be considered broad [22, 23]. A Gaussian distribution is assumed with a standard deviation of 150 meV [22].

The mobility gap of μc-Si:H is usually found to be higher than the band gap of crystalline silicon. The mobility gap of μc-Si:H is typically found to be around 1.2 eV [21]. As, according to the percolation theory, conduction only takes place through the crystalline phase, it follows that the effective density of states in μc-Si:H should scale with the crystalline volume fraction [21].

23.3.3 Modeling Recombination in a-Si:H and μc-Si:H

23.3.3.1 Recombination Statistics for Single-Electron States: Shockley–Read–Hall Recombination

Shockley–Read–Hall (SRH) recombination considers two capture and two emission processes as illustrated in Figure 23.3. Recombination occurs when a trap state occupied by an electron captures a hole or vice versa. The capture and emission rates can be described by the equations in Table 23.1 for both single-electron trap states. In Table 23.1, N_t is the concentration of traps with electron occupation probability f; σ_n and σ_p are the electron and hole capture cross sections, respectively; and e_n and e_p are the electron and hole emission coefficients, respectively. In thermal equilibrium, there is no net recombination and the principle of *detailed balance* applies, meaning $r_1 = r_2$ and $r_3 = r_4$. Furthermore, in thermal equilibrium, the electron occupation probability of a trap at energy E_t is described

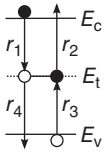

Figure 23.3 Schematic illustration of capture and emission processes on a single-electron trap state.

Table 23.1 Capture and emission rates of single-electron trap states.[a)]

Process		Rate
Electron capture	r_1	$n\nu_{th}\sigma_n N_t(1-f)$
Electron emission	r_2	$e_n N_t f$
Hole capture	r_3	$p\nu_{th}\sigma_p N_t f$
Hole emission	r_4	$e_p N_t(1-f)$

a) The rates $r_1 - r_4$ are defined in Figure 23.3.

by the Fermi–Dirac distribution $f = \left(1 + \exp\left(\frac{E_t - E_f}{kT}\right)\right)^{-1}$. Applying the principle of detailed balance and using the Fermi–Dirac distribution for the occupation probability function yields for the emission coefficients

$$e_n = \nu_{th}\sigma_n N_c \exp\left(\frac{E_t - E_c}{kT}\right)$$
$$e_p = \nu_{th}\sigma_p N_v \exp\left(\frac{E_v - E_t}{kT}\right), \tag{23.13}$$

where ν_{th} is the thermal carrier velocity.

The recombination efficiency, η_R, is defined as the net recombination rate per trap state. In nonequilibrium steady-state conditions, the recombination efficiency is equal to the net rate at which electrons are captured by a trap state. Under steady-state conditions, the net electron capture rate must be equal to the net capture rate of holes (i.e., the average charged state of trap states is not changed); therefore it follows that

$$N_t\eta_R = r_1 - r_2 = r_3 - r_4. \tag{23.14}$$

Using the equations from Table 23.1 and Equation 23.14, the electron occupation function can be determined as

$$f = \frac{n\nu_{th}\sigma_n + e_p}{n\nu_{th}\sigma_n + p\nu_{th}\sigma_p + e_n + e_p}. \tag{23.15}$$

The recombination efficiency of single-electron trap states is then determined as

$$\eta_R = \nu_{th}^2\sigma_n\sigma_p\frac{np - n_i^2}{n\nu_{th}\sigma_n + p\nu_{th}\sigma_p + e_n + e_p}. \tag{23.16}$$

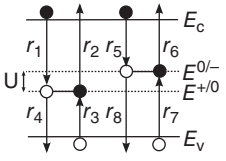

Figure 23.4 Schematic illustration of capture and emission processes on an amphoteric trap state.

The total recombination on single-electron trap states can be obtained by integrating the recombination over all the single-electron trap states in the band gap:

$$R = \int_{E_v}^{E_c} N(E)\eta_R(E)\mathrm{d}E. \tag{23.17}$$

For the modeling of a-Si:H, the donor-like trap states of the valence band and the acceptor-like states of the conduction band not necessarily have the same capture cross sections. In that case, the integral of Equation 23.17 should be computed for both tail-state distributions separately. When we refer to capture cross sections of trap states, we usually distinguish between the charged states of the trap. Acceptor-like traps that capture an electron must be empty and thus positively charged and acceptor-like traps that capture a hole must be filled and thus neutral. Therefore we refer to the capture cross sections of donor-like states as σ_n^+ and σ_p^0 for the electron and hole capture cross sections, respectively. Likewise, for acceptor-like states, the capture cross sections are referred to as σ_n^0 and σ_p^- for the electron and hole capture cross sections, respectively.

23.3.3.2 Recombination Statistics for Amphoteric States

Sah and Shockley [24] developed a model that can describe recombination and trapping statistics on amphoteric states. Figure 23.4 illustrates an amphoteric trap level and the capture and emission processes that can occur for an amphoteric trap level. Table 23.2 lists the rates for each capture or emission process of an amphoteric trap level. The symbols $F^{+,0,-}$ denote the occupation functions and represent the probability F^+ that the trap is empty, F^0 that the trap is occupied by a single electron, or F^- that the trap is occupied by two electrons.

In a similar fashion as for single-electron states, the emission coefficients can be derived from the equilibrium electron, n_{eq}, and hole, p_{eq}, concentrations and the equilibrium occupation probabilities, F_{eq}^+, F_{eq}^0, and F_{eq}^- (see Equation 23.12). The emission coefficients are found as

$$\begin{aligned}
e_n^0 &= \nu_{th}\sigma_n^+ n_{eq}\frac{F_{eq}^+}{F_{eq}^0} = \frac{1}{2}\nu_{th}\sigma_n^+ N_c \exp\left(\frac{E^{+/0}-E_c}{kt}\right)\\
e_n^- &= \nu_{th}\sigma_n^- n_{eq}\frac{F_{eq}^0}{F_{eq}^-} = 2\nu_{th}\sigma_n^0 N_c \exp\left(\frac{E^{0/-}-E_c}{kt}\right)\\
e_p^+ &= \nu_{th}\sigma_p^0 p_{eq}\frac{F_{eq}^0}{F_{eq}^+} = 2\nu_{th}\sigma_p^0 N_v \exp\left(\frac{E_v-E^{+/0}}{kt}\right)\\
e_p^0 &= \nu_{th}\sigma_p^- n_{eq}\frac{F_{eq}^-}{F_{eq}^0} = \frac{1}{2}\nu_{th}\sigma_p^- N_v \exp\left(\frac{E_v-E^{0/-}}{kt}\right).
\end{aligned} \tag{23.18}$$

Table 23.2 Capture and emission rates of amphoteric states.[a)]

Process		Rate
Electron capture	r_1	$n\nu_{\mathrm{th}}\sigma_{\mathrm{n}}^{+}N_{\mathrm{DB}}F^{+}$
Electron emission	r_2	$e_{\mathrm{n}}^{0}N_{\mathrm{DB}}F^{0}$
Hole capture	r_3	$n\nu_{\mathrm{th}}\sigma_{\mathrm{n}}^{0}N_{\mathrm{DB}}F^{0}$
Hole emission	r_4	$e_{\mathrm{n}}^{-}N_{\mathrm{DB}}F^{-}$
Electron capture	r_5	$p\nu_{\mathrm{th}}\sigma_{\mathrm{p}}^{0}N_{\mathrm{DB}}F^{0}$
Electron emission	r_6	$e_{\mathrm{p}}N_{\mathrm{DB}}F^{+}$
Hole capture	r_7	$p\nu_{\mathrm{th}}\sigma_{\mathrm{p}}^{-}N_{\mathrm{DB}}F^{-}$
Hole emission	r_8	$e_{\mathrm{p}}N_{\mathrm{DB}}F^{0}$

a) The rates $r_1 - r_8$ are defined in Figure 23.4.

In steady-state situations, the net recombination rate is zero, and therefore the rate equation of the occupation functions should be zero. The rate equations of the occupation functions are given by

$$\begin{aligned}\frac{\partial F^{+}}{\partial t} &= -n\nu_{\mathrm{th}}\sigma_{\mathrm{n}}^{+}F^{+} + e_{\mathrm{n}}^{0}F^{0} + p\nu_{\mathrm{th}}\sigma_{\mathrm{p}}^{0}F^{0} - e_{\mathrm{p}}^{+}F^{+}\\ \frac{\partial F^{-}}{\partial t} &= n\nu_{\mathrm{th}}\sigma_{\mathrm{n}}^{0}F^{0} - e_{\mathrm{n}}^{-}F^{-} - p\nu_{\mathrm{th}}\sigma_{\mathrm{p}}^{-}F^{-} + e_{\mathrm{p}}^{0}F^{0}.\end{aligned} \tag{23.19}$$

By further taking into account that the sum of the occupation functions should be unity ($F^{+} + F^{0} + F^{-} = 1$), the occupation functions are obtained as

$$\begin{aligned}F^{+} &= \frac{P^{0}P^{-}}{N^{+}P^{-} + P^{0}P^{-} + N^{+}N^{0}}\\ F^{0} &= \frac{N^{+}P^{-}}{N^{+}P^{-} + P^{0}P^{-} + N^{+}N^{0}}\\ F^{0} &= \frac{N^{0}N^{+}}{N^{+}P^{-} + P^{0}P^{-} + N^{+}N^{0}},\end{aligned} \tag{23.20}$$

where, for readability, the terms P^{0}, P^{-}, N^{0}, and N^{+} are introduced, which are defined as

$$\begin{aligned}P^{0} &= p\nu_{\mathrm{th}}\sigma_{\mathrm{p}}^{0} + e_{\mathrm{n}}^{0}\\ P^{-} &= p\nu_{\mathrm{th}}\sigma_{\mathrm{p}}^{-} + e_{\mathrm{n}}^{-}\\ N^{0} &= n\nu_{\mathrm{th}}\sigma_{\mathrm{n}}^{0} + e_{\mathrm{p}}^{0}\\ N^{+} &= n\nu_{\mathrm{th}}\sigma_{\mathrm{n}}^{+} + e_{\mathrm{p}}^{+}.\end{aligned} \tag{23.21}$$

The recombination efficiency is given by $\eta_{\mathrm{R}} = (r_1 - r_2 + r_5 - r_6)/N_{\mathrm{t}}$. Using the derived occupation functions, we obtain

$$\eta_{\mathrm{R}} = \nu_{\mathrm{th}}^{2}(pn - n_{\mathrm{i}}^{2})\frac{\sigma_{\mathrm{n}}^{+}\sigma_{\mathrm{p}}^{0}P^{-} + \sigma_{\mathrm{n}}^{0}\sigma_{\mathrm{p}}^{-}N^{+}}{N^{+}P^{-} - P^{0}P^{-} + N^{+}N^{0}}. \tag{23.22}$$

The total recombination rate can be obtained by integration of the recombination efficiency over all dangling-bond states, that is, as done in Equation 23.17 for single-electron states.

Often amphoteric states are modeled with two uncorrelated single-electron states [25–27]. The pair consists of one donor-like state and one acceptor-like state. The energy levels of the uncorrelated states should be slightly shifted compared to the transition levels of the correlated state. By equating the emission coefficient of the acceptor-like state (Equation 23.13) to the emission coefficient of the negatively charged amphoteric state (Equation 23.18), one can find that the acceptor-like state should be at $E^{0/-} + kT\ln(2)$. Likewise one can find that the donor-like state should be located at $E^{+/0} - kT\ln(2)$. The effective correlation energy of the uncorrelated pair is therefore $U + kT\ln(4)$. Note that modeling a correlated defect with two uncorrelated defects leads to errors as the two states are independently capable of trapping carriers. This leads to higher recombination rates for the pair of uncorrelated states and may lead to the physically impossible situation that the $E^{0/-}$ (acceptor-like) state is occupied, while the $E^{+/0}$ (donor-like) state is unoccupied. Willemen [2] showed that modeling an amphoteric state with a pair of uncorrelated states is only accurate under the condition that the capture cross section of the neutral state is much smaller than the charged states and the correlation energy is positive and considerably larger than kT.

23.3.4 Modeling $Cu(In,Ga)Se_2$ Solar Cells

A chalcopyrite-based solar cell is a rather complex system, consisting of several layers of various materials. This creates several heterointerfaces, which require quite some effort to model. Not only both adjacent materials are important but also the interface itself and the band lineup at the interface. The defect physics of $Cu(In,Ga)(S,Se)_2$ exhibits several particularities. They are usually native defects; they can be multivalent [28] and metastable [29]. Additionally $Cu(In,Ga)(S,Se)_2$ is to be considered as a material system rather than as a material. The exact composition of the material can vary widely, and together with the composition, other properties can be varied. The composition is easily changed, often unintentionally due to diffusion from an adjacent layer. Sometimes, however, the composition is deliberately changed throughout the absorber layer, leading to a graded structure. This section will focus on the modeling aspects of such graded solar cells.

23.3.4.1 Graded Band-Gap Devices

One of the main properties depending on the composition of the $Cu(In,Ga)(S,Se)_2$ is the band gap. Increasing the Ga/In ratio results in a conduction-band raise, without much changing the valence band. Increasing the S/Se ratio results in both a conduction-band raise and a valence-band lowering, dominated by the valence-band effect.

Varying the band gap throughout the absorber layer can have two main beneficial effects: The recombination probability can be reduced in regions where this probability is higher, and additional electric fields can be built in by changing the conduction-band level:

1) Increasing the band gap near the junction reduces the junction-recombination rate, which usually dominates the cell recombination and governs the open-circuit voltage. Only increasing the band gap locally ensures that the absorption is not significantly reduced. In order to preserve the band alignment at the heterointerface, the band-gap raise is preferred to be a valence-band lowering and thus originating from an increased sulfur content.
2) Varying the conduction-band level leads to the introduction of an additional electric field. This field can be used to push back charge carriers from the back contact, where the recombination probability can be high. This is possible by increasing the Ga content toward the back of the absorber.

23.3.4.2 Issues When Modeling Graded Band-Gap Devices

When varying the band gap by means of a composition change, it is paramount to know the link between the band gap and the composition. Unfortunately, there is a rather large spread on the reported band-gap values for $Cu(In,Ga)(S,Se)_2$ in literature. Moreover, most of the time a band-gap value is reported at only one composition or only as a function of the Ga/In or the S/Se ratio. In Ref. [30], a general formula for the band gap of $Cu(In_{1-y},Ga_y)(Se_{1-x},S_x)_2$ is proposed combining the reports of several authors and reproduced in Equation 23.23:

$$\begin{aligned} E_g(\text{eV}) =& 1.04(1-x)(1-y) + 1.68(1-x)y + 1.53x(1-y) \\ &+ 2.42xy - 0.14x(1-x)(1-y) - 0.15y(1-y). \end{aligned} \tag{23.23}$$

A second problem arising when modeling graded structures is to find the absorption ($\alpha(\lambda)$) characteristic of a material which is a mixture of two other materials. There are two properties of importance for a $\alpha(\lambda)$-characteristic: the cutoff wavelength which is determined by the band gap and the absorption for high-energy photons. The former will be badly reproduced when performing an interpolation between the characteristics of the pure materials along the α-axis, and the latter when interpolating along the λ-axis. An adequate interpolation scheme is reported in Ref. [31] and is implemented in the solar-cell simulator SCAPS (see Section 23.5.5).

A third issue appears when interpreting the results of simulations for graded band-gap devices. As a high band gap favors the open-circuit voltage and harms the short-circuit current, there exists a compromise between both, leading to an optimum band gap. If the goal of the modeling is to find the influence of the grading on the cell performance, the result will thus be veiled by the band-gap dependence of the I–V characteristics on nongraded solar cells. Hence it is important to compare the results for the graded structure with the results for a uniform reference cell. This reference cell should be designed with great care, however, and is dependent on the investigated structure as well as on the property studied. For example, according to whether the defect concentration is thought to originate from the introduction of the grading, the uniform reference should take this defect concentration into account as well. If one wants to investigate the effect of grading on the short-circuit current, one could require the reference to have the

same open-circuit voltage as the graded structure. An advanced way of constructing an adequate reference cell, which leads to objective results for most graded structures, involves a combination of two structures carefully selected based on their maximum power point behavior [32].

23.3.4.3 Example

Simulations reveal the principal design problem when grading the absorber of a $Cu(In,Ga)(S,Se)_2$ device, that is, the influence of nongraded and graded parameters is equally important.

In the following example, the influence of a grading at the front of an absorber is investigated. The absorber band gap is locally increased from a certain depth in the absorber, called the *grading depth*, up to the buffer–absorber interface. This increase is assumed to originate from an increasing sulfur concentration. The maximum sulfur concentration (which appears at the buffer–absorber interface) and the grading depth are varied, and the efficiency of a uniform reference structure is subtracted from the resulting efficiency. All details about this model can be found in Ref. [33].

Whether the grading is beneficial and what are the optimum values for the grading depth and the maximum sulfur concentration are questions which do not seem to have an unanimous answer. It is largely dependent on parameters not belonging to the grading structure. In Figure 23.5, the simulations have been performed thrice, each time with a different electron-diffusion length in the part of the absorber where no grading is present, thus the back part of the absorber. The optimum parameters governing the grading as well as the absolute value of the efficiency gain/loss are largely different in all three cases. As a conclusion, one could observe that implementing a graded band-gap structure in order to improve the cell performance is not straightforward, but should be done while keeping in mind the entire cell structure.

23.3.5 Modeling of CdTe Solar Cells

Thin-film cadmium telluride solar cells seem to be rather tolerant to imperfections and defects: A decent cell performance is obtained by a wide variety of fabrication technologies, if these include some form of "activation treatment," usually with $CdCl_2$. However, this apparent simplicity should not distract from the complexity in the cell structure and operation. This is illustrated already by the appearance of room temperature $I-V$ measurements under standard illumination: There is a kink in both the dark and illuminated $I-V$ curves at forward bias ("roll-off"), and quite often the light and dark $I-V$ curves intersect ("crossover"). These phenomena are related with the key technology aspects of CdTe cells: the $CdCl_2$ activation treatment and especially the structure and properties of the back contact to CdTe. A phenomenological two-diode model was set up to explain the gross features of the $I-V$ [34] and $C-V$ measurements [35], but full numerical modeling was necessary to explain all observed phenomena. This has been reviewed in Ref. [36]. In

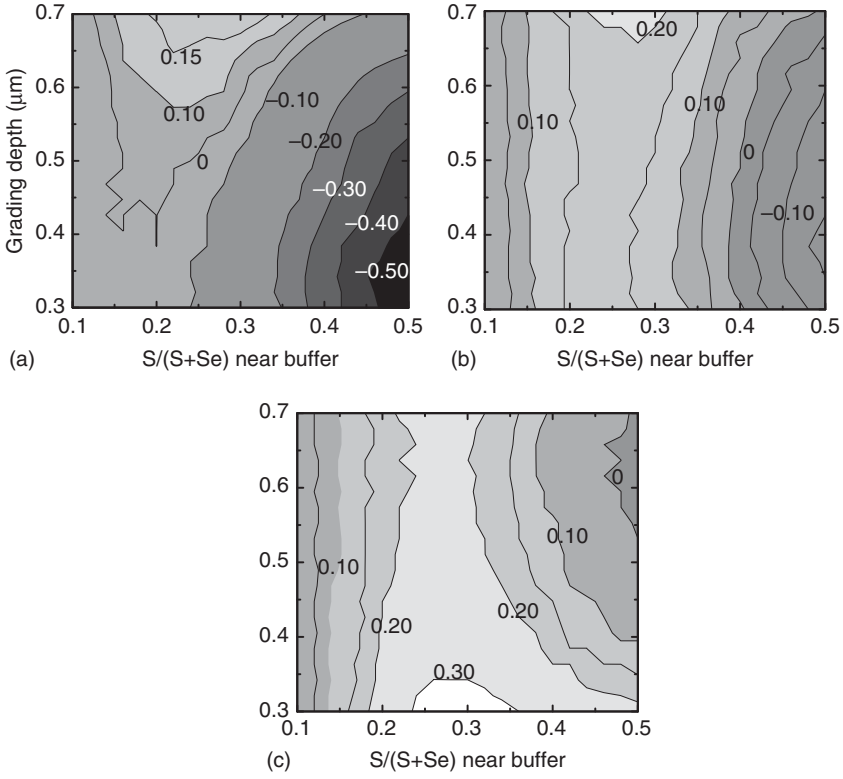

Figure 23.5 Example of the influence of the electron-diffusion length in the nongraded part of the absorber on the effect of grading on the cell performance. The electron-diffusion length is smallest in figure (a) intermediate in (b) and largest in (c). Figures are taken from Ref. [33].

this section, we will use numerical modeling to illustrate the interrelation between uncommon aspects observed in $I-V$ and in $C-V$ measurements; these aspects are typical for CdTe cells but are occasionally also observed in other cells [37].

23.3.5.1 **Baseline**

An elaborated parameter set was developed [38] for Antec CdTe cells that were treated with $CdCl_2$ in both air and vacuum; see, for example, [39]. In setting up this parameter set, only defect levels were introduced that were confirmed with DLTS, and no unphysical assumptions were made, such as neutral defects or an assumed light or voltage dependence of some parameter. This parameter set could successfully explain a variety of measurements: dark $I-V(T)$ and light $I-V(\lambda)$, $I_{sc}-V_{oc}(T)$, $C-V(T)$, $C-f(T)$, and $QE(V)$. It has been used as a baseline set for a numerical parameter exploration [40]. We will use this parameter set here to illustrate the influence of two key parameters: the energy barrier ϕ_b at the CdTe back contact and the acceptor density N_{Ac} in the CdTe layer close to the back contact.

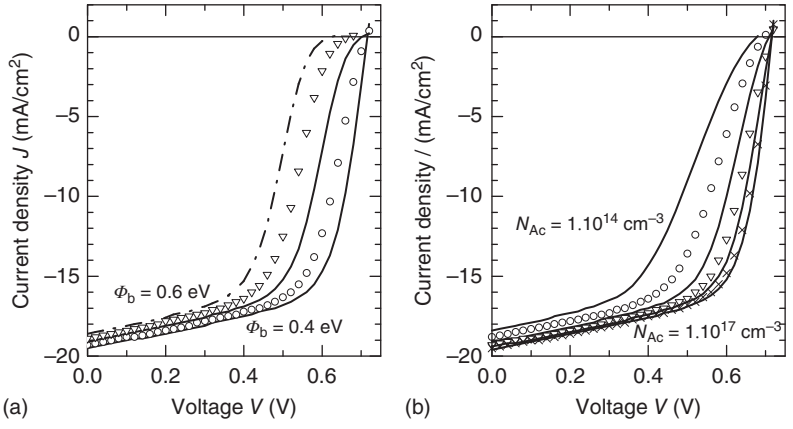

Figure 23.6 Variation of the $I-V$ characteristics with the energy barrier ϕ_b (a) and the doping density N_{Ac} at the CdTe back contact (b). The other parameters have their baseline values. (a): $\phi_b = 0.40, 0.45, \ldots, 0.60$ eV. (b): $N_{Ac} = 1\times10^{14}$, 3×10^{14}, 1×10^{15}, $\ldots$, 1×10^{17} cm^{-3}.

23.3.5.2 The ϕ_b–N_{Ac} (Barrier–Doping) Trade-Off

Simulated $I-V$ curves under AM1.5G illumination have been presented in Ref. [40]. In Figure 23.6, all parameters had their baseline values but for ϕ_b (a) and N_{Ac} (b). It is obvious that the effect of a low doping density at the contact can be erroneously interpreted as an effect of a high contact barrier.

This is further illustrated in Figure 23.7: A too large barrier ϕ_b and a too low doping density N_{Ac} can cause a very comparable efficiency loss. From the shape of the illuminated $I-V$ curve in the active quadrant alone, it is not possible to distinguish

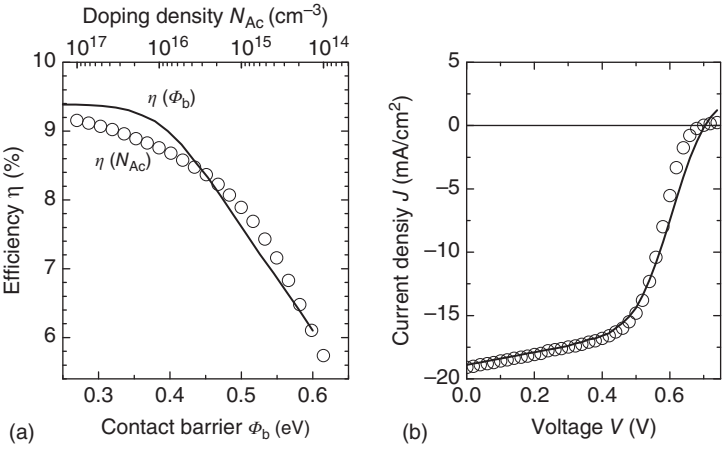

Figure 23.7 (a) Dependency of efficiency η on the contact barrier ϕ_b (bottom axis; solid line) or on the CdTe doping density N_{Ac} (top axis; open symbols). (b) An $I-V$ curve simulated with $\phi_b = 0.4$ eV, $N_{Ac} = 3\times10^{14}$ cm^{-3} (solid line) and $\phi_b = 0.55$ eV, $N_{Ac} = 1\times10^{17}$ cm^{-3} (open symbols).

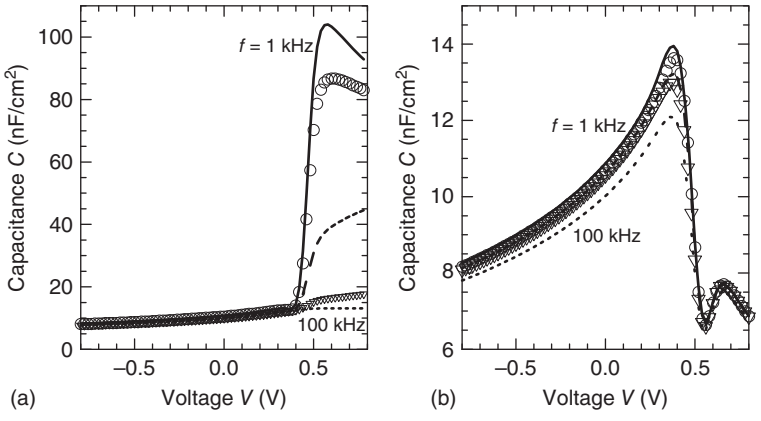

Figure 23.8 (a) $C-V$ curves calculated with "bad ϕ_b, good N_{Ac}" (see text). (b) $C-V$ curves calculated with "good ϕ_b, bad N_{Ac}" (see text). The parameter is the frequency, ranging from 1 (upper curve) to 100 kHz (lower curve).

between the effects of a high ϕ_b and of a low N_{Ac}: The $I-V$ curve calculated with $\phi = 0.4$ eV, $N_{Ac} = 3 \times 10^{14}$ cm^{-3} ("good ϕ_b, bad N_{Ac}") almost coincides with the curve calculated for $\phi_b = 0.55$ eV, $N_{Ac} = 1 \times 10^{17}$ cm^{-3} ("bad ϕ_b, good N_{Ac}").

23.3.5.3 *C–V* Analysis as an Interpretation Aid of *I–V* Curves

Although the two situations, "bad ϕ_b, good N_{Ac}" and "good ϕ_b, bad N_{Ac}," have very similar $I-V$ curves, they have very different $C-V$ and $C-f$ curves (Figure 23.8). The gross features of $C-V$ curves dominated by contact effects were explained in Refs [35, 36]: The $C-V$ curve in general shows two maxima separated by a minimum. On the left of the first maximum, the low-frequency $C-V$ behavior is in circumstances determined by the CdS–CdTe junction capacitance, while on the right of the second maximum, the CdTe-contact capacitance is dominating the $C-V$ behavior. The shape of the $C-V$ curves at forward voltage clearly is a much better indicator than the $I-V$ curves to distinguish the situation of "bad ϕ_b, good N_{Ac}" from "good ϕ_b, bad N_{Ac}."

The same holds for the $C-f$ curves measured in an extended temperature range (Figure 23.9). The $C-f(T)$ curves calculated with "good ϕ_b, bad N_{Ac}" show an additional step at high-frequency/low-temperature step, which can be ascribed to an RC time constant with the CdS–CdTe junction capacitance and the resistance of the CdTe bulk.

The normal procedure to analyze a possible effect of a too high contact barrier is to measure the temperature-dependent dark $I-V(T)$ curves. The curves for our two situations only differ in the high-voltage range $V > 0.5$ V (no illustration), and even then the shape of the $I-V(T)$ does not allow to distinguish between the two situations. We have shown here that impedance measurements, especially $C-V(f)$ and $C-f(T)$, together with numerical simulation, provide better criteria for assessing the contact effects.

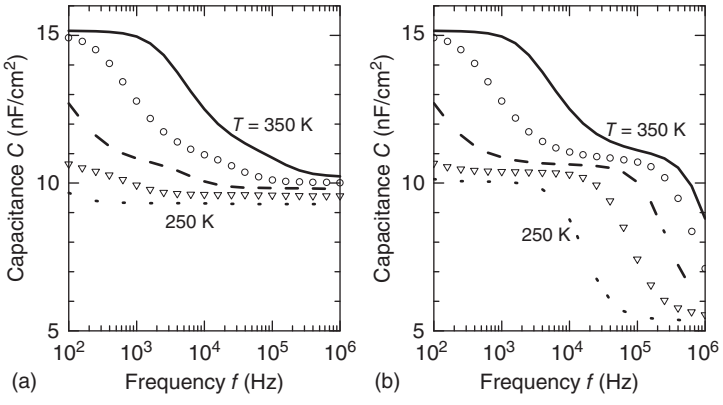

Figure 23.9 (a) C–f curves calculated with "bad ϕ_b, good N_{Ac}" (see text). (b) C–f curves calculated with "good ϕ_b, bad N_{Ac}"; the data of (a) are also shown in open symbols, for comparison. The parameter is the temperature, ranging from 350 (upper curve) to 250 K (lower curve), step 25 K. The dc bias voltage is 0 V.

23.4 Optical Modeling of Thin Solar Cells

The optical generation rate in a solar cell is also an important input parameter for electrical modeling. It is determined from the absorption profile of the photons in the solar cell. When assuming that every photon generates one and only one electron–hole pair, the generation rate profile is equal to the absorption profile. Calculation of the absorption profile in a-Si:H-based solar cells is complicated by the commonly used light-trapping techniques, making a-Si:H-based solar cells complex optical systems.

23.4.1 Coherent Modeling of Flat Interfaces

For flat solar cells, the multilayer thin-film optics model can be used. The multilayer thin-film optics model uses the complex refractive indices of the media and the effective Fresnel coefficients to calculate the optical generation rate profile. This model includes multiple internal reflections and interference. See for details, for example, Refs [41, 42]. Although all practical solar cells use textured substrates and therefore their interfaces are rough, solar-cell structures with flat interfaces are a very useful experimental tool for examining the optical models, extracting unknown optical parameters, and showing the trends in optical behavior.

23.4.2 Modeling of Rough Interfaces

The textured structures used in thin-film solar cells are generally difficult to describe. It is possible to compute the light intensities in a solar cell using

Maxwell solvers; see, for example, Ref. [43]. However, solving Maxwell's equations for the disordered rough interfaces of the commonly used substrates requires a significant computation effort. Because of this limitation of the Maxwell's equations, the scalar scattering theory is quite popular [44–46]. In this chapter, we introduce the multirough-interface model which is based on the scalar scattering theory.

In the multirough-interface model, it is often assumed that a rough interface reflects (transmits) the same *amount* of light as a flat interface. When light is reflected (transmitted) at a rough interface, a certain amount of light is scattered where the remainder to the reflected (transmitted) light will continue in the specular (nonscattered) direction. In the multirough-interface model, the light is assumed to be incoherent. The haze for the reflectance and transmittance can be described by scalar scattering theory [47, 48]

$$H_{\mathrm{R}} = 1 - \exp\left[-\left(\frac{4\pi\delta_{\mathrm{rms}} n_0 \cos\left(\theta^{\mathrm{in}}\right)}{\lambda}\right)^2\right]$$
$$H_{\mathrm{T}} = 1 - \exp\left[-\left(\frac{4\pi\delta_{\mathrm{rms}} |n_0 \cos\left(\theta^{\mathrm{in}}\right) - n_1 \cos(\theta^{\mathrm{out}})|}{\lambda}\right)^2\right], \tag{23.24}$$

where n_0 is the refractive index of the medium of incidence, δ_{rms} is the root-mean-square (rms) roughness of the interface, and θ^{in} and θ^{out} are the incident angle and the angle of the outbound reflected or transmitted light, respectively.

Unfortunately, with commonly used textured substrates, scalar scattering theory does not work very well to describe the haze. The reason for this is that for scalar scattering theory to hold, it is required that:

- The interface should be completely random and have a normal (Gaussian) height distribution; this is generally not the case for commonly used rough substrates used in solar cells.
- The correlation length of the interface morphology, which is a measure of the lateral feature size, has to be much larger than the wavelength of light; also this condition is often violated for the commonly used substrates.

In order to describe the haze more accurately, it has been proposed to use [49]

$$H_{\mathrm{R}} = 1 - \exp\left[-\left(\frac{4\pi C_{\mathrm{R}} \delta_{\mathrm{rms}} n_0 \cos\left(\theta^{\mathrm{in}}\right)}{\lambda}\right)^2\right]$$
$$H_{\mathrm{T}} = 1 - \exp\left[-\left(\frac{4\pi C_{\mathrm{T}} \delta_{\mathrm{rms}} |n_0 \cos\left(\theta^{\mathrm{in}}\right) - n_1 \cos(\theta^{\mathrm{out}})|}{\lambda}\right)^3\right], \tag{23.25}$$

where C_{R} and C_{T} are fitting parameters which depend on the two media and both approach 1 when $|n_0 - n_1|$ is large. Note that this correction is empirical in nature and the appropriate correction depends on your substrate.

The amount of scattered light at a rough interface is incident angle dependent and has an angle distribution. This means that the reflected and transmitted scattered light, R_{scatt} and T_{scatt}, respectively, are proportional to

$$R_{\text{scatt}} = H_{\text{R}} f_{\text{R}}^{\text{in}}(\theta^{\text{in}}) f_{\text{R}}^{\text{out}}(\theta^{\text{out}}) R_{\text{tot}}$$
$$T_{\text{scatt}} = H_{\text{T}} f_{\text{T}}^{in}(\theta^{\text{in}}) f_{\text{T}}^{\text{out}}(\theta^{\text{out}}) T_{\text{tot}}, \tag{23.26}$$

where $f_{\text{R,T}}^{\text{in}}$ describes the dependence of scattering on incident angle for reflection and transmittance; $f_{\text{R,T}}^{\text{out}}$ is the angular distribution of the scattered reflected or transmitted light; θ_{in} and θ_{out} are the incident angle and the angle of the outbound reflected or transmitted light, respectively; and R_{tot} and T_{tot} are the total reflectance and transmittance of the interface (scattered and specular), respectively. For both angle distribution functions, $f_{\text{R,T}}^{\text{in}}$ and $f_{\text{R,T}}^{\text{out}}$, we will assume a $\cos^2(\theta)$ distribution unless otherwise specified.

In practical thin-film solar cells, interference effects are often observed despite the application of surface texture. In order to account also for these interference effects, coherent nature of specular light has to be included in the simulation. In this case, a semicoherent model is required, where specular light is assumed to be coherent and scattered light is incoherent. A semicoherent model can be obtained by combining the multilayer thin-film optics model to analyze the specular light propagation, with the multirough-interface model to analyze the scattered light propagation.

23.5 Tools

In this section, we introduce several tools for the simulation of thin-film solar cells. Many 1D simulation tools for solar cells have been developed over the years, and as a result we cannot provide a list that is anywhere near to complete. We attempted to provide a list of the better known and readily available programs.

23.5.1 AFORS-HET

AFORS-HET (automat for simulation of heterostructures) is a one-dimensional numerical computer program for modeling multilayer homo- or heterojunction solar cells and solar-cell substructures, as well as a variety of solar-cell characterization methods. Thus different measurements on solar-cell components as well as on the whole solar cell can be compared to the corresponding simulated measurements in order to calibrate the parameters used in the simulations and thus to obtain reliable predictions. Originally, it was developed in order to treat amorphous/crystalline silicon solar cells; however all types of thin-film solar cells (i.e., a-Si, CIS, and CdTe) can as well be appropriately treated. AFORS-HET (current version 2.4, launched on December 2009) is an open-source on-demand program. It is distributed free of charge and it can be downloaded via the Internet:

http://www.helmholtz-berlin.de/forschung/enma/si-pv/projekte/asicsi/afors-het/index_en.html.

AFORS-HET solves the one-dimensional semiconductor equations (Poisson's equation and the transport and continuity equations for electrons and holes) with the help of finite differences under different conditions: (i) equilibrium mode; (ii) steady-state mode; (iii) steady-state mode with small additional sinusoidal perturbations; (iv) simple transient mode, that is, switching external quantities instantaneously on/off; and (v) general transient mode, that is, allowing for an arbitrary change of external quantities. A multitude of different physical models have been implemented:

1) Optical models: The generation of electron–hole pairs can be described either by a ray-traced Lambert–Beer absorption including rough surfaces and using measured reflection and transmission files (neglecting coherence effects) or by calculating the plain-surface incoherent/coherent multiple internal reflections using the complex indices of reflection for the individual layers (neglecting rough surfaces).
2) Semiconductor bulk models: Local profiles within each semiconductor layer can be specified. Radiative recombination, Auger recombination, SRH, and/or dangling-bond recombination with arbitrarily distributed defect states within the band gap can be considered. Super band gap as well as subband-gap generation/recombination can be treated.
3) Interface models for treating heterojunctions: Interface currents can be modeled to be either driven by drift diffusion or by thermionic emission. A band to trap tunneling contribution across a heterointerface can be considered.
4) Boundary models: The metallic contacts can be modeled as flatband or Schottky-like metal/semiconductor contacts or as metal/insulator/semiconductor contacts. Furthermore, insulating boundary contacts can also be chosen.

Thus, all internal cell quantities, such as band diagrams, quasi-Fermi energies, local generation/recombination rates, carrier densities, cell currents, and phase shifts, can be calculated. Furthermore, a variety of solar-cell characterization methods can be simulated, that is, current/voltage, quantum efficiency, transient or quasisteady-state photoconductance, transient or quasisteady-state surface photovoltage, spectral resolved steady-state or transient photo- and electroluminescence, impedance/admittance, capacitance–voltage, capacitance–temperature and capacitance–frequency spectroscopy, and electrical detected magnetic resonance. The program allows for arbitrary parameter variations and multidimensional parameter fitting in order to match simulated measurements to real measurements.

AFORS-HET is capable of treating full time-dependent problems and can thus implement a huge variety of different solar-cell characterization methods. Furthermore it offers different physical models in order to adequately describe recombination and transport in thin-film semiconductor layers. It can treat graded layers. However, in order to describe amorphous silicon within pin cells,

the defect-pool model should be implemented. Furthermore, a tunnel junction model in order to describe pin/pin tandem cells is still missing. The optical model "coherent/incoherent internal reflections" is very slow if coherent and noncoherent layers have to be considered simultaneously (i.e., treating thin-film layers on glass) and could be significantly improved.

If one expects a numerical computer simulation to give reliable results, a good model calibration, that is, a comparison of simulation results to a variety of different characterization methods, is necessary. The solar cell under different operation conditions should be compared to the simulations. Also different characterization methods for the solar-cell components, that is, for the individual semiconductor layers and for any substacks should be tested against simulation. Only then the adequate physical models as well as the corresponding model input parameters can be satisfactorily chosen. Thus AFORS-HET is especially capable to simulate most of the common characterization methods for solar cells and its components and compare them to real measurements.

23.5.2 AMPS-1D

AMPS-1D is a well-known device simulation program for thin-film (silicon) solar cells developed at Penn State University. The program provides an easy-to-use graphical user interface. The program has a particularly flexible system to define the gap-state distribution of donor and acceptor levels, where, apart from continuous distributions like exponential tails and Gaussian distributions of dangling-bond defects, also (banded) discrete levels can be introduced. However, the program does not provide defect-pool models or amphoteric states.

The software is available free of charge. For further information, see http://www.ampsmodeling.org/.

23.5.3 ASA

The ASA program was specifically designed for modeling of thin-film silicon solar cells, that is, the program is designed to model both electrical and optical properties of multilayered heterojunction device structures. The ASA program is a full-featured and versatile program for the simulation of inorganic semiconductor solar cells in general and thin-film silicon-based solar cells in particular. ASA is written in C and is relatively fast. Furthermore it implements several defect-pool models and Shah and Shockley statistics for amphoteric defects. Several optical models are implemented, including a thin-film optics model and a semicoherent optical model. Although ASA is supplied with a graphical user interface, it is also available as a command-line-driven program which can take an ASCII text file as input. The command-line version is particularly flexible as it allows for an easy integration of the ASA program in (mathematical) script languages like GNU Octave [50] and MATLAB® [51]. This allows, for example, using the

built-in routines of MATLAB for nonlinear optimization of simulation parameters. A nice example of this is a simulation program for bulk heterojunction solar cells written in GNU Octave, which makes use of iteratively calls to the command-line version of ASA [52]. This way we effectively added models to the ASA program without modifying the ASA program itself. The ASA program is commercially available from Delft University of Technology.

23.5.4 PC1D

PC1D is *de facto* the industry standard for the simulation of solar cells. Its primary focus, however, is on crystalline silicon solar cells, making the program not very suitable for most thin-film technologies. The program was developed starting from 1982 at the University of New South Wales. In 2007, the source code was released under the General Public License (GPL), meaning that the program can be freely distributed and modified, provided that the modified source code is made available under the terms of the GPL. The program can be obtained from http://sourceforge.net/projects/pc1d/.

23.5.5 SCAPS

SCAPS is a numerical simulation tool that is developed at the University of Gent [53] that is widespread in the thin-film photovoltaics (PV) research community. It was developed especially for thin-film Cu(In,Ga)Se_2 and CdTe cells. However, it has also been used for Si and III–V cells, and recently its applicability was further enhanced to amorphous and micromorphous Si cells. Its advantages are that it is fast and interactive, with an intuitive user interface, and that it can simulate various measurements from everyday's PV practice: $I-V$, $C-V$, $C-f$, and QE, all under a wide variation of excitations (voltage, illumination intensity, spectrum, wavelength, and frequency). Also, many users experience a low threshold to use it. Since it became available [53, 54], its capabilities have been continuously extended and now also include intraband tunneling [55], the impurity photovoltaic effect [55], and graded properties ("graded band gaps") [56]. The last extension is the implementation of multivalent defects [57], which is crucial in simulating a-Si cells and appears to be important in Cu(In,Ga)Se_2 cells as well [58].

SCAPS is freely available to the PV research community on request from the authors.

23.5.6 SC-Simul

SC-Simul is a program developed by the University of Oldenburg, which is suitable for steady-state and transient simulations of solar cells. The software was developed for simulations of amorphous silicon–crystalline silicon heterojunction

solar cells and is therefore capable to simulate amorphous semiconductors. The models for recombination of charge carriers include band-to-band and Auger recombination as well as recombination via tail states and Gaussian dangling-bond distributions. However, a defect-pool model for the calculation of the defect-state distribution in a-Si:H is not implemented. The optical model used to determine the generation rate is a simple Lambert–Beer's law, that is, no interference effects are taken into account. The software is delivered with an intuitive graphical user interface. The user is, however, able to run the simulations from the command line, which allows a similar flexibility as ASA in combining the drift-diffusion solver with external programs as MATLAB.

The software is available free of charge. For further information, see http://www.physik.uni-oldenburg.de/greco/.

Acknowledgments

The authors are grateful to Rudi Brüggemann for discussions on solar-cell simulations. Marc Burgelman and Koen Decock acknowledge the support of the Research Foundation – Flanders (FWO; PhD fellowship).

References

1. Mott, N. (1987) The mobility edge since 1967. *J. Phys. C: Solid State Phys.*, **20**, 3075.
2. Willemen, J.A. (1998) Modelling of amorphous silicon single- and multi-junction solar cells. PhD thesis. Delft University of Technology.
3. Tiedje, T. (1981) Evidence for exponential band tails in amorphous silicon hydride. *Phys. Rev. Lett.*, **46**, 1425.
4. Stutzmann, M. (1992) A comment on thermal defect creation in hydrogenated amorphous silicon. *Philos. Mag. Lett.*, **66**, 147.
5. Aljishi, S., Cohen, J., Jin, S., and Ley, L. (1990) Band tails in hydrogenated amorphous silicon and silicon–germanium alloys. *Phys. Rev. Lett.*, **64**, 2811.
6. Winer, K. (1990) Defect formation in a-Si:H. *Phys. Rev. B: Condens. Matter Mater. Phys.*, **41**, 12150.
7. Powell, M.J. and Deane, S.C. (1993) Improved defect-pool model for charged defects in amorphous silicon. *Phys. Rev. B: Condens. Matter Mater. Phys.*, **48**, 10815.
8. Powell, M.J. and Deane, S.C. (1996) Defect-pool model and the hydrogen density of states in hydrogenated amorphous silicon. *Phys. Rev. B: Condens. Matter Mater. Phys.*, **53**, 10121.
9. Schumm, G. (1994) Chemical equilibrium description of stable and metastable defect structures in a-Si:H. *Phys. Rev. B: Condens. Matter Mater. Phys.*, **49**, 2427.
10. Stutzmann, M. (1987) Weak bond-dangling bond conversion in amorphous silicon. *Philos. Mag. B*, **56**, 63.
11. Kakalios, J., Street, R.A., and Jackson, W.B. (1987) Stretched-exponential relaxation arising from dispersive diffusion of hydrogen in amorphous silicon. *Phys. Rev. Lett.*, **59**, 1037.
12. Street, R.A. (1991) Hydrogen chemical potential and structure of a-Si:H. *Phys. Rev. B: Condens. Matter Mater. Phys.*, **43**, 2454.
13. Bar-Yam, Y. and Joannopoulos, J. (1987) Theories of defects in amorphous semiconductors. *J. Non-Cryst. Solids*, **97**, 467.

14. Shockley, W. and Last, J.T. (1957) Statistics of the charge distribution for a localized flaw in a semiconductor. *Phys. Rev.*, **107**, 392.
15. Okamoto, H. and Hamakawa, Y. (1977) Electronic behaviors of the gap states in amorphous semiconductors. *Solid State Commun.*, **24**, 23.
16. Overhof, H., Otte, M., Schmidtke, M., Backhausen, U., and Carius, R. (1998) The transport mechanism in microcrystalline silicon. *J. Non-Cryst. Solids*, **227–230**, 992.
17. Dylla, T., Finger, F., and Schiff, E.A. (2004) Hole drift-mobility measurements and multiple trapping in microcrystalline silicon. *Mater. Res. Soc. Symp. Proc.*, **808**, 109.
18. Dylla, T., Finger, F., and Schiff, E.A. (2005) Hole drift-mobility measurements in microcrystalline silicon. *Appl. Phys. Lett.*, **87**, 032103.
19. Reynolds, S., Smirnov, V., Main, C., Finger, F., and Carius, R. (2004) Interpretation of transient photocurrents in coplanar and sandwich pin microcrystalline silicon structures. *Mater. Res. Soc. Symp. Proc.*, **808**, 127.
20. Merdzhanova, T., Carius, R., Klein, S., Finger, F., and Dimova-Malinovska, D. (2005) A comparison of model calculations and experimental results on photoluminescence energy and open circuit voltage in microcrystalline silicon solar cells. *J. Optoelectron. Adv. Mater.*, **7**, 485.
21. Pieters, B., Stiebig, H., Zeman, M., and Swaaij, R. (2009) Determination of the mobility gap of intrinsic μc-Si:H in p–i–n solar cells. *J. Appl. Phys.*, **105**, 044502.
22. Kanschat, P., Mell, H., Lips, K., and Fuhs, W. (2000) Defect and tail states in microcrystalline silicon investigated by pulsed ESR. *Mater. Res. Soc. Symp. Proc.*, **609**, A27.3.
23. Dylla, T. (2005) Electron spin resonance and transient photocurrent measurements on microcrystalline silicon. PhD thesis. Forschungszentrum Jülich.
24. Sah, C.-T. and Shockley, W. (1958) Electron–hole recombination statistics in semiconductors through flaws with many charge conditions. *Phys. Rev.*, **109**, 1103.
25. Fantoni, A., Vieira, M., and Martins, R. (1999) Simulation of hydrogenated amorphous and microcrystalline silicon optoelectronic devices. *Math. Comput. Simul.*, **49**, 381.
26. Chatterjee, P. (1994) Photovoltaic performance of a-Si:H homojunction p–i–n solar cells: a computer simulation study. *J. Appl. Phys.*, **76** (2), 1301.
27. Hernandez-Como, N. and Morales-Acevedo, A. (2010) Simulation of heterojunction silicon solar cells with AMPS-1D. *Sol. Energy Mater. Sol. Cells*, **94**, 62.
28. Zhang, S.B., Wei, S.-H., and Zunger, A. (1998) Defect physics of the $CuInSe_2$ chalcopyrite semiconductor. *Phys. Rev. B: Condens. Matter Mater. Phys.*, **57** (16), 9642.
29. Zabierowski, P., Rau, U., and Igalson, M. (2001) Classification of metastabilities in the electrical characteristics of ZnO/CdS/Cu(In,Ga)Se_2 solar cells. *Thin Solid Films*, **387**, 147.
30. Decock, K., Lauwaert, J., and Burgelman, M. (2009) *Modelling of Thin Film Solar Cells with Graded Band Gap*. Proceedings of the 45th MIDEM, Postojna, Slovenia, p. 245.
31. Burgelman, M. and Marlein, J. (2008) *Analysis of Graded Band Gap Solar Cells with SCAPS*. Proceedings of the 23rd EUPVSEC, Valencia, Spain, p. 2151.
32. Decock, K., Khelifi, S., and Burgelman, M. (2010) *Uniform Reference Structures to Assess the Benefit of Grading in Thin Film Solar Cell Structures*. Proceedings of the 25th EUPVSEC/WCPEC-5, Valencia, Spain, p. 3323.
33. Decock, K., Lauwaert, J., and Burgelman, M. (2010) Characterization of graded CIGS solar cells. *Energy Procedia*, **2**, 49.
34. Stollwerck, G. and Sites, J. (1995) *Analysis of the CdTe Back Contact Barriers*. Proceedings of the 13th EUPVSEC, Nice, France, p. 2020.
35. Niemegeers, A. and Burgelman, M. (1997) Effects of the Au/CdTe back contact on IV- and CV-characteristics of Au/CdTe/CdS/TCO solar cells. *J. Appl. Phys.*, **81**, 2881.

36. Burgelman, M. (2006) Cadmium telluride thin film solar cells: characterization, fabrication and modeling, in *Thin Film Solar Cells: Fabrication, Characterization and Applications* (eds J. Poortmans and V. Arkhipov), John Wiley & Sons, Ltd, Chichester, UK, p. 277, Chapter 7.
37. Eisenbarth, F.T., Unold, T., Cabballero, R., Kaufmann, C.A., and Schock, H.W. (2010) Interpretation of admittance, capacitance–voltage, and current–voltage signatures in $Cu(In,Ga)Se_2$ thin film solar cells. *J. Appl. Phys.*, **107**, 034509.
38. Nollet, P. and Burgelman, M. (2004) *Results of Consistent Numerical Simulation of CdTe Thin Film Solar Cells*. Proceedings of the 19th EUPVSEC, Paris, France, p. 1725.
39. Bonnet, D. and Harr, M. (1998) *Manufacturing of CdTe Solar Cells*. Proceedings of the 2nd WCPEC, Wien, Austria, p. 397.
40. Burgelman, M., Verschraegen, J., Degrave, S., and Nollet, P. (2005) Analysis of CdTe and CIGS solar cells in relation to materials issues. *Thin Solid Films*, **480–481**, 392.
41. Tao, G. (1994) Optical modeling and characterization of hydrogenated amorphous silicon solar cells. PhD thesis. Delft University of Technology.
42. Heuvel, J. (1989) Optical properties and transport properties of hydrogenated amorphous silicon. PhD thesis. Delft University of Technology.
43. Rockstuhl, C., Lederer, F., Bittkau, K., and Carius, R. (2007) Light localization at randomly textured surfaces for solar-cell applications. *Appl. Phys. Lett.*, **91**, 171104.
44. Tao, G., Zeman, M., and Metselaar, J.W. (1994) Accurate generation rate profiles in a-Si:H solar cells with textured TCO substrates. *Sol. Energy Mater. Sol. Cells*, **34**, 359.
45. Schropp, R.E.I. and Zeman, M. (1998) *Amorphous and Microcrystalline Solar Cells: Modeling, Materials, and Device Technology*, Kluwer, Dordrecht.
46. Zeman, M., Swaaij, R.A.C.M.M., Metselaar, J.W., and Schropp, R.E.I. (2000) Optical modeling of a-Si:H solar cells with rough interfaces: effect of back contact and interface roughness. *J. Appl. Phys.*, **88**, 6436.
47. Bennett, H.E. and Porteus, J.O. (1961) Relation between surface roughness and specular reflectance at normal incidence. *J. Opt. Soc. Am.*, **51**, 123.
48. Carniglia, C.K. (1979) Scalar scattering theory for multilayer optical coatings. *Opt. Eng.*, **18**, 104.
49. Zeman, M., Swaaij, R.A.C.M.M., Metselaar, J.W., and Schropp, R.E.I. (2000) Optical modelling of a-Si:H solar cells with rough interfaces: effect of back contact and interface roughness. *J. Appl. Phys.*, **88**, 6436.
50. Eaton, J.W. (2002) *GNU Octave Manual*, Network Theory Limited: Bristol, United Kingdom.
51. MATLAB release 2016b (2016), The MathWorks, Inc., Natick, Massachusetts, United States.
52. Kirchartz, T., Pieters, B.E., Taretto, K., and Rau, U. (2008) Electro-optical modeling of bulk heterojunction solar cells. *J. Appl. Phys.*, **104**, 094513.
53. Burgelman, M., Nollet, P., and Degrave, S. (2000) Modelling polycrystalline semiconductor solar cells. *Thin Solid Films*, **361–362**, 527–532.
54. Burgelman, M., Verschraegen, J., Degrave, S., and Nollet, P. (2004) Modeling thin film PV devices. *Prog. Photovoltaics*, **12**, 143–153.
55. Verschraegen, J. and Burgelman, M. (2007) Numerical modeling of intra-band tunneling for heterojunction solar cells in SCAPS. *Thin Solid Films*, **515** (15), 6276–6279.
56. Burgelman, M. and Marlein, J. (2008) *Analysis of Graded Band Gap Solar Cells with SCAPS*. Proceedings of the 23rd European Photovoltaic Solar Energy Conference, Valencia, Spain, pp. 2151–2155.
57. Decock, K., Khelifi, S., and Burgelman, M. (2011) *Modelling Multivalent Defects in Thin Film Solar Cells*. Thin Solid Films, **519**, 7481.
58. Wei, S.-H., Zhang, S.B., and Zunger, A. (1998) Effects of Ga addition to $CuInSe_2$ on its electronic, structural, and defect properties. *Appl. Phys. Lett.*, **72**, 3199–3201.

24
Two- and Three-Dimensional Electronic Modeling of Thin-Film Solar Cells

Ana Kanevce and Wyatt K. Metzger

Research and development to expand solar-cell use is based on finding ways to create more efficient devices, eliminate as many losses as possible, lower material usage, and use cheaper production processes. Empirical optimization is important but can be misguided and require significant time, effort, and cost. Modeling can give insight to the physical processes, has a power to predict the impact of different parameters on the output results, and thus can help guide experimental investigations. The need for modeling solar cells in two and three dimensions is constantly increasing as solar technology matures. A description of multidimensional modeling and its applications is given here.

24.1
Applications

A standard 1D model simulates the electron and hole motion in the direction perpendicular to a planar junction. An enormous amount has been learned from this type of model. However, 1D models must also eliminate the inherent 3D nature of solar cells. Figure 24.1 shows a schematic of a typical thin-film solar cell. The carriers generated in the absorber will not only move perpendicular to the junction plane (the z-direction) but also in directions parallel to the junction plane (x- and y-directions). In a standard thin-film module, individual cells are just several microns thick, but the cell width is usually several millimeters to several centimeters across and can be several feet wide. The lateral distance traveled by the carriers may impose additional requirements on material quality and alter the optimal distance between contacts. Consequently, it is important to consider motion in all directions.

Modeling in more than one dimension is also necessary for understanding the impact of grain boundaries (GBs) and nonuniformities on device performance. The nonuniformities have been observed for $Cu(In,Ga)Se_2$ (CIGS), $Cu_2(Zn,Sn)(Se,S)_4$ (CZTS), perovskite, polymer, CdTe, and other solar cells with many experimental methods such as OBIC, electron-beam-induced current

Advanced Characterization Techniques for Thin Film Solar Cells, Second Edition.
Edited by Daniel Abou-Ras, Thomas Kirchartz, and Uwe Rau.

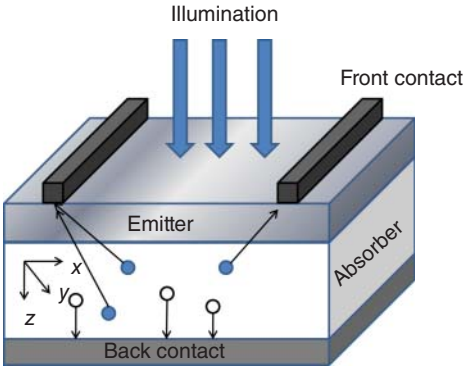

Figure 24.1 A cross section of a solar cell. The *z*-direction is perpendicular to the planar junction, the *x*-direction runs from left to right, and the *y*-direction comes out of the page. A 1D model takes into account motion only along the *z*-axis.

(EBIC), LBIC, and STM. For examples of experimentally observed inhomogeneities and grain boundaries, the reader is referred to Chapters 11, 13, and 14. Grain boundaries run both vertically and horizontally relative to the solar cell in the absorber layer. Voids and pinholes often appear in different layers of CdTe and CIGS solar cells under certain growth conditions.

Nonuniformities may be manifested in the thickness of all the layers, as well as in the electronic parameters such as band gap, carrier density, and carrier lifetime. The impact of inhomogeneity on device performance can be analyzed by a 2D or 3D model.

Although planar cell geometry (as in Figure 24.1) is generally the most amenable to manufacturing, there can be benefits to more complex designs. For example, by positioning the front and back contacts on the same side of a cell, losses connected to the series resistance of the emitter can be avoided, and the photocurrent can increase because the shading of the grid is avoided.

Numerical modeling is also useful to simulate different electro-optical experiments, in the presence of grain boundaries and nonplanar junctions and geometries, and to help interpret data obtained in such experiments. In addition, multidimensional models can be used to examine novel grid designs, the effects of nonuniform illumination, and advanced technologies such as nanowires.

Methods for effective multidimensional modeling are presented in Section 24.2. Examples of the aforementioned problems and the modeling efforts directed toward their solutions are presented in Section 24.3.

24.2 Methods

The first step in creating a computational model is defining and providing discretization of a 2D area or a 3D volume. Two main approaches to the

discretization have been used for studying solar cells: equivalent-circuit modeling (Section 24.2.1) and solving semiconductor equations (Section 24.2.2).

Equivalent-circuit modeling represents a solar-cell device or module as a collection of circuit elements. Diodes are inserted to the circuit to represent the photovoltaic (PV) effect from the semiconductor layers, and resistors are inserted to simulate series and shunt resistance between and within individual cells. The most commonly used software package for circuit simulations is SPICE. This and other packages can handle numerous circuit elements in very little time. This makes circuit modeling amenable to simulating modules, systems, and problems with a large number of discrete units. For example, circuit modeling has often been used to examine how local nonuniformities and shunts impact module performance.

By solving the semiconductor equations, one can get more information about the electron–hole dynamics occurring within a solar cell, but solving very complex problems with many discrete parts is much more cumbersome and can lead to numerical convergence issues. Obtaining these solutions also requires detailed input on the properties of each material in the device. The semiconductor equations can be solved by commercial software packages, by generic partial differential equation (PDE) solver packages, or by custom code. In the literature (e.g., Refs [1–12]), one can find studies executed with Sentaurus Device by Synopsys [13], COMSOL Multiphysics [14], Crosslight APSYS [15], Atlas by Silvaco [16], and other programs. Sentaurus Device uses the finite-difference method, while COMSOL Multiphysics and Crosslight APSYS use finite element method to solve the differential equations. Some commercial software packages allow combining both semiconductor and equivalent-circuit modeling.

24.2.1
Equivalent-Circuit Modeling

The equivalent-circuit approach is based on representing regions in a solar cell simply as diodes. A current source parallel with the diode represents light generation, and resistors can be connected to simulate parasitic resistances. A nonuniform device can then be represented as a network of nonuniform diodes. Figure 24.2 shows part of such a network, where six diodes are connected in parallel. The current density (J) flowing through the different diodes is defined with the diode equation

$$J = J_0 \left(\exp\left(\frac{qV}{n_{\mathrm{id}} kT} \right) - 1 \right) - J_{\mathrm{sc}}. \tag{24.1}$$

The different diodes are defined with their saturation current densities (J_0) and ideality factors (n_{id}) as well as with their local short-circuit current density J_{sc}. In a nonuniform device, the characteristics of each diode may be varied. A part of the device with characteristics different than the rest is highlighted in Figure 24.2. A local leakage current, which could be caused by something like a pinhole in CdS, can be simulated with a shunt resistor added to one of the diodes. The parallel diode model is most valid when the fluctuations have a scale greater than several

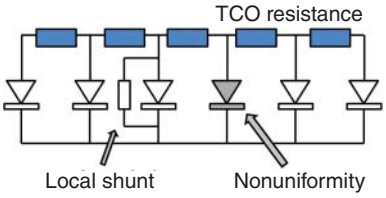

Figure 24.2 A schematic of an equivalent circuit of a nonuniform solar cell represented as a network of diodes. The cells are connected with resistors that represent the transparent conductive oxide (TCO).

diffusion lengths. The network program SPICE has been widely used for this type of simulation. Although some device physics is lost in representing unit cells with the exponential diode law, this approach has given some important results. Some of these will be reviewed in Section 24.3.1.

24.2.2 Solving Semiconductor Equations

The output of the equivalent-circuit method is limited to calculating the current density–voltage (J–V) characteristics of the device. To model cells more precisely, calculate physical properties such as band alignment, carrier density, photogeneration, and recombination, and simulate different characterization experiments such as quantum efficiency (QE), photoluminescence, admittance spectroscopy, and others, one needs to solve equations that describe the electrostatics and carrier transport in the semiconductor layers. The number and precise form of these equations depend on the specific physics that needs to be captured in the simulations. The most common set of equations applied in thin-film solar-cell simulations are three interdependent nonlinear PDEs [17], namely, the Poisson equation

$$\nabla\cdot(-\varepsilon(\vec{r})\nabla\varphi(\vec{r})) = q(p(\vec{r}) - n(\vec{r}) + N_{\mathrm{d}}(\vec{r}) - N_{\mathrm{a}}(\vec{r})) \tag{24.2}$$

and the continuity equations for holes

$$\nabla\cdot J_{\mathrm{p}}(\vec{r}) = \nabla\cdot(q\mu_{\mathrm{p}}(\vec{r})p(\vec{r})E(\vec{r}) - qD_{\mathrm{p}}(\vec{r})\nabla p(\vec{r})) = q\left(G\left(\vec{r}\right) - R(\vec{r}) - \frac{\partial p(\vec{r})}{\partial t}\right) \tag{24.3}$$

and electrons

$$\nabla\cdot J_{\mathrm{n}}(\vec{r}) = \nabla\cdot(q\mu_{\mathrm{n}}(\vec{r})n(\vec{r})E(\vec{r}) + qD_{\mathrm{n}}(\vec{r})\nabla n(\vec{r})) = -q\left(G\left(\vec{r}\right) - R(\vec{r}) - \frac{\partial n(\vec{r})}{\partial t}\right). \tag{24.4}$$

Here φ is electrostatic potential, ε is dielectric constant, p and n are electron and hole densities, N_{a} and N_{d} are densities of ionized acceptors and donors, J_{n} and J_{p} are electron and hole current densities, E is electric field, and G and R are the generation and recombination rates, respectively. All of the physical properties can vary as a function of the position $\vec{r}$.

24.2.2.1 Creating a Semiconductor Model

To create a structure, one first defines the materials and contacts in the model. Then, the geometry and position for each material layer and contact need to be

specified. After the structure is defined, the next step is defining the electronic properties such as doping profiles and band structure. The optical properties such as the absorption coefficient of different materials involved as well as reflection coefficient of the layers and contacts also need to be included in the model. The user inputs the incident illumination spectrum, usually the standard spectrum AM1.5 for terrestrial applications or AM0 for space applications [18].

For most thin-film materials, the dominant recombination mechanisms are nonradiative. In order to define the recombination mechanisms, the modeler needs to input the density of different types of defects and their spatial and energetic distribution, as well as capture cross sections, or lifetime values that represent the overall recombination rates. Then, the interfaces need to be defined by properties such as the interface states, interfacial recombination velocity, and the transport mechanism(s) across the interfaces.

For single-crystal materials like Si or GaAs, many material properties are well established in the literature. For thin-film polycrystalline materials, experimental input is sometimes absent or not clear, and the material properties may vary largely based on deposition methods and conditions. The lack of good input can present a difficulty for modeling; conversely, modeling can help determine what values are important to measure and the range of values that are realistic. Once the parameters are set, one needs to approach the solution techniques.

To attain solutions, the device is discretized in two or three dimensions by creating a mesh. Numerical algorithms calculate solutions to the equations at the mesh vertices. Hence, while increasing the mesh density can improve accuracy, it also increases the computational time and memory requirements. Fewer dimensions and less complicated models require far less computational time and effort.

An example of a meshed model is shown in Figure 24.3. The meshing needs to be denser where one expects rapid changes in variables, as well as at the heterointerfaces. To improve the calculation time, the mesh should be less dense when possible such as in bulk material with uniform properties. In this example, the mesh is significantly denser at the junction and at the grain boundaries within the absorber. Equations 24.2–24.4 describe transport in the bulk of the device and are solved at every mesh point. In addition, boundary conditions and transport at each material interface (such as CdTe and CdS) must also be specified, and ohmic or Schottky contacts must be defined with appropriate parameters. Band offsets are typically determined using the Anderson model based on the band gap and

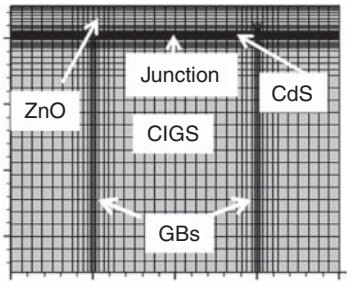

Figure 24.3 An example of a meshed structure used in 2D simulations. A model of a CIGS cell. The cell has two columnar grain boundaries perpendicular to the junction.

electron affinities for each material. One must also specify current and energy flux equations and thermionic or tunneling transport if necessary. Boundary conditions must also be specified for the sides of the device. A detailed description of boundary conditions is given in Ref. [19].

24.3 Examples

This section will give some examples of problems that were addressed with 2D or 3D modeling and the knowledge that was gained through them. It does not by any means list all of them.

24.3.1 Equivalent-Circuit Modeling Examples

In an equivalent-circuit model, like the one shown in Figure 24.2, a nonuniform device is represented with diodes having different properties. If the highlighted diode has a lower turnup voltage (defined as a weak diode) than the rest of the diodes in the device, it will be forward biased by the surrounding diodes [20–24]. The efficiency loss due to nonuniformities depends on the area taken by the weak diodes, the difference in voltages of the weak diode compared to the strong ones, as well as on the resistance in the transparent conductive oxide (TCO). An example is shown in Figure 24.4. In this example, PSPICE simulations are used to calculate how the ratio of the weak area A_w versus the total device area A_t affects the device efficiency. The $\Delta V_{oc} = V_{oc}(s) - V_{oc}(w)$ is the difference in open-circuit voltage between the strong and the weak diodes. In the case of intrinsic transparent conductive oxide (i-TCO), as the resistivity increases, the voltage drop across the TCO layer will increase as well, which can localize the voltage difference into a smaller area.

Rau *et al.* [25], Werner *et al.* [26], and Grabitz *et al.* [27] have reported that it is difficult to avoid potential fluctuations in CIGS cells, which have a detrimental effect on performance. These studies have also reported that moderate series resistance in a window layer (e.g., i-ZnO layer) can reduce the losses caused by

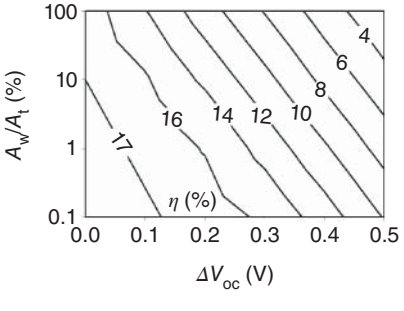

Figure 24.4 Impact of area and voltages of the weak diodes on nonuniform device performance. [20].

these fluctuations. However, large TCO resistance also reduces the device fill factor (FF). In certain cases, there is an optimal TCO resistance value that minimizes the damage due to fluctuations while maintaining a low FF loss.

Circuit simulations have also been used to predict alternative module designs to decrease the impact of partial shading [28, 29] and local shunts[30]. Hybrid methods, where circuit simulations are combined with device simulations, have been used to correlate cell characteristics to module performance [31–35].

24.3.2 Semiconductor Modeling Examples

One of the problems that call for modeling in more than one dimension lies in the polycrystalline nature of CIGS, CZTS, perovskite, CdTe, and other thin-film cells. The GBs in these materials have been observed by several scanning techniques. GB studies of CIGS cells can be found in Refs [3, 6, 8, 36–39], for CdTe cells in Refs [40, 41], for CZTS cells in Refs [10, 42], and for polycrystalline Si in Refs [2, 7].

The boundaries between different grains disturb the periodicity of the crystal lattice and can create energy states within the band gap. This can result in electronic charge on the boundaries and a creation of electric fields and potentials within the absorber material. A significant amount of research has been directed toward understanding the role and the importance of grain boundaries in polycrystalline thin-film solar cells. The debate on whether grain boundaries are detrimental, innocuous, or beneficial to device performance has been ongoing for over a decade. Clearly, one motivation for extending modeling beyond one dimension is to understand grain-boundary properties, composition, defect densities, and potentials and provide a direct correlation between these proprieties and device performance. The defect density at the GBs can increase the total nonradiative recombination rate and decrease V_{oc} and FF [3, 41]. The quantitative impact of GB recombination on V_{oc} is directly connected to other cell parameters such as the grain size, bulk lifetime, and surface recombination. Therefore, although one can intuitively connect the GB recombination with V_{oc} and conversion efficiency loss, the magnitude of this effect can vary significantly among different devices. Figure 24.5 shows 2D simulation of GB recombination impact on the conversion efficiency of a CdTe device. The grain size is 2 μm, and the layer stack is composed of SnO_2/Cd_2SnO_4/CdS/CdTe (see inset in Figure 24.5). The relative loss in conversion efficiency due to GB recombination is higher for the device with high lifetime. This means that as the bulk properties are improved, the device performance limitations are shifted to surface, interface, and GB recombination and their passivation becomes more important.

In addition to creating recombination centers, GB defects can create local potentials. The impact of charged GBs on the device performance depends on the type of charges at the boundaries and their energy distribution. If the GBs are positively charged, the resulting GB potential can repel holes and attract electrons. These charged GBs can create channels for minority-carrier flow and potentially improve minority-carrier collection. This should result in an

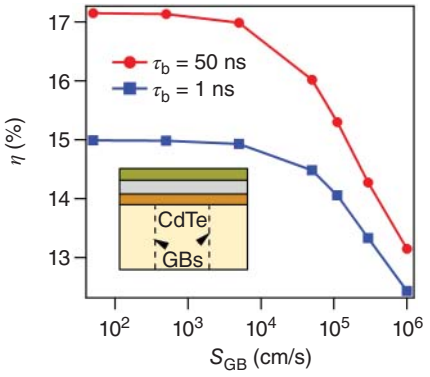

Figure 24.5 The impact of GB recombination on the conversion efficiency η of a CdTe solar cell when the GI lifetime τ_b is 50 ns (circles) and 1 ns (squares).

increased J_{sc}. However, in forward bias, these GBs will attract minority carriers flowing from the TCO into CdTe and thereby increase forward current, which reduces V_{oc} [43]. An example of simulated impact of grain boundary potential on device performance is shown in Figure 24.6. The results demonstrate the complex relationships between GB potential, GB recombination, and device performance that can be manifested by modeling and difficult to predict by intuition. If positively charged grain boundaries are oriented perpendicular to the plane of the junction, the GB and/or the region adjacent to it may act as a collection channel for minority carriers, thereby increasing photocurrent. But, in general, the negative effects on V_{oc} and FF outweigh the positive effects on photocurrent, and efficiency decreases.

In addition to recombination centers and local potentials, the material composition along the GBs differs compared to the grain interior (GI). In CIGS, the GBs are found to be Cu poor, with increased band gap in the valence band. This creates a barrier for hole recombination at the grain boundary, reducing the GB recombination rate and its impact on device performance [3]. To effectively passivate the GB recombination, the barrier needs to be at least 3 nm thick and 300 meV high to minimize the tunneling probability [6]. Unlike in CIGS devices, in kesterites the GBs are predicted to be Cu rich and have a lower band gap than the bulk. The lower band-gap regions can be detrimental for the devices V_{oc}, even without increased defect density at the GBs [10, 42].

Local phases with different composition are not only limited to the GBs but can form throughout the material and have detrimental effect on the device performance especially on V_{oc} [10]. Their impact is dependent on the location within the absorber material, band gap, and size. The most detrimental secondary phases are located in the vicinity of the heterointerface.

Local voids in CIGSSe absorbers in the vicinity of the back contact can have impact on the performance as well as on the capacitance and EBIC measurements [44]. 2D modeling was also used to analyze the impact of roughness at the interface. Although interface roughness can increase interface recombination in

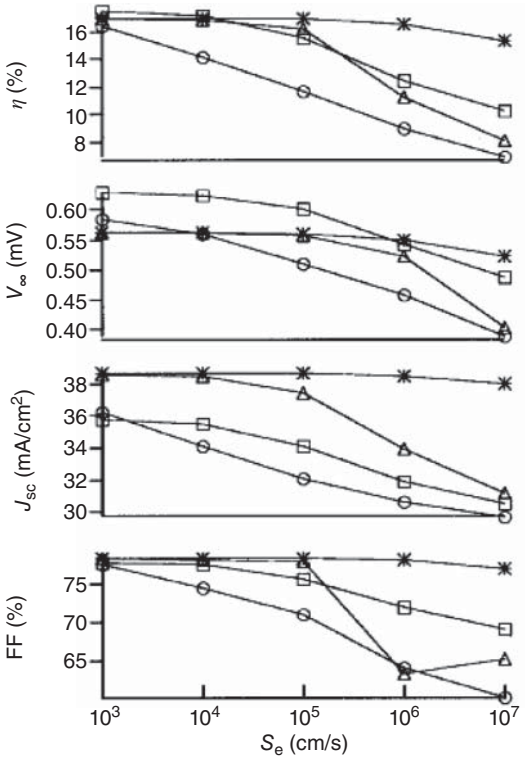

Figure 24.6 Simulated impact of recombination velocity at the grain boundaries on V_{oc}, J_{sc}, and FF and conversion efficiency of a CIGS for four different values of grain boundary potential: 0 V (square), 200 mV (circle), 400 mV (triangle), and 550 mV (asterisk). (Reprinted with permission from Metzger [36]. Copyright 2005, American Institute of Physics.)

$Cu(In,Ga)(Se,S)_2$ devices, it also improves light absorption and increases carrier collection. Modeling has indicated that the beneficial effects outweigh the negative effects [44].

In addition to simulating current–voltage curves, 2D modeling is very important to understand other characterization techniques such as QE, EBIC, cathodoluminescence (CL), time-resolved photoluminescence, and near-field scanning microscopy performed on polycrystalline films or devices [36, 41, 45, 46]. Some examples are given below.

Analysis of quantum efficiency (QE) data is usually performed in one dimension, and its interpretation is based on carrier motion in the z-direction. Therefore, the losses for low photon energies (long wavelengths) are mainly assigned to incomplete carrier collection and back contact recombination, while the higher energy losses are assigned to the front layers, such as absorption in buffer and window layers. 2D simulations have revealed that band bending at the GBs can provide a

possible explanation of the differences observed in QE measurements with different buffers [39].

Sozzi *et al*. [11] used 2D modeling to investigate the temperature dependence of the current–voltage behavior and suggested that donor-type defects at the GBs in CIGS in combination with a Schottky back contact barrier can reproduce observed $J-V-T$ curves. It was suggested that these defects are a source of a shunt leakage current in CIGS and that the $J-V-T$ curves are very dependent on the energetic distribution of the traps.

2D (3D) modeling is necessary to simulate and interpret the measurements based on local carrier generation, including, but not limited to, CL, EBIC, and two-photon excitation time-resolved photoluminescence (2PE TRPL). Local carrier generation is used in several characterization techniques to enable access to the local recombination mechanisms separately, to determine the specific location where the dominant performance sinks occur, and to suggest how to alter and optimize deposition processes and conditions to minimize the recombination rates.

In a CL experiment, the excitation spot moves along the material and across the GBs. The measured CL signal is proportional to the total radiative recombination rate. When the excitation spot is over the GB, because the recombination at the GBs is usually higher than at the GI, the CL signal will be smaller compared to the signal at the GI. Figure 24.7 shows simulated radiative recombination rates in a CdTe material when the excitation spot is in the middle of the grain (Figure 24.7a) and at the GB (Figure 24.7b). The difference in CL intensities can give qualitative

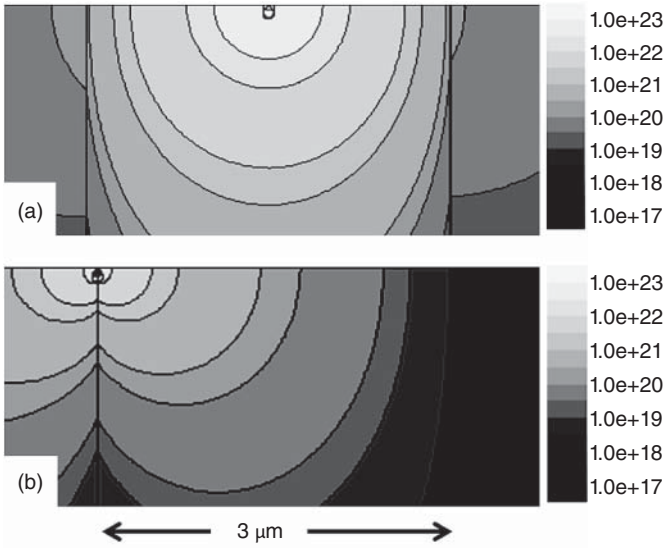

Figure 24.7 Calculated radiative recombination rate in units of $1/(cm^3 \times s)$ in a CdTe material in a CL measurement, when the excitation spot is (a) in the middle of the grain and (b) at the grain boundary.

information about the GB recombination, but modeling can assign quantitative values and connect them to device performance [41].

Another experimental technique requiring 2D modeling is 2PE TRPL microscopy. This method generates carriers away from the material surface and enables experimentalists to probe bulk, GB, and interface (front or buried) recombination separately [47]. However, carrier diffusion out of the excitation region and local potentials can affect the measurement, and recombination mechanisms can be convoluted. Numerical simulations are able to find the optimal measurement conditions and help separate and quantify the different recombination mechanisms. For example, at first it may seem most attractive to focus the laser beam to the smallest spot size possible to provide the best spatial resolution. However, modeling has revealed that the optimal excitation spot size (compared to the carrier diffusion length) should not be smaller than 1/3 of the diffusion length. This is needed to distinguish between carrier diffusion and recombination rates in the measured results. For smaller spot sizes, diffusion can dominate the measured decays and make it difficult to accurately assess recombination rates [48].

During the deposition of $Cu(In,Ga)Se_2$, different phases with different Cu/In/Ga/Se ratios might form. These phases have different band gaps and electronic structures. The impact of band-gap fluctuations on device performance is analyzed in Ref. [49]. The Cu content can influence the conductivity. The higher and lower Cu domains will have p-type and n-type conductivity, respectively [50]. Therefore, as opposed to a single p–n junction at the heterointerface, the device could have multiple p–n junctions [50]. A schematic is shown in Figure 24.8. What this means for the device performance is difficult to tell without a model.

Analysis of the implications caused by the possible existence of nanodomains has been addressed by 2D modeling [1]. The model can simulate details such as currents and carrier densities for a range of material properties and domain sizes. An example in Figure 24.9 shows electron flow for p-type and n-type domains that extend perpendicular to the junction plane into the absorber material. If the domains are on the nanometer scale and have small relative band offsets, transport will be similar to a uniform material with the average properties of the constituent domains, and the device can be treated as a planar junction. If the domains have strong relative band offsets or are larger than tens of nm across, they can form a multidimensional network of p–n junctions. This network may

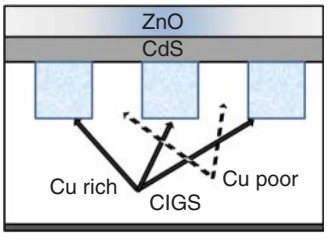

Figure 24.8 A schematic of an interdigitated CIGS solar cell.

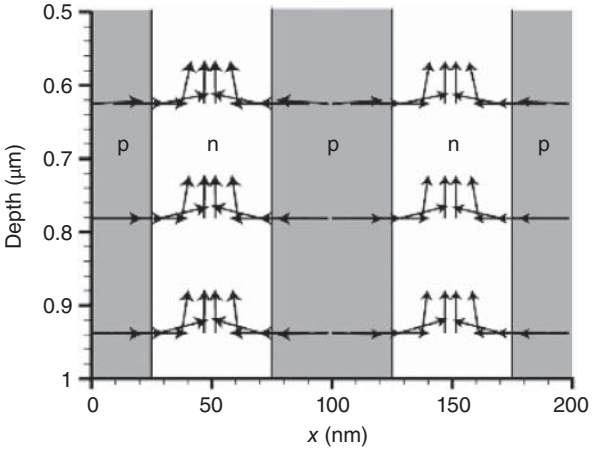

Figure 24.9 Simulated electron transport in a CIGS solar cell. The depth represents the distance into the CIGS interdigitated region relative to the CIGS/CdS interface, and p and n refers to regions doped p- and n-type, respectively. (Reprinted with permission from Metzger [1], Copyright 2008, American Institute of Physics.)

either increase or decrease efficiency depending on the material properties of the constituent domains.

As mentioned in Section 24.1, there are several benefits that can be gained by placing the cathode and anode contacts only on the bottom of the cell. An example of such a design is shown in Figure 24.10. In this case, sunlight is able to enter the top of the cell without shading from top contacts. However, absorption occurs preferentially at the top of the cell. As the current collecting junction is now at the bottom of the cell, rather than the top, the carriers must travel further in the material before being collected. The doping profile, contact thickness, and distance between contacts will all influence the device performance, and optimal design and loss analysis requires a 2D model.

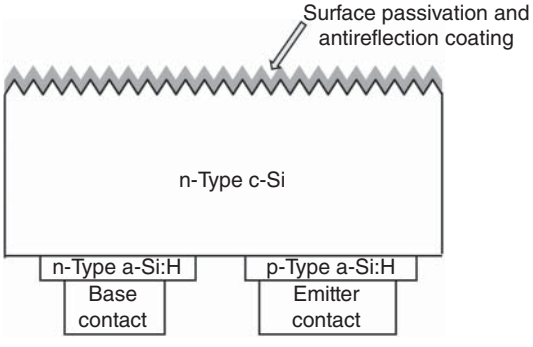

Figure 24.10 A schematic of a silicon heterojunction cell with an interdigitated back contact. (Figure courtesy of Hao-Chih Yuan.)

Nichiporuk *et al*. [51] used a 2D model to calculate the optimal geometry and doping and to analyze the impact of several parameters on the interdigitated cell with p-type c-Si used as a base. They have found that with their parameters, the optimum width of the emitter should be couple of times larger than the one of the base contact, regardless of the distance between them. Kim *et al*. [52] have found that for minority-carrier lifetimes higher than 50 μs in Si devices, the interdigitated geometry outperforms their standard planar device. Allen *et al*. [53] provided guideline on how to decrease FF losses in interdigitated solar cell.

24.4 Summary

Modeling can provide physical insight to device operation, help distinguish important material properties from unimportant properties, predict trends, and help interpret experimental data. Multidimensional modeling including GBs and other material variations is necessary to explain the device physics and experimental results present in diverse thin-film technologies. The examples in this chapter have shown how modeling has improved our understanding of experimental results and device design. Multidimensional modeling has expanded rapidly in the past decade and is likely to become more common to address complex issues as PV technology develops.

Acknowledgments

This work was supported by the US Department of Energy under contract number DE-AC36-08GO28308 to NREL.

References

1. Metzger, W.K. (2008) The potential and device physics of interdigitated thin-film solar cells. *J. Appl. Phys.*, **103** (9), 094515.
2. Christoffel, E., Rusu, M., Zerga, A., Bourdais, S., Noel, S., and Slaoui, A. (2002) A two-dimensional modeling of the fine-grained polycrystalline silicon thin-film solar cells. *Thin Solid Films*, **403** (2002), 258.
3. Gloeckler, M., Sites, J.R., and Metzger, W.K. (2005) Grain-boundary recombination in Cu(In,Ga)Se_2 solar cells. *J. Appl. Phys.*, **98** (11), 11704.
4. Lu, M., Bowden, S. and Birkmire, R. (2007) *Two Dimensional Modelling of Interdigitated Back Contact Silicon Heterojunction Solar Cells*, in Proceedings of 7th International Conference on Numerical Simulation of Optoelectronic Devices, p. 55.
5. Malm, U. and Edoff, M. (2009) 2D device modelling and finite element simulations for thin-film solar cells. *Sol. Energy Mater. Sol. Cells*, **93** (6–7), 1066.
6. Taretto, K. and Rau, U. (2008) Numerical simulation of carrier collection and recombination at grain boundaries in Cu(In,Ga)Se_2 solar cells. *J. Appl. Phys.*, **103** (9), 094523.
7. Taretto, K., Rau, U., and Werner, J.H. (2001) Two-dimensional simulations

of microcrystalline silicon solar cells, in *Polycrystalline Semiconductors IV Materials, Technologies and Large Area Electronics* vols 80–81, Trans Tech Publications, p. 311.

8. Taretto, K., Rau, U., and Werner, J.H. (2005) Numerical simulation of grain boundary effects in $Cu(In,Ga)Se_2$ thin-film solar cells. *Thin Solid Films*, **480**, 8.
9. Malm, U. and Edoff, M. (2009) Simulating material inhomogeneities and defects in CIGS thin-film solar cells. *Prog. Photovoltaics*, **17**, 306.
10. Kanevce, A., Repins, I., and Wei, S.H. (2013) Impact of bulk properties and local secondary phases on the $Cu_2(Zn,Sn)Se_4$ solar cells open-circuit voltage. *Sol. Energy Mater. Sol. Cells*, **133**, 119.
11. Sozzi, G., Menozzi, R., Cavallari, N., Bronzoni, M., Annoni, F., Calicchio, M. and Mazzer, M. (2015) *On the Temperature Behavior of Shunt-Leakage Currents in Cu(In,Ga)Se_2 Solar Cells: The Role of Grain Boundaries*, in IEEE PVSC, New Orleans, LA.
12. Richter, M., Schubbert, C., Eraerds, P., Parisi, J., Riedel, I., Dalibor, T., and Palm, J. (2015) Comprehensive simulation model for $Cu(In,Ga)(Se,S)_{(2)}$ solar cells. *Sol. Energy Mater. Sol. Cells*, **132**, 162.
13. www.synopsys.com (accessed 4 March 2016).
14. www.comsol.com (accessed 4 March 2016).
15. http://www.crosslight.com (accessed 4 March 2016).
16. http://www.silvaco.com/products/device_simulation/atlas.html (accessed 4 March 2016).
17. Streetman, B.G. (1990) *Solid State Electronic Devices*, 3rd edn, Prentice-Hall, Englewood Cliffs, NJ.
18. ASTM (2008) *Standard G173-03, in: Standard Tables for Reference Solar Spectral Irradiances: Direct Normal and Hemispherical on 37° Tilted Surface*, ASTM International, West Conshohocken, PA, DOI: 10.1520/G0173-03E01.
19. Selberherr, S. (1984) *Analysis and Simulation of Semiconductor Devices*, Springer Vienna, New York.
20. Karpov, V.G., Compaan, A.D., and Shvydka, D. (2004) Random diode arrays and mesoscale physics of large-area semiconductor devices. *Phys. Rev. B: Condens. Matter Mater. Phys.*, **69** (4), 045325.
21. Shvydka, D., Compaan, A.D., and Karpov, V.G. (2002) Nonlocal response in CdTe photovoltaics. *J. Appl. Phys.*, **91**, 905.
22. Karpov, V.G., Rich, G., Subashiev, A.V., and Dorer, G. (2001) Shunt screening, size effects and I/V analysis in thin-film photovoltaics. *J. Appl. Phys.*, **89** (9), 4975.
23. Karpov, V.G. (2003) Critical disorder and phase transitions in random diode arrays. *Phys. Rev. Lett.*, **91** (22), 226806.
24. Kanevce, A. and Sites, J.R. (2007) *Impact of Nonuniformities on Thin Cu(In,Ga)Se_2 Solar Cell Performance*, vol. 1012, (eds. T. Gessert, K. Durose, C. Heske, S. Marsillac, and T. Wada), Materials Research Society Symposium Proceedings, Warrendale, PA, 1012-Y08-02.
25. Rau, U., Grabitz, P.O., and Werner, J.H. (2004) Resistive limitations to spatially inhomogeneous electronic losses in solar cells. *Appl. Phys. Lett.*, **85** (24), 6010.
26. Werner, J.H., Mattheis, J., and Rau, U. (2005) Efficiency limitations of polycrystalline thin film solar cells: case of $Cu(In,Ga)Se_2$. *Thin Solid Films*, **480**, 399.
27. Grabitz, P.O., Rau, U., and Werner, J.H. (2005) A multi-diode model for spatially inhomogeneous solar cells. *Thin Solid Films*, **487**, 14.
28. Dongaonkar, S. and Alam, M.A. (2015) Geometrical design of thin film photovoltaic modules for improved shade tolerance and performance. *Prog. Photovoltaics*, **23**, 170.
29. Dongaonkar, S., Deline, C., and Alam, M.A. (2013) Performance and reliability implications of two-dimensional shading in monolithic thin-film photovoltaic modules. *IEEE J. Photovolt.*, **3**, 1367.
30. Dongaonkar, S. and Alam, M.A. (2014) In-line post-process scribing for reducing cell to module efficiency gap in

monolithic thin-film photovoltaics. *IEEE J. Photovolt.*, **4**, 324.

31. Koishiyev, G.T. and Sites, J.R. (2009) *Effect of Shunts on Thin-Film CdTe Module Performance*, in: Materials Research Society Symposium Proceedings, Warrendale, PA, 1165-M05-22.
32. Galiana, B., Algora, C., Rey-Stolle, I., and Vara, I.G. (2005) A 3-D model for concentrator solar cells based on distributed circuit units. *IEEE Trans. Electron Devices*, **52**, 2552.
33. Brecl, K. and Topic, M. (2008) Simulation of losses in thin-film silicon modules for different configurations and front contacts. *Prog. Photovoltaics*, **16**, 479.
34. Koishiyev, G.T. and Sites, J.R. (2009) Impact of sheet resistance on 2-D modeling of thin-film solar cells. *Sol. Energy Mater. Sol. Cells*, **93**, 350.
35. Mungan, E.S., Wang, Y.B., Dongaonkar, S., Ely, D.R., Garcia, R.E., and Alam, M.A. (2014) From process to modules: end-to-end modeling of CSS-deposited CdTe solar cells. *IEEE J. Photovolt.*, **4**, 954.
36. Metzger, W.K. and Gloeckler, M. (2005) The impact of charged grain boundaries on thin-film solar cells and characterization. *J. Appl. Phys.*, **98** (6), 063701.
37. Nerat, M., Cernivec, G., Smole, F., and Topic, M. (2008) Simulation study of the effects of grain shape and size on the performance of Cu(In, Ga)Se_2 solar cells. *J. Appl. Phys.*, **104** (8), 083706.
38. Nerat, M., Smole, F., and Topic, M. (2011) A simulation study of the effect of the diverse valence-band offset and the electronic activity at the grain boundaries on the performance of polycrystalline Cu(In,Ga)Se_2 solar cells. *Thin Solid Films*, **519**, 7497.
39. Harndt, S., Kaufmann, C.A., Lux-Steiner, M.C., Klenk, R., and Nurnberg, R. (2015) Grain boundary assisted photocurrent collection in thin film solar cells. *EPJ Photovoltaics*, **6**, 60101.
40. Troni, F., Menozzi, R., Colegrove, E., and Buurma, C. (2013) Simulation of current transport in polycrystalline CdTe solar cells. *J. Electron. Mater.*, **42**, 3175.
41. Kanevce, A., Moseley, J., Al-Jassim, M., and Metzger, W. (2015) Quantitative determination of grain boundary recombination velocity in CdTe by combination of cathodoluminescence measurements and numerical simulations. *IEEE J. Photovoltaics*, **5**(6), 1722–1726.
42. Cozza, D., Ruiz, C.M., Duché, D., Neuschitzer, M., Saucedo, E., Simon, J.J. and Escoubas, L., (2015) *1D and 2D Numerical Simulations of $Cu_2ZnSnSe_4$ Solar Cells*, in IEEE PVSC, New Orleans, LA.
43. Metzger, W.K. (2008) How lifetime fluctuations, grain-boundary recombination, and junctions affect lifetime measurements and their correlation to silicon solar cell performance. *Sol. Energy Mater. Sol. Cells*, **92**, 1123.
44. Richter, M., Riedel, I., Schubbert, C., Eraerds, P., Parisi, J., Dalibor, T., and Palm, J. (2015) Simulation study of the impact of interface roughness and void inclusions on Cu(In,Ga)$(Se,S)_{(2)}$ solar cells. *Phys. Status Solidi A*, **212**, 298.
45. Metzger, W.K., Ahrenkiel, R.K., Dashdorj, J., and Friedman, D.J. (2005) Analysis of charge separation dynamics in a semiconductor junction. *Phys. Rev. B: Condens. Matter Mater. Phys.*, **71** (3), 035301.
46. Metzger, W.K., Repins, I.L., Romero, M., Dippo, P., Contreras, M., Noufi, R., and Levi, D. (2009) Recombination kinetics and stability in polycrystalline Cu(In,Ga)Se_2 solar cells. *Thin Solid Films*, **517**, 2360.
47. Kuciauskas, D., Farrell, S., Dippo, P., Moseley, J., Moutinho, H., Li, J.V., Motz, A.M.A., Kanevce, A., Zaunbrecher, K., Gessert, T.A., Levi, D.H., Metzger, W.K., Colegrove, E., and Sivananthan, S. (2014) Charge-carrier transport and recombination in heteroepitaxial CdTe. *J. Appl. Phys.*, **116**, 123108.
48. Kanevce, A., Kuciauskas, D., Levi, D.H., Motz, A.M.A., and Johnston, S.W. (2015) Two dimensional numerical simulations of carrier dynamics during time-resolved photoluminescence decays in two-photon microscopy measurements in semiconductors. *J. Appl. Phys.*, **118**, 045709.

49. Rau, U. and Werner, J.H. (2004) Radiative efficiency limits of solar cells with lateral band-gap fluctuations. *Appl. Phys. Lett.*, **84**, 3735.

50. Yan, Y.F., Noufi, R., Jones, K.M., Ramanathan, K., Al-Jassim, M.M., and Stanbery, B.J. (2005) Chemical fluctuation-induced nanodomains in $Cu(In,Ga)Se_2$ films. *Appl. Phys. Lett.*, **87** (12), 121904.

51. Nichiporuk, O., Kaminski, A., Lemiti, M., Fave, A., and Skryshevsky, V. (2005) Optimisation of interdigitated back contacts solar cells by two-dimensional numerical simulation. *Sol. Energy Mater. Sol. Cells*, **86**, 517.

52. Kim, D. S., Meemongkolkiat, V., Ebong, A., Rounsaville, B., Upadhyaya, V., Das, A. and Rohatgi, A. (2006) *2D-Modeling and Development of Interdigitated Back Contact Solar Cells on Low-Cost Substrates*, 4th World Conference on Photovoltaic Energy Conversion Waikoloa, Hawaii, p. 1417.

53. Allen, J., Shu, B., Zhang, L., Das, U. and Hegedus, S. (2011) *Interdigitated Back Contact Silicon Hetero-Junction Solar Cells: The Effect of Doped Layer Defect Levels and Rear Surface i-layer Band Gap on Fill Factor Using Two-Dimensional Simulations*, in: 37th IEEE PVSC, p. 002545.

Index

Advanced Characterization Techniques for Thin Film Solar Cells, Second Edition.
Edited by Daniel Abou-Ras, Thomas Kirchartz, and Uwe Rau.